Proceedings of:

The Sixeenth Annual Meeting

The American Society for Precision Engineering

November 10-15, 2001
Hyatt Regency Crystal City
Arlington, Virginia

The American Society for Precision Engineering (ASPE) is a multidisciplinary professional and technical society concerned with research and development, design, manufacture and measurement of high accuracy components and systems. ASPE activities encompass relevant aspects of mechanical, electronic, optical and production engineering, physics, chemistry, and computer and materials science. Membership is open to anyone interested in any aspect of precision engineering.

Founded in 1986, ASPE provides a new focus for a diverse but important community. Other professional organizations have covered aspects of precision engineering, always as a sideline to their principal goals. ASPE is based on the core of generic concepts necessary to achieve precision in any application; independent of discipline, ASPE intends to be the focus for precision technology — and to represent all facets from research to application.

ASPE — The American Society for Precision Engineering
301 Glenwood Avenue, Suite 205, Raleigh, NC 27603
P.O. Box 10826, Raleigh, NC 27605
Telephone: (919) 839-8444 Fax (919) 839-8039

Preface

This book comprises the proceedings of the 2001 Annual Meeting. The contributions reflect the authors' opinions and are published as presented to ASPE, without change. Their inclusion in this publication does not necessarily constitute endorsement by the ASPE, or its editorial staff.

Individual readers of this book and nonprofit libraries acting for them are permitted to make fair use of the material contained in this book to be used in teaching or research; provided they copy said paper in total, as written by the author. Permission is granted to quote excerpts from the scientific or technical works in this book with proper acknowledgment of the source to include: The author's name, the book name, and the ASPE tag line. Reproduction of figures and tables is likewise permitted from the contents of this book, provided that the same acknowledgment of the same source and content is permitted.

Any other type reproduction, systematic copying or multiple reproduction of any material in this book is expressly prohibited except with the written permission of the ASPE editorial staff, addressed to the Society's headquarters.

ISBN 1-887706-27-5

2001

American Society for Precision Engineering
301 Glenwood Avenue, Suite 205
Raleigh, NC 27603

Printed in the United States of America

Welcome Note

The American Society for Precision Engineering celebrates its Sixteenth Annual Meeting this year in Crystal City, Arlington, Virginia. The remarkable growth and success of the Society is reflective of the increasing importance of precision engineering in a wide variety of fields of endeavor, from manufacturing to microelectronics to basic science. The Society serves as a focus for precision engineers across all of these fields. The Annual Meeting has evolved into a premier international forum for the exchange of ideas and presentation of research results relating to precision engineering, metrology, controls, and system integration. Precision engineers and scientists from private industry, government laboratories, and universities meet to learn about the latest developments and to exchange ideas about the future directions of these technologies.

This year's meeting continues the tradition of offering two full days of tutorials presented by some of the foremost precision engineers and scientists in the world. Many participants cite the tutorial program as one of the most valuable features of the meeting. The technical sessions and poster presentations offer the latest research results in the areas of ultraprecision machining, metrology, controls, precision grinding, micro-positioning, material processing, design, precision transducers, surface profilometry, machine tool metrology, and error compensation. The commercial exhibit will provide attendees with the opportunity to view and discuss the latest precision engineering equipment, products, and services that are commercially available. The open forum will give attendees the opportunity to express their opinions and pose questions for discussion by the group, enhancing the exchange of information.

The conference organizing committee is proud to present the program for the Sixteenth Annual Meeting of the ASPE. We welcome your participation.

Welcome to Crystal City.

2001 Organizing & Technical Program Committee

James F. Cuttino, Chairman,
University of North Carolina at Charlotte

Jones B. Arnold, Lockheed Martin Energy Systems, Inc.
Vivek G. Badami, Corning Tropel Corporation
Jeffrey W. Carr, Lawrence Livermore National Laboratory
S. Hossein Cheraghi, Wichita State University
Robert D. Day, Los Alamos National Laboratory
Thomas A. Dow, North Carolina State University
Joseph D. Drescher, UTC-Pratt & Whitney
Helen E. Fawcett, Axsun Technologies, Inc.
Steven C. Fawcett, Axsun Technologies, Inc.
Kenneth P. Garrard, North Carolina State University
Anthony E. Gee, Cranfield University
Bradley H. Jared, Corning Inc.
Don A. Lucca, Oklahoma State University
Eric R. Marsh, The Pennsylvania State University
Michele H. Miller, Michigan Technological University
Edward P. Morse, University of North Carolina at Charlotte
Dietmar Paehler, Fraunhofer IPT
Zhi-Jian Pei, Kansas State University
James G. Salsbury, Mitutoyo America Corporation
Alex Sohn, North Carolina State University
Andrew D. Woodfin, Corning Inc.

2001 Scholarship Recipients

David D. Gill, North Carolina State University
R.V. Jones Memorial Scholarship

Bryan P. O'Connor, The Pennsylvania State University

2001 Annual Meeting
Contents

Preface . . . . . *ii*

Welcome Note . . . . . *iii*

Organizing Committee — 2001 Scholarship Recipients . . . . . *iv*

Sponsor Members . . . . . *vi*

Cooperating Sponsors—Technical Exhibitors . . . . . *vii*

Program . . . . . *viii*

Keynote Address . . . . . *ix*

2001 Lifetime Achievement Award . . . . . *x*

Commercial Session/Open Forum *1*

Technical Paper Index *2-11*

Technical Papers *15-548*

Authors Index *549-552*

Sponsor Members of the ASPE

3M Company
St. Paul, MN 55144-1000
Contact: William J. Bryan
(651) 575-1465

ADCOLE Corporation
Marlborough, MA 01752
Contact: Addison D. Cole
(508) 485-9100

ADE Technologies, Inc.
Newton, MA 02466
Contact: Jon Allen
(617) 831-8012

Agilent Technologies
Santa Rosa, CA 95403
Contact: Paul Lomeli
(707) 577-5514

Chardon Tool & Supply Company, Inc.
Chardon, OH 44024
Contact: Weldon Bennett
(216) 286-6440

Contour Fine Tooling, Inc.
Marlborough, NH 03455
Contact: Jeffrey Tomlin
(603) 876-4908

Corning Inc.
Corning, NY 14831
Contact: John Thomas
(607) 974-3842

Corning Tropel Corporation
60 O'Connor Road
Fairport, NY 14450
Contact: John H. Bruning
(716) 388-3400

Cranfield Precision, Div. of Landis Lund
A Western Atlas Corporation
Cranfield, Bedford MK43 OAL, England
Contact: Edric M. E. Brown
011-44-1234-754222

DAC International, Inc.
Carpinteria, CA 93013
Contact: James W. Drain
(805) 684-8307

Dover Instrument Corporation
Westboro, MA 01581
Contact: Michael Townsend
(508) 366-1456

Fabreeka International, Inc.
Stoughton, MA 02072
Contact: Robert P. Haley
(781) 341-3655

Fisba Optik, LLC
Rochester, NY 14623
Contact: John J. Nemechek
(716) 427-9155

ITW Polymer Castings
Cincinnati, OH 45252
Contact: Loren Power
(513) 385-4577

Lion Precision
St. Paul, MN 55126
Contact: Don L. Martin
(612) 484-6544

Mahr Federal, Inc.
Providence, RI 02940-9400
Contact: Robert A. Frick
(401) 784-3313

Micro-Metric, Inc.
San Jose, CA 95112-1404
Contact: Thomas Pelton
(408) 452-8505

MicroE Systems, Inc.
Natick, MA 01760-1313
Contact: Donald K. Mitchell
(508) 903-5000

Mitutoyo America Corporation
Aurora, IL 60504-9102
Contact: Mark T. Izumi
(630) 820-9666

Moore Tool Company, Inc.
Bridgeport, CT 06607-0088
Contact: Thomas L. Hannon
(203) 366-3224

Nano Corporation
Tokyo 146-0085, Japan
Contact: Akira Hayashi
011-81-3-3751-3311

New Way Machine Components
Aston, PA 19014
Contact: Andrew J. Devitt
(610) 494-6700

Precitech, Inc.
Keene, NH 03431
Contact: David W. Davis
(603) 357-2511

Professional Instruments Company
Hopkins, MN 55343
Contact: James Arneson
(612) 933-1222

Reflexite-Precision Technology Center
West Henrietta, NY 14586
Contact: Steven M. Scott
(716) 272-0309

Seagate Technology
Scotts Valley, CA 95067
Contact: Bernd M. Seeger
(831) 439-3781

Zygo Corporation
Middlefield, CT 06455-0448
Contact: Robert A. Smythe
(860) 704-8506

Cooperating Sponsors

Elsevier Science, Inc.

euspen – European Society for Precision Engineering and Nanotechnology

Japan Society for Precision Engineering

Technical Exhibitors

ADE Phase Shift

ADE Technologies

Aerotech, Inc.

Center for Precision Metrology—University of N. C. at Charlotte

Chardon Tool

Contour Fine Tooling, Inc.

CoorsTek

Corning Tropel Corporation

Fabreeka International, Inc.

Heidenhain Corporation

Lion Precision

Machine Dynamics Research Lab.—Penn State University

Mitutoyo America Corporation

Moore Nanotechnology Systems, LLC

New Way Machine Components, Inc.

Philips Electronics

Precision Engineering Center—N.C. State University

Precitech, Inc.

Professional Instruments Company, Inc.

QED Technologies

SNU Precision Company, Ltd.

Veeco Metrology Group

Zygo Corporation

Program

2001 ASPE Annual Meeting

Time	Sat., Nov. 10	Sun., Nov. 11	Mon., Nov. 12	Tues., Nov. 13	Wed., Nov. 14	Thurs., Nov. 15
8:00			Continental Breakfast			
9:00	Tutorials	Tutorials	Session I Instrument Design & Testing	Session III Surface & Form Metrology	Session VI Machining	Technical And Companion Tours
10:00			Break	Break	Break	
11:00			Session II Novel Systems	Session IV Precision Fab. Processes	Session VII Optics	
12:00						
1:00			Lunch and Committee Meetings	Awards Lunch and Business Meeting	Lunch and Roundtable Discussions	
2:00	Tutorials	Tutorials	Commercial Session & Open Forum	Poster Papers	Session VIII Novel Actuators	
3:00			Break	Break		
4:00			Poster Papers	Session V Large Scale Dim. Metrology		
5:00			Hospitality Hour	Hospitality Hour		
6:00		Informal Reception				
7:00	Student Reception	Keynote Address	Dinner			
8:00						
9:00						

Keynote Address

Phillip R. Hannah

Sunday, November 11, 6:30 p.m.

Session Chair: James F. Cuttino, University of North Carolina at Charlotte

Precision in Time

I hope, through the medium of this talk to take the listener on a journey through time, a journey exploring the application of precision engineering and fabrication to the keeping of time. The assembling of these notes has led the writer down many paths, all of which are very interesting in and of themselves. A quote that I find appropriate at this point was made by the father of the Synchronome clock Frank Hope-Jones "..... Just as I refrain from metaphysics, so will I will refrain from all references to sundials, clepshydras, candle-clocks, and sand glasses. They have a literature of their own, and it is assumed that my readers (or listeners) are more concerned with the scientific side of time measurement than its archaeology."[1]

During my tenure at The Perkin-Elmer Corporation I became acquainted with John Rawlings, who some of you may realize was the brother of A. L. Rawlings the author of an extremely interesting book, The Science of Clocks and Watches.[2] Through John I became fascinated with the clocks; later he asked me to repair a Synchronome clock with its detached gravity escapement. It was then that the horological bug bit harder, but more on this clock later. John also gave me several books by Hope-Jones that belonged to his brother as well as some interesting papers, one on circular pendulum error. I also owned and maintained a Riefler astronomical clock which we shall see played a significant role in our quest for "Precision in Time."

Over the years I have kept involved in the field of horology having attained the title of Certified Master Watchmaker from the American Watchmakers Institute, and in my retirement (ha) am actively repairing mechanical clocks and watches, and starting construction of a Synchronome electric clock.

On our journey we will only briefly mention the motive power of the clock (springs and weights) and the attempts to provide a uniform driving force to the time train and escapement. We will however, spend some time looking at significant developments like the design of clock escapements and the addition of electricity that provided the needed uniform driving force, and their effects on precision timekeeping. I have chosen not to take you on a journey through the development of the watch escapement or with Harrison and his quest for keeping accurate time at sea, the history of which is well documented.

Finally I hope the records of data kept on these clocks' performance will give the listener an appreciation for precision mechanics, as they did me, and be recognized as a tribute to those precision engineers who have gone on before, their understanding of the problem and their unique solution as we end our quest for "Precision in Time". None of the presented historical data is original to me, but is a compendium of the works and labors of many, especially Hope-Jones, Rawlings, Howse, Landes, Bruton, Britten and Bucheron.

[1] ***Hope-Jones, Frank*** *Electrical Timekeeping, London N.A.G. Press, 1940*
[2] ***Rawlings, A.L.*** *The Science of Clocks and Watches, British Horological Institute. Ltd. 1993*

2001 Lifetime Achievement Award

E. Ray McClure

In recognition for his efforts to define the field of precision engineering, his leadership in the creation of the ASPE and his technical contributions in the area of thermal effects on manufacturing accuracy. Ray has been a passionate spokesman for precision engineering and his technical and organizational skills have had a profound impact on the field and those involved in it.

Ray was born on December 31, 1933, in North Dakota. He moved around because he was an Air Force brat. He finished high school in Spokane, Washington, in 1951 and entered Washington State College with the intent of getting an Air Force commission via the ROTC. After failing the eye exam, he had to lower his sights to only a BSME degree in 1955. Ray was employed at Boeing in Flight Test until he received a fellowship to Ohio State University in 1957. While at OSU, Columbus, he worked at North American Aviation (now Rockwell/Boeing) and Battelle Institute.

Before graduating with a MSME, he was appointed to the faculty of Mechanical Engineering at Oregon State University. While an Assistant Professor at Oregon State University, took a summer job at the Lawrence Livermore National Laboratory and received a NSF grant that allowed him to pursue a doctorate at the University of California, Berkeley, finishing in 1969. Before graduation from UCB, he joined the Mechanical Engineering Department at LLNL in the Metrology Group, headed by Jim Bryan. Over the next twenty-five years, he had several positions within LLNL, including Deputy Head of the Mechanical Engineering Department, Division Leader of the Energy Systems Division and Program Leader of the Precision Engineering Program. He retired from LLNL in 1988 and joined the Moore Special Tool Company as Vice President for Engineering and Technical Director. He retired from Moore in 1996.

His technical experience started with his interest in aircraft, which led to work in the flight testing of aircraft, design of jet propulsion engines and a Master's thesis on air breathing engines at Mach 2 to Mach 7. During his tenure at Oregon State University, he progressively learned aerodynamics and flight testing, moved to mechanical design and then to automatic controls. The summer of 1961 brought him into contact with Jim Bryan and the world of metrology, which sealed his fate. His doctoral dissertation was entitled "Manufacturing Accuracy Through Control of Thermal Effects." Over 500 copies of this thesis has been distributed worldwide and has served as a reference for several standards pertaining to machine tool performance testing and metrology environments, especially the ASME B89.6.2.

Measurement, testing and design have always been key elements of his work. Beginning with aerodynamic performance, propulsion system and structural testing, his career has included applications to rotary lawn mowers, free piston engines, radio telescopes and, while a consultant to the Bureau of Mines in 1963, the development of a fringe counting laser interferometer dilatometer to make the first measurements of thermal expansion of Columbium (now Niobium) at 1500 degrees Celsius. The actual "fringe counting" was done by a graduate student, who counted the wiggles of a line on a strip chart recording. The original light source for this instrument was an "ozone" lamp from a clothes dryer. This was replaced with a prototype HeNe 130 mm laser from Spectra Physics; Spectra Physics at the time had only three employees working in a rented garage.

He met his wife, Amelia, at Boeing and was married in 1956. Amelia passed away after a fight with cancer on September 1, 2001. They have two sons, Michael and Steven.

Commercial Session / Open Forum

Monday, November 12, 2:00 - 3:30 p.m.

Session Chairman: Newman Marsilius, Moore Tool Company, Inc.

The Commercial Session / Open Forum will take place early in the week on Monday afternoon. This is a special session where companies and participants are free to open discussions on a less-formal basis and to promote interaction on a variety of topics. In the first part of this session, company representatives are invited to make brief presentations (5 minutes) on new products associated with precision engineering. This provides participants with the opportunity to receive timely information on new technologies that have been commercialized into products and services, as well as information on advances that can be expected in the near future. In the second half, the floor is open to conference participants to discuss any topic of interest to the society. So bring your overheads, problems, and experiences to this enlightening hour and a half of impromptu discussions! Signup sheets will be available at the conference.

Technical and Poster Sessions Index

The technical program for the 2001 ASPE Annual Meeting contains over 130 papers on precision engineering advances. Papers that lent themselves to significant verbal interaction, concise but important discoveries, or strongly visual or tactile subjects have been selected for the poster session. Authors will be present to discuss their work on Monday, November 12, from 3:30 to 5:00 p.m., and again on Tuesday, November 13, from 1:30 to 3:00 p.m.

Session I
Instrumentation Design and Testing

Monday, November 12, 2001, 8:15 AM - 10:00 AM

Session Co-Chairs: Vivek G. Badami (Corning Tropel Corporation), and Andrew D. Woodfin (Corning Inc.)

1. **Scanning Beam Interference Lithography (Invited Paper)**
   Konkola, P. T.; Chen, C. G.; Heilmann, R. K.; Pati, G. S.; Schattenburg, M. L. (Massachusetts Institute of Technology) . . . . . page 15
2. **Molecular Measuring Machine Design and Performance**
   Kramar, J. A.; Jun, J.; Penzes, W. B.; Scheuerman, V. P.; Scire, F. E.; Teague, E. C. (National Institute of Standards and Technology). . . . . page 19
3. **Nanomeasuring Technology — Nanomeasuring Machine**
   Jäger, G.; Menske, E.; Hausotte, T.; Büchner, H.-J.; Grünwald, R., Schott, W. (Technical University of Ilmenau) . . . . . page 23
4. **The Polar Profilometer "Polaris"**
   Sohn, A.; Garrard, K. P.; Dow, T. A. (North Carolina State University) . . . . . page 28

Session II
Novel Systems

Monday, November 12, 2001, 10:30 AM - 12:00 PM

Session Co-Chairs: Joseph D. Drescher (UTC-Pratt & Whitney), and Helen E. Fawcett (Axsun Technologies)

1. **Planar and Spatial Three-degree-of-freedom Micro-stages in Silicon MEMS**
   Jokiel, Jr., B.; Benavides, G. L.; Bieg, L. F.; Allen, J. J. (Sandia National Laboratories) . . . . . page 32
2. **Micro Screw Pump to Discharge Effusion from Human Middle Ear**
   Nakao, M.; Okusa, T.; Rahim, A.; Matsumoto, K.; Hatamura, Y. (The University of Tokyo) . . . . . page 36
3. **High Precision Assembly and Metrology of X-ray Foil Optics**
   Mongrard, O.; Butler, N.; Chen, C. G.; Heilmann, R. K.; Konkola, P. T.; McGuirk, M.; Monnelly, G.; Pati, G. S.; Ricker, G. R.; Schattenburg, M. L. (Massachusetts Institute of Technology); and Cohen, L. (Harvard-Smithsonian Astrophysical Observatory) . . . . . page 40

Session III

Surface and Form Metrology

Monday, November 12, 2001, 3:30 PM - 10:00 AM

Session Co-Chairs: S. Hossein Cheraghi (Wichita State University), and Kenneth P. Garrard (North Carolina State University)

1. ***Precision Relational Metrology of Flatness, Thickness, Parallelism and Step Height***
   Colonna de Lega, X.; de Groot, P. J.; Grigg, D. A. (Zygo Corporation) . . . . . *page 44*
2. ***A Recommendation Inspection to Control Sub-Surface Damage in Sapphire****
   Polvani, R. S. (National Institute of Standards and Technology) . . . . . *page 48*
3. ***Development of Intelligent Precision Vision Inspection System for Micro Optics Parts Using New Optical Probe Implemented to Have Multiple Fields of Views and Mutual Calibration Scheme***
   Pahk, H. J.; Lee, I.-H. (Seoul National University) . . . . . *page 50*

Session IV

Precision Fabrication Processes

Tuesday, November 13, 2001, 10:30 AM - 12:00 PM

Session Co-Chairs: Jeffrey W. Carr (Lawrence Livermore National Laboratory), and Michele H. Miller (Michigan Technological University)

1. ***High Throughput Surface Structuring in Solar Cell Manufacture***
   Weck, M.; Leifhelm, B. (Fraunhofer-Institut für Produktionstechnologie (IPT)) . . . . . *page 54*
2. ***Superabrasive Grinding Process Optimization Through Force Measurement***
   Knapp, B. R.; Marsh, E. R.; Grejda, R. D.; Schalcosky, D. (The Pennsylvania State University) . . . . . *page 58*
3. ***Development of Automatic Image Processing System for Evaluation of Wheel Surface Condition in Ultra-smoothness Grinding***
   Yasui, H.; Hiraki, Y.; Sakata, M. (Kumamoto University) . . . . . *page 62*
4. ***Replication of Precision Optical Features Through Injection Molding***
   Gill, D. D.; Dow, T. A.; Sohn, A. (North Carolina State University) . . . . . *page 66*

Session V

Large Scale Dimensional Metrology

Monday, November 12, 2001, 3:30 PM - 5:15 PM

Session Co-Chairs: James G. Salsbury (Mitutoyo America Corporation), and Edward P. Morse (University of North Carolina at Charlotte)

1. ***Good Things Come in Small Packages — A Table Top CMM with Sub-Micron Capability (Invited Paper)***
   Youden, D. H. (Eastman Kodak Company) . . . . . *page 70*
2. ***Design and Testing of a One Dimensional Measuring Machine for Determining the Length of Ball Bars***
   Ziegert, J. C.; Rea, D. (University of Florida); and Phillips, S. D.; Borchardt, B. R.; Stoup, J. (National Institute of Standards and Technololgy) . . . . . *page 82*
3. ***Methods for Correcting the Group Index of Refraction at the PPM Level for Outdoor Electronic Distance Measurements****
   Parker, D. H. (The National Radio Astronomy Observatory) . . . . . *page 86*
4. ***The Grid Bar, Calibration and Application***
   Weikert, S.; Knapp, W. (Swiss Federal Institute of Technology (ETHZ)) . . . . . *page 88*

* *Extended abstract not available at press time*

Session VI
Machining

Wednesday, November 14, 2001, 8:30 AM - 10:00 AM

Session Co-Chairs: Alex Sohn (North Carolina State University), and Bradley H. Jared (Corning Inc.)

1. **Vibration Assisted Diamond Turning Using Elliptical Tool Motion**
   Dow, T. A.; Cerniway, M. A.; Sohn, A.; Negishi, N. (North Carolina State University) . . . . . page 92
2. **Numerical Simulation of Ductile Machining of Silicon Nitride**
   Kumbera, T. G.; Patten, J. A.; Cherukuri, H. P. (University of North Carolina-Charlotte); and Brand, C. J.; Marusich, T. D. (Third Wave Systems, Inc.). . . . . page 98
3. **Effects of Rotating Unbalance on Turning Precision: Analytical and Experimental Investigations and Real-Time Compensation***
   Winzenz, W., Dyer, S. W. (BalaDyne Corporation) . . . . . page 102

Session VII
Optics

Wednesday, November 14, 2001, 10:30 AM - 12:00 PM

Session Co-Chairs: Vivek G. Badami (Corning Tropel Corporation), and Andrew D. Woodfin (Corning Inc.)

1. **Techniques for the Reduction of Cyclic Errors in Laser Metrology Gauges for the Space Interferometry Mission (Invited Paper)**
   Halverson, P. G.; Zhao, F.; Spero, R.; Shaklan, S. B.; Lay, O. P.; Dubovitsky, S.; Diaz, R. T.; (California Institute of Technology, Jet Propulsion Laboratory); and Bell, R.; Ames, L.; Dutta, K. (Lockheed Martin Advanced Technology Center). . . . . page 103
2. **Compact Absolute Length Measuring Machine by Combining Regular Crystalline Surface and Laser Interferometry**
   Aketagawa, M.; Rerkkumsup, P.; Takada, K.; Takagi, T.; Watanabe, T. (Nagaoka University of Technology) . . . . . page 107
3. **Laser-CCD Based Sensor System for Real Time Detection of Motion Linearity**
   Kagawa, Y.; Yamazaki, K.; Yang, Y. (University of California-Davis); and Matsumiya, S. (Mitutoyo Corporation) . . . . . page 111
4. **Measurements Using Fourier Transform Phase Shifting Interferometry**
   Deck, L. L. (Zygo Corporation) . . . . . page 115

Session VIII
Novel Actuators

Wednesday, November 14, 2001, 1:30 PM - 3:00 PM

Session Co-Chairs: John C. Ziegert (University of Florida), and Anthony E. Gee (Cranfield University)

1. **Picometer Positioning System Using Aerostatic Guideway as Motion-Reduction Mechanism**
   Mizumoto, H.; Arii, S. (Tottori University); and Yabuya, M.; Kami, Y. (Nachi-Fujikoshi Corporation) . . . . . page 119
2. **Design of a Linear High Precision Ultrasonic Piezoelectric Motor**
   Bauer, M. G.; Dow, T. A. (North Carolina State University) . . . . . page 123
3. **A Micromachined Thermoelastic Inchworm Actuator**
   Kwon, H. N.; Lee, J. H.; Jeong, S. H.; Lee, S. K. (Kwang-Ju Institute of Science & Technology (K-JIST)) . . . . . page 127
4. **Rotary-Linear Hybrid Axes for Meso-scale Machining**
   Liebman, M. K. (Novalux, Inc.); Vona, M. A. (Jet Propulsion Laboratory); and Trumper, D. L. (Massachusetts Institute of Technology) . . . . . page 131

* *Extended abstract not available at press time*

Poster Session

Monday, November 12, 2001, 3:30 PM - 5:00 PM
Tuesday, November 13, 2001, 1:30 PM - 3:00 PM

Equipment, Machines & Instruments

Analysis & Modeling

1. ***Kinematic Modeling and Analysis of a Planar Micro-positioner***
   Dagalakis, N. G.; Kramar, J. A.; Amatucci, E. G.; Bunch, R. (National Institute of Standards and Technology) . . . . . *page 135*
2. ***Modeling, Identification, and Control of Ballscrew Drives***
   Varanasi, K. K.; Nayfeh, S. A. (Massachusetts Institute of Technology) . . . . . *page 139*
3. ***Preliminary Design of a Very Low Frequency Vibration Calibration System****
   Rhorer, R. L.; Payne, B. F. (National Institute of Standards and Technology) . . . . . *page 143*

Controls

1. ***A Study on Model-based Analysis of the Dynamic Motion Accuracy of CNC Machine Tools***
   Johnston, G.; Kagawa, Y.; Yamazaki, K. (University of California-Davis); Liu, J. (Digital Technology Laboratory (DTL)); and Mori, M. (Mori Seiki Co., Ltd.) . . . . . *page 144*
2. ***Precision Manufacturing and Electronic Gaseous Fuel Injection System Reduces Emission While Improving Fuel Economy for SI Engine***
   Kumarappa, S. (Bapuji Institute of Engineering and Technology); Prabhukumar, G. P. (University B.D.T College of Engineering) . . . . . *page 148*
3. ***Development of Nanometer Positioning System Driven by Force Operational Water Hydraulic Actuator with Rigid Slide Guide-way - Simulation and Experimental Evaluation of Non-linear Positioning Characteristics***
   Tsukahara, S.; Hara, K.; Tomita, Y.; Isobe, S. (Sumitomo Heavy Industries, Ltd.); Kanai, A. (Ashikaga Institute of Technology); and Miyashita, M. (Nano-Tec Associates). . . . . *page 152*

Design & Testing

1. ***Long Range Stage for the Metrological Atomic Force Microscope***
   Eom, T. B.; Kim, J. Y. (Korea Research Institute of Standards and Science); and Choi, H.-S.; Lee, S.-K. (Kwang-Ju Institute of Science & Technology (K-JIST)). . . . . *page 156*
2. ***A Study on a Novel 5-Axis Machine Tool Using Direct Drive***
   Fitsos, P.; Yamazaki, K. (University of California-Davis); Sugimoto, Y.; Mori, M. (Mori Seiki Co., Ltd.) . . . . . *page 160*
3. ***Nanometer Cutting Machine Employing Parallel Mechanism***
   Furutani, K.; Kudoh, R.; Mohri, N. (Toyota Technological Institute). . . . . *page 164*
4. ***Design of a Kinematic Spindle for Low-force, Low-speed Applications***
   Hii, K.-F.; Wolsing, E.; Vallance, R. R. (University of Kentucky). . . . . *page 168*
5. ***Error Compensation of the Maglev Stage Supported by Permanent Magnet Biased Magnetic Bearing***
   Lee, S.-H.; Chang, J.-U.; Lee, S.-W.; Kim, O.-S.; Han, D.-C. (Seoul National University); Chang, I.-B.; (Kangwon National University) . . . . . *page 172*
6. ***Design of Ultraprecision Modular, Freeform® Machine Tool***
   Koning, R. J.; Walter, M. M. (Precitech, Inc.). . . . . *page 176*
7. ***Absolute Strain Measurement for Fiber Bragg Grating Sensor Using a String Resonator With High Accuracy***
   Lee, Y.-K.; Song, I.-C.; Jeong, S.-H.; Lee, B.-H.; Lee, S.-K. (Kwang-Ju Institute of Science and Technology (K-JIST)) . . . . . *page 180*

* *Extended abstract not available at press time*

8. ***Development of a Design Tool for Conceptual Design Stages of Machine Tools***
Mishima, N. (Institute for Mechanical Systems Engineering) . . . . . *page 184*

9. ***A New Optimal Design Technique for the Pneumatic Vibration Isolation System Implementing the Full Mathematical Analysis and Nonlinear Modeling***
Moon, J. H.; Pahk, H. J. (Seoul National University) . . . . . *page 188*

10. ***Desk-Top NC Milling Machine With 200 krpm Spindle***
Okazaki, Y. (National Institute of Advanced Industrial Science and Technology); Mori, T. (Tokyo Metropolitan Industrial Technology Research Institute); and Morita, N. (Chiba University) . . . . . *page 192*

11. ***Development of a High-Speed Micro-Machining System for Brittle Materials***
Warisawa, S.; Karino, T.; Takenaka, R.; Mitsuishi, M. (The University of Tokyo) . . . . . *page 196*

Mechatronics

1. ***Kinematic Modeling of a 6 Degree of Freedom Tri-Stage Micro-Positioner***
Dagalakis, N. G.; Amatucci, E. G. (National Institute of Standards and Technology) . . . . . *page 200*

2. ***Design and Control of Versatile Micro Robot for Microscopic Manipulation***
Fuchiwaki, O.; Aoyama, H. (University of Electro-Communications) . . . . . *page 204*

MEMS & Nanotech

1. ***Development of a Micro-screw and a Micro-pitch-rack Utilized Tungsten Wires***
Honda, S. (Tokyo Metropolitan Institute of Technology) . . . . . *page 208*

2. ***Polishing TiN for Nanotube Synthesis***
Smith, P.; Trinkle, C.; Vallance, R. R. (University of Kentucky); and Gaillard, J.; Sadanand, B.; Rao, A. M. (Clemson University) . . . . . *page 212*

Novel Systems

1. ***A Novel Sub-microradian Beam Diagnostic and Alignment System***
Chen, C. G.; Heilmann, R. K.; Konkola, P. T.; Pati, G. S.; Schattenburg, M. L. (Massachusetts Institute of Technology) . . . . . *page 216*

2. ***Experimental Ductile Grinding of Glass Specimens on the Cranfield Tetraform C Machine***
Gee, A. E.; Delalandre, J.; Corbett, J.; Stephenson, D. J. (Cranfield University) . . . . . *page 220*

3. ***Development of Miniature Actuator for Cryogenic Applications***
Heinrich, M. D.; Dow, T. A. (North Carolina State University) . . . . . *page 224*

4. ***Precision Robot Calibration Using Kinematically Placed Inclinometers***
Robertson, A. P. (ABB Robotics); and Willoughby, P. J.; Slocum, A. H. (Massachusetts Institute of Technology) . . . . . *page 229*

5. ***A Novel Single Degree-of-freedom Active Vibration Isolation System***
Sato, T. (Toshiba Corporation); and Trumper, D. L. (Massachusetts Institute of Technology) . . . . . *page 233*

Metrology

Analysis & Modeling

1. ***A Statistically Based Proposal for Checking the Need of CMM Calibration***
Abackerli, A. J.; Orrego, R. M. M. (Univerisdade Metodista de Piracicaba); Camargo, C. A. (Starrett Indústria e Comércio Ltda.) . . . . . *page 237*

2. ***Deriving the Parametric Errors of a Co-ordinate Measuring Machine from the Mathematical Models Fitted to Represent the Volumetric Error Components***
Bosco de Aquino Silva, J. (Federal University of Paraiba) . . . . . *page 241*

3. ***An Examination of the Effect of Variation in Datum Targets' Locations on Part Acceptance***
Gardner, T. E. (Boeing Commercial Aircraft Group); and Cheraghi, S. H. (Wichita State University) . . . . . *page 245*

4. ***Wavelet Analysis with Different Wavelet Bases for Engineering Surfaces***
Fu, S.; Liu, X.; Muralikrishnan, B.; Raja, J. (University of North Carolina-Charlotte) . . . . . *page 249*

5. ***Translating Machine Tool Errors Into Part Errors by Enhanced Virtual Machining for Sculptured Surfaces***
Lin, Y.; Shen, Y.-L. (The George Washington University) . . . . . page 253

6. ***Modeling of Coolant Flows for In-process Optical Measurement***
Tao, Z.; Gao, Y. (Hong Kong University of Science and Technology) . . . . . page 257

7. ***Nonlinear Error in Eight-pass Heterodyne Interferometers***
Wang, C.; Hocken, R. J. (University of North Carolina-Charlotte). . . . . page 261

8. ***Systematic Error Estimation Based on Grey Relational Analysis***
Wang, Z. (Luoyang Institute of Technology); Gao, Y.; Tse, S. (Hong Kong University of Science and Technology); and Qin, P. (Xi'an Jiaotong University) . . . . . page 265

9. ***Uncertainty Assessment for the Roundness Measurement of Crankshafts Using a Virtual Gaging System***
Zhang, X.; Cole, A. D. (ADCOLE Corporation) . . . . . page 269

10. ***Software Frameworks for Integrated Measurement Processes***
Zhao, X.; Wilhelm, R. G.; Martin, O. A.; Bullock, J. B. (University of North Carolina-Charlotte) . . . . . page 273

11. ***2D Extension of GapSpace Model for Tolerance Analysis***
Zou, Z.; Morse, E. P. (University of North Carolina-Charlotte) . . . . . page 277

Form & Geometry

1. ***Geometric Quality Analysis and Process Control for Ultra-precision Laser Micromachining***
Bordatchev, E. V.; Nikumb, S. K. (National Research Council of Canada) . . . . . page 281

2. ***In-situ Self-calibration of Two-dimensional Angle Probe for Profile Mesaurement of Large Silicon Wafers***
Gao, W.; Yamada, T.; Kiyono, S. (Tohoku University); and Huang, P. S. (SUNY at Stony Brook) . . . . . page 285

3. ***Systematic Form Error Estimation for Circular Parts Using Fourier Components***
Desta, M. T.; Feng, H.-Y. (The University of Western Ontario) . . . . . page 289

4. ***Form Error Measurement by Comparison with a Reference Object***
Horikawa, O. (University of São Paulo). . . . . page 293

5. ***Evaluation of Cylindricity Error Based on MRS, LSC, MCC, and MIC***
Jiang, G.; Cheraghi, S. H. (Wichita State University) . . . . . page 297

6. ***Evaluation of Variations Specified by Non-Uniform Profile Tolerance Boundaries***
Kethara Pasupathy, T. M.; Wilhelm, R. G.; Morse, E. P.; Hetland, G. A. (University of North Carolina-Charlotte). . . . . page 301

7. ***Development of a Cylindricity Measurement System for Parallel Rollers Based on a V-Block Method***
Mitsui, K.; Katsurada, K. (Keio University); and Hayashi, A. (Nano Corporation). . . . . page 305

8. ***Measurement of Drilling Burr by Image Pocessing Technique***
Nakao, Y. (Kanagawa University) . . . . . page 309

9. ***A Study on Evaluation of Sphericity and Related Features of Shaft with Spherical End Faces***
Takahashi, M. (Institute of Technologists); Sasajima, K. (Tokyo Institute of Technology); and Tsukada, T. (Meiji University) . . . . . page 313

10. ***Optical Metrology of Micro-Electro-Mechanical Torsional Mirrors***
Zhang, X.; Shen, Y.-L.; Nagel, D. J. (The George Washington University); and Rensing, N. M. (Micro Optical Engineering Corporation) . . . . . page 317

Instrumentation, Design & Testing

1. ***Calibration of CMM by 3-Dimensional Coordinate Comparison***
Abbe, M. (Mitutoyo Corporation); Takamasu, K. (The University of Tokyo); and Ozono, S. (Tokyo Denki University) . . . . . page 321

2. ***First Generation Micro-machine Tool Characterization***
Caballero-Ruiz, A. (Universidad Autónoma de México) . . . . . page 325

3. ***Use of Fluid Beams to Establish a Clean Zone for In-process Optical Measurement***
Gao, Y. (Hong Kong University of Science and Technology). . . . . page 329

4. ***A New Surface Encoder for Multi-Axis Position Detection***
Shimizu, Y.; Gao, W.; Kiyono, S. (Tohoku University) . . . . . page 333

5. ***Correlation of Spindle Errors to Piece-Part Accuracy***
Wang, K.; Morse, E. P. (University of North Carolina-Charlotte) . . . . . page 337

6. ***A Nanometer Profiling Device with Contact Force Controlled at the Level of Millinewtons***
Yang, L., Xie, T. (Huazhong University of Science and Technology); and Gao, Y. (Hong Kong University of Science and Technology) . . . . . page 341

7. ***Demonstration of Sub-Angstrom Cyclic Nonlinearity Using Wavefront-division Sampling with a Common-path Laser Heterodyne Interferometer***
Zhao, F. (Jet Propulsion Laboratory) . . . . . page 345

8. ***Development of Sub-nanometer Racetrack Laser Metrology for External Triangulation Measurement for the Space Interferometry Mission***
Zhao, F.; Diaz, R. T.; Dumont, P.; Halverson, P. G.; Shaklan, S. B.; Spero, R. (Jet Propulsion Laboratory); and Ames, L.; Barrett, S.; Barrett, R.; Bell, R.; Benson, R.; Cross, G.; Dutta, K.; Kvamme, T.; Holmes, B.; Leary, D.; Perkins, P.; Scott, M.; Stubbs, D. (Lockheed Martin Advanced Technology Center) . . . . . page 349

Machine Tool Metrology

1. ***An Alternative Technique to the Geometric Test of Machining Centers***
de Sousa, A. R.; Schneider, C. A. (Federal University of Santa Catarina) . . . . . page 353

2. ***Evaluating the Tool Point Dynamic Repeatability for High-speed Machining Applications***
Medicus, K. M; Schmitz, T. L. (National Institute of Standards and Technology) . . . . . page 357

3. ***De-Coupling of an Optical Grating Based Measurement Normal from the Machine Tool Structure***
Mueller, U.; Kagawa, Y.; Yamazaki, K. (University of California-Davis) . . . . . page 361

Measurement Uncertainty

1. ***Uncertainty Evaluation of Calibration of the Optical Projector***
Fang, C.-Y.; Lui, K.-W.; Chang, K.-M. (Center for Measurement Standards / ITRI) . . . . . page 365

Surface & Subsurface

1. ***Laser Digitizer Based Strain Measurement***
Chan, H.-L.; Spence, A. D.; Sklad, M. P. (McMaster University) . . . . . page 369

2. ***3-D Measurement and Quantitative Description of Disk Micro-Waviness***
Hara, S. (Tokyo Institute of Technology); Oosone, T. (Union Tool Company); and Yanagi, K. (Nagaoka University of Technology) . . . . . page 373

3. ***Surface Roughness Profile Measurement Based on Microscopic Shearing Interferometry***
Liu, X.; Gao, Y. (Hong Kong University of Science and Technology) . . . . . page 377

4. ***Scale-space and Multi-resolution Techniques for Outlier Analysis in Surface Metrology***
Muralikrishnan, B.; Fu, S. Y.; Orji, N. G.; Raja, J. (University of North Carolina-Charlotte) . . . . . page 381

Optics

Optics / Interferometry

1. ***Off-axis White Light Scatter Interferometry with 0.5m Transmissive Optical Elements***
Gee, A. E. (Cranfield University) . . . . . page 385

2. ***Zone Plate Interferometer Using a Liquid Crystal Panel as a Diffraction Grating — Proposal on the Compensation Method of Systematic Error***
Kamiya, K.; Nomura, T.; Okuda, S. (Toyama Prefectural University); and Tashiro, H.; Yoshikawa, K. (Toyama University) . . . . . page 389

Processes

Grinding

1. ***A Study of Grinding Marks in Semiconductor Wafer Grinding***
Chidambaram , S.; Pei, Z. J. (Kansas State University) . . . . . page 393

2. ***Optimization of Cooling Effect in the Grinding with Mist Type Coolant***
Choi, H. Z.; Lee, S. W.; Kim, D. J. (Korea Institute of Industrial Technology (KITECH)) . . . . . page 397

3. ***Grinding Temperature Measurement in MgO-PSZ Using Infrared Spectrometry***
Curry, A. C.; Shih, A. J.; Kong, J.; Scattergood, R. O. (North Carolina State University); and McSpadden, S. B.; Dinwiddie, R. B. (Oak Ridge National Labotatory) . . . . . page 401

4. ***Force Modeling in Vibration Assisted Cutting***
Fan, X; Miller, M. H. (Michigan Technological University) . . . . . page 405

5. ***Water Jet Assisted In-Process Cleaning and Dressing of Grinding Wheels***
Gho, L. M.; Miller, M. H. (Michigan Technological University) . . . . . page 409

6. ***Abrasive Wear and Forces in Grinding of Silicon Carbide***
Handigund, P. B.; Miller, M. H. (Michigan Technological University) . . . . . page 413

7. ***Study on a Measuring Method for Grain Cutting Edges in Grinding Wheel Surface***
Izumi, M. (Hiroshima Institute of Technology); Lee, H.-S. (Nihon University); and Inoue, S. (Makino Seiki Co., Ltd.) . . . . . page 417

8. ***In-situ Three-dimensional Observation of Active Abrasive Grains on a Grinding Wheel During Grinding of Brittle Materials***
Kanai, A.; Inaba, F. (Ashikaga Institute of Technology); and Miyashita, M. (Nano-Tec Associates) . . . . . page 421

9. ***Fighting Surface Damages of Silicon Wafers - Fine-tuned Wafer Processing with Rotational Grinding***
Klocke, F.; Pähler, D. (Fraunhofer Institut für Produktionstechnologie-IPT) . . . . . page 425

10. ***Wire Electrical Discharge Truing of Metal Bond Diamond Grinding Wheels***
Rhoney, B. K.; Shih, A. J.; Scattergood, R. O. (North Carolina State University); McSpadden, S. B.; Ott, R. (Oak Ridge National Laboratory); Akemon, J. A.; Gust, D. J.; Yonushonis, T. M.; Grant, M. B. (Cummins, Inc.) . . . . . page 429

11. ***Machining of Aspherical Opto-device Utilizing Parallel Grinding Method***
Saeki, M.; Kuriyagawa, T.; Syoji, K. (Tohoku University); and Lee, J.-S. (Nambu University) . . . . . page 433

12. ***Precision Grinding of Micro Fresnel Shape and Precision Glass Molding of Micro Fresnel Lens***
Suzuki, H.; Shibutani, H.; Horiuchi, O. (Toyohashi University of Technology); Higuchi, T. (University of Tokyo); Nishioka, M. (Toshiba Machine Tool); and Kitajima, T.; Yui, A.; Okuyama, S. (The National Defense Academy) . . . . . page 437

13. ***Evaluation of Grinding Conditions Using Dynamic Components of Grinding Force in Centerless Grinding***
Wu, Y.; Kato, M. (Akita Prefectural University); Syoji, K.; Kuriyagawa, T. (Tohoku University); and Tachibana, T. (Micron Machinery Co., Ltd.) . . . . . page 441

14. ***Development of Dead-end Grinding Machine with Linear Motor Driven Table***
Yui, A.; Okuyama, S.; Kitajima, T. (The National Defense Academy); and Kosugi, K. (Okamoto Mashine Tool Works, Ltd.) . . . . . page 445

Machining

1. ***Material Development of Si_3N_4-SiC Composites for Machining Application***
Kwon, W. T.; Park, J. S.; Kim, K. J.; Kim, Y.-W. (University of Seoul) . . . . . page 449

2. ***Burr Formation in Micro-milling***
Lee, K.; Dornfeld, D. A. (University of California at Berkeley); and Essel, I. (University of Technology at Aachen (RWTH)) . . . . . page 453

3. ***Reduction of Tensile Residual Stress and Cutting Force Under High Speed Cutting***
Nakao, M.; Chen, Y.; Konno, J. (The University of Tokyo); Hatamura, Y. (Kogakuin University); and Morita, N. (Chiba University) . . . . . page 457

4. **Single-Point Diamond Machining of Silicon**
O'Connor, B. P.; Grejda, R. D.; Knapp, B. R.; Marsh, E. R. (The Pennsylvania State University) . . . . . page 461

5. **Profile Generation for Brittle Materials by Using Ultra-precision Lathe with On-machine Measurement System**
Ogura, I.; Okazaki, Y. (National Institute of Advanced Industrial Science and Technology) . . . . . page 465

6. **Micromachining by CNC Slotting Using a Steered Tool**
Schaller, T.; Schubert, K. (Forschungszentrum Karlsruhe GmbH) . . . . . page 469

7. **Burr Formation in Micro-drilling**
Stirn, B. (University of Technology at Aachen (RWTH)); and Lee, K.; Dornfeld, D. A. (University of California at Berkeley) . . . . . page 475

8. **A Basic Study on Slurry Actions and Slicing Characteristics of Multi-wire Saw**
Suwabe, H.; Ishikawa, K.; Kitajima, A. (Kanazawa Institute of Technology); and Uneda, M. (Japan Defense Agency) . . . . . page 477

9. **Chatter Modeling and its Diagnostics in Endmilling**
Yoon, M.-C.; Kim, Y. G. (Pukyong National University); Cho, H. D. (Kyungil University); and Kim, S. K. (Hoseo University) . . . . . page 481

Manufacturing

1. **Compensation of Spindle Unbalance-induced Vibration using an Electromagnetic Exciter**
Ahn, J. S.; Kim, S. M.; Mahalik, N. P.; Lee, S. K. (Kwang-Ju Institute of Science & Technology (K-JIST)) . . . . . page 485

2. **Errors in Aluminum Micro-Scale Grooves Produced with Wire EDM for Subsequent Grinding**
Barraja, M.; Rachakonda, P. K.; Vallance, R. R. (University of Kentucky) . . . . . page 489

3. **The Fabrication of Nano-roughness Standards for the Calibration of Atomic Force Microscopes**
Gatzen, H. H.; Kourouklis, C. (Hannover University) . . . . . page 493

4. **Analysis of Cutting Forces in Ball End Milling**
Onozuka, H.; Asakawa, Y.; Sawa, M.; Yamanaka, T.; Maeda, Y. (Hitachi , Ltd.); and Watanabe, K.; Tajima, T. (Hitachi Via Mechanics, Ltd.) . . . . . page 497

5. **Cylindrical Wire Electrical Discharge Machining Process Development**
Qu, J.; Shih, A. J.; Scattergood, R. O. (North Carolina State University); and McSpadden, S. B. (Oak Ridge National Laboratory) . . . . . page 501

Manufacturing (precision mass production)

1. **Dimensional Control for Composite Manufacturing**
Dong, C.; Zhang, C.; Wang, B. (Florida A&M University - Florida State University) . . . . . page 505

2. **2D Error Models and Monte Carlo Simulations for Budgeting Variation in Optical-Fiber Array Connectors**
Rachakonda, P. K.; Barraja, M.; Vallance, R. R. (University of Kentucky); and Kiani, S.; Lehman, J. (Teradyne, Inc.) . . . . . page 509

3. **Basis for Micro-Factory: CNC Micromachine Tools**
Ruiz-Huerta, L. (Universidad Autónoma de México) . . . . . page 513

Non-conventional

1. **An Internet Based Collaborative Filtering Scheme for Surface and Form Metrology Information**
Bui, S. H.; Raja, J. (University of North Carolina-Charlotte) . . . . . page 517

2. **Abrasive Process for Reclaiming Semiconductor Wafers**
Kremen, G. Z.; Igelshteyn, L.; Feigyn, S. (Scientific Manufacturing Technology Inc.); McSpadden, S. B.; Parten, R.; Bai, J. M. (Oak Ridge National Laboratory) . . . . . page 521

3. **Micro Ultrasonic Abrasive Machining for Three-dimensional Milli-structures of Hard-brittle Materials**
Kuriyagawa, T.; Syoji, K. (Tohoku University); Shirosawa, T. (Hitachi Cable, Ltd.); and Saito, O. (Tohoku Gakuin University) . . . . . page 525

4. ***Productive Anisotropic Etching with Excimer Laser Assist***
Moronuki, N.; Uchiyama, K.; Takayama, A. (Tokyo Metropolitan University) . . . . . *page 529*

5. ***Using Drop-on-Demand Technology for Manufacturing GRIN Lenses***
Trost, H.-J.; Ayers, S.; Chen, T.; Cox, W. R.; Grove, M. E.; Hoenigman, R. (MicroFab Technologies, Inc.) . . . . . *page 533*

Polishing, Lapping and ECM

1. ***Laser Assisted Chemical Mechanical Polishing for Planarization***
Kimura, K. (Sony Corporation); and Miyoshi, T.; Takaya, Y.; Takahashi, S. (Osaka University) . . . . . *page 537*

2. ***Digital Polishing Method for CMP System Using a Smaller Diameter Polishing Pad***
Uda, Y.; Senga, T.; Ishikawa, A.; Yamamoto, E.; Mitsui, T.; Hoshino, S. (Nikon Corporation) . . . . . *page 541*

3. ***High Removal Rate Ultra-Smoothness Polishing of NiP Plated Aluminum Magnetic Disk Substrate with Colloidal Silica***
Yasui, H.; Fukamachi, T.; Sakamoto, S. (Kumamoto University) . . . . . *page 545*

Technical Papers

A S P E

Scanning Beam Interference Lithography

Paul T. Konkola[1], Carl G. Chen, Ralf K. Heilmann, G.S. Pati, and Mark L. Schattenburg
Massachusetts Institute of Technology, Cambridge, MA 02139

1 Introduction

We are developing a system for patterning large-area, nanometer-accuracy gratings that are appropriate for semiconductor metrology [1]. Our system, termed Scanning Beam Interference Lithography (SBIL), uses the interference fringes between two coherent laser beams to define highly coherent gratings in photoresist. The substrate is step-and-scanned under the interference pattern to produce large gratings.

The ultimate goal of the SBIL system is to write gratings and grids with sub-nanometer distortions over substrates up to 300 mm in diameter. These ultra-low distortion gratings would enable important advances in metrology, electro-optics, spectroscopy, and many other applications.

Figure 1 depicts the SBIL concept. The optics closely resemble those of the traditional interference lithography system [2, 3] but the image is much smaller than the total desired patterning area. The grating image diameter is typically designed to be between 200 μm and 2 mm. Large gratings are fabricated by scanning the substrate at a constant velocity under the image. At the end of the scan the stage steps over by an integer number of grating periods and reverses direction for a new scan. The interference pattern has a Gaussian intensity envelope since we interfere Gaussian beams. A maximum step size is constrained by the desired dose uniformity. For instance, a step size of 0.9 times the Gaussian beam $1/e^2$-radius produces dose uniformity of better than 1%.

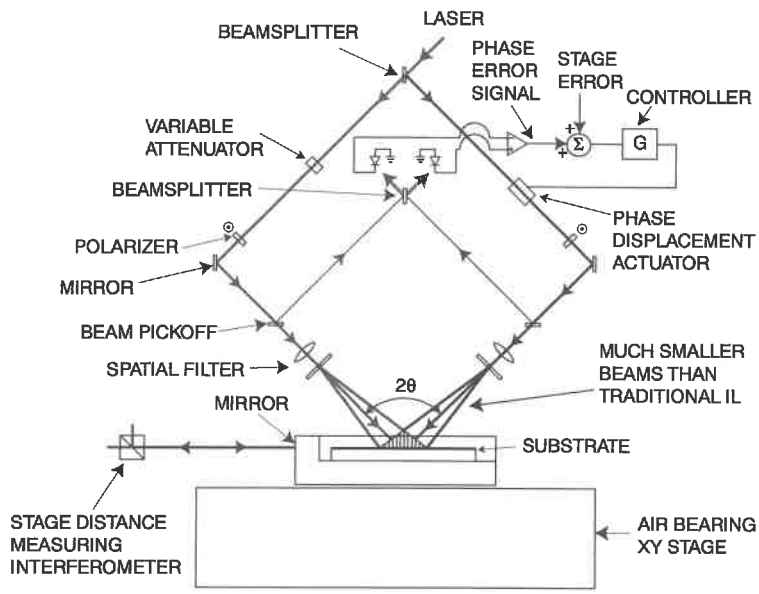

Figure 1: SBIL system concept

The system has the significant added problem over previous interference lithography systems of accurately synchronizing the interference image to the moving substrate. Therefore, the design includes correction for stage error and the lithography interferometer's phase error by feedback to a high bandwidth fringe locking controller.

The optical design incorporates means for spatial filtering and adjustment of intensity, polarization, wavefront curvature, and spot size. The nominal period, Λ, of the interference fringes is controlled by the beam incident angle θ and is given by

$$\Lambda = \frac{\lambda}{2\sin\theta}. \tag{1}$$

Here λ is the wavelength of the laser.

The relatively small beams used in SBIL provide a major benefit in ease of obtaining small wavefront distortions [4]. Furthermore, by scanning the image, distortions along the scan direction can be averaged out. The overlap of scans provides even further averaging of the wavefront distortions. Also, critical alignments such as lens positioning and angle of interference are much relaxed for the small beams.

In our approach, we aim to demonstrate nanometer-level repeatable grating writing first. Then, self-calibration methods [5] will be implemented to correct systematic errors and achieve nanometer-level accuracy. We are designing and implementing a system with a CW 351.1 nm wavelength argon-ion laser that

[1]email: konkola@mit.edu.

is intended to achieve nanometer level distortions for arbitrarily selected grating periods in the range of 200 nm to 2 μm. Realizing our performance goals is a major challenge because of the many error sources in lithography. We elaborate on the major error sources in the next section.

2 System Errors

There are many sources of errors in our system. We break them down into six categories: stage interferometer, fringe locking, metrology frame, substrate frame, period control, and image distortion.

Figure 2 illustrates definitions of error coordinate systems. The distance, x_d is the displacement between the stage and column reference mirrors. We define errors in this measurement as stage interferometer errors. The distance x_f is the displacement of the fringe pattern at the substrate-interference image interface relative to the column reference. During writing, we shift the fringes with a high speed acousto-optic fringe locking system [6] such that

$$x_d - x_f + x_o = NM\Lambda. \tag{2}$$

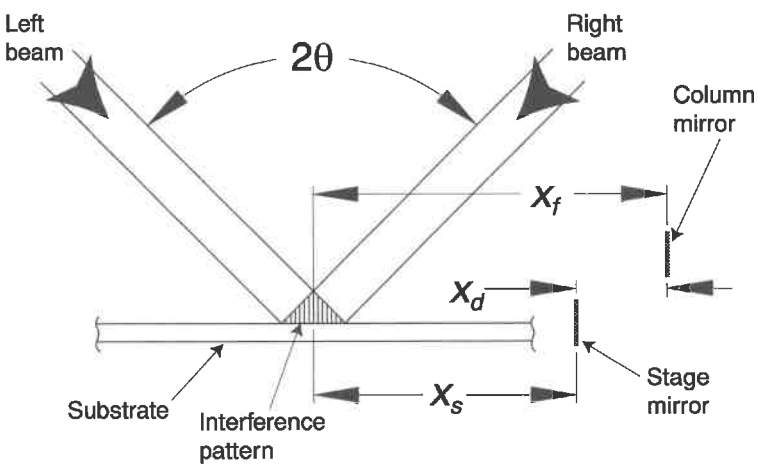

Figure 2: Definition of coordinate systems for error terms.

Here x_o is a constant depending on the location of the first scan and N is the integer scan number incremented from zero. The distance $M\Lambda$ is the step size between scans, where M is an integer and Λ is the period of the interference image.

Inaccuracy in the fringe position, x_f, comprises two error categories. The first is the fringe locking error, which is due to inaccuracy in the fringe locking sensor signal and the controller's inability to lock out the total fringe locking error signal. Inaccuracy in the fringe locking sensor signal is due to air index variations and electronic inaccuracy. The metrology frame error category contains the remaining sources of errors in x_f. These errors are due to the non-collocation of the sensor with the fringes on the wafer, alignment errors, and disturbance of the sensor optics with respect to the column reference.

The position of a substrate location relative to the stage mirror is x_s. Inaccuracy in this position is the substrate frame error; during writing the substrate must accurately track the stage mirror for this error to be zero. Furthermore, the substrate must be clamped during writing in substantially the same way that it will be used as a metrology reference, otherwise clamping distortions will limit the accuracy of the reference.

Another category of error is period control. Variations in λ and interference angle, θ, limit the period control. For 1 nm of accumulated phase error across a 1 mm image radius we must control the period to 1 ppm [3].

The image distortion category is due to nonlinearity of the interference image. To some extent, the image nonlinearity can be averaged out by tightly overlapping adjacent scans but this approach limits throughput and image contrast is sacrificed. Therefore, we are trying to achieve image linearity on the same order as for the other error categories.

3 System Design

Our accuracy goal requires fringe locking to the substrate with nanometer-level spatial phase errors while controlling the fringe period to approximately one part per million. Furthermore, our system design faces severe requirements on the design of the substrate and metrology frames, stage and vibration controls, environmental controls, displacement interferometry, lithography interferometer phase locking, planarity of the interfering waves, and control of the fringe period. We review how our design, shown in Figure 3, addresses some of these error categories.

The system employs an X-Y air bearing stage, four axes of column referencing heterodyne laser interferometry, beam alignment systems [7], period measurement system [3], image distortion measurement system, acousto-optic fringe locking [6], environmental controls, active and passive vibration isolation with feed-forward, and beam steering [8].

We require a length scale repeatable to ± 1 nm/.150 m or ± 7 ppb to ensure that we can repeatably write gratings. Moreover, the index of air and laser vacuum wavelength are unstable and we must have an accurate way to scale the phase readings from our heterodyne electronics. A grating length-scale reference is included on the chuck to calibrate the wavelength of the stage interferometer. Our system is designed to read the phase of a grating that is nominally the same period that we are setup to write [6]. This scale calibration method replaces air-index calculations that may have experimental uncertainties of ± 30 ppb [9]. Furthermore, the grating length scale allows us to use a commercial heterodyne laser in place of a less convenient but highly wavelength-stable iodine-stabilized laser system. We continuously take measurements from our refractometer once we establish our length scale from the grating reference. Thus, in real-time we can correct for the wavelength change of the stage interferometer. The writing interferometer uses an achromatic grating-based interferometer configuration where the image period is insensitive to air index changes and vacuum wavelength instability of the UV laser.

Our system's repeatability is determined by reading the phase of a previously exposed substrate. This direct measurement of the grating phase allows us to assess the repeatability of the stage's displacement interferometer. We present measurements from our stage and grating-based interferometers .

4 Conclusions

Our accuracy goal requires fringe locking to the substrate with nanometer-level spatial phase errors while controlling the fringe period to approximately one part per million. We have designed and are in an evolutionary process of implementing a SBIL system for producing gratings with repeatability of a few nanometers.

We are in the process of major upgrades to our system. We are incorporating thermally stable and higher resonant frequency metrology frames. Also, an environmental enclosure is being installed to control temperature (± 0.005 °K), relative humidity ($< \pm 0.8\%$), and pressure gradient (< 15.5 Pa/m). Acoustic suppression is also a necessary feature of the enclosure in our noisy lab [6]. We will present the latest repeatability results in grating reading, writing, and stage interferometry.

References

[1] M. Schattenburg *et al.*, J. Vac. Sci. Technol. B **17**, 2692 (1999).

[2] J. Ferrera, PhD dissertation, Massachusetts Institute of Technology, Department of Electrical Engineering and Computer Science, 2000.

[3] C. G. Chen *et al.*, to be published in J. Vac. Sci. Technol. B (2001).

[4] C. G. Chen, Master's thesis, Massachusetts Institute of Technology, Department of Electrical Engineering and Computer Science, 2000.

[5] C. J. Evans, R. J. Hocken, and W. T. Estler, CIRP Annals **45**, 617 (1996).

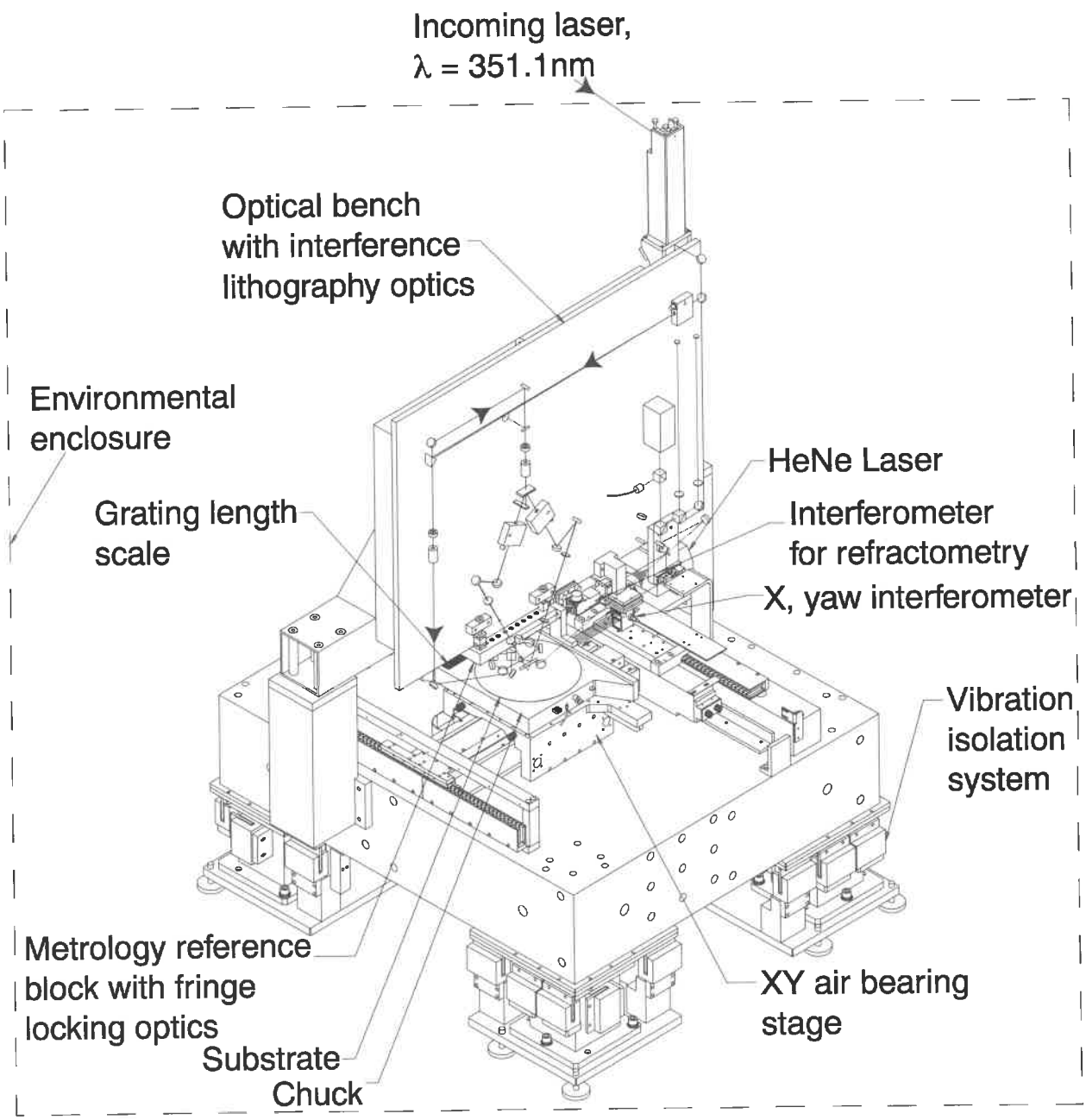

Figure 3: SBIL design showing optics and some subsystems. Details such as optical mounts, fasteners, and holes may not be shown.

[6] R. K. Heilmann *et al.*, to be published in J. Vac. Sci. Technol. B (2001).

[7] C. G. Chen *et al.*, submitted to these proceedings (2001).

[8] P. Konkola, C. G. Chen, R. Heilmann, and M. L. Schattenburg, J. Vac. Sci. Technol. B **18**, 3282 (2000).

[9] K. P. Birch and M. J. Downs, Metrologia **31**, 315 (1994).

MOLECULAR MEASURING MACHINE DESIGN AND PERFORMANCE

John A. Kramar, Jay Jun, William B. Penzes, Vince P. Scheuerman, Fredric E. Scire,
E. Clayton Teague
National Institute of Standards and Technology, Gaithersburg, MD 20899

Introduction

The trend toward product miniaturization is pervasive across many fields, most notably in the microelectronics arena, but also in mechanical systems [micro-electro-mechanical systems (MEMS)], microoptics, and microfluidics to name a few. As an alternative to the top-down approach of shrinking sizes, many researchers are striving to jump ahead to molecular nanotechnology, where commercially viable products would be made from the bottom-up by placing each molecular building block in its place through self-assembly or nano-manipulation.[1] In any case, as the dimensions of manufactured features decrease, the need will increase for tools, procedures, and standards for measuring these ultra-small features to assure proper function and for manufacturing process control.

At the National Institute of Standards and Technology, we are developing an instrument to address some of these emerging measurement needs. We call the tool the Molecular Measuring Machine (M^3). It combines the sub-nanometer feature-resolution capability available from scanning probe microscopy with the better than 1 part in 10^9 displacement measuring capabilities of high-resolution interferometry. The overall performance goal is for sub-nanometer probe and interferometer resolution and one nanometer combined uncertainty for two-dimensional point-to-point measurements within the 50 mm by 50 mm measurement area. With this tool, we can characterize and validate industry-developed calibration artifacts. The instrument is now operating and we present here some aspects of its design and its current performance capabilities.

Design

The Molecular Measuring Machine has a unique design.[2] A cut-away view is shown in Fig. 1. The machine core is a copper sphere with othogonal vee and inverted-vee slideways for the upper and lower carriages, respectively. The carriages rest on kinematically placed Teflon[3] pads and are driven by a piezoceramic stepping motors having 50 mm ranges. Each of the carriages carries a one-dimensional, flexure-constrained sub-carriage, whose motion is aligned with the carriage motion. The sub-carriages are directly driven by piezoceramic stacks and have 10 µm ranges. The lower sub-carriage carries the sample inside a Zerodur box. The four inside mirrored surfaces of the box serve as the reference mirrors for the interferometry system. The beam-splitter assemblies are suspended from the upper sub-carriage. The Michelson interferometers measure differentially the location of the beam-splitter assemblies relative to the two opposing metrology box mirrors. Also suspended from the upper sub-carriage is the Z-axis assembly. This is a complex yet compact assembly that includes a vertical piezoceramic-stepping-motor coarse-motion stage with 3 mm range; a flexure-constrained, piezoceramic fine-motion stage with 5 µm range; a capacitance gage sensor for measuring the fine motion displacement relative to the coarse stage; and a potentiometer sensor for measuring the coarse motion relative to the upper sub-carriage. The Z fine motion carries the scanning tunneling microscope probe tip. Also on the upper sub-carriage is the pre-amplifier for measuring the nanoampere-level tunneling current, and a charge-coupled-device array video camera for providing a visual indication of the position of the probe tip relative to the sample.

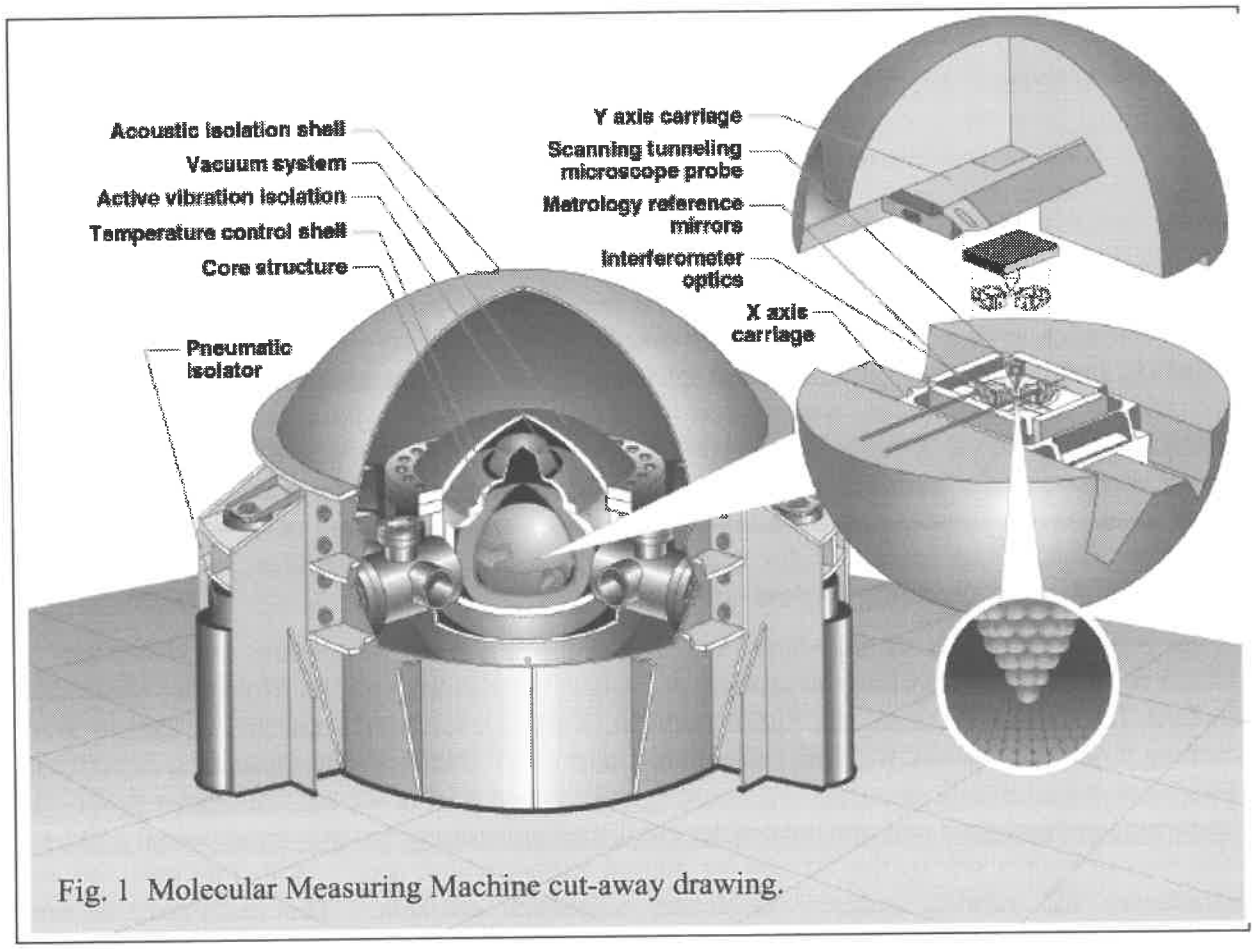

Fig. 1 Molecular Measuring Machine cut-away drawing.

The core of the instrument just described is housed inside several layers of environmental isolation. A thin copper heater shell used for temperature control immediately surrounds the core with a 25 mm gap. Room temperature is kept at 17 °C to act as a heat sink and the temperature of the core is maintained at 20 °C ± 0.005 °C by servo control of the current in thin wires wrapping the heater shell. Surrounding this there are, in order, an active vibration isolation suspension system; a vacuum system capable of better than 10^{-5} Pa; and an acoustic isolation shell supported by pneumatic vibration isolation legs.

The instrument control and data acquisition system uses independent digital signal processors (DSPs) for specific processing and control tasks. These DSPs are controlled by an overall system controller and can intercommunicate through a common VME bus and shared memory. There are two DSPs for processing the raw X and Y interferometer signals to determine the stage positions; one DSP that acts as the controller for the X and Y axes, generating scan trajectories and collecting data; another DSP assigned to the Z axis for control of the coarse and fine motion stages, including the probe servo control; and a last DSP used to control the active vibration isolation system. Each of the DSPs has its own separate input/output bus for independent communication with the M^3 hardware through analog-to-digital, digital-to-analog, and digital input and output ports, thus minimizing VME bus traffic. The top-level control is written within the Matlab language environment, using its command-line interpreter, data plotting and display, and graphical-user-interface capabilities. Matlab callable functions written in C are used to interface with the DSP controllers.

Performance

Several artifacts have been examined to validate the instrument performance. Initially, an average pitch measurement was made on a one-dimensional grating that had been produced by laser-focused atomic deposition of chromium atoms on a silicon substrate.[4] To measure the average line pitch on this sample, a large composite image was acquired of an area 1 mm in length and 5 μm wide. The image was taken in overlapping 6 μm sections, continuously over a period of 8 days. The average pitch was determined by taking the interferometrically-ascertained distance between two end lines and dividing by the total number of line spaces between them. The grating uniformity was checked by comparing the coordinates of lines at intervening locations. The orientation of the grating with respect to the coordinate system was determined by taking a series of images along the lines. The average pitch was measured to be 212.69 nm, with an estimated fractional standard uncertainty of 25×10^{-6}, or 5 pm. The biggest uncertainty sources were the Abbé error, the interferometer alignment, and the motion coupling from the Z-actuator into the X and Y axes (Table 1). Based on the fabrication method, the expected pitch for this grating was 212.78 nm with a standard uncertainty of 10 pm. Clearly, the difference of 90 pm exceeds the combined uncertainty bounds. This discrepancy is under investigation. On the other hand, an informal comparison was also made with the NIST Line Scale Interferometer through measurement comparisons of a 10 mm stage micrometer. Here the measurements were in agreement to within the estimated fractional standard uncertainty of 15×10^{-6}.

Most recently, we have turned our attention to nanometer-scale features. We have demonstrated that the mechanical stability of M^3 is adequate for making atom-resolved images of the graphite lattice ($a = 0.25$ nm) in the topographical scan mode. However, noise in the interferometer

Table 1 – M^3 Uncertainty Estimate for a 1 mm Measurement

Uncertainty Component	Estimated Value, EV (nm)	Comments
Wavelength of Light	0.1	$\delta\lambda/\lambda = 10^{-7}$; EV = $(\delta\lambda/\lambda)$(1 mm); (very conservative)
Polarization Mixing	1	δx = 0.5 nm (peak); EV = 2 (δx)
Interferometer Cosine Error	20	Optical Path = 300 mm; Maximum beam separation at optics = 2 mm; θ =? 2/300; ? EV = $(\theta^2/2)$(1 mm)
Abbé Offset Error	9	Abbé Offset = 10 mm; $\delta\theta = 5 \times 10^{-7}$ ea. for the X coarse, X fine, and Y fine carriages; EV = v3 ($\delta\theta$)(10 mm)
Z-to-X Coupling Uncertainty	13	$\alpha_{XZ} = 0.10 \pm 0.02$; ΔZ = 650 nm for the 1 mm displacement; EV = $(\Delta Z)(\delta\alpha_{XZ})$
Temperature Instability Uncertainty	4	δT = 5 m°C; $CTE_{Cu} = 2 \times 10^{-5}$/°C; 25 mm Cu; $CTE_{SS} = 1 \times 10^{-5}$/°C; 25 mm SS; EV = (δT)(25 mm)$(CTE_{Cu}+CTE_{SS})$
Specimen Cosine Error	0.01	$\delta\theta = 10^{-4}$; EV = $(\delta\theta^2/2)$(1 mm)
Line Center Determination	4	δx = 3 nm; EV = v2 (δx)
$\sigma = (\Sigma EV_i^2)^{1/2}$	26	

readings at about the 1 nm level between 1 Hz and 20 Hz have precluded a lattice measurement. This is not due to direct mechanical vibrations, as indicated by the stable open-loop images of graphite atoms. The interferometer noise is instead related to the pointing stability of the lasers, and is under investigation. In the meantime, we have examined the electrically-conductive molecular crystal[5], (TEET)[Ni(dmit)$_2$]$_2$, which has larger lattice constants of $a = 1.02$ nm ± 0.01 nm, $b = 0.75$ nm ± 0.01 nm, and ?= 106° ± 0.5° (from x-ray crystallographic measurements). With this sample we have been able to obtain lattice-resolution images while scanning the surface under closed-loop control from the interferometers (Fig. 2). Now for the first time, M^3 measurements can be compared with a crystal lattice. Measured surface lattice parameters of $a = 1.1$ nm ± 0.1 nm, $b = 0.7$ nm ± 0.1 nm, and ?= 106° ± 3° from initial small-area scans were in agreement with bulk x-ray-crystallography. The quoted standard uncertainties are dominated by Type A (statistically estimated) effects.

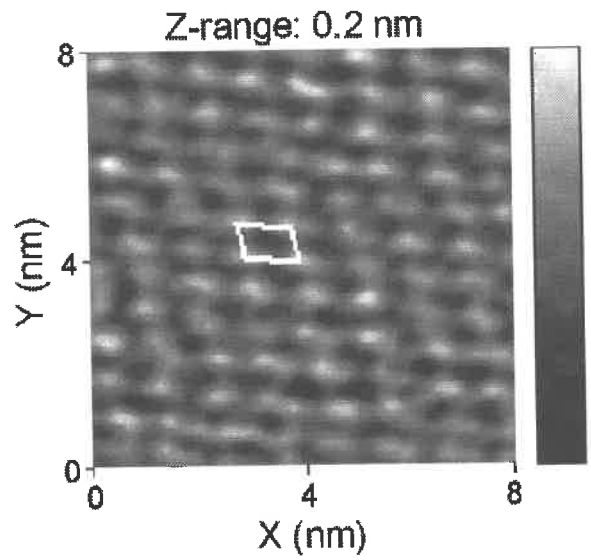

Fig. 2 M^3 metrology scan of (TEET)[Ni(dmit)$_2$]$_2$. Measured unit cell dimensions are $a = 1.1$ nm ± 0.1 nm, $b = 0.7$ nm ± 0.1 nm, ?= 106° ± 3°

The Molecular Measuring Machine is now beginning to fulfill its designed powerful measurement capability of resolving and measuring sub-nanometer features over square-centimeter areas.

References

[1] For a broad review and critique of nanotechnology and the bottom-up approach, see several articles in *Scientific American*, September 2001.

[2] John Kramar, Edward Amatucci, David Gilsinn, Jau-Shi Jun, William Penzes, Fredric Scire, E. Clayton Teague, and John Villarrubia, "Toward Nanometer Accuracy Measurements," *Proceedings of the SPIE Conference on Metrology, Inspection, and Process Control for Microlithography XIII,* SPIE **3677**, 1017–1028 (1999)

[3] Certain commercial equipment, materials and software are identified in this paper in order to specify the experimental procedure adequately. Such identification does not imply recommendation or endorsement by NIST, nor does it imply that the materials or equipment specified are necessarily the best available for the purpose.

[4] J.J. McClelland, R.E. Scholten, E.C. Palm, and R.J. Celotta, "Laser Focused Atomic Deposition," *Science*, **262**, 877-880, (1993).

[5] A.M. Kini, J.P. Parakka, U. Geiser, H.H. Wang, F. Rivas, E. DiNino, S. Thomas, J.D. Dudek and J.M. Williams; "Tetraalkyl- and dialkyl-substituted BEDT-TTF derivatives and their cation-radical slats: synthesis, structure, and properties," *Journal of Materials Chemistry*, **9**(4), 883-892, (1999).

Nanomeasuring technology - Nanomeasuring machine

Prof. Gerd Jäger, Dr. Eberhard Manske, DI Tino Hausotte, Dr. Hans-Joachim Büchner,
Prof. Rainer Grünwald, Dr. Walter Schott
Technische Universität Ilmenau

Summary

At the Institute of Process Measurement and Sensor Technology of the TU Ilmenau, a scanning force microscope (measuring range 15 µm x 75 µm x 15 µm) having a laser-interferometric 3D-nanomeasuring system free from Abbe errors has been developed in cooperation with the PTB Braunschweig. The extended measuring uncertainty (K = 2) is only 0.2 nm and was obtained with a structure standard. To achieve a considerable extension of the measuring range up to 25 mm x 25 mm x 5 mm, a nanopositioning and –measuring machine was developed. The measuring axes have a resolution of 1.24 nm. The laser-interferometric measurement is free from Abbe errors of 1st order in all measuring axes. The deviations of the guides used are compensated by means of a precision mirror corner.

1 Introduction

The big advances made in the fields of microelectronics, microtechnology, nanotechnology and precision engineering require the exact measurement of ever smaller structures, with those structures being localized in increasingly large spatial areas. According to the International Technology Roadmap for Semiconductors of 1999, the positioning ranges to be realized already in the years from 2010 to 2014 will cover an area of 450 mm x 450 mm. Furthermore, it will be necessary to measure and to manufacture structure widths of about 35 nm with nanometer accuracy. Such extreme requirements are closely linked with technologies such as electron ray or X-ray lithography. However, also Nanoimprint Lithography, which is a very promising new approach to the creation of nanostructures /1/ , will place great demands on measurement and positioning technology.

There is not only a lack of nanomeasuring and positioning systems, but also of 1D to 3D-mechanically tactile and optical sensing systems primarily necessary for measuring small parts having a sophisticated geometry.

In the following, some developments made at the Institute of Process Measurement and Sensor Technology of the TU Ilmenau in the fields of nanomeasuring and positioning technology will be described.

2 3D-nanomeasuring system free from Abbe errors for the scanning force microscope type VERITEKT

Figure 1 shows the simplified principle of the VERITEKT scanning force microscope. A 3D-monolithic scanner carries the x-, y- and z-drive and measuring systems. All three drive and measuring systems function nearly separately. Each axis is driven by piezoactuators combined with capacitive sensors for position measurement. In the x- and y-axes, the infringement of the Abbe comparator principle results in considerable measuring errors when tilts occur during movement:

$$f_x = L_x \cdot \sin \beta \quad (1)$$

$$f_y = L_y \cdot \sin \beta \quad (2)$$

In the z-axis, errors of 2nd order occur:

$$f_z = L_z \cdot (1 - \cos \beta) \tag{3}$$

L_x, L_y, L_z - distances between the measuring systems and the probe tip
β - angle of tilt of the axes

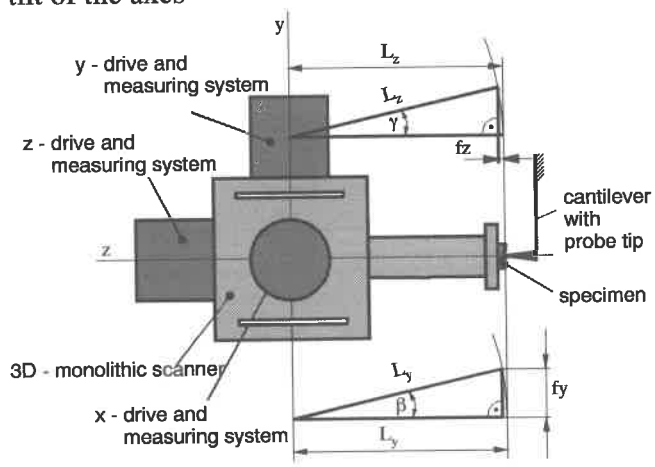

Fig. 1: Abbe errors on the 3D-monolithic scanner of the VERITEKT microscope

As in case of the VERITEKT microscope, the distances L_x, L_y and L_z are approximately 60 mm, considerable errors result even if the angle of tilt is small. Those errors can greatly be reduced only if the distances L_x, L_y and L_z are short. From this, it follows that the measuring systems must be positioned as close to the measuring object (specimen) as possible. Ideally, the measuring axes should intersect in the point of contact of the probe tip.
At the Institute of Process Measurement and Sensor Technology of the TU Ilmenau, a suitable laser-interferometric three-coordinate measuring system was developed and manufactured by the SIOS Messtechnik GmbH Ilmenau company /2, 3, 4/.

The fundamental mode of action of the 3D-nanomeasuring system free from Abbe errors of the VERITEKT microscope is shown in Fig. 2.

A measuring cube (8 mm x 8 mm x 8 mm) is firmly positioned in the moving specimen holder as close to the measuring object as possible. The measuring beam of the z-miniature interferometer is directed perpendicularly to the mirrored z-surface of the measuring cube, with its virtual extension hitting the tip of the sensing needle. L_{zo} being the distance between the z-mirror surface and the probe tip, the following cosine error f_{zo} results:

$$f_{zo} = L_{zo} (1 - \cos \beta) \tag{4}$$

In order to be able to make measurements free from Abbe errors also in the x-y plane, i.e., to avoid errors of 1st order, a 90°-corner mirror with silvered external faces is firmly attached to the specimen holder. This mirror as well as the miniature interferometers are to be adjusted to the specimen holder in such a way that the measuring beams of the miniature y-interferometer and

of the miniature x-interferometer hit the mirror surfaces at an angle of 90° and the virtual extensions of both measuring beams intersect in the tip of the sensing needle. Thus, only cosine errors will occur in the x-y measuring plane:

$$f_{xo} = L_{xo} (1 - \cos \beta) \quad (5)$$
$$f_{yo} = L_{yo} (1 - \cos \beta) \quad (6)$$

with L_{xo} and L_{yo} being the perpendicular distances between the mirror surfaces and the probe tip.

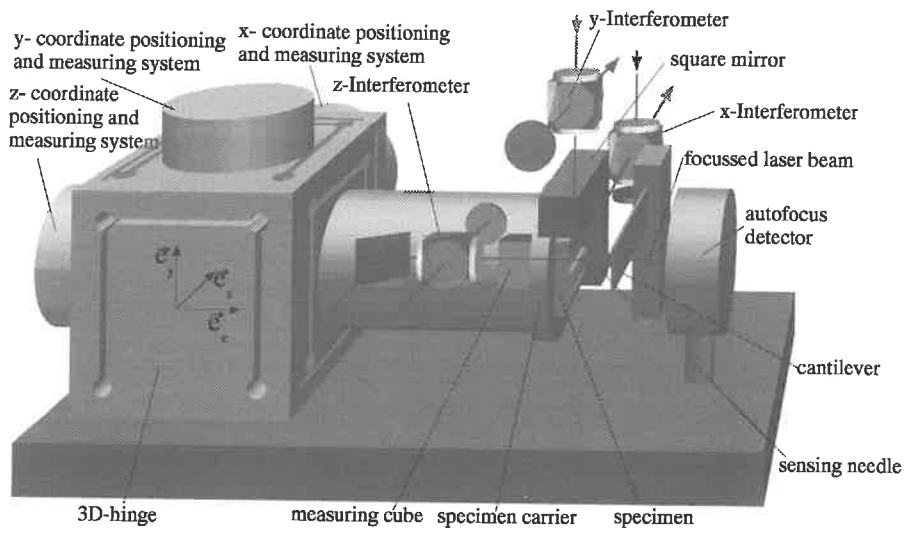

Fig. 2: VERITEKT microscope with laser-interferometric 3D-measuring system free from Abbe errors

In cooperation with the PTB Braunschweig, department 5 (manufacturing metrology), two VERITEKT microscopes were equipped with the Abbe error-free measuring systems and tested successfully. By means of suitable structure standards, scientists of the PTB achieved an extended measuring uncertainty (K = 2) of only 0.2 nm using the laser-interferometric 3D-measuring system /5/. The measurements made at the PTB clearly show that a scanning force microscope which performs exact measurements in a metrological sense was developed.

3 Nanomeasuring machine

3.1 Structure and functioning /6, 7/

As reported above, it was possible to achieve extremely small measuring uncertainties by means of the metrological VERITEKT microscope. However, its measuring range amounts to 15 µm x 75 µm x 15 µm only. As it was said in the introductory paragraph, considerably larger measuring ranges to be realized at the same metrological certainty are required today. Those ranges amounting, for example, to several centimeters can no longer be realized by means of spring guides. Therefore, precision ball guides were used with the nanomeasuring machine. However, such guiding systems present systematic deviations. We were able to largely compensate these deviations in the functional principle we have chosen to realize a nano-measuring machine. The basic principle of the nanomeasuring machine is illustrated in Fig. 3.

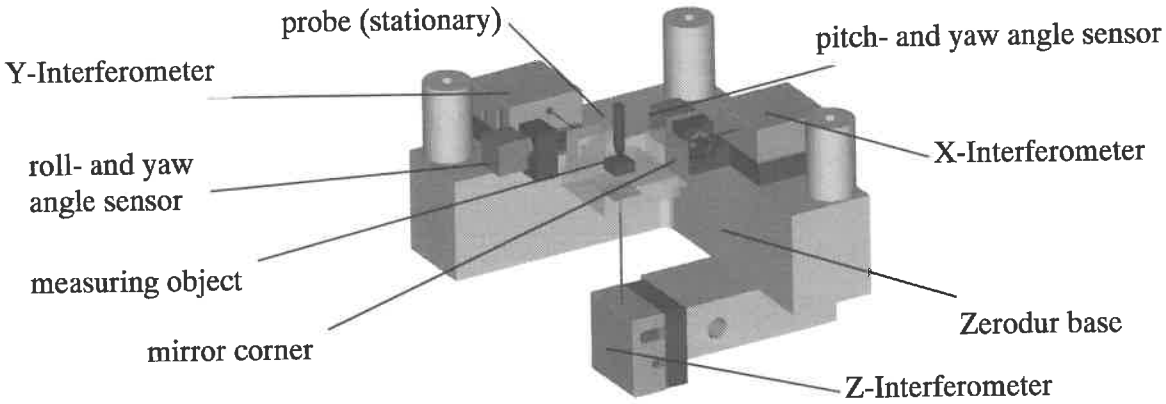

Fig. 3: Basic set-up of the nanomeasuring machine

The standard of the nanomeasuring machine is constituted by a mirror corner consisting of three plates arranged perpendicularly. The external faces of the plates are mirrored.
The measuring object is positioned on the base plate of the mirror corner and sensed by a stationary sensing system (AFM, STM, autofocus, tactile probes). The probes are employed only as zero systems. As the point of contact of the probe with the surface of the measuring object is stationary, a measurement free from Abbe errors can be achieved in all three axes. For this, three plane mirror interferometers type SP 500 made by the SIOS Meßtechnik GmbH company are fixed to a Zerodur base. The measuring beams sent out by the interferometers are reflected by the external faces of the mirror corner. The virtual extensions of the measuring beams hit the surface of the measuring object in the point of contact of the probe. As a result, any Abbe errors of 1st order will be avoided in all measuring axes.
To measure the measuring object, the mirror corner must be guided parallel to the object, with great attention being paid to the fact that the contact of the probe is maintained at any time. If this is the case, possible height deviations of the guides will not have any influence on the result of measurement. For compensating the tilt errors of the guides, pitch, yaw and roll angle sensors are attached to the Zerodur base. The drives for the guides are of an electrodynamic type.
The complete nanomeasuring machine is represented in Fig. 4.

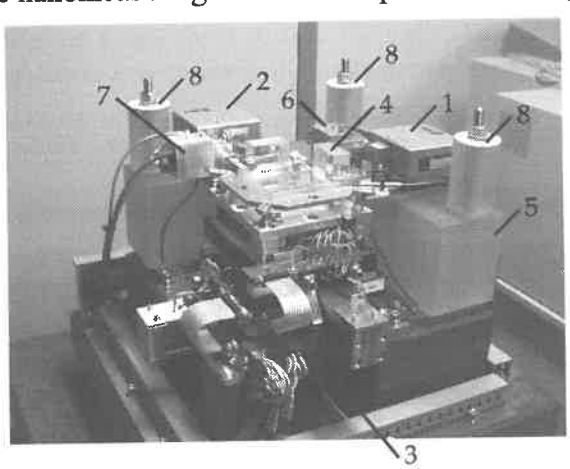

1 x-Interferometer
2 y-Interferometer
3 z-Interferometer
4 mirror corner
5 Zerodur base
6 pitch- and yaw angle sensor
7 roll- and yaw angle sensor
8 fixing points for probe system

Fig. 4: Nanomeasuring machine

3.2 Metrological properties

The nanomeasuring machine has a measuring range of 25 mm x 25 mm x 5mm and a resolution of 1.24 nm in all measuring axes. The laser-interferometric measurement is free from Abbe errors of 1st order in all three coordinates. When the machine was tested, crosstalk occurred also to the other axes within the digital uncertainty of 1.24 nm, with the measuring table being moved linearly. Thus, within its measuring range, the nanomeasuring machine is able to fulfil the requirements of microelectronics, microtechnology, nanotechnology and precision engineering with highest possible measuring uncertainty.

4 Acknowledgements

The authors wish to thank all those colleagues from the TU Ilmenau who have contributed to the developments described. Our special thanks are due to the Thüringer Ministerium für Wissenschaft, Forschung und Kultur for promoting the nanocoordinate metrology in the framework of joint projects.

Bibliographical reference

/1/ Zankoviych, S.; Hoffmann, T.; Seekamp, J.; Bruch, I.U.; Sotomayor Torres, C.M.: Nanoimprint lithography: challenges and prospects. Nanotechnology 12 (2001). S. 91 - 95.

/2/ Büchner, H.-J.; Jäger, G.; Manske, E.: Laser-interferometrically assisted 3D-nanometrology on the atomic force microscope type VERITEKT. euspen 1st international conference. May 1999.

/3/ Jäger, G.: Lasernanomesstechnik - Möglichkeiten, Grenzen und Anwendungen in der modernen Gerätetechnik. In: 44. Internationales Wissenschaftliches Kolloquium. TU Ilmenau. September 1999. S. 43 - 54.

/4/ Bienias, M.; Gao, S.; Hasche, K.; Seemann, R.; Thiele, K.: 3D calibration of a Scanning Force Microscope with Internal Laser Interferometers. Surface andInterface Analysis. Vol. 25. 1997. S. 606 - 616.

/5/ Herrmann, K.; Hasche, K.; Pohlenz, F.; Seemann, R.: On Some Metrological Applications of Scanning Force Microscopy. Workshop "Scanning Probe Microscopy in Nanometrology and Nanofabrication". Breslau (Polen). Juli 2001.

/6/ Jäger, G.; Manske, E.; Hausotte, T.; Büchner, H.-J.: Nanomessmaschine zur abbefehlerfreien Koordinatenmessung. tm 7-8. 2000. S. 319 - 323.

/7/ Jäger, G.; Manske, E.; Hausotte, T.: Nano Measuring Machine. Invited Paper. MICRO.tec 2000. VDE World Microtechnologies Congress. Hannover. September 2000.

THE POLAR PROFILOMETER *POLARIS*

Alexander Sohn, Kenneth P. Garrard, Thomas A. Dow
Precision Engineering Center, North Carolina State University, Raleigh, North Carolina

Introduction

Profilometers for form and roughness measurements have traditionally been based on cartesian geometry. Measuring parts with large aspect ratios presents a significant challenge for commercial measurement systems. Optical profilometers are slope limited to a few degrees by the ratio of fringe spacing to camera resolution. Mechanical profilometers are usually limited by the clearance angle of the tip and the non-perpendicular loading direction of the probe – both of which usually limit the measurable slope to less than 45°. Certain industries, those making high aspect-ratio optics in particular, require the measurement of geometries more polar than cartesian in nature. A polar profilometer, called *Polaris*, has been designed and built at the Precision Engineering Center to address this need. The device is capable of measuring figure as well as roughness on hemispheres and aspheres both concave and convex inside a circular measurement field 50 mm in diameter. The instrument can measure surfaces to a resolution of 22 nm and an overall accuracy of 200 nm.

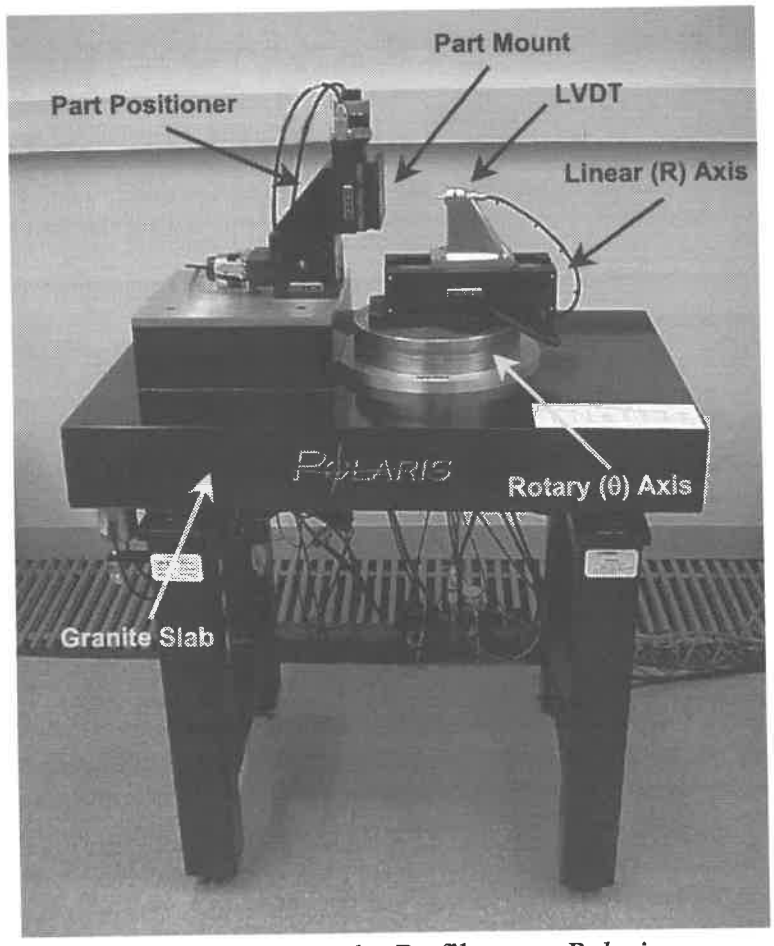

Figure 1. The Polar Profilometer *Polaris*.

Design

As shown in Figure 1, *Polaris* consists of an air bearing linear slide (R-axis) stacked atop an air bearing rotary table (θ-axis). The linear slide supports an air bearing LVDT sensor with 1.5 nm resolution at a measurement range of ±5 μm. Position feedback on the linear and rotary axes is via encoders with 20 nm and 1 μrad resolution, respectively. The axes are actuated by brushless, frameless motors to prevent disturbances from motor bearings or brushes. A three-axis part

positioning stage with vertical part mounting plate is actuated by stepper motors. The purpose of the positioning stage is to align the part with the measurement axes. The air bearing axes are then used to trace out a nominal cross-section of the part with the LVDT measuring deviations from this nominal path. Data acquired from the R- and θ- axis feedback signals and the LVDT can then be reduced to form both polar and cartesian surface profiles.

Error Budget

To evaluate a precision machine design's ability to meet specifications requires an error budget. Constructing an error budget involves adding the individual errors of the components in an appropriate manner to create the error for the entire system. Roll, pitch, yaw, straightness, and displacement errors in the linear air bearing slide were added to radial, axial, and tilt errors in the rotary air bearing to obtain geometric errors. Thermal errors have also been evaluated by defining a thermal circuit. The following strategy was followed. Based on the specifications of maximum errors of each component, a typical geometric error form was constructed. The shapes of the errors are somewhat subjective, but the maximum amplitudes are those given by the specifications. These geometric errors are then combined in three dimensions for the entire range of motion of the machine to give an estimate of the maximum obtainable errors and their directions. The target accuracy of the machine was 0.5 μm over the full measurement range.

Figure 2 shows the total predicted radial error (sum of the errors from all of the sources that influence the position) as a function of rotary axis position from -90° to +90° and linear axis position from -25 mm to +25 mm. The P-P magnitude in the radial direction is approximately 2 μm. The tangential direction and the vertical direction were also evaluated, but turned out to contribute substantially less to the total machine error.

From the geometric error evaluation, it is clear that the errors in the radial direction are larger than the error budget allows. However, this error can be compensated by moving the R-axis. All that is required is an error map in the control system that will issue a correction value according to the R- and θ- positions. Since the prime contributor to the radial

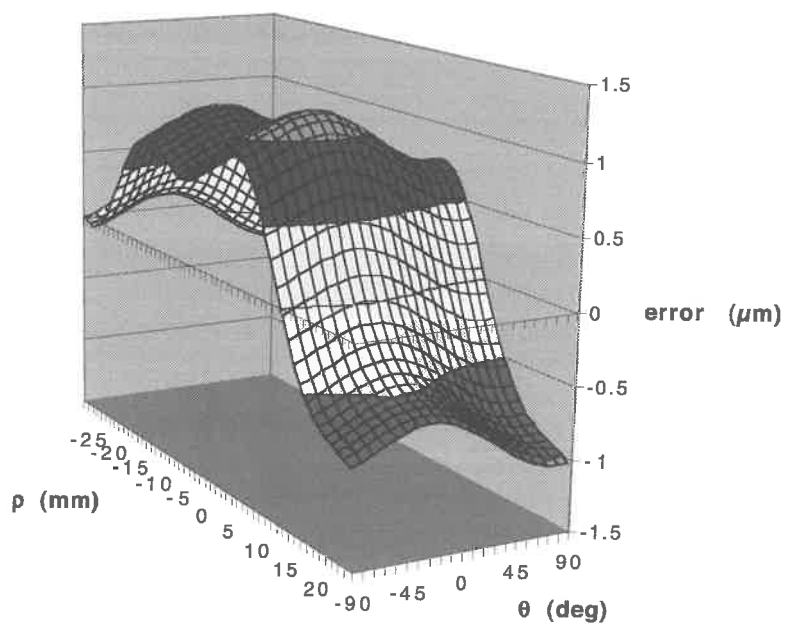

Figure 2. Predicted radial error. This error is dominated by errors in the linear slide pitch.

direction error is the pitch of the linear axis, this error was measured using an electronic level. The results of the measurement are shown in Figure 3 and indicate an error smaller than the prediction from manufacturing specifications.

LVDT Load

The LVDT probing force is critical since a 0.8 μm radius cylindrical tip is used. For coarse adjustments to the probing force, a setscrew at the rear of the LVDT housing is rotated. Fine adjustments are made by adjusting the air pressure to the probe with a precision air regulator. To measure the force, a flexure of known stiffness is placed into contact with the probe tip after it is adjusted to zero load. As the air pressure is increased, the flexure deflection is measured by the LVDT. Increasing air pressure increases deflection and thus the probing force proportional to the spring constant of the flexure increases. This allows the probing force to be adjusted to 0.1 mN (10 mg).

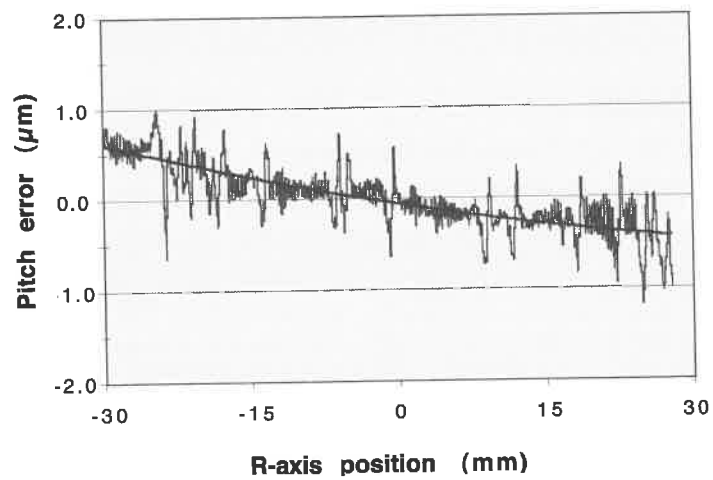

Figure 3. Pitch measurement results over the entire travel of the R-axis of *Polaris*. The pitch error at the probe tip is approximately 1 μm.

Controls

The machine hardware has been interfaced to a Delta Tau UMAC motion controller and a relay-based hardware emergency stop circuit has been built. PLCs to monitor the status of axis overtravel limits, the E-Stop loop, axis home status and the incremental handwheel jogger have also been implemented. Closed-loop control for the R- and θ- axes is handled by the UMAC's enhanced PID servo code. The axes are driven with a pair of linear amplifiers. The R-axis has a closed loop bandwidth of 50 Hz and the θ-axis has a bandwidth of 25 Hz. Both axes track desired motion profiles with sub-micrometer following error at a reasonable velocity which easily enables measurement scans to be taken with the LVDT probe set to a 10 μm range. Currently, the instrument is programmed in polar coordinates and data analysis is performed on the host PC with the JMP® statistical analysis software. Development of a comprehensive user interface that includes programming in cartesian coordinates and automatically generated post-measurement plots is currently in progress.

Calibration

Polaris was calibrated using a spherical calibration standard supplied with the Precision Engineering Center's Form Talysurf profilometer. The radius of this spherical standard is

specified to be 21.99220 mm ±25 nm. With the probe center positioned directly above the rotational axis of the rotary table, the part was independently crowned in the horizontal and vertical planes. This procedure locates the apex of the sphere relative to the axis of rotation in the measurement plane. Then the R-axis was moved to +21.99220 mm and the part moved an equal distance to maintain contact with the LVDT. At constant R, the θ-axis was rotated, scanning the LVDT probe across the surface of the part while data was collected on all axes. The collected data was combined and a circular radius of 21.99220 mm fit to the data. The resulting error plot shown in Figure 4 reveals the total measurement error (assuming a perfect calibration artifact). The measurement accuracy over the 90 degree measurement range is ±100 nm, well within the target machine accuracy of 500 nm.

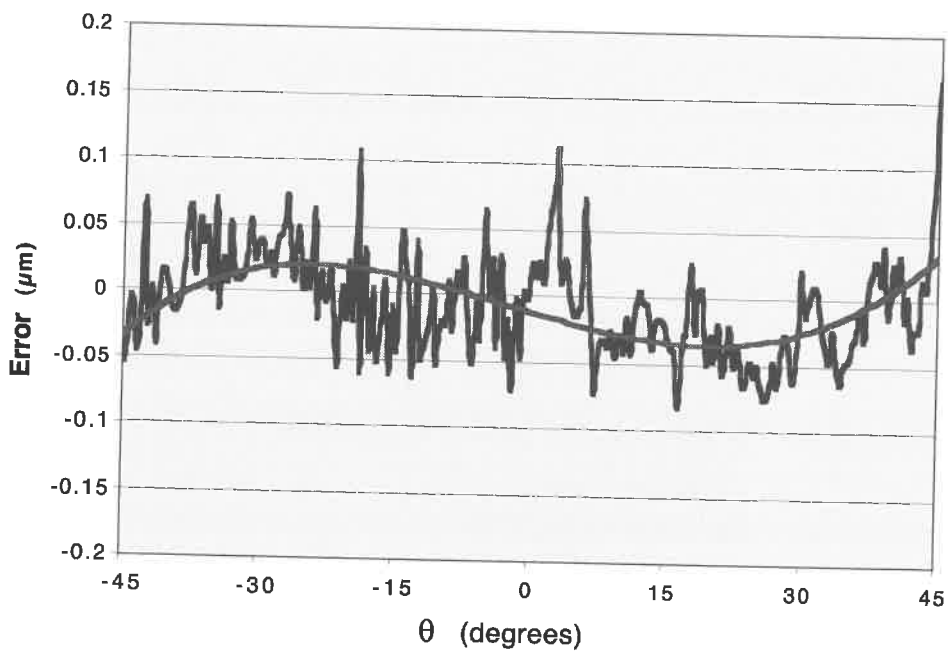

Figure 4. Measurement results obtained from a 21.99220 mm radius calibration sphere. The filtered deviation (smooth line) is less than 40 nm.

Conclusions

Final adjustments and calibration of Polaris have revealed that the machine has exceeded the goals for accuracy and resolution specified by the design. Previously difficult to measure parts such as large-aperture aspheres with binary surfaces can now be measured over a large included angle to an accuracy of better than 200 nm.

PLANAR AND SPATIAL THREE-DEGREE-OF-FREEDOM MICRO-STAGES IN SILICON MEMS

Bernhard Jokiel, Jr., Gilbert L. Benavides, Lothar F. Bieg, James J. Allen
Sandia National Laboratories*, NM

1 Introduction

Work in progress at Sandia National Laboratories (SNL) has led to the development of a family of micro-stages in silicon MEMS capable of multi degree-of-freedom (DOF) planar and spatial motions. The devices are built using parallel kinematic mechanisms (PKM) and are built in polysilicon using SNL's SUMMiT-V™ silicon surface micromachining process. The devices take up less than $3mm^2$ on the surface of a microchip. Included herein is an overview of the SUMMiT-V™ process, description of and experimental results for two planar devices, and design methodology for multi-DOF joints and spatial MEMS mechanisms.

2 Overview of SUMMiT-V™ Silicon Surface Micromachining

SUMMiT-V™ consists of five layers of structural polysilicon (n-type) separated by sacrificial silicon oxide layers built-up on a silicon-nitride coated, <100>, n-type, 6" silicon wafer substrate (Figure 1). Each of the layers are patterned and etched as is commonly done in integrated circuit production, which provides the means to create complex, interconnected, micro-mechanisms complete with motors, drive linkages containing spinning and translating elements with minimum feature sizes of 1μm.

Conformal layer Poly0 provides the ground plane. Conformal structural layers Poly1 and Poly2 may be laminated together to form a single layer, separated by SaxOx2 to form two separate structural layers, or connected together through a "pin joint cut" allowing the creation of free-spinning hubs for gears and rollers in Poly2 (Figure 1). Between the applications of the SaxOx3, Poly3, SacOx4, and Poly4 layers the patterned wafer undergoes chemical-mechanical polishing (CMP) to remove topology. Each layer may be connected to the layer beneath by patterning and etching the SaxOx layer below (Figure 1).

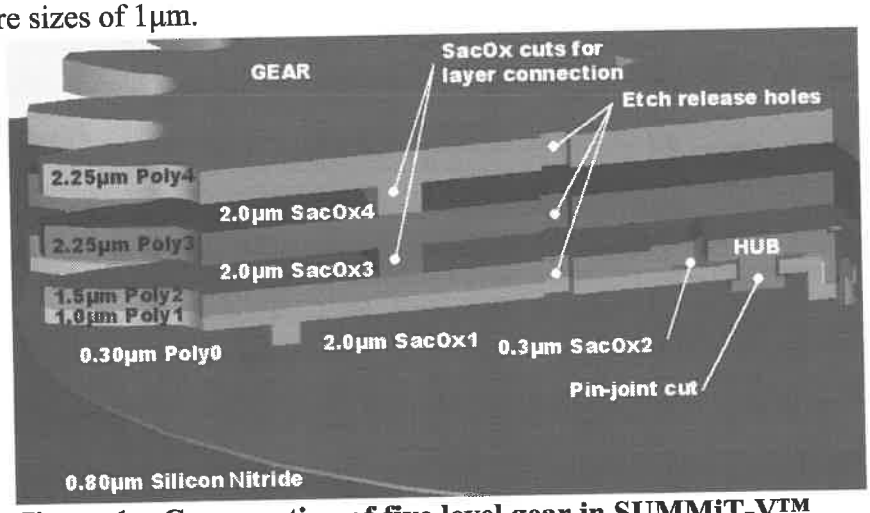

Figure 1 – Cross section of five level gear in SUMMiT-V™.

3 Planar Three-DOF Devices

By "planar" it is meant that the devices are constrained to move in a plane with three independently controllable DOF including translations along the X- and Y-axes and one rotation

---

* Sandia is a multiprogram laboratory operated by Sandia Corporation, a Lockheed Martin Company, for the United States Department of Energy under contract DE-AC04-94-AL85000.

Keywords: MEMS, SUMMiT-V, PKM, spatial, stages, silicon, Sandia, motion, position, control

about the Z-axis. This motion was accomplished by connecting each of the corners of a triangular, free-floating platform to a stationary linear drive by connecting rods and pin joints. By varying the extension of each of the three linear drives, the platform is moved around the workspace and controlled in both rotation and position in the X-Y plane (Figure 2a). Using this design two generations have been built using four layers of structural polysilicon, differing mainly by their actuation methods.

The first generation is powered directly by electrostatic combdrives (Figure 2a). This has the advantages of high velocity (at least 1kHz or 30mm/sec), six drive signals (two per actuator) plus one ground, but has the disadvantages of limited workspace due to combdrive stroke of 60μm and lack of positional control (combdrives lack position sensors). The second generation is powered by a stepping track drive (Figure 2b). Each stepping track drive utilizes three high performance combdrives (HPCD). Teeth connected to the HPCD's impinge a toothed track when actuated moving the track 1.6μm. Firing the combdrives in the order "1-2-3" moves the track forward. Reversing the firing order reverses the track motion. The track displacement is determined by multiplying the number of steps by the least-count motion (similar to a stepper motor). The stepping track drive has the advantages of positional control, allows workvolume scalability and flexible least-count motion. The trade-offs are reduced maximum velocity (at least 1.6mm/sec) and the need for nine drive signals instead of six.

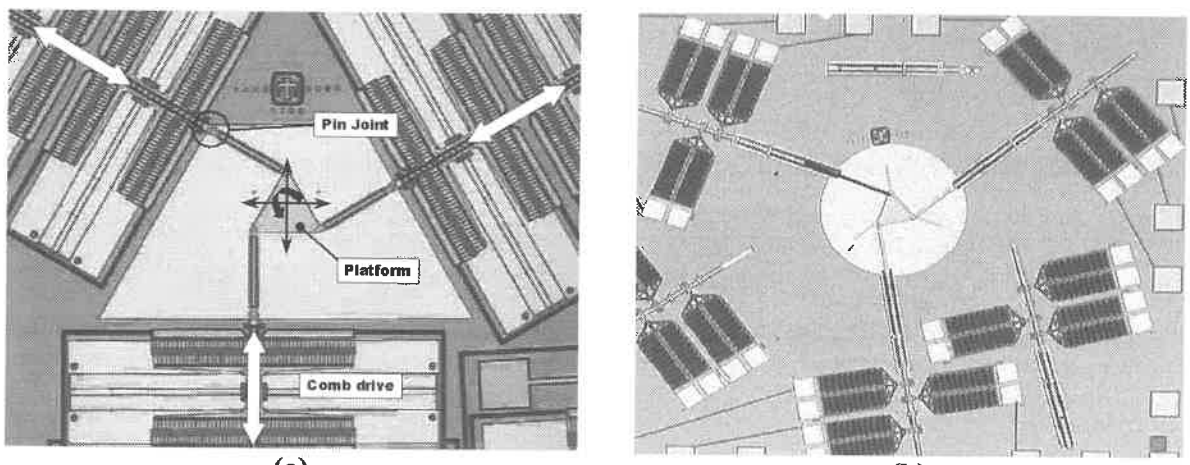

(a) (b)

Figure 2 – Planar three-DOF devices: (a) first generation; (b) second generation.

In testing, the first generation was found to be more reliable due in part to fewer components, but mainly to the flexibility in the toothed track. The HPCDs were strong enough to bend the track during actuation, causing it to jam in the guides and cause erratic motion of the track. In the second generation of the track drive, all of the HPCD's were moved to one side and push into the track. The new track is supported along its entire length on one side and incorporates a guide groove. This stiffer design and guide should solve the jamming problem.

4 Spatial Three-DOF Devices

By "spatial" it is meant that the platform is "popped-out" of the fabrication plane after release and may be moved along arbitrary, three-dimensional (3D) paths in space. Three unique, four layer designs were explored producing: (1) XYZ translational motion, (2) piston-tip-tilt (PTT) with Z translation and two rotations, and (3) spherical motion with variable radius and two rotations, and are powered using the second generation of the stepping track drive. Similar to the planar devices the corners (or sides) of the triangular platform are connected to linear drives by a

linkage, however due to the more complex platform motions, single-DOF hinge or pin joints are not sufficient (Table 1). Three-DOF spatial mechanisms have three legs, two independent kinematic loops, requiring a total of 15 independent DOF. Three of these DOF are driven by linear motors, leaving four DOF per leg that must be constrained, which leads to the need for two and three DOF compound rotational joints to construct any spatial PKM device. In response to this need four different joints were created (Figure 3).

Table 1 – Classification of Spatial Parallel Manipulators [1,2]

Platform DOF	# of Loops	Total Joint DOF	DOF per Leg
2	1	8	4,4; 5,3; 6,2
3	**2**	**15**	**5,5,5**; 6,5,4; 6,6,3
4	3	22	6,6,5,5; 6,6,6,4
5	4	29	6,6,6,6,5
6	5	36	6,6,6,6,6,6

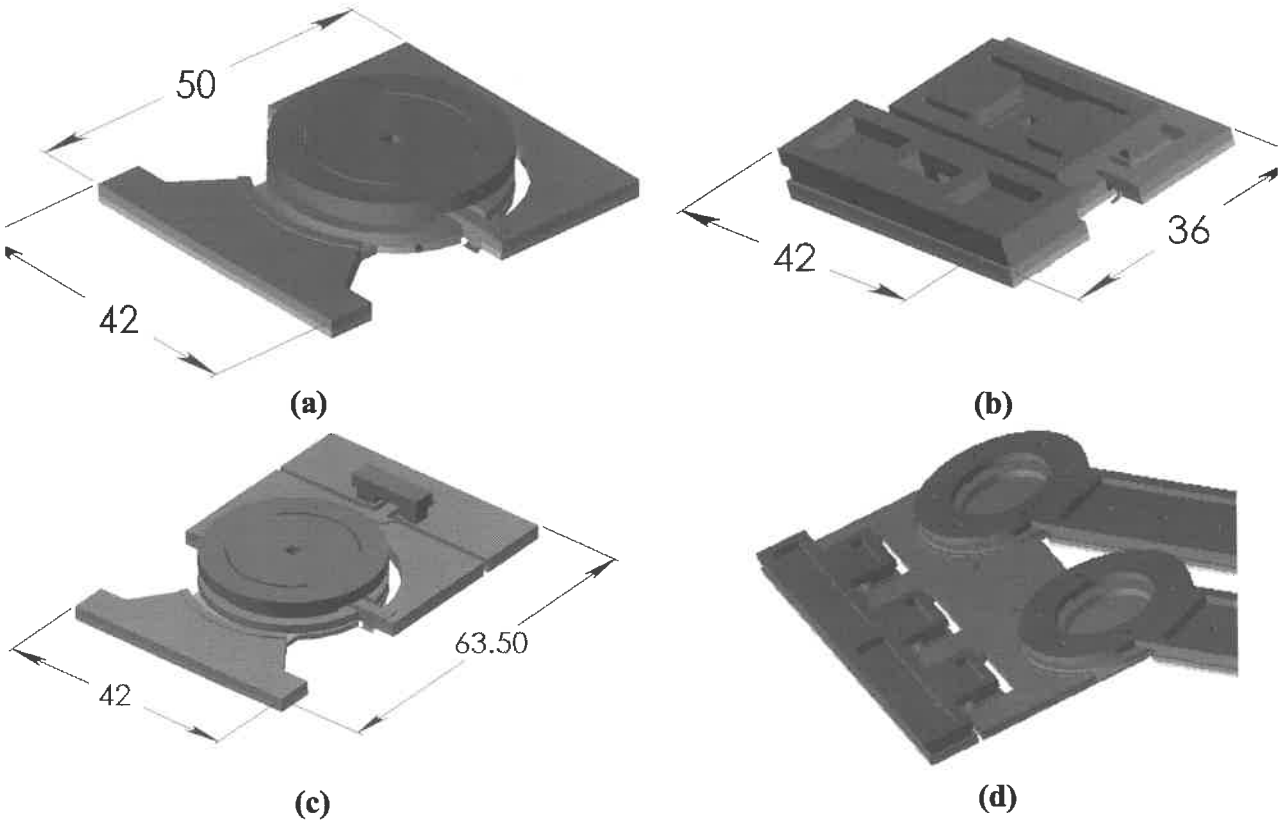

Figure 3 – Multi DOF SUMMiT-V™ rotary joints with intersecting and mutually orthogonal axes (units in μm): (a) C and A; (b) A and B; (c) A, B and C.

The XYZ stage consists of three, spatial four-bar linkages made from four joints (Figure 3d) to connect a platform to the wafer surface (Figure 4a) while allowing each linkage to rotate out of plane about its respective guideway line of action. This construction forces each side of the triangular platform to remain parallel to its respective guideway, constraining the unwanted three rotational platform DOF, while allowing the three translational DOF (XYZ) to remain controllable. Legs 300um long and a platform 230um wide, the device has a workvolume (approximated by a cylinder) of approximately 250μm high by 150μm in diameter.

Similar to the XYZ stage is the PTT stage. However the particular combination of joints allows the PTT stage to execute independently controllable, spatial, out-of-plane, Z translation plus two rotational DOF. Where the joints on the XYZ stage have two DOF that were perpendicular but not intersecting (Figure 3d), the PTT stage uses two different joint designs (Figures 3a and 3b) where the joint axes are perpendicular and intersecting. This constrains different platform DOF, allowing its unique motion. Again note each leg still has five DOF. Legs 188μm long and a platform 86μm wide allow the platform to move to 150μm above the wafer with approximately ±5° tip and tilt angles.

The spherical device is similar to a surveyor's transit tripod and is nearly identical to the PTT (Figure 4c). The important difference again lies in the joint construction. Moving one DOF from the platform joint to the base joint allows for three-DOF rotational motion of the base joint emulating a spherical joint - three mutually perpendicular joint axes intersecting at a single point (Figure 3c). The platform joints then become simple one-DOF hinges. This particular combination of joints allows the SD3 platform to execute motion in a spherical coordinate frame (R, phi, theta). Legs 200μm long and a platform 86μm wide create approximately a 150μm radius, 50° cone work volume.

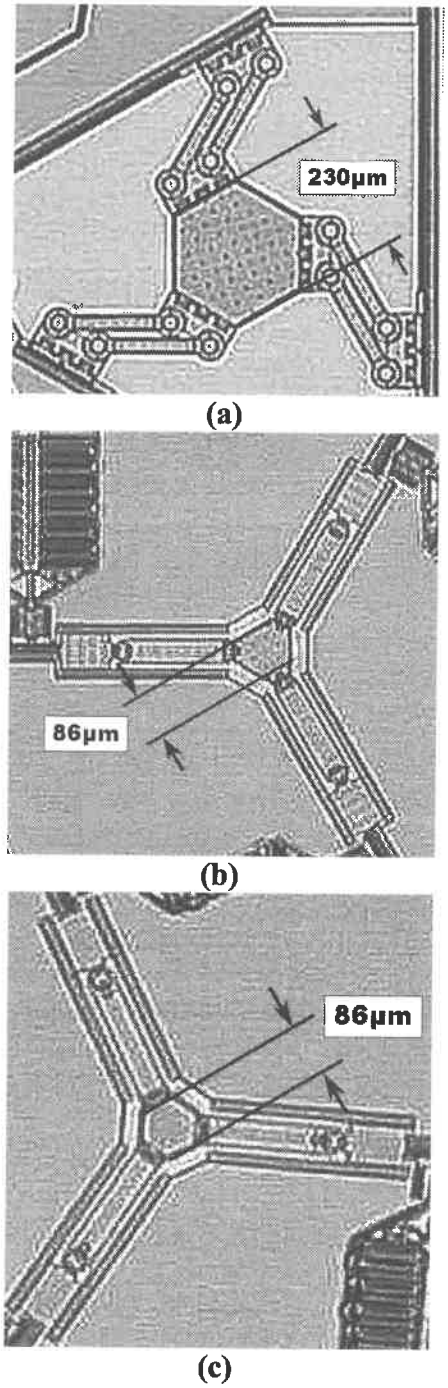

Figure 4 – SUMMiT-V™ spatial devices: (a) XYZ; (b) PTT; (c) Spherical.

5 Conclusions and Future Work

The construction and methodology of the devices is sound and provides the basis for continued improvement and refinement of planar and spatial MEMS devices. At the time this paper was written, the spatial devices had just finished being fabricated and had not yet been released. Upon release, the devices will all be fully tested and performance of the second-generation track drive will be assessed. This project will continue through 2002 and will produce more devices over two more fabrication cycles and will exhibit flexible multi-DOF joints and improved actuators. Before the end of 2002 we will have demonstrated a fully operational spatial microstage with sub-micron positional resolution.

6 References

[1] Tsai, L., 1999, Robot Analysis, John Wiley, pp. 121-125.
[2] Hunt, K. H., 1983, "Structural Kinematic of In-Parallel-Actuated Robot Arms,"*ASME J. Mech. Transm. Autom. Des.*,Vol. 105, pp. 705-712.
[3] Merlet, J., 2000, Parallel Robots, Kluwer, pp. 15-62.

Micro Screw Pump to Discharge Effusion from Human Middle Ear

M. Nakao, T. Okusa, A. Rahim, K. Matsumoto and Y. Hatamura
Department of Engineering Synthesis, Graduate School of Engineering
The University of Tokyo
Email nakao@hnl.t.u-tokyo.ac.jp

In this paper we report the development of a micro screw pump for discharging effusion from middle ear for treatment of otitis media. This tool extrudes effusion using a newly designed screw, which rotates at 90,000 rpm in a pipe penetrated through tympanic membrane. This tool satisfies the discharge performance especially for high viscosity effusion while it has smaller diameter such as about 0.5 mm. We also performed clinical application to prove its feasibility usage.

1. Introduction

For treatment of otitis media, suction of effusion is conventionally performed after puncture or myringotomy through tympanic membrane [1]. However cutting its radial fiber bundles causes unnecessary hypertrophy, scar and sclerosis [2]. Doctor needs to cut as small as possible, using a small penetrating pipe. But the small pipe can not suck high viscosity effusion. Doctor also needs to discharge effusion within 20 seconds. Generally, effusion volume inside middle ear is about 50 mm^3, so that discharge rate should be more than 2.5 mm^3/s. Also sound pressure level in the operation should be not harmful for patient's middle ear. Environmental Protection Agency suggests 75 dB as permissible sound pressure level.

To satisfy requirements above, we add a rotating screw inside the pipe. In this research we introduced the micro screw pump for discharging effusion from middle ear and verify its clinical application.

2. Design of micro screw pump

As the screw, we designed twisted wires as shown in Fig.1. To prevent their separation, we fixed them with acrylic resin cured by an ultra violet light. Next we inserted the twisted wire into a pipe as shown in Fig. 2. The pipe is an injection needle used in the hospital routinely. The twisted wires screw is flexible even in rotating; doctor can bent the pipe/screw at an angle in Fig. 2, operating it in a best posture while watching the tympanic membrane.

In the research, we designed three types of the micro screw pump appeared in Fig. 3. Type A using a DC motor has maximum rotation speed of 24,000 rpm. In results, this speed was not able to achieve enough discharge rate. Type B using an air turbine can increase rotation speed to 60,000 rpm, producing enough discharge rate. But in results, this is too noisy so that it needs a thick cover to reduce noise. Type C using a synchronous motor can increase to 90,000 rpm with a gearbox. The motor is designed for dentists to handle like a pencil; The tool satisfied doctors with its silence and its disinfection procedure. Each pump can sucked effusion using negative pressure made by a vacuum pump.

Consequently, we checked various design parameters: rotation speed (less than 90,000 rpm), inner

diameter of pipe (ID; 0.23, 0.3, 0.38, 0.45, 0.46, 0.56, 1.23 mm), outer diameter of twisted wires (OD; 0.16, 0.2, 0.24, 0.28, 0.32, 0.36, 1.1 mm), twisted angle (TA; 10, 15, 20, 25 degree), negative pressure (NP; less than 60 kPa). As standard viscosity fluid, we used 85, 450, 1800, 13000 mPa.s standard fluids.

3. Evaluation of micro screw pump

We evaluated the micro screw pumps as presented in Fig. 4 to Fig. 9. Especially we checked influence on its discharge rate under various design parameters mentioned above.

Fig. 4 shows discharge rate at various fluid viscosity under suction only, extrusion only and both. As sucking higher viscosity, discharge rate becomes lower drastically. But extrusion only performs constant discharge rate even at high viscosity. When using both suction and extrusion, we can get the summation of discharge rate each.

Fig. 5 indicates the same tendency with various screws/pipes. We calculated an ideal discharge rate assuming that the screw can extrude the volume inside its lead. Compared with the ideal rate, the experimental rate was by 1 – 3 % much smaller. The slip between screw and fluid should happen. For future plan to increase the rate much more, we are trying a square cross-section wire for another thick pump. The square one has higher rate by 3 – 7 times than the round one.

To increase the discharge rate, we increase negative pressure and rotation speed. Fig. 6 shows negative pressure is effective at lower viscosity. The rate increases twice at 100 mPa.s.

Fig. 7 shows, as rotation speed increases, the rate increases linearly. So faster type C is better than type A or B.

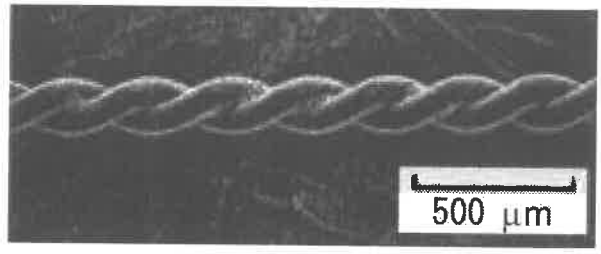

Fig. 1 SEM image of twisted wires for micro screw pump

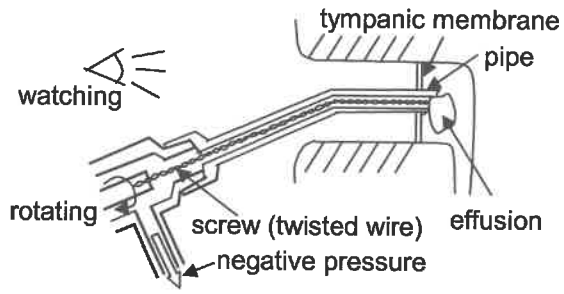

Fig. 2 Illustration of micro screw pump penetrating through tympanic membrane

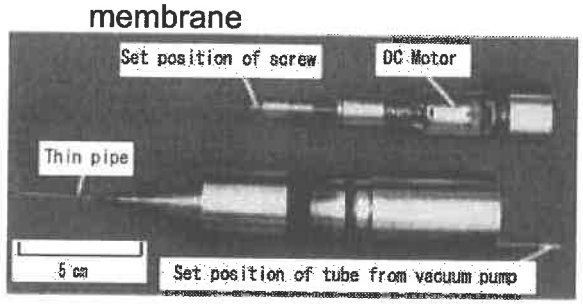

a. Type A using DC motor

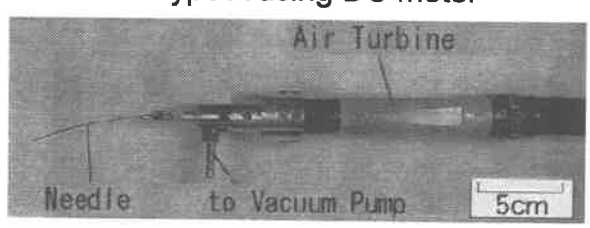

b. Type B using air turbine

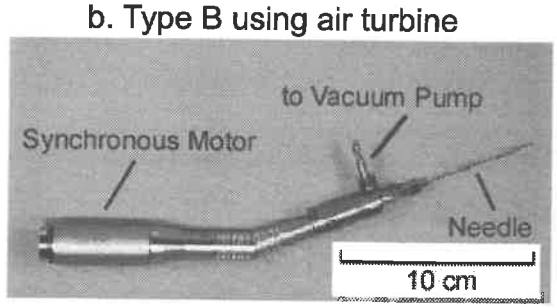

c. Type C using synchronous motor

Fig. 3 Appearances of three types of micro screw pump

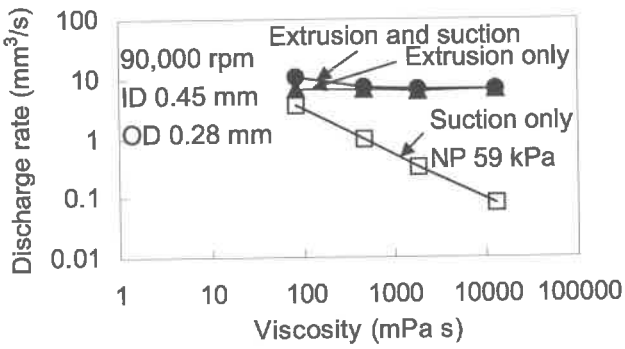

Fig. 4 Discharge rate at various fluid viscosity under extrusion and suction

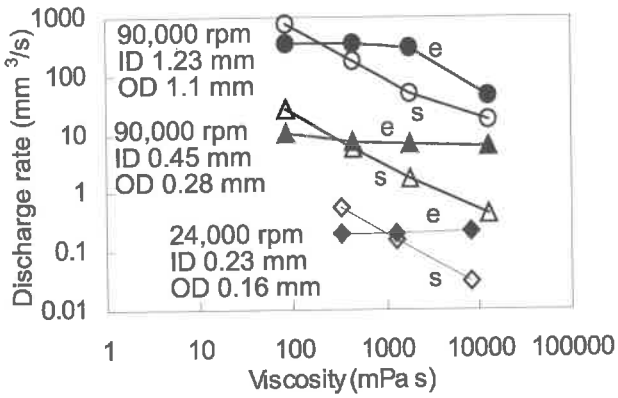

Fig. 5 Discharge rate at various fluid viscosity under extrusion (e) and suction (s)

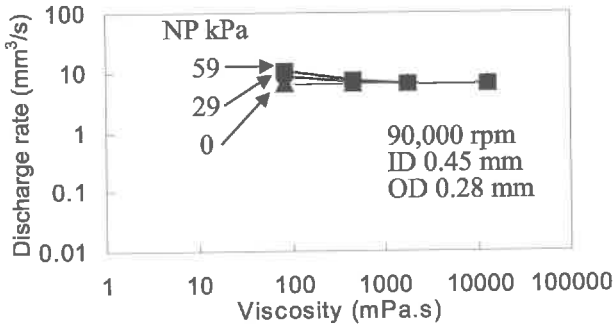

Fig. 6 Discharge rate at various fluid viscosity under suction of negative pressure

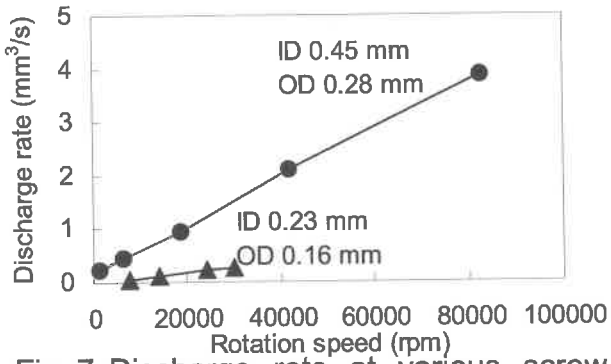

Fig. 7 Discharge rate at various screw rotation speed

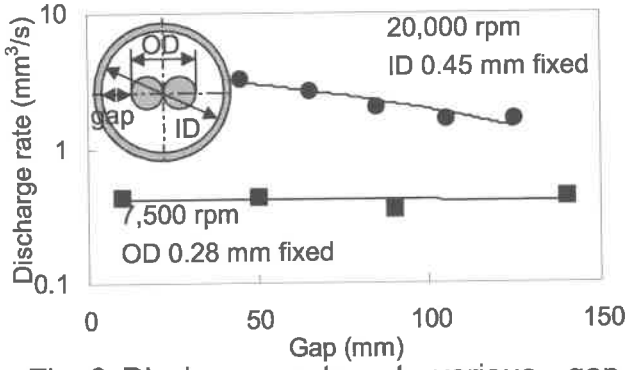

Fig. 8 Discharge rate at various gap between pipe and screw

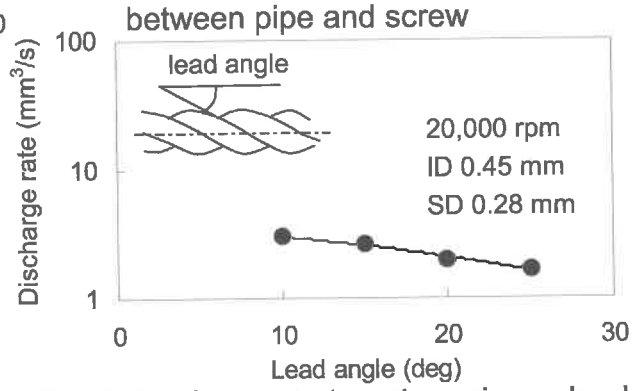

Fig. 9 Discharge rate at various lead screw

Fig. 10 Clinical application

Fig. 8 indicates that the gap between the screw and the pipe almost doesn't affect the rate. We observed the flow inside the pipe using a 450 mPa·s fluid with aluminum powders; the fluid which was 10 μm away from the screw didn't move; the large slip happened; the gap of more than 10 μm is not effective for the discharge rate, but it is necessary for easy insertion of the screw into the pipe. Fig. 9 shows the influence of lead angle of the screw on discharge rate; lower angle is twice better in 10-25 degrees range.

Now we clinically applied the micro screw pump as shown in Fig. 10. Its parameters were the following: type C, 90,000 rpm, ID 0.45 mm, OD 0.28 mm, NP 51 kPa, TA 20 degree. We successfully performed 27 cases (80 %) out of 34 cases. The failure cause of 7 cases was high viscosity of effusion which looked like a solid, or small volume of effusion which stayed on the inside wall of middle ear.

We need more cases, but now we conjecture from effusion viscosity distribution measured by us that conventional suction using the ID 0.6 mm pipe could discharge only about 25 percent of 12 cases, and the micro screw pump could also discharge the rest of cases.

Sound pressure level of type C was 72 dB. It was below tolerable level. It was measured at 15 mm distance from tip of the pipe, namely near ear of the patient.

4. Conclusions

To discharge effusion from middle ear under minimum invasion, we developed the micro screw pump using twisted rotating wire. This tool successfully treats the 80 % operations within 20 seconds under the 90,000 rpm rotating screw and the 0.45 mm inner diameter of pipe.

5. Acknowledgment

We thank to Prof. Ishii, Prof. Takayama and Dr. Kawano of Tokyo Women Medical College for design suggestion and for clinical application. This research was supported by Organization for Pharmaceutical Safety and Research (OPSR) of Japan.

6. Reference

1. Cummings, Charles W. et.al., "Otolaryngology-Head and Neck Surgery Volume 4", The C.V. Mosby Company, St. Louis, pp. 2963-2988, 1986.
2. Takayama, M. et.al., "Clinical Application of A Micro-pump for Aspiration of Fluid in Otitis Media with Effusion", Abstract Otitis Media 2001, Sendai, pp. 78, 2001.

High Precision Assembly and Metrology of X-ray Foil Optics

Olivier Mongrard[a], Nat Butler[a], Carl G. Chen[a], Ralf K. Heilmann[a], Paul T. Konkola[a], Mike McGuirk[a], Glen Monnelly[a], G.S. Pati[a], George R. Ricker[a], Mark L. Schattenburg[a] and Lester Cohen[b]

[a]Center for Space Research, Massachusetts Institute of Technology, Cambridge, MA 02139, USA

[b]Harvard-Smithsonian Astrophysical Observatory, Cambridge, MA 02138, USA

Keywords: x-ray telescopes, x-ray optics, Constellation-X, microstructures, mirror alignment, precision assembly, MEMS

1. INTRODUCTION

Achieving arcsecond angular resolution in a grazing-incidence foil-optic x-ray telescope (such as the segmented mirror approach being considered for the NASA Constellation-X mission) requires accurate placement of thousands of individual foils. We have developed a method for assembling large numbers of nested, segmented foil optics with sub-μm accuracy using lithographically defined and etched silicon alignment microstructures, called microcombs (Fig. 1). A system of assembly tooling incorporating the silicon microstructures, called an assembly truss, is used to position the foils that are then bonded to an engineered flight structure. The advantage of this procedure is that the flight structure has relaxed tolerance requirements while the high accuracy assembly tooling can be reused.

2. MICROCOMB DESIGN

Our high accuracy alignment technique is enabled by silicon microcombs that are etched from a silicon wafer using microelectromechanical systems (MEMS) technology.[1] They offer two distinct advantages over other techniques for mounting segmented foil optics. First, our fabrication technique provides the sub-μm accuracy which is a general characteristic of the lithographic process used in the MEMS industry, allowing for highly accurate foil placement. Second, it is possible to make intricate structures such as the leaf springs on the spring microcombs and the precisely round reference surfaces of the reference microcomb.

2.1. Design requirements

Many of the requirements of the microcombs design relate directly to the properties of the foil optics being mounted, particularly edge roughness, thickness variation, and figure errors. The baseline for the Constellation-X/SXT design is to use epoxy replication with a glass substrate. Because the edges of the foil are generally rough compared to interior surfaces, the mounting point should ideally be a small distance away from the edge so that contact can be made with the smooth mirror surface. The alignment bars of previous generation had no provision to mount the foils with a contact point other than the edge.

Replicated foils have typical thickness variations of 20 μm, which is due mostly to the glass substrates. Conventional spacer techniques would therefore lead to large placement errors. Even the novel "stack-up and grind" assembly method considered for the High Energy Focusing Telescope (HEFT)[2] has an accuracy limited to a few microns. To accommodate the thickness variations, we use micromachined leaf springs that force the foil against the reference surface of the reference microcomb (Fig. 2).

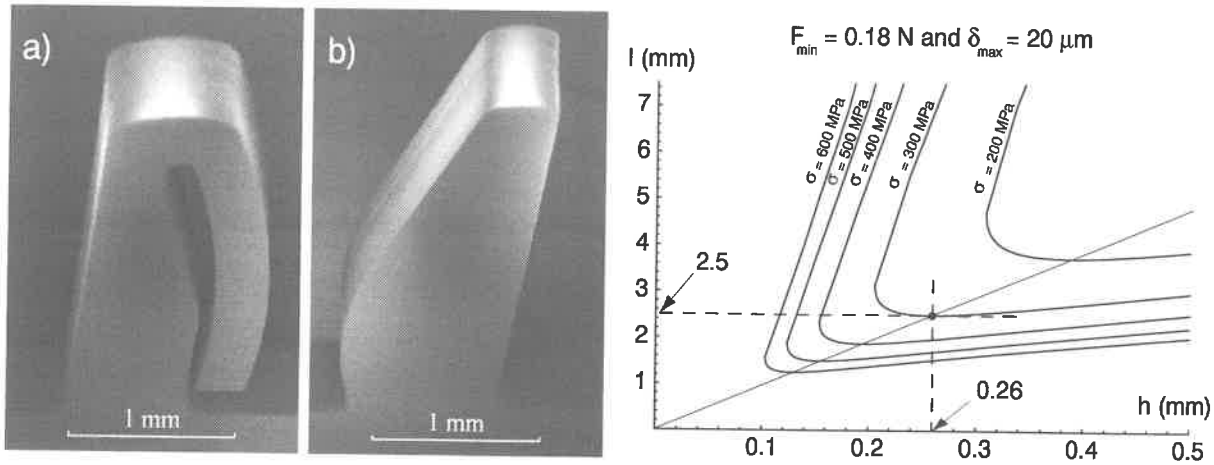

Figure 1. (*Left*) Scanning electron microscope (SEM) images of our silicon spring (a) and reference (b) microcombs. (*Right*) Leaf spring length l vs width h curves calculated for five different stress values.

2.2. Leaf spring design

We have developed a simple description of the mechanical requirements of the spring microcombs leaf spring that is used to optimize its dimensions. The foil optics will generally have figure errors where the shape of the foil differs from the ideal, so that the foil will have to be distorted to make contact with the reference microcomb. The leaf springs are designed so that for the expected range of thickness variation, enough force is applied to the foil to move it into place, overcoming frictional forces and the effects of figure errors in the foils.

Our analysis, based on analytic and finite element calculations, allows us to search all possible leaf spring geometries (parameterized by spring length and thickness) to minimize internal stresses given the substrate mounting requirements. The minimum load F_{min} is the force required to force a foil into its desired shape. The leaf spring displacement must accommodate not only an "equilibrium" displacement, $\delta^* = \delta^*(F_{min})$, but also the maximum foil-to-foil thickness variation δ_{max}. Knowing both F_{min} and δ_{max}, we can design the leaf spring such that the maximum stress encountered, when applying to it a displacement $\delta = \delta^* + \delta_{max}$, remains below an allowable stress level, defined as $\sigma_A = 300$ MPa, inferior to the nominal breaking strength of silicon, $\sigma_{max} = 566$ MPa.

An analytical analysis of the leaf spring, modeled as a flexible cantilever, is used to generate, for each stress σ input, a corresponding leaf spring length l vs width h curve.[3] For $\sigma = \sigma_A$, the most compact design is $l = 2.5$ mm and $h = 0.26$ mm (Fig. 1). Subsequent finite-element modeling refined these values to $l = 3.5$ mm and $h = 0.35$ mm.

3. PLACEMENT ACCURACY TESTS

Direct measurements of the dimensions of the microcombs using a microscope and precision translation stage have shown that the microcombs are fabricated to a higher tolerance than the 2 μm resolution of the measurement. To more accurately characterize microcombs, we have designed a series of experiments that uses our breadboard test assembly system to specifically measure the alignment capabilities of the microcombs.

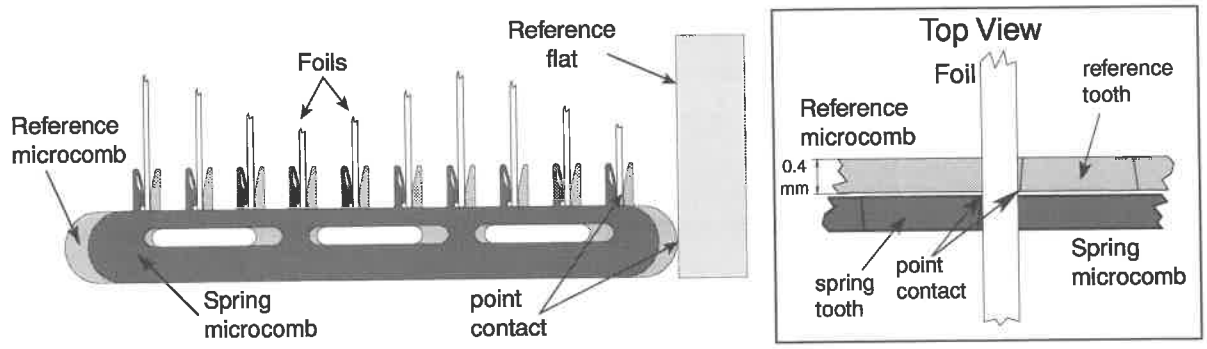

Figure 2. Foils are referenced by the spring microcombs against the reference microcombs which in turn are referenced against a flat reference surface. All the references are made by point contacts as illustrated in the top view of a foil being clipped in between a reference tooth and a spring tooth.

The system has a rectilinear geometry and is designed to mount a nest of parallel foil optics. Since we are currently not able to manufacture foils with accuracy comparable to the alignment accuracy of the microcombs, we instead used rigid flat plates. The plates are $102\times102\times2.3$ mm^3 fused silica and are held inside the assembly truss using three spring-reference microcomb pairs (Fig. 3). The tests are designed to measure the parallelism of a plate mounted in different "slots" of the assembly truss. A microcomb slot is the space between one reference tooth and its corresponding spring tooth. Angles are measured with an autocollimator which reads out μrad in pitch and yaw with a resolution of 0.1 μrad.

The repeatability of mounting of a plate in a given slot was measured by a repeated process of sliding a rigid flat plate against the reference microcomb teeth in a given slot, measuring its angle, then removing it. Results of repeatability tests show a typical 1 σ mounting repeatability error of about 0.11 μm in both axes. To measure mounting variations between slots, the plate was installed in several different slots and for each slot, five measurements were made. Variation between slots corresponds to a 1 σ slot-to-slot mounting error of less than 0.5 μm in both pitch and yaw. To measure alignment between the mounted plate and the reference flat (Fig. 2), the angle of the plate and reference flat were compared with the plate mounted in several different slots. Results of reference flat measurements, corrected to only show errors due to the microcombs,[4] shows a mounting accuracy standard deviation of 0.3 μm in pitch and 0.4 μm in yaw. This result is encouraging. It suggests that the reference between the microcombs and reference flat is as good as the reference between the microcombs and the rigid plate, both being accurate to about 0.5 μm.

Another series of experiments has addressed the impact of the spring microcomb on the alignment capacity. It has consistently shown that the force applied by the spring microcomb (Fig. 3) affects the placement accuracy. In fact, the error introduced is quasi-linear with respect to the leaf spring displacement and therefore with respect to the force. The maximum error is about 0.7 μm and is obtained when the leaf bottoms out, i.e. when the force is $\sim$0.36 N.

It is hypothesized that the distortion of the contact interface between the reference microcomb and the foil is due to contact stresses. Contact stresses occur when curved surfaces of two bodies are pressed together by external loads. The Hertz theory provides a useful set

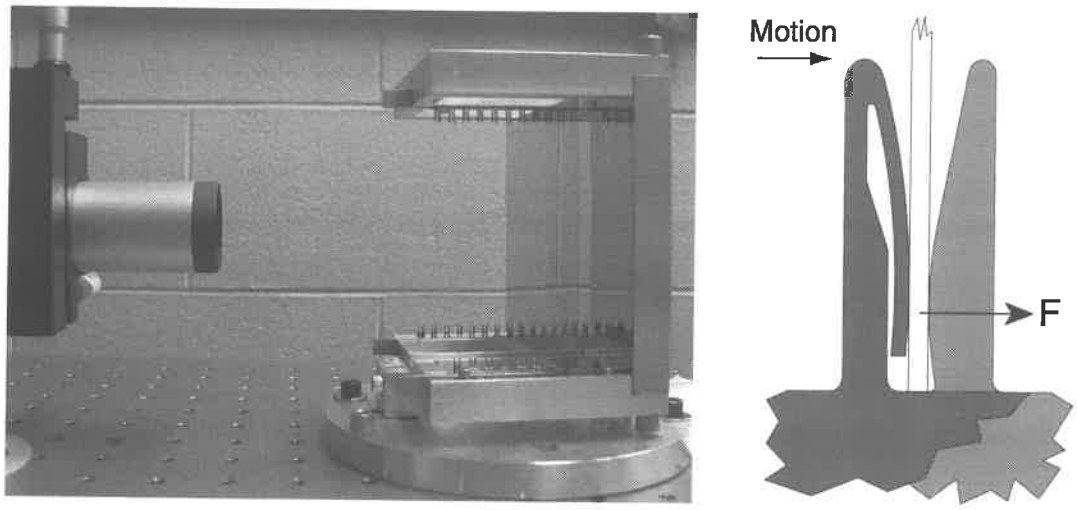

Figure 3. (*Left*) Autocollimator pointing at a rigid flat plate in the assembly truss. (*Right*) Spring microcomb applying a force on the back of a foil.

of equations for the contact stresses between surfaces with only one radius of curvature each which allowed us to confirm our hypothesis.[3]

On the one hand, since the main component of the forces applied to the foils during the assembly process can be predicted, we can take their effect into account while designing the reference microcombs. On the other hand, some effects such as friction or thickness variation cannot be predicted and therefore could introduce errors. For example, the effect of the thickness variation of the substrate would lead to an error between the placement of the thicker and the thinner substrates of about 0.26 μm.

4. CONCLUSION

We have described the requirements and design process of the microcombs used inside an assembly truss to provide subarcsecond foil placement. Tests performed thus far have demonstrated that the alignment system can mount rigid flat plates with a positioning tolerance typically better than 0.5 μm, resulting in a high degree of parallelism that for the Constellation-X design would correspond to a $\sim$1 arcsecond resolution. These tests have also underlined the effects of Hertzian contact stresses on the placement accuracy.

REFERENCES

1. C. G. Chen, R. K. Heilmann, P. T. Konkola, O. Mongrard, G. P. Monnelly, and M. L. Schattenburg, "Microcomb design and fabrication for high accuracy optical assembly," *J. Vac. Sci. Technol. B* **18**, pp. 3272–3276, 2000.
2. W. W. Craig, F. E. Christensen, T. Decker, C. J. Hailey, F. A. Harrison, R. M. Hill, M. Jimenez-Garate, P. Mao, and S. Schindler, "Hard X-ray Optics for the HEFT Balloon Borne Payload: Prototype Design and Status," *Proc. SPIE* **3445**, 1998.
3. O. Mongrard, "High-accuracy foil optics for x-ray astronomy," Master's thesis, Massachusetts Institute of Technology, 2001.
4. G. P. Monnelly, O. Mongrard, D. Breslau, N. Butler, C. G. Chen, L. Cohen, W. Gu, R. K. Heilmann, P. T. Konkola, G. R. Ricker, and M. L. Schattenburg, "High-accuracy x-ray foil optic assembly," *Proc. SPIE* **4138**, pp. 164–173, 2000.

Precision relational metrology of flatness, thickness, parallelism and step height

Xavier Colonna de Lega, Peter de Groot, David Grigg
Zygo Corporation, Laurel Brook Rd, Middlefield CT 06455

1. Introduction

Using Geometric Dimensioning and Tolerancing as a common language, engineers design, manufacture and qualify precision-machined parts. This framework defines the allowable deviation of actual part features from their ideal geometrical form, such as profile or flatness, as well as deviations from ideal relationships between features, such as parallelism or size. The traditional metrology tools used to verify compliance to these tolerances include a large range of tactile, pneumatic and electronic gages. However, certain tolerances have reached the micron level, requiring new metrology solutions for the production floor and the quality control lab. A good example is the automotive industry, where tighter emission levels drive the efficiency requirements of fuel systems, resulting in more demanding mechanical designs.

Because the tolerances of interest are on the order of 1-10 microns, new metrology solutions must achieve sub-micron accuracy, which is well within the capability of interferometers. However, an interferometer suitable for form and relationship measurements on machined parts must possess a number of unique features. Primarily, this optical tool must accommodate varying degrees of surface roughness and yet provide high-resolution surface measurements, look at parts from different viewpoints and relate the data collected from these viewpoints to a common coordinate system.

In this context, we present an instrument that combines two surface profilers with a 2-axis displacement measurement interferometer, effectively allowing the profilers to share a common datum plane. This metrology frame enables the simultaneous measurement of flatness, thickness, parallelism and step height on a variety of machined parts.

2. IR scanning interferometry

There is a large number of optical techniques that could be used to design a rough surface profiler. However, we can narrow the choice down fairly rapidly given the requirements stated above. Moiré, fringe projection, visible wavelength low-coherence interferometry, holographic or speckle contouring do not consistently provide the required sub-micron resolution[1,2]. Grazing incidence interferometry, while capable of meeting resolution requirements, is strongly limited by shadowing effects, precluding the measurement of most recessed surfaces. Geometrically desensitized interferometers[3] and infrared interferometers[4] are thus better suited for our application. The additional requirement of locating the measured surface without fringe ambiguity with respect to an optical datum further narrows the spectrum of solutions. Multi-wavelength infrared interferometry[5] is one but we opted for a different route, based on low-coherence interferometry.

The mode of operation of the profiler is very similar to that of white-light interference microscopes. In practice, this profiler can be described as a Michelson interferometer where the

source is a simple glowing filament – providing a quasi-infinite lifetime at a negligible cost. The interferometer is scanned by translating the reference mirror over a couple hundreds of microns. The acquisition system detects the presence of an interferogram at each pixel and records the corresponding intensity samples. The data is then processed using Frequency Domain Analysis[6], which provides an absolute height estimate for each pixel, relative to the starting point of the scan. Note that each pixel is processed independently from its neighbors.

In our experience, most tightly-toleranced ground or lapped metal parts become mirror-like at wavelengths longer than 5 µm. Also, metals, ceramics and ground glass surfaces that exhibit large reflectivity variations at visible wavelengths appear uniform in the infrared. There are some benefits to using the 3-5 micron wavelength band given both the high sensitivity of InSb and PtSi cameras and the peak emission of simple blackbody sources around 800K. On the other hand, the longer wavelength band (8-12 micron) provides improved robustness for rougher surface finishes.

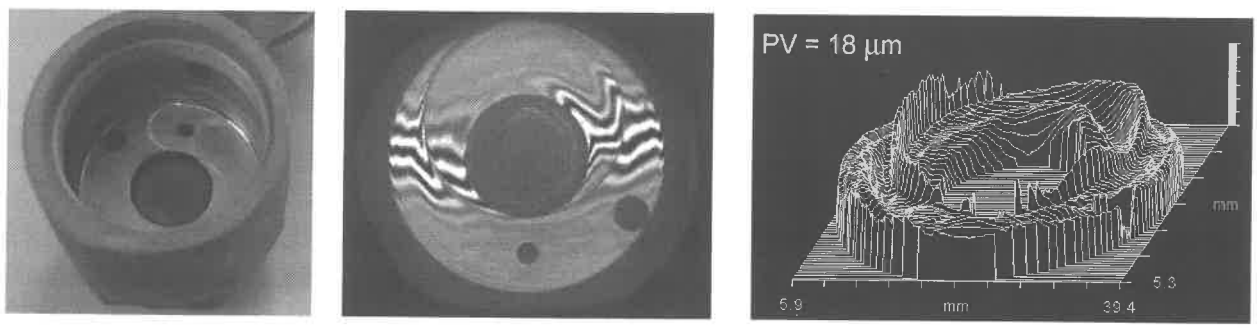

(a) (b) (c)

Figure 1: (a) Recessed machined surface; (b) Infrared interferogram; (c) Absolute height map.

As an example, Figure 1 shows the fringe pattern and height map obtained with a 10-µm Michelson interferometer when measuring a recessed surface that presents tool marks and burrs. The IR scanning technique consistently demonstrates 1-σ repeatability better than 0.01 µm for flatness measurements, and is thus suitable for characterizing precision-engineered parts down to 0.5-µm flatness tolerances.

3. Measurement of parallelism and size

Let us now consider a flexible tool capable of measuring the flatness of two opposing surfaces on a part, as well as their parallelism and the corresponding size (or thickness). Starting with two profilers facing each other and sharing a common measurement volume, we can imagine measuring a reference part with each device simultaneously. The knowledge of this reference artifact flatness, thickness and parallelism allows to unambiguously relate the measurement volume of one profiler with respect to the other. In effect, this procedure allows to "zero" the instrument. We can then place other parts in the common measurement volume and characterize their flatness, parallelism and size. There are however two limitations with this approach. First, given the limited range of the scanning stages used in each profiler (300 µm), it is only possible

to measure parts that have the nominal dimensions of the reference part. Second, small mechanical drifts of one profiler with respect to the other could easily compromise the system accuracy.

For these reasons we add to the system a displacement measurement interferometer (DMI). The purpose of this tool is to constantly track the relative position of the two profilers, allowing to take into account any drift from one measurement to the next. In fact, thanks to this tracking capability, we actually gain the freedom to purposely move one profiler with respect to the other. Going one step further it is now possible to move the two profilers to accommodate for different part size and position. This is the basis for our design.

In practice, we merge the two profilers such that they share the reference mirror, beam splitter and camera. The sketch in Figure 2 shows the key elements of the interferometers (the illumination system has been removed for clarity; the two lenses are the first elements of the imaging system). The ray fans materialize the two optical paths that image two opposite sides of a part side by side on the camera. The rays going to the reference mirror symbolize the reference legs of the two embedded interferometers. The two roof mirrors are mounted on translation stages, which allows covering a 100-mm part thickness range, as well as periodically "zeroing" the instrument by measuring one side of the reference window (as shown in Figure 2b). In effect, this surface behaves as the reference artifact described earlier, with the benefit of perfectly well known parallelism and thickness characteristics (both zero in this case).

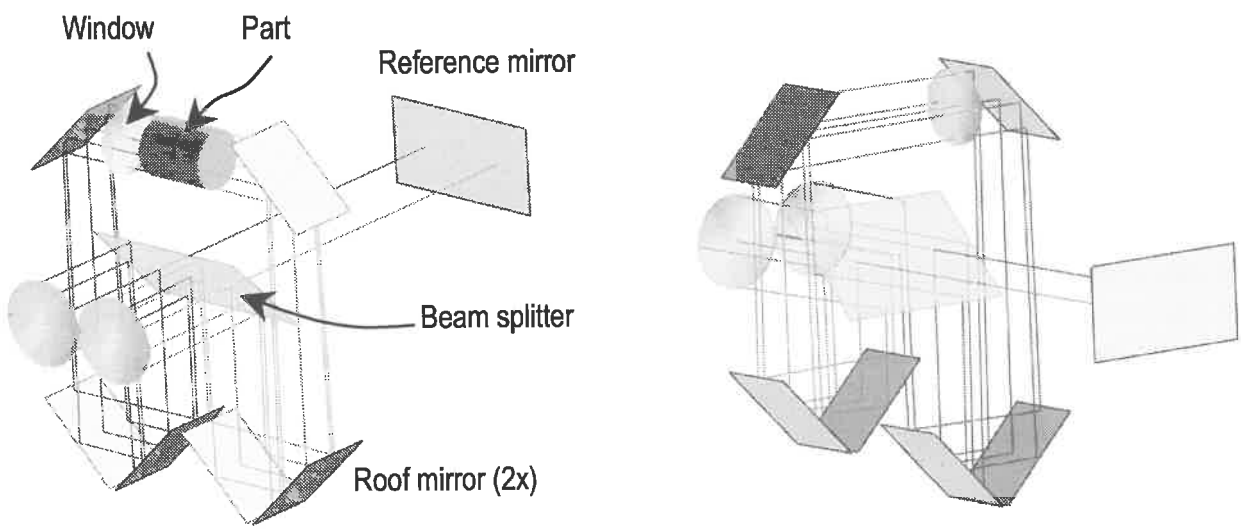

Figure 2: (a) Dual-profiler setup with common reference mirror; (b) Reference measurement.

The DMI system (not shown on the figure) snakes through the test and reference legs to monitor any drift of the two cavities as well as the effective displacement of the two roof mirrors when adjusting thickness. A careful study of the system symmetries shows that only two DMI axes are required to monitor the system. Indeed, certain mirror and beam splitter motions only result in an apparent tilt of the part with respect to the instrument, leaving parallelism and size unaffected. This greatly simplifies the system design.

4. Capabilities

The sketch shown above forms the basis of a shop floor instrument dedicated to the measurement of flatness, thickness and parallelism[7]. The measurement volume is 100-mm long with a maximum part diameter of 75 mm. The 1-σ repeatability (measured with part loading and unloading) is 0.02 μm for flatness, 0.06 μm for thickness and 0.03 μm for parallelism. The 2-σ uncertainty is respectively 0.10 μm, 0.30 μm and 0.15 μm for these same 3 parameters. The complete measurement cycle takes less than 10 seconds per part.

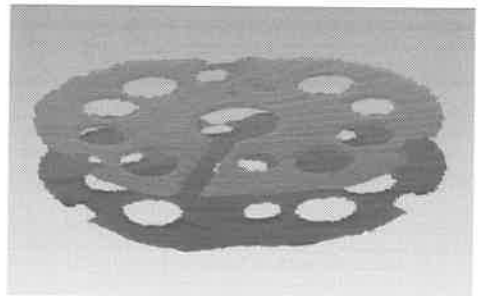

Figure 3 3D reconstruction of a part showing machining tool marks.

It is important to note that since both sides of a part are fully characterized, the user has absolute freedom in the definition of the datum surfaces used for the determination of parallelism and size. For example, one can choose a plane defined by the three highest points on the surface instead of a simple RMS fit plane. Finally, because of the high spatial sampling associated with optical techniques, the user collects a wealth of information about his process capability, including machining defects such a burrs and taper (see tool marks in Figure 3).

5. Conclusion

The approach outlined in this paper is the basis for an instrument that measures simultaneously flatness, parallelism and size of precision-engineered parts. Using the same metrology framework it is straightforward to extend the technique to step height measurements. The practical performance of this tool allows controlling and binning tightly tolerance-machined parts in a production environment.

6. References and notes

[1] Häusler, G.: About the scaling behaviour of optical range sensors. In: Fringe'97. Jüptner, W.; Osten, W., Ed., Akademie Verlag Series in Optical Metrology, 1997, 147-155.

[2] Flatness is frequently measured as the peak-valley deviation of the surface from its RMS-fitted plane. In this case, according to typical industry Gauge Repeatability & Reproducibility procedures, a 1-micron flatness tolerance requires the metrology instrument to be repeatable to better than 20 nanometers (1-sigma).

[3] de Groot, P.: Diffractive grazing incidence interferometer. Applied Optics, 39(2000)10, 1527-1530.

[4] Ai, Chiayu: IR interferometers using modern cameras. Proc. SPIE, 3134(1997), 461-464.

[5] Bourdet, G. L.; Orszag, A. G.: Absolute distance measurements by CO2 laser multiwavelength interferometry. Applied Optics, 18(1979)2, 225-227.

[6] de Groot, P.; Deck, L.: Surface profiling by analysis of white-light interferograms in the spatial frequency domain. J. Mod. Opt. 42 (1995) 2, 389-401.

[7] Infrared scanning, FDA and the Simetra product line are covered by issued and pending patents assigned to Zygo Corporation.

A Recommendation Inspection to Control Sub-Surface Damage in Sapphire

Nat'l Institute of Standards & Technology, Manufacturing Metrology Division
Gaithersburg, MD 20899 – E-mail: robert.polvani@nist.gov

We will recommend an inspection practice for single-crystal optics, we do this with a hope: that it is a good start on developing a generally useful sub surface damage inspection standard serviceable for all single crystal based optics. The approach, which is now well demonstrated as effective for sapphire, requires test pieces successfully progress through four separate inspection steps. Passage from one step to the next is conditional on passing the current one. Failure at any step requires rejection and return for reworking. These steps range from using shop floor practices - a careful visual inspection - onto use of x-ray topography, an advanced diagnostic. The possibility to rework inspected parts is the key argument for just inspecting, over using proof testing. Preferably, both are and would be used as complementary methods.

This approach to inspection distills our experiences with the Sapphire Statistical Characterization And Risk Reduction (SSCARR) Program. SSCARR tried to establish a fracture-strength database for sapphire windows and domes, and to develop means to detect and control subsurface damage. SSCARR specifically raised the questions: what allowances in both the fabrication of parts and performance expectations for parts must be made for subsurface damage? NIST's role was to identify and evaluate ways to non-destructively inspect sapphire for sub surface damage, SSD, and to then recommend a "practical" detection practice. Eleven different forensic methods were considered. A second task was to correlate pre-inspection results/observations with actual fracture performance which will also be briefly reported here.

Optical components frequently use brittle materials, and fabrication involves damaging the surface material to shape parts. A residue of SSD is expected from the processing. In sapphire, this damage can be surface stresses, large scratches, twins, cracks, edge chips, and digs - craters in the surface. Subsequent fabrication steps always try to remove the SSD from a preceding step or all of the preceding steps. Just how much material to remove and in what way affects the cost and time to make parts. Effective SSD control is your best reason for inspecting optical components.

The practice has four inspection steps. First, parts are visually examined for significant flaws. Second, a Polariscope is used to reveal sub-structure and "large" bulk strains. Third, light microscopy is used to detail significant flaws. Fourth, the component is examined using x-ray topography at the NIST, Materials Science Beamline at the National Synchrotron Light Source of the Brookhaven National Laboratory.

To illustrate the technical points and to establish credibility for the approach, we will draw solely on our SSCARR experiences, where ASTM Type B modulus of rupture bars to measure fracture strength in four point bending. The bars were supplied by the prime vendors for each missile system and were to exactly "represent" flight components. Our inspection was to address surface quality. The bars were made in groups of 25 or more pieces, of one gauge surface condition and

crystallo-graphic orientation. Each groups represented different vendor, and specific window or dome areas. Since THAAD and ARROW use octagonal planar windows, there are three geometrical regions to consider. Each area had a specific and different surface finish. The Block IVA missile uses a hemispherical dome; and nominally one surface condition. But this shape uses all crystallographic orientations, which predictably leads to different local surface conditions. The specific test pieces for our task were selected for two reasons. One was to represent key SSCARR factors, the other to define the Diagnostics performance envelopes.

Using just finish proved to be a serious obstacle to effective inspection. The MOR bar finishes ranged from ground through to super-polished. In between were the edge, bevel and side finishes. We force fit "finish" into three grades: ground, intermediate and polished. Surface finish numbers obtained from non-contacting profilometry proved useful numerical descriptors of the surface relief, but not the mechanical performance. Finish values ranged from 0.7 nm Ra, THAAD optical faces; down to 1.4 m, ARROW side finish. The range of finish was the key obstacle to using just one inspection method. For this inspection recommendation, we are simplifying the problem to inspecting parts with a less than 10 nm Ra surface finish.

Keywords: Sub-Surface Damage, Sapphire, Single Crystal Optics, and Fracture Strength

Development of Intelligent Precision Vision Inspection System for Micro Optics Parts using New Optical Probe Implemented to Have Multiple Fields of Views and Mutual Calibration Scheme

Heui Jae Pahk, Il Hwan Lee
School of Mechanical and Aerospace Eng. Seoul National University, Seoul, Korea

Abstract

The Micro optics parts such as ferrules and pigtails are required to be manufactured within very small tolerances, as the slight deviation of the tolerance would give very large amount of loss in communication efficiency. Thus we developed an automatic inspection system to evaluate shape parameters of the optical fiber connectors up to sub-micrometer accuracy using machine vision. The new optical probe of multi fields of views has been developed and the image processing and data analysis algorithms have been implemented in real time basis. The developed system is successfully used in the optical parts manufacturing industry, and about 0.1um accuracy can be obtained with very fast inspection time.

Introduction

Small micro optics parts are increasingly in need in optical communication industry and optical parts manufacturing industry, as the optical telecommunication and wireless optical units are expected to have enormous market size in few years of time. The micro optics parts such as ferrules, pigtails, and optical parts are required to be manufactured within very small tolerances, as the slight deviation of the tolerance would give very large amount of loss in communication efficiency. The ferrules, for example, are glass/ceramic/metallic/plastic tubes in which optical fibers are inserted and connected. For efficient optical communication, outer diameter, fiber diameter, fiber separation, eccentricity, etc. are vital to be inspected and quality controlled with sub-micrometer accuracy. This is the typical example of small micro optical parts, and thus a new optical inspection probe of multiple fields of views (FOVS) has been developed in this research. The developed system consists of two fields of views: one is LFOV (Large Field of View), and the other is SFOV (Small Field of View), where the two FOVS are optically interconnected each other. The LFOV scans the large area such as outer diameter and outer form tolerances, while the SFOV scans the small area such as the fiber separation, eccentricity at the same time. The two FOVS scan results are combined to give the global image data for inspection, and the image processing algorithms have been processed in real time basis for the inspection analysis, where some new image processing algorithms have been designed. In order to level up the accuracy and reliability of the developed inspection system, precision mutual algorithms are designed for the precision mutual calibration. For the In-process Inspection of the developed system, a XYZ robot mechanism is designed, where fast and accurate positioning of the inspection unit is possible, and positional error calibration module is also interfaced to the robot in order to give higher accuracy. The jigs are also intelligently designed which are to give easy insert/removal of micro parts, uniform illumination, and easy setups, etc.

Inspection System

The developed inspection system has been designed to measure the shape parameters of micro optical parts using the optical probe, XYZ robot and jig/tray unit.

As fig.1 shows, the optical probe consists of two CCD cameras of different filed of views, illuminator and frame grabber. The CCD cameras simultaneously capture the images where one image of LFOV is analyzed to measure the diameter and the roundness of outer circle, and the other image of SFOV is analyzed to measure the diameters, roundness and the separation of fiber holes. Two image data transformed by dual camera calibration are combined to calculate the eccentricity. The system has multiple illuminations. Coaxial, front, backlight illuminations are equipped, so optical parts of various shapes can be inspected with optimal typed illumination.

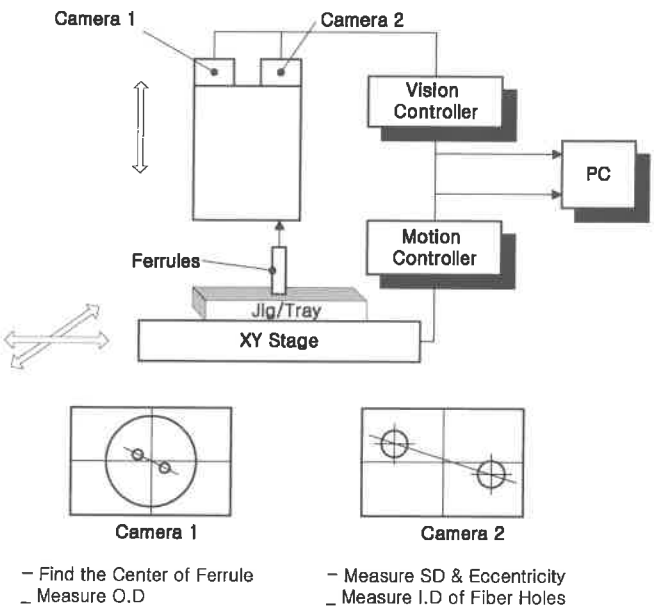

Fig. 1: Schematic diagram of the developed system

The XYZ robot consists of XY stage and Z- axis at which jig/tray unit and dual cameras are fixed respectively. For the defocused image inherently have distorted information of object, and aggravate the efficiency of edge detector, so the focus position providing the sharpest image must be calculated in advance. The optimum focusing position can be calculated with the image focus measurement function using sequential images captured by moving Z-axis. Jig/tray unit has been designed to fix the optical parts, in which spring has been inserted to control the height of the optical parts constantly. Automatic inspection process has been implemented using RS232C serial communication between the XYZ robot and Windows based PC.

Analysis

The image processing algorithms for shape measurement of optical parts analyze the two images acquired from dual CCD cameras. Fig.2 shows the ferrule images of multi fields of views. In order to measure the eccentricity, which is the distance between the center of the outer circle and the center of two fiber holes, the calibration process of dual camera should be performed to transform the data of SFOV into the data of LFOV. For the calibration process, as fig.3 shows, precisely designed calibration artifact of grid type is used to select the control points, which are intersection points of grid and have same real position but different image coordinates values in FOVS. Using these control points, transformation matrices between LFOV and SFOV can be acquired.

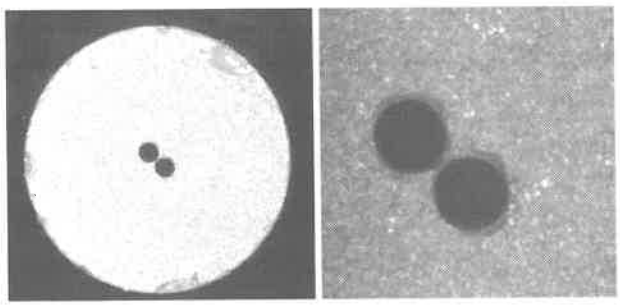

Fig. 2: Images of multi fields of views

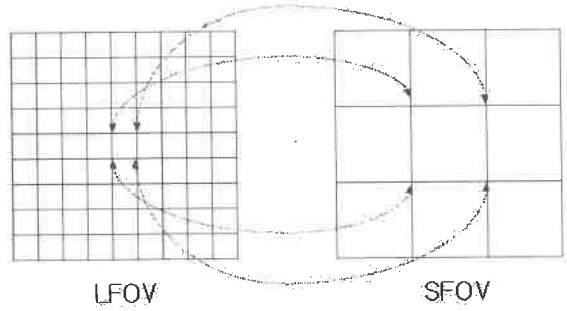

Fig. 3: Dual cameras calibration

In the vision inspection system, the focused image is required for precise detection. The defocused images inherently have distorted border information of object, and aggravate the efficiency of edge detector. Thus the focus position providing the sharpest image must be calculated in advance. The optimum focusing position can be calculated by the IFMF (image focus measurement function). In the developed system, sequential images are captured at the displaced capturing locations, and the IFMF finds the location of the focused image. The IFMF is based on the Sum of Laplacian operator, and the edge detection is based on the LoG (Laplacian of Gaussian) operator and the location of Zero-Crossing. The LoG operator is defined below.

$$\nabla^2 G(x,y) = \frac{1}{\pi\sigma^4}(1-\frac{x^2+y^2}{2\sigma^2})\exp(-\frac{x^2+y^2}{2\sigma^2}),$$ where σ is space constant.

At the Zero-Crossing location, the intensities of 8-connected neighborhood points are modeled as the continuous polynomial function. With this polynomial function, we can divide the pixel into 9 sub-pixels. Using these sub-pixels, the edge detection is performed once more, and the edge with sub-pixel accuracy can be determined. In the edge detection, determinant threshold often doesn't work well because of irregular illumination and time-variant illumination intensity. In this research, the optimal threshold is applied to the edge detection process, and so reliable border data of object can be detected. The developed system samples more than 1,000 data being detected in edge detection process, and with least squares method, can measures the shape parameters such as diameter, roundness, fiber separation and eccentricity. In the raw images, however, there may be noise and undesirable corrupted data caused by unclean optical parts and hardware limitations. So measurement process including the automatic removal of the noise and corrupted data has been intelligently implemented. Fig.4 shows the removal process of corrupted data of fiber hole.

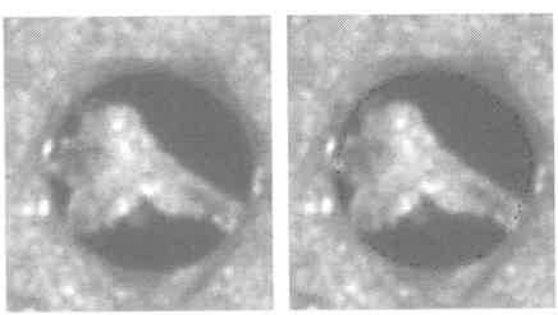

Fig. 4: Intelligent removal process of burr and noise

Experiments and Results

The developed inspection system can be applied to inspection of various optical parts such as

ferrules, pigtails and etc. The fundamental parameters of 100 pieces of optical parts can be measured simultaneously with just one setup and one calibration process. To demonstrate the performance of the system, ferrule inspection test has been performed.

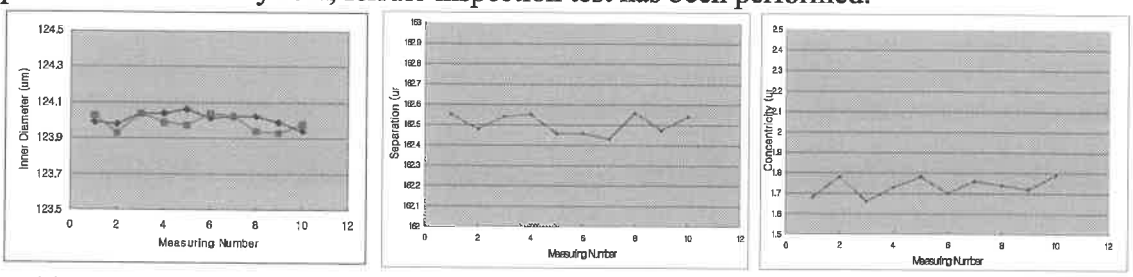

(a) Inner diameters (b) Separation (c) Concentricity

Fig. 5: Inspection results of ferrules

The ferrule inspection test has been repeated 10 times to evaluate the repeatability accuracy. The inspection time is about 10 seconds per each test and the results show in fig.5.

The concentricity that is crucial parameter to determine the communication efficiency in ferrules has the mean value of 1.771um, and the standard deviation of 0.0615um. The other parameters such as Outer Diameter, diameters of fiber holes and separation distance, are measured with less than 0.1um accuracy.

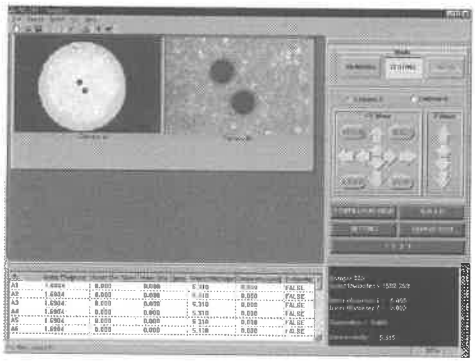

Fig. 6: The developed software window

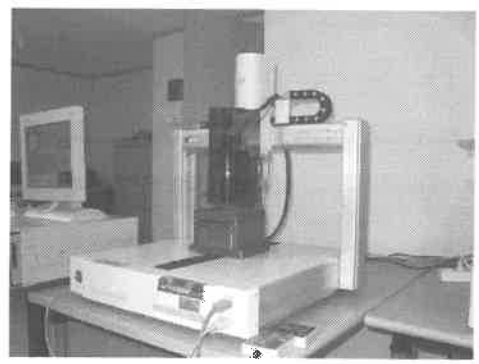

Fig. 7: The developed system for ferrule inspection

Fig.6 shows the developed software window and fig.7 shows the figure of the developed system.

Conclusion

The vision inspection system has been developed to measure the fundamental parameters of micro optical parts using optical probe, XYZ robot and jig/tray unit

The high precision and intelligent image processing algorithms analyzing objects with sub-pixel accuracy has been designed, thus about 0.1um accuracy can be achieved.

An auto focus technique has been implemented. The optimal focus position of CCD cameras has been determined very fast and efficiently.

A dual camera calibration technique has been implemented. The eccentricity for which data needs to be acquired from LFOV and SFOV and to be analyzed simultaneously has been measured successfully with sub-micrometer accuracy.

HIGH THROUGHPUT SURFACE STRUCTURING IN SOLAR CELL MANUFACTURE

Manfred Weck, Burkhard Leifhelm
Fraunhofer-Institute of Production Technology (IPT), Aachen, Germany

Abstract
Sun light, the »renewable energy« source, and photovoltaics are attracting more and more interest, which in turn produces cost pressure for more efficient solar panel production due to the competitive situation. Solar cells structured with V-shaped grooves show a significant improvement in efficiency thanks to better light collection. But the costs of the additional operation for structuring have to be minimised, so high-throughput machining is essential. At the same time, the dimensions of the structure require high-precision machining of silicon wafers.

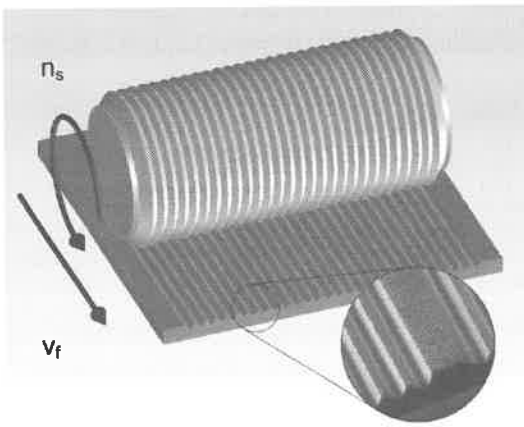

Fig. 1 Mechanical surface structuring

In colaboration with solar cell manufacturers and process designers a structuring system was built up, which meets the requirements for a brittle material such as silicon. The structuring process is carried out by grinding with profiling tools, for accurate and high-speed generation of the desired surface topology. The machine is designed for production-line operation. The process, which was until now in the experimental stage, is automated and provides a high level of reliability due to process monitoring.

Motivation

Today, the manufacture of crystalline silicon solar cells and modules is mostly based on the technologies derived from the generic process flow [2]. As substrate material, cast multicrystalline silicon wafers in the thickness range of 330±30 µm and a size of 100*100 mm^2 and 125*125 mm^2 are dominating. High efficiencies and high yield have to be achieved with a low cost high-throughput processes. A critical process step is the surface texturing to reduce surface reflection. Usually performed in the same way as for <100>-oriented monocrystalline silicion wafers by etching in an alkaline solution with organic additives, this process is much less efficient on multicrystalline substrates because of the different grain orientations. In this case the mechanical structuring is applied, whereby an efficiency gain of 5 % relative after encapsulation can be reached [3].

Wafer structuring machine

The system specifications are derived from multiple demands. The mechanical structuring process requires a rigid machine design and good geometrical characteristics. In-process measurements reveal machining forces of up to 1.5 $N/mm_{structuring\ width}$, so the machining width of 280 mm leads to comparably high load. Furthermore, wafer contamination with oil, grease and non-ferrous metals has to be avoided, which would impair the following chemical process and the cell function. And finally, industrial users want to have an economic machine setup for automatically machining with high yield and high reliability. This requirements were taken into consideration in the machine setup. Fig. 2 shows the arrangement of the axes.

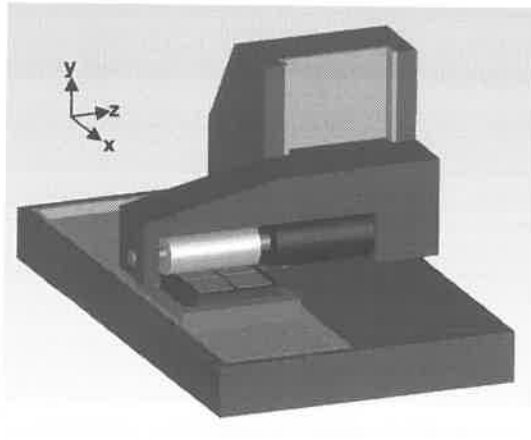

Fig. 2: Machine set-up

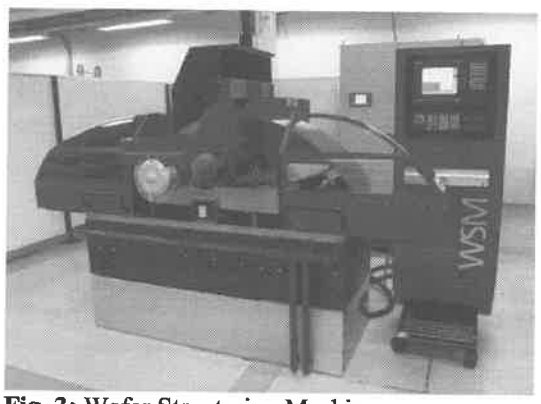

Fig. 3: Wafer Structuring Machine

The mechanical wafer structuring system is designed for utilisation in an automatic solar cell production line with high throughput. The machine base material is granite. The machine is provided with three controlled linear axes X, Y and Z. The X-axis is the oscillating main machining axis with a travel range of 900 mm and is ball screw driven. The Y- and Z-axis are positioning respectively shift axes with a stroke of 215 mm and 70 mm. The Y-axis is equipped with a roller screw and the Z-axis is provides with a linear motor. Incremental linear scales are integrated in all three axes. The main spindle exhibits a 33 kW built-in motor and a maximum rotation speed of 10,000 rpm.

The spindle as well as the linear axis are equipped with precision rolling bearings to provide a high stiffness of the system (hybrid spindle bearing and rail guides). The X-Z-linear axis system carries a vacuum chuck which is able to hold four wafers.

The Y-slide carries the spindle. Due to the dimensions and the weight of the tool and the requirement of stiffness a counter bearing is necessary. It is equipped with hybrid spindle bearings as well. The structuring tool is clamped by an arbor which is mounted into the machine by hollow shank interfaces. The tool can consist of one part or several segments. To facilitate the tool change especially of large rollers, the counter bearing cartridge can be removed and guides the tool arbor out of the machining housing. The repeatable positioning of the counter bearing part is guaranteed by spur wheels. The Wafer Structuring Machine (WSM) is shown in tool change position in fig. 3.

Process reliability

Different process monitoring systems are integrated in the system. One detects the balancing of the tool and compensates balancing caused disturbance. The balancing head of the control system is integrated into the clamping arbor. Also, the system shows an acoustic emission evaluation that detects contact between wafer and tool as well as wafer breakage. It controls the condition of the grinding process, too. The third element of the process monitoring system is the vacuum control. A broken or missing wafer leads to vacuum loss that is indicated.

Fig. 4: WSM - machining area

To avoid wafer breakage one has to ensure to fix the wafers on a clean chuck surface. A vacuum field cleaning is done in three steps. First rotating brushes remove wafer fragments or accumulated crusts. A water jet removes remaining small dirt particles. In the third step an air jet dries the chuck surface and prepares it for new wafer feeding. The process control system guarantees the full automatically machining of

the silicon wafers.
The machining strategy has a large influence on the cycle time. Two strategies are suitable, that take the four wafer clamping fields of the chuck into consideration. The first strategy features two clamping fields prepared with wafers. After the wafers are machined, the vacant clamping fields are scavenged by cleaning units that are located bilateral of the machining area. The machining area is shown in fig. 4. The feeding and unloading processes take place simultaneously. This strategy realises the synchronous wafer machining and chuck preparation. Another mode considers the four wafers machined simultaneously, which makes an additional cleaning step necessary.
The wafer handling proves to be the bottleneck of a high throughput system. Its tasks are the wafer separation, wafer measuring, pre-alignment, wafer feed and removal, wafer cleaning and wafer storage. Various systems will be evaluated.

Structuring process and tool

To enhance the efficiency of multicrystalline silicon wafers a grinding tool is used. A typical V-shaped structure has an structure width of 160 µm and a depth of about 100 µm, depending on the groove angle. The grinding roller shows the structure shape. The roller material is brass or steel. In the case of brass a single point diamond turning process is used to structure the tool, and micro wire EDM in case of steel. The Ni-diamond abrasive layer granulation comprises of grain size of 5 µm to 25 µm. A coarse grain causes larger saw damage which has to be removed by etching. Purified water is used as coolant. In conjunction with a tool diameter of 200 mm, a maximum cutting speed of 100 m/s is available and the cutting infeed is up to 120 mm/s. The parameter choice depends on the cutting mode. In case of a single-cut-mode the tool profile exhibits the complete wafer structure. The index-cut tool provides half the structure pitch. The wafer is machined in two steps with a shift of the z-axis. The index cut lead to higher feed rates due to lower process load, that has to be counterbalanced by the vacuum fields. A section of the structure is shown in fig. 6. The V-shaped grooves improve the light collection, while the plateau is used for printing of the contact fingers, which collect the current.

Fig. 5: Structuring tool

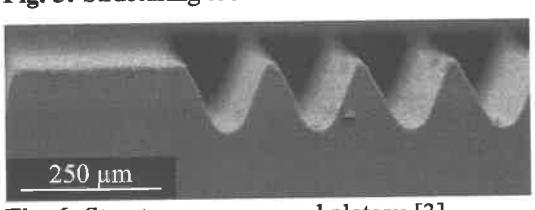

Fig. 6: Structure: grooves and plateau [3]

Applications

Several applications - not only in the field of photovoltaics - stand to benefit from the system. The V-structure of solar cell surfaces leads to an improvement of the efficiency due to the physical effects of surface respectively emitter enlargement, multiple light reflection, light trapping and improved light collection probability. Especially the sharpness of the slot tips determines the cell efficiency gain.
Planarization - face grinding without structuring - of the silicon wafers is used to standardise and prepare the material for the further processing. It is recommended especially for foil substrates (RGS, EFG, APex) that show a high waviness of the surface. After levelling the wafers, the

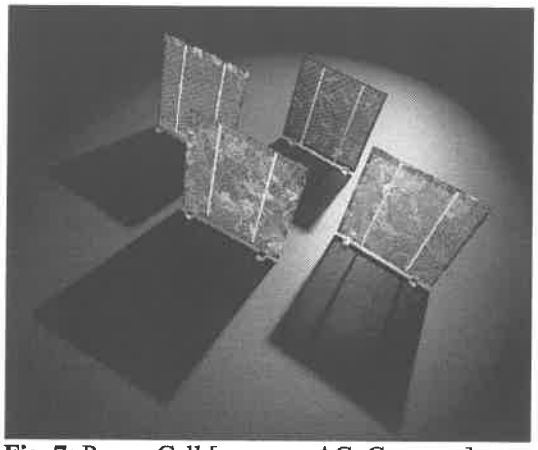

Fig. 7: Power Cell [sunways AG, Germany]

subsurface damage is considerably smaller, so that the time of the following saw damage etching step can be reduced.

Due to the mechanical wafer structuring step the conventional screen printing of contact fingers can be substituted by roller printing in the future solar cell process flow. Screen printing requires a plain surface and an accurate pre-alignment of the wafers. In the case of roller printing, elevated finger plateaus are made by structuring and the paste is applied by a roller. Furthermore the finger shadowing is reduced due to smaller finger width.

POWER (POlycrystalline Wafer Engineering Result) cells are double-sided structured solar cells types. The grooves show a square shaped cross section and the directions of the grooves are perpendicular between front and backside. At the cross-over the structures interpenetrate and holes emerge. The regular distribution of the small hole lead up to 30 % translucent solar cell utilised, e.g. for direct facade integration of photovoltaics [5]. POWER cells are shown in fig. 7.

Conclusion

The introduced wafer structuring machine in a system to apply small precise structures on extended surface areas in a high-throughput line. The focus was laid on rigidity and process reliability. The throughput aspired is 12 m^2/h. The system is designed to integrate a wafer handling system, that considerably influences the performance of the system. The utilisation in the manufacture of innovative products contributes to the launch of solar wafer and non-solar wafer applications.

Acknowledgement

This development was founded by the EC within the HIT project under contract number JOR3-CT98-0223.

References

[1] Weck, M., Leifhelm, B.,
New lights in solar cell manufacturing:
High throughput surface structuring system for solar cell wafers
Proceedings of the euspen 2nd International Conference, Turin, Italy, 2001, pp. 766-769

[2] Szlufik, J., Sivoththaman, S., Nijs, J.F., Mertens, R.P., Van Overstraeten, R.,
Low-Cost Industrial Technologies of Crystalline Silicon Solar Cells
Proceedings of the IEEE 85(5), 1997, pp. 709-730.

[3] Gerhards, C., Fischer, A., Fath, P., Bucher, E.,
Mechanical microtexturization for multicrystalline SI solar cells
16th EPVSEC, Glasgow, UK, 2000

[4] Nakaya, H., Nishida, M., Takeda, Y., Moriuchi, S., Tonegawa, T., Machida, T., Nunoi, T.,
Polycrystalline silicon solar cells with V-grooved surface
Solar Energy Materials and Solar Cells 34, 1994, pp. 219-225

[5] Boueke, A., Kühn, R., Fath, P., Willeke, G., Bucher, E.,
Latest Results of Semitransparent POWER Silicon Solar Cells
Technical Digest 11th International PVSEC, Sapporro, Japan 1999, pp. 135-136

Superabrasive Grinding Process Optimization through Force Measurement

Byron Knapp, Eric Marsh, Robert Grejda, and David Schalcosky

The Pennsylvania State University

University Park, PA 16802

Abstract

Several obstacles complicate the task of optimizing a particular superabrasive grinding process. Grinding wheel manufacturers provide valuable guidance in setting up a new process; however, there are numerous issues requiring better insight into machine setup and wheel selection. This paper presents a promising approach to investigating grinding brittle materials with superabrasives. In this work, a grinding machine is used with a specially designed air bearing spindle featuring embedded sensors calibrated for measuring grinding forces. The sensor output provides valuable feedback and is especially valuable in configurations that are not easily instrumented by other methods (such as ID, OD, and rotary grinding). In this article, an example is presented along with a brief review of the technical approach.

Introduction

The motivation for developing and building instrumented spindles is found in the many challenges facing the precision grinding community. Difficult materials, complex part geometries, and a wide variety of abrasive wheel types and coolants are found in every industry. Grinding process development is facilitated through the use of modern instrumentation and analysis tools [1-3]. Unfortunately, some of the most common grinding configurations, such as ID or OD grinding are difficult to instrument because of the rotation of both the workpiece and abrasive wheel. New commercial offerings of rotating cutting force dynamometers are available to measure the relatively large forces of milling (hundreds of Newtons), but there remains a need for a system suited to the light forces of precision grinding [4].

The instrumentation described in this article addresses the need for a precision grinding feedback system through the use of a spindle with embedded non-contact sensors that measure the relative axial motion between the rotor and stator. The advantage of using specially-calibrated displacement sensors to estimate grinding force is that the displacement is measured without introducing a compliant element into the structural loop. Using the known stiffness of the grinding spindle, force is computed without increasing the compliance of the machine.

This instrumentation approach allows efficient study of the grinding process with the benefit of an accurate and stiff machine tool. The air bearing spindles offer several additional characteristics favorable to grinding brittle materials including high speeds, high damping, and minimal synchronous and asynchronous error motions [5].

With this custom machine tool it is possible to measure and analyze a number of parameters critical to successful grinding with superabrasive wheels. It can also provide insight on the effect of a variety of operating parameters including wheel type, condition, and speed; dressing and coolant; workpiece properties; and machine characteristics including stiffness and damping. The instrumented spindle also detects the onset of grinding contact and grinding vibration, including chatter, and may offer valuable insight into mechanism of material removal during grinding.

Precision Grinding Machine and Spindles

Figures 1 and 2 show the plain way Moore grinding machine used in this testing. The grinding machine is outfitted with two Professional Instruments 10,000 RPM, motorized air bearing spindles. Customizable spindle mounting hardware allows a variety of grinding operations to be run, and both straight and cup wheels can be tested (typically 100 mm to 200 mm diameter superabrasive wheels are used).

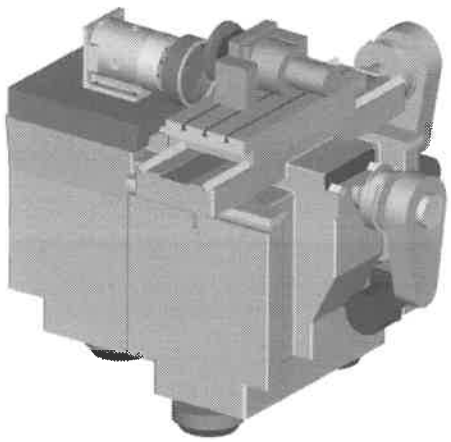

Figure 1. Instrumented Moore grinding machine.

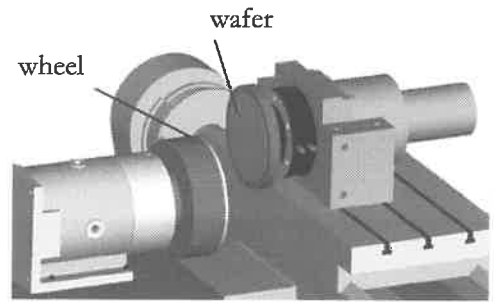

Figure 2. Close-up view of instrumented spindle used in diamond grinding of silicon.

The work spindle has embedded Lion Precision capacitance gages that sense relative motion between the spindle rotor and stator. The complications due to coolant and swarf contamination that arise when using capacitance gages are eliminated by sensing in the high pressure air film of the spindle. Figure 3 shows the important design features of the instrumented spindle used in this testing. The capacitance gages are embedded in the stator and target the thrust plate. The spindle features a spherical piloting wheel mount that allows interchanging of workpieces and grinding wheels with a repeatability of 0.1 microns. This allows for convenient off-line preparation and truing of workpieces and wheels, which can later be reliably mounted on the spindles for grinding. The piloting mounts are also used for interchanging wheels between grinding tests without the need for re-balancing.

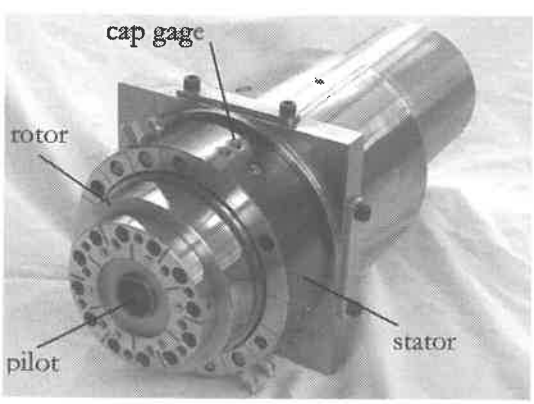

Figure 3. Instrumented spindle with lapped carbide piloting mount.

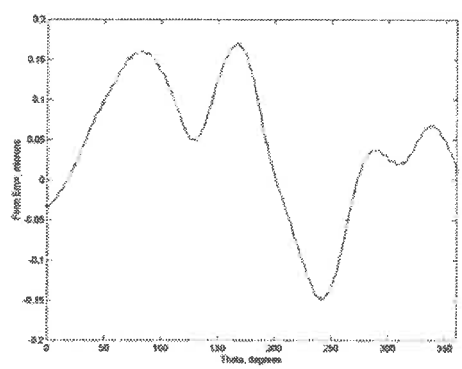

Figure 4. Error map of the lapped spindle thrust plate.

Figure 4 shows the error map of the thrust plate that is removed from the capacitance gage output for calculation of the force measurement. The static stiffness of the spindle, along with the measured relative displacements between rotor and stator are used to estimate the grinding forces. The first structural resonance of the machine occurs at 300 Hz, so the usable bandwidth of the force measurement is approximately 75 Hz (one-fourth of the resonant frequency).

Experimental Results

Figure 5 shows the results of plunge rotary grinding a 150 mm silicon wafer with a 200 mm superabrasive cup wheel. The wheel spindle is running at 5825 RPM (62 m/s) and workpiece is running at 600 RPM with an infeed of 170 nm/s. Because of the alignment of the spindles, the forces steadily increase to 500 mN where the wheel is in contact with half of the wafer. The spectral content of the force measurement before contact of the wheel and workpiece (a) and during the grind (b) is shown in Figure 6. The waterfall plots clearly show workpiece speed (10 Hz) and its harmonics during the grind.

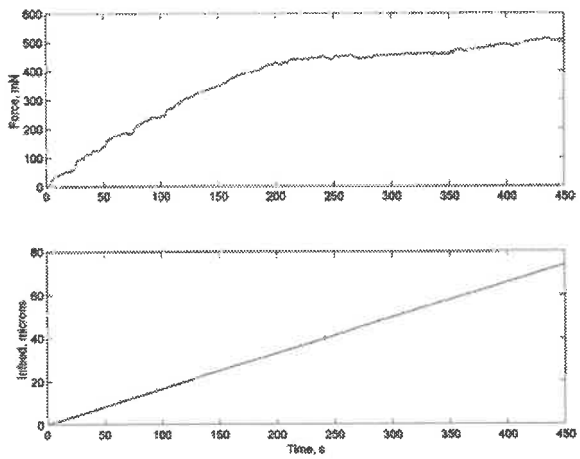

Figure 5. Normal force and infeed while grinding silicon.

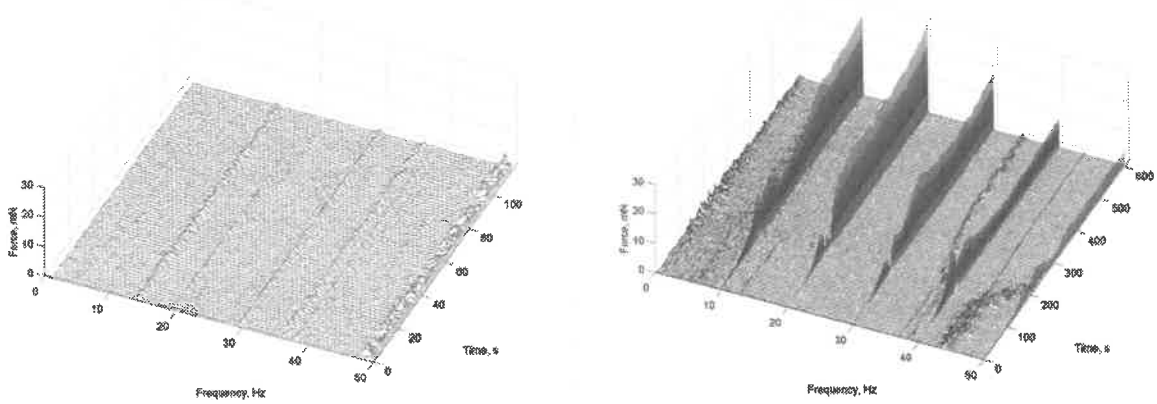

a) b)

Figure 6. Spectral content a) before contact and b) during grind.

In order to determine the quality of the surface finish obtained during the test, the specimen was examined with a Nomarski microscope and an SEM. A surface finish with grinding marks typical of those produced with rotary grinding were found on the specimen [6]. The surfaces shown in Figures 7 and 8 had an average roughness of Ra = 18 nm.

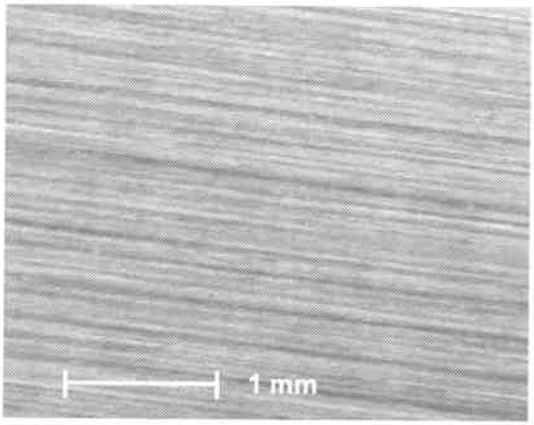

Figure 7. Nomarski microscopy picture of ground surface.

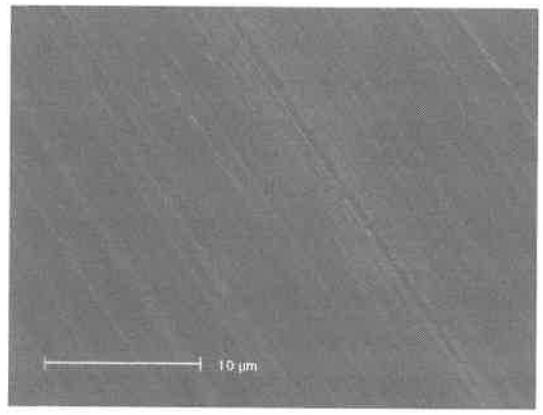

Figure 8. SEM picture of ground surface.

Conclusion

This paper describes an instrumented grinding machine that features an air bearing spindle with embedded capacitance probes used to measure grinding forces in applications that cannot be instrumented with traditional techniques. The machine is well suited for grinding model verification because the instrumentation is tightly coupled to a high performance spindle and machine tool. This combination allows measurement of subtle, yet high frequency phenomena in the grinding process.

Acknowledgements

The authors thank Dave Ameson, Mel Liebers, and Dan Oss of Professional Instruments, and Don Martin of Lion Precision for their continued support of this research.

References

1. Shaw. M.C., Brach, K., Pai, D.M., and Ratterman, E. "Grinding Forces and Energy." *ASME Journal of Engineering for Industry* 110 (1988): 25-31.
2. Tönshoff, H.K., Peters, J., Inasaki, I., and Paul, T. "Modelling and Simulation of Grinding Processes." *Annals of the CIRP* 41.2 (1992): 667-688.
3. Shaw. M.C. "Precision Finishing." *Annals of the CIRP* 44.1 (1995): 343-348.
4. Blaedel, K.L., Taylor, J.S., and Evans, C.J. "Ductile-Regime Grinding of Brittle Materials." *Machining of Ceramics and Composites.* Ed. Said Jahanmir, M. Ramulu, and Philip Koshy. New York: Marcel Dekker, Inc., 1999. 139-176.
5. Tönshoff, H.K., Leirse, T., and Inasaki, I. "Grinding of Advanced Ceramics." *Machining of Ceramics and Composites.* Ed. Said Jahanmir, M. Ramulu, and Philip Koshy. New York: Marcel Dekker, Inc., 1999. 85-118.
6. Tönshoff, H.K., v. Schmieden, W., Inasaki, I., König, W., and Spur, G. "Abrasive Machining of Silicon." *Annals of the CIRP* 39.2 (1990): 621-635.

DEVELOPMENT OF AUTOMATIC IMAGE PROCESSING SYSTEM FOR EVALUATION OF WHEEL SURFACE CONDITION IN ULTRA-SMOOTHNESS GRINDING

Heiji YASUI, Yutaka HIRAKI and Masato SAKATA
Department of Mechanical Engineering & Material Science,
Kumamoto University, Kumamoto 860-8555, Japan

1. Introduction

The grinding wheel surface condition characterized by the distribution and wear of cutting edges has strong influence on grinding results such as surface roughness, grinding force and temperature, and so on. Recently the wear extent of cutting edge has been found to influence the quality of ductile-mode ultra-smoothness grinding of fine ceramics with coarse grain size diamond wheel [1]. Thus to optimize the ultra-smoothness grinding process, it is necessary to clear the relation between the wheel surface condition and grinding results.

The quantitative evaluation of the wheel surface condition, however, is not easy because of the difficulty of quantitative measurement of numerous cutting edges more than several thousands, which are distributed irregularly over the wheel surface. One of the authors reported the wheel surface monitoring system [2] but it was not enough for practical experiment in order to clear the influence on the grinding results. In this research, the automatic image processing system is newly developed for the evaluation of the distribution and wear of the cutting edges by means of measuring the numerous microscopic images on the wheel quickly and precisely.

2. Automatic image processing system

2.1 Apparatus and monitoring system

Figure 1 shows the view of the automatic image processing system. The system consists of four components, that is, (1) the surface grinder having the wheel spindle driven with the servo-motor positioned in the accuracy of 0.01 degree under the computer control, (2) the observation system of wheel surface using the image transformation technique of CCD camera to the computer for digital handling of microscope image, (3) the newly developed software program for extracting of cutting edges from the image transformed into the computer and (4) the whole system control computer operated by multi-task Windows-OS.

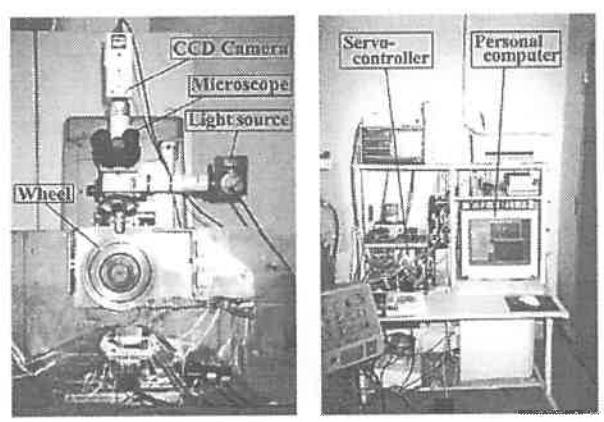

(a) Surface grinder with microscope and CCD camera (b) Servo-controller and personal computer

Fig. 1 Appearance of the automatic image processing system

The servo-motor with a rotary encoder is connected to the axis of the grinding wheel. The motor is driven by the computer through the servo-controller and makes it possible to position the location of wheel precisely. The wheel surface image is picked up by CCD camera through the microscope. The output video signal of the image is digitized on the video-capture-board and processed in the same computer directly.

Figure 2 shows a sample of the microphotograph-image of the metal-bonded diamond wheel surface used in this research. It is found that the bright portions of cutting edges emerging clearly from the wheel surface have almost the same brilliance as some bright parts from metal-bond surface around the grains. The frame size is 670x500μm square and one image has 640x480 pixels with 24bits-color mode (8bits resolution for Red, Green, Blue). In the experiment, it is necessary to measure about 900 images for examining the change of numerous cutting edges on 200-mm-diameter-wheel surface.

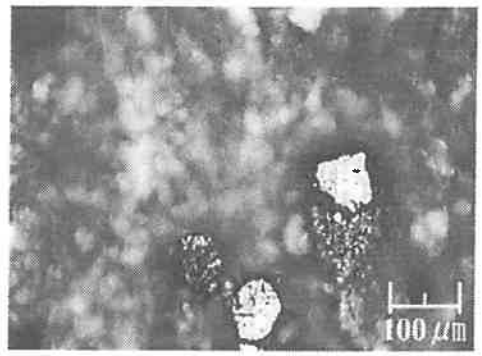

Fig.2 Original microscopic photo-image of the metal-bonded diamond wheel surface in ultra-smoothness grinding (Frame size is 670x500μm square)

2.2 Digital image processing

The wear-flat area of active grains is recognized as the cutting edges in the case of ultra-smoothness grinding with the coarse grain size diamond wheel. Figure3 shows the image processing process for extracting of the cutting edges from the wheel surface image.

The image processing is done in the two steps. In the first step, the pixels which are lighter than the brilliance of threshold are displayed as white shown in Fig. 3 (a). From the figure, it is found that some bright parts from metal-bond surface are remained as the same as the wear-flat area on active grains. In the second step, outline image is obtained by calculating the difference of the neighborhood pixels shown in Fig. 3 (b). It is found from the figure that the cutting edge areas have the distinct outlines. Therefore, the extraction of cutting edges is realized by overlapping both images as shown in Fig. 3 (c).

The simple image processing method is newly developed in this research and can extract distinctly the wear-flat areas of cutting edges on the metal-bonded diamond wheel surface with high accuracy and in the short time below a second.

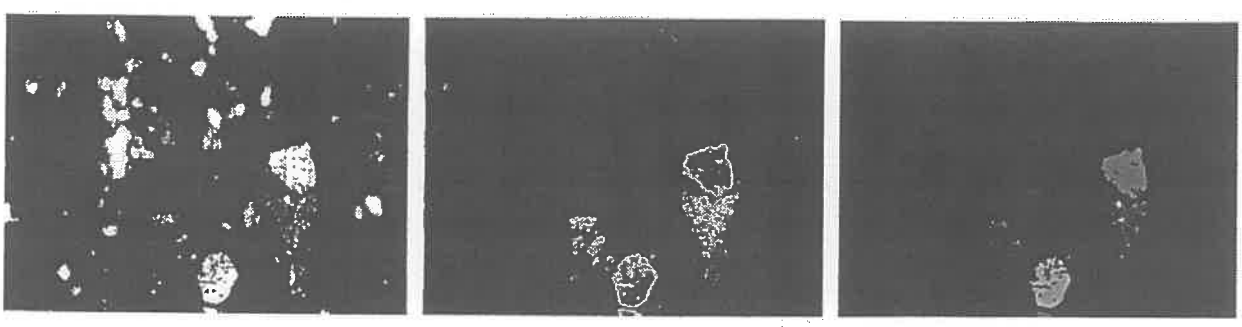

(a) After brilliance image processing (b) After outline image processing (c) After final image processing

Fig.3 Image processing for extraction of cutting edges by means of thresholding of brilliance and outline image

The flowchart of the software program is shown in Fig. 4. The basic procedures are as follows:

(1) Initialization of the system: Setting the servo-motor and controller on, positioning the wheel to the initial location and setting up the number of sampling images.

(2) Sampling and Image processing: Positioning the wheel to the photographing location, sampling a wheel surface image and extracting of cutting edges from the image explained above.

(3) Calculation of the following parameters: a) Cutting edge density n_p mm^{-2}; the number of cutting edge per unit area, b) Successive cutting edge spacing a mm; the average cutting edge distance along a circumferential scanning line on the wheel surface, c) Cutting edge ratio η %; the proportion of total wear-flat area of cutting edges to total viewing area.

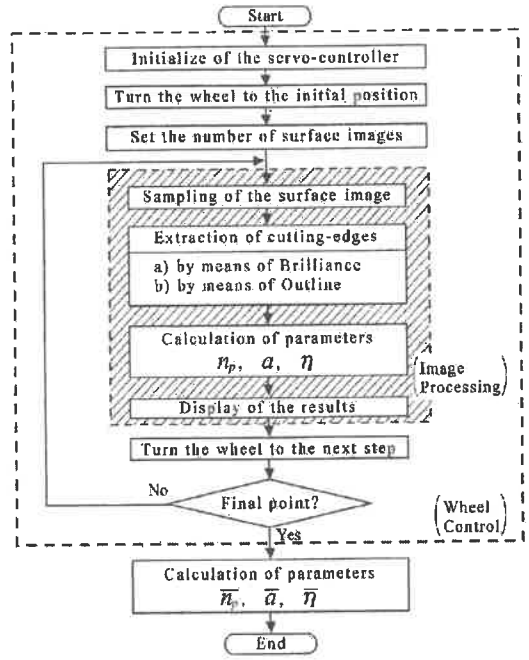

Fig.4 Flowchart of the software program in the automatic image processing system

3. Results and discussions

3.1 Evaluation of wheel surface

In order to precisely evaluate the periphery of a wheel surface, the photographic images are sampled at 895-location on the wheel surface so that the continuous images can be obtained along the circumferential line on the 200-mm-diameter-wheel. The sampling is done after grinding the silicon carbide ceramics with the coarse #140-mesh grain size diamond wheel.

In the circumferential-line-area, numerous cutting edges of more than three thousands are observed. Figure 5 (a) and (b) show the histograms of cutting edge density n_p and cutting edge ratio η, obtained by means of processing the 895 images. From the figures, it is found that the cutting edge density and the cutting edge ratio per each image are within a relatively wide range.

Figure 6 (a), (b) and (c) show the distributions of the mean values of cutting edge density n_p, cutting edge spacing a and cutting edge ratio η at every 16 point along the circumferential wheel location. The mean values are calculated by the 56-images nearby every point. From the figures, it is found that the mean values of the cutting edges density and cutting edge spacing change depending on the periphery location of the wheel surface.

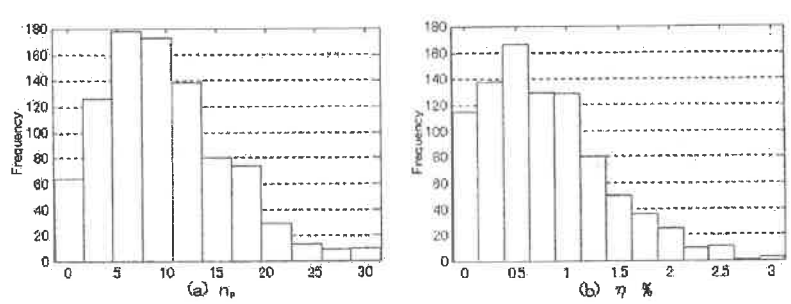

Fig.5 Histograms of cutting edge density and cutting edge ratio

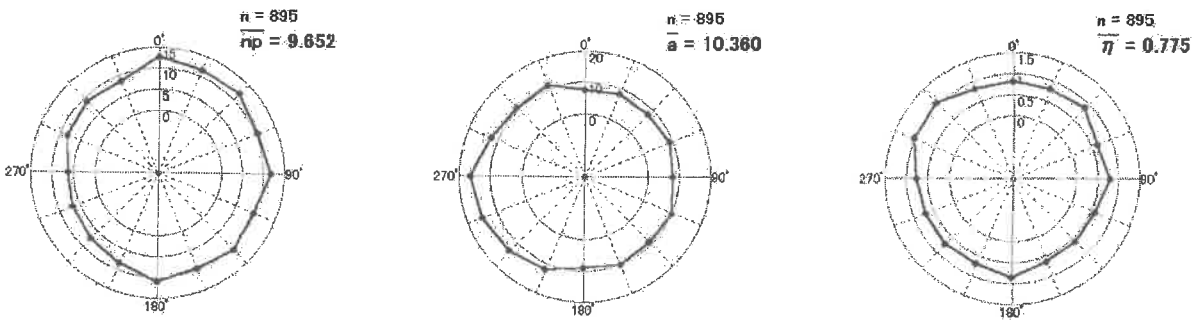

(a) Cutting edge density (b) Cutting edge spacing (c) Cutting edge ratio η

Fig.6 Distributions of the mean values of the parameters at every 16 point on the wheel surface obtained by automatic image processing of the whole 895-point data

3.2 Application of the ductile-mode ultra-smoothness grinding of fine ceramics

Figure 7 shows the comparison of the silicon carbide ceramic surfaces ground at feed speed v_w = 0.05mm/s under cutting edge ratio η = 0.82% and η =1.4% with #140-mesh grain size diamond wheel. It is found that the grinding cracks caused by the wheel condition of η = 1.4% are fewer than those of η = 0.82% and the ductile-mode ground surface is produced. Therefore, the system is considered to be useful for clearing the influence of the wheel surface conditions on ultra-smoothness grinding of fine ceramics below 10nm(P-V) as reported previously [1].

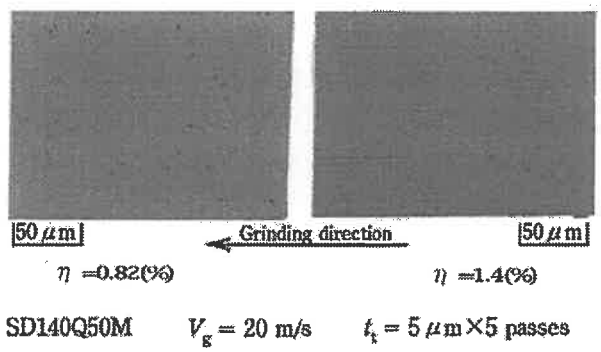

Fig.7 Influence of cutting edge ratio on the ground surface of the silicon carbide ceramic

4. Conclusion

The newly developed automatic image processing system can evaluate precisely, in the short time, the cutting edge density, successive cutting edge spacing, cutting edge ratio and so on. It is proved experimentally that the system is available for the evaluation of wheel surface in the ultra-smoothness grinding of fine ceramics with coarse #140-mesh grain size diamond wheel of 200 mm diameter, which can be done by means of processing of about 900 images around the wheel periphery by every 670μm width in the accuracy of 19μm within 120 minutes. Most of the evaluation time, however, is used for positioning of wheel surface though an image processing can be executed in the short time of below 1 second.

Acknowledgement

A part of this research is supported by Grant-In-Aid for Scientific Research, 2001, in Japan.

Reference

[1] H.YASUI, G.YAMAZAKI, Y.HIRAKI et al: Ultra-Smoothness Grinding of Silicon Carbide Ceramic with #140-mesh Grain Size Diamond Wheel, Proc. of 9th ICPE (1999), 120.

[2] A.HOSOKAWA, H.YASUI et al; Development of the wheel surface monitoring system with image processing for the purpose of grinding operation control, Proc. of 8th ICPE (1997), 207.

REPLICATION OF PRECISION OPTICAL FEATURES THROUGH INJECTION MOLDING

David D. Gill, Thomas A. Dow, Alex Sohn
North Carolina State University, Raleigh, NC

INTRODUCTION

The objective of this research is to study the process of replicating precision optics using injection molding. The technology to produce optical devices for the communication and photonics industries must allow high volume production of thin, highly transmissive, and environmentally stable (uniform properties throughout a range of temperature and humidity) components at low cost and high speed. The details of the current technology and methods used in industry are typically closely held and research that reveals a greater understanding of the processes involved and creates new replication methods is needed. This research must include an investigation of the replication of nanometer-sized optical features and a determination of the transfer function between the shape of the mold and that of the molded lens.

EXPERIMENTAL APPARATUS

To address the research goals, a series of experiments have been carried out on a laboratory-scale Nissei hydraulic injection molding machine at the Precision Engineering Center at North Carolina State University. This machine has a 6.2cm^3 shot volume and a 14mm screw that allows very thin optics to be produced in a single cavity mold while still staying within common design practices regarding the ratio of shot volume to screw volume. The available mold clamping force is 69 KN with a maximum injection pressure of 175 MPa. The tie-bar spacing is 102mm. The machine has an integrated mold heating and cooling system that employs water as the heat transfer medium. The parts replicated to date have been single and double cavity parts approximately 1800mm^2 in area with varying thicknesses below 350μm.

A series of diamond turned aluminum and hard-copper mold inserts have been fabricated and thousands of optical components have been created. The mold inserts were populated with optical features representing many different shapes, aspect ratios (depth divided by width), sizes, f numbers, and groupings that are common in micro-optical devices. An example mold insert is shown in Figure 1 with a representative cross-section and detailed information about each of the features in the mold. The features included in this copper insert are a spherical lens, a spherical Fresnel lens, a blaze diffraction grating, and a lenticular (cylindrical lens) array. Non-optical features are also included for the purpose of studying the effects of aspect ratio and shape. These non-optical features include a wedding cake structure and grooves of various geometries. The features range in overall depth from 300nm to 600μm, have aspect ratios between 0.026 and 0.87, and contain both rounded and sharp corners in various combinations. Several of the features are also included to reveal any replication effects due to different widths and depths of features that have the same aspect ratio.

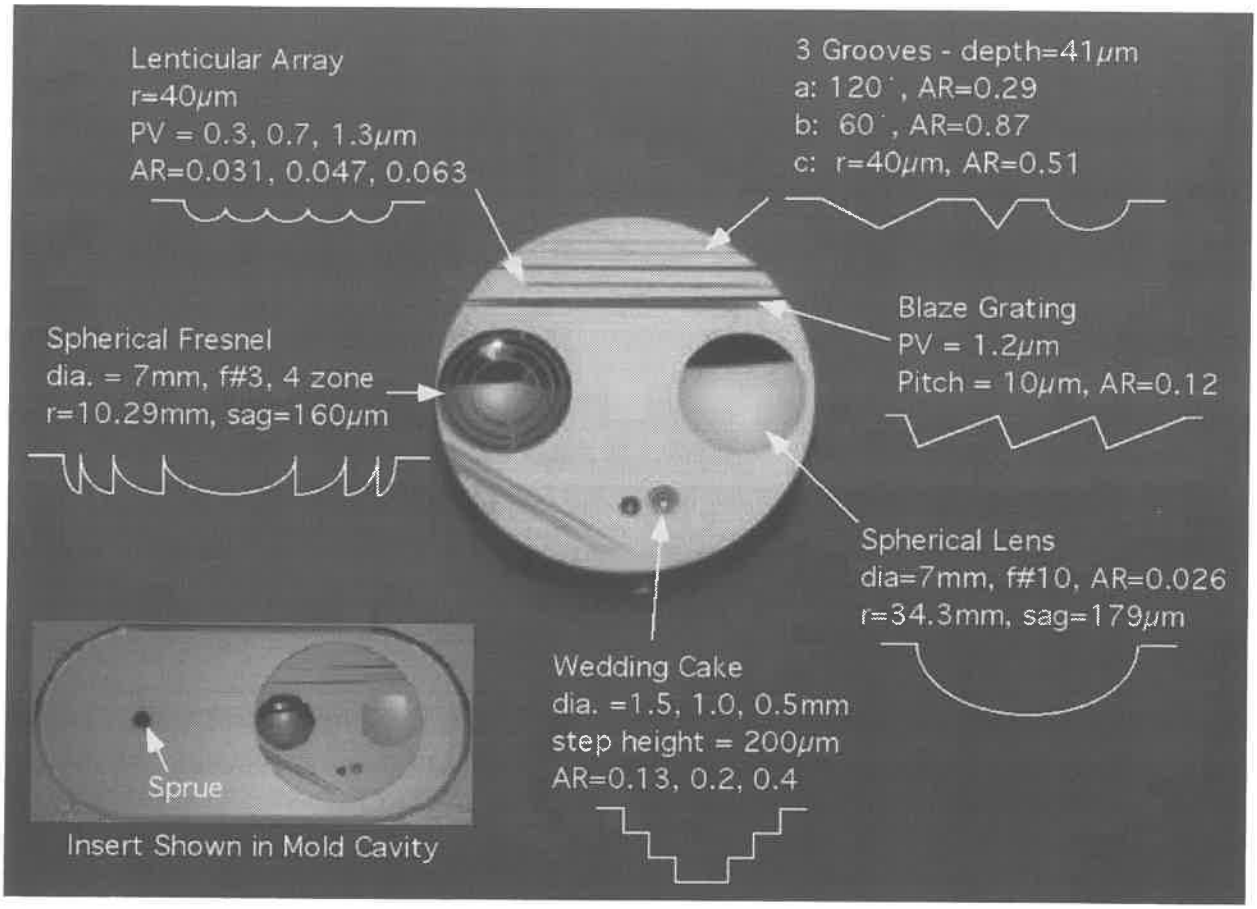

Figure 1. Mold Insert with Optical Features and Their Dimensions

The features were designed to be measured using stylus profilometry, interferometry, scanning probe microscopy, and optical transmission tests. The copper mold insert is fitted into a diamond turned aluminum mold cavity as shown in the lower left hand corner of Figure 1 and mounted in the injection molding machine. Because this insert is circular, it can be mounted in the mold cavity with the mold features located at different positions with respect to the polymer flow as it enters through the sprue and proceeds to fill the mold cavity.

EXPERIMENTAL PROCEDURE

Experiments are being conducted with the molds described above to investigate the effects of different molding variables on the replication of optical features. Nine variables or factors were chosen for this study due to their importance in general purpose injection molding. A design of experiment was developed for the nine factors and initial high and low values were determined for each factor using Atohaas Plexiglas VLD poly(methyl methacrylate) (PMMA). The factors and their high and low values are given in Table 1.

Table 1. Injection Molding Factors for Design of Experiment

Factor	*Low*	*High*
Polymer Temperature (deg F)	470	523
Mold Temperature (deg F)	120	176
Injection Pressure (MPa)	88	175
Injection Speed (cm^3/s)	5.85	13
Cooling Time (s)	0	10
Hold Time (s)	0.35	1.89
Hold Pressure (MPa)	5.6	14
Screw Rotation (RPM)	20.5	205
Feature Position (deg)	0, 90, 180, 270	

The high and low factor values for the first eight factors were determined as the minimum and maximum values at which the optical features could be replicated with reasonable fidelity. The features must be replicated well enough to be measurable so that test will make known any correlation between molding factors and replication fidelity. To determine the low values of the factors, all factors were initially set to low values and then individual factors were lowered in a stepwise manner until the part was no longer acceptable. The factor was left at the lowest acceptable value and the process was repeated with the next factor. At several points during this search, all of the factors were reset to the initial low values to assure that the factor values determined previously were not preventing the later factors from reaching their potential low. By this process, acceptable low values were found for each factor. The high values were determined by the limits of the molding machine except for the polymer temperature and the cooling and hold times. The high polymer temperature is a high temperature for this polymer, but not so high as to cause polymer degradation. The high cooling time was chosen as the maximum that would be desirable in a production setting. The high hold time was determined as a time longer than was necessary for the sprue to freeze, at which point the polymer in the part is cut off from the pressure being exerted by the injection ram. The ninth factor is feature position. The mold insert is circular and is designed so that it can be rotated in the mold. This allows the features to be placed at different locations in the mold with respect to the polymer flow direction. This factor was chosen to be incremented through 360 degrees in 90 degree intervals.

A combination of all of the factors with each factor set to one of its extreme values is called a treatment. Using these maximum and minimum values, a design of experiment was developed, which reduced the number of treatments from 1024 (testing each factor at both of its values against every other condition in the table) to 32 by making the following assumptions: the factors do not interact and the effects of the factors vary linearly between the high and low value given in the table. Through statistical analysis of the chosen 32 treatments, it was shown that two variables in the test were not constrained by the first assumption and could interact without compromising the test results. Injection speed and injection pressure were chosen as the variables most likely to interact. In the experiment, each treatment consisted of the production of more than 100 parts to allow the process to reach equilibrium. Five of the final 25 parts were collected and 3 of those 5 were measured, the extra 2 parts being backups in case of handling damage during removal from the mold or during the measuring process. The measured parts

were then compared to measurements of the mold features to reveal the linkage between injection molding process factors and feature replication fidelity.

Each replicated feature is compared to the matching mold; however, the method of quantifying that measurement is different for each feature type. For example, Figure 2 shows an interferometer measurement of a spherical lens feature in the mold and its replicated PMMA lens. The lens can be compared to the mold by measuring the mean radius of a sphere fit to the data, the error in overall feature height, the chi squared value showing the deviation from the fit sphere, and by subtracting the corresponding errors in the mold from these replication errors. The sphere can also be tested for optical transmission using optical tests such as the Air Force Targets, error in focal length, and dispersion of a beam at the focal point. The Fresnel can be measured with the same techniques as the spherical lens with the additional measurement of step height at each of the zone changes. Sharp features such as the blaze grating and V-shaped grooves are measured for PV error, feature edge form, and face angle and flatness. The lenticular array can be measured for the radius of curvature of each cylinder and error in the replication of the height of the peaks between the cylinders. On all features, analysis of both the feature itself and the array of features is important. For example, the shape of each peak in the blaze grating is important, but it is the form of all of the peaks together that causes the grating to function.

Through this experiment a greater understanding of the relationship between injection molding factors and the replication of precision optical features is being developed. Through this understanding, it will be possible to better predict the moldability of optical features in new molds.

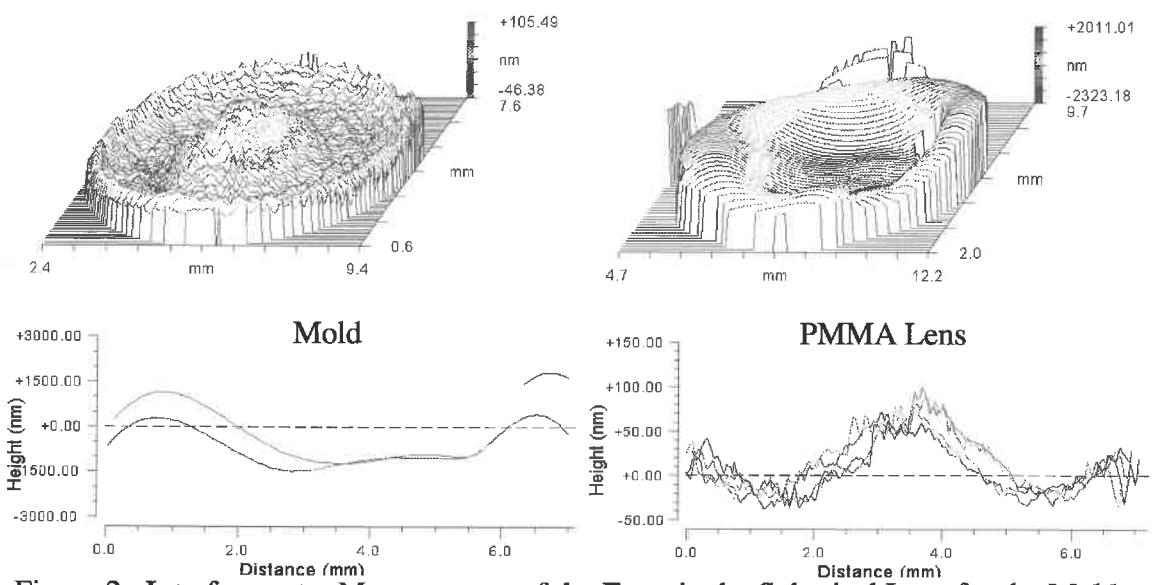

Figure 2. Interferometer Measurement of the Error in the Spherical Lens for the Mold and a Replicated PMMA Lens

ACKNOWLEDGEMENT

The authors wish to acknowledge the support of this research by the National Science Foundation (grant #9908223, Dr. K. P. Rajurkar, Program Director)

Good Things Come in Small Packages

A Table Top CMM With Sub-Micron Capability

David H. Youden
Eastman Kodak Company

Abstract

For Presentation at the 16th Annual Meeting
Of the
American Society for Precision Engineering
November 10-15, 2001

Background

It has long been stated, and it is generally agreed, that a large majority of the manufactured parts in the world are small enough to fit into a 50 mm cube. For some reason, however, most coordinate measuring machines (CMMs) have a capacity much greater than 50 mm. Capacities of 500, or even 2000 mm cubes are not all that uncommon. This is probably true because, if an organization commits the funds necessary to purchase a good CMM, there must be assurances that it will be capable of inspecting the largest part that anyone can ever imagine manufacturing. I submit that this is a poor approach to the issue. As good precision engineers, we know that size comes at a significant price in terms of accuracy and repeatability. Therefore, I submit that, to maximize the accuracy of the CMM, it should be as small as possible while still having the capacity to inspect a large percentage of the work at hand.

In mid 1998, I got a chance to prove my point. There developed a need within Kodak for a small CMM with exceptional accuracy, and as the resident precision engineers, it fell to Karl Falter and myself to design, build, and qualify such a machine. Other members of our team included Bob Smarcz, who oversaw our interface with the purchasing and manufacturing systems; Marty Wilk, our draftsman; and Joe Coffey, the technician responsible for actually building the machine. Many others from the Kodak organization contributed to the project and I wish to take this opportunity to thank everyone for their individual contributions to the project.

Machine overview

The Ultra Precision Coordinate Measuring Machine is a three-axis device with a work envelope of 50 mm (X) by 50 mm (Y) by 50 mm (Z). The gauge is carried on the Z axis while the work piece is located on the compound XY axis. Many different gauge heads can be accommodated. The gauge used initially with the machine is a three-axis analog LVDT-based design. All of the axes of the machine are supported on air hydrostatic bearings and are driven in translation by linear DC servomotors. The position feedback consists of four axes of laser plane mirror interferometry. In addition to the three linear axes (X, Y, and Z) the yaw motion of the XY compound axis is measured and used to correct the drive current to the two Y axis servomotors. The linear interferometers have a resolution of 0.31 nanometers and the angular interferometer has a resolution of 0.02 arc seconds

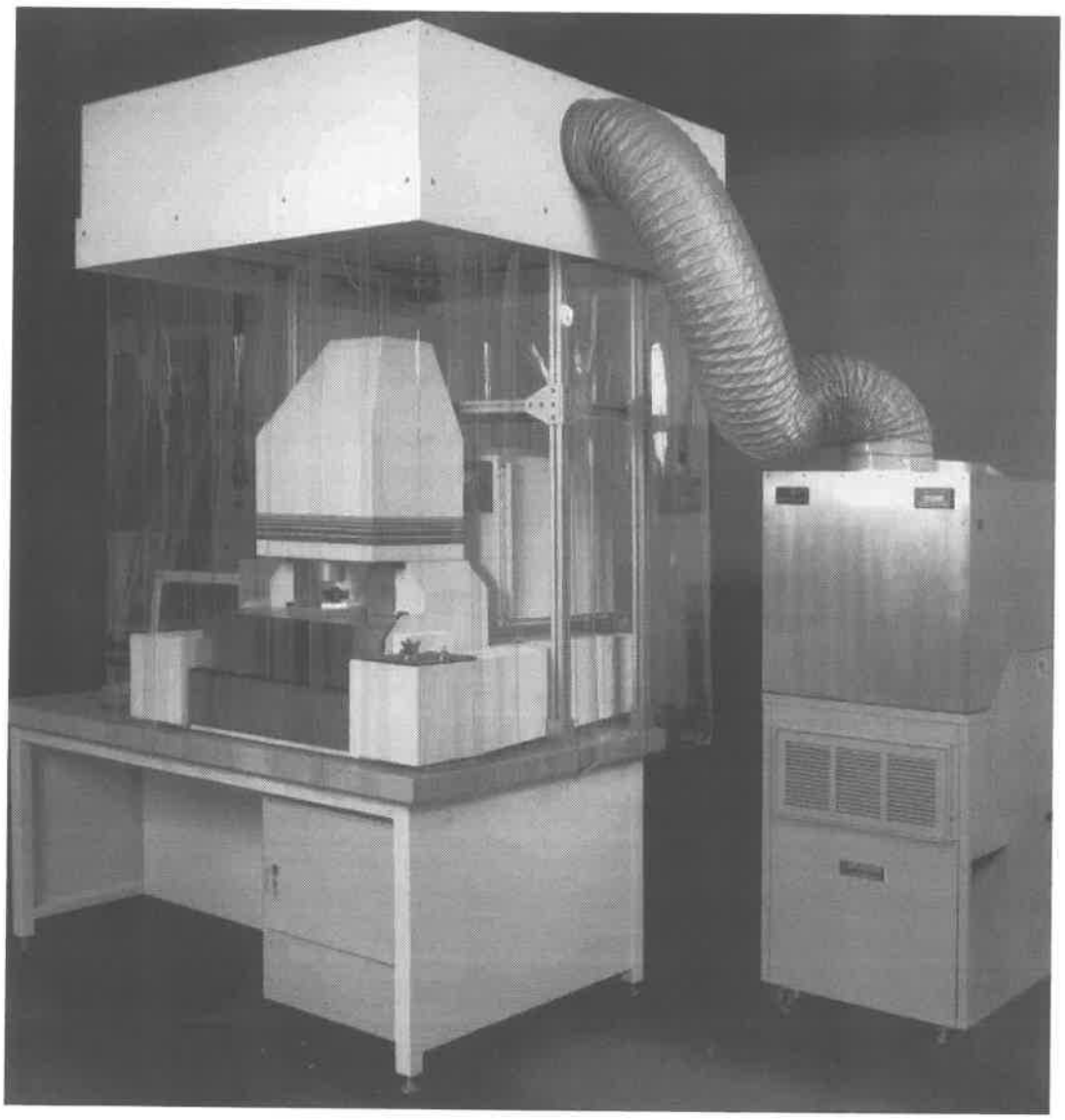

Y axis

The Y axis is an H shaped structure that is driven by two motors, one on each leg of the H. The crossbar of the H is the guide bearing for the compound main slide. Air bearings around three sides of each of the legs support and guide the assembly. There are shock absorbing stops at each end of the assembly's motion. A home switch is provided for initializing the position registers associated with the laser feedback sub-system. The bearing components of the Y axis are constructed of aluminum which has been hardcoated to provide wear resistance, and lapped to achieve superior geometry.

X axis

X axis motion is attained by the motion of the main slide along the guide way of the Y axis. The main slide is an aluminum block that is supported on air hydrostatic bearings. This block has a recess along its bottom surface that accepts the guide way of the Y axis. Three axes laser interferometry impinge upon a ULE glass square that is carried on the top surface of the main slide. These are the X and Y position feedback and the XY yaw feedback. The work stage is mounted directly above the glass square minimizing the Abbe offset of the stage.

Machine base

The XY compound stage is mounted on the machine base plate, which is a granite surface plate 700 mm wide, 700 mm long, and 150 mm thick. This plate is, in turn, supported by three pneumatic vibration isolation and leveling devices that are mounted on the supporting steel base assembly. The base assembly contains the electronic sub-systems and the air preparation equipment. At the rear of the base is the laser support bracket. This bracket serves to attach the rear vibration isolation mount to the base as well as supporting the laser head and the electronics termination panel.

Column support

The column support weldment mounts on the top of the machine base plate to the rear of the XY compound slide assembly. This steel fabrication supports the column and the Z axis.

Column

The column is also a steel fabrication. Three identical adjustable mounting assemblies kinematically mount it on the top surface of the column support.

Z axis

The Z axis is located on the front face of the column. Two 45 degree angle blocks and two L shaped preload blocks contain the air bearings that constrain the aluminum moving slide. At the front end of the moving slide is the gauge head mounting block. This block also carries the plane mirror that is the target for the Z axis interferometer, and the shutter for the Z axis home switch. The interferometer itself is mounted on a bridge that spans the moving slide and mounts atop the two preload blocks. The drive motor is located behind the interferometer bridge. At the rear end of the moving slide is the attachment point for the counterbalance band. The counterbalance band is made of stainless steel. It is .05 mm thick and 40 mm wide. The band passes up from the moving slide to the top of the column where it bends 180 degrees around a cylindrical air bearing and then down inside the column to the counterweight. Thus, when the slide moves, the band slides around the cylinder without friction, stick-slip, or bearing noise. The counterbalance weight may be bolted it to the interior wall of the column during transportation of the machine.

Gauge head

The gauge head is mounted to the front of the z axis directly in front of and in line with the Z axis target mirror. It is a three-axis device. Each of the three axes is comprised of an identical pair of flexures that allows plus or minus 0.25 mm of travel. Each axis has an LVDT that provides a linear displacement signal. The excitation voltages to the three LVDTs are phase locked together to minimize cross talk between the axes. A variety of other gauge heads may be fitted to the machine.

Covers

There are five main covers on the machine. The largest cover is the column and Z axis cover that mounts on the top of the column riser and covers the front and sides of the machine upper structure. The rear of this cover is open to allow air to flow over the upper structure. The XY compound slide is covered with a sheet stainless steel cover that protects it from dust, dirt, and falling parts. Each of the two front vibration isolation supports has a cover to prevent items from becoming pinched between the machine and the table when the isolation system is turned off. Finally, there is a transparent cover that encompasses the work area. This cover has doors to allow access to the stage on the top of the XY compound slide. It protects the work area from air movement and dust. In addition to these, there is a small cover over the front of the column riser that serves to complete the work area containment.

Table

The entire machine is mounted on a rigid table 1525 mm (60") wide, 762 mm (30") high and 1067 mm (42") deep. Air filtering and monitoring components are also mounted on this table.

Control electronics

The electronic equipment that controls the machine is contained, for the most part, in cabinets located beneath the table that supports the machine. The electronic equipment includes a personal computer, the Zygo laser control system, several Delta Tau PMAC printed circuit boards that are mounted in a personal computer expansion chassis, the gauge head control electronics, and miscellaneous other electrical and electronic components. The personal computer, the video display and a keyboard are located on the table adjacent to the machine.

Temperature control system

The machine is surrounded by an enclosure containing an open loop air shower. Temperature controlled air flows from an overhead plenum down around the machine, exiting the enclosure several inches below the table top. The air cooling and tempering equipment is located in a free standing cabinet that can be located near the machine. Temperature control is achieved by mixing the cold air from the evaporator of the air conditioner with the hot air stream from the condenser. The mixing fans are driven by the output of a cascaded dual loop PID controller. This system has proven to be able to hold ±0.01° F for long periods of time.

Axis straightness and noise

Axis straightness and noise measurements were made by placing a glass straight edge on the XY compound slide and mounting an LVDT displacement probe on the Z axis. The appropriate axis was then moved and a recording was made of the probe signal. In the case of the Z axis, the straight edge was mounted on the stationary frame of the compound slide. The straight edge was known to be straight within about 50 nm over its 330 mm length. The following table summarizes the results of these measurements.

AXIS	DIRECTION	STRAIGHTNESS	NOISE	DATE
X	HORIZONTAL	53 nm	30 nm	11/17/00
X	VERTICAL	25 nm	20 nm	12/7/00
Y	HORIZONTAL	125 nm	50 nm	12/5/00
Y	VERTICAL	75 nm	40 nm	12/7/00
Z	L-R	250 nm	65 nm	12/6/00
Z	F-B	125 nm	25 nm	12/6/00

Straightness measurements refer to long wavelength features where the wavelength is longer than the length of travel of the axis. Noise measurements refer to features with a wavelength less than 5 mm. Note that the X and Y axes each have a travel of 50 mm, and the Z axis has a travel of 100 mm. Note, also, that there are no guide bearings to provide control the Y axis horizontal travel. These numbers are a result of servo system response only.

Squareness

The squareness of the X axis to the Y axis is completely dependent upon the squareness of the stage mirror. This mirror is square to about 0.1 arc seconds. We have no way to verify this number. The squareness of the Z axis to the X and Y axes is adjustable by use of the column mounts. At the time of the testing no precision square was available, so no attempt was made to square the Z axis travel to the X and Y axes.

X-Y error map

The motion of the XY compound slide should be such that the distance from the gauge mounting surface to the surface of the work platen does not change as the X and Y axes move. The actual change in this distance was measured on a grid with a spacing of 12 mm. A best fit plane was calculated and subtracted from the measured data.

The raw, uncorrected data showed a range of 214 nm peak to valley. The best fit plane had a peak to valley range of 196.4 nm. The corrected data displayed a total error, or deviation from a plane, of +21.2 nm, -21.4 nm. This indicates that careful lapping of the platen feet can bring the uncorrected X-Y plane of the machine to within 25 nm of perfection, leaving only the remaining few nanometers to be removed by error mapping. It was elected to leave the implementation of the error map for a future project.

Repeatability

The repeatability of the Ultra Precision Coordinate Measuring Machine was tested in accordance with paragraph 5.3 of ASME B89.4.1-1997. The results are presented below. The spreadsheet lists the minimum and maximum values for the X, Y, and Z coordinates of the center of the test sphere along with the calculated value of its radius. There are 10 sets of readings reported. Each set of readings required about 41 seconds of machine time. The temperature in the work enclosure is also reported, but the value reported is raw analog to digital converter output. The reported value for temperature must be divided by -327, and then an offset value of 141.2 must be subtracted from the result to arrive at degrees Celsius.

The test ball used for this test was not a precision ball, therefore we are slightly limited in our ability to calculate its radius because the ball is not truly spherical. Nevertheless, the repeatability of the X and Y axes is on the order of 25 nanometers, and the Z axis repeatability is about 35 nanometers. The temperature did not drift more than about 0.003° C during the 7 minutes of the test.

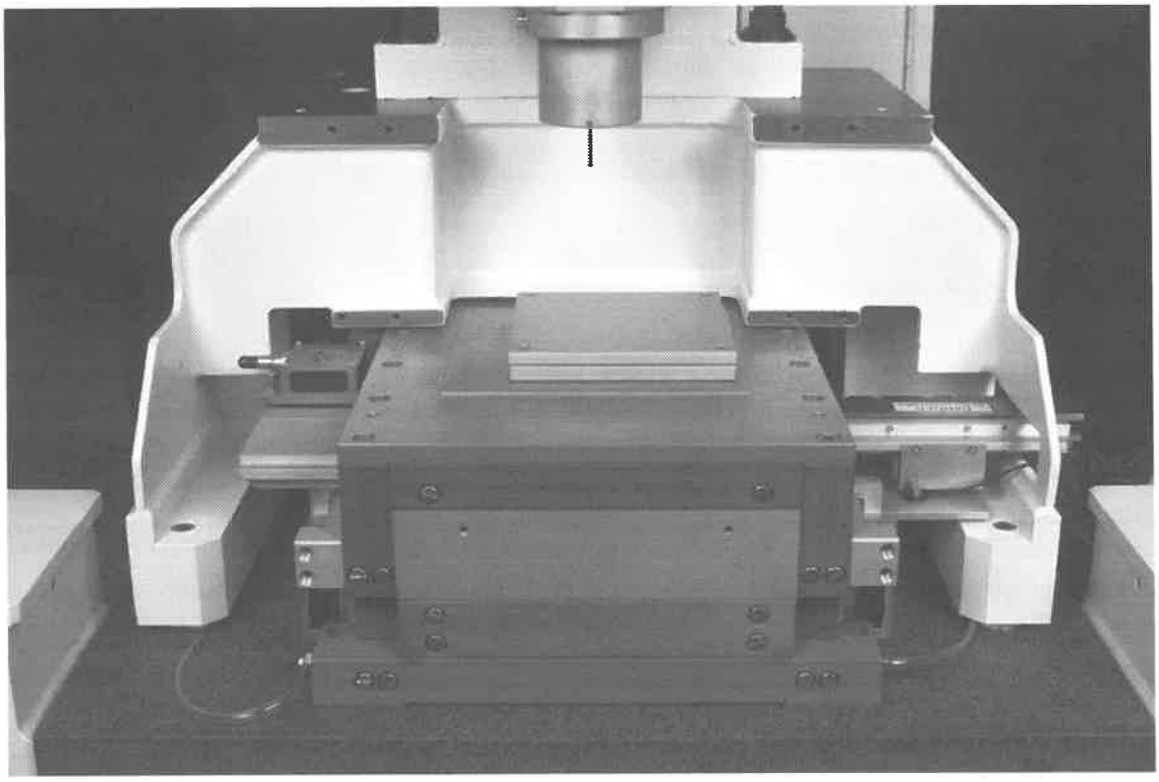

Number of Sphere Readings: 10
Calibration File: C:\WINDOWS\Desktop\probe_cal\calibration_file_feb15_lo_defl.txt
Date this file was generated: 2/16/2001 7:59:45

Min/Max Values:

min/max x center	min/max y center	min/max z center	min/max radius	min/max time	min/max temp	min/max_err
22.77146	24.58646	68.78945	4.762665	66.71875	39519.25	3.55E-15
22.77148	24.58649	68.78948	4.762678	480.5937	39520.25	2.75E-14

(Max - Min) Ranges:

range_x	range_y	range_z	range_r	elapsed time	range_temp	range_err
2.21E-05	2.56E-05	3.49E-05	1.30E-05	413.875	1	2.40E-14

List of Spheres:

center_x	center_y	center_z	radius	time	temp	max_radius_error
22.77146	24.58649	68.78947	4.762670	66.71875	39520.25	2.31E-14
22.77148	24.58648	68.78948	4.762678	104.3437	39519.5	4.44E-15
22.77147	24.58648	68.78946	4.762675	141.9687	39519.25	9.77E-15
22.77148	24.58648	68.78945	4.762672	179.5937	39520.25	5.33E-15
22.77148	24.58648	68.78945	4.762672	217.2187	39520.25	3.55E-15
22.77147	24.58648	68.78946	4.762670	254.8437	39519.75	2.75E-14
22.77148	24.58647	68.78947	4.762674	367.7187	39519.5	9.77E-15
22.77148	24.58646	68.78948	4.762671	405.3437	39519.75	1.33E-14
22.77148	24.58646	68.78945	4.762671	443	39519.75	3.55E-15
22.77147	24.58648	68.78946	4.762665	480.5937	39519.5	1.07E-14

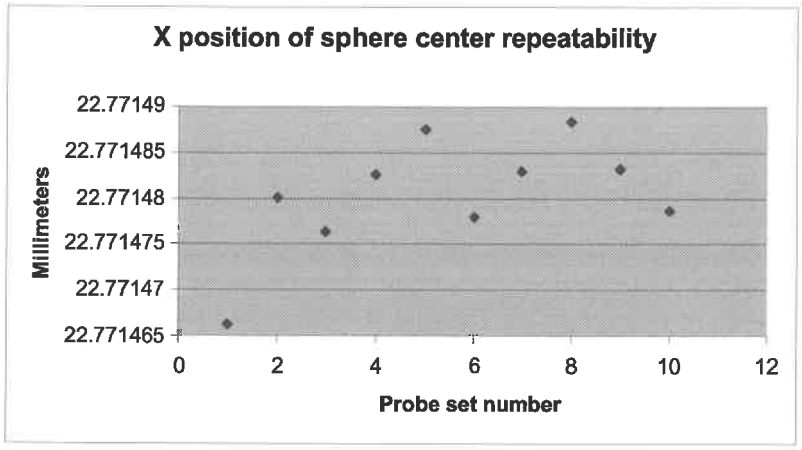
X position of sphere center repeatability
22.77149
22.771485
22.77148
22.771475
22.77147
22.771465
Millimeters
0
2
4
6
8
10
12
Probe set number

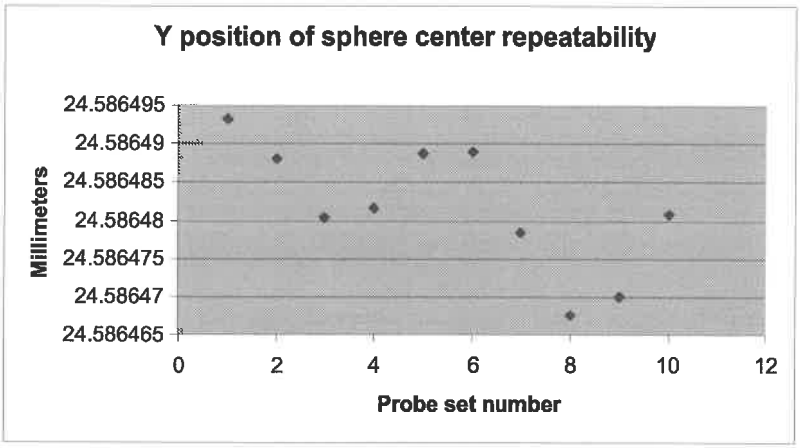
Y position of sphere center repeatability
24.586495
24.58649
24.586485
24.58648
24.586475
24.58647
24.586465
Millimeters
0
2
4
6
8
10
12
Probe set number

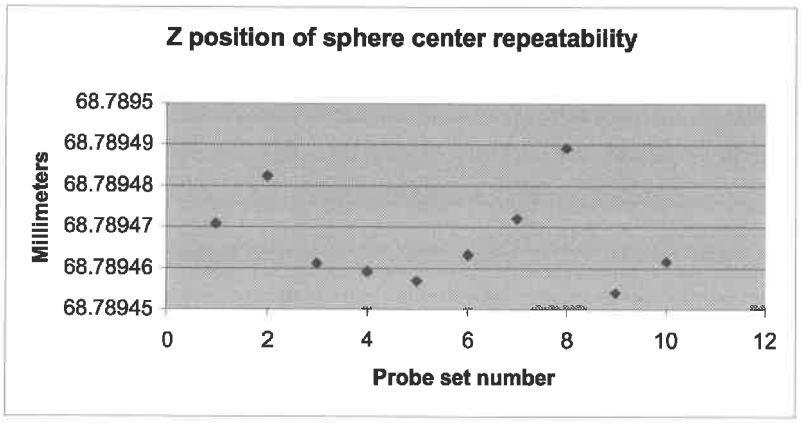
Z position of sphere center repeatability
68.7895
68.78949
68.78948
68.78947
68.78946
68.78945
Millimeters
0
2
4
6
8
10
12
Probe set number

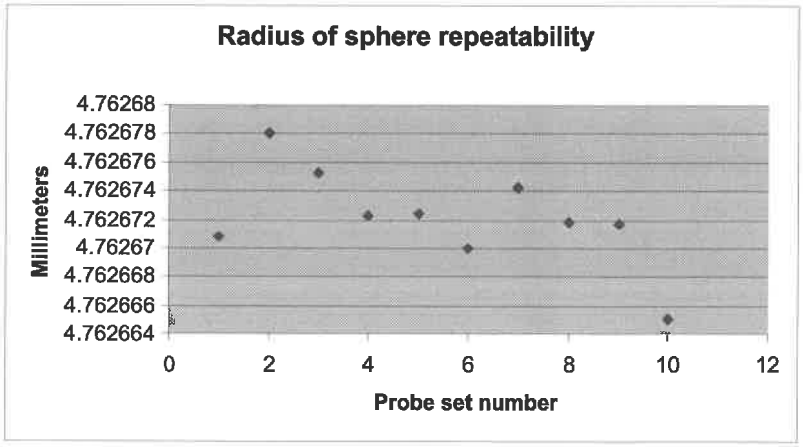
Radius of sphere repeatability
4.76268
4.762678
4.762676
4.762674
4.762672
4.76267
4.762668
4.762666
4.762664
Millimeters
0
2
4
6
8
10
12
Probe set number

Temperature variation error

The temperature variation error (TVE) test was performed using a 3/8" (9.525 mm) diameter ball mounted near the center of the machine's working volume. This ball was probed at the pole, and at 3 points near its equator. From this information, the location of the center of the ball, and the radius of the ball were calculated. Each set of four measurements took 41.81 seconds to complete. Two long tests were run during which about 945 measurement sets were made. An additional short run was also made which had 110 measurement sets. The long runs took about ten and one-half hours to complete, and the short run was one hour and a quarter long. The first long run was made with the local room air conditioner running normally, which for this room produced a temperature swing of about two and one-half degrees Celsius. Results are shown for the X, Y, and Z directions, as well as for the ball radius and the temperature within the machine measurement enclosure.

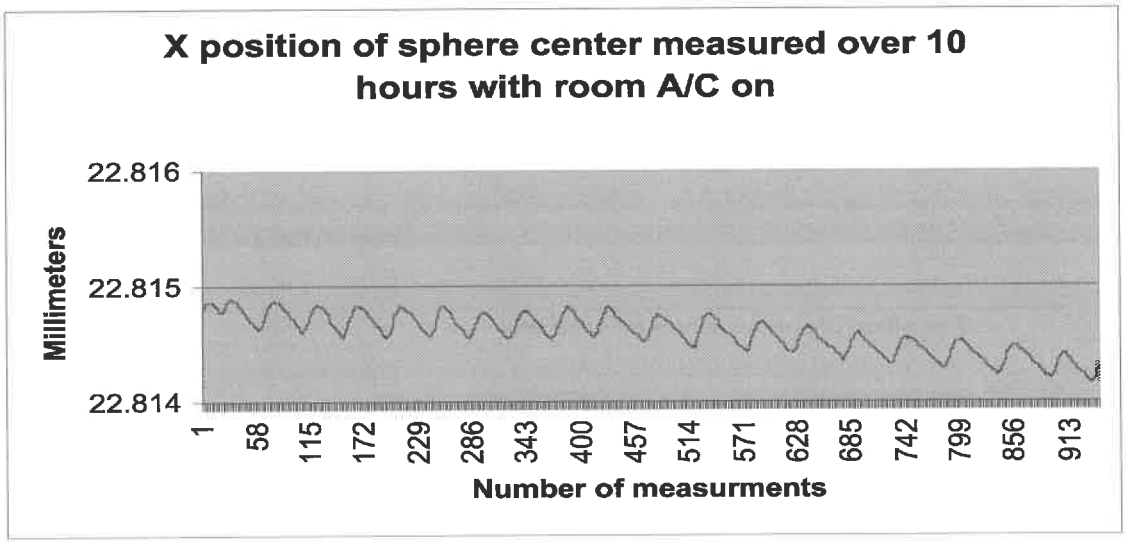

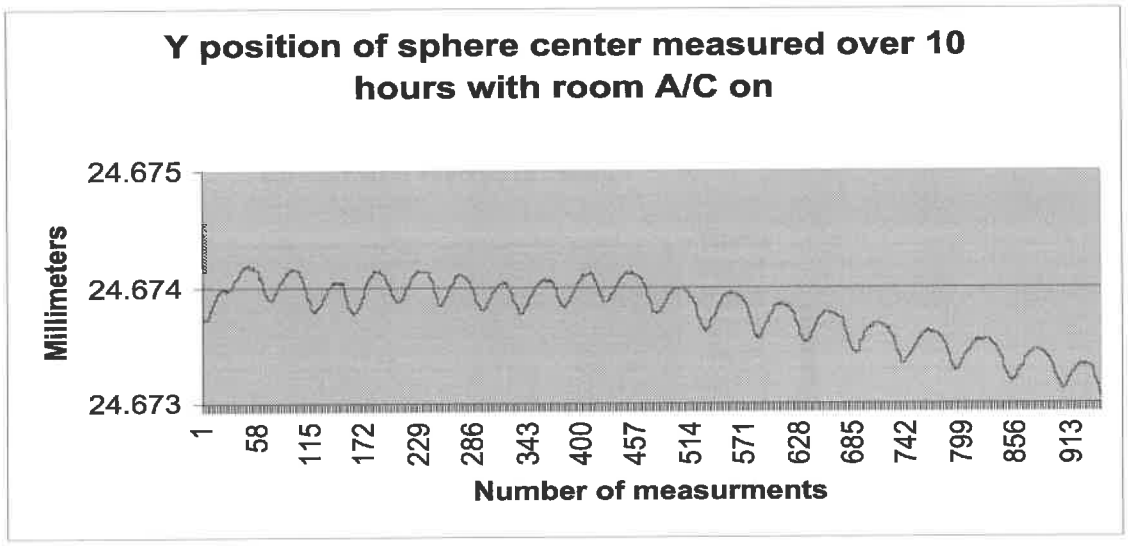

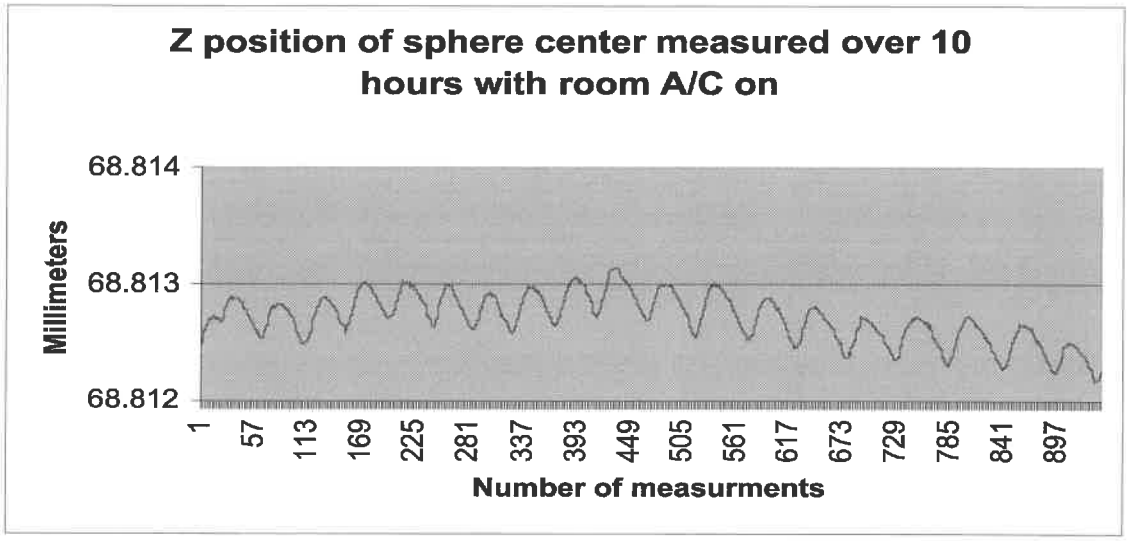
Z position of sphere center measured over 10 hours with room A/C on
Millimeters
68.814
68.813
68.812
1
57
113
169
225
281
337
393
449
505
561
617
673
729
785
841
897
Number of measurments

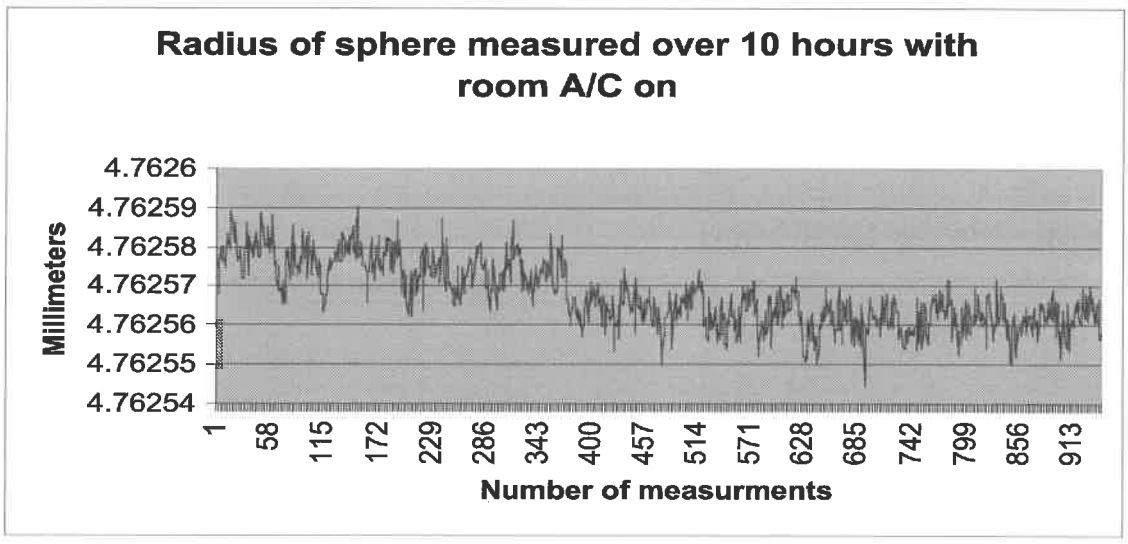
Radius of sphere measured over 10 hours with room A/C on
Millimeters
4.7626
4.76259
4.76258
4.76257
4.76256
4.76255
4.76254
1
58
115
172
229
286
343
400
457
514
571
628
685
742
799
856
913
Number of measurments

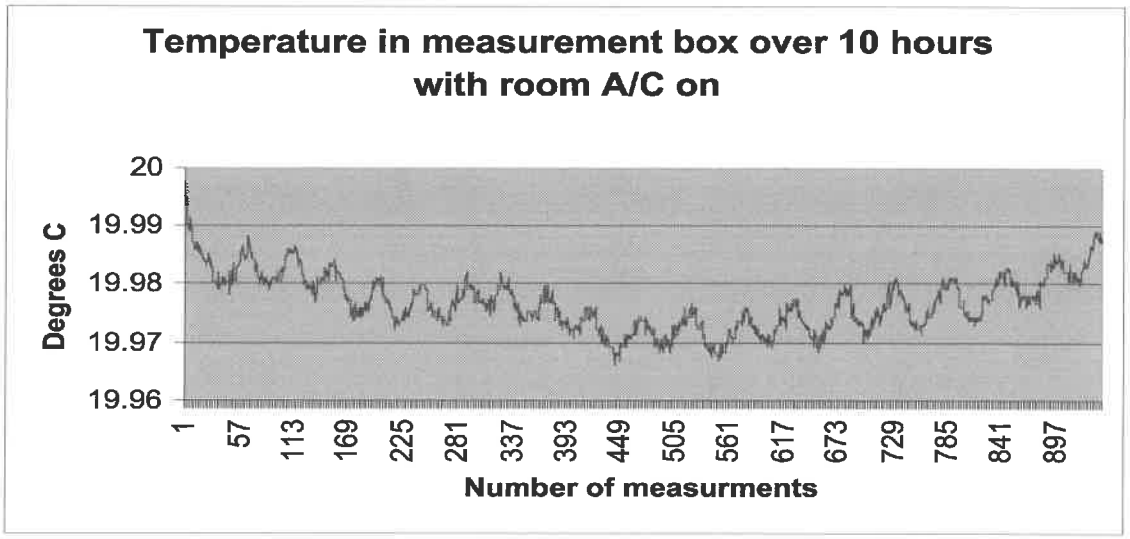
Temperature in measurement box over 10 hours with room A/C on
Degrees C
20
19.99
19.98
19.97
19.96
1
57
113
169
225
281
337
393
449
505
561
617
673
729
785
841
897
Number of measurments

Note that the temperature within the machine measurement box faithfully followed the room temperature with an amplitude of about 0.01° C. This may be due to radiative heat transfer through the vinyl curtains.

The following night the room air conditioner was shut down and the test was repeated. The results from this second test are shown below. During this test the room temperature increased by at least 10 degrees F. This gross temperature change overpowered the temperature control system on the machine and the temperature rose during the test by about 0.3 degrees C compared to the previous night when there was a 0.025 maximum temperature swing.

TVE Results	X Axis	Y Axis	Z Axis
RUN 1 (A/C On)	0.702 _m	1.08 _m	0.905 _m
RUN 2 (A/C Off)	2.201 _m	5.10 _m	4.304 _m

The results stated above are peak-to-valley readings for the two 10 hour tests. I estimate that, in a properly temperature controlled environment, the results would be about 50% of those shown for run 1. This is because the short term variations caused by room temperature variations would, for the most part, be gone.

Volumetric performance

Volumetric performance of the machine was evaluated using an artifact which is a cube with 9.55 mm balls, numbered 1 through 4, mounted on the top four corners. The four balls were measured, and the six distances between their centers were calculated. This gave us the four sides of a box and the two diagonals. This procedure was done twice and then the artifact was rotated about 90° (By eye) and the process was repeated. The results obtained are reported below.

	Distance 1-2	Distance 1-3	Distance 1-4	Distance 2-3	Distance 2-4	Distance 3-4
Run 1	28.12652	39.80367	28.19226	28.13287	39.79336	28.11556
Run 2	28.12575	39.80366	28.19211	28.13249	39.79217	28.11517
Run 3	28.12400	39.80310	28.19475	28.13388	39.79224	28.11217
Run 4	28.12356	39.80285	28.19395	28.13414	39.79226	28.11282
Deviation	0.00296	0.00082	0.00264	0.00165	0.00119	0.00339

Gauge head issues

The gauge head approach velocity used for all testing was 0.25 mm/sec. The gauge spring constant is about .004 Newton/Micron in each direction. The gauging force used for these tests was .01 Newton's (1 Gram force). The stylus was 30 mm long and had a 0.75 mm diameter ruby ball on the end of the shaft.

Error sources

The following items have been identified as potential sources of errors in our characterization of the small CMM:

1. The variation of the temperature of the room where the machine is located. The temperature change in this room is extreme for our purposes. Steps have been taken to correct the situation, but as the machine has been moved to a new location the results are unknown.

2. The squareness of the Z axis to the X-Y plane. This is readily adjustable but we do not have a good squareness standard to use for the adjustment.

3. Velocity of light calculation for the laser. We may, at some time, want to consider adjusting the laser scale factor as a function of barometric pressure. Temperature is not a big concern as we control it quite well. Relative humidity is a factor, but not a large one. Each machine axis should be independently adjustable because the Z axis of the machine uses a slightly different wavelength of light than the X and Y axes. This is because of the way the differently polarized laser beams are steered around the machine.

4. Tooling balls. None of the balls used for our testing had any degree of precision. This probably did not affect the results for repeatability and TVE but it did affect the volumetric data where the balls are probed at different places during different parts of the testing.

Conclusions

The small coordinate measuring machine meets the criteria for which it was designed. While there is no doubt that further significant improvements could still be made in the performance of the machine, this effort must be viewed as an academic exercise.

Design and Testing of a One Dimensional Measuring Machine for Determining the Length of Ball Bars

John Ziegert, David Rea
Department of Mechanical Engineering
University of Florida
Gainesville, FL 32611

Steven D. Phillips, Bruce Borchardt, John Stoup
National Institute of Standards and Technology
Gaithersburg, MD

ABSTRACT

A new machine for the rapid calibration of ball bars has been built. By means of comparisons to CMM measurements, it has been shown to work as an accurate special purpose machine for the calibration of ball bar lengths.

INTRODUCTION

One of the most common artifacts used to evaluate the volumetric measuring performance of coordinate measuring machines is the ball bar (ANSI/ASME B89.1.12M). This procedure involves measuring the distance between two precision spheres held a fixed distance apart by the connecting rod of the ball bar. The measurement is repeated at numerous positions and orientations in the workzone of the machine. Because the ball bar is a fixed length, any measured deviations in the ball bar center-to-center length indicate measuring errors of the CMM. When used for this purpose, the absolute length of the ball bar need not be known. However, more information about the CMM can be gained by examining the measurement errors using a calibrated length ball bar. The current best method for calibrating the length of ball bars is by measurement on very high performance CMMs. This procedure is expensive and time consuming, and is unsuitable for adoption by individual corporate standards laboratories.

The goal of the work reported here is to provide a simpler and lower cost instrument capable of measuring the absolute length of ball bars ranging from 300 to 1000 mm nominal length with an expanded uncertainty for the measurement of $U = 0.2\ \mu m + 0.2\ L\ \mu m$, where L is given in meters. An additional goal is to design an instrument which does not act as a length comparator, thus requiring a calibrated ball bar to "master" the instrument, but introduces the length metric directly into the measurement process.

DESIGN CONCEPT

The instrument we have developed is essentially a 1 dimensional measuring machine (1DMM). It is composed of a long stiff granite beam (approx. 150mm X 300mm X 2000mm) with 2 air bearing stages riding on its top surface (Figure 1). Each stage carries a kinematic mount to accept the end of a ball bar, and a retroreflector mounted so that its center is coaxial with the axis of the ballbar, minimizing Abbe errors during measurement. A fixed block at the center of the beam holds another kinematic mount to accept a ball bar end. A metrology frame is kinematically mounted to the top of the granite beam. The metrology frame consists of two endplates connected by 3 Invar rods. Each endplate of the metrology frame holds a

Michelson interferometer whose measurement axis is aligned with the ballbar axis and stage motion, thus minimizing cosine errors. (Figure 2)

The granite beam is sized so that deflections due to the weight of the ball bar and the moving sled cause negligibly small errors in the measurements. Appropriate adjustment degrees of freedom are provided on the sleds and optical mounts to allow the three kinematic mounts to be aligned in a straight line and the interferometer beams to be aligned to the stage motions.

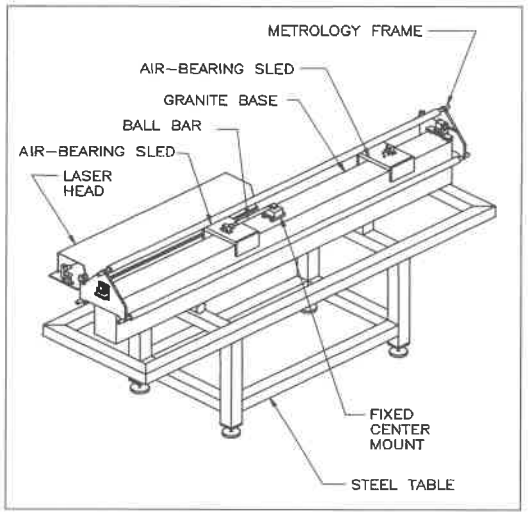

Figure 1. Conceptual design of 1DMM

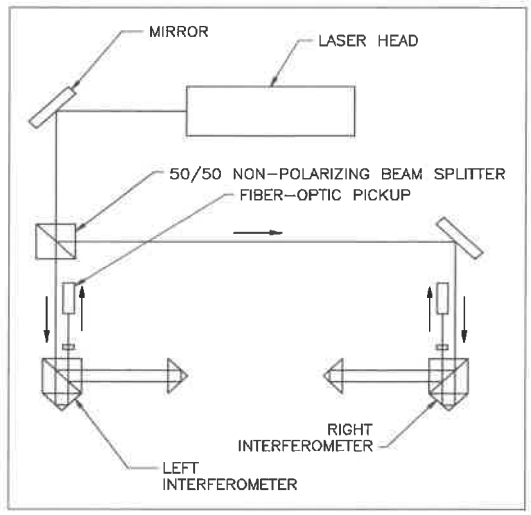

Figure 2. Interferometer layout of 1DMM

The measurement procedure is as follows:

1. Place the ball bar ends in the kinematic mounts on the left movable stage and fixed center point and initialize the left interferometer to zero.
2. Move the right end of the ball bar to the right movable stage, and simultaneously initialize the right interferometer to zero and record the displacement, $\boldsymbol{a}$, measured by the left interferometer.
3. Move the left end of the ball bar to the fixed center mount and record the displacement, $\boldsymbol{b}$, of the right interferometer.
4. The length between ball centers of the ball bar is $\boldsymbol{L} = \boldsymbol{a} + \boldsymbol{b}$.

UNCERTAINTY ANALYSIS

In the design stage, we generated an uncertainty analysis based entirely on Type B uncertainties. This analysis takes into account laser system errors, environmental effects, stage misalignments and error motions, cosine and Abbe errors of the measurement beam, thermal effects in the ballbar and metrology frame, sag of the ball bar, and mechanical repeatability of the system. (Table 1) The assumed measurement conditions for the uncertainty analysis are:

1. Room at 20 °C ± 0.05 °C.
2. Temperature of air and ballbar measured to ± 0.01 °C.
3. Barometric pressure measured to ± 0.255 mm Hg (34 Pa).
4. Relative humidity measured to ± 5%.
5. Uncertainty of Coefficient of Thermal Expansion (CTE) of material = 1 x 10^{-6} /°C.

6. Negligible vibrations.
7. Dead path length for each interferometer = 10 mm.
8. CO_2 content of atmosphere = 355 x 10^{-6}
9. Time required for complete measurement is assumed to be less than 10 minutes.

Table 1. Uncertainty analysis for a 1000 mm ballbar measurement.

Wavelength stability	0.027
Polarization mixing	0.00164
Resolution	0.00124
Environmental Error	0.161
Deadpath Error	0.001
Stage Misalignment	0.02
Laser Alignment	0.007
Thermal Errors	0.176
Ball Sphericity	0.1
Ball Bar Sag	0.07
Combined Standard Uncertainty: $u_c = 0.270$ µm Expanded Standard Uncertainty: $U = 2\,u_c = 0.540$ µm Target Expanded Standard Uncertainty: $U = 0.400$ µm	

Although the uncertainty analysis shows that the target expanded uncertainty is not met, it can be seen that the most significant contributors to the error are environmental and thermal effects. Changes in the basic design of the machine will have a small effect on these sources of error. Therefore, it was decided to build and test a prototype 1DMM to assess its accuracy and repeatability.

TEST RESULTS

Figure 3 shows a photograph of the prototype 1DMM. The instrument was delivered to NIST and assembled in a room with the temperature controlled to approximately ± 0.05 °C. The temperature, pressure, and humidity of the air were monitored and appropriate corrections to the index of refraction were made using Edlen's equation. The temperature of the ball bar was also monitored and its length corrected using the best available estimate of the CTE. Noise and drift tests were performed to assess the stability of the instrument and to determine the optimal sampling time for interferometric measurements. Based on these tests, it was decided to read the laser interferometers by sampling them 150 times over a 15 second period and averaging the readings. This procedure was selected to reduce the sensitivity of the measurements to variations in the air along the laser path due to imperfect mixing of the air in the room, yet still be rapid enough to minimize the effect of thermally induced changes in the instrument components.

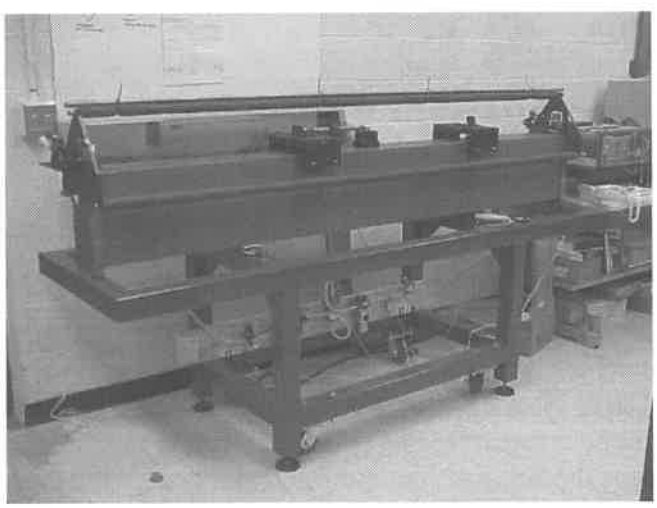

Figure 3. Prototype 1DMM

Six ball bars of varying lengths and materials were measured by NIST on a Moore M-48 CMM. These ball bars were then measured on the 1DMM. Each ball bar was measured 10 times on the 1DMM, which required approximately 30 minutes. The measured length of the ball

bar is reported as the mean of the 10 measurements. Table 2 shows the results of these measurements.

Table 2. Results of 1DMM measurement of 6 ball bars. (All lengths in mm)

Ball bar material	Nominal length	1DMM length	1DMM 2*S.D.	CMM measured length	1DMM length – CMM length
Steel	400	400.54437	0.00020	400.54454	-0.00017
Invar	400	400.09760	0.00017	400.09759	0.00001
Invar	500	499.93388	0.00030	499.93403	-0.00015
Invar	600	599.98659	0.00021	599.98635	0.00014
Steel	700	698.90277	0.00015	698.90290	-0.00013
Invar	900	899.93887	0.00025	899.93857	0.00030

In all cases the 1DMM measurements were within 0.30 μm of the CMM measured lengths. The expanded uncertainty of the CMM measurements ($k = 2$) is 0.2 μm + 0.2 L μm (L in meters). Two standard deviations of the 1DMM repeatability were all less than or equal to 0.30 μm, which is significantly less than predicted by the uncertainty analysis of Table 1, and is most probably due to better environmental conditions than were assumed in that analysis. Furthermore, in all cases the 1DMM-CMM differences for these measurements are less than the target value established at the beginning of the project.

The 1DMM achieves satisfactory results as a special purpose machine for highly accurate certification of the length of ball bars at a small fraction of the cost of high accuracy, general purpose CMMs.

References

1. ASME B89.4.1M-1997. Methods for Performance Evaluation of Coordinate Measuring Machines, ASME, New York, 1997.
2. Edlen, B. The Refractive Index of Air, Metrologia, Vol. 2, No. 2. 71-80.
3. Estler, W. Tyler. High-accuracy displacement interferometry in air, Applied Optics, Vol. 24, No. 6., 15 March 1985. 808-815.
4. Phillips, Steven D., Borchardt, B., Doiron, T., Henry, J. Properties of Free-Standing Ball Bar Systems, Journal of the American Society for Precision Engineering. Vol. 15, No. 1, January, 1993. 16-24.
5. Slocum, A. Precision Machine Design. Prentice-Hall, Inc., Englewood Cliffs, NJ, 1992.
6. Taylor, Barry N., Kuyatt, Chris E. Guidelines for Evaluating and Expressing the Uncertainty of NIST Measurement Results, NIST Technical Note 1297. U.S. Government Printing Office, Washington, DC, 1994.
7. Rea, L.D., "Design, Assembly, and Testing of a Ball Bar Measuring Machine", MS Thesis, University of Florida, August 2001.
8. Certain trade names and company products are mentioned in the text or identified in illustrations in order to adequately specify the experimental procedure and equipment used. In no case does such identification imply recommendation or endorsement by National Institute of Standards and Technology nor does it imply that the products are necessarily the best available for the purpose.

Methods for Correcting the Group Index of Refraction at the PPM Level for Outdoor Electronic Distance Measurements

Parker, David H.
The Nat'l Radio Astronomy Observatory, Green Bank, WV 24944-0002, dparker@nrao.edu

The Green Bank Telescope (GBT)[1] is a recently completed 100-meter radio telescope built by the National Radio Astronomy Observatory in Green Bank, WV. The GBT incorporates a first-of-its-kind active surface and precision-pointing system based on a custom designed system of 18 automated electronic distance measurement (EDM) instruments. Twelve EDMs are mounted on stable monuments equally spaced on a 120-meter radius around the telescope. These ground-based instruments measure cardinal points on the structure to correct for thermal and gravitational deflections in the structure and thus correct the pointing with respect to the stable earth reference. Six additional instruments mounted on the deflecting structure measure the surface of the main reflector and generate corrections which are used to move 2209 actuators to correct the shape of the main reflector. By tying the 12 stable ground instrument measurements to the 6 structurally mounted instruments, they are referenced to the same coordinate system and thus the absolute pointing of the reflector is determined. The system can best be described as a large *in situ* coordinate measurement machine working in a 240-meter diameter X 150-meter high cylindrical volume (6 million cubic meters). The desired accuracy is of the order of 1 part per million (ppm) (0.100 mm at 100 meters). Due to the nature of the application, the EDMs must operate under outdoor ambient conditions.

The instrument is based on a phase measurement of a 1.5 GHz modulated laser, and therefore the phase of the 1.5 GHz return beam depends on the speed of light - more specifically, the group index of refraction for the modulated beam. To first order, the group index of refraction depends on the temperature, humidity, and pressure integrated through the path. For outdoor measurements, temperature is the primary limitation to the accuracy of EDM instruments. The group index of refraction changes by about 1 ppm/degree C - our entire error budget. The group index of refraction as a function of temperature, humidity, and pressure, has been worked out to about 0.001 ppm. The problem is that the temperature is not uniform throughout the volume. For example, the temperature near the ground can vary significantly from the temperature 150 meters higher at the top of the telescope. The 100-meter reflector cast a large shadow, which produces radical gradients in the temperature profile. Temperature profiles across the reflector surface depend on shadows and angle of the sun. Melting snow, standing water, ground cover, etc. can produce large gradients in the water vapor pressure. Clearly, a simple measurement of temperature, humidity, and pressure is insufficient to model the group index of refraction at the 1-ppm level throughout the volume.

The GBT system does have some advantage over general surveying problems. Unlike a general surveying problem where one is working from temporary tripods and limited bench marks, the 12 ground-based monuments were built to be very stable and can be used as bench marks, and up to 60 bi-directional base-lines can be constructed. Due to the automated control system and speed of the measurements (5 points/second), vast amounts of data can be generated and used in a model. The geometry of the base-lines can be measured under ideal conditions, and the base-lines can be used as ambient refractometers to measure the group index of refraction directly. A

fixed retroreflector on an adjacent mountain can be used as a macro refractometer. Temperature, humidity, and pressure can be measured at a number of locations. Acoustic thermometry is also an option. Experimental data will be presented which puts bounds on the accuracy of the model under various weather conditions.

The grid bar, calibration and application

Sascha Weikert, Wolfgang Knapp
Institute for Machine Tools and Manufacturing (IWF),
Swiss Federal Institute of Technology (ETH), Zurich, Switzerland

Keywords: machine tools, metrology, three-dimensional measurement

1. Introduction

For the evaluation of trajectories of machine tools and robots, the grid bar measuring device has been developed. A single grid bar (figure 1) allows the measurement of absolute spatial distances between the centres of the two spheres at it's ends over a range of 420 to 640mm, described in [1].

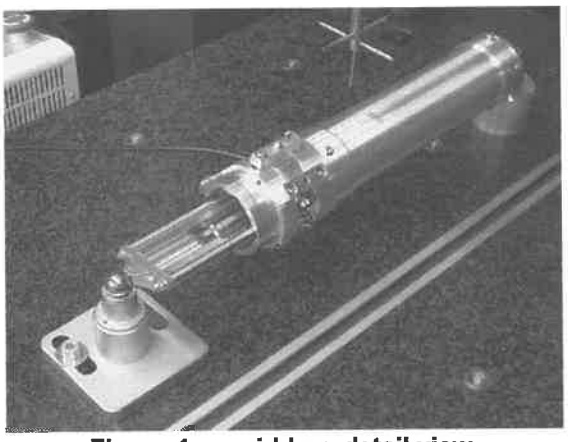

Figure 1 grid-bar, detail view

Combining two or three grid-bars at the same time (bipod or tripod application) hence permits the measurement of planar or spatial movements of the tool tip. Especially for measurements on parallel structures, specified alignment demands for the measurement equipment should be avoided.

In this paper, the design of the device for combined application of two and three bars is shown and uncertainty estimates concerning calibration and measurement results are given.

2. Calibration of single grid bar

2.1 Calibration for nominal bar length

For the calibration for the nominal bar length between the centres of the two precision spheres at the grid bar's ends a Leitz PMM864 coordinate measuring machine (CMM) is used. The grid bar is aligned parallel to the X axis of the CMM. The length measurement uncertainty on an end gauge is given by U_{95} = 1,2 µm + L/400 where L is the measuring length in mm. This value is given for any direction of the length measurement. From this a conservative estimate for the ball bar distance uncertainty can be derived as follows:

The measurement uncertainty U (k=2) for a point on the first sphere = 0,84 µm, i.e. the constant value of the length measurement uncertainty divided by $\sqrt{2}$, as the probing is just in one direction; the standard uncertainty u(point on 1st sphere) = 0,42 µm. The second sphere is assumed to be at a distance of 500 mm, hence U (k=2) for a point is 0,84 µm + 500/400 = 2.09 µm, or the standard uncertainty u (point on 2nd sphere) = 1.05 µm. The spheres can be measured on partial arcs of up to 270° at 25 points per arc. Therefore the uncertainty of the centre coordinates of the spheres are according to [2] just 80% of the uncertainty of the single point of contact. Therefore u (x coordinate, 1st sphere) = 0,34 µm and u (x coordinate, 2nd sphere) = 0.84µm. The centre distance uncertainty of the CMM measurement is the root of the squared sum, therefore u (centre distance, CMM) = 0.91 µm.

The run out of the spheres in the sockets is about 0.4 µm (range), therefore u(roundness) = 0.12 µm assuming a rectangular distribution. Following [3], and assuming a temperature of 20°C, the resulting measurement uncertainty for the nominal bar length U(nominal) (k=2) = 1.84 µm.

2.2 Calibration for measuring range

Using the Leitz PMM 864 for the calibration of the measuring range of 250 mm, the measurement uncertainty U(k=2) for the calibration for the measuring range is 1.40 µm. This task can be also carried-out using a HP 5529 laser interferometer as reference, accurately aligned to the measuring axis of a single grid bar. The set-up would have been located on a CMM in an air conditioned environment in order to reduce configurational and environmental influences on the measurement. Following ISO230-2 [4] an uncertainty U (k=2) for the calibration for the measuring range of 250 mm of 0.42 µm is obtained, assuming a calibration at 20°C.

3 Design and Construction of bipod configuration

The most intuitive way to combine three single-dimensional measurement devices would be to combine them to form three edges of a tetrahedron [5]. This configuration simplifies the calculation of the tool tip position very much, but necessitates the simultaneous attachment of three bars to the tool tip, typically using a precision sphere. Additionally, the angles of rotation are strongly restricted due to collision between the sockets connected with the bars and the shaft reaching for the tool holder. To overcome these restrictions in the actual design the two or three bars respectively are aligned as shown in figure 2. The location of the tool tip is determined by measuring absolute lengths of telescopic bars equipped with incremental linear scales.

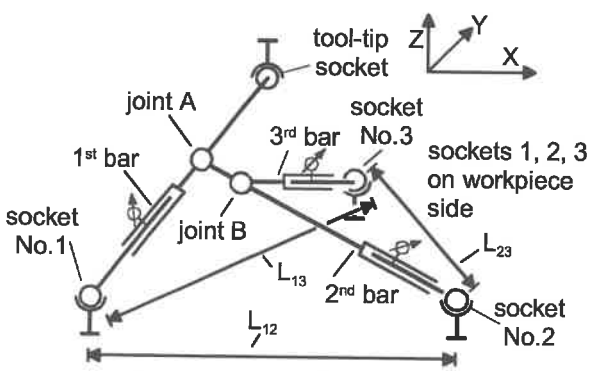

Figure 2 tripod configuration, lay-out

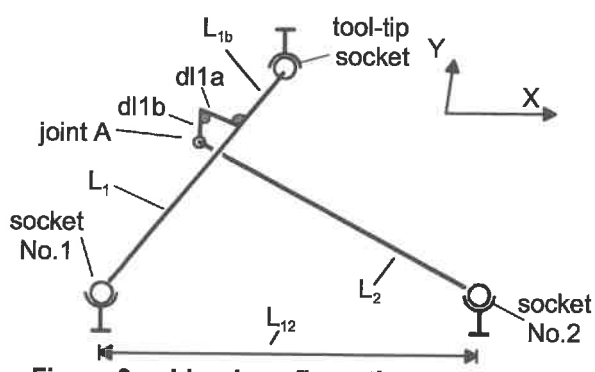

Figure 3 bipod configuration, parameters

For the bipod configuration, six geometric parameters are required to calculate the planar position (figure 3): L_{12}, the distance between the sockets 1 and 2; distance L_1 and it's component L_{1b} between joint A and the tool-tip socket; distance L_2, between socket 2 and joint A.

The offset dl1b is orthogonal to L_1 and L_2 and is realised by a hinge-type joint, the other offset dl1a of joint A is held orthogonal to dl1b. By this, the accuracy requirements for the joint location are strongly reduced. The influence of a small rotation of grid bar 1 is also minimised by this arrangement.

3.1 Measurement uncertainty and sensitivity analysis for bipod configuration

In table 1, the bipod's contributors u_i to the measurement uncertainty and the result of a sensitivity analysis are listed.

The alignment of the sockets 1 and 2 on the machine tool is checked by a dial gauge within a range of 1 mm in Z-direction, thus the standard uncertainty u(alignment in z) = 0.57 µm (cosine error).

The uncertainty of the calibration of the nominal bar length (u = 0.85 µm) and of the calibration of the measuring range (u = 0.21 µm) are included in the uncertainties of L1 and L2 respectively (u(L1, L2) = 0.88 µm). The uncertainties of L12 to L2 in table 1 are based on the measurement uncertainties of the CMM and the relevant distances.

The design restricts the rotation of grid bar 1 to a maximum of ±1 mrad, introducing a standard uncertainty u(rotation of 1st bar) = 0.58 mrad.

The sensitivity values indicate the ratio between the size of the single uncertainty contributor (expressed by the standard uncertainty) and it's effect on the measuring value. As can be seen, the influences of the orthogonal joint offset dl1b and the Cosine error only have very little influence on the measuring results.

Table 1 contributors to bipod's measurement uncertainty and results of sensitivity analysis

Contributors	u_i	ranges of sensitivity values [-]		
		x-direction	y-direction	x-y-plane
L_{12} basis distance between sockets 1 and 2	1.0 [µm]	0.06 – 0.89	0.05 - 0.35	0.09 - 0.91
L_1, distance between socket 1 and joint A	0.88 [µm]	0.87 – 1.30	0.05- 0.82	1.06 - 137
L_{1b}, distance between joint A and ball at tool tip	0.54 [µm]	0.04 – 0.68	0.67- 0.98	~ 1
dl1a, offset of joint A	0.54 [µm]	0.71 – 1.07	0.05- 0.72	1.06 - 1.09
dl1b, offset of joint orthogonal to L_1 and L_2	0.54 [µm]	~ 0.002	~ 0.002	~ 0.002
L_2, length between socket 2 and joint A	0.88 [µm]	0.89 – 1.36	0.06 – 0.89	1.15 - 1.42
rotation of 1st bar	0.58 [mrad]	0.71 - 1.07	0.05 - 0.73	1.07 - 1.09
Cosine error (alignment of the measuring plane)	0.57 [µm]	~ $1{,}7 \cdot 10^{-4}$	0.8·- 1.2	0.8·- 1.2

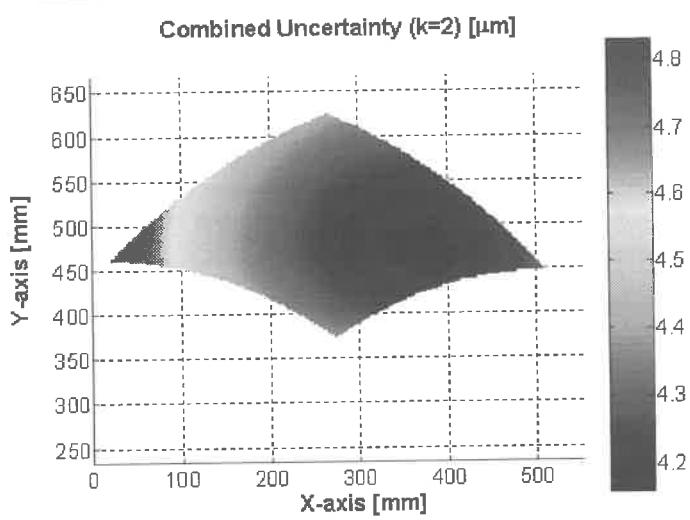

Figure 4 **Combined measurement uncertainty of the bipod device, alignment error included**

As can be seen in Figure 4, the combined uncertainty U (k=2) ranges between 4.2 and 4.6 µm. (values of 4.8 µm in local areas) including influences due to cosine-error (alignment error = 1 mm). Without alignment influences U(k=2) ranges between 3.5 and 4.2 µm.

In this case, the distance between the two sockets on the work-piece side is 500 mm. The square planar measuring range is 200 x 200 mm. In this area, tool tip rotations may vary about ±90° around X- and Y-axis.

4. Tripod application

While the use of two bars offers planar path information, for the measurement of spatial positions three bars are used (figure 5 and 6). The influence of additional six dimensional components flows into the uncertainty budget, corresponding to the two-dimensional case described in clause 3. As in the bipod case, the accuracy requirements for the joint location are low.

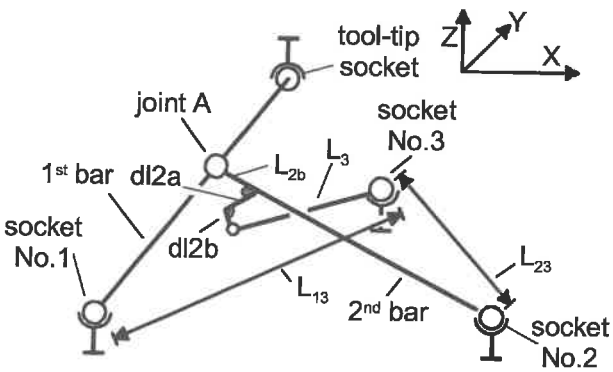

Figure 5 tripod application, additional parameters

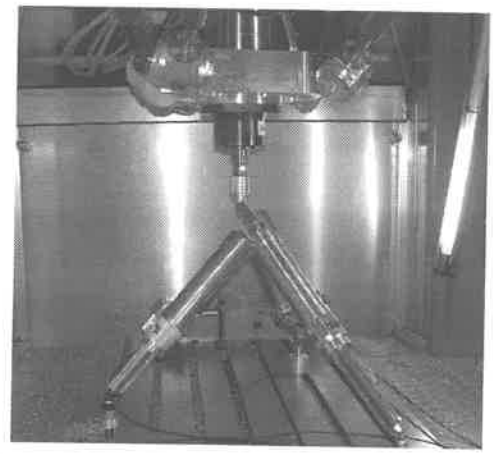

Figure 6 tripod configuration, mounted on HEXAGLIDE [6] for measurements

5. Conclusion and Future Work

A new kind of a two and three-dimensional measurement device for the evaluation of the path accuracy on machine tools has been developed. Due to simplified lay-out and kinematic correct design of the device, a measuring uncertainty U (k = 2) below 5µm for 2D application has been obtained. The next steps will be various applications in accuracy assessments of machine tools and calibration of the IWF-Hexaglide [6]

6. Acknowledgements

This project was supported by the Swiss Commission for the Promotion of Applied Research (KTI) and by the partners Agie SA, DIXI SA, Heidenhain (CH) AG, Mikron AG and Starrag.

7. References

[1] Weikert, S.; Knapp, W.: The Grid-bar, a New Device for Machine Tool Testing, Proc. of 2nd euspen Internat. Conference, Torino, Italy, May 27th – 31st, 2001

[2] Lotze,W,: Unsicherheit des Ausgleichskreises aus Koordinatenmessungen. Feingerätetechnik, Berlin 32 (1983) 2

[3] ISO, (International Standards Organisation), *Guide to the Expression of Uncertainty in Measurement*," ISBN 92-67-10188-9, Geneva, Switzerland, 1993

[4] ISO, (Int. Stand. Org.), ISO 230-2, Test code for machine tools – part 2: Determination of accuracy and repeatability of positioning numerically controlled axes; Addition of Annex C (informative), measurement uncertainty estimation for linear positioning measurement (ISO/TC39/SC 2 N1294)

[5] Schmitz, T.; Ziegert, J.: Dynamic evaluation of spatial CNC contouring accuracy, Prec. Eng. 24 (2000) 99-118

[6] Institute for Machine tools and production, Swiss Federal Institute of Technology (ETH), Zurich, Switzerland http://www.iwf.bepr.ethz.ch

VIBRATION ASSISTED DIAMOND TURNING USING ELLIPTICAL TOOL MOTION

Thomas A. Dow, Matthew Cerniway, Alex Sohn, Nobu Negishi
Precision Engineering Center, North Carolina State University, Raleigh, NC

1 INTRODUCTION

Diamond turning has been used to create optical quality surfaces quickly and efficiently. However, it is limited to certain workpiece materials [9] based on tool wear. To expand the choice of workpiece materials, several innovative machining methods and equipment modifications have been tried to varying degrees of success. Evans attempted to machine stainless steel at cryogenic temperature [1] and Casstevens experimented with diamond turning of carbon steel in a carbon-saturated environment [2]. Another approach taken by Moriwaki and Masuda utilized CBN tools, with their low chemical reactivity to iron, to produce an optical quality surface on steel [3,4]. While acceptable surface finishes were produced and tool life was extended, no single method achieved both [6].

In the mid-70's, a new class of machining was born. This new technique involved independent, cyclic displacement of the cutting tool with respect to the workpiece. This class of machining was referred to as vibration cutting. Early experiments were primarily carried out at frequencies greater than 20 kHz. However at these "ultrasonic" frequencies, little practical value was demonstrated. It took nearly two decades of slow growth before the technology started to show promise. Finally in the early 90's, research into vibration cutting at both low and high frequency produced results sufficient for industrial applications [5]. This mature class of machining is called Vibration Assisted Machining (VAM).

The VAM path motion can be either 1D or 2D; that is the tool can be vibrated in a line or in a circular or elliptical path. Moriwaki has shown that 2D vibration cutting produces lower cutting forces and longer tool life than 1D vibration assisted cutting [6,7]. But what makes elliptical vibration cutting superior? What is the relationship between elliptical path, surface finish and tool forces? It is by understanding the dynamics and mechanics of an elliptically driven tool servo that these questions will be answered.

2 DESCRIPTION OF THE APPARATUS

A sketch of the cutting tool actuator is shown in Figure 1. A steel frame (A) is attached to the tool post on the DTM. A cam mechanism is used to apply approximately 45 N of tension to a pair of 0.25 mm diameter music wires (B). These wires serve two purposes: 1) to preload the piezoelectric stacks, and 2) to keep the head firmly seated on the stack ends during the elliptical motion. Two 44-layer piezoelectric actuators (C) form the engine of this tool servo. These 6.35 mm diameter stacks measuring 25.4 mm in overall length and produce 22 μm of displacement. Seated on the end of each

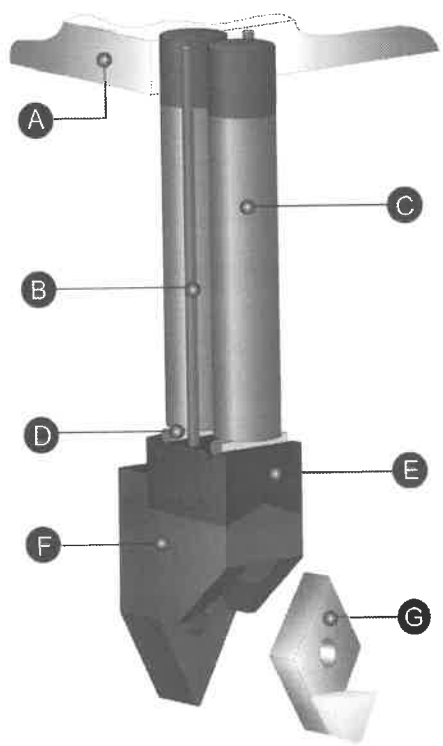

Figure 1. Elliptical cutting apparatus

stack is a 6 mm long, 1.58 mm diameter half round hardened steel pivot pin (D), that mates to a V-notched groove in the tool head mount (E). The aluminum tool head (F) is attached to this mount using a kinematic mount for precise realignment. A standard diamond tool insert (G) completes the assembly. The first natural frequency limits the operating range from 0-400 Hz.

2.1 Tool Motion

The tool motion derived from this design depends on the excitation of the two actuators and the geometry of the mount. The specific geometry of interest is the horizontal distance between pins at the end of each actuator and the vertical distance from this line to the cutting edge of the tool. For the mechanism described here, the pins are 6.3 mm apart and the tool is 23 mm above the pivot line. This geometry should produce an ellipse with a major axis, a = 50 μm, and a minor axis, b = 7 μm. The actual motion is slightly distorted due to small differences in response of the two actuators.

For elliptical cutting, the motion of the end of the tool is a combination of the elliptical motion from the actuator and the linear motion from the workpiece. Figure 2 shows the motion of the tool (exaggerated in the vertical direction for clarity) and defines some important parameters discussed next. Only two cycles of the tool are shown in this figure and the emphasis is on the second revolution shown as a dotted line. This is the steady-state motion that removes material from the workpiece.

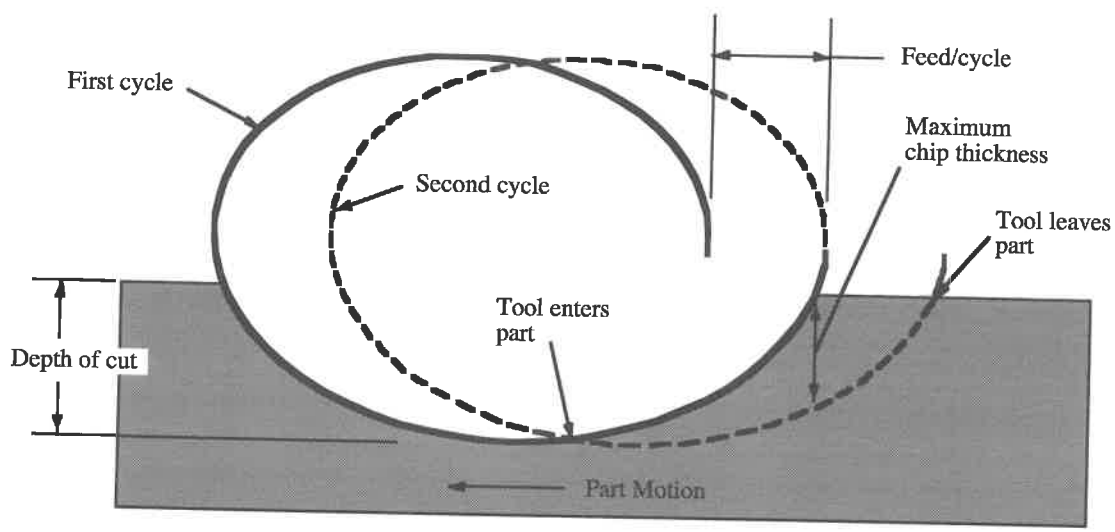

Figure 2. Tool motion and chip definitions for elliptical cutting

2.1.1 Duty Cycle

One of the important parameters defined for vibration cutting is the duty cycle. For linear vibration cutting, the duty cycle was defined as the percentage of one vibration cycle that the cutter rake face of the tool contacted the chip. This definition is somewhat misleading because the flank face of the tool is always in contact with the workpiece. For elliptical cutting, a new definition has been adopted to be more like flycutting; that is, the duty cycle is defined as the percentage of tool/workpiece contact during one vibration cycle. From Figure 2 this means the difference between the time the tool enters and leaves the part divided by one period of tool operation. This new definition will produce larger values of duty cycle than the old definition.

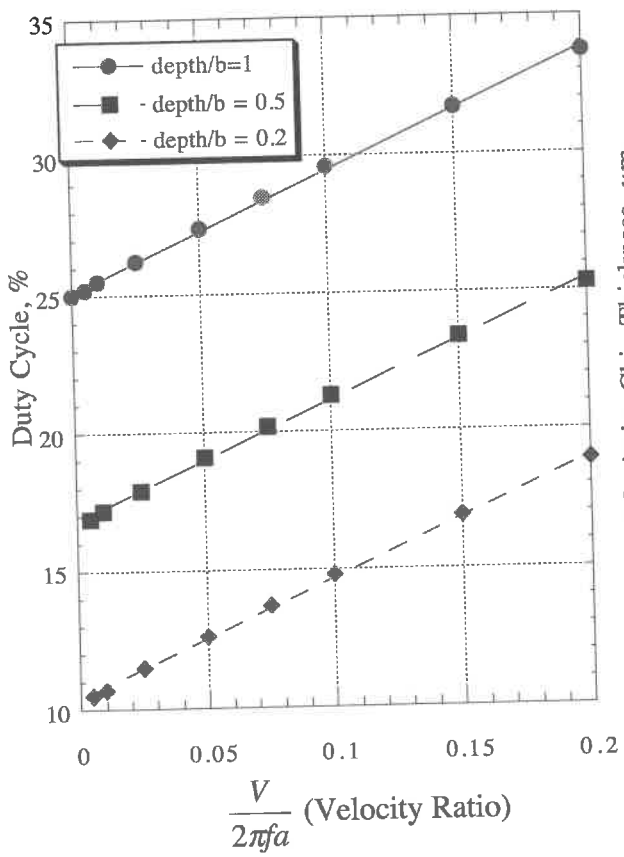

Figure 3. Duty Cycle as a function of velocity ratio and depth of cut

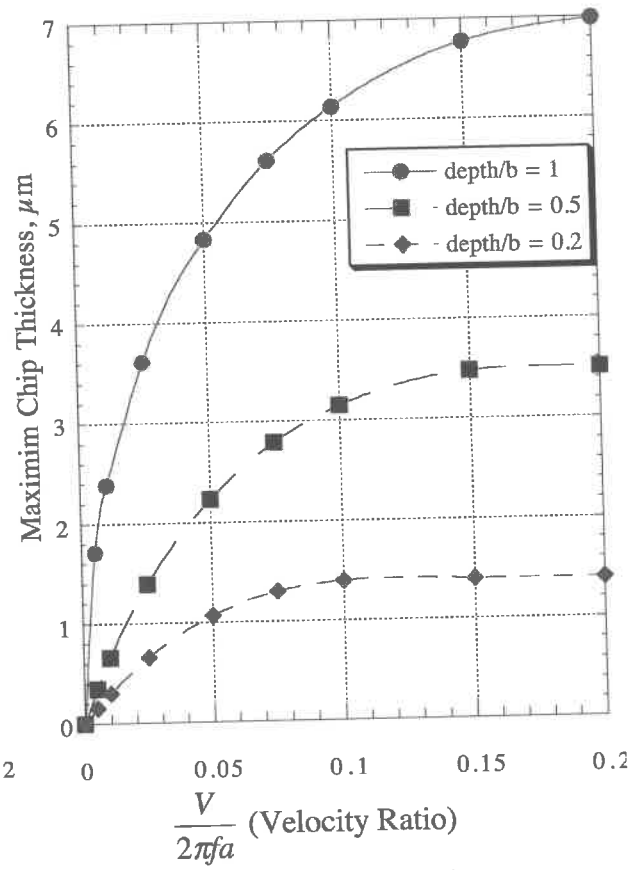

Figure 4. Maximum chip thickness as a function of the velocity ration and depth of cut

(major axis of ellipse = a, minor axis = b, part speed = V, frequency = f)

Figure 3 shows the duty cycle as a function of the tool ellipse, the workpiece speed and the vibration frequency. The horizontal axis is the ratio of the part speed to the maximum speed of the tool vibration along the tool motion direction. The three lines represent different depths of cut with respect to the minor axis of the ellipse; a range from 20 to 100%. For a given depth ratio, decreasing the speed of the part or increasing the frequency of vibration will reduce the duty cycle. However, the graph shows that there is a lower limit to the duty cycle that is a result of the new definition. For example, at a depth equal to the minor axis of the elliptical motion (depth/b = 1), the minimum duty cycle is 25%; that is, the tool will always touch the workpiece for at least one-quarter of each vibration cycle.

2.1.2 Chip Geometry

Figure 2 also shows the definition of the maximum chip thickness as the tool moves through its elliptical path. Figure 4 indicates the change in this thickness as a function of the same variables as in Figure 3. In this case, the chip thickness is reduced as the tool frequency is increased or the part speed is reduced. The chip thickness can also be made thinner by reducing the depth of cut. Notice that as the speed parameter on the horizontal axis gets larger, the chip thickness approaches the depth of cut. This means that the chips do not overlap and the chip shape looks like the first cycle of the tool in Figure 2.

3 TOOL FORCES

The tool geometry is needed to calculate the tool forces during elliptical cutting. A simple explanation for the force reduction for VAM is that the cutting distance is increased. For example, if the blade of a circular saw is locked and pushed through the board, the cutting distance is the board width, the chip thickness is the board thickness and the force is high. However, if the blade is rotating, each tooth creates a thin chip and the cutting force is low, but the total length of the cut, that is, the sum of each individual tooth contact, is much higher.

3.1 FORCE MODEL

The force model is based on work done by Carroll, Drescher and Arcona [8] to develop a tool force model for diamond turning. For the case of elliptical cutting, the chip geometry was first calculated and then the model was applied to this time varying geometry. Figure 2 illustrates the change in the chip size along the centerline of the tool and this geometry can also be easily expanded to create the 3D chip geometry. Depending on the duty cycle, only a portion of each period of vibration will produce a force and that force will depend on the tool geometry (including wear) and the material properties.

3.2 FORCE MEASUREMENTS

To see if the model can be used to predict the forces during vibration cutting, a series of experiments were conducted using different workpiece materials and operating conditions. A three-axis tool force dynamometer was mounted on the fixed spindle of the DTM and the tool was moved across the surface at a given depth of cut. A picture of the apparatus is shown at the right.

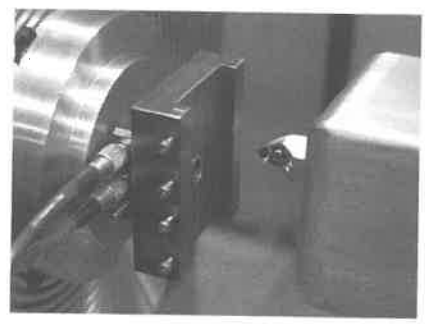

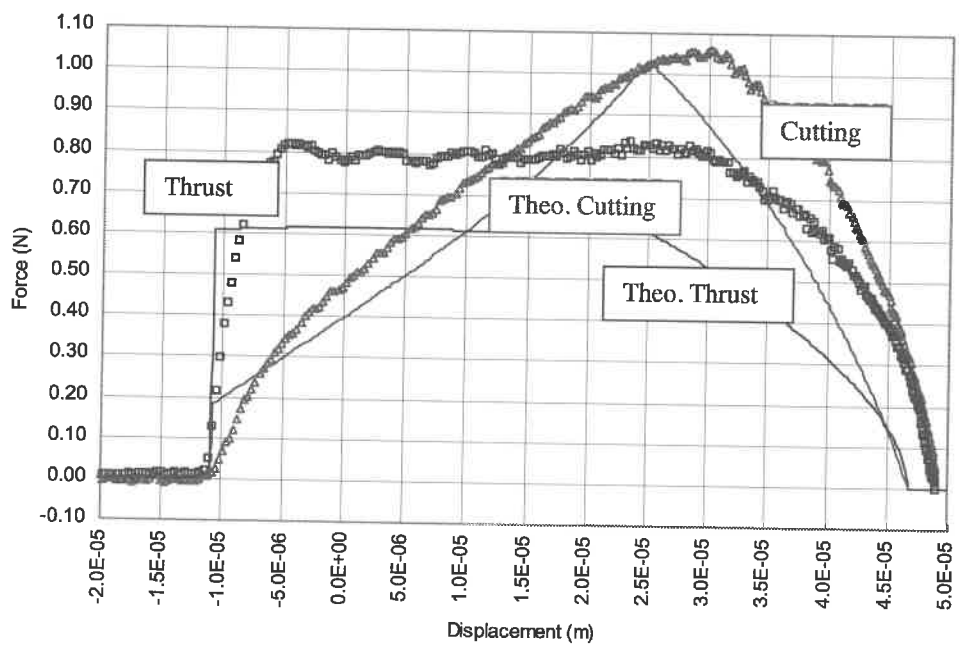

Figure 5. Theoretical and measured forces cutting copper workpiece

One example of the forces measured and predicted is shown in Figure 5. The workpiece was copper, the vibration frequency was 10 Hz, the depth of cut is 6 μm (depth/b = 0.85) and the

velocity ratio was 7.5%. From Figures 3 and 4, the duty cycle is 26% and the maximum chip thickness is 4.7 μm. The measured forces as a function of tool displacement are shown in Figure 5 as a series of points and the predicted forces are the solid lines. For these cutting conditions, the maximum force was on the order of 1 N and the predicted values were in agreement with the shape and within 0.2 N of the magnitude of the measurements.

4 STEEL MACHINING EXPERIMENTS

One of the advantages reported for vibration cutting is a reduction in the wear of diamond cutting tools. To test this hypothesis, a series of machining experiments was performed using both standard diamond turning and vibration assisted diamond turning of steel. The workpieces were mounted in the spindle of the DTM and turned at low spindle speeds as indicated in Figure 6. Two 5 mm wide bands were machined on each sample that were centered at 22.5 mm and 16 mm from the center of rotation. Each band required about 10 meters of machining. A higher cross feed was chosen for the conventional turned work piece to put the theoretical radial surface roughness of both specimens in the same range. Figure 6(a) and 6(b) show a comparison of the reflectivity of the two surfaces created indicating the advantages of VAM.

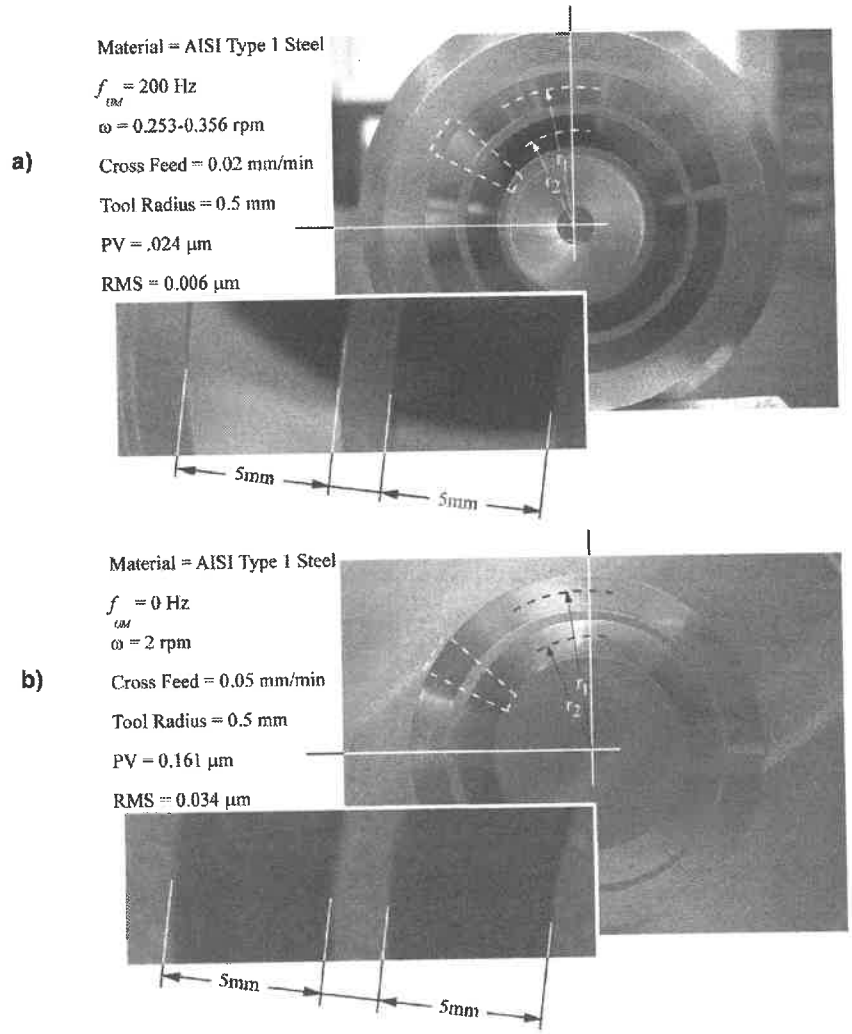

4.1 SURFACE FINISH

The conventionally machined sample, Figure 6(b), has a peak-to-valley roughness of 0.161 μm and RMS roughness of 0.034 μm. This is an order of magnitude higher than the VAM steel sample, Figure 6(a), which has a peak-to-valley roughness of 0.024 μm and a RMS roughness of 0.006 μm. Optimizing the VAM parameters could make this difference even larger.

5 TOOL WEAR

Conventional diamond turning cannot achieve a high quality finish due to high tool wear. SEM micrographs comparing the cutting edges of the tools used in the steel cutting experiments are shown in Figure 7. The dramatically worn edge on the diamond used in conventional turning, Figure 7(a) can be compared to more uniform wear on the tool used during the VAM process in Figure 7(b). The tool used for conventional turning shows indication of wear regions at the 25 μm feed spacing and a greatly enlarged edge radius. The VAM diamond tool, on the other hand, shows uniform wear across the width of the contact region and a smaller change in edge radius.

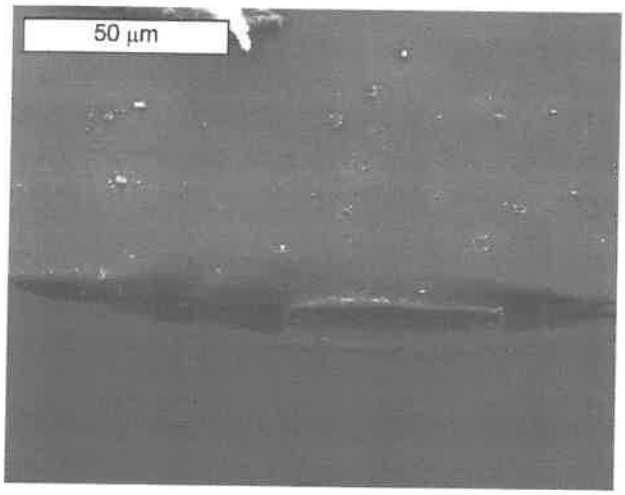

a) Tool used for conventional DT

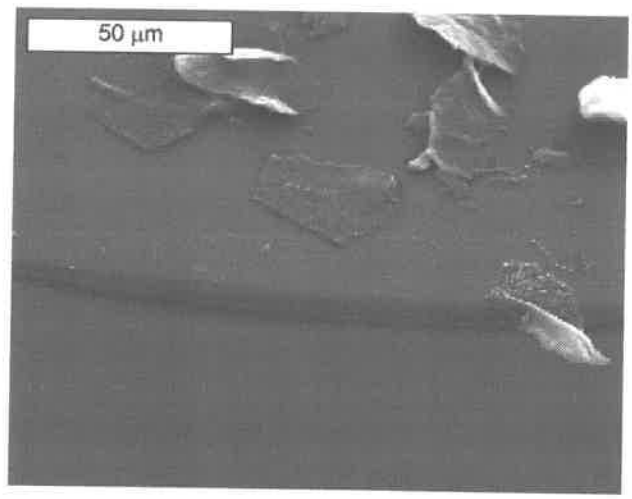

b) Tool used for Vibration Assisted Machining

Figure 7. Comparison of Worn Diamond Tools (SEM images at 800x)

6 REFERENCES

1. Evans, C., "Cryogenic Diamond Turning of Stainless Steel", Annals of the CIRP, Vol. 40, pg. 571-575, 1991
2. Casstevens, J., "Diamond Turning of Steel in Carbon-saturated Atmospheres", Precision Engineering, Vol. 5, pg. 9-15, 1983.
3. Masuda, M., "Ultra-precision Cutting of Steel with CBM Tools" (in Japanese), JSPE, Vol. 52, pg. 384-389, 1986.
4. Moriwaki, T., "Machinability of CBN Tools in Precision Engineering of Stainless Steel", Proc. 5th International Conf. on Mfg. Engineering, Wollongong, pg. 129-133, 1990.
5. Moriwaki, T. and Shamoto, E., "Ultra-precision Diamond Turnign of Stainless Steel by applying Ultrasonic Vibration", Annals of the CIRP, Vol. 40, Pg. 559-562, 1991.
6. Moriwaki, T and Shamoto, E., "Ultra-precision Diamond Cutting of hardened Steel by applying Elliptical Vibration Cutting", Annals of the CIRP, Vol. 48, Pg. 441-444, 1999.
7. Shamoto, E. and Moriwaki, T., "Study on Elliptical Vibration Cutting", Annals of the CIRP, Vol 43, pg. 35-38, 1994.
8. Arcona, C., "Tool Force, Chip Formation and Surface Finish in Diamond Turning", Ph.D. Dissertation, North Carolina State University, 1996.
9. Evans, C., Paul, E.,Mangamelli, A., McGlaufin, M., "Chemical Aspects of Tool Wear in Single Point Diamond Turning", Precision Engineering, Vol. 18, pg. 4-19, 1996.

NUMERICAL SIMULATION OF DUCTILE MACHINING OF SILICON NITRIDE

Thimmaiah G.Kumbera, John A.Patten*, Harish P. Cherukuri
University Of North Carolina at Charlotte
Charlotte NC 28223 USA

Christopher J.Brand, Troy D.Marusich
Third Wave Systems
Minneapolis, MN 55439 USA

Abstract: Recent experiments into the ductile-regime machining of Silicon Nitride have confirmed that Silicon Nitride behaves in a ductile manner under high pressure and micrometer depths of cut. This paper reports results from a series of numerical simulations carried out to model and understand the ductile machining of Silicon Nitride. The cutting process is modeled using the commercial software package ADVANTEDGE. Effects of various parameters like cutting speed, feed, rake angles and tool tip radius that favor brittle-to-ductile transitions are the focus of the parametric study. Feed, tool tip radius and depth of cut are in the range of tens of microns while speeds are in the range of 1m/min to 300m/min. Results from this study indicate that ductile cutting may be possible at high speeds, small tool tip radii, high negative rake angles and small depths of cut.

Keywords: Silicon Nitride, High pressure phase transformation, Diamond turning, Simulation, Brittle to ductile transition.

1. Introduction

Brittle materials, by their inherent properties, are difficult to machine while maintaining the desired surface roughness. Recently, single point machining techniques such as laser assisted machining and diamond turning of brittle materials like Silicon Nitride (Si_3N_4) have been reported as an alternative to finishing processes such as grinding and polishing [2,3]. Ductile machining of brittle materials, where material removal is by plastic deformation is possible at very low material removal rates, usually in the micrometer range [7,8]. The ductile behavior of nominally brittle materials is due to high-pressure phase transformations at the tool-chip interface and is metallic in nature [6]. For the Silicon Nitride samples reported in this paper, phase transformation occurs under hydrostatic stress state conditions at approximately the hardness value of 22GPa. In addition, brittle fracture can also occur during machining. Such fractures can occur at two zones relative to the tool – in front of the tool, where chip formation occurs due to a compressive stress field and in the wake of the tool due to a trailing tensile stress field [4]. Brittle behavior in front of the tool is governed by rake angle and the uncut chip thickness and may not cause surface cracks as the fracture is sometimes constrained inside the chip. Brittle behavior behind the tool typically occurs at a threshold value of depth of cut and causes extensive surface and subsurface damage.

This paper reports a series of numerical results from a parametric study carried out to model the ductile regime machining of Silicon Nitride. The commercial general purpose machining software ADVANTEDGE [1,5,9] is used to model the process. The constitutive model assumes ductile material behavior and does not include phase transformation or brittle fracture models. However, it is expected that the numerical results will provide information on the threshold values for ductile to brittle transition as a function of various parameters like rake angle, tool tip radii, cutting speeds and feed.

2. Finite Element Model

The machining of silicon nitride is modeled as an orthogonal cutting process assuming plane strain conditions. A schematic of the tool-workpiece configuration is as shown in Figure 1, where the v is the cutting velocity, r the tool tip radius, f is the feed, α and β the rake and clearance angles respectively. The length of the workpiece is l and the height is h.

The commercial finite element package ADVANTEDGE from Third Wave Systems is used for the numerical simulations. ADVANTEDGE is a Lagrangian finite element package used for two-dimensional modeling of orthogonal cutting. The element topology used is a six-noded quadratic triangle element with three corner and three midsize nodes. Continuous adaptive remeshing is used to correct the problem of element distortion due to high deformations. The larger elements are refined and smaller elements coarsened at regular intervals.

For the model, Si_3N_4 is assumed to behave in a ductile manner. The material behavior is modeled by using the constitutive equation,

$$\left(1+\frac{\dot{\varepsilon}^p}{\dot{\varepsilon}_o^p}\right)=\left[\frac{\bar{\sigma}}{g\left(\varepsilon^p\right)}\right]^{m_1} \quad \text{for } \dot{\varepsilon}^p \le \dot{\varepsilon}_t^p$$

$$\left(1+\frac{\dot{\varepsilon}^p}{\dot{\varepsilon}_o^p}\right)\left[1+\frac{\dot{\varepsilon}_t^p}{\dot{\varepsilon}_o^p}\right]^{\frac{m_2}{m_1}}=\left[\frac{\bar{\sigma}}{g\left(\varepsilon^p\right)}\right]^{m_2} \quad \text{for } \dot{\varepsilon}^p > \dot{\varepsilon}_t^p \tag{1}$$

where the function g (ε^p) accounts for the thermal softening and strain-hardening effects and the function $\theta(T)$ is the thermal softening function.

Only strain hardening effects are considered in this paper. Thus the strain rate sensitivity exponent's m_1 and m_2 are set to large values in equation (1). Thermal softening effects are neglected until the temperature reaches the cutoff temperature.

The material model for Si_3N_4 is as given by Table 1. Cutting tool material is single point diamond which is assumed to be elastic and the material properties are E = 1.2E+12 Pa, ν = 0.2, κ = 1500 W/m-^{0}C, c = 471.5 J/Kg-^{0}C, ρ =3520 Kg/m^3. The work tool friction coefficient value is 0.4 and is modeled as per Coulomb friction law.

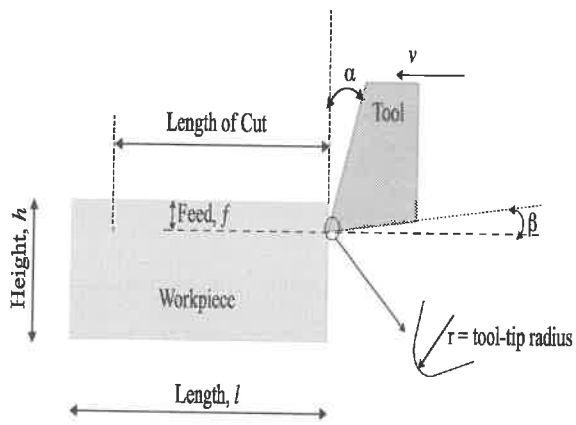

Figure 1. Schematic orthogonal cutting model used for numerical simulations.

E	3.1E+11Pa
ν	0.27
κ	26 W/m-^{0}C
c	800 J/Kg-^{0}C
ρ	3210 Kg/m^3

$\dot{\varepsilon}_0^p$	1 /s
$\dot{\varepsilon}_t^p$	1E+7 /s
m_1, m_2	300
ε_0^p	0.006
n	5
σ_0	1E+10

C_0	1.0
C_i, $1 \le i \le 5$	0
T_{cut}	1800^{0}C
T_{melt}	2500^{0}C
T_{ref}	0^{0}C

Table 1. Material Properties of Si_3N_4 used in numerical model.

3. Numerical Results

3.1 Effect of Cutting Speed

The parameters for the study of effects of cutting speed are: feed=20μm, rake angle=0^0 and tooltip radius=10μm. Figure 2 shows the corresponding maximum temperatures and pressures. Temperatures increase as the cutting speed increases. The maximum temperature distribution is along the shear plane and varies from 300^{0}C at low speeds to melting temperatures at high speeds. Pressure plots indicate that phase transformation pressures of 20GPa are possible at higher speeds. Hydrostatic pressure distribution

into the workpiece as a percentage of feed increases with increase in cutting speeds, i.e., the zone of high pressure increases in extent. The fluctuation of temperature and pressure between the speed ranges of 5m/min to 15m/min is possibly due to mesh density. This is currently being studied. Figure 3 shows the plot of machining forces as a function of cutting speed. Cutting forces decrease with decrease in cutting speeds. Thrust forces increase marginally as speed is increased.

3.2 Effect of Feed

The effect of feed was studied setting the parameters as: cutting speed=6m/min, tooltip radius=10μm, Rake angle= 0^0. Maximum temperatures and pressures are plotted as a function of feed in Figure 4. As the feed increases, maximum temperatures increase while maximum pressure values do not change significantly. This marginal change in pressure values is possibly due to numerical approximation. The machining forces are plotted as a function of feed in Figure 5. Cutting forces increase with the increase in feed due to an increase in chip load. Thrust forces follow a minimally increasing trend.

3.3 Effect of Rake Angle

The effects of rake angle are studied at speed=300m/min, tooltip radius=1μm, feed=10μm. Figure 6 shows a plot of maximum temperature and pressure. Maximum temperatures are along the shear plane and are close to melting temperature. This may be due to the high speed at which the simulation was run. Temperatures decrease with high negative rake angles. The fluctuation of temperature is possibly due to numerical approximation. Pressures show a gradual increase as rake angle is decreased from 15^0 to -45^0. Values for pressure at -45^0 approach the phase transformation pressure of 20GPa indicating more efficient machining at high negative rake angles. Machining forces as a function of rake angles are shown in Figure 7. Cutting and thrust forces increase with decrease of rake angle with a crossover at -45^0.

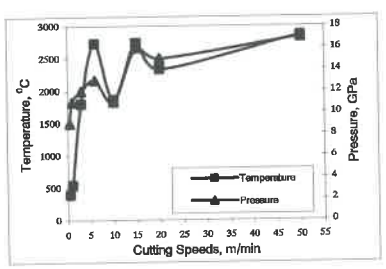

Figure 2. Maximum temperature and pressure plot for varying cutting speeds.

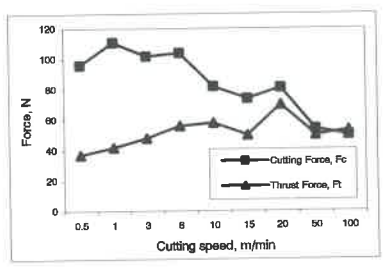

Figure 3. Maximum cutting and thrust force plot for varying cutting speeds.

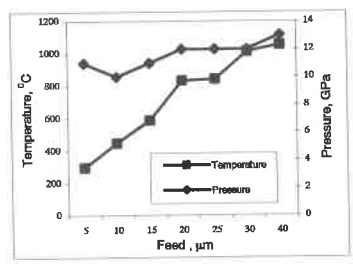

Figure 4. Maximum temperature and pressure plot for varying feeds.

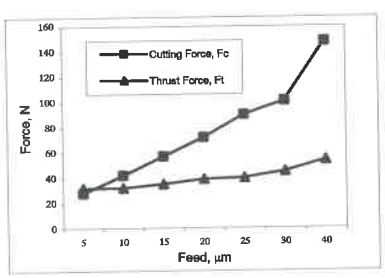

Figure 5. Maximum cutting and thrust force plot for varying feeds.

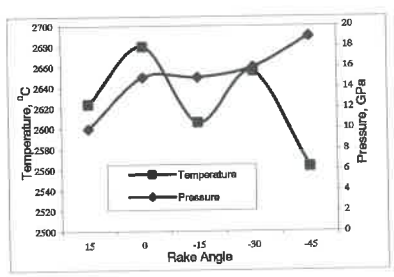

Figure 6. Maximum temperature and pressure plot for varying rake angles.

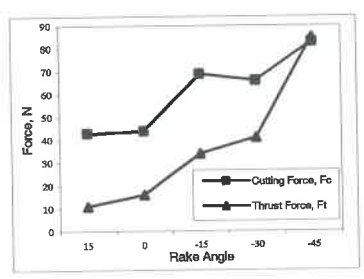

Figure 7. Maximum cutting and thrust force plot for varying rake angles.

3.3 Effect of Tooltip Radius

The effect of tooltip radius are studied by setting speed=1m/min, feed=70μm, Rake angle= -45^0. Figure 8 shows the maximum temperature and pressure values as a function of increasing tool tip radius. Temperatures in general decrease with the increase in tooltip radius. Pressures increase with decrease in tooltip radius indicating that brittle-ductile transition due to high-pressure phase transformation is

possible at small tooltip radii. This decrease in pressure for larger tooltip radius is expected since this is analogous to cutting with a blunt tool. Figure 9 shows the plot of machining forces. While the cutting forces show a marginal change in values, thrust forces increase slightly with increasing tooltip radius.

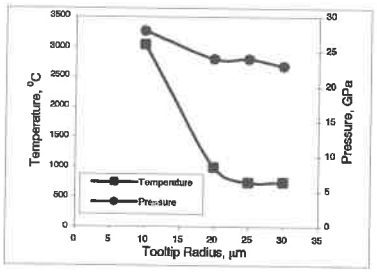

Figure 8. Maximum temperature and pressure plot for varying tooltip radius.

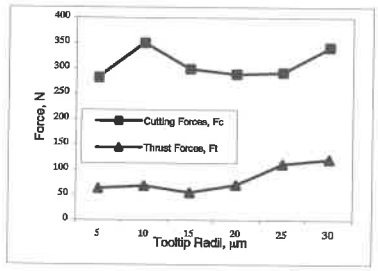

Figure 9. Maximum cutting and thrust force plot for varying tooltip radius.

4. Discussion

Ductile-regime orthogonal cutting (single point diamond turning) of Silicon Nitride is modeled parametrically to study the effects of various machining parameters such as cutting speed, feed, rake angles and tooltip radius on the process. Results indicate that for small values of feed, small tooltip radius and at high speeds, conditions of pressure and temperature exist that facilitate ductile behavior during machining. Negative rake angles are more likely to cause a brittle to ductile transition when compared with the positive or zero degree rakes.

Acknowledgements

The authors would like to acknowledge the support of NSF through grant EEC 9903838. The authors are also grateful to the Center for Precision Metrology at UNC-Charlotte for supporting this effort.

References:

[1] Kumbera, T.G, Cherukuri, H.P, Patten, J.A, Brand, C.J, Marusich, T.D, 2001, Numerical Simulation of Ductile machining of silicon nitride with a cutting tool of defined geometry, Proceedings of 4th CIRP International workshop on Modeling of machining operations, Pp 7.

[2] Shin, Y.C., et al., 2000, Laser Assisted Machining, Machining Technology, 11/3:1-6.

[3] Patten, J., 2000, Ductile regime machining of silicon nitride, 87-90, Advances in Abrasive Technology III, Eds. N. Yasunaga, J. Tamaki, K. Suzuki, T. Uematsu, The Society of Grinding Engineers, Tokyo, Japan.

[4] Patten, John, 1998, Cutting tool edge radius and depth of cut influence on the generation of the high pressure phase transformation during ductile machining, Proceedings ASPE Spring Topical Meeting on Silicon Machining, 17/88-91.

[5] Marusich, T.D. and Ortiz, M., 1995, Modeling and Simulations of High-Speed Machining, Int. J. Num. Meth. Eng. 38:3675-3694.

[6] Morris, J.C., Callahan, D., J. Kulik, Patten, J.A., Scattergood, R.O., 1995, Origins of the Ductile Regime in Single Point Diamond Turning of Semiconductors, J. Am. Ceram. Soc. 78/8:2015-2020.

[7] Zhang, B., Howes, T.D, 1994, Material Removal Mechanisms in Grinding Ceramics, Annals of CIRP, 43/1:305-308.

[8] Syn, C.K, Taylor, J.S, Donaldson, R.R, Shimada, S., 1988, Ductile-Brittle Transition of Cutting Behavior in Diamond Turning of Single Crystal Si, Japan Society of Precision Engineering, Annual Spring Meeting, Meiji University, Kawasaki, Japan, Pp735-736.

[9] ADVANTEDGE Software, Theoretical Manual, Version 3.5, 2001, Third-wave Systems.

Effects of Rotating Unbalance on Turning Precision: Analytical and Experimental Investigations and Real-Time Compensation

W. Winzenz and S. W. Dyer
BalaDyne Corporation
1665 Highland Drive
Ann Arbor, MI 48108

Past research has been conducted on the effects of rotating unbalance on precision machining using rotating tools. Real-time balance compensation methods have been applied for decades on precision grinding machines and, more recently, on high-speed milling machines. However, such active balance control has not been extensively applied to metal turning applications. This paper first presents results from traditional analytical machining models to predict the effects of rotating unbalance on various measures of turning precision. Active compensation is described that mitigates the negative effects on precision while not significantly impacting process cycle-time. Experimental results are presented that validate the trends predicted by the analytical models and also suggest other indirect effects of unbalance on process precision. The experimental results also demonstrate the effectiveness of active balance compensation.

The "dynamic" runout caused by rotating unbalance is shown to potentially have a more harmful effect on precision than traditionally measured "static" runout. Dynamic runout is dependent on rotational speed and, thus, can change during a variable-speed turning operation. Furthermore, when spindle and machine stiffness is not symmetric between the X- and Y-directions, the unbalance-induce runout will not be a perfect circle but rather an ellipse. This condition is shown to effect workpiece circularity.

Aside from harming machining precision, the constant excitation of unbalance forces as the spindle rotates exacts a toll on spindle bearing life and transmits vibration throughout the machine. Since bearing fatigue life is proportional to the load cubed, the addition of even small unbalance loads relative to cutting forces can cause premature spindle bearing failure. This leads to the expense and down-time of changing out the spindle or rebuilding the spindle bearings. Machine vibration can also cause other secondary results such as affecting surface finish and tool life.

Balancing is most important for eccentric parts or workpieces that have particularly tight concentricity, roundness, or surface finish tolerances. After setup changes with such parts it is often necessary to rebalance the chuck/workpiece assembly. Workpiece casting weight variation can also lead to significant variation in unbalance from part to part. Unbalance variation is even possible while machining a single part if interrupted cutting is involved.

Off-line manual balancing of each part or setup is usually too time-consuming to be a viable solution. Another method of compensating for lathe setup unbalance is to implement active balance control. Such systems correct for rotating unbalance automatically after a setup or part change and prior to metal cutting. Active balancing is shown to address the problems related to unbalance without the time penalty of off-line balancing. Application case studies of prototype production active lathe balancing systems are presented to provide examples of the economic justification of such systems.

Key words: turning, balancing, vibration, vibration control

TECHNIQUES FOR THE REDUCTION OF CYCLIC ERRORS IN LASER METROLOGY GAUGES FOR THE SPACE INTERFEROMETRY MISSION

Peter G. Halverson[1], Feng Zhao, Robert Spero, Stuart Shaklan,
Oliver P. Lay, Serge Dubovitsky, Rosemary T. Diaz
California Institute of Technology, Jet Propulsion Laboratory,
4800 Oak Grove Drive, Pasadena, CA 91109
Ray Bell, Lawrence Ames, Kalyan Dutta
Lockheed Martin, 3251 Hanover St., Palo Alto, CA 94304-1191.

The Space Interferometry Mission ("SIM", see http://sim.jpl.nasa.gov) requires displacement metrology gauges with linearity ~10 picometers (pm) over a distance of several meters. Displacement measuring interferometers are under development meeting these requirements, while also meeting thermal stability, robustness, size and geometry requirements. A persistent difficulty in attaining picometer-class performance with laser interferometric metrology gauges is the problem of "cyclic error" caused by the leakage of a small fraction of light to the photodetectors via routes that do not represent the distance being measured. We survey a variety of approaches to reducing this cyclic error and their application in reaching SIM's 10 pm goal.

Statement of the problem: a generic SIM gauge.

We seek to measure the relative distance between two fiducial corner cube retro reflectors, with a systematic error less than 10 picometers (pm). (Commercial systems typically exhibit a cyclic nonlinearity of order 1 nm.) Fig. 1 shows a generic metrology gauge, a Michelson interferometer, which informs us of changes in L, the distance to be measured. To achieve picometer accuracy, the JPL metrology group has constructed a stable wavelength reference[2,3] and stable signal processing electronics[4]. The two remaining challenges are the 10 pm linearity requirement, which requires near perfect beam split and recombination, and the ~2 nm/K temperature coefficient, which requires good beam overlap after recombination. Quantitatively, the goals are:

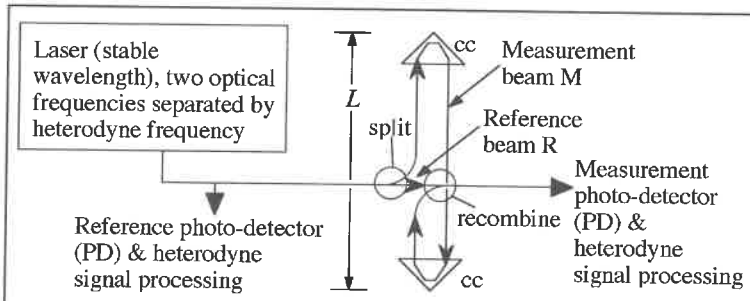

Fig. 1. Generic metrology gauge measuring the distance L between two retro-reflectors. Laser light is split into two paths: a short **reference** beam (R) and a **measurement** beam (M) which have optical frequencies offset by ~10^4 to ~10^6 Hz for heterodyne interferometry. The problem to be solved is how to cleanly split and recombine the beams, without introducing errors. Usually, a small portion of the M beam leaks into the R beam, and R leaks into M, causing cyclic non-linearity of order ~1 nm.

Beam overlap goal:

To minimize the effect of transverse drift of the measurement beam (M) after traveling between the fiducials, and to achieve good visibility, the angle between the two beams must satisfy $\theta \ll \lambda/d$=(1.3 microns)/1cm≈100 μRad where d is the beam diameter. In practice, 10 uRad alignment is readily achieved.

Beam separation goal:

This goal is usually stated as a limit on power leakage between the R and M beams, but it also includes cross-talk between the analog electronic channels. If the photodetector output has a "good" heterodyne component of amplitude V, and a "bad" leakage component of amplitude v, the measurement error will be (to first order) $\varepsilon=2^{-1/2}(1/2)(1/2\pi)(v/V)\approx(\lambda/18)(v/V)$ where the constants account for conversion to RMS, the double pass through L and the worst-case change in the zero-crossing phase of the heterodyne signal for a contaminating signal of amplitude v. Hence the cross-

talk between electronic channels must be <(18)(10pm)/(1.3 microns) $\approx 1.4\times10^{-4}$, requiring ~80 dB isolation.

For optical leakage we have to first order $v/V = (B\alpha + A\beta)/(AB)$, where A and B are the electric field amplitudes of the R and M beams respectively, and α and β are the amplitudes of R light leaking into M and vice-versa. Higher order errors are also present[5], but will not be considered here. Treating the two errors separately, we have $v/V=\alpha/A=p_{RM}^{1/2}$ and $v/V=\beta/B=p_{MR}^{1/2}$, where p_{RM} and p_{MR} are the R and M power leakage fractions. For ε<10 pm we need $p_{RM}\approx(18\varepsilon/\lambda)^2 \approx 2\times10^{-8}$; again ~80 dB of isolation. Similarly p_{MR} must be ~80 dB.

Others have met these goals and obtained~10 picometer linearity results[6,7], but constraints set by the practical needs of SIM rule out the use of their configurations. The constraints include:

1. The need to measure distance *between* corner cube fiducials.
2. The need for minimal sensitivity to metrology head mis-orientation. This eliminates schemes where the reference and measurement beams are not co-axial.
3. Homodyne interferometers have achieved good linearity[8,9], but working near DC presents difficult stability requirements for the laser source and detection electronics.
4. Additional requirements include low power dissipation and simple, robust construction.

Meeting all these requirements has been extremely challenging. We now consider the central question: How do we separate, then recombine the R and M beams, while working within SIM's practical constraints?

Our options: Space, Time, Energy (frequency) and Polarization

We have contradictory goals. For low thermal and alignment drift sensitivity, we seek near-perfect overlap of the R and M beams at the "split" and "combine" points of figure 1, but near-perfect separation of the beams between the "split" and "overlap" points. To achieve this we have the properties of electromagnetic radiation at our disposal: Space, Time, Energy and Polarization.

Polarization: the "conventional" approach.

Used in commercial distance measuring interferometers, this approach has the R and M beams assigned orthogonal polarization states: P and S respectively. A polarizing beamsplitter is used to achieve overlap (before the "split" point) and another is used to accomplish both the "split" and "combine" functions. SIM's implementation has been described elsewhere[10,12]. The overlap goal is easily met but the 80 dB separation goal is unattainable because (a) polarizing beam splitters with better than 30 to 40 dB extinction ratio are unavailable and (b) delivering 80 dB purity polarized beams to the metrology head is not feasible.

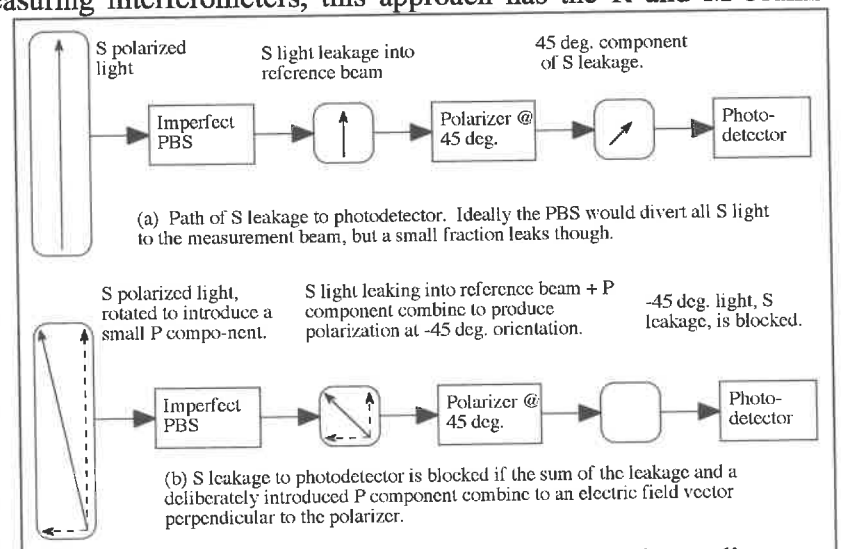

Figure 2: Technique used to minimize effect of imperfect beamsplitters.

Minimizing effect of finite polarization extinction ratio.

The negative impact of ~30 dB extinction ratio PBS can be minimized if (a) the S light (measurement beam) is polarized to better than the extinction ratio of the PBS (i.e., >30 dB) and if the beam's S direction can be finely adjusted.

It was found by one of the authors that under these circumstances the polarization leakage signal is nearly eliminated when the S beam is slightly rotated about the propagation axis. Explained in figure 2, the effect also applies to leakage of reference beam P light into the measurement beam. The effectiveness of this "trick" is not easily predicted as it will be affected by component variations, but it has been used to improve SIM launchers by a factor of ~10 (from 3

nm RMS cyclic error down to 300 pm). We were limited by the coarseness of the adjustments and extraneous cross-talk effects, so further improvement is expected.

Space: a wavefront division approach.
The M and R beams can be spatially separated yet combined, with the compromise described in the accompanying paper[11] where low (~90 pm RMS) cyclic error results are presented.

Energy (frequency): cyclic averaging.
The error caused by M and R beam leakage has the form $e = \Sigma m_n \sin(n2\pi L/\lambda)$, n=1,2... representing 1st and 2nd order optical mixing and the combined effects of electronic crosstalk and distortion. The error integrated over a cycle is zero, as illustrated in fig. 3 for the n=1 case. Cyclic averaging consists of imposing a 10 to 1000 Hz dither such that the apparent $L(t)$ is either a sawtooth or triangle function, by modulating the laser wavelength[2] (or by moving one of the retro-reflectors). An average position measurement $\langle L \rangle$ is obtained by combining N (roughly 100 to 1000) measurements while the dither is within the one cycle window in fig. 3: $\langle L \rangle = (\Sigma L_n)/N$. To do this, the JPL phasemeter board[4] has hardware windowed averaging. Typical parameters would be a dither ramp time of 5 ms, a 4 ms averaging window T_W, during which N=400 measurements are taken, if F_{HET}=100 kHz.

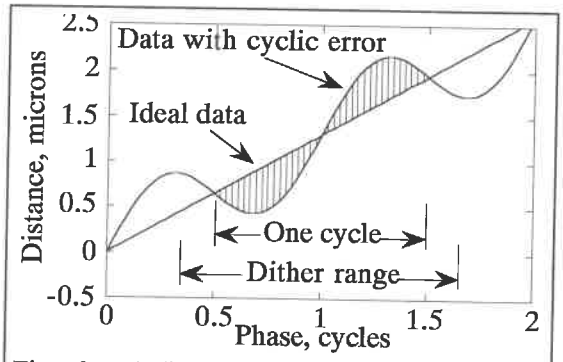

Fig. 3: Idealized gauge output for a linear displacement, and output with cyclic error, exaggerated ~1000 times for clarity. For cyclic averaging, the apparent distance is dithered by modulating the laser wavelength (or by moving one of the retro-reflectors). Data is accumulated over one cycle so that, in principle, the error averages to zero.

Error reduction by ~200, applied to polarizing-type gauges with ~20 nm cyclic errors, yielding linearity of 100 pm RMS have been achieved[12]. The limiting factor appears to be the determination of an optimum averaging window. For reasons that are not clear (may involve ghost reflections) the optimum was found to vary with time so that <100 pm class performance could not be maintained for more than a few minutes. An undesirable side-effect of the windowed dithering is an increase in noise. The exact time of the first and last measurements in an average is a function of the rapidly varying measurement heterodyne phase and is non-deterministic. This introduces a measurement uncertainty $\varepsilon=\lambda/2T_W F_{HET}\approx 1.6$ nm, assuming the previous dither and window parameters and λ=1.3 microns, thus adding noise to $\langle L \rangle$.

Time: phase modulation[13].
Photons traveling the measurement beam path take *longer* to arrive at the measurement photo-detector (PD) than those taking the reference beam path. This allows us to exclude M beam light that leaks into the R beam: the "good" M photons have time delay $\Delta t=2L/c$ while the "bad" photons have Δt=0. (This discussion also applies to R beam light leaking into M.) Phase modulating the laser allows us to select delayed light, while ignoring undelayed leakage, as outlined in fig. 4.

To understand the mechanism, consider the same interferometer with no frequency shifters, and no phase modulator. The measurement PD signal varies from V_{min} (when the M and R wavefronts are out of phase) to V_{max} (when they are in phase). Adding phase modulation causes the R and M wavefronts to move 1/2 wave past each other (because of the M beam time delay) at frequency F_ϕ, so we have a rapidly changing PD output whose amplitude and phase depends on the average relative phase of the R and M wavefronts. Demodulating the PD signal with a phase sensitive detector (the mixer & filter in fig. 4) produces a DC output voltage proportional to the average phase difference between R and M, modulo one wave. Leakage light has no time delay difference, hence no RF signal and is removed by the demodulator.

Adding the frequency shifters introduces a continuously increasing phase difference between the M and R wavefronts, which is seen as a periodic change of amplitude and phase on the PD's RF output, demodulates as a sinusoid at frequency F_{HET}, and is treated as the measurement heterodyne signal in the usual way.

The phase modulation amplitude and frequency are chosen for maximum PD RF output, which happens when the M and R beam wavefront motions at the PD (a) are in opposite directions requiring $1/F_\phi=4nL/c$, n=1,2…, and (b) have zero-to-peak excursions of 1/4 wave. In practice, this modulation is easily applied with $LiNbO_3$ modulators.

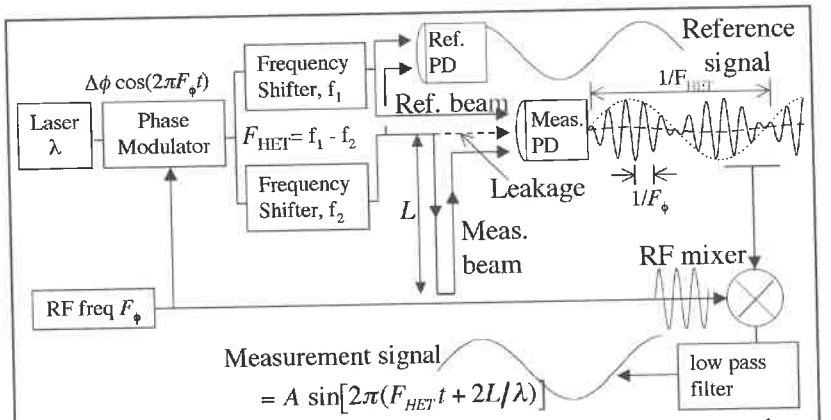

Fig. 4: Phase modulation rejection of cyclic error. Laser output phase varies $\Delta\phi$≈1/4 wave at frequency F_ϕ≈c/(4L). (For L=2m, F_ϕ=37.5 MHz.) (Note that F_{HET}<<F_ϕ.) The meas. photodiode output consists of a RF carrier modulated by the heterodyne signal (dots). Demodulation with a mixer & filter recovers the "good" heterodyne signal, which is then compared with the ref. PD output. The leakage signal (dashes), is also present but only at the much lower heterodyne frequency and is removed by the mixer/filter.

Conclusion

Various techniques for reducing cyclic nonlinearity have been tested at JPL. Each offers 10 to >50 fold improvements and have particular advantages and disadvantages, summarized in table 1.

	Advantages	Disadvantages	Cyclic error	Probable limiting factors
Polarization	Gaussian beam profile gives low pointing sensitivity	Polarization leakage causes cyclic error	130 pm	Polarization leakage, coarse adjustments
Polarization w/phase mod.	Robust, flight qualifiable	Requires phase modulator & fast photodetector	80 pm	Electronic cross-talk
Polar. w/cyclic averaging		Increased noise. Requires frequency modulator.	100 pm	Averaging window drift
Wavefront division	No polarizing components	Annular/segmented M pointing sensitivity	90 pm	Diffraction, electronic x-talk

Table 1. Cyclic error reduction techniques discussed, RMS cyclic error achieved to date.

The research described in this paper was carried out by the Jet Propulsion Laboratory, California Institute of Technology, under a contract with the National Aeronautics and Space Administration.

[1] Email: pgh@aip.org, halver@huey.jpl.nasa.gov

[2] S. Dubovitsky, et al. "Metrology Source for High-Resolution Heterodyne Interferometer Laser Gauges," SPIE **3350** 973-984, 1998.
[3] However: SIM will not require long-term laser source wavelength stability since wavelength drift will introduce metrology errors that are common-mode and self-canceling.
[4] P.G. Halverson, et al. "A Multichannel Averaging Phasemeter for Picometer Precision Laser Metrology," *Opt. Eng. for Sensing and Nanotech. (ICOSN '99)* SPIE **3740** 646-649, 1999.
[5] C. Wu, R.D. Deslattes, Applied Optics **37**, 28 (1998).
[6] C. Wu, J Lawall, R.D. Deslattes, Applied Optics **38** (1999) 4089-4094.
[7] J. Lawall, E. Kessler, Rev. Sci. Inst. **71** (2000), 2669-2676.
[8] C.Wu, C. Su, G. Peng, Meas Sci. Technol. **7** (1996) 520-524.
[9] W. Augustyn, P. Davis, J. Vac. Sci. Technol. B **8** (**6**) (1990) 2032-2036.
[10] Y.Gürsel, "Laser metrology gauges for OSI", SPIE **1947**, pp. 188-197, 1993.
[11] F. Zhao et al. "Development of Sub-nanometer Racetrack Laser Metrology for External Triangulation Measurement for the Space Interferometry Mission", ***this conference***.
[12] P.G. Halverson et al., Int. Conf. on Space Optics (ICSO 2000), Toulouse, France pp. 417-428
[13] S. Dubovitsky, NPO-20740. NASA Tech Briefs **25** (2), Feb. 2001.

COMPACT ABSOLUTE LENGTH MEASURING MACHINE BY COMBINING REGULAR CRYSTALLINE SURFACE AND LASER INTERFEROMETRY

Masato AKETAGAWA*, Pongpun RERKKUMSUP, Koji TAKADA,
Toshio TAKAGI, Tomonori WATANABE
Department of Mechanical Engineering, Nagaoka University of Technology
Kamitomioka 1603-1, Nagaoka, Niigata, 940-2188 JAPAN

1. Introduction

Since nanotechnology has progressed rapidly, new methods for length measurement applicable to the millimeter range with sub-nanometer resolution are required. Currently, the standard method for length measurement is laser interferometry. A heterodyne interferometer with a Zeeman laser [1] or a homodyne interferometer using the bi-fringes counting method [2] is widely used in the industry. However, it is difficult to determine arbitrary length with the sub-nanometer accuracy using the interferometers, because they have the non-linearity problem of the fringe interpolation [3]. A phase modulation homodyne interferometer, that can determine the optical path difference of wavelength times integer with the accuracy of 10 picometer or less, is proposed [4].

The lattice spacing of approximately 0.2 nanometer for some regular crystalline lattices is uniform and stable over a long range, when the crystals are stress free. These crystals can be used as reference scales with a sub-nanometer resolution instead of laser interferometry. X-ray interferometry (XRI) using silicon crystal has been developed to determine the lattice spacing of silicon at National Metrological Laboratories [5]. Moreover, the combined optical and x-ray interferometer (COXI) [6] has been developed for absolute length measurement with sub-nanometer accuracy at European metrological laboratories. However, XRI is very delicate for an adjustment to obtain x-ray fringe, and not commonly used in the industry. On the other hand, a scanning tunneling microscope (STM) [7] and an atomic force microscope (AFM) [7] are becoming a powerful and popular tool in surface engineering fields and can be used to obtain "images of atoms" on a regular crystalline surface. Therefore, such crystalline lattice can be used as a "crystalline lattice scale" with sub-nanometer resolution by combining them with STM/AFM. We have shown the feasibility of the crystalline lattice scale using a graphite crystal (highly oriented pyrolytic graphite: HOPG) as the reference scale and a dual-tunneling-unit scanning tunneling microscope as the detector [8]. In this article, we propose a compact absolute length measuring machine (ALMM) with sub-nanometer accuracy and sub-millimeter travel by combining "the crystalline lattice scale" as a fine scale and the phase modulation homodyne laser interferometry (= optical fringe) as a coarse scale.

2. Basic design and operation principle

Figure 1 and **2** illustrate the side and top views of the ALMM planned to construct. The sample of interest and reference crystal (HOPG) are set on piezo-driven stages A and B, respectively, which are just beneath AFM and STM heads with tips and *YZ* scanners. Both stages travel along 1-dimensional motion axes X_A and X_B. (A coarse motion mode with millimeter travel may also be added in stage A in Fig. 2.) The stage A and B are independently controlled and their motion

axes X_A and X_B are aligned to be parallel with the two arms of the Michelson interferometer. The interferometer can measure motion (= displacement) difference between the X_A and X_B axes. 3-dimensional images of the both samples can be obtained using the combined motions of the stages A/B and AFM/STM heads. The compact thermo-stabilized vacuum cell with a temperature stability of 1 mK and a vacuum of 10^{-5} torr is employed to remove thermal deformation and fluctuation of refractive index of air. The beam path of the interferometer is shown in Figure 2. The linear polarized beam (polarization angle : 45 degree) emitted from the frequency-stabilized He-Ne laser passes through the Pockels cell and the single-mode polarization preserving fiber. The Pockels cell is used to supply phase modulation and a phase bias shift between the two polarization components p and s. Removing the instability of beam pointing and a heat source of the He-Ne laser can be attained using the fiber. The beam passes through the non-polarizing beam splitter 1 (NPBS1), and a part of the beam is split into the photodiode 1 (PD1) through polarizer 1 (P1: 45 degree) for the reference phase detection with the lock-in amplifier 1 (LIA1). The beam incident on the polarized beam splitter 1 (PBS1) is divided into two beams, s and p components. The two beams go along the two arms of the interferometer via PBS2 and 3, quarter wave plates 1 and 2 (QWP1/2), moving prism 1 and 2 (MP1/2) on the stages and trapezoid prism 1 and 2 (TP1/2). The beams travel back and fourth four times between MP1/2 and TP1/2. The two beams re-passed through QWP1/2 and the PBS2/3 are recombined at the PBS4. The recombined beam is divided at NPBS2 into two parts, one goes to PD2 via P2(45 degree) and the other to PD3 via QWP3 and P3 (45 degree), respectively. Output signals form the PD2 and 3 are fed into the LIA2 and 3 to determine the phase shift corresponding to the motion difference between the stage A and B using phase modulation and lock-in detection. The output signal of the LIA1 is used to control the bias phase shift of the Pockels cell so that amplitudes of the s and p components at the PBS1 should be the same. The output signals of LIA2 and 3 are the cosine and sine function of the optical path difference. The motion difference can be measured and controlled

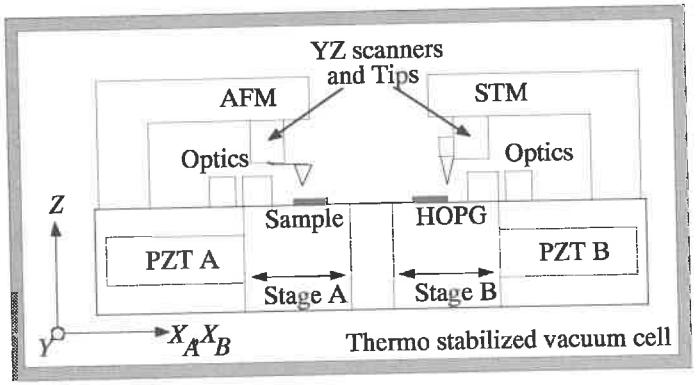

Figure 1. Side view of the absolute length measuring machine.

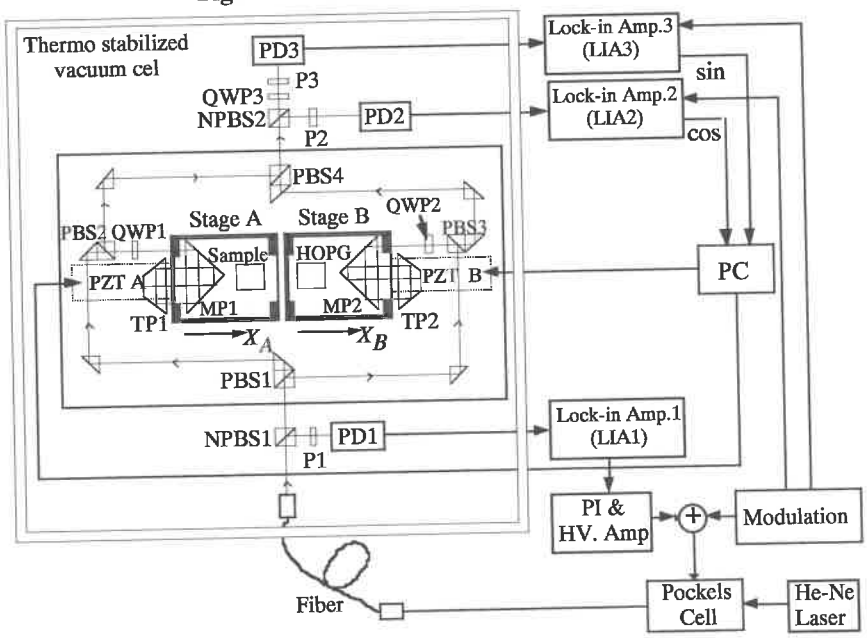

Figure 2. Top view of the absolute length measuring machine.

at the dark fringes points (= null points) with picometer resolution. In our design, the motion difference between the stages A and B, which is corresponding to 1 fringe should be (wavelength/8). The following steps represent the measurement procedure of the ALMM.

(1) Initial to zero calibration point: At the starting position x_{A0} of scan for stage A, displacement of stage B x_B is controlled and locked so that the fringe of the interferometer should be dark (null point). The stage B is then at position x_{B0}.

(2) Scanning of the stage A for the AFM: The stage A is then scanned for the AFM imaging to the ending position x_{A1}. The moving translation (x_{A0} -x_{A1}) will consist of integer part n of optical fringe n*(wavelength/8) and fractional part f of an optical fringe f*(wavelength/8). n is then determined from the output of the LIA2 and LIA3.

(3) Scanning of the stage B for the STM: The stage B is then scanned for the STM atomic imaging to position x_{B1} to shift the optical fringe to the next dark (null point). The translation (x_{B0} -x_{B1}) equals to the fractional part f of the optical fringe and it can be determined by counting the number m of atoms in the STM image, in which lattice spacing is d.

(4) Determination of total translation length: The total translation equals to n*(wavelength)/8 + md.

3. Pre-experiments

In order to realize the ALMM project, a lattice spacing on crystalline surface must be determined. The lattice spacing of a bulk state may not be same as the one of a surface state. To research the problem, we preliminary made a measuring machine for lattice spacing on crystalline surface [9], which consist of a flexure piezo-driven X axis-stage, a STM head with tip and a YZ-scanner and a phase modulation homodyne interferometer. In the interferometer, a differential-4-path configuration is used. **Figure 3** shows the outline of the machine, which are almost same as the ALMM, except an AFM head and another flexure stage. The stage is fabricated from low linear expansion cast iron whose linear expansion coefficient is less than $0.8*10^{-6}$ K^{-1}. A first resonance frequency of the stage is about 2 kHz. A maximum travel of the stage is about 10 micrometers. Pitch and yaw motion are less than 1.5 radian for maximum travel. We can obtain a good quality image of HOPG for counting the number of atomic array. **Figure 4** shows a part of atomic image of HOPG obtained using the machine, whose length is 1 micrometer.

Figure 3. Photograph of the measuring machine for lattice spacing on crystalline surface.

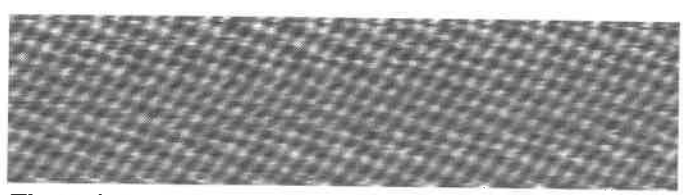

Figure 4. Part of a long atomic image of HOPG. The lateral axis was selected as the measurement and the fast scanning direction. The scanned area was 1 micrometer (lateral axis) * 2 nanometer (vertical axis). Tip speed was 2 micrometer/s. The scanned time for one line along the fast scanning axis and the scanning period of the complete image were 0.5 and 256 s, respectively.

Figure 5 shows a demonstration of the phase modulation homodyne interferometer used on the stage shown in Fig. 3. In Fig. 5, signals (A), (B) and (C) are from capacitive displacement sensor set on the stage, photodiode ended at the interferometer (PD2 in Fig. 2) and the lock-in am-

plifier (LIA2 in Fig.2). In Fig. 5, the *X* axis stage moves with triangular motion. About (2+1/4) fringes (=(2+1/4)*(1/16)*wavelength) from PD2 can be observed. The result almost agrees with the output of 90 nanometer from the displacement sensor. The LIA2 signal crosses null line when the PD2 signal reaches at bright and dark points. The S/N ratio for LIA2 signal is not sufficient in Fig. 5, because the modulation amplitude is not so high. We believe it is possible to improve the S/N ratio by tuning the modulation method. By combining the results from Fig. 4 and 5, we can report determination process for lattice spacing on HOPG crystalline surface in the near future, and we can also realize the ALMM project.

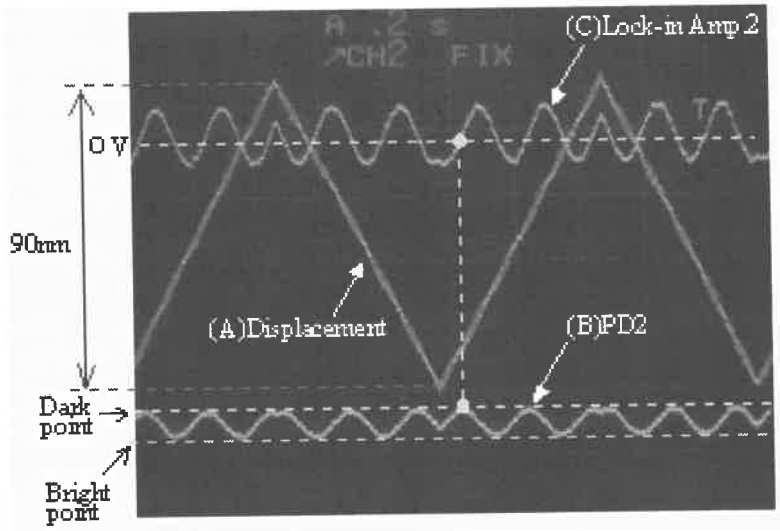

Figure 5. A demonstration of the phase modulation homodyne interferometer set on the stage shown in Fig. 3. Signals (A), (B) and (C) are from capacitive displacement sensor set on the stage, photodiode ended at the interferometer (PD2 in Fig. 2) and the lock-in amplifier (LIA2 in Fig.2). A differential-4-path configuration is used in the interferometer. With the configuration, optical one fringe equals (1/16)*wavelength. In the interferometer, two $LiNbO_3$ crystals (5 *5*30 milimeters*2 piece) was used for the Pockels cell. A half-wavelength voltage for the cell is about 180 V. Modulation amplitude and frequency applied to the cell were 10 V and 10 kHz, respectively. Amplitude of LIA2 signal (C) is about 0.5 V.

Acknowledgment

The partial financial supports of the Saneyoshi Scholarship Foundation and the Mitutoyo Association for Science and Technology are gratefully acknowledged.

References

1) For example, Agilent Technologies, Model 10897B; 2001.
2) For example, Gonda S et al.. Real-time, interferometrically measuring atomic force microscope for direct calibration of standards. Rev. of Sci. Instrum. 1999; **70**: 3362.
3) Thalmann R, Hou W. Limitations of interpolation accuracy in heterodyne interferometry. Proc. of the 7th International Precision Engineering Seminar; May 1993; Kobe, Japan: 11.
4) Basile G, Bergamin A, Cavagnero G, Mana G. Phase modulation in high-resolution optical interferometry. Metrologia 1991-2; **28**: 455.
5) NIST, PTB, NPL, IMGC, NRLM et al..
6) Basile G, Becker P, Bergamin A et al.. Combined optical and X-ray interferometry for high-precision dimensional metrology. Proc. Royal Society Lond. A 2000; 456: 701
7) Binnig G, Rohrer H.
8) Aketagawa M, Takada K et al.. Long atomic imaging over a 5-um-long region using an ultralow thermally drifted DTU-STM. Rev. of Sci. Instrum. 1999; **70**: 133.
9) Hashida T et al., Proc. Spring meeting of JSPE; 2000 March 22-24; Tokyo: 589. [in Japanese]

LASER-CCD BASED SENSOR SYSTEM FOR REAL TIME DETECTION OF MOTION LINEARITY

Yoshihito Kagawa[(1)], Sadayuki Matsumiya[(2)], Kazuo Yamazaki[(1)], Yue Yang[(1)]
(1): Department of Mechanical and Aeronautical Engineering,
University of California, Davis CA 95616-5294
(2): Mitutoyo Corporation, Kawasaki, 213 –0012 Japan

1. Introduction

The major goal of manufacturing science and technology is to achieve high productivity and high machining accuracy. In these days, while high productivity is being achieved, precision machining depends substantially on the reduction of motion errors induced by thermal and time dependent deformation. In order to minimize such an inaccurate machining results, the error compensation based on the in-process identification of the error cause is most effective.

Currently, there are two methods used in error detection. The first one is based on the utilization of laser interferometric instrument [1]. By this method, error detection usually cannot be performed in a real-time fashion during the machining process. The second method is based on the pre-established relationship between temperature distribution and thermal deformation errors, such as thermal error model [2]. Although this approach has found some application in machine tool industry, the enhancement of accuracy is limited, since the thermal behavior and deformation of machine tool systems are highly nonlinear in machine conditions [3] and this method can only detect thermal errors.

The purpose of this research is to propose and develop a novel Laser-CCD based 6 Degree-of -freedom motion Measuring System (LC6DMS) for real time, directly and simultaneously detection of motion linearity for machine error measurement and compensation.

2. A proposal of novel sensor system for real time detection of motion linearity

2.1 Conceptual design

Figure 1 shows a conceptual design of the proposed sensor, LC6DMS. This sensor is composed of two main modules in addition to computer system, which are a laser module and a CCD measuring module. The laser model is stationery on the global coordinate system and the CCD measuring module is rigidly mounted onto machine slider. The laser module produces two laser beams, B1 and B2, by using two splitters, BS1 and BS2, as two metrology bases for measurement. A laser beam B2 has inclination angle γ against B1 to measure the linear motion in Z-axis of the slider. The CCD measuring module consists of three CCD cameras, CCD1, CCD2 and CCD3, and two beam splitters, BS3 and BS4. The 6 degree-of-freedom (DOF) erroneous motions of machine slider, which are 3 linear motions $(\delta x, \delta y, d)$ and 3 angular motions (α, ϕ, θ), are measured as the relative motion between B1 and BS3 at the lowercase coordinate system o_{1B}-$x_{1B}y_{1B}z_{1B}$. During the measurement is being performed, the position of the laser beam is always captured by each CCD to measure the motion linearity of the machine slider.

2.2 Measurement principle

Figure 2 shows the coordinate system of the proposed sensor system, LC6DMS. O-XYZ is a world coordinate system attached at the center of BS1 and the others are moving coordinate

systems attached at the center of BS3, BS4, CCD1, CCD2 and CCD3. W, H, L, L0 and γ are the geometric parameters of the sensor system and d is a distance of slider from the laser module.

The kinematics relationship between a six-dimensional motion of the slider, a three-dimensional translation $(\delta x, \delta y, d)$ and a composite rotation (α, ϕ, θ), and three laser positions $(y_{1C}, z_{1C}), (y_{2C}, z_{2C}), (x_{3C}, y_{3C})$ captured by three CCD cameras can be written in a following equation (1).

$$\begin{Bmatrix} y_{1C} \\ z_{1C} \\ y_{2C} \\ z_{2C} \\ x_{3C} \\ y_{3C} - \gamma(L+L0) \end{Bmatrix} = \begin{bmatrix} 0 & -1 & 0 & H & 0 & 0 \\ -1 & 0 & 0 & 0 & -H & 0 \\ 0 & -1 & 0 & H+L & 0 & 0 \\ -1 & 0 & 0 & 0 & -(H+L) & 0 \\ -1 & 0 & 0 & 0 & -(L+L0) & W \\ 0 & -1 & \gamma & L+L0 & 0 & 0 \end{bmatrix} \begin{Bmatrix} \delta x \\ \delta y \\ d \\ \alpha \\ \phi \\ \theta \end{Bmatrix} \tag{1}$$

The transformation equation from the three laser positions to a six-dimensional motion can be obtained by solving equation (1). Following equation (2) is the theoretical basis of LC6DMS for simultaneous measurement of 6 DOF machine slider motion. Once laser beam center coordinates are obtained from CCD image processing, the 6 DOF machine slide motion can be found immediately and simultaneously.

$$\begin{Bmatrix} \delta x \\ \delta y \\ d \\ \alpha \\ \phi \\ \theta \end{Bmatrix} = \begin{Bmatrix} -\frac{H+L}{L} z_{1C} + \frac{H}{L} z_{2C} \\ -\frac{H+L}{L} y_{1C} + \frac{H}{L} y_{2C} \\ \frac{L0-H}{\gamma L} y_{1C} - \frac{L+L0-H}{\gamma L} y_{2C} + \frac{1}{\gamma}\{y_{3C} - \gamma(L+L0)\} \\ -\frac{1}{L} y_{1C} + \frac{1}{L} y_{2C} \\ \frac{1}{L} z_{1C} - \frac{1}{L} Z_{2C} \\ \frac{L0-H}{LW} z_{1C} - \frac{L+L0-H}{LW} z_{2C} + \frac{1}{W} x_{3C} \end{Bmatrix} \tag{2}$$

3. Design and simulation study of LC6DMS

3.1 Optimization of structural parameters

In order to achieve highest measurement accuracy, the 5 structural parameters W, H, L, L0 and γ were optimized through simulation study. First, assuming a set of motion components,

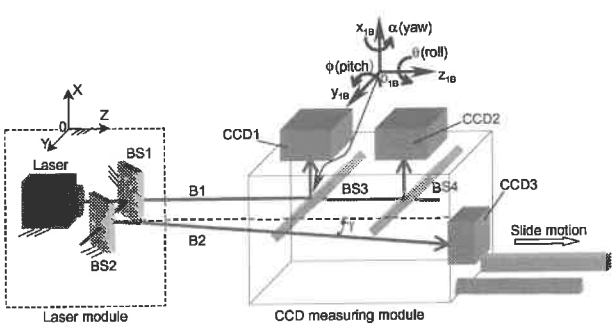

Figure 1: Conceptual design of LC6DMS

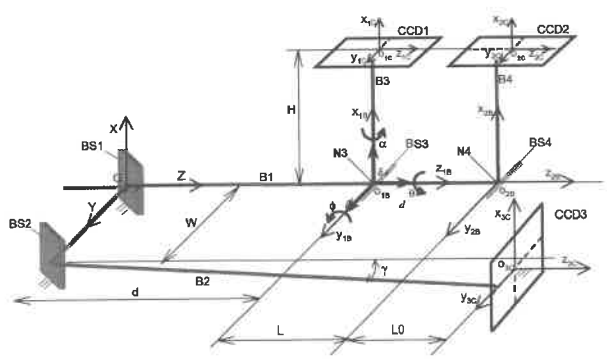

Figure 2: Coordinate system of LC6DMS

the theoretical beam center positions on each CCD are calculated by equation (1). Then, the beam center coordinate are obtained through calculation of intensity centroids of the beam images captured by each CCD in consideration of a diameter and divergence of a He-Ne laser beam and specifications of CCD cameras such as the count resolution and pixel size. Second, the 6 DOF erroneous motions are calculated by substituting the laser beam center coordinate obtained above into equation (2). The criteria of optimal design of the structural parameters are defined by following equation.

$$\delta x_{re} = \left|\frac{\delta x_o - \delta x_m}{\delta x_o}\right| \times 100\%,\ \delta y_{re} = \left|\frac{\delta y_o - \delta y_m}{\delta y_o}\right| \times 100\%,\ d_{re} = \left|\frac{d_o - d_m}{d_o}\right| \times 100\%$$
$$\alpha_{re} = \left|\frac{\alpha_o - \alpha_m}{\alpha_o}\right| \times 100\%,\ \phi_{re} = \left|\frac{\phi_o - \phi_m}{\varphi_o}\right| \times 100\%,\ \theta_{re} = \left|\frac{\theta_o - \theta_m}{\theta_o}\right| \times 100\% \quad (3)$$

where subscripts o and m shows the given motion error initially and the measurement results obtained from simulation respectively.

Figure 3 ~ Figure 6 shows the simulation results and its simulation parameters listed under the figures. The following structural parameters were designed based on these results and the overall module size requirement;

$$L = 60\text{mm},\ H = 54\text{mm},\ W = 46\text{mm},\ L0 = 28.5\text{mm},\ \gamma = 200\text{arcsec} \quad (4)$$

3.2 Theoretical measurement accuracy

The theoretical measurement accuracy of 6 DOF motion linearity was analyzed. Figure 7 and Figure 8 shows the theoretical measurement accuracy for linear motion. From Figure 7, it can be seen that the relative measurement errors for δx and δy are less than 0.09% over a range of 1~25 μm. Figure 8 shows that the relative error is less than 1.4% when the distance d is smaller than 2000 mm. The other theoretical measurement accuracy for three angular motions have achieved less than a 0.05% error over the range from 1 to 100 arecsec.

4. Conclusions

(1) A laser-CCD based novel sensor system for the direct and simultaneous detection of 6 DOF motion linearity was proposed.

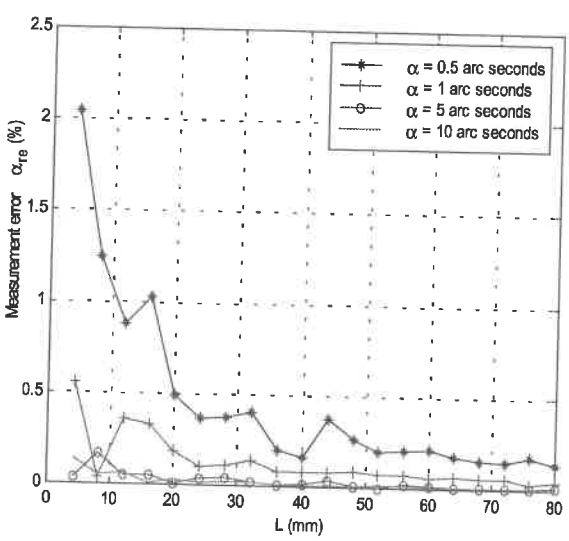

Figure 3: Relationship between L and α_{re} (d=100mm,δx=5μm,δy=5μm,ϕ=10arcsec, θ=15arcsec,H=50mm)

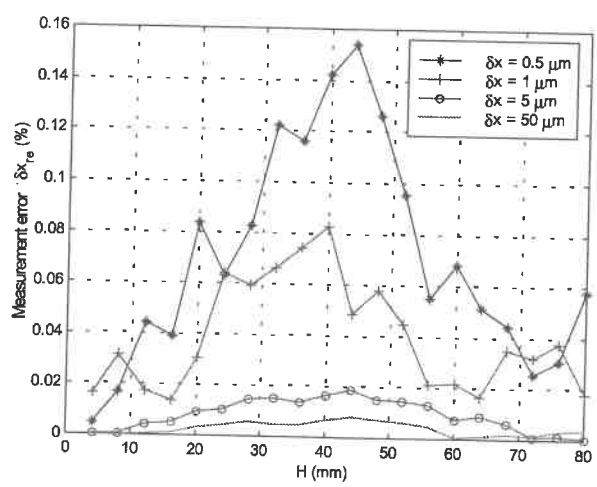

Figure 4: Relationship between H and δx_{re} (d=100mm,δy=0.5μm,α=10arcsec,ϕ=10arcsec, θ=15arcsec,L=60mm)

(2) The theoretical bases of the proposed sensor system for simultaneous measurement of 6 DOF machine slider motions were established based on the kinematics relationships.
(3) In order to achieve highest measurement accuracy, the key structural parameters were designed through simulation.
(4) The theoretical measurement accuracy of the proposed sensor system was analyzed.

References

[1] Zhang, G., Wang, C., Hu, X., And Jing, F., Error Compensation Of Coordinate Measuring Machines. Annals Of The Cirp, 1985. 34(1): P. 445-448

[2] Chen, j.s., j. Yuan, and j. Ni, Thermal Error Modeling For Real-Time Error Compensation. International journal of advanced manufacturing technology, 1996b. 12(4): p. 266-275.

[3] Attia, M.H.A.K., L., Nonlinear Thermoelastic Behavior Of Structural Joints--Solution To A Missing Link For Prediction Of Thermal Deformation Of Machine Tools. ASME Journal Of Engineering For Industry, 1979. 101: P. 348-354.

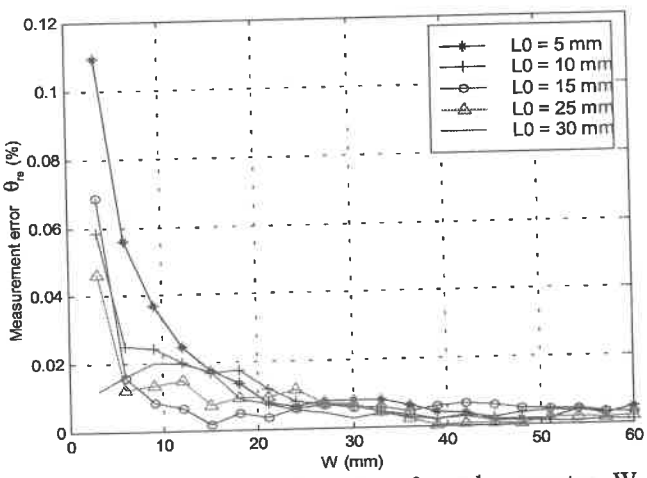

Figure 5: Relationship between θ_{re} and parameters W and L0
(d=100mm,δx=5μm,δy=0.5μm,α=10 arcsec, ϕ=10arcsec,θ=15arcsec,L=60mm,H=54mm)

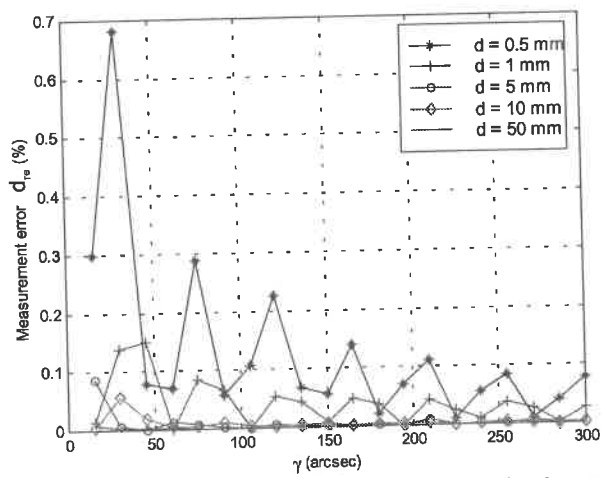

Figure 6: Relationship between d_{re} and beam inclination angle γ
(δx=0.5μm,δy=0.1μm,α=10arcsec,ϕ=10arcsec, θ=15arcsec,L = 60mm,H=54mm,W=46mm, L0=28.5mm)

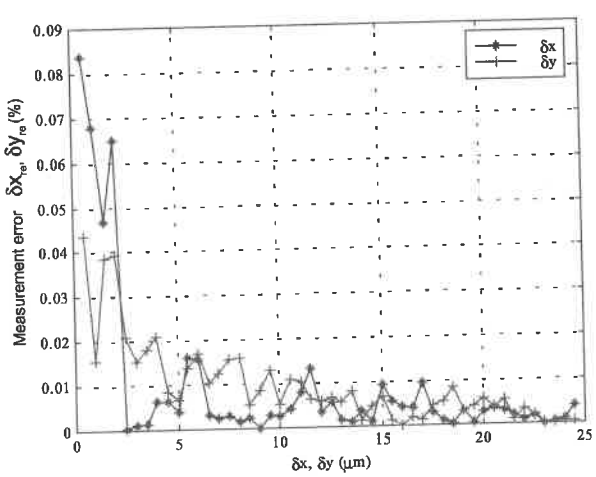

Figure 7: Theoretical measurement accuracy of δx and δy
(d=50mm, α=1arcsec, ϕ=5arcsec, θ=10arcsec)

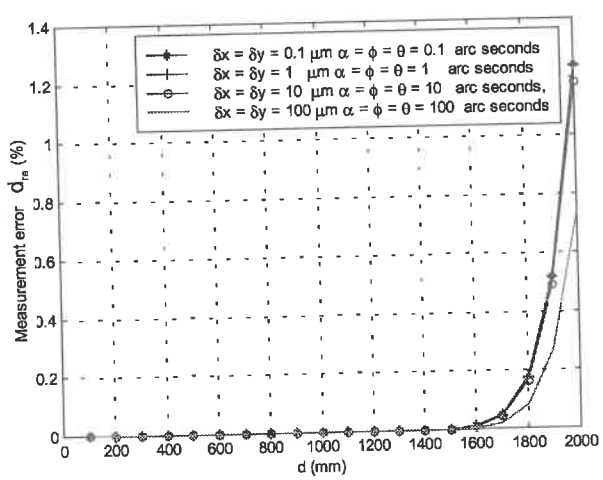

Figure 8: Theoretical measurement accuracy of d

Measurements using Fourier Transform Phase Shifting Interferometry

Leslie L. Deck
Zygo Corporation, Laurel Brook Road, Middlefield, CT. 06455-0448

Phase shifting interferometry[1] (PSI) using wavelength tuning is a preferred technique for high-precision surface form measurements of large optics[2]. Recently, a new phase shifting interferometry technique was described that has a significantly greater flexibility and measurement precision than traditional PSI[3]. Called Fourier transform phase-shifting interferometry (FTPSI)[4], the technique combines phase shifting via wavelength tuning with specific cavity geometries and a flexible Fourier based analysis technique to identify and extract surface features from many surfaces simultaneously. In addition, FTPSI preserves the spatial relationships between the physically separated surfaces so that measurements of surface profiles, physical wedge and homogeneity can be easily extracted. These measurements have been demonstrated for a parallel plate in Ref. 3. In this paper, I describe these and several additional measurement possibilities using FTPSI.

1. Fourier transform phase-shifting interferometry

The technique is based on the realization that to first order, a multi-surface cavity is just a combinatorial collection of elemental (2-surface) cavities, and that with wavelength tuning, each elemental cavity generates interference with a phase variation directly related to the cavities' total optical path difference (OPD) nT and the optical frequency tuning rate $\dot{\nu}$ via

$$\dot{\varphi} = 2\pi nT\dot{\nu}/c\,, \tag{1}$$

where n is the index and T is the cavity physical thickness. If the OPD of each elemental cavity is unique, each cavity then produces interference at a frequency f_C given by,

$$f_C = nT\dot{\nu}/c\,. \tag{2}$$

A Fourier analysis of the interference variation from a single wavelength-tuned measurement extracts the spectrum of interference frequencies. Each spectral peak corresponding to the interference from an elemental cavity of interest is individually analyzed for the interferometric phase φ using a windowed discrete Fourier transform evaluated at the frequency of the peak;

$$\varphi = \tan^{-1}\left(\frac{\mathrm{Im}(\mathrm{DFT}(f_C))}{\mathrm{Re}(\mathrm{DFT}(f_C))}\right), \tag{3}$$

with

$$\mathrm{DFT}(f_C) = \sum_{j=0}^{N-1} I_j W_j \exp\left(i2\pi j f_C / f_S\right). \tag{4}$$

The I_j represent the N intensity samples acquired during the wavelength tune, W_j are the sampling weights and f_S is the sampling rate. The optical frequency variation $\dot{\nu}$ is assumed linear throughout the acquisition. As with PSI, surface profiles are obtained from the spatial variation of the interferometric phase. Figure 1 shows the apparatus used to demonstrate the technique, incorporating a conventional Fizeau interferometer outfitted with a wavelength tunable laser.

To minimize the effect of higher order interference frequencies disturbing the phase evaluation, cavity geometries are used which separate all the 1st and 2nd order frequencies from each other. This entails selecting the total optical frequency excursion, the primary gaps L_1 and L_2 and the number of intensity samples N, depending on the value of the test optic OPD, nT. The details of this selection procedure are discussed in Ref. 3, the main result being that the optimal cavity geometry is one in which the ratio of the optical path lengths of any two primary gaps is a unique power of three.

2. Relative Measurements

The 4-surface cavity shown in Figure 1 can be used to measure many properties of a test optic that is bounded by two parallel surfaces – a parallel plate being the canonical example. The four surfaces making up the cavity decompose into six elemental 2-surface cavities, each producing a unique 1st order interference frequency. The interferogram recorded at each pixel is spectrally decomposed with a Fourier transform and the interference frequency peaks corresponding to the elemental cavities are identified. Figure 2 shows the interference frequency spectrum obtained when using the 4-surface geometry. The spectrum of 2nd order cavity frequencies is also shown to highlight the excellent separation between the 1st and 2nd order peaks.

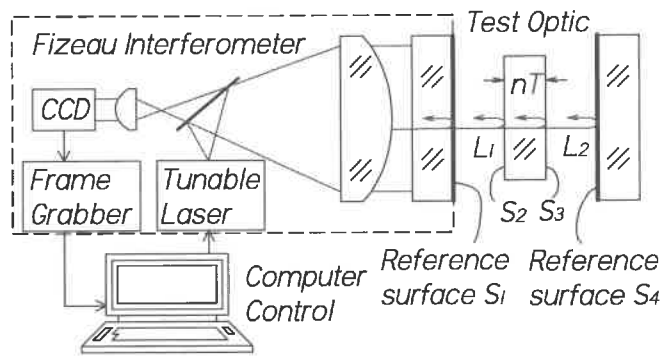

Figure 1: Apparatus used to demonstrate the method.

Each 1st order frequency peak corresponds to a particular elemental cavity. The spatial phase variation of each 1st order peak evaluated at the 1st order frequency represents the OPD variation between those two surfaces. For example, assuming $nT < L_1 < L_2$, the first leftmost peak corresponds to interference between the two surfaces of the test optic S_2 and S_3. As such, the spatial phase map can be used to measure the optical thickness variation. The second peak from the left corresponds to interference between the first reference surface S_1 and the first surface of the test optic S_2. Its phase variation corresponds to the first surface profile of test optic. Similarly, the profile of the second surface of the test optic S_3 relative to the second reference S_4 is found from the fourth peak. If necessary, S_3 can be referenced to S_1 with an additional measurement of the

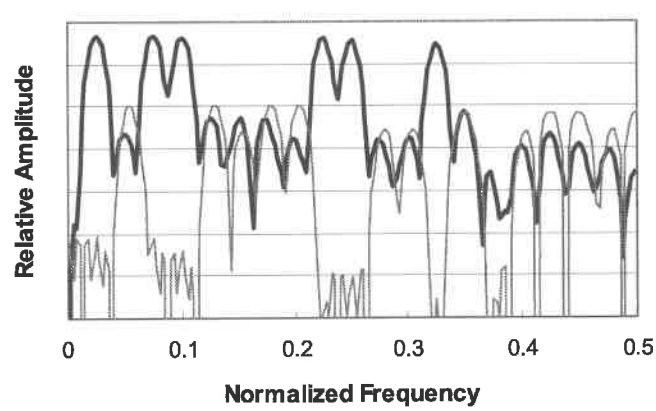

Figure 2: Log plot of the interference spectrum for the optimum 4-surface geometry normalized to the sampling rate. The heavy curve is the full spectrum and the light curve is the spectrum of 2nd order frequencies.

cavity with the test optic removed.

The information for each elemental cavity is obtained with a single wavelength tuned acquisition. The simultaneous nature of these measurements implies that spatial relationships between the surfaces are preserved. This allows the measurement of index homogeneity from the difference between the optical thickness variation and the physical thickness variation obtained from the empty cavity measurement and the measurements of the two outermost primary elemental cavities, S_1:S_2 and S_2:S_3. Surface profiles, physical and optical wedge and relative homogeneity measurements were demonstrated in Ref. 3, this paper will concentrate on additional measurement capabilities of the technique.

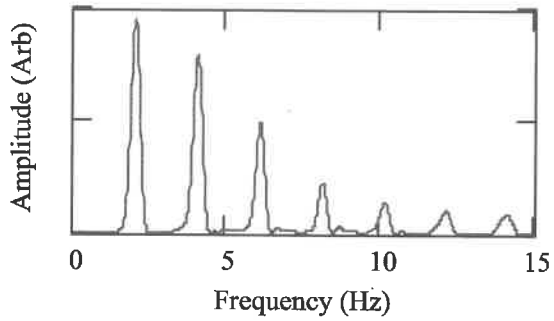

Figure 3: Plot of the interference spectrum from a high finesse cavity.

3. High finesse cavities

When the reflectivities of the surfaces making up an elemental cavity are high, the optical power transferred to higher order multiple interference events increases, producing interference at harmonics of the 1st order frequency. The distorted fringe pattern produced cannot be analyzed with conventional PSI without significant error. FTPSI separates these harmonics so that the 1st order frequency can be analyzed in isolation, producing distortion free profiles of the surfaces. Figure 3 shows the frequency spectrum obtained from a high finesse cavity whose interference pattern is shown in Fig. 4

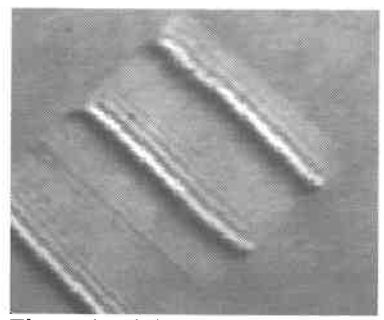

Figure 4: High finesse fringes.

4. Internal angle measurements

By selecting which elemental cavity to analyze, measurements of internal angles of various optical elements can also be realized. Figure 5 shows one possible geometry for measuring the 90° angle and the pyramidal error of a right angle prism. To 1st order, a ray encounters 4 surfaces before leaving the cavity, S1, S2, S2` and S1`. The S1:S2 cavity provides a measure of the S2 surface, which acts as the orientation referent for the non-retro direction for the pyramidal error. The tilt of the S1:S1` cavity in the retro direction determines the 90° angle. Note that the direct return of the beam back to the camera forces the use of a camera with good dynamic range. The dashed line to the left of S1 indicates where a beam stop can be used to remove the direct return if necessary. A traditional PSI measurement of this angle requires the removal the S1 surface and measures the S2:S2` cavity, however the geometry shown here allows us to simultaneously qualify the S2 surface against a known reference.

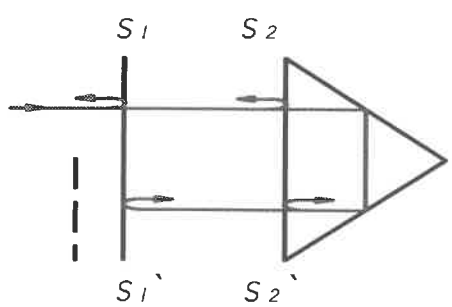

Figure 5: Cavity geometry for measuring the 90° angle and pyramidal error of a right angle prism.

5. Absolute measurements

Equation 1 implies that the total cavity OPD can be obtained if the total phase shift is measured during a known optical frequency excursion. This process is known as coherent ranging[5]. To account for the spectral dispersion of the test optic, Eq.1 must be modified to

$$\dot{\varphi} = \frac{2\pi n T \dot{\nu}}{c}(1 + \alpha\nu/n) \tag{5}$$

where α is the 1st order dispersion coefficient of the test optic material. The magnitude of this correction is of order 1% for typical glasses at wavelengths from the visible through the near-IR. The test optic absolute physical thickness T can be found with the 4-surface cavity geometry via

$$T = \frac{c}{2\pi\dot{\nu}}(\dot{\varphi}_{14} - \dot{\varphi}_{34} - \dot{\varphi}_{12}). \tag{6}$$

Here $\dot{\varphi}_{14}$ is the phase variation observed in the empty cavity and the 1st order dispersion coefficient for air is assumed to be zero. The absolute index of the test object is obtained by solving Eq. (5) for nT and dividing by Eq. (6)

$$n = \frac{\dot{\varphi}_{23}}{(\dot{\varphi}_{14} - \dot{\varphi}_{34} - \dot{\varphi}_{12})} - \alpha\frac{c}{\bar{\lambda}}, \tag{7}$$

where $\bar{\lambda}$ is the mean value of the wavelength used. Note that for the absolute index, the actual wavelength used must be known, while for the thickness only the change in the wavelength during the measurement is required.

6. Summary

I have outlined a new general methodology for optical profiling using wavelength tuning combined with specific cavity geometries and an effective Fourier based analysis technique. Called Fourier transform phase-shifting interferometry (FTPSI), the method is a general replacement for traditional PSI. This paper has outlined some of the more interesting measurement possibilities of the technique, including;

1) Surface profiles from multiple surface cavities
2) Surface profiles from high finesse cavities
3) Internal angle measurements
4) Measurements of relative and absolute optical thickness
5) Measurements of relative and absolute physical thickness
6) Measurements of relative and absolute index homogeneity

7. References

[1] J. E. Greivenkamp and J. H. Bruning, "Phase Shifting Interferometry," *Optical Shop Testing*, D. Malacara, 501-598, J. Wiley, New York, 1992

[2] L. Deck, J. A. Soobitsky; "Phase-shifting via wavelength tuning in very large aperture interferometers," Proc. SPIE, 3782-58, 432-442 (1999)

[3] L. Deck, "Multiple surface phase-shifting interferometry," to be published in Proc. SPIE, 46th Annual, San Diego, (2001)

[4] FTPSI is the topic of US and Foreign patents pending assigned to Zygo Corporation

[5] P. de Groot, "Chromatic dispersion effects in coherent absolute ranging," Opt. Lett., **17**, 898-900 (1992)

PICOMETER POSITIONING SYSTEM USING AEROSTATIC GUIDEWAY AS MOTION-REDUCTION MECHANISM

Hiroshi MIZUMOTO, Shiroh ARII
Tottori University, Koyama, Tottori, JAPAN
Makoto YABUYA, Yoshihiro KAMI
Nachi-Fujikoshi, Namerikawa, Toyama,JAPAN

1. Introduction

Precision positioning is one of the basic functions of machine tools and measuring instruments used in the field of nanotechnology. Positioning resolution of these machines should be less than one nanometer. In the present paper, a picometer positioning system is proposed, where the table of an ultraprecision machine tool is positioned with 10pm of resolution. The proposed picometer positioning system uses an aerostatic guideway with an Active Inherent Restrictor (abbreviated as "AIR"). The AIR was invented by the authors for improving the stiffness and the rotational accuracy of air-bearing spindles [1]. A piezoelectric transducer incorporated into the AIR controls the restriction gap on the bearing surface, then the position of the machine table. Owing to aerostatic mechanism, the table displacement can be much less than the deformation of the transducer; therefore, the aerostatic guideway with the AIR acts as motion-reduction mechanism. Characteristics of the proposed positioning system such as positioning resolution and dynamic response are reported.

2. Motion-Reduction Mechanism using Aerostatic Guideway

Figure 1 shows the proposed picometer positioning system. A ceramic machine table (size: 300mm x 350mm x 100mm, mass: c.50kg) of an ultraprecision machine tool [2] is guided by an aerostatic guideway in X direction (normal to the paper). This X-table can also be positioned in Z-direction (horizontal, cutting direction) by the Active Inherent Restrictor (AIR) incorporated into the aerostatic guideway. A positioning instruction output from a microcomputer is converted into the supply voltage to the piezoelectric transducer (PZT) in the AIR. The X-table moves according to the deformation of the PZT. The table movement in Z-direction is detected by a fiber optic sensor and fed back to the computer. Thus a closed-loop control system is completed. Then the computer outputs the instruction for correcting the table position. The movement of the table is monitored by an FFT analyzer.

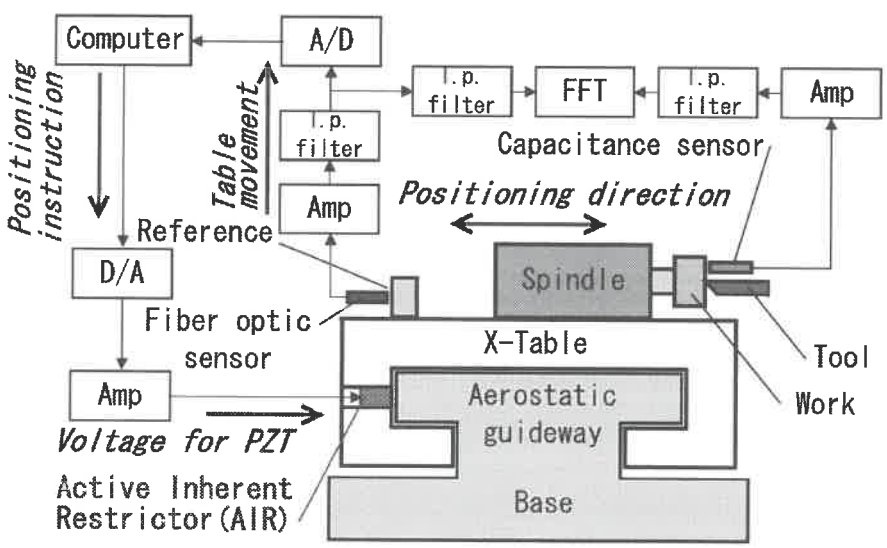

Fig. 1 Ultraprecision positioning system using aerotatic guideway

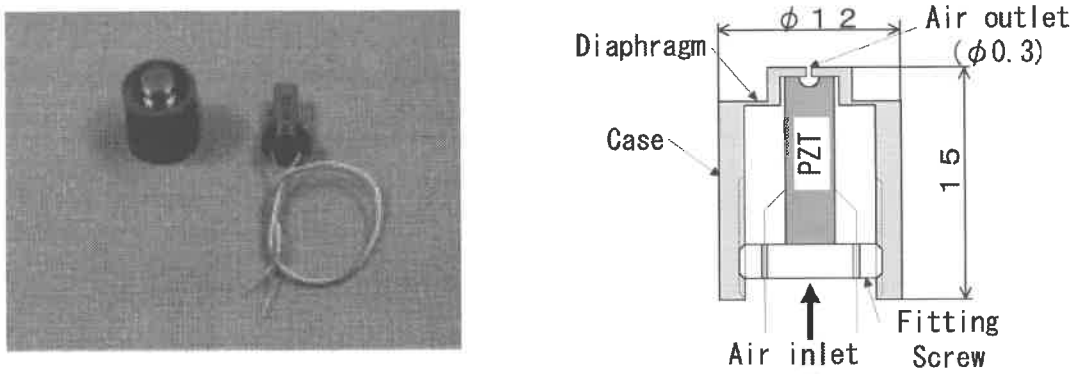

(a) Piezoelectric transducer and diaphragm case **(b) Cross section of assembled AIR unit**

Fig. 2 Unit and elements of Active Inherent Restrictor (AIR)

The elements and the assembled view of the AIR are shown in Fig. 2; the AIR unit consists of a piezoelectric transducer (PZT) and a diaphragm case that has an air outlet. The hole is small enough to function as an orifice when the transducer is embedded in the bearing surface. The positioning mechanism using the AIR is shown in Fig. 3. A table is supported by an aerostatic guideway with an inherent restrictor. Orifice area of the inherent restrictor formed on the bearing surface is $\pi d h_d$, where, d is the diameter of the air outlet and h_d is the restriction gap that can be controlled by PZT. When the length of PZT decreases by Δh_d, the airflow rate and the pressure on the bearing surface increases. Then, the air film thickness h increases by Δh, and the table moves upward.

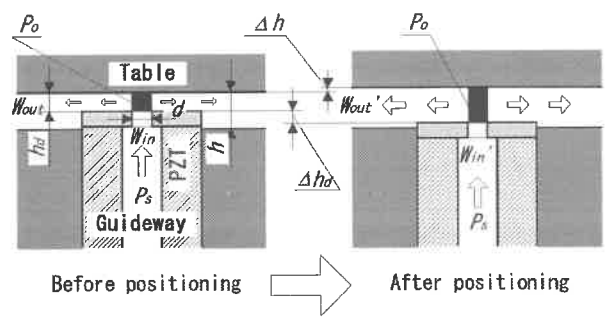

Fig. 3 Motion reduction mechanism of AIR

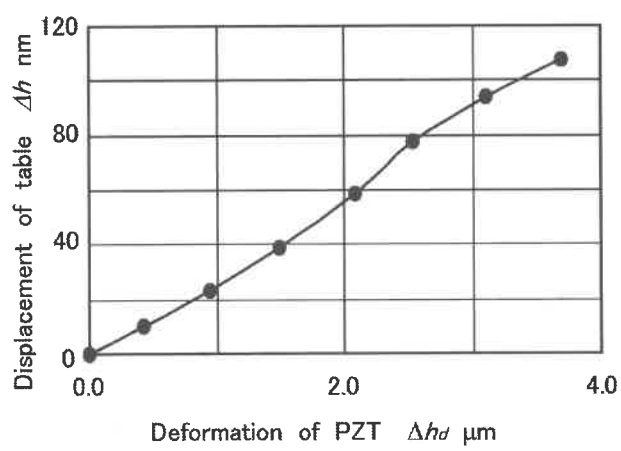

Fig. 4 Characteristic of motion reduction by AIR

Owing to aerostatic mechanism, the table displacement Δh in Z-direction can be much less than the deformation of the transducer Δh_d. Figure 4 indicates an experimental relationship between Δh_d and Δh: full stroke of the piezoelectric transducer is 3.5 μm, while the maximum movement of the table is 110nm. This means that the aerostatic guideway with the AIR acts as motion-reduction mechanism. The reduction rate shown in Fig. 4 is about thirty.

3. Dynamic Response

Figure 5 shows a dynamic step response of the positioning system, where the width of the step is 10nm. From the rising of the curve, the slew rate is calculated to be about 4.5nm/ms. Settling time, the time for completing the step movement, is about 20ms. The frequency response of the

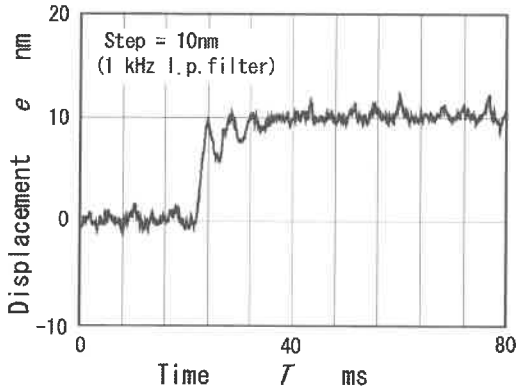

Fig. 5 Step response of the system

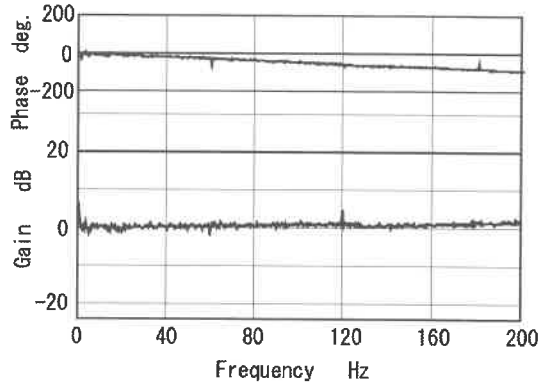

Fig. 6 Frequency response of the system

system is shown in Fig. 6, where the amplitude of sinusoidal instruction is 5nm. As the frequency increases, the amplitude of the table vibration slightly increases. Phase lag also increases, however, the phase lag at 50Hz is only 20deg. Therefore, maximum controllable frequency is at least 50Hz. In spite of large phase lag, the amplitude of vibration does not reduce at 200Hz. The response for a series of rectangular positioning instructions is also examined. Maximum pulse rate that the X-table can follow after is about 25HZ.

4. Positioning Resolution

Results of static step positioning with various step widths (100pm, 50pm, 20pm and 10pm) are shown in Fig. 7. Steps of the same width are repeated five times in one direction then in the reverse direction. Low pass filter is used to decrease noise. Steps larger than 20pm are clearly resolved. Steps of 10pm are degraded by noise and not so clear as others, however, every step can be recognized. Therefore, the positioning resolution of this system is considered to be 10pm.

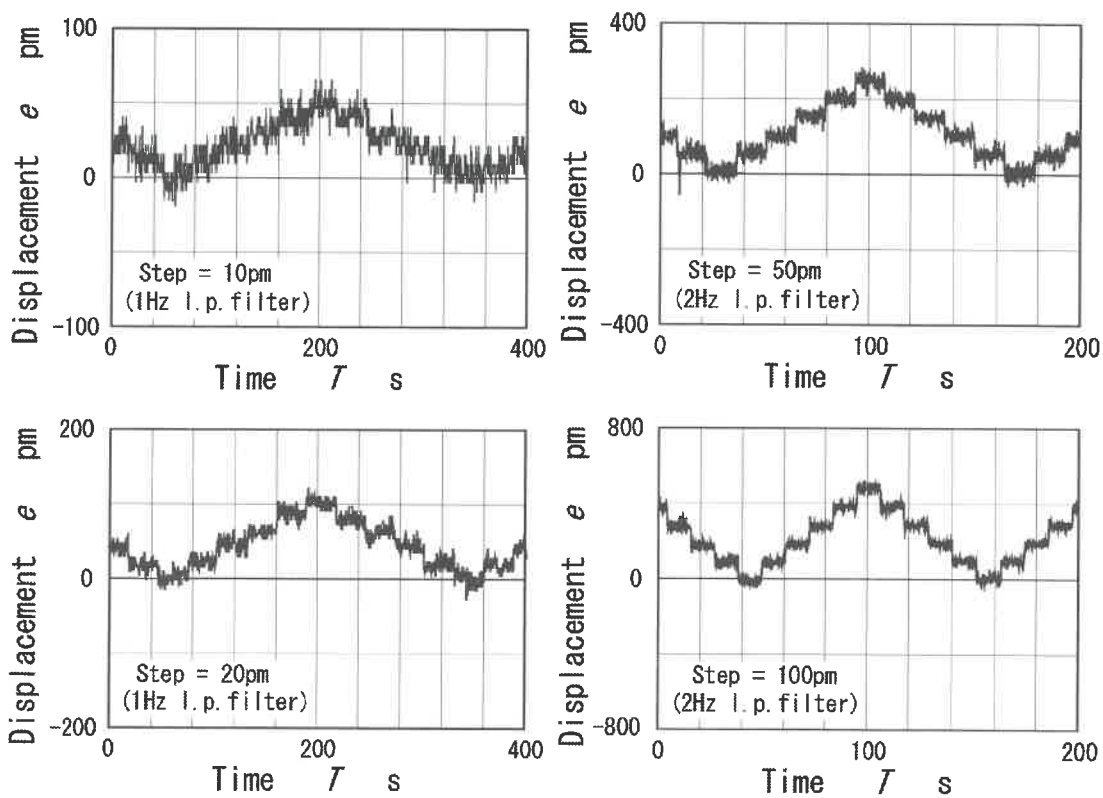

Fig. 7 Picometer step positioning (step width: 10pm, 20pm, 50pm and 100pm)

5. Micro Step Cutting

As shown in Fig.1, an aluminum alloy mounted on the X-table can be turned. During single point diamond turning, micro steps can be made on the turned surface by positioning the X-table in the cutting direction. Figure 8 shows the table displacement measured at the reference point for the positioning system (a) and the cutting point (b). Step positioning of 10nm is repeated five times then reversed. At the cutting point, the width of step is about 16nm, which is larger than at the reference point. This is because some rotation of the X-table occurs. Three-dimensional expression of the turned surface is shown in Fig. 9, where, about 18nm width of steps can be recognized. Therefore, this positioning system can also be used as a micro cutting device.

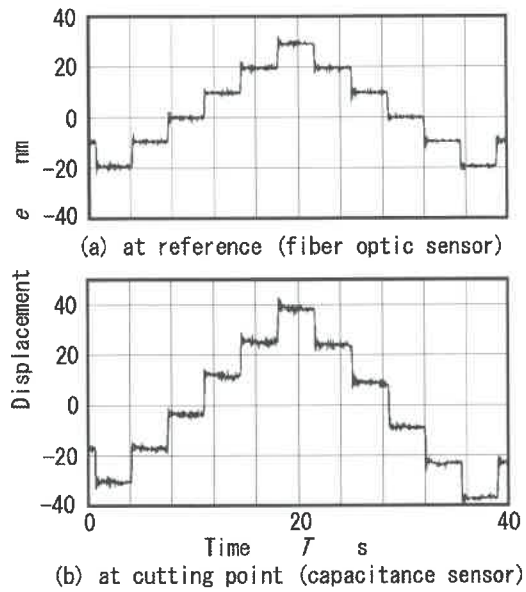

Fig. 8 Cutting of micro step using positioning system

6.Conclusions

The effect of the proposed motion-reduction mechanism using the active aerostatic guideway on the characteristics of the positioning system is analyzed and following results are obtained:

(1) The motion-reduction mechanism effectively reduces the deformation of the piezoelectric transducer. Measured reduction rate is about thirty.

(2) The dynamic step response indicates that the settling time is about 20ms and the frequency response indicates that the maximum controllable frequency is about 50Hz.

(3) Stroke (maximum movement of the table) is only about 100nm, however, static step positioning in various step widths shows that the resolution of the positioning system is 10pm.

Thus, picometer positioning resolution is realized. Therefore, this picometer positioning system using the proposed motion-reduction mechanism will be useful in the field of nanotechnology.

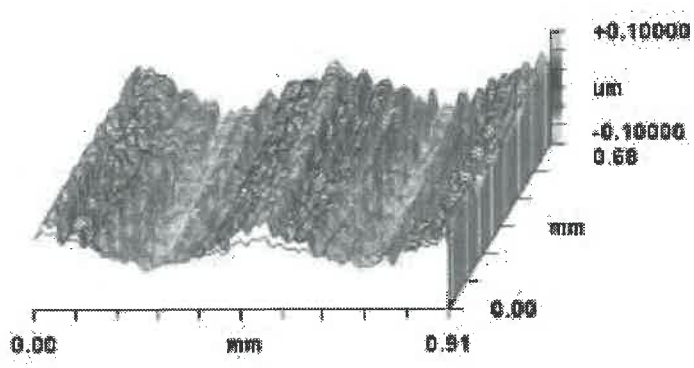

Fig. 9 Micro steps turned on aluminum alloy

References

[1] H. Mizumoto, et. al., Precision Engineering, Vol.19, No.2/3, pp141-146 (1996).

[2] H. Mizumoto, et. al., Proceedings of 1st euspen, Vol.1, pp28-31 (1999).

DESIGN OF A LINEAR HIGH PRECISION ULTRASONIC PIEZOELECTRIC MOTOR

Markus G. Bauer, Dr. Thomas A. Dow
Precision Engineering Center, North Carolina State University
Raleigh, NC

1 INTRODUCTION

Piezoelectric standing wave motors generate motion using a combination of flexural, torsional and/or longitudinal vibrations of a piezoelectric actuator. One of the vibration components produces a normal force, while the other vibration component generates motion (or thrust force) that is perpendicular to the normal force. This combination creates a friction based driving force between one stationary component, the motor, and the slideway to be moved [1]. Piezoelectric standing wave motors have the potential to achieve both high velocities (1m/s) and sub-μm resolution in a small, compact and inexpensive package. The operation of these motors is absolutely silent, if the operating frequency is above the audible spectrum, typically around 40kHz. Although commercially available piezoelectric standing wave motors, such as a motor made by Nanomotion Ltd. [2], perform very well at high slideway velocities, fine positioning requires additional features and advanced control algorithms.

2 MOTOR DESIGN

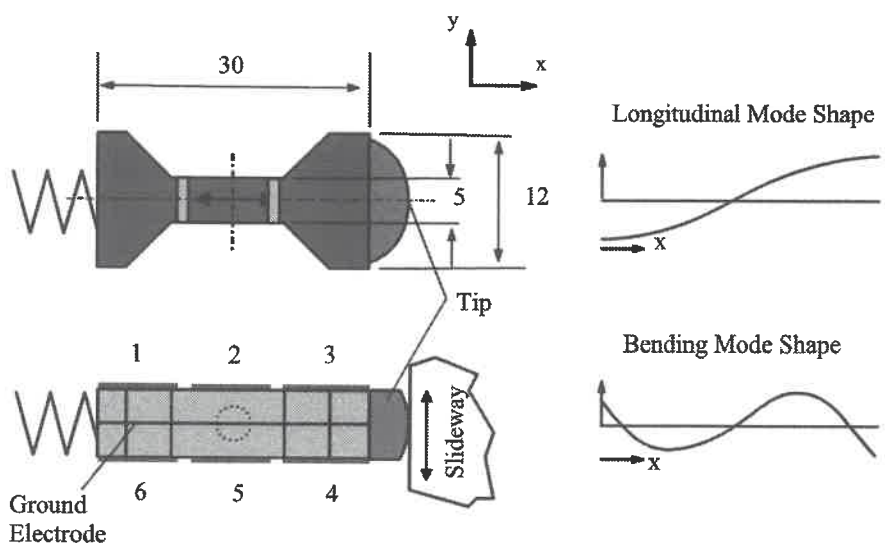

Figure 1. Actuator Design and Operating Modes (dimensions are in mm)

The ultrasonic motor, as shown in Figure 1, uses a bimorph type actuator that allows separate excitation of the first longitudinal mode of vibration and the second bending resonance. Exciting electrodes 2 and 5 with a sinusoidal excitation voltage excites only the longitudinal vibration mode. This allows the adjustment of the dynamic normal force at the tip such that the normal force alternates between almost no compression and twice the preload. The bending vibration is effectively excited with a sinusoidal voltage at electrodes 1 and 4 and with the inverse of this

voltage at electrodes 3 and 6. Variation of the bending excitation amplitude or the phase between bending and longitudinal excitation can be used to control the slideway velocity. In either case, once per cycle the normal load goes to zero and even a small thrust force will initiate sliding between motor tip and slideway. The most efficient motor operation can be achieved when the phase is close to 90° and variation in the amplitude of the bending vibration is used to set the slideway velocity.

3 OPEN LOOP PERFORMANCE

Figure 2 shows series of measurements of the slideway velocity when a different, but constant, bending excitation is applied to an initially motionless slideway. In this experiment, an air bearing spindle is used as the slideway. The inertia is equivalent to that of a linear slideway with a mass of 2.28 kg. When the excitation voltage is applied, the slideway accelerates until a steady state velocity, which is linearly proportional to the bending excitation, is reached. This becomes apparent when the steady-state slideway velocity from the measurement in Figure 2(a) is plotted as a function of the excitation voltage as done in Figure 2(b). It should be noted that the initial acceleration is virtually independent of the excitation amplitude. Instead, it depends on the preload, the accelerated mass, the coefficient of friction and the phase.

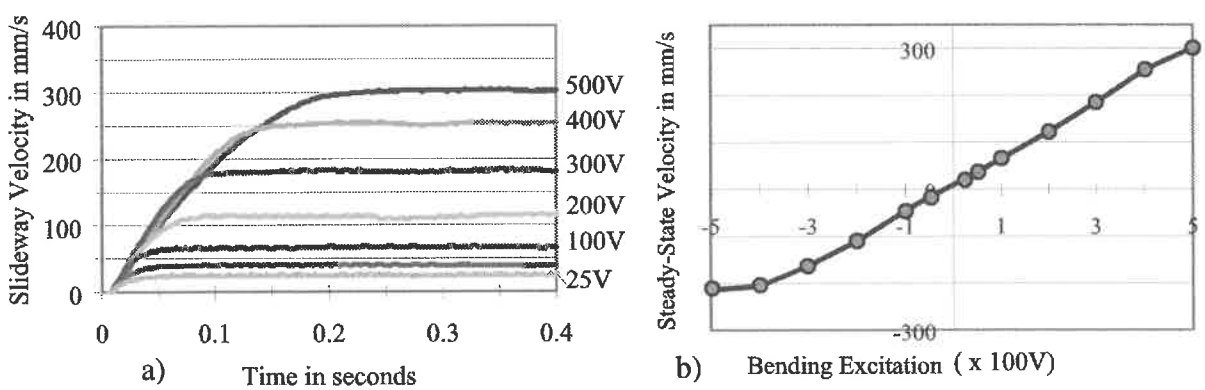

Figure 2. Slideway Velocity for Constant Bending Excitation

The measurements show that unlike other standing wave motors, any excitation of the bending amplitude or thrust force results in slideway motion. The smallest obtainable constant slideway velocity is limited by the noise and the linearity of the electric components that generate and amplify the sinusoidal excitation voltage.

4 CLOSED LOOP POSITION CONTROL

To evaluate the ability of the motor to position the slideway, it was tested in a closed loop control system using simple control algorithms. A block diagram of this system is shown in Figure 3. The computer/motor interface transforms the control parameter into the motor drive signals. The two voltages that oscillate at the motor frequency of 40kHz are modulated such that the control parameter is proportional to either the phase angle between both motor vibrations or to the amplitude of the signal that excites the thrust force. A sampling rate of 500Hz was chosen. Three power amplifiers were used to achieve a maximum output voltage of +/- 500V at the actuator. The slideway position was measured using an incremental encoder with a resolution of

11 μm and compared to the commanded position. Error is defined as the difference between commanded and measured slideway position and is the input to the control algorithm to compute the appropriate motor control value.

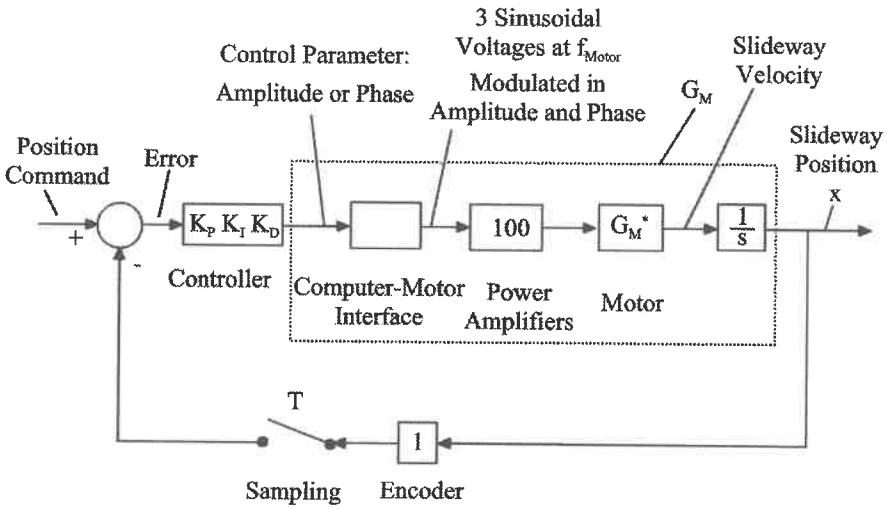

Figure 2. Block Diagram for Motor-Slideway System

A single transfer function was used to represent the behavior of the computer-motor interface, the power amplifiers and the motor-slideway system. This transfer function $G_M(s)$ describes the slideway position (x) as a function of the control parameter (bending amplitude). As sketched in Figure 2, excitation of the bending mode amplitude leads to a slideway velocity. The slideway position is proportional to the integral of the actuator excitation. If a proportional gain controller is used, any position error results in an actuator excitation (proportional to the error). Because the motor generates slideway motion until the error is zero, the steady state error will be driven to zero for an ideal implementation of this principle. In this respect, the ultrasonic standing wave motor resembles an electromagnetic motor.

5 CLOSED LOOP SYSTEM RESPONSE

Initial measurements were performed using a proportional gain controller. The gain was empirically adjusted to yield the fastest response time without overshoot. Despite nonlinearities in the transfer function of the system and saturation of the power amplifiers for large stepsizes, measurements showed that the proportional gain algorithm leads to a stable, responsive positioning system. However, a small steady-state position error was observed. This error is a result of misalignment of the motor and coupling between the two motor vibrations, creating tip motion in the slideway direction. The result is a slow slideway velocity (up to about 3mm/s) that is independent of the motor control input. Applying a PID-controller eliminated the steady state errors but caused a significant amount of overshoot.

A gain scheduling control strategy [3] combines the advantages of the proportional gain controller for large position errors and the PID controller to avoid steady-state errors. The response of the slide to step input commands of different magnitudes is shown in Figure 3a). A straight line means that the control parameter is at its maximum and the slideway moves at maximum velocity. Figure 3b) shows the position error as a function of time. The curves show

that the position error approaches zero. The overshoot of 150 μm maximum can be reduced by increasing the derivative gain without significantly reducing the response time.

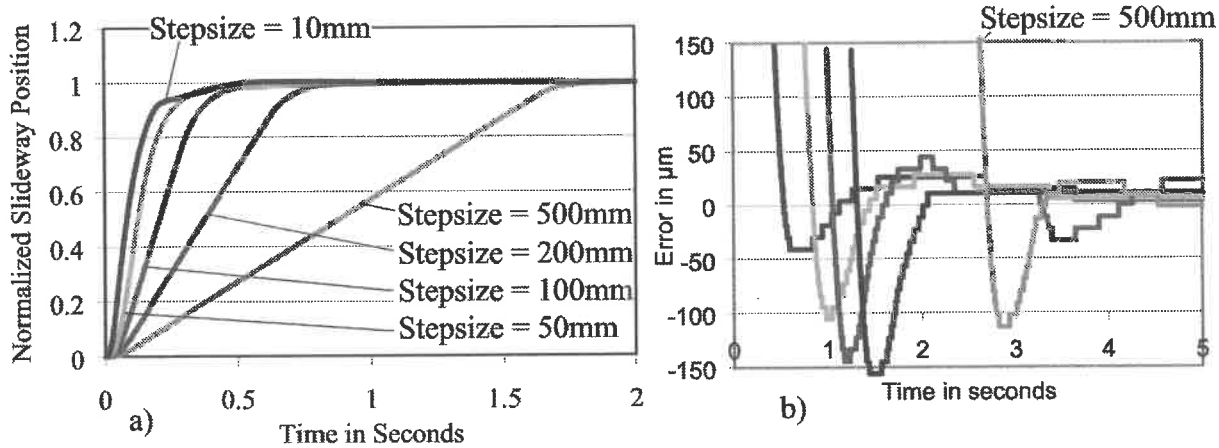

Figure 3: System Response using a Gain Scheduling Control (K_P=0.15, K_I=1,K_D=0.02) Motor Preload = 10N, Slideway Mass = 2.28kg

5 CONCLUSION

This research shows that it is possible to design ultrasonic standing wave motors whose slideway velocity is linearly proportional to the excitation voltage. This is possible by designing an actuator that allows independent excitation of two orthogonal vibration modes at the same frequency. The quality of the operation of the motor depends on the separation of these vibrations. Coupling between longitudinal and bending vibrations creates slideway motion, which is responsible for a small steady-state position error that cannot be eliminated using a proportional gain feedback controller. Despite saturation of the control input and nonlinearities in the dynamics of the motor-slideway system, it was shown that a simple feedback control system is stable and suitable for controlling the slideway position. A gain-scheduling controller, which is based on a PID-algorithm, can be used to achieve a steady-state error within one encoder increment while maintaining the overall performance shown for the proportional-gain controller.

With overall dimensions of about 35x30x6mm, and a mass of 13g, the final prototype actuator comes in a small and light package that can be used to accelerate any slideway, rotational or linear, to a velocity of 500mm/s with a maximum force of 5N. In addition, the motor is insensitive to changes in the frictional properties and changes in the surface. At this point, the maximum force is limited by the physical strength of the actuator; however, multiple motors can be used to produce larger forces. The motor generates a constant slideway velocity over a range from 1mm/s to 500mm/s, a speed which is linearly proportional to the control input.

REFERENCES

1. Ueha, S., Tomikawa, Y., Kurosawa, *Ultrasonic Motors--Theory and Applications*, Clarendon Press, Oxford 1993.
2. US Patent #5616980, April 1, 1997
3. William Levine, *The Control Handbook*, CRC Press 1995, p. 393ff

A MICROMACHINED THERMOELASTIC INCHWORM ACTUATOR

Ho Nam Kwon, Jong Hyun Lee, Sung Ho Jeong, Sun Kyu Lee
K-JIST, Gwangju, Korea
E-mail : jonghyun@kjist.ac.kr

Abstract

A new micromachined inchworm motor has been designed and fabricated for micro assembly applications. In order to implement inchworm motions, two thermoelastic actuators are contrived to have five-linkage mechanism with two-dimensional motions in tangential and normal directions. The thermoelastic actuators consist of two amplification bars and two coupling bars with four hinge springs. A forked tip, located on the apex of the linkage, is used to fit the teeth of shuttle mass for inchworm operation. The thermal expansion of the active bar generates the displacement of the actuator, which is then transformed into a bending of the active hinges to be finally amplified by the amplification bar. The inchworm actuator progressed by the designed steps of 5 um and latched up by the teeth. The estimated driving force was 50 uN with less than 0.2 um tolerance.

1. Introduction

For micro assembly applications, an actuator should be able to translate a small workpiece with an appropriate chucking force not to drop the workpiece during operation. The micro chuck needs to have a gripping force greater than tens of uN to grip the workpiece and a stroke longer than tens of um [1]. In order to realize a high precision and long stroke translation system, electrostatic driven comb drivers and inchworm motors were suggested as driving actuators [2][3][4]. Unfortunately, the driving force from electrostatic actuator tends to be small, and it is necessary to either apply a high voltage to attain a large displacement. Meanwhile, a thermoelastic actuator was fabricated for considerably large force and long stroke applications [5]. However, this actuator still provides insufficient force and non-rectilinear motion.

In this work, a new micromachined inchworm motor has been designed, fabricated and characterized for micro assembly applications of high force and long stroke.

2. Design of the inchworm motor

The proposed inchworm motor consists of one shuttle mass suspended by four leaf springs and a pair of five-linkage actuators, as shown in Fig. 1(a) [6]. The five-linkage mechanism provides the motion of two degree of freedom using two active hinge points, two shoulder hinges, and one neck hinge. And additional neck hinge and the forked tip (end effector) were added to grip the shuttle mass. Because the link between two neck hinges is so short that it works as one hinge point, we can consider the proposed mechanism as a five-linkage. When an input voltage is applied to two electrical pads of the actuator, induced electric current flow raises the temperature of the active bar and two active hinges, and t amplified displacement can be obtained from the thermal expansion of active bars and rotation of the amplification bar.

To secure the actuation without slipping, we contrived the teeth structure at the interface between the shuttle mass and the forked tip.

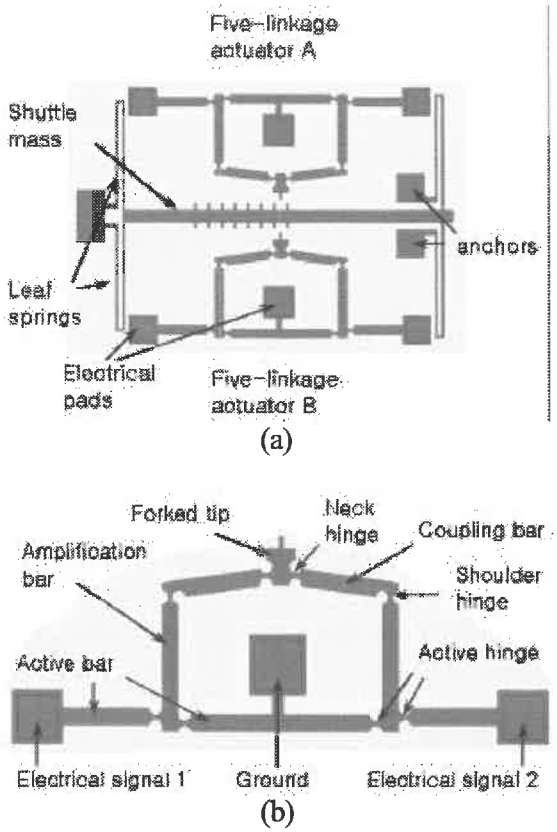

Figure 1. Schematics of proposed inchworm motor with thermoelastic actuators, (a) overall view of the inchworm motor, and (b) five-linkage mechanism for 2-dim actuation.

If the two amplification bars rotate in-phase, the forked tip will either move leftward/ rightward with/without the shuttle mass or return to its initial state, as shown in Fig. 2(b), (d) and (f), respectively. On the contrary, if the two amplification bars rotate out-of-phase, the forked tip moves either inward for fitting or outward for releasing the shuttle mass, as shown in Fig. 2(c) and (e), respectively.

One pair of actuators is capable of four kinds of motion, such as fitting a forked tip, rectilinear driving of shuttle mass, releasing the shuttle mass, and returning to its initial state, as illustrated in Fig. 3. In this way, one cycle of stepping motion enables the inchworm motor to have a large stroke by accumulating many stepping movements. In addition, the teeth may reduce power consumption by latch-up after driving.

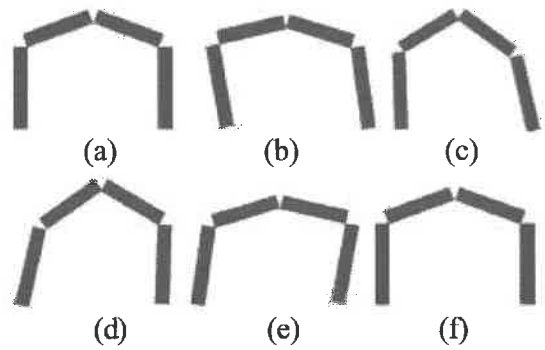

Figure 2. Unit steps of the linkage mechanism, (a) initial state, (b) leftward motion, (c) closing motion for fitting, (d) rightward motion for driving, (e) opening motion for releasing, and (f) in-phase leftward motion for returning to initial state.

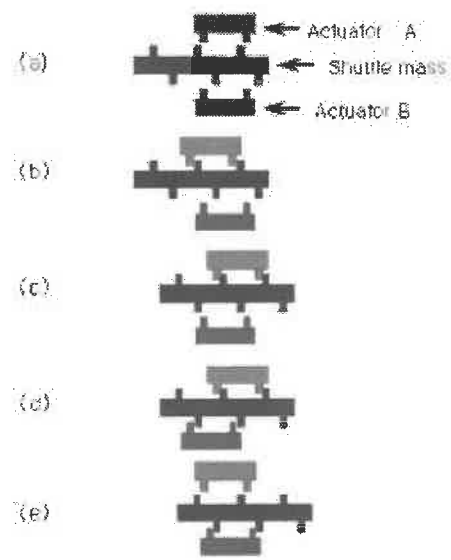

Figure 3. Inch-worm actuation with forked tips, (a) initial state, (b) fitting of the forked tip into the shuttle mass by actuator A, (c) rightward driving by actuator A, (d) fitting by actuator B, and (e) extracting and returning to initial state by actuator A, and rightward driving by actuator B.

3. Theoretical analysis

3.1. Operational schemes

In order to utilize the proposed thermoelastic actuator for inchworm motors, the required trajectory was investigated for one cycle of operation, as shown in Fig. 4. The trajectory consists of 4 unit steps, such as 1) extrusion for fitting, 2) driving for transportation, 3) retraction for release, and 4) contraction to initial location. Fig. 4 also shows the required voltages for right and left linkage actuators to perform inchworm motion according to the cyclic sequence. We can see from the diagram that the required strokes are about 5 um and 2 um in tangential and normal directions, respectively. This mechanism is very useful for the microsystem to meet the requirements from large force applications or switching devices with discrete displacement.

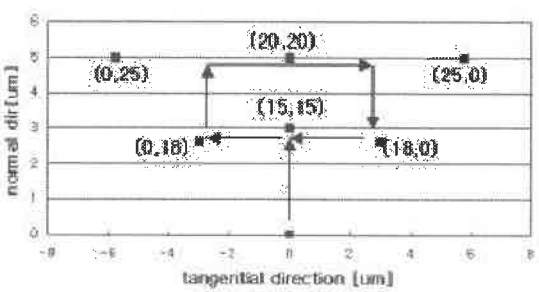

Figure 4. Estimated trajectory of one cyclic motion for inchworm motors based on FEA.

3.2. Stiffness of the actuator

The stiffness at the top of the forked tip is used to estimate the maximum force that the thermoelastic actuator can exert to the shuttle mass. The resultant stiffness of the forked tip can be estimated to be 286 N/m from FEA. We also found that the actuator can generate a driving force over 50 uN with a placement tolerance of 0.2 um.

4. Device fabrication

We fabricated the proposed thermoelastic actuators using SOI (silicon-on-insulator) wafers. The minimum feature size was 2 um, which corresponds to the width of one tooth. The device layer of 40 um in thickness was micromachined with DRIE (Deep Reactive Ion Etching) process and was doped with phosphorus to control its electrical resistance. The sacrificial oxide layer was removed using HF GPE (Gas-Phase etching) process with no virtual stiction of microstructures.

5. Experimental characterization

Fig. 5 shows that the response time of the fabricated actuator is about 4 msec by 90% of rising time criterion from step response. Dynamic characteristics of the fabricated micro inchworm motor were experimentally investigated to evaluate its performance. First of all, the upper actuator A drove the shuttle mass one step, and the counterpart actuator B drove another step, next the actuator A drove one more step and latched up the shuttle mass as shown in Fig 6(a),(b),(c) respectively. By three steps of the inchworm motion, the accumulated displacement was 15um as shown in Fig 6(d).

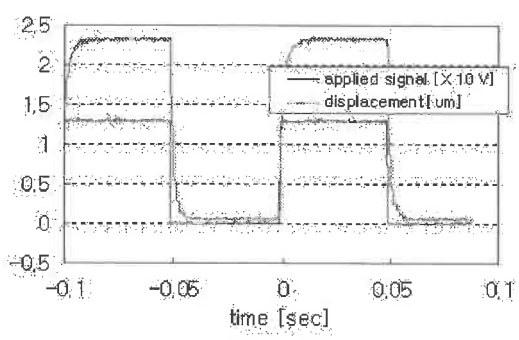

Figure 5. Step response of a thermoelastic actuator with a linkage mechanism

Using the fabricated micro inchworm motors, the gripping of a workpiece like an optical fiber is under investigation as shown in Fig. 7.

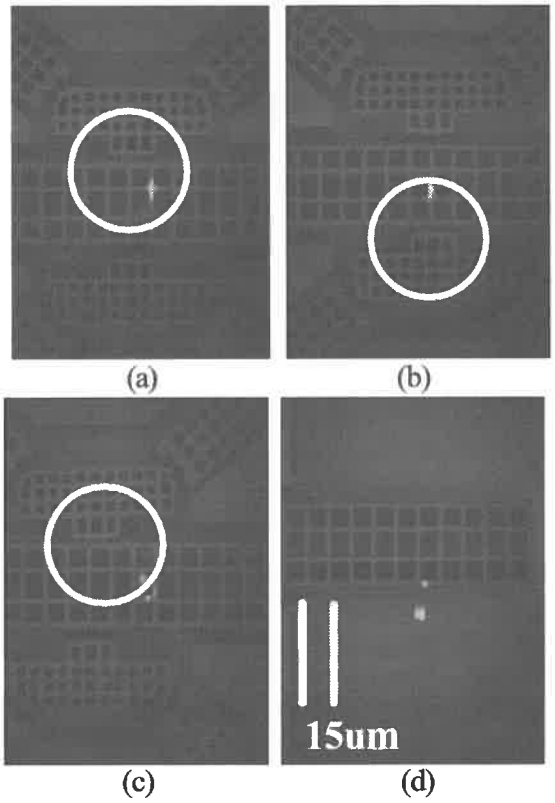

Figure 6. Video images of the inchworm motions, (a) 1st step by top actuator, (b) 2nd step by bottom actuator, (c) 3rd step and latch up by the top actuator, and (d) accumulated stroke of 3 steps. Notice the difference between the locations of the end effector in (a) and (c).

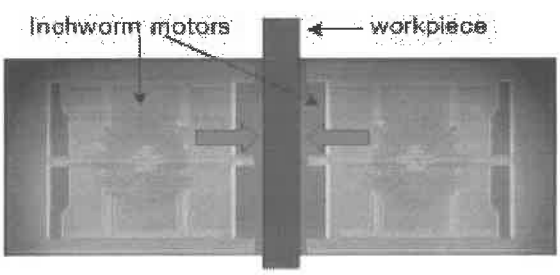

Figure 7. Schematic of gripping a workpiece with one pair of the inchworm motors.

6. Conclusion

A micromachined thermoelastic inchworm motor was fabricated and characterized SOI wafer with the structural layer 40 um thickness was used to fabricate the proposed inchworm motors, and the inchworm motion was experimentally investigated by the cyclic motion. The motor is applicable to the micro precision stage for micro assembly or switching devices. As a further study, gripping a workpiece with the motors is under investigation using the fabricated actuators and the control circuit.

Acknowledgement

This work was supported by BK21 project. The authors would like to thank ETRI and LG Elite for their technical supports in connection with fabrication of the device presented in this paper.

References

[1] K. Tsuchiya, M. Nakao, T. Okusa, Y. Hatamura, and K. Matsumoto, SPIE MMF, pp.147-156, Jan. 1997.

[2] W. C. Tang, Tu-Cuong, H. Nguyen, and R. T. Howe, Proc. MEMS, pp.53-59, Jan. 1989.

[3] N. R. Tas, A. H. Sonnenberg, A. F. M. Sander, and M. C. Elwenspoke, Proc. MEMS, pp.215-220, Jan. 1997.

[4] R. Yeh, S. Hollar, and K. S. J. Pister, Proc. MEMS, pp. 260-264, Jan. 2001.

[5] E. S. Kolesar, P. B. Allen, J. T. Howard, J. M. Wilken, and N. C. Boydston, J. Vac. Sci. Technol. A, 17(4), pp.2257-2263, Jul/Aug. 1999.

[6] H. N. Kwon, J. H. Lee, S. H. Jeong, S. K. Lee, W. I. Jang, and C. A. Choi, 32nd ISR, pp. 796-801, Apr. 2001.

ROTARY-LINEAR HYBRID AXES FOR MESO-SCALE MACHINING

Michael K. Liebman
Novalux, Inc., Sunnyvale, CA

Marsette A. Vona
Jet Propulsion Lab, Pasadena, CA

David L. Trumper
Massachusetts Institute of Technology, Cambridge, MA

1 Introduction

We have designed and built a prototype hybrid rotary-linear machine tool axis; this axis is a key subsystem for high speed, 5-axis machine tools intended for fabricating meso-scale parts. The hybrid rotary-linear axis is a cylinder driven independently in rotation and translation. This hybridization minimizes machine inertias and thereby maximizes accelerations allowing for the production of meso-scale parts with complex surfaces rapidly and accurately. We define *meso-scale* parts as having a size on the order of centimeters and thus falling between the domains of microfabrication and standard machining. Such parts might include dental restorations, molds, dies, and turbine blades.

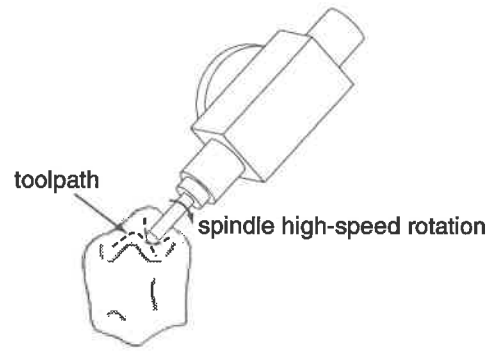

Figure 1: A high speed spindle traverses toolpaths on the complex occlusal surface of a dental restoration.

This research was motivated by the desire to build a 5-axis machine tool for grinding customized dental restorations. If a machine existed which could automatically grind dental restorations from ceramic blanks as shown in Figure 1, it would revolutionize dentistry by eliminating the high costs of manual fabrication. Such a machine needs 5 axes of motion to generate the complex shape of teeth, and it needs to obtain shape accuracies of 20 μm. Existing 5-axis machine tools cannot achieve the high feedrates and accelerations required for fabrication in acceptable cycle times.

Existing 5-axis machine tools typically have axes stacked on top of each other, as shown in Figure 2(a). In this situation the bottom axis must accelerate the mass of all the axes and actuators further up the kinematic chain. Thus, bottom axes tend to have low accelerations which limit attainable feedrates and lengthen production times of small parts with complex surfaces. One way to achieve high accelerations in two axes is with a hybrid axis consisting of one moving part driven in two axes: the rotary-linear axis consists of a cylinder driven independently in rotation and translation as shown schematically in Figure 2(b). By eliminating one level of the machine tool's kinematic chain in this fashion we allow for significantly higher accelerations than would otherwise be possible.

We have invented a 5-axis machine topol-

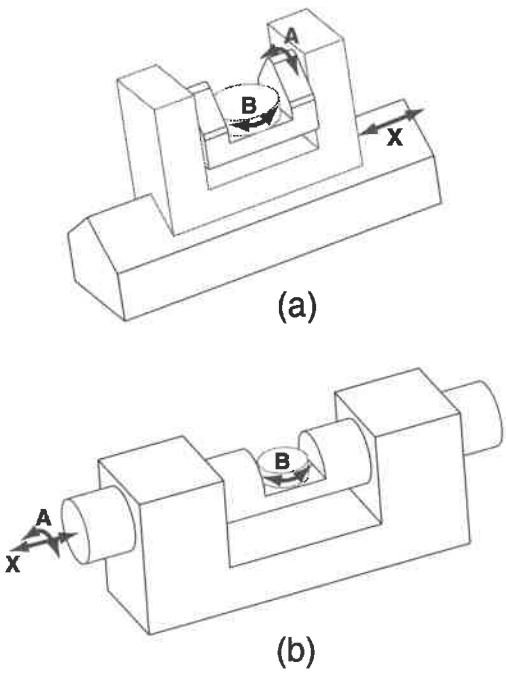

Figure 2: (a) Conventional stacked axis arrangement with a rotary table (B) stacked on a trunnion (A) riding on an X-axis. (b) Rotary-linear (A-X) axis with a rotary table (B).

ogy which we envision will have higher accelerations, control bandwidths, and accuracies than are currently possible. This improved performance is achieved by using two hybrid rotary-linear axes, each of which eliminates one level of stacking from the machine's kinematic chain. The envisioned topology, shown in Figure 3, is kinematically similar to existing horizontal spindle 5-axis machine tools with trunnions. The envisioned topology combines the conventional trunnion (A) and linear axis (X) into a rotary-linear (A-X) axis to position the workpiece. Furthermore, it eliminates the conventional moving column providing infeed motion (Z) by combining this linear degree of freedom with the high speed spindle rotation using a second rotary-linear axis. The spindle is mounted to a conventional vertical slideway (Y) riding

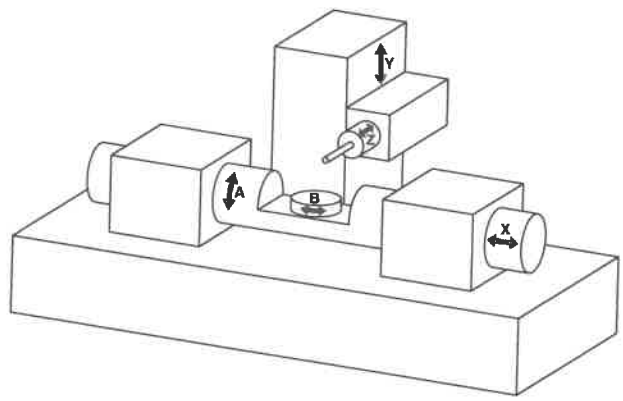

Figure 3: Envisioned 5-axis machine tool topology using two rotary-linear axes.

up and down a fixed column. The conventional rotary table (B) is replaced by a small indexing rotary axis. By indexing this fifth axis we lighten the A-X rotary-linear axis and thereby allow for higher accelerations in the A- and X-axes.

2 Prototype Axis

We built a prototype of the A-X rotary-linear axis for positioning the meso-scale workpiece in the machine topology shown in Figure 3. The hybrid rotary and linear motion provides special challenges for precision actuation and sensing. Our prototype rotary-linear axis is shown in Figures 4 & 5 and described in detail in [1]. It consists of a central shaft 3/4 inch (1.91 cm) in diameter and 15 inches (38.10 cm) long, supported by two cylindrical air bearings. The axis has one inch (2.54 cm) of linear travel and unlimited rotary travel. Two frameless permanent magnet motors respectively provide up to 41 N continuous force and 0.45 N·m continuous torque. The rotary motor is composed of commercially available parts; the tubular linear motor is completely custom-built. The permanent magnet rotors of the rotary and linear motors are shorter than their stators so that the axis can trans-

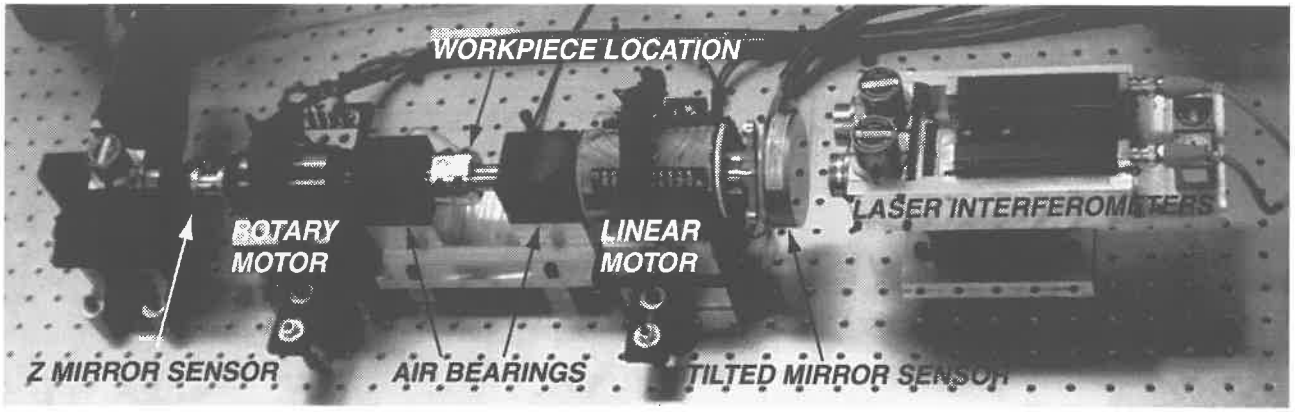

Figure 4: Prototype rotary-linear axis. The axis uses two separate permanent magnet synchronous motors to provide force and torque. On the far left is a 1 inch (2.54 cm) diameter mirror for z measurement, and on the far right is a 3 inch (7.62 cm) diameter slightly tilted mirror for θ measurement.

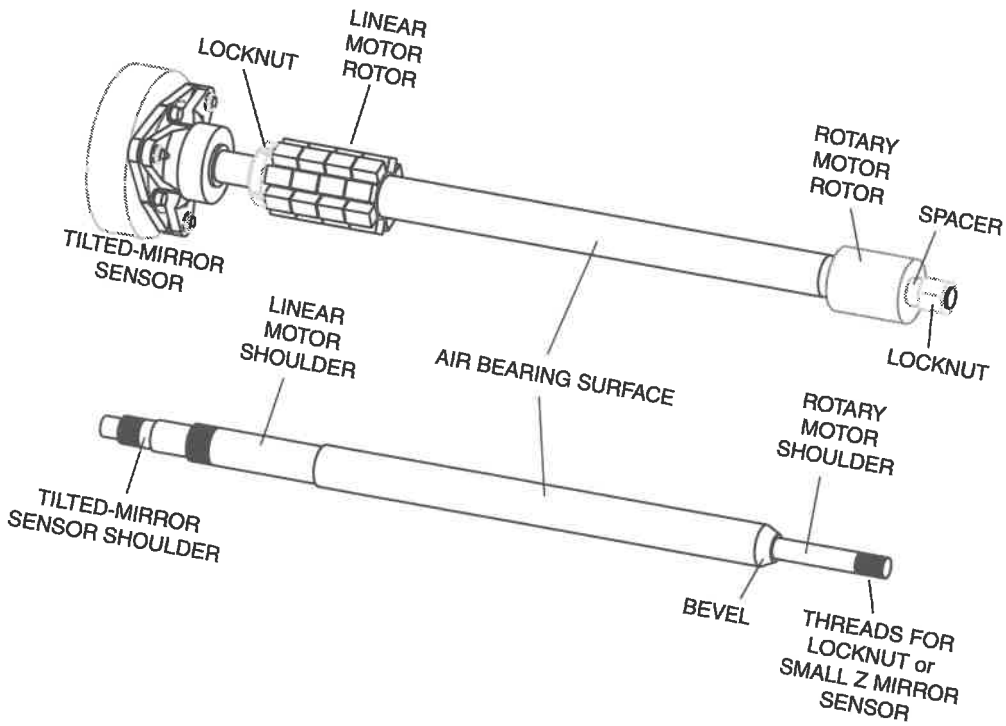

Figure 5: Prototype rotary-linear axis shaft geometry and assembled components. The motors are designed for high accelerations, and the masses and inertias of the moving shaft and attached components have been minimized. The magnetic rotors and mirror mounts are axially clamped to shoulders in the shaft. Thus, they can be disassembled and used on future prototypes.

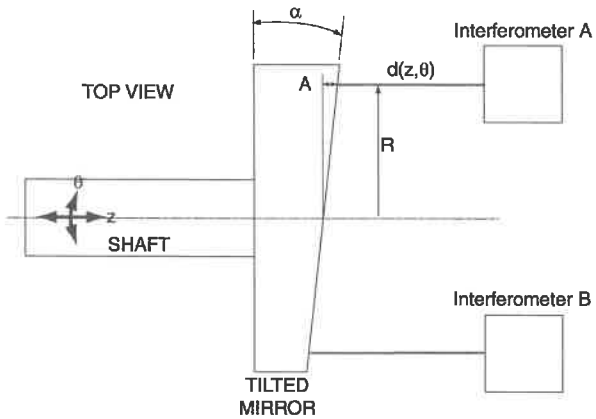

Figure 6: Tilted-mirror rotary sensor. The shaft's rotation angle θ is sensed by measuring the distance in two places to a slightly tilted mirror. Maximum mirror tilt is $\alpha = 4.7$ mrad.

late axially without losing motor force. The prototype axis achieves a linear acceleration of 3 g's and a rotary acceleration of 1,300 rad/s^2. With higher power current amplifiers and reduced sensor inertia, we predict the axis could attain peak accelerations of 12 g's and 17,500 rad/s^2 at low duty cycles.

We examined several concepts for developing a precision rotary-linear sensor that can tolerate axial translation. Our prototype sensor, shown schematically in Figure 6, uses two laser interferometers to measure the orientation of a 3 inch diameter slightly tilted mirror attached to the shaft. The details of the sensor design are presented in [2]. This sensor has a resolution of 1,366,000 counts/rev (4.6 μrad) corresponding to a linear resolution of 0.046 μm at a 1 cm radius. Unfortunately, the inertia of this sensor dominates that of the rest of the axis, so we anticipate using a different sensor in future prototypes. A third interferometer measures shaft translation from a 1 inch diameter mirror on the opposite end of the shaft.

A program running on a DSP controls the hybrid axis. At the top level it uses finite state control to run automatic calibration routines and respond to events such as a blocked laser. The automatic calibration routines determine parameters such as the mirror tilt which are used to calculate angular position during normal operation. The rotary axis has a closed-loop control bandwidth of 40 Hz; the linear axis has a bandwidth of 70 Hz. The rotary-linear axis has 2.5 nm rms linear positioning noise and 3.1 μrad rms rotary positioning noise.

3 Conclusions

The precision positioning and high acceleration capabilities of rotary-linear axes make them an enabling technology for rapidly producing complex meso-scale parts to micron-level accuracies. Our rotary sensor is successful at achieving sufficient angular resolution, but its large mass and inertia limit the accelerations and control bandwidths that can be achieved with this first prototype.

4 Acknowledgments

This research was funded by NSF grant award number DMI-0084981, *Rotary-Linear Hybrid Axes for Meso-scale Machining.*

References

[1] Michael K. Liebman. *Rotary-Linear Axes for High Speed Machining.* PhD thesis, Mechanical Engineering Dept., Massachusetts Institute of Technology, September 2001.

[2] Marsette Arthur Vona. Metrology techniques for compound rotary-linear motion. Master's thesis, Electrical Engineering and Computer Science Dept., Massachusetts Institute of Technology, June 2001.

KINEMATIC MODELING AND ANALYSIS OF A PLANAR MICRO-POSITIONER

Nicholas G. Dagalakis, John A. Kramar, Edward Amatucci, and Robert Bunch
National Institute of Standards and Technology, Gaithersburg, Maryland 20899

1. Introduction

The tremendous growth of opto-electronic devices manufacturing has raised the need for high performance micro-positioners, which are used in their assembly and alignment. The static and dynamic performance of micro-positioners depends in part on the quality of operation of their controllers, which in turn depends to a significant degree on the accuracy of the kinematic and dynamic mathematical models upon which they are based. The objective of this work was to evaluate the accuracy of two kinematic mathematical models of a planar X-Y micro-positioner under a variety of testing conditions.

A fully instrumented X-Y Parallel Cantilever Bi-axial Micro-Positioner[1] (PCBMP), was used for the tests (Fig. 1). The performance of the stage was evaluated by measuring the output motions as a function of input displacements over a two-dimensional grid of test positions. Second-order and linear kinematic models were developed through an examination of the stage geometry. The performance test data was used to identify the unknown parameters of the kinematic models using least-squares fitting algorithms. The accuracy of the fits was examined under the conditions of varying the number of input test data or adding white noise.

2. Stage Performance

The static performance of the stage was evaluated by examining its input and output displacements while moving it throughout its motion range of about 130 μm by 130 μm. The input actuators are servo-controlled based on built-in capacitance gage sensors, thus eliminating the typical piezoceramic effects of hysteresis, non-linearity, and creep.[2] At each test position, along with the input position commands and capacitance gage data, we also recorded six output data: the X and Y position of the output stage, measured by separate capacitance gages[3]; and the angular orientation of the output stage in all three angular axes, with a redundancy in yaw (rotation about the Z-axis). The angles were measured using two orthogonally placed, two-dimensional, high-resolution autocollimators, which tracked a cube reflector on the stage. A LabView[4] program was written to scan the stages and read the data. The entire array of data was swept multiple times over a period of several hours to verify repeatability and correct for drift.

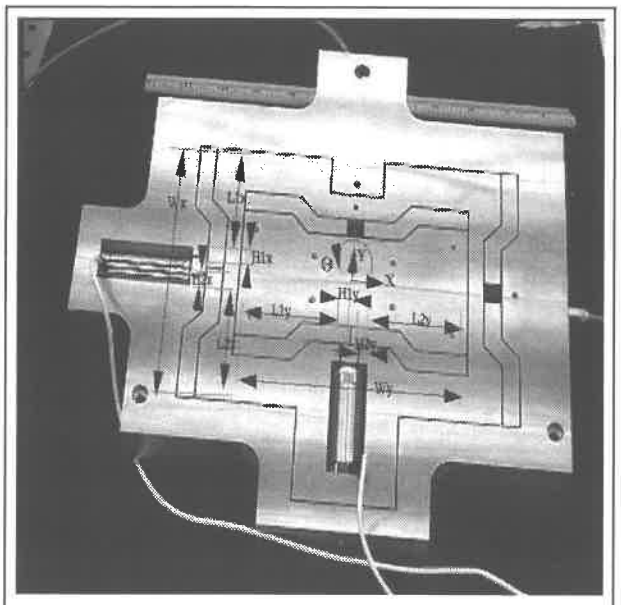

Fig. 1 Picture of a PCBMP stage with dimensions.

In initial tests, the motion actuators were coupled to the stage through a single universal joint (SUJ) on one end, the other end being hard mounted. The universal joint is a flexure device made from cross-bored pairs of holes to define the flexures and electron-discharge machined slots to release the motion. The sizes of the bores and their placements were optimized to achieve the required axial stiffness and lateral flexibility.[1] Later, since we had doubts about the ability of this coupling to

transmit pure axial loads, the tests were repeated with dual universal joint (DUJ) actuators, having flexure universal joint decoupling on both ends.

Fig. 2 shows plots of the angular stage errors as a function of position for the DUJ coupled stage. The maximum error is 0.1 arc seconds (0.5 microradians). The roughly periodic errors in the roll and yaw(2) measurements are auto-collimator noise, and are within specifications. That the error is not due to the stage is clearly evident by comparing with the yaw(1) measurements that were simultaneously acquired by the other autocollimator. These data demonstrate the exceptional absence of angular cross-talk in these stages.

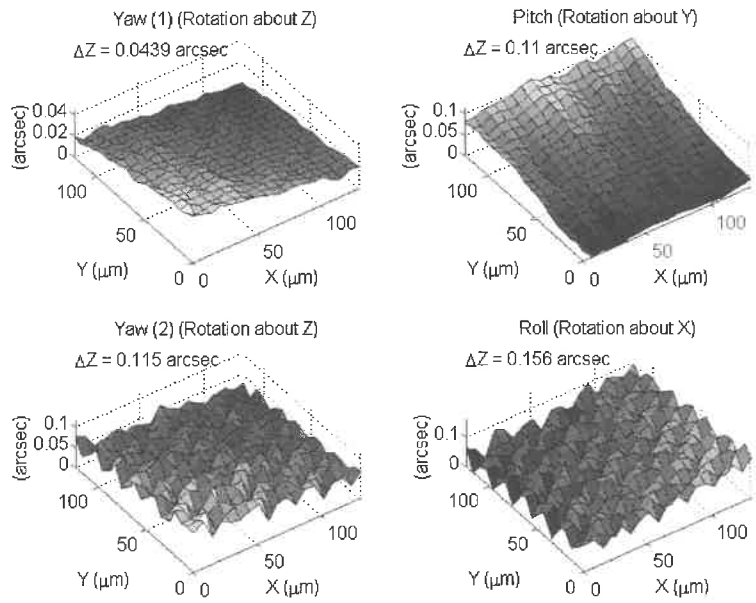

Fig. 2 Angular errors of the stage motion.

3. The Kinematic Model

The kinematic mathematical model equations are derived through an analysis of the stage geometry. Fig. 3 shows a schematic drawing of the stage. Only the Y-axis motion mechanism is shown for clarity. The input displacement is generated by the piezo-electric actuator (AC) and transmitted to the moving stage (MS) through flexures a_1 and a_2 of levers A_1 and A_2, respectively. These levers pivot about flexures b_1 and b_2, transmitting the actuator force to the moving stage through flexures c_1 and c_2. If not further constrained, due to the pivoting action, the attachment points of flexures c_1 and c_2 would generate arcuate motion. However, these arcs operate symmetrically on a rigid body. We therefore expect balanced elastic deformation, finally resulting in the approximate cancellation of the parasitic cross-axis motion. Levers A_{1t} and A_{2t} similarly constrain the other end of this stage of motion.

The approximate planar output motions as a function of the actuator inputs can be described by the following matrix equation:

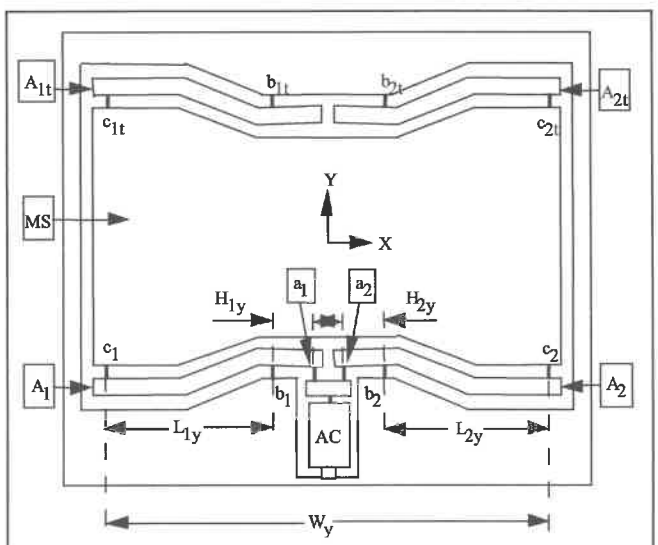

Fig. 3 Schematic drawing of the PCBMP Y-axis motion mechanism.

$$\begin{bmatrix} X_o \\ Y_o \\ \Theta_o \end{bmatrix} = \begin{bmatrix} \left(-\frac{L_{1x}}{2H_{1x}} - \frac{L_{2x}}{2H_{2x}}\right) & 0 & 0 & \left(-\frac{L_{1y}}{2H_{1y}^2} + \frac{L_{2y}}{2H_{2y}^2}\right) \\ 0 & \left(-\frac{L_{1y}}{2H_{1y}} - \frac{L_{2y}}{2H_{2y}}\right) & \left(-\frac{L_{1x}}{2H_{1x}^2} + \frac{L_{2x}}{2H_{2x}^2}\right) & 0 \\ \left(\frac{L_{1x}}{W_xH_{1x}} - \frac{L_{2x}}{W_xH_{2x}}\right) & \left(\frac{L_{1y}}{W_yH_{1y}} - \frac{L_{2y}}{W_yH_{2y}}\right) & 0 & 0 \end{bmatrix} \begin{bmatrix} X_i \\ Y_i \\ X_i^2 \\ Y_i^2 \end{bmatrix} . \qquad (1)$$

X_o, and Y_o, are the output stage motions in the X and Y axes and and Θ_o is the stage yaw. The parameter definitions can be gotten by reference to Fig. 3. Out of plane motion (Z_o) and rotations (pitch and roll) are ignored in this analysis. Eq. (1) includes first and second order terms in X_i and Y_i, which are the stage inputs generated by the actuators. In developing Eq. (1) we have assumed that certain nominally equal parameters, *e.g.* L_{1y} and L_{2y}, are in fact slightly different due to fabrication errors. The fabrication errors explicitly treated here are only a small subset of the possible errors. Other potential fabrication errors could be invoked which would result in additional terms, including terms where there are currently zeros in the matrix. On the other hand, for the first-order model, all the second order terms are forced to be zero.

The values of the kinematic model parameters were determined by first- or second-order fits in the X_i and Y_i input positions to the measured X_o and Y_o output positions and yaw of the stage. Six different least-squares techniques available in LabWindows CVI[5] were compared for curve-fitting. All the techniques generated similar results except for the "Square Root Free Givens Decomposition," which generated significantly worse fits. We define the accuracy of the fits as the root mean square difference between the modeled position and the measured position.

4. Variation of the Number of Test Data and the Amplitude of Sensor Noise

The identification of the kinematic model parameters was repeated four times with varying numbers of test data. Each time two columns of position test data located farthest from center and directed along the Y-axis were removed from the pool of data. These were the data where we would expect the largest amount of cross-talk error, since they involve the largest translation of the stage that carries the largest mass. Conversely, in typical applications, the central region would be the most used.

Fig. 4 shows a plot of the mathematical model evaluation error for the simple linear model (XY) and the second-order model (XY2). For each model the error is plotted for the case of SUJ and DUJ couplings. The more advanced model leaves smaller residual errors until the number of test data drops below approximately 65 to 75 (18% DUJ to 44% SUJ), at which point the situation is reversed. This raises questions that we will discuss in a future publication.

A possible explanation for this result is pointed to by an examination of the distribution of errors for the case of the linear model, using the complete set of test data, shown in Fig. 5. The highest magnitude of the errors appears to concentrate along a column at the end of travel of the X-axis actuator, near 60 micrometers. That is the region where we expect the maximum loading of the flexures, which can generate non-linearities. The linear model cannot describe these non-linearities, which now appear as errors. The removal of these

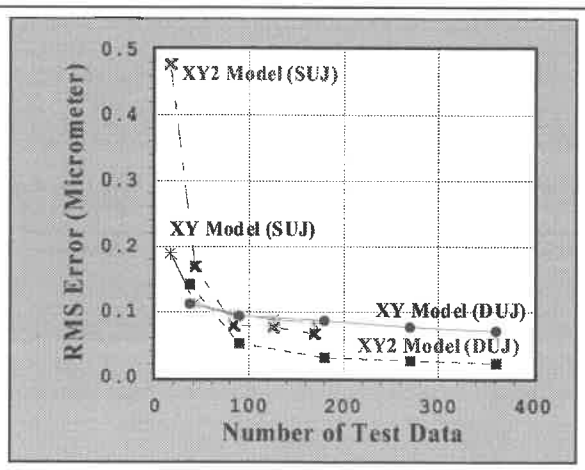

Fig. 4 Model error *vs.* the number of test data.

boundary regions from the pool of test data apparently hurts the advanced model more than the simple linear model. If the error plot of Fig. 5 is repeated for the case of the advanced model with the complete set of test data, the column of the high error region disappears, as well as the error droop in the central region. This will be explained in a future publication.

The plots of Fig. 4 also show that for the cases of the DUJ coupling, the errors tend to be lower than the for the SUJ coupling, *i.e.*, the mathematical models are in better agreement with the DUJ-coupling test data. One explanation for this is that the DUJ couplings come closer to satisfying the basic modeling assumption that the actuators exert a pure axial force.

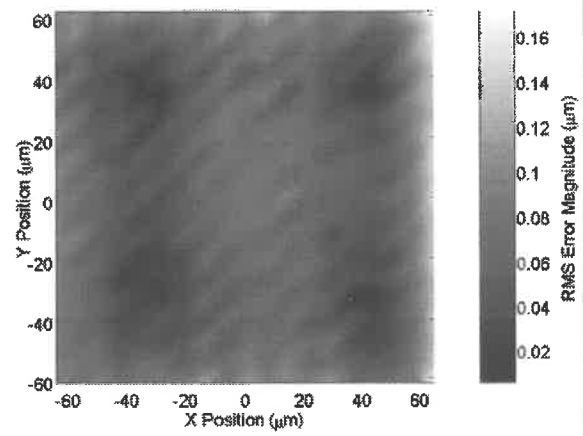

Fig. 5 Distribution of error after planar fit.

The effect of feedback sensor noise on the identification of the mathematical model parameters was also examined. This effect was simulated by adding white noise to the measured output displacements before solving for the kinematic model parameters. Arrays of random numbers that were uniformly distributed between the values of ± 2, ± 4, ± 6, ± 8 and ± 10 μm were used. The results show that the second-order model is more sensitive to sensor noise and generates higher estimation errors than those generated by the simple model for noise amplitudes exceeding approximately ± 1 μm. A possible reason for this result might be the sensitivity of the higher order terms of the advanced model to sensor noise.

5. Conclusions

The static performance for the stage using the DUJ coupling was significantly better than with the SUJ coupling, and the predictions of the mathematical models were also more accurate. It was found that the number of test locations plays a significant role in the accuracy of the kinematic model. The more advanced mathematical model is more accurate above a critical threshold for the number of test locations data used. Any further decrease results in significantly higher errors for the advanced model than for the simple model. It was found that the accuracy of both mathematical models decreases as the level of the noise increases. The more advanced model was more sensitive to noise, performing worse than the simple linear model, indicating that it should be used with caution and only when sufficiently good data is available.

6. Acknowledgements

This work was supported by the NIST Advance Technology Program, Office of Electronics and Photonics Technology.

7. References

[1] Amatucci E., Dagalakis N.G., Kramar J.A., Scire F.E., "Performance Evaluation of a Parallel Cantilever Biaxial Micropositioning Stage," ASPE 2000 Annual Meeting, Oct. 22-27, 2000, Scottsdale, Arizona.

[2] DPT actuators from Queensgate, Ltd. This and certain commercial products are identified in this paper to specify experimental procedures adequately. Such identification is not intended to imply recommendation or endorsement by the National Institute of Standards and Technology, nor is it intended to imply that the products identified are necessarily the best available for the purpose.

[3] ADE non-contact probes.

[4] LabView, National Instruments.

[5] LabWindows CVI, National Instruments.

MODELING, IDENTIFICATION, AND CONTROL OF BALLSCREW DRIVES

Kripa K. Varanasi, Samir A. Nayfeh
Massachusetts Institute of Technology, Cambridge, MA

The closed-loop bandwidth of a servomechanism is a measure of how faithfully it tracks commands. Most measures of control performance (such as the rise time or disturbance rejection) are correlated with high bandwidths. But the axial compliance of a ballscrew (or roller screw) combined with the inertias of the carriage, motor, and screw give rise to a resonance that limits the system bandwidth. In this paper, we present a method for selection of the key design parameters of a ballscrew drive to achieve a specified bandwidth, robustness, velocity, and acceleration.

We begin by presenting a model of a leadscrew system that accurately accounts for the distributed inertia of the screw as well as the compliance of all of the major elements of the structural loop. We then reduce the model and employ a perturbation expansion to obtain approximate expressions for the open-loop poles of the system. Based on the open-loop poles, a graphical design technique yields a formula for the highest bandwidth controller that meets a given set of robustness requirements. This result combines with requirements for speed and acceleration to yield a set of acceptable designs for the lead and diameter of the screw as well as the motor inertia.

We consider a ballscrew drive such as that sketched in Fig. 1. The end of the screw nearest the drive motor is axially constrained to a thrust bearing. But to accommodate thermal expansion, axial motion of the end of the screw farthest from the drive motor is either unconstrained or partially constrained by a damper as suggested by Nayfeh and Slocum (1998). Feedback can be taken either from the angle of rotation of the motor or the linear position of the carriage relative to the base (or both, see Chen and Tlusty 1995). But unless the screw is pre-stretched against stiff thrust bearings at both ends, thermal expansion of the screw makes it difficult to accurately determine the position of the carriage from the angle of rotation of the motor. Therefore, it is most common to use the carriage position for feedback, hence we focus on the design of this "non-collocated" feedback system for the remainder of this paper.

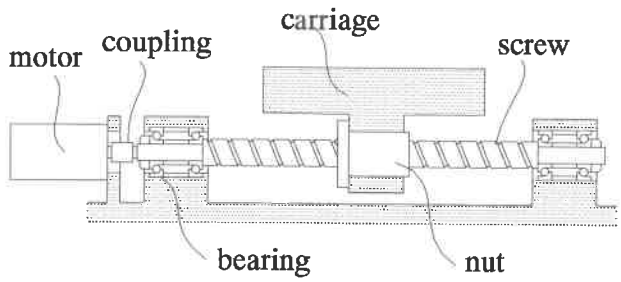

Fig. 1: sketch of a ballscrew drive

Modeling

For the purposes of motion control it suffices to accurately characterize the first axial resonance. We begin by modeling the ballscrew

as a distributed stiffness and inertia linked via the compliances of the thrust bearings, ball-nut, and coupling to the inertias of the motor and carriage. The damping that arises in the raceways of the carriage bearings, ball-nut, and support bearings are difficult to model, but we lump them into "effective" viscous dash-pots between the carriage, motor, and base. A damper mounted to the end of the ballscrew may be either viscous or hysteretic, and can be modeled with some accuracy (see Nayfeh and Slocum, nnn). This model is described by longitudinal and torsional wave equations of the screw along with appropriate boundary conditions, and is far too cumbersome for use in our design study.

We therefore apply Galerkin's method to reduce the model to fourth order. The shape function employed corresponds to the quasi-static deformation when an axial force is applied to the carriage and a restraining torque is applied to the motor. The states of the model are the position and velocity of the carriage and motor, and are given in the frequency domain by

$$(-\omega^2[M] + \jmath\omega[C] + [K])\{Q\} = \{F\} \qquad (1)$$

The mass and the stiffness matrices are functions of the stiffnesses of the bearings (and their mounts), coupling, nut and the screw parameters. This model which we call the "full" model can be used at a later stage for verification purposes. However, at the initial design stages such a model involves too many parameters to be used directly for sizing of the screw and motor.

To further simplify the model, we note that the ballscrew can usually be made the dominant compliance in the stiffness loop by careful design; that is, one can usually select thrust bearings and torsional couplings that are several times stiffer than the screw itself without incurring inertia or packaging problems. Hence a further simplification of the model (in terms of the number of design parameters) is possible, and we can express the elements of the mass, damping, and stiffness matrices in Eq. (1) in terms of the length of travel, lead and diameter of the screw, inertia and stall acceleration of the motor, and so on. Finally, we employ a perturbation expansion to obtain approximate expressions relating the open-loop poles to the design parameters, forming a link between the mechanical design and the controller design that we describe in the next section.

Because of the distributed inertia of the screw, the inertia matrix is not diagonal and non-minimum phase zeros can arise in the open-loop transfer function. If the non-minimum phase zero occurs at a frequency comparable to the first axial resonance, it becomes extremely difficult to achieve closed-loop performance. Therefore, the designer should always make sure that the non-minimum phase zero occurs well above the desired bandwidth by satisfying

$$\left(\frac{2\pi}{l}\right)^2 J_s \left[\frac{1}{6K_t} + \frac{K_T}{3K_aK_t}\right] - M_s\frac{K_T}{3K_a^2} \ll \frac{1}{\omega_b^2}$$

where l is the lead of the screw; J_s and M_s are the total rotary and linear inertia of the screw; and K_T, K_t, and K_a are the total, torsional, and the axial stiffnesses of the screw when the carriage is at the end farthest from the motor.

Mechanical and Controller Design

We quantify performance in terms of three important parameters: the bandwidth, phase margin (PM), and resonance gain margin (RGM). The first two parameters are very widely known in the controls literature. Phase margin is related to the effective damping of the closed-loop system and is a very useful measure of the degree of stability. We define the RGM as the gain by which the loop transmission can be multiplied without

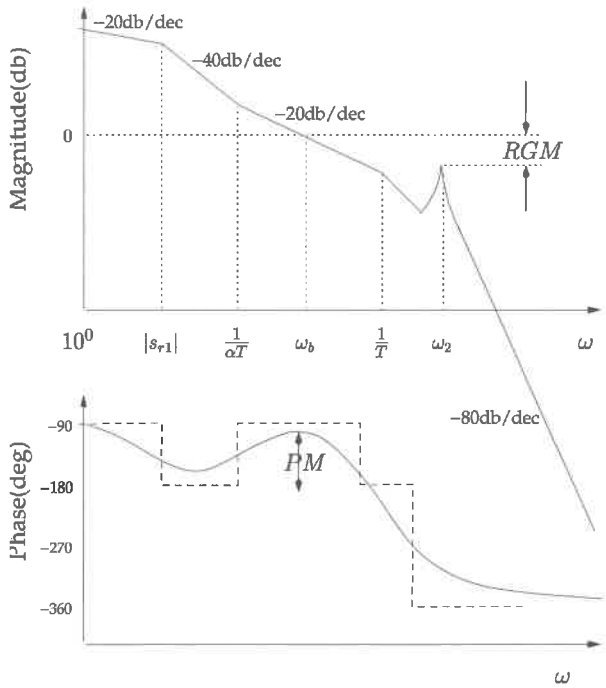

Fig. 2: design of a lead compensator in the frequency domain

resulting in multiple crossovers at resonance. Figure shows a frequency-domain design of a lead compensator for the ballscrew drive for a given PM and RGM. The graphical design method yields the following expression for the highest bandwidth attainable with this form of controller:

$$\omega_b = \sqrt{\frac{2\zeta(1-\zeta^2)^{1/2}\omega_n^2}{1+RGM}}\sqrt[4]{\frac{1-\sin(PM)}{1+\sin(PM)}} \quad (2)$$

where ζ and ω_n are the damping and natural frequency of the axial resonance of the open-loop system. This formula can be used to obtain a first-cut design of the ball-screw drive that attains a required closed-loop specification. The same methodology can be extended to higher-order controllers.

In addition to a bandwidth specification, we usually wish to achieve a given speed and acceleration. There are a number of factors which can limit the traverse speed, but one of the most common is the critical speed of rotation at which the ballscrew undergoes transverse vibration. The achievable acceleration

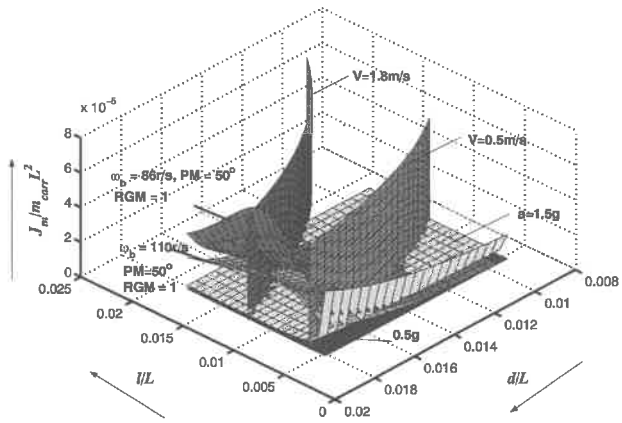

Fig. 3: design space and constraint surfaces

is determined by the ratio of the motor torque (minus frictional losses) to the total inertia of the system. A survey of commercially available servomotors shows that (for a given family of motors) the motor torque scales approximately linearly with inertia. Hence, for a given type of motor, we can characterize the motor by its inertia.

Therefore the key design parameters become the motor inertia J_m and the lead l and diameter d of the screw. We normalize these parameters by the length of travel L and the mass of the carriage and plot each on an axis as shown in Figure 3. To achieve a given velocity, acceleration, and bandwidth, a design must lie to the left of the corresponding velocity surface, above the corresponding acceleration surface, and below the corresponding bandwidth surface. The enclosed volume represents the family of designs which can achieve the required closed-loop specifications.

Identification

The test stand includes a ball-screw with lead and diameter of 25.4 mm and free length of 1100 mm. A carriage weighing approximately 80 kg is mounted on Schneeberger rails and clamped to the ballnut. The bearing support at the motor end consists of four sixty-degree

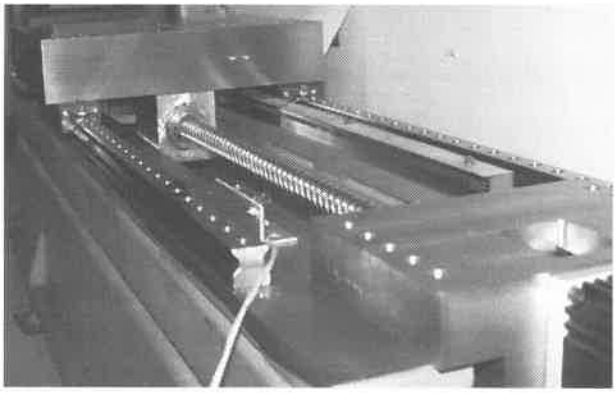

Fig. 4: photo of test stand

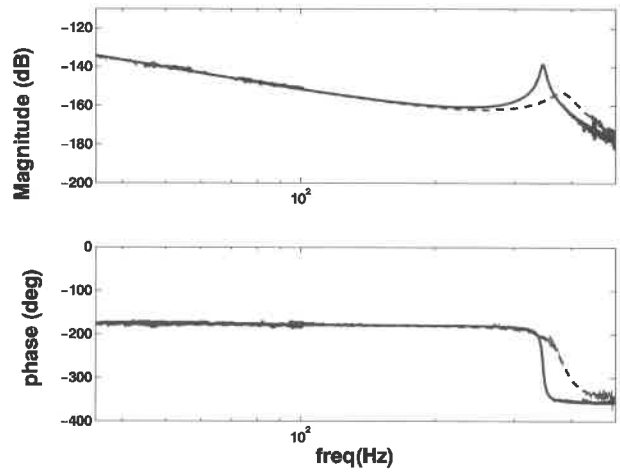

Fig. 5: measured loop transmission with and without damper

angular contact bearings mounted back to back. The damped end is formed by combining the above mentioned bearings with a viscoelastic damper. A brushless servomotor (inertia 13.9e-5 kg·m^2) is attached to the screw by means of a bellows-type coupling (with torsional stiffness of approximately 6800 N·m). A photograph of the experimental setup is shown in the Fig. 4.

Two kinds of experiments were conducted on the test setup to validate the theoretical model: experimental modal analysis and sine sweeps. Experimental modal analysis was conducted by placing an accelerometer at various positions on the machine and exciting it with a shaker to measure the mode shapes. The theoretical prediction of the axial mode is within 4% percent of that measured. The other set of experiments involve measuring the loop transmission by using a sinusoidal torque input at the motor and measuring the response from the linear encoder. Figures 5 shows a comparison of the measured loop transmission with and without damping respectively.

Conclusion

In this paper, we have outlined the solution of the inverse problem of designing the ballscrew drive for closed-loop performance. In order to attain a robust design, the plant and the controller must be designed simultaneously; that is, the focus should be on the design of the loop transmission. To this effect, we have obtained a reasonably accurate model of the system which is supported by extensive experimental evidence. Graphical design techniques then allow us to link the closed-loop performance to mechanical design parameters so that a designer can rapidly lay out a machine that meets the desired closed-loop specifications.

References

Nayfeh, S. A. and Slocum, A. H., 1998, "Enhancing Ballscrew Axial Dynamics," *Proceedings of the ASPE 13th Annual Meeting*, St. Louis, Missouri.

Chen, Y., and Tlusty, J., 1995, "Effect of Low-Friction Guideways and Leadscrew Flexibility on Dynamics of High-Speed Machines," *Annals of the CIRP*, Vol. 44.

Preliminary Design of a Very Low Frequency Vibration Calibration System

Dick Rhorer and Bev Payne
National Institute of Standards and Technology
Gaithersburg, MD 20899-8220

Measuring vibration is important to many precision-engineering enterprises. For example, accelerometers are often used to measure and analyze the vibration of precision machine tool structures. As with any measurement, the calibration of the vibration transducer is a key component of the overall measuring process. The National Institute of Standards and Technology (NIST), originally the National Bureau of Standards, has been calibrating reference level accelerometers for over half a century.

This paper is an overview of the preliminary design for a new motion generating and measuring system for the NIST vibration laboratory. The goal of this project is to develop the capability for the high accuracy calibration of vibration transducers in the low frequency range—down to 0.1 hertz (Hz) or below. This will extend the current frequency range for NIST calibration of accelerometers by at least one order of magnitude.

The calibration of vibration transducers usually involves placing the transducer on a motion generating system—often called a shaker—and comparing the transducer output to a standard motion measuring system. The design of both the shakers and the motion measuring systems involve the application of precision engineering principles to achieve the levels of accuracy necessary for NIST level calibrations. Measuring the displacement of the accelerometer as a function of time with a laser interferometer can be used to perform an absolute calibration. The second derivative of the displacement signal is compared to the accelerometer output signal for calibration. The uncertainties of the calibration measurement results depend on many factors, including the purity of the motion imparted by the shaker during calibration. An ideal situation is to have pure rectilinear harmonic motion of a carriage that supports the accelerometer. Specifying the maximum allowable deviations from pure rectilinear motion, needed to produce the required level of accuracy in the acceleration, is an important part of the design specification for the shaker.

The current lowest frequency capability at NIST is 2 Hz for acceleration levels 2 to 20 m/s^2 (or 0.2 to 2 g). For a harmonic vibration of 2 Hz at an acceleration level of 2 m/s^2, the displacement required is 12.6 mm and the maximum velocity is 159 mm/s. To lower the frequency and maintain the same level of acceleration the length of motion and velocity capability will increase. To produce a motion with the same acceleration of 2 m/s^2 and a harmonic frequency of 0.1 Hz, a displacement of 5.06 m would be required (a total stroke of about 10 m) with a maximum velocity of 3.18 m/s. Because of the difficulties and expense of such a large shaker, the preliminary designs being considered will limit the stroke to about 1 m, which would allow the calibration of transducers to an acceleration amplitude of 400 mm/s^2 at 0.1 Hz. Maximum velocity would be approximately 630 mm/s. This range would cover many of the instruments designed to measure earthquake motions. Also, it is interesting that these length of travel and velocity requirements for the shaker are similar to parameters for modern high-speed precision machine tools.

Key Words: precision motion, accelerometer calibration, vibration measurement

A STUDY ON MODEL-BASED ANALYSIS OF THE DYNAMIC MOTION ACCURACY OF CNC MACHINE TOOLS

Gabriel Johnston[1], Yoshihito Kagawa[1], Jiancheng Liu[2], Masahiko Mori[3]
Kazuo Yamazaki[1]
(1): Department of Mechanical and Aeronautical Engineering,
University of California, Davis CA 95616-5294
(2): DTL, A Division of Mori Seiki U.S.A. Inc., Sacramento, CA 95833
(3): Mori Seiki Co., Ltd., Nara, 639-1160, Japan

1. Introduction

In the past, the solution to increase machine tool accuracy and speed has been to make incremental innovations to both the machine design and the numerical controller. There have been many improvements to the feed-drive mechanism including ball screw, supporting member, and coupling design and material improvements, rotary motor and encoder developments, and guideway redesigns (air and lubrication oil additions) to minimize friction. From the controller side, additional peripheral functions have been included to compensate for non-linearities such as backlash (quadrant protrusion compensation), guide-way stiction, and pitch errors.

One cause for machine tool inaccuracy lies in the area of the feed-drive system. In today's machine tool industry, the most common mechanism to actualize the table position is still the conventional ball screw mechanism, which introduces three main sources of error: thermal expansion, static/dynamic friction, and elastic deformation of the components such as ball nut, supporting bracket and bearings, ball screw, etc.

During high-speed machining, the machine table is required to accelerate and decelerate extremely rapid. Due to the sudden high torque applied to the end of the shaft, some of the motor's energy is employed to elastically twist the ball screw material. The severity of this elastic deformation of the ball screw depends not only on the magnitude of the torque, but additionally the table position. With increased table position the effective ball screw length is increased and thus the rigidity of the ball screw shaft decreases. Consequently, the decreased rigidity is a source of machining errors: it creates an initial time delay in the response and a transient oscillation of the table around the desired position as the shaft 'untwists.' Therefore the problem exists to enhance the feed-drive mechanism to significantly improve the machining precision and reduce these dynamic motion errors.

The objective of this research is to develop an accurate simulation model for multi-axis feed drive system motion in a CNC vertical machining center by accounting for the torsional deformation that occurs within the ball screw shaft during the high acceleration and deceleration process. This model can be used to improve the positioning accuracy of the ball screw feed drive system.

2. Modeling of the feed drive system

There are four basic components of a CNC feed-drive system. These are the Interpolator and Trajectory Generator, the Servo Controller, the Actuator System (containing the amplifier), and the Mechanism for both the X and Y axes which operate independently.

2.1 Machine Tool Interpolator and Trajectory Generator

The first part of the model is the command creation, which is achieved by a Trajectory Generator. In the physical system the Interpolator reads the program code and the Trajectory Generator creates the motion command accordingly. In the simulation model only the motion command creation is necessary to serve as the input to the feed-drive model in order to conduct tests. Among the interpolated motions, a circular interpolation will be modeled because circular tests are most popularly used to evaluate the machine motion performance. The X and Y positions are determined at each time step based on the equations:

$$X = Radius \cdot \cos(t \cdot Feed / Radius/60)$$

$$Y = Radius \cdot \sin(t \cdot Feed / Radius/60) \qquad (1)$$

The feed-rate (Feed) and radius are first specified. In the model, after these values are calculated they are compared to a function to check if it is the end of the circle. If not, they are each multiplied by a filter which has the form: $1/(t_a s+1)$, and generates the radius reduction phenomenon that occurs in the real machine. The outputs from both X and Y axes are used as inputs to the model's feed-drive system.

2.2 PID Servo Controller

The first component of the machine tool that receives the motion command from the Interpolator and Trajectory Generator is the servo controller. A simplified diagram of the CNC machine tool controller is shown in Figure 1. Multi-loop feedback is used to control position, velocity, and current of the motor and mechanism. The parameter values input to the simulation model are the same values as the machine in which we are trying to model.

2.3 Actuator System

The third component of the CNC Machine Tool Feed-drive System is the Actuator System, which consists of an amplifier and an electric servomotor to drive each axis. A model of DC motor was used.

2.4 Feed-drive Mechanism

The last component of the feed-drive system is the mechanism The mass-spring-damper model of a precise feed-drive mechanism to account for the friction existing on the guide surfaces and brackets, which would affect the response of feed-drive mechanism is given in Figure 2. This model includes the parameter of ball screw torsional stiffness K_θ. The dynamic calculation of this parameter is crucial in this research. Furthermore, the axial rigidity of the supporting members (ball screw, supporting bearings and bracket) between a ball screw and machine base, K_S, and the axial rigidity between the ball screw and table, K_n, are included. The following are the governing equations of this new model.

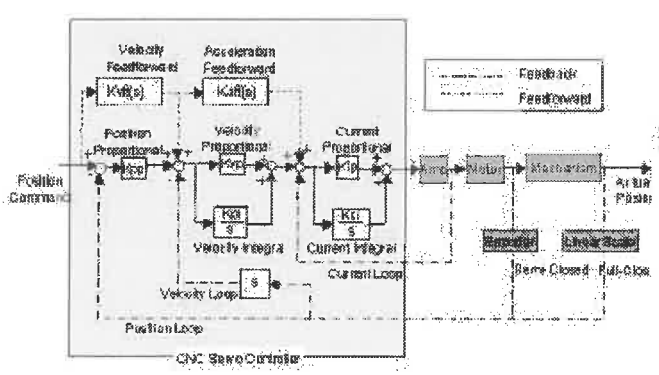

Figure 1: CNC Machine Tool Servo Controller

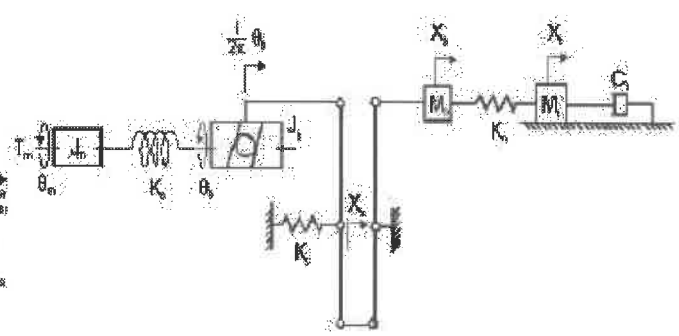

Figure 2: Mass-Spring-Damper Model of Feed-Drive Mechanism[1]

$$
\begin{aligned}
&J_m \ddot{\theta}_m + K_\theta(\theta_m - \theta_b) + T_{mf}(\dot{\theta}_m) = T_m \\
&J_b \ddot{\theta}_b + K_\theta(\theta_b - \theta_m) + \frac{l}{2\pi} K_s (\frac{l}{2\pi}\theta_b - X_b) + T_{bf}(\dot{\theta}_b) = 0 \\
&M_b \ddot{X}_b + K_s(X_b - \frac{l}{2\pi}\theta_b) + K_n(X_b - X_t) + F_{bf}(\dot{X}_b) = 0 \qquad (2) \\
&M_t \ddot{X}_t + C_t \dot{X}_t + K_n(X_t - X_b) + F_{tf}(\dot{X}_t) = 0
\end{aligned}
$$

Where T_m is the motor torque, J_m is the inertia of the motor, J_b is the inertia of the load (Coupling, Ball Screw, and Table), M_n is the mass of the nut, M_t is the mass of the table, and l is the pitch of the ball screw shaft.

The states are θ_m (position of the motor in radians), θ_b (ball screw position in radians), X_b (ball screw position in millimeters), X_t (table position in millimeters).

These equations also consider four frictional non-linearities T_{mf} (frictional torque on the motor), T_{bf} (bracket frictional torque on the ball screw), F_{bf} (frictional force on the nut and supporting parts) and F_{tf} (frictional force between the guide and table).

The followins is the torsional rigidity equation that calculates the ball screw stiffness from the table position, which affects L.

$$K_\theta = \pi r^4 G / 2L \qquad (3)$$

3. Evaluation and optimization of simulation model

3.1 Parameter optimization of simulation model

Because this research also investigates how the ball screw mechanism contributes to machining errors, variables considered for comparison are the motor's position at each point along the trajectory

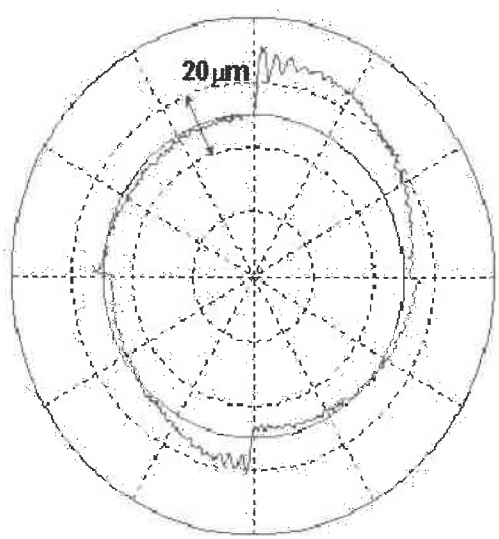

Figure 3: Physical Result Magnified 2-Axes Error Plot for F=5, R=50, XP0=2769, YP0=1584

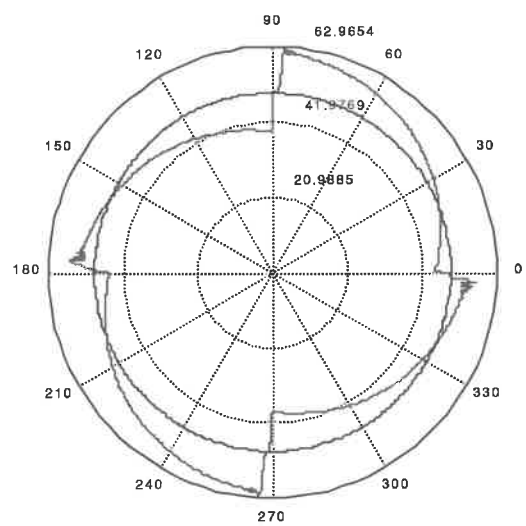

Figure 4: Simulation Result Magnified 2-Axes Error Plot for F=5, R=50, XP0=2769, YP0=1584

(in order to gage the difference between the table and motor position at each instance), and the time delay between the motor and table positions. After comparing the motion curves of the machine and model, the simulation model parameters were optimized. The parameters considered were the friction model parameters, namely the dynamic and static friction constants, and the stiction velocity because these were the most difficult to predict.

In the two-axes case, the magnitude of the error at the quadrant changes and the reduction in error after each quadrant will be considered. The plot of the 2-axis physical results with the experimental conditions of F=5000mm/min, R=50mm is shown in Figure 3. After changing the X frictional constants, increasing the supporting member rigidity, and changing the Y frictional constants, increasing the supporting member rigidity the simulation result is very close to the physical result and is shown in Figure 4. The main differences between the two plots are the magnitude of the stiction after crossing the x-axis, and the amount of radius reduction after crossing the desired trajectory, the moldel exhibite the same fieature of machine circular motion. The magnitude of the stiction errors at the y-axis are 23 microns compared to the physical results of 16 and 20 microns.

3.2 Table position error trend

In order to reveal how this trend-line behaves in the simulation model, and estimate how much affect the ball screw elasticity has on the motion errors, the simulation model was used for estimate of the contribution of the ball screw. Figure 5 and 6 shows the simulation model's stiction error verses ball screw length (table initial position). The stiction error increases linearly with table position and increases over the entire length of the ball screw.

4. Conclusions

(1) In order to devrlope an accurate similation model for multi-axis feed drive system motion in a CNC vertical machining center, the model of each component of the machine tool were generated and the entire model was revealed.

(2) Each parameter of the model was optimized by comparing to physical test results and the simulation model exhibited the same feature of machine tool.

(3) The effect of the ball screw elasticity on the motion error was clarified.

References

[1] Tsutsumi, M., Ohtomo, S., Okazaki, Y., Sakai, K., Yamazaki, K. and Ge, D., [1996], "Mathematical Model of Feed Drive Mechanical System and Friction for CNC Machine Tools," Journal of Japan Society for Precision Engineerin

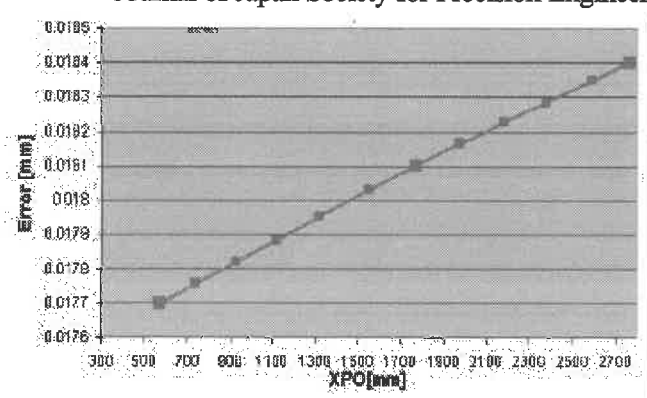

Figure 5: Simulation Stiction Error Verses Table Initial Position For F=5000mm/min, R=50

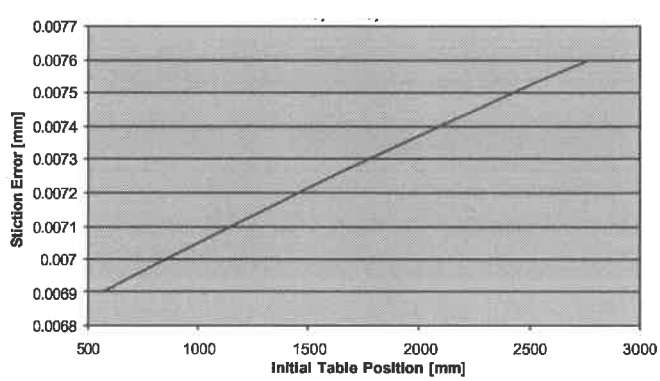

Figure 6: Simulation Stiction Error Verses Table Initial Position For F=10000mm/min, R=50

PRECISION MANUFACTURING AND ELECTRONIC GASEOUS FUEL INJECTION SYSTEM REDUCES EMISSION WHILE IMPROVING FUEL ECONOMY FOR SI ENGINE

S.Kumarappa
Bapuji Institute of Engineering and Technology, Davangere-577 004, Karnataka State, INDIA.
Fax: (08192) 23261, E-mail: kumarappa_sdvg@yahoo.com , kumarsdvg@indiatimes.com
G.P. Prabhukumar
University B.D.T. College of Engineering, Davangere. 577 004, Karnataka State, INDIA.

Abstract

Today's automobile engines have parts with tolerances of one micron. This precision manufacturing has enabled auto companies to reduce total emissions, improve fuel economy and make engines more reliable. Improvements in cutting tools, grinding systems and CNC technology let today's engine builders routinely achieve levels of precision that could not even be measured a decade ago. Automobile vehicles today are 96% cleaner and 50% more fuel efficient than in the 1970s because of innovations in fuel injection system, multiple valves and lighter materials.

Introduction

The high standard of living of developed nations can be traced to the great contribution made by engineering manufacture, through innovation in product design and development and adoption of advanced manufacturing technologies. In the field of engineering manufacture, Flexible automation and application of precision engineering have emerged in the last decade. Flexible automation was necessitated by the customer preference for varieties and variants in products. It has led to the introduction of computer numerical control machine tools, flexible-manufacturing systems, and computer integrated manufacturing systems.

Precision engineering

Precision engineering has contributed greatly to product developed through greater interchangeability, high service life, high reliability, better product quality and comfort to the user. Precision engineering forms a vital role in the field of automobile applications. The major emerging areas of application of precision engineering in automobile are in the field of sensors and actuators. The level of precision required for these products could be achieved through an effective synthesis of high precision manufacturing techniques and dimensional metrology associated with careful material processing techniques. The various manufacturing processes generally include high precision force machining, selective precision machining, ultra high precision machining, elastic emission machining, dry mechano-chemical polishing, lithographic etching technique, energy beam machining and ion processing. The ultra high precision has greatly enhanced the value added to achieve the required precision with minimal effect. It is important to select an appropriate design and the machining process to obtain maximum performance or life (1).

Precision engineering generally involves

i) High precision and ultra precision engineering

Precision engineering as applied to general engineering products, relates to manufacturing to a tolerance of 1 to 10 microns over dimensions of 100 mm. In the manufacture of automobile products, high precision and ultra precision machine tools such as diamond turning machines, diamond-milling machines, ultra precision grinding and lapping machines and high precision Electro-discharge machines are used. Apart from the human skill, the other important ingredients for precision manufacture are good metrology practices and special environmental conditions such as controlled temperature, humidity, ground vibrations and dust level.

ii) Micro engineering

Micro engineering is a subset of precision engineering. This new field, also known as Micro system technology and Micro electro mechanical system, relates to devices and machines of extremely small size comprising tiny but highly sophisticated elements which allow to perform minute and complicated tasks. They are invariably integrated with signal processing electronic circuitry. Miniaturization trough micro engineering imposes simplicity in design and brings about reduction in the cost of manufacture.
The applications in automobiles alone will justify the investments on facilities and processes to fabricate micro mechatronic devices, accelerometers for smart automobile suspensions, for safety air bag development and for antilock braking systems, micro actuators, micro gears, sensors, transducers, connectors, electronic fuel injectors, flow sensors, micro valves and gas sensors to control the optimal engine operation and emission control in automobiles.

iii) Micro fabrication techniques

Integrated circuit batch processing techniques such as photolithography, oxidation, diffusion, ion implantation, epitaxy and film deposition are used in making micromachined devices. In addition to the standard Integrated circuit processes, silicon fusion bonding, anodic bonding of silicon to pyrex glass, electrochemical drilling of glass wafers are also used for making microelectronic devices. Various approaches to micro electro mechanical systems such as Polysilicon surface micromachining, high aspect–ratio techniques Photolithography, Maskes, Photoresists, Etching, Diffusion, Vapor deposition, lithography, electroplating, and molding process.

Electronic fuel injection

To meet the demands of high specific output, low exhaust emission, modest fuel consumption and good driveability of the vehicle, modern electronics technology is opening up new perspectives in automotive design. Electronic fuel injection is generally more efficient than carburetors because it is able to compensate for a variety of operating conditions. This compensating ability allows the system to deliver the optimum fuel mixture needed, resulting in good throttle response and fuel economy. Over the years various technologies such as ceramic coating of piston and cylinder wall, use of catalytic converters, exhaust gas recirculation, charge stratification, use of intake resonators, active thermo-atmosphere combustion, use of air assisted

fuel injection etc., have been suggested to improve fuel economy and reduction of pollutants for SI engine. Amongst all, precision manufacturing, precision sensor and electronic gaseous fuel injection system proves to be most effective (2).

In daily life, the reliability of sensor systems even under extreme conditions is of vital importance for automobile applications. The success of most technical applications depends strongly on the technology used to develop a suitable sensor system. Sensor technology increases process efficiency and reduces cost of products. High measuring accuracy and long term consistency characterize the sensors used in electronic control. For electronic system to play a major role in fuel control the following requirements have to be met: High precision and reproducibility, higher safety, wide working temperature region, corrosion resistance, vibration resistance, interference suppression, friction free sensors, long working life.

The extreme accuracy of fuel delivery by the electronic control unit, at any load and speed, provides the engine with air-fuel mixtures that fall within a tiny window of accuracy required for maximum power or maximum economy. Electronic fuel injection system (Fig (1)) generally permits greater flexibility of intake manifolds designed to achieve higher inlet airflow rates and consistent cylinder to cylinder air-fuel distribution. More efficient, higher compression ratios are usable, due to accurate fuel metering (3). The most commonly sensed inputs are Engine speed, Engine load, Throttle position, Intake manifold pressure, Air temperature, Fuel pressure, mass of airflow, Crank position.

The microcontroller receives the signals from these sensors and determines the precise quantity of fuel to be injected per cycle for the particular load and speed conditions of the engine. The injection starts on receiving the signal from the crank position sensor. The injection duration pulse width is controlled by the microcontoller through one of the ports. On line control of the injection duration is also provided through another port for optimization of the engine performance.

Results and discussions

Figure (2) shows improvement in tolerances in machining the automobile components over the years, and Fig (3) shows reduction of pollutants with machine tooling accuracy. Figure (4) shows a comparison of CO emissions. In electronic gaseous fuel injection mode, significant lower concentration of CO is observed. This shows that a better-controlled air-fuel ratio can be maintained over entire range of operation. Figure (5) shows a comparison of HC emissions. Lower HC emissions were observed in electronic gaseous fuel injection mode.

Conclusion

The advantage of the electronic gaseous fuel injection system is precise online control of the quantity of fuel injected per cycle and the air-fuel ratio for any particular load, speed and can be optimized for the best engine performance and low emissions.

References:

1. A Journal of Micro electromechanical system, December 2000, volume 19, number 4.
2. L.M.Das andY.V.R.Reddy,"Evaluation of Alternative fuels for internal combustion engine". Terabzan, International energy and environment symposium, Turkey, July 29-31,1996.
3. R.D. Fleming and G.B.O Neal . "Potential for improving the efficiency of spark ignition engine for natural gas fuel" SAE 852073 Vol.94, 1995.

Key words: Precision manufacturing, electronic gaseous fuel injection, calibration of sensors, microcontroller, SI engine.

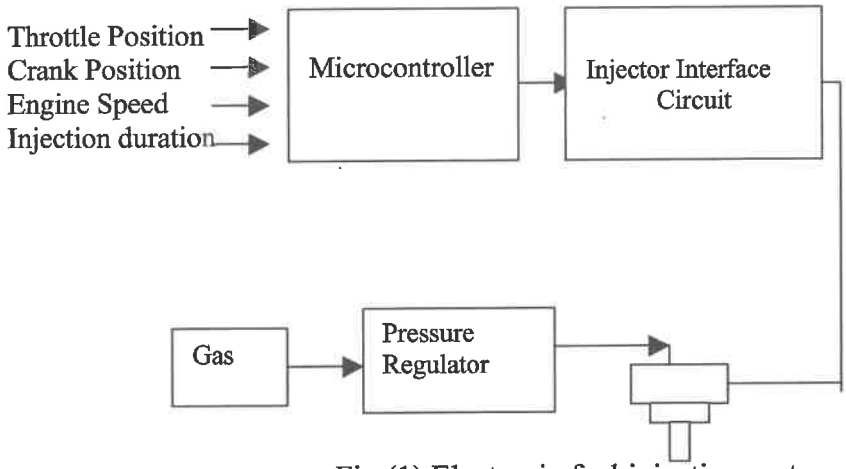

Fig (1) Electronic fuel injection system

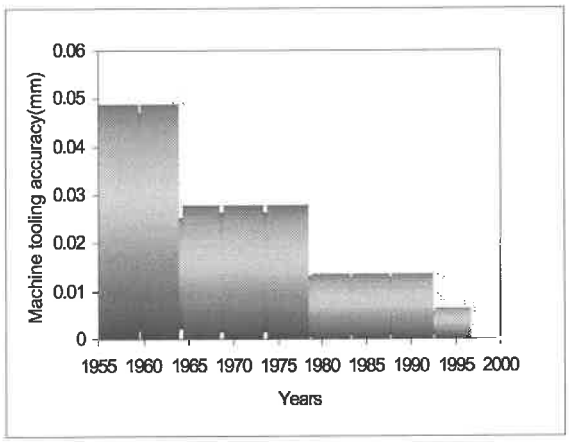

Fig(2) Machine tooling accuracy

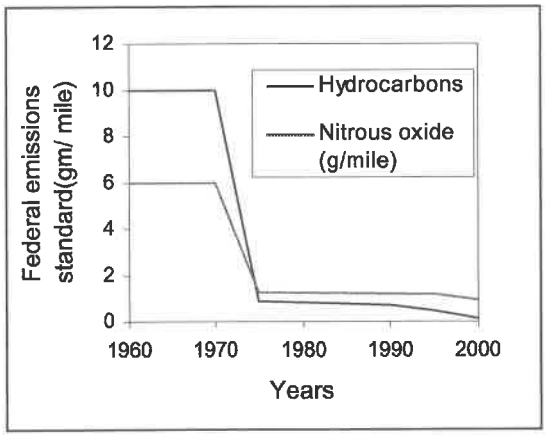

Fig(3) Reduction of pollutants with machine tooling accuracy

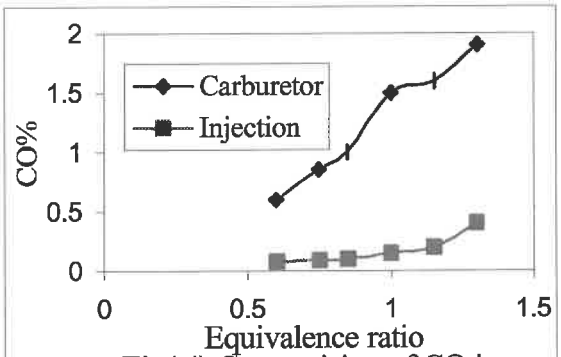

Fig(4) Comparision of CO in Carbutetor and Injection mode

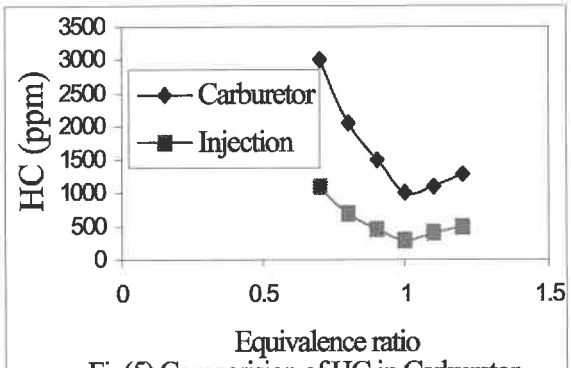

Fig(5) Comparision of HC in Carburetor and Injection mode

Development of Nanometer Positioning System Driven by Force Operational Water Hydraulic Actuator with Rigid Slide Guide-way, -Simulation and Experimental Evaluation of Non-Linear Positioning Characteristics-

Shinichiro Tsukahara, Kazutoshi Hara, Yoshiyuki Tomita, and Sho Isobe
Sumitomo Heavy Industries, Ltd., 19 Natsushima, Yokosuka, Kanagawa 237-8555 Japan
Akira Kanai Ashikaga Institute of Technology, 268 Ohmae, Ashikaga, Tochigi 326-8558 Japan
Masakazu Miyashita Nano-Tec Associates, 1-13-5 Higashi-Motomachi, Kokubunji, Tokyo 185-0022 Japan

1. Introduction

Most of conventional machine tools use slide guide-way system in order to obtain both high positioning rigidity and damping characteristics to suppress reaction force and oscillation due to cutting and/or grinding process. However, the nonlinear friction load of slide guide-way causes stick-slip motion, and as a result decreases motion accuracy as well as stability of the positioning system. A new control system design is required to realize nanometer-positioning system with high rigidity and high damping characteristics. Kanai et al. proposed a new theoretical model which can simulate the nonlinear friction characteristics of the slide guide-way in several hundreds nm displacement region.

The goal of our research is to develop a nanometer positioning system that is applicable to the ductile mode grinding system of next generation. The newly developed simulation system includes the nonlinear friction characteristics model and the elastic model of the saddle structure. In this paper, the new nonlinear simulation method is proposed and its validity is experimentally evaluated.

2. Positioning system

Fig.1 shows the schematic of the experimental positioning system. A force operation type water hydraulic cylinder, which is exempt of unwanted heat source, generates huge force by the differential pressure control operated by a servo-valve (MOOG, E061-007). The saddle is guided by the double-V type slide guide- way that realizes high stiffness and high damping toward the operation axis, and high motion accuracy toward the guide axis (both horizontal and vertical). A digital controller operates the servo-valve with PID position feedback control, where a linear scale is used as the feedback sensor with the resolution of 2.5nm.In this

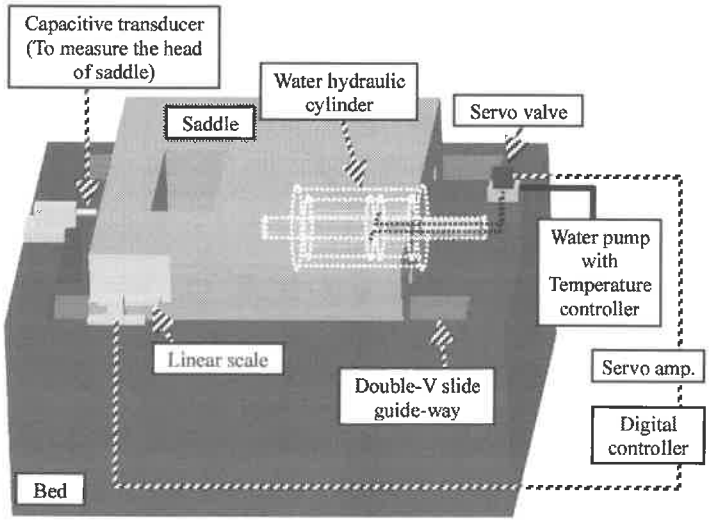

Fig.1 Schematic of the positioning system

positioning mechanism, the frictional load is so huge that the saddle is forced to be deformed. Through the experiment, the static rate of the deformation has turned out to be 0.14nm at operational force of 1N.

3. Simulation model

Fig.2 indicates the simulation model of the whole positioning system. In Fig.2, C_q and C_p are the flow gain and the pressure gain of the servo-valve. ω_n and ζ are the characteristic frequency and the damping ratio of the flapper in the servo-valve. A represents the piston area of the cylinder. V and K_v are the volume and the volume elasticity of water.

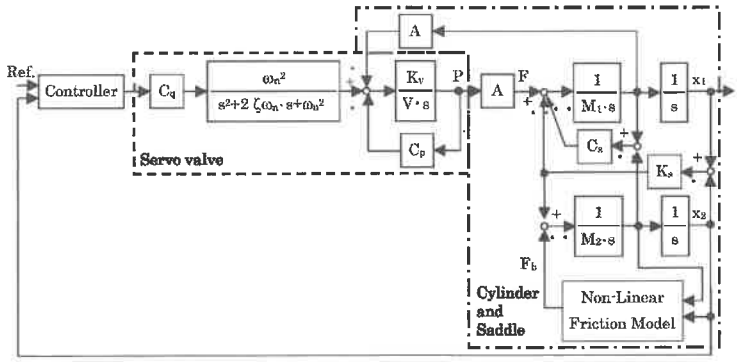

Fig.2 Schematic of simulation model of the positioning system

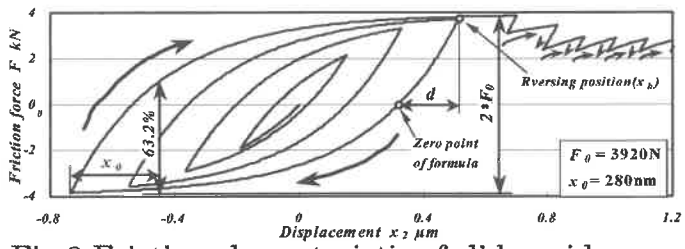

Fig.3 Friction characteristic of slide guide-way (Swaying and stepping motion)

The dynamics of the saddle is modeled as the two masses (M_1, M_2) linked by a spring with the spring constant of K_s, and associated with a damper with damping ratio of C_s. The cylinder is connected to M_1, and M_2 is placed on the slide guide-way. x_1 and x_2 ,which are the displacement of the masses M_1 and M_2, express the displacement of the head and that of the side of the saddle. In order to prevent an unwanted momentum from arising, it is better to align the axis of the cutting/grinding with that of operation. However the aligned position of two axis puts the restriction on the freedom of the placement of the sensor.

The block named "Non-linear friction model" is the one of the displacement for the frictional load characteristics in the sub μm range, which is expressed by the formula (1)[1] and which depends on both the history and the direction of saddle motion. Fig.3 is the typical fluctuation of the characteristics.

$$F(x) = \pm F_0 \cdot \left(1 - 2 \cdot \exp\left(\mp \frac{x}{x_0}\right)\right) \quad \ldots(1)$$

$F(x)$: frictional load
F_0 : stationary frictional load
x : displacement after reversing feed direction
x_0 : displacement constant

With regard to the positioning system of this development, stationary frictional load (F_0) is 3920N, displacement constant (x_0) is 290nm.

4. Experimental and simulation result

The characteristic behavior of the positioning system in this development appears at the motion including some "start-and-stop" actions like step feed, because the non-linearity of the

huge frictional load affects on the response. Fig.4 displays the experimental result of the displacement and operational force fluctuation at 50nm step feed. Similarly, Fig.5 shows the simulation result. Fig.6 represents the results of both the experiment and simulation. And also plotted in Fig.6 is the behavior of formula (1). To be note is that the operation force is plotted against the displacement of the side of the saddle. On these figures, first 20 steps are directed to the positive, and the after, 20 steps are directed to the negative. In both experiment and simulation, before turning to the positive stepping, the saddle moves several micrometers, which are much larger than the transient domain, by the positive continuous feed to saturate the frictional load.

In Fig.4 showing the fluctuation of the motion, the side of the saddle, which is closely controlled, among the motion direct to the positive follows well the commanded position without the significant over-shoot larger than 10nm. The head of the saddle follows the commanded position with the deviation less than several ten nanometers and over-shoot larger than 50nm. Then if the fluctuation of the operational force is observed, it increases about 0.5kN and decreases almost same in one step, and its shape of the fluctuation remains almost equal at each step.

The observed fluctuations are explained as follows. First, the side of the saddle keeps well up with the commanded step motion with a little over-shoot. With the displacement of the step motion, the frictional load increases according to the formula (1), therefore the operation force also increases according to the formula (1). Next, the side of the saddle is controlled to compensate the over-shoot, therefore both the frictional load and the operation force decrease in line with the formula (1). The saturation of the frictional load makes the shape of the each response similar to one another. And the fluctuation of the operation force (about 0.5kN) and the elasticity of the saddle (0.14nm/N) cause the large over-shoot (70nm) at the head of the saddle.

After the step direction is reversed, if the operation force is observed, it decreases without increasing toward the positive until the 3rd step. From the 4th step, the increase starts and becomes larger and larger. And as steps progress, the increase becomes almost equal to the decrease. The fluctuation of the operation force toward the negative seems to show the behavior typical to the step response curve of first order delay with a time constant. If the displacement in the zoomed view of Fig.5 is observed, the side of

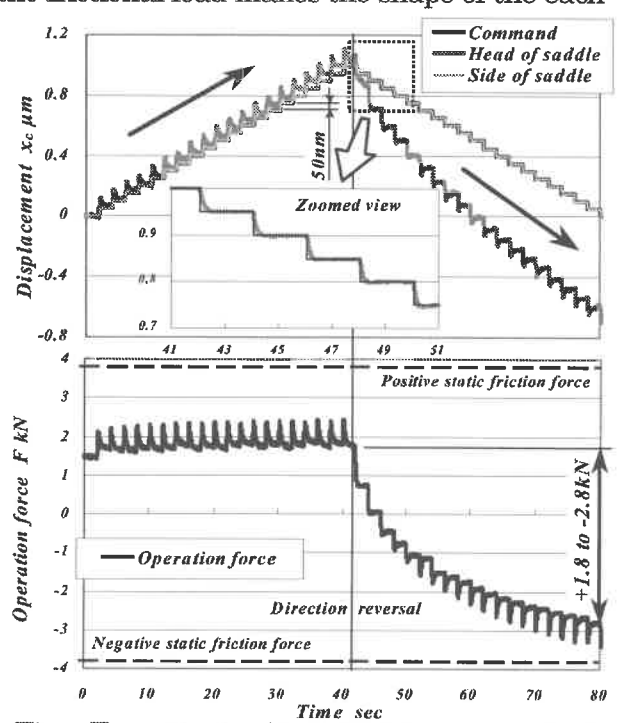

Fig.4 Experimental result of 50nm step feed

the saddle follows well the commanded position, changing the response at each step. The head of the saddle moves about two times as much distance as the command. It also changes the response at each step.

In Fig.6, the operation force considerably fluctuates to the negative along with the curve of the formula (1). After over-shoot starts, the fluctuation gradually deviates because the reversing position shifts. The equivalent spring stiffness according to the frictional load in the formula (1) changes so significantly for the positioning system dynamics that the response of the saddle changes depending on the shift of the frictional load. When the frictional load becomes close to the stationary frictional load, the equivalent spring stiffness becomes so soft that the over-shoot happens easily. But if the over-shoot is very large, the decrease of the frictional load on the compensation motion becomes large and the equivalent spring stiffness increases. Therefore at the step feed which travels over the transient domain, the frictional load is saturated near the stationary frictional load.

If the fluctuation of the operation force and saddle motions in Fig.5 and 6 are observed, there is a good agreement between the experiment and simulation results. It can be thought that the errors of the two results are caused by the characteristics that are not included in this simulator, which is the non-linearity of the servo-valve, the viscosity of the lubricating oil and the distribution of the frictional load along the slide guide.

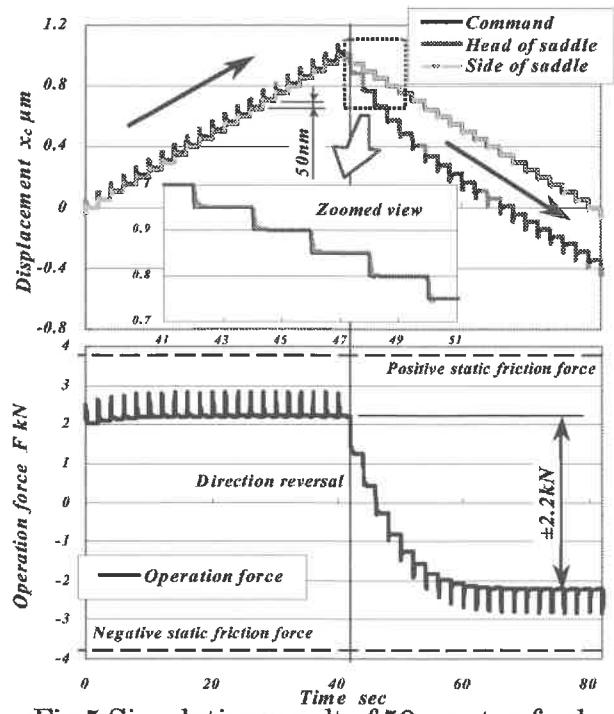

Fig.5 Simulation result of 50nm step feed

5. Conclusions

By comparing the simulated positioning characteristics with the experimental one, it has been shown that both results describes good agreement each other, although the associate phenomena include the non-linearity in the positioning that depends on the direction of stepwise motion, the step height, and the history of motion.

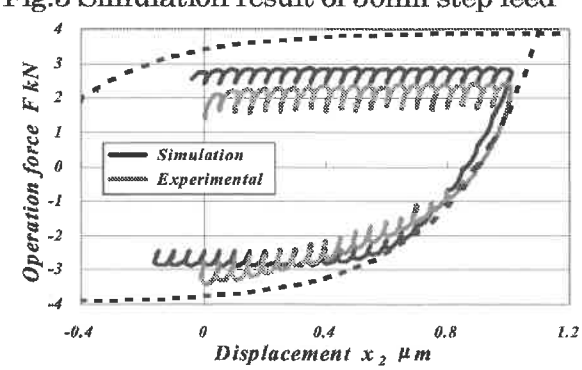

Fig.6 Simulation and experimental result of 50nm step feed

6. References

1) Akira Kanai, Masakazu Miyashita, Sadaaki Hatai and Masato Yoshida, Proc. ASPE 1997 Annual Meeting

Long Range Stage for the Metrological Atomic Force Microscope

T.B. Eom and J. Y. Kim
Korea Research Institute of Standards and Science, Yousong , Taejeon 305-666, Korea
H. S. Choi and S. K. Lee
K-JIST, 1 Oryong-dong, Puk-gu, Kwangju 500-712, Korea

Abstract

We are constructing the AFM based nano-measuring machine with long measuring range for the metrological applications. In this project, our aim is to develop the measuring system with sub-nm resolution to measure three-dimensional positions of the artifacts used for semiconductor metrology. For developing the nano-measuring machine, a high precision positioning stage with a travel range of 200 mm x 200 mm x 30 μm is also fabricating. On designing the system, we mainly consider an Abbe offset free arrangement and a simple structure with low vibration and low deformation. In stead of the traditional two level stages, we adopted a single level stage using a surface plate as the reference of the stage. Therefore, it has low profile, and small pitch and roll error motion. The X-Y stage consists of a micro-stage driven by the PZTs and a global stage driven the DC geared motors and lead screws. The position and angular motion of the X-Y stage can be measured and controlled by laser interferometers. The positioning of AFM tip is achieved by 3 PZTs and capacitance type gap sensors, and the approaching AFM tip to the sample and retracting it is achieved by a inchworm motor.

Introduction

Scanning probe microscopes (SPMs) have been used frequently to observe the surface texture over past years. With the development of nanotechnology, there has been growing demand for measuring the dimension of the very small structure. For this purpose, several national metrology institutes have developed the metrological SPMs upgrading the commercial machines with precision flexure stage and displacement measuring system such as capacitance type sensor or laser interferometer [1, 2]. These metrological SPMs are used mainly for measuring critical dimensions, pitch and step-height. However, the disadvantage of these measuring systems are the small measuring range of a few μm. For measuring the image placement of the photomask and wafer, a special metrological system having long measuring range is required. National Institute of Standards and Technology is developing a STM based Molecular Measuring Machine having an accuracy of 1 nm and a measuring range of 50 mm x 50 mm x 0.1 mm [3]. PTB also developed a SEM based Electron-Optical Metrological System with a measuring range of 300 mm x 300 mm [4]. At present, we also are constructing a metrological system similar to NIST

Molecular Measuring Machine. The aim of the project is to develop a nano-measuring system presenting a resolution of about 0.1 nm with a measuring range of 200 mm x 200 mm x 30 μm.

Structure of the stages

We designed the measuring system to apply to semiconductor metrology. Fig.1 shows X-Y translation system. On designing the system, we mainly consider an Abbe offset free arrangement and a simple structure with low vibration and deformation. In stead of the traditional two level X and Y stages, we used one level X-Y stage. The surface plate is used as the reference of the stage. Therefore, It has low profile, and small pitch and roll error motions. Surface plate was made of the cast iron and its flatness is below 1.5 micrometer over the size of 650 mm x 650 mm. The X-Y stage is positioned on the surface plate. It is guided horizontally by a cross structure with two precision bars rectangularly linked and vertically by the surface plate. The X-axis guide bar with a moving plate is fixed on the surface plate. The Y-axis guide bar is attached to the X-axis moving plate and moved to the X direction by motion of the X stage. Finally the y-axis guide bar guides the Y-axis moving plate on which the X-Y moving plate is fixed, so the X-Y moving plate can be moved to two directions. The sliding pads, which are made of PTFE, are used at X- and Y-axes moving plates, and also used for vertically supporting the X-Y stage on the surface plate. Each stage is driven by the lead screws with the geared DC servo motors. In this structure, by the movement of the X-axis moving plate, the position which the driving force for the Y-axis movement is applied to MAY be changed. It usually induces the yaw error. To prevent this error motion, we incorporate a special guiding system that is fixed on the surface plate parallel to the

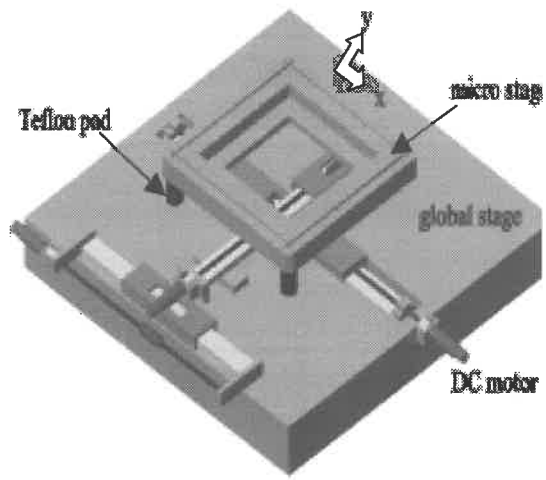

Fig. 1 Schematic diagram of 2-axis translation system.

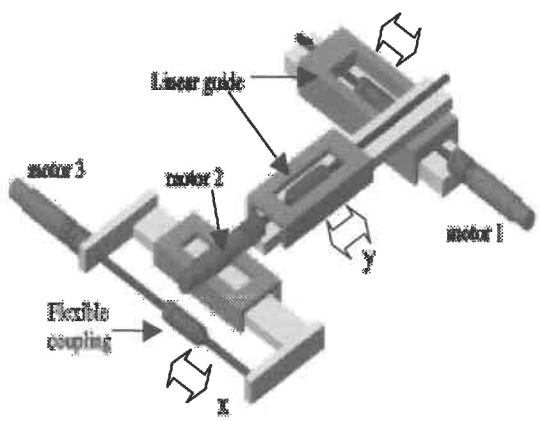

Fig. 2 Schematic diagram of the translation system for global stage.

main X-axis guide. This second X-axis driving system is controlled to move at the same speed with the main X-axis driving system. And it carries a geared DC servo motor for the Y-axis driving. As a result, the driving force for Y-axis is always applied to the center of the stage (see Fig. 2). And this structure can prevent the vibration of the motor from transferring to the X-Y stage. The X-Y stage plate has the two-axis flexure stage machined by the precision wire-cutting machine. The flexure stage provides a total moving range of 30 μm x 30 μm and angular motion for adjusting yaw error motion (see Fig. 3). The stage plate and the flexure stage are made of a single aluminum block. By both of them, the stage provides the fast movement and the fine positioning. Three-axis tilt stages for adjusting the two pitch motions of the stage are fixed on the flexure stage and a square mirror for laser interferometer is positioned on the tilt stage. The Z-stage has a design based on three pairs of capacitance type gap gauges and PZTs driving a kinematic assembling of two plates. The lower plate is fixed on the tilt stage and upper one supports on the measuring target. The distance from the surface to the top of the square mirror is 55 mm. The Z stage based on inchworm mechanism is fixed on a bridge which is kinematically coupled on the surface plate. The inchworm stage is used to approach the AFM tip to the sample and retract the tip from sample. It was made of a PZT tube with large diameter, two flexures for clamping and fixed ring. It has a large through-hole to view the sample surface and tip by an optical microscope (see Fig. 4).

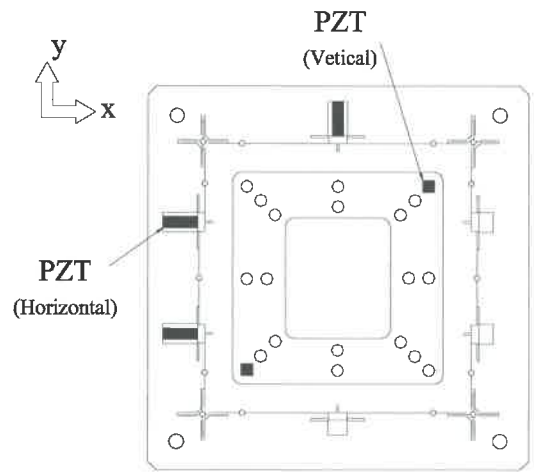

Fig. 3. Configuration of micro stage structure.

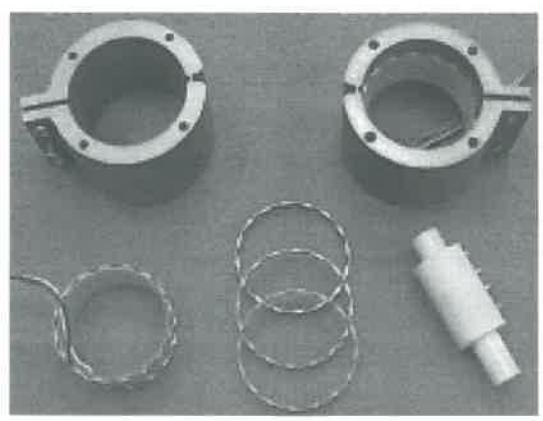

Fig. 4 Inchworm motor. In the figure, the developed inchworm motor and commercial motor are shown.

The laser interferometer measures the position of the stage and also measures the angular motions such as two pitch errors of the two axes and one yaw error. For this purpose, we also are developing the heterodyne laser interferometer having two frequencies. The transverse Zeeman stabilized laser is used as a light source of which frequency

is stabilized by thermally controlling the plasma tube length. Its beat frequency is about 170 kHz. Now we are evaluating the nonlinearity compensation technique and phase encoding electronics.

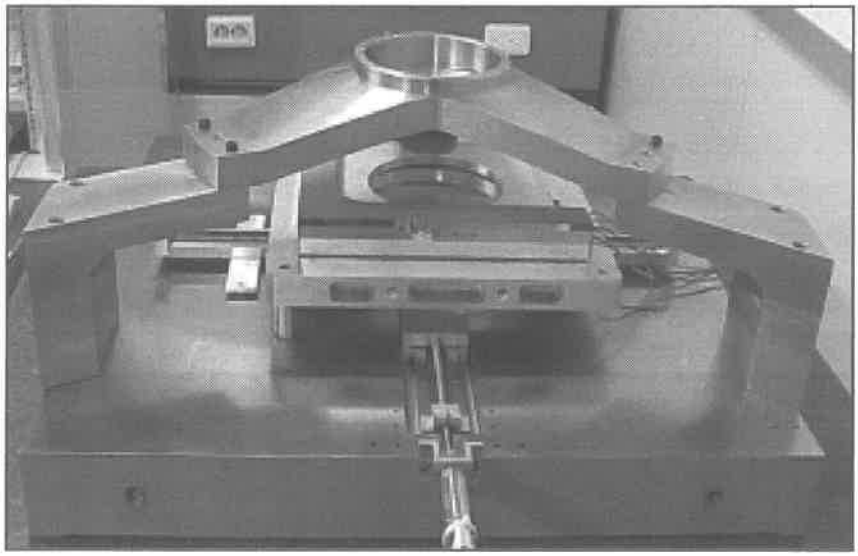

Fig. 5 prototype nano-measuring machine under developing.

Further works

Now we are constructing the prototype nano-measuring machine for semiconductor metrology applications. The preliminary test shows that the long range stage works well. Further study is to combine the stage with laser interferometer and develop the control algorithm. After that, we will design the final system.

References

[1] T. V. Vorburger, *et al.,* Industrial uses of STM and AFM, Annals of the CIRPS, 46(1997) pp 597-620.

[2] G. B. Picotto and M. Pisani, A metrological SPM for dimensional surface measurement, Proceedings of the EUSPEN, 1(2001), pp 402-405.

[3] E. C. Teague, Nanometrology, Scanning Probe Microscopy, Gaithersburg, MD 20899, NIST (1991)

[4] W. Häßler-Grohne and H. Bosse, An electron optical metrology system for pattern placement measurements, Meas. Sci. Technol. 9(1998) pp1120-1127

A STUDY ON A NOVEL 5-AXIS MACHINE TOOL USING DIRECT DRIVE

P. Fitsos[1], K. Yamazaki[1], Y. Sugimoto[2], M. Mori[2]
[1]IMS-Mechatronics Laboratory, Department of Mechanical & Aeronautical Engineering
University of California, Davis CA 95616-5294
[2]Mori Seiki Co., Ltd., Nara, 639-1160, Japan

INTRODUCTION

In an effort to improve the manufacturing productivity of precise and complex parts, manufacturers would like to use precision machine tools as high volume, versatile manufacturing tools. The productivity of precision machine tools can be improved by applying high speed machining methods to the classical orthogonal multi-axes machines. Machine versatility can be enhanced with a machine design that allows the cutting tool to approach the workpiece from many angles, quickly and precisely. In this design versatility is achieved by using a novel method to rotate and position the spindle as much as 90 degrees from the horizontal through the use of linear motors and electro-pneumatic clamping. Thus creating a machine tool that approaches the rigidity of the classic machine tool structure with some of the versatility found in parallel kinematic machine tools.

BACKGROUND

The two most common methods used for powering movement in machine tools are the ball screw and linear motor drives. Ball screw drives are less expensive and can provide accelerations as high as 1 g. But they also can introduce errors from gear wear and backlash and have low natural frequencies, which make them less suitable for precision high speed machining. Linear motors can provide high accelerations, high thrust forces and are very stiff dynamically. Therefore they may be more suitable for precise high speed machining [1]. However they are more expensive, generate more heat and can produce high attractive forces between the moving and stationary sides of the motor.

The two most common structural designs discussed in the literature are the classic orthogonal multi-axis machine and the hexapod parallel kinematic design [2,3,4]. The classic multi-axis machine is more rigid statically, dynamically and thermally. However the less rigid, less thermally stable hexapod design has the advantage that it can provide more machining flexibility through its ability to provide a larger variety of paths that the cutting tool can approach the work piece [3,4]. The classic machine tool design in its 5-axis form can provide a wider variety of cutting tool paths. But may not be able to provide these paths in a manor suitable for high-speed precision machining due to the error and relatively slow movement of conventional drive systems. Therefore the idea of this design is to create a machine that combines the rigidity of the classic machine tool with some of the flexibility of hexapod and use a linear motor drive system to provide the acceleration and accuracy needed for high speed precision machining.

DESIGN APPROACH

A digital design approach was used for the design and analysis of this device. This entailed creating virtual prototypes of components and assemblies using

IDEAS CAD software. This distributed model of the device was used for static and modal analysis using the finite element method. Large motion analysis of the device was done by creating a lumped model using ADAMS software. Lumped masses where used to represent the major components and stiffness matrices were used to represent the compliance of the rail carriages. ADAMS was also used to model the performance of the pneumatic ballast actuators of the system using an analytical model of the actuators inserted into ADAMS. For all of the analyses done, a performance criteria was used to judge the virtual performance of the component or assembly. Thereby testing aspects of the design without creating a physical prototype.

CONCEPTUAL DESIGN

A conceptual design of the device is shown below with a 500 by 500mm square work piece that shows the working range of the device. In Figure 1 the spindle is in its full vertical position for machining on the top surface. Figure 2 shows the lower horizontal position. By supporting the work piece with a 2-axis table, which can rotate about its vertical axis, the device has the ability to machine on the top horizontal surface of the work piece and the 4 vertical surfaces. Thus achieving 5-face machining.

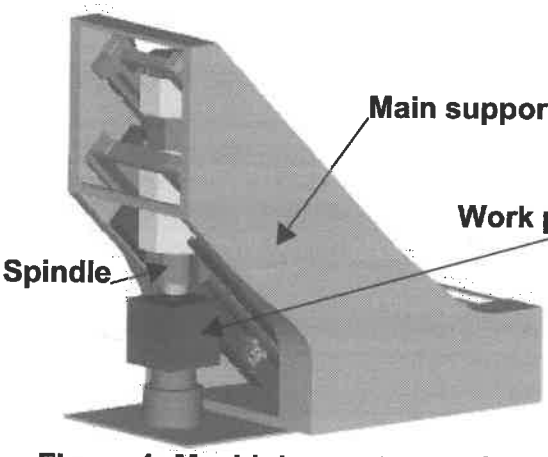

Figure 1: Machining on top surface

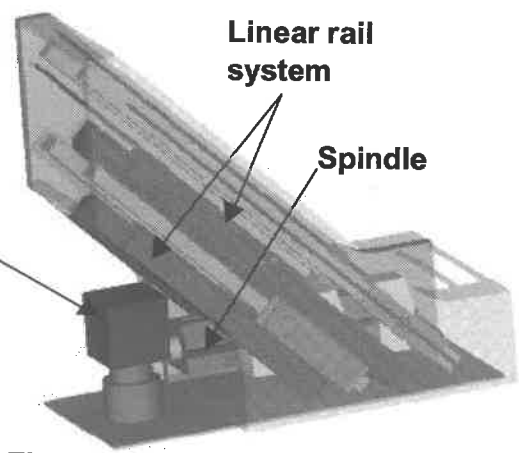

Figure 2: Lower horizontal position

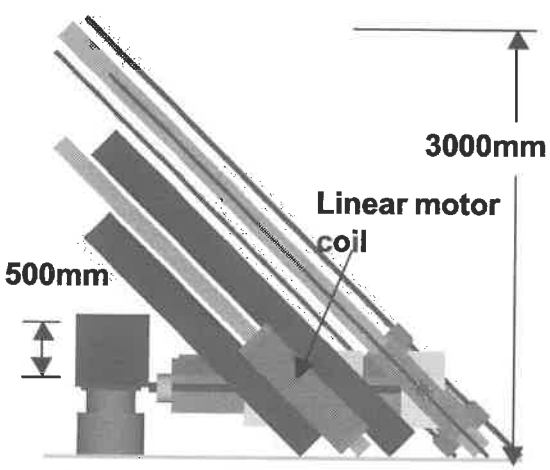

Figure 3: Lower horizontal position

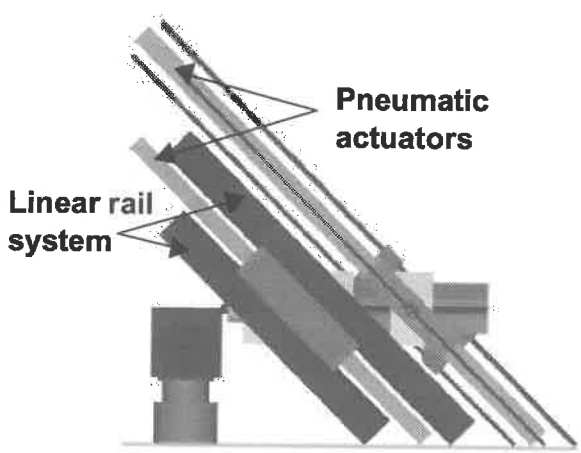

Figure 4: Upper horizontal position

Figure 2 also shows the main support of the device as partially translucent to show the placement of the linear guide rails. Figure 3 and 4 show the device without its main support. It shows the guide rails, pneumatic actuators and the linear motors. Figure 5 and 6 below show the device in intermediate positions at 45 degrees and 90 degrees respectively.

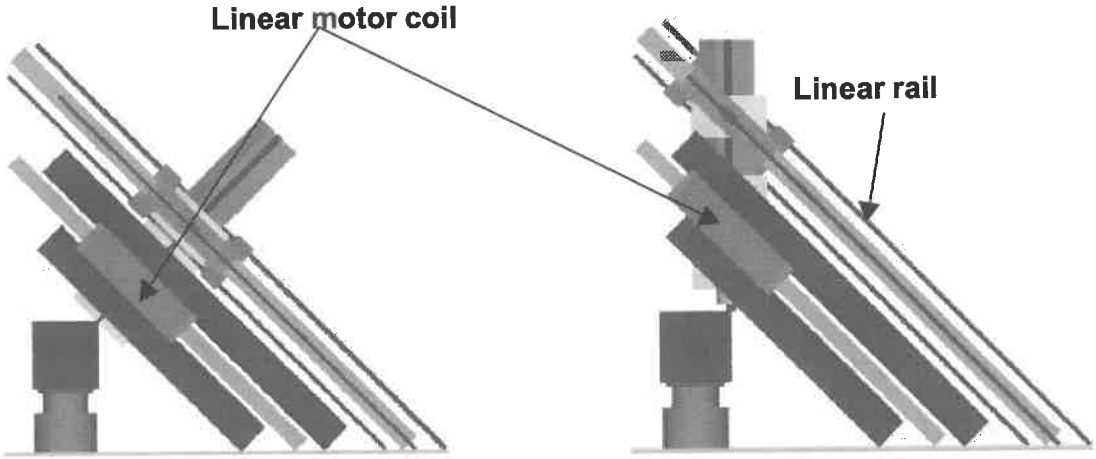

Figure 5: 45 degree position **Figure 6: 90 degree position**

Figure 7 shows the major components of the device: the spindle, the spindle supports, the frames and the linear motor coils. The frames support the motors and the pneumatic actuators and moves along the linear guide ways. The attached spindle supports, hold the spindle and can rotate up to 90 degrees while moving vertically. In addition, the spindle slides on rails in the spindle supports. Thus 3 axes of independent motion are possible. When combined with a 2-axis table, a 5-axis machine is created.

OPERATION OF THE DEVICE

The operation of the device is as follows:

1. The spindle can move towards or from the work piece under the power of a GE Fanuc 3000B linear motor located under the spindle (not shown).
2. Vertical movement occurs through the combined thrust from the pneumatic actuators and linear motors that move the frames and spindle assemblies along the linear guide rails. The pneumatic actuators act as a ballast, offsetting the weight of the spindle and its assemblies against gravity. Thus allowing the linear motors to only work against the inertia of the assembly. There are three linear motors that provide vertical thrust. Two GE Fanuc 15000C linear motors in the front, on either side of the spindle and one 15000C linear motor in the rear along the side of the spindle.
3. Rotation of the spindle is caused by differential thrust from the front and rear linear motors and can be done while the spindle is being extended or withdrawn. Thus allowing for 2-axis motion of the spindle.

Rotation of spindle support is possible due to a 3 degree of freedom joint (3 DOFJ) as shown in Figure 8. This device allows for linear movement along 2 axis and rotation about another. This joint connects the spindle supports with the linear rail systems (not

shown together). For precise single axis machining, the Zimmer electro-pneumatic clamps on the 3 DOFJ are activated, locking all movement except for the spindle on its linear rails. Thus allowing the spindle to move toward or from the work piece.

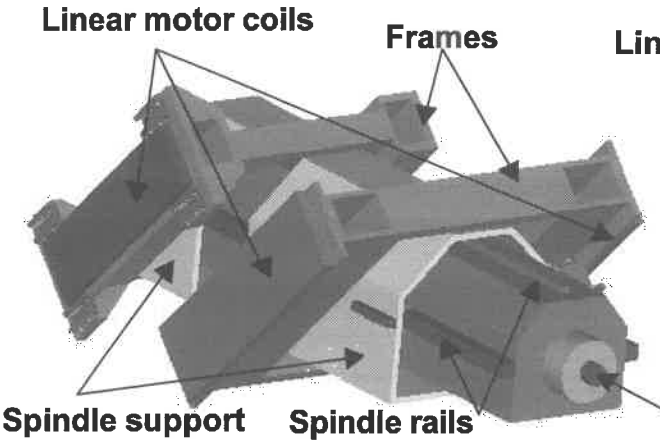

Figure 7: Main components

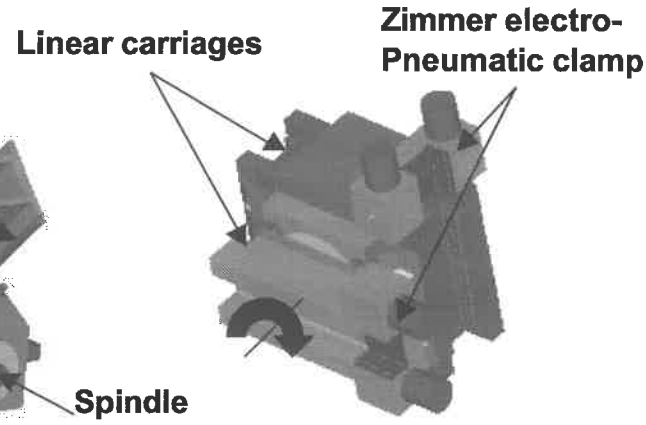

Figure 8: 3 Degree of freedom joint

SIMULATED PERFORMANCE

Using the simulation approach previously discussed, a static, modal and large motion analysis of this device was performed. The static deflections of the spindle where shown to be less than 10 microns due to cutting loads and gravity. A motion analysis using 2-axis movement, to trace a 100mm circle showed deviations less than 5 microns at tracing velocities up to 167mm/sec. Positioning performance of the spindle, under power form the pneumatic actuators and linear motors, showed a maximum acceleration of 1.5 g's. These performance results were deemed acceptable.

CONCLUSION

This design has been successfully simulated as a digitally engineered prototype. This work will be expanded to include an error budget analysis, which will be used to evaluate the ability to manufacture the device and the expected accuracy. This analysis will incorporate the static, dynamic, kinematic and thermal errors of device as derived from simulation work.

REFERENCES

[1] Pritschow, G.,"A Comparison of Linear and Conventional Electromechanical Drives", Annals of CIRP Vol. 47/2/1998.

[2] Warneche, H., Neugebauer, R., Wieland, F., "Development of Hexapod Based Machine Tools", Annals of the CIRP Vol. 47/1/1998, pp.337-340.

[3] Tlusty, J., Ziegert, J.C., Ridgeway, S., "Stiffness of Structures and Drives in Fast Milling Machines", Paper 1999-01-2273, SAE Aerospace Manufacturing Technology Conference & Exposition, Bellevue, WA, June 1999.

[4] Heisel, U., Ziegler, F., Hestermann, J.-O., "Optimization Possibilities of Parallel Kinematic Machine Tool Structures", Paper 1999-01-2276, SAE Aerospace Manufacturing Technology Conference & Exposition, Bellevue, WA, June 1999.

NANOMETER CUTTING MACHINE EMPLOYING PARALLEL MECHANISM

Katsushi Furutani, Ryusei Kudoh, Naotake Mohri
Toyota Technological Institute, Nagoya 468-8511 Japan

1. Introduction

Today, fabrication of nanometer-scale structures using scanning probe microscope (SPM) instruments are actively investigated [1]-[3]. A tripod or a tube type piezoelectric actuator is generally used to scan a specimen with fine *xyz*-motions. An interference among the three orthogonal motions exists for both the tripod and the tube type and it becomes significant particularly for a large displacement. Therefore, the authors has proposed a SPM type machine tool employing a parallel mechanism with 6 degrees of freedom [4]. Small angles of elevation of links is designed to make a resolution in the *z*-direction fine in the prototype. However, its motion was sometimes unstable due to singular points.

In this paper, a structure of a fine motion device employing the parallel mechanism is improved at first. Then the performance of the device is discussed. Finally, the application of the stage to a nanometer cutting machine with an atomic force microscope (AFM) structure is described.

2. Structure of nanometer cutting machine

Fig. 1 shows an overview of a fine motion stage for a nanotemer cutting machine. The stage supported with 6 links with an elevation angle of 35° stands on a base platform. The machine measures 170×170×108 mm. A table weighs 103 g. The movable range of the table is 30×40 μm in the *x*- and *y*-directions and 100 μm in the *z*-direction. Stacked piezoelectric actuators with dimensions of 5×5×20 mm are used to change the link length. They extend 16 μm at an applied voltage of 150 V. Displacement of the piezoelectric actuator is magnified over 8.6 times (approximately 100 μm) with a lever mechanism with flexure hinges made of ANSI 304 stainless steel. The generative force of the lever mechanism is 3.3 N. Its residual vibration is absorbed with a friction damper. Both ends of the links are connected with the base platform and the table by flexure joins which spring constant is 3.5×10^4 N/m. The motion of the stage is controlled by a feedback of link displacements. The displacement of each link is measured with an eddy current sensor with a frequency range up to 18 kHz.

Fig. 2 illustrates a block diagram of a control system. A given posture of the table is resolved into the link lengths by inverse kinematics. Then, the link lengths are given as references in each

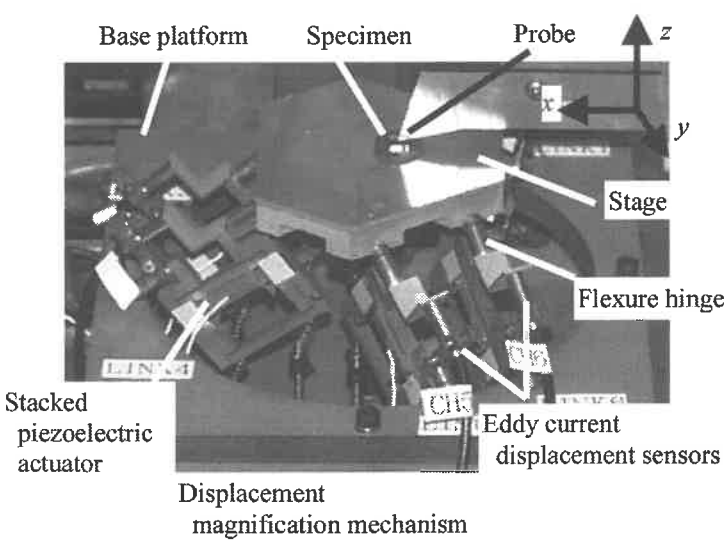

Fig. 1 Appearance of fine motion stage

servo systems with a proportional-integral (PI) controller. In each servo systems, a digital low pass filter with a cutoff frequency of 100 Hz precedes each controller in cascade in order to prevent the vibration of the lever mechanisms which resonant frequency is approximately 300 Hz.

The controller is installed in a personal computer (80586, 100 MHz). The manipulation signal through a 12 bit D/A converter is given to the piezoelectric actuator through a voltage amplifier. The feedback signal is obtained with a 12 bit A/D converter.

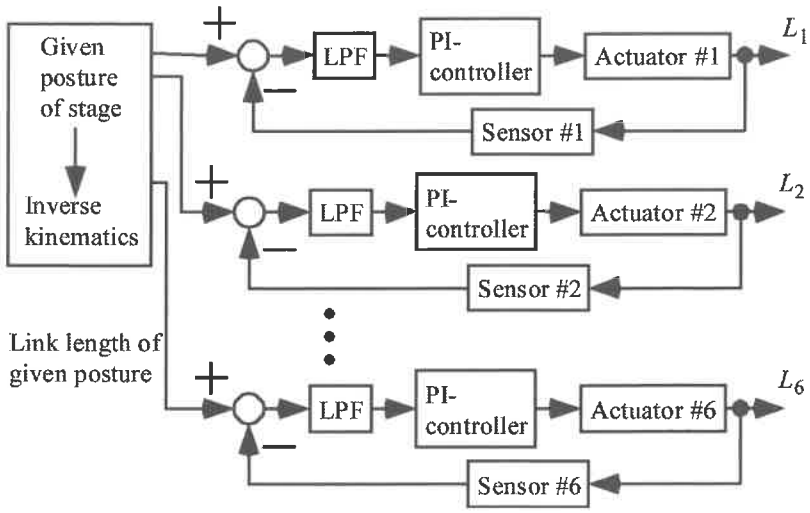

Fig. 2 Block diagram of control system

3. Displacement performance

Fig. 3 shows an example of displacement of the stage in the case of driving in the x-direction. Displacement of the stage is measured with capacitance displacement sensors. Interference in the y- and z-directions are 10 and 14 %p-p, respectively. A pitching error is 7.5×10^{-5} rad. Position errors of the link ends form the designed ones in assembly process cause the motion error. Though a resolution of the lever mechanism is 170 nm, resolutions of the stage are 100 nm, 143 nm and 115 nm in the x-, y- and z-directions, respectively.

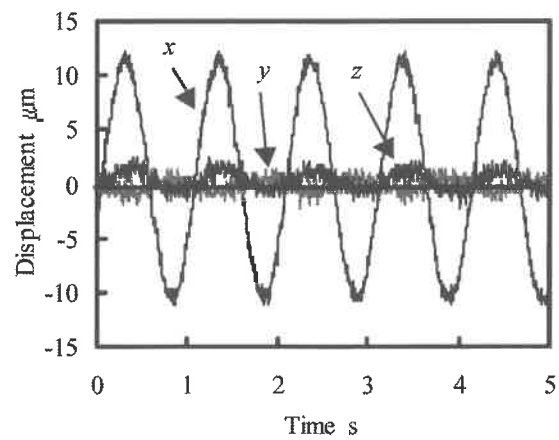

Fig. 3 Example of stage displacement driven in x-direction

To evaluate the displacement performance in detail, an atomic force microscope (AFM) is composed with the stage. Fig. 4 shows a configuration of the AFM. A contact mode cantilever with a length of 200 μm and a spring constant of 0.16 N/m is arranged above the stage. A probe tip mounted on the end of the cantilever is made from Si_3N_4. A beam from a semiconductor laser irradiates the back of the free end of the cantilever. A deflection of the cantilever is detected as a position of the reflected light with a quadrant photodiode. The probe is scanned within 10×10 μm on an optical flat with an accuracy of $\lambda/20$. The stage is scanned on the horizontal plane by triangular waves with frequencies of 2 and 0.05 Hz in the x- and y-directions, respectively. The standard deviation of a motion error from the plane is 34 nm.

A force curve is also measured to evaluate the z-motion. Fig. 5 shows an example of the force curve measured in air. The vertical and horizontal axes indicate the output of the quadrant

photodiode and the commanded displacement of the table in the z-direction, respectively. A silicon wafer cut along (001) plane is used for a specimen. The stage is driven by a triangular wave with a frequency of 1 Hz and an amplitude of 4 μmp-p in the *z*-direction. The output of the photodiode is proportional to the deflection of the cantilever. The positive deflection corresponds to the repulsive force between the probe and the specimen. The probe approaches the specimen when the table moves upward. The linearity of the motion is 3.8 % between 1.3 (A) and 1.8 μm (B).

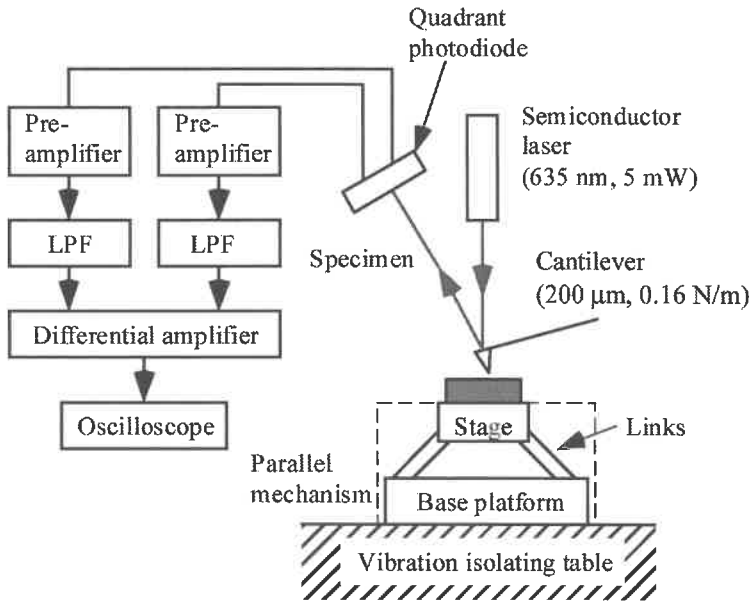

Fig. 4 Configuration of AFM

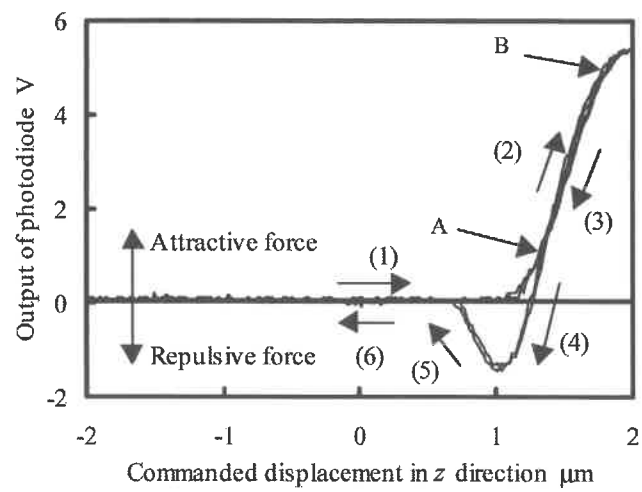

Fig. 5 Example of force curve

4. Nanometer cutting experiments

Because polymer resin is light, and has good machinability and chemical stability, it is expected to apply to precision parts and materials for micro-machines. Acrylic resin is scratched with the probe. At first, an inclination of a workpiece is measured by scanning roughly. Then the stage is moved in parallel to inclined surface of the workpiece and the probe scratchs it. Finally, the scratched area is observed.

Fig. 6 shows an example of scratching. The probe is scanned within 10×10 μm for the observation and within 5×5 μm for the scratching with a pressing force of 450 nN. The scanning frequencies are 2 and 0.05 Hz in the *x*- and *y*-directions, respectively. A pocket with a depth of 28 nm can be machined after 100 scratches. A stack of debris is observed near the pocket. Fig. 7 shows a change of depth against the number of scratch. The surface is seldom machined below 25 times. However, the depth of the pocket is linearly increased over 25 times. Once a scratch occurs by some reason, machining proceeds constantly.

5. Conclusions

The following conclusions can be drawn through the experiments.

(1) A stage for an AFM by using a parallel mechanism with 6 degrees of freedom is build as a trial.
(2) The movable range of the prototype is 40×30×100 μm in the *x*-, *y*- and *z*-directions.
(3) A pocket with dimensions of 5×5×0.03 μm is machined by scratching 100 times.
(4) The motion performance is evaluated by composing an AFM.

The authors will improve the motion accuracy of the stage.

Acknowledgment

This study is financially supported by Electro-Mechanic Technology Advancing Foundation, the Grant-in-Aid for Academic Frontier for "Future Data Storage Materials Research", for High-tech Research Center for "Space Robotics" and for Scientific Research (C)(2)(13650289) by the Ministry of Education, Sports, Culture, Science and Technology of Japan.

References

[1] D. M. Eigler, E. K. Schweizer: Positioning Single Atoms with Scanning Tunneling Microscope, Nature, 334, p. 524 (1990).

[2] B. Bhushan, V. N. Koinkar: Tribological Studies of Silicon for Magnetic Recording Applications, J. Appl. Phys., 75, pp. 5741-5746 (1994).

[3] K. Asamoto, K. Furutani, N. Mohri: A Basic Study on Nanometer Cutting of Brittle Materials, Proc. 12th ASPE, Norfolk, VA, USA, pp. 466-469 (1997).

[4] K. Yamakawa, K. Furutani, N. Mohri: XYZ-stage for Scanning Probe Microscope by Using Parallel Mechanism, Proc. 1999 ASME DETC99/MOVIC, Las Vegas, NV, USA, pp. 8425/1-6 (1999).

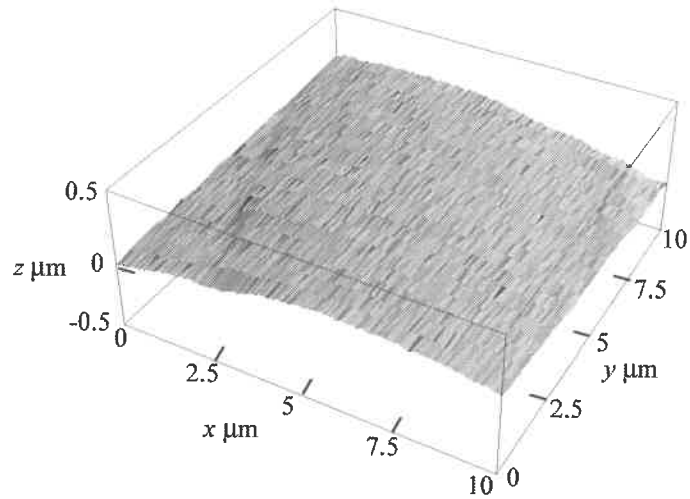

(a) Before scratching

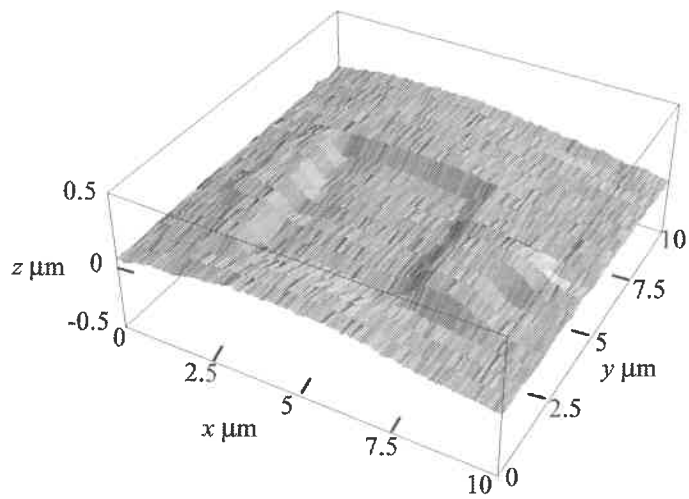

(b) After 100th scratching

Fig. 6 Example of scratching

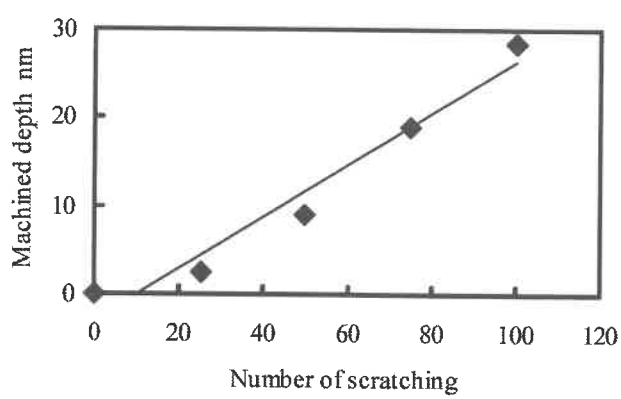

Fig. 7 Progress of machined depth

DESIGN OF A KINEMATIC SPINDLE FOR LOW-FORCE, LOW-SPEED APPLICATIONS

King-Fu Hii, Eric Wolsing, and R. Ryan Vallance
Precision Systems Laboratory, University of Kentucky, Lexington, KY *

Abstract

This paper describes a spindle for low-force, low-speed applications that is kinematically constrained and therefore based on the principles of exact constraint. The position and orientation of the spindle shaft is constrained at five contact points; four constraints are arranged radially around the shaft, and one constraint is located at the end of the shaft. In this paper, we describe the concept, detailed design of a prototype spindle, and analyses conducted during the detailed design. A simple 2D simulation is presented, which suggests that a shaft with a dominant periodic, multi-lobed roundness profile should cause the shaft's centerline to trace simple linear or circular trajectories. If the prototype spindle demonstrates repeatable error motions that are functions of the shaft rotation angle, then compensation may enable a spindle that is both highly repeatable and highly accurate. In addition, this spindle concept is amenable to micro positioning applications by incorporating position-controlled actuation at the constraint points. Although a prototype spindle was completed, experimental testing is not yet complete.

Keywords: machine design, spindle, kinematic constraint, exact constraint, axis of rotation

Introduction

In several ultra-high precision systems, linear motion is guided with sliding or rolling contact bearings that are arranged in a kinematic or exact constraint fashion [1]. A kinematic arrangement typically assures high repeatability, and accuracy is then attainable with accurate ways and rollers. In metrology applications, linear bearings employing thin polymer coatings have demonstrated that point contact between a bearing pad and way is sustainable with little wear [2]. The Nanostep profilometer from Rank Taylor Hobson (originally Nanosurf 2 [3]) and the NIST Molecular Measuring Machine [4] apply this technique. Despite the success of this approach in linear bearing systems, rotary bearings based on these principles have received little attention.

In the Precision Systems Laboratory at the University of Kentucky, we are designing an electro discharge micro milling machine [5]. The machine entails three axes of Cartesian motion and uses a pre-existing XY stage. Unlike a machine tool's spindle, a spindle in the micro EDM machine is not subjected to large forces, and high speeds are not necessary. Furthermore, there is an opportunity to simplify the machine configuration if the fine motion in the Z-axis is incorporated into the spindle. We are therefore interested in designing a high precision spindle for low-force and low-speeds that can eventually allow translation along the axis of the rotary motion.

In considering these requirements, we became interested in a spindle that used sliding contact constraints similar to those employed in linear bearings [2]. This paper describes the concept, design of a prototype spindle, and analyses conducted during the design. Results from a simple 2D simulation suggest that a shaft with a periodic, multi-lobed roundness profile should cause the shaft's centerline to trace simple linear or circular trajectories. A prototype spindle is fabricated, but measurement of error motions [6] is not complete and will therefore be presented in future work.

Conceptual Design of the Spindle

The kinematic spindle employs the principles of exact constraint [1] in establishing the position and orientation of a rotating shaft. Five constraints should be applied to the shaft so that the only free degree of freedom is rotation about the shaft's centerline. One approach to arranging the five constraints is to position a constraint acting axially along the centerline of the shaft and to position two pairs of constraints acting radially on the shaft. A finite distance along the shaft must separate the pair of radial constraints.

With appropriate nesting forces, the constraints can be established using five points of contact. This arrangement of constraints on a rotating shaft is illustrated in Fig 1. The axial constraint is simply a

* *Precision Systems Laboratory, Mechanical Engineering, University of Kentucky, 210-A CRMS Building, Lexington, KY 40506. http://www.engr.uky.edu/psl.*

rotating ball placed between the shaft's end and a rigid plate (magnetic base). The radial constraints are contact between the shaft and cylinders. Appropriate nesting forces are established by tension in the flexible drive belt and permanent magnets that lift the shaft towards the magnetic base. The shaft is free to rotate by sliding on the contact points when torque is transmitted from a servomotor through an o-ring belt. Radial and axial motions of the shaft are constrained by these five contact points. A similar configuration using line contact rather than point contact is used in a commercial μEDM machine [7].

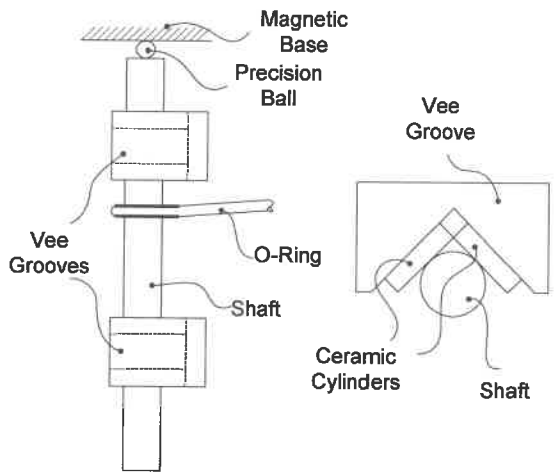

Fig 1: Kinematic Spindle Constrained with Five Contact Points

The principal advantage of the kinematic approach illustrated in Fig 1 is that repeatable error motions should be obtained. This means that radial and axial errors during shaft rotation should be repeatable functions of the shaft rotation angle. If repeatable motions are obtained, then compensation can provide further reduction in error motion. The disadvantage, however, is that sliding contact limits the rotational speed and loads that can be applied to the spindle shaft.

Detailed Design of a Prototype Spindle

To explore the repeatability of the shaft's error motions and the limits imposed by sliding contact, we designed and fabricated prototype spindles as illustrated in Fig 2. The 2 inch (50.8 mm) long shaft was machined from 1.5 inch (38.1 mm) diameter 440C stainless steel, case hardened to Rc 55-60 (Thomson 60 Case Shaft). A final grinding operation will be done in the Machine Dynamics Lab at Penn State to hopefully obtain roundness errors of about 10 micro inches (0.25 μm).

An o-ring belt wraps around the shaft, and tension in the belt preloads the shaft against the radial contact points. Axial preload is established by an array of permanent magnets mounted above the shaft in the top plate. We will investigate the spindle performance with sliding on ceramic rods and a thin layer of polymer (e.g. Nylon, UHMW, Delrin, etc). The contact surfaces are mounted into the vee-groove foundation and top plate. A 0.23 HP (175 W) brushless, slotless motor (Aerotech BMS60) and PWM amplifier drive the shaft. A 3:1 transmission is achieved with a 0.5 inch diameter pulley on the motor's shaft. The tension in the o-ring belt is adjustable by sliding the motor mount away from the spindle shaft.

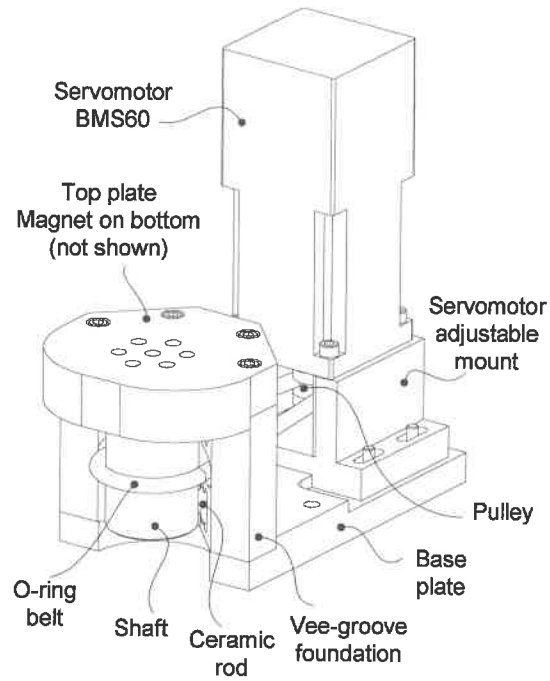

Fig 2: Prototype model for kinematic spindle

Analysis of the Detailed Design

The deterministic nature of exact constraint devices allows a thorough analysis during design. In analyzing the kinematic spindle, one should consider the following analyses:

1. Determine amount of tension required for transmitting power from motor to spindle shaft
2. Determine reaction and friction forces at five contact points based on belt tension and magnets
3. Analyze Hertzian contact
4. Size motor and transmission ratio

The tension in the o-ring belt can be determined using the Eq (1)-(3) where all values are in English units [8]. F_1 is the tight-side tension, F_0 is the slack-side tension, F_s is the minimum required tightening force, V is the belt velocity, θ is the wrap angle, μ is the coefficient of friction, F_c is centrifugal tension, A

is the belt cross section area, *pwr* is the power, and γ is the belt unit weight. The maximum tension necessary for the prototype spindle was estimated to be 3 lbs (13.6 N).

$$F_c = 0.104 \times 10^{-3} \gamma A V^2 \quad (1)$$

$$F_s = \frac{pwr}{2V} \frac{e^{\mu\theta}+1}{e^{\mu\theta}-1} + F_c \quad (2)$$

$$F_1 = F_s + \frac{pwr}{2V} \; and \; F_0 = F_s - \frac{pwr}{2V} \quad (3)$$

A static analysis, which considers belt tension, magnetic preload, and dynamic friction forces, yields the components of the five reaction forces at the contact points.

Once the reaction forces are known, the Hertzian contact stresses can be determined and compared with material yield strength. A comprehensive contact analysis should include both the reactions that act normal to the contact surfaces and tangential forces due to friction. The designer should refer to comprehensive references on contact mechanics [9]. Since the centerline of the shaft is perpendicular to the centerline of the constraint rods, an elliptical contact region is expected.

2D Simulation of Shaft Error Motion

Unlike other spindles, the error motion of the kinematic spindle's shaft should be deterministic and predictable a priori. The principal source of error motion is the out-of-roundness in the shaft. We can therefore simulate the error motion of the shaft centerline for particular roundness profiles. The roundness of a shaft can be modeled with Eq (5) [10].

$$r(\theta_i) = R + \sum_{k=1}^{\infty} C_k \cos(k\theta_i - \Phi_k) \quad (4)$$

Where,

$i = 1, 2, \ldots, N \qquad 0 \le \theta_i \le 2\pi$

R = nominal shaft radius

C_k = amplitude of k-th harmonic

Φ_k = phase angle of a harmonic

A typical roundness profile for a ground shaft might have multiple lobes. In this paper, the shaft is assumed to have a dominant 2-lobe, 3-lobe, 4-lobe, or 5-lobe roundness profile. We expect that as the shaft rotates on the vee-grooves, the shaft's center will follow a path that depends upon the roundness profile of the shaft. Fig 3 shows an example of the error motion produced by a 2-lobed roundness profile for two particular angular positions of the shaft. The position of the shaft centerline will oscillate horizontally (along the X' axis) as the 2 lobed shaft rotates counter clockwise.

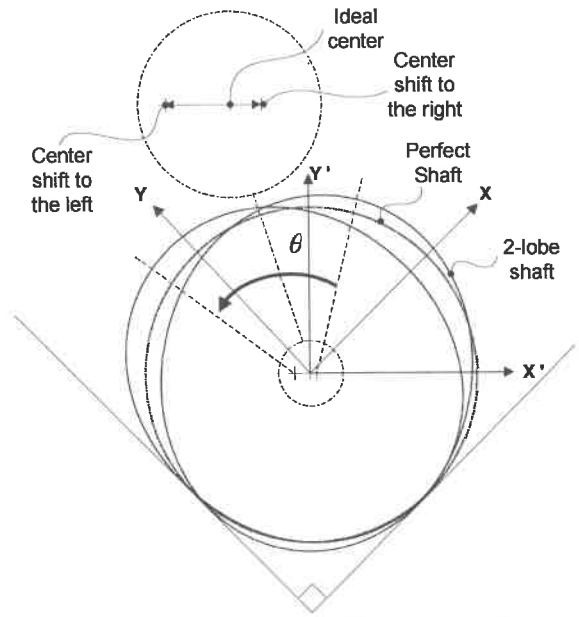

Fig 3: Displacement of Shaft Centerline for a Roundness Error with 2 Lobes

The shaft displacement error in the X and Y directions is given in Eq (6) and (7).

$$r_x(\theta_i) = \sum_{k=1}^{\infty} C_k \cos(k\theta_i - \Phi_k) \quad (5)$$

$$r_y(\theta_i) = \sum_{k=1}^{\infty} C_k \cos\left(k\left(\theta_i - \frac{\pi}{2}\right) - \Phi_k\right) \quad (6)$$

The magnitude of the shaft's displacement error at a particular shaft position is given in Eq (8).

$$r_{error}(\theta_i) = \left[\left(\sum_{k=1}^{\infty} C_k \cos(k\theta_i - \Phi_k)\right)^2 + \left(\sum_{k=1}^{\infty} C_k \cos\left(k\left(\theta_i - \frac{\pi}{2}\right)\right) - \Phi_k\right)^2\right]^{1/2} \quad (7)$$

For the simulation, the amplitude of the dominant mode and groove angle were assumed to be 10 μin and 90°. Fig 4 illustrates the predicted trajectories of the shaft centerline for various quantities of lobes in the roundness profile. For shafts having (4n-2) lobes, the trajectory of the shaft's centerline should oscillate along the X' axis (Fig 3) with a peak displacement of 14.1 μin (C_k/cos(45°)). For shafts with 4n lobes, the trajectory of the shaft's center oscillates in and out of the groove, along the Y' axis (Fig 3) with maximum displacement of 14.1 μin. And, for shafts with 2n-1 lobes, the shaft's center should trace 2n-1 circles

around the ideal shaft center with a radius equal to the amplitude of the dominant harmonic mode (C_k).

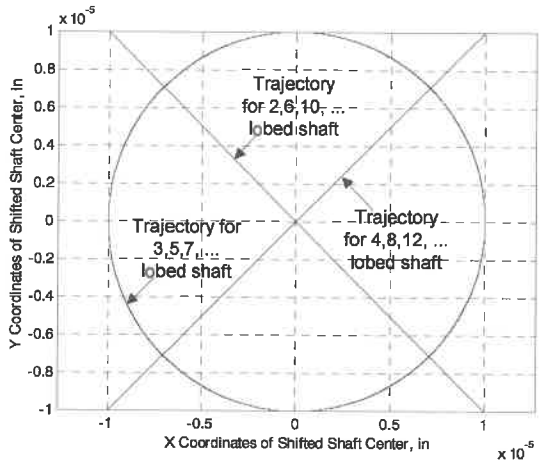

Fig 4: Trajectory of Shaft Centerline for Shafts with Various Quantities of Lobes

Fig 5 illustrates the magnitude of the shaft's displacement from the ideal center for a full rotation of the shaft for various quantities of lobes.

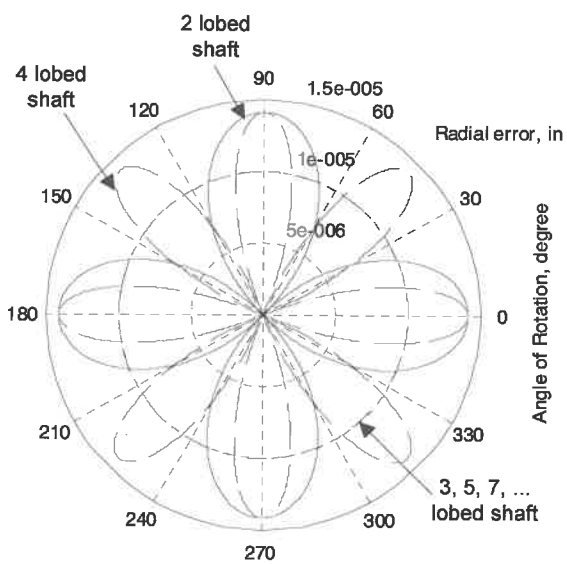

Fig 5: Magnitude of shaft displacement for any given angle of rotation for multi-lobed shafts

Conclusions and Future Work

Since sliding contact bearings with kinematic arrangement have been successful in ultra-high precision applications, we are now considering the performance of a spindle with sliding contact at kinematic constraints. This paper described the conceptual design and detailed design of a prototype spindle. A simple 2D simulation, suggests that shafts with multi-lobed roundness profiles should produce error motions with linear or circular trajectories of the shaft centerline. Future experiments conducted on the prototype spindle will test this hypothesis and be used to study the wear due to sliding at the contact points. If repeatable error motions are observed experimentally, then future work will consist of passive and/or active compensation for attaining a precise and accurate axis of rotation.

References

[1] Blanding, D.L. *Exact Constraint: Machine Design Using Kinematics Principles*. ASME Press. New York. 1999.

[2] Smith, S.T., H. Yang, and R.M. Seugling. "Polymeric Bearings for Nanotechnology Applications". *Proceedings of the American Society for Precision Engineering Summer Topical Meeting on Precision Bearings and Spindles*. State College, PA. June 18-19, 2001. p. 70-75.

[3] Lindsey, K., S.T. Smith, and C.J. Robbie. "Sub-Nanometer Surface Texture and Profile Measurement with 'Nanosurf 2'. *Annals of the CIRP*. Vol. 37. p. 519-522.

[4] Evans,C.R., R.S. Polvani, F.E. Scire, A.W. Ruff, X.Z. Hu, and E.C. Teague. "Way Systems for the Molecular Measuring Machine". 5th Int. Precision Engineering Seminar. Sept. 18-22, 1989. Monteyrey, CA.

[5] Hii, K.F., X. Zhao, and R.R. Vallance. "Design of a Precision Electro Discharge Micro Milling Machine". *Proceedings of the American Society of Precision Engineers Annual Conference*. Scottsdale, Arizona. October 22-27, 2000. p. 353-356.

[6] "Axes of Rotation – Methods for Specifying and Testing". ASME 89.3.4-1985. American Society of Manufacturing Engineers. 1985.

[7] Masaki, T., T. Mizutani, K. Yonemaochi, and A. Tanaka. "Electric Discharge Machining Method and Apparatus for Machining a Microshaft". U.S. Patent #4,900,890. Issued Feb. 13, 1990.

[8] Burr, A. H. and Cheatham, J. B. *Mechanical Analysis And Design*. 2nd Edition. Prentice Hall. Englewood Cliffs, New Jersey. 1995.

[9]Johnson, K.L. *Contact Mechanics*. Cambridge University Press. Cambridge, Great Britain. 1987.

[10] Cho, N. and J. Tu. "Roundness modeling of machined parts for tolerance analysis". Precision Engineering. 25 (2001). p. 35-47.

ERROR COMPENSATION OF THE MAGLEV STAGE SUPPORTED BY PERMANENT MAGNET BIASED MAGNETIC BEARING

Sang-Ho Lee*, Jee-Uk Chang*, Sang-Wook Lee*, Oui-Serg Kim*, Dong-Chul Han** and In-Bae Chang***

* Graduate student, School of mechanical and aerospace eng. Seoul National Univ, Seoul, Korea

** School of mechanical and aerospace eng. Seoul National Univ. Seoul, Korea

*** School of mechanical and aerospace eng. Kangwon National Univ. Chuncheon, Kangwon, Korea

Abstract

This paper provides the design of permanent magnet biased magnetic bearing and the error compensation of the maglev (magnetically levitated) stage supported by this bearing. A magnetic bearing composed of only two electromagnets needs large amount of bias current to support its own weight so that its load capacity is limited and the energy consumption becomes large. To eliminate these drawbacks of the electromagnetic bearing, the permanent magnet is proposed to provide a bias flux generating a bias force. In this paper, the two-dimensional configuration of the permanent magnets is designed to make the analysis simple and is adopted to the linear motion stage as a magnetic suspension. This paper will show the traveling error compensation of the maglev stage supported by the permanent magnet biased bearings with experimental test.

Keywords : permanent magnet biased magnetic bearing, linear motion stage, error compensation

1. Introduction

It is common to use the bias linearization method that linearizes the non-linear characteristics of the magnetic bearing. The bias current of the electromagnetic bearing limits the load capacity and causes the heat problem.

Many research have been studied to reduce the energy loss due to the bias current. Sotore [1] decreases the power consumption and heat problem successfully superposing the flux paths of the electromagnet and the permanent magnet.

The magnetic bearing using permanent magnetic bias flux can reduce the energy consumption and Pang [2] adopts it to the flywheel energy storage device. The research mentioned above are the application in the rotation machinery only and Han et al [3] adopt the permanent magnet biased magnetic bearing to the linear motion system firstly. They use NdFeB the rare earth permanent magnet with three-dimensional arrangement and make a flux path of the electromagnet does not pass through the permanent magnets to prevent the demagnetization of the permanent magnets. They also show the linearity of the displacement stiffness and current stiffness from the static load tests. However, there is uncertainty in the modeling and the analysis with three-dimensional arrangement of the permanent magnets.

In this paper, the new actuator can be modeled more accurately with two-dimensional arrangement of the permanent magnets and the magnetically levitated stage using the permanent magnet biased magnetic actuator is designed for the high precision linear motion system. Moreover, the error occurred during the positioning of the stage is compensated for by dual servo controller which compares with the signals from the external metrology frame and built-in sensor each other.

2. System Configuration

Permanent magnet biased magnetic bearing

An electromagnetic bearing needs large amount of bias current to support its own weight so that its load capacity is limited and problems caused by heat generation can be arose. In order to remove these

drawbacks of the electromagnetic bearing, we developed a new permanent magnet biased electromagnetic bearing using a rare earth permanent magnet. The permanent magnet provides a bias flux and generates a bias force. The electromagnet can increase or reduce a flux of the permanent magnet and the flux path of the electromagnet does not pass through the permanent magnet that the permanent magnet will not be demagnetized. The permanent magnet biased magnetic bearing consists of three laminated steel cores, two electromagnet coils and two permanent magnets as shown in Fig. 1.

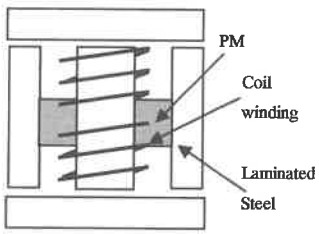

Fig. 1 Schematic of the permanent magnet biased actuator

The two electromagnet coils are located in the upper and lower legs of the center steel core and connected in serial with the same direction. The two permanents are located between legs of center and outer side steel cores. The thickness of the permanent magnet is selected as much as the thickness of the air gap is negligible. The flux of the permanent magnet is gathered at center steel core and then forms the same magnitude of the magnetic fields both at the upper and lower side following the black colored arrows shown in Fig.2.

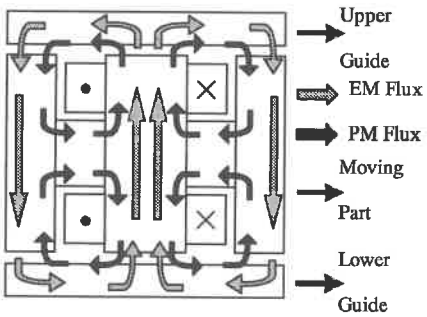

Fig. 2 Flux paths of the actuator

Maglev Stage

The magnetic bearing module to support the magnetically levitated stage is manufactured and is consists of one permanent magnet biased actuator and one conventional electromagnetic bearing to support the vertical and the horizontal load respectively. Three capacitive sensors are built in the same module to perform the closed-loop control for stabilization of the magnetic bearing measuring the displacement against the guideway. Fig. 3 shows the schematics of newly designed magnetic bearing module.

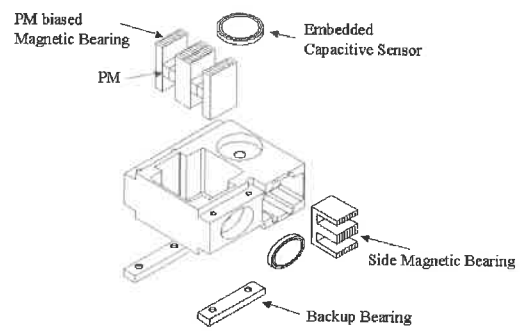

Fig. 3 Schematics of the magnetic bearing module

Providing that there must be no coupled motion to the each mode direction, the stage has to be designed the mass center symmetrically so that the coupled components of the inertia moment can be vanished. Therefore, the stage is designed symmetrically as possible as we can and the simplified model is analyzed for the size of the whole system and for the location of the each sensor, actuator and the motor with little coupled components.

The moving part of the stage shown in Fig.4 has four magnetic modules that consist of twelve capacitive sensors, four permanent magnet biased magnetic bearing for vertical direction and four electromagnetic bearings that form two pairs for horizontal direction.

(a)top view (b) bottom view

Fig. 4 Photos of the stage

Dual servo control using external metrology frame

Using the built-in sensors on the magnetic bearing module, the servo controller for the stage always has the Abbe error and the manufacturing error of the guideway. To compensate for the positioning error of the stage, it essentially needs reliable sensor system that is located on the metrology frame. If the sensor signal can be acquired

in real time and the signal bandwidth of the sensor that communicates with the stage is wide enough, then the dual servo control can be performed.

Fig.5 and Fig.6 show the configuration of the servo control using embedded sensors and the dual servo controller using external sensors respectively.

The external sensor signal can remove the steady-state error after it passes through the servo controller as it introduces the control command of the servo controller that uses the internal built-in sensor. $K_1(s)$ is the robust controller considering the disturbances and the noise in the system for the stabilization of the magnetic bearing.

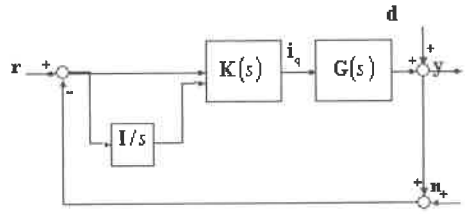

Fig. 5 Servo controller by embedded sensors

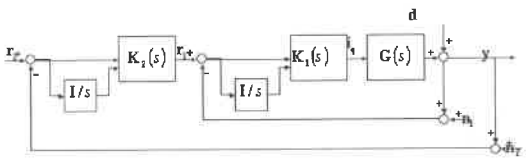

Fig. 6 Dual servo controller used additional external sensors

$K_2(s)$ is the command follower for the external measurement system. The transfer function that comes from r_1 to y has higher order than that of the system G so that an implementation of the robust controller K_s makes Ks of the higher order states and it is not desirable. Thus, the conventional PI (proportional-integral) controller is selected. The servo controller shown in Fig. 7 uses the robust controller $K_1(s)$ including no integral term and use a PI controller $K_2(s)$ as a command follower.

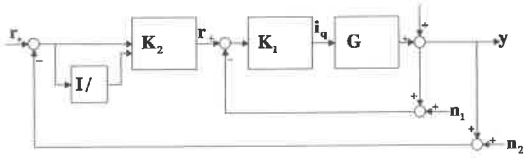

Fig. 7 Servo controller using external sensors

3. Plant modeling and control

The stage is assumed and can be modeled as a rigid body that has a six-degrees-of freedom in three-dimensional space. Fig. 8 shows the coordinates system of the magnetically levitated stage. The rotational motion of the stage can be assumed as a infinitesimal angle because it is much smaller than the total size of the system so that the equation of the motion can be linearized about the minute angle. The linearized equation of the motion is given by eq(1)

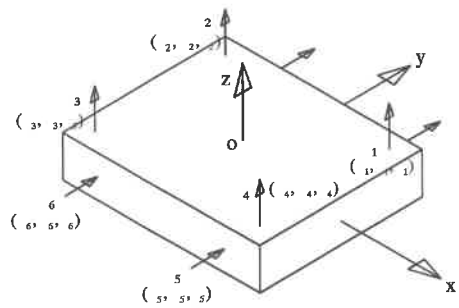

Fig. 8 Coordinates of the stage system

$$\begin{matrix} & 0 & 0 & 0 & 0 & & 0 & 0 & 0 & 0 & 1 & 1 & 1 \\ 0 & & 0 & 0 & 0 & & 1 & 1 & 1 & 1 & 0 & 0 & 2 \\ 0 & 0 & 11 & 12 & 13 & 1 & 1 & 2 & 3 & 4 & 5 & 6 & 3 \\ 0 & 0 & 21 & 22 & 23 & 2 & 1 & 2 & 3 & 4 & 0 & 0 & 4 \\ 0 & 0 & 31 & 32 & 33 & 3 & 0 & 0 & 0 & 0 & 5 & 6 & 5 \\ & & & & & & & & & & & & 6 \end{matrix} \qquad (1)$$

The stage has no mechanical contract and there is no mechanical stiffness and damping term but external force term only. Using the displacement feedback control with six external force $_1 \sim {}_6$, the stiffness and the damping term can be utilized as given in eq(2).

$$(\quad =1\sim6) \qquad (2)$$

4. Experiments

The stage moves following the differential sensor signal which means the centerline of the both sides of the guideways and the manufacturing and assembling errors of the guideways affect the positioning accuracy. In this paper, the external sensor signal is compared with the internal capacitive sensor signal and then the compared signal is used to compensate for the positioning errors during the motion. The external metrology frame shown in Fig.9 can measure the vertical displacement error, rolling and pitching error.

Error compensation

The strategy of the error compensation is to use the feedback control of the external sensor signal comparing with the internal sensor signal. The feedback control forms the dual servo controller basically as mentioned in section 2. Fig.10~Fig.12 show the positioning errors

including noise band of the stage when the dual servo control is adopted. The error in the vertical direction is 20nm, the rolling error is 0.02 arcsec and the pitching error is 0.04 arcsec respectively.

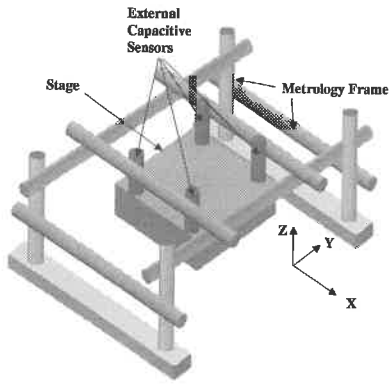

Fig. 9 Schematics of the metrology frame sensors

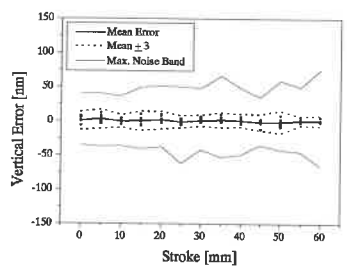

Fig. 10 Vertical traveling error compensation

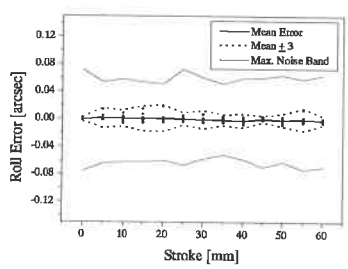

Fig. 11 Rolling error compensation of the stage

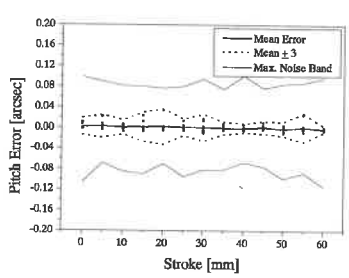

Fig. 12 Pitching error compensation of the stage

It is common to measure the target position at the work and the accuracy of the stage will be increased when the active feedback by the target position is performed.

5. Conclusion

The permanent magnet biased linear magnetic bearing has been designed and manufactured to apply to the linear motion stage. The positioning error compensation using dual servo controller has been also performed by the external sensor system located on the metrology frame. The stage provides the built-in capacitive sensors and tracks the centerline of the guideways following the differentiated sensor signal. The measured positioning profile differs from the desired profile because the guideways always include the manufacturing and assembling errors so that the error compensation is needed. The extra sensor system on the metrology frame located on the vibration isolation table is equipped and the compensation using a dual servo control is performed successfully.

Acknowledgment

This research is based upon BK21 and national research projects supported by the Institute of Advanced Machinery & Design at Seoul National University and Samsung electronics.

References

1.C.K. Sortore, P.E. Allaire, E.H. Maslen, R.R. Humphris, P.A. Studer, "Permanent magnet biased magnetic bearings-design, construction and testing", 2'nd International Symp. On Magnetic Bearing, July, 1990, Tokyo, Japan.

2.Pang, Da-Chen, "Magnetic Bearing System Design for Enhanced Stability", Ph.D Thesis, University of Maryland, 1994

3.Dong-Chul Han, In-Hwang Park, Hyeong-Joon Ahn, Sang-Ho Lee, Oui-Serg Kim and In-Bae Chang, "The high precision linear motion table with a novel rare earth permanent magnet biased magnetic bearing suspenstion" Proceedings of ASPE 13th annual meeting, Oct, 1998, St.Louis, MO, USA

Design of ultraprecision modular, Freeform® machine tool

R. Koning and M. Walter
Precitech Inc, Keene, NH 03431

Key words: ultra precision machining, free form optics, diamond milling, modular

Abstract

The Freeform® 3000 ultra precision machine tool has been developed to satisfy a need for a unified affordable multi-axis machine with the capability of milling, grinding and turning ultra precision surfaces. Demand for a universal ultra-precision machine emerges from developments in grinding and milling conformal optics, lens arrays, grooved patterns and diamond turning. This paper discusses the design challenges of the Freeform® 3000 machine and the culmination of enabling technologies. The final machine configuration was determined by evaluating precision, stiffness and modularity. Ultra precision machine elements have been reinvented to accommodate the new configuration. Finite element models were used to evaluate static and dynamic performance of machine components. A steady state thermal analysis of the machine has been compiled which pinpointed areas for thermal error reduction. A thermal environment has been created to hold the machine temperature stable to less than ±.05 C°(.1 F°). Cutting tests display that the machine is appropriate for milling three dimensional forms, diamond turning axis-symmetric components and grinding in a flood-cooled environment.

Configuration

Several machine configurations have been evaluated for the following criteria: Flood coolant compatible, commonality of parts, ease of build, ability to single point diamond turn, ability to diamond mill, and modularity. It is common to think of machine configurations in a conventional manner, however this can lead the ultra-precision designer down the wrong path. Fundamental to ultra-precision machine design is that relative motion between moving elements be facilitated by a fluid film and be free of contact. The fluid film provides an averaging effect, which in turn produces straightness and truth-of-motion in excess of the individual elements. Contact between moving elements through a seal or service loop produces undesirable forces and error motion. Sealing slides from machining debris must be facilitated through the use of non-contacting labyrinths. Service loops must be supple and the number of cables minimized when ever possible. Finally, cables must be bundled in a manner to provide a neutral axis that remains parallel throughout the slide travel.

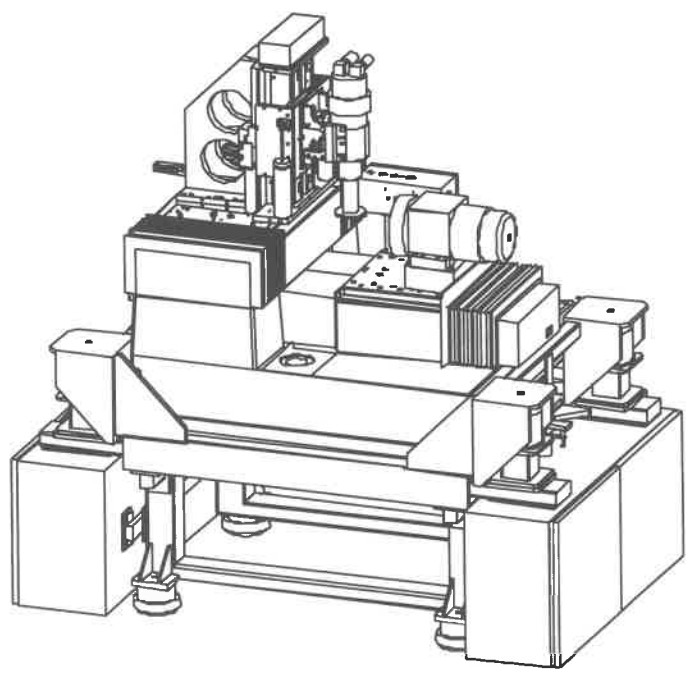

Figure-1
Freeform®-3000 machine
Guards and covers removed

To produce three axes of motion, at least one axis must be mounted onto another. However, if the moving slide way causes a transfer of mass, then a compromise in slide straightness will result. The Freeform® 3000 was designed with a 150 mm vertical slide mounted onto a 350 mm horizontal slide and a third 250 mm horizontal slide mounts orthogonal to the other two slides to produce the final axis of motion. During the conceptual phase of the Freeform® 3000, it was determined that a non-contacting bulkhead design would separate the cutting process from the combination slideways, to provide isolation for flood coolant[1].

The Freeform® 3000 is based on a modular design. The machine base, oil hydrostatic box slides, frame, electrical and pneumatic cabinets were designed to be common for a family of three separate machine tools, Nanoform® 350, Nanoform® 700 and the Freeform® 3000. The common modular design facilitates economies of scale for the components and an ability to build up the machine subassemblies to a level and then quickly react to customer demands.

Machine Elements

All three linear slideways utilize oil hydrostatic pads, at a supply pressure of 250 psi, and linear motors to produce ultra-precision contouring and positioning. Hydrostatic "box type" slide ways were chosen in each axis for their stiffness and ability to provide straight slide travel.

A small high stiffness vertical slide was developed to mount onto a horizontal axis via an angle bracket. Emphasis for the vertical slide design was placed on reducing the moving mass, which would enable the servo bandwidth to remain high. Several counterbalance design concepts were evaluated for their ability to produce a neutralizing force, be non-influencing, convenient and inexpensive. A counter-balance air piston was chosen because it would not contribute a significant amount of inertia. Other frictionless designs such as a cable mass counterbalance double the moving mass and create a second order harmonic. Finally, the air piston counterbalance would be convenient and inexpensive to implement.

A standard commercially available cylinder was initially used which was rated for a frictional force equal to 1-2% of applied load. During implementation of the cylinders on the vertical slide, it was found that the friction produced an undesirable slide error. Several efforts to reduce the friction resulted in a design of a non-contacting aerostatic piston that was non-influencing[2] (Figure 2).

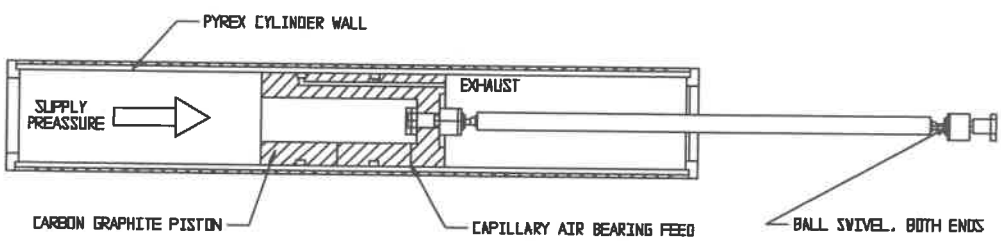

Figure-2
Frictionless air piston counter balance

To avoid reversal error and hysteresis, a design was employed which provides constant pressure to the air piston. The system includes a precision regulator, which maintains constant pressure to a bleed valve. The bleed valve allows an excess of 10 times the volume displaced by the maximum traverse rate, to be exhausted to the environment (Figure-3). The

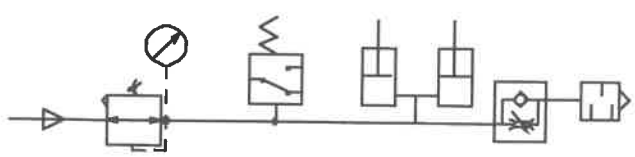

Figure-3
Counterbalance air piston schematic

[1] Alexander H. Slocum, "Precision Machine Design", Prentice Hall, 1992, P.
[2] Julius C. Boonshaft, U.S. Patent No. 3,319,534, 1967

constant non-reversing flow through the system reduces variations in force as a function of slide travel direction.

The new generation of lens and reflector elements is the free form surface shape, that has no axis of revolution but is instead a surface shape that could be defined by a map of points, an equation, or a computer model represented in solid form[3]. Freeform components require part cuts of up to several days and complete thermal stabilization. The Freeform® 3000 required a thermal enclosure and temperature controller which produced an environment within ±.05 C°(.1 F°)(Figure-4). Key machine elements such as the spindle riser and flycutter wheel were manufactured with Invar-36, a low coefficient of expansion nickel based alloy.

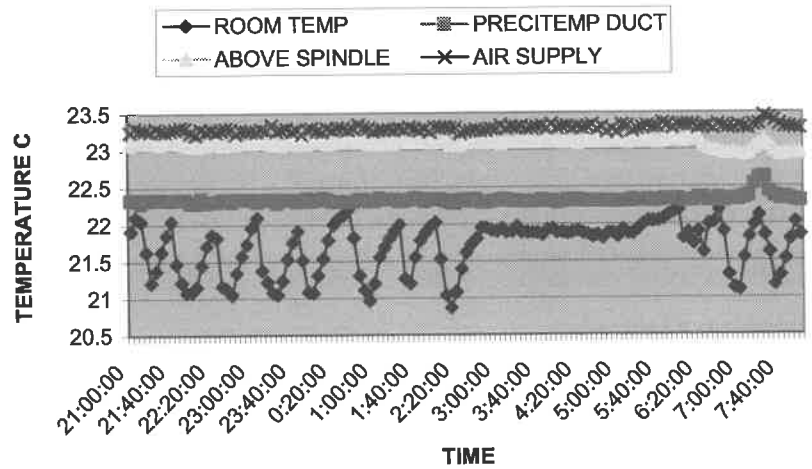

Figure-4
10 Hr machine temperature stability chart

With a diamond tool holder mounted onto the milling spindle riser (Figure-5) and a spindle mounted onto the horizontal slide, the Freeform® 3000 can be configured as a lathe. A tool holder design was evaluated using finite element analysis for stiffness and modes of vibration. Base line design parameters derived from a known diamond turning lathe have a stiffness greater than 150,000 lbs/in and first mode of vibration greater than 700 Hz. Several iterations were required to produce a tool holder, which met these criteria and still maintained a small moving mass. (Figure-6).

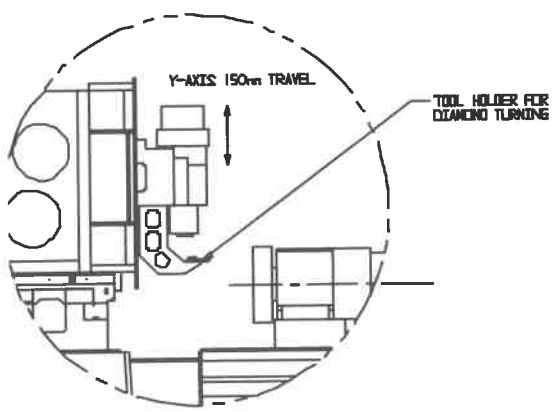

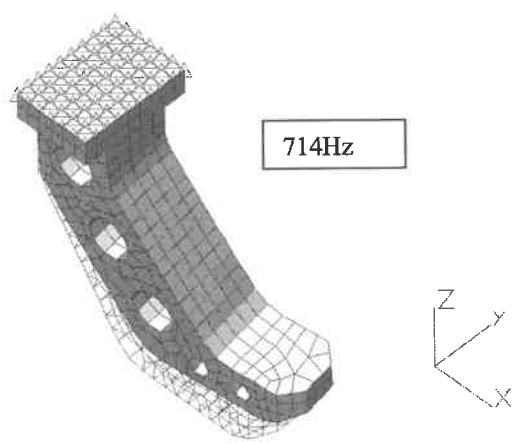

Figure-6
Tool holder for diamond turning

[3] P.D.Brehm, The Single Point Diamond Machining of Optical Microstructures and Freeform Surfaces, Euspen Conference Proceedings, Vol. 2, 1999

Machining Results

Diamond milled surfaces have been generated to a form accuracy of 0.204 µm per 1500 mm^2 in an 8-hr cycle with a surface finish of 15 nm RMS. Diamond turned surfaces have been created to a form accuracy of .057 µm P-V with a surface finish of 3nm on a Ø 75mm (250mm convex radius) spherical aluminum part. Peripheral ground parts have been generated to a form accuracy of .214 µm and a surface finish of 4.4 nm RMS. A repeatability test displayed that freeform parts can be created consistently in a 2.5 hr cutting test. Total variation for five part cuts, was 0.038 um P-V.

Surface finish for freeform machining is defined by the cusp height of the interrupted cut. Thermal stability of the machine is required for long part cuts. Surface finish can be predicted using the following equations:

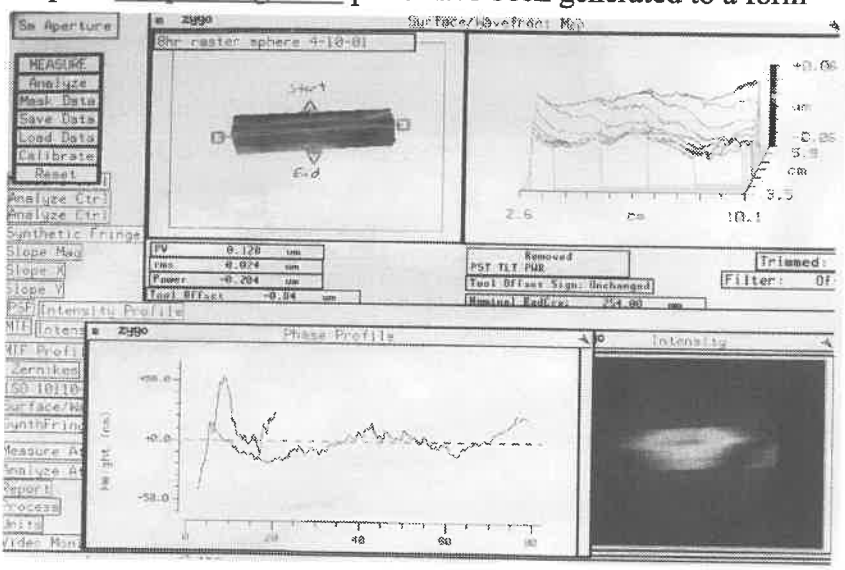

Figure-8
Freeform Cutting results

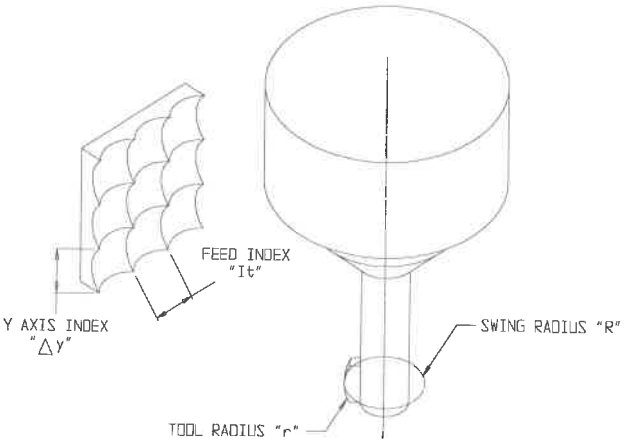

Cusp height in X feed direction.

$$Hcx := R - \frac{1}{2}\cdot\sqrt{4\cdot R^2 - \left(\frac{Fx}{S}\right)^2}$$

$$Hcx = 5\cdot 10^{-6}\ \cdot mm$$

Index (Δy) so that index cusp matches feed cusp.

$$\Delta y := 2\cdot\sqrt{Hcx\cdot(2\cdot r - Hcx)}$$

$$\Delta y = 0.014\cdot mm$$

Tool Advance:

$$It := \frac{Fx}{S}$$

$$It = 0.014\ \ mm/rev$$

Surface finish (rms)

$$Rq := \sqrt{\frac{It^4}{720\cdot R^2} + \frac{\Delta y^4}{720\cdot r^2}}$$

$$Rq = 2.09\cdot 10^{-9}\ \ rms$$

Figure-9
Cusp height definition

Conclusion

The Freeform® 3000 establishes an ultra precision diamond machining platform which is versatile in configuration, thermally stable, and easy to operate. The machine has been developed to meet the need for conformal freeform optics, lens arrays and grating patterns, while maintaining utility as a turning/grinding platform. Precision engineering disciplines have been applied to produce a cost-effective robust design. Machining results have produced components that exceed initial expectations.

ABSOLUTE STRAIN MEASUREMENT FOR FIBER BRAGG GRATING SENSOR USING A STRING RESONATOR WITH HIGH ACCURACY

Yeong-Kyoon Lee, In-Cheon Song, Sung-Ho Jeong, Byung-Ha Lee and Sun-Kyu Lee
Kwang-Ju Institute of Science and Technology, Gwangju, Korea

ABSTRACT

This paper describes a string resonator that is used for the interrogation system of a Fiber Bragg Grating (FBG) strain sensor. The strain on the fiber piece is calculated from the measured frequency based on that the natural frequency of a string is a function of the applied absolute strain. Existing research considered a fiber as a string, but a fiber is not a string in the strict sense due to its bending stiffness, thus the fiber should be modeled as a beam accompanied with an axial force. In the vibration modeling, the relationship between the strain and the natural frequency is derived, and then the resonance condition is described in terms of both the phase and the mode shape for sustaining resonant motion. Several experiments verify the effectiveness of the proposed model of the fiber.

Keywords: absolute strain, string resonator, fiber Bragg grating sensor, tunable-filter, high accuracy, resonance, beam model, string model

1. INTRODUCTION

Fiber Bragg Grating (FBG) is an optical fiber element, which is fabricated to show periodic change of the refractive index of the fiber core and reflects a narrow band of wavelength, called Bragg wavelength, when illuminated with a broadband light source. The principle of a FBG sensor is based on the fact that the Bragg wavelength of the sensing element shifts when strain or temperature change arises in the element. FBG sensors provide advantages such as distributed sensing using only single fiber line, ease of insertion and attachment, self-referencing capability independent of the total power level of the source and the loss of coupler or connection, high sensitivity, electromagnetic interference immunity, and multiplexing capability [1][2].

With wavelength interrogating method using Fiber Fabry-Perot (FFP) filter, a real-time strain measurement was achieved for wavelength division Multiplexing (WDM) with four FBG's, and quasi-static resolution of ~0.3με and ±3με was obtained for single and four FBG's, respectively [3]. However, this method shows inaccuracy in wavelength interrogation due to the hysteresis and the non-linearity of piezo actuator. To overcome this problem, a new interrogation system consisting of a FBG as the filter replacing FFP and a string oscillator for an absolute strain measurement was suggested[4]. By introducing the string oscillator that automatically sustains the fiber motion in phase with the excitation, an accuracy of ±2με and a quasi-static resolution of ~0.05με in 1200με dynamic range were reported. Despite the improvement, there exists a problem in this new system that the measured absolute strain was based on a modeling of the fiber as an ideal string, which could affect the validity of the measured strain.

In this work, a robust modeling of the string resonator is conducted, considering the stiffness of the string. A string resonator is designed and implemented to evaluate the effectiveness of the proposed model and the actual performance of the strain measurement system.

2. VIBRATION ANALYSIS

2.1 Natural frequency and strain.

Neglecting the damping of an ideal string, the motion equation for free vibration and the corresponding natural frequency are given by

$$P\frac{\partial^2 w(x,t)}{\partial x^2} = \rho_L \frac{\partial^2 w(x,t)}{\partial t^2} \tag{1}$$

$$f_i = \frac{i}{2L}\sqrt{\frac{P}{\rho A}} \tag{2}$$

where P is tension, L is length of the string, ρ and ρ_L are the density and linear density of the string material respectively, and

f_i is the i-th mode natural frequency in Hz. Eqn.(2) can be rewritten in terms of the strain as follows,

$$f_i = \frac{i}{2L_0(1+\varepsilon)}\sqrt{\frac{E\varepsilon}{\rho}} = \left(\frac{i}{2L_0}\sqrt{\frac{E}{\rho}}\right)\frac{\sqrt{\varepsilon}}{(1+\varepsilon)} \tag{3}$$

where L_0 is length of the string without strain. Under the assumption of small strain, the natural frequency varies linearly to the square root of the strain. Therefore, it is possible to calculate the strain from the measured natural frequency [4].

In case of a fiber, however, it is difficult to neglect the bending stiffness because the fiber cannot be assumed as an ideal string any more. Instead, the fiber should be considered as a beam, and then the equation of vibration is rewritten as

$$EI\frac{\partial^4 w(x,t)}{\partial x^4} + \rho A\frac{\partial^2 w(x,t)}{\partial t^2} - P\frac{\partial^2 w(x,t)}{\partial x^2} = 0 \tag{4}$$

The solution of Eqn.(4) can be expressed as $w(x,t) = W(x)(A\cos\omega t + B\sin\omega t)$. Using an assumed mode method, the general solution of Eqn.(4) is represented by

$$w(x,t) = \sum_{i=1}^{\infty}\Phi_i(x)q_i(t) \tag{5}$$

$$\int_0^L \rho A\Phi_i(x)\Phi_j(x)dx = \delta_{ij} \tag{6}$$

where, Φ_{ij} is mode shape of the vibration, and δ_{ij} is Kronecker's delta. Eigenvalue problem is drived from Eqn. (4) as follows [5].

$$[I]\{\ddot{q}\} + [K]\{q\} = \{0\} \tag{7}$$

$$K_{ij} = \omega_{b,i}^{\ 2}\delta_{ij} + P\int_0^L \Phi_i'\Phi_j'dx = \omega_{b,i}^{\ 2}\delta_{ij} + P\Gamma_{ij} \tag{8}$$

$$q(t) = A\cos\omega_i t + B\sin\omega_i t \tag{9}$$

In above equation, $\omega_{b,i}$ is the natural frequency of the beam without axial tension and matrix Γ_{ij} is defined by Eqn. (10), (11).

$$\Gamma_{ij} = \int_0^L \Phi_i'\Phi_j'dx \quad (i \neq j) \tag{10}$$

$$\Gamma_{ij} = \int_0^L (\Phi_i')^2 dx \quad (i = j) \tag{11}$$

By applying the boundary conditions for clamped beam, the characteristic equation of the beam with an axial force is derived as

$$\left|P\Gamma_{ij} - \left(\Lambda - \omega_{b,i}^{\ 2}\right)\delta_{ij}\right| = 0 \tag{12}$$

where, Λ is the eigenvalue and equal to the square of the natural frequency $\omega_{b,j}$ (rad/sec) of the beam with tension. Considering that the length and cross-sectional area of the beam vary with the strain change, Eqn.(12) becomes,

$$\left|\left\{\frac{\varepsilon}{(1+\varepsilon)^2}\right\}EA_o\Gamma_{o,ij} - \left\{\Lambda - \frac{\omega_{bo,i}^{\ 2}}{(1+\varepsilon)^3}\right\}\delta_{ij}\right| = 0 \tag{13}$$

The solution of Eqn.(13) obtained using MATLAB is compared to that of Eqn.(3)

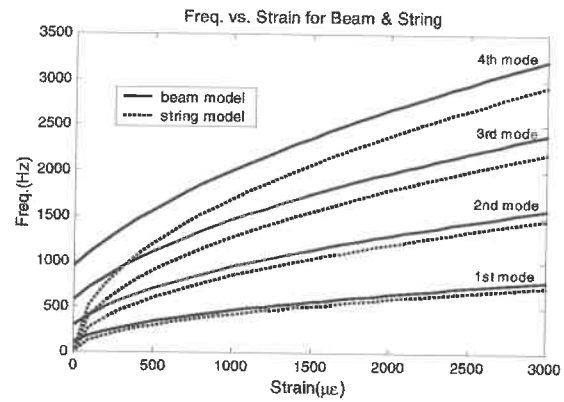

Fig.1 Natural frequency vs. strain
(solid line: beam model, dotted line: string model)

The main difference between the beam and string model is that the natural frequency of the beam model has nonzero values while that of the string model is always zero when no strains exist on the fiber.

2.2 Resonance Condition

When a fiber is constrained at both ends while one of the them is excited according to Eqn.(14), the relative motion of the fiber can be represented by Eqn.(15) [6],

$$w_g = \delta(x)g(t) \tag{14}$$

$$w^* = -\sum_{i=1}^{4}\frac{\rho A\Phi_i(x)}{\omega_i}\left[\int_0^L \delta(x)\Phi_i(x)dx\int_0^t \ddot{g}(t')\sin\omega_i(t-t')dt'\right] \tag{15}$$

where $\delta(x)$ is a displacement influence function. Thus, the total displacement of the fiber is represented as the sum of a rigid-body motion, Eqn.(14), and the relative motion, Eqn.(15), as follows

$$w = w_g + w^* = \delta(x)g(t) + w^* \tag{16}$$

Assuming that the excitation can be represented by a sinusoidal function as $g(t) \equiv A_g \sin \Omega t$, the total motion in Eqn.(16) can be rewritten as

$$w = A_g \delta(x) \sin \Omega t + \sum_{i=1}^{4} \rho A \Phi_i(x) \left[\int_0^L \delta(x) \Phi_i(x) dx \right] A_g H(\Omega, t) \quad (17)$$

$$H(\omega_k, t) \approx \frac{\omega_k t}{2} \sin\left(\omega_k t - \frac{\pi}{2} \right) \quad (18)$$

From Eqn.(18), it is shown that the fiber motion is delayed as much as $\pi/2$ than the excitation motion for 1st mode. And for 3rd mode, fiber motion is faster as much as $\pi/2$ than the excitation motion..

3. EXPERIMENTS AND RESULTS

3.1 Experimental setup

The functional diagram of automatic string resonator is shown in Fig.2. The flexure stage of the string resonator is composed of two elastic hinges of notch type [7]. One flexure is for fiber stretching with a piezo actuator, PZT1, and another is for excitation motion, PZT2.

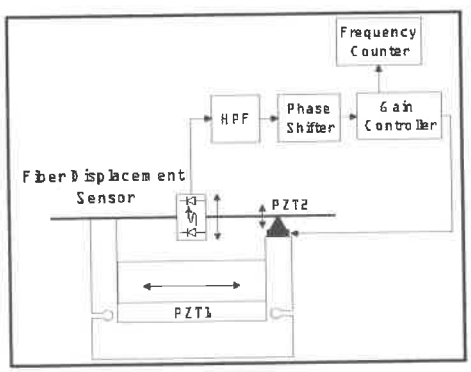

Fig. 2 Functional diagram of string resonator

A photo interrupter, which is composed of a pair of a LED and a phototransistor, was used as the displacement sensor measuring the fiber's oscillating motion. The signal from the photo interrupter, which represents the displacement of fiber center, goes through high-pass filter so that DC offset is removed. The phase of the AC signal from the high-pass filter shifts by 90° by the integrator for resonant condition. The automatic gain controller makes the amplitude of the output signal be constant regardless of frequency.

3.2 Results

Using the string resonator circuit the resonant frequencies with respect to the strain are measured. The relative strain to the initial value is calculated from the displacements read by a capacitance sensor, and the resonant frequency is read from a frequency to voltage converter [8]. The experiments are mainly to detect the 1st mode and 3rd mode resonance frequency.

Fig.3 and Fig.4 shows measured natural frequency with respect to strain, and error from fitting equation, Eqn.(13) at 1st and 3rd modes.

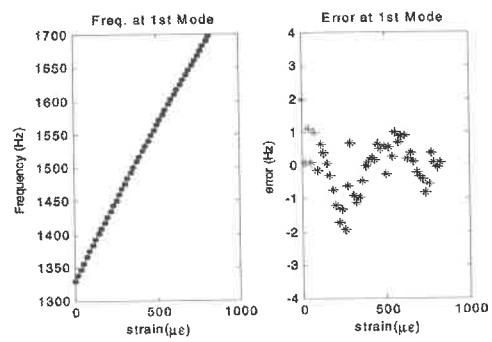

Fig. 3 Fitting of the experimental data at 1st mode

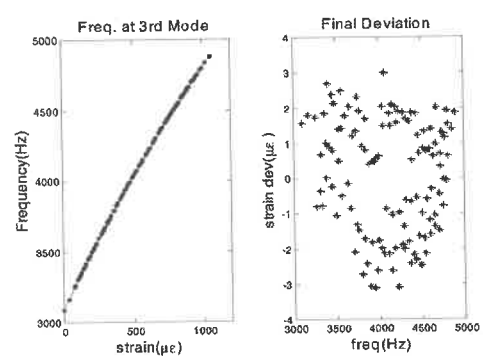

Fig. 4 Fitting of the experimental data at 3rd mode

To test resolution, the frequency variation with respect to a small step strain (0.7με) is measured in each mode, Fig.5 and Fig.6. For 1st and 3rd mode, it shows accuracy of 4με and 3με and quasi-static resolution of 0.2με(rms) and 0.1με(rms), respectively.

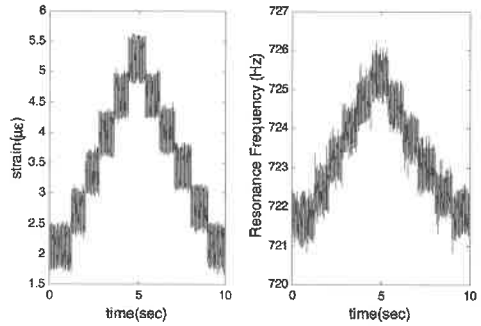

Fig. 5 Response to small step strain at 1st mode

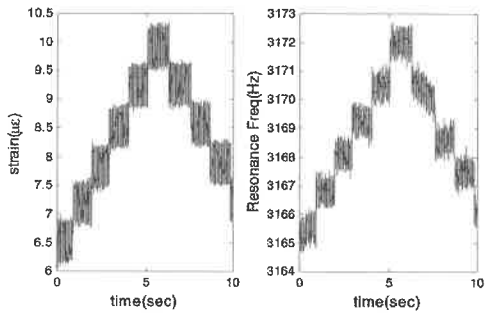

Fig. 6 Response to small step strain at 3rd mode

Frequency response of the 3rd mode with respect to a dynamic strain is measured for input signal with the amplitude of 25με. The frequencies of the strain input were changed from 1Hz to 16 Hz, Fig.7. For frequencies smaller than 8Hz, excellent locking capability is achieved, with an accuracy of ~3με and almost no phase difference.

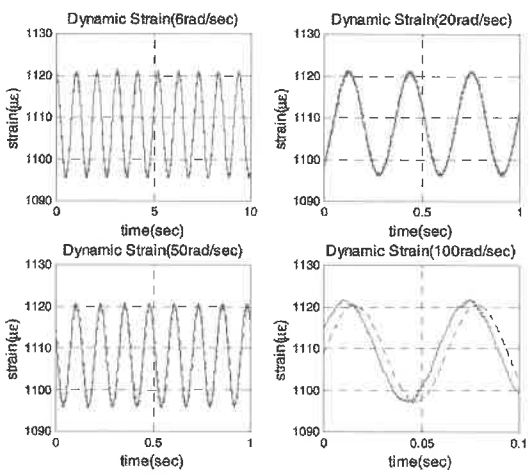

Fig. 7 Response to dynamic strain

4. CONCLUSION

By the vibration analysis, the measuring scheme for the absolute strain was established, from which the string resonator for the locking filter interrogation system was implemented. The measurement system of 3rd mode detection provides the sensitivity of three times compare with 1st mode, the accuracy of ±3με, and the quasi-static resolution of ~0.1με which are better than 1st mode. For dynamic strain it provides accuracy of ~3με below than 8Hz input. Consequently, the performance of the string resonator for the absolute strain measurement with high sensitivity and high accuracy can be advanced by the design improvement of the flexure and the novel scheme for resonance detection of 3rd mode.

ACKNOWLEGMENT

This research has been done by supports of Korea Science and Engineering Foundation (KOSEF). The authors express their gratitude.

REFERENCES

1. A. D. Kersey et al., "Fiber Grating Sensors", Journal of Lightwave Technology, Vol.15, No.8, pp.1442-1463, 1997
2. G. Meltz, "Overview of Fiber Grating-Based Sensors", SPIE's Symposium on Smart Structures and Materials, Vol. 2838, pp. 2-22, Aug. 1996
3. A. D. Kersey, T. A. Berkoff, and W. W. Morey, "Multiplexed Fiber Bragg Grating Strain-Sensor System with a Fiber Fabry-Perot Wavelength Filter", Optics Letters, Vol.18, No.16, pp.1370-1372, 1993
4. Byeongha Lee, "Absolute Strain Measurement Using Fiber Bragg Grating", Ph.D Thesis, Univ. of Colorado, 1996
5. Leonard Meirovitch, "Analytical Methods in Vibrations", Macmillan Publishing, 1967
6. W. Weaver JR., S. P. Timoshenko, and D. H. Young, "Vibration Problems in Engineering", Wiley, 5th Ed., 1990
7. Stuart T. Smith, Vivek G. Badami, Jami S. Dale, and Ying Xu, "Elliptical Flexure Hinges", Rev. Sci. Instrum., Vol.68, No.3, pp.1474-1483, 1997
8. R. Mark Stitt, and Rod Burt, "Frequency -to-Voltage Conversion", Burr-Brown Application Bulletin, 1993

DEVELOPMENT OF A DESIGN TOOL FOR CONCEPTUAL DESIGN STAGES OF MACHINE TOOLS

Nozomu MISHIMA
Fine Manufacturing System Group,
Institute of Mechanical Systems Engineering, 1-2 Namiki, Tsukuba, Ibaraki

1. Introduction

In the former research [1], the author proposed and have examined a new design tool for machine tools combining the form-shaping theory of machine tools; an analytical procedure representing the machining motions, with the Taguchi method [2]; a well-known robust tool to optimize processes or design parameters. Using the design tool, machine tool designers can evaluate how design parameters, local error factors and structures affect the machine performances without prototyping. The design tool was applied to the two designs of miniature mills which were used in the "microfactory" [3], and predicted that the design with distributed degrees of freedom (DOF) had better machining tolerances than the other. This paper first describes about measurement of positioning errors between the product and the cutting tool of each micro mill. Comparison of the measured and the calculated errors shows that the positioning errors of machine tools are roughly predictable by the proposed design tool. Secondly, the paper focuses on a conceptual design creating process of a lathe. In creating a design concept, there are many possible structures that have different sequences of motion axes. After considering every possible structure, the design tool compares three major structures of a lathe. Assuming that all designs use same machine components and being same sizes, the comparison based on the design tool leads us to conclude that one design has better theoretical performance than the other two. Throughout the measurement of the micro mills and the design trial of the lathes, the proposed design tool is proved to be a useful method to create conceptual designs of miniature machines.

2. Microfactory and miniature machine tools

Microfactory is a name of an ultra miniature manufacturing system consists of miniature machine tools and manipulators and benefits to reduce energy consumption and space occupied by the machines. The first microfactory was prototyped by author's research group in 1999 as fig. 1. The system contains three machine tools including the micro-lathe [4] and the micro mill. The total area of the factory was approximately 50cm x 70cm. The factory was able to produce miniature mechanical parts by machining and assembled them into a miniature pivot ball bearing that was 0.9mm in diameter and 3mm in length. Through the test production, the microfactory indicated its capability as a rather practical miniature manufacturing system. Consecutively in 2000, the group prototyped the portable microfactory shown in fig.2 to demonstrate the concept of future manufacturing systems which enable "on-site" or "on-demand" manufacturing. However, especially for these miniature

Fig. 1 Desktop microfactory

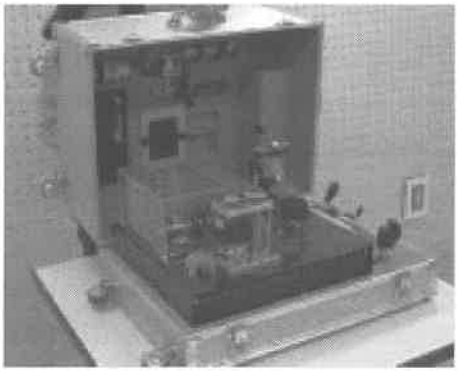

Fig. 2 Portable microfactory

machine tools for the microfactory, designers may not have enough design experience and conceptual design procedure of machine tools has not been well examined. So, a design tool to evaluate the performances of machine tools and tell which size and structure is appropriate for the target product must be helpful for designers. Having this purpose, the author proposed a design tool that can predict machine tool performances without prototyping in the former research and applied to miniature machines shown in fig. 3 and 4.

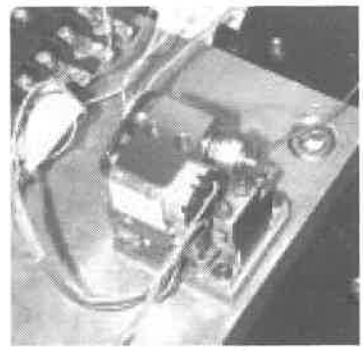

Fig. 3 Micro-lathe

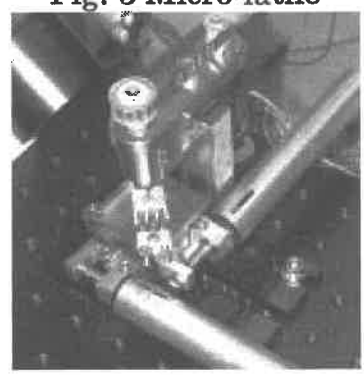

Fig. 4 Micro mill

3. Design evaluation method

A machine tool structure can be considered as a chain of directly linked rigid components extending from a product through a cutting tool. Defining local coordinate system to each component, transformation between two next coordinates can be represented by a homogeneous transformation matrix. Calculating the transformation consecutively from the product towards the cutting tool, it is possible to express the relative displacement or motion between the product and the tool. The result of the matrices calculation is the definition of the form-shaping function that expresses the cutting motions of machine tools mathematically. However, actual machine tools have many error sources. In order to describe actual cutting motions, one must consider these errors. Such errors may be treated as errors in transformations between elements. And the form-shaping error function, expressing the shift from the target value of the machine tool motion, is defined as the difference between the form-shaping function not containing errors and that containing errors. By defining the design parameters, error factors and dimensions of the product, the form-shaping theory can calculate the form-shaping error function of the machine tool. The next step is to evaluate the calculated function by using a robust design method. The Taguchi method; a well-known robust design tool frequently used to optimize process parameters in manufacturing processes, is applied to the form-shaping error function to clarify how design parameters, machine structures and error factors affect the machining tolerances, which are the critical performance indicators of machine tools.

4. Robustness comparison of machine tool structures

4.1 Comparison of two design candidates of micro milling machines

By using the form-shaping theory and the Taguchi method, it was possible to evaluate the effects of design parameters of an existing design. However, the tool did not provide a design suggestion to choose one design from design candidates, or to create an alternative design when the performance of the old design is insufficient. This stage of a design procedure is often called "Conceptual design". The Taguchi method does not mention about the conceptual design and some researchers [5] tried to create a design method for conceptual stages. Though, one can compare performance of several designs by the Taguchi method with some assumptions. The method was applied to two design candidates of the micro mill used in the microfactory. To obtain a design guideline, I compared two different designs with same parts, same dimensions and different distribution of DOF. Following the machine tool elements from the product towards the cutting tool, one has two axes before the static part, whereas the other has all three axes

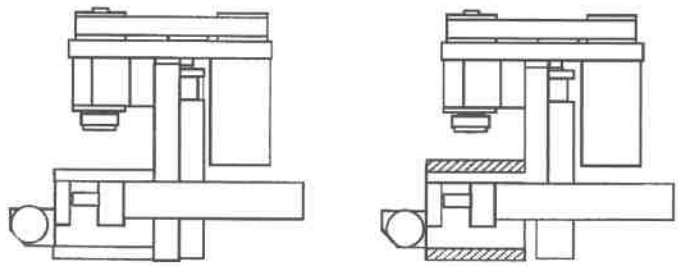

(a) Type 1 with distributed DOF (b) Type 2 with concentrated DOF

Fig.5 Two designs of the micro milling machines

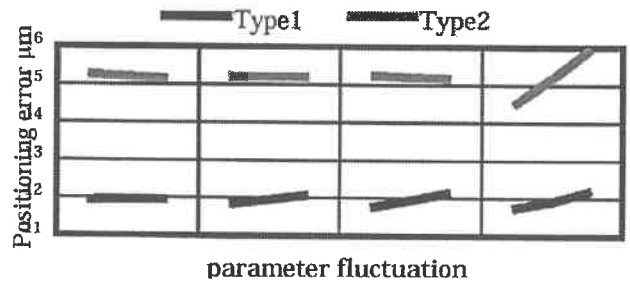

Fig. 6 Machining error comparison

concentrated after the static part. Fig. 5 shows the overview of the two designs. Fig. 6 indicates the result of the analysis comparing the predicted tolerance holding capability of two designs, when design parameters varies within certain ranges.

4.2 Measurement of positioning errors

Since, the analytical results shown in fig. 6 depend on some assumptions made in determining the ranges of error factor fluctuation, it is necessary to measure the positioning error directly and prove that the prediction made by the design tool was reasonable. For the purpose, relative positioning errors between the products and the cutting tools for both machines were measured, using laser displacement sensors fixed to the table on which products are usually placed. Fig. 7 shows the comparison between measured and predicted value of errors to y-direction when coordinate value of x are fixed. The figure indicates that there is a difference between predicted and measured value, though, the accuracy of prediction seemed enough for the purpose to aid conceptual design stage. The figure also tells that type 1 had smaller error than the type 2 had, as it was calculated. So, it can be concluded that the prediction based on the design tool matches the results of the measurement. It means that the proposed design tool is helpful to determine which of several designs has better performance in its conceptual design stage.

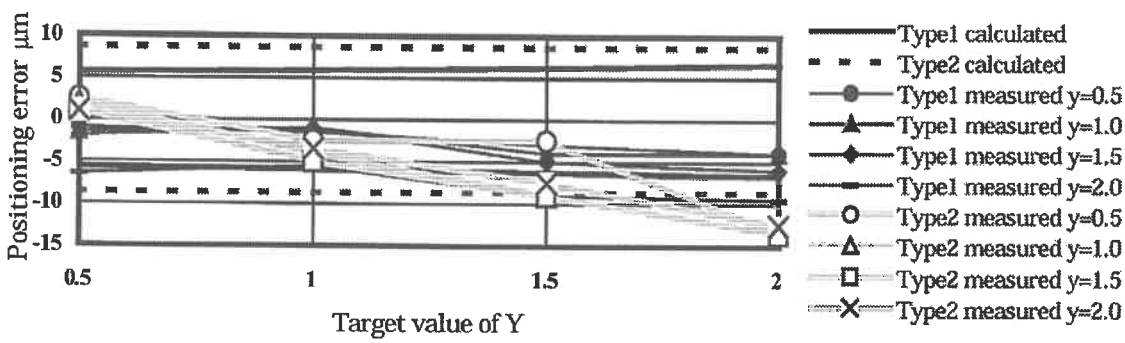

Fig. 7 Comparison of predicted and measured error

4.3 Creating a deign concept of a miniature lathe

The next issue is to applying the above-mentioned design tool to create a design concept of a machine tool. Assuming to create a new design concept of a miniature lathe, the paper tried to make the use of the design tool to evaluate a few design concepts. Basically, a lathe must have three motion axes. And as the definition of a lathe, following a link of components from a product towards a cutting tool, a main spindle must come first. Expressing transitional motion

axis along X as 1, along Y as 2 and so on, structure of machine tools can be expressed by those numbers from 1 to 6 focusing on the sequence of the motion axes. A static part being expressed as 0, the micro-lathe shown in fig. 3 can be written as 6310. Using this expression, possible structures of a lathe are categorized into 6 types; those are 6013, 6031, 6301, 6103, 6310 and 6130. Further, assuming the x-axis and the z-axis would have the same characteristics, those 6 will be integrated to 3, shown in fig. 8. Following the machine tool elements from the main spindle towards the cutting tool, the first design has two linear motions after the base. The second one has one linear motion before and the other motion after, whereas the last design has two linear motions and the main spindle concentrated. Using the proposed design evaluation method, it was possible to predict the mean positioning error of each structure. Fig. 9 is the theoretical performance comparison, based on the calculation. The figure shows that type 6031 evidently has the smallest positioning error, and type 6301 has the next best theoretical performance.

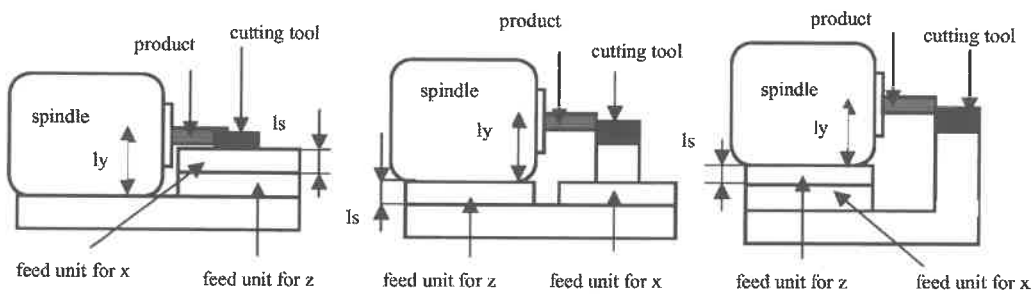

a) type 6031 **b) type 6301** **c) type 6310**

Fig. 8 Three different structures of lathes

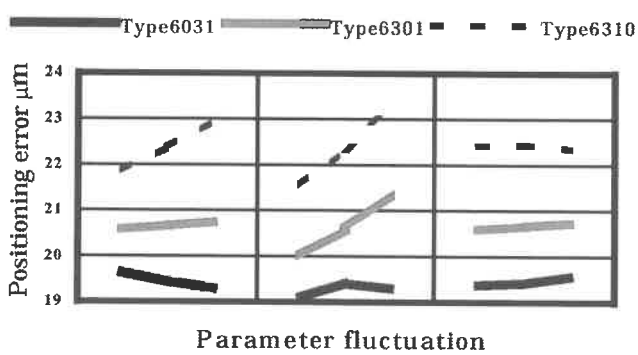

Fig. 9 Machining error comparison

5. Conclusions and future work

A) Using the proposed design tool, it was able to show that among two designs of micro mills, distributed DOF type has a smaller error.

B) Above-mentioned result was followed by the measurement, and the prediction accuracy was enough for usage in the conceptual design stages.

C) Typical design variations of a lathe are categorized to three types and the type 6031 (or 6013) has the best theoretical performance.

References

1. Mishima, N. and Ishii K., *Robustness Evaluation of a Miniaturized Machine Tool*, Proc. for ASME Design Engineering Technology Conference, Las Vegas, Sept. 1999, DETC/DAC-8579.

2. Taguchi, G. and Konishi, S. (1994) *Quality Engineering Series* Vol.1-4, ASI Press.

3. Mishima, N., Asida, K., Tanikawa, T., Maekawa, H., Kaneko, K. and Tanaka, M., *Micro-factory and a design evaluation method for miniature machine tools*, Proc. for ASPE 15th Annual Meeting, Phoenix, Oct. 2000, pp. 567-570.

4. Kitahara, T., Ishikawa, Y., Terada, K., Nakajima, N., and Furuta, K. (1996). *Development of Micro-lathe,* Journal of Mechanical Engineering Lab., Vol. 50, No. 5, p. 117-123.

5. Ford, R.B. and Barkan, P. (1995). *Beyond Parameter Design --A Methodology Addressing Product Robustness at the Concept Formation Stage,* Proceedings of ASME National Design Engineering Conference.

A New Optimal Design Technique for the Pneumatic Vibration Isolation System Implementing the Full Mathematical Analysis and Nonlinear Modeling

Jun Hee Moon, Heui Jae Pahk
School of Mechanical and Aerospace Engineering, Seoul National University, Seoul, Korea

1. Introduction

All precise machining and measurement equipments are much influenced by environments such as temperature, vibration, humidity, dust and so on. As for vibration, the amplitude of the vibration that resides in buildings and ground is from about 0.1 um to 10 um in general, which is bigger than the resolution of the precision equipments, and thus the vibration isolation systems are widely used in industry and laboratories.
The pneumatic vibration isolators are most widely used for the vibration isolation of small areas. However, their design depends on the empirical method and human experience. Many mechanical and mathematical analyses have been performed for the optimal design of the pneumatic vibration isolator, but the correspondence with real system is still weak.
The pneumatic vibration isolation system has nonlinear elements while the elements of the mass-spring-damper system are almost linear. For example, the orifice in the pneumatic system is a nonlinear element that the pressure drop between its both sides is proportional to the square of the flow rate. In previous researches, this element was regarded as only a linear element or as nonlinear one whose coefficients were assigned arbitrarily or artificially, so that the modeling might have less physical meaning. As a result, the full nonlinear characteristics of the pneumatic vibration isolation system has not been shown clearly.
In this research, a new analysis method is developed by modeling the nonlinear elements and calculating nonlinear algorithms numerically in order to show the full characteristics of the isolation system. These analyses and methods have achieved the optimal design of pneumatic vibration isolation system.

2. Description and modeling of the pneumatic vibration isolation system.

2.1 Composition

A typical vibration isolation system is shown in Fig.1, where it consist of two air chambers, an orifice between them, an elastomeric diaphragm which enables the sealing of air and the free movement of the payload, and a mass mounted on the piston.

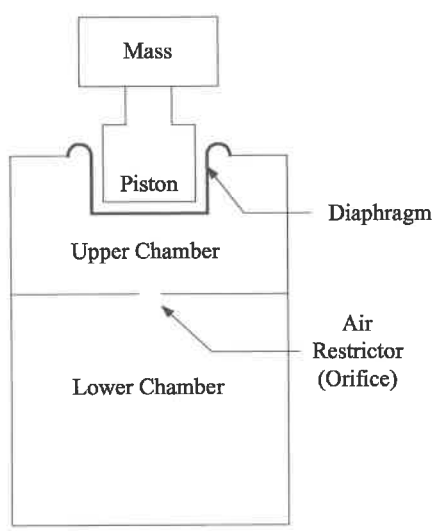

Fig. 1 Schematic diagram of a pneumatic vibration isolator

2.2 Air chambers

A sealed chamber with volume change behaves like a mechanical spring, where the relationship between pressure and volume in an air chamber can be described as follows.

$$P_0 V_0^{\,k} = P V^k \tag{1}$$

where k is the specific heat ratio of air, 1.4.
From this equation, we can derive the pressure change formula.

$$\Delta P = P - P_0 = P_0 \left(\left(1 + \frac{\Delta V}{V_0} \right)^{-k} - 1 \right) \tag{2}$$

2.3 Air restrictor (Orifice)
The flow rate through an sharp-edge orifice may be expressed as follows.

$$Q = \frac{C_d A_2}{\sqrt{1-(A_2/A_1)^2}} \sqrt{\frac{2(P_1 - P_2)}{\rho}} \tag{3}$$

where A_1, A_2: Pipe/Orifice Area [m^2]
P_1, P_2: Pressures in Pipe/Orifice [Pa]
C_d: Discharge Coefficient

In the case of the pneumatic vibration isolator, the pressure difference ratio of the upper and lower chamber does not exceed 10% and the ratio of the orifice diameter and the pipe diameter is very small. Thus we can set the discharge coefficient to be about 0.65.
And, equation (3) can be expressed like this by squaring both terms.

$$\Delta P_{ori} = -C_{ori} \left(\Delta \dot{V} \right)^2 sign(\Delta \dot{V}) \tag{4}$$

Because the pressure difference P is analogous to the weight and the flow rate d(V)/dt to the velocity, we can regard the orifice as a damper whose damping force is proportional to the square of velocity. This is the reason why the pneumatic system has nonlinear characteristics.

2.4 Diaphragm
The elastomeric diaphragm can be regarded as a damper and a spring. But, the stiffness of the diaphragm is constant in all loads while the stiffness of the air chamber changes in proportion to weight. Thus, the lighter is the mass, the more is the effect of the stiffness of diaphragm.

3. Simulation

3.1 Equations
As described above, the governing equations in the pneumatic vibration isolation system are as follows:

Relationship between the acceleration of the mass and the air pressure difference

$$\Delta P_1 = \frac{M}{A_p} \ddot{x}_{piston} \tag{5}$$

Pressures in the pneumatic vibration isolator

$$\Delta P_1 = \Delta P_2 + \Delta P_{ori} \tag{6}$$

where

$$\Delta P_1 = P_0\left(\left(1+\frac{\Delta V_1 - \Delta V_2}{V_1}\right)^{-k} - 1\right) \tag{7}$$

$$\Delta P_1 = P_0\left(\left(1+\frac{\Delta V_2}{V_2}\right)^{-k} - 1\right) \tag{8}$$

$$\Delta P_{ori} = -C_{ori}\left(\Delta \dot{V}_2\right)^2 sign(\Delta \dot{V}_2) \tag{9}$$

Relationship between the ground excitation and the upper chamber volume change

$$\Delta V_1 = A_p(x_{piston} - x_{ground}) \tag{10}$$

3.2 Algorithm

Using the relationship equations in section 3.1, a simulation has been carried out in the time domain by MATLAB/Simulink. Followings are the steps in the program:

- Ground excitation invokes the volume change of the upper air chamber and its pressure change.
- The pressure change makes the air flow through the air restrictor.
- The flow changes the volume of upper and lower air chambers and their pressure changes.
- The change of the pressure difference between two chambers results in the change of the air flow through the orifice
- The pressure change of the upper air chamber makes the change of the supporting force under the piston.

These steps have been accomplished iteratively by numerical analysis and Runge-Kutta method was used to solve differential equations.

3.3 The calculation of the transmissibility

The result data of ground excitation and table-top vibration by the time-domain simulation goes through FFT algorithm because the transmissibility can be attained in the frequency domain. The transmissibility versus the excitation amplitude and frequency is shown in Fig. 2.

If the elements of the pneumatic system are assumed as linear ones, the transmissibility has nothing to do with the amplitude, because the amplitude coefficients in the linear differential equations can be vanished by division. The transmissibility, however, has been found out to be dependent on the amplitude.

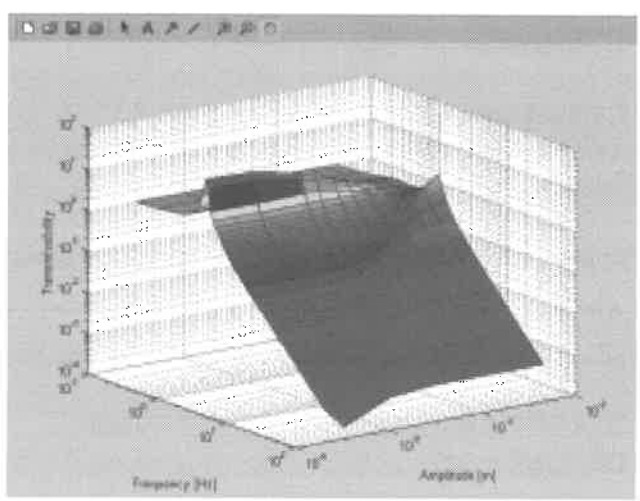

Fig. 2 Transmissibility of a vibration isolator

4. Comparison

4.1 Trend

As seen in the transmissibility graph, when the orifice area is small or the excitation amplitude is large or the excitation frequency is high, the effect of the upper air chamber alone is dominant. In the opposite case, however, the net volume of the both air chambers comes to be in effect. It shows good accordance with the description of one pneumatic vibration isolator maker catalog.

4.2 Natural frequency

We simulated the pneumatic system with following conditions.

- Effective piston area: 1.742e-3 m^2
- Mass: 61.3 Kg
- Upper chamber volume: 71.44e-6 m^3
- Lower chamber volume: 507.6e-6 m^3
- Orifice area: 384.8e-9 m^2

From the simulation, the resonant frequencies are 1.0 Hz in the small excitation amplitudes and 2.9 Hz in the large excitation amplitude respectively. For the verification of the simulation, a prototype has been made with the same specification. In the large amplitude of excitation, the resonant frequency of the system was measured as about 3.0 Hz, producing very close value of simulation. Thus it can be stated that the simulation can be a good tool to optimize the vibration isolation system.

5. Optimal design

Because all design parameters such as chamber volume, operation air pressure, and so on, can be input to the simulation program, the influence of the each design parameter can be known.
Followings are the representative design parameters to be optimized:

- Chamber volumes
- Piston Area
- Orifice Area

6. Conclusion

The proposed modeling and nonlinear simulation made clear the effect of each components of the pneumatic vibration isolation system enabling the optimal design based on the good agreement between experiments and simulation. When the design parameters are input to the simulation program, their effects can be observed successfully. Therefore, the design parameters can be optimally chosen by the simulation results.

References

1. K. Peter Heiland, "Recent Advancements in Passive and Active Vibration Control Systems", SPIE Vol.1619, Vibration Control in Microelectronics, Optics and Metrology, 22-33, 1991
2. G. Popov and S. Sankar, "Modelling and Analysis of Non-linear Orifice Type Damping in Vibration Isolators", J. Sound and Vibration, 183(5), 751-764, 1995
3. E. O. Doebelin, *Measurement Systems : Application and Design,* 4th Ed., McGraw-Hill, p.566, 1990
4. Kinetic Systems Inc., *Vibration Isolation Products Catalog,* 1999

Desk-Top NC Milling Machine with 200 krpm Spindle

Yuichi Okazaki
The National Institute of
Advanced Industrial Science and Technology
1-2 Namiki, Tsukuba, 305-8564, Japan
okazaki-u1@aist.go.jp

Toshimichi Mori
The Tokyo Metropolitan Industrial
Technology Research Institute
3-13-10 Nishigaoka, Kita-ku, Tokyo, 115-8586 Japan
Mori.Toshimichi@iri.metro.tokyo.jp

Noboru Morita
Chiba University
1-33 Yayoi-cho, Inage-ku, Chiba, 263-8522 Japan
nmorita@meneth.tm.chiba-u.ac.jp

1 Background

Downsizing of machine tools can improve space utilization factor, and reduce the price and energy consumption including air conditioning and facility investment. The agility in reconfiguring the manufacturing lines in the factories will be elevated. Furthermore, location of the machines can be spread off the factory floor, to the design office, classrooms and distributed to small manufacturing laboratories, even in residential areas. As technical aspects, the downsizing makes it easier to achieve high-speed machining and high-precision/rigidity motion control due to reduce inertia, and in turn, it leads to higher precision, quality and productivity. With these objectives, a desktop NC milling machine has been developed, using a miniature high-speed spindle. The purpose of the development is to evaluate the technical possibility of extremely downsized machine tools in practice.

2 Mechanical Design

The machine as a prototype consists of a stacked X-Y stage and Z-axis drive unit, which holds a spindle unit at the end. The Z-axis drive unit is mounted on the top of a housing surrounding the XY stage (**Fig. 1**).

X and Y stages are commercial ones using crossed roller guides and ball screws, driven by directly coupled 30W AC servomotors.

The Z-axis drive unit uses a vertical hollow drive screw of M40x1.5, and is driven by a brush-type direct drive torque motor (**Fig. 2-3**). The sliding part of the unit is guided by four crossed roller guides, which are located at the four corner of the slide. The drive screw is supported by a thin rotary ball bearing. The screw, the spindle unit and the DD motor are allocated in a line.

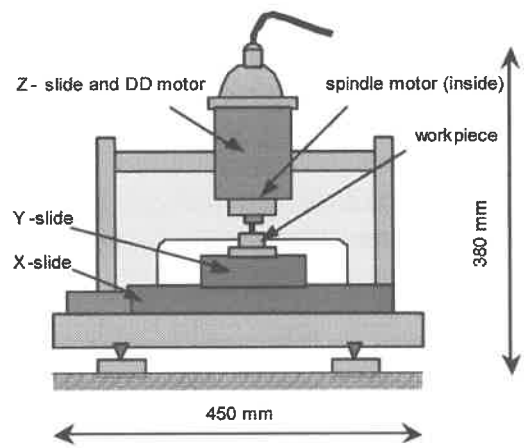

Fig. 1 Structure of the desktop milling machine

This configuration is kinematically over-constrained. The motion is ruled in a way so that guiding errors of each element are absorbed in elastic components of the elements. These designs provide with sufficient structural stiffness and thermal symmetricity.

The spindle is a miniature high frequency AC motor specially designed to provide 60W rated power and 200 krpm of maximum rotation speed. It is 27mm in

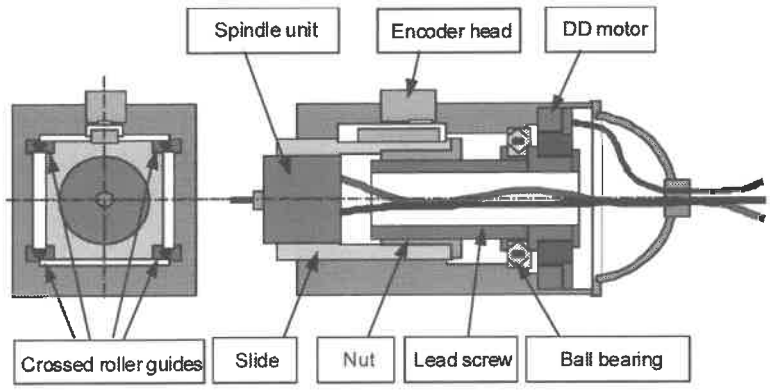

Fig. 2 Structure of Z axis drive

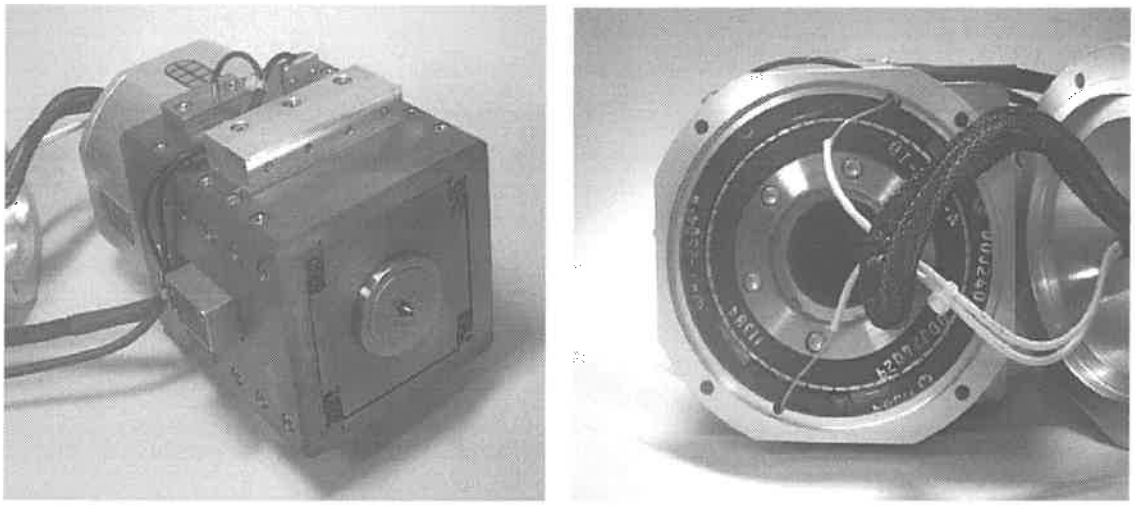

Fig. 3 Views of Z axis drive (from bottom and top with cover removed)

Table 1 Specification of axis mechanisms

Axis	X (lower)	Y (upper)	Z (top)
Guide	Crossed roller guides (2)	Crossed roller guides (2)	Crossed roller guides (4)
Travel	60mm	100mm	30mm
Feed mechanism	Ball screw (lead: 2mm)	Ball screw (lead: 1mm)	Lead screw (lead: 1.5mm)
Actuator	AC servomotor (30W)	AC servomotor (30W)	DC torque motor (57W)
Maximum feed rate	50mm/s	50mm/s	3mm/s
Command acceleration	$2mm^2/s$	$2mm^2/s$	$0.5mm^2/s$
Encoder (resolution)	Optical linear scale (50nm)	Optical linear scale (50nm)	Optical linear scale (50nm)

diameter and 26 mm long. The motor is slightly cooled by airflow in a jacket, and the air is also used as a clearing jet at the cutting point. The spindle end holds a milling tool by a directly machined collet chuck of 1.0 mm shank diameter.

The rugged machine base made of magnesium alloy sizes 450mm x 300mm. The cutting point is totally enclosed (**Fig. 4**), so that the workpiece is loaded and unloaded by drawing out the Y stage. The cutting point is monitored by a CCD camera of 7 mm diameter.

Fig. 4 Outlook of the milling machine

3 Motion Control System

3.1 Numerical Controller

Full closed loop numerical control system with 0.1-μm resolution is installed. The feedback is given by both optical linear scales with 50 nm resolution (MicroE S132-M400) at the stages and 16 bit rotary encoders at the motor shafts (for X and Y drive). The compact

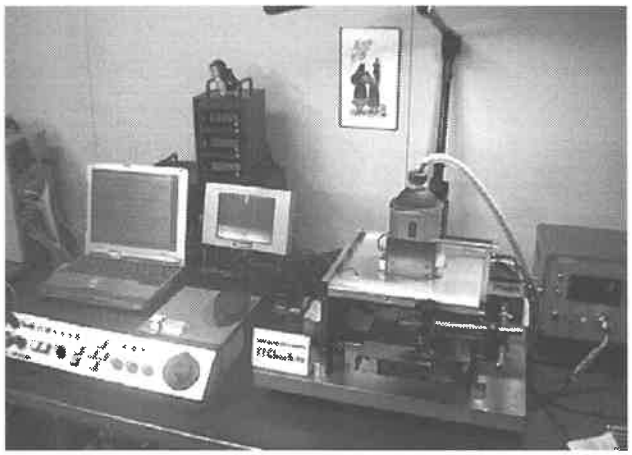

Fig. 5 View of the whole system

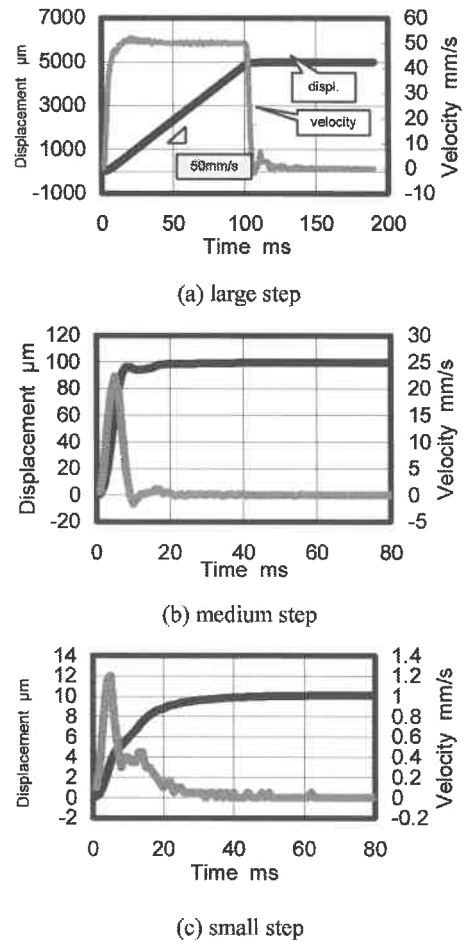

Fig. 6 Response of X stage

custom made NC system consists of a microprocessor-based controller, operational panel, a notebook PC for monitoring and program control (**Fig. 5**). DNC operation is available. **Table 1** summarizes the specifications of the axes. For X and Y axes, the maximum feed rate is limited by the maximum acceptable pulse rate (500 kpps) of the drivers. The maximum feed rate and acceleration are limited by the large friction torque of the drive screw and the maximum torque of the DD motor.

Response of the axis motion control was evaluated observing the encoder signals for each axis. Actually, positioning resolution of 0.1 μm is achieved for all the axes, due to the high loop stiffness.

3.2 Step response

Dynamically, settling time for a step command is ruled by different factor depending on the step size (**Fig. 6**). For a large step (a), the rule is the maximum feed velocity. For an intermediate step size (b), smaller than 200μm, the settling time is determined by acceleration, because the velocity does not reach to the limit. For a small step size (c), response of servo system dominates the settling. Due to the nature of the mechanism, the system becomes "stiffer" in a very small displacement region, and settling time becomes longer than for larger step size. In the figure, the convergence goes slower when the servo error enter within about 5 μm range.

4 Machining

4.1 Plane machining

Preliminary machining tests have been made on hard aluminium alloy (A7075-T651: HB 165) and pre-hardened steel (NAK55: HRC40), using ball end mill tools with R0.2mm. Spindle rotation was selected as 50 krpm and 200 krpm. Depth-of-cut (d), feedrate (f) and pick peed (pf) were scanned. Surface profile was measured and evaluated by a scanning stylus profilometer (TalyScan) in terms of Sa (average aerial surface roughness). Though motion copy was finely made on aluminium alloy for a wide range of feed rate of 0.3 to 50mm/s, the surface roughness was smaller with higher feed rate. For example, with both pick feed and depth-of-cut of 50 μm, surface roughness measured was 2 μm Rz, calculated as 120% of theoretical surface roughness 1,56 μm. Feed amount for a single cutting edge is as small as 7.5 μm at the maximum feed rate of 50 mm/s. On pre-hardened steel, the machining was fine when the pick feed was reduced down to 0.05mm.

4.2 High aspect-ratio machining

Thin walls were machined out of high strength aluminium alloy (**Fig. 7**). The tool used was a straight two-flute end mill of 0.5 mm diameter with straight edges. Thin walls of 80 μm thick and 2 mm high were perfectly machined

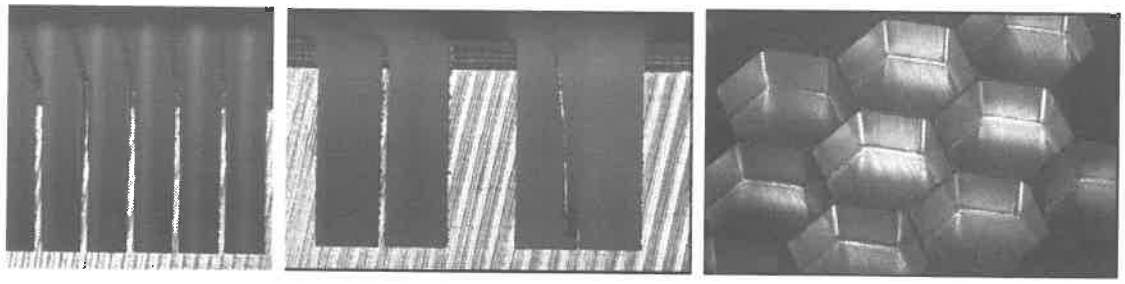

(a) 80μm (b) 50 and 20μm (c) Honeycomb (4mm pitch, 2mm deep)

Fig. 7 Thin wall machining

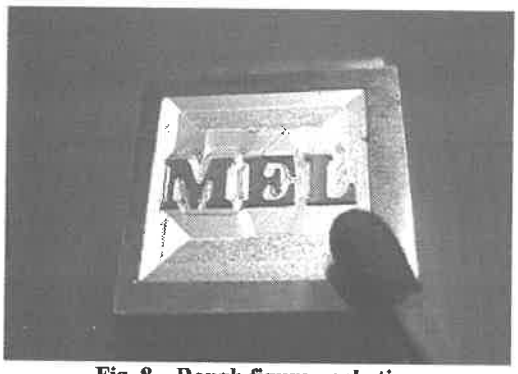

Fig. 8 Rough figure pocketing

Table 2 Cutting conditions for pocketing

Material of workpiece	A7075
Depth of cut	0.1 mm x 2
Feed rate	50 mm/s
Pick feed	0.1 mm
Nose radius of tool	0.2 mm
Spindle rotation speed	200,000 rpm

in the manner that the slots were finished one by one. No thinner walls could be machined in this manner. By deepening the both sides alternatively, the wall of 50 μm thick was machined up, but slightly deformed by the cutting force from the side that hits the wall as downcut. The cutting force damages thinner walls. Honeycomb rib is an application of thin wall machining.

4.3 Pocketing

Three-dimensional milling was also made using DNC function, processing machining program files generated by a CAM system. The pocketing sample shown in **Fig. 8** was completed in 130 s, under the condition in **Table 2**. As a result, the developed prototype of downsized milling machine has been proved to have machining capability comparable to regular sized milling machines.

5 Power consumption

One of advantages of downsized machine tools is their minimized power consumption. In this system, the total power consumption under high speed machining condition was only 120 W. The components were: 30 W for spindle, 25 W for servo motor drives, 32 W for NC, 18 W for PC, and 15 W for monitoring devices.

6 Conclusion

Taking advantages of downsized machine tool, the developed milling machine features high acceleration due to the reduced moving mass even using small actuators, and minimized power consumption, Furthermore, ultra-high speed spindle enables high speed milling on hard materials. High aspect ratio machining was also performed.

7 Acknowledgements

The authors would like to express their heart full thanks to Dr. H. Aramaki and Mr. H. Yui of NSK for supplying the spindle, and Prof. K. Muto of Polytechnic University for his useful advises on machining.

Development of a High-Speed Micro-Machining System for Brittle Materials

Shin'ichi WARISAWA, Takashi KARINO, Ryo TAKENAKA and Mamoru MITSUISHI
Department of Engineering Synthesis, Faculty of Engineering
The University of Tokyo
Hongo 7-3-1, Bunkyo-ku, Tokyo 113-8656, Japan

1. Introduction

It is well known that brittle materials can be machined without any cracks using a sharp cutting tool with a small depth of cut. It is called "ductile mode cutting." The ductile mode cutting has been already applied to the grinding process. The grinding process can realize the high productivity because a wide machining surface at one process is maintained in spite of its small depth of cut. Furthermore, because of the self-dressing capability of the grinding process, it is not necessary to consider the chipping effect. In the cutting process, smaller number of cutting edges contribute to the machining process compared with the grinding process and thus the productivity of the cutting process is much less than the grinding process. The cutting process, however, has an advantage of producing a complex shape part compared with the grinding process. It enables to manufacture a micro-optical part which is required in IT industries. Many researches have been executed concerning the cutting of brittle materials. They have paid much attention to the basic mechanism of cutting a brittle material and, therefore, the cutting speed is rather slow such as less than several mm/min, which is not applicable for a practical use. Our research goal is to develop a new technology to realize a ductile mode cutting with high cutting speed.

2. Related work

Many researches have been conducted concerning the ductile mode cutting. The relationship between cutting speed and depth of cutting while cutting a single crystal silicon was executed by Ichida, et al.[1]. Shirakashi, et al. have reported that the critical depth of cut became larger in case of cutting a single crystal silicon under the high hydro static pressure condition[2]. The atmosphere dependency of the cutting mode for an optical glass was investigated by Ogura, et al.[3]. Eda, et al. developed a shaping machine with sub-nanometer order depth of cut which worked under SEM. They investigated the relationship between the material properties and the critical depth of cut[4]. In those cases, however, the cutting speed is very slow such as in the order of several mm/s. There are no discussion regarding the cutting behavior of a brittle material at higher cutting speed. There are no experimental setup considering the high speed cutting for a brittle material, either. On the contrary, in this paper, a high speed shaping machine was developed for a brittle material and the capability of ductile mode cutting using the developed system was reported.

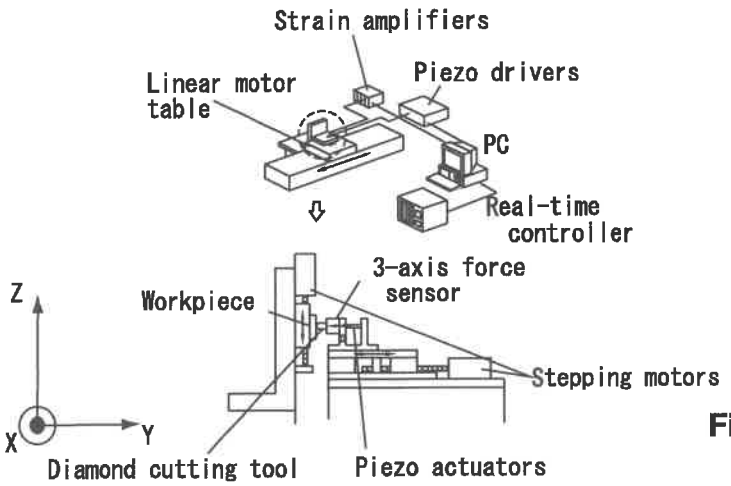

Fig.1 Overview fo the developed system

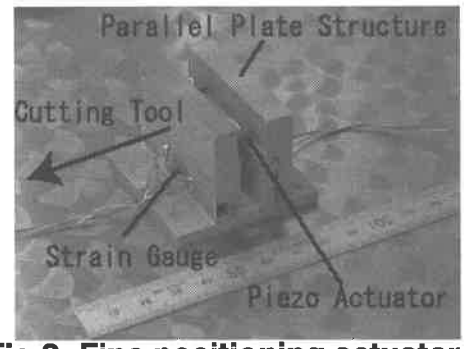

Fig.2 Fine positioning actuator to control the depth of cut

3. System overview

Figure 1 shows the shaping machine system which was newly developed. The system consists of 3 orthogonal axes; (i) a linear motor driven table system to realize high speed cutting in X direction, (ii) a hybrid-type tool positioning system composed of a ball screw mechanism for the coarse positioning and a piezo-electric actuator for the fine positioning in Y direction, and (iii) a ball screw mechanism for positioning a workpiece in Z direction. A single crystal diamond byte was used as a cutting tool which was fixed on the linear motor driven table system. A strain gauge type 3-axis force sensor was installed on the tool post to observe the cutting phenomena. The following part of this section will explain the developed system in detail.

3.1 Linear motor driven table system

In order to realize a high cutting speed in an appropriate stroke, high acceleration capability is required. Therefore, a linear motor was adopted in the developed system. Advantages of the linear motor system compared with other systems such as a high-lead ball screw mechanism are a long stroke without resonance and a high acceleration to produce high speed. The stroke, positioning resolution and the maximum feed speed of the linear motor system are 1050mm, 1 micrometer, and 120 m/min, respectively.

3.2 Cutting depth control mechanism

A hybrid feed mechanism with a coarse and a fine positioning unit is adopted to control the cutting depth. The coarse positioning unit, using a ball screw with 1mm lead, is installed for tool setup and rough approaching. The fine positioning unit, using a piezo-electric actuator, determines the depth of cut. Figure 2 shows the overview of the fine positioning unit. The hysteresis of the piezo-electric actuator was compensated by monitoring the displacement of the parallel plate structure unit. Strain gauges are attached on the due place of the unit. The fine positioning function is realized by examining the relationship between the displacement and the ouput strain. Figure 3 shows the relationship between the displacement and the strain. Proportional relationship between them, represented by the following equation, was

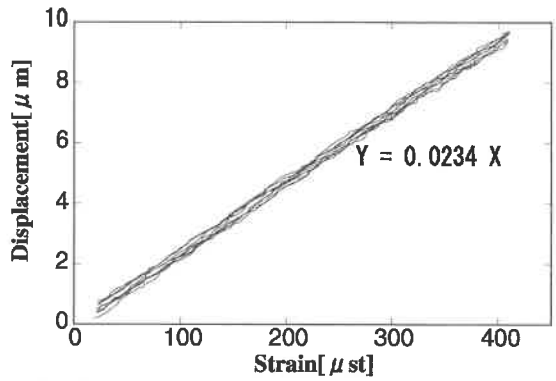

Fig.3 Relationship between strain and displacement

Fig.4 A groove produced by the developed system

detected: $Y = 0.0234X$, where X and Y are strain and displacement, respectivity. In the developed system, 0.1 micrometer resolution was realized.

3.3 3-axis force sensor

A strain gauge type 3-axis force sensor is installed between a cutting tool and the cutting depth control mechanism. The purposes of the sensor are to observe the cutting behavior and also to perform a feedback control for cutting conditions to maintain the ductile mode cutting. The nominal resolution of the force sensor is 4mN in each direction.

4. Experiment results

Cutting experiments were performed using the developed system. The workpiece material is soda-lime glass. Specification of the cutting tool used in the experiments is shown in Table 1. The feed speed is set as 1mm/s to verify the performance of the developed system. The speed is known as a condition of the ductile mode cutting for a brittle material. In the experiments, both brittle mode cutting and ductile mode cutting were observed. The experiment proved the capability of ductile mode cutting using the developed system. Figure 4 shows a photomicrograph of the transient mode from ductile to brittle. Figures 5 and 6 show the cross section of the groove in the ductile and the brittle mode cutting in Fig.4, respectively. The measured depth of cut in ductile mode cutting was approximately 3.7 micrometer, which is larger than that reported by many other researchers. Generally, it is said 0.1 micrometer. The reason of the observed phenomena is not still clear. It was difficult to obtain the valid force information because of the noise from the magnetic field of the linear motor.

Table 1 Specification fo the cutting tool

Tool angle	118 deg.
Rake angle	−30 deg.
Nose radius	3mm
Edge radius	less than 80mm
Material	single crystal diamond

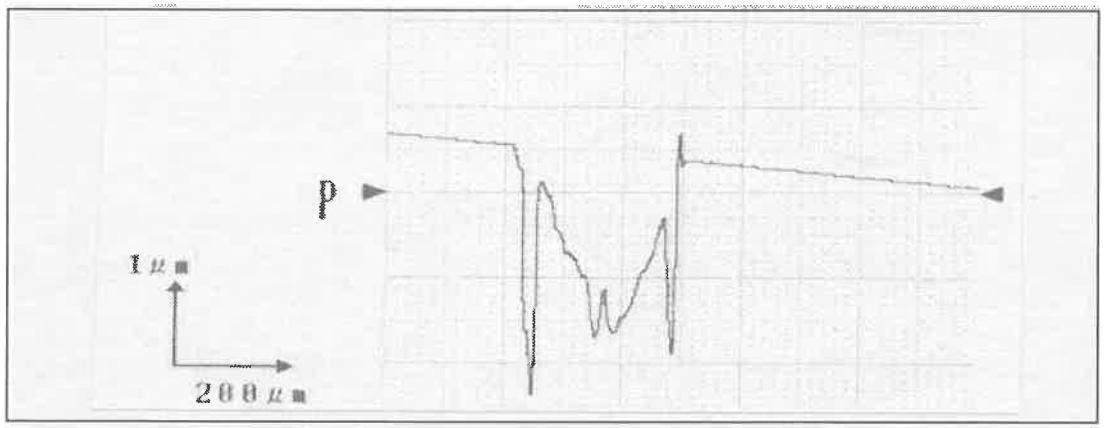

Fig.5 Cross section of the groove in brittle mode cutting

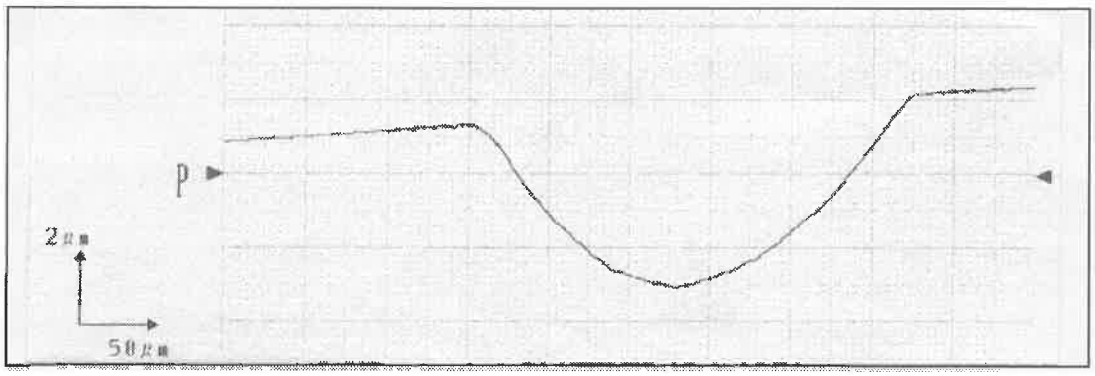

Fig.6 Cross section of the groove in ductile mode cutting

5. Conclusions

A high-speed micro-machining system for a brittle material was newly developed by the authors. Cutting experiments show the capability of the ductile mode cutting using the developed system. In the experiment, the observed depth of cut of the groove in the ductile mode cutting was larger than that reported by others. High-speed cutting will be conducted in the future.

References

[1] Yoshio ICHIDA, Nabil BEN FREJ and Reza YOUSEFI, "Ductile-Mode Mirror Cutting of Single-Crystal Silicon," *J.JSPE*, vol.64, no.4, pp.608–612, 1998.

[2] Masahiko YOSHINO, Takayuki AOKI, Taisuke SUGISHIMA and Takahiro SHIRAKASHI, "Scratching Test on Hard-brittle Materials under High Hydrostatic Pressure," *J.JSPE*, vol.65, no.10, pp.1481–1485, 1999.

[3] Ichiro OGURA and Yuichi OKAZAKI, "The study on cutting brittle materials," *Autumn meeting of JSPE*, p.126, 2000.

[4] Hiroshi EDA, Lotfi CHOUANINE and Jun SHIMIZU, "Verification of Ductile-Regime Generation on Scratching Process of Glasses – In Case of Using Sharply Pointed Tip Diamond Indenter –," *J.JSPE*, vol.64, no.4, pp.613–618, 1998.

Kinematic Modeling of a 6 Degree of Freedom Tri-Stage Micro-Positioner

Nicholas G. Dagalakis, Edward Amatucci
National Institute of Standards and Technology
Gaithersburg, Maryland 20899

Abstract

The 6-Degree of Freedom Tri-Stage Micro Positioner (6DFTSMP) can generate high accuracy, small displacement, and high-resolution motions. The moving platform of the device has six degrees (6-D) of freedom motions (translation and rotation about three orthogonal axes, X-Y-Z). The 6DFTSMP is unique because it derives its input motion from a monolithic tri-stage base plate and has struts that may have specially designed flexures. The 6DFTSMP capitalizes on the availability of inexpensive high quality planar micro-positioning stages for the control of its moving platform. Because the struts, which connect the planar micro positioning stages with the moving platform are oriented in a parallel mechanism fashion the in plane motion of the stages is converted into a translation and rotation about three orthogonal axes. Two experimental prototypes of the 6DFTSMP have been built and various mathematical models have been developed. A micro-position and orientation measurement sensor nest has been developed, which will be used to test various calibration and performance testing methods for this type of micro-positioners.

Introduction

Opto-Electronic Manufacturing and Assembly is quickly becoming part of the critical path in advancing the manufacturing practices of many photonic manufacturers. Without reliable and inexpensive solutions to their manufacturing needs, many of their advanced photonic designs and products will be impractical for production and consumer applications. Usually manufacturing has been overlooked and is an after thought in the development of advances in industry. A critical component of Opto-Electronic Manufacturing and Assembly is the micro-positioner. A reliable, easy to calibrate, five to six degrees of freedom micro-positioner can significantly enhance the alignment and assembly of Opto-Electronic devices. The focus of the work we report in this paper is the development of sensors, calibration and performance testing techniques for parallel mechanism micro-positioners, like the 6DFTSMP.

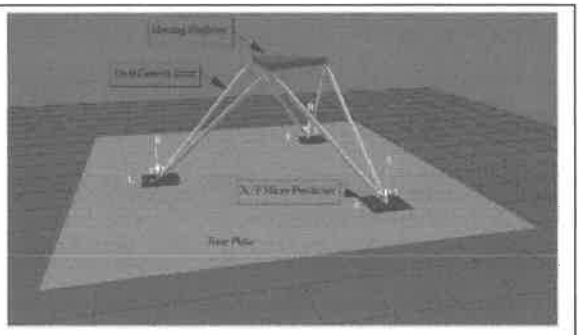

Figure 1. Schematic drawing of the 6DFTSMP

Figure 1 shows a schematic drawing of the 6DFTSMP with struts, which have flexures at both attachment points. The device consists of a base plate, six struts and a moving platform. The base plate is equipped with three X-Y micro positioning stages. Each of these stages is capable of generating motion in two orthogonal directions. The range of these motions depends on the design and size of these stages. The moving plate of each X-Y stage supports two struts, which are firmly attached to the plate on one end and the moving platform on the other and allow motion to take place through elastic deformation of the struts and their flexures thus eliminating backlash and stiction. The moving platform is the load carrying part of the device.

The coordinates of the base plate support points of the struts form the base of the 6DFTSMP. The size and shape of the 6DFTSMP base changes, the struts deform, and the position and orientation of the moving platform changes when the moving plate of each X-Y stage moves. With proper calibration and sensors it is possible to control the position and orientation of the moving platform by commanding appropriate displacements of each X-Y stage moving plate. The three X-Y micro positioning stages are machined on the monolithic base [1]. This simplifies the design and makes the 6DFTSMP more compact. Also the use of a monolithic actuating base and a deformable three dimensional parallel mechanism structure eliminates backlash and stiction during motion. Because the actuation of motion takes place at the base there is no inherent limit to the size of the micro positioning stages, thus permitting a wider range of motion of the moving platform.

Experimental Prototypes

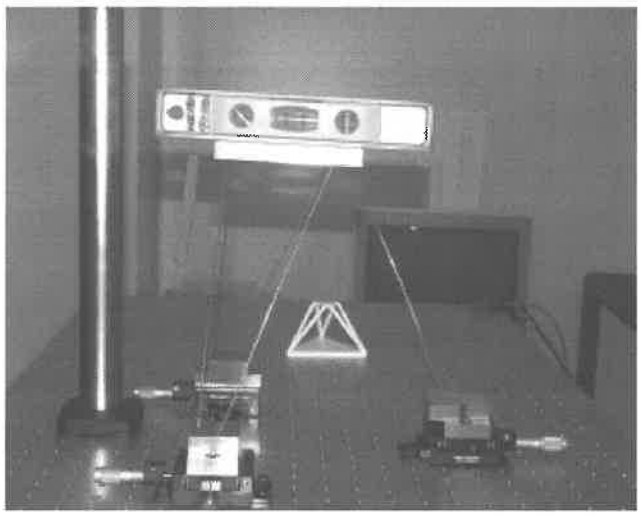

Figure 2. Steel wire 6DFTSMP prototype

Two functioning experimental prototypes have been constructed. Figure 2 shows a prototype that uses six Steel wire struts. The base plate X-Y micro positioning stages are simulated by three manual micro-meter stages. The use of these stages allows us to vary the size of the base plate without having to build one every time we make a change. Depending on the length and the diameter of the wires it is possible to achieve significant translations and rotations of the moving platform, as it is demonstrated in Figure 2. Because the wires act as parallel actuators the stiffness and payload capacity of the micro-positioner can be significant too.

Figure 3 shows the second prototype that uses six 6.35 mm (0.25 in) diameter steel rod struts. The base plate X-Y micro positioning stages are simulated by three motorized stages. The steel rods have their diameter reduced to 1.53 mm (0.006 in) at both ends, which are then attached to the base plates and the lower side of the moving platform. The reduction in the rod diameter forces the strut deformation to take place near the strut attachment points while the strut rod remains virtually rigid. A simple digital controller has been developed, which uses data from the kinematic models of these experimental prototypes

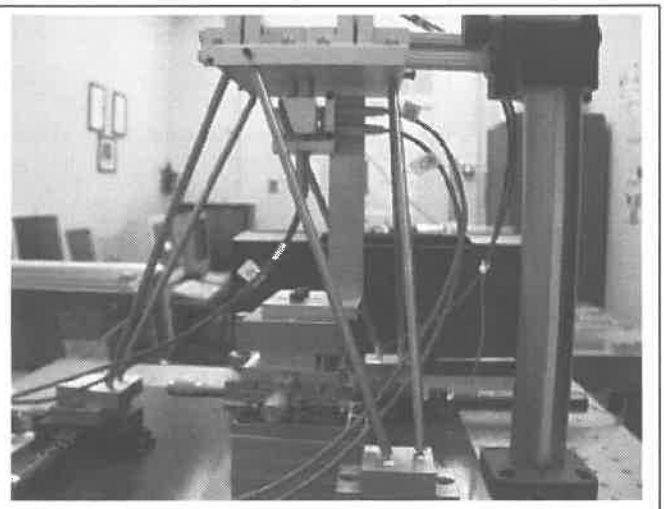

Figure 3. Steel rod 6DFTSMP prototype

to drive the X-Y micro positioning stages that result in a rotation and translation of the moving platform.

Micro Translation and Rotation Sensor

A good calibration requires a sensor that will measure the position and orientation of the moving platform stage. This is not a trivial operation especially when some applications might require accuracy of the order of 1 micrometer or less.

It is always possible to use several laser interferometers and autocollimators to measure the components of translation and rotation of the moving platform. This type of sensor though will be difficult to setup and very expensive. We needed a relatively simple, low cost sensor that can be used by manufacturers and users to calibrate and check the performance of 6-D micro-positioners. The solution was to modify a robot metrology sensor [2] to meet the above mentioned requirements. Based on our experience from the calibration and performance of planar micro-positioners we were able to build a compact sensor that can be installed and removed in a few minutes and which can serve an additional important function to protect the mechanism from overloading. Overloading can result from excessive actuator torque or impact with another object, like for example a robot arm. The sensor can be seen in Figure 3 underneath the centroid of the moving platform.

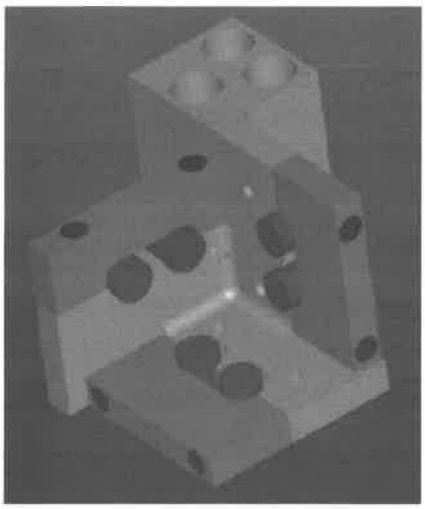

Figure 4. Close-up of clamps that hold the proximity sensors. Black cylinders represent proximity sensors.

To avoid interfering with the motion of the moving platform we decided to use non-contact proximity sensors. The main choices are capacitive gages and opto-electronic reflective sensors. The capacitive gages are excellent proximity sensors, but can cost 10 times or more the cost of opto-electronic reflective sensors.

The reflectors of our sensor are the polished sides of a true square cube. The cube has five highly polished reflecting sides orthogonal to each other within 3 arc seconds. The sixth side has three tapped holes for mounting underneath the moving platform. The cube is attached to the lower side of the moving platform plate and translates and rotates with the platform as a single rigid body. Three orthogonal adjacent sides of the cube face three orthogonal adjacent plates of a sensor nest (see CAD image in Figure 4) mounted on a beam, which is attached to the base plate through an X-Y-Z position adjustment stage. The sensor nest remains stationary while the cube moves with the micro-positioner moving platform. Two proximity sensors are mounted on each sensor nest plate with their sensitive front side facing the moving cube. The six distance signals from the sensors can be combined to estimate the position and orientation of the moving platform reflecting cube rigid body with respect to a sensor nest reference coordinate frame. Each sensor nest plate consists of two parts, a plate with two V shape groves and a clamp. The proximity sensors are placed in the V shape groves and are held in place by the clamps. Loosening the screw that corresponds to each proximity sensor allows adjustment of its position until the desired output signal is detected. The sensor nest has to be calibrated first and then used to calibrate the micro-positioner. Once the sensor nest is calibrated epoxy glue drops are used to detect any change in the position of the proximity sensors within the sensor nest.

Kinematic Models

Kinematic mathematical models have been developed for two different versions of the 6DFTSMP. The intersecting struts design and the non-intersecting struts design. Figure 1 shows an example of an intersecting struts 6DFTSMP. In that case the neighboring struts are joined at the center of their upper and lower flexures and then attached to the base plate and the moving platform. Figure 3 shows an example of a non-intersecting struts 6DFTSMP. In that case the struts are attached to the base plate and the moving platform at separate points, which are determined by the desired geometry of the mechanism. The objective of our work is to develop calibration and performance testing techniques for a variety of these designs. At this stage our calibration effort is focused on the identification of the parameters of kinematic and dynamic mathematical models of the micro-positioners and the use of the performance tests to evaluate the accuracy of these models. Since it is not possible to fully predict the shape of the deforming 6DFTSMP under various loading conditions it will take several iterations in order to come up with models that meet tight performance specifications. These models are necessary for the control of these type micro-positioners and for the detection of defects that are difficult to detect by simple inspection, like for example plastic deformation of strut flexures.

The most simple of the mathematical models is that of the intersecting struts 6DFTSMP. It can be shown that the coordinates d_{ix}, d_{iy}, of the base plate attachment points for i = 1, 2, 3, with respect to the base plate coordinate system are given by:

$$\left(s_{ix}^{2}+1\right)d_{iy}^{2}+2\left(s_{ix}\left(h_x+p_{ix}\right)-\left(h_y+p_{iy}\right)-q_{ix}s_{ix}\right)d_{iy}+\left(q_{ix}^{2}-2\left(h_x+p_{ix}\right)q_{ix}+g_i\right)=0 \quad (1)$$

$$d_{ix}=q_{ix}-s_{ix}d_{iy} \quad (2)$$

Where p_{ix}, p_{iy}, are the coordinates of the three moving platform attachment points and h_x is the X-axis coordinate of the centroid of the moving platform. s_{ix}, q_{ix}, g_i, are complex functions of the kinematic parameters of the mechanism, which cannot be listed here due to the page limitation, but will be described in later publications.

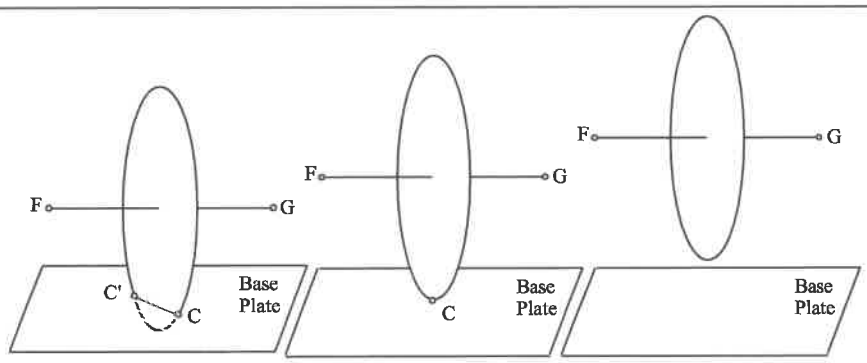

Figure 5. Two, single and no point intersection representation

Equation (1) can have two, one or no solutions. This is depicted by the three schematic drawings of Fig. 5, where F and G represent moving platform attachment points and C, C' solutions.

References

1. Amatucci E., Dagalakis N.G., Kramar J.A., Scire F.E., "Performance Evaluation of a Parallel Cantilever Biaxial Micropositioning Stage," ASPE 2000 Annual Meeting, Oct. 22-27, 2000, Scottsdale, Arizona.

2. Ranky, P. G. "Test Method and Software for Robot Qualification," The Industrial Robot, pp. 111-115, June 1984.

Acknowledgements

This work was supported by the NIST-ATP, Office of Electronics and Photonics Technology.

Design and Control of Versatile Micro Robot for Microscopic Manipulation

Ohmi Fuchiwaki and Hisayuki Aoyama
Applied Micro Systems
Dept. of Mechanical Engineering and Intelligent Systems
University of Electro-Communications,
1-5-1,Chofugaoka,Chofu, Tokyo 182-8585
Japan

Abstract:
In this paper, we describe design and control of the newly developed versatile micro robot which can be applied to microscopes. In order to provide microscopic manipulation, the unique locomotion mechanism which is composed of four piezo elements and two electromagnets is proposed. Here two legs arranged on cross each other are connected by four piezo elements so that it can move in any directions, i.e. in X and Y directions as well as rotate at the specified point precisely with the manner of inch worm. Moreover the combination of particular wave forms for piezo elements can provide "arc trajectory", that is important for the micro manipulator to keep its tip end within the microscopic area. In the primary experiments, several performances such as motion accuracy, reliability and precise dexterity are checked by the CCD camera based microscope image tracker. The design procedure, basic performance and biomedical application of this tiny robot also are discussed to open the new field for micro-robotics in precision region.

Key word : versatile micro robot, piezo element, electromagnet, arc trajectory, microscopic manipulation

1. Introduction

In the field of micro system and precision engineering, there are many reports concerning micro robotics and its trial applications. Some of them are based on the advanced technology including micro battery, micro motor and tiny computational facility[1], the others are made by the sophisticated precision machining techniques[2-4] However it is still very important to find the industrial application where such micro robots can provide effective benefits. It is well known that the *Desk top Factory* [5] has the potential application not only for the production engineering but also for the chemical and biotechnology. For these years, our group has developed insect size robots equipped with various micro tools and instruments[6]. Particularly the in-situ micro processing in the scanning electron

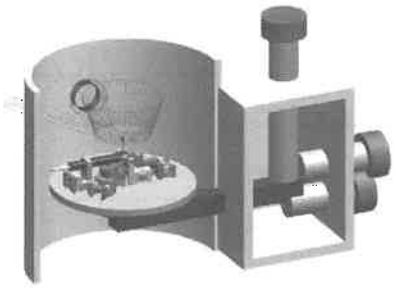

Fig.1 Flexible micro processing system by micro robots in SEM vacuum chamber

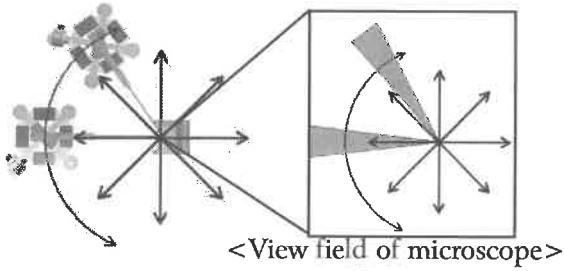

Fig.2 Motion pattern required at microscopic operation

microscope is one of interesting application although it needs much of cost to install the fine mechanism into the small chamber[7]. For these years, we have proposed the flexible micro-processing system organized by multiple miniature robots in SEM vacuum chamber as shown Fig.1[8]. And we provide a simple manipulation system for micro objects and micro processing system assisted by fiber guided YAG-laser. In these previous experiments, we concluded that we needed to arc trajectory motion as well as XY orthogonal motions with facing center to keep its tip end within the microscopic monitoring area. In this paper, we describe design and control of the newly developed versatile micro robot which can move any direction. In the experiment, several performances such as motion accuracy, reliability and precise dexterity are checked by the CCD based image analyzer.

2. Design and Principle of Versatile Micro Robot

2-1. Design and Structure

Fig.2 shows the motion pattern required at microscopic operation and in order to realize these motion pattern at the same time, we need to design the structure which can move in XY directions and in rotation independently.

Fig.3 shows the structure of the micro robot. Here two closed loop electromagnets which are arranged to cross each other are connected by four piezo elements so that it can move in any direction with the manner of inch worm. Also we design the special joint at one of the 4 legs to get the stable 4 legs contact on the surface at once.

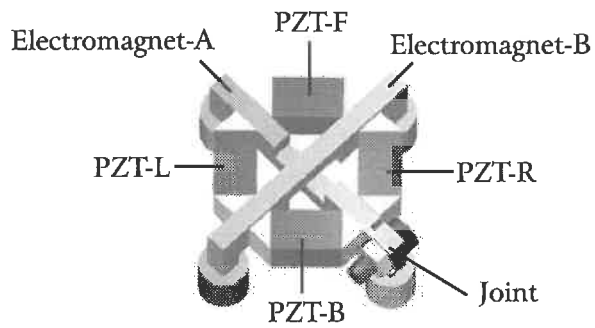

Fig.3 Structure of versatile micro robot

2-2. Principle of Versatile Motions

(1) Basic Motion

Fig.4 shows the motion sequence of forward motion. Here we use right and left PZT actuators. At first the robot can

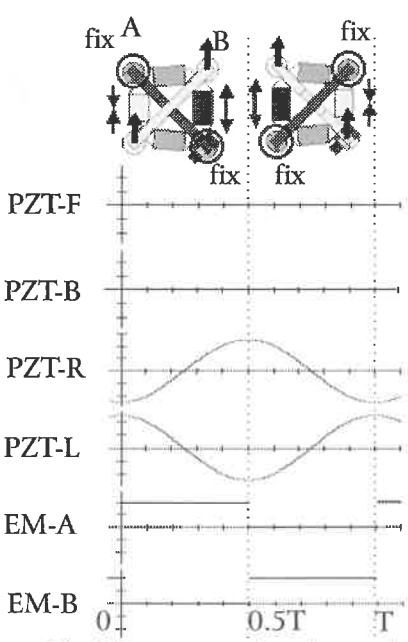

Fig.4 Sequence of orthogonal motion

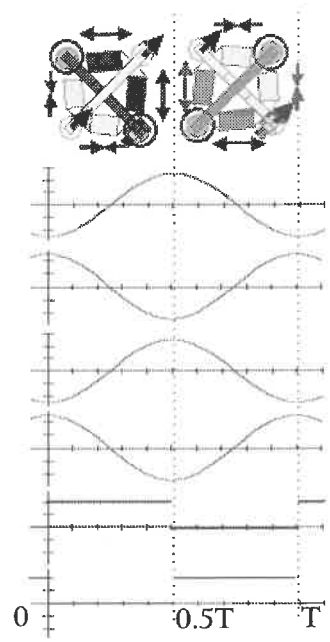

Fig.5 Sequence of diagonal motion

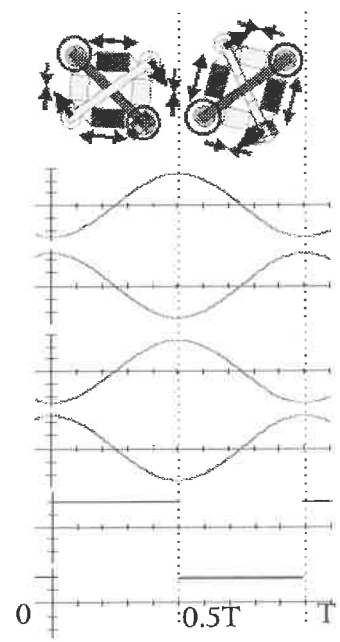

Fig.6 Sequence of rotation

fix the electromagnet-A and constrict the PZT-L and expand PZT-R, then the body can move one step forward. In the next step, the robot can fix the electromagnet-B, expand the PZT-L and constrict the PZT-R, then the electromagnet-A can be moved forward. The robot can repeat the sequence, then the robot can move forward precisely with the manner of inch worm. If the similar sequence are operated, the robot can move in the diagonal direction as depicted in Fig.5.

(2) Arc Trajectory

We also give the unique signal to the small robot so that it can rotate as in Fig.6 Additionally we can consider the specified model of this piezo based small robot as depicted in Fig.7 to move on the arc trajectory. In this figure, we give the approximation that the two points, K1, K2 on the contact point of magnets can move to the K1', K2' on the arc. We can tune the amplitudes and the phase difference of 4 PZT elements' sine wave. Then the small robot can move on the arc path with respect to the center point for rotation.

3. Experiments

As shown in Fig.8, we provided the versatile robot to check its primary performance. The robot is 30mm in

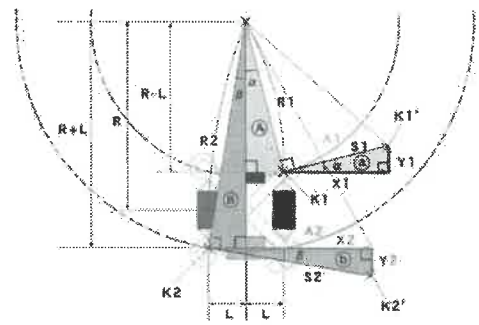

$$V-F = (Pmax)\left(\frac{R-L}{R+L}\right)\sin t$$

$$V-B = (Pmax)\sin(t+\pi)$$

$$V-R = (Pmax)\left(\frac{L}{R+L}\right)\sin t$$

$$V-L = (Pmax)\left(\frac{L}{R+L}\right)\sin t$$

Fig.7 The mechanical model of arc trajectory

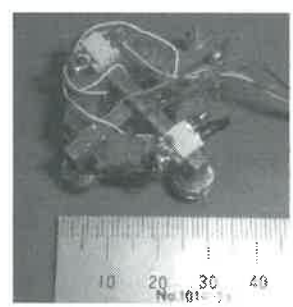

Fig.8 Versatile micro robot provided for microscopic operation

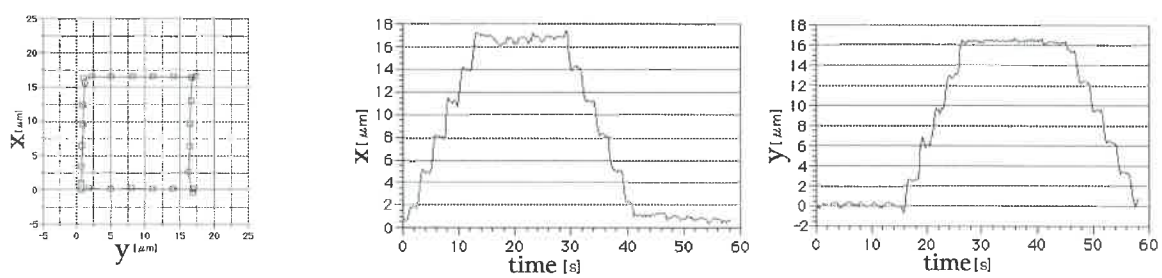

Fig.9 Experimental result of square path motion (5 steps at each movement, 0.5[Hz])

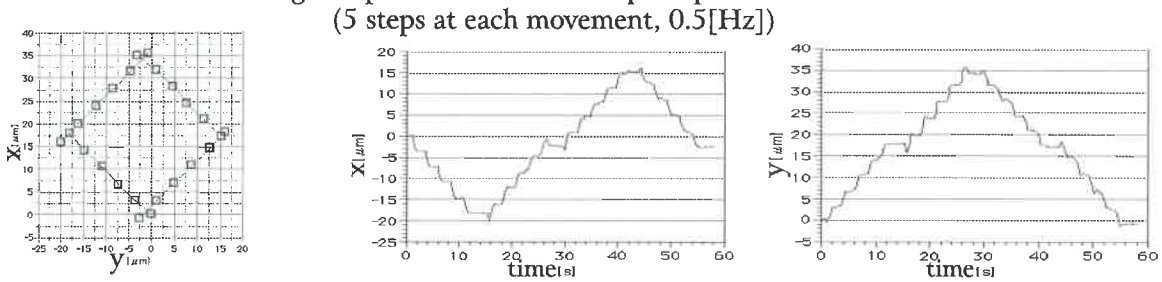

Fig.10 Experimental result of diagonal movement (5 steps at each movement, 0.5[Hz])

length, 30mm in width and 15mm in height. We use the stacked type PZT elements of 5mm x 5mm x 10mm. Each piezo element is connected with the electromagnet leg with the plastic insulator.

3.1 Fine motion accuracy

In the experiment, we used the microscope with CCD based image analyzer to measure its motion accuracy. Fig.9 and Fig.10 show the results of fine motion experiment. We can confirm that the robot can move in both the orthogonal and the diagonal directions.

3.2 Arc trajectory motion

In another experiment, we succeeded in controlling the small robot to move on the arc trajectory with fixing center point as depicted Fig.11. This performance should be useful to manipulate the small object in the focused area such microscope.

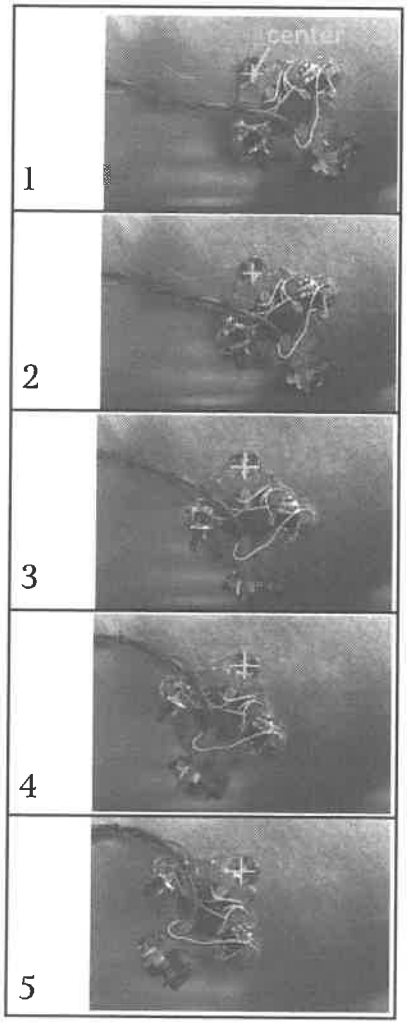

Fig.11 Experimental result of arc trajectory motion (150[Hz])

4. Conclusion & Future Works

Versatile micro robot which can move any direction and rotate with respect to the specified point precisely was proposed and developed. And the typical performances of this robot were confirmed by the experiments. Furthermore in order to realize more advanced and complicated motion such as any angle diagonal movement or any radius arc trajectory motion at any point, we will improve our robot, develop the PC controlled system with the help of the visual feedback system. We are also developing micro tools which can be implemented on the robot to achieve the flexible micro processing system under the collaboration by this versatile micro robots.

References

(1)H. Ishihara, T. Fukuda: Miniaturized Autonomous Robot, Proc. of SPIE, Vol.3202,(1997)pp.191-196

(2)S. Martel, K. Doyle, G. Martinez, I. Hunter, and S. Lafontaine: Integrating a complex electronic system in a small scale autonomous instrumented robot: the NanoWaker Project, Proc. of SPIE, Vol.3834(1999) pp. 63-73

(3)S. Fatikow: Automated micromanipulation desftop-station based on mobile pie zoelectric microrobots, Proc. of SPIE, Vol.2906,(1996) pp.66-77

(4)Nobuyuki KAWAHARA, Takayuki SHIBATA, Takanari SASAYA: In-pipe Wireless Micro Robot, Proc. of SPIE, Vol.3834(1999)pp. 166-171

(5)T.Kitahara,K.Ashida,M.Tanaka,Y.Ishikawa, N.Oyama and Y.Nakazawa;Microfactory and Microlathe, Proc. of Int. Workshop on Microfactories, (1999)pp. 1-8

(6)H. Aoyama, F. Iwata, and A. Sasaki: Desktop flexible manufacturing system by movable miniature robots, Proc. of Int. Conf .on Robotics and Auto mation(1995) pp. 660-665

(7)Y.Hatamura,M.Nakao and T.Sato: Construction of Nano Manufacturing World as a Desk-top Factory , Microsystem technologies 1, (1995)pp. 155-162

(8)H.Aoyama and O.Fuchiwaki: Flexible Micro Processing by Multiple Micro Robots in SEM, 2001 IEEE International Conference on Robotics & Auto mation, (2001)FP04

DEVELOPMENT OF A MICRO-SCREW AND A MICRO-PITCH-RACK UTILIZED TUNGSTEN WIRES

Satoshi Honda
Tokyo Metropolitan Institute of Technology, Tokyo, Japan

1. Introduction

Micro-mechanical parts for a micro-machine are mostly produced by two methods of the LIGA process or an ultra-precise grinding/milling. If we choose the LIGA process to make the micro-parts, the LIGA process requires lithography equipments for IC manufacturing system; besides, their equipment must be kept in a clean room. The cost of the lithography equipment is over ten million dollars and running cost for the clean room runs up to considerable sum. Therefore, advanced researches for the micro-machine which parts are produced by the LIGA process are only proceeding at a few research institutes. If we choose the ultra-precise grinding/milling method to make the micro-parts, the method requires the special designed machine tool and special whetstone wheels or exclusive cutting tools. Therefore, advanced researches for the micro-machine which parts produced by the ultra-precise grinding/milling methods are only proceeded by limited researchers. The third method for providing the micro-mechanical parts is waited for eagerly.

A novel method to make the micro mechanical parts utilized superfine wires is thought up in this paper. Several trial products of micro-screws, micro-pitch racks and internal gears with micro-teeth utilized a tinning lead wire are mentioned as prompt results. Possibility of the micro-mechanical parts utilized a tungsten wire which diameter is less than 50 micrometers is investigated.

2. Micro-screw utilized a superfine wire

A micro-screw utilized a superfine wire is made as follows. A superfine wire is coiled around a needle pin, and the superfine wire and the needle pin are brazed with bonding metal. Figure 1 shows the micro-screw brazed a tinning lead wire and a standardized screw of M1.4 in normal size. The micro-screw has dimensions of 0.85 millimetres in diameter and of 0.22 millimetres in

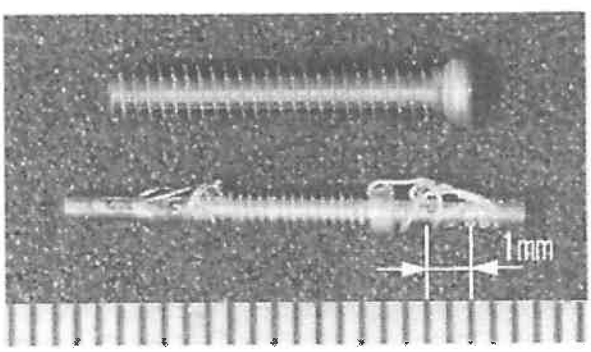

Figure 1. Micro-screw brazed a tinning lead wire and the standardized screw of M1.4.
(Diameter of the micro-screw is 0.85 mm.)
(Pitch of the micro-screw is 0.22 mm.)

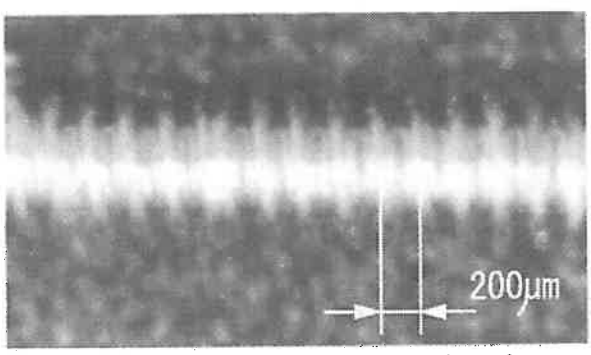

Figure 2. Enlarged photograph of the micro-screw.
(Diameter of the tinning lead wire is 0.1 mm.)
(Diameter of the needle pin is 0.6 mm.)

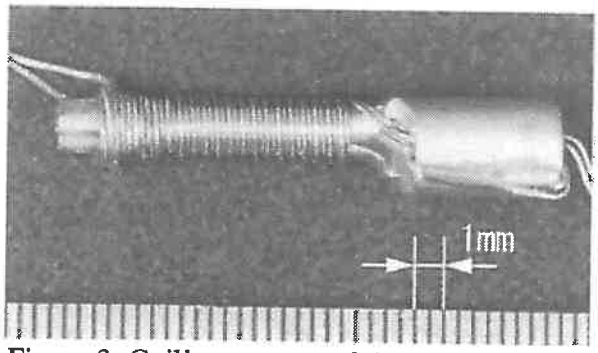

Figure 3. Coiling process of the tinning lead wire and the polyurethane lead wire

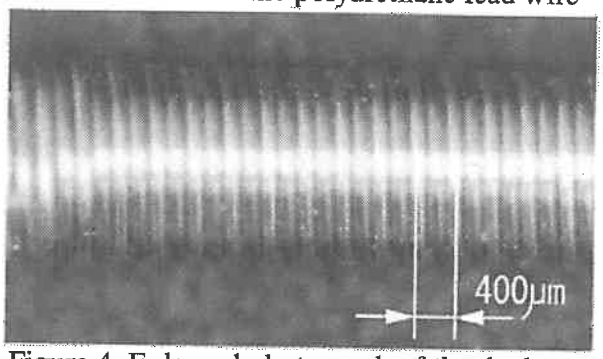

Figure 4. Enlarged photograph of the dual coiled micro-screw

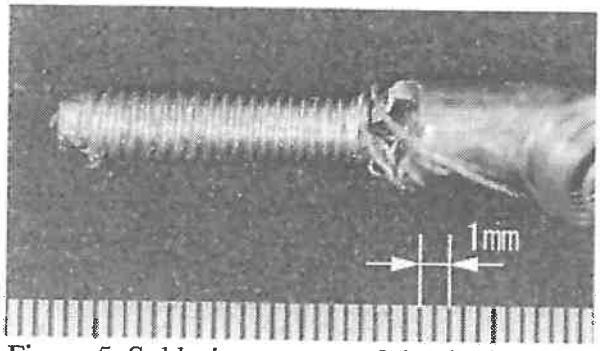

Figure 5. Soldering process of the tinning lead wire and peeling process of the polyurethane lead wire.

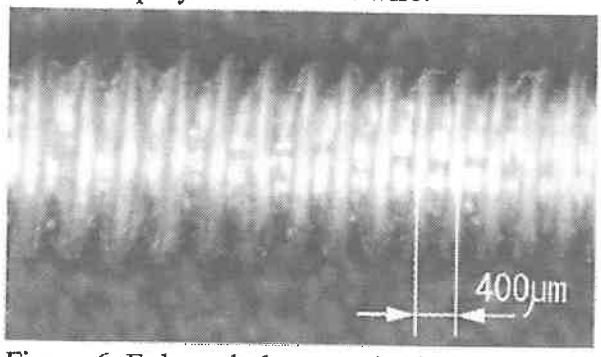

Figure 6. Enlarged photograph of the micro-screw

pitch. Just for reference, diameter of the standardized screw is 1.4 millimetres and its pitch is 0.3 millimetres. An enlarged photograph of the micro-screw is shown in figure 2.

3. Processes for making the micro-screw utilized the tinning lead wire

The micro-screw utilized a tinning lead wire is made as follow. A pin type of an electrical terminal is used as the needle pin. The electrical terminal is plated with tin, and its diameter is 1.85 millimetres. A pair of a tinning lead wire and an insulated lead wire filmed with polyurethane is coiled around the needle pin by hand like a double-threaded screw. Both diameters of the tinning lead wire and the insulated lead wire are same size of 200 micrometers. The micro-screw coiled by double wire is produced as shown in figure 3 and figure 4.

Solder melted upon the dual coiled micro-screw flows into gaps between the electrical terminal and the coiled wires. The tinning lead wire is soldered around the electrical terminal, but, the insulated lead wire is not soldered around the electrical terminal. The insulated lead wire is peeled from the dual coiled micro-screw. The micro-screw to solder the tinning lead wire is produced as shown in figure 5 and figure 6. The micro-screw has dimensions of 400 micrometers in pitch and 2.35 millimetres in diameter. Axial section of the micro-screw becomes the profile connected semicircle concave ditches and semicircle convex ridges alternatively.

4. Several trial products of micro-screws, micro-pitch racks and internal micro-gears

Figure 7 and figure 8 show the micro-screw to coil and to solder the tinning lead wire around the electrical terminal in the same processes mentioned above. Pitch of the micro-screw is 200 micrometers.

Figure 9 and figure 10 show a micro-pitch

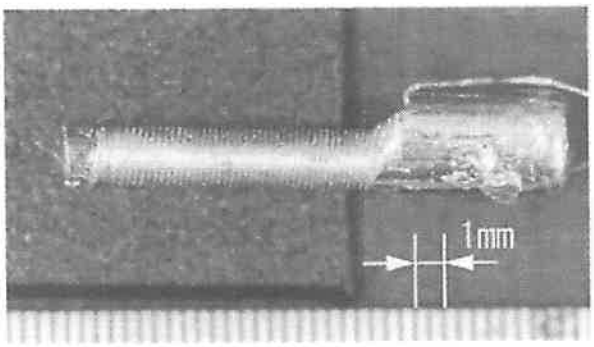

Figure 7. The micro-screw to solder the tinning lead wires
(Diameter of the tinning lead wire is 0.1 mm.)

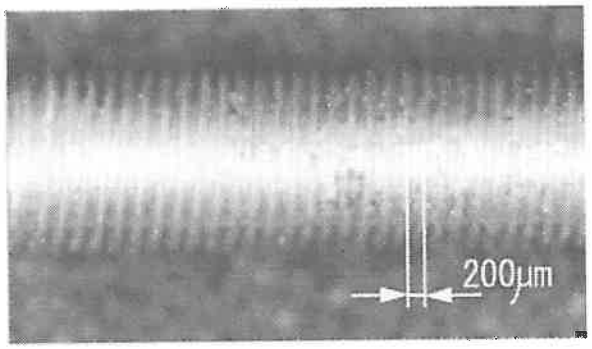

Figure 8: Enlarged photograph of the micro-screw showed in figure 7

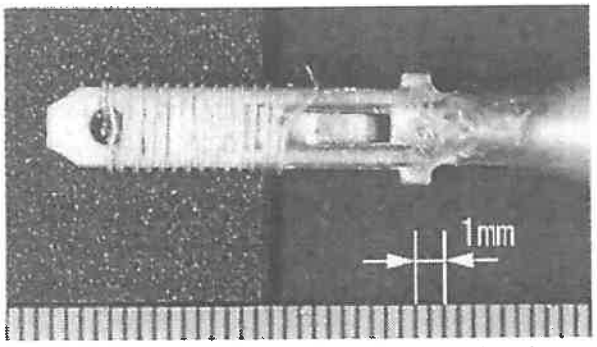

Figure 9. The micro-pitch rack to solder the tinning lead wires
(Diameter of the tinning lead wire is 0.2 mm.)

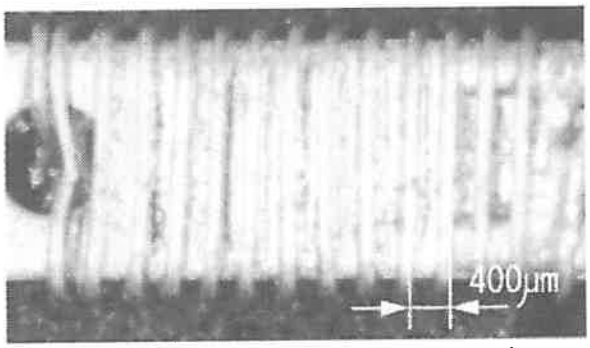

Figure 10. Enlarged photograph of the micro-pitch rack showed in figure 10

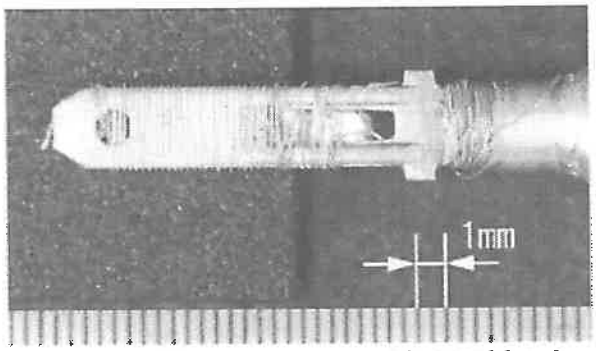

Figure 11. The micro-pitch rack to solder the tinning lead wires
(Diameter of the tinning lead wire is 0.1 mm.)

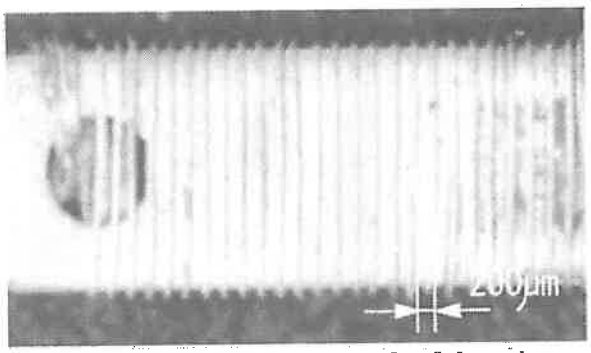

Figure 12. Enlarged photograph of the micro-pitch rack showed in figure 11

rack to coil and to solder the tinning lead wire around a flat face type of the electrical terminal. Pitch of the micro-pitch rack is 400 micrometers.

Figure 11 and figure 12 show a micro-pitch rack to coil and to solder the tinning lead wire around the flat face type of the electrical terminal. Pitch of the micro-pitch rack is 200 micrometers.

As the tinning lead wire was coiled by hand, pitch of the micro-screw and the micro-pitch rack is of unevenness value, and actual pitch of the micro-screw and the micro-pitch rack is a little longer than theoretical pitch. The theoretical pitch means an interval between one tinning lead wire and next coiled tinning

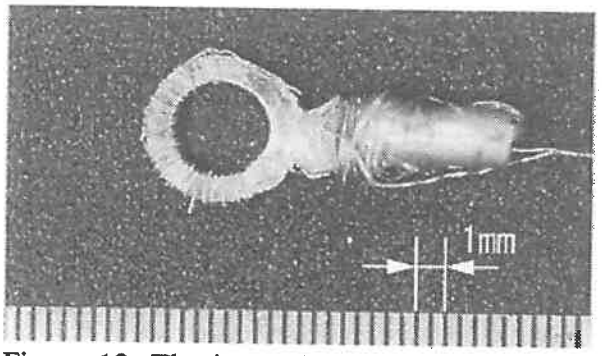

Figure 13. The internal micro-gear to solder the tinning lead wires
(Diameter of the tinning lead wire is 0.2 mm.)

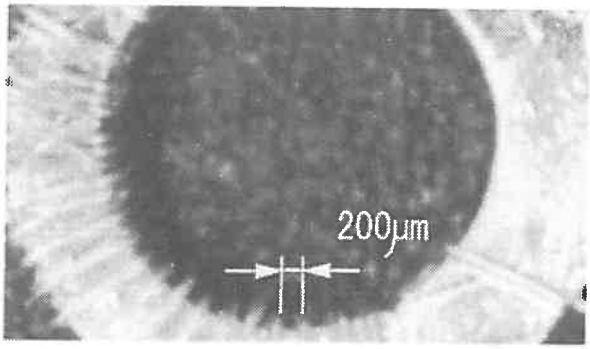

Figure 14. Enlarged photograph of the internal micro-gear showed in figure 13

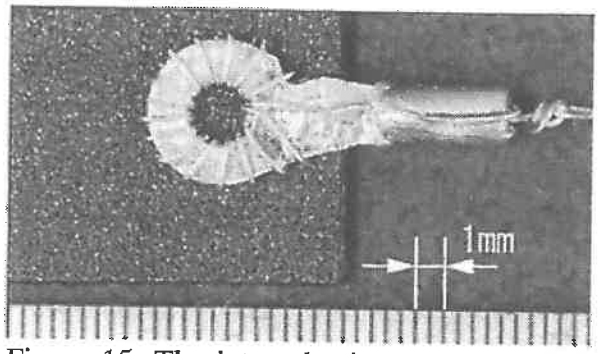

Figure 15. The internal micro-gear to solder the tinning lead wires
(Diameter of the tinning lead wire is 0.1 mm.)

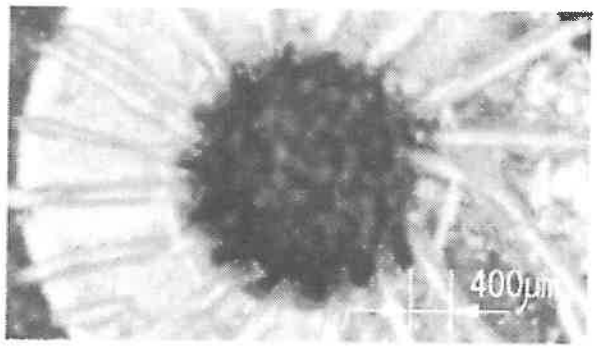

Figure 16. Enlarged photograph of the internal micro-gear showed in figure 15

lead wire when the tinning lead wire and the insulated lead wire are coiled without slit.

Figure 13 and figure 14 show the internal micro-gear to coil and to solder the tinning lead wire around a ring of a circular type of the electrical terminal. In the coiling process, the pair of the tinning lead wire and the insulated lead wire is coiled without slit on the inside of a centre hole.

Figure 15 and figure 16 show the internal micro-gear to coil and to solder the tinning lead wire around the ring of the circular type of the electrical terminal.

As we coiled the pair of the tinning lead wire and the insulated lead wire around the ring of the electrical terminal by hand, we could not coiled both lead wires without crossing or twisting of both lead wires.

5. Possibility of the micro-mechanical parts utilized tungsten wires

It is easy to coile the tungsten wire which diameter is 50 micrometers or 20 micrometers even if the tungsten wire is coiled by hand. The tungsten wire which diameter is 2 micrometers has been already commercialised. The micro-screw and the micro-pitch rack which pitch is 4 micrometers will be developed if the brazing method in which the tungsten wire is brazed with silver solder around the needle pin is developed

6. Conclusions

The method for making the micro-mechanical parts utilized a superfine wire is developed. The micro-screws, the micro-pitch racks and the internal micro-gears are produced as prompt results by soldering the tinning lead wire around the needle pin.

POLISHING TiN FOR NANOTUBE SYNTHESIS

Phil Smith, Chris Trinkle, R. Ryan Vallance
Precision Systems Laboratory, University of Kentucky, Lexington, KY *

Jay Gaillard, Bindu Sadanand, and A. M. Rao
Department of Physics and Astronomy, Clemson University, Clemson, SC †

Abstract

Carbon nanotubes have excellent mechanical and electrical properties for applications requiring the smallest probe tips in scanning probe microscopy or electron discharge. Large quantities of aligned multi-walled nanotubes are often synthesized on flat substrates made of quartz, but electrically conductive substrates are preferable for field emission applications. Polished substrates made from compacted titanium nitride (TiN), a conductive ceramic traditionally used for coating cutting tools, were previously used to produce excellent field emitters. However, nanotubes could not be synthesized on surfaces sputtered with TiN, suggesting that the topography of polished surfaces might play some role in enabling nanotube synthesis. To test this hypothesis, we synthesized nanotubes on three sets of TiN substrates that were polished with three processes to obtain different surface roughness parameters. Although nanotubes were successfully synthesized on all TiN substrates, the vertical alignment was inferior to those typically synthesized on quartz substrates. The highest degree of alignment was observed on the roughest samples. This paper describes the polishing processes, characterizes the surface topography, and shows nanotubes synthesized on polished TiN surfaces.

Keywords: titanium nitride, polishing, nanotubes, field emission

Introduction

Carbon nanotubes, first identified in 1991 [1], are a hexagonal lattice of carbon atoms similar to a graphene sheet rolled upon itself to form long narrow tubes. The ends of nanotubes are typically closed by a geodesic arrangement of carbon atoms, similar to one-half of another carbon nanostructure called a "buckyball". Nanotubes are synthesized in inert atmospheres using CVD, pulsed laser vaporization and electric arc discharge [2].

Depending on the synthesis technique, the resulting nanotubes will either be composed of a single layer of atoms or concentric layers of atoms. Nanotubes with a single layer are referred to as single walled nanotubes (SWNTs), and those with multiple layers are referred to as multi-walled nanotubes (MWNTs). SWNTs are usually less than 2 nm in diameter, and MWNTs are typically less than 100 nm in diameter. While SWNTs may be conductors or semiconductors depending on their arrangement of atoms, MWNTs are excellent conductors and are considered ideal electron emitters for many applications. Their small tip diameters enhance the electric field, and in a sealed gas environment they were shown to be robust electrodes [3]. Current applications include flat panel displays, actuators, gas sensors, nano-diodes and transistors, and atomic force microscopy (AFM) probes [4].

Rao et al. have developed a CVD technique to grow aligned MWNTs on several substrate materials at 675°C in a xylene-argon-hydrogen mixture [5]. The aligned nanotubes shown in Fig 1 were synthesized on a quartz substrate using this process. In field emission applications, a conductive substrate is necessary, and so Rao et al. later synthesized nanotubes on polished titanium nitride (TiN), which is a conductive ceramic [6]. Experiments demonstrated that MWNTs on polished TiN substrates were superb field emitters [6]. However, later experiments

* *Precision Systems Laboratory, Mechanical Engineering, University of Kentucky, 210-A CRMS Building, Lexington, KY 40506. http://www.engr.uky.edu/psl.*
† *107 Kinard Laboratory of Physics, Physics and Astronomy, Clemson University, Clemson, SC 29634-0978. http://physicsnt.clemson.edu.*

using substrates with sputtered TiN did not successfully grow MWNTs. This suggests that the topography of polished TiN surfaces, which are rougher than sputtered TiN surfaces [7], are more amenable to nanotube growth. The surface parameters of these polished TiN surfaces and any relation to successful synthesis of MWNTs were not known. This paper investigates the 3D surface topography resulting from polishing compacted TiN and its affect on MWNT growth.

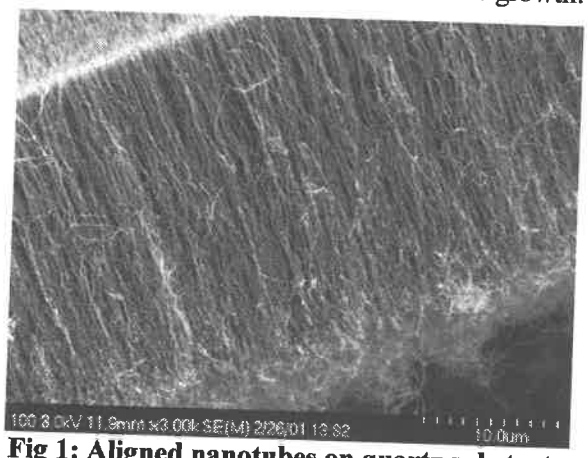

Fig 1: Aligned nanotubes on quartz substrate

Polishing Procedures

We begin with commercially available TiN discs (99.5% pure) used as sputtering targets for coating other surfaces. The targets were either 3.18 mm (0.125 inches) or 6.35 mm (0.25 inches) thick. These targets are formed from TiN powder with particles less than 44 microns in diameter. The powder is pressed and sintered to form a solid approximately 70% dense, with a structure as shown in the scanning electron microscope (SEM) image in Fig 2. 5mm square samples were produced by cutting the targets using wire EDM or a diamond cutoff saw.

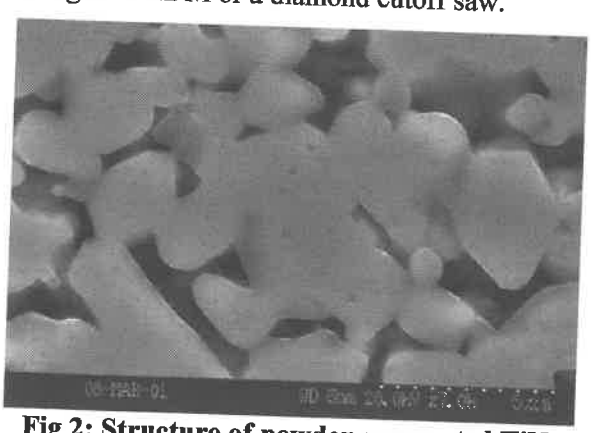

Fig 2: Structure of powder compacted TiN

The samples were labeled and grouped into three sets before grinding and polishing with three different procedures. The procedures were varied for each set to obtain samples with three distinct surface finishes. The duration and the particle size during the final polishing steps were varied. The steps in the finishing procedure for all three sets of samples are shown in Table 1.

Fig 3 is a SEM micrograph of a polished TiN surface viewed at an oblique angle, showing relatively smooth and flat regions interspersed with crevices due to the spacing between particles. It is possible that these crevices, which are not present on sputtered TiN surfaces, may enhance nanotubes growth on polished surfaces.

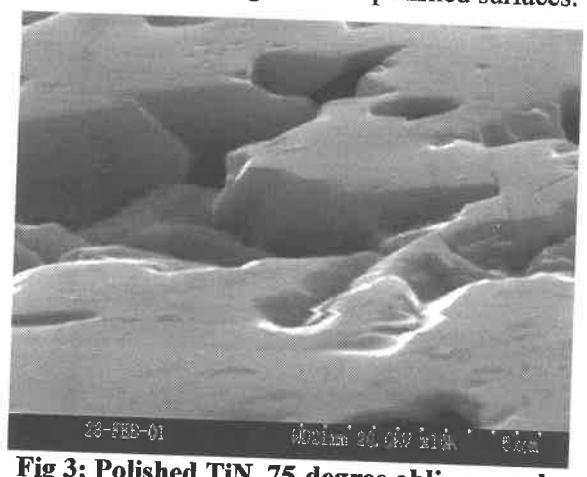

Fig 3: Polished TiN, 75-degree oblique angle

Surface Roughness Measurements

The roughness of the TiN surfaces after polishing was studied with a light microscope, SEM, AFM and a surface profilometer. Light microscope images provide convenient feedback during the polishing process and are easily collected between polishing steps. SEM images give higher resolution and a good indication of feature sizes, but still only provide qualitative information regarding the depth of the features. Atomic force microscope images that show the force on the scanning tip in tapping mode, give quantitative data on specific surface features. The surface profilometer gives quantitative data over a larger area (122 μm x 93μm) and includes surface waviness and roughness. Profilometer measurements in Fig 4 and Fig 5 contrast the surface roughness of samples from Set 1 and Set 2. Roughness parameters as measured with the surface profilometer for the samples from the three sets are shown in Table 2 [8,9].

Table 1: Polishing Procedures for Three Sets of TiN Samples

Step #	Operation	Wheel	Abrasive	Lubricant	t, min.	Force, N
1 (set 1)	Planar grind	MD-Piano 120	Diamond	Water	Plane	120
2	Fine grind 1	MD-Allegro	9 micron DP-suspension	Green/Blue	5	180
3	Fine grind 2	MD-Allegro	3 micron DP-suspension	Green/Blue	10	180
4	Diamond polish	MD-Allegro	1 micron DP-suspension	Green/Blue	8	120
5	Oxide polish	MD-Chem	OP-S or OP-U	-	1	140
1 (set 2)	Planar grind	MD-Piano 120	Diamond	Water	Plane	120
2	Fine grind 1	MD-Allegro	9 micron DP-suspension	Green/Blue	5	180
3	Fine grind 2	MD-Allegro	6 micron DP-suspension	Green/Blue	18	180
1 (set 3)	Planar grind	MD-Piano 120	Diamond	Water	plane	120
2	Fine grind 1	MD-Allegro	9 micron DP-suspension	Green/Blue	5	180
3	Fine grind 2	MD-Allegro	3 micron DP-suspension	Green/Blue	10	180
4	Diamond polish	MD-Allegro	3 micron DP-suspension	Green/Blue	8	150
5	Oxide polish	MD-Chem	OP-S or OP-U	-	1	140

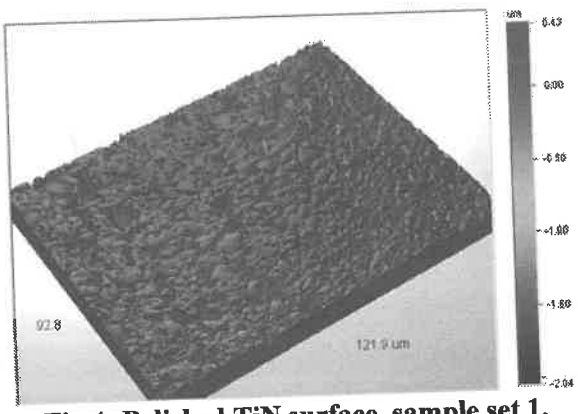

Fig 4: Polished TiN surface, sample set 1.

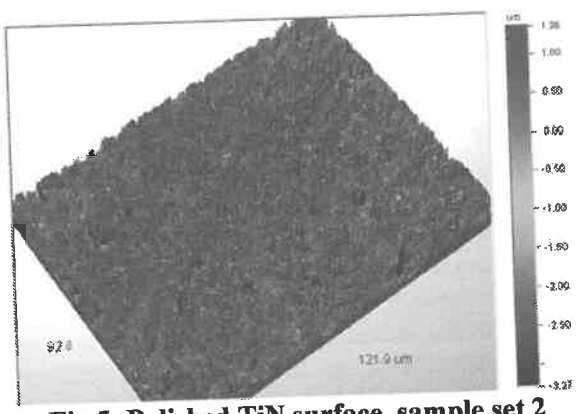

Fig 5: Polished TiN surface, sample set 2

Synthesis of Carbon Nanotubes

Following the polishing process, MWNTs were synthesized on samples from each of the three sets in a 1 m long two-stage reactor [5]. A preheater operating at 200°C heats a mixture of xylene and ferrocene. Argon gas is used to carry this mixture into the reaction chamber, which operates at 675-700°C. After an initial layer of Fe nanoparticles are deposited on the surfaces of the chamber (and any substrates present in the reactor), the nanoparticles catalyze the growth of aligned MWNTs on these surfaces [5].

This technique does not require a separate processing step to seed a catalyst layer on the surface of the substrate since the catalyst is deposited *in-situ* during operation of the reactor. Typical operation times for the reactor are on the order of 2 hours [5,6].

Assessment of Nanotube Alignment

In the case of well-aligned nanotubes (such as Fig 1), a profile image facilitates measurement of the length of nanotubes and density of nanotubes. So after synthesizing nanotubes on the polished surfaces, several cross-sectional cuts were made to achieve a profile view of the aligned nanotubes under the SEM. It is possible to disrupt the alignment of the nanotubes during cutting.

Fig 6 shows aligned nanotubes from a polished TiN substrate from Set 2. For samples in Set 2, typical lengths ranged from 5-10 microns, with knotting in the upper layer. The same style of knotting is observed in the nanotubes synthesized on quarts as shown in Fig 1. On the quartz substrate, nanotube lengths range from 20-100 microns.

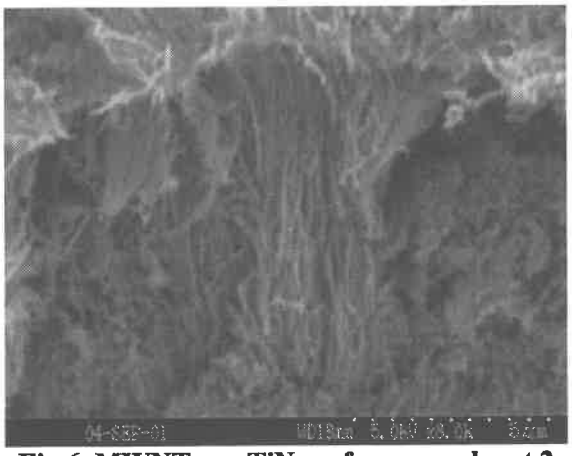

Fig 6. MWNTs on TiN surface, sample set 2

Conclusions

Planar grinding and polishing of TiN is a predictable and repeatable process to achieve smooth surfaces. As indicated by the roughness parameters in Table 2, samples in Set 2 were rougher than samples from Sets 1 and 3. The smoothest TiN surface achieved a "mirror finish" with an Ra of 85 nm, and the roughest surfaces had an Ra of about 400 nm.

MWNTs were synthesized on all polished TiN samples, but none were able to duplicate the same precise alignment observed when synthesizing MWNTs on quartz substrates. The samples that showed some degree of alignment were those in the roughest set (Set 2). Hence, we conclude that some amount of roughness is beneficial when synthesizing MWNTs. This conclusion is in agreement with experimental observations that MWNTs could not be synthesized on smooth TiN sputtered surfaces.

Table 2: Roughness parameters obtained from three different polishing procedures

	Ra	Rq	Rt	Rz	Rku	Rsk	Volume	Bearing Ratio Htp
Units	nm	nm	nm	nm			um3	Nm
Set 1	84.48	139.48	2724.64	2211.98	29.81	-3.76	1383.25	2724.64
Set 2	399.78	503.03	4233.09	3769.79	3.97	-0.93	5462.62	4233.09
Set 3	92.47	146.77	3060.34	2355.24	26.56	-3.40	1501.15	3060.34

References

[1] S. Iijima. "Helical Microtubules of Graphitic Carbon." *Nature* 354 (1991) 56-58.

[2] M. S. Dresselhaus, G. Dresselhaus, and P. C. Eklund. *Science of Fullerenes and Carbon Nanotubes*. Academic Press. San Diego, 1996. p. 778.

[3] R. Rosen, W. Simendinger, C. Debbault, H. Shimoda, L. Fleming, B. Stoner, and O. Zhou. "Application of Carbon Nanotubes as Electrodes in Gas Discharge Tubes." *Applied Physics Letters* 76 (2000) 1668-1670.

[4]Various papers of Symposium A in the *Proceedings of the Fall 2000 Materials Research Society Conference*. Boston, USA.

[5] Andrews, R., D. Jackques, A.M. Rao, F. Derbyshire, D. Qian, X. Fan, E.C. Deickey, and J. Chen. "Continuous Production of Aligned Carbon Nanotubes: A Step Closer to Commercial Realization". *Chem. Phys. Letters*, 303, 1999. p. 467-474.

[6] Rao A.M., D. Jacques, R.C. Haddon, W. Zhu, C. Bower, and S. Jin. "In-Situ Grown Carbon Nanotube Array with Excellent Field Emission Characteristics". *Applied Physics Letters*. V. 76, No. 25. p. 3813-(2000).

[7] T. Takahashi, K. Masugata, H. Kawai, S. Kontani, J. Yamamoto. "Surface Morphology of TiN Films Reactively Deposited by Bias Sputtering." *Vacuum* 59 (2000) 777-784.

[8] W.P. Dong, B. Griffiths, X. Jiang, N. Luo, E. Mainsah, P. S. Scott, P. J. Sullivan. *Three Dimensional Surface Topography, 2nd Ed.* Penton Press. London, 1994

[9] K. J. Stout. Development of the Methods for the Characterisation of Roughness in Three Dimensions. Penton Press. London, 2000.

A NOVEL SUB-MICRORADIAN BEAM DIAGNOSTIC AND ALIGNMENT SYSTEM

Carl G. Chen[1], Ralf K. Heilmann, Paul T. Konkola, G. S. Pati and Mark L. Schattenburg
Space Nanotechnology Laboratory
Massachusetts Institute of Technology, Cambridge, MA 02139

I. INTRODUCTION

By interfering a pair of millimeter-diameter laser beams, scanning beam interference lithography (SBIL) is capable of exposing linear gratings and grids in photoresist with extremely low phase distortions. (Please see our other paper [1] in these proceedings for a more detailed description of the SBIL architecture.) Our ultimate design goal calls for sub-nanometer accumulated phase distortions across a 300 mm substrate when compared to a grating with a perfect linear phase. These accurate periodic structures, when patterned onto ultra-low thermal expansion substrates, can be used as absolute metrology standards [2]. They may also enable advances in other fields such as the making of high precision optical encoders.

Elsewhere [3], we have demonstrated the ability to diagnose *in-situ* the spatial period and phase of a grating image via the use of interferometry. For a grating period of approximately 2 μm, we have reported a period measurement repeatability of three parts per ten thousand, one sigma, and a grating phase drift of 0.25 mrad/sec. Both the repeatability error and the phase drift are expected to decrease by three orders of magnitude after some major system upgrades, including the installation of an environmental enclosure and the addition of thermally stable metrology frames. Ultimately, the beam diagnostic system is capable of resolving the overall phase of a 1 mm radius grating to around 1 nm, corresponding to a period measurement accuracy of one part per million.

The diagnostic system is an integral part of a sub-microradian beam alignment system (Fig. 1 [4, 5]), which is composed of a series of beamsplitters, mirrors, lenses, position sensing detectors (PSD), and picomotors. The system is designed to sense beam position fluctuations and angle shifts with resolutions of 61 nm and 61 nrad, respectively. Based on the sensor readings, a network of eight picomotors, each with an angular resolution of 0.74 μrad, adjusts four tip-tilt steering mirrors so as to overlap the beams in position and to equalize their incident angles, thus setting the grating period and ensuring vertical fringes. To obtain good fringe contrast, beam centroids must be overlapped to within a small fraction of the beam radius, typically 1%, which corresponds to 10 μm for a 1 mm radius beam. A PSD located in the substrate plane is used to directly verify the beam overlap with a resolution of 61 nm. Slow drifts in the lithography station, thermal or otherwise, once diagnosed, can be corrected by periodically registering the beams to a reference beamsplitter cube on the interferometer stage [3], ensuring ultra-low phase distortions. The approach is similar to that used in electron-beam mask writers [6] whereby in order to compensate for drifts, the electron beam is periodically referenced to a fiducial mark on the stage.

II. SYSTEM DESIGN

Data acquisition from the PSDs is handled by two National Instruments 6034E 16-bit I/O boards. The PSD used to sense the beam overlapping in the plane of the substrate is an

[1]Email: gangchen@mit.edu

On-Trak Photonics UV2L4 duolateral position sensing detector. To rid the errors that may be introduced if the beam reflects multiple times off the PSD's protective window, we have acquired a special no-window version of the detector. Once the beams are overlapped, the picomotors, purchased from New Focus, Inc., are driven so as to equalize the incident angles, without shifting the positions of the beams at the substrate.

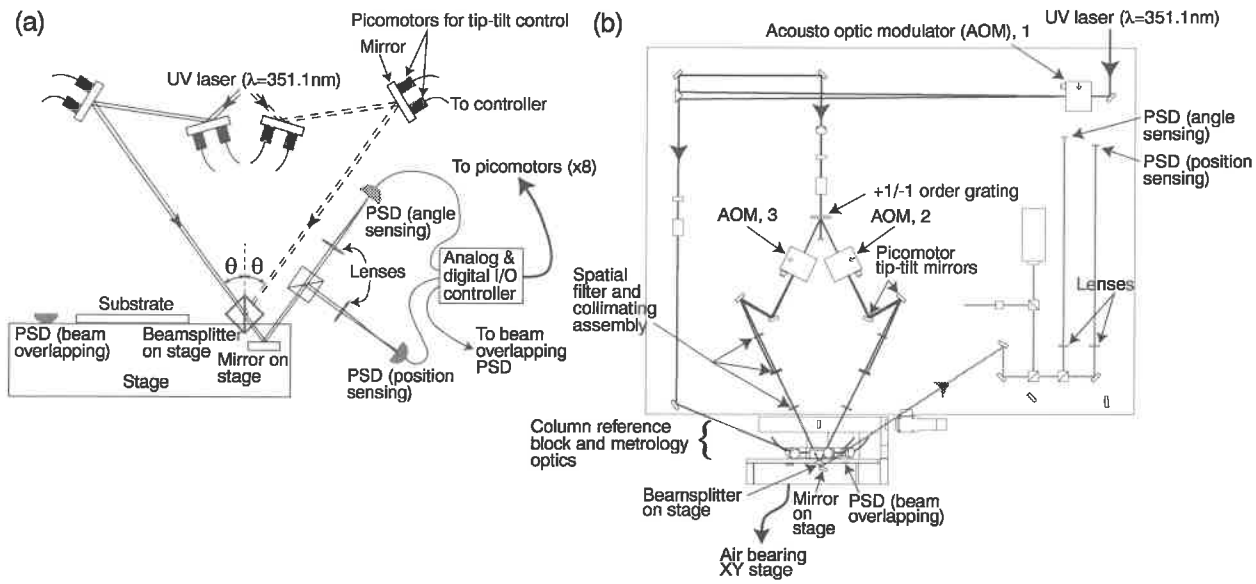

Figure 1: (a) A schematic of the SBIL beam alignment system. The PSD used for beam overlapping, the substrate, a reference beamsplitter cube and a steering mirror are attached to the interferometer stage. All other components are attached to an optical bench. During beam diagnostics and alignment, the stage is moved so that the beams intersect the cube as shown. (b) Actual design of the alignment system. The grating beamsplitter provides greater tolerance on the beam angular instability and temporal coherence than the traditional cube beamsplitter. Three acousto optic modulators (AOM) provide digital heterodyne interference fringe control. Furthermore, by nulling AOM 2 and 3 control signals, each beam can be individually shuttered to provide position and angle readouts.

The alignment system adopts the same position and angle decoupling topology as that described in our earlier work [4]. The theory of angle decoupling is straightforward. After passing through a thin lens of focal length f, a beam's angle (α), not its position, is converted to a displacement (r) at the back focal plane of the lens, where $r = f\alpha$. Position decoupling is best understood via the ABCD matrix formalism [7]. Defined in Fig. 2(a), the output position and angle of the beam, r and r', can be written in terms of the input beam position and angle, d and α, geometric distances L_0 and L_1, and the focal length f,

$$\begin{aligned}\begin{pmatrix} r \\ r' \end{pmatrix} &= \begin{pmatrix} 1 & L_1 \\ 0 & 1 \end{pmatrix}\begin{pmatrix} 1 & 0 \\ -1/f & 1 \end{pmatrix}\begin{pmatrix} 1 & L_0 \\ 0 & 1 \end{pmatrix}\begin{pmatrix} d \\ \alpha \end{pmatrix} \\ &= \begin{pmatrix} 1 & L_1 \\ 0 & 1 \end{pmatrix}\begin{pmatrix} 1 & 0 \\ -1/f & 1 \end{pmatrix}\begin{pmatrix} 1 & L_0 - \Delta \\ 0 & 1 \end{pmatrix}\begin{pmatrix} d + \Delta\alpha \\ \alpha \end{pmatrix}. \end{aligned} \tag{1}$$

Therefore, if L_0 and L_1 are chosen such that the beam's position at the output plane (r) is only a function of the position at the input plane (d), then this particular choice of position decoupling is strictly maintained across all possible input planes. Two On-Trak Photonics UV2L2 duolateral PSDs are used as position and angle sensors, with resolutions of 61 nm and 61 nrad, respectively, limited by the resolution of the 16-bit I/O board.

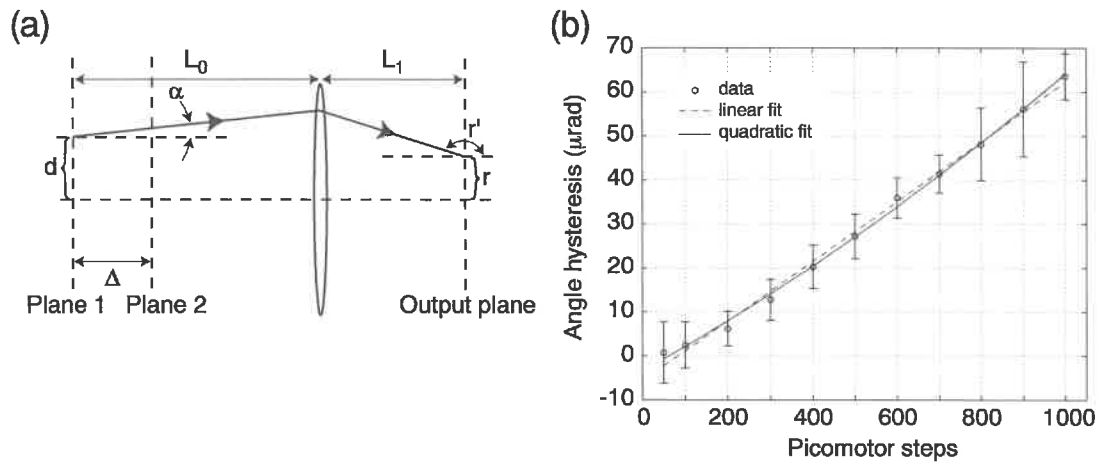

Figure 2: (a) Position decoupling. (b) Picomotor repeatability study. For each data point, the picomotor is first commanded forward by the indicated number of steps, then backward by the same number of steps. Difference between the initial and final angles is recorded by the angle sensing PSD. Before a new set of measurement, the picomotor is commanded so as to return the beam spot to the same location on the PSD. This is to ensure that the starting load on the picomotor remains the same for all measurements.

The picomotors have a displacement resolution of better than 30 nm, which translates into an angular adjustability of 0.74 μrad. The technology enables us to equalize the incident beam angles and correct for beam drifts with sub-microradian accuracy, which is necessary given a one-part-per-million overall phase distortion budget [4]. Each beam is steered in position and angle by four picomotors, interfaced to a New Focus Picomotor Driver (Model 8732), which is itself controlled via external TTL signals from a National Instruments PCI-DIO-96 digital I/O board. Analog and digital control algorithms have been implemented using LabVIEW. Prior to the actual alignment, each of the four picomotors is commanded in sequence to move by an amount. The recorded position and angle data is used to compute a calibration matrix. Once the system is calibrated, we can then coordinate picomotor movements in order to equalize the angles while maintaining the beam overlap.

Due to the nature of its frictional drive, a picomotor's step size varies. As shown in Fig. 2(b), motions in opposite directions by the same number of steps are not equivalent. Repeatability is thus an issue with the picomotors. Open-loop control of the alignment system is impractical. One can not, for example, calibrate the system using a fixed number of picomotor steps as a calibration unit, since the device behaves unrepeatably. We implement a close-loop controller which calibrates not to a unit of picomotor step, but to a unit of sensor distance. The latter is an invariant, assuming we can effectively control drifts of thermal, vibrational, mechanical and acoustic origins. Prior to the alignment, each of the four picomotors is stepped until the beam intensity has decreased by 10% on the position sensor, in other words, the beam has started to fall off the sensor. (Because of the particular optical topology that we are using, the beam always falls off the position sensor first.) The position and angle readouts before and after the picomotor movement help define a 'unit' vector, which is expressed in terms of sensor distances. In this fashion, a 4×4 calibration matrix can be obtained, without any link to picomotor step size. During alignment, an individual picomotor is commanded to move till a desired sensor output is obtained. This effectively rids the picomotor non-repeatability pitfall. For speed, a successive approximation type of algorithm is implemented to drive the picomotors, much similar to that used on most

A/D converters [8]. Special care is taken such that the beams never fall off the two sensors while any one of the picomotors is driven.

III. CONCLUSIONS AND FUTURE WORK

We have constructed a system to satisfy the need of microradian level beam angle alignment during scanning beam interference lithography. Analog and digital control algorithms have been implemented based on a close-loop control scheme that effectively circumvents the problem of picomotor step non-repeatability. Critical testing of the system will be carried out once major upgrades to SBIL, such as the installation of an environmental enclosure and thermally stable metrology frames, are done. Latest test results will be presented.

IV. ACKNOWLEDGMENTS

We gratefully acknowledge the outstanding student, staff, and facility supports from the Space Nanotechnology Laboratory. This work was supported by DARPA under Grant No. DAAG55-98-1-0130 and NASA under Grant No. NAG5-5271.

REFERENCES

1. P. T. Konkola, C. G. Chen, R. K. Heilmann, G. S. Pati, and M. L. Schattenburg, "Scanning Beam Interference Lithography," these proceedings.

2. M. L. Schattenburg, C. Chen, P. N. Everett, J. Ferrera, P. Konkola, and H. I. Smith, "Sub-100 nm metrology using interferometrically produced fiducials," J. Vac. Sci. Technol. B **17,** 2692–2697 (1999).

3. C. G. Chen, P. T. Konkola, R. K. Heilmann, G. S. Pati, and M. L. Schattenburg, "Image metrology and system controls for scanning beam interference lithography," to be published in J. Vac. Sci. Technol. B, Nov/Dec 2001.

4. P. T. Konkola, C. G. Chen, R. K. Heilmann, and M. L. Schattenburg, "Beam steering system and spatial filtering applied to interference lithography," J. Vac. Sci. Technol. B **18,** 3282–3286 (2000).

5. R. K. Heilmann, P. T. Konkola, C. G. Chen, G. S. Pati, and M. L. Schattenburg, "Digital heterodyne interference fringe control system," to be published in J. Vac. Sci. Technol. B, Nov/Dec 2001.

6. H. Pearce-Percy, R. Prior, F. Abboud, A. Benveniste, L. Gasiorek, M. Lubin, and F. Raymond, "Dynamic corrections in MEBES 4500," J. Vac. Sci. Technol. B **12,** 3393–3398 (1994).

7. H. A. Haus, in *Waves and fields in optoelectronics* (Prentice-Hall, Inc., 1984), Chap. 5.

8. P. Horowitz and W. Hill, in *The art of electronics*, 2nd ed. (Cambridge University Press, 1989), Chap. 9.

Experimental Ductile Grinding of Glass Specimens on the Cranfield Tetraform C Machine

A.E.Gee*, J.Delalandre, J Corbett & D J Stephenson

School of Industrial and Manufacturing Science, Cranfield University,
Cranfield, Bedford, MK43 0AL UK
(*corresponding author a.e.gee@cranfield.ac.uk)

Introduction: Preceding Work

In the 1980s, Dr A Franks at the UK National Physical Laboratory (NPL) led a programme of research into the machining of brittle glass materials. Parallel collaborative studies at the University of Surrey, Guildford, UK by Prof K Puttick and colleagues modelled machining type material deformation to show that crack-formation was scalar-dependent. Using pyramidal diamond indenter tools, they demonstrated that single point incursions to depths to some critical value of the order of 1μm in both glasses and crystalline semiconductors could be made with crack formation controlled in apparently ductile plastic mode as shown in Fig.1 (Puttick et al 1989). This was extended to include dead-load ruling (Chao & Gee 1989, Gee et al 1992) and to semiconductors (Puttick et al 1994).

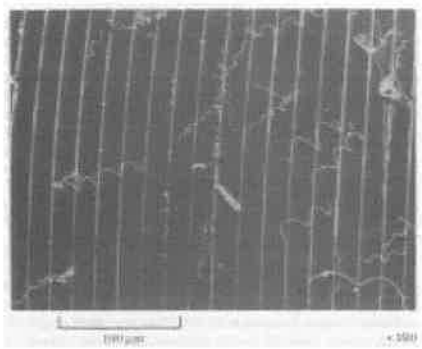

Figure 1 Single Point Ductile Machining of Glass (Puttick et al 1989)

Blackley and Scattergood (1991) provided an additional model for a curved tool producing an extended 'D' cut section profile, showing critical 'depth' could be more fully defined as a critical incursion dimension.

At NPL a stiff radical concept machine-tool was designed and built on which to extend studies aimed at producing optical surfaces approaching polished standards of surface finish. The 'Tetraform' machine tool (Lindsey 1992) employed a stiff tetrahedral structure comprised of substantive cylindrical members with internal damping, a vertical spindle carrying a cup-grinding wheel and two translation axes: a leadscrew horizontal traverse of 150mm and a high pressure hydraulic vertical in-feed of 100μm. On it Lindsey (1992) reported grinding Spectrasil B silica glass flats using a 104mm diameter 15-30μm diamond cup-wheel at feed-rates of 30mm/min (500μm/s) with surface roughness of 5nm R_a and sub-surface damage of 0.25-0.95μm for cut-depths of 0.5-10μm.

Design studies of the Tetraform concept continued at Cranfield University resulting in Tetraform C, an extended design based on the high stiffness obtainable with such a structure but employing two horizontal traverse axes (220mm x 120mm) and a 25mm vertical axis to permit form generation. The resulting structural design, coupled with the use of hydrostatic leadscrews and guideways for each axis, provides very high static and dynamic stiffnesses. The machine is shown in Fig 2 and details have been given by Corbett *et al* (1999).

Figure 2 Tetraform 'C'

Experimental Work

To classify glass specimens indentation and ruling were employed, depth-controlled by applied dead-load, indentation being a standard materials test procedure. Ruling is a specialised process performed on a machine originally developed for generating diffraction-gratings (Horsfield 1965) and suitably modified (Chao & Gee 1989, Gee *et al.* 1992).

Grinding on the Tetraform C machine was performed with samples initially set inclined so as to machine a wedge leaving recognisable regimes on the sample: (1) unground reference surface, (2) ductile ground surface, (3) transitional region (of increasingly frequent brittle damage) and (4) brittle ground region. Angles of surfaces generated were checked interferometrically and samples were examined using by Wyko optical interferometer and atomic force microscope. Examination of the areal extent of brittle fracture was by optical microscopy. From the results, constant depth machining parameters were selected and employed on further samples.

Materials employed were commercial float glass and Spectrosil B. The first was chosen for reasons of its production process: melt-formed on liquid tin, few surface structure defects were to be expected. This and its surface roughness formed a datum base from which to study the effects of subsequent mechanical incursion processes.

Results - Indentation

Averages of four readings of Vickers indenter load, indentation diagonal and lateral crack length were as follows:

Float Glass			Spectrosil B	
Load (g)	Diagonal (µm)	Crack Length (µm)	Diagonal (µm)	Crack Length (µm)
25	9.7		8.1	
50	13.7		10.4	
100	19.2		15.8	
200	26.7	13.5	23.1	
300	32.2	21.0	27.2	11.5
500	41.7	28.3	35.8	17.5

Results - Ruling

On float glass, loads of between 10 and 150g produced ductile material removal. Loads of above 180g produced brittle fracture and were tested to 350g.

On Spectrasil B, the ductile range was 10 to 250g with brittle damage observed above 250g and tested to 350g.

Results - Grinding

Float glass (initial R_a = 0.42nm):

For various feed-rates, the ductile ranges of depths and achieved roughnesses were as follows:

Feed-rate (mm/min)	Transitional depths (µm)	Roughness R_a (nm) Wyko
3	1-10	2.1 - 5.2
6	1-9	1.2 - 2.5
12	1-6.6	1.6 - 6.7

At 2µm constant depth, 3 and 6mm/min feed-rates yielded a surface free of damage with R_a between 3 and 6nm.

At 1µm constant depth and12mm/min feed-rate a damage-free surface was observed throughout but with some observed blemishes and R_a increased to between 13 and 22nm.

Spectrasil B (polished R_a = 0.62nm):

At feed-rates of 3 and 6 mm/min, wedge-depths to 4.5µm only were investigated due to set-up problems. These showed no brittle fracture. R_a was between 3 and 7nm with one sample achieving 1.04nm (see Fig 3).

2µm constant depth and 6mm/min feed-rate yielded a surface free of damage with R_a of 3.5 - 8.8nm.

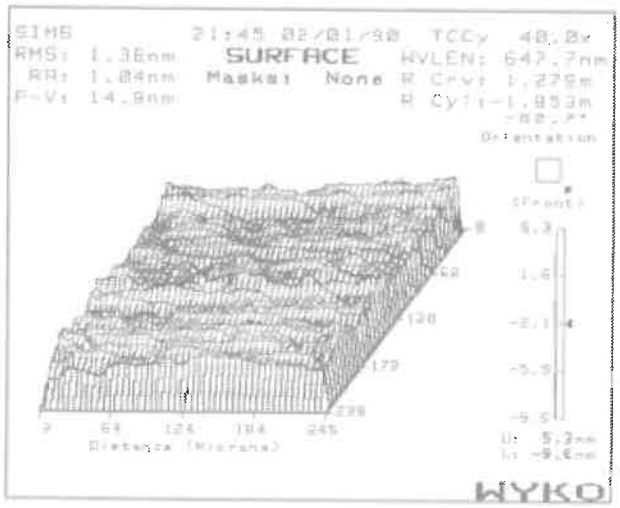

Figure 3 Wyko Interferometer plot showing surface finish obtained on Spectrosil diamond ground surface (1.04 nm Ra)

Discussion

The surface finish of the float glass samples (R_a ~0.4nm) was comparable with conventional polishes. Spectrasil B samples were polished to R_a ~0.6nm. 1nm R_a is typical of a quality optical glass surface produced by traditional free-abrasive polishing. Since that process also exploits ductile mode material removal, it is to be expected that an alternate machining process will either show results approaching this or manifest brittle damage (Gee 1996).

The work showed that on the Tetraform C machine, Spectrasil B could be readily ground with 2μm cut-depth at a cross-feed rate of 3-6mm/min to a finish of R_a~3nm, overlapping well with the earlier results of Lindsey (1992) on the original Tetraform at NPL. Underlying this, it should be pointed out that the Tetraform C machine has an extended (25mm) vertical axis to enable it to be employed for form generation. The current work indicates that these additional capabilities have not compromised target surface finish and damage performance.

References

Blackley W S and Scattergood R (1991) *Ductile-regime Machining Model for Diamond Turning of Brittle Materials* Prec Engg vol 13 pp95-103

Corbett J, Stephenson D J, Sweet J and Wills-Moren W (1999) *An Ultraprecision Machine Tool Demonstrating a Novel Vibration Resistant Structure* Proc 1st EUSPEN Conf vol 1 pp159-162

Chao C-L and Gee A E (1989), *Investigation of the Brittle-Ductile Transition in Single Point Machining of Glassy Materials Using a Ruling Engine*, Intl Precision Engineering Seminar/Am Soc Prec Engg Conf. IPES5/ASPE89, Monterey, CA, USA, Sept 1989; Proc. pp 259-263 (ASPE Raleigh NC)

Corbett J, Stephenson D J, Sweet J and Wills-Moren W J (1999) *An Ultra Precision Machine tool Structure Demonstrating a Novel Vibration Resistant Structure*, in McKeown P, Corbett J, Bonis M, Sartori S, Kunzmann H, Weck M, Brinksmeier E, Preuss W and Riemer O (Eds) 'Precision Engineering Nanotechnology' (Proc 1st Intl Euspen Conf, May 1999, Bremen, Germany), Shaker Verlag, Aachen, Germany vol 1 pp159-162.

Gee A E (1996) *Modelling the Mechanics of Free Particulate Abrasive Polishing from the Viewpoint of Single Point Processes* Proc SPIE vol 2775 pp611-618 .

Gee A E, Spragg R C, Puttick K E, and Rudman M R (1992) *Single-point Diamond Form-finishing of Glasses and other Macroscopically Brittle Materials* Proc SPIE vol 1573 pp 39-48

Horsfield W R (1965) *Ruling Engine with Hydraulic Drive* App Opt vol 4 pp 189-193

Lindsey K (1992) *Tetraform Grinding*, Proc SPIE vol. 1573 pp 129-135

Puttick K E, Rudman M R, Smith K J, Franks A and Lindsey K (1989) *Single-point Diamond Machining of Glasses* Proc Roy Soc A vol 426 pp19-30

Puttick K E, Whitmore L, Chao C-L and Gee A E (1994) *Transmission Electron Microscopy of Nanomachined Silicon Crystals* Phil Mag A, Vol 69, pp91-103

Acknowlegement

The authors are indebted to Prof A Franks for continued supporting discussions and for providing polished Spectrasil B samples.

DEVELOPMENT OF MINIATURE ACTUATOR FOR CRYOGENIC APPLICATIONS

Matias D. Heinrich*, Thomas A. Dow
Precision Engineering Center, North Carolina State University

INTRODUCTION

A goal of Next Generation Space Telescope (NGST)is to detect objects 400 times fainter than what is detectable from other infrared, ground-based telescope systems such as the Keck Observatory or the Gemini Project. The proposed design includes a mirror 8 meters in diameter, much larger than the 2.4 m mirror on the Hubble Space Telescope. NGST will be transported using the space shuttle orbiter or other Evolved Expendable Launch Vehicles (i.e. Titan and Atlas rockets). However, the cargo bay capacities cannot accommodate either the size or weight of a single piece 8 meter mirror. The solution is to build the primary mirror from an adjustable, reflective surface. Tentative designs include a flexible, thickfilm like plate or several smaller mirrors, each with a fixed reflective surface shape that can be adjusted independently from other sections. In either case, the primary mirror shape will have to be adjusted using many smaller actuators. These actuators are one of the major challenges of the NGST project and a number of requirements and goals have been set. The requirements are the specifications that are needed for the design to be effective and the goals are the specifications that would aid in the final design, assembly and testing but are not absolutely critical. The key requirements of interest in this design: resolution less than 20 nm, a range larger than 6 mm and the capability to hold position in a power-off condition. Since the intended environment for the device is space, it must operate under cryogenic conditions.

DESCRIPTION OF THE DESIGN

The prototype is designed around a precision ¼"-80 pitch screw that provides inherent power-off holding when transferring an axial load of the screw through a matching nut connected to ground. The system uses two sets of piezoelectric actuators to provide motion. Using the clamping set of actuators, the screw is locked by pushing the two clamping brass nuts apart. To rotate the screw, the rotation actuators push the rotational nut by pushing against the integrated front endplate (connected to ground). The rotational nut has flexures that allows the nut to rotate about the center of the screw. If the screw is locked by the clamping actuators, the rotational nut will slide on the screw but if the screw is unlocked, rotating the nut will rotate the screw with it. Using a series steps that includes rotating the screw, locking the screw, repositioning the rotational nut and unlocking the screw, the screw will displace axial in small steps. A sketch of the design is shown in Figure 1.

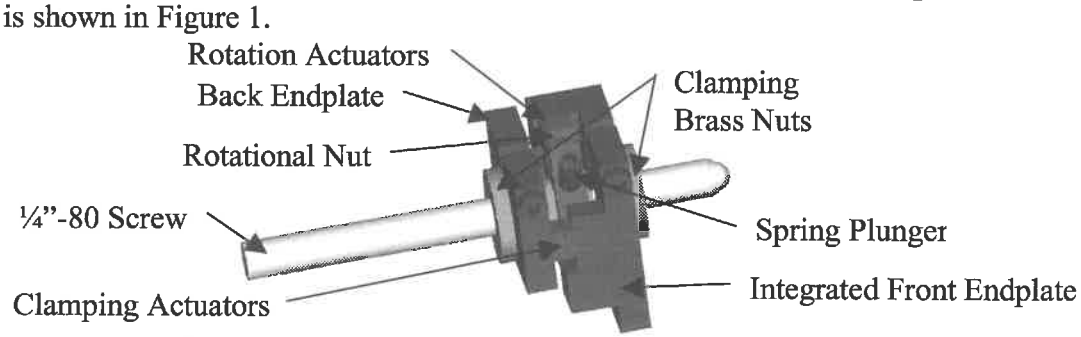

Figure 1: Overall view of the actuator prototype

* Currently at Vistakon, Johnson & Johnson

ACTUATOR OPERATION

Operation of the actuator involves four steps:
1) the rotational nut is forced to rotate around the center of the screw by a pair of piezoelectric actuators and it carries the screw along with it; 2) the clamping actuators push the front and rear clamping nuts apart increasing the friction needed to rotate the screw; 3) the rotational nut is deactivated and it rotates back to its initial position but without the screw; and 4) the clamping actuators are released.

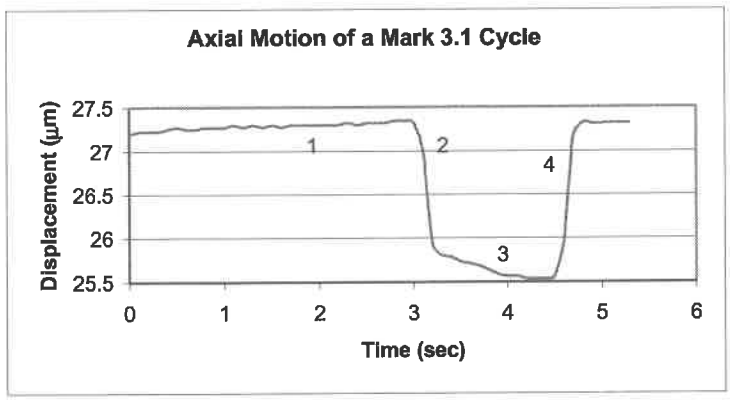

Figure 2: Motion of Mark 3.1 for one Cycle

Each step of the actuator can be viewed in the axial motion of the screw as observed in Figure 2. The first step (rotating the screw) is seen as a small upward sloping motion displacement (1). The next step (2) is to clamp the screw which sends it away from the load as a sharp downward motion of about 1 µm. This is caused by the clamping actuators pushing the clamping brass apart and increases the axial force on each. The screw/nut interface at the front clamping brass nut is supporting the axial load F. When the clamping actuators are energized, the force on the front nut is increased, and as a result, the nut is pushed away from the load. The third step (3) in the displacement motion of Figure 2 is a resut of de-energizing the rotational actuators to move the rotational nut its nominal position. Because the screw is clamped, there should be no axial motion of the screw. However, some motion is evident in Figure 2,which has two possible sources. The first is creep of the clamping actuators; that is, rapid displacement for the majority of their stroke (from step 2) followed by slow creep for the remainder. The continuing downward slope from segment 2 to segment 3 of the cycle could be attributed to creep. Another possible source of motion is radial forces on the screw generated when the rotational nut and modified brass rotate back to their nominal position. If the two tensile forces used to generate the moment and rotate the screw are not equal, then the rotational nut will tend to pull the screw radially. Radial forces on the screw create relative motion between the screw and the clamping brass nuts and move the screw. However, this is unlikely because the clamping brass nuts are firmly locked with the screw during this stage of the cycle. Whatever the source, the prototype displaces a small amount axially during the derotation of the screw. The final step (4) in the motion is a large positive jump in displacement upon relieving the clamp load. The positive jump has approximately the same magnitude as the negative jump seen from step 2.

When a series of steps such as illustrated in Figure 2 are strung together, the motion of the actuator can be determined. Figure 3 shows the axial displacement of the Mark 3.1 design using

the ADE 3940 capacitance gage to read the displacement of the screw. The axial load in this case is 0.2 N.

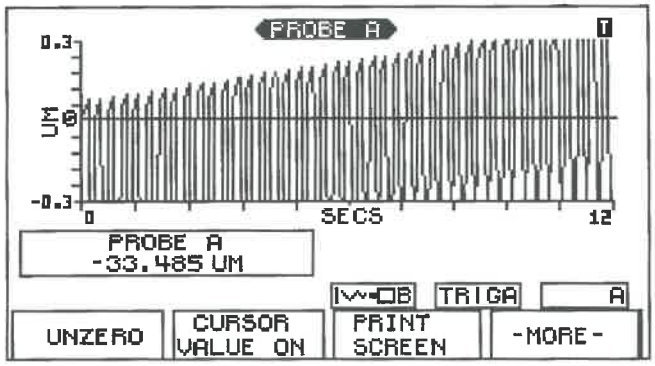

Figure 3: Axial Displacement (0.2 N Preload)

Figure 3 shows displacement of the actuator from 60 nm to 300 nm in 31 cyclesor 7.7 nm per cycle. The motion of the screw shows evenly displacing steps. A second test is shown in Figure 4 with a 0.5 N preload on the screw. The added load creates additional friction at the interface between the screw and the front clamping nut that leads to slippage when the rotational actuators are energized to rotate the screw. Consequently, a reduction in displacement is noticed with an average step size of 5 nm/cycle measured from Figure 4.

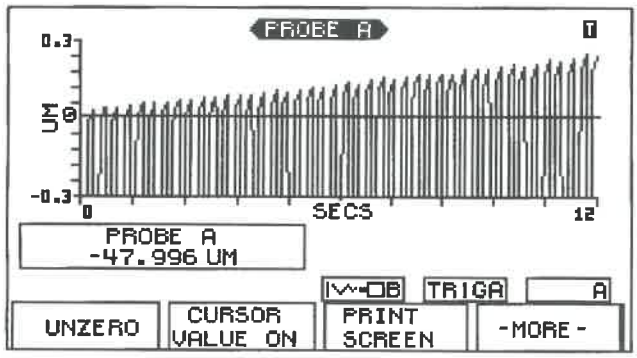

Figure 4: Axial Displacement (0.5 N Preload)

CRYOGENIC PERFORMANCE

To measure the performance of the actuator under cold conditions, the prototype was mounted on a piece of aluminum that rested in a plastic dish filled with liquid nitrogen. The aluminum served as a thermal conductor to extract heat from the prototype to the liquid nitrogen. The dish and the prototype where placed inside of a chamber (150 mm x 150 mm x 100 mm) made from 19 mm R4 closed cell styrofoam. One hole was bored to allow the screw to project outside of the box and another hole to carry wiring as well as a tube transporting nitrogen gas into the chamber. The nitrogen gas was used to purge the chamber for 10 minutes prior to adding the liquid nitrogen to eliminate any water vapor that could condense and freeze on the prototype. A 25 mm diameter hole was cut into the top cover to add liquid nitrogen but minimizing ambient air entering the chamber during the filling.

To measure displacement, a small silicon mirror was attached to the portion of the screw exposed to the ambient air. A laser beam was pointed at the mirror and the reflected light was spotted on a large flat wall 3.53 m from the center of the screw. As the prototype is powered and begins to displace, the rotation of the screw is tracked by the reflected image on the wall. The technique gives the advantage of magnifying the rotation of the screw because a one degree rotation of the screw will cause a two degree sweep of the laser beam. Knowing the distance from the wall to the center of the screw and measuring the change in position of the laser beam on the wall, the angular rotation of the screw can be easily calculated. The axial displacement is calculated from the angular rotation and pitch of the screw.

Cryogenic Testing Procedure

The test procedure began by marking the laser beam on the wall. A stopwatch was started when the compressed nitrogen was started. After 10 minutes, the one inch hole in the lid was uncovered and two cups of liquid nitrogen where poured into the chamber. Every five minutes, a half-cup of liquid nitrogen was added into the chamber. Forty minutes into the experiment, the prototype was started by sending the clamping and rotation signals from controller with a frequency of 1 Hz. The reflected laser beam disappeared due to the condensation and frost buildup on the silicon mirror so the actual minute-by-minute displacement could not be tracked. After 5 minutes, the actuator was stopped having undergone 300 cycles. The apparatus was then left undisturbed allowing everything to warm up to room temperature. As the ice melted off the silicon mirror and the water evaporated, the laser beam reappeared and a final reading was taken the apparatus reached equilibrium with the room temperature; approximately 3 hours was needed for the entire experiment.

Performance at Cryogenic Temperatures

To verify the design of the experiment, three experiments where preformed. The first was done at room temperature. The displacement of the laser beam was tracked on a minute-by-minute basis. The displacement was 28 mm/min at a distance of 3.53 m from the wall. Based on the laser path and the pitch frequency of the threads (317.5 μm/rotation),the displacement was 6.7 nm/cycle; that is, it reproduced the results discussed in Figures 3 and 4. The second experiment was performed using cryogenic conditions but the minute-by-minute data could not be captured due to mirror icing. The distance between the start and finish point of the laser beam was measured to be 23 mm or 0.5 nm/cycle. A third experiment was run to verify that the measured displacement of the actuator during cryogenic testing was true displacement rather then thermal drift. This experiment was identical to that of the second experiment but in this case the prototype was never operated. There was some drift during the test and the distance between the start and finish point of the laser beam was 3 mm. However, this displacement is much smaller then the 23 mm displacement of the second experiment described above and thus could be ignored.

CONCLUSIONS

A piezoelectric cryogenic motor has been developed to meet the actuator requirements of the Next Generation Space Telescope. The design objectives for actuator have been met as follows:

- Position resolution requirement of 20 nm with a goal of 10 nm-The piezoelectric actuator testing has shown that in a cryogenic environment (~80 K)the actuator can take step sizes less then 1 nm/cycle and at room temperature this value is on the order of 10 nm/cycle.

- The stroke of the design must be at least 6 mm with a goal of 10 mm -The actuator is built around a threaded screw and therefore the stroke of the design is governed by the length of the screw minus the length of the chassis. For the Mark 3.1 prototype, the screw length is 65 mm with a chassis length of just under 25 mm. The effective stroke of the design is thus 40 mm, four times greater then the 10 mm requirement.

- Operating temperature range of 20-60 Kelvin with a goal of 20-300 Kelvin -The structure of the design was calculated to have little thermal mismatch in the critical areas of the design (i.e. brass nut on the steel and axial straining of the screw versus the surrounding structure). The same setup was used during both the room temperature testing and the cryogenic testing. While no liquid helium facility was available to test the design at 20 K, the design was tested at 77 K and steps as small as 0.5 nm were measured.

- Capable of holding a load in place with no power supplied to the actuator -This is a major requirement of the motor and allows for a satellite telescope to have large quantities of the motor but not require power to hold position. The design of an actuator around a precision high pitch screw using a threaded nut attached to ground allows for built-in power off holding capability.

Precision Robot Calibration Using Kinematically Placed Inclinometers

Alec P. Robertson[1], Patrick J. Willoughby[2], Alexander Slocum[2]
[1]ABB Robotics, Västerås, Sweden
[2]Massachusetts Institute of Technology, Cambridge, MA

Introduction

In the field of industrial robotics, many different calibration methods exist to reduce error in the robot system. Locating the manipulator home position is a common calibration technique, which can be divided into three main categories — relative, optimal and leveling based methods. The home position of an industrial manipulator is a position where all joint angles have a pre-defined value (e.g. zero or 90 degrees), which can be transformed into Cartesian space via the robot kinematics. Large industrial manipulators, with a working range in the order of several meters, require an accurately defined home position that can be restored with repeatability in the order of 0.2mm in Cartesian space or 0.01 degrees in Joint space.

Relative calibration methods locate each robot link in a predefined position, relative to the previous link in the kinematic structure. This requires highly accurate robot parts, an expensive proposition for high volume manipulators. Optimal methods require a measurement system to measure a set of robot poses and use mathematical models of the robot kinematics to determine the link angles. The resultant home position is sensitive to the chosen calibration poses, leading to difficulties in maintaining a repeatable calibration. Leveling based techniques utilize inclinometers to position each link parallel or perpendicular to the gravity vector and provide a simple, accurate, and repeatable recalibration of the robot's home position.

In order to achieve the required accuracy using a leveling system, several key accuracy and repeatability aspects must be considered — the robot control system, the inclinometer unit and the mounting interface to the robot. The robot control system is a function of the accuracy of the motor resolvers and is expressed as the repeatability of the manipulator. This is typically of the order of 100 micrometers as defined by various ISO standards, which test the robot at a defined speed and with a defined payload. This value cannot be compensated for using a calibration system and can be considered to be a stochastic error about the chosen home position.

Testing of the existing leveling system method revealed a mean recalibration error of 1.0mm measured at the robot flange. The existing system makes use of two sensors mounted on separate right-angle plates that are placed sequentially on various mounting plates bolted to the robot structure. Each joint of the robot is then manually jogged until the robot stands in a home position that is parallel and perpendicular to the gravity vector. Analysis of the existing process revealed that placement of the sensors on the mounting plates represents over half the total error; tolerances of the right-angle and mounting plates represent over a third of the total error; with the remainder considered to be stochastic.

Kinematic Design of Prototypes

The inclinometer unit was designed in three successive stages in order to progressively prove the feasibility of various aspects of the concept. The first cube prototype, shown in Figure 1, involved mounting both sensors to a modified right angle plate. The robot mounting plates were retained and the measurement process automated via software. Although it was constructed essentially to prove the automation concept, the system also yielded a slightly improved recalibration error by eliminating the error due to manual jogging of the robot and eliminating one of the right-angle plates.

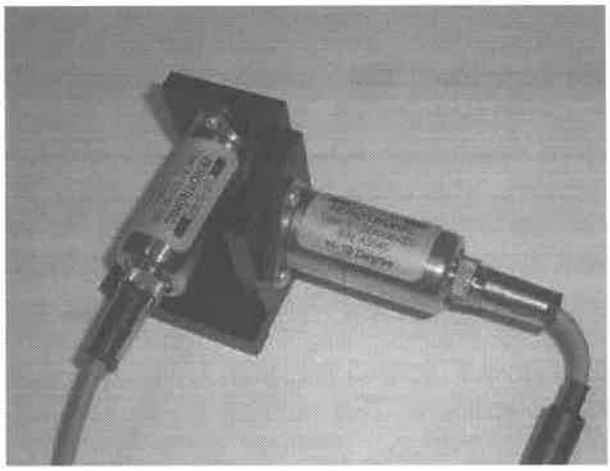

Figure 1: Initial prototype

To improve the accuracy and repeatability of the mounting procedure, the second prototype was designed based on kinematic, or exact constraint, design principles. The new design comprises an integrated inclinometer unit and separate V-groove mounting interface plates bolted to the robot structure. The inclinometer unit consists of three plates accurately mounted in an open-cube structure, with three spheres placed on the outer surface of the bottom and front plates. Each set of spheres is arranged in a standard circular kinematic coupling arrangement as shown in Figure 2(a), with the original prototype shown in Figure 2(b).

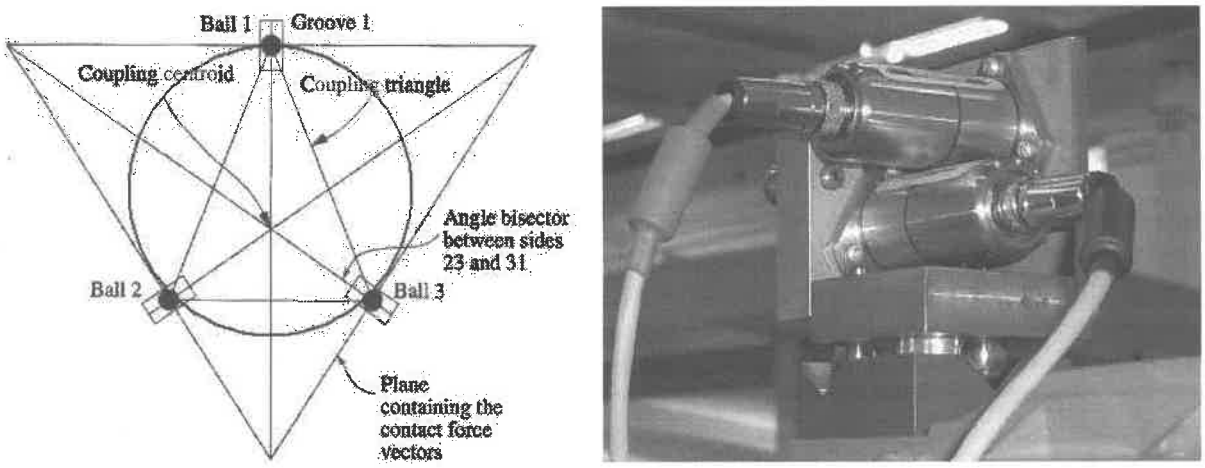

Figure 2: (a) Standard Kinematic Coupling Schematic and (b) Prototype

At the center of the circle, a magnet provides the necessary attractive preload between the cube and the robot to secure the contact between the spheres and the 90-degree V-grooves. The supplied magnet preload (approximately 35N) is sufficient to secure the unit to the robot, but is minimized to keep the Hertz contact stress under 50% of the material limit. To provide optimal repeatability at a reasonable cost, the balls and grooves were chosen to be readily available hardened steel tooling balls.

Mounted inside the cube, two inclinometers measure the roll and pitch angles with respect to the gravity vector. A "dynamic V-groove" variation, shown in Figure 3, is used for axes that are not subject to gravity (e.g. the first axis), converting axis rotation parallel to gravity to a rotation that can be measured by the inclinometers. Furthermore, the design of the groove-sphere interface causes large inclinometer measurements from small axis motions, resulting in improved calibration accuracy. This is particularly important for larger robots where a small angular error is dramatically magnified at the robot flange resulting in large positioning errors. A concern for the dynamic measurement is the instability caused by excessive movement of the coupling halves relative to each other, causing separation of the cube from the V-grooves. However, the required working range of the relative motion was sufficiently less than required to reach the instability point.

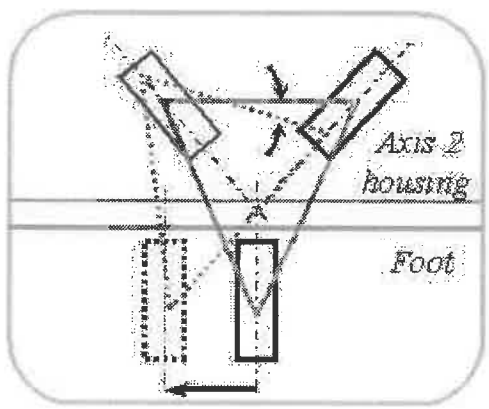

Figure 3: Dynamic first-axis calibration

The mounting repeatability of the kinematic coupling interface offers micrometer accuracy for both horizontal and vertical placements. Variation between cube individuals represents the largest source of error, predominantly due to the machining tolerances of the three cube surfaces, which can account for more than the desired 0.2mm recalibration error. This was the key issue addressed in the design of the product prototype shown in Figure 4, which utilizes a single piece of Aluminum as the chassis for the cube. Only three outer surfaces are required to be accurate hence enabling the entire cube to be machined in a single pass with an NC milling machine. Furthermore, the mounting of the sensors on the outer surface of the cube reduces the size of the structure to approximately that of a credit card, reducing weight and allowing the cube to be used on robots with smaller accessible calibration areas.

Figure 4: (a) Product prototype and (b) size relative to credit card

The product prototype is integrated with existing large robots through an add-on kit wherein the V-groove plates are permanently bolted to the robot structure. For optimal cost and performance V-grooves are directly machined into the robot structure on newer robot models. The results of recalibration tests satisfy the original specifications, revealing an error of 0.2mm, which represents a five-fold improvement on the existing system.

Key words: robot calibration, kinematic coupling, inclinometer, leveling devices

References:

1. T. Poovey, M. Holmes, D. Trumper "A kinematically-coupled magnetic bearing calibration fixture", Precision Eng., April 1994, Vol. 16, No. 2, pp 99-108
2. Patent 4,574,625: Surface Finish, Displacement, and Contour Scanner
3. A. Slocum, Precision Machine Design, Prentice Hall, 1992
4. A. Slocum, "Design of Three-Groove Kinematic Couplings", Precision Eng., April 1992, Vol. 14, No. 2, pp 67-76

A NOVEL SINGLE DEGREE-OF-FREEDOM ACTIVE VIBRATION ISOLATION SYSTEM

Tsuyoshi Sato* and David L. Trumper †

* TOSHIBA CORPORATION, Yokohama, Kanagawa, JAPAN
† Massachusetts Institute of Technology, Cambridge, MA, USA

Abstract: A prototype of a single degree-of-freedom active vibration isolation system is developed with a novel actuator design and control algorithm. In our actuator design, two variable reluctance actuators face each other with two thin sheets of elastomeric material placed between each actuator and the suspended mass. Using the tunable negative spring of the variable reluctance actuators, we can realize the required soft spring even with the thin elastomeric material sheets and can dramatically downsize the actuator unit. Hybrid position and velocity control system is developed to enable both good vibration isolation performance and platform re-leveling. We demonstrate our system's disturbance rejection performance against floor vibration and on-board generated disturbance force and show our actuator-design concept and control algorithm have significant promise.

Introduction

Active vibration isolation technology is receiving increasing attention as the means to insulate precision machines from floor vibration and at the same time reject on-board-generated disturbance forces. This is happening because conventional passive mounts such as elastomers and pneumatic isolators have a fundamental trade-off between rejecting these two classes of disturbance [1].

Many present-day active isolation systems use a parallel architecture of soft passive springs to support the static load and electromechanical actuators to provide the active force control. However there is a problem with this configuration in terms of the difference of traveling distance between the passive mount and the actuator. In most environments for precision machines, the floor motion never exceeds 25 μm [1], therefore the required traveling distance for active isolation actuators is about tens of microns. Meanwhile the traveling distance of the passive mount is generally from hundreds of microns to tens of millimeters and it is thus much larger than that of the actuator. This is because the dimensions of the passive mount are determined by the natural frequency and damping requirements of the system. In general, the lower the natural frequency, the better the isolation system performance. In order to realize the required soft springs, the passive springs typically require a large packaging volume.

Another issue relates to the system actuators. Typically, Lorenz-type actuators (voice coils or linear motors) are used to drive the active control forces. However, such actuators have low force per power as compared with variable reluctance actuators. Thus we have investigated the possibility of using variable reluctance actuators to drive our isolation system.

The downside of such actuators is their nonlinear force/current/air-gap relationship, which makes it hard to achieve high isolation performance. The actuators also have a negative equivalent spring constant which makes the open-loop system unstable. To address this, we have paired the variable reluctance actuators with a thin sheet of elastomeric material. If we can realize sufficiently low natural frequency even with thin elastomers, and with good damping, we could dramatically downsize the isolation system. This point is our motivation to develop a novel compact actuator for active vibration isolation; this compact actuator could gain wider application in many industries such as electronics, semiconductors and optics.

Actuator design and experimental hardware

Our actuator design is shown in Fig. 1. The basic idea of our design is that relative high positive spring constant of the thin damping material, k_d, can be counterbalanced with the tunable negative spring constant of the variable reluctance actuators, k_x. The total spring constant, $k_l = k_d - k_x$, and is thereby set to small positive value which leads to the required low natural frequency of the isolation system even with the thin damping material sheets.

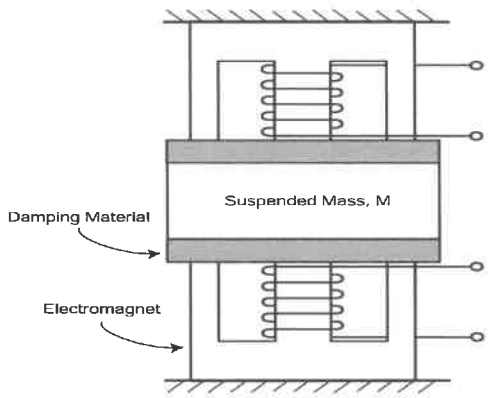

Fig. 1. A novel actuator unit for a single dof active vibration isolation system. Two electromagnets face each other with a thin damping material sheet placed between each electromagnet and the suspended mass.

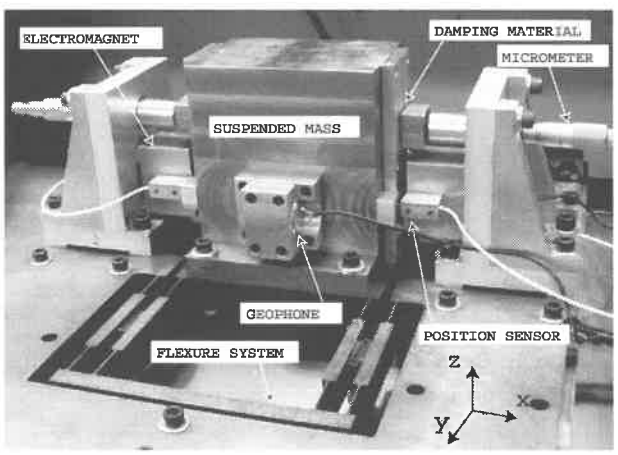

Fig. 2. A single dof platform of the active vibration isolation. The suspended mass weighs 20 kg and the center of gravity is 50.8 mm high from the upper surface of the low carbon steel plate. All sensors and actuators are placed at this height. Without damping material, the estimated 1st-mode natural frequency is 3.5 Hz according to the planar analysis detailed in [2]. The experimental result of the 1st-mode is 3.0 Hz and well matched to the calculated value.

Based on the same principle, we have built the prototype of the single dof active vibration isolation system shown in Fig. 2. The double compound rectilinear spring is made from 1 inch-thick low carbon steel plate to realize x-direction motion of the suspended mass and to constrain other five uncontrolled dof.

Commonly used Sorbothane with 50 durometer is used as damping material for our system. Each 1.5 mm-thick Sorbothane sized to 18 $mm \times 18$ mm is placed between the suspended mass and a fixture with a tapered hole. This fixture forms kinematic coupling with a steel ball glued to the tip of a micrometer. The damping material sheets are preloaded by the micrometers and are compressed by about 20 %.

The position of the suspended mass is controlled via two electromagnetic actuators. Each electromagnet consists of a 12.7 μm-thick stack of E-core laminations, made from 50 % Ni, 50 % Fe material.

The position and the velocity of the suspended mass are sensed by a pair of eddy current-type position sensor and geophone, model GS30CT 10-395 HORZ made by OYO Geospace, respectively.

Control algorithm

Since general active vibration isolation system is AC-coupled, its control system loop transmission must cross unity gain with positive slope at low frequencies and then cross unity gain with negative slope at high frequencies. The active control bandwidth is between the two crossover points. Thus the suspended mass could be moved by the disturbance vibration with lower frequency than the active control bandwidth. We thereby need position control to eliminate the mass drift caused by the low frequency disturbance and build the hybrid position and velocity control system with the parallel configuration, as shown in Fig. 3.

When the suspended mass separates from the center to either side, negative spring constant, k_x, exponentially increases and k_l goes to be negative

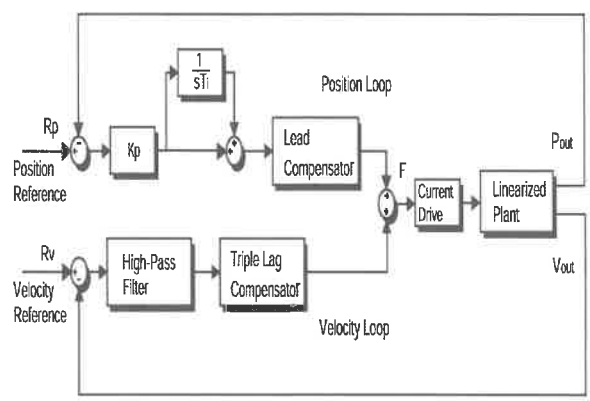

Fig. 3. Hybrid (position/velocity) control diagram. Triple lag compensator of the form $K_c(\frac{\tau_1 s+1}{\alpha\tau_1 s+1})^3$, with $\alpha = 10$ and $\tau_1 = 0.026$ sec to get 75°phase margin at 13 rad/s. The controller gain $K_c = 1.3 \times 10^4$ is chosen to set the loop crossover at 13 rad/sec. High-pass filter of the form $\frac{\tau_2 s}{\tau_2 s+1}$, with $\tau_2 = 1$ sec is to prevent any undesirable DC control action. PI controller with proportional gain $K_p = 0.4$ and integral time $T_i = 0.008$ sec is used as the compensator for the position loop. This controller is implemented to dSPACE DS1103 board with a selected sample rate of 10 kHz.

according to the above-mentioned $k_l = k_d - k_x$. This means that the system turns to be unstable and the suspended mass sticks to either actuator's pole. Thus we also need to produce a linear negative spring constant to mitigate the exponential increase of negative spring, k_x. To do so, we linearize the system by feedback linearization and then the position signal is positively feedbacked inside linearized plant block in Fig. 3 . The application of feedback linearization to the dual magnetic suspension system like our system is well described in [3].

In order to get good isolation performance, we need to make the active bandwidth wide and the loop gain as large as possible in the bandwidth. However, the upper unity-gain frequency is limited by structural resonances and the lower one is limited by noise in the inertial sensor [4]. With these limitations, we set the active control bandwidth at between 13 rad/s (2 Hz) and 1885 rad/s (300 Hz). Modeling and controller design for a single dof active vibration isolation system using geophone as velocity sensor are well described in [5].

Fig. 4 indicates that we successfully change the natural frequency by tuning negative spring. It also shows that an interesting phase drop occurs with the increasing negative spring value. Our estimated reason for this phenomenon is the following. As well known, the damping material has the dynamic modulus [6] and thus its stiffness decreases with the decreasing frequency. Since the negative spring of the electromagnets is constant, the total stiffness would become negative somewhere in low frequencies and the phase of the system would approach $-180°$. The larger negative spring makes this phase drop faster to $-180°$.

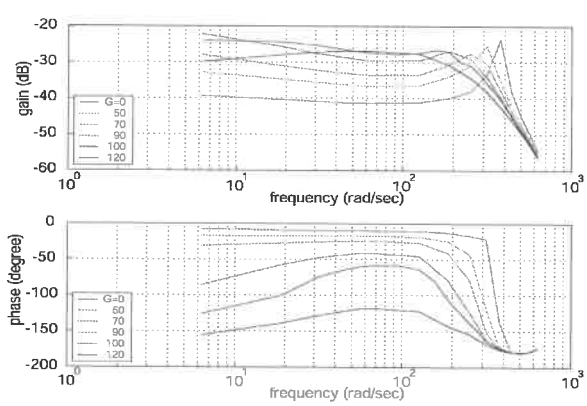

Fig. 4. Measured plant transfer functions from desired force F to the output of the position sensor P_{out}. In this experiment, the system runs only with the position loop. Undescribed feedback gain G is varied to change the value of the negative spring constant. ($G = 0$ indicates the original natural frequency.) Note that the position controller gain K_p is equal to 3 for every value of G, except for $G = 120$ where K_p is set to 15 to avoid instability.

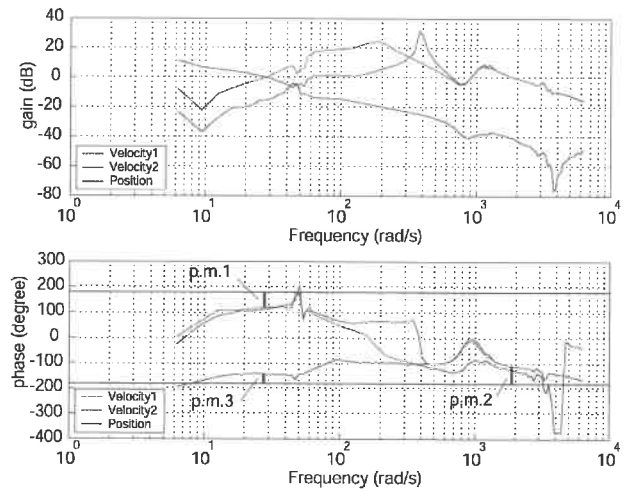

Fig. 5. Measured open-loop transfer functions of the hybrid system. The loop transfer function of the velocity loop with the shifted natural frequency is labeled as Velocity 1 ($G = 130, P = 1.5$). The loop transfer function of the velocity loop without the shift of the natural frequency is marked as Velocity 2 ($G = 0, P = 1.5$). The loop transfer function of the position loop with the shifted natural frequency is labeled as Position. The measured phase margins of the velocity loop are $p.m.1 = 61°$ at 28 rad/s and $p.m.2 = 70°$ at 1885 rad/s. That of the position loop is $p.m.3 = 37°$ at 28 rad/s.

In the hybrid system, this phase drop significantly effects the stability of the system because it directly reduces the phase margin of the position loop. In order to compensate for this phase drop, a lead compensator of the form $\frac{\alpha\tau_3 s+1}{\tau_3 s+1}$, with $\alpha = 15$ and $\tau_3 = 0.022$ sec, is placed in the position loop. This lead compensator gives us $+60°$ phase lead at 12 rad/s.

Experimental result

We measure loop transfer functions of the hybrid system using digital signal analysis program [7] under MATLAB and SIMULINK environment. As shown in Fig. 5, the active bandwidth of Velocity 1 is between 28 rad/s (4.5 Hz) and 1885 rad/s (300 Hz) and this hybrid system is stable according to the measured phase margins.

In order to ascertain the performance of the active vibration isolation system, we perform two sets of experiments, a seismic transmissibility test and a transient performance (settling time) test. The result of the transmissibility test is plotted in Fig. 6. The passive transmissibility (dashed line) clearly shows the resonant peak due to the passive mount. The active transmissibility (solid line) with the

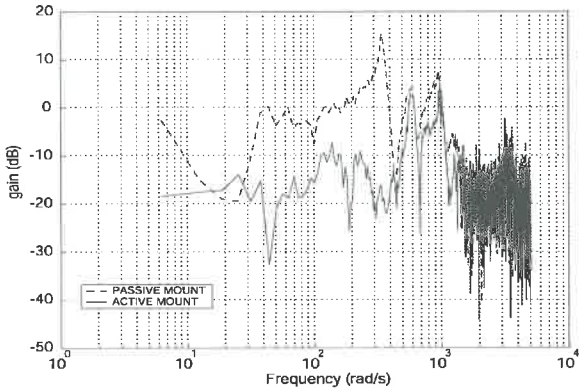

Fig. 6. Measured transmissibility. Floor vibrations in the horizontal direction are measured using a seismic accelerometer attached to the surface plate on which the testbed is placed. The horizontal vibrations of the suspended mass are similarly measured by a accelerometer attached to the suspended mass. The transfer function between these two accelerations is calculated by the HP 35665A signal analyzer. The surface plate is excited by PCB 086C20 impact hammer, which provides uniform excitation by about 1257 rad/s (200 Hz). The average number of this test is 20 times.

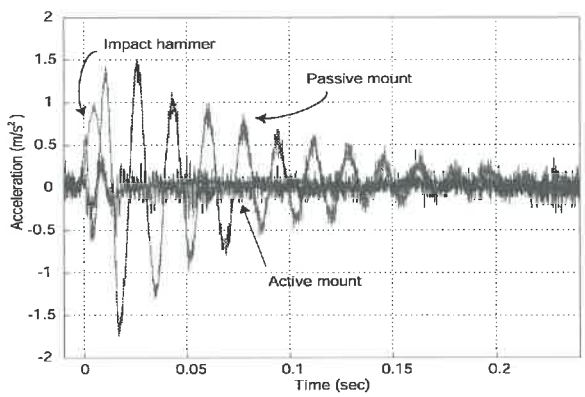

Fig. 7. Isolation performance in time domain after impact. The acceleration of the suspended mass is measured by the same setup in the seismic transmissibility test. The force disturbance is provided by hitting the suspended mass using the impact hammer and the profile of the impact hammer's output is monitored in time domain to confirm the input level of the disturbance force.

shifted natural frequency indicates a clear attenuation in the active control region and the maximum attenuation is about 35 dB.

The result of the transient performance test is shown in Fig. 7 where the acceleration of the passive mount, active mount and impact hammer are plotted. When the active system is turned off, the rocking of the acceleration plot of the suspended mass is consistent with its natural frequency due to the passive mount. When the active system is turned on, the rocking at the natural frequency is found to be arrested just after the moment when the acceleration provided by the impact hammer turns to be negative. For convenience to quantize the transient performance, let's assume the settling time is the time when the absolute value of acceleration becomes smaller than 0.5 m/s^2. Using this criteria, the settling time is 16 ms with the active system turned on and 146 ms without.

Conclusion and further work

Our novel idea to produce soft spring using thin elastomeric material sheets and the variable reluctance actuators has been introduced. We have built the prototype of the single dof active vibration isolation system and have performed two sets of experiments showing significant benefits of the active vibration isolation. Since our system has possibility to make the isolation system much smaller than present-day isolation systems, it is a promising candidate as means of disturbance rejection for next-generation precision machines.

The next step is to add bias flux using permanent magnets to support large static load without excessive generation of heat caused by drive currents in case of a vertical setup.

Acknowledgment

The first author wishes to acknowledge members of Precision Motion Control Laboratory in MIT for their helpful discussions about flexure design and a hybrid control issue. This work is supported by Corporate Manufacturing Engineering Center of TOSHIBA CORPORATION.

Selected bibliography

1. Subrahmanyan,P.K., Ph.D. dissertation, Dept. Mech. Eng. MIT, Cambridge, MA, Sept. 1999.
2. Smith,S.T., Flexure, Gordon and Breach Science Publishers, 1st edition, 2000.
3. Trumper,D.L., Olson,S.M. and Subrahmanyan,P.K., " Linearizing Control of Magnetic Suspension Systems ", IEEE Transactions on Control Systems Technology, vol.5, no.4, pp. 427-438, July 1997.
4. Nelson,P.G., " An active vibration isolation system for inertial reference and precision measurement ", Rev. Sci. Instrum., volume 62, Sept. 1991.
5. Trumper,D.L. and Sato,T., " A vibration isolation platform ", Mechatronics 2000, Sept. 2000.
6. Nashif,A.D., Jones,D.I.G. and Henderson,J.P., Vibration Damping, John Wiley & Sons, 1985.
7. Lillienkamp,K., " Dynamic Signal Analyzer Implemented on dSPACE System ", MS thesis, Dept. Mech. Eng. MIT, Cambridge, MA, Jan. 1999.

A STATISTICALLY BASED PROPOSAL FOR CHECKING THE NEED OF CMM CALIBRATION

Alvaro J. Abackerli, Roxana M. M. Orrego*
Universidade Metodista de Piracicaba – UNIMEP - Piracicaba/SP - Brazil
Carlos A Camargo
Starrett Indústria e Comércio – Itú/SP - Brazil

INTRODUCTION

International standards for CMM testing guide people to have their machine verified, but there are still some doubts to define when to get it calibrated. In many cases, the calibration interval is defined on formal basis, disregarding the actual machine use.

This becomes complicated when the working conditions are not quite the specified by the CMM manufacturer. In those cases, it becomes important to have a simple but reliable test to check the machine performance.

To help users to identify the right time to have their machines calibrated, according to manufacturer's specifications, quick tests have been proposed [1,2,3] in which simple master pieces are used to generate CMM performance information. In those works, ring gauges were measured to provide information about the errors influencing the CMM performance. Figure 1 illustrates the main concepts. The underlying assumption is that a machine influenced by non-negligible errors will provide results reflecting those errors, distorting the machine's dimensional space.

If a perpendicularity error of δ does exist between directions **i** and **j**, the resulting measured diameter will show an ellipse rotated of α, Figure 1-b. If the error δ makes the angle between **i** and **j** greater than 90 degrees, the resulting ellipse will be rotated of 90 degrees counterclockwise. If a CMM error or a set of errors enlarges one CMM axis, the measured data will show an ellipse according to Figure 1-c, resulting h > d. Infinite combinations of results can be obtained depending on the CMM error.

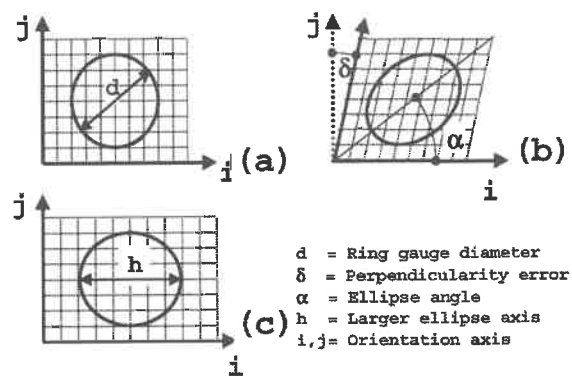

Figure 1: Concepts of CMM testing using ring gauges.

Some authors [1] claimed to identify the most important sources of machine errors observing the dimensions and angles of the generated ellipse. In those tests, no special care was taken regarding sampling strategies since they were designed to check machine tools and large CMMs subjected to errors from 20 to 50 µm magnitude. Other authors [5] apply statistical tools to improve tests reliability, providing additional information to decide about the CMM performance.

The proposal discussed here [4] aims the evaluation of medium sized CMMs influenced by smaller errors, making the issues regarding sampling strategy very important to the test effectiveness. To make it practical for users, common measurement procedures and regular dimensional

* Corresponding author

standards are used (master spheres, ring gauges, and gauge blocks). A sampling strategy and statistical data treatment are applied to improve comprehension about the CMM behavior, associating confidence levels to indicate the validity of test information. A guidance procedure to lead the user to the final decision, with little efforts on statistical processing, was implemented.

THE TEST PROCEDURE

The procedure discussed here can be defined in four steps, as following:

Step 1 – Sample size definition: it is based on the verification of homogeneity among the effective stylus ball diameters, obtained when the probe is qualified with its styli aligned to the main CMM axis, in positive and negative directions. The criterion here is to verify which probe orientation provides stylus ball diameters as repeatable as another, after several qualifications in each direction (spread of data).

The probe is qualified 5 times in each direction to get samples of probe styli ball diameter. Their variances are evaluated and compared to each other, testing for differences between pairs using Bartlett's Test [6]. If the test does not indicate statistical differences, the compared directions (styli) are said to be homogeneous. Resampling test results with 4 and 3 elements, the new variances can be evaluated by the same statistical procedure. If the variances are homogeneous with sample of 3 elements, the sample size $N = 3$ is adopted. Otherwise, the sample size is increased to 4 or 5 until having indication of homogeneity among the qualified directions (styli). If the homogeneity is not concluded the test must be repeated under better experimental conditions.

Step 2 – Identification of comparable results: similar comparisons are made using the averages obtained from probe qualifications in each direction, in order to identify which results taken in the planes XY, XZ and YZ can be compared. The criterion here is to use single-factor Analysis of Variance [6] to verify which set of probe orientations can be said homogeneous, using the defined sample size N at the chosen confidence level. If the homogeneity among all orientations (styli) cannot be accepted by the statistical test, it is necessary to apply the Tukey Test [6] to identify the differences.

Step 3 – Working volume mapping: here, a gauge block and two ring gauges are positioned at the volume areas defined in Figure 2, and measured using regular measuring procedures.

A gauge block of 100 mm is positioned and measured in each area, as shown in Figure 2, by the center points of its calibrated faces. One of the ring gauges is chosen with a 100 mm diameter and the other one with a diameter between 1/2 and 1/3 of the shortest axis of the machine. They are measured N times in each orientation, according the planes XY, XZ and YZ, within each area.

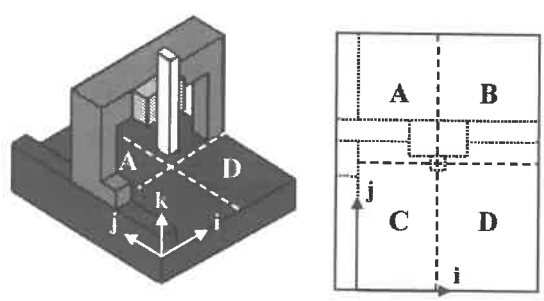

Figure 2: CMM areas for volume mapping

The distances G1-G2, G3-G4, G5-G6 and G7-G8 of the ring gauges are measured, Figure 3, besides their diameters and volume positions. The average results are also compared to each other by Analysis of

Variance [6] and possible influences on the machine performance are identified as already described.

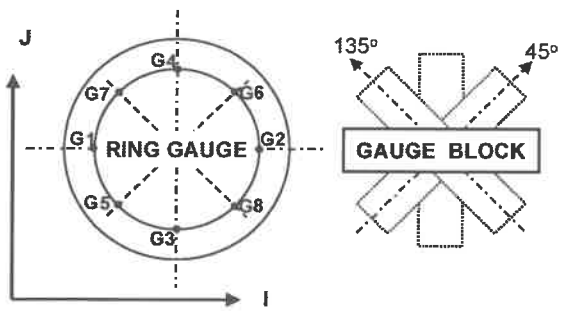

Figure 3: Ring gauge diagonals and gauge block alignments

Step 4 – Performance diagnostic: a comparative analysis identifies the most likely influences on the machine behavior, under the specific test conditions. The criterion is to use redundant information and statistical analysis to conclude about the machine performance against its specification and the evaluated test uncertainty [7]. Similar behaviors obtained from different tests give indication of identifiable CMM errors. The more the agreement of information, the strongest is the indication of presence of machine errors. A similar comparison is made using the diagonals information, G5-G6 and G7-G8, and the gauge block length, obtained at 45 and 135 degrees, to provide indication of possible perpendicularity errors.

If no conclusive indication is obtained, the machine performance is taken as appropriate and no further action is necessary. Otherwise, the appropriate action may be defined from the results. The timely repetition of the complete procedure gives indication of the CMM reproducibility; from which one can evaluate the right time to have the machine calibrated according the manufacturer's specification.

It is important to emphasize that this test is proposed only to indicate the machine performance under specific test conditions and the eventual need of a machine calibration. Therefore, it is also important to note that any conclusion should be made against the CMM expanded uncertainty evaluated according the ISO GUM [7] and considering influences of the environmental conditions, about the specified limits of the machine and the declared uncertainty of each test standard. Its most important aspect is the confidence on statistical validation to accept test results. This allows the optimization of the number of necessary measurements, depending on the CMM working conditions, besides adding confidence limits on the performance statement. Finally, it is worth to mention that the final diagnosis from the proposed test is user dependent, making some experience on dimensional measurements a necessary condition to the procedure application.

EXPERIMENTAL TESTS AND RESULTS

The evaluated machine was started up to get operational equilibrium together with auxiliary devices, master standards and fixtures. Probe configuration, measuring speed, probe force and approach distance were adjusted and/or selected as close as possible to their usual working conditions.

A 20 mm long stylus with a 3 mm ball diameter was selected. The approach distance was set to help the elimination of vibration, due to the machine movements. Further consideration on parameters can be found in literature [8]. Master standards with calibration uncertainty small than 20% of the machine specification were also selected to perform the discussed tests.

The probe qualification was performed 5 times in each direction and tested applying Bartlett's test [6] on samples of 5, 4 and 3 elements, resulting in a B_C of 3.94, 3.53 and 2.17, respectively. Taking a confidence level

α of 5%, a critical value of 9.45 was found, indicating that all tested sample sizes satisfy the homogeneity criterion, and giving the smallest sample size (N = 3) as sample size for the analysis of the probe orientations averages and for the gauges tests in the different volume areas.

With the defined sample size the comparable test results were chosen after applying analysis of variance [6]. Using the same confidence level of 5%, a critical value of 3.45 was selected, indicating non-homogeneity of averages on the tested probe orientations. Tukey's test was applied to identity the comparable results, reaching non-comparability between the data collected in the XY and XZ planes.

To get the final performance diagnostic test results have been compared using the discussed analysis of variance, providing statistical evidences of CMM errors. Tests show statistical confidence of ring gauge ovalization on the XY plane, but not in the other ones, indicating a probable perpendicularity error between axis X and Y. The measurements initially indicated the probable existence of displacement errors, which were not confirmed later by the experimental uncertainty [7]. Further analysis indicates the experimental standard deviation as the largest portion of the combined uncertainty, showing the need of better experimental conditions for a better CMM diagnostic.

FINAL REMARKS.

The discussed test provides a statistically oriented selection of sample size and some useful information about CMM performance, making the decision to calibrate the machine easier to the regular user. It also emphasizes the dependence of diagnostic on the actual experimental conditions. It is important to mention that further analysis on test results can be made to investigate other aspects of the machine behavior, even though the detailed identification of each error source is not the objective of the discussed test procedure.

Keywords: CMM testing, performance evaluation, kinematic errors, statistical methods.

Acknowledgments: the authors would like to thank the financial support received from the *Starrett Indústria e Comércio, Ltda*, UNIMEP and FAPESP for the development of this work.

REFERENCES

[1] Knapp, W. Test of the three-dimensional uncertainty of machine tools and measuring machines and its relations to the machine errors. Annals CIRP.v.2, n.1, 459-464, 1983.

[2] Pahk, H., Kim, J. Development of computer integrated system for error diagnosis of a CMM using calibrated mechanical artifacts. Int. Journal Man. v.33, n. 6, 733-790, 1993.

[3] Lotze, W. Circle form test for testing of coordinate measuring machines and machine tools. Proc.Int. Symp. on Metrol. for Quality Control in Prod., 289-293, Tokyo, 1984.

[4] Abackerli, A.J. Qualificação estatística de máquinas de medir a três coordenadas – MM3Cs. Projeto de Pesquisa, Versão 1.6. UNIMEP, 1997.

[5] Poole, A. B. The calibration of co-ordinate measuring machines by statistical method. Quality Assurance, v.9, n.2, 1983.

[6] Zar, J. H. Biostatistical analysis. 4th Edition, Prentice Hall Inc., New Jersey, 1999. 663 pp.

[7] _____ ISO GUM. Guide to the expression of uncertainty on measurements. Switzerland, 1995.

[8] Phillips, S. D. Performance Evaluations in: Bosch, J. A. Coordinate Measuring Machines and Systems. New York – NY: Marcel Dekker Inc, 1995, 444 p., Chap. 7

DERIVING THE PARAMETRIC ERRORS OF A CO-ORDINATE MEASURING MACHINE FROM THE MATHEMATICAL MODELS FITTED TO REPRESENT THE VOLUMETRIC ERROR COMPONENTS

JOAO BOSCO DE AQUINO SILVA **e-mail: jbosco@ct.ufpb.br**
FEDERAL UNIVERSITY OF PARAIBA
DEPARTMENT OF MECHANICAL ENGINEERING
58059-900 - João Pessoa –Pb -Brasil

Abstract

In this paper, an approach to volumetric determination of CMMs, which permits interpolation between measured points, has been developed. Mathematical and statistical techniques, such as Response Surface Methodology, have been used to represent the relationship between each volumetric error component (Ex, Ey and Ez) at a point, within the measuring volume, and the co-ordinates of the point (X_i, Y_i, Z_i). Also, a method to derive the parametric errors of a CMM from the volumetric error data is presented.

Keywords: Co-ordinate Measuring Machines, Parametric Errors, Response Surface Methodology

1. Introduction

This paper present a methodology to deriving the parametric errors of a co-ordinate measuring machines from the mathematical models fitted to represent the volumetric error components. These error components are obtained by measuring a novel form of space frame, which has been designed and manufactured, as described by (Silva (1997). This space frame has the form of a tetrahedron, which contains a sphere at each apex. The base of the tetrahedron comprises a ball plate that contains three spheres. Each tetrahedron contains three magnetic ball links. A simple magnetic ball link comprises a link, connecting magnetically, to two spheres. One sphere is located on the ball plate and the other at a space point where three links are connected together

2. Fitting mathematical models to represent the volumetric accuracy

Response Surface Methodology (RSM) has been applied to fit a mathematical model to represent the volumetric errors of CMMs. RSM, is a collection of mathematical and statistical techniques that are useful for the modelling and analysis of problems in which a response of interest is influenced by several variables and the objective is to optimise this response [1], [2]. By comparing the calibrated and measured tetrahedron configurations of the modular space frame it is possible to determine the volumetric error components (Ex_i,Ey_i,Ez_i) of the machine under test. The volumetric error at each point defined by the modular space frame is given as follows:

$$Ex_i = X_{mi} - X_i \quad (1)$$

$$Ey_i = Y_{mi} - Y_i \quad (2)$$

$$Ez_i = Z_{mi} - Z_i \quad (3)$$

where,

X_i, Y_i, Z_i, are the calibrated co-ordinates of the points generated by the calibrated modular space frame.

X_{mi}, Y_{mi}, Z_{mi}, are the measured co-ordinates of the points generated by the measured modular space frame.

The general equation that represents each volumetric error component (Ex, Ey, Ez) can be written either by using a first-order mathematical model, that is,

$$E_k(X_1, X_2, X_3) = \beta_{ko} + \beta_{k1}X_1 + \beta_{k2}X_2 + \beta_{k3}X_3 \quad (4)$$

or by using a second-order mathematical model,

that is,

$$E_k(X_1, X_2, X_3) = \beta_{ko} + \beta_{k1}X_1 + \beta_{k2}X_2 + \beta_{k3}X_3 + \beta_{k4}X_1^2 + \beta_{k5}X_2^2 + \beta_{k6}X_3^2 + \beta_{k7}X_1X_2 + \beta_{k8}X_1X_3 + \beta_{k9}X_2X_3 \quad (5)$$

where, k=x, y or z

In both equation (1) and (2) the coefficients β's are to be estimated by the method of least squares where the basic formula is given by the following equation:

$$\beta_k = (XX^T)^{-1} X^T Y_k \tag{6}$$

where,

k=x, y or z and it is related to X, Y and Z direction , respectively.

$\mathbf{Y_k}$= the vector of error component Ex, Ey or Ez in X, Y or Z direction, respectively.

X^T= Transposed of matrix **X**

X= the matrix of independent or predictor variables X_1, X_2 and X_3.

X_1, X_2, X_3 = coded co-ordinates of the ith experimental point in the X, Y and Z direction, respectively.

2. **Deriving the parametric errors from the mathematical models fitted to represent the volumetric error components.**

Two cases have been considered to represent the volumetric error component in the X, Y and Z direction. Initially a first-order mathematical model was fitted. Next, a second-order mathematical model was developed. In both cases the residuals (Y_i - Y_{if}) were plotted against the fitted value, Y_{if}, obtained from the fitted mathematical model. By analysing the residual plots as shown in Silva (1999), it was found that the second-order model more adequately represents the measured data. The analysis of variance concerning the second-order mathematical model was established and it was observed that the overall regression is statistically significant. Therefore, the second-order mathematical model has been selected to represent the volumetric error component in the X, Y and Z direction.

Once the mathematical models that represent the volumetric error components (Ex, Ey, Ez) of a CMM has been fitted, it is possible to derived the parametric errors of the machine under test. To achieve this objective a particular method has been developed and applied as part of this research. This method is founded on the physical meaning of each parametric error component. Basically, the following steps must be performed when applying the proposed method. First, a reference plane within the measuring volume of the machine is selected. Second, measurement lines on the reference plane are defined. These measuring lines are defined by taking into account the physical meaning of each parametric error to be determined. Third, the boundary conditions are applied on the fitted equations that represent the volumetric error components(Ex, Ey, Ez). The parametric errors can be derived as following:

- Positioning error in X direction, $\delta_x(X)$, at plane Z=0.

Boundary conditions: Z=0, Y=0, 0<=X<=X_{max}, Then,

$$\delta_X(X)\Big|_{Z=0;Y=0} = Ex(X, Y=0, Z=0) \tag{7}$$

- Positioning error in Y direction, $\delta_y(Y)$, at plane Z=0.

Boundary conditions: Z=0, X=0, 0<=Y<=Y_{max}, Then,

$$\delta_Y(Y)\Big|_{Z=0;X=0} = Ey(X=0, Y, Z=0) \tag{8}$$

- Positioning error in Z direction, $\delta_z(Z)$, at plane X=0.

Boundary conditions: X=0, Y=0, 0<=Z<=Z_{max}, Then,

$$\delta_Z(Z)\Big|_{X=0;Y=0} = Ez(X=0, Y=0, Z) \tag{9}$$

b) Straightness errors

- Straightness error in the X direction when moving along the Y axis, $\delta_x(Y)$, at plane Z=0.

Boundary conditions: Z=0, X=0, 0<=Y<=Y_{max} Then,

$$\delta_X(Y)\Big|_{Z=0;X=0} = Ex(X=0, Y, Z=0) \tag{10}$$

- Straightness error in the direction Y when moving along the X axis, $\delta_Y(X)$, at plane Z=0.

Boundary conditions: Z=0, Y=0, 0<=X<=X_{max} , Then,

$$\delta_Y(X)\Big|_{Z=0;Y=0} = Ey(X, Y=0, Z=0) \tag{11}$$

- Straightness error in the direction X when moving along the Z axis, $\delta_X(Z)$, at plane Y=0.

Boundary conditions: X=0, Y=0, 0<=Z<=Z_{max} ,Then,

$$\delta_X(Z)\Big|_{Y=0;X=0} = Ex(X=0,Y=0,Z) \tag{12}$$

- Straightness error in the Y direction when moving along the Z axis, $\delta_Y(Z)$, at plane X=0.
Boundary conditions: X=0, Z=0, 0<=Y<=Y_{max}, then,

$$\delta_Y(Z)\Big|_{X0;Y=0} = Ey(X=0,Y=0,Z) \tag{13}$$

- Straightness error in the direction Z when moving along the X axis, $\delta_Z(X)$, at plane Y=0.
Boundary conditions: Y=0, Z=0, 0<=X<=X_{max}, then,

$$\delta_Z(X)\Big|_{Y0;Z=0} = Ez(X,Y=0,Z=0) \tag{14}$$

- Straightness error in the direction Z when moving along the Y axis, $\delta_Z(Y)$, at plane X=0.
Boundary conditions: X=0, Z=0, 0<=Y<=Y_{max}, then,

$$\delta_Z(Y)\Big|_{X=0;Z=0} = E_Z(X=0,Y,Z=0) \tag{15}$$

c) Angular errors

- Pitch and Yaw errors

In this research, a method to determine pitch and yaw errors has been applied. This method consists in deriving the positioning error along two measuring lines that are parallel to the axis of motion. A distance, h, in the appropriated orthogonal distance, separates these measuring lines. Pitch and yaw errors can be calculated by using the following equations:

- Pitch error in X axis

$$E_Y(X) = \frac{\delta_X(X)\Big|_{Z=h,Y=0} - \delta_X(X)\Big|_{Z=0,Y=0}}{h} = \frac{Ex(X,Y=0,Z=h) - Ex(X,Y=0,Z=0)}{h} \tag{16}$$

Pitch errors in Y and Z axes can be determined following similar procedure.

- Yaw error in X axis

$$E_Z(X) = \frac{\delta_X(X)\Big|_{Y=h,Z=0} - \delta_X(X)\Big|_{Y=0,Z=0}}{h} = \frac{Ex(X,Y=h,Z=0) - Ex(X,Y=0,Z=0)}{h} \tag{17}$$

Yaw error in Y and Z-axes can be determined following similar procedure.

- Roll error in X axis

The roll error of the X axis can be derived by considering the straightness error, $\delta_Y(X)$, on two parallel planes, which are separated by an orthogonal distance, h. That error can be calculated by the following equation:

$$E_X(X) = \frac{\delta_Y(X)\Big|_{Z=h,Y=0} - \delta_y(X)\Big|_{Z=0,Y=0}}{h} = \frac{Ey(X,Y=0,Z=h) - Ey(X,Y=0,Z=0)}{h} \quad (18)$$

Roll errors in Y and Z axes can be determined following similar procedure.

d) Squareness errors between axes of motion

In this research, a method to determine the squareness errors α, β_1 and β_2 in the planes XY, XZ and YZ, respectively, has been proposed. Basically, this method uses the straightness errors, which are obtained from the mathematical models fitted to represent the volumetric error components. To describe this method, let us consider the straightness errors $\delta_x(Y)$ and $\delta_y(X)$ at plane XY. The slope of the best fit least square line to the curves defined by $\delta_y(X)$ and $\delta_x(Y)$ are θ_{yx} and θ_{xy} , respectively. The squareness error α is given by the following equation:

$$\alpha=\theta_{yx}-\theta_{xy} \quad (19)$$

Similarly, by applying the same method the squareness errors β_1 and β_2 can be determined. These errors are defined as follows:

$$\beta_1=\theta_{xz}-\theta_{zx} \quad (20)$$

$$\beta_2=\theta_{yz}-\theta_{zy} \quad (21)$$

where,

θ_{xz},θ_{zx},θ_{yz} and θ_{zy} are the slopes of the best fit least squares line to the curves defined by $\delta_x(Z)$, $\delta_z(X)$, $\delta_y(Z)$ and $\delta_z(Y)$, respectively.

3. Conclusions

In using mathematical and statistical techniques, such as response surface methodology, it can be concluded that a second-order mathematical model more adequately represents the volumetric error data obtained by measuring the modular space frame. The developed method to derive the parametric errors from the volumetric error data constitutes an efficient and rapid tool in diagnosing the sources of error of a CMM.

The technique developed for volumetric error calibration does not have to assume that the CMM under investigation has to behave as a rigid body kinematic system.

4. References

Silva, J. B. A., 1997, Volumetric accuracy measurement and analysis of co-ordinate measuring machines, Ph. D. thesis, Department of Mechanical Engineering, UMIST, UK.

Montgomery, D. C. (1991). Design and Analysis of Experiments, 3rd Ed. New York: Wiley.

Box, G. E. P. and Draper, N. (1987). Empirical Model-Building and Response Surfaces. New York: Wiley.

Silva, J. B. A, (1999). Proposal and Application of a Mathematical Model for Volumetric Accuracy Analysis of CMMs. 15th Brazilian Congress of Mechanical Engineering. CD-ROM, paper code AACIIJ. November, 1999, São Paulo, Brazil.

AN EXAMINATION OF THE EFFECT OF VARIATION IN DATUM TARGETS' LOCATIONS ON PART ACCEPTANCE

Tom E. Gardner
Boeing Commercial Aircraft Group, Wichita

S. Hossein Cheraghi
Industrial and Manufacturing Engineering Department
Wichita State University, Wichita, Kansas

Any method of dimensioning and tolerancing is designed to assure that parts manufactured to the stated dimensions and within the stated tolerances will assemble to mating parts and result in a final assembly that satisfies some desired requirement. To accomplish this, dimensions must be described in a way that reflects the functionality of the part and eliminates any confusion as to what and where to measure. Proper tolerance analysis should then guarantee with a reasonable certainty that a measurement for a given dimension that is within the stated tolerance should result in a suitable assembly. Only when this is accomplished can a measurement be useful as an assessment of the suitability of a part. If this is not the goal of dimensioning and tolerancing, then any measurements taken will be a waste of effort.

The use of datum targets to establish datums is commonplace in industry today. Datum targets are used primarily for manufacturing and inspection setups where it is impractical to use the entire part feature and corresponding datum feature simulator. More complex parts can now be dimensioned and toleranced using GD&T since the advent of the CMM. Using the CMM, datums can now be established mathematically using point measurement data rather than requiring the physical mating of the part datum feature and the simulated datum feature. Parts with irregular surfaces and parts that are flexible are primary candidates for use of datum targets. The use of datum targets in these cases is designed to reduce dimensional variation of the part due to locating the part in manufacturing and inspection processes. Care must be taken to assure that the datum target points preserve the functionality of the part.

Establishing a simulated datum from datum target points may be done physically or mathematically, as is the case when using a datum feature on a part. The process is the same but the datum feature points used are now limited in number and have a defined position on the part surface. Establishing a datum feature using datum target points becomes a fairly simple task of calculating a datum plane that passes through the datum target points.

In the process of establishing a simulated datum, there are several possible sources of variation. This variation in establishing a datum will have an effect on any feature that references that datum. Any variation or error in establishing the datum will manifest itself as variation or error in the measurement of the distance between the feature and the datum.

Datum variation can occur from actual variation in the part datum feature itself, from the process of locating the part datum feature to the datum feature simulator, from the measurement error in measuring the part datum feature or datum target points, or from the algorithm used to calculate the mathematical definition of the simulated datum. These types of variation may be referred to *as datum feature error* or *datum target point error*.

When using datum targets, the decision must be made as to where on the part datum feature the datum targets should be located. This type of variation may be referred to as *datum target point location*. Datum target point location will be a significant factor only if the datum target points are located in such a manner that small variations in datum target measurements cause large variation in the simulated datum. An example of this would be to place secondary datum targets very close to each other and at a distance from the feature that references the datum.

Other than the analysis of measurement error, common practice ignores these sources of variation and includes them in the resulting variation of the feature measured. As long as the feature in question meets engineering requirements, this may not be viewed as a problem. However, having the ability to calculate the amount of variation due to datum target point location and error may be valuable in assessing how to improve the process. In addition, understanding the effects and sources of variation will give the manufacturing and measurement process owners the knowledge required to assess tolerance requirements for manufacture and use of part datum features.

The objective of this paper is to understand and quantify the variation of a measured feature e.g., hole true position, that is due to the variation of the datum target points. This information will be used to develop a predictive model that may be used when there is a priori knowledge of datum target point variation. These objectives may be stated as follows:

1. Develop a mathematical model for the evaluation of hole true position GD&T callout in terms of datum target point coordinates.
2. Evaluate and quantify the amount of feature variation due to datum target point variation.
3. Develop a methodology to predict true position variation given a priori knowledge of datum target point variation.
4. Evaluate the methodology and its implications.

First, a two-dimensional model is developed to analyze the effects of datum target point location and datum target point error on a hole true-position tolerance. For this analysis there are several assumptions that are being made. In the case where parts are not flexible and tooling is used to locate the part for processing and measurement, the location and error of datum target points probably aren't of much concern. Since these types of parts may be located with good repeatability, the variation discussed here is minimal. This is certainly true if the datum targets truly reflect the functionality of the part and tooling is manufactured with sufficiently close tolerances. However, there are two cases where variation in datum targets may cause problems.

Case 1 – Flexible Parts

Flexible parts cause special problems when trying to assess compliance to engineering specifications and fitness for use. Since it is not practical to have tooling that contacts an entire surface, datum targets are frequently used for both processing and inspection. In the case of large contoured sheet metal parts, there can sometimes be dichotomy between the functionality of the part and the use of datum targets to aid in the manufacturing and inspection process. When parts require multiple processes, the variation induced by this relocation and the subsequent location for inspection may influence part acceptance decisions.

Case 2 – Datums and Features Produced in the Same Process
Today's machines may take a sheet of material or an extrusion and manufacture a part complete. In cases such as these, both the datums and features produced are relative to machine datums, and as such, cannot be recreated for inspection purposes. Datum targets or even datum simulators used for measurement purposes may show that parts do not meet engineering requirements even though the features may be acceptable. Since a machine may be capable of several different processes - drilling, milling, etc. – the machine process used to manufacture datum features and part features may have different capabilities relative to the machine datums. Axis specific movement may even have quite different capabilities, so the possibilities of different process specific capabilities are quite numerous.

As the first step in the analysis process, the mathematical model of hole position in terms of the coordinates of the datum target points is developed. In this model the primary datum is considered to have no variation. This assumption was relaxed later, and a three-dimensional model was developed. An exact mathematical model is developed to give the deviation from nominal in terms of the datum target point error. From this exact model, an approximate model is developed which is used to give the variation of hole position error in terms of the variation of the datum target point errors. Analysis of these models gives an explanation of the hole position error location and variation in terms of the datum target point error location and variation.

The mathematical model is then used to quantify the amount of variation that can be attributed to datum target point error. The results show how the datum target point errors affect the hole position errors. The effect is not constant for a given hole pattern and increases as the hole position moves away from the center of the pattern. The conclusion may be drawn that the secondary datum target points should be placed as far apart as possible with their midpoint located at the average of the X-coordinates of the hole pattern. Likewise, the tertiary datum target point should be placed at the average of the Y-coordinates of the hole pattern. The datum target point error of the tertiary datum target point affects only the X-direction of hole position error. It affects all hole positions equally, and therefore may be thought of as the largest single contributor to variation. The datum target point error of the secondary datum target points affects both the X- and Y-direction of hole position error. As the hole location deviates further from the center of the hole pattern, the greater the effect of secondary datum point target error will be on the hole position error.

These results may be used to aid in location of datum target points on engineering drawings. The conclusions support the accepted practice of datum target location as shown in many textbooks. If the case arises where datum feature variation is at such a magnitude that hole positions tolerances cannot be met, it is recommended that the engineering drawing be changed to establish a more stable datum system. In the cases discussed here, the most likely candidate for datums would be the holes themselves. Of course, the functionality of the part must be examined and preserved with any changes in datums.

In addition, the knowledge of sources of variation can be used to determine part orientation when machining a part. If there is a priori knowledge of differing machine axis capabilities, the part may be oriented in such a way that it minimizes the effect on hole position errors. The knowledge can also be used to allocate tolerances for fixtures that locate parts during

manufacturing since it can be calculated just how much variation between fixtures locating the same part to the same datum target points will affect the hole position error.

An estimation technique was also presented that uses summary statistics of datum target point error to predict the number of holes that can be expected to meet a given tolerance requirement. This estimation technique may also be used to estimate the amount of tolerance consumed by datum target point error. That information is valuable in tolerance allocation and analysis exercises.

The previous discussion assumed no variation in the primary datum. In some cases, this may not be a valid assumption. In addition, it may be necessary to evaluate the effect of datum target variation on holes that are not perpendicular to the primary datum. Based on the analysis for the secondary and tertiary datums, the mathematical model for three datums was calculated using fixed datum target points.

This model may be used to quantify the amount of variation in hole position that may be attributed to datum target point error. It is shown that the variation in hole position due to the datum target point error of the primary datum target points is very minimal. Therefore, unless the variation in the primary datum target points is of some particular concern, the estimates from using only the secondary and tertiary datum target point variation are satisfactory. Both the two-dimensional and the three-dimensional models developed in this research are valuable tools in understanding how datum target point error can influence hole position error when referencing those datums.

Wavelet Analysis with Different Wavelet Bases for Engineering Surfaces

Shengyu Fu, Xiangyang Liu, B.Muralikrishnan, J.Raja
Center for Precision Metrology
The University of North Carolina at Charlotte
Charlotte, NC 28223

1. Introduction

Wavelets are mathematical functions that separate data into different frequency components, and then present each component with a resolution matched to its scale. They have advantages over traditional Fourier methods in analyzing physical situations where the signal contains discontinuities and sharp spikes. Wavelets were developed independently in the fields of mathematics, quantum physics, electrical engineering, and seismic geology. In recent years, some efforts have been taken to apply wavelet analysis to surface profile analysis [1][2][3]. The goal of this paper is to address the difference between wavelet basis in terms of transmission characteristics associated with their filter bank.

2. Wavelet Analysis Overview

The idea of approximation using superposition of functions has existed since the early 1800's, when Joseph Fourier discovered that he could superpose sines and cosines to represent other functions. However, the sines and cosines that comprise the bases of Fourier analysis are non-local functions. Therefore, frequency information obtained by Fourier transform is the average of the total spatial domain and the sharp change in the spatial domain will be lost due to the averaging. It is ruled by the Heisenberg uncertainty principle that multiplication of the temporal variance and the frequency variance will always be greater than 1/2. Therefore a tradeoff exists between temporal (spatial in surface analysis) localization and frequency localization of a basis function. Wavelets overcome the shortcoming of sines and cosines by having compact support in both spatial and frequency domain. And by varying the size of the support in both domains you can get different emphasis in the representation of spatial domain information or frequency domain information.

Multiresolution analysis in digital signal processing (DSP) is a major application with wavelets. It is introduced by Mallat and Meyer after discovering the unexpected equivalence between pyramid algorithm used in discrete multi-rate filter banks and wavelet transform [4][5]. While the pyramid algorithm enables fast implementation of multiresolution analysis, the wavelet theory builds strong mathematical ground for it. The details of the relation between wavelets and filter banks are given in the book written by Strang/Nguyen [6].

3. Wavelet Bases

Many wavelet families with various characteristics are known. Some wavelet families are especially useful for specific application. Most wavelets are based on FIR

filters although research work is also done for wavelets constructed by IIR filters. The orthogonal and biorthogonal wavelets are the two basic categories of wavelets. Table 1 summarizes the main properties of most well-known wavelets.

The primary consideration in the use of wavelets for surface profile analysis is the amplitude and phase transmission characteristics of the wavelet basis. A combination of good amplitude and linear phase transmission is always desired to achieve minimum distortion of surface features. Among the listed wavelets in Table 1, Haar wavelet is the oldest and simplest wavelet that is not continuous [7]. The Symlet and Coiflet wavelet come from Daubechie wavelet, but are more symmetric [8]. Both the scaling function and wavelet of Meyer are defined in frequency domain. Although the scaling function and wavelet of Meyer are symmetric, no fast algorithm is available for its wavelet transform [9]. The Morlet and Mexican wavelets only have wavelet functions and the corresponding scaling functions don't exist [10]. Four wavelets in three categories are selected for study here. They are orthogonal Daubechies wavelets and Butterworth wavelets with nonlinear phase, orthogonal Coiflets wavelets with near linear phase, and biorthogonal Spline wavelets with linear phase. All of them are associated with FIR filters except Butterworth wavelets.

Type	Filter	Symmetry	Orthogonality	Fast algorithm
Haar	FIR	Symmetric	Orthogonal	Yes
Daubechies	***FIR***	***Asymmetric***	***Orthogonal***	***Yes***
Symlets	FIR	Near symmetric	Orthogonal	Yes
Coiflets	***FIR***	***Near symmetric***	***Orthogonal***	***Yes***
Spline	***FIR***	***Symmetric***	***Biorthogonal***	***Yes***
Morlet	IIR	Symmetric	No	No
Mexican Hat	IIR	Symmetric	No	No
Meyer	IIR	Symmetric	Orthogonal	No
Butterworth	***IIR***	***Asymmetric***	***Orthogonal***	***Yes***

Table 1. Main properties of wavelet families

4. Comparison of Wavelet Bases

The comparison of $h_0(z)$ (low-pass filter for decomposition) for Db6, Coif4, Spline5.5 and Butterworth12 is illustrated in Figure 1. In order to show the difference between the phase linearity of Spline5.5 and Coif4, the relative errors of phase linearity are given in Figure 2. X. Chen used the most popular Daubechies wavelet to explore the potential application of wavelet transform in engineering surface analysis [1]. But Daubechies wavelet is not an ideal choice for application in engineering surface analysis because their amplitude transmission characteristics are not very sharp and phase responses are nonlinear. Butterworth wavelet has excellent transmission characteristics that lead to good frequency selectivity. But the disadvantage is the nonlinearity in the

phase characteristics that are even worse than that of Daubechies wavelet families. For biorthogonal Spline5.5, the phase is linear. But the amplitude responses are rather poor. There are big variations in stopband and passband, and the gentle slope in transition band. The Coiflets has near linear phase. Although the amplitude response is not as good as that of Butterworth wavelet, it is much better than the transmission characteristics of Daubechies wavelet and Spline wavelet. Table 2 shows the results of the comparision.

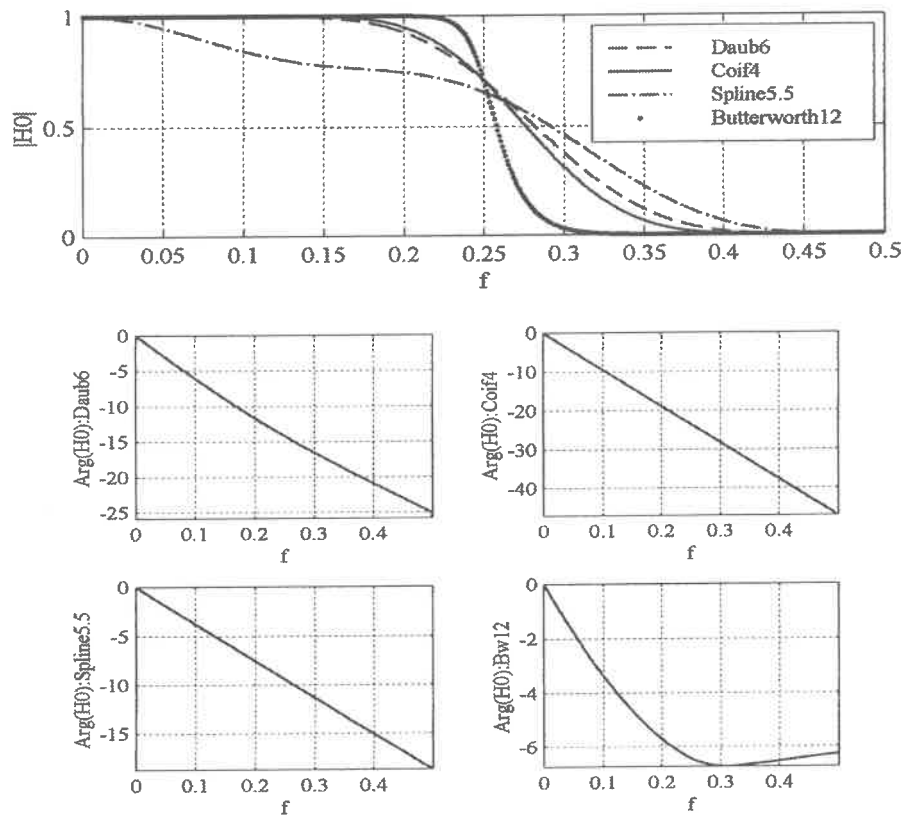

FIGURE 1. Comparison of Db6, Coif4, Spline5.5 and Butterworth12 wavelets

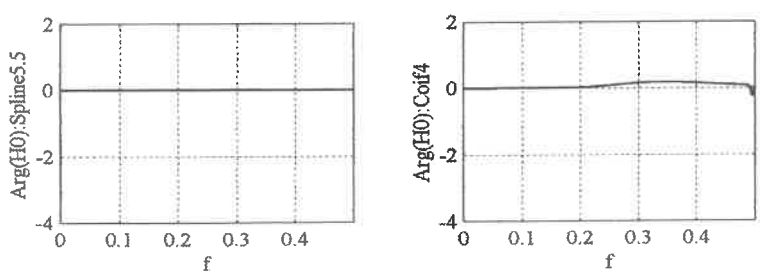

FIGURE 2. Relative phase errors of Spline5.5 and Coif4

	Db6	Coif4	Butterworth12	Spline5.5
Amplitude	not good	good	excellent	poor
Phase	nonlinear	near linear	nonlinear	linear

TABLE 2. Comparison of the wavelet features

5. Conclusion and Future Works

Wavelet analysis is a novel technique introduced into surface analysis in recent years. There are different wavelet bases for us to choose for analysis. This paper studied a set of wavelet bases in terms of the transmission characteristics associated with their corresponding scaling filter. There are other characteristics such as regularity and vanishing moments of the wavelets to be studies in terms of their impacts in surface analysis. Moreover, a set of surface analysis applications with wavelets needs to be done to validate the difference of applying different bases.

6. References

[1] Chen, X., Raja, J. and Simanapali, S., "*Multi-scale analysis of engineering surfaces*", Int. J. Mach. Tools Manufact., Vol. 35, No. 2, 231-238, 1995.

[2] Liu, X. and Raja J., "*The Application of Wavelet Filter Bank in Surface Metrology*", SPIE Vol. 2825, Aug. 1996.

[3] X.Q.Jiang, L.Blunt, K.J.Stout, "*Development of a lifting wavelet representation for surface characterization*", Proc. R. Soc. Lond. A (2000) 456, 2283-2313.

[4] S. G. Mallat, "*Multifrequency channel decompositions of images and wavelet models*", IEEE Trans. Acoust. Speech Signal Process, 37(12):2091-2110, 1989.

[5] Y. Meyer, "*Ondelettes et Operateurs, I: Ondelettes, II: Operateurs de Calderon-Zygmund, III: Operateurs multilineaires*." Hermann, Paris, 1990.

[6] Strang, G. and Nguyen, T. Q., Wavelets and Filter Banks, Wellesley-Cambridge Press, Wellesley, 1996.

[7] Akansu, A. N., and Haddad, R. A., Multiresolution Signal Decomposition, Transforms, Subbands, and Wavelets, Academic Press, Inc., London, UK, 1992.

[8] Daubechies, I., "Orthonormal Bases of Compactly Supported Wavelets II. Variations on a Theme," Technical Memo., #11217-891116-17, AT&T Bell Labs., Murray Hill, and preprint, 1989.

[9] Dabuchies, I., Ten Lectures on Wavelets, Notes from the 1990 CBMS-NSF Conference on Wavelets and Applications at Lowell, MA, SIAM, Philadelphia, PA, 1992.

[10] Grossmann, A., Kronland-Martinet, R., and Morlet, J., "Reading and Understanding Continuous Wavelet Transform, in Wavelets, Combes, J. M., Grossmann, A., and Tchamitchian, Ph., eds., Springer-Verlag, Berlin, 2-20, 1989.

TRANSLATING MACHINE TOOL ERRORS INTO PART ERRORS ENHANCED VIRTUAL MACHINING FOR SCULPTURED SURFACES

Yizhen Lin, Yin-Lin Shen

Dept. Of Mechanical and Aerospace Engineering
The George Washington University
Washington, DC 20052

Sculptured surface machining is a time-consuming and costly process. It requires simultaneously controlled motion of the machine axes. However, positioning inaccuracies or errors exist in machine tools. The combination of error motions of the machine axes will result in a complicated pattern of part geometry errors. On the other hand, little progress has been made in qualitatively translating the machine tool errors into the part geometry errors in the research community. Therefore, in order to quantitatively predict the shape errors of the sculptured surfaces from the machine tool errors, the enhanced virtual machining framework integrates machine tool error models into NC simulation so that part errors can be predicted and shown on a graphic output by simulating the cutting process. It is defined as an "enhanced" system because the virtual part includes information on part geometry errors contributed by machine tool errors when compared with the perfect-cut part geometry obtained by current virtual machining techniques.

In principle, a machining process (removing the material from the stock) can be simulated by taking the Boolean difference of the tool swept volume from the stock. Two different cutting tools, flat-end and ball-end tools, are often used in sculptured surface machining. Therefore, the swept volume model for these two cutting tools are developed. Based on the envelope theory, the task of computing the swept volume can be further reduced to determining the boundary surface of the swept volume, frequently denoted as the envelope surface. For a cylindrical flat-end tool, the boundary surfaces of the tool can be decomposed into the cylindrical surface and top and bottom discs. For ball-end tools, the boundary surfaces of the tool can be decomposed into the cylindrical surface and the top disc and the bottom semi-sphere. The parametric equation for the envelop surface swept by these boundary surface were then derived based on the geometry, trajectory and the orientation of the cutting tool. This parametric form can be used in scan-rendering or forming an approximate polyhedron in machining simulation. For every complete tool path (i.e. one NC block), the tool swept volume is generated and subtracted from the stock, yielding the updated part geometry with the corresponding material volume removed.

Generally, the cutting path for sculptured surfaces is composed of a sequence of linearly interpolated movements. However, due to the machine tool volumetric errors, instead of being straight line as designed, the actual tool path will be a nonlinear motion. The geometric errors $\boldsymbol{VE}$ and tool rotational errors $\boldsymbol{RE}$ of five-axis machine tools can be written as $\boldsymbol{VE} = \boldsymbol{F}(X,Y,Z,A,B)$, where X, Y, Z are the nominal motions of machine linear slides, A and B are nominal rotations of machine rotary axes. These arguments of $XYYAB$ will change as the cutting tool moves along the designed tool path. Therefore, the ideal cutter path in the NC

program for surface machining is discretized and multiple straight lines are used to approximate the actual path. For each newly interpolated cutter location, the machining errors are predicted from the machine tool error model. After the machine tool volumetric errors have been superimposed on the ideal tool path to generate a series of sub-paths, the tool swept volume can be computed as the Boolean union of the swept volumes created by these discretized sub-paths. As the straight-line sub-paths are used to approximate the curve of the actual tool path, the equations describe the envelope surface created by each straight-line tool path can be further simplified.

The next step in geometric simulation of the machining process would be the conversion of the analytic form of tool swept volume into computable graphic object, such as an approximation of polyhedron. This polyhedral approximation of the swept volume is then converted into pixel data by the scan-line conversion algorithm in computer graphics. After the tool swept volume has been converted into pixel data, the workpiece stock model is built by constructive solid geometry (CSG) modeling and converted to pixel data, too. Finally, the machining process can be simulated by carrying out Boolean subtraction of the tool swept volume from the stock model. Fig. 1 shows the general solid-based machining simulation approach for the enhanced virtual machining system.

The solid modeling approach has the advantage of capturing all the errors including the machine tool geometric errors and the approximation errors in the cutting path generation. However, the solid modeling approach has a few down sides. The very complex geometries swept out by the cutting tool impose a heavy burden on computing resources. With the tool path further broken into sub-paths, the computational problem for CSG-based solid model systems will become out of control since the calculation time is estimated to increase as $O(N^4)$ (N is the number of tool path segments) for general tool movements. Also, the comparison between the finished workpiece and the designed part is difficult. Small machining errors (e.g. less than 100 μm) are unlikely to be detected by a visual inspection of the 3-D solid image. Therefore, based on these observations, a surface-modeling based approach is proposed to quickly simulate the machining errors of sculptured parts. . The surface modeling approach approximates the actual cutter contact points by calculating the cutting tool motion and geometry. The approximated part geometry errors contributed by machine tool errors can be written as the functions of cutting tool radius, machine tool volumetric errors and cutting tool orientation errors. Color-coded images are used to visualize and evaluate machining errors, where green means perfect cut, blue means overcut and read means undercut.

Finally, a sculptured surface machined by a five-axis machining center is used to demonstrate the methodology of enhanced virtual machining with error representation. Both the solid modeling approach and the surface modeling approach are used to present the machining errors for sculptured surface. By means of the solid modeling approach, the machine tool error model is integrated into the MasterCAM software package. The final result of the machined surface with machining errors incorporated is shown in Fig. 2. Because the machining errors are very small compared with the overall part geometry, they can not be clearly visualized. Therefore, all the errors are exaggerated by 100 times and presented in Fig. 2. A standalone

computer program is developed to render the machining errors into color-coded image by the surface modeling approach. Figure 3 shows the color-coded images indicating both the undercut and overcut machining errors. These simulation results show that the machine tool error model can be effectively integrated into sculptured surface machining to predict part geometric errors before the physical cutting happens.

In summary, this research work provides the quantitative way to translate machine tool errors into part geometric errors. It integrates machine tool metrology into the CAD/CAM system so that quality assurance can be accomplished in the virtual domain.

ACKNOWLEDGEMENT

This work was supported in part by the National Science Foundation under Grant No. DMII-9624966. The support is appreciated.

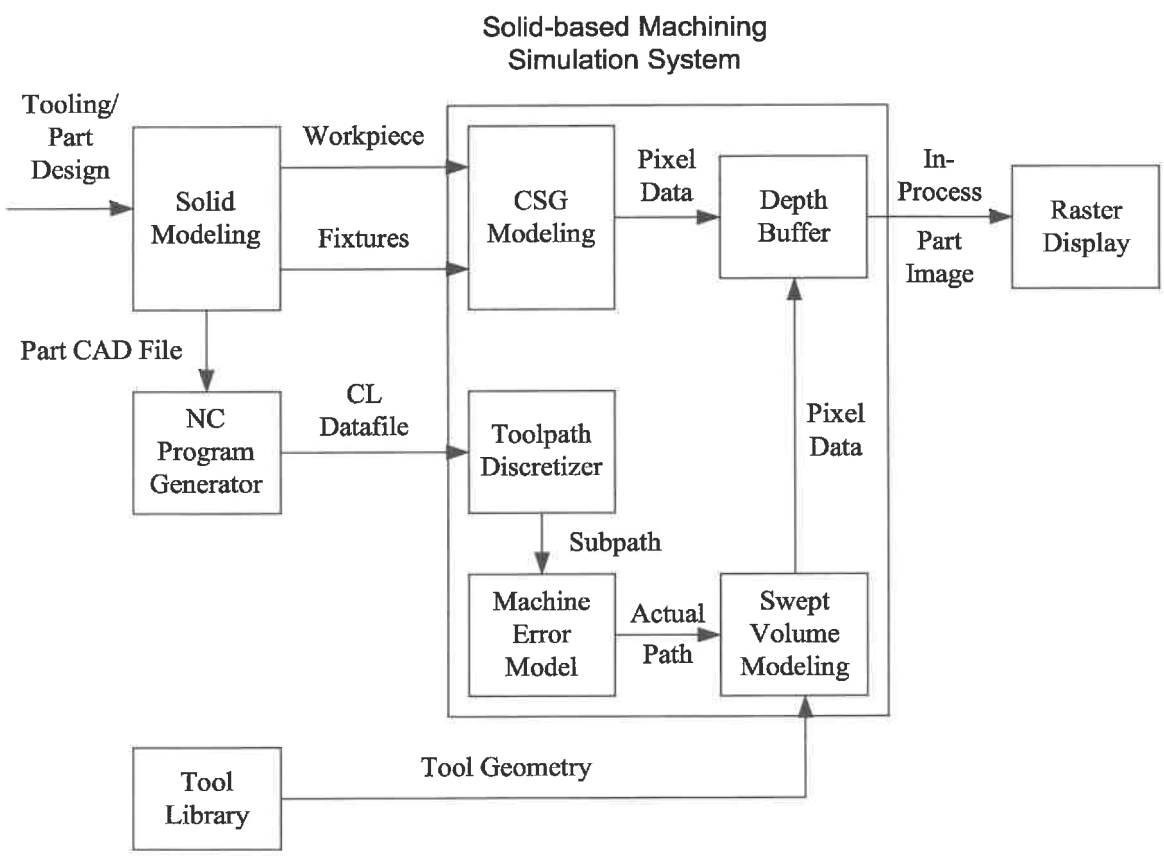

Figure 1. Solid Based Machining Simulation System

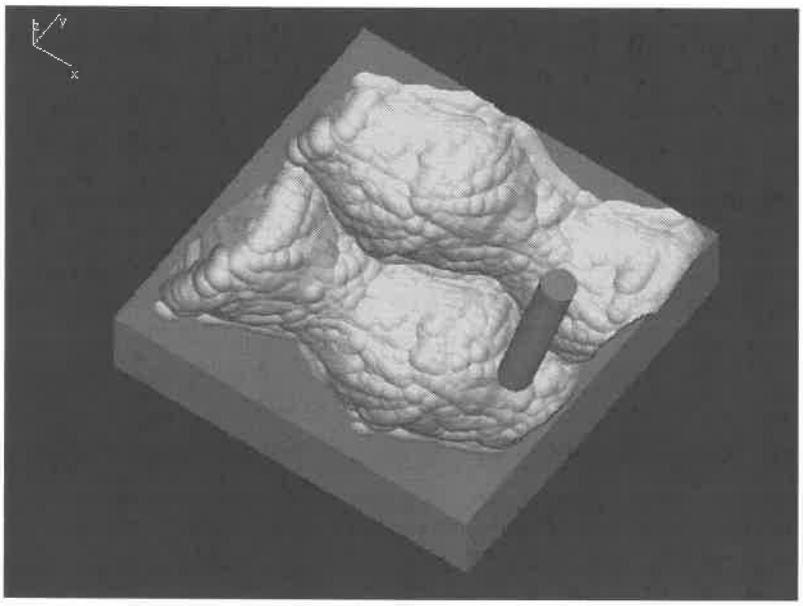

Figure 2. Machined Surface with Machining Errors (Exaggerated by 100 times)

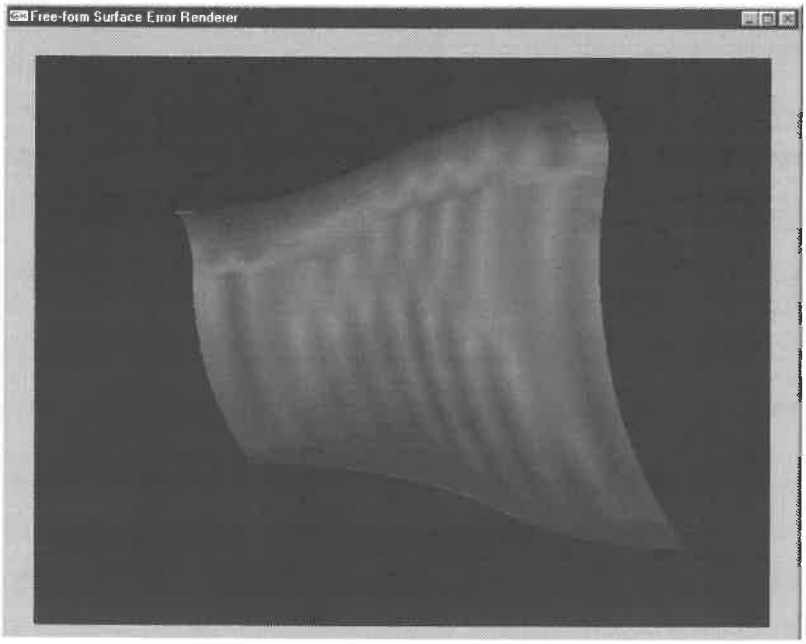

Figure 3. Color-coded Image for Machining Errors
Green: Perfect Cut, Red: Under Cut; Blue: Over Cut

MODELING OF COOLANT FLOWS FOR IN-PROCESS OPTICAL MEASUREMENT

Z. Tao * and Y. Gao **

Department of Mechanical Engineering, Hong Kong University of Science and Technology
Clear Water Bay, Kowloon, Hong Kong

E-mail: * zstao@ust.hk and ** meygao@ust.hk

Abstract: Mathematical models to describe the fluid flows are presented. The models are derived based on fluid dynamics principles. The purpose of the work is to provide a theoretical basis for parameter adjustment for a newly developed method for in-process optical measurement under coolant conditions. In this method, the coolant fluids are removed using a fluid stream to build a transparent window for measurement. It shows that the size of the transparent window is a function of the flow, the velocity, the gap, and the viscosity of the coolant. In the experimental testing, images of the coolant flows were obtained and results were compared with those of the theoretical models. The comparison shows good agreement between them.

Keywords: in-process measurement, surface profile, fluid flow, coolant

Introduction

In general, the coolant fluids must be applied at the grinding zone during grinding operation. However, the coolant fluids are opaque and cover the surface of the workpiece. This causes in-process optical measurement of the surface profiles impossible. In order to realize in-process optical measurement, a device is designed [1], in which, as shown in Fig. 1, the optically transparent fluid is used to remove the coolant fluids, then, a transparent window is generated. The laser beam can go through the transparent window and reach the surface of workpiece for the measurement.

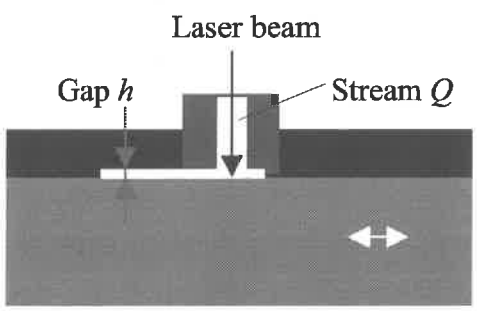

The transparent window is a hyperbolic curve opening along the coolant movement direction and governed by many factors. Q, h, V_w are three main parameters. The parameter Q is the flow rate of the transparent fluid with the unit ml/s, h is the gap between measurement device and the test surface, and V_w is the velocity of test surface, which is the same as the velocity of coolant fluid flow. The relationships between the transparent window parameters and the transparent fluid flow rate Q, the machine table movement speed V_w, and the gap between the transparent window device and workpiece surface h are to be examined.

Mathematical Models of the Coolant Flows

According to the basic analysis [2-5], the transparent fluid flow Q is a point source. In the real system, the gap h is quite small, so we can admit it to be as a line source. The complex potential for a line source located at the position $z=z_0$ is

$$F = \frac{m}{2\pi}\ln(z - z_0) \tag{1}$$

On the other hand, the coolant flow can be simplified to a uniform flow at V_w velocity and along the direction of workpiece movement. This flow and the line source are combined to a flow potential field as described in Fig. 2.

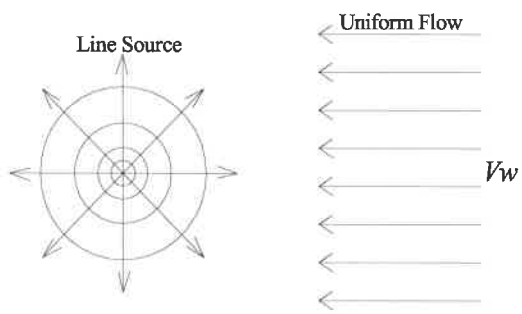

Fig. 2 Flow potential field

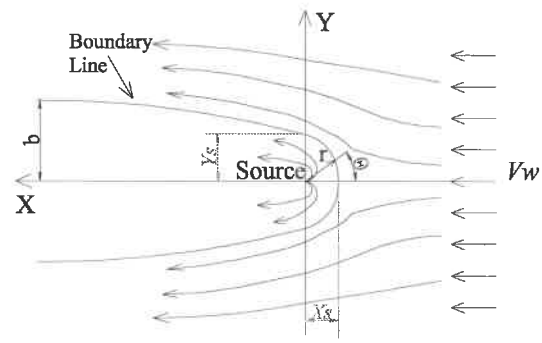

Fig. 3 Stream lines and boundary line

The stream function [2, 4-5] is

$$\psi = V_w y + \frac{Q}{2\pi h}(\pi - \theta) + C \tag{2}$$

The interface boundary of the two fluids includes the stagnation point. So the boundary line, as shown in Fig. 3, can be computed from $\psi=0$. Therefore,

$$y = \frac{Q}{2\pi h V_w}\theta \tag{3}$$

where $\theta \to \pi$, $y = b = \frac{Q}{2hV_w}$. $\theta=0$, $y_0=0$, $x_0 = \frac{Q}{2\pi h}\frac{1}{V_w}$. $\theta=\pi/2$, $y_1 = \frac{Q}{4hV_w}$, $x_1=0$. The parameters $X_s=x_0$ and $Y_s=y_1$ will be used to describe the transparent window form in the future.

For the above basic models, the flow potential field is supposed as an ideal flow field. In fact, this flow field is in a narrow region between two plates, which is quite small from workpiece surface to the bottom of transparent window device. Owing to the viscosity, boundary layer effect should be one of main factors for transparent window. In the gap between the two plates, the coolant fluid flow is a plane Couette flow because of viscosity; its velocity is variable at different laminar layer. The velocity profile is plotted in Fig. 4. According to the no-slip boundary condition, it is a linear relationship. Therefore,

$$V_x = \frac{V_w}{h}z \tag{4}$$

Specially, $v_x(z=0)=V_w$ and $v_x(z=h)=0$.

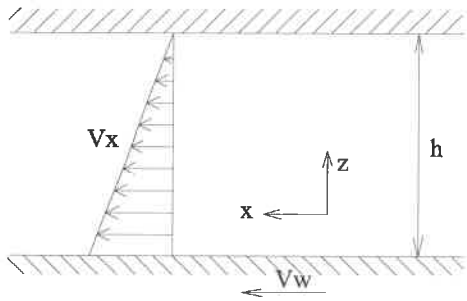

Fig. 4 Coolant fuid flow velocity

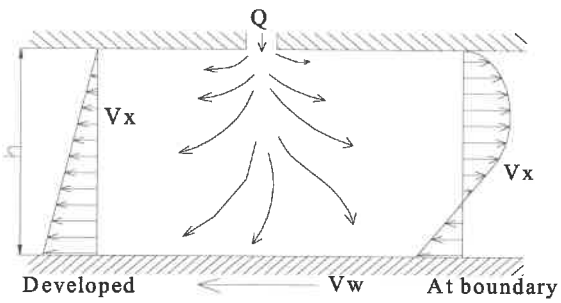

Fig. 5 Transparent fluid flow velocity

Similar to coolant fluid flow, transparent fluid flow is affected by two plates too. As a line source, transparent fluid flow is complex around jet point and at a narrow region between a moving plate and a steadying one. The flow is a composite flow, which consist of a Couette flow and a line source flow. Let the Couette flow velocity be v_{x1} and the line source velocity be v_{x2}, then the sum represents the flow $v_x = v_{x1} + v_{x2}$, as shown in Fig. 5. The Couette flow is a shear flow, which is governed by shear stress from viscosity. In this case, shear stress $\tau_{zx} = \mu dv_x / dz$. Thus, the velocity will be governed by fluid viscosity μ and velocity V_w of the moving plate.

According to the above analysis, the boundary line of transparent window is the function of parameters Q, h, V_w. Furthermore, owing to the effect of boundary layer, the viscosity of fluid affects the velocity profile. So, the transparent window will be governed of Q, h, V_w and μ. It can be described as:

$$x_s = \frac{Q}{2\pi h}\frac{1}{V_w}.C_x \tag{5}$$

$$y_s = \frac{Q}{4hV_w}.C_y \tag{6}$$

where C_x and C_y are the coefficients that depend on the fluid viscosity μ and the plate materials.

Experimental Results and Discussion

An experimental system has been set up to investigate the flow fields. The flow field images under different conditions covering parameters Q, h, V_w have been measured [3]. Let parameters h and V_w V_w be constant and change the Q, we get the different transparent window regions. Fig.6 to Fig. 9 are the sample images of flow field when h=0.3mm and V_w =111mm/s. Similar to the Q experiments, let Q and V_w be constant, a serial of X_s and Y_s under different h can be measured.

Let Q and h be constant, another X_s and Y_s under different V_w are measured and shown in Fig.10 and Fig.11, where X_{sv} and Y_{sv} are the curve of real data; X_{so} and Y_{so} are the theoretically line depending on the model equation.

It can be seen that within the effective region that are 4mm and 5mm at x and y axis, respectively, in this experiment, the actual data are suitable with the models.

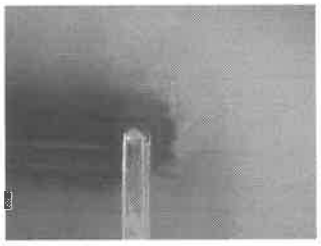

Fig. 6 Q=2.25ml/s

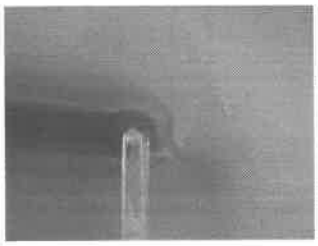

Fig. 7 Q=1.305ml/s

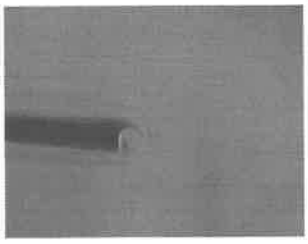

Fig. 8 Q=0.562ml/s

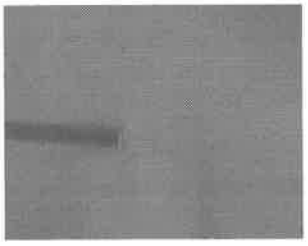

Fig. 9 Q=0,250m

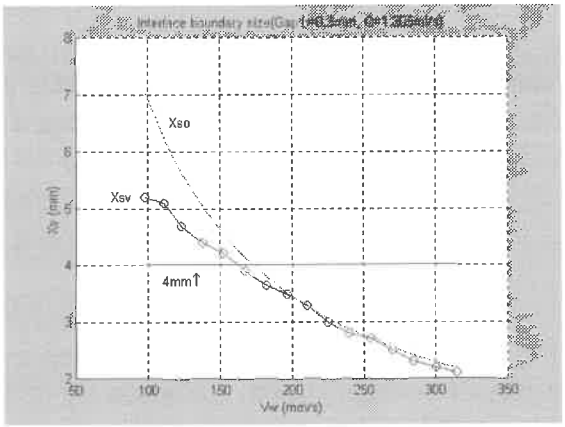

Fig. 10 X_s and X_{so}

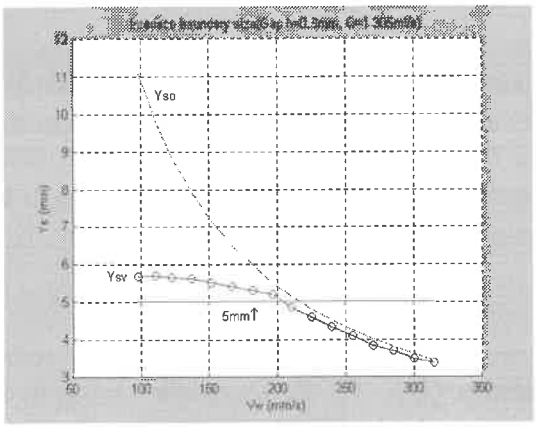

Fig. 11 Y_s and Y_{so}

Conclusions

The coolant fluid field has been analyzed. The models are developed based on the fluid dynamics principles. The models can be used to calculate the size of the transparent window, if the one is within the effective region. The research work should be useful to design a suitable system based on the parameters Q, h, and v_w to create a required transparent window.

Acknowledgement

This work has been supported by the Research Grants Council of Hong Kong SAR of China (Project no. HKUST6100/97E).

References

[1] Gao, Y., and Tao, Z., Tests of flow patterns of grinding coolant interfered using an injection of stream, Proc EUSPEN 2001, 2001.

[2] Tao, Z., and Gao, Y., Analysis of transparent fluid patterns for optical in-process measurement, Proc ISMTII 2001, 2001.

[3] Tao, Z., and Gao, Y., Recognition of fluid images for in-process surface profile measurement, Proc ISMQC 2001, 2001.

[4] Panton, R. L., Incompressible flow, 2e, John Wiley and Sons Inc, New York, 1996.

[5] Johnson, R. W., Handbook of fluid dynamics, CRC Press, New York, 1998.

NONLINEAR ERROR IN EIGHT-PASS HETERODYNE INTERFEROMETERS

Chunhai Wang, Robert J. Hocken,
Center for Precision Metrology, University of North Carolina, Charlotte

Abstract: Optical mixing error is one of the major concerns when using heterodyne interferometers in sub-nanometer applications. This paper focuses on optical mixing error in eight-pass interferometers. A mathematical model is built. Experimental data are obtained and compared to the model. It is found that, unlike two-pass interferometers, the eight-pass interferometer has eight error components due to optical mixing and it still takes half a wavelength displacement for the slowest component to complete a cycle of variation.

1. Introduction

With the advance of science and technology, the demand for sub-nanometer metrology is accelerating. Laser interferometers, a backbone in high precision metrology, are experiencing challenges. Due to the unavailability of stabilized short wavelength lasers, the resolution of interferometers is more and more dependent on the subdivision of the optical wavelength. Optical multiplexing offers an effective way to increase interferometer resolution. Eight-pass interferometers have been adopted at UNC Charlotte for a long-range scanning stage [1].

One of the major concerns when using polarization encoded heterodyne interferometers is the nonlinearity error, also called beam-mixing. Much research has been focused on the problem, mainly for two-pass interferometers [2-8]. Little work has been reported for more than two-pass interferometers. This paper will explore the optical mixing phenomenon in eight-pass interferometers. A mathematical model is developed and verified with experimental data.

2. Eight-pass interferometer

Figure 1 shows the configuration of an eight-pass interferometer used at UNC Charlotte. This interferometer is composed of polarizing beamsplitter PBS, two quarter-wave plates Q_1 and Q_2, coated cube corner reflector CCR, measuring mirror M_1, reference mirror M_2, a roof prism and a fold mirror. A two-frequency laser (not shown in Figure 1) serves as its light source, giving two linearly polarized beams 1 and 2 with a frequency difference of about 20MHz. The CCR, Q_1, Q_2, roof prism and fold mirror reroute the beams inside the interferometer so that beam 1 will travel four returns between PBS and M_1 and beam 2 four returns between PBS to M_2 before they emerge out of the interferometer. Then the two beams combine and form a heterodyne signal, which is processed by decoding electronics to calculate the displacement information.

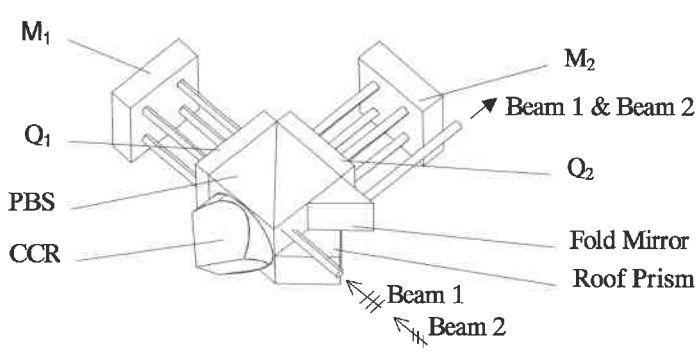

Figure 1 Eight-pass interferometer

3. Optical mixing error

Ideally beam 1 should travel only between PBS and M_1 and beam 2 only between PBS and M_2, so that beam 1 carries the position information of M_1 and beam 2 carries that of M_2. But this is based on an assumption that everything is perfect: the laser beams are perfectly linearly polarized and aligned perfectly with beamsplitter, and the beamsplitter, quarter wave plates and other optical components are perfect and aligned perfectly in the interferometer. Any imperfection will lead a beam to travel not only in the arm where it should be but also in the other arm, causing optical mixing. In this case, the optical route of a beam becomes more complex, as shown in figure 2, where T denotes a passage through PBS, R a reflection at PBS, Q_1 a passage though quarter wave plate Q_1, Q_2 a passage though quarter wave plate Q_2, ϕ_1 a round trip between Q_1 and M_1, ϕ_2 a round trip between Q_2 and M_2, CCR a reflection by CCR, and $ROOF$ a reflection by the roof prism.

$$\begin{aligned}
Input \rightarrow\ & \begin{matrix} T\rightarrow Q_1\rightarrow \phi_1\rightarrow Q_1\rightarrow R \\ R\rightarrow Q_2\rightarrow \phi_2\rightarrow Q_2\rightarrow T \end{matrix} \rightarrow CCR\rightarrow \begin{matrix} R\rightarrow Q_1\rightarrow \phi_1\rightarrow Q_1\rightarrow T\rightarrow ROOF\rightarrow T\rightarrow Q_1\rightarrow \phi_1\rightarrow Q_1\rightarrow R \\ T\rightarrow Q_2\rightarrow \phi_2\rightarrow Q_2\rightarrow R\rightarrow ROOF\rightarrow R\rightarrow Q_2\rightarrow \phi_2\rightarrow Q_2\rightarrow T \end{matrix} \rightarrow \\
\rightarrow CCR\rightarrow\ & \begin{matrix} R\rightarrow Q_1\rightarrow \phi_1\rightarrow Q_1\rightarrow T \\ T\rightarrow Q_2\rightarrow \phi_2\rightarrow Q_2\rightarrow R \end{matrix} \rightarrow Output
\end{aligned}$$

Figure 2 Optical route of a laser beam in the eight-pass interferometer

To calculate the optical mixing, the Jones Matrices are employed. Following the optical route in figure 2, the eight-pass interferometer can be described as:

$$\begin{aligned}
\mathbf{J} = (&\mathbf{J}_{thru}\underbrace{\mathbf{J}_{\lambda/4}\mathbf{J}_{\phi 1}\mathbf{J}_{\lambda/4}}_{\text{4th travel to M1}}\mathbf{J}_{refl} + \mathbf{J}_{refl}\underbrace{\mathbf{J}_{\lambda/4}\mathbf{J}_{\phi 2}\mathbf{J}_{\lambda/4}}_{\text{4th travel to M2}}\mathbf{J}_{thru})\mathbf{J}_{ccr}(\mathbf{J}_{refl}\underbrace{\mathbf{J}_{\lambda/4}\mathbf{J}_{\phi 1}\mathbf{J}_{\lambda/4}}_{\text{3rd travel to M1}}\mathbf{J}_{thru}\mathbf{J}_{roof}\mathbf{J}_{thru}\underbrace{\mathbf{J}_{\lambda/4}\mathbf{J}_{\phi 1}\mathbf{J}_{\lambda/4}}_{\text{2nd travel to M1}}\mathbf{J}_{refl} \\
&+ \mathbf{J}_{thru}\underbrace{\mathbf{J}_{\lambda/4}\mathbf{J}_{\phi 2}\mathbf{J}_{\lambda/4}}_{\text{3rd travel to M2}}\mathbf{J}_{refl}\mathbf{J}_{roof}\mathbf{J}_{refl}\underbrace{\mathbf{J}_{\lambda/4}\mathbf{J}_{\phi 2}\mathbf{J}_{\lambda/4}}_{\text{2nd travel to M2}}\mathbf{J}_{thru})\mathbf{J}_{ccr}(\mathbf{J}_{refl}\underbrace{\mathbf{J}_{\lambda/4}\mathbf{J}_{\phi 1}\mathbf{J}_{\lambda/4}}_{\text{1st travel to M1}}\mathbf{J}_{thru} + \mathbf{J}_{thru}\underbrace{\mathbf{J}_{\lambda/4}\mathbf{J}_{\phi 2}\mathbf{J}_{\lambda/4}}_{\text{1st travel to M2}}\mathbf{J}_{refl})
\end{aligned} \tag{1}$$

where $\mathbf{J}_{thru}$ denotes the Jones matrix for a passage through PBS, $\mathbf{J}_{refl}$ the Jones Matrix for a reflection by PBS, $\mathbf{J}_{\lambda/4}$ the Jones matrix for quarter wave plate Q_1 and Q_2, $\mathbf{J}_{\phi 1}$ the Jones matrix for a round travel between M_1 and Q_1, $\mathbf{J}_{\phi 2}$ the Jones matrix for a round travel between Q_2 and M_2, $\mathbf{J}_{ccr}$ the Jones matrix for coated cube corner reflector CCR, and $\mathbf{J}_{roof}$ the Jones Matrix for the roof prism. Since the two laser beams are only 20MHz different in frequency, they see virtually the same polarizing effect when propagating in the interferometer. Some Jones Matrix value for both the ideal and non-ideal optical components are shown in Table 1.

Table 1 Jones Matrices

Symbol	$\mathbf{J}_{thru}$	$\mathbf{J}_{refl}$	$\mathbf{J}_{\lambda/4}$	$\mathbf{J}_{\phi 1}$	$\mathbf{J}_{\phi 2}$	$\mathbf{J}_{ccr}$	$\mathbf{J}_{roof}$
Ideal components	$\begin{bmatrix}1 & 0\\0 & 0\end{bmatrix}$	$\begin{bmatrix}0 & 0\\0 & 1\end{bmatrix}$	$\begin{bmatrix}0.5+0.5i & 0.5-0.5i\\0.5-0.5i & 0.5+0.5i\end{bmatrix}$	$\begin{bmatrix}e^{i\phi_1} & 0\\0 & e^{i\phi_1}\end{bmatrix}$	$\begin{bmatrix}e^{i\phi_2} & 0\\0 & e^{i\phi_2}\end{bmatrix}$	$\begin{bmatrix}1 & 0\\0 & 1\end{bmatrix}$	$\begin{bmatrix}1 & 0\\0 & 1\end{bmatrix}$
Non-ideal components	$\begin{bmatrix}1 & 0\\0 & \alpha\end{bmatrix}$	$\begin{bmatrix}\alpha & 0\\0 & 1\end{bmatrix}$					

Let $\mathbf{E}_1$ and $\mathbf{E}_2$ denote the Jones vectors for input beam 1 and 2, the polarizing effect of the interferometer on the two beams can be expressed as

$$\mathbf{E}_1' = \mathbf{J}\mathbf{E}_1 \tag{2}$$

$$\mathbf{E}_2' = \mathbf{J}\mathbf{E}_2 \tag{3}$$

The heterodyne signal is formed by synthesizing $\mathbf{E}_1'$ and $\mathbf{E}_2'$. Restoring the time dependence, the electric field of the heterodyne signal will possess the mathematical form

$$\begin{aligned} E_h = {} & E_{14}e^{-i(\omega_1 t+4\phi_1)} + \varepsilon_{13}e^{-i(\omega_1 t+3\phi_1+\phi_2)} + \varepsilon_{12}e^{-i(\omega_1 t+2\phi_1+2\phi_2)} + \varepsilon_{11}e^{-i(\omega_1 t+\phi_1+3\phi_2)} + \varepsilon_{10}e^{-i(\omega_1 t+4\phi_2)} \\ & + E_{24}e^{-i(\omega_2 t+4\phi_2)} + \varepsilon_{23}e^{-i(\omega_2 t+3\phi_2+\phi_1)} + \varepsilon_{22}e^{-i(\omega_2 t+2\phi_2+2\phi_1)} + \varepsilon_{21}e^{-i(\omega_2 t+\phi_2+3\phi_1)} + \varepsilon_{20}e^{-i(\omega_2 t+4\phi_1)} \end{aligned} \tag{4}$$

where ω_1 is the angular frequency of beam 1, ω_2 is the angular frequency of beam 2, E_{14} denotes the amplitude of the light component that originates from beam 1 and travels 4 returns only between PBS and M_1, ε_{1k} (k = 1, 2, 3, 4) the light components that originate from beam 1 and travel 4-k returns between PBS and M_1 and k returns between PBS and M_2, E_{24} is the amplitudes of the light components that originates from beam 2 and travels 4 returns only between PBS and M_2, and ε_{2k} (k =1, 2, 3, 4) the amplitudes of the light components that originate from beam 2 and travel 4-k returns between PBS and M_2 and k returns between PBS and M_1. The intensity of the heterodyne signal is

$$\begin{aligned} I \propto |E_h|^2 = {} & |E_{14}|^2 + |\varepsilon_{13}|^2 + |\varepsilon_{12}|^2 + |\varepsilon_{11}|^2 + |\varepsilon_{10}|^2 + |E_{24}|^2 + |\varepsilon_{23}|^2 + |\varepsilon_{22}|^2 + |\varepsilon_{21}|^2 + |\varepsilon_{20}|^2 \\ & + 2E_{14}E_{24}\cos[(\omega_1-\omega_2)t + 4(\phi_1-\phi_2)] \\ & + 2(E_{14}\varepsilon_{23} + E_{24}\varepsilon_{13})\cos[(\omega_1-\omega_2)t + 3(\phi_1-\phi_2)] \\ & + 2(E_{14}\varepsilon_{22} + E_{24}\varepsilon_{12} + \varepsilon_{13}\varepsilon_{23})\cos[(\omega_1-\omega_2)t + 2(\phi_1-\phi_2)] \\ & + 2(E_{14}\varepsilon_{21} + E_{24}\varepsilon_{11} + \varepsilon_{12}\varepsilon_{23} + \varepsilon_{13}\varepsilon_{22})\cos[(\omega_1-\omega_2)t + (\phi_1-\phi_2)] \\ & + 2(E_{14}\varepsilon_{20} + E_{24}\varepsilon_{10} + \varepsilon_{11}\varepsilon_{23} + \varepsilon_{12}\varepsilon_{22} + \varepsilon_{13}\varepsilon_{21})\cos[(\omega_1-\omega_2)t] \\ & + 2(\varepsilon_{12}\varepsilon_{21} + \varepsilon_{13}\varepsilon_{20} + \varepsilon_{11}\varepsilon_{22} + \varepsilon_{10}\varepsilon_{23})\cos[(\omega_1-\omega_2)t - (\phi_1-\phi_2)] \\ & + 2(\varepsilon_{11}\varepsilon_{21} + \varepsilon_{12}\varepsilon_{20} + \varepsilon_{10}\varepsilon_{22})\cos[(\omega_1-\omega_2)t - 2(\phi_1-\phi_2)] \\ & + 2(\varepsilon_{11}\varepsilon_{20} + \varepsilon_{10}\varepsilon_{21})\cos[(\omega_1-\omega_2)t - 3(\phi_1-\phi_2)] \\ & + 2\varepsilon_{10}\varepsilon_{20}\cos[(\omega_1-\omega_2)t - 4(\phi_1-\phi_2)] \\ & + 2E_{14}\sum_{k=0}^{3}\varepsilon_{1k}\cos[(4-k)(\phi_1-\phi_2)] + 2E_{24}\sum_{k=0}^{3}\varepsilon_{2k}\cos[(4-k)(\phi_1-\phi_2)] \\ & + 2\sum_{j=0}^{3}\sum_{k=0}^{j}\varepsilon_{1j}\varepsilon_{1k}\cos[(j-k)(\phi_1-\phi_2)] + 2\sum_{j=0}^{3}\sum_{k=0}^{j}\varepsilon_{2j}\varepsilon_{2k}\cos[(j-k)(\phi_1-\phi_2)] \end{aligned} \tag{5}$$

The right hand side of the first line is the DC component, the second line is the main heterodyne signal, the third to the tenth are optical mixing signals, and the last two lines are quasi-DC components. Usually the DC and quasi–DC components are filtered away by the electronics, and the high frequency signals (line 2 to line 10) are left. Nonlinear error can be expressed in angular phase, which is equal to the sum of optical mixing components (line 3 to 10) divided by the main heterodyne signal. In the worst case, it is the sum of the amplitudes from line 3 to 10 divided by the amplitude in line 2. The smaller $\varepsilon_{13}, \varepsilon_{12}, \varepsilon_{11}, \varepsilon_{10}$ $\varepsilon_{23}, \varepsilon_{22}$ ε_{21} and ε_{20}, the smaller the nonlinear error. We can also note that different mixing components have different perodicities. The line 10 signal takes 1/8 wavelength displacement ($4(\phi_1-\phi_2) = 2\pi$) to complete a cycle while line 3 and 9 take 1/6 wavelength displacement ($3(\phi_1-\phi_2) = 2\pi$), line 4 and 6 take 1/4 wavelength displacement ($2(\phi_1-\phi_2) = 2\pi$), and line 5 and line 7, the slowest error components, take 1/2 wavelength displacement ($(\phi_1-\phi_2) = 2\pi$), that is to say, a complete nonlinear error cycle in eight-pass interferometer will be 1/2 wavelength displacement.

To verify equation (5), an experiment was designed. According to equation (5), if measuring mirror M_1 is moved at a constant speed, equation (5) will present nine spectral lines (line 2 to 10). Adjacent frequencies are spaced by v/λ, where λ is the mean wavelength of the two frequency laser and v the velocity of M_1. The measured spectrum is shown in figure 3. The largest peak 1 in the figure is the main heterodyne signal, corresponding to the term in line 2 of equation (5). Other significant peaks 2,

3, 4 and 5 correspond to the error terms in line 3, 4, 6 and 10 respectively. The error terms in line 5, 7, 8 and 9 are not significant in this interferometer. Nonlinear error, by figure 3, is about 0.039 radians in phase corresponding to a displacement error about 0.5nm.

Various imperfections that might affect optical mixing errors were analyzed based on the model. Details will not be given here due to length constraints. It was found that the optical mixing errors are more sensitive to the misalignment between the laser polarization orientation and the beamsplitter, but less sensitive to the imperfections of the beamsplitter. Slight misalignment and imperfection of quarter wave plates theoretically have no contribution to optical mixing errors.

4. Summery

A mathematical model was developed to study optical mixing errors in an eight-pass interferometer. An experimental spectrum was compared to the model. It was found that the eight-pass interferometer has eight optical mixing components and a complete cycle of the slowest mixing component requires a measurement mirror displacement of 0.5 Wavelengths. The influence of misalignment and imperfection of the optical components on the nonlinear error is slightly different from that of a two-pass interferometer.

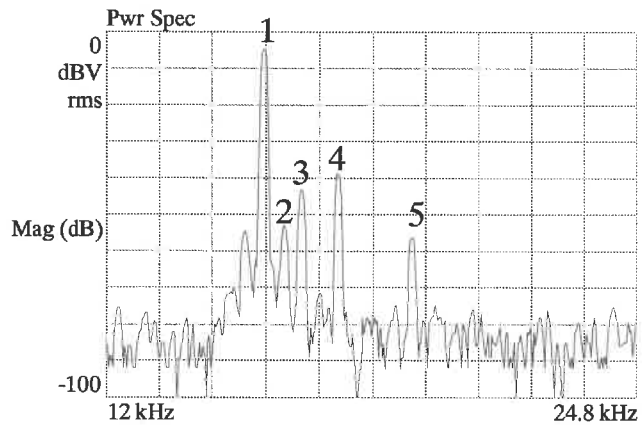

Figure 3 The spectrums of heterodyne signal

5. Acknowledgments

The research is funded by the National Science Foundation under the grant No.2975990126, and carried out in the Center for Precision Metrology, University of North Carolina at Charlotte.

6. Reference

[1] Mike Holmes, Robert Hocken, David Trumper, "The long-range scanning stage: a novel platform for scanned-probe microscopy", *Precision Engineering*, Vol. 24, No. 3, 2000, pp 191-209

[2] Bobroff N, "Recent advances in displacement measuring interferometry", *Measurement Science and Technology*, Vol 4, No. 9, 1993 pp.907-926

[3] Tanaka M., Yamagamai T., and Nakayama K., "Linear interpolation of periodic error in a heterodyne laser interferometer at subnanometer level", *IEEE Trans. Instrum. Meas.*, Vol. 38, No.2, 1989, pp552-554

[4] Hou W., and Wilkening G., "Investigation and compensation of the nonlinearity of heterodyne interferometers", *Precision Engineering*, Vol. 16, No. 1, 1994, pp25-35

[5] Badami, V. G., "Investigation and compensation of periodic nonlinearities in heterodyne interferometry", PhD's Thesis, Department of Mechanical Engineering and Engineering Science, UNCC Charlotte, NC, 1999

[6] Bobroff N., "Residual errors in laser interferometry from air turbulence and nonlinearity", *Appl. Opt.*, Vol. 26, No. 13, 1987, pp2676-2682

[7] J.A. Stone, L.P. Howard, A simple technique for observing periodic nonlinearities in Michelson interferometers, *Precision Engineering* Vol. 22, No. 4, 1998, pp. 220-232.

[8] V.G. Badami, S.R. Patterson, A frequency domain method for the measurement of nonlinearity in heterodyne interferometry, *Precision Engineering* Vol. 24, No. 1, 2000, pp. 41-49.

SYSTEMATIC ERROR ESTIMATION BASED ON GREY RELATIONAL ANALYSIS

Z. Wang *, Y. Gao **, S. Tse **, and P. Qin ***

* Luoyang Institute of Technology, Luoyang, 471039, China
** Hong Kong University of Science and Technology, Clear Water Bay, Hong Kong
Email: meygao@ust.hk
*** Xi'an Jiaotong University, Xi'an, 710049,China

Introduction

It is known that systematic errors could cause the measurement results deviating from the true values. This could decrease the validity of the measurement. Systematic errors are due to the adverse effects in the measurement methods, apparatus, environments, etc. In measurement practices, due to the complexity of error sources, systematic errors are found difficult to determine or sometimes ignored under the assumption that such errors do not exist. In terms of solutions, simply increasing the number of repeated measurement, which is common in a traditional test, may not be able to reduce or eliminate the systematic error. Based on data distribution, the statistical criteria such as the experimental contrast, the residual error check-up, and the t-distribution inspection are often used to estimate the systematic errors in a measurement. The working principle is based on the statistics principle that the existence of systematic error in a measurement sequence would destroy the quality of randomness. To improve accuracy in a modern test, it is very important to examine the characteristics of the systematic errors and find an effective method to reduce their effects on the measurement.

In recent years, there are several investigations on the systematic error estimation and removal [1-5]. Rothe [6] introduced a multivariate estimation method to determine the systematic error of a surface profile using a covariance matrix. Bechhoefer [7] proposed a method to estimate the random error that exists in the experimental data along with the relative proportion of systematic error using an auto-covariance function of the residual errors in a number of least-square curve fittings. Kojro [8] discussed a number of digital statistical correlations and algorithms with respect to the systematic errors. The standard deviation of the statistical errors in the correlation estimators was also computed. Kadis [9] investigated the criteria to see if the random and systematic components of the total measurement error are sufficiently small to neglect. The method is within the framework of an approach to estimate the measurement errors. Rekkas [10] presented an algorithm to deal with the problem of systematic errors in radar measurement. The performance of the algorithm was assessed in several cases and the result was satisfactory. The above research work and the corresponding estimation methods are based on the statistics principle. To do a statistical analysis with sufficient confidence, the measurement number must be large enough, so that the distribution could be confirmed. In addition, to simplify the numerical computation, and in many cases to permit an analytical solution, the distributions are required to conform to some typical distributions such as the Gauss distribution and the t-distribution. In practical measurement, in particular in the tests where the data samples are only a few, such as in the destructive tests and in the blast-off examination, it is very difficult to obtain a large number of data samples. On the other hand, if the sample size of the measurement data is

large, but it is not sure if it fits a typical statistical distribution, the statistical criteria may still be difficult to use. The result may not be true if the statistical methods are used to analyze the measurement data.

To solve this problem, a new method using the grey system theory is proposed to estimate the systematic errors in a dynamic measurement. In this method, a grey relational analysis is performed for a measurement sequence. Due to the use of the grey relational analysis, the requirements of large samples and conformance to typical distributions are no longer needed. As such, the systematic errors can be successfully determined for different measurement sequences without the stringent requirements. Theoretical analysis and experimental investigation are presented. It shows that the proposed method can be used to estimate systematic errors with high confidence where the statistical methods are found not suitable to use. The proposed method can be seen as a viable supplement to the statistical methods.

Working Principle

Measurement errors from apparatus, environmental factors and so on, make measurement results uncertain in certain degrees. Measurement systems could be regarded as grey systems. Measurement processes could also be regarded as grey processes [11]. The data would be correlated in certain degrees in a repeated measurement if systematic errors do not exist in the measurement sequence. Thus a grey relational analysis can be applied. The essence is comparing the geometric curves shape among sequences to get the quantitative description with grey relational coefficient and grey relational grade [12]. Assume the measurement is carried out using several different methods, where each method is done with repeated measurements. The sequence of a specific method can be expressed as:

$$x_i = x + \delta_i + \theta_i \tag{1}$$

where i=1,2,...,n, x_i is the sequence of the measured values, i is the sequence number, x is the true value sequence of the measurand, δ_i and θ_i is the sequence of random error and systematic error, respectively. If the referenced sequence is

$$x_0 = x + \delta_0 + \theta_0 \tag{2}$$

where x_0 is the referenced sequence of the measured value, δ_0 and θ_0 is the referenced sequence of random error and the systematic error, respectively. To analyze the systematic error, a pretreatment is to be done. The absolute difference between the measured sequence and the referenced sequence is expressed as:

$$\Delta_i = | x_i - x_0 | = |\delta_i + \theta_i - (\delta_0 + \theta_0)| \tag{3}$$

The grey relational coefficient between the two sequences can be defined as:

$$\gamma(x_i, x_0) = \frac{\min \Delta_i + \zeta \max \Delta_i}{\Delta_i + \zeta \max \Delta_i} \tag{4}$$

The grey relational grade [12] can be obtained from the equations. Since the absolute difference Δ_i is related to both the random and systematic error (Eq. (3)), the grey relational grade would be also influenced by both random and systematic error. The random error would be much less than the systematic error if it could be reduced into neglected degree by many-repeated measurement. The relational grade would mainly depend on the systematic error if the random error were able

to be neglected. A specific type of systematic error in the measuring process would change the grey relational grades in the sequence. The grey estimation of systematic errors can be done using the grey relational grade and grey relational coefficient.

Measurement Results and Discussion

The measurement results of an experimental testing are examined to demonstrate the use of the method for the systematic error estimation. In the testing, a workpiece was measured repeatedly for a number of times using two different methods. The measuring results were as: $y_1(k)$ = [0.27, -0.78, 0.11, -0.71, 0.03, 0.07, 0.08, 0.56] (μm) and $y_2(k)$ = [-0.90, 0.20, 0.96, 0.86, -0.06, -0.90, -0.17, -0.03] (μm). A pretreatment mapping of the original sequences was used as:

$$\begin{aligned} x_i(1) &= (2y_i(1) + y_i(2))/3 \\ x_i(k) &= (y_i(k-1) + y_i(k) + y_i(k+1))/3 \\ x_i(8) &= (y_i(7) + 2y_i(8))/3 \end{aligned} \tag{5}$$

After above transformation, two new data sequences were obtained as $x_1(k)$=[-0.08, -0.13, -0.46, -0.19, -0.20, 0.06, 0.23, 0.40] (μm) and $x_2(k)$=[-0.53, 0.08, 0.67, 0.58, -0.03, -0.37, -0.36, -0.07] (μm). The smallest data point in the above sequence was assumed to compose the referenced sequence as $x_0(k)$ = -0.53, k=1,2,...,8. The grey relational coefficient between the measured sequence and the referenced sequence [12] was obtained as:

$$\gamma(x_i(k), x_0) = \frac{\min_i \min_k |x_i(k) - x_0| + \zeta \max_i \max_k |x_i(k) - x_0|}{|x_i(k) - x_0| + \zeta \max_i \max_k |x_i(k) - x_0|} \tag{6}$$

where ζ is a coefficient, and $\zeta \in [0,1]$. In general, ζ=0.5. The grey relational coefficients between the data of the measured sequence and that in the referenced sequence can be obtained. The grey relational coefficient curves are as shown in Fig. 1. The grey relational grades between the measured sequence and the referenced sequence are given as:

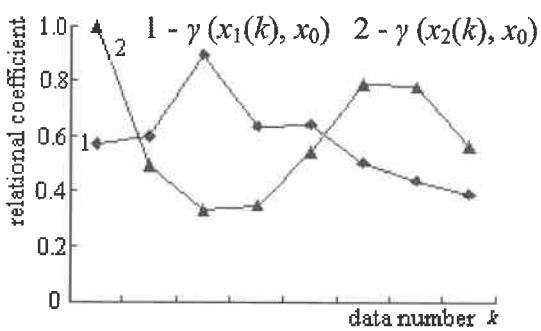

Fig. 1 Grey relational coefficient curves

$$\gamma_i = \frac{1}{8}\sum_{k=1}^{8} \gamma(x_i(k), x_0) \tag{7}$$

For the two sequences, γ_i =[0.586,0.608]. From Fig. 1, it can be seen that there were no linear or periodical features in the two curves. From Eq. (7), the difference between two relational grades is very small. In addition, there was no constant systematic error since the two measurement sequences were obtained using two different methods. Therefore, it can be said that there was no systematic error in the measurement process. The conclusion was the same, if the statistic criteria were used to estimate the systematic errors in the measurement process. Additional experiments show that if the difference is less than 0.4, there would be no remarkable systematic errors in a measurement process. The method can be served as an alternative method to estimate systematic errors for the cases where the statistical methods cannot be used due to unknown distribution and very small number of samples.

Conclusions

A new method is proposed to estimation the systematic errors in a measurement process. The method is based on a grey relational analysis of a measurement sequence using the grey system theory. Multiple data sequences can be analyzed. The proposed grey relational estimation does not require the measurement data to conform to the normal distribution and does not require a large sample size. It is therefore a good alternative to estimate systematic errors where the statistical methods could not be successfully applied.

Acknowledgement

This project is supported by the National Natural Science Foundation of China (Project No. 59805007).

References

[1] Abdou, I. E., Comment on the paper 'Elimination of systematic error in subpixel accuracy centroid estimation', *Optical Engineering*, 1995, **34**(11), pp. 3347-3348, USA.

[2] Agupov, V. A., and Lotonov, H. A., Estimate of the systematic error of dosimetric measuring instruments in the absence of reference standards, *Izmeritel'naya Tekhnika*, 1998, **41**(8), pp. 50-52, Russia.

[3] Tao, R., and Tong, G., A new method for testing systematic errors caused by multifactors, *Chinese Journal of Scientific Instruments*, 1999, **20**(6), pp. 564-567, China.

[4] Liu, J., Owe, Fruhauf, and Andreas, Schonecker, Accuracy improvement of impedance measurements by using the self-calibration method, *Measurement*, 1999, **25**(3), pp. 213-225.

[5] Wang, J., and Fiebig, M., Measurement of the thermal diffusivity of liquids with a laser-induced thermal-grating technique, an experimental investigation of systematic errors, *International Journal of Thermophysics*, 1996, **17**(6), pp. 1229-1239, USA.

[6] Rothe, Hendrik, Multivariate estimation of the systematic error of scanning probes microscopes, *Thin Solid Films*, *Proc the Workshop on Development and Industrial Application of Scanning Microscopes*, SXM-1, 1995, **264**(2), pp. 282-290, Germany.

[7] Bechhoefer, J., Curve fits in the presence of random and systematic error, *American Journal of Physics*, 2000, **68**(5), pp. 424-429, USA.

[8] Kojro, Z., Riede, A., Schubert, M., and Grill, W., Systematic and statistical errors in correlation estimators obtained from various digital correlators, *Review of Scientific Instruments*, 1999, **70**(12), pp. 4487-4496, USA.

[9] Kadis, R. L., Criteria for negligible smallness of random and systematic components of measurement errors, *Izmeritel'naya Tekhnika*, 1996, **39**(7), pp. 3-7, Russia.

[10] Rekkas, C. M., Kyriakopoulos, K., and Krikelis, N. J., An algorithm for the estimation of systematic errors in radar measurements, *International Journal of Systems Science*, 1994, **25**(6), pp. 1105-1112, UK.

[11] Wang, Z., Qin, P., and Gao, Y., Grey evaluation of measurement uncertainty, *Journal of Grey System*, 1999, **11**(4), pp. 347-352, UK.

[12] Deng, J., Grey systems, China Ocean Press, Beijing, 1988.

UNCERTAINTY ASSESSMENT FOR THE ROUNDNESS MEASUREMENT OF CRANKSHAFTS USING A VIRTUAL GAGING SYSTEM

Xianping Zhang and Addison D. Cole
ADCOLE CORP.
Marlborough, MA 01752

Introduction

Crankshafts are one of the critical components in reciprocating engines, and their accuracy greatly affects the fuel consumption, dynamic performance and reliability of the engines. Adcole Corporation's Cylindrical Coordinate Measuring Machines (CCMMs) are specifically designed for measuring crankshafts of reciprocating engines. Many parameters including the roundness, diameter, cylindricity and straightness of journals and parallelism and perpendicularity among the journals can be measured during one set-up.

In this paper, we attempt to assess the uncertainty of roundness measurement of crankshaft journals using a virtual gaging system we reported earlier [1]. The virtual gaging system is basically a mathematic model of the real gages, and each data point is obtained by actually moving the follower and part models and mathematically detecting the contact condition. By varying the errors of different components, we can assess the uncertainty of roundness measurement through simulations using the virtual gaging system. In the following, some factors affecting the roundness measurement uncertainty are discussed first. Then the uncertainty assessment is demonstrated through examples. It is shown from demonstration that assumption of normal distribution is inappropriate for uncertainty assessment of roundness measurement, and uncertainty assessment using virtual gaging system gives better result.

Some Factors Affecting the Roundness Measurement Uncertainty

The roundness is a type of form error of circular shapes such as crankshaft journals, and the factors affecting the uncertainty in the roundness measurement is much more complicated. Currently the common practice is to use a single number such as total indicator reading (TIR) to represent the roundness, and this is in accordance with the national standards such as ANSI Y14.5M [2]. In the following, we will discuss some factors that affect the roundness measurement uncertainty of crankshaft journals. The factors to be discussed include the assumption of normal distribution , measurement method, sampling scheme, spindle error motion, and follower straightness error.

Assumption of Normal Distribution: In the assessment of measurement uncertainty, normal distribution is often assumed to derive the expanded uncertainty of the final results. This is true for many applications, but it falls apart when it is assumed for applications such as roundness measurement uncertainty assessment. The problem is that under normal distribution, the uncertainty interval extends on both sides of the mean value in order to include all the probable values; while in roundness measurement, we know that the roundness of a perfectly round part will be zero, which is the lower bound of the uncertainty interval. Therefore, using assumption of normal distribution would lead to erroneous expanded uncertainty for roundness measurement result.

Effect of Methodology: This means how the roundness data are collected and processed. For instance, in the roundness measurement the data points may be collected using two diametrically opposing probes. This method actually measures the diametric variation of the cross section, and it will not reveal the odd-lobed shapes. In other word, for any odd-lobed shapes it will look perfectly round. Adcole gages measure the radial variation and will reveal both odd and even-lobed shapes.

Sampling Scheme: Sampling scheme normally includes the number of sampling points and their distribution, and is a critical factor affecting the roundness measurement error in crankshaft journals. In Adcole gages, the sampling points are uniformly distributed along the whole circle of the cross section being measured for a journal, so in the following the different sampling schemes will only mean the different number of sampling points. Assume that the journal has a three-lobed shape and the journal is sampled with three points uniformly distributed around the journal. Then, we can see that the journal will look perfectly round even though it is not. According to sampling theorem, in order to reveal the three lobes of the journal, the number of sampling points has to be at least six. In order to measure higher frequencies, the number of sampling points has to be large enough. Many CMMs equipped with

only touch trigger probes are limited by the maximum number of sampling points and consequently have a very limited frequency response for roundness measurement. In Adcole gages, the number of sampling points is up to 3600; therefore, the maximum number of detectable lobes, according to the sampling theorem, can reach 1800. This is very useful when the detection of high harmonics is important such as chatter analysis.

Spindle Error Motion: Spindle error motion causes a perfectly round journal to look non-round. This is true for all roundness measuring instruments. In Adcole gages, the spindle error motion has the maximum effect at the headstock end and the minimum effect at the tailstock end. If no other error sources exist, the roundness of the journal at the headstock end would be approximately the same as spindle error motion.

Follower Straightness: In Adcole gages the follower is the component in contact with the part being measured, and the coordinates of the contact points are recorded during the rotation of the part. For main journals the contact points on the follower are within an extremely small region so the follower form error can be neglected. However, when pin journals are measured the contact points are distributed along the follower, and therefore the follower form error (straightness) will be mapped to the roundness of the journals if it is not corrected. In Adcole gages the follower straightness is strictly controlled and can also be compensated in the software, so the uncertainty of the roundness measurement for pin journals can be minimized.

There are also other factors affecting the roundness measurement. The factors include, but not limited to, vibration and gravitational effects, and so on. These factors will not be discussed here.

Uncertainty Assessment of Roundness Measurement Using A Virtual Gaging System

In uncertainty assessment of roundness measurement using virtual gaging system, the error sources are varied and combined and then plugged into the virtual gaging system to produce the roundness result of journals. For each input error source, the standard uncertainty is assigned with either a type A uncertainty or type B uncertainty according to the ISO document, "Guide to the Expression of Uncertainty in Measurement" (GUM) [3]. Uncertainty of roundness is obtained from the output of the virtual gaging system. In the following, we will demonstrate the process of uncertainty assessment through examples , and show the inappropriate assumption of normal distribution for roundness measurement.

Example 1

In this example, we will show a general but very simple case. This case also applies to other roundness measuring instruments. The part will assume a 2nd harmonic roundness error, and the gage also has its only error in the spindle and it assumes a 2nd harmonic error motion in the measurement direction. We will also assume the spindle error motion is repeatable, which indicates that it is fixed in the gage coordinate system. It is obvious that the roundness data can be analytically expressed as follows:

$$r(\theta) = e_p \cos(2\theta - \phi_p) + e_s \cos(2\theta - \phi_s) \tag{1}$$

where, e_p is the amplitude of the 2nd harmonic of part roundness error, e_s is the amplitude of the 2nd harmonic of spindle error motion, θ is the angle position in the gage coordinate system, ϕ_p is the phase of the part error and ϕ_s is the phase of the spindle error. The right side of the above equation can be simplified as

$$r(\theta) = [e_p^2 + e_s^2 + 2e_p e_s \cos(\phi_p - \phi_s)]^{1/2} \cos(2\theta - \alpha) \tag{2}$$

where α is the resultant phase. The measured roundness value is then

$$e_r = 2[e_p^2 + e_s^2 + 2e_p e_s \cos\phi]^{1/2} \tag{3}$$

where $\phi=\phi_p-\phi_s$. This indicates that the measured roundness value varies as the phase relationship between the part form error and the spindle error motion changes. The measured roundness value will fall within the interval of

$[2|e_p-e_s|, 2(e_p+e_s)]$. Now let us assess the roundness uncertainty from a common procedure. We will repeat the measurement process 10000 times, record the roundness each time, and then calculate the mean and standard deviation of the roundness values from these 10000 measurements. We will let the virtual gaging system do the job. Assume that the amplitude of the 2nd harmonic of the part form error is 2 μm, the amplitude of the 2nd harmonic of the spindle error motion is 0.15 μm, and the phase difference, ϕ, uniformly varies from 0 to 2π. The uniform distribution of ϕ simulates repeated roundness measurement process since in the repeated measurement the part is repositioned on the gage and then the phase difference ϕ could be anywhere from 0 to 2π. Substituting these parameters into the virtual gaging system, we obtain the following result from one simulation:

$$max = 4.3\ \mu m;\quad min = 3.7\ \mu m;\quad mean = 4.009\ \mu m;\quad std = 0.213\ \mu m.$$

If the minimum and maximum values are used for the roundness uncertainty, we conclude that the roundness values will fall within the interval of [3.7μm, 4.3 μm]. However, if we assume normal distribution and use a coverage factor of 3, we will obtain an interval of [3.370 μm, 4.648 μm]. Comparing the two intervals, we find that the second one is more than two times wider than the first one. Obviously the normal distribution is not applicable in this case. Figure 1 shows the histogram of this 10000 simulated results and it is clearly seen that the distribution is not normal. On the other hand, the interval obtained using the maximum and minimum values is the same as the one obtained from the analytical result. This example shows that using the virtual gaging system gives a better uncertainty assessment and it might be true for other cases.

Since this is a simple case, it is easy to show that when uniform distribution is assumed for phase difference ϕ the probability density of the roundness e_r can be expressed as following:

$$p(e_r) = \frac{2e_r}{\pi}[(8e_p e_s)^2 - (e_r^2 - 4e_p^2 - 4e_s^2)^2]^{-1/2} \tag{4}$$

and for the parameters given in the example, the probability density is plotted in Figure 2. Note that at the lower and upper bounds, the distribution density goes to infinity. Comparing Figure 1 and Figure 2 we find that the simulation using the virtual gaging system gives the correct distribution for roundness uncertainty.

Figure 1

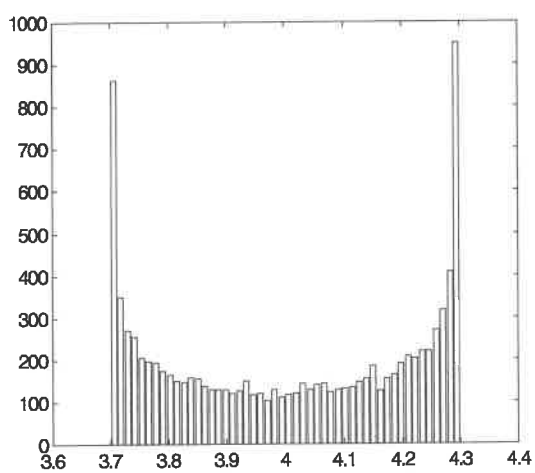

Figure 2

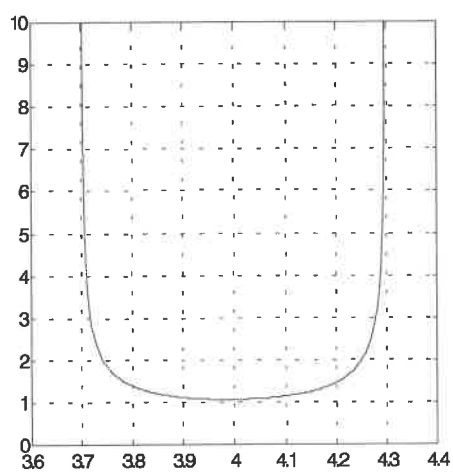

Example 2

In this example, in addition to the part form error and spindle error motion, follower straightness error is also considered. In the simulation we will assume 0.5 μm of follower straightness in a 50-mm span as shown in Figure 3. Two cases are compared; one case is with the follower straightness correction enabled and the other with the

follower straightness correction disabled. The variation of roundness measurement is still due to the random initial phase position of the part, which is assumed to have a uniform distribution within [0, 2π].

Figure 3

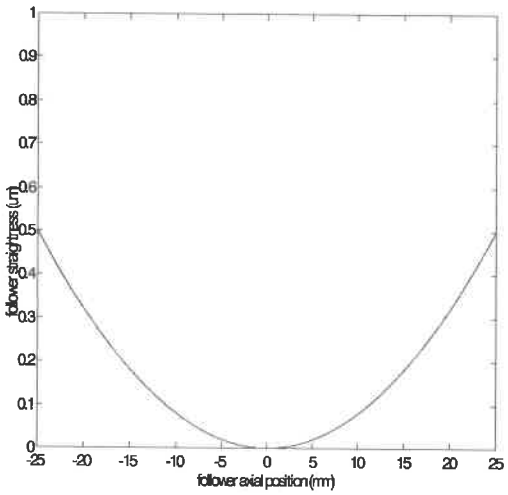

The simulation result using the virtual gaging system is summarized in Table 1. It is seen that both cases give the same range (0.6 μm) and standard deviation (0.212 μm). However, the mean, minimum and maximum values differ between the two cases. When the follower straightness correction is enabled, the interval of [3.7μm, 4.3μm] is obtained, which includes the true roundness of the part (4 μm); while the follower straightness correction is disabled, the interval then is [3.276μm,3.876μm], which does not include the true roundness of the part (4μm). This indicates that in order to accurately assess the roundness uncertainty, the known systematic effects should be corrected. This agrees with the ISO GUM. The histograms of these simulations have the similar shape as the one in Example 1; therefore, the distribution is also not normal in these cases. However, if normal distribution is assumed, the assessed uncertainty will be larger than that obtained directly from the simulation.

Table 1: Summary of Simulation Result (Unit: μm)

Case	Min	Max	Range	Mean	Std
Follower Straightness Correction Enabled	3.7	4.3	0.6	4.006	0.212
Follower Straightness Correction Disabled	3.276	3.876	0.6	3.582	0.212

Closing Remarks

Normal distribution is usually assumed to assess the uncertainty in dimensional measurement results. This assumption is quite accurate for many applications such as in diameter measurement. However, when it comes to roundness measurement, it falls apart since the roundness has no negative values. This is true for similar applications such as parallelism, perpendicularity, cylindricity, and so on. We demonstrated using virtual gaging simulation that the roundness distribution is far different from normal, and that the assumption of normal distribution would give much larger roundness uncertainty. The examples also showed that using the virtual gaging system might be able to directly give better results in uncertainty assessment. When more error sources are involved in the measurement process, it is probably easier to assess uncertainty using virtual gaging than using other means such as building an accurate mathematical model and then propagating the uncertainty according to the law of propagation of uncertainty.

References

1. Zhang , Xianping and Cole, Addison D., "Development of A Virtual Gauging System for Cylindrical Coordinate Measuring Machines", Proceedings of American Society for Precision Engineering, Vol. 18, St. Louis, MO, 1998, pp475-478.
2. American Society of Mechanical Engineers, ANSI/ASME Y14.5M-1994: "Dimensioning and Tolerancing", New York, 1994
3. International Organization for Standardization, "Guide to the Expression of Uncertainty in Measurement", Geneva, Switzerland, 1993. (corrected and reprinted 1995), This document is also available as an American National Standard: ANSI/NCSL Z540-2-1997.

Software Frameworks for Integrated Measurement Processes

Xiaoping Zhao, Robert G. Wilhelm, Osborne A. Martin, Jonathan B. Bullock
Center for Precision Metrology and Intelligent Manufacturing
University of North Carolina at Charlotte, Charlotte, NC 28213

1. Introduction

With the continuous diffusion of CAD technology into industry and increasing requirements for higher efficiency, integrated measurement processes (IMP) are becoming more and more important. High performance IMP implies reduced measurement uncertainty, dynamically configured plans for different parts, and shared measurement data among different application departments in an enterprise. A new software framework is needed to meet these requirements.

Currently, there is no complete system architecture or transport protocol defined to integrate CAD, CAM and CMM applications although several partial solutions are available from commercial vendors such as Brown & Sharpe, IMS, and Technomatix.

In this paper, we describe a project that is underway to provide software frameworks for integrating the measurement process in the automotive and aerospace industries. Several technologies that have tight relationships with this project are examined. Based on these technologies, some important aspects of the project are described. Finally, the effect of IMP on measurement uncertainty is discussed.

2. Existing Technologies to IMP

The design philosophy behind the IMP is to leverage the best features of existing technologies and standards, while at the same time, preserving the principles and semantics of measurement processes.

2.1 Web and XML

The use of the Internet, the World Wide Web and XML is a de facto requirement in new system integration projects that address application interoperability and data exchange. The reason for this is that the ubiquity and acceptance of the Internet and World Wide Web provide the furthest reaching and lowest cost integration platform in the world.

XML is a good approach for deploying structured information on the web because it marries the presentation-free content management view of SGML to the de facto language systax of the web established by HTML. XML data may exist either independently or using a separate DTD file to define its data structure. The presentation of XML data is accomplished either directly or by using an HTML file that has been transformed by an XSL file.

2.2 STEP Technologies

STEP (STandard for the Exchange of Product model data) is a set of standards (ISO 10303) for a computer-interpretable representation and exchange of product data to provide a mechanism capable of describing product data through out its life cycle while independent of any specific system. STEP consists of different parts including a description method, integrated resources, and application protocols, as well as implementation methods and abstract test suites. It can be expected that STEP will become the industrial standard for product data exchange. Seeing this

trend, many CAD/CAM systems now provide interfaces to STEP data models in order to keeping their systems in the market.

STEP defines a set of Application Protocols (AP) to represent a domain in different industrial fields. Each AP includes an application activity model (AAM), an application reference model(ARM) and an application integrated model(AIM). In practice, industrial applications may use only a subset of an AP or may combine aspects of more than one AP to create a given system. A new AP (Ap219) currently under development in the STEP group is quite useful for IMP.

AP219 will specify information requirements to manage dimensional inspection of solid parts (or assemblies) that includes administering, planning, and executing dimensional inspection as well as analyzing and archiving the results. Ap219 is a comprehensive application protocol, which may use information from other application protocols, such as AP203, AP214, AP224 and other resources.

The AP AIM is what a user employs to define product data. It is written by using the EXPRESS or EXPRESS-G languages, which provide an object-oriented information modeling language and mechanisms for specialization and generalization of entities that represents product data. A typical geometrical model represented with EXPRESS is hierarchical.

2.3 DMIS

DMIS (Dimensional Measurement Interface Standard) is a standard (ANSI/CAM-I 101-1995) created by the Consortium for Advanced Manufacturing International to enable coordinate measuring machines (CMMs) to communicate seamlessly with each other. Traditionally, each CMM manufacturer developed its own programming language and embedded it within its measuring-application software. As a result, most installed CMMs were unable to execute each other's inspection part programs. Fortunately, CMM software vendors have reacted to this situation and begun to provide interfaces for two-way communication via DMIS.

3. Divisions of IMP

IMP will need to consider the integration of many applications. Normally, incremental implementations are most successful for this kind of system integration project. In this type of approach, integration designs of limited scope are defined and implemented using a spiral development model. Each incremental step in the integration brings greater sophistication to the integration framework and touches a larger number of information sources within the enterprise.

An important aspect of this IMP is the dimensional control process flow proposed by DaimlerChrysler (see Figure 1), which summarizes the measurement issues in IMP and is the starting point for other applications department. Some important aspects of this process, applicable to the whole project are shown.

3.1 Inspection Data Exchange

Based on above discussion, one good solution could use STEP AP219 as the standard data for CAD/CAM software and DMIS as the standard data format for CMM operating software. Some mappings between AP219 and DMIS are necessary as suggested in Figure 2. Since AP219 is still at the proposal stage, the architecture of this model may be subject to changes in the future.

Since AP219 is still under development, direct data transformation from DMIS to STEP AP may also be helpful.

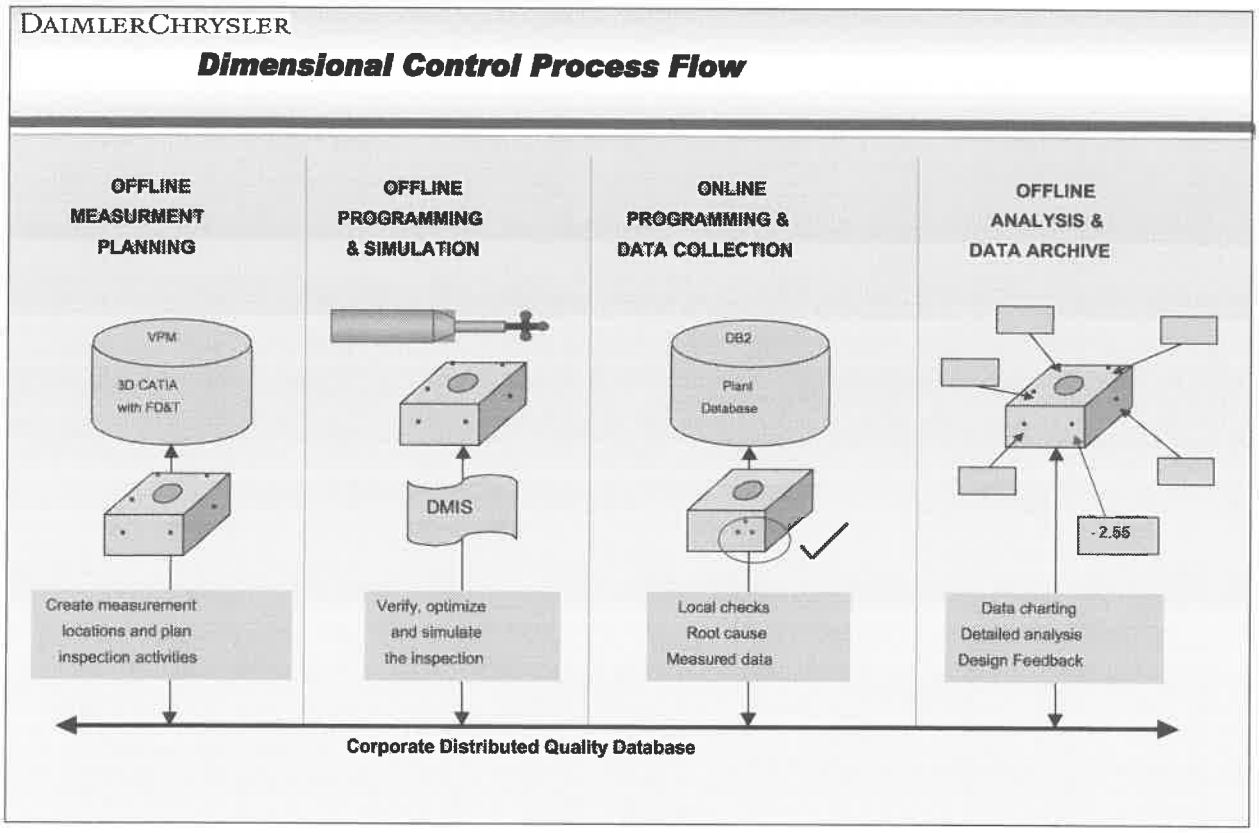

Figure 1. Typical Process Flow for Dimensional Control

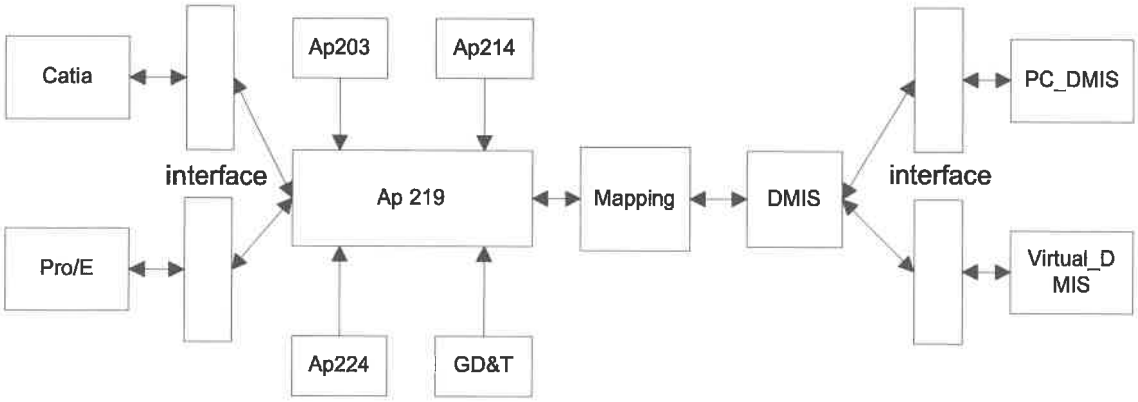

Figure 2. Adapter Model for Data Exchange

3.2 Data Representation

The AIM for each STEP AP is written in the EXPRESS language while XML/XSL/DTD is a more suitable neutral data format solution for communication among heterogeneous applications. Hence, a conversion process is needed to turn the EXPRESS schema into an XML/DTD data format. Early-binding-based conversion is a candidate solution for this issue. The resulting DTD using this method is robust and complete with respect to the product data semantics and constraints in the EXPRESS schema.

In a typical enterprise application, one or several databases may be used to store different kinds of information. The design of applications and databases must address the issue of partitioning, storing, and accessing these different data. An intuitive approach is to store the data in the lowest physical level objects (e.g. AIM entities) though this may cause a large database and make the operations inefficient. The use of some intermediate level of granularity, called Units of Functionality in object-relational database design, appears to be a better candidate solution.

3.3 Data Usage and Sharing.

This part mainly deals with types of analysis and how efficiently different application departments in an enterprise can use the measurement data. The data mentioned here not only refer to the discretely measured point data, but also the measurement program. Two main factors will be considered here. One factor is to consider algorithms to analyze the data based on functional requirements while another is to consider the overall structure of data flow and how the data flow can efficiently and correctly travel among or even outside enterprises. Some distributed component deployment technologies may be used to address this problem.

4. Measurement Uncertainty and IMP

Measurement uncertainty is a long-standing topic in coordinate metrology. Each complete measurement value must be reported with its uncertainty. There are several components contributing to measurement uncertainty that include machine components, probe components, part components and repeatability components. Among them, the measurement uncertainty caused by repeatability components can be reduced by IMP since operator influence, thermal errors, errors in recording, and analysis variations may be compensated for or eliminated by an automatic measurement process. Also, IMP may produce a more efficient measurement and reduce the negative effects caused by environment influences.

5. Conclusions

In this paper, the idea of an integrated measurement process is presented. Several current available technologies that are useful for this project are described. Important research issues in this project are discussed and some conceptual solutions and frameworks are presented. Also, the relationship between IMP and measurement uncertainty is discussed briefly.

References

[1] Robert G. Wilhelm, "Software Framework for Integrated Measurement Process", *Proposal for DaimlerChrysler Challenge Fund University Project Proposal*, September, 2000.

[2] J.Liang, J.J.Shah, etc. "Synthesis of Consolidated Data Schema for Engineering Analysis from Multiple STEP Application Protocols", *Computer-Aided Design* 31 (1999) 429-447.

[6] ISO, "Industrial Automation Systems and Integration – Product Data Representation and Exchange". *http://www.nist.gov/sc4/www/stepdocs.htm*

[7] Consortium for Advanced Manufacturing International, "Dimensional Measurement Interface Standard", *http://www.cam-i.org/standards.html*

[11] James G. Salsbury, "A Simplified Methodology for the Uncertainty Analysis of CMM Measurements", *Precision Metrology/Applying Imaging & Sensoring*, June 6-8, 1995, Indianapolis, Indiana

2D EXTENSION OF THE GAPSPACE MODEL FOR TOLERANCE ANALYSIS

Zhihua Zou & Edward Morse
Center for Precision Metrology, Department of Mechanical Engineering
The University of North Carolina at Charlotte, NC 28223, USA

Introduction

To insure interchangeable assembly and proper function of mechanical components, designers use tolerances to specify allowable limits for variations in geometric form and material properties. Effective use of tolerance analysis tools will allow the designer to balance acceptable variation in the part geometry with the requirement for production at lower cost. The GapSpace model described in the paper is an extension of the 1D model developed in [Morse 99]. Our 2-D extension bears some similarity to the Physical Constraints Faces Set method (PCFS) method from [Mullins 98] as both approaches use graph to represent the functional requirements of assembly. Because of the gap-based nature of the GapSpace model, the development of graph traversal rules and analysis methods is more direct.

The GapSpace model in 1D uses gaps to define the adjacency for a pair of opposing features, which are from different components and may potentially interfere when assembling. After identifying all gaps, an assembly graph is generated. Each assembly cycle in the graph represents a physical requirement for assembly, independently of how the components are dimensioned. The physical requirements are called Fits Conditions (FC) because they represent the necessary and sufficient conditions for the parts 'fitting' together in an assembly. Both worst case and statistical tolerance analysis can be implemented based on these FCs [Morse 99] [Zou 01].

In this paper we present the extension of these assembly cycles and Fits Conditions to assemblies of "two-dimensional" parts (i.e. prismatic parts with a constant polygonal cross-section).

The 2-D GapSpace Model

In this model, we only consider components that are polygonal, although they may be either convex or concave. This is because we use gap to describe a constant distance between two planar surfaces. We first introduce the ideas of Constraining Triangles and their relationship to the GapSpace Sine Law.

1. Constraining Triangle (CT)

If three faces in a polygonal component are constrained, the motion of the component may be restricted. We call the triangle generated by the three faces a constraining triangle, or CT. Because the constraint for each face is related to a gap between that face and the rest of the assembly, we can represent the Constraint Triangle in terms of these gaps. Equation (1) shows a validity test for a CT formed by three gaps. The directions of gaps g_1, g_2 and g_3 in Equation (1) are decided by the normals of the respective faces, pointing away from the material side of the part. The three gaps g_1, g_2 and g_3 in Figure 1 form a valid CT, called *CT_A*.

$$\sum_{i=1}^{3} a_i * \vec{g}_i = 0 \quad \text{where } a_i > 0,\ \overline{g_i} \text{ is gap associated with the face i} \tag{1}$$

$$CTL = L2\sin(a1)\sin(a3) \tag{2}$$

Each CT is associated with a value represented by the component's geometric parameters. This

value is called the constraint triangle length (CTL). The CTL of CT_A in Figure 1 is shown in Equation (2). If the normal directions for two faces are opposite, their gaps generate a 1-D constraint triangle whose CTL is the distance between the faces. A CT is represented by its associated 3 (or 2, for the opposing case) gaps.

2. *The GapSpace Sine Law*

If a component is assembled with other components, the gaps (g_1, g_2, g_3) associated with any CT are related by the expression in Equation (3), where angles a1, a2 and a3 are those shown in Figure 1. The constant is the difference between the lengths of *CT_A* and the "outside" CT. The "outside" CT is formed when we treat other components as one pseudo-component (think of this as a subassembly). These outer faces form a CT which we call the *outside_pseudo_CT.*

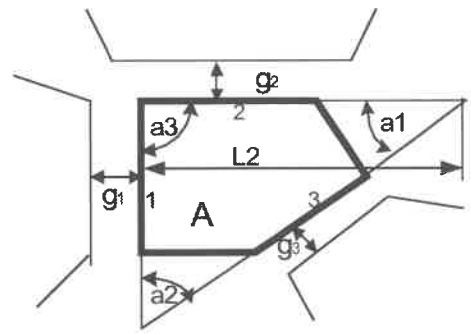

Fig 1. One part A is assembled with others

The equation (3) means that the value of left side keeps a constant wherever component A translates in any direction (no rotation) with respect to the rest of the assembly. As all coefficients are related to sine values, we call it the *GapSpace Sine Law.*

$$g_1 \sin(a1) + g_2 \sin(a2) + g_3 \sin(a3) = \textbf{\textit{constant}} = \text{CTL(outside_pseudo_CT)} - \text{CTL(CT_A)} \quad (3)$$

Combination of two components with a common gap

If CTs from different components share a common gap, the two CTs can be combined together by counting the common gap once and sum up all other gaps after making the coefficients for the common gap equivalent. In Figure 3, Part B has one CT (g_1, g_2, g_3) while C has one CT with (g_3, g_4, g_5). Using the Sine Law for both CTs as shown in Equation (4) we combine these two CTs as shown in Equation (5). The value of the left side of Equation (5) remains constant if either component B or C moves.

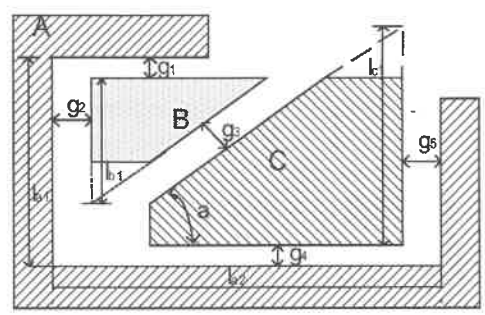

Fig 3. A real 2D assembly with 3 components

$$\begin{cases} g_1 \sin(\pi/2 - a) + g_2 \sin(a) + g_3 \sin(\pi/2) = c1 \\ g_3 \sin(\pi/2) + g_4 \sin(\pi/2 - a) + g_5 \sin(a) = c2 \end{cases} \quad (4)$$

$$g_1\cos(a) + g_2\sin(a) + g_3 + g_4\cos(a) + g_5\sin(a) = c1 + c2 \quad (5)$$

Liaison graph

The constraint triangle is used to describe the constraints on the dimensions of individual component. As we showed above, the constraint of two components with a common gap is also possible. The next step is to find a way to combine the constants for all components in an assembly. An assembly graph is used to capture the assembly relationships, and a method for inducing assembly-level constraints is presented.

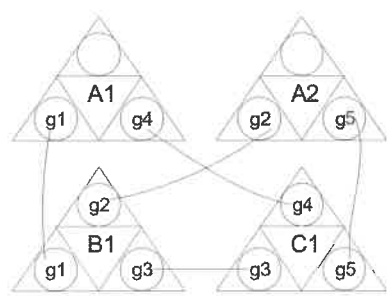

Fig 4. Assembly graph of Fig 3

In an assembly graph, each CT for a component will be one **node** of the assembly graph. Each node has 2 or 3 **ports** that reflect the gaps related to the CT. Any two ports belonging to different CTs in different components should be connected by an arc if they include the same gap. There is no arc between CTs from the same component. Each arc is associated with a single gap, but a gap may map many arcs in the graph. The assembly in Figure 3 has the assembly graph shown in Figure 4, where the CTs A1 and A2 are from Part A, B1 is from Part B, and C1 is from Part C. The CTs are connected by arcs representing the gaps in the assembly.

Fits Conditions (FCs)

After the assembly graph is constructed, the next step is to search the graph to find a constant expression (or expressions) for the assembly, called the Fits Condition (FC). A Fits Condition is a subgraph of the assembly graph with some restrictions. The sub-graph should satisfy the following conditions to be a FC:

1. The sub-graph is comprised of one or more assembly cycles (explained below).
2. If one port in any node is included in the sub-graph, any other ports in the node should be included in an assembly cycle that is included in the sub-graph.
3. The sub-graph can't be divided into more sub-graphs that satisfy conditions 1 and 2.

The third condition above is to prevent the search of the assembly graph from finding redundant FCs. The basic element in a FC, the assembly cycle, is a general cycle in the graph theory plus these constraints:

1. The assembly cycle must enter from one port of a node, exit from another port of the node
2. The assembly cycle can pass through at most one node in the same component.

If we follow the definitions for FCs and assembly cycles, we are able to find that the assembly graph in Figure 4 has just one Fits Condition, and 2 assembly cycles are included in this Fits Condition.

The properties of FCs

While a Fits Condition is comprised of assembly cycles, it is also comprised of Constraint Triangles that include gaps. A FC may be represented by the weighted sum of the included gaps if we repeatedly perform the combination of CTs as shown in Equations (4) and (5). The combination can be aborted when we've reduced the problem to two (possibly pseudo-) components, because these components or sub-assemblies will share common gaps. For example, in the Equation (5), after the CTs in B and C are combined, it is not necessary to combine the CTs from part A. The Equation (5) is already an FC after the CTs in parts B and C have been combined.

Some important properties of FCs follow:

1. An FC can be represented by weighted sum of included gaps. The value of FC is independent of the relative positions of components in the assembly.
2. If and only if all FCs for an assembly are non-negative, the components can be assembled without interference. Fits Conditions are so named because they guarantee fitting among components when the value is nonnegative.
3. The value of a FC is represented by the geometric parameters of related Constraint Triangles inside. Every Constraint Triangle has a contribution coefficient (CC) for the FC, representing the weight of

its Constraint Triangle Length in the FC.

Analysis Example

For the assembly in Figure 4, the only FC is shown in Equation (5). The expression of this FC in terms of the components' geometric parameters (dimensions) is shown in Equation (6). The contribution coefficients and CT Lengths are listed in Table 1 for all CTs.

Table 1. CCs and CTLs

CT	Contribution Coefficients	CT Length
A1	cos(a)	l_{a1}
A2	sin(a)	l_{a2}
B1	-1	$l_{b1}\sin(a)$
C1	-1	$l_{c1}\cos(a)$

$$FC = \cos(a)l_{a1} + \sin(a)l_{a2} - \cos(a)l_{b1} - \cos(a)l_{c1} \qquad (6)$$

Some basic tolerance analysis questions are listed below. The answers may be found easily, given that we've already developed Equations (5) and (6).

Table 2: The questions that are answered by the 2D GapSpace model

Question	Answer
Is there interference in the assembly?	Only if an FC has a negative value.
What is the maximal value of a gap?	The minimum of the FCs divided by its coefficient if the FCs contain the gap
What is the relative sensitivity of each gap with respect to part dimensions?	Expressed as a ratio of the coefficients of the gap.

Conclusions

We have presented the GapSpace modeling technique in 2-D, which is a direct extension of 1-D GapSpace. The representation of an assembly in 2 dimensions using an assembly graph is shown. One or more FCs are found for the assembly graph. These FCs are represented by the weighted sum of the gaps, where the weights are determined using the *GapSpace Sine Law*. Each FC can also be represented by the components' dimensions. The tolerance analysis is easy to execute after both representations of FCs are available. The algorithms to search FCs and combination of two CTs have already been implemented using C++ programming by the authors. The limitations of the model described in the paper are that the components must be polygons and no rotation is considered. We are extending the method to more complicated components and have begun work to apply it to 3 dimensional assembly.

References:

[Morse 99] Morse, E. P.; "Models, Representations, and Analyses of Toleranced one-dimensional Assemblies", Ph.D. Thesis, Sibley School of Mechanical and Aerospace Engineering, Cornell University, Ithaca, NY, 1999.

[Mullins 98] Mullins, S. H.; Anderson, D. C.; "Automatic identification of geometric constraints in mechanical assemblies", *Computer-Aided Design*, vol. 30, no. 9, pp715-726, August, 1998.

[Zou 01] Zou, Z. H.; Morse, E. P.; "Statistical Tolerance Analysis Using GapSpace", 7th CIRP Seminar, ENS de Cachan, pp 313-322, France, April, 2001.

GEOMETRIC QUALITY ANALYSIS AND PROCESS CONTROL FOR ULTRA-PRECISION LASER MICROMACHINING

Evgueni V. Bordatchev and Suwas K. Nikumb
Integrated Manufacturing Technologies Institute, National Research Council of Canada
800 Collip Circle, London, Ontario, Canada N6G 4X8

1. INTRODUCTION

For ultra-precision laser micromachining, the need to control the process is very high because the operator has to make a host of complex decisions, based on trial-and-error methods, to set process control parameters related to the laser, workpiece material, and motion system. In addition, factors such as power fluctuations, intensity distribution, and thermal effects, not controlled by the operator, also influence the machining process. Further, the problem of choosing the optimal process parameters becomes more complicated when parts and features dimensions become smaller (less than a few tens of microns), and the thermodynamic processes within machining zone could significantly change the part geometry. To produce parts with nano/micro-scale geometric quality, using laser micro-processing technologies, a thorough understanding of the machining process and control of the entire system performance is essential. This paper describes a method for geometric quality analysis and process control aimed at improving the accuracy, precision, and surface finish of laser machined micro parts with dimensions less than 100 μm using simulation of surface profile and analysis of the machining system performance.

2. DETERMINISTIC AND STOCHASTIC CONCEPT OF LASER MICROMACHINING

During the laser machining process, laser pulses are applied according to a prescribed toolpath for material removal. Each laser pulse removes a certain amount of material. The geometry and the volume of the material removed depend on the material and laser pulse characteristics. Therefore, it is important to model and control the effect of each individual laser pulse in order to control the accuracy and precision. The deterministic concept of laser micromachining modelling, shown in Figure 1a, assumes that all machining parameters such as the pulse energy, E, the frequency of laser pulses, f, the focal spot diameter, d, and the travel speed, v, are constant. Therefore, the geometric parameters, d, v, and volume of the crater, and 2D and 3D geometry of the spot overlaps, S^{2D}, S^{3D}, are constant. The final surface profile of the machined part is a deterministic combination of n craters and is defined as

$$\mathrm{P}(x,y,z)=\sum_{i=1\ldots n}\mathrm{P}_i\left(x_i^c,y_i^c,z_i^c,h_i,d_i\right) \tag{1}$$

where x,y,z are the surface profile coordinates; x_i^c,y_i^c,z_i^c are the crater center coordinates. 2D/3D spot overlap is a percentage of overlapped area/volume between two consecutive craters.

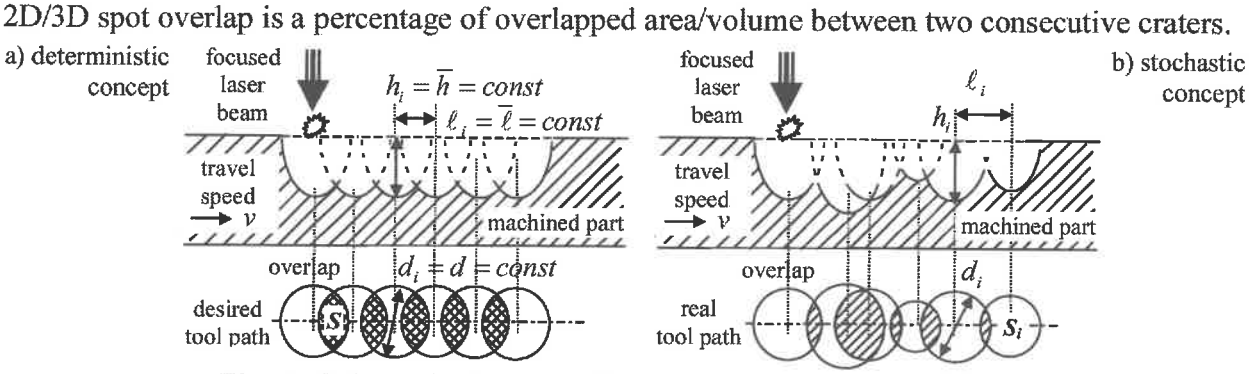

Fig. 1. Schematic diagram of laser micromachining modelling.

Experimental results [1] indicate that all process parameters of laser micromachining are non-deterministic. They are stochastic with certain mean value and variance. Based on these facts, the stochastic concept of laser micromachining modelling is shown in Figure 1b. The proposed concept is based on a realistic assumption that the variations within process parameters such as pulse energy and travel speed cause variations in each crater's geometry. Therefore, variations within the travel speed, $\tilde{v}$, are a source of variation of 2D spot overlap, $\tilde{S}^{2D}$, even if energy is constant. If energy varies then the crater geometry and 3D spot overlap also have random components, e.g. $\tilde{d}$, $\tilde{h}$, and $\tilde{S}^{3D}$. Likewise, the final geometry of the machined part is modeled as a linear combination of deterministic, $\overline{\mathrm{P}}(x,y,z)$, and stochastic, $\tilde{\mathrm{P}}(x,y,z)$, components:

$$\mathrm{P}(x,y,z)=\sum_{i=1\ldots n}\mathrm{P}_i\left(x_i^c,y_i^c,z_i^c,h_i,d_i\right)=\overline{\mathrm{P}}(x,y,z)+\tilde{\mathrm{P}}(x,y,z) \tag{3}$$

Deterministic component is the ideal (desired) geometry of the machined part, and can be derived from the deterministic modelling of laser micromachining. On the contrary, the stochastic component represents a difference between ideal and actual (machined) geometry. Alternatively speaking, it is the 2D/3D inaccuracy of laser machining.

3. GEOMETRIC QUALITY ANALYSIS AND PROCESS CONTROL

In order to analyze the final geometric quality and to implement proper control actions, a comparison of ideal, $\overline{\mathrm{P}}(x,y,z)$, semi-actual, $\hat{\mathrm{P}}(x,y,z)$, and actual, $\mathrm{P}(x,y,z)$, geometries of the machined part is performed. The ideal geometry is developed from the conformance of the laser beam focal spot into the workpiece surface in accordance with the desired toolpath trajectory, to serve as a reference point for the geometric quality analysis. The ideal geometry is calculated as

$$\overline{\mathrm{P}}(x,y,z)=\sum_{i=1\ldots n}\mathrm{P}_i\left(\overline{x}_i^c,\overline{y}_i^c,\overline{z}_i^c,\overline{h},\overline{d}\right) \tag{4}$$

The semi-actual geometry, $\hat{\mathrm{P}}(x,y,z)$, is a result of a simulation, which utilizes the parameters of the actual dynamic performance of the laser machining system, e.g. actual variations within travel speed and the statistical results from the machinability study. Therefore, it is necessary to complete the two steps before simulation. The first step consists of the analysis of variations within workpiece translation movement, by measurement of the non-uniformity of travel speed to obtain $v=\overline{v}+\tilde{v}$ and $S^{2D}=\overline{S}^{2D}+\tilde{S}^{2D}$. The second step is the statistical machinability study in order to obtain $d=\overline{d}+\tilde{d}$ and $h=\overline{h}+\tilde{h}$ as a function of E. Experimental results show that each of these parameters randomly fluctuates around the mean value for certain pulse energy and for a particular material. Afterwards, the semi-actual geometry is calculated as

$$\hat{\mathrm{P}}(x,y,z)=\sum_{i=1\ldots n}\mathrm{P}_i\left(x_i^c,y_i^c,z_i^c,\overline{h}+\tilde{h}_i,\overline{d}+\tilde{d}_i\right) \tag{8}$$

The actual geometry, $\mathrm{P}(x,y,z)$, is obtained by measuring the machined part. Each surface profile has a unique data structure in the form of a polygon register that allows geometric quality parameter calculations with minimal loss of geometric information. Figure 2 shows the structure of the geometric quality analysis and process control. In order to produce a machined part at ultra-high accuracy, the appropriate correction of the toolpath trajectory and pulse energy must be implemented based on the analysis of the difference between ideal and actual geometry.

To verify the performance, a micro-pyramid (height of 28.0 μm, base area of 53x53 μm, slope of faces of 46.04°, peripheral area of 70x70 μm) was machined with a pulse energy of 16 μJ by

removing nine layers of material. To improve the accuracy of micro-pyramid, appropriate correction of the toolpath trajectory and pulse energy was applied. Figure 3 shows the ideal, actual non-corrected and corrected geometries, and profiles correspondingly in the X-X and Y-Y direction of the micro-pyramid. Table 1 contains the comprehensive analysis of these geometries. It can be seen that the machining depth is a more complex parameter to control and needs combined correction of toolpath and pulse energy simultaneously. Dimensional geometry (base and peripheral areas) is more accurate and consistent and can be adjusted by using the correction of toolpath trajectory only. Therefore, our control actions were primarily concentrated on achieving the desired height. As a result, an error in height was reduced from 10.65 μm to 2.4 μm. Also, the accuracy of peripheral area was improved from 71.25 +/- 0.55 μm to 70.2 +/- 0.6 μm. Accordingly, the slopes of pyramid faces were improved from 55.7° to 49.1°. The remaining inaccuracy is attributed to the agglomeration of burrs and heat-affected zone as a result of instabilities within laser-material interaction and pulse energy.

4. SUMMARY AND CONCLUSIONS

A method for geometric quality analysis and process control has been presented. The method improves the accuracy and precision of laser machined parts with microscale dimensions (< 100 μm). Deterministic and stochastic concepts of laser micromachining have been introduced for simulation of ideal and semi-actual geometries of a machined part. The geometric quality analysis is based on a comparison of ideal, semi-actual and actual geometries. The process control utilizes the results of geometric quality analysis and provides appropriate correction of toolpath trajectory. Experimental results confirm the usefulness and reliability of this method.

REFERENCES

1. E.V. Bordatchev and S.K. Nikumb, 2001, Improving Geometric Quality Of Laser Micromachined Parts Using High-Precision Motion System Dynamic Performance Analysis, Proc. of the 3rd World Manufacturing Congress'2001, Sept. 24-27, Rochester, NY, USA.

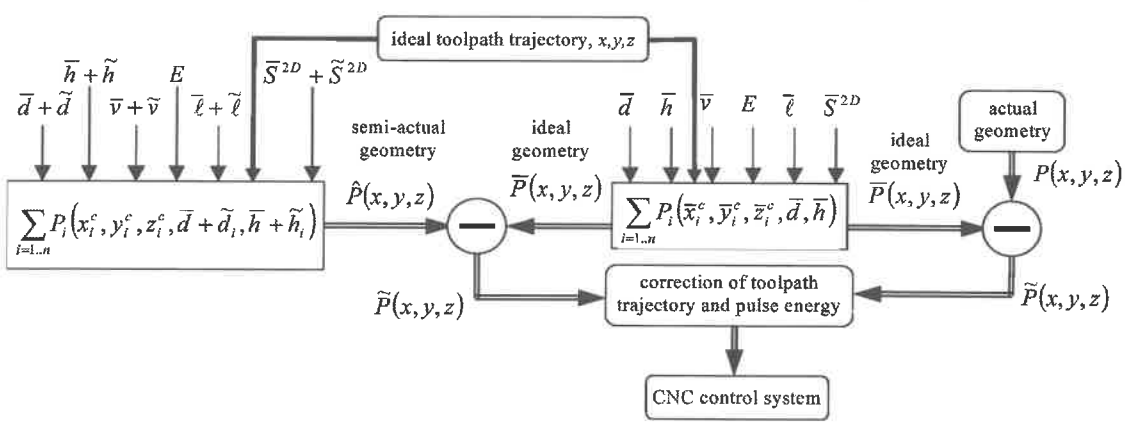

Fig. 2. Schematic diagram of geometric quality analysis and process control.

Parameters of geometry — Table 1

	height, μm		base area, μm		peripheral area, μm		slope, degree	
	X-profile	Y-profile	X-profile	Y-profile	X-profile	Y-profile	X-profile	Y-profile
ideal	28.0		53.0		70.0		46.04	
non-corrected	38.1	39.2	52.1	53.2	72.8	71.7	55.64	55.84
corrected	30.2	30.6	53.2	52.3	70.8	69.6	48.63	49.48

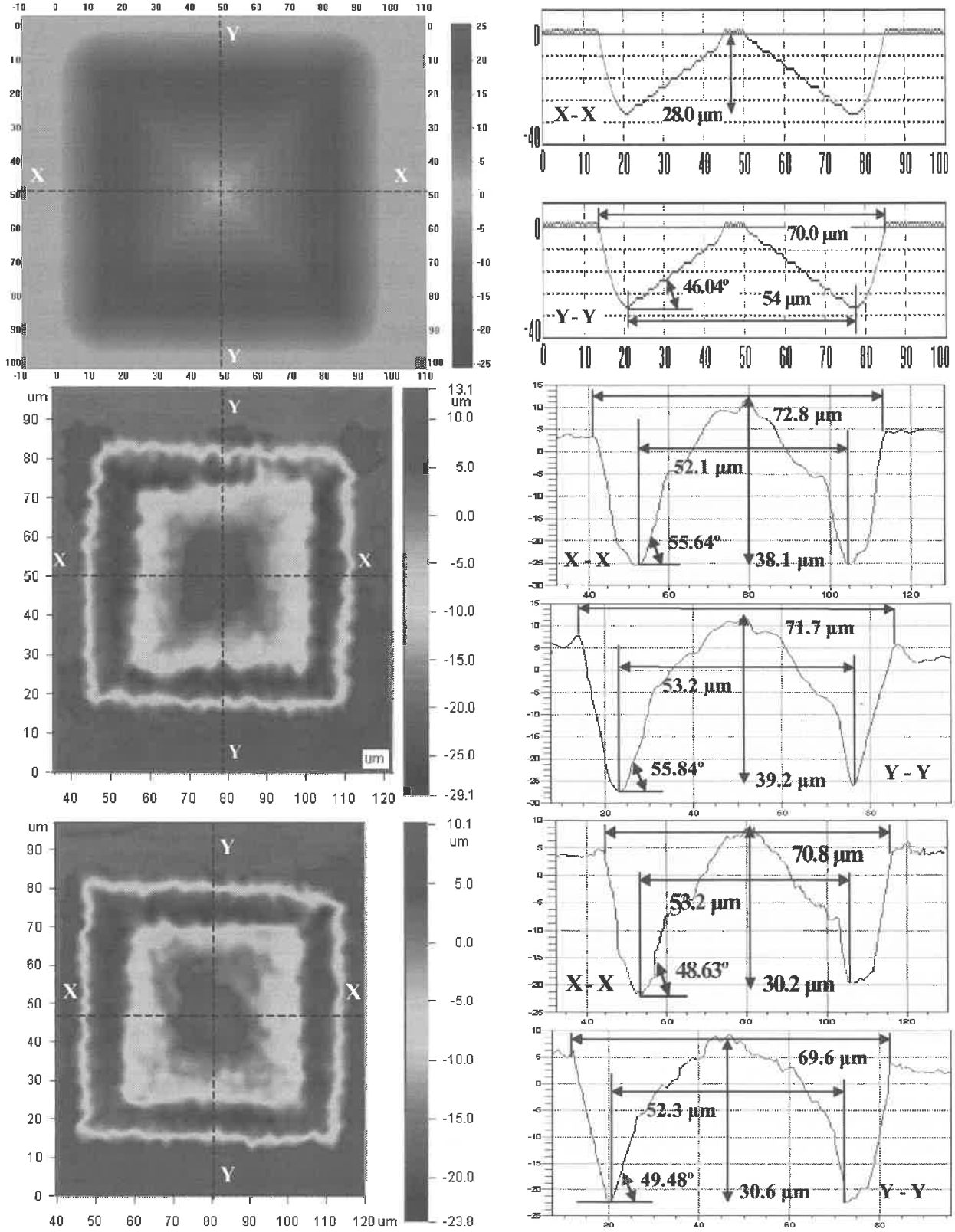

Figure 3. Ideal, actual non-corrected and corrected geometries and profiles of the micro-pyramid.

IN-SITU SELF-CALIBRATION OF TWO-DIMENSIONAL ANGLE PROBE FOR PROFILE MEASUREMENT OF LARGE SILICON WAFERS

Wei Gao*, Tomohiko Yamada*, Satoshi Kiyono* and Peisen S. Huang**
* Dept. of Mechatronics & Precision Engineering, Tohoku University, Sendai, JAPAN
** Dept. of Mechanical Engineering, SUNY at Stony Brook, New York, USA

1. Introduction

Flatness metrology of silicon wafer substrates is an essential process for semiconductor manufacturing [1]. The undergoing transition from 200 mm diameter wafers to 300 mm diameter wafers has being brought about a great challenge to the flatness measuring technology. Comparing with interferometer-based systems, the scanning probe systems are much easier to be advanced to measure large wafers through expanding the travel of the scanning stage.

The authors are developing a scanning angle probe system for flatness metrology of large silicon wafers [2-4]. The proposed system employs two two-dimensional (2D) angle probes, which detect the 2D local slopes (X- and Y-directional local slopes) at two points on the wafer surface. In this angle-based measuring system, the translational error motions of the probe carriage (straightness error motions) and the wafer spindle (axial error motion) will not appear in the probe outputs. Based on the concept of error separation [5], the 2D local slopes of the wafer surface can be separated from the angular error motions of the probe carriage (pitch, roll) and the wafer spindle (angular error motion) using the 2D outputs of the angle probes [4]. The cross-sectional height profiles of the wafer surface along radial directions can be obtained through integrating the X-directional local slopes of the wafer surface, and the cross-sectional height profiles along concentric circles can be obtained through integrating the Y-directional local slopes. The height profile of the entire wafer surface can thus be evaluated from combining the sectional profiles in these two directions.

To realize the 2D angle-based scanning probe method with nanometer accuracy, highly sensitive and accurate 2D angle probes are necessary. The authors have successfully developed a compact and sensitive 2D angle probe [2,4]. In this paper, we apply an in-situ self-calibration method [6] to the calibration of the 2D angle probe when the angle probe and the wafer are mounted in the scanning system.

2. Principle of the in-situ self-calibration

Figure 1 shows the 2D angle-based scanning probe system. For the sake of clarity, only one of the two angle probes is shown in the figure. The angle probe is mounted on a linear X-carriage, and the wafer is mounted on a wafer spindle.

Assume that the X- and Y-directional calibration curves of the 2D angle probe are described by functions $A_X(v_X)$ and $A_Y(v_Y)$, in which v_X and v_Y are outputs of the angle probe. Figure 2 shows an example of the calibration curves. In Fig. 2, the vertical axis represents the detected angle τ_X (the angle around Y-axis) (or τ_Y: the angle around X-axis), and the horizontal axis represents the corresponding probe output v_X (or v_Y). When use an angle probe, it is necessary to evaluate the detected angle τ_X (or τ_Y) from the probe output v_X (or v_Y) based on the function $A_X(v_X)$ (or $A_Y(v_Y)$). To obtain the function $A_X(v_X)$ ($A_Y(v_Y)$) is the objective of the calibration.

Here, we propose an in-situ self-calibration method that can realize the calibration in the wafer measuring system shown in Fig.1, where the angle probe is moved by the X-carriage to scan the wafer surface while the wafer is being rotated by the spindle. Differing from a conventional calibration process, in which the angle τ_X (or τ_Y) in Fig. 2 needs to be measured by

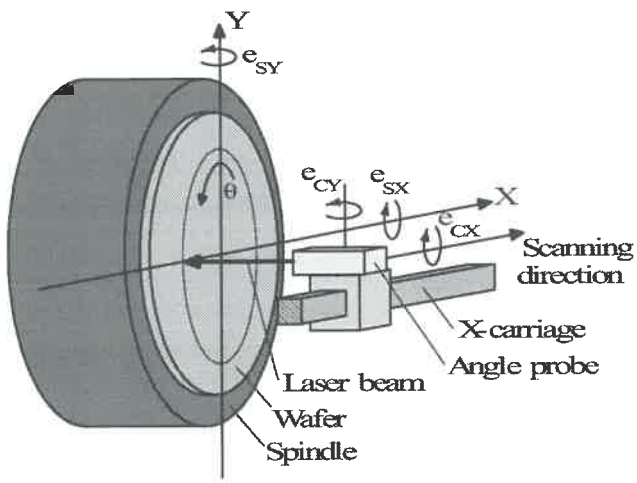

Figure 1 The scanning angle probe system

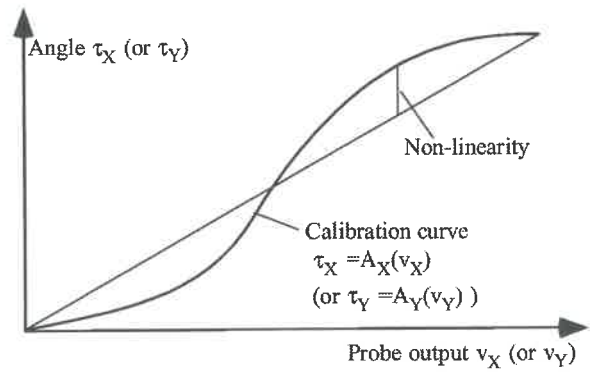

Figure 2 An example of the calibration curve

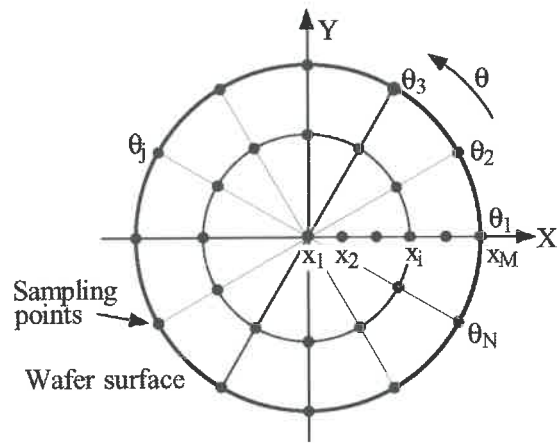

Figure 3 Sampling positions on the wafer surface

an accurate reference angle sensor, the proposed calibration technique utilizes the profile measurement data of a wafer surface.

Assume that the scanning in X-direction starts from the center of the wafer and the sampling positions are numbered as x_i (i=1, 2, ..., M) as shown in Fig. 3. At each position x_i, the 2D angle slopes of the wafer surface at points along a circle are sampled by the angle probe. If the sampling positions along the circle are numbered as θ_j (j=1, 2, ..., N), the following equations can be obtained.

$$A_X(v_X(x_i,\theta_j)) = f'_X(x_i,\theta_j) + e_{CY}(x_i) + e_{SY}(x_i,\theta_j) \quad (1)$$

$$A_Y(v_Y(x_i,\theta_j)) = f'_Y(x_i,\theta_j) + e_{CX}(x_i) + e_{SX}(x_i,\theta_j) \quad i=1,2,\ldots, M, j=1,2, \ldots N \quad (2)$$

where $v_X(x_i,\theta_j)$ and $v_Y(x_i,\theta_j)$ are the X- and Y-directional outputs of the angle probe at sampling position (x_i,θ_j), respectively. $A_X(v_X(x_i,\theta_j))$ and $A_Y(v_Y(x_i,\theta_j))$ are the corresponding X- and Y-directional angles detected by the angle probe. $e_{CX}(x_i)$ and $e_{CY}(x_i)$ are the roll error and yaw error of the X-carriage, respectively. $e_{SX}(x_i,\theta_j)$ and $e_{SY}(x_i,\theta_j)$ are the angular motion components of the wafer spindle around X- and Y-axes. $f'_X(x,\theta)$ and $f'_Y(x,\theta)$ are the X- and Y-directional local slopes of the wafer surface, which are defined as:

$$f'_X(x,\theta) = \partial f(x,\theta)/\partial x, \quad f'_Y(x,\theta) = \partial f(x,\theta)/\partial y \quad (3)$$

After the first scanning, we tilt the wafer or the probe by a small angle $\Delta\phi$ around the Y-axis, and then perform the second scanning to get the following equations.

$$A_X(v_{X+}(x_i,\theta_j)) = f'_X(x_i,\theta_j) + e_{CY}(x_i) + e_{SY}(x_i,\theta_j) + \Delta\phi\cos\theta_j \quad (4)$$

$$A_Y(v_{Y+}(x_i,\theta_j)) = f'_Y(x_i,\theta_j) + e_{CX}(x_i) + e_{SX}(x_i,\theta_j) + \Delta\phi\sin\theta_j \quad (5)$$

$$i=1,2,\ldots, M, j=1,2, \ldots N$$

where $v_{X+}(x_i,\theta_j)$ and $v_{Y+}(x_i,\theta_j)$ are the X- and Y-directional outputs of the angle probe at sampling position (x_i,θ_j) in the second scanning, respectively. $A_X(v_{X+}(x_i,\theta_j))$ and $A_Y(v_{Y+}(x_i,\theta_j))$ are the corresponding X- and Y-directional angles detected by the angle probe.

The data shown in Eqs. (1) and (4) are used to evaluate the calibration function $A_X(v_X)$ of the X-directional output of the angle probe. Taking the difference of Eqs. (4) and (1) gives :

$$A_X(v_{X+}(x_i,\theta_j)) - A_X(v_X(x_i,\theta_j)) = \Delta\phi\cos\theta_j \qquad (6)$$

where the terms of surface slopes and motion errors are removed.

In most cases, for a fixed θ_j, the raw data of the voltage output $v_X(x_i,\theta_j)$ and $v_{X+}(x_i,\theta_j)$ with respect to the sampling position x_i will have a relationship shown in Fig. 4(a), which do not progressively increase or decrease with respect to x_i. As shown in Fig. 4(b), before conducting the calculation of the calibration function, we rearrange the data as $v_X(m,\theta_j)$ and $v_{X+}(m,\theta_j)$ (m=0, 1, ..., M) so that the data progressively increase or decrease with respect to the new X-data number m (the case of increase is taken as an example in the figure).

For a fixed θ_j (θ_j is not equal to 90 and 270 degrees), an approximate derivative of $A_X(v_X(m))$ can be obtained from:

$$A'_X(v_X(m)) \approx \frac{A_X(v_{X+}(m,\theta_j)) - A_X(v_X(m,\theta_j))}{v_{X+}(m,\theta_j) - v_X(m,\theta_j)} = \frac{\Delta\phi\cos\theta_j}{v_{X+}(m,\theta_j) - v_X(m,\theta_j)} \qquad (7)$$

$$m=1,2,\ldots, M$$

As shown in Fig. 4(c), the calibration function of the X-directional output $A_X(v_X)$ can thus be obtained through integration of $A'_X(v_X)$ with respect to $v_X(m)$ as:

$$A_X(v_X(m)) = \sum_{w=1}^{m} A'_X(v_X(w))(v_X(w+1,\theta_j) - v_X(w,\theta_j)) \qquad m=1,2,\ldots, M-1 \quad (8)$$

On the other hand, the calibration function of the Y-directional output $A_Y(v_Y)$ can be obtained through using the data of Eqs. (2) and (5), in which x_i is fixed:

$$A_Y(v_Y(n)) = \sum_{u=1}^{n} A'_Y(v_Y(u))(v_Y(x_i,u+1) - v_Y(x_i,u)) \quad n=1,2,\ldots, N-1 \qquad (9)$$

where the probe output data are rearranged to progressively increase or decrease with respect to the new θ-data number n, and

$$A'_Y(v_Y(n)) \approx \frac{A_Y(v_{Y+}(x_i,n)) - A_Y(v_Y(x_i,n))}{v_{Y+}(x_i,n) - v_Y(x_i,n)} = \frac{\Delta\phi\sin\theta_n}{v_{Y+}(x_i,n) - v_Y(x_i,n)}$$

$$n=1,2,\ldots, N \qquad (10)$$

As can be seen from above, the calibration result in each sensitive direction of the angle probe can be obtained from two sets of angle probe outputs of sampling the wafer surface before and after a small tilt of the wafer (or the angle probe) without the influence of the wafer surface slopes and the error motions of the X-carriage and the spindle.

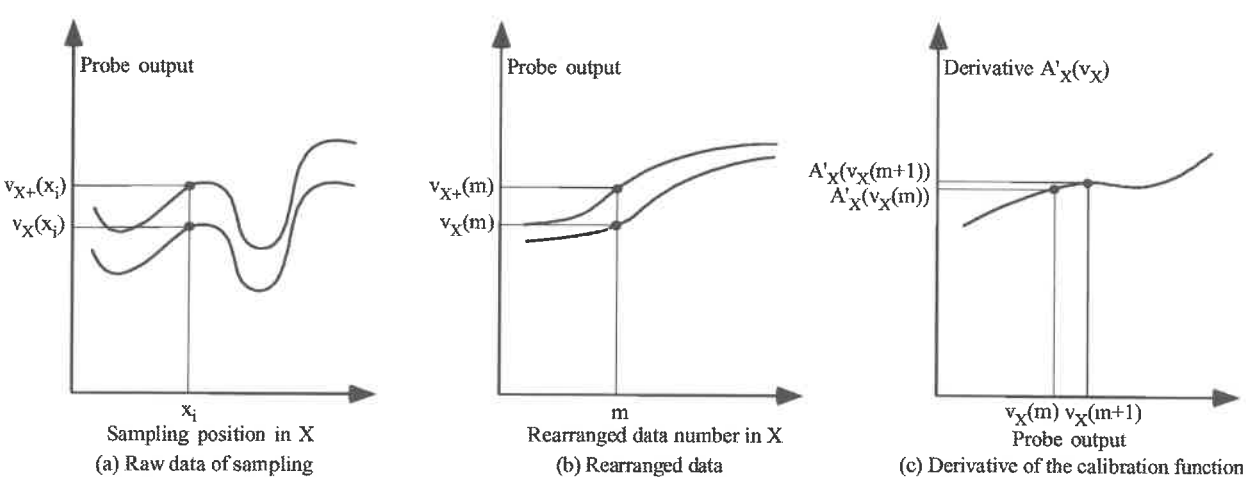

Figure 4 Data processing procedure of calibrating the X-directional output of the angle probe

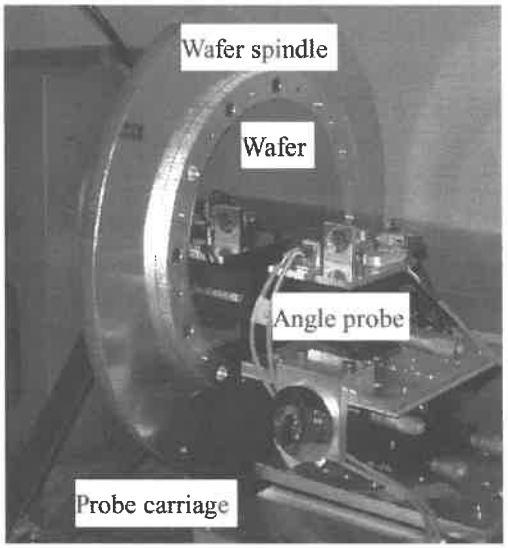

Figure 5 Experimental system

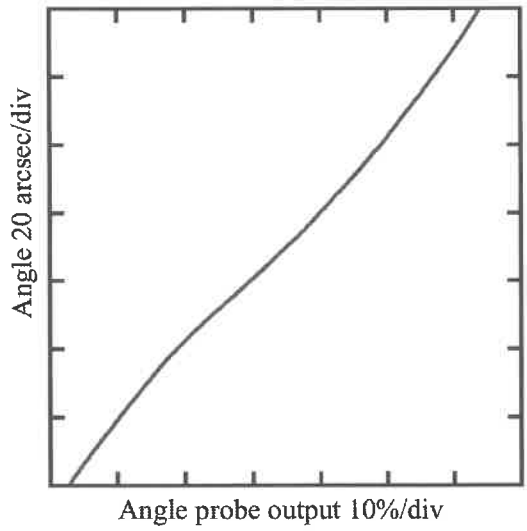

Figure 6 An X-directional calibration result

3. Experiments

Figure 5 shows a photograph of the experimental system. The wafer was mounted vertically on an air-spindle. A stepping motor-driven stage was used as the X-carriage. A 200 mm diameter wafer was used as the specimen. In the experiments, the tilt $\Delta\phi$, which is necessary for the calibration, was applied to the angle probe. The tilt was measured by a Nikon autocollimator.

Figure 6 shows one of the in-situ self-calibration results. The result of the X-directional output was shown in the figure. The vertical axis shows the detected angle in arc-second, and the horizontal axis shows the probe output in percentage. The non-linearity was approximately 10 arc-seconds in a calibration range of 140 arc-seconds.

4. Conclusions

An in-situ self-calibration technique has been proposed to calibrate a 2D angle probe developed for flatness metrology of large silicon wafers. The two-dimensional outputs of the angle probe can be calibrated from two repeated sampling of the wafer surface before and after a small tilt of wafer or the angle probe. The only condition for the calibration is the repeatability of the scanning motion, and this is not an issue for the air-bearing based probe carriage and wafer spindle.

Acknowledgements

This project is conducted under a JSPS Grant-in-Aid for Scientific Research (No.12555032) and a grant from the Mazda Science Foundation. It is also supported by a NSF/JSPS Joint Research Grant.

References:

[1] International SEMATECH: International Technique Roadmap for Semiconductors.

[2] W. Gao, E. T. Kanai, P. S. Huang and S. Kiyono: Development of 2D angle probe for flatness metrology of large silicon wafer, Proc. of ASPE 15th, Scottsdale, (2000), 35-38.

[3] W. Gao, P. S. Huang, T. Yamada and S. Kiyono: Flatness metrology of large silicon wafer using an absolute error separation method, Proc. of 2nd euspen Conf., Torino, (2001), 430-433.

[4] W. Gao, T. Yamada, S. Kiyono and P. S. Huang: Profile measurement of silicon wafer by laser autocollimation, to appear in Proc. of ISMTII' 2001, Cairo, (2001).

[5] C. J. Evans, R. J. Hocken and W. T. Estler, Self-calibration: Reversal, Redundancy, Error Separation, and 'Absolute Testing', Annals of the CIRP 45-2, (1996), 617-634.

[6] S. Kiyono, W. Gao, S. Zhang and Toru Aramaki: Self-calibration of a scanning white light interference microscope, Optical Engineering, 39 (2000), 2720-2725.

SYSTEMATIC FORM ERROR ESTIMATION FOR CIRCULAR PARTS USING FOURIER COMPONENTS

Mesay T. Desta, Hsi-Yung (Steve) Feng
Department of Mechanical and Materials Engineering
The University of Western Ontario, London, Ontario, Canada N6A 5B9

Abstract: This paper presents a new approach to characterize the systematic form error in manufactured parts with circular features. A mathematical model using a combination of Fourier components is formulated to capture the unknown and significant systematic form error present in discrete coordinate measurement data collected from the manufactured surfaces. An objective measure, based on principles of statistical hypothesis testing, is established to identify the Fourier components to be included in this mathematical model. The effect of random form error on the accuracy of the estimation of systematic form error parameters is thoroughly investigated using simulated data.

Keywords: Systematic form error; Coordinate metrology; Fourier components

Introduction

It is widely recognized that the actual form of manufactured features deviates from the ideal form specified in the CAD model. With existing manufacturing facilities, geometric errors are inevitable no matter how small they are. Therefore, a reliable inspection system is essential to evaluate the geometric errors precisely and then generate the necessary meaningful feedback information to improve faulty production processes and make accurate conformance decision against the required tight tolerances. A typical inspection system involves a device to take discrete coordinate measurement data as well as error analysis software to construct the geometry defined by these data points and compare with the design specifications to find out any discrepancy that may exist. To this end, the geometry constructed from the discrete data points has a significant influence in the correct identification of the geometric errors.

Most existing form error estimation methods are based on fitting an ideal substitute feature to the measured data points with an implicit assumption that manufacturing form error is totally random [1]. However, such assumption is impractical in most manufacturing cases, and very often leads to significant variation of inspection results [2,3]. For example, results obtained using various sampling distribution strategies are not identical, or different estimation techniques produce different results. This is basically because the correlation between errors in neighboring locations is not recognized and considered. Therefore, it is imperative to construct the surface profile that considers this correlation in order to reduce inspection uncertainty substantially. This requires characterizing the systematic form error due to reproducible imperfect production processes. However, it should be noted that manufacturing processes fundamentally consist of random error sources besides the reproducible ones [3]. Therefore, in parallel with characterizing the systematic form error, it is necessary to express the uncertainty due to unexplainable (random) form error.

This paper presents a new and systematic approach to characterize the systematic form error in manufactured parts with circular features and investigate the influence of the random form error component in the estimation of systematic form error parameters.

Systematic form error representation

Since it is difficult to predict and consider all types of manufacturing errors in advance, a robust mathematical model is required to capture the unknown form error from the measurement data. In this work, a combination of Fourier components is selected to represent radially fluctuating systematic from error. Using the polar coordinate system, the deterministic profile, $\boldsymbol{R}(\theta)$, is expressed as

$$\boldsymbol{R}(\theta) = R + dR + SFC \tag{1}$$

where R and dR represent, respectively, the design radius and change in radius of the nominal circle during manufacturing. A sum of dR and the SFC term give the resultant systematic form error. SFC denotes fluctuations in the radial direction and is given by:

$$SFC = \sum_{i=1}^{M} a_i FC(m_i \theta) \tag{2}$$

where M designates the number of significant Fourier components that are necessary to approximate the radial fluctuation errors. FC stands for either a sine or a cosine term. a_i and m_i represent the coefficient magnitude and spatial frequency of the corresponding Fourier component, respectively.

Model determination

The deterministic profile model can be estimated by fitting the mathematical model given in Eq. (1) to the measurement discrete data points. However, the exact mathematical form of the model must be known before fitting proceeds; i.e. a specific and appropriate combination of Fourier components to be included in the model must be identified in advance. Such information is not available and also very difficult to determine. Therefore, the main focus of this research work is to develop a systematic approach that can identify the right combination of Fourier components to efficiently represent the fluctuating portion of the deterministic profile model. The major strategy adopted to accomplish this task is to first fit a candidate model with the simplest form to the data points. Then, the form of this candidate model is modified iteratively and refitted to the data points until a valid least squares fit is obtained. The form of the deterministic model can easily be modified by sequentially adding more Fourier components to the candidate deterministic profile model. The properties of the residual errors, such as correlation, distribution of residual errors around their mean, residual mean squares statistics, are examined to monitor the progress of the fitting process as more Fourier components are added to the model. Threshold values are set on these statistics to terminate the iterative fitting process based on principles of statistical hypothesis testing. The termination point indicates the adequacy of the candidate model to approximate the deterministic profile.

Since both form (FC, a_i, m_i, M, dR) and location (x_o, y_o) parameters of a manufactured circular feature are not known in advance and must be estimated from the same data set, the estimates of location parameters will have an effect on the subsequent estimates of the form parameters, or vise versa. If a single numerical procedure is used to determine all these parameters simultaneously, the interaction between location and form parameters will create convergence problems. To overcome this problem, two separate optimization functions are formulated for finding the values of location and form parameters independently. These objective functions are expressed as

$$\min_{dR,a_i}\left(\sum_{i=1}^{N}\left[R_m^i - R(\theta)^i\right]^2\right) \tag{3}$$

$$\min_{x_0,y_0}\left(\sum_{i=1}^{N}\left[R_m^i - R(\theta)^i\right]^2\right) \tag{4}$$

where N represents the number of data points and R_m^i the radial distance from the origin of the local coordinate system (x_0, y_0) to the ith measured point.

Implementation of the proposed approach involves three important tasks to be carried out sequentially in each major iteration step. These tasks can be described as construction, localization, and validation of a candidate deterministic profile model. In a given iteration step, construction and localization of deterministic profile are first performed one after the other until the percentage error between the corresponding estimates obtained through consecutive repetition stabilizes. Thereby, the effect of correlation between location and form parameter estimates is considered. The model validation process then proceeds to check the randomness of the fitting residuals and hence test the adequacy of the candidate model in representing the deterministic profile. This is conducted using the serial correlation and chi-square ratio tests.

The flow chart given in Fig. 1 summarizes the overall procedure used to determine the appropriate deterministic model. The form error characterization process begins with preliminary evaluation of all candidate Fourier components. Then, the Fourier components are rearranged based on the magnitude of Fourier coefficients calculated in the preliminary evaluation process. In the last, but the most important, section of the algorithm, statistically significant Fourier components are determined with the serial correlation and chi-square ratio tests. Moreover, in a parallel and separate procedure to the determination of statistically significant Fourier components, the dominant Fourier components are identified using F-ratio test.

Simulation studies

The proposed procedure has been implemented using several simulated point data sets. In order to generate the simulated data set, a hypothetical form error with specified characteristic is superimposed on an ideal circle. In this study, both periodic and non-periodic systematic form error combined with various proportions of random form error have been considered to investigate the effectiveness of this method in identifying the systematic form error accurately. Based on these simulation studies, the following observations have been made.

The proposed method reduces the influence of the systematic form error in the estimation of the center position of the circle. The center position estimated with the present method and the traditional least squares method has been compared. This comparison suggests that the estimated center position using this method has less uncertainty and is very close to the ideal position.

The proposed method can effectively characterize systematic form error when the "signal to noise ratio" is high and the form error is periodic. The performance of the procedure is fairly acceptable at lower signal to noise ratio and can also satisfactorily approximate non-periodic systematic form error. However, when the systematic form error is non-periodic and signal to noise ratio is very low, the coefficients of some of the statistically significant Fourier components become too variable and their values may considerably differ from their true values.

In such cases, it is recommended to construct the deterministic profile from the dominant Fourier components so that consistent and relatively reliable estimation is achieved.

The random form error influences the systematic form error characterization in two ways. It affects the values of the systematic form error parameters and it tends to introduce the wrong form parameters (Fourier components). However, the criteria used in this method satisfactorily prevent the latter incident. Furthermore, the effect of random form error depends on the signal to noise ratio used to simulate the data and the kind of systematic form error present.

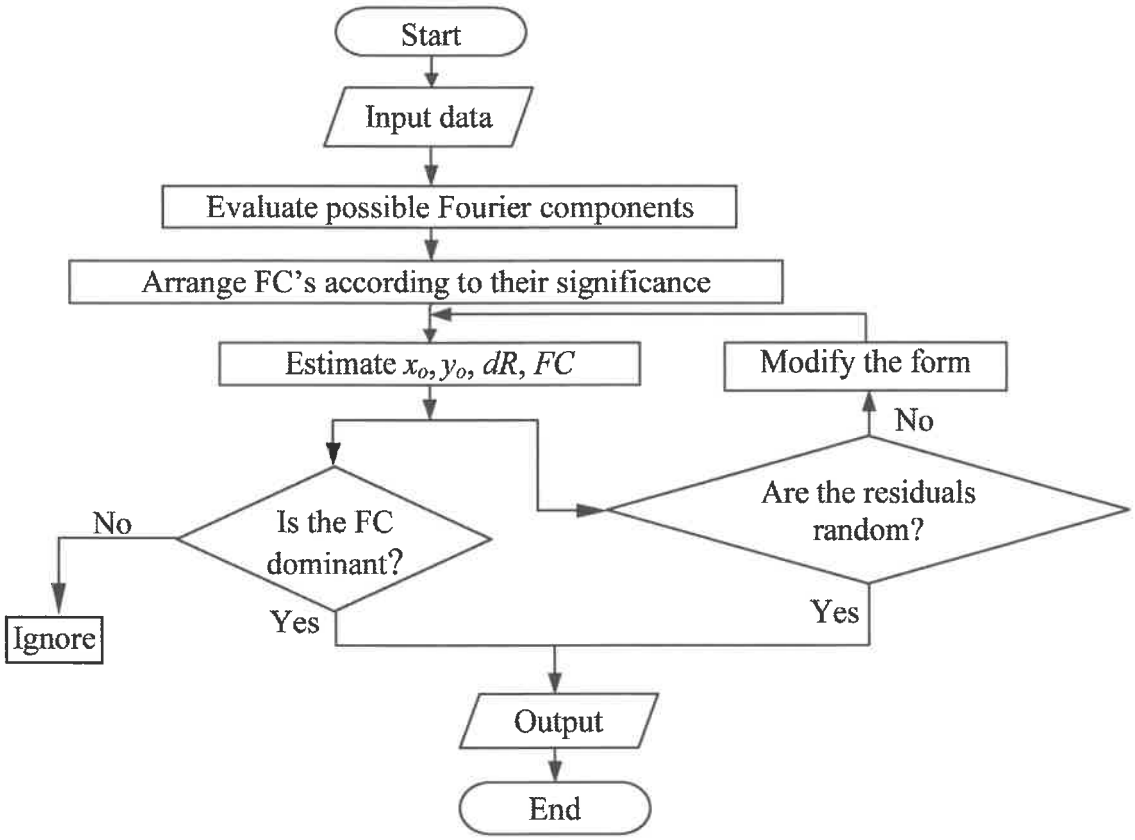

Figure 1 Procedure for determining deterministic profile model.

Conclusions

In this paper, a systematic procedure is proposed to characterize the systematic form error in manufactured parts with circular features. The simulation studies suggest that this method performs well for a wide variety of form variations. Experimental verification is essential to illustrate the effectiveness of this method in practice. The related work is underway.

References:

[1] Yang, T. H. and J. Jackman, *ASME Journal of Manufacturing Science and Engineering*, 119, 375 (1997).

[2] Dowling, M. M., P. M. Griffin, K. L. Tsui, and C. Zhou, *Technometrics*, 39(1), 3 (1997).

[3] Yan, Z., Yang, B. D., and Menq, C. H., *International Journal of Machine Tools and Manufacture*, 39, 1199 (1999).

FORM ERROR MEASUREMENT BY COMPARISON WITH A REFERENCE OBJECT

Oswaldo Horikawa
Escola Polécnica - University of São Paulo
Av. Prof. Mello Moraes, 2231, CEP05508-900, SP, BRAZIL

Traditionally, form error measuring machines compares the form of the object with a precise linear or rotary motion generated by a precision bearing. As an alternative strategy, this paper presents a strategy based on the comparison of the object form with the form of a second object. This makes the measurement accuracy independent of the motion accuracy of the measuring machine, opening possibilities for keeping conventional measurement accuracy but using bearings of lower accuracy – this means measuring machines of lower cost. A roundness measuring system based on this new strategy is presented. Even using a ball-bearing with non-repetitive motion errors larger than 2μm, the presented system, shows a final measurement repeatability better than 0.3μm, proving the effectiveness of the proposed strategy.

Keywords: *form measurement, roundness measurement, error separation technique*

1. Introduction

In conventional measuring machines such as roundness measuring machine (RMM) or straightness measuring machine (SMM), the measurement accuracy is affected by repetitive and non-repetitive motion errors of the measuring machine. Therefore, in such machines, high measurement accuracy is assured by using precision bearings (oil-film and air-film bearings) and isolating the machine from external disturbance sources.

In recent years, a sort of techniques was developed to compensate systematic measurement error caused by motion errors present in the measuring machine. The motion error is previously measured by comparing it to an external datum and then, the measurement result is compensated. The external datum can be a masterpiece like a straight edge or a master sphere. However this strategy is effective only to reduce systematic measurement errors.

Therefore, this work identifies a strategy to compensate measurement errors of both, repetitive and non-repetitive, nature induced by motion errors. While in the conventional strategies, the form of the object is compared to a motion, in the present strategy, the form of the object is measured by comparing it to the form of a second object, i.e. an auxiliary reference. This strategy is referred here as FFC, Form – Form Comparison, strategy.

Some measurement methods follow FFC strategy, making the measuring accuracy independent of the motion accuracy of the bearing. In the multi point method[1),2)], the influences of motion errors are removed from sensor readings by measuring the object simultaneously by two or more sensors. An another method consists on the direct comparison of the object with a masterpiece such as a master sphere[3)]. However these methods has some problems. The multi point method has the problem of different gain for each harmonic existent in the form of the object. The direct comparison with a masterpiece has a serious practical problem on maintaining the original profile of the masterpiece. The profile of a masterpiece may change when fixed to the machine or suffers some damages. At least in the case of roundness measurement, the problems are minimized by the Improved Reversal Method – IRM[4)], described later.

In order to demonstrate the effectiveness of the FFC strategy, this work presents an example of a roundness measurement system that was designed according to the strategy and uses the IRM to measure the roundness of objects.

2. The Improved Reversal Method –IRM[4)]

In the IRM, the object is firstly set on a second round object, which works as an auxiliary reference (see Fig.1(a)). Then, both objects are rotated and measured simultaneously resulting in the following sensor readings:

$$s_1(\theta) = h(\theta) + t(\theta) \qquad (1)$$

$$s_2(\theta) = q(\theta) + t(\theta) \qquad (2)$$

Where, θ is the angular position, $s_1(\theta)$ is the reading of sensor 1, $s_2(\theta)$ is the reading of sensor 2, $h(\theta)$ is the object roundness, $q(\theta)$ is the roundness of the auxiliary reference and $t(\theta)$ is the radial motion error of the table.

In the next step, the object is reverted with respect to the auxiliary reference and the sensor installed in the opposite side (Fig.1(b)). Then, both elements are rotated and measured again resulting in the following sensor readings:

$$s_1'(\theta) = h(\theta) + t'(\theta) \qquad (3)$$

$$s_2'(\theta) = q(\theta) - t'(\theta) \qquad (4)$$

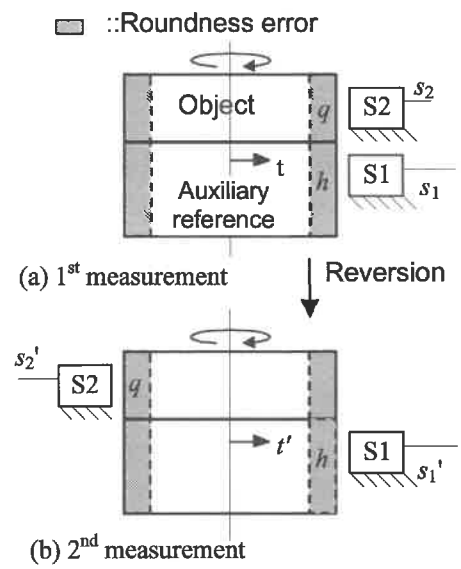

Figure 1 The IRM

$s_1'(\theta)$ and $s_2'(\theta)$ are new readings respectively of the sensors 1 and 2. $t'(\theta)$ is the motion error during the 2nd measurement executed after the reversion. $t'(\theta)$ is not necessarily equal to the motion error $t(\theta)$.

Finally, using all sensor readings (Eqs.(1)~(4)), the roundness is obtained as follows.

$$h(\theta) = [(s_1(\theta) - s_2(\theta)) + (s_1'(\theta) + s_2'(\theta))] / 2 \qquad (5)$$

The operations $(s_1(\theta) - s_2(\theta))$ and $(s_1'(\theta) + s_2'(\theta))$ executed in Eq.(5) represent a comparison between the profile of the object and of the auxiliary reference. Therefore, the IRM follows the proposal of this work, i.e. the comparison between forms.

3. The prototype

According to the FFC strategy and assuming the use of the IRM, a prototype of a roundness measuring system is developed (Fig.2). Similar to a conventional RMM, the system consists of a rotary table, displacement sensors and a computer system. The most significant difference with respect to a conventional RMM is related to the motion accuracy of the table. Instead of a high accuracy bearing, this system uses ball bearings. The use of a ball bearing is particularly interesting since it ensures reasonable motion accuracy (on the order of μm), is robust, is easily maintainable and is largely available in the market. A lathe finished table of ϕ150mm of diameter is fixed to a shaft and the shaft is suspended by a pair of ball bearings (NSK/6305Z, radial run-out less than 1μm). The shaft is equipped in its lower extremity with an encoder that generates 256 pulses/rev and an origin reference pulse. By using these pulses for synchronization, signals from two non-contact capacitive gap sensors (ADE3800, gain: 0.4V/μm, resolution 0.05μm) are

sampled and stored in the computer. During experiments, the table is rotated manually at a speed of approximately 5rpm.

4. Results

Readings of the sensor 1 and 2 are sampled simultaneously during 20 successive rotations. Figure 3 shows readings of the sensor 2. It indicates the presence of non-repetitive motion errors with a peak-to-peak value of approximately 2μm. These errors are mainly consequence of the clearance in the ball bearings. If the equipment presented in Fig.2 is used as a RMM, the reading of sensor 2 is used directly as the object roundness. Even assuming that the table does not have repetitive motion errors, non-repetitive errors limit the measurement accuracy to 2μm.

After sampling, sensor readings are processed according with the IRM (Eq.(5)) using sensor readings collected along 20 successive rotations, before and after the reversion. Results are shown in Fig.4. The peak-to-peak value of the measurement repeatability is about 0.3μm, which is almost 10 times better than the direct measurement (Fig.3). The largest standard deviation (σ) along 20 measurements is 0.084μm. These results, show that a measurement accuracy superior to that of the motion accuracy is obtained by the IRM, showing the effectiveness of the FFC (Form-Form Comparison) strategy.

Although it is not a relevant result in practical applications, the IRM can isolate motion error of the table during the measurement. The motion errors before the reversion are presented in Fig.5. Similar motion errors are observed after the reversion, suggesting the presence of motion error components of repetitive nature. The repeatability of the motion error in terms of peak-to-peak value is close to 2μm.

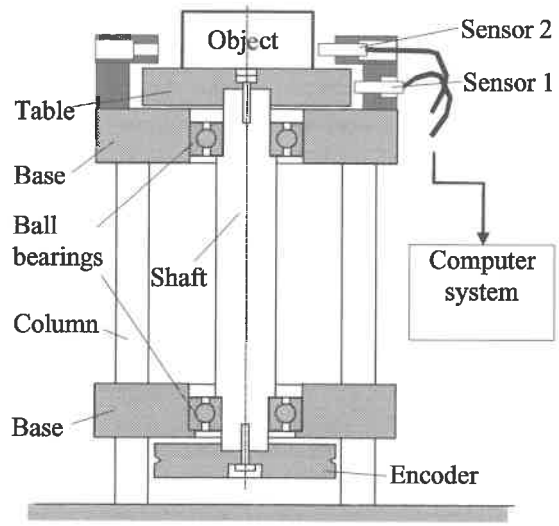

Figure 2 The prototype

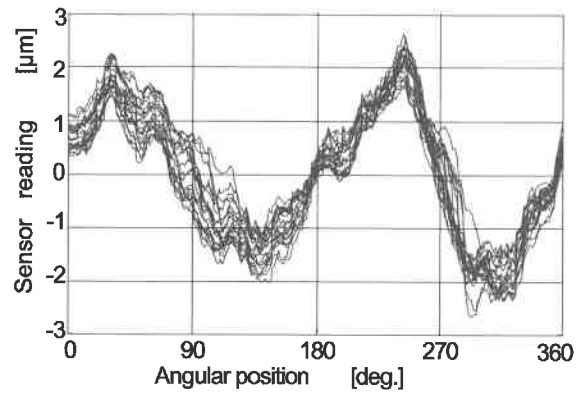

Figure 3 The readings of sensor 2.

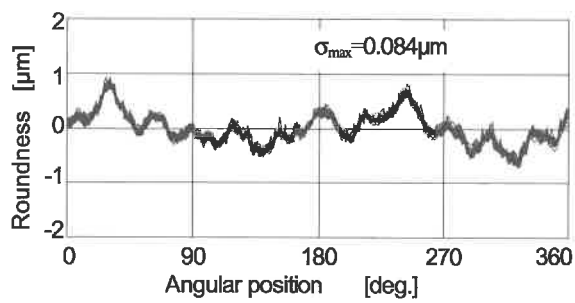

Figure 4 The roundness.

Repetitive motion errors can be eliminated from sensor readings by using the Reversal Method – RM[5]. Using the same readings of sensor 2 that are used in Figs.4 and 5, 20 object roundness are obtained using the RM. The results are shown in Fig.6. These results are very similar to those obtained using the IRM (Fig.4), suggesting the validation of the measurements executed by the IRM. A lower repeatability, larger than 1μm, is observed in the case of the RM because of non-repetitive motion errors present in the measuring machine.

In Fig.7, the measurement by the IRM is compared to that obtained by a conventional RMM (Taylor-Hobson, Talyrond 200). The maximum deviation between results is around 0.2μm. The deviation is explained by the difference in the sensor used in the measurement. The IRM uses non-contact sensor with a circular sensitive area of approximately 5mm diameter, while the RMM uses a stylus type contact sensor. Despite the deviation, the measurement by the IRM is in good conformity with that obtained by the RMM.

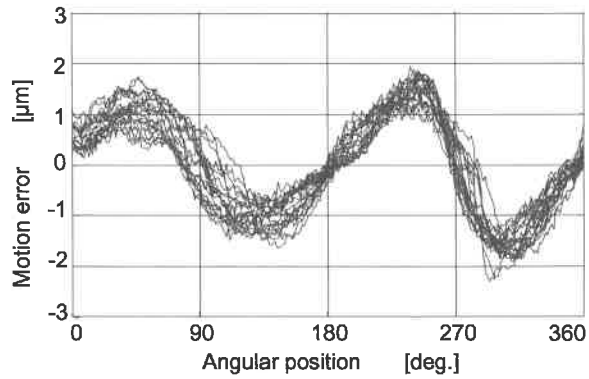

Figure 5 Motion errors.

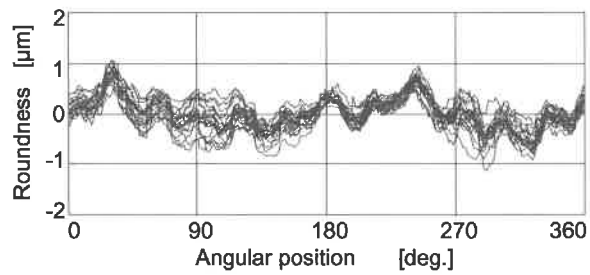

Figure 6 Measurements using the RM.

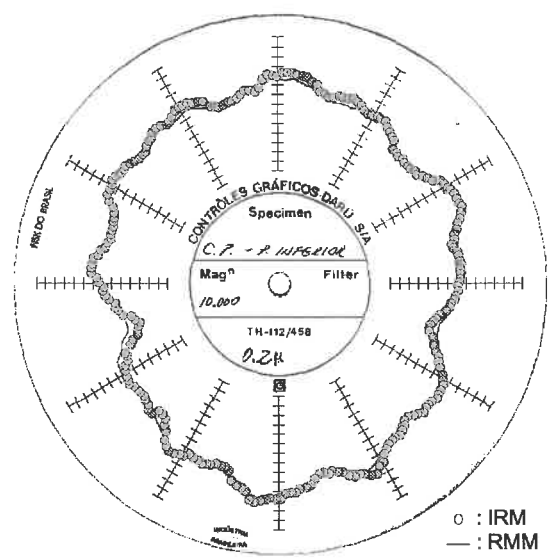

Figure 7 Measurement by a RMM.

5. Conclusions

This work presented a form measuring strategy that is based on the comparison of the form of the object with the form of a second object. By the strategy, the measuring accuracy becomes independent of the repetitive and non-repetitive motion errors of the motion mechanism used in the measurement. As consequence, the present strategy opens possibilities for developing measuring machines with accuracy similar to the traditional ones but of lower cost because of the use of bearing of lower accuracy. This is the most interesting aspect of this strategy.

7. Acknowledgements

The author acknowledges the Conselho Nacional de Pesquisa e Desenvolvimento Científico e Tecnológico - CNPq for the financial support ("Produtividade em Pesquisa"), Fundação de Amparo à Pesquisa do Estado de São Paulo - FAPESP for the financial support ("Auxílio participação em reunião científica ou tecnológica") and the NSK do Brasil for supplying the bearings end executing measurements.

8. References

1. Obi, M., Kobayashi, T. and Furukawa, S., "On a New Method of Roundness Measurement Based on the Sequential-Three-Points Method", *Trans Japan Soc Mech Eng, Part C*, 54 *(506)*, 1988, 2475.
2. Gao, W., Kiyono, S. and Sugawara, T., "High - accuracy roundness measurement by a new error separation method", *Prec Eng*, 21(*2/3*), 1997, 123.
3. Bifano, T. G. and Dow, T. A., "Real Time Control of Spindle Runout", *Opt Eng*, 24*(5)*, 1985, 888.
4. Horikawa, O., Sato, K. and Shimokohbe, A. An Active Air Journal Bearing, *Nanotechnology*, 3, 1992, 84.
5. Chetwynd and Siddall, G., "Improving the Accuracy of Roundness Measurement", J Physics E: Scientific Instruments, 9, 1976, 537.

EVALUATION OF CYLINDRICITY ERROR BASED ON MRS, LSC, MCC, AND MIC

Guohua Jiang and S. Hossein Cheraghi
Industrial and Manufacturing Engineering Department
Wichita State University, Wichita, KS. 67260-0035

Abstract

In this paper, we present an efficient methodology for the evaluation of cylindricity error. Based on the proposed methodology, the cylindricity error can be assessed using any of the existing criteria (LSC, MCC, MIC or MRS). The results indicate that the proposed procedure is fast and the results it provides are very accurate.

Key words: cylindricity, straightness, median line, geometric dimensioning and tolerancing

Introduction:

A great majority of mechanical parts comprise of cylindrical features. A basic geometric characteristic that is used to control form and function of cylindrical features is cylindricity. Significant error associated with this characteristic may result in the failure or inadequate functioning of the corresponding part. Accurate measurement of this error is not a trivial task due to the three dimensional nature of the characteristic.

Methods for the assessment of form errors can be generally divided into the intrinsic datum and extrinsic datum methods. In the intrinsic datum method, points on the surface of the part are used as a datum. The most commonly used intrinsic techniques are diametrical measurement, V-block measurement, and bench center measurement. The intrinsic methods are generally inaccurate due to the existence of multiple sources of error with the measurement process.

In the extrinsic method, an external member is used as the datum reference. The most common extrinsic methods for the evaluation of cylindricity error are Minimum Radial Separation cylinders (MRS), Least Square Cylinder (LSC), Maximum Inscribed Cylinder (MIC), and Minimum Circumscribed Cylinder (MCC). All these techniques try to find two coaxial cylinders at minimum separation within which the surface of the measured feature is to fall. The difference is in the method of finding the location and orientation of the common axis. Among these methods, only MRS is based on the ASME Y14.5-1994 standard on Geometric Dimensioning and Tolerancing (GD&T).

Researchers have developed procedures for the evaluation of cylindricity error based on these criteria. Wang [2] proposed a general-purpose algorithm for constrained nonlinear optimization problems for minimum zone evaluation of form tolerances. Shunmugam [3] proposed a method based on the minimum average deviation for evaluating the form error of lines, circles, planes, cylinders and spheres. He used linearizations and the simplex search method to minimize the sum of the absolute deviation values. Karr and Ferreira [4] discussed the nonlinear optimization models for cylindricity and straightness of a median line, developed a verification methodology for computing the minimum zone for the problem, and proposed two linear programs for implementation. Their basic idea is to solve the nonlinear optimization problem using successive linear programs. A strategy proposed by Lai and Chen [4] for minimum zone evaluation of circles and cylinders employs a non-linear transformation to convert a circle into a line and a cylinder into a plane, and then uses straightness or flatness evaluation schema to obtain

appropriate control points and minimum zone deviation for the feature concerned. This strategy is an approximation to the minimum zone circles or cylinders. Roy and Xu [6] proposed a computational geometry based technique to generate a pair of concentric cylinders for checking the cylindricity tolerance. In this method, the cylindrical surface is divided into several cross-sections normal to the coordinate measuring machines local Z-axis. Then 2-D convex hulls and voronoi diagrams are used to generate pairs of concentric circles, and these circles are used to find a pair of concentric cylinders to create the minimum zone required for form tolerance analysis. This method requires the axis of the cylindrical feature to be parallel to Z-axis of measurement.

Proposed Approach:

Geometrically speaking, the cylindricity error evaluation problem based on minimum radial separation criteria may be stated as follows: Given a set of three dimensional points collected from the surface of a cylinder, find two concentric cylinders with minimum radial separation within which all the measured points shall fall. The radial distance between these two cylinders defines the cylindricity error.

The proposed methodology for the evaluation of cylindricity error uses the circularity error evaluation problem as a subroutine. The methodology is constructed based on the following fact. If we rotate a cylinder with a perfect form to a position such that its axis parallels the z-axis and then project all points on the cylindrical surface onto the x-y plane, the projection points will form a circle on the x-y plane. It is clear that this circle has a circularity error equal to zero. As the orientation of the axis of the cylinder is changed, the projected points would no longer have a circularity error of zero. Hence, according to this discussion, to find cylindricity error, one can find minimum value of circularity error of the projected points as the cylinder is rotated around x and y axes.

Based on this logic, an efficient algorithm has been developed. The procedure consists of two loops: an inner loop and an outer loop. The outer loop searches for optimal value of rotation angles around x and y axes. The inner loop calculates the value of circularity error for a given set of rotation angles. Given a set of rotation angles, the data points are first rotated around x and y axes. The points are then projected onto the x-y plane. Circularity error of the projected points is calculated and saved in an array. The rotation angles are changed and the steps are repeated until optimal value of circularity error is calculated. The generalized procedure is as follows:

Step 1: Select a set of initial rotation angles and assume a large number as the minimum circularity error value
Step 2: Rotate the collected points around the x and y axes by the rotation angles
Step 3: Project the rotated points onto the x-y plane
Step 4: Calculate the circularity error. Compare this value with the minimum circularity error value. Keep the minimum value.
Step 5. Change the rotation angles and go to step 2.
Step 6: Continue this process until no improvement in the circularity error value can be found.

The inner loop finds the circularity error of the projected points of the surface of the cylinder based on a selected method. As mentioned in the previous section, there are several methods available for the calculation of circularity error, such as minimum circumscribed circle (MCC), maximum inscribed circle (MIC), least-squares circles (LSC) and minimum radial separation circle (MRS). Any of these techniques can be used in the inner loop. In this research, only the

MRS and LSC techniques have been implemented. Many procedures exist for the calculation of the minimum radial separation circles. Wang and Cheraghi [7] proposed an efficient algorithm for calculating minimum zone circles. We used Wang and Cheraghi's algorithm for calculating minimum zone circles in the inner loop. Similarly, there are efficient procedures for the calculation of LSC [8,9], MCC [10] and MIC [11] that can be utilized in the inner loop.

Performance Evaluation:

The proposed procedure for the evaluation of cylindricity error has been implemented into a computer program. To validate the results from the proposed procedure and to study the efficiency of the proposed procedure several example problems were solved. Some of the data sets for these problems were taken from published articles while other others were measured from real parts. The results of these studies are shown in the following sections.

To validate the developed procedure it was applied to a set of data taken from the literature using MRS in the inner loop [4, 13]. The results were then compared with the published results as shown in Table 1. As shown in the table the developed procedure accurately calculates the cylindricity error values.

Table 1. Comparison of the cylindricity error results with the published results

	Cylindricity error - Proposed procedure	**Cylindricity error - Published results**
Data set 1 [4]	0.00100	0.00100
Data set 2 [4]	0.18395	0.18396
Data set 3 [4]	0.00944	0.00941
Data set 4 [13]	0.002788	0.002788

To test the efficiency of the proposed procedure, a program was developed to randomly generate data under different conditions. The developed procedure was tested on data sets containing 25, 50, 75, 100, ..., 250 points. The computer program was run on a PC with a 450 MHz Pentium processor. The results are shown in Figure 2. As shown in the figure, the correlation between the number of points and computation time seems to be linear. For a data set containing 250 points it took the procedure only four seconds to arrive at solution.

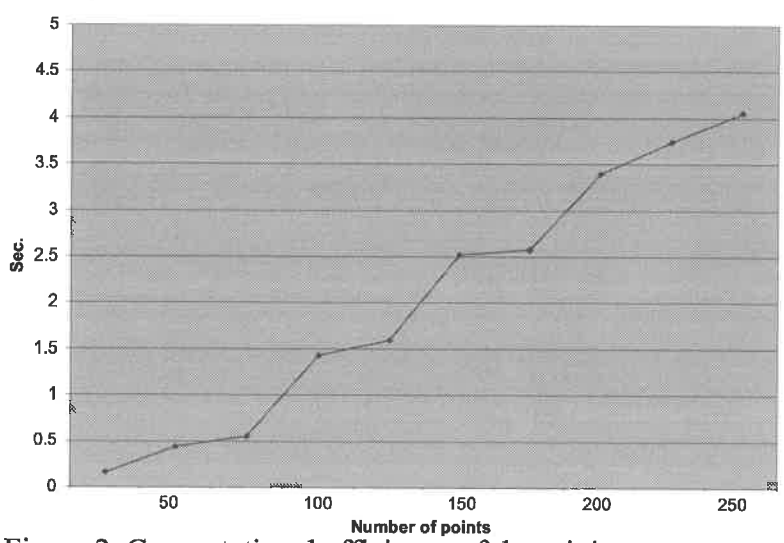

Figure 2. Computational efficiency of the minimum zone method

Conclusions:

This paper presented an efficient procedure for the evaluation of cylindricity error. The procedure uses as a subroutine a circularity error evaluation procedure. The results from the evaluation of the procedure indicate that it is capable of providing accurate results efficiently. An important advantage of the proposed procedure is that it allows different procedures for the evaluation of cylindricity error such as minimum circumscribed cylinder, maximum inscribed cylinder, minimum radial separation or least squares cylinders be used.

References

1. American Society of Mechanical Engineers, ANSI Y14.5, Dimensioning and Tolerancing ANSI Y14.5, New York, N.Y., 1994.
2. Wang, Y., 1992, "Application of Optimization Techniques to Minimum Zone Evaluation of Form Tolerances", Quality Assurance Through Integration of Manufacturing Process and Systems, ASME 1992, PRD-Vol. 56.
3. Shunmugam, M. S., 1987, "New Approach for Evaluating Form Errors of Engineering Surfaces", Computer-Aided Design, Vol. 19, p 368-374.
4. Carr, K and Ferreira, P., 1995, "Verification of Form Tolerances Part II: Cylindricity and Straightness of a Median Line", Precision Engineering, Vol. 17, No. 2, p 144-156.
5. Lai, J. and Chen, I., 1995, "Minimum Zone Evaluation of Circles and Cylinders", The International Journal of Machine Tools and Manufacture, Vol. 36, No. 4, p 435-451.
6. Roy, U. and Xu, Y., 1995, "Form and Orientation Tolerance Analysis for Cylindrical Surfaces in Computer-aided Inspection", Computer in Industry, Vol. 26, p 127-134
7. Wang, M., Cheraghi, S. H. and Masud, Abu S. M., 2000, "Circularity Error Evaluation: Theory and Algorithm," Precision Engineering, 25, 1999.
8. Murthy, T.S.R., 1986, "A Comparison of Different Algorithms for Circularity Evaluation", Precision Engineering, Vol. 8, No. 1, p 19-23.
9. Kim, N. and Kim, S., 1996, "Geometrical Tolerances: Improved Linear Approximation of Least Squares Evaluation of Circularity By Minimum Variance". The International Journal of Machine Tools and Manufacture, Vol. 36, No. 3, p 355-366.
10. Elzinga, J. and Hearn, D., 1972, "The Minimum Covering Sphere Problem", Management Science, Vol. 19, p 96-104.
11. Preparata, F.P. and Shamos, M.I., 1985, Computational Geometry: An Introduction, Springer-Verlag, New York.
12. Lai, H., Jywe, W., Chen, C. and Liu, C., 2000, "Precision Modeling of Form Errors for Cylindricity Evaluation Using Generic Algorithms", Precision Engineering, 24, p 310-319.

Evaluation of Variations Specified by Non-Uniform Profile Tolerance Boundaries

T. M. Kethara Pasupathy, Robert G. Wilhelm, Edward P. Morse and
Gregory A. Hetland*
Center for Precision Metrology and Intelligent Manufacturing
The University of North Carolina at Charlotte
9201 University City Blvd., Charlotte, NC 28223-0001
*Formerly of Hutchinson Technologies Ltd.
40 West Highland Park, Mail Stop 403
Hutchinson, MN 55350-9784

1. Introduction

Profile tolerance specification is a heavily utilized scheme to represent allowable geometric variation of manufactured parts as it simultaneously controls form, orientation and location of actual features of a manufactured part. The specification is applied on implicit features such as planes, straight lines and also on freeform curve and surface features. Examples of such freeform features include airfoils and bathtubs.

In our previous work [1], we showed that offsets (uniform boundaries) as defined by the ANSI or the ISO for profiles do not adequately define the tolerance zone as per the designer's intent in several cases. Furthermore, the applicability of non-periodic B-splines [2] was demonstrated to overcome the problems caused by offsets and to meet the needs for computer interpretable representation. Non-periodic B-splines can be used to specify non-uniform boundaries.

The deviation of the actual feature within a non-uniform or uniform zone is essential to map the relationship between parts and performance. Determination of deviation of actual features lying in certain regions of the tolerance zone and the parametric form of the curves renders this task a non-trivial problem.

In this paper we first group 2-D parts based on the type of the tolerance boundary. Later we explain deviation in the context of non-uniform tolerance boundaries followed by the application of two algorithms to determine deviations of actual features. Results from some example cases are also presented.

2. Profile Tolerance Boundaries

In industrial practice, a part is sub-divided into features and tolerances are specified to represent the extreme boundaries within which the feature should lie. Additional rules are provided on how adjacent features are to merge for example, chamfer and radius controls. These controls are provided to handle singular zones as described below.

Consider the hatched region in Figure 1. While any point in the rest of the tolerance zone can be associated with a point on the nominal geometry in the normal direction, the entire hatched region may be associated with the corner point of the nominal feature. Manufactured parts will not have distinct corners and hence extraction of co-ordinates of any actual point in this region is difficult. Furthermore, even if an actual point in this region is available, its deviation cannot be estimated, as it is difficult to associate the point with any particular feature. Such points are singular points and the associated zones are singular zones.

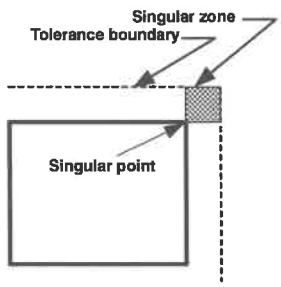

Figure1, Singular zone within the tolerance boundary

The occurrence of these instances can be distinguished. In part A of Figure 2, a corner point is shown on the nominal feature while in part B a point is shown on the tolerance boundary. These points on the curve do not posses a derivative. It is common practice not to include points in these zones in measuring deviations though resources are spent to control this region. While all parts with singular points on the boundary and on the nominal geometry can be grouped into a class, it is also possible to define parts without singular points and zones. Part C in Figure 2 is one such part and it has a tolerance boundary specified using B-spline that has a smooth transition between sections of varying tolerances. (Uniform boundaries need not have singular points and zones.)

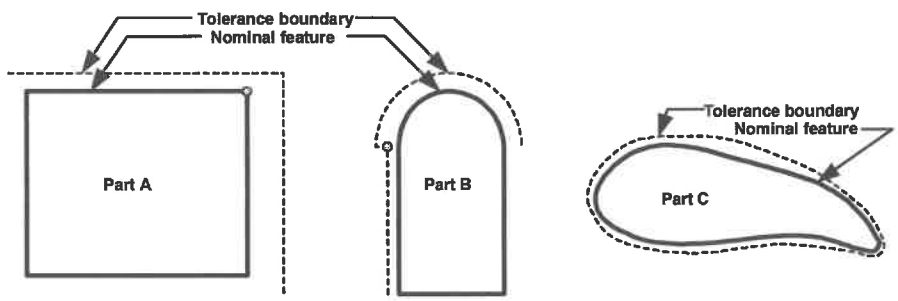

Figure2, Parts A and B with uniform boundaries and singular points; Part C has non-uniform boundary without singularities

Non-periodic B-splines can be used to specify profile tolerances for both classes of parts. While it is possible to arrive at the maximum deviation as per the conventional practice for parts with singularities, no single actual value can meaningfully characterize a part with non-uniform boundaries. The following section is a discussion on the deviation for non-uniform boundaries.

3. Deviation of the Actual Feature in *t*+ Boundary

The distance L (refer Figure 3a) between a point NP_i, on the nominal feature and a point AP_i of the actual surface that lies in the direction normal to nominal surface at NP_i is the deviation that can be inferred from the ANSI standard for uniform boundaries. Note that no unique normal exits at the singular points. Hence the occurrence of the maximum deviation within the restricted length of the profile feature is tested for conformance and reported.

In case of features that fall into the subgroup of smooth tolerance boundaries, as shown in Figure 3b, we do the following. The deviation of a measured point of the actual feature can be shown as a vector whose magnitude represents the ratio

$$|AP_i - NP_i| / |t+_i - NP_i| \qquad (1)$$

in the direction normal to the nominal feature with the initial point NP_i. The vectors are shown in Figure 3c. For conformance all the points of the actual feature should lie within the zone. The above discussion can be easily extended to bilateral tolerances. For deviations inside the nominal feature, deviation vectors will point in the direction of the *t*- zone boundary points.

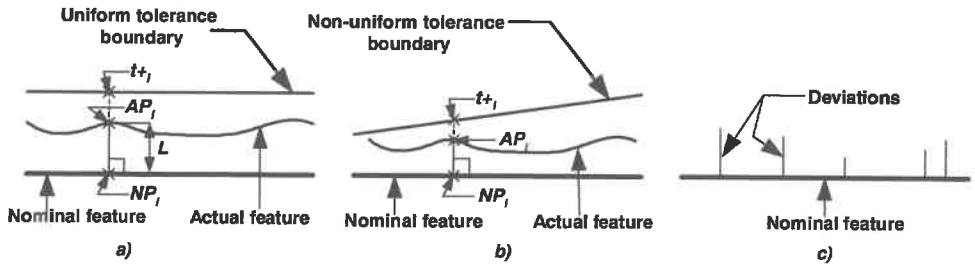

Figure 3, a) Deviation in the case of uniform tolerance boundary, b) Deviation in non-uniform tolerance boundary and c) presenting deviations for non-uniform boundaries

4. Procedure for Evaluating Deviations

Classification of actual points with respect to tolerance boundary defined by B-splines i.e., if it lies within the tolerance zone or not, is not easy as in the case of implicitly defined curves. In the paper [1] for an actual point say a_i, we showed that if the closest point on the tolerance boundary b_i is known, we can check the containment of a_i in the zone.

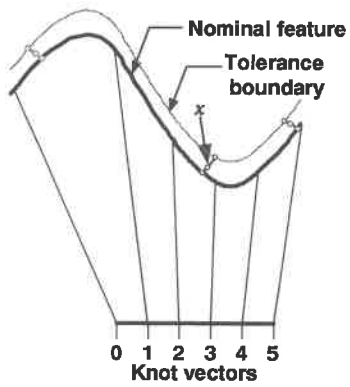

Figure 4. Determination of closest points on the tolerance boundary

Refer Figure 4 where the nominal feature is a non-uniform B-spline with a knot vector that varies from 0 to 5. A linear scale shows how a parameter varying within the knot vector range maps to points on the nominal feature. In this example the tolerance boundary varies uniformly with respect to the nominal feature. Procedure_*profile*_evaluation below describes a method to determine the closest point and later we use it to calculate the deviations.

Procedure_*Profile*_evaluation

1. Set **range, delta_segment_length.** /* Range = a very small value, delta_segment_length = limiting condition */
2. Substitute each element in a knot vector set that does not repeat, $K_{sp} = [k_1..k_j..k_n]$, in the B-spline formulation of the boundary, to obtain a set of points $Kp = [(Px, Py)_1,.. (Px, Py)_j,...(Px, Py)_n]$ on the curve.
3. Of all the points in Kp, determine the point $(Px, Py)_j$ that is closest to the actual point.
4. If $j = 0$; choose the interval $[0, 1]$; else-if $j = n$, choose the interval $[n-1, n]$; else substitute (k_j - **range**) and (k_j + **range**) in the B-spline formulation to obtain two points on the curve. If the point corresponding to (k_j - **range**) is closer to the actual point than the point from (k_j + **range**), choose the interval $[j-1, j]$; else choose $[j, j+1]$. The case of point x in Figure 4 is an example of $j \neq 0,1$.
5. Application of Adaptive subdivision: Recursively subdivide the selected interval from step 4 by half and find the closest half, for example if $j = 0$, the first subdivided interval would be $[0,0.5, 1]$ or say $[P, Q, R]$. Substitute (Q - **range**) and (Q +**range**) in the B-spline formulation and test as in step 4 if the interval $[P, Q]$ or $[Q, R]$ is close. Say if $[P, Q]$ is closer, we subdivide the interval to obtain $[0,0.25,0.5]$ or $[P, P+ ((Q-P)/2), Q]$. Meanwhile, the points on the curve corresponding to P and R, i.e., $[U, V]$ on the curve is updated after every subdivision. This process is continued till the distance between U and V equals **delta_segment_length.** This method converges to the closest point quickly and paper [3] provides details on the performance of the adaptive subdivision.

Having obtained the closest point b_i close to a_i, the deviation can be calculated. In contact measurements, like co-ordinate measuring machines, the co-ordinates of the actual point is obtained with respect to the normal of the known point n_i on the nominal geometry. With a_i, b_i and n_i, the deviation can be calculated as described in the previous section.

Note that this method will work for actual points that are within the radius of curvature of the curve defining the tolerance boundary.

5. Results

The above algorithms can be used for both tolerance boundaries that are uniform and non-uniform. Figure 5a shows an implicit feature for which a uniform boundary is considered sufficient. The offset of end points of the feature can either be converted to an implicit form or a B-spline form of degree 1. For this example we used the theoretical inspection procedure (**Procedure_*Profile*_evaluation**) to determine the closest point on the tolerance boundary and later calculated the deviation. The result agrees with the deviation to be reported as per the ANSI standard. Figure 5b shows a higher degree nominal curve. In this case, using the **Procedure_*Profile*_evaluation,** closest points on both nominal and tolerance boundary was determined. Vectors as defined in section 3 are desirable to present the deviations for the example in Figure 5b. Figure 5c shows the deviations.

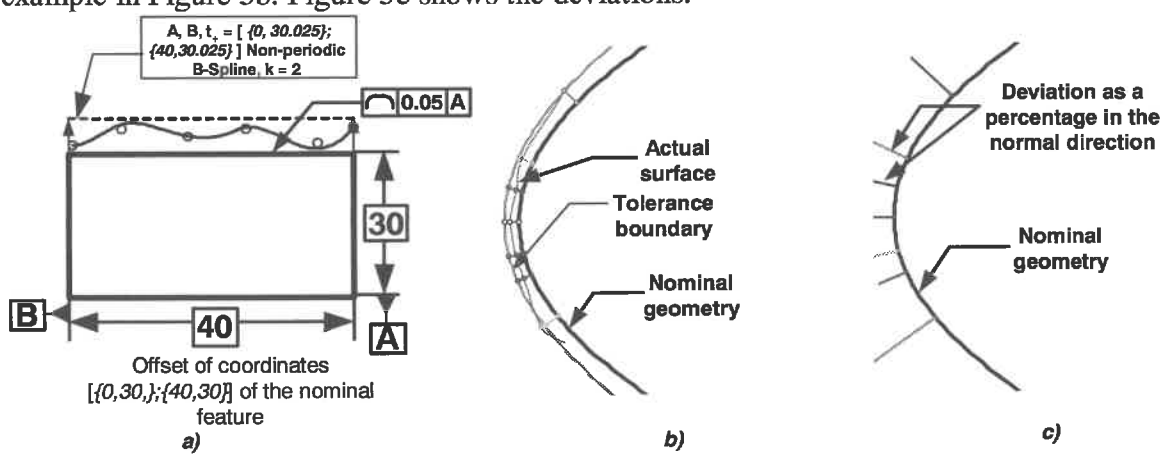

Figure 5, a) Deviation for an implicit feature, b) Closest points on tolerance boundary and nominal geometry and c) Presentation of deviations

6. Conclusions

Non-uniform B-splines can be used to represent uniform and non-uniform 3-D tolerance boundaries. A method to present deviations of non-uniform boundaries was illustrated. Two algorithms for inspection and evaluation of an actual feature were presented, as were results from the application of algorithms.

7. References

1. Kethara Pasupathy T M, Wilhelm R G, Curves for profile tolerance boundaries, 7th CIRP International seminar on computer aided tolerancing, ENS de Cachan, France, April 2001,pp.275-284.
2. Farin G E, Curves and surfaces for Computer aided geometric design, 3rd Ed, Academic Press.
3. Cohen E and Schumaker L, Rates of convergence of control polygons, Comp. Aid. Geom. Des., 2(1-3), 229-235,1985.

Development of a Cylindricity Measurement System for Parallel Rollers Based on a V-Block Method

Kimiyuki Mitsui [1], Ken Katsurada [1], and Akira Hayashi [2]

[1] Department of Mechanical Engineering, Keio University,
3-14-1 Hiyoshi, Kohoku-ku, Yokohama, 223-8522 JAPAN
[2] Nano Corporation, 5-12-5 Kugahara, Ota-ku, Tokyo, 146-0085 JAPAN

Introduction

Cross section roundness profile and cylindricity measurement is generally considered a significant procedure in the processing of parallel rollers requiring the highest quality in dimensional accuracy. This becomes a difficult procedure due to the fact that such rollers show extremely small dimensional error, resulting in expensive and time consuming measuring methods or, in most cases, the ignorance of the procedure itself. Such rollers are incorporated into precision stages for ultra-precision machining tools or measuring instruments, and thus we believe it is important to realize a practical method to evaluate such dimensional error precisely.

In this report, we attempt to evaluate the dimensional error of high-precision parallel rollers with a newly developed cylindricity measurement device based on a V-block three point method. The roller was supported at two points by two independent V-blocks, and measurements are simultaneously taken at three points; namely the two cross-sections supported by the V-blocks and a third cross-section. These results were analyzed to determine the roundness and average radius of the respective cross-sections, while the centers of the cross-sections were calculated and used to determine coaxiality. Furthermore, these results were combined to provide the cylindricity of the measured roller.

We started off with a device designed to support the roller at both ends. Experiments proved that this configuration provided high repeatability for the two cross-sections supported by the V-block, while the third cross-section in between showed rather lower performance.

Experimental results matched well with results from a commercially available high accuracy roundness measuring instrument, thus proving the validity of the proposed device. Repeatability of average radius, roundness and cylindricity measurement was approximately 20 nm. Furthermore, more than 300 parallel rollers of a uniform standard were measured to analyze the distribution of average radius, roundness, and cylindricity.

Measuring principle

We have already reported about the principle, hardware system configuration and basic experimental results of roundness profile measurement method based on a V-block three point method [1]. Figure 1 illustrates the cross-section of a cylindrical workpiece placed in a V-block with a taper angle of α. The cross-section of a cylindrical workpiece can be looked upon as a periodic function with a period of 2π and thus its radius $r(\theta)$ can be expressed in a Fourier series as shown in equation (1).

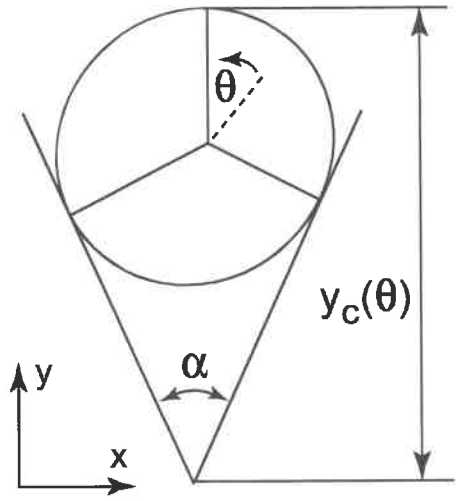

$$r(\theta) = r_0 + \sum_{k=1}^{\infty} (A_k \cos k\theta + B_k \sin k\theta) \qquad (1)$$

By arranging the measured $y_c(\theta)$ values into a Fourier series, the resultant Fourier coefficients, A_k and B_k can be easily calculated using equation (2).

$$y_c(\theta) = \left\{1 + \frac{1}{\sin(\alpha/2)}\right\} r_0 + \sum_{k=2}^{\infty} \left\{1 + \frac{\cos k(\pi/2 + \alpha/2)}{\sin(\alpha/2)}\right\} \times (A_k \cos k\theta + B_k \sin k\theta) \qquad (2)$$

If section L , M and R are the measuring points on a parallel roller, we can express cross-section roundness profiles of section L and R as eq.3 and 4.

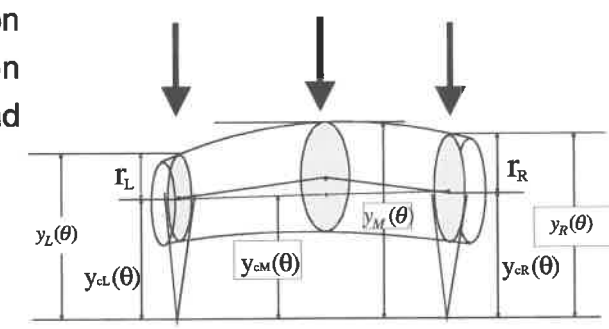

Fig.2 Cyclindricity measuring method

$$y_L(\theta) = \hat{r}_{L0} + \sum_{k=1}^{\infty} (\hat{A}_{Lk} \cos k\theta + \hat{B}_{Lk} \sin k\theta) \qquad (3)$$

$$y_R(\theta) = \hat{r}_{R0} + \sum_{k=1}^{\infty} (\hat{A}_{Rk} \cos k\theta + \hat{B}_{Rk} \sin k\theta) \qquad (4)$$

In contrast, section M is not supported by V-block. Roundness profile of section M is now calculated by $y_L(\theta)$ and $y_R(\theta)$. Central points at section L and R are given by eq. 5 and 6.

$$y_{CL}(\theta) = y_L(\theta) - r_L(\theta) \qquad (5) \qquad\qquad y_{CR}(\theta) = y_R(\theta) - r_R(\theta) \qquad (6)$$

Tentative center of section M is given by eq. 7 with central points at section L and R ($y_{cL}(\theta)$ and $y_{cR}(\theta)$).

$$y_{cM}(\theta) = \frac{1}{2}\{y_{cL}(\theta) + y_{cR}(\theta)\} \qquad (7)$$

Roundness profile of section M, $r_M(\theta)$ is expressed as eq. 8.

$$r_M(\theta) = y_M(\theta) - y_{cM}(\theta) \qquad (8)$$

Measuring instrument

Figure 3 shows the test stand based on above theory for precision parallel rollers. The instrument consists of two V-blocks, three measuring bars, capacitance type displacement sensors with a sensitivity of 0.01μm, and a miniature DC motor to rotate roller.

Our proposed device possesses double enlargement mechanism, where parallel roller is enlarged first by a V-block, and furthermore by a measuring bar which act as a lever. The former gives an enlargement rate which is a function of V-block angle α and lump order *k*. Enlargement due to the measuring bar is a constant which is determined by the distances from the supporting point of the bar to the V-block position and measuring position. In our device, the measuring bars at section L and R enlarge the y_c value to 5 times and middle bar enlarges 6 times.

The V-block was cut out of a SUJ2 steel composite block, with the contacting planes lap processed to a roughness of Ra=0.01μm. The contacting plane of the measuring bar, also lap processed. Contact length of V-block and roller is 3 mm. The measuring bars contact the roller at a width of 1 mm on section L and R and 0.8 mm on middle bar as shown in Fig. 4. Figure 5 shows photograph of the measuring

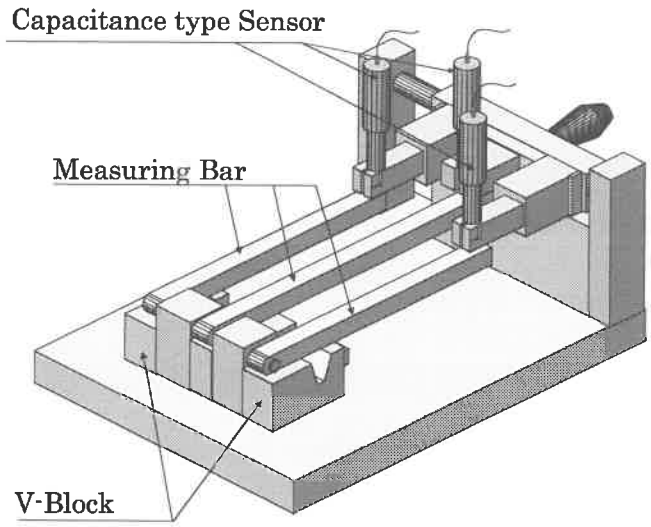

Fig.3 Conceptual design of the measuring system

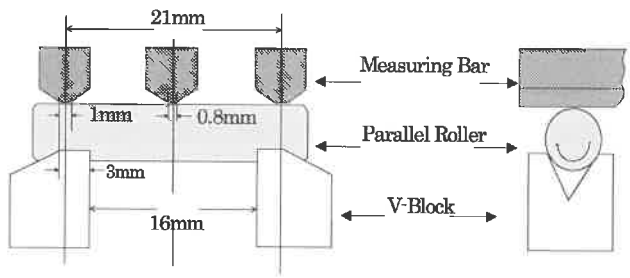

Fig.4 Enlargement of V-block

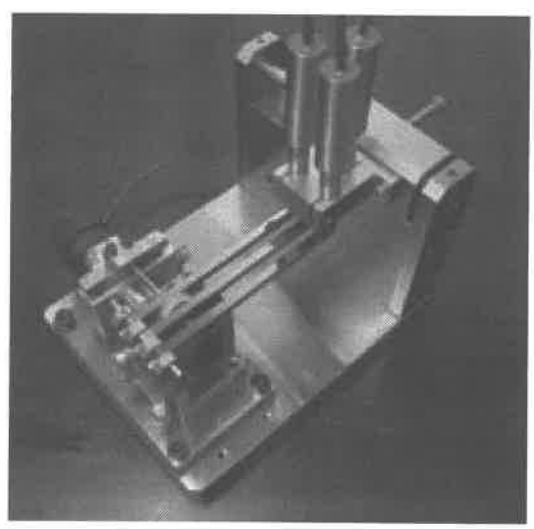

Fig.5 Photograph of the device

system.

Figure 6 shows the measured middle cross-section profiles of a single roller. These measurements were repeated 3 times, where the roller was taken off the V-block after each measurement. The results in the figures prove high repeatability, thus demonstrating the validity of the device.

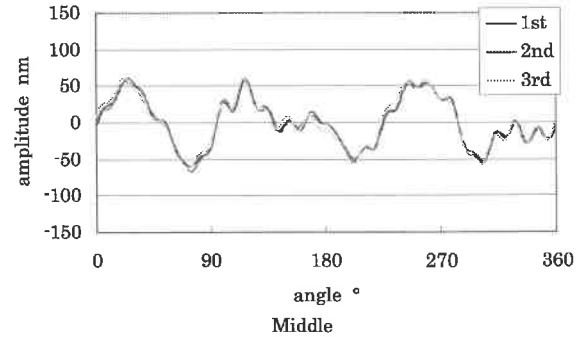

Fig.6 Repeatability

Experimental results

Measurement experiments were conducted on JIS P1 grade high-precision parallel rollers, 4 mm in nominal diameter and 25.7 mm in length and processed from SUS 440J2 bearing steel. Tolerance zone in diameter is $4^{+0}_{-0.001}$mm. The surface of the rollers were lapped. The measurement on each roller was done by four consecutive rotations. Sampling rate of the data was 256 points in a roller rotation. Figure 7 illustrates the base radius values of the 344 sample rollers.

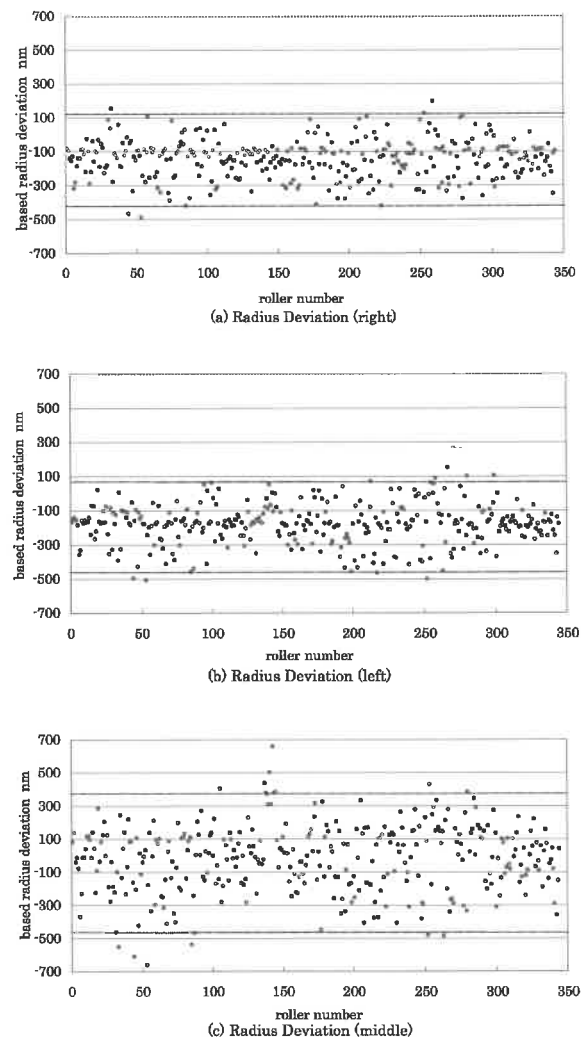

Fig.7 Relative radius distribution

Conclusions

In this report, the measuring principle and the test stand for the cylindricity measurement of parallel rollers are described, followed by analyzed results of roundness and base radius deviation at three cross sections for 344 sample rollers were shown.

Reference

[1] K. Goho, K. Mitsui and A Hayashi: Development of a Roundness Profile Measurement System for Parallel Rollers Based on a V-Block Method, JSME International Journal, Series C, Vol.42, No.2(1999)410.

MEASUREMENT OF DRILLING BURR BY IMAGE PROCESSING TECHNIQUE

Yohichi Nakao
Kanagawa University, Yokohama, Japan

1. Introduction

Drilling operations are used as the most common machining processes for making circular holes to parts. Because of plastic deformation of the workpiece during drilling, drilling burrs are generated at both sides of the entrance and exit of machined workpieces. In particular, the burr size at the exit side tends to be large, which requires deburring processes to finish the parts. The deburring processes are additional machining operations, consequently it results in an increase of machining costs. Therefore, the drilling technique that requires few or no deburrings must be a key for reductions of machining costs. It is important to study the mechanism of the burr formations to develop the effective drilling technique. Many experimental and theoretical studies on drilling burr formations have therefore been conducted [1]-[4].

Measurements of size and profile of every drilling burr created in the experimental studies are vital to evaluate the experimental results. Two measurement methods for the burr size have been mainly used in these studies. Direct burr measurements have been conducted with universal profile projectors. In another method, resin mold of the burr have been cut and then used for indirect burr measurements by universal profile projectors. These methods require inconvenient processes and much time to measure.

The purpose of this work is to develop an effective measurement technique for drilling burr profiles; a burr thickness and height. The present paper describes simple and convenient measurement technique of the drilling burr profiles and a developed drilling burr measurement system based on image processing techniques. Measurement tests using the developed system have then been conducted. An outline of the technique and the developed system will be described with measurement results in the following sections.

2. Measurement Method

Figure 1 shows a schematic of the setup consisting of a measured burr specimen and four mirrors. An image of the measured burr specimen is taken with a CCD camera located right above the burr specimen. A feature of the present measurement method is in the method for taking side images of the burr specimen. A key idea of the measurement method is to take image of the side surfaces of the burr by means of the set of four mirrors, in which the angle between mirror surface and setup base is 45 degrees, located around the measured burr. In this case, images of four side surfaces of the burr are projected to upper direction by the mirrors. Consequently, both images of top and side surfaces of the burr can be taken by CCD camera, simultaneously. An original three-dimensional burr image can be therefore transformed to a two-dimensional image, which is effective to avoid complicated calculations of three-dimensional image data. A rod with circular cross section is inserted into the drilled hole of the specimen in order to shut out the

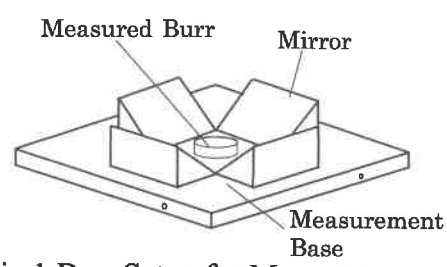

Fig.1 Burr Setup for Measurement

opposite side surface of the burr for convenience in the following calculations.

3. Calculation of Burr Thickness and Height

Figure 2 shows a flowchart of a series of calculations for burr profile measurements. In advance of an analysis of the burr profile at a last step of the calculations, conventional image processing techniques such as the binary image processing, the noise reduction and the labeling are applied for measured image data. Top surface and four-side surface images of the burr profile are obtained as shown in Fig. 3(a). The binary image processing is applied for the measured image data. Examples of binary imaged burr profiles are shown in Fig. 3(b). Here, each image as shown in Fig. 4 is then named as I, II, III, IV and V, respectively. After the noise reduction and the labeling process, the labeled images of the burr; I, II, III, IV and V; are analyzed at the final step.

A two-dimensional coordinate system in Fig. 4 is then defined for the analysis of the binary imaged and labeled burr profiles. Burr height and thickness are calculated based on the defined coordinate system. By the image processing techniques, the pixels corresponding to the burr areas become 'black', whereas all other pixels become 'white'. Analyzing the area I, the burr thickness can be given by the length between point A and B. Burr heights are obtained from the analysis of the pixel of each area labeled as II, III, IV and V. In this case, the burr thickness is given by length between point C and D in the case of the area II, for example.

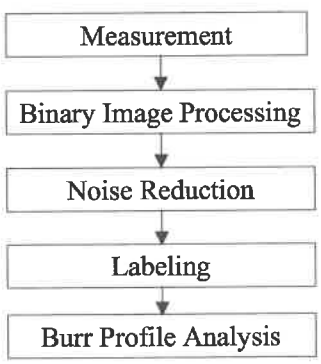

Fig. 2 Flowchart

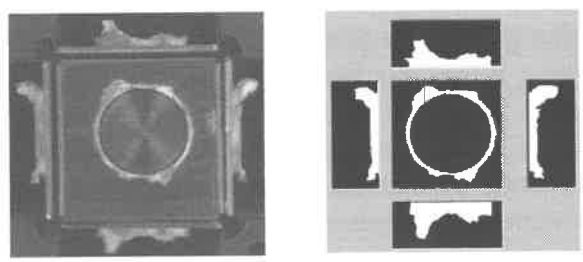

(a) Original Burr Image (b) Binary Imaged Burr

Fig. 3 Sampled Burr Image

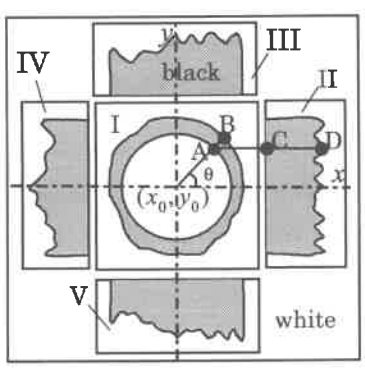

Fig.4 Coordinate System for Analysis

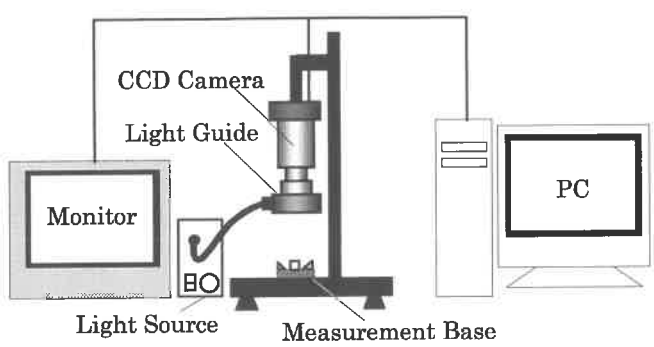

Fig.5 Schematic of Measurement System

4. Measurement System

4.1 Measurement Instrument

Figure 5 shows a schematic of the developed measurement system. A measured specimen is set on a designed base in which four mirrors are fixed at particular positions. Consequently, whole side surface images of the burr specimen on the base are projected to upper direction. Controlled light is supplied to the measured burr through optical fiber cables from a light source device. A CCD camera is fixed right above the measured burr. A taken burr image is recorded in a computer memory and then analyzed by the developed software. A resolution of measured burr image using the system is approximately 40 μm.

4.2 Measurement Accuracy

Total measurement accuracy of the system depends on the accuracy of both the measurement process using developed instrument and the analyzing processes using developed software. The accuracy of each process has been examined. Simple objects have been measured and analyzed instead of actual drilling burrs in these tests.

Accuracy of the analyzing processes has first been examined using a simple image data. For the test, precise image data was made as a model of actual drilling burr. The modeled burr image is an ideal uniform burr with 1.81mm burr thickness and height. Calculated results are given in Fig. 6 (a) and (b), respectively. Average values of the analyzed burr thickness and height are 1.84 mm and 1.81 mm. Each calculation error is 30 μm and 0 μm in average.

Similarly, accuracy of the measurement processes has been examined using a specimen as a model of an actual drilling burr with ideal uniform burr. A thickness and a height of the model are 1.93 mm and 2.0 mm, respectively. Calculated results are shown in Fig. 7(a) and (b). Average values of calculated burr thickness and height are 1.875 mm and 2.037 mm. Each calculation error is 55 μm and 37 μm.

5. Measurement of Drilling Burr

Figure 8(a) shows an example of a measured drilling burr. Using the developed instrument, both a top surface image and four side surface images have been obtained as shown in Fig. 8(b) and then have been analyzed by the developed software. Calculated burr thickness and height are given in Fig. 9(a) and (b), respectively. The standard deviations of the calculated burr thickness and height are 0.254 mm, 0.258 mm, respectively. In contrast, another burr as shown in Fig. 10 has been also measured and the result is given in Fig. 11(a) and (b). In this case, the standard deviations of the calculated burr thickness and height are 0.071 mm, 0.057 mm, respectively. It is considered that uniformity or other features of the burr profiles can be represented by these standard deviations or other statistical values. Using these values, for example, it is possible to investigate repeatability of the drilling burr formation by same machining condition and classify types of created burrs such as "uniform-type burr" and "crown-type burr", in more objective ways.

6. Summary

A measurement method for drilling burr profile was presented and a measurement system was developed. The measurement method is based on image processing techniques. In particular, a set of mirrors is used to take side surface images of measured burrs. Measurement accuracies of the measurement system and results of actual drilling burr measurement tests are presented. Developed system will be a useful tool for studies on drilling burr.

References

[1] Shikata, M. F. DeVries and S. M. Wu, "An Experimental Investigation of Sheet Metal Drilling", Annuals of the CIRP, 29, 1, 1980, pp.85-88.

[2] T. Miyake et. al., "Study on Mechanism of Burr Formation in Drilling", Journal of the Japan Society of Precision Engineering", 57, 3, 1991, pp.485-490 (in Japanese).

[3] H. Takeyama et. al., "Study on Oscillatory Drilling Aiming at Prevention of Burr", Journal of the Japan Society of Precision Engineering", 59, 10, 1993, pp.1719-1724 (in Japanese).

[4] Y. Guo, D. A. Dornfeld, "Finite Element Modeling of Drilling Burr Formation Process in Drilling 304 Stainless Steel", Trans. ASME. J. Mfg. Sci. & Eng., 122, 2000, pp. 612-619.

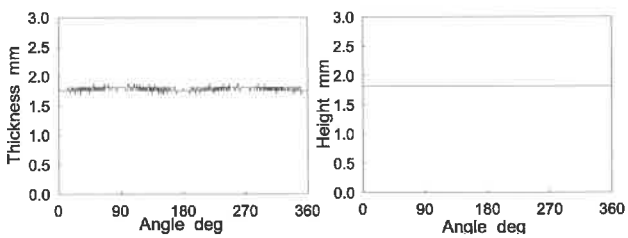

(a) Burr Thickness (b) Burr Height

Fig. 6 Calculated Profile
(Measured Object: Image Data)

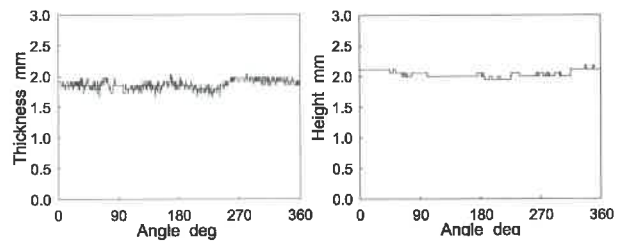

(a) Burr Thickness (b) Burr Height

Fig. 7 Calculated Profile
(Measured Object: Burr Model)

(a) Burr Sample

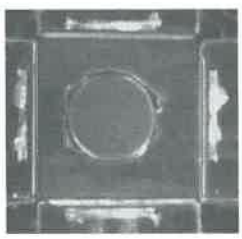

(a) Projected Burr Image

Fig. 8 Measured Burr

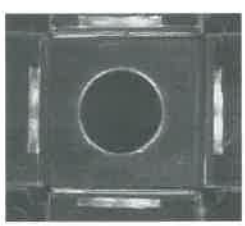

Fig. 10 Projected Burr Image

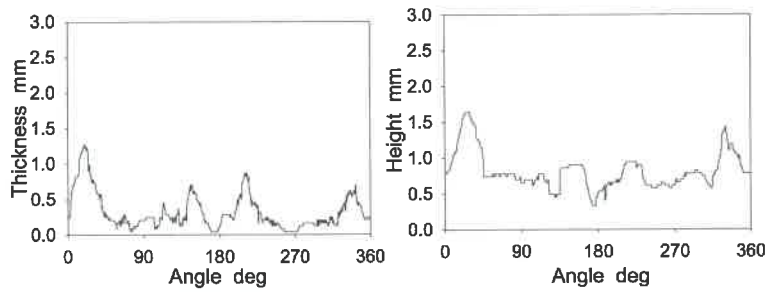

(a) Burr Thickness (b) Burr Height

Fig. 9 Calculated Burr Profile
(Measured Object: Actual Burr)

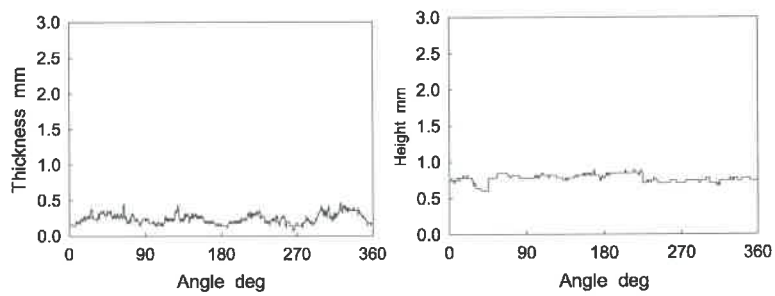

(a) Burr Thickness (b) Burr Height

Fig. 11 Calculated Burr Profile
(Measured Object: Actual Burr)

A Study on Evaluation of Sphericity and Related features of Shaft with Spherical End Faces

Masaaki TAKAHASHI
Institute of Technologists, Saitama,Japan
Kazuyuki SASAJIMA
Tokyo Institute of Technology, Tokyo,Japan
Tadao TSUKADA
Meiji University, Tokyo,Japan

Introduction

Recently, for introducing the G.P.S. (Geometrical product specification) to the technical drawings and the machining, the assessment of the related features (position, concentricity, symmetry) is getting more important. For example, this paper describes assessing of spherical parts that have the shaft and spherical end face. For assessing this part, it is very important not only measuring a form of the sphere, but also estimating a related feature between sphere and shaft.

The authors have developed the spherical coordinate instrument. Using with this system, the form deviation of the specimen is obtained in the spherical coordinates. Furthermore, the technique is presented to assess the related feature between the straight shaft and the sphere of end faces .

Measuring System

As shown in Fig.1 , the instrument has a vertical and a horizontal high accuracy air spindles. These two spindle axes cross perpendicularly to each other. The spherical specimen is set on the vertical spindle. And the measuring probe is mounted on the horizontal spindle. By rotating these tow spindles, the probe generates a sphere datum. The form deviation of specimen surface from an accurate sphere form is obtained. In this system, it is possible to use the sensor which has a very high resolution with short measurement range. In this paper, the laser type sensor with 0.005μm (max.) resolution is used. For the experiment, the measurement range is set to +30μm~-30μm.

In this system, the measuring area covers the whole sphere except holding part of the spindle. Also, it is possible to measure the form of asphere within a limited range of the probe.

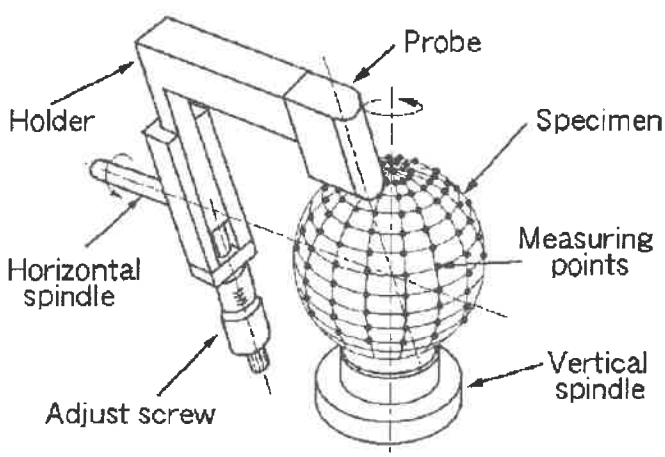

Fig.1 Measuring system

Specimen

As mentioned above, for introducing the G.P.S. (Geometrical product specification) to the technical drawings and the machining, the assessment of the related features (position, concentricity, symmetry) is getting more important. A typical example of this problem, the assessment of spherical parts that have the shaft and spherical end faces (Fig.2) is selected. It is very important not only measuring a form of the sphere, but also estimating a related feature between sphere and shaft.

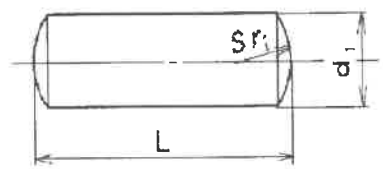

Fig.2 Specimen

Measurement setup

It is necessary for assessing the form of the sphere and the related feature to measure the sphere and shaft at the same time. For this purpose, the measuring system is arranged as shown in Figure 3. The specimen is mounted to the vertical spindle. For measuring the spherical end face, the probe rotates around the horizontal spindle and the specimen rotates around the vertical spindle. For assessing the related feature between sphere and shaft, the probe is set to the horizontal direction. Then the measurement data of shaft is obtained by rotating the vertical spindle. If exceed sensor range, the probe is adjusted by the adjust screw (Fig.1).

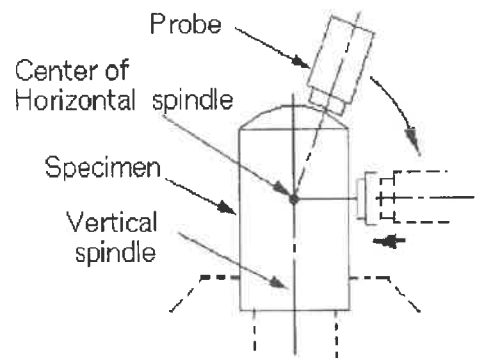

Fig.3 Measuring probe and specimen

Analysis

For the measurement and evaluation of sphericity, a best fit sphere by the least square method is applied. The data close to pole are not situated in equi-distance when the data measured by the spherical coordinate instrument. Then , we introduced weight function related to region of a data point area.[1]

For the estimation of a related feature between the sphere and the shaft, it is necessary to get a position of sphere center and a position of the shaft center . From the former data of sphericity measurement, the sphere center is obtained. From the latter data of the shaft measurement, the shaft center is defined. The roundness of shaft part of specimen is measured and calculate the position of the shaft center using a best fit circle by the least square method.

Result of experiments

Table 1 shows the specification of shaft for experiments. This specimens has been ground with center-less grinder and specially provided grinder.

The measuring data of the end faces of the sphere have gotten 200 point (interval 1.8 degree) during a one revolution of the vertical spindle. And the horizontal spindle have been positioning from pole(θ =0 degree) to θ =24.3 (S1), 35.1 (S2) degree (interval 0.9 degree).

Figure 4 shows the contour map of form errors of spherical end face. The error of local sphere form assessed by means of least square method fitting a sphere form to measured data.

Table 2 shows the result of experiments. P.D.S.(Profile deviation of Any surface) shows the form errors of spherical end face. The data of position deviation shows the related feature between sphere and shaft.

Figure 5 shows the cross-section form through the pole in Figure 4. Figure 6 shows the cross-section form measured with Form talysuf for the same specimen. It shows good similarity.

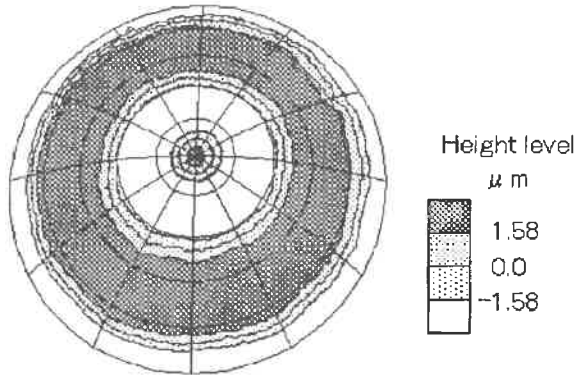

Fig.4 Contour map for S1

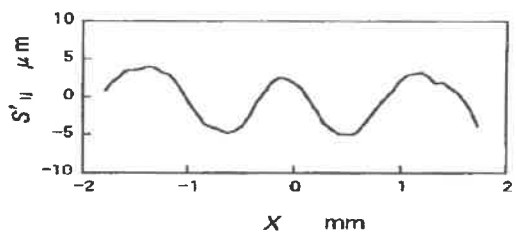

Fig.5 Cross-sectioned form through the pole in Fig.4

Tab.1 Specimens

Specimens No.	d1 mm	L mm	r1 mm
S 1	ϕ 5	71	4.5
S 2	ϕ 4	17	2.8

Tab.2 Result of experiments

Specimens No.	Profile deviation of Any surface(P.D.S.) PV μm	rms	Position deviation e s mm
S 1	13.0	1.58	0.79
S 2	6.5	0.70	1.48

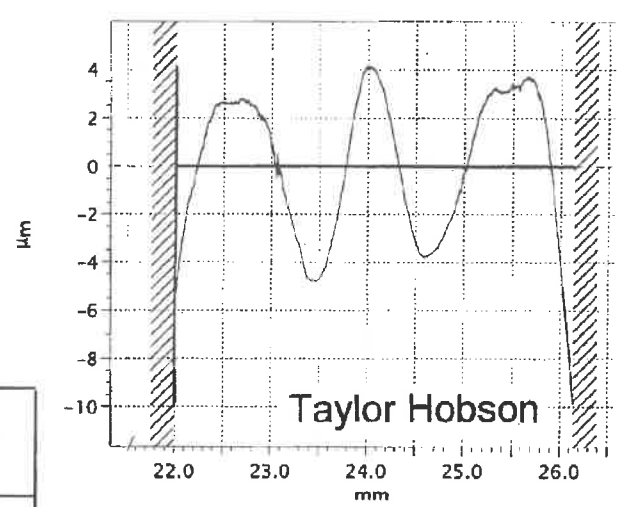

Fig.6 Cross-sectioned form through the pole with the Form talysuf

Effect of shaft's form error

Getting data from experiment setup as shown as Figure 3, it is expected the measuring error of shafts center. To consider of this effect, the form error of shaft is assessed. Using with cylindricity measuring instrument with a air rotating table (Rondcom 50A-150: Tokyo Seimitu), the form data of the shaft of the specimen is measured. For every section data, it is fitting circle by least square method as shown in Figure 7.

Figure 8 show the experimental result for shaft S1. The center of position error is smaller than 0.03μm.

From this study, it is obvious that effect of the form error of shaft is small, in this case.

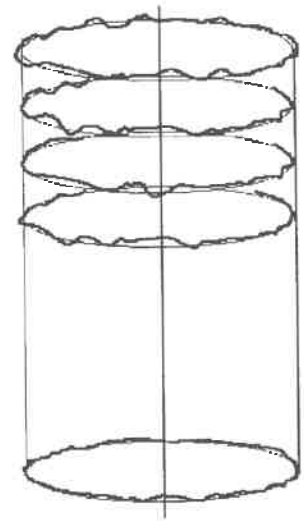

Fig.7 Fitting circle for section

Conclusion

This paper presented the study on the evaluation of spherical part that have the shaft and spherical end face. A new measuring technique using with spherical coordinate system is presented.

Acknowledgment

The author thanks to M. Daito of TNK SANWA PRECISION CO. LTD. for his knowledge.

1. Masaaki Takahashi,Tadao Tsukada,Kazuyuki Sasajima, Measurement of Partial Sphere by Spherical Coordinate System (3rd Report) Journal of Japan Society for Design Engineering, 34(6),196(1999) (in Japanese)

Keyword: Sphere, form, measuring, related features

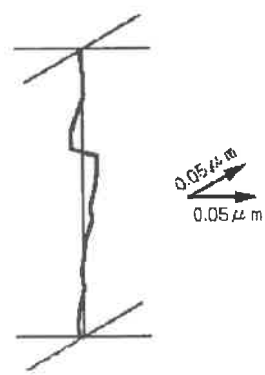

Fig.8 Center line of shaft

OPTICAL METROLOGY OF MICRO-ELECTRO-MECHANICAL TORSIONAL MIRRORS

X. Zhang, Y. Shen*, D. J. Nagel
George Washington University, Washington D.C., 20052
N. M. Rensing
MicroOptical Engineering Corporation, Westwood, MA 02090

Abstract — An optical reflectometer was designed, built and calibrated for measurement of the dynamics of MEMS resonant torsional micro-mirrors. The resonant frequency of the micro-mirror used for this study was measured as 3.997 kHz, the maximum rotation angle was measured as ± 4.32° (± 8.64° optical) and the quality factor (Q) was measured to be 88.8. The mechanical behavior of the MEMS torsional mirror, including normal modes, frequency and static response, were simulated by using finite element analysis (FEA) software MSC NASTRAN/PATRAN. The computed resonant frequency is within 0.1% of the measured frequency. The computed rotation angle is within 6% of the measured angle.

Key words — Micro-Electro-Mechanical Systems (MEMS); Optical metrology; Reflectometer; Finite element analysis; Torsional micro-mirror.

I. INTRODUCTION

Precise characterization of the dynamic mechanical response is a primary concern in MEMS metrology. Dynamic parameters such as displacement, rotation angle, resonant frequency and quality factor must be determined for better understanding of MEMS devices. However, the size of MEMS structures and their high frequencies make measurements difficult. As a result, there is a need for the development of metrology tools specifically designed for the dynamic measurement of MEMS devices. This research employs a laser reflectometer to measure the motion of a MEMS mirror, and compares the experimental results with FEA calculations.

II. DESIGN OF MICRO-MIRRORS

Torsional scanning micro-mirrors are small, highly reflective, and offer interesting opportunities for small display devices used in head mounted displays [1]. Fig. 1 shows the schematic of the torsional mirror designed by the MicroOptical Engineering Corporation (Westwood, MA). The mirror was fabricated at the Northeastern University (Boston, MA) Microfabrication Laboratory [1]. The central mirror is 1 mm on a side and about 20 μm thick. The mirrors are electrostatically driven at frequencies in the range from 4 to 8 kHz and can achieve mechanical rotation angles up to ± 4° (± 8° optical) at their resonant frequencies [1].

The mirror body is made out of single silicon substrate material by bulk micromachining. The thickness, mass, and stiffness of the mirror are defined by a patterned etch from the backside of the wafer. An etch from the front defines the mirror's length and width. To support and actuate the mirror, two torsional support bridges are made by electroplating nickel on top of the silicon layer. Two anchors connect each support bridge to the wafer and the mirror, and also serve as the actuators. These anchors are equal in height and define the gap of the actuating

* Correspondence to: Yin-Lin Shen, Academic Center T727, MAE Dept., GWU, 801 22nd Street, NW, Washington, DC 20052. Phone: (202) 994-5995, Fax: (202) 994-0238, Email: shen@seas.gwu.edu

capacitors. Two electrodes underneath each bridge and on either side of the axis of rotation can be used either to excite or sense the motion of the mirror. The actuation of these devices is electrostatic. The actuating electrostatic force is provided by applying a voltage to one of the electrodes on the wafer surface and grounding the mirror support electrode. This force results in a torque which then causes the mirror support and mirror to rotate. The sensing electrode is used to detect the motion of the mirror by measuring the capacitance [1].

III. DESIGN OF OPTICAL REFLECTOMETER SYSTEM

Reflective sensing is widely used in measurement applications, because of its characteristics of high accuracy, simplicity, and non-contact. The photograph of the reflectometer arrangement is shown in Fig. 2. A light beam from a solid-state laser is focused through a pinhole, passes through focusing lenses, and converges to a spot of 20 μm in diameter on the mirror surface. The incident light spot can be positioned on the center of the oscillating mirror by carefully adjusting the mirror position under a microscope. A second lens refocuses the reflected light on a transmission screen which is imaged by a computer-based CCD camera. The image is a streak, whose length is proportional to the angle through which the driven mirror oscillates. A commercial image analysis software, namely the Andromeda Measurement Filter, is used for the construction of the calibration curve based on the characteristics of the focused spot from the mirror when it is stationary, and to measure the extent of the streak formed by the oscillating mirror. A micrometer-controlled calibration device was used to relate the mirror deflection angle to displacement of the reflected and focused light along the screen.

IV. MEASUREMENT AND DATA ANALYSIS

A. Calibration

The output signals of the laser reflectometer system are optical streaks, with length determined by the angle through which the driven mirror oscillates. The length of the optical streak on the screen should, preferably, be linearly related to the rotation angle of mirror surface. Linearity depends upon the geometry and placement of the screen, the quality of the optics system used to refocus the light spot onto the screen, and on the quality of the CCD camera, i.e. any optical distortion introduced by camera lenses. A calibration function or table over the whole angular range must be employed to correct for non-linearity.

The calibration device consists of a glass plate reflector, provided with a micrometer is used to control its displacement and rotation angle. To generate the rotation, the micrometer is used to move a probe tip, which presses down on the glass plate. A spring underneath the glass plate ensures tight contact between the probe and the glass plate. Displacement as small as 1 μm can be achieved at the probe tip, corresponding to an angle of 0.0056°. The resultant displacement of the laser dot in the image is captured by the CCD camera and used to calibrate the system.

B. Rotation Angle and Resonant Frequency Measurements

The maximum rotation angle and resonant frequency can be determined by measuring the length of the light streak as a function of excitation frequency. For this data, the rotation angles can be obtained using the calibration curve obtained. The resonant frequency is the frequency where rotation angle achieves the maximum value. The averaged data from several measurements are shown in Fig. 3. The resonant frequency of the mirror is found to be 3.997 kHz. The maximum full sweep rotation angle of the mirror was 4.32°. The quality factor (Q) of

the system can be obtained by measuring the frequency bandwidth (B) about the resonant frequency. The quality factor is calculated as 88.8. The relationship between rotation angle and drive voltage magnitude was studied by varying the magnitude of drive voltage from 65 V to 170 V (peak). The frequency of drive voltage was fixed at the resonant frequency of 3.997 kHz. The result curve shows a non-linear behavior as expected. The force in an electrostatic actuator is a function of V^2, where V is the drive voltage.

The experimental rotation angle *vs.* frequency curve can be decomposed into several components to study the dynamic characteristics of the micro-mirrors. For this mirror the response contains six decomposed curves, as shown in Fig. 3. It can be seen that most of the additional components in the response are at frequencies higher than the resonant frequency. The best fit number and location of the peaks can vary depending on the specific operations used to calculate the decomposition of the averaged data. Hence, these details are less important than the appearance of the additional near-resonance peaks.

V. FEA SIMULATION OF MICRO-MIRRORS

Normal mode, frequency response, transient response and static simulations of the micro-mirrors were done by using FEA program MSC NATRAN/PATRAN [3]. The resonant frequency of the mirror was calculated to be 3.994 kHz. This value is within 0.1% of the measured resonant frequency of this micro-mirror, which is 3.997 kHz.

In frequency response simulation, the micro-mirror was excited under a frequency-varying excitation in a range of 0 ~ 300 kHz. A damping factor of $\zeta = 0.006$ is used. The result shows the micro-mirror reaches a resonant peak at 4.02 kHz, a second peak at 20.32 kHz and a third peak at 38.46 kHz. The maximum displacement of the edge of the mirror is 40.03 μm at the resonant frequency. The rotation angle at the resonant frequency can be calculated as 4.58°. This value is within 6% of measured maximum rotation angle of 4.32°. The error is mainly due to the selection of the damping factor. Since the mirror was packaged in a vacuum, a small damping factor of 0.006 is used in this work. However, the damping factor of 0.006 is not verified and it is not an accurate value. This simulation shows that the real structural damping factor may be slightly larger than 0.006.

To compare the dependence of rotation angle on the drive voltage, the drive frequency was set to the measured resonant frequency of 3.997 kHz. Simulation shows the FEA result values are slightly higher than experimental curve. The rotation angle difference between the two curves is 0.1°. The simulated maximum rotation angle is 4.4°, which is within 2.3% of the measured value. The result of this simulation also verifies that the structural damping factor 0.006 is smaller than the actual damping factor of the device. Had we increased the damping factor to some extent, the simulation result would have matched the experimental result more precisely.

VI CONCLUSIONS

Measurements, simulations and analysis were employed to characterize a MEMS torsional mirror. The resonant frequency of a micro-mirror was measured to be 3.997 kHz, the maximum rotation angle was 4.32°, and a quality factor (Q) of 88.8 was obtained from the frequency response data. The computed resonant frequency is within 0.1% of the measured frequency. The computed rotation angle is within 6% of the measured angle. Simulation shows the damping factor of 0.006 is smaller than the actual damping factor of the device. The reflectometer and NASTRAN were proved to be effective experimental and computational tools. The micro-mirror exhibited a more complex frequency dependence than expected. Its origin is not understood.

ACKNOWLEDGEMENT

This work was supported in part by the National Science Foundation under Grant No. DMII-9624966. The support is appreciated. The mirrors were fabricated by MicroOptical Corporation under DARPA contract DAAK60-96-C-3018. The devices were fabricated by Robert McClelland of MicroOptical Corporation at the Northeastern University Microfabrication Laboratory. We would also like to thank Dr. J. D. Lee, Dr. Y. P. Chen, C. Behnke, B. Rutkowski, J. Petrella, Y. Zou and B. Ruppel for their contributions.

REFERENCES

[1] N. M. Rensing, S. Dodson, G. G. Adams, P. M. Zavracky, R. W. McClelland, and A. Lemoncelli, "Modeling, simulation and testing of non-Linear resonance behavior in MEMS torsional mirrors with mechanical-electrostatic coupling," *1999 ASME International Congress and Exposition,* MEMS-- vol. 1, pp. 143-150, 1999.

[2] X. Zhang, "Characterization of MEMS torsional mirrors by optical metrology and finite element analysis," Master Thesis, The George Washington University, Washington D.C., May 2001.

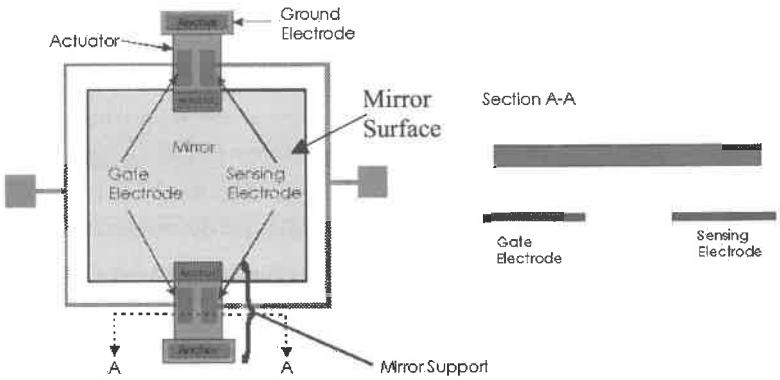

Fig. 1. Schematic of the Torsional Mirror.

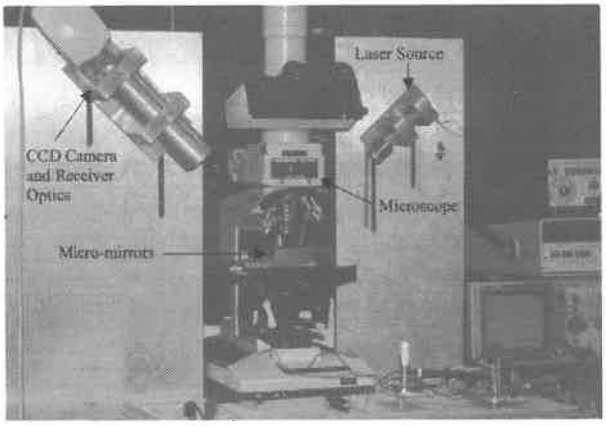

Fig. 2. Photograph of the Optical Reflectometer.

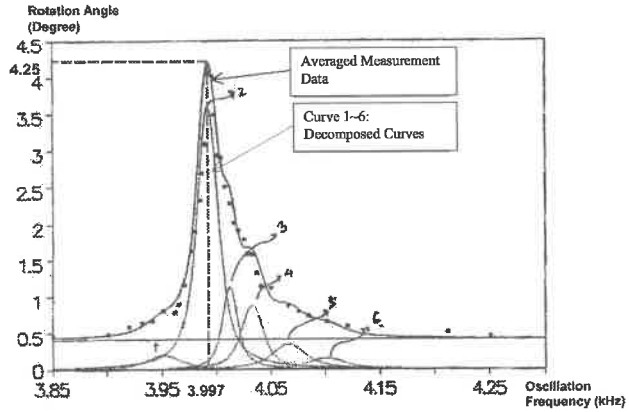

Fig.3. Component Peaks in Micro-mirror Frequency Response Curve.

CALIBRATION OF CMM BY 3-DIMENSIONAL COORDINATE COMPARISON

Makoto Abbe*, Kiyoshi Takamasu** and Shigeo Ozono***
* Tsukuba Institute of Research and Development, Mitutoyo Corporation
430-1, Kamiyokoba, Tsukuba, Ibaraki, 305-0854, JAPAN
** The University of Tokyo
7-3-1, Hongo, Bunkyo, Tokyo, 113-0033, JAPAN
***Tokyo Denki University
2-2, Kanda-Nishikicho, Chiyoda, Tokyo, 101-8457, JAPAN

1 INTRODUCTION

This paper presents a new calibration method particularly for up to middle size CMM. The method is able to provide the 21 parametric errors only by performing the coordinate comparison. An automated calibration system for production stage of CMM is realized.

Numerical compensation of geometry for CMM has been popular in these days. Still, each specific mechanical component may show peculiar shape in its geometry due to manufacturing reasons. This fact requires manufacturers to calibrate and map the naked geometric error of CMM on the production stage each respectively.

Several methods have been proposed [4]. Direct assessment of the error component by adequate instruments e.g. laser interferometer or electric level are adopted. This method has been widely used since each error component can be detected directly with reasonably high accuracy and high spatial density instead its tedious operation complexity. Other trend in the recent years is introduction of the artefact method typically performed on the ball plate [1]. Reasons the method become popular can be: 1) tools with inexpensive and ease to use realizes rapid calibration, 2) well known mathematical processes are able to distribute indication error obtained by the artefact measurement into the parametric errors of CMM, e.g.[2][3].

Paying attention to robustness and automation possibility of the artefact method, authors consider building a new calibration method which utilizes a kind of programmable three dimensional sphere grid maintained by the reference CMM. The object CMM can then be calibrated by means of three dimensional coordinate comparison. Handing over portability, such as possibility of onsite calibration at customer site, to already proposed artefact method, the study is to be focused on the parametric calibration of up to middle size CMM in the production floor.

2 COORDINATE COMPARISON

Figure 1 shows a schematic of the proposed calibration system. The reference CMM attaching a touch trigger probe and a sphere on its measurement spindle traverses and positions successively to form a virtual sphere grid. The calibration of an object CMM is carried on by performing three dimensional coordinate comparison through the sphere feature as shown on Fig. 2. The system superimposes the measurement volume of the reference CMM into that of the object CMM. While the appearance bears some resemblance to that of the calibration with the ball cube, the method introduces characteristic which is able to obtain higher data density in space as the conventional direct method.

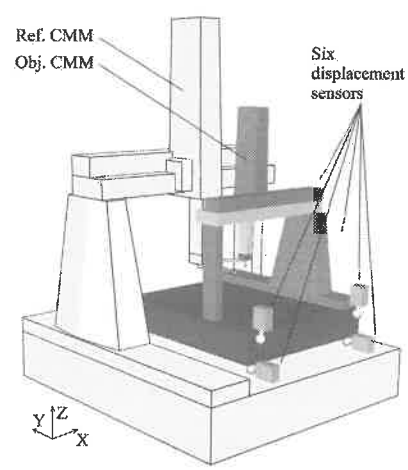

Fig. 1 Schematic of three dimensional coordinate comparison

2.1 Relative sphere position

Relative position information of sphere is essential to quantify indication error of the object CMM in the measuring volume since observed indication error is input to the whole calibration procedure. The parametric error of the CMM is acquired as the final calibration result. The parametric error obtained only by using the relative position information may provide Cartesian coordinate frame to the object CMM. It is necessary to consider way to keep traceability to the length standard.

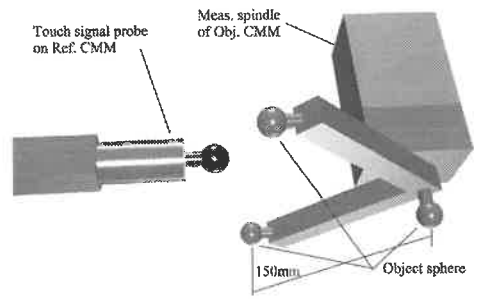

Fig. 2 Example of three probe vectors on object CMM

2.2 Traceability to Length Standard

Geometric calibration activity generally demands a standard gauge with smaller uncertainty, typically one fifth or one third, than that of the object to be calibrated. It seems however economically not to be wise to require small enough uncertainty for every measurement task on the reference CMM for the three dimensional coordinate comparison. Based on fact that it is not difficult to maintain reasonably accurate Cartesian coordinate frame on the reference CMM the traceability of the calibration system to the length standard can be kept by adopting an end gauge. The other possibility is to describe statistically propagated uncertainty through linear system [6].

2.3 Calculation of Parametric error

There are two major methods to calculate parametric errors of CMM. One is *step by step calculation* and the other is *linear regression*. The former evaluates each parametric error by corresponding measurement. The latter estimates parametric errors at once from a batch of observation data. Referenced reports[1,4] indirectly compare some aspects of these two methods as *direct method* and *self calibration method*. With all their differences, [4] reports that there is no significant different result observed. Authors take a similar view about result of the calibration of CMM. It seems safe to say that either calculation principle provides comparable result.

However, actual measurement procedure required by the adopted calculation principle shows different view. Adopting *step by step calculation* a set of the measured points have direct relation with the corresponding parametric error. It means that measurement strategy drawing spatial distribution of observation points is fixed depending on the kinematic structure of the CMM. On the other hand, adoption of *linear regression* allows us to arrange positions for measurement almost arbitrary if proper response is kept for the focused parametric error. A kind of programmable sphere grid is going to be built. Noticing the flexibility, the latter method is chosen here to calculate the parametric error.

Adopted model includes 21 parametric error components and typical components for thermal expansion. Major components are described by piecewise polynomials with proper order respectively. The model is so designed as to be solved by conservative linear regression technique. Estimated components can be transferred to a CMM controller to execute error compensation.

3 CALIBRATION EXPERIMENT

The calibration method and the measurement strategy mentioned in the above are applied on CMM in the production floor. Here, one of the typical example is presented.

3.1 Measurement strategy

Observation of the indication error of the object CMM carries on like that of the ball plate

method as follows. The reference CMM traverses and positions a sphere supported on the measurement spindle. The object CMM measures this sphere by co-operating with a touch signal probe and the other sphere on it. Simple least squares give the center coordinate of the sphere as the indication error of the object CMM. Fixing the approaching procedure to measure the sphere, major systematic errors caused by the touch signal probe can be rejected from the calibration result.

An example of the designed measurement strategy is shown in Fig. 3. Approximately 400 points are positioned and measured to accumulate indication error of the object CMM. Calibration measurement on CMM requires us to adopt at least three different probe vector if all 21 parametric errors are to be evaluated. The requirement is also fulfilled on the measurement strategy shown in Fig.3 although it is not visible.

3.2 Observed indication error

Figure 4 shows an example of indication error of the object CMM. The data is obtained on the measurement line along the X axis. A couple of figures a) on the left side is measured at Z=400mm that is the top of the volume. The b) on the right side is at Z=0mm the bottom of the volume. Each plot from the top to the bottom corresponds to deviation in X, Y and Z direction respectively. The circle and the square indicates measurement direction in forward and reverse. It is clear that three dimensional indication error of the object CMM is measured with high spatial density under the fully automated operation.

3.3 Measured and Predicted Error

Figure 5 shows the indication error of the object CMM actually measured by the three dimensional coordinate comparison and the predicted error calculated from the estimated parametric errors. The estimated parametric error can be used to compensate the CMM. When the model explains geometrical error of the object CMM perfectly the measured error and the predicted error become a pair of vectors with equal length in opposite direction. Figure 6 shows the estimation residual by subtracting them. As far as visually observing distribution of residual error there seems not to be systematic trend.

3.4 Verification by Conventional Calibration

Since it seems not simple to compare the whole consequence from the three dimensional coordinate comparison method and that from the conventional calibration method. Adopting both calibration method on a CMM, spatial distribution of the estimated parametric errors are compared to see some aspects of the verification. Figure 7 presents a comparison example of one of the X

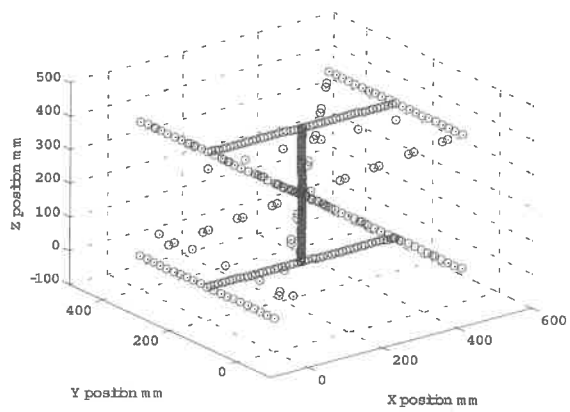

Fig. 3 Measurement strategy for coordinate comparison

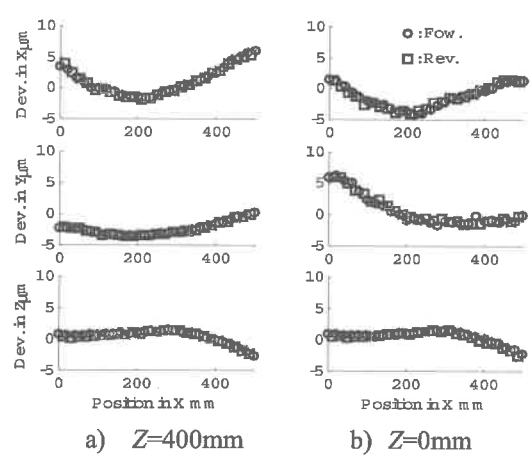

a) Z=400mm b) Z=0mm

Fig. 4 Observed three dimensional deviation along X axis of object CMM

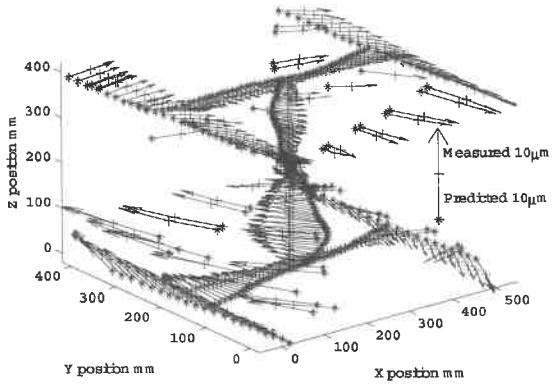

Fig. 5 Measured and predicted deviation

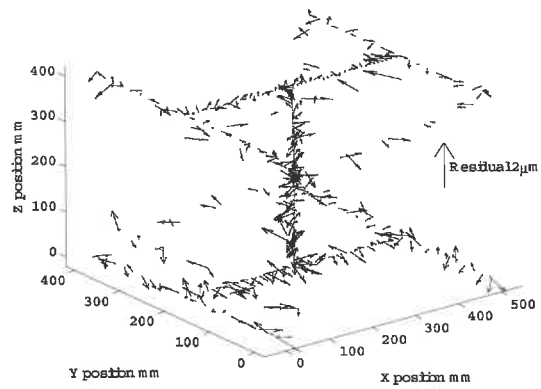

Fig. 6 Estimation residual after calibration

straightness component. With in the top plot, the solid line shows the component obtained by the three dimensional comparison method. The broken one does the component obtained by the conventional laser interferometer respectively. The bottom plot shows difference of the two components in the top plot. Both components agree with each other well.

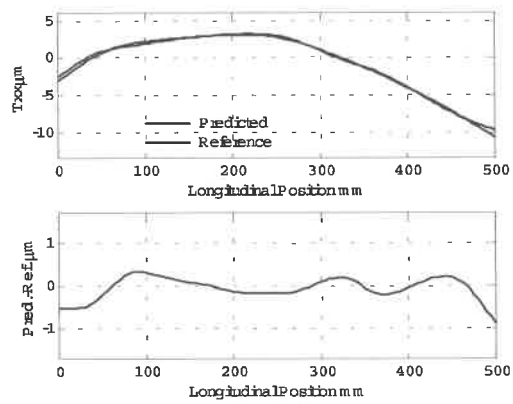

Fig. 7 Example of component comparison, *X* axis straightness in *Z* direction

4 SUMMARY

A new calibration method for CMM is proposed. A fully automated calibration system for up to a middle size CMM is realized by direct coordinate comparison between two CMMs. The system does not require any human operation after its starting till the end. The method may contribute to improve productivity of CMM in the production floor. The parametric error obtained by the three dimensional comparison method shows satisfactory coincidence with that obtained by the conventional direct measurement. Sufficient reliability of the calibration performance is confirmed.

REFERENCES

[1]Balesmo, A. et al., Results of the CIRP-Euromet intercomparison of ball plate-based techniques for determining CMM parametric errors, Ann. CIRP, Vol. 46/1, (1997) 463.

[2]Zhang, G. et al., A displacement method for machine geometry calibration, Ann. CIRP Vol. 37/1 (1988) 515.

[3]Soons, J. et al., Modeling the errors of multi-axis machines: a general methodology, Precision Engineering, Vol. 14, 1, (1992) 5.

[4]Sartori, S. and Zhang, G., Geometric error measurement and compensation of machines, Ann. CIRP Vol. 44/2 (1995) 599.

[5]EAL-G17, Coordinate measuring machine calibration, (1995)

[6]Abbe, M. et al., Reliability of parametric error on calibration of CMM, IMEKO 2000 Proc. Vol. 8 (2000) 3.

FIRST GENERATION MICRO-MACHINE TOOL CHARACTERIZATION

A. Caballero-Ruiz,
Laboratory of Mechatronics, Instrumentation Center, National Autonomous University of Mexico.
Circuito Exterior s/n, Cd. Universitaria, Coyoacán, 04510, A.P. 70-186 México, D.F.
Tel. (+52) 5622-8602 to 07 ext 115 E-mail. albcaru@servidor.unam.mx

1. INTRODUCTION

The development of methodologies to characterize micro-systems has become a need for the investigation around the world. UNAM has been developed an investigation line focused on the technology generation for micro-equipment at Mechatronics Laboratory of the Center of Instruments. As result of this investigation has been developed a micro-machine tool of first generation with three work axes, which is automated with the help of stepping motors. Until this moment there are few methodologies that allow to evaluate the capacities of these kind of devices, so that, here we present a proposition of characterization of a micro-machine tool.

2. CASE OF STUDY

The development of micro-mechanic systems is pointed out as a part of the researching lines of the Mechatronics Laboratory at the Instruments Center, UNAM. Its main goal is to generate the high performance technology in order to fabricate pieces of smaller dimensions than one millimeter. Those pieces are used in the development of the completely automated production technology and they are focused on the development of equipment and instruments, highly efficient and low cost. During the last year it has been developed a prototype of a micro-machine tool with the capability of performing machining such as lathe, milling, and drilling. This work (lathe, milling, drilling) depends on the kind of tool and the configuration, which the equipment works with. Some specifications to the first generation micro-machine tool prototype were proposed by the Mechatronics Laboratory at the Instruments Center. Those specifications are: Capability of producing pieces on a size range from 100 micrometers to 5 millimeters; 2 micrometers resolution; the equipment must have 4 grades of freedom (3 translation axes and, at least, one rotation axe.); the prototype must include automation software; and the automation software must work on a Pentium system with 32 RAM megabytes.

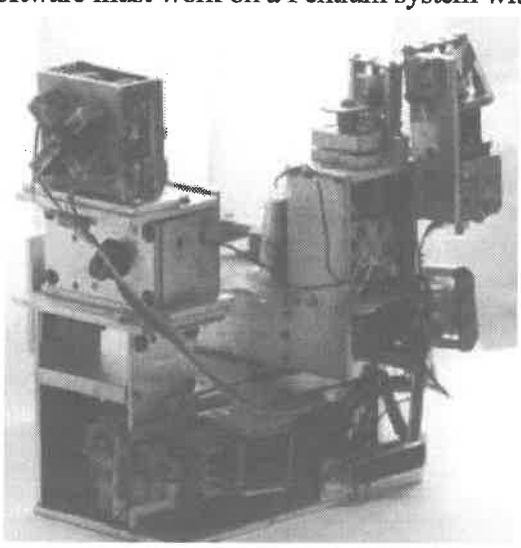

Figure 1. Micro-machining center developed by the Mechanic Engineer Laboratory at the Instruments Center

As a result of the application of those specifications, we obtained a micro-machining prototype on the approximated dimensions of 130x160x85 ?mm^3? (figure 1).

Some pieces have been fabricated on an automatic way with this equipment but the real characteristics of the machine were unknown. Therefore, it is necessary to characterize it as well as to establish the performance parameters in order to use that information for the software design to reduce errors, for the establishing of error sources, and for the improvements proposal. This study is the main part of this paper.

3. CHARACTERIZATION

There are two methods for machine characterization. The first one is called 'direct method', which is focused on the quantification of each one of the qualities of the machines, through this quantification, we can estimate precisely the machine errors. The second method is called 'indirect method', and it helps to determine the work accuracy and the machine tool capability [1].

We tested the micro-machine tool by indirect method. In other words, we characterized the micro-machine tool by evaluating test pieces producing with the same equipment. Once that was made, we knew some characteristics of the equipment.

According to the parameters that the proposed method gave us we were capable to know the following characteristics of the equipment:

Positional characteristics: "Y" axis accuracy, resolution (linear displacement for each motor step) and Backlash.

Geometric inspection: Geometric analysis of the pieces fabricated on the equipment and of its conceptual design in order to know the accuracy characteristic by comparing both pieces.

The characterization tests of the micro-machining center prototype were made on the base of the fabrication of 20 similar pieces with approximately known geometric characteristics. With the help of statistic analysis we determined the needed parameters. The testing piece implemented to determine the positional characteristics was a cylindrical shape with 3 radial marks, as is shown in the figure 2.

For the geometric inspection study, micro-rings were designed. Those rings were employed in a micro-mechanic filter, which is an application of this technology. This measurements were made with an optical contrast. The solid model of a micro-ring is shown on the figure 3. This kind of pieces was tested with a profile projector.

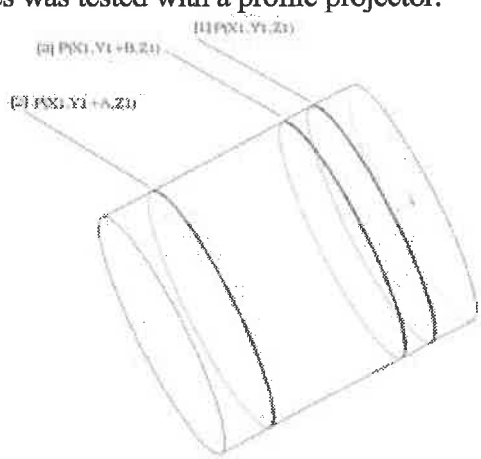

Figure 2: Testing piece used to determine the positional characteristics of the micro-machining center.

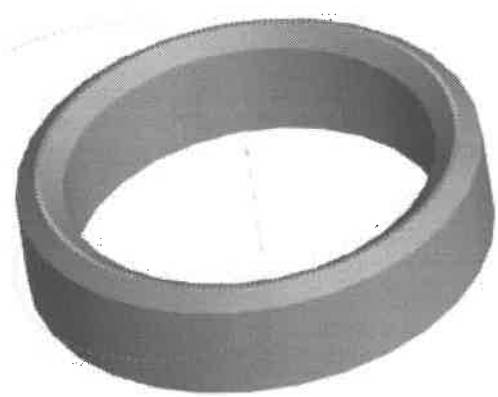

Figure 3. Testing piece for the geometric inspection

The test pieces machined shown below.

Figure 4. Testing piece used in the measurement of the determination of the positional characteristic tests.

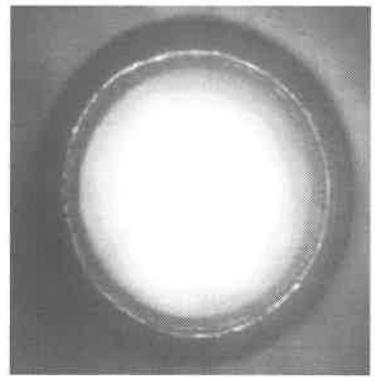

Figure 5. Testing piece used in the geometrical analysis.

4. RESULTS

The results shown below were determined by a statistic analysis of the parameters gotten with the help of the measurement tools. Among the different results we got from the statistic analysis, we focused on the average values and standard deviations.

A. Positional characteristics

The results of the positional characterization are shown below.

Accuracy	18.21 [?m]
Resolution	1.88 [?m]
Backlash	345.27 [?m]

To establish de accuracy in the "Y" axis we made measurement the distance between the 1 and 2 marks of de first test piece (1050 steps programmed). The accuracy is an average of the 3?[1], and it can work as the error of the "Y" axis working length because it was always machinated on different axis positions. The resolution was obtained by the relation between the distance 1-2 and the number of esteps programmed. In order to define the backlash presented on the "Y" axis, it was measured the distance between the marks 1 to 3 of the testing pieces.

After analyze the gotten results it was determined that there are different backlash error sources in the machining-center. The first source is located in the gear box. The second one, and the most important, is located between the transmission and the carrier on each axis. The third one is located between the leading screw and the nut that is coupled to the carrier on each axis.

B. Geometrical analysis

It is shown below a table containing the measurements effected to the testing micro-rings. The results of the measurements are shown on the table below.

[1] Standard deviation

Measurement name	Description
M	Exterior diameter of the micro-ring base.
S	Distance between the diameters (interior, and exterior of the micro-ring base)
N1, N2	Diameter conforming the conic cutting vertice located on the superior micro-ring's base
P	Distance between the conic cutting vertice and the interior diameter of the micro-ring's base
Q	Height form the micro-ring's conic part

Table 1. The measurements to the testing micro-rings for determining the geometrical analysis.

Machining kind	Measurement average [?m]	Expected error ?[?m]
Cylinder machining (M)	1258.45	20.11
Drill machining (S)	205.47	38.28
Cone machining (N)	981.30	62.19
Cone machining (P)	64.63	37.00
Cone machining (Q)	476.79	34.82

Table 2. Measurement's results

Because the machining errors of the pieces correspond to the mode of machining, we found errors resulted of the kind of tool employed on the fabrication of the piece, besides the errors resulted of the micro-machining center characteristics. Therefore, the errors the micro-machining center showed are also related with the tools employed in the machining.

CONCLUSIONS

The proposal to characterize a micro-machining center was presented. This is an alternative permitting to know some parameters about this kind of devices like they are accuracy, backlash, among others. This parameters help us to develop improvements to reduce the micromachine tools errors via software or hardware. It's necessary development methodologies that permits to characterize micromachines tools by direct method to decrease de errors that depend on the design of the equipment. The development of micro-equipment raises the need of generating the technology that allows us to learn its behavior. As a part of our future work, it is going to be developed an auto-evaluation system for this equipment..

ACKNOWLEDGEMENTS

Special thanks to Ph. D. Ernst Kussul and Leopoldo Ruiz-Huerta by your support in this work.
This work was supported by CONACyT project 339944-U and DGAPA UNAM project IN-118799.

REFERENCES

1. Dohi T. Computer Aided Surgery and Micro Machine. // Proceedings of the 6-th International Symposium on Micro Machine and Human Science, 1995. MHS'95, pp 21-24.
2. E.M.Kussul, D.A.Rachkovskij, T.N.Baidyk et al. Micromechanical engineering: a basis fot the low cost manufacturing of mechanical microdevices using microequipment. // J. Micromech. Microeng. - 1996. - 6. - P. 410-425.
3. Fukuda, T.; Micro Mechanical Systems, Principles and Technology; ELSEVIER; 1998.
4. Kussul E., Ruiz L., Caballero A., Kasatkina l., Baydyk T; CNC machine tools for low cost micro devices manufacturing; First International Conference on Mechatronics and Robotics; Saint-Petesburg, Russia; May 29-June 2, 2000; Proceedings Volume1; pp 98-103.
5. Some Micro Machine Activities in Japan. //Report ATIP96.021.

USE OF FLUID BEAMS TO ESTABLISH A CLEAN ZONE FOR IN-PROCESS OPTICAL MEASUREMENT

Y. Gao
Department of Mechanical Engineering, Hong Kong University of Science and Technology
Clear Water Bay, Kowloon, Hong Kong
E-mail: meygao@ust.hk

Introduction

It is known that in precision machining, a large sum of energy could be transformed into thermal energy, generating excessive heat that induces thermal deformations. Due to the thermal deformation of the machine and the workpiece, the machining accuracy could be affected. The thermal deformation can be related to various sources including an uncontrolled environment, the friction that results from the interaction between the cutting tool and the workpiece, and the shear fracture that results from the formation of chips during machining. If coolants are applied at the intersection of the cutting tool and the workpiece, the heat generation can be reduced by the lubrication function of the coolant and the effect of the heat that causes the thermal deformation is removed by the cooling function of the coolant. Using coolants can be effective to improve the machining accuracy.

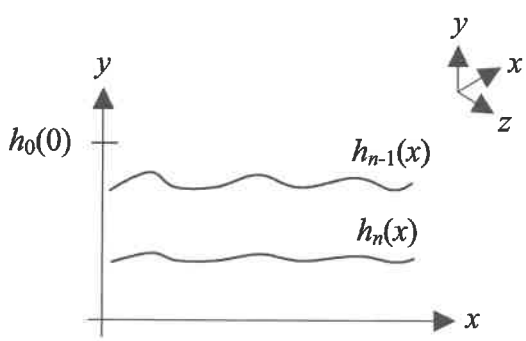

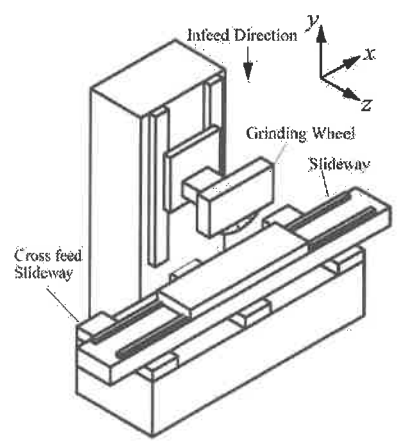

Fig. 1 Surface profiles during machining **Fig. 2** High speed table motion in surface grinding

However, the use of coolant could make the in-process optical measurement of the workpiece surface profiles difficult. In order to control the process to improve the machining accuracy, it is desirable to measure the workpiece profiles [$h_{n-1}(x)$, n =1,2,...] during the process of machining, as shown in Fig. 1, where n is the pass number.

In-process measurement has been investigated in two areas, condition monitoring and workpiece surface measurement. The condition monitoring is to achieve optimal machining states, while the workpiece surface measurement is to provide control the workpiece surface profiles. In the latter case, a detecting probe either in a wave form, or in a mechanical stylus form, is used to measure workpiece surface profiles. Due to the high speed motions typically involved in precision machining, as the table motion in the x direction in Fig. 2, the mechanical stylus methods cannot be used in order to avoid scratches, likely caused by the contacting styluses on workpiece

surfaces, and as a consequence, excessive wear of the stylus tips in contact with the workpiece. It seems that the non-contact measurement methods have to be utilized. The non-contact methods utilize waves in two ways, waves are originated from the interaction between the workpiece and the cutting tool, or waves come from an external source. The latter type has the advantage of being in the category of non-contact measurement, avoiding scratches and wear, which are the disadvantages associated with the stylus probes. However, under the condition of wet grinding, where coolant would be used to remove the heat generated, and when the probe is made of light waves, the light, which is from an external source, would not reach the workpiece surface, as, it is very often, the coolant used for machining is optically opaque and the light is stopped by the layer of coolant (Fig. 3). A detecting probe in the form of ultrasonic waves may be considered. Since ultrasonic waves, typically at the frequency of 50kHz or above but far below that of light, are able to propagate in the liquid and reach the workpiece surface, although the liquid is optically opaque. It has been seen that workpiece surface roughness can be detected by measuring the changes in the echoed beam intensity. In addition, the distance between the sensor and the workpiece surface could be obtained if the flight time of the ultrasonic beam reflected from the workpiece surface is measured [1]. The ultrasonic probe has the advantage that the coolant does not have to be optically transparent. However, the accuracy may be limited in the ultrasonic method. The flow of coolant could adversely affect the propagation of the ultrasonic waves in the coolant layer. The ultrasonic waves are of mechanical. The frequency is typically 5-1000MHz, far below the frequency of the light waves. For these reasons, the achievable measurement accuracy of an ultrasonic method would not be as high as that of an optical method. Optical measurement has long been investigated and commercially available products are capable to reach very high resolution, often nanometers. This indicates that the ultrasonic method, which is compatible with the optically opaque coolant, may not be the best choice, if there is a solution for the problem of light being stopped by the coolant layer before reaching the workpiece surface, making the workpiece surface inaccessible. In this sense, it is proposed to use an assisting fluid system to overcome the opaque barrier. In this new approach, a fluid beam is established through the use of an applicator (Fig. 3) to build a small zone that is optically clean, termed as transparent window, to enable the workpiece surface accessible to optical measurement systems. The advantages of the proposed method are that the wear problem of the contact methods and the inaccessibility problem of the non-contact methods are removed. This could permit the in-process optical measurement to reach to very high precision, since the optical methods can be applied.

Transparent Window

In order to generate a necessary transparent window, the applicator is used to position in the coolant layer along the direction of the table movement (Fig. 2-3) and maintain a clearance d between the applicator and the workpiece surface (Fig. 3). A transparent fluid is then applied to a small area on the workpiece surface through the applicator. The clearance is to be small so that the transparent fluid can be easily directed to the workpiece surface. The applicator is also used to redirect the majority of the coolant to the two sides. This will be beneficial for the establishment of the transparent window and for the minimum use of transparent fluid. Since the range of the clearance d is small, a fine adjustment mechanism is required. If d is too large the transparent window will be difficult to establish. Conversely, if too small, the possibility of contacting the workpiece will be large.

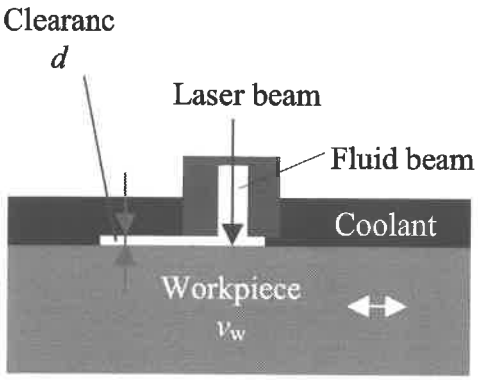

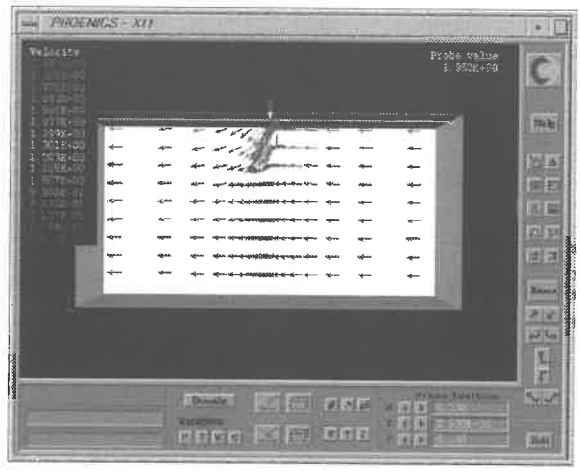

Fig. 3 In-process optical measurement **Fig. 4** Flow pattern of the fluid beam at v_w=5m/s

For this reason, a small servo motor may be used with feedback from an inductive sensor mounted on the applicator. To control the servo system, one method is to use optimal dc values established through experiments, and as such a large number of tests are necessary. Another method is to use optical sensors to measure the workpiece surface directly, based on a strategy that if no reflection is received, the applicator is lowered down by a step and this is repeated until reflection signals are detected, indicating that a transparent window is established. This approach will require a safety switch to avoid the applicator too low, a possibility to contact the workpiece. This approach is advantageous since the control algorithm adjusts to the actual situation, and as such the number of tests can be reduced. A fluid system is used to deliver the transparent fluid to the workpiece surface through the applicator. Due to the pressure in the system, the fluid would flow out evenly from the bottom of the applicator. The fluid beam can be affected by several factors including the coolant speed and the clearance between the workpiece surface and the fluid beam applicator. Due to two fluid flows are involved, the interactions between them can be complex. This requires a computational fluid dynamics approach (CFD) be utilized. In this investigation, a CFD package, PHOENICS, was used. The CFD models were established and the mesh model generated. The flow patterns and the velocity profiles were obtained (Fig. 4). It was found that the velocity of the fluid beam should be set at 5m/s approximately or higher, when the velocity of the coolant is 0.64m/s, to enable the beam to reach the workpiece surface [2]. Under this condition, the clearance between the workpiece surface and the applicator can have many choices. In the actual situation, it was quite small [3].

Experimental Testing and Discussion

Experimental testing has been carried out on an ESG-818ASD surface grinding machine to test the proposed method. In the experimental tests, a Keyence LB-70 laser triangulation sensor was used to measure the test workpiece surface profiles under the coolant condition (Fig. 5). The profiles were compared with those obtained without any coolant being applied. In Fig. 5, the effect of the machine vibrations was involved. If two laser sensors were used to measure the workpiece profile derivatives through the clean zone, the effect could be removed. The results of the experiments (Fig. 5), although at the scale of millimeter due to the limitation in the resolution

of the LB-70 laser sensor, confirm the computational model for the fluid beam to be established, demonstrating that the proposed method can be a suitable solution to the problem.

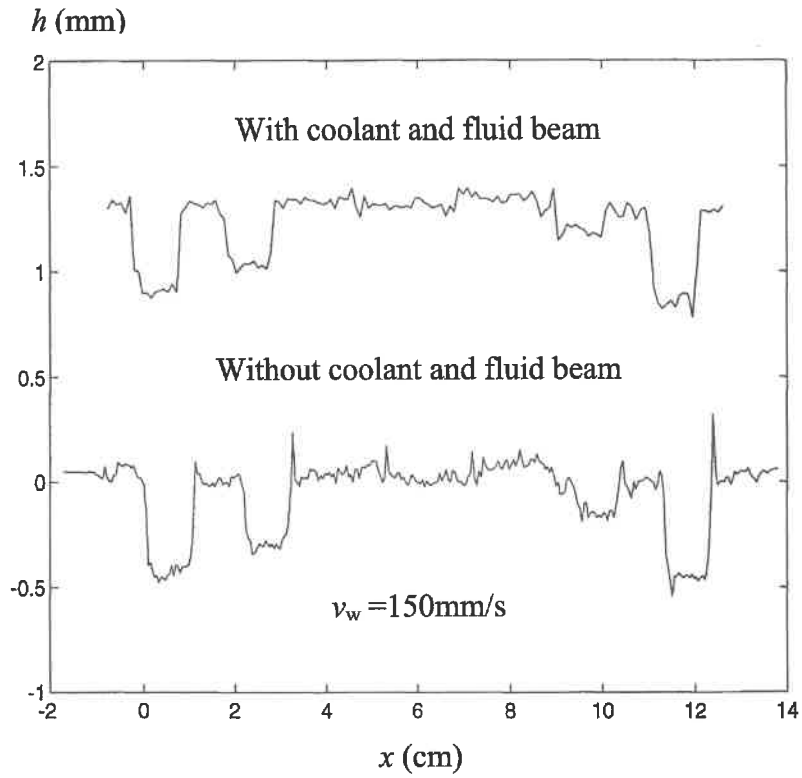

Fig. 5 Workpiece surface profiles obtained with coolant and without coolant

Conclusions

In-process optical measurement is desirable but has several main difficulties to overcome. The proposed use of a fluid beam to establish an optically clean zone can be a good solution for the in-process optical measurement problem. Preliminary tests show that the proposed approach is feasible.

Acknowledgement

This work has been supported by the Research Grants Council of Hong Kong SAR of China (Project no. HKUST6100/97E).

References

[1] Pettengill, J., and Shin, Y. C., 1996, Surface contour measurement by an ultrasonic technique, Proc Japan/USA Symposium on Flexible Automation, **2**, pp. 1181-1188.

[2] Gao, Y., Tse, S., and Lai, K., 2001, A computational investigation of the parameters to establish a transparent window for in-process optical measurement, Proc ISMQC 2001.

[3] Gao, Y., and Tao, Z., 2001, Tests of flow patterns of grinding coolant interfered using an injection of stream, Proc ESUPEN 2001, pp. 684-687.

A NEW SURFACE ENCODER FOR MULTI-AXIS POSITION DETECTION

Yuki Shimizu, Wei Gao and Satoshi Kiyono
Department of mechatronics and Precision Engineering,
Faculty of Engineering, Tohoku University, Sendai, 980-8579 Japan

1. Introduction

Improvement of speed and precision of multi-axis stages for precision machine tools and photolithography steppers is strongly required. To fulfill this requirement, it is necessary to measure multi-degree-of-freedom (MDOF) translational and rotational motions of the stage precisely, and feedback the measurement results to the control system[1].

Conventional MDOF measurement systems consisting of multiple sensors (laser interferometers, linear/rotary encoders, autocollimators, etc.), however, are complicated and expensive. It is also difficult to integrate such sensors in the stage system.

The authors have proposed a new method for MDOF measurement named the surface encoder[2]. The surface encoder is composed of a two-dimensional (2D) optical angle sensor and a 2D angle grid. The angle sensor has the ability of detecting the 2D local slopes at a point on the angle grid surface, on which 2D sinusoidal angular patterns are generated. Since the angle profiles of the grid surface along X- and Y-axes are independent from each other, the X- and Y-outputs of the angle sensor provide the X- and Y-directional positions/displacements of the angle sensor relative to the angle grid, respectively. In other words, the 2D translational X- and Y- motion can be detected by a single surface encoder.

The authors have also proposed a modified surface encoder employing a scanning laser beam-type angle sensor. At each measurement position, the sensor scans a laser beam on the angle grid surface at a constant speed. In such a surface encoder, the lines along X- or Y-directions on the grid surface, at which the X- or Y-angles are zero, are used as the encoder graduations. The interpolations between the zero-lines (graduations) are carried out by counting the traveling time of the laser spot. Since only the zero-lines on the grid surface are used for position detection, the influence of the form error of the angle grid on the accuracy of position detection can be greatly reduced[3].

In this paper, the scanning laser beam-type surface encoder is improved to measure the three-directional rotational motions (pitch, roll, and yaw) in addition to the X- and Y-directional translational motions. Principle of the 5-degree-of-freedom (5-DOF) surface encoder and some experimental results are presented.

2. Principle of the 5-DOF surface encoder

Fig.1 shows a schematic principle of the 5-DOF surface encoder. The surface encoder system consists of a 2-D angle sensor and a 2-D angle grid. The profile height of the 2-D angle grid at the measurement position P(x,y) is represented as follows:

$$h(x,y)=A_X \sin\left(\frac{2\pi}{D_X}x\right)+A_Y \sin\left(\frac{2\pi}{D_Y}y\right) \quad (1)$$

Here, D_X, D_Y are the wavelengths of the angle grid in the X- and Y-directions, respectively. A_X, A_Y are the amplitudes. Assume that the position of the angle sensor is kept stationary and the angle grid moves in the

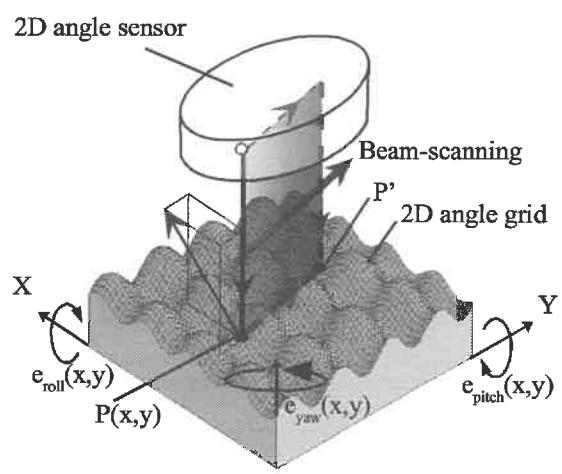

Fig.1 The surface encoder

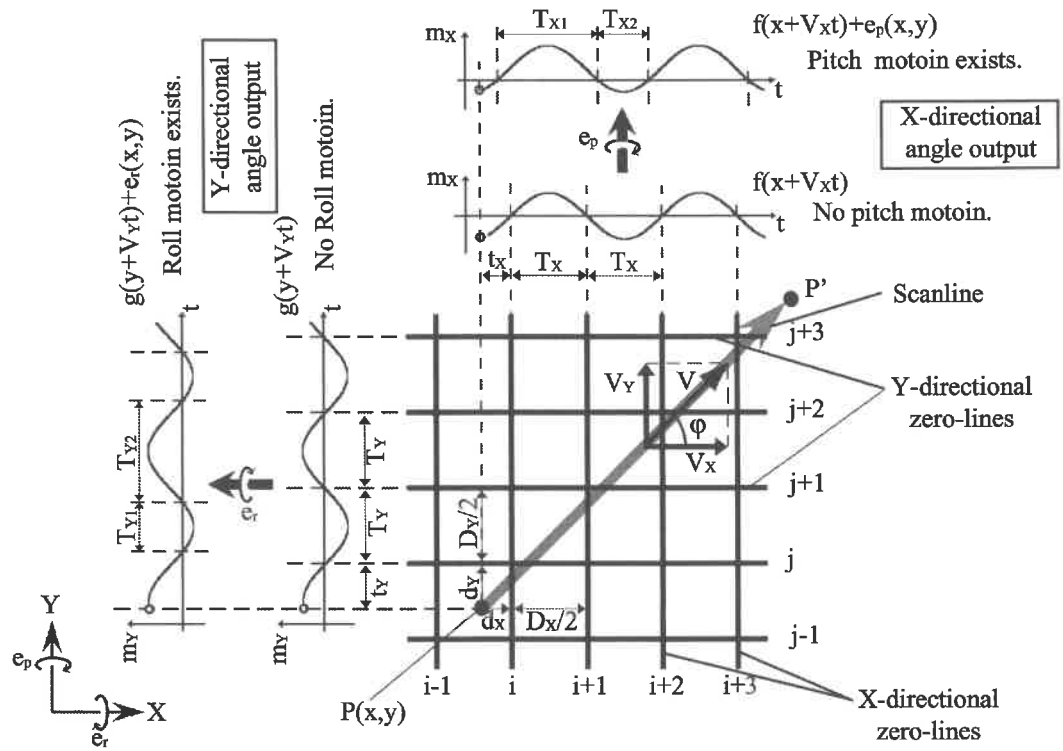

Fig.2 Measurement principle of 5DOF translational and rotational motions

XY plane, the X- and Y-directional outputs of the angle sensor ($m_X(x,y)$, $m_Y(x,y)$) at the measurement point P, which correspond to the X- and Y-directional local slopes of the grid surface, can be expressed as follows:

$$m_X(x,y)=\frac{\partial h}{\partial x}=\frac{2\pi A_X}{D_X}\cos\left(\frac{2\pi}{D_X}x\right)=f(x),\ m_Y(x,y)=\frac{\partial h}{\partial y}=\frac{2\pi A_Y}{D_Y}\cos\left(\frac{2\pi}{D_Y}y\right)=g(y) \qquad (2)$$

Although it is possible to directly evaluate the position of the measurement point P from Eq.(2), the evaluation accuracy is influenced by the form error of the grid surface. To resolve this problem, we scan the laser beam of the angle sensor over the grid surface along a straight line at a constant speed V. Assume that the scan starts at the measurement point P and ends at a point of P'. The scanning length PP' is kept the same at all the measurement points. The angle between the scanline PP' and X-axis is let to be φ as shown in **Fig.2**. Also assume that the beam scanning speed is much faster than the movement speed of the angle grid so that the angle grid can be considered to be stationary during the scanning. In **Fig.2**, the X-directional and Y-directional zero-lines of the angle grid are numbered by i and j, respectively. The outputs of the angle sensor at time t after the scanning can be written as

$$m_X(x+V_Xt,y+V_Yt)=\frac{2\pi A_X}{D_X}\sin\left(2\pi\cdot\frac{x+V_Xt}{D_X}\right),\ m_Y(x+V_Xt,y+V_Yt)=\frac{2\pi A_Y}{D_Y}\sin\left(2\pi\cdot\frac{y+V_Yt}{D_Y}\right) \qquad (3)$$

where V_X and V_Y are the X- and Y- directional components of V. Assume that the time distances for the spot to travel from the measurement P to lines i and j is t_X and t_Y, respectively. The position of the measurement point P relative to lines i and j can thus be evaluated from

$$dx=\frac{D_X}{T_X}\cdot t_X(x,y),\ dy=\frac{D_Y}{T_Y}\cdot t_Y(x,y) \qquad (4)$$

where, T_X and T_Y are the time for the beam to travel between two adjacent zero-lines in the X- and Y- directions, respectively.

If rotational motions pitch e_p and roll e_r exist, the outputs of the angle grid become

$$m_X(x+V_Xt,y+V_Yt)=f(x+V_Xt)+e_p(x,y)=\frac{2\pi A_X}{D_X}\sin\left(2\pi\cdot\frac{x+V_Xt}{D_X}\right)+e_p(x,y) \quad (5)$$

$$m_Y(x+V_Xt,y+V_Yt)=g(y+V_Yt)+e_r(x,y)=\frac{2\pi A_Y}{D_Y}\sin\left(2\pi\cdot\frac{x+V_Yt}{D_Y}\right)+e_r(x,y) \quad (6)$$

As can be seen in **Fig.2**, when a pitch motion exists, the time distance between adjacent zero-points in the X-directional angle output will be different from T_X, and can be expressed as

$$T_{X1}(x,y)=\frac{D_X}{V_X}\left\{\frac{1}{2}\mp\frac{1}{\pi}\arcsin\left(-\frac{D_Xe_p}{2\pi A_X}\right)\right\},\ T_{X2}(x,y)=\frac{D_X}{V_X}\left\{\frac{1}{2}\pm\frac{1}{\pi}\arcsin\left(-\frac{D_Xe_p}{2\pi A_X}\right)\right\} \quad (7)$$

If e_p is small, combining T_{X1} and T_{X2} gives:

$$e_p(x,y)\approx\pm\frac{\pi^2A_X}{D_X}\cdot\frac{T_{X2}(x,y)-T_{X1}(x,y)}{T_{X2}(x,y)+T_{X1}(x,y)}=k\cdot\frac{T_{X2}(x,y)-T_{X1}(x,y)}{T_{X2}(x,y)+T_{X1}(x,y)}\ \text{(k: const)} \quad (8)$$

Eq.(8) means that e_p can be detected by counting T_{X1} and T_{X2}. The same calculations can be applied to e_r (roll) through counting T_{Y1} and T_{Y2}.

On the other hand, when a yaw error e_{yaw} around Z-axis exists, the angle between the scanline and X-axis will change to $\varphi+e_{yaw}$, and e_{yaw} can be obtained from

$$e_{yaw}=\arcsin\frac{D_Y}{(T_{Y1}(x,y)+T_{Y2}(x,y))}-\varphi=\arccos\frac{D_X}{(T_{X1}(x,y)+T_{X2}(x,y))}-\varphi$$

$$=\arctan\frac{T_{X1}(x,y)+T_{X2}(x,y)}{T_{Y1}(x,y)+T_{Y2}(x,y)}\cdot\frac{D_Y}{D_X}-\varphi \quad (9)$$

As can be seen from above, 5-DOF motions (x, y, pitch, roll and yaw) at each measurement point P(x,y) can be measured by a single surface encoder.

3. Experiments

The experimental surface encoder designed and manufactured in this study is shown in **Fig.3**. The angle sensor is based on the principle of auto-collimation. By using an acousto-optical deflector (AOD), the beam from the light sources(LD) can be scanned at a constant and high speed on the angle grid. The wavelength and the amplitude of the angle grid were the same in X- and Y-axes, which were 300μm, 0.3μm, respectively.

Fig.4 shows the results of pitch detection. The scanning frequency of the beam, which was generated by the AOD, was 50Hz. The sampling number was 400 points at one-scanning. Pitch motions were applied to the angle grid. The horizontal axis

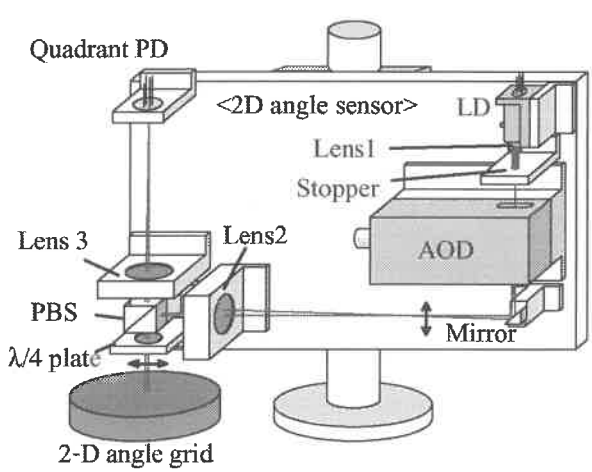

Fig. 3 The scanning optical 2-D angle sensor

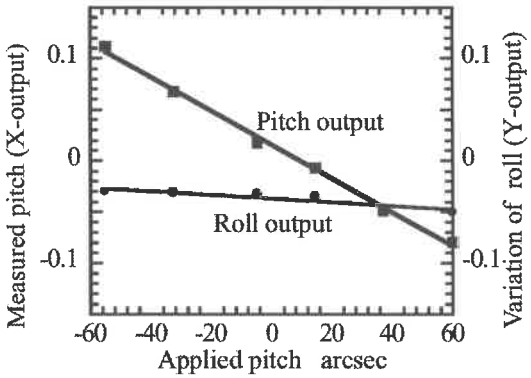

Fig. 4 Results of pitch measurement

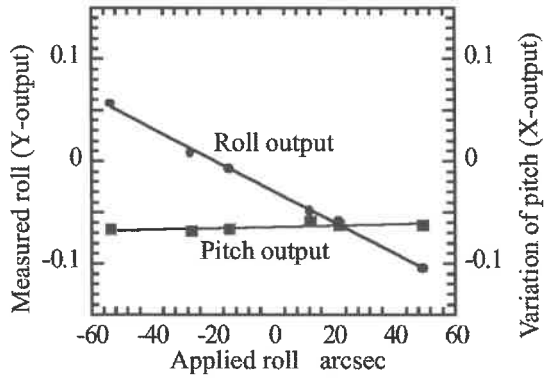

Fig. 5 Results of roll measurement

represents the result measured by an autocollimator placed outside the surface encoder. The vertical axis shows the pitch motion detected by the surface encoder. The corresponding roll output of the surface encoder, which should be constant if a pure pitch motion is applied to the angle grid, is also plotted in the figure. Three repeated measurements were made at the same location of the angle grid. Repeatability was about 5".

Fig.5 shows the results when roll motions were applied. The results shown in **fig.4 and 5** indicate that pitch and roll were detected separately.

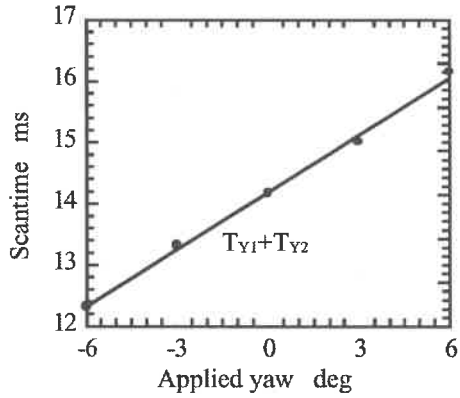

Fig. 6 Results of yaw measurement

Fig.6 shows the results of yaw detection. The horizontal axis represents the yaw motion of the angle grid applied by a rotary stage, and the vertical axis shows the corresponding change in the scanning time ($T_{Y1}+T_{Y2}$). The result indicates the possibility of yaw detection by the surface encoder.

5. Conclusions

1) A 5-degree-of-freedom surface encoder consisting of a scanning laser beam-type 2D angle sensor and a 2D angle grid has been developed. In addition to the X- and Y-translational motions, the rotational motions (pitch, roll and yaw) can also be simultaneously detected by such a surface encoder.
2) An experimental surface encoder has been constructed. The possibility of detecting 5-DOF motions has been verified.

Acknowledgement

This research was supported by a Grant-in-Aid for Scientific Research (A)(2) from the JSPS (No. 11305013).

References

1) H. Kunzman, T. Pfeifer and J. Flugge: Scales vs. Laser Interferometers, Performance and Comparison of Two Measuring Systems, Annals of the CIRP, Vol.**42**, No 2, (1993), pp.753-767.
2) S. Kiyono, P. Cai and W. Gao: An Angle-Based Position Detection Method for Precision Machines, International Journal of the Japan Society for Mechanical Engineers, Vol.**42**, No.1, (1999), pp.44-48.
3) S.Kiyono, T.Hoshino and W.Gao: A New Method of Position Detection Based On an Optical Angular Sensor System, Proc.of Int.Conf.Mechatronics 2000, warsaw, No 2,(2000),pp.359-362.

Correlation of Spindle Errors to Piece-Part Accuracy

Ke Wang & Edward Morse
Center for Precision Metrology
The University of North Carolina at Charlotte
Charlotte, NC 28223

Keywords: Axis of Rotation Errors, In-Process Measurement, Part Geometry

Introduction

Spindle error measurement technology, utilizing a cylindrical or spherical target artifact with non-contact gauges (capacitance gauges, eddy current gauges, etc.) to measure a machine tool spindle's "axis of rotation" errors (including radial, axial, and tilt errors: ANSI/ASME B89.3.4 [1]), plays an important role in metrology and precision engineering. There are a variety of testing methods and equipment available for measuring these errors for a freely rotating machine tool spindle [1] [2]. These methods are widely used by manufacturing industries and precision engineers to determine spindle errors of an *unloaded* machine tool spindle. It is very likely that the error motions of a machine tool spindle during the machining process will be different from those in free rotation. Some attempts has been made to simulate the loading conditions that a machine tool could experience during its cutting process [3] [4], as well as measuring the radial errors induced by cutting [5]. We are not aware of the successful measurement of all five error motions of a machine tool spindle during the machining process. This absence of knowledge prevents us from understanding how a machine tool spindle really behaves when it is carrying out machining applications and, ultimately, how these in-process spindle errors affect the accuracy of the parts manufactured by this machine tool.

In this paper we describe an approach for measuring spindle errors during machining process. The motivation for the development of this instrumentation is to better understand how cutting forces influence the deviations from ideal rotor-to-stator spindle motion.

Design of Experimental Instruments

The measuring apparatus we developed in this study is designed for performing in-process spindle error measurements on a Bostomatic M-270 CNC vertical machining center. Our design is based on the conventional method for testing unloaded spindle errors, which is described in appendix A of ANSI/ASME B89.3.4 [1]. This measuring device consists of two parts, the target artifact which rotates with the tool and tool holder, and a mounting fixture that holds five capacitance gauges that measure changes in distance between the stationary mount and the rotating target surface.

- Target Artifact

The target artifact is a disk shape, which permits measurement of all five error motions while protecting the gauges from chips and other debris. While every effort is made to ensure that the surfaces of the target are smooth and the circumference of the disk is centered on the spindle axis, we rely on reversal techniques and information about the spindle's errors from earlier unloaded measurements in lieu of requiring perfect form for the artifact. Figure 1 shows models

of the target mounted on the tool holder, and also shows the relative positions for the capacitance gauges that are used to measure the motion of the disk.

Fig 1.1 BT-40 Tool Holder (Pro-E)

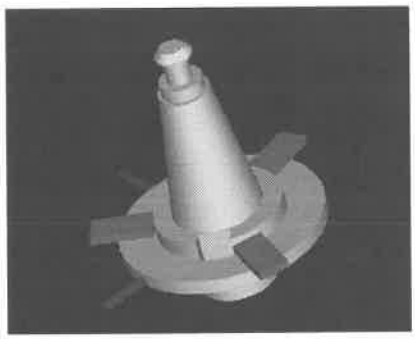

Fig 1.2 Target disk mounted on the tool holder with rectangular and cylindrical capacitance gauges targeting at it (Pro-E)

Fig 1.3 BT-40 tool holder with target disk mounted on it (Actual photo)

Fig 1. Target artifact

The thickness of this target disk is 0.375 inch and its diameter is 4.25 inch; the rim of the disk is machined to a spherical surface – i.e., the disk is really a slice of a sphere. This prevents tilt errors from being interpreted as radial errors, and gives a more uniform target for the capacitance gauges as tilt motion increases.

- Mounting Fixture for the Capacitance Gauges

In order to measure all five error motions simultaneously, we use five capacitance gauges (provided by Lion Precision) to collect error motion data. Three of these gauges are flat, rectangular bodied model R1-A gauges and the other two are cylindrical bodied model C1-B gauges [6]. The relative positions of these gauges are shown in Figure 1.2. The R1-A gauges look "down" at the flat top surface of the target disk to measure Z axis error motions and tilt error motions, while the C1-B gauges target at the edge of the target disk to measure X- and Y-axis radial error motions. Driver units of the capacitance gauges are model DMT-10 [7], also provided by Lion Precision. A PC data acquisition board, standard to the spindle error analyzer, is used to record and process error motion data collected by the gauges. The mounting fixture for the gauges consists of three parts: a connector plate, the mount for the R1-A gauges, and the mount for the C1-B gauges.

1. Connector Plate

In order to make our instrumentation more flexible, we use a connector plate to fix the gauge mounts to the quill of the spindle. This connector plate is unique to the machine tool used for testing, while the remaining components can be used with any tool. This design allows us to easily test spindles on different machine tools without major redesign. For the M270, we use a connector plate with a six-hole pattern. Three of the holes are used to mount the plate to the lower end cover of the quill. Three other holes are tapped and used to fix the mount of R1-A gauges to the connector plate (Fig 2.2).

Fig 2.1 M-270 machine spindle

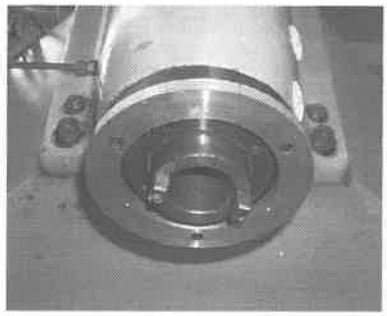

Fig 2.2 Connector plate

Fig 2.3 Mounts for the R1-A capacitance gauges

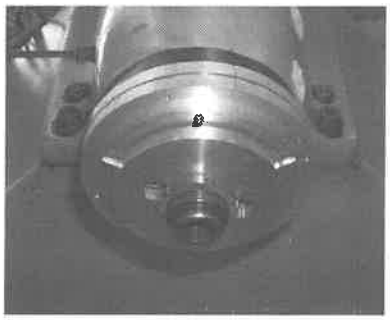

Fig 2.4 Target disk and tool holder

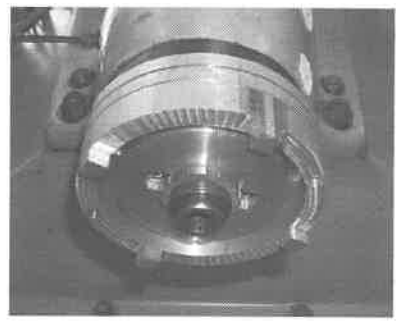

Fig 2.5 Mounts for the C1-B Capacitance gauges

Figure 2: Mounting fixture for the capacitance gauges

2. Mounting for the R1-A Capacitance Gauges

This mount locates the three rectangular R1-A gauges. The locations of these three gauges are distributed evenly at 120 degrees (Fig 2.3). We use three bolts to fix this mount to the connector plate. These three bolts are also used to adjust the distance and parallelism between those R1-A gauges and the target disk (Fig 2.4). Near the rim, there are four boltholes distributed evenly at 90 degrees, which are used to receive the C1-B gauge mount.

3. Mounting for the C1-B Capacitance Gauges

This mount locates the two cylindrical C1-B gauges. These two gauges are located parallel to the X and Y axis of the CNC machine, targeting at the spherical rim of the target disk to pick up X and Y axis error motions. Four bolts are used to fix this part to the mount of R1-A gauges. These four bolts are also used to make small adjustments of the relative positions between the C1-B gauges and the target disk (Fig 2.5).

Testing Procedures and Data Analysis

Before we employ our measuring device on the CNC machine, we need to make sure that the spindle and tool holder combination we use for these experiments has repeatable behavior. We use the dual sphere Spindle Error Analyzer (SEA) system made by Lion Precision to measure the unloaded spindle errors. We perform several measurements at various spindle speeds to ensure that the results we obtain are repeatable. Data from the unloaded spindle error measurements are used to map any mechanical errors that occur in the target artifact and the mounting fixture of

our design. This mapping operation is applied to the capacitance gauge measurements taken from the disk target artifact when the spindle is rotating without load. We are also able to easily rotate the tool holder and target disk 180 degrees with respect to the spindle to confirm that the geometric errors we assign to the target are distinguishable from the spindle errors.

We next acquire capacitance gauge data during machining process. The standard PC data acquisition and interface provided with the SEA hardware is used. These data (from our new apparatus) are transformed to match those data that would be obtained from the standard two-sphere artifact. The method used to perform this transformation is described in [8] and, after these data are transformed, they can be displayed with the existing graphics routines for the two-sphere artifact. The spindle's behavior during free rotation is compared with that observed during machining process.

Current and Future Work

After machining the test parts, we will measure them to determine both geometric and surface finish characteristics. Our focus will be to determine what correlation exists between the in-process spindle errors and the geometry and surface finish characteristics of the part. As we are only measuring rotor-to-stator spindle errors, differences between the observed spindle errors and the part geometry can be associated with unwanted motion in the structural loop of the machine. An initial outcome realized by comparing the magnitude of the different errors contributing to the final part geometry will be to guide the machine tool user as to the origin of errors and uncertainty for specific combinations of tool, workpiece, and materials.

Acknowledgements

This research is conducted at UNC Charlotte and is supported by the affiliates of the UNCC Center for Precision Metrology. We are grateful to Lion Precision for providing us with technical information, advice, and measuring equipment.

References

[1] ANSI/ASME B89.3.4, "Axes of Rotation, Methods for Specifying and Testing" American Society of Mechanical Engineers, NY, 1985.

[2] Bryan, J., Clouser, R., Holland, E., "Spindle Accuracy", American Machinist, December 4, 1967.

[3] Sharma, A.K., "An Experimental Investigation into Thermal Spindle Growth Under Load", Master Thesis, The University of North Carolina at Charlotte, 1997.

[4] Marsh, E., Grejda, R., "Experience with the Master Axis Method for Measuring Spindle Error Motions", Precision Engineering 24 (2000) 50~57.

[5] Davies, M. A., *et al.*, "On the Dynamics of High-Speed Milling with Long, Slender Endmills", Annals of the CIRP, vol. 47, no. 1, pp. 55-60, 1998.

[6] "Probe Selection Chart", Lion Precision, Inc., St. Paul, MN, 2000.

[7] "Spindle Error Analyzer, Instructions Manual", Lion Precision, Inc., St. Paul, MN, 1996.

[8] Morse, E. P., and Wang, K., "Using alternative artifacts for error motion analysis", *Proc. ASPE Summer Topical Meeting on Precision Bearings and Spindles*, pp. 100-103, State College, PA, June 2001.

A NANOMETER PROFILING DEVICE WITH CONTACT FORCE CONTROLLED AT THE LEVEL OF MILLINEWTONS

L. Yang *, Y. Gao **, and T. Xie *

* Huazhong University of Science and Technology, Wuhan, Hubei, 430074, China
** Hong Kong University of Science and Technology, Clear Water Bay, Kowloon, Hong Kong
E-mail: meygao@ust.hk

Introduction

It is known that in order to measure the surface profiles or the 3D topography, contact or non-contact type profiling devices can be considered. The non-contact type instruments are typically optical ones and rely on the reflected lights from the measured surfaces. Due to the lights being used, the non-contact profile devices are advantageous as no force is involved in the measurement. For many applications, in particular, for the micro-system applications where the steep steps and transparent thin films are involved, the non-contact profiling devices may not work effectively. In these cases, the contact profiling devices have to be utilized. Contact profiling devices utilize a contact profiling probe or a stylus to make contact with the surfaces under measurement. Inevitably, a contact force is induced. Due to the contact force, scratches may be produced on the surface and the measurement results distorted. It is clear that the contact force should be maintained as small as possible. A number of research efforts have been aimed to deliver improved stylus designs to reduce the contact force. However, due to the feature of the surfaces under measurement, the contact force would vary in a measurement process. This would make the measurement results very unstable and the uncertainty deteriorated.

In order to have a high precision and a large measurement range, some research has been conducted and new probes or devices have been developed. A stepper motor [1] could be used to extend measurement range. When measuring signal exceeds measurement range, the probe moves up or down by driving motor. As a result, measuring signal changes smaller and return into the measuring range, the measuring range is enlarged. The disadvantage of this method is lower system accuracy due to lower moving precision and control precision, inconvenience of control of measuring force. Piezoelectric ceramics, glass ceramics with super-lower inflation coefficient, and capacity sensors could be used [2-4]. It adopts PI reactive control circuit to adjust measuring force. This method has higher precision, and the probe can maintain a constant tip-to-sample force. The measuring force was at 100nN approximately. The disadvantages of the design of the type were high cost, difficult to manufacture, and small measurement range. In order to solve the problem, a new profiling device with constant contact force is proposed and developed. In this device, the contact force is controlled using an inductive probe of high resolution and a voice coil servo system to reduce and to control the contact force to the level of millinewtons. The voice coil servo system and the probe are built in the device to be an integrated part of the profiling device to ensure consistent performance in a profiling process.

Working Principle

The structure of the proposed device is shown in Fig. 1. It consists of a voice coil motor (VCM) with a short and movable coil and an electric inductance sensor. As an executive mechanism, the VCM consists of a magnet core, a coil, a moving part, and springs. The VCM avoids the wear in a driving mechanism, has low noise, a simple structure, a high working frequency. Compared to other VCMs, the motor with short and movable coil has advantages of good dynamic response due to lighter mass of moving part and less inductance due to short moving coil. This is good to improve the dynamic stability of the control system and simplify the design of compensatory network of phase. In the profiling device, the VCM was used as a part of the servo control system used to enlarge the measurement range.

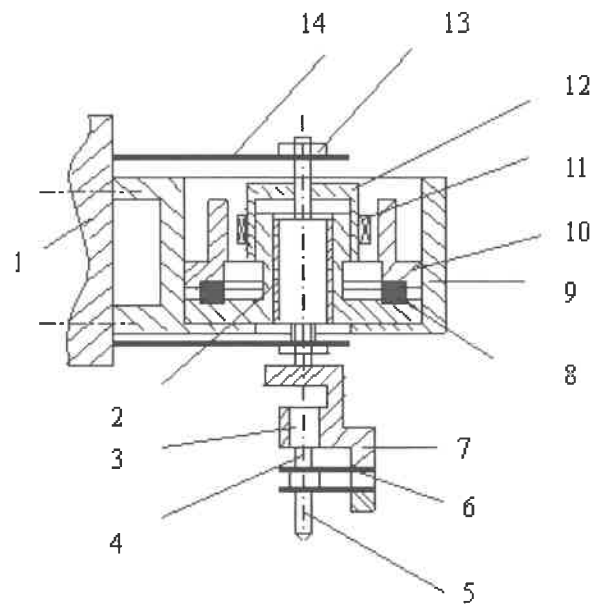

1 - installation rack 2 - framework 3 - coil of induction 4 - induction magnetic core
5 - stylus 6 - reed 7 - holding rack 8 - iron post 9 - shell
10 - alnico 11 - coil 12 - moving part 13 - nut 14 - reed

Fig. 1 Structure of the profiling device

The stylus is connected to the magnet core of the electric inductance through two reeds installed on holding rack. When the stylus moving through the measured surface, at the same time, through two reeds installed on holding rack, stylus pulls magnet of inductive sensor to move, displacement signal is generated. This signal is transmitted to processing circuit of electric inductance. In order to improve measurement accuracy, electric inductance should be high precise and should work in very little and linear range. Usually, the measurement range of electric induction should be smaller than 3μm according to the precision profiling device required. The VCM consists of coil, magnet, alnico, iron post, moving part, etc. The coil of this motor used in the profiling device is movable and short. Electric induction sensor is installed at the bottom of the framework of the VCM.

In order to extend the measurement range of the device, the holding rack and the electric induction, connected with holding rack, are connected with the moving part of VCM. The moving part of the motor is connected with two reeds installed on installation rack. In addition to

the structure as the above, other types of structures can be used. For example, the VCM can have a long coil. Other sensors, such as a differential transformer or a capacity displacement sensor, could be used, although the precision may be affected. No matter which structure used, the moving part of VCM must be connected with moving part of electric induction or differential transformer. The sensor used in this profiling device must have high precision, little measuring range as small as possible, fine linearity. The enlargement of measuring range must be conducted by driving moving part of VCM up or down. In addition, the electric induction or capacity displacement sensor must be working in very little measuring range in order to improve resolution of profiling device. The holding rack and electric induction sensor are connected with moving part of VCM. When voltages are applied to the coil of the motor, the moving part will be located at corresponding position due to magnetic force. As a result, the force between the stylus and workpiece will vary. When the moving part moves, it drives the holding rack up and down. Therefore, the electric induction sensor would be moved up or down.

Signal processing

Signals of the electric induction are transmitted to a computer after they are processed by the signal processing circuit, and converted by the A/D converting circuit. The signal processing circuit is required for high stability, lower electric noise, and high resolution. When the magnet of electric induction located at the predetermined limit position, the voltage input of signal processing circuit is also a predetermined voltage, such as 1-4V. The output of A/D converter is also a predetermined value near to LSB and MSB of A/D converter. When measuring a workpiece, if displacement varies in measuring range of electric induction, the moving part of the motor will not be adjusted. When the output of A/D converter exceeds predetermined value, the voltage applied to coil of VCR will be adjusted through D/A converting circuit. As a result, the moving part will be driven up or down. Making use of a digital PID control algorithm, the adjustment value of the moving part is determined by the computer, according to the voltage applied to the coil of the VCM.

Therefore, the electric induction will work in the pre-determined measurement range. The measurement force will be adjusted. Because the measuring force of the profiling device can be known by a computer from the value of A/D converter and the moving part of the motor may be adjusted, the measuring force between stylus and surface of workpiece can be adjusted to the level of millinewtorns, due to using the PID feedback algorithm, and can be maintained almost at a constant value. Therefore, the stylus would not damage the surface of a workpiece. There are a number of error sources in this profiling device. The friction on the magnet, the damping of the reeds, the fluctuation of voltage, magnetic lag of the VCM, resolution and instability of the electric induction sensor are the typical error sources. The magnetic lag is an important factor. There is a hysteresis error between the moving parts of VCM moving up and down. In order to solve the problem, the VCM position must be calibrated with high precision.

Applications

The proposed profiling device has been used in a measurement system to trace marks on bullets for forensic investigations (Fig. 2). Typical measurement results are as shown in Fig. 3. The application required a measurement range at least at 200μm. In addition, good longitudinal and

lateral resolutions were required. In the measurement system, the probe responsible for the contact force control was set to a 10μm range to ensure a sensitivity level necessary for the application.

Due to the use of a high stability signal processing circuit, the signal of the probe output could be controlled within 1mV. The probe output was used as feedback signal to control the voice coil servo system to reduce the measurement force. As a result, the indention of the probe was controlled to be less than 5μm, and the measurement force was estimated to be at the 0.0lmN level, at least at the level of millinewtons. In a series of experiments, measurement marks could not be traced using a 40x optical microscope. The resolution of the profiling device was 10nm, and the measurement range was up to 2mm. The proposed profiling system can be a good supplement for high precision, low cost profiling applications.

Fig. 2 A system utilizing the profiling device

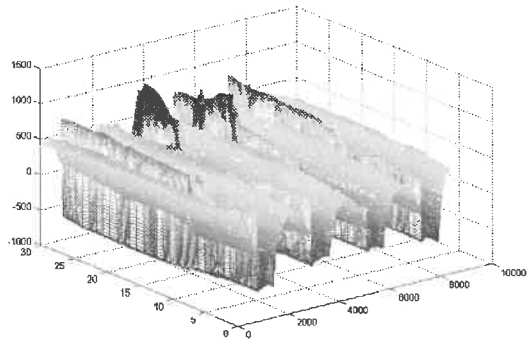

Fig. 3 Measurement results of the system

Conclusions

A profiling device with a resolution of 10nm and a measurement range up to 2mm has been developed. The device should have a precision better than 0.1μm. It has been used successfully in a demanding measurement application. In this device, an inductive probe of high resolution and a voice coil servo system were used to achieve millinewton level measurement forces. The device has a simpler structure and is easy to use and manufacture.

References

[1] Chuard, M., Mignot, J., Nardin, P., and Rondot, D., 1986, Range expansion and automation of a classical profilometer, Journal of Manufacturing Systems, **6**(3), pp. 223-230.

[2] Howard, L. P., and Smith, S. T., 1992, Long range constant force profiling for measurement of engineering surfaces, Review of Science Instrument, **63**(10), pp. 4289-4295.

[3] Chetwynd, D. G., Liu, X., and Smith, S. T., 1996, A controlled-force stylus displacement probe, Precision Engineering, **19**(2-3), pp. 105-111.

[4] Howard, L. P., and Smith, S. T., 1994, A metrological constant force stylus profiler, Review of Science Instrument, **65**(10), pp. 892-902.

DEMONSTRATION OF SUB-ANGSTROM CYCLIC NONLINEARITY USING WAVEFRONT-DIVISION SAMPLING WITH A COMMON-PATH LASER HETERODYNE INTERFEROMETER

Feng Zhao
Jet Propulsion Laboratory, California Institute of Technology, Pasadena, CA 91109

Several NASA's missions such as the Space Interferometry Mission, call for a displacement measuring interferometer (DMI) with a linear accuracy better than 0.1nm. Traditional implementations of DMI are based on laser heterodyne techniques and polarization to separate and combine the measuring beams. However, traditional interferometers suffer from periodic nonlinear errors on the order of a few nanometers due to optical self-interference. Polarization leakage has been found to be the dominant source for the periodic nonlinear error. With even state-of-the-art polarizing optics, the nonlinear error is still difficult to be reduced to less than 1nm. In addition to having large nonlinear error, traditional DMIs are quite sensitive to temperature changes and are far-off from meeting the stability requirement imposed by these proposed missions.

A novel common-path heterodyne interferometer (COPHI) was proposed at JPL as a multi-purpose, high-resolution laser interferometer [1-2]. In this paper, we describe a new approach to address both the cyclic error and thermal stability problems. Figure 1 shows the schematic of COPHI configured as a displacement measuring interferometer. Figures 2 and 3 show the pictures of the prototype COPHI we have developed at JPL.

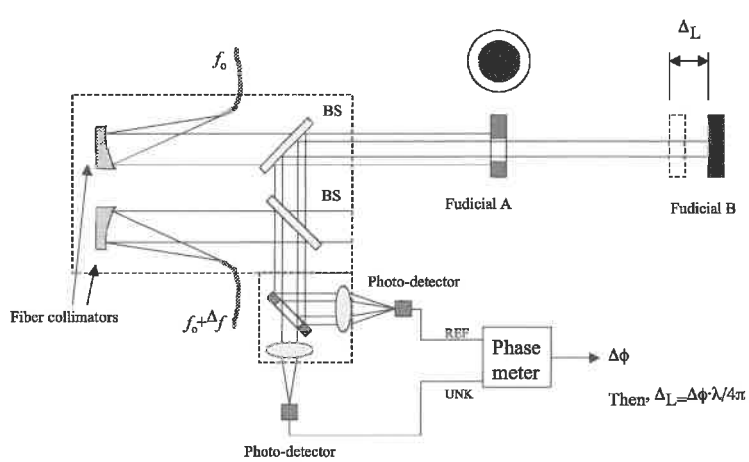

Figure 1. Schematic of a common-path heterodyne interferometer, configured for displacement measurement.

In this interferometer, both the measurement and reference beams are collimated from a pair of polarization-maintaining fibers with two Zerodur off-axis parabolic mirrors. In the displacement measurement configuration, we use a flat mirror with a center hole as fiducial A and a second flat mirror as fiducial B, as shown in Figure 1. The center hole in fiducial A allows the center portion of the beam at frequency f_o to reach fiducial B. This way the measurement beam f_o is split into two symmetric sections. Both

mirrors are aligned to retro-reflect the beams back to the interferometer to combine with reference beam at frequency $f_o + \Delta f$, which serves as a local oscillator. At this point, two interference fringes are formed, the annular fringe formed by fiducial A and the center fringe formed by fiducial B. Then the heterodyne fringes are spatially separated with a truncated mirror and focused into separate photo-detectors. The phase difference ($\Delta\phi$) between the reference and measurement signals is then used to calculate the displacement (ΔL) between the fiducials:

$$\Delta L = \Delta\phi \frac{\lambda}{4\pi}.$$

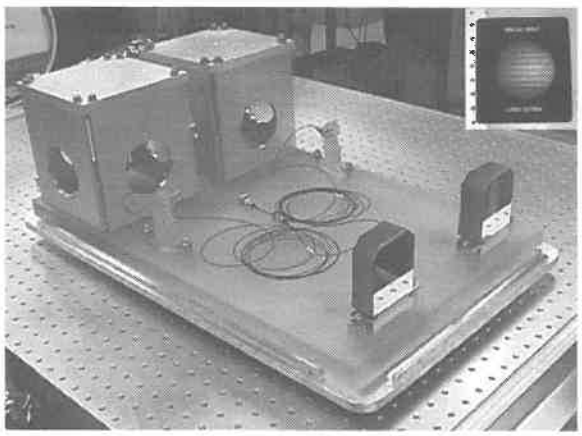

Figure 2 . Picture of the collimator/beam-splitter assembly. They are mounted on a Zerodur plate to ensure good thermal stability. The beams are 50mm in diameter and the shear interference fringes (top right) show the wavefront quality is better than λ/5 P-V for both beams.

Figure 3. Picture of the interferometer. The collimator/beam-splitter assembly is covered with multi-layered insulator (MLI) to isolate the optics from the ambient temperature flucturations. The heterodyne beams are generated with two acousto-optic modulators with their RF frequencies separated by Δf=10kHz.

To measure the residual periodic nonlinear error, a PZT is used to translate fiducial B "linearly" over a distance of many laser wavelengths. The distance is then measured with a phase meter. A periodic error in this "linear" translation can be estimated by looking at the power spectral density of the displacement data. In our experiment, the laser wavelength is 0.532μm, and the total stroke of the PZT is about 5μm with a triangle wave modulation at 0.05Hz. Thus cyclic error with λ/2 periodicity can be found at about 2Hz in the spectral domain.

Figure 4 shows the measured displacement of the PZT. We select an arbitrary linear displacement, e.g., between 27 and 36 seconds in Figure 4 for analysis. Figure 5 shows its residual after removing its linear to cubit terms. The power spectral density of the residual is calculated and plotted in Figure 6, in which the peak at 2Hz indicates the existence of λ/2 periodic nonlinear error. The total energy of this cyclic error is estimated to be about 730pm^2, which translates into a periodic nonlinear error of only 27pm RMS. This result represents a roughly 100 times improvement over traditional DMIs.

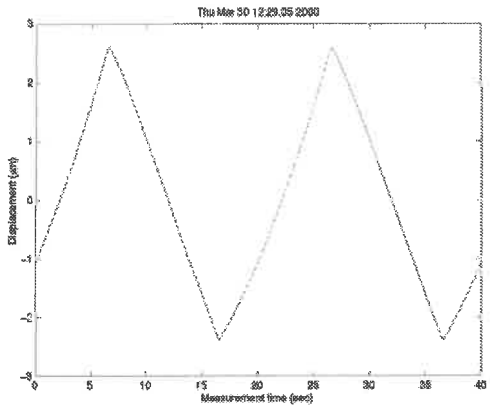

Figure 4 . Displacement of the PZT measured with the interferometer.

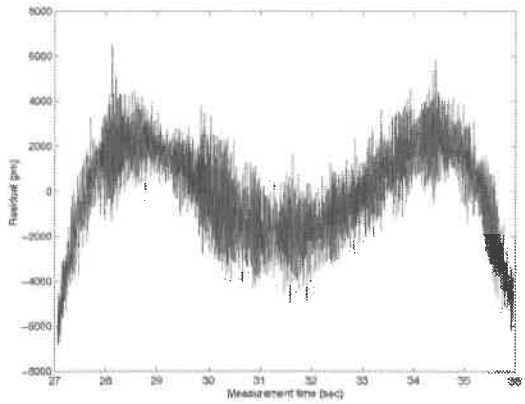

Figure 5. Residual of the displacement between 27 and 36 seconds after removing its linear to cubic terms.

This implementation of the DMI eliminates once the largest error source, i.e., polarization leakage. Nevertheless, several other sources such as ghost reflections, diffraction induced cross-talk between the two measurement beams can still cause self-interference thus periodic nonlinear error. In the above proof-of-concept demonstration, we use a guard-band between the two measurement beams to lower the diffraction cross-talk. The beam splitters have a small wedge and good anti-reflection coatings are applied to the back surfaces to minimize the effect of ghost reflections. The 27 pm periodic nonlinear error may be attributed to diffraction and ghost reflections in the interferometer.

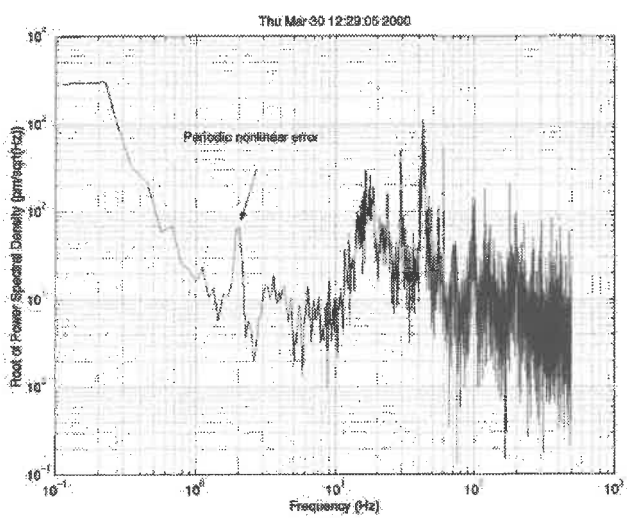

Figure 6. Power spectral density of the displacement data. As the PZT moves "linearly", the periodic error distinguishes itself from the noise background in the spectral domain. This result indicates a cyclic error of about 27pm RMS. Background noise measurement with PZT driver off indicates that peaks above 10Hz are attributed to vibrations in this setup.

It should be noted that in COPHI, the two measurement beams (annular and central) are derived from the same wavefront using wavefront-split approach. In other words, thermal expansion of the optical components in the interferometer is common-mode. This feature greatly improves the temperature stability of the interferometer.

In the thermal stability measurement, we replace fiducials A and B with a single Zerodur mirror. This single mirror ensures that there is no change in the fiducials during the measurement. Changes of the phase between the annular and central fringes are due to the drift of the interferometer itself. Figure 7 shows a measurement of the drift over 10 hours. The result indicates that the interferometer is stable to better than 100pm over 1 hour period.

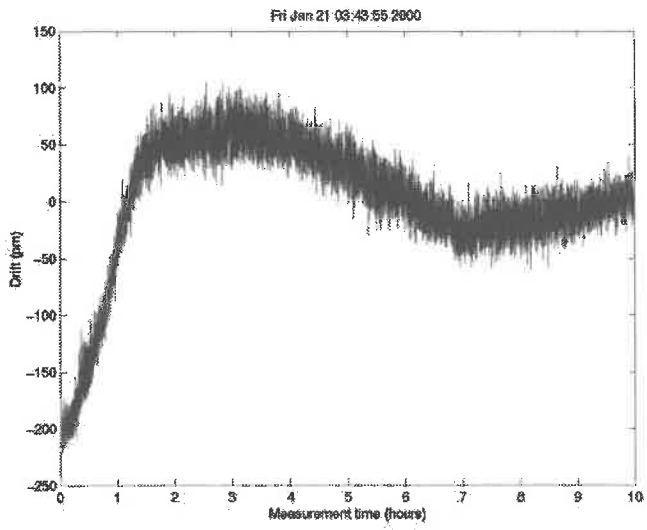

Figure 7. Stability measurement of the interferometer. The drift is less than 100pm over 1 hour period.

In this paper, we proposed and demonstrated a novel displacement interferometer with extremely low periodic nonlinear error (~27pm RMS) and ultra high temperature stability (better than 100pm over 1 hour). These results represent more than an order of magnitude improvement over traditional interferometers. In addition, this interferometer is simple and quite easy to implement. It may find wide applications in a variety of ultra-high precision measurement ranging from atomic force microscope calibration to gravitation wave sensors, etc.

The author would like to thank Robert E. Spero for his help on data analysis. This research was carried out at the Jet Propulsion Laboratory, California Institute of Technology, under a contract with the National Aeronautics and Space Administration.

REFERENCES:

[1] F. Zhao, "A common-path, multi-channel heterodyne interferometer," NASA Tech. Briefs, Vol. 25, No. 7, pp12 (2001).

[2] F. Zhao, J. Logan, S. Shaklan, and M. Shao, "A common-path, multi-channel heterodyne laser interferometer for sub-nanometer surface metrology," SPIE Proceedings, Vol. 3740, pp 642-645 (1999).

DEVELOPMENT OF SUB-NANOMETER RACETRACK LASER METROLOGY FOR EXTERNAL TRIANGULATION MEASUREMENT FOR THE SPACE INTERFEROMETRY MISSION

Feng Zhao, Rosemary Diaz, Philip Dumont, Peter G. Halverson, Stuart Shaklan, Robert Spero
Jet Propulsion Laboratory
California Institute of Technology
Pasadena, California 91109
Lawrence Ames, Stephanie Barrett, Robert Barrett, Ray Bell, Robert Benson, Gene Cross, Kalyan Dutta, Todd Kvamme, Buck Holmes, David Leary, Patrick Perkins, Mark Scott, and David Stubbs
Lockheed Martin Advanced Technology Center
3251 Hanover Street, Palo Alto, California 94304

The external metrology for NASA's Space Interferometry Mission (SIM, http://sim.jpl.nasa.gov) uses a laser heterodyne metrology system to measure the distance between fiducials on the siderostat mirrors and a reference fiducial. Figure 1 illustrates an early version of the SIM external metrology truss. The relative orientation of multiple interferometer baselines is computed by triangulation of the measurements between these fiducials.

To accomplish micro-arcsecond astrometric measurements, SIM requires the external metrology to provide an accuracy better than 0.1 nm in relative distance measurement. A novel common-path heterodyne interferometer was proposed at JPL to address the cyclic error problem, which has been one of the major error sources in laser interferometers. This concept is based on wavefront-division sampling as shown in figure 2.

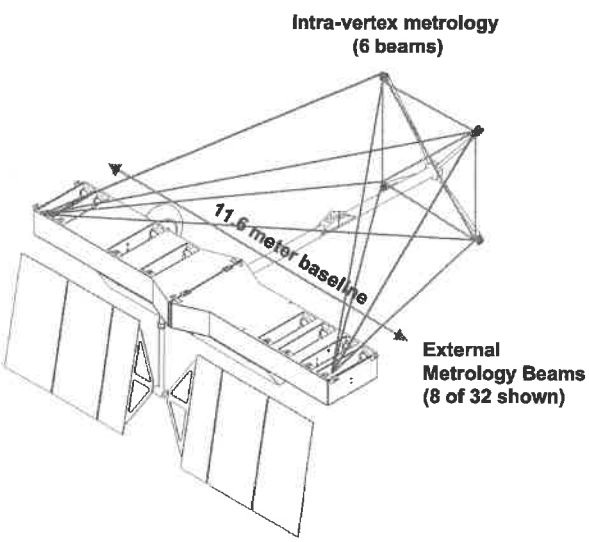

Figure 1. An early version of the SIM external metrology truss. The interferometer baseline is monitored with triangulation measurement between the reference fiducials.

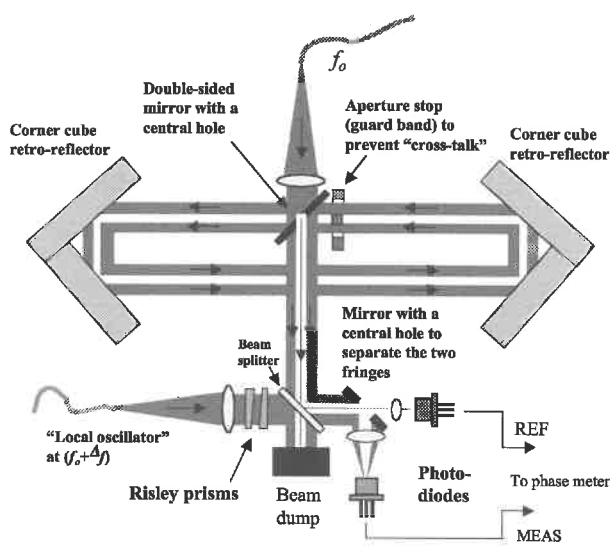

Figure 2. Schematic of the proposed laser heterodyne interferometer for use in the SIM external metrology system. Corner cube retro-reflectors are used as the measurement fiducials.

Unlike traditional displacement measuring interferometers using polarization to separate and combine interfering beams[1], this new scheme divides the wavefront of a collimated beam into annular measurement (M) and core reference (R) portions. The R beam is coaxially situated inside M before and after recombination. The gauge measures the optical path difference (OPD) between the M and R beams, which is twice L, the distance between the corner cube fiducials. To determine the OPD, the R and M beams are mixed with a "local oscillator" beam which has optical frequency offset by Δf, and the interference is detected with photodiodes. The resulting heterodyne signals are sent to a phasemeter which determines ϕ, the relative phase of the heterodyne signals, in cycles. Thus we get $L=\phi\lambda/2+L_0$ where L_0 is the initial fiducial separation. (In SIM, L_0 will be determined off-line during astrometric data reduction.)

Compared to traditional metrology heads, this approach[2,3,4] has the advantage of not having polarization leakage which has been the major source of cyclic nonlinearity. In addition, the use of wavefront division reduces sensitivity to temperature drifts. However, new challenges arise because the segmented beams experience diffraction which (a) causes beam mixing (resulting in cyclic nonlinearity) and (b) causes sensitivity to slight changes in the transverse position of the M beam, after it has traveled several meters and reaches the measurement photodiode.

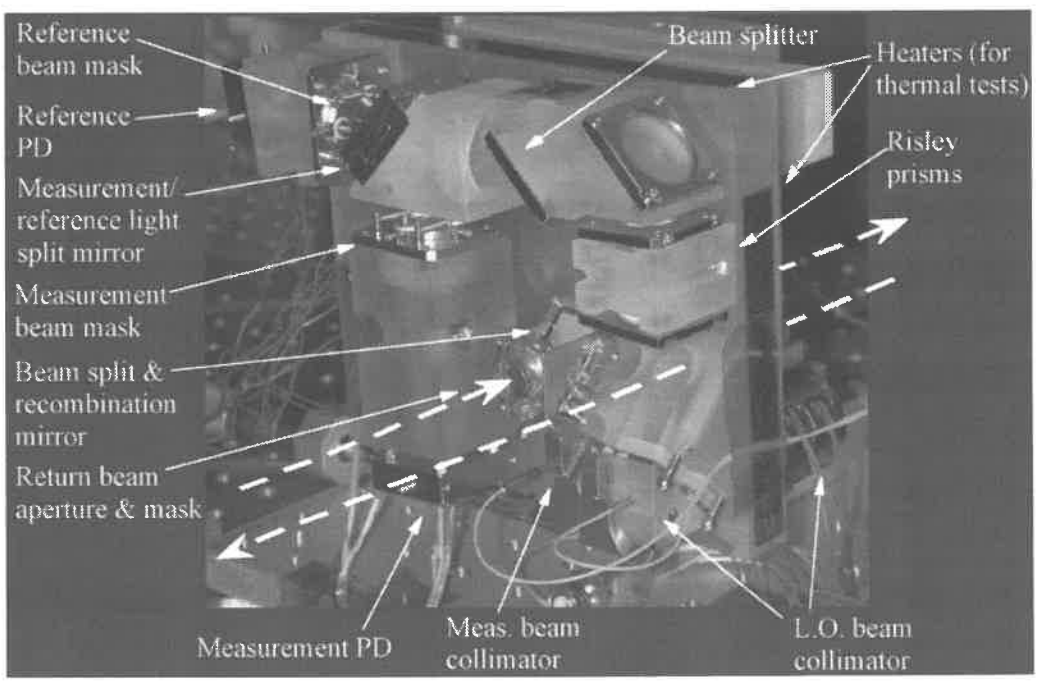

Figure 3. Prototype metrology head. 1.3 μm laser light from the laser source is delivered by optical fibers to collimators (lower right). The measurement (M) beam leaves the back of the assembly, reflects off the first corner cube (not shown) offset 25mm to the right and passes through the assembly bench on its way to the 2nd corner cube. After the 2nd cube, the M beam enters the return aperture, and reflects (up) off an annular mirror. It is now traveling with the reference R beam, which is inside the annular M beam. The beam splitter mixes the M and R beams with the local oscillator beam. The mixed beams travel to the left, and are separated by a 2nd annular mirror which redirects the M beam down to the measurement photodiode, and allows the R beam to travel unimpeded to the reference photodiode.

There are several methods to reduce the error caused by the diffraction effect. First, use a guard band (including baffles, etc.) between the M and R beams to keep the diffraction contamination small. Second, use small photo-detectors and place them at the back focal plane of

the focusing lenses. This spatial filtering approach will reduce the effect of the diffraction ripples and other high spatial frequency components on both M and R since the high frequency components do not fall on the detector. Third, use an imaging lens to reverse the diffraction effect, in which the lens forms a clear image of the first wavefront separating mirror on the second fringe separating mirror. In our prototype metrology gauge shown in Figure 3, we use only the simple guard band (mask) approach.

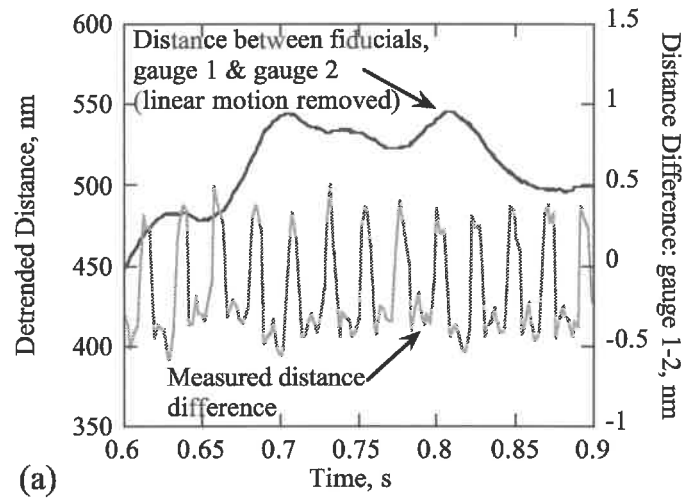

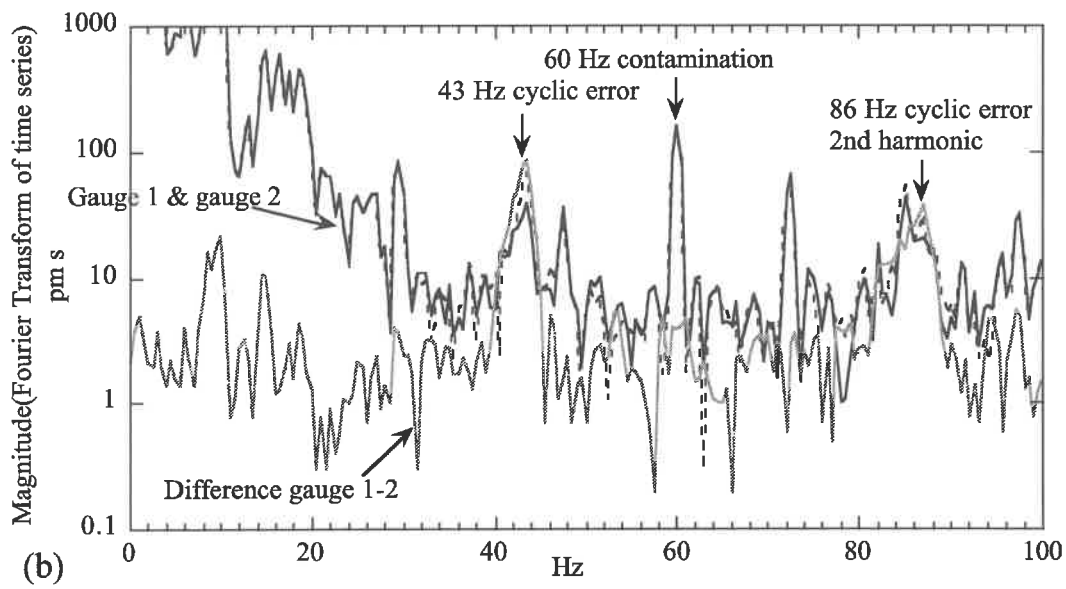

Figure 4: Data taken from two prototype gauges during linear motion of one corner cube fiducial. (The two gauges concurrently observe the distance between the *same* two fiducials.) Cube velocity was ~28 microns/second, causing 43 cycles of OPD change per second for the 1.3 micron source wavelength. (a) shows the data as a function of time. The cyclic nonlinearity is too small to be observed in the individual gauges, where it is hidden by vibrations and the nonlinearity of the piezo moving the fiducial. However these obscuring artifacts cancel in the *difference* data, where nonlinearity is easily seen. (Note 100x scale change.) In (b), the Fourier transform of the same data, cyclic nonlinearity is seen as peaks at 43 and 86 Hz (determined by the cube velocity) in each gauge indicating cyclic errors of 57 and 98 pm rms for gauges 1 (solid) and 2 (dashed) respectively. Higher harmonics are also seen, but at much lower amplitudes.

To determine the cyclic nonlinearity of the interferometer, we use the well-known approach in which a linear displacement over many wavelengths is introduced by moving one corner cube with a PZT[5]. The residual cyclic nonlinearity can be measured by looking at the corresponding periodic structure in the power spectrum of the displacement data. Figure 4 shows the measurement results of two interferometers co-aligned to measure the same corner cube displacement. (The two metrology heads have holes which allow the beams to be interlaced,

hence they observe the same pair of corner cubes.) The results indicate that the cyclic nonlinearity is less than 100pm RMS in both interferometers.

The temperature sensitivity of the interferometer is measured by introducing an intentional temperature change to the metrology head. The results are shown in Figure 5, where the top curve is the temperature of the interferometer, and the bottom curve is the optical path length error caused by the change in temperature. This measurement indicates that the temperature sensitivity is about –8 pm/mK.

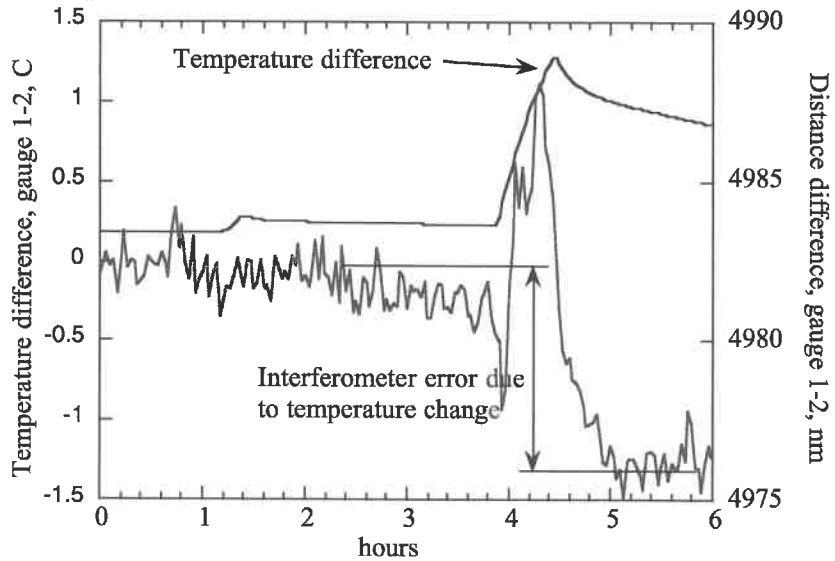

Figure 5. Temperature sensitivity measurement. Heating gauge 1 (while gauge 2 stays at constant temperature), causes a disagreement between the gauge outputs. The transient maximum disagreement at 4.4 hours is due to gradients, uneven heating of the optics. The gradients dissipate after the heater power is turned off. For SIM, we are mainly interested in the gradient-free (soak) temperature coefficient.

We have developed a prototype displacement measuring interferometer for use in SIM's external metrology system. This interferometer is based on wavefront-division rather than polarization to separate and combine interfering beams. Both experimental data and theoretical calculations confirm that the cyclic nonlinear error is smaller than 100pm. This is about a factor of 50 improvement over traditional polarization type interferometers. Our temperature sensitivity measurement also indicates that this interferometer is quite immune to ambient temperature variations. The results so far suggest that the wave-front-division approach is very promising in providing a flight qualifiable metrology gauge suitable for SIM external metrology systems.

The research described in this paper was carried out by the Jet Propulsion Laboratory, California Institute of Technology, under a contract with the National Aeronautics and Space Administration.

---

[1] P.G. Halverson et al., "Techniques for the Reduction of Cyclic Errors in Laser Metrology Gauges for the Space Interferometry Mission", **this conference**, and references therein.
[2] F. Zhao, NASA Tech. Briefs **25**, 7, pp12 (2001).
[3] F. Zhao, J. Logan, S. Shaklan, and M. Shao, SPIE **3740**, 642-645 (1999)
[4] F. Zhao et al., ODIMAP III, Pavia, Italy, Sept. 20-22, 2001 pp 39-44.
[5] P.G. Halverson et al., ODIMAP III, Pavia, Italy, Sept. 20-22, 2001 pp 63-68.

AN ALTERNATIVE TECHNIQUE TO THE GEOMETRIC TEST OF MACHINING CENTERS

Sousa, A.R.[1]; Schneider, C.A.[2]
LABMETRO - Metrology and Automation Laboratory
UFSC - Federal University of Santa Catarina - Brazil
[1]ars@certi.ufsc.br and [2]cas@certi.ufsc.br

Abstract

An alternative technique for the geometric test of machining centres was developed, to congregate metrological reliability with operational and economical advantages, when comparing to methods classically used for such task. A touch probe is used on a 3-axis vertical machine center to check against artifacts calibrated on a coordinate measuring machine (CMM). By comparing the results obtained from the machine tool and CMM, the main machine tool error components are measured, attesting the machine accuracy. The method is easy to use, has lower cost than classical test techniques, and the results have shown that its uncertainty is comparable to well established techniques.

1. INTRODUCTION

The development of the Computer Numerical Controls (CNC) has made possible to correct some of the mechanical errors of the machine tools, taking their accuracy beyond mechanical limitations [1]. However, to take advantage of these means, the users should periodically test their machines but, in spite of most CNCs have these means available, most users do not test their machines to update the CNC error compensation table. The economic, metrological and operational limitations of the geometrical test techniques used to verify the machine accuracy are the main reasons for this problem. Classical techniques usually are expensive or very time consuming or are not metrological reliable. More, usually the results are not formatted for compensation at the CNC.

This work describes an alternative technique for the geometric test of machining centres, developed to congregate metrological reliability with operational and economical advantages, when comparing to methods classically used for such task. A system called QUALIMAQ was developed to make this operation easy and time efficient, combining the coordinate metrology with the use of calibrated artefacts [2]. The method is an alternative to the expensive and/or very time consuming classical techniques that are the main reasons for what the machine tool user do not undertake tests with greater frequency.

The QUALIMAQ method was applied to the geometric test of a vertical machining centre, tested also with classical techniques (laser interferometer, straightedge and square). The results showed that the uncertainty of QUALIMAQ is comparable to well established techniques, with significant advantages in operational and economic aspects. Its time efficiency is 7 times better and the costs involved with the operation are 6 times lower than the same geometric tests performed with the classical techniques.

In order to verify the efficiency of the CNC correction, the errors were used to correct the machine and two plates with holes were machined, one of them before and the other one after the correction. The measurement of both workpieces on a Zeiss CMM indicated that a maximum error in the first workpiece has decreased in more than 70%.

2. THE ALTERNATIVE TEST TECHNIQUE

The use of probes on machine tools for *automatic workpiece setup*, *tool setting*, *digitalisation* and *in-process measurement* has increased in the last years, improving the machine productivity, as non-cutting times are reduced by up to 50% [3]. In this paper, the touch probe is used for another (important) function: verify the geometric accuracy of the machine and update its CNC error compensation table.

In the QUALIMAQ system, a touch probe is installed on a 3-axis vertical machine centre to check against calibrated artefacts (an aluminium hole plate and a vertical detachable artefact), previously calibrated on a Coordinate Measuring Machine. The artefacts are measured on the machine tool and the coordinate points are transferred via serial interface, to a portable computer where a software acquire and process these points, comparing them to the calibrated values.

As a result, the errors of positioning, straightness and squareness are measured, attesting the machine tool accuracy. These errors can be easily formatted to update the error compensation table at the CNC, enhancing the geometric behaviour of the machine. The software also give reports of the errors, monitoring the machine accuracy condition. The figure 1 illustrates the system, and the artefacts.

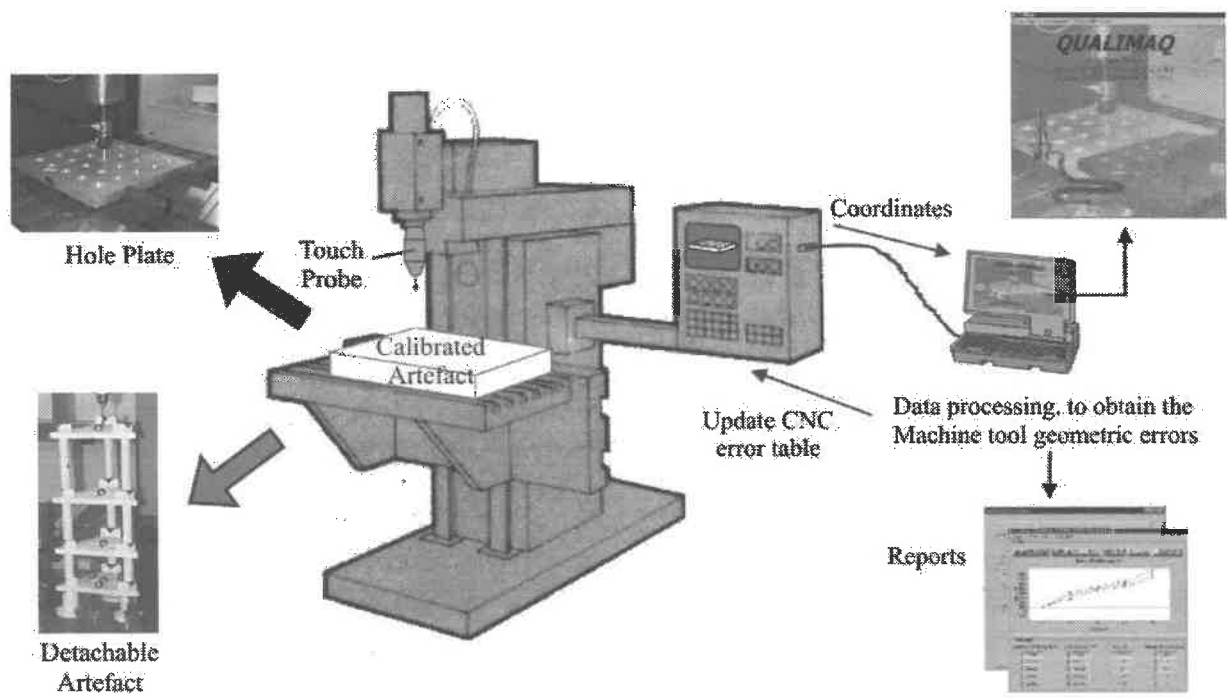

Figure 1 - Basic configuration of QUALIMAQ system

A **Hole Plate** and a **Vertical Detachable Artefact** are calibrated in a Coordinate Measuring machine and used in the geometric test of the machine tool. The **Plate** has 25 holes disposed in a square grid, with the position of the centers calibrated, and is used to test the horizontal plane (XY) of the machine. The **Detachable Artefact** was developed to test the vertical planes of the machine (XZ and YZ) and has dismounted parts with kinematics mounting, that can be repositioned very precisely [4]. Both artefacts have their temperature measured and the thermal expansion compensated.

3. EXPERIMENTAL RESULTS

In order to compare the time efficiency and to evaluate the metrological reliability of QUALIMAQ system, a same machine tool was tested with different methods. A CNC vertical milling machine was tested with laser interferometer (linear positioning), square (squareness) and straightedge (straightness). After that, these errors were verified with QUALIMAQ system and all of the results compared. These experiments are illustrated in the figure 2 and typical results for linear position and straightness can be seen in the figure 3 and 4. As described previously, in the horizontal plane of the machine tool (XY) the hole plate was used and for the horizontal planes, the vertical detachable artefact.

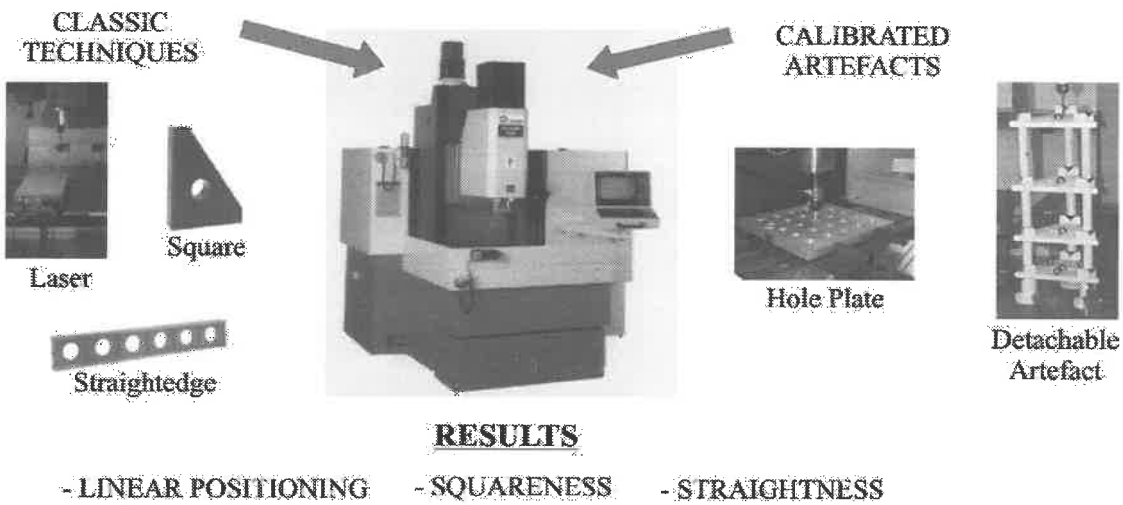

Figure 2 – Comparisons between QUALIMAQ and Classical Techniques

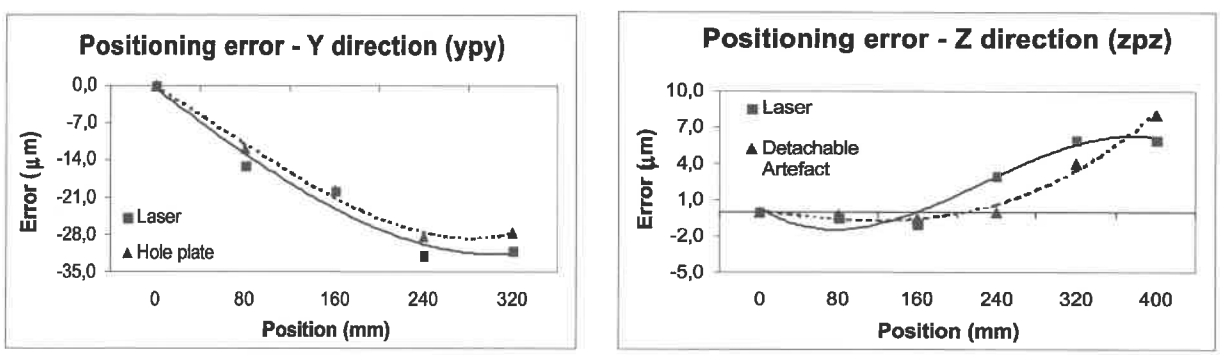

Figure 3 – Typical results obtained with Laser and artefacts for the linear positioning test

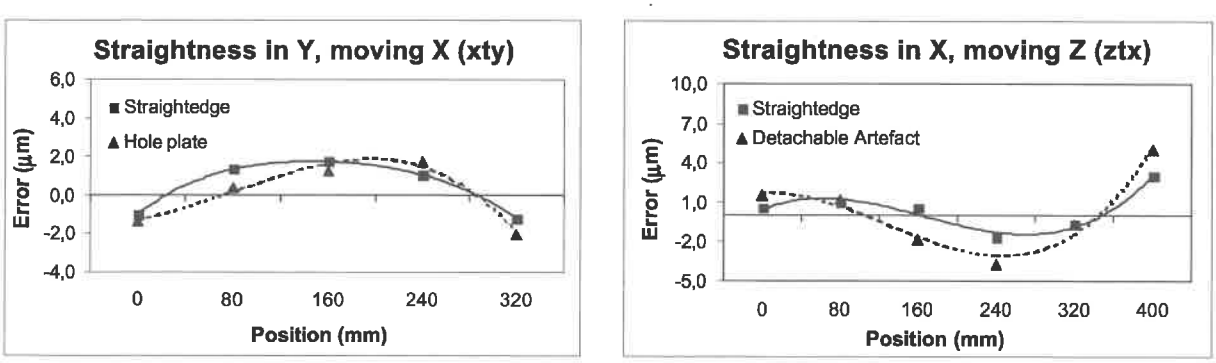

Figure 4 – Typical results obtained with Straightedge and artefacts for the straightness test

In all these graphics, the results obtained with classical methods and QUALIMAQ have a very close concordance and the measurement uncertainties are also similar. But, when operational and economical aspects are analysed, the numbers are very different.

The figure 5 shows the time necessary to perform all of geometric tests on the milling machine, employing classical and QUALIMAQ methods, as well as the cost of the equipment involved in the experiments. From these numbers can be concluded the higher operational and cost efficiency of the QUALIMAQ method for this size of CNC machine tools, when compared to that classical techniques.

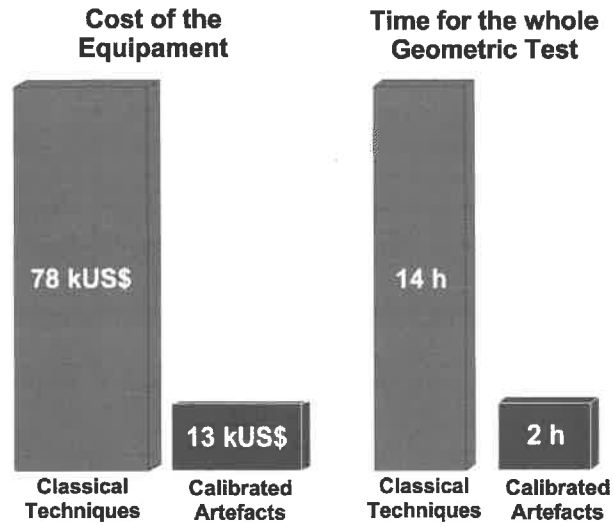

Figure 5 – Operational and economical comparisons

4. CONCLUSIONS

The results obtained in this work showed that the geometric test with calibrated artefacts can be a low cost, easy to use and reliable method to verify the accuracy performance of machine tools. A vertical machining center with a touch probe was tested with the method proposed and, for comparison, also with classical techniques. The results revealed a promising method not only in the metrological aspect, but in operational and economical aspects also.

The uncertainty of QUALIMAQ is comparable to well established techniques, with significant advantages in operational and economic aspects. Its time efficiency is 7 times better and the costs involved with the operation are 6 times lower than the same geometric tests performed with the classical techniques. A geometrical test technique with such advantages could motivate the machine tool users to more frequent tests, and to update periodically the CNC error compensation table.

To motivate the machine users to undertake testing with greater frequency, several techniques have been developed and applied, trying to congregate operational advantages, low price and reliability. The research and development of such techniques is important for the users to explore that new error compensation resources of machine controllers, important for the quality assurance in machining processes.

5. REFERENCES

[1] **Drescher, Joe and Malloch, Charles**. *Application of performance testing to maintain and improve machine tool accuracy*. International Manufacturing Engineering Conference - Proceedings, pp. 151 - 153, 1996.

[2] **Sousa, A.** *Calibrated artifacts with Coordinate Metrology innovating the Geometric tests of Machining Centers*. Doctor Thesis, Federal University of Santa Catarina - Brazil, 2000 (in Portuguese).

[3] **Beard, Tom**. *In touch with quality and productivity*. Modern machine shop, January, 1998.

[4] **Sousa, A. and Schneider, C. A.**. *A detachable step gage for the calibration of vertical machining centers and bridge type coordinate measuring machines*. Proceeding of the Annual Meeting of the American Society for Precision Engineering, ASPE 2000, Scottsdale - AZ, USA, November, 2000.

EVALUATING THE TOOL POINT DYNAMIC REPEATABILITY FOR HIGH-SPEED MACHINING APPLICATIONS

Kate M. Medicus, Tony L. Schmitz
National Institute of Standards and Technology, Gaithersburg, MD

Introduction

Unstable cutting (chatter) can be a primary limiting factor in reaching high material removal rates (MRR) in high-speed milling. Chatter may be avoided by proper selection of machining parameters [1,2] or by tuning the tool point dynamics to increase stability at the desired machining conditions [3-6]. Both methods use the setup-specific stability lobe diagram, which divides the machining parameter space into stable and unstable regions, to select the commanded spindle speed and axial depth of cut. The stability lobes are calculated from the tool point Frequency Response Function (FRF) and specific cutting energy coefficients for the selected machining operation [7,8]. Variations in the tool point FRF, which occur due to removing and replacing the holder in the spindle, tool changes, and deviations in tool length and collet torque, change the stability lobe diagram and, therefore, affect the selection of machining parameters. In this study we replicated these variable conditions and measured the resultant FRFs. Comparisons between the FRFs indicate the dynamic repeatability of each change.

The tool point FRF was measured using an instrumented hammer/accelerometer setup (Fig. 1). An instrumented hammer was used to excite the tool while an accelerometer measured the acceleration at the tool point. The FRF was then calculated from the complex ratio of the displacement (twice-integrated acceleration) and hammer Fourier transforms. The variability of the FRFs that occurred without changing the setup was established as the baseline measurement repeatability.

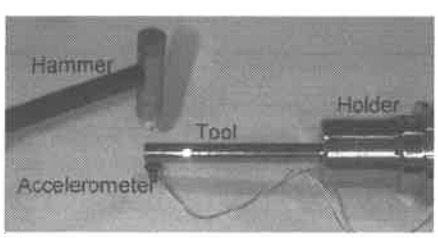

Figure 1. Hammer and accelerometer setup.

Two types of tool holding systems, a traditional collet tool holder and a new interference fit Schunk Tribos[1] tool holder, were tested for their dynamic repeatability. Both systems used an HSK 63A holder/spindle connection. All experiments were performed on a Makino A55[1] high-speed CNC mill. A 12.7 mm diameter carbide tool blank was used in the collet holder, 12.0 mm blanks in the Tribos holder. In both cases, the angular orientation of all components was maintained throughout the measurements.

Tool Overhang Variation

A schematic of the Schunk Tribos tool holding system is shown in Fig. 2. In the resting position (Fig. 2a), the holder restricts entry of the tool. When force is applied as indicated in Fig. 2b, the holder elastically deforms and the tool is inserted. After the force is relieved, the holder relaxes to clamp the tool along three contact lines (Fig. 2c). The Tribos holder dynamic repeatability was tested at tool overhangs ranging from 6:1 to 11:1 length to diameter (L:D) ratios, in steps of one diameter using two tool blanks with lengths of 115 mm and 153 mm. At each tool length, the variation in the FRF was found when: 1) the tool holder was removed from the spindle to the tool rack and replaced (to simulate a break in machining), and 2) the tool was removed from the holder (simulating a tool change), which also required removing the holder from the spindle.

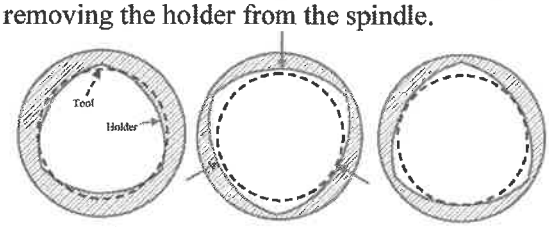

(a) (b) (c)

Figure 2. Schematic of Schunk Tribos tool holding system operation (not to scale): a) rest position, b) force applied, and c) tool clamped.

[1] Certain commercial equipment, instruments, or materials are identified to adequately specify the experimental procedure. Such identification is not intended to imply recommendation or endorsement by the National Institute of Standards and Technology, nor is it intended to imply that the materials or equipment identified are necessarily the best available for the purpose.

A representative FRF (magnitude component) for each tool length tested in the Tribos holder is shown in Fig. 3. Characteristic differences between the data sets are seen. In particular, the 7, 8, and 11:1 tools are single mode systems (shown by a single peak) and the 6, 9, and 10:1 tools are dual mode systems (two peaks). The dual mode systems occur due to the dynamic absorber effect [5,6] that occurs when the natural frequency of the tool approaches or matches a natural frequency of the spindle. The spindle then acts as a dynamic absorber for the tool, which results in increased dynamic stiffness. Evaluating the dynamic repeatability becomes more complicated due to this two mode behavior. Unlike the single mode data, a simple fit to determine the dynamic stiffness can not be performed. Therefore, a point-by-point comparison of the FRFs was performed.

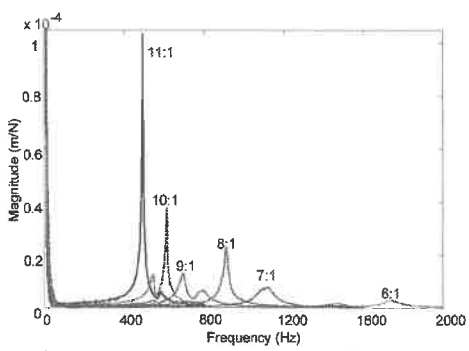

Figure 3. Magnitude component of FRFs for the Tribos tool holder.

To find the baseline repeatability, five FRFs (which were each an average of ten measurements) were acquired without changing the setup. When calculating the holder change repeatability, a single FRF (which was an average of 50 measurements) was measured, the tool/holder was moved to the rack and back, and the process was repeated for a total of five FRFs. The tool change repeatability analysis followed the same process as the holder movement repeatability evaluation except the tool was removed and replaced each time.

The FRF comparisons were performed by calculating the standard deviation of the set of five magnitude plots at each frequency (i.e., a point-by-point analysis). Fig. 4 shows the measurement, holder change, and tool change repeatability for the Tribos 9:1 and 11:1 tools using the point-by-point standard deviation method. As expected, the standard deviation curves follow the same shape as their respective FRFs; the uncertainty is higher at the natural frequency(s).

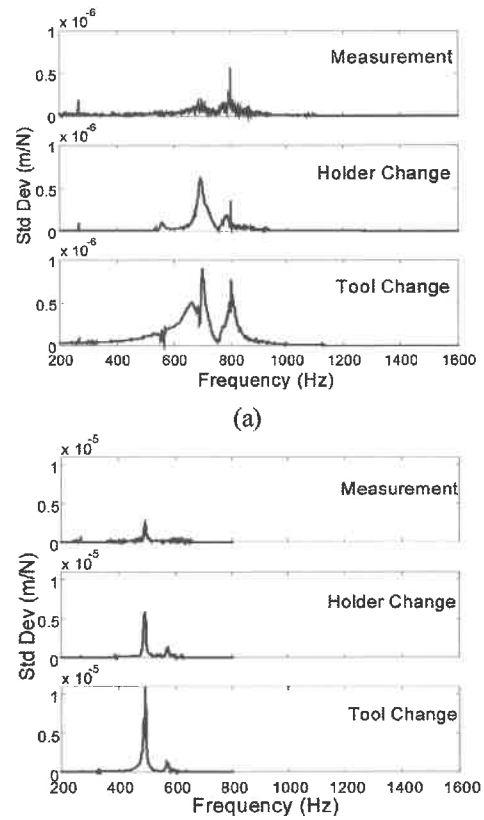

Figure 4. Standard deviation of magnitude FRFs showing measurement, holder movement, and tool change repeatability for: a) Tribos 9:1 tool and b) Tribos 11:1 tool. (Note different vertical scales.)

One possible method to compare between tool lengths and between the three repeatability levels is to use the maximum standard deviations from Figure 4. But, as before, the dual mode system changes the behavior of the standard deviation curve and makes this type of comparison unacceptable. For example, an order of magnitude separate the maximum standard deviation of the 9:1 (dual mode) and 11:1 (single mode) tools. Therefore, we used the area (calculated numerically) under the standard deviation curves to make the dynamic

repeatability comparisons. See Fig. 5. As expected, the repeatability decreases (i.e., standard deviation area increases) as the mechanical complexity of the change increases from the measurement to holder change to tool change. Additionally, the repeatability generally decreases with tool length.

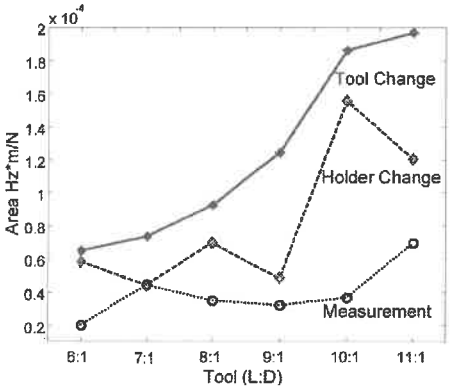

Figure 5. Area under standard deviation of magnitude FRF curves for multiple tool lengths.

Collet Torque Variation

Collet-type holders clamp the tool by creating uniform pressure around its circumference. In this study, we used a torque wrench to set the collet torque, although this may not always be the case in practice. We tested the tool point dynamic repeatability for this holder type over a reasonable range of torques for this collet: (47.5, 61.0, 67.8, and 74.6) N-m. The repeatability was also determined for holder and tool changes, but only at a set torque of 61.0 N-m.

The collet holder was tested with a tool overhang of 113.3 mm (9:1 L:D ratio). At this overhang, the system can be modeled as single mode; therefore, we used the dynamic stiffness directly to compare between data sets. Assuming a single mode, the minimum value of the imaginary part of the FRF (A), shown in Fig. 6, is inversely proportional to the dynamic stiffness of the system ($k\zeta$). See Equation 1, where dynamic stiffness is the product of the stiffness (k) and the damping ratio (ζ).

$$A = \frac{-1}{2k\zeta} \qquad \text{(Eq. 1)}$$

Fig. 7 plots collet torque versus dynamic stiffness for the collet holder data. As the torque increases we expect stiffness to increase while damping decreases. Here, the dynamic stiffness of the system increases overall, which indicates the stiffness is increasing faster than damping is decreasing.

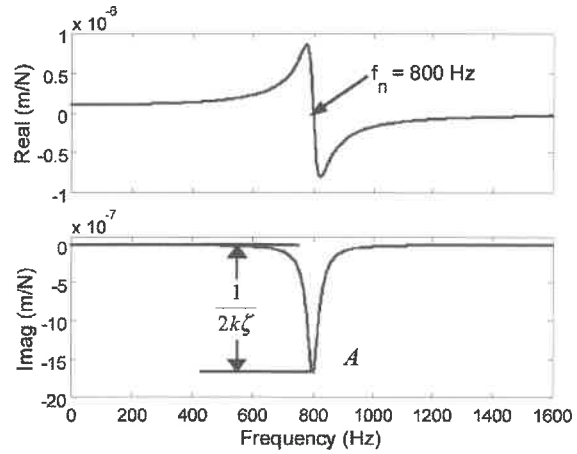

Figure 6. Typical FRF showing dynamic stiffness and natural frequency.

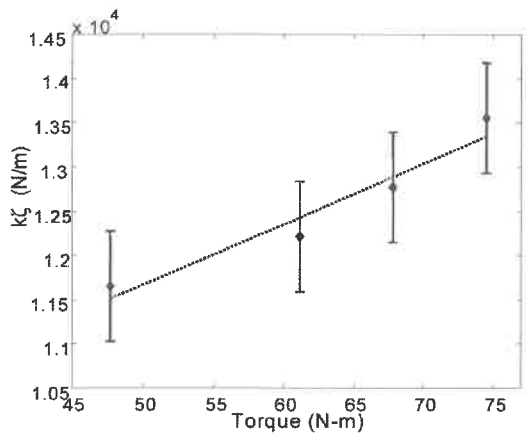

Figure 7. Variation in dynamic stiffness with applied collet torque. Data was not collected at 54 N-m.

The error bars on the data in Fig. 7 were developed from the standard deviation of the dynamic stiffness at 61.0 N-m. The dynamic stiffness standard deviation for the measurement, holder change, tool change were, $1.99\text{x}10^{-2}$ N-m, $3.87\text{x}10^{-2}$ N-m, $6.22\text{x}10^{-2}$ N-m, respectively. As with the Tribos system, the uncertainty increases with the complexity of the mechanical change. The error bars in Fig. 7 are

$\pm 6.22 \times 10^{-2}$ N-m, corresponding to the maximum value.

Tribos Holder vs. Collet Holder

In comparing the two tool holding systems, the decrease (percent change) in repeatability from the holder change to the tool change was examined. The percent decrease in repeatability from the measurement to holder change was not compared because it was believed that a large portion of that increase is due to the removal and replacement of the accelerometer between FRF measurements.

For the collet holder, the percent change was calculated from the standard deviation of the dynamic stiffness term at a torque of 61.0 N-m. For the Tribos holder, the percent change at each tool length was calculated from the area under the standard deviation curve; these values were then averaged to obtain an overall percent change. The percent change in repeatability from holder change to tool change was 37% for the collet holder and 33% for the Tribos holder. These results suggest two conclusions: 1) the dynamic stiffness variability associated with tool changes is not trivial and future research could focus on tool/holder interfaces that offer improved repeatability, and 2) the dynamic repeatability of the new Tribos holder compared favorably with the more well-established collet holder. Future testing should also compare these results with thermal shrink fit holders, which are common in high-speed machining applications.

Conclusions

In this work, the dynamic repeatabilities of two tool holding systems, a standard collet and the new Tribos holder, were evaluated under various conditions. For the collet holder, the effect of collet torque on the tool point dynamic stiffness was explored. For the Tribos system, the tool overhang was varied over a wide range. Evaluations of the dynamic repeatability were completed for: 1) no system change, 2) removal and replacement of the holder from the spindle, and 3) removal and replacement of the tool from the holder.

The results showed the expected decrease in dynamic repeatability with increased mechanical complexity in the system change. Additionally, the percent variation between tool and holder changes from the collet (37%) and Tribos (33%) were similar in magnitude, which implies comparable dynamic repeatabilities. The relatively high variability in dynamic response between tool changes for both systems suggests future research on tool/holder interfaces with improved dynamic repeatability may be justified.

References

1. S. Smith and T. Delio, "Sensor-Based Control for Chatter-Free Milling by Spindle Speed Selection", Symposium on Control Issues in Manufacturing, DSC-Vol. 18, ASME, WAM (1989).
2. S. Smith and J. Tlusty, "Stabilizing Chatter by Automatic Spindle Speed Regulation", Annals of the CIRP, 41/1 (1992) 433-436.
3. M. Davies, B. Dutterer, J. Pratt, and A. Schaut, "On the Dynamics of High-Speed Milling with Long, Slender Endmills", Annals of the CIRP, 47/1 (1998) 55-60.
4. T. Schmitz, M. Davies, K. Medicus, and J. Snyder, "Improving High-Speed Machining Material Removal Rates by Rapid Dynamic Analysis", Annals of the CIRP, 50/1 (2001), 263-268.
5. T. Schmitz and R. Donaldson, "Predicting High - Speed Machining Dynamics by Substructure Analysis", Annals of the CIRP, 49/1 (2000) 303-308.
6. S. Smith, W. Winfough, and J. Halley, "The Effect of Tool Length on Stable Metal Removal Rate in High Speed Milling", Annals of the CIRP, 47/1 (1998) 307-310.
7. Y. Altintas and E. Budak, "Analytical Prediction of Stability Lobes in Milling", Annals of the CIRP, 44/1 (1995) 357-362.
8. E. Budak and Y. Altintas, "Analytical Prediction of Chatter Stability Condition of Multi-Degree of Freedom Systems in Milling, Part I: Modeling, Part II: Applications", Journal of Dynamic Systems, Measurement and Control, 120 (1998) 22-36.

DE-COUPLING OF AN OPTICAL GRATING BASED MEASUREMENT NORMAL FROM THE MACHINE TOOL STRUCTURE

Ulrich Mueller, Yoshihito Kagawa, Kazuo Yamazaki
IMS-Mechatronics Laboratory,
University of California, Davis, CA

Keywords: measuring instrument, motion calibration, flexures

Introduction

Precision machine tools use optical encoders for accurate position feedback [1,2]. A novel encoder based on three cross grid gratings mounted on a thin wall beam and a sensor head consisting of six optical sensing elements was developed to calibrate the linear machine tool axis in six Degrees of Freedom (Figure 1). The feasibility of this device has been tested and verified under laboratory conditions [3]. However, in order to use the device under varying environmental conditions.it has to be guarenteed that the measurement normal is decoupled from the mounting surface in order to prevent induced forces to distort its shape. Therefore this paper descripes the design procedure for such de-coupling mounts based on slip stick free flexures.

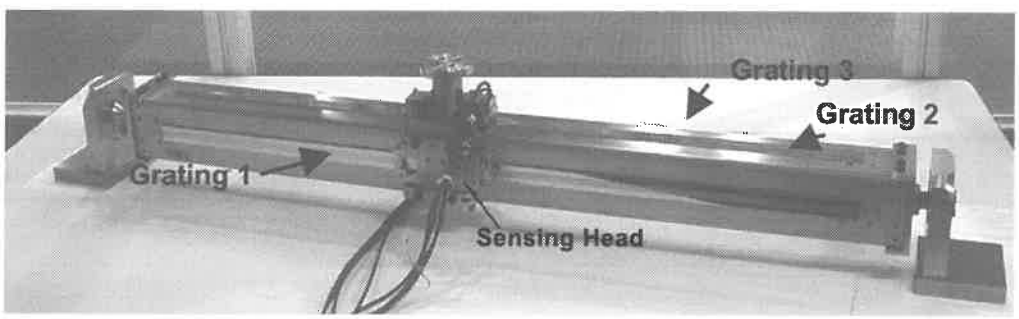

Figure 1. Encoder Prototype (1m long)

Principle

During calibration the encoder base is mounted on the table of a machining center and the bracket that holds the sensing heads is attached to the machine spindle. The three optical glass gratings on the stainless steel thin wall beam act as measurement normal. Therefore a mounting scheme which de-couples the measurement normal from the machine structure itself is necessary. For in-process calibration the de-coupling unit has to be slip stick free. To de-couple the measurement normal from the mounting surface, 2-Degrees of Freedom (DOF) must be provided at the side with the thermal reference, whereas the other end should provide only support in horizontal and lateral direction (Figure 2). As far as the basic motion range requirements are concerned a maximum thermal change of 15 Kelvin is assumed. Giving this particular steel beam of one-meter length an expansion of approximately 200μm. The mounting beam has a weight of about 10kg. We also assume an offset of 100μm between the two ends of the beam due to mounting misalignment and due to the deformation of the mounting surface on the machine table. This would cause the beam to bend about 100μrad over 1m.

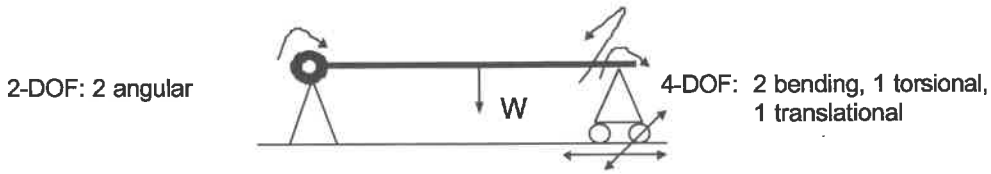

Figure 2. The de-coupling model

To provide the necessary DOF while maintaining a slip stick free setup the use of flexures is proposed. In order to provide the desired degrees of freedom, while maintaining rigidity and providing a defined thermal and geometrical reference the mounting flexures have to be properly dimensioned [4]. The 2-DOF mount consists of a toroidal two-axis flexure (Figure 3), and it allows small bending deflections about a point located at the thinnest point with the thickness t. In order to size the mount, the axial, torsion, and bending stiffness must be calculated. Goal is to keep the torsional and axial stiffness high while maintaining a low bending stiffness to prevent deformation of the measurement normal due to bending. The equations for the bending stiffness k_b can be approximated from Paros and Weissbord [5]

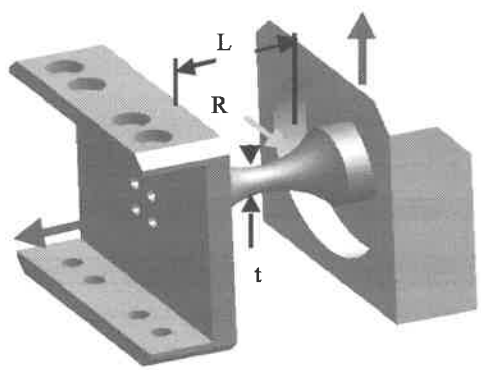

Stiffness

Axial: $k_a = \frac{Et^{3/2}}{20R^{1/2}}$

Torsion: $\phi = \int_0^L \frac{Tdx}{GI_{px}}$

Bending: $k_b = \frac{Et^{7/2}}{20R^{3/2}}$

Figure 3. 2-DOF mount

The parameter G is the shear modulus, T is the applied moment and I_{px} the polar moment of inertia that varies over the length L. With the mathematical descriptions, one can create graphs for each bending, torsion, and axial stiffness depending on the individual geometric variables such as length, diameter, and thickness (Figure 4).

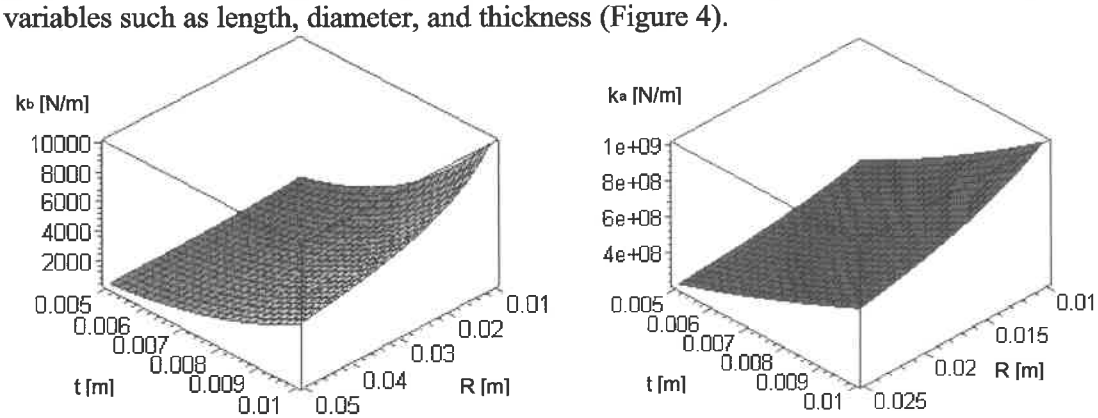

Figure 4. Bending and axial stiffness versus radius R and min. diameter t

Analogous the same can be done for the torsional stiffness.

The 4-DOF flexure consists of a cruciform type of flexure for torsional motions and a disk type flexure for translational motion as well as bending.

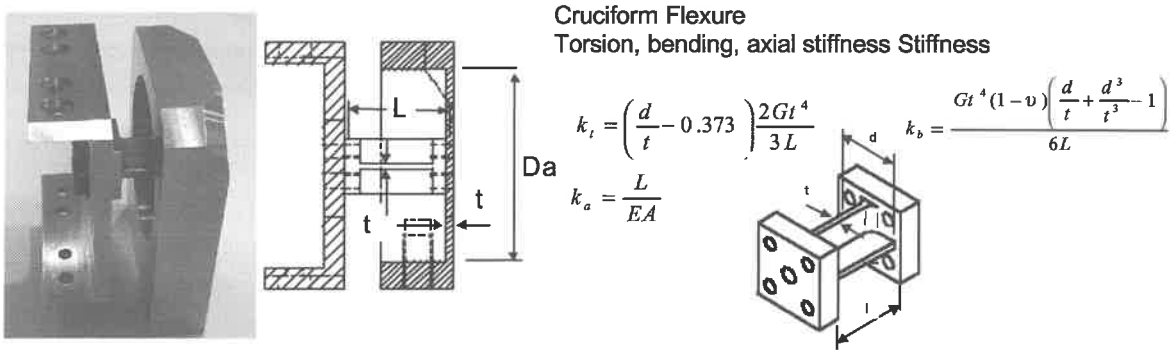

Figure 4. Three Degree of freedom mount

Evaluation

The axial, torsion, and bending behavior of these structures has to be evaluated simultaneously in order to validate the functionality of the proposed mounts. From the previously derived figures, the individual geometry can be selected to achieve the desired deflections. The general requirements for the flexure designs are:

1. Nearly all axial deformation should be provided by the disk flexure.
2. All torsion deformation due to movement of the mounting base has to be provided by the cruciform flexure.
3. Axial deflection should not lead to a substantial in- or decrease of the bending deflection of the measurement normal.

The evaluation of the axial deformations is simple because the elongation of each individual element adds. Knowing the individual stiffness, one can calculate the total Force F_{axial} that correlates to the axial elongation:

$$F_{axial} = \delta_{tot}\sum_{i=1}^{4} k_i \qquad \delta_{Ai} = \frac{F}{k_i},\ i=1..4 \qquad (1)$$

The plot of the axial force versus a total deflection of 0 to 200µm, which corresponds to an approximate thermal elongation caused by a change of temperature of about 15K is shown in Figure 5. The individual deflections are then determined for each flexure as well as the beam. This allows the evaluation of the functionality of the flexure mechanism. Plotting the individual deflections for a total deflection of 200 µm shows that nearly all-axial deformation (more than a factor 100) is provided by the disk flexure.

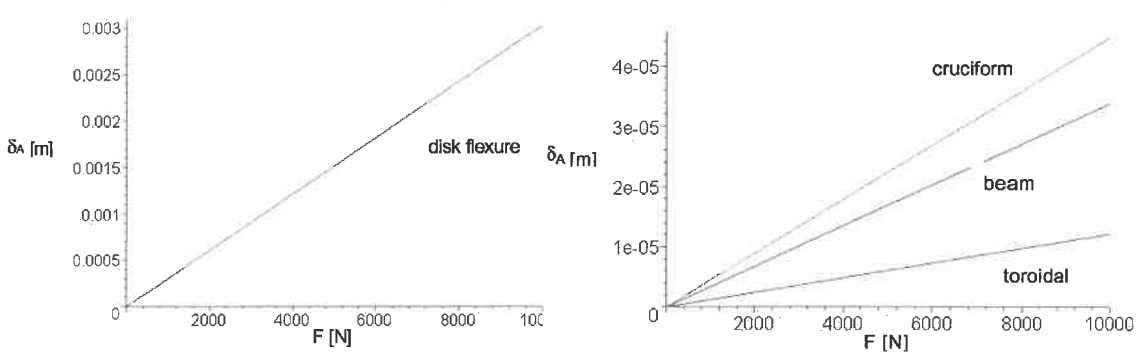

Figure 5. Axial deflection of the disk flexure, Axial deflection of the beam, the toroidal and the cruciform flexure

The effect of torsion and bending can be analyzed analogous to axial deformations. The flexures and the beam act as torsion springs, which are connected in series. As noted, the cruciform flexure is the most elastic torsion element provides nearly all flexibility in torsion. Figure 6 shows the cruciform flexure's angular displacement if a total torsion deflection of up to 0.8mrad is induced into the structure. Compared to the disk, the bending, the beam and the toroidal flexure its angle of twist ϕ is almost 1000 fold larger (Figure 6). This verifies its functionality as a decoupling element.

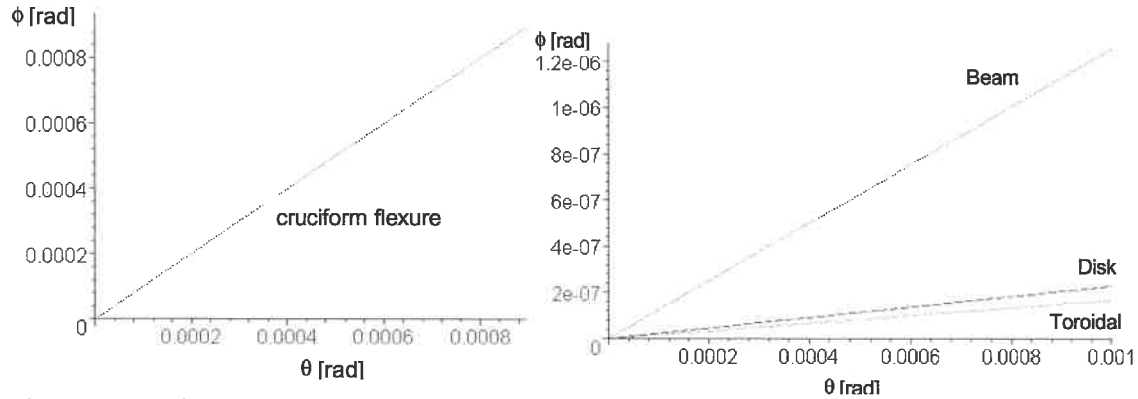

Figure 6. Torsion displacement of the cruciform flexure, Twist ϕ of the beam the disk flexure and the toroidal flexure

In order to evaluate the thermal behavior of the measurement device it was mounted on the granite base of a CMM. Than the measurement beam was fitted with two fluid fittings on both sides. Water at various temperatures was run through the beam to simulate a thermal expansion similar to that of a machine tool. While the water was running, the average temperature of the beam was closely monitored. An increase in temperature led to an elongation of the beam, whereas the mounts stayed at a steady position due to the minimal expansion of the granite surface. Therefore, the elongation must be compensated by the disk flexure. In order to insure that the elongation doesn't lead to a distortion of the beam, a touch probe measured its shape. The test showed promising results and ongoing tests are caried out to investigate the behavior over time.

Conclusion

A procedure for the design of flexure mounts for a volumetric encoder was proposed. The mounts enable the de-coupling of a measurement body from the mounting forces induced during mounting on the machine table.

References

[1] M. Weck, P. Mckeown, R. Bonse, U. Herbst, Annals of The CIRP, 44/2:589 (1995).

[2] A. Spies, Feinwerktechnik & Messtechnik, 98/10:406 (1990).

[3] Ulrich Mueller, Yoshihito Kagawa, Kazuo Yamazaki, Jan Braasch, Proceedings of the 10th JSPE conference, A Novel Approach For Simultaneous Measurement Of The Linear Guideway Errors Of A Machine Tool With A Volumetric Optical Encoder, (2001).

[4] S.T. Smith, D.G. Chetwynd, Foundations Of Ultraprecision Mechanisms, Gordon & Breach Science Pub., (1991).

[5] J.M. Paros, L. Weissbord, How To Design Flexure Hinges, Machine Design, 151-156 (Nov), (1965).

Uncertainty Evaluation of Calibration of the Optical Projector

Cheng-Yen Fang, Kam-Wa Lui, and Kuo-Ming Chang
Center for Measurement Standards/ITRI, Hsinchu, Taiwan

ABSTRACT

An optical projector has been widely used in electronics, semi-conductors and mechanical industry. It is the basic inspection equipment for factories and laboratories. The accuracy of optical projector is very important, since it influences the quality of products directly. Therefore, optical projector should be calibrated periodically to guarantee that the quality of inspections and measurements is well known by industries. Recently, the requirements for quality, especially for calibration, have become much more important. Thus, it's well known that the uncertainty, which is an indication of calibration quality, has also become more important. The uncertainty should be estimated before the calibration results were used. Then, we can make sure the validation of the calibration.

This paper describes the evaluation model of uncertainty of magnification calibration of optical projector. The mathematical models and the procedures for uncertainty estimation are derived according to the ISO "*Guide to the Expression of Uncertainty in Measurement*", usually abbreviated *ISO GUM*, which is a worldwide standard method to estimate measurement uncertainty. Then the uncertainty budget was decided and the effect of each influential factor on uncertainty evaluation was also estimated. Finally, the uncertainty of calibration of magnification is estimated to be 0.015% at a 95% confidence level.

Keywords: *optical projector, calibration, uncertainty*

1. INTRODUCTION

The shadow images are produced by the lens system in an optical projector. Any misalignment in the lens system will cause the image distorted and influence measurement results. They must be inspected and fine adjusted first. Then the calibration items are shown as follow.

(1) Magnification error
(2) Positioning error
(3) Angle error

The magnification error is most important one to be calibrated. So the estimation of the uncertainty of magnification error calibration is described in this paper.

2. THE ESTABLISHMENT OF UNCERTAINTY MODELS

According to the ISO GUM, the first step of uncertainty estimation is to establish the mathematical model of measurement. From the standard calibration procedure we can find the measurant in the calibration is ΔL the measured length deviation of standard scale image from reading scale. ΔL can be expressed as below:

$$\Delta L = ML_1(1+\alpha_1\Delta T_1) - L_2(1+\alpha_2\Delta T_2)$$

where M : Magnification measured

ΔL : Length deviation of standard scale image from reading scale(Measurant)

L_1, L_2 : Length of standard and reading scale at 20℃

α_1, α_2 : Thermal expansion coefficient of standard and reading scale

ΔT_1 : Temperature difference between standard scale and reference temp.(20℃)

ΔT_2 : Temperature difference between reading scale and reference temp.(20℃)

And then the mathematical model of magnification of optical profile is expressed in Eq.(1).

$$M = \frac{\Delta L + L_2(1+\alpha_2\Delta T_2)}{L_1(1+\alpha_1\Delta T_1)} \tag{1}$$

The magnification error of optical projector is described in JIS B7184 specification, denotes ΔM, and is defined as below:

$$\Delta M = \frac{M - M_N}{M_N} \times 100\% \tag{2}$$

where M_N : Nominal magnification(constant)

Equation (2) can be modified to Eq.(3) by substitute the term M with Eq.(1).

$$f = \Delta M = \left(\frac{\Delta L + L_2(1+\alpha_2\Delta T_2)}{L_1(1+\alpha_1\Delta T_1)M_N} - 1 \right) \times 100\% \tag{3}$$

Equation (3) can also be written in the form of a function as shown in Eq.(4).

$$\Delta M = f(\Delta L, L_1, L_2, \alpha_1, \alpha_2, \Delta T_1, \Delta T_2) \tag{4}$$

The combined standard uncertainty, denotes u_c, is given by

$$u_c(\Delta M) = \sqrt{\left(\frac{\partial f}{\partial \Delta L}\right)^2 u(\Delta L)^2 + \left(\frac{\partial f}{\partial L_1}\right)^2 u(\Delta L_1)^2 + \left(\frac{\partial f}{\partial L_2}\right)^2 u(\Delta L_2)^2 + \left(\frac{\partial f}{\partial \alpha_1}\right)^2 u(\alpha_1)^2 + \left(\frac{\partial f}{\partial \alpha_2}\right)^2 u(\alpha_2)^2 + \left(\frac{\partial f}{\partial \Delta T_1}\right)^2 u(\Delta T_1)^2 + \left(\frac{\partial f}{\partial \Delta T_2}\right)^2 u(\Delta T_2)^2} \tag{5}$$

where f is the function given in Eq.(4)

$u(x_i)$ is the standard uncertainty of each factor x_i

The partial derivatives $\frac{\partial f}{\partial x_i}$ are called sensitivity coefficients and also expressed as c_i.According to the suggestion of the ISO GUM, the standard uncertainty $u(x_i)$ in Eq. (5) can be estimated by Type A evaluation or Type B evaluation. The term $u(\Delta L)$in Eq. (5) is related to the behavior of a measurement process by way of repeated measurements. It can be classified to Type A evaluation. The other six terms $u(L_1)$、$u(L_2)$、$u(\alpha_1)$、$u(\alpha_2)$、$u(\Delta T_1)$, and $u(\Delta T_2)$can be estimated by Type B evaluation.

After calculating all the terms $\frac{\partial f}{\partial x_i}$ and $u(x_i)$ for each factor x_i, these are substituted into Eq. (5) to get the combined standard uncertainty $u_c(\Delta M)$.

3. THE ESTIMATION OF STANDARD UNCERTAINTY

Before calculating the standard uncertainty of each factor, the values of all the parameters presented in Eq.(6)'s should be given. These values are assumed as follows.

M_N : Nominal magnification is 10X

ΔL : The maximum measurant value= 0.009 mm = 9×10^{-6} m

L_1=30 mm =0.03 m; L_2=300 mm =0.3 m

$\alpha_1 = \alpha_2 = 8.75\times10^{-6}$ ℃$^{-1}$; ΔT_1=15 ℃; ΔT_2=10 ℃

Effects of each influential factor on uncertainty evaluation are estimated in the following.

3.1 The term, ΔL, can be estimated by repeat measurements for a long-term period. The standard deviation of 53 measurements is 0.003 mm. Then, the standard uncertainty of ΔL, $u(\Delta L)$ is $\pm3\times10^{-6}$ m。Since 53 measurements were taken, the degree of freedom, $\nu_{\Delta L}$=52。

3.2 Both of the standard and reading scales are traceable to National Measurement Laboratory (NML). The standard uncertainty can be obtained from the calibration reports.

A. The total uncertainty of standard scale (50 mm) listed on the report (Report No.: B860851) is ±1.2 μm with a 99.7% confidence level, i.e. k =3. Then $u(L_1)$ = ±0.4 μm = $\pm4\times10^{-7}$ m.

B. The total uncertainty of reading scale (300 mm) listed on the report (Report No.: B860852) is ±0.9 μm with a 99.7% confidence level, i.e. k =3. Then $u(L_2)$ = ±0.3 μm = $\pm3\times10^{-7}$ m.

Since these two uncertainty components come from the calibration report of traceability. Assume that this uncertainty estimation is reliable to 10%, thus the degrees of freedom $\nu_{L1} = \nu_{L2} = 50$.

3.3 All of the scales used in this system are made of quartz glasses. So the thermal expansion coefficient of the scales are obtained from the catalogues of Mitutoyo Japan Company. In the absence of further information, we apply a Type B evaluation procedure. We will estimate the bounds on both of the values of α_1 and α_2 to be $\pm0.25\times10^{-6}$ °C^{-1} with an uncertainty represented by a rectangular distribution. The standard uncertainty is $u(\alpha_1) = u(\alpha_2) = \pm1.4434\times10^{-6}$ °C^{-1}. Assume that this uncertainty estimation is reliable to 20%, thus the degrees of freedom $\nu_{\alpha1}$ and $\nu_{\alpha2}$ are both 12.5.

3.4 Since the optical projectors are precision instrument, they should be not calibrated in an unstable environment. So a range of 15～30 ℃ is the minimum request to execute calibration. That is to say, we assume the change of temperature is ±10 ℃ with an uncertainty represented by a rectangular distribution. The standard uncertainty is then $u(\Delta T_1) = u(\Delta T_2)$ =5.7735 °C. Assume that this uncertainty estimation is reliable to 20%, thus the degrees of freedom $\nu_{\Delta T1}=\nu_{\Delta T2}$ is 12.5.

The uncertainty budget is as shown in Table 2. All the calculated terms are substituted into Eq.(5) to get the combined standard uncertainty u_c.

$u_c = 7.3405\times10^{-5}$

The effective degrees of freedom is obtained from the Welch-Satterthwaite formula, we get

$\nu_{eff}=27$

Refer to the t-distribution table which shows that the value of $t_{95}(27)$ for a 95% confidence interval is 2.05, thus k is equal to 2.05. Hence, the expanded uncertainty is

$U_{95} = k\cdot u_C = (2.05)(7.3405\times10^{-5}) = 0.00015 = 0.015\%$.

Table 2. Summary of standard uncertainty components (10X)

Source of uncertainty x_i	Estimate bounds	Value of standard uncertainty $u(x_i)$	Sensitivity coefficient $\frac{\partial f}{\partial x_i}$	Degrees of freedom ν_i
ΔL	$\pm 3\times10^{-6}$m	$\pm 3\times10^{-6}$m	3.3329m^{-1}	52
L_1	$\frac{\pm 1.2\times10^{-6}\text{m}}{3}$	$\pm 4\times10^{-7}$m	-33.3329m^{-1}	50
L_2	$\frac{\pm 0.9\times10^{-6}\text{m}}{3}$	$\pm 3\times10^{-7}$m	2.3332m^{-1}	50
Thermal expansion coefficient				
•α_1	$\pm 0.25\times10^{-6}$℃$^{-1}$	$\pm1.4434\times10^{-7}$℃$^{-1}$	-14.9978℃	12.5
•α_2	$\pm 0.25\times10^{-6}$℃$^{-1}$	$\pm1.4434\times10^{-7}$℃$^{-1}$	9.9987℃	12.5
Temperature difference				
•ΔT_1	± 10℃	±0.5774℃	-8.7487×10^{-6}℃$^{-1}$	12.5
•ΔT_2	± 10℃	±0.5774℃	8.7489×10^{-5}℃$^{-1}$	12.5

6. CONCLUSIONS

The uncertainty of magnification error calibration is estimated to be 0.015% at a 95% confidence level. From the result we find that the estimated standard uncertainty, $u(\Delta T_1)$ and $u(\Delta T_2)$, are quiet big compared to the others. These imply that the temperature variation is really a great influential factor on dimensional measurement. Thus, the temperature should be controlled at its minimum requirement to get fine calibration results. Hence, if the measurements are done be well practiced operator, the Type A estimated uncertainty, such as $u(\Delta L)$ can also be reduced. Therefore, the operator is also a great influential factor.

REFERENCES

1. Guide to the Expression of Uncertainty in Measurement, ISO,1995。
2. Y.H.Weng, W.R.Liaw, The Calibration Procedure for Optical Projector, L-IP-86-02-002, 1st edition, Mitutoyo Taiwan Co., Ltd., 1997.
3. Measuring Projector, JIS B7184-1972, Japanese Standard Association.

LASER DIGITIZER BASED STRAIN MEASUREMENT

Hau-Lam Chan, Allan D. Spence, Mateusz P. Sklad
Department of Mechanical Engineering, McMaster University, Hamilton, Ontario, Canada

Abstract

Automotive sheet panel strain measurement usually involves large surface areas. For high resolution analysis, using the circle grid analysis method, several hundred elements must be measured. Existing technologies are limited to the small surface that area can be measured in one setup. As well, the (X,Y,Z) location on the part is not accurately available. This paper reports a new surface strain measurement system based on use of a laser digitizer attached to a Coordinate Measuring Machine (CMM). A Forming Limit Diagram is automatically generated. The thickness strain is calculated, and displayed as a color shaded part surface image. There is a very good agreement with a dial gauge measurement of thickness.

Keywords: metal forming, coordinate measuring machines, strain measurement, laser digitizing

2. Introduction

The sheet metal forming process is widely used in the production of automobiles and other high volume manufactured items. Although computer prediction of formability is advancing, there remains a need for experimental "try out" when dies for a new part are first used. This involves checking that the part is within dimensional tolerance, and that the sheet has not been strained beyond the Forming Limit for the material and process combination. Obtaining the strain experienced during forming is therefore an important process measurement.

The traditional approach to strain measurement begins with electrochemical etching of 0.1 inch diameter circle grid pattern onto the undeformed sheet. After forming, the circles will deform into ellipses. The strain is obtained by manually reading the ellipse major and minor axis lengths with dividers and rulers, a graduated mylar tape, or a microscope [1]. The differences in length from the undeformed circle radius are the local strain value. This process is repeated for every circle in the area of interest, and the results are typically plotted on a Forming Limit Diagram.

Because the manual approach is time consuming, tedious, error prone, and not repeatable, automation of the process has been investigated. One example is the Grid Circle analyzer [2]. This system uses a camera to obtain the image for one ellipse at a time. A least-squares fit is used to calculate the major and minor axis lengths and hence the strain. No information on the (X,Y,Z) part location, or local curvature, is available. Vogel and Lee [3] proposed a stereo video camera and frame grabber. By analyzing a square grid from two images of the same surface area, the part location can be obtained by triangulation. More recently, this approach has been improved by moving to higher resolution digital camera [4]. Existing approaches share the common deficiencies that only a limited surface area can be measured in one setup, and the (X,Y,Z) location on the part is not accurately available.

The new approach of strain measurement uses a laser digitizer that operates with a CMM. The output of laser digitizer is

(X,Y,Z) co-ordinates and the associated intensity value. Using intensity data, the location of the deformed circles can be measured precisely. The remainder of paper is organized as follows. Section 2 describes the measurement system. Section 3 describes curve detection for the grid location. Section 4 data points segmentation will explains how to group the ellipse data points. Section 6 is strain calculation. Section 7 concludes the paper.

3. Measurement System

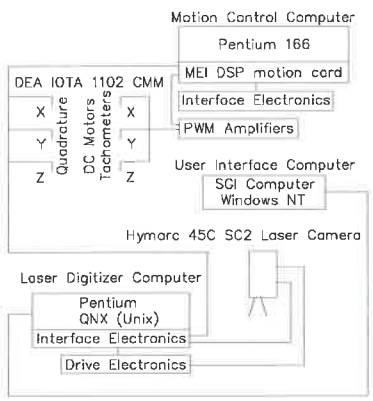

Fig. 1. System architecture.

Fig. 1 shows the overall system architecture. The Co-ordinate Measuring Machine employed is a DEA IOTA model 1102. The configuration has a standard bridge Z vertical axis on Y, on X and granite table. Each axis consists of a rack and pinion drive, linear scale and air bearings. The linear scales are interpolated to a 1 μm resolution. The CMM controller uses a Pentium 166 MHz based computer, and Motion Engineering Inc. (MEI) Digital Signal Processor (DSP) based motion interface card [5]. It provides scale quadrature counting, probe switch latching, digital control system interval timing, analog to digital (A/D) tacho-generator input and digital to analog (D/A) output to the Pulse Width Modulated (PWM) DC motor servo amplifiers. The laser digitizer employed is a Hymarc Hyscan 45C SC2 [6].

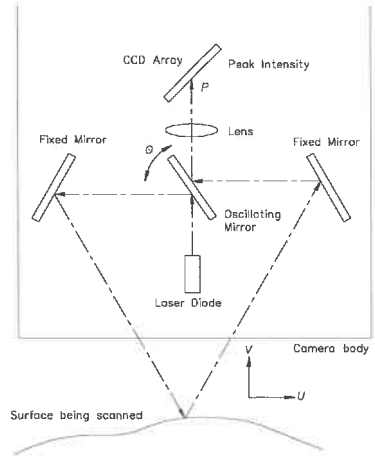

Fig. 2. Camera body.

The camera body (Fig. 2) of the laser digitizer includes a Charge Coupled Device (CCD) array, two fixed mirrors, lens, oscillation mirror, and laser diode. The oscillating mirror is rotated about its center and sweeps out the scan line along the surface being scanned. The laser digitizer applies the principle of active triangulation with synchronization of projection and detection. Beginning at the laser diode, the beam travels to the bottom of the oscillating mirror, left fixed mirror, part surface, right fixed mirror, to the top of the oscillating mirror, ending at the CCD array. The Hyscan system (U,V) coordinates are determined from the orientation θ of the scanning mirror and position P that has the greatest intensity value on the CCD array. Using calibration data, the (U,V) coordinates are converted to (X,Y,Z) position. Data samples along the scan line are normally separated by 100 μm.

4. Curve Detection

The curve detection algorithm uses the local image threshold strategy. The algorithm starts by choosing a threshold value ε. This depends on the contrast of the image and gray level of the CCD camera. The next step is to establish the size of the curve detector threshold window. This

depends on the diameter of the circles. During detection, the square window will move from left to right and top to bottom on the data structure. In this case, the data points are stored in a format scan line by scan line. At the current location the curve detector takes the data points and performs intensity normalization. Let $I(i,j)$ is the intensity value. The normalized intensity value is

$$I_{norm}(i,j) = \frac{I(i,j)}{SI},\ SI = \sum_{i=1}^{m}\sum_{j=1}^{n} I(i,j) \qquad (1)$$

Retained curve data points satisfy the condition

$$I_{norm} < \varepsilon \qquad (2)$$

For the research reported herein, $\varepsilon = 0.016$ and $m = n = 7$.

5. Ellipse data points grouping

For neighboring ellipses, the closest edge to edge distance is approximately 500 μm. The closest data point neighbor within an ellipse is 100 μm. A midpoint threshold is therefore 300 μm. Using this relationship, the data points can be grouped into ellipses. If the point separation distance is less than 300 μm, the data points are grouped into a single ellipse. If the distance is larger, a new ellipse group is created.

An orthogonal least squares fitting algorithm [7] is applied to compute the ellipse center and length of major and minor axis for each group of ellipse data points.

6. Strain Computation

Once, the ellipse centers and length of major and minor axis is available, the strain of each ellipse elements can be calculated. For each axis, the true strain is

$$\varepsilon_s = \int_{L_0}^{L} \frac{dL}{L} = \ln\left(\frac{L}{L_0}\right) \qquad (3)$$

where L_0 and L are original and elongated length, respectively.

7. Experiment Results

Fig. 3 shows scanned area of the part. Comparing the center with the circumference of part, the center region has the highest strain since the size of ellipse is larger. Fig. 4 shows the result after curve detection and the extra pieces of line are erased. Fig. 5 is a Forming Limit Diagram corresponding to scanned area. Fig. 6 is a 3-D thickness strain color plot, and illustrates the promising results.

To evaluate the result of laser digitizer based strain measurement, manual dial-gauge strain measurement is performed. The results of the measurement are shown in Fig. 7. Comparing the result with the laser digitizer measurement, Fig. 6 and Fig. 7 shows good agreement.

8. Conclusions

In conclusion, this paper has presented a new laser digitizer based strain measurement system. The key procedures of the new technology consist of curve detection, ellipse data point grouping, ellipse fitting and 3-D graphical display of the results. Compared to existing CCD camera methods, the laser digitizer based strain measurement method has the advantage of high accuracy measurement of (X,Y,Z) coordinates. This information is needed so that detailed die forming geometric errors, such as spring back, can be investigated. As well, using a CMM to carry the laser digitizer permits accurate measurement of large part areas.

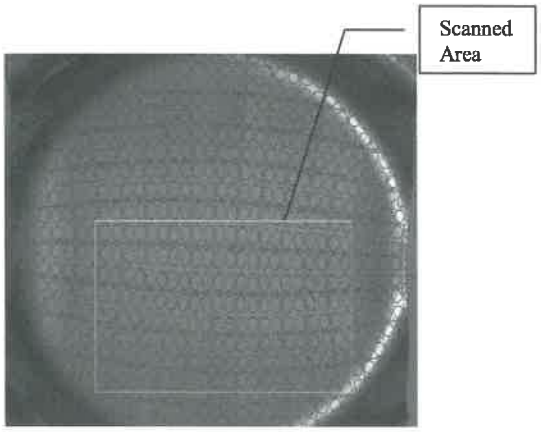

Fig. 3. Scanned Object.

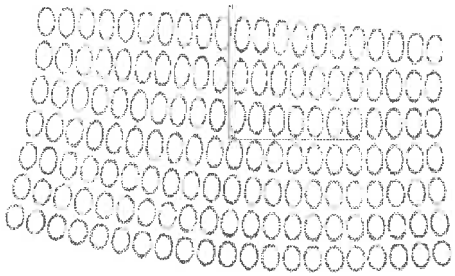

Fig. 4. The ellipse data points.

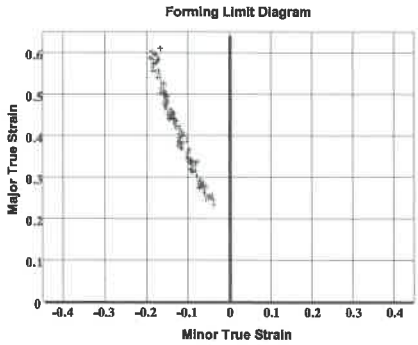

Fig. 5. Forming Limit Diagram.

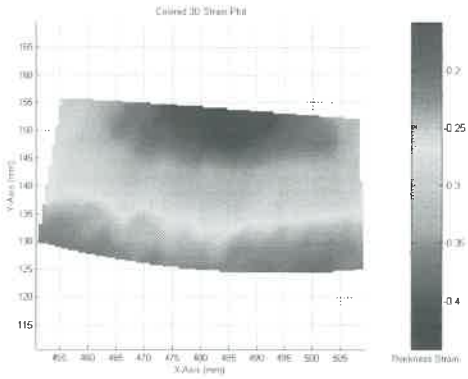

Fig. 6. 3-D thickness strain color plot.

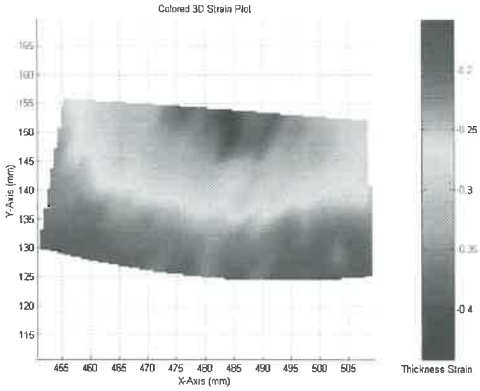

Fig. 7. 3-D thickness strain color plot from dial-gauge manual strain measurement.

Reference

[1] S. Dinda, K.F. James, S.P. Keeler, P.A. Stine, "How to use circle Grid Analysis for Die Tryout", *American Society for Metals*, 1981.

[2] R.A. Ayres, E.G. Brewer and W.W. Holland, "Grid Circle Analyzer: Computer Aided Measurement of Deformation", *Trans. SAE*, 88(3), pp. 2630-2634, 1979.

[3] J.H. Vogel and D. Lee, "The Automated Measurement of Strains from Three-Dimensional Deformed Surfaces", *Journal of Metals*, 42, pp. 8-13, 1990.

[4] D.W. Manthey and D. Lee, "Vision Based Surface Strain Measurement System", The Journal of The Minerals, Metals, & Material society (JOM), vol.47, No 7, pp.46-49, 1995.

[5] Motion Engineering, Inc., 520 East Montecito Street, Santa Barbara CA 93103, United States.

[6] Hymarc3-D Vision Systems, www.hymarc.com.

[7] W. Gander, G. H. Golub, R. Strebel, "Least Squares Fitting of Circles and Ellipses", *BIT*, vol 34, pp. 558-578, January 1994.

3-D MEASUREMENT AND QUANTITATIVE DESCRIPTION OF DISK MICRO-WAVINESS

Seiichiro Hara*, Tomoaki Oosone** and Kazuhisa Yanagi***
* Tokyo Institute of Technology, Tokyo, Japan
** Union Tool Co., Shizuoka, Japan
*** Nagaoka University of Technology, Niigata, Japan

Introduction

To achieve larger recording capacity while reducing the price, higher recording density of the hard disk is demanded. For the realization of that, it is one of the important requirements to keep the spacing between the magnetic layer on the disk and the magnetic head on the head slider narrowly and constantly. Though all the disk surface profile undulation can cause the fluctuation of the spacing, components those wavelength bands are about 5mm to 80μm, called "micro-waviness", is noticed as the major cause of the fluctuation. Authors had reported that the amplitude fluctuation of the head readout signal is closely related to the amplitude of the micro-waviness of the 2-D profiles [1].

Considering that aerodynamics and tribology phenomena would be related to the surface profiles in 3-D rather than 2D, measurement and characterization of the micro-waviness should be discussed in 3-D. In this paper conditions of measurements and processing of the micro-waviness of the disk surface are assessed. In addition, relationship between the amplitude of the micro-waviness and the touch down height is discussed.

Measurement conditions

Common instruments employed to measure the disk micro-waviness are white light microscope interferometers. But the measurement results of the instruments from different manufacture are usually not considered to agree with each other. Authors thought that this situation could be caused by the disagreement of the measuring and filtering conditions in addition to the disregard of error-compensation. Three popular commercially available instruments are used in this paper. MicroXAM (ADE PhaseShift), NT-3000 (Veeco), NewView5000 (Zygo).

Considering the size of the head slider, table 1 shows the rational sizes of measurement area of the disk surface profile. Though actual sizes of measuring area are slightly different to each instrument, almost same measuring area can be selected.

To compensate the measurement error, utilization of the reference standards is very important. It is possible to identify and compensate the optical error of lens and reference mirror by measuring a standard flat. Figure 1 shows an example of error of an instrument. The warp of the error is usually comparable to that of the disk surface. A standard step is used to identify and compensate the vertical amplitude error of the instruments.

Table 1 Selection of measurement area

No.	Area mm	Objective× zoom	Resolution μm	Compared to the slider	Examples of usage
1	5.6× 4.2	2.5×0.5	9.8	Larger than slider	Aerodynamics simulation
2	2.8× 2.1	2.5×1.0	4.9	Same as slider	Contact simulation
3	0.70× 0.53	10×1.0	1.22	Same as one side of slider	Contact simulation

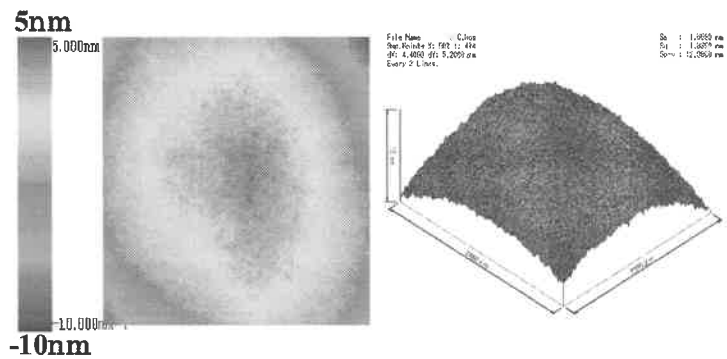

Fig. 1 Example of an error of the measuring instrument (2.4×2.2mm)

Filtering conditions

Selection of the filter to extract the micro-waviness from the measured data is also important. High-pass filter is applied to remove the waviness and warp of the disk profile. Low-pass filter is applied to remove the roughness and noise component. Considering the resolution of the measurement area and resolution of the data, examples of proper cut-off of the filters can be defined as shown on table 2.

Table 3 shows the comparisons of area filters. In the viewpoint of the "Edge effect", spline filter [2] and, Gaussian regression filter of 2-order [3] showed advantage compared to the conventional Gaussian filter that have "Edge-effect" as shown in figure 2.

Table 2 Measurement area and wavelength band.

No.	Area mm	Resolution μm	Wavelength μm
1	5.6×4.2	9.8	500 to 2000
2	2.8×2.1	4.9	80 to 500
3	0.70×0.53	1.22	15 to 80

Table 3 Comparison of area filters

	Long wave length residual	Edge Effect	Method*	Speed*	Order of calculation*	Axially symmetric al transfer function
Gaussian filter	Yes	Yes	1	Fast (5s)	$n\ w$	Yes
			2	Slow (30min.)	$n^2\ w^2$	Yes
Gaussian regression filter of 2 order	Small	No	1	Fast (20s)	$n\ w$	No
			2	Slow (2hour)	$n^2\ w^2$	Yes
Spline	No	No	1	Fast (5s)	n	No
			2	Not defined		

Method* 1: apply filter in x and y directions successively
2: apply filter to each data point like original definition
Speed* Approximate time for 500×500 data points using standard PC
Order of calculation* n: number of data points in one axis,
w: number of data points in cutoff wavelength

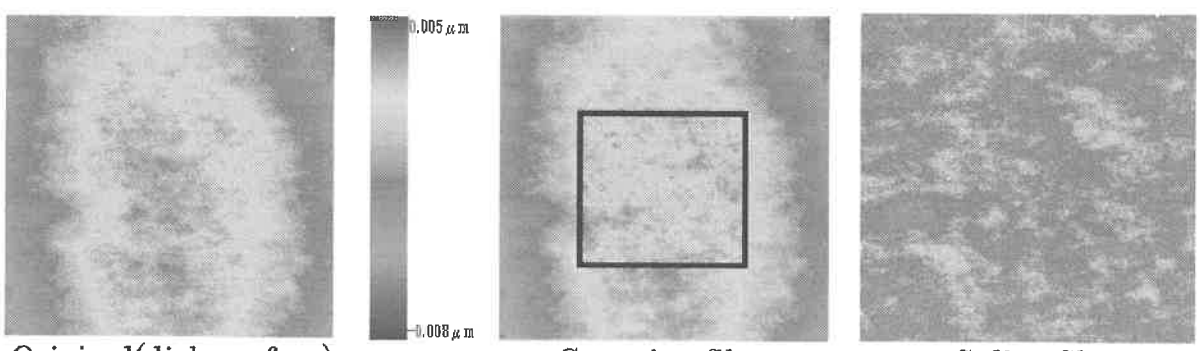

Original(disk surface) Gaussian filter Spline filter

Fig. 2 Edge effect of Gaussian high-pass filter

Experiment

3-D profile measurements of the magnetic disk surfaces were carried out using 3 kinds of white light microscope interferometer under the proposed condition, the error compensation and the filtration. Four sample disks that have different roughness and micro-waviness are used. Four areas are measured on each disk. As a result of the comparison for each measurement data, it was shown that the value of *Wa* from different instruments agreed almost. Figure 3(a) shows an example of the agreement. In contrast, figure 3(b) is an example in which no LPF are used. The *Wa* values are different to each instrument. Amount of the noise is thought to be the main cause of the disagreement. Under the proper measuring conditions and error compensation, the result of those measuring instrument are compatible with each other.

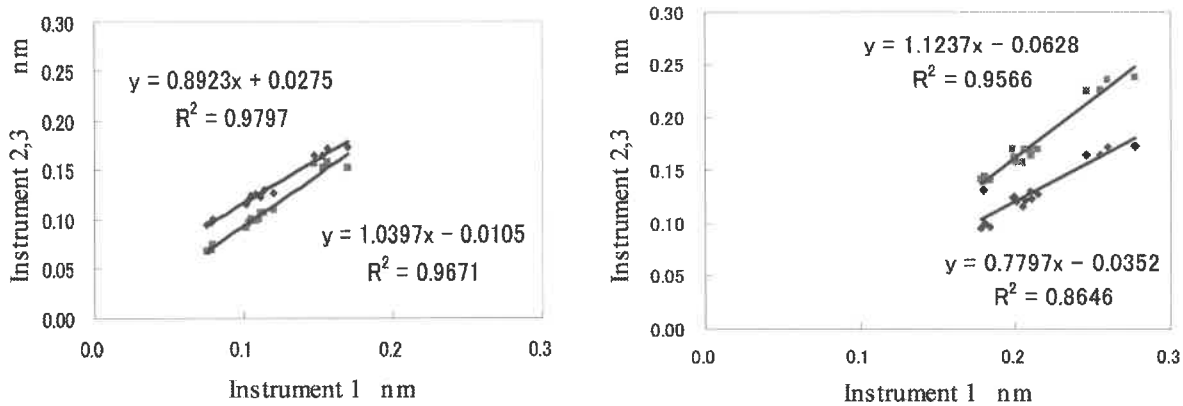

(a) 80μm HPF and 15μm LPF (b) 80μm HPF

Fig. 3 Comparison of the measured *Wa* values

Relation to the touch down height

Relationship between the amplitude of the micro-waviness and the touch down height, i.e. minimum average flying height to avoid the severe contact between the slider and the disk surface, are investigated. The RMS output of the Piezo-electric transducer on the slider suspension to detect the contact is recorded while changing the rotational speed of the disk. Influence of the micro-waviness to the touch down height was investigated.

[1] S. Hara, K. Yanagi, and Tomoaki Oosone, *Proc. ASPE,* 312, 22(2000)
[2] M. Krystek, *Measurement,* 9, 18(1996)
[3] S. Brinkmann, H. Bodschwinna, H. Lemke, *Intl. Coll. On Surfaces,* 31, (2000)

SURFACE ROUGHNESS PROFILE MEASUREMENT BASED ON MICROSCOPIC SHEARING INTERFEROMETRY

X. Liu * and Y. Gao **

Department of Mechanical Engineering, Hong Kong University of Science and Technology
Clear Water Bay, Kowloon, Hong Kong
Email: * mexjl@ust.hk and ** meygao@ust.hk

Introduction

Surface roughness is an important feature of engineering surfaces. For surface roughness profile measurement, most of the exiting methods [1-6] would require isolated conditions to reduce the effect of base vibrations. The scattering interference method [7-8], based on a statistical algorithm together with comparison, may be used in a production environment, but the accuracy and reliability are limited. More importantly, the existing methods could not obtain roughness profiles for further analysis.

For an accurate measurement of roughness profiles in a production environment, a new method is proposed. It is based on microscopic interferometry and lateral shearing interferometry. The interference microscope technique has been applied to surface roughness profile measurement successfully [2]. Lateral shearing interference [9] is the self-interference technique. In the proposed interferometry that combines the two techniques, a wavefront with roughness information of the test surface is obtained by a microscope objective. The wavefront enters the shearing interference optical path for shearing interference. By interferograms analysis and corresponding phase recovery algorithm, the wavefront can be rebuilt and so the roughness can be evaluated.

Due to the self-reference characteristic of the shearing interference and complete common-path polarized interference design, the interferometry has excellent anti-disturbance ability while it keeps high accuracy as the interference microscope. So the interferometry is suitable for high precision surface quality monitoring in the manufacturing environment. The working principle of the proposed interferometry is presented and analyzed. The structure of new shear generator is introduced. The wave front recovery algorithm is described to obtain the roughness profile. Experimental results are also presented to demonstrate the feasibility of the proposed method.

Measurement Principle

The proposed interferometer (Fig. 1) has a microscopic objective to obtain the wavefront with the roughness information of the test surface. The wavefront is expanded by a beam expander consisting of lens L_1 and L_2. After being reflected by the polarized beam splitter PBS, the wave front enters a purpose-build shear generator SP made of a birefringence crystal and is sheared into two wavefronts parallel to each other. After passing through quarter wave plate Q_3 and polarized plate P_1, the two wavefront overlap and shearing interference happens between them. By CCD, the shearing interferogram is grabbed. Then a phase analysis and recovery algorithm

will be utilized to rebuild the wave front of the roughness profile to permit surface roughness assessment.

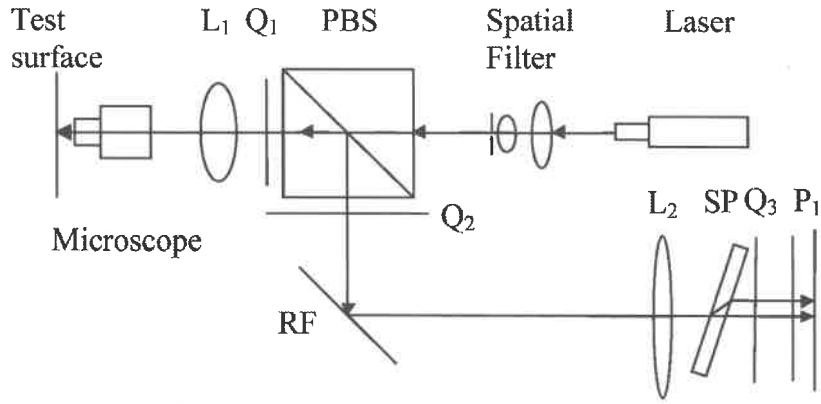

Fig. 1 Schematic diagram of the proposed interferometer

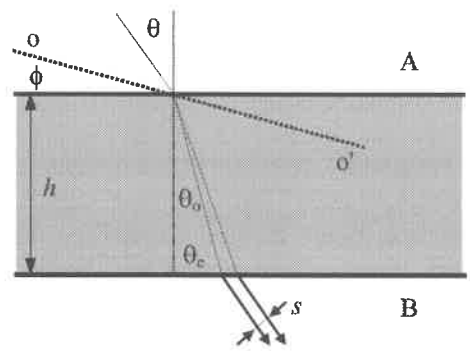

Fig. 2 New shear generator

In the proposed interferometer (Fig. 1), the He-Ne laser, the spatial filter, and the collimate lens consist of the light source. Quarter wave plate Q_1 changes the polarized direction of the wavefront to make it be reflected into the shearing circuit, another quarter wave plate Q_2 continues to change it to circular polarized, and Q_3 and the polarizer P_1 consist of a polarized phase shifter. When P_1 is rotated by an angle α, the interfering phase is shifted by 2α. When the wavefront with information from the test surface is sheared laterally by a shear quantity s into two wavefronts B_1 and B_2, the two wavefronts will interfere with each other in the overlapping field. The interference intensity can be obtained [6] as:

$$I(x, y)=I_0(x, y)+I_1(x, y)\cos(k\Delta w(x, y)) \tag{1}$$

where $\Delta w(x, y)= w(x, y)-w(x-s, y)$, $w(x, y)$ is the original wave front, $w(x-s, y)$ is the sheared copy of $w(x, y)$, $k=4\pi/\lambda$ is wave number, $I_0(x,y)$, $I_1(x,y)$ is the mean intensity and the modulation intensity, respectively. Once $\Delta w(x,y)$ is determined by analyzing the interferograms, $w(x,y)$ can be obtained as:

$$w(x, y) = \frac{1}{s}\int \Delta w(x, y)dx \tag{2}$$

The shear generator of the proposed method is made of calicite crystal (Fig. 2). Assume A and B are the two working faces parallel to each other, h is the thickness, OO′ is the optic axis of the crystal. The angle with the working faces A and B is ϕ. According to the birefringence characteristics of the calicite crystal [10], when a light beam gets onto the surface A of the

generator in a incident angle of θ, its two mutually perpendicular polarization compositions will refract in different refraction indexes of n_o and n_e, respectively. When the beam comes out from the surface B, it will be laterally sheared into two beams with their polarization directions orthogonal and ray directions parallel to each other, so the lateral shearing happens. The shear quantity s is equal to the splitting distance between the two beams and can be obtained as:

$$s = h(\tan\theta_e - \tan\theta_o)\cos\theta \tag{3}$$

where h is the thickness of the generator, θ is the angle of incident of the beam, and θ_o, θ_e is the refract angles of the two polarization components, respectively. θ_o, θ_e can be obtained according to Huygens principle [10]. By the special design, common-path, shear quantity adjusting and phase shifting can all be realized conveniently. A Fourier transformation method [11] is adopted for wavefront reconstruction from the phase differences. From the lateral shearing interferograms, the phase differences can be obtained as:

$$\Delta w(x,y) = w(x+s/2,y) - w(x-s/2,y) \tag{4}$$

The Fourier transforms of the phase differences are as:

$$\begin{aligned} F[w(x-s/2,\ y)](v) &= \int w(x-s/2,\ y)\exp(-2\pi i v x)dx \\ &= \int w(x,\ y)\exp(-2\pi i v x)\exp(i\pi v s)dx \end{aligned} \tag{5}$$

$$\begin{aligned} F[w(x-s/2,y)](v) &= \int w(x+s/2,y)\exp(-2\pi i v x)dx \\ &= \int w(x,y)\exp(-2\pi i v x)\exp(i\pi v s)dx \end{aligned} \tag{6}$$

where s is the shear quantity, F donates the Fourier transform, x is a length coordinate, and ν is the spatial frequency. From Eq. (4-6), the Fourier transform of the wave front can be obtained as:

$$F[w(x,y)](v) = T(v)F[\Delta w(x,y)](v) \tag{7}$$

Using an inverse Fourier transformation, the wavefront of the test profile can be obtained as:

$$w(x,y) = F^{-1}[T(v)F[\Delta w(x,y)](v)] \tag{8}$$

where $T(v) = 1/(\exp(i\pi v s) - \exp(-i\pi v s)) = 1/(2i\sin(\pi v s))$. $T(\nu)$ represents the shearing transfer function, which is undefined for $\sin(\pi\nu s)=0$. As a consequence, $F[w(x,y)](ks^{-1})$ remains unknown for $k \in Z$ of the integer domain, and no information about these s-periodic parts can be obtained from the difference function. Fortunately, only roughness features are cared about in our measurement, which has a definite spatial frequency domain. So we can choose a suitable shear quantity s which is far from wavelength corresponding roughness, so that $\sin(\pi\nu s)\neq 0$, and roughness profile information can be obtained.

Experimental Results and Discussion

To demonstrate the feasibility of the proposed method, a standard roughness sample with a R_a value of 0.34μm was used. A 10x microscopic objective was used. The shear quantity s=0.004mm. A set of results of the preliminary tests are as shown in Fig. 3. It can be seen that roughness profiles were obtained. Based on the results, the roughness parameter R_a=0.297μm. It can be seen that the obtained R_a result was quite close to the original R_a value. With more accurate estimation of the shear that was applied in the testing, better results could be obtained.

Conclusions

Taking the advantages of shearing interferometry and those of microscopic interferometry, a new non-contact roughness profile measurement method is presented. Due to the self-reference and common path polarized interferometric design, the proposed interferometric method should be immune to external disturbances while have high measurement accuracy. The interferometer is suitable for surface quality monitoring in a production environment. The experimental results demonstrated that the proposed method is feasible.

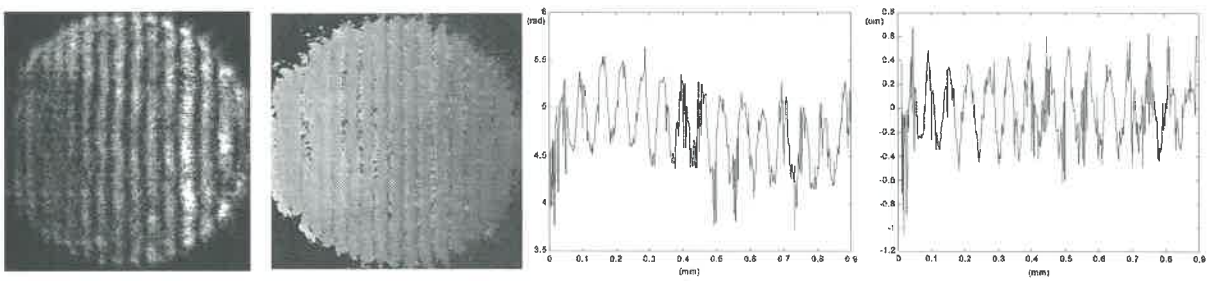

(a) Interferogram (b) Phase difference (c) 1D phase difference (d) Roughness profile

Fig. 3 Experimental results of a roughness specimen

References

[1] Garatt, J. D., 1982, A new stylus instrument with a wide dynamic range for use in surface metrology, *Precision Engineering*, **4**, pp. 384-9.

[2] Ding, Z. H., Wang, G. Y., and Wang, Z. J., 1996, Microscopic interferometer for surface roughness measurement, *Optical Engineering*, **35**(10), pp. 2956-2961.

[3] Fujii, T., Yamaguchi, M., and Suzuki, M., 1995, Scanning tunneling microscope with 3-dimensional interferometer for surface roughness interferometer for surface roughness measurement, *Review of Scientific Instrument*, **66**(3), pp. 2504-2507.

[4] Jolic, K. I., Nagarajah, C. R., and Thompson, W., 1994, Non-contact, optically based measurement of roughness of ceramics, *Measurement Science and Tech*, **5**(6), pp. 671-684.

[5] Chen, S. H., Lin, H. N., and Yang, C. R., 2000, Surface roughness measurement on microchannels by atomic force microscopy using a bent tapered fiber probe, *Review of Scientific Instrument*, **71**(10), pp. 3953-3954.

[6] Poon, C. Y., and Bhushan, B., 1995, Comparison of surface roughness measurements by stylus profiler, AFM and non-contact optical profiler, *Wear*, **190**(1), pp. 76-88.

[7] Rao, C. B., Kalyanasundaram, P., and Raj, B., 2001, Laser scattering for surface roughness measurement, *Insight*, **43**(4), pp. 265-269.

[8] Wong, P. L., and Li, K. Y., 1999, In-process roughness measurement on moving surfaces, *Optics and Laser Technology*, **31**(8), pp. 543-548.

[9] Malacara, D., and Devore, S. L., 1992, Phase-measurement interferometry, *Optical Shop Testing*, 2e, Daniel Malacara, John Wiley and Sons Inc., New York.

[10] Longhurst, R. S., 1973, Geometrical and Physical Optics, 3e, Longman Inc, New York.

[11] Elster, C., and Weingartner, I., 1999, Solution to the shearing problem, *Applied Optics*, **38**(23), pp. 5024-5031.

Scale-space and multi-resolution techniques for outlier analysis in surface metrology

B. Muralikrishnan, Shengyu Fu, N.G.Orji and J.Raja
Center for Precision Metrology
The University of North Carolina at Charlotte
Charlotte, NC 28223

1. Introduction

Scale-space techniques and multi-resolution analysis are entirely different techniques, yet they share certain similarities. Scale-space approach relies on viewing a profile at different scales, much like the methodology used by wavelets. However, there is no clear transmission characteristic at each level. Both methods let us break down a signal into different scales and later reconstruct the signal. This permits us to analyze signal according to scale. The objective of this work is to demonstrate the applicability of scale-space technique and multi-resolution approach for outlier analysis in surface metrology.

2. Morphological Filters

Morphological filters [1] are a superset of the envelope filters used in surface metrology in the late 70s. They typically involve finding the contact between a structuring element (ball or line) and the profile. Two basic operations are dilation (locus of points of a ball rolling over a surface) and erosion (locus of points of a ball rolling under a surface). Closing and opening are combinations of these two fundamental operations. A closing filter produces an outer mean line and an opening filter produces a lower mean line. These mean lines can be used for identifying peaks and valleys, as they are not average mean lines such as those produced by conventional filters. Instead local peaks and valleys very heavily influence the morphological mean lines.

3. Alternating Symmetrical Filters (ASF)

ASF is a sequence of opening and closing filters [1] applied to a profile. ASF produces a ladder structure that is very similar to that produced by multi-resolution analysis using wavelets. At each step of the ladder, an approximation and a difference profile are created. The approximation is obtained by passing the approximation from the previous step through an opening filter of certain size followed by a closing filter of the same size. The sequence of closing and opening filter removes all peaks and valleys whose sizes are smaller than the size of the structuring element. The difference profile at any step is simply the difference between the approximation at the previous step and the approximation at that step. The next rung of the ladder is obtained by

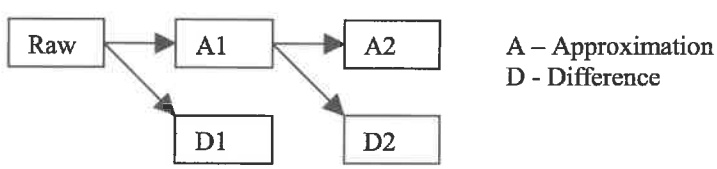

Figure 1 Schematic of alternating symmetrical filter

using a structuring element of larger size. Figure 1 shows the schematic of alternating symmetrical filters.

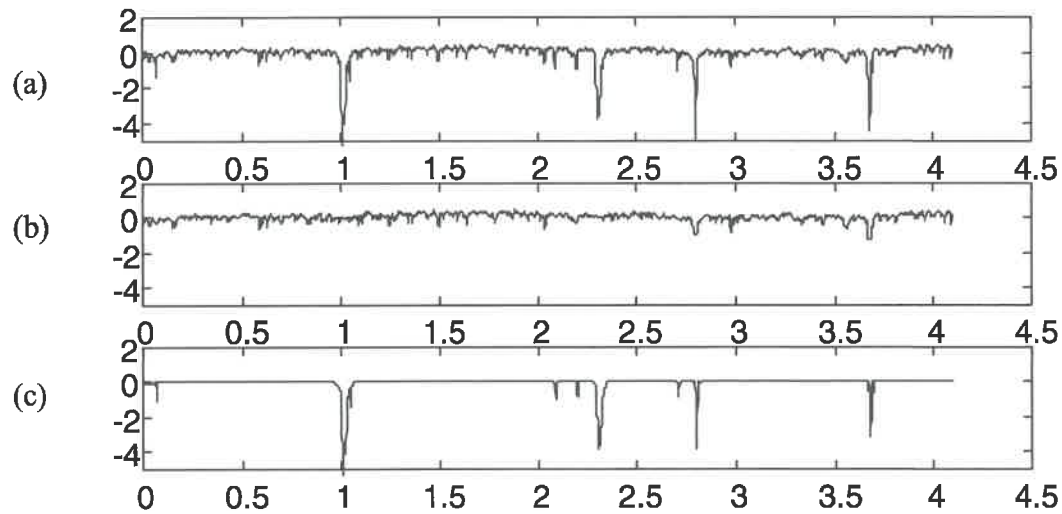

Fig 2 (a) Original profile (b) final profile after valley removal (c) and the difference

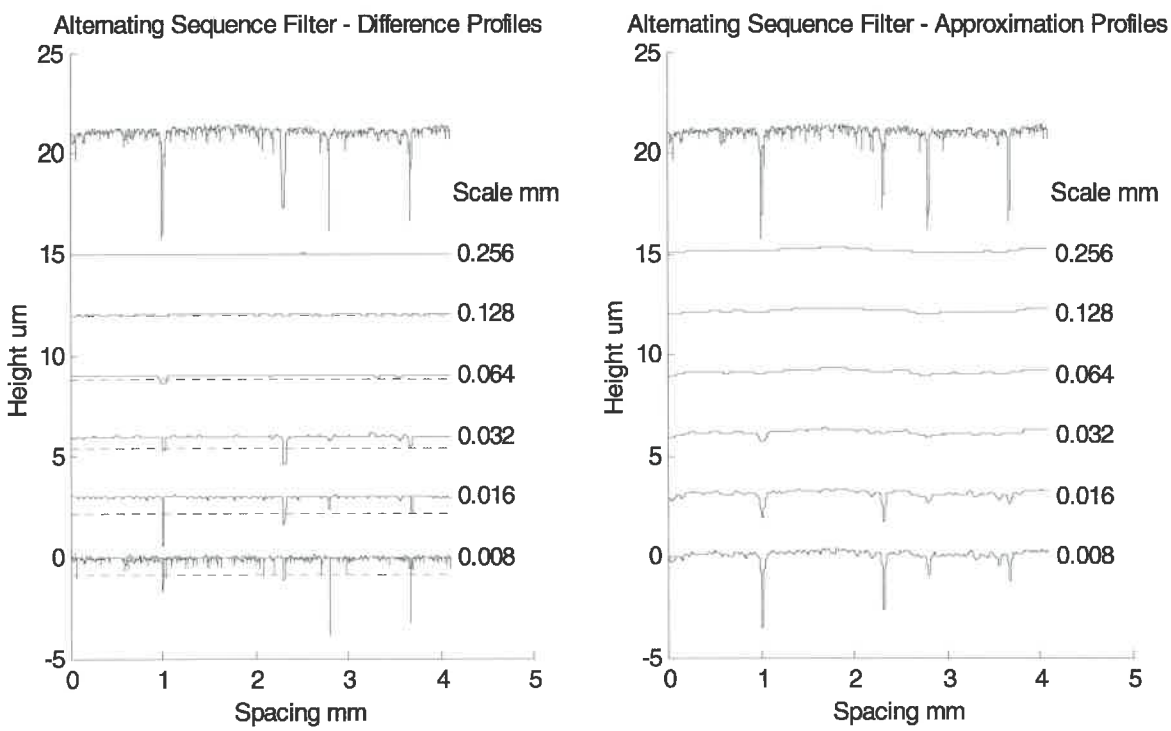

Fig 3 Scale space analysis to remove outliers – the difference profiles with the 4 sigma threshold is plotted on the left, the approximation profiles on the right

Outlier suppression is performed by thresholding the difference profile at each scale and reconstructing the signal. An example profile shown in figure 2(a) is sent through an ASF and the resulting ladder structure is shown in figure 3. The structuring

elements considered are 0.008mm, 0.016mm, 0.032mm, 0.064mm, 0.128mm and 0.256mm. It can be seen that the valleys are mainly present in the second and third rung from the top. In this example, a global four-sigma threshold is applied to all levels. This, however, need not be the case. The thresholded difference profiles along with the final approximation are added to generate the modified profile as shown in the figure 2(b). The data points that are removed are shown in the figure 2(c).

4. Multi-resolution approach to outlier removal

Multi-resolution analysis [2] involves breaking down a signal into several scales. At each scale, an approximation and a detail are created that is very similar to the scale-space concept. One fundamental difference between the two techniques is that each scale of the multi-resolution ladder can be correlated to a certain cutoff frequency while each scale of the scale-space ladder is related to the size of the structuring element. Figure 4(a) shows a profile with deep valleys that are sent through 9 levels of the multi-resolution ladder using coif4 wavelets. The choice of the wavelet is based on the recommendation by Liu [3] in his dissertation. Level 1 corresponds to a cutoff of 0.004mm and each subsequent level is double the cutoff of the previous level. The different levels are shown in figure 5. Figure 4(b) shows the reconstructed profile and figure 4(c) shows the points that are discarded.

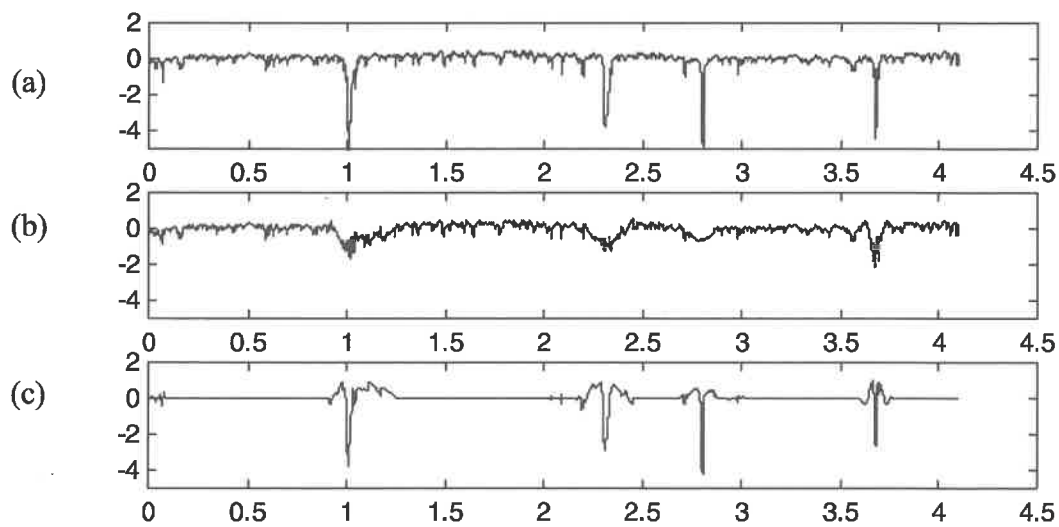

Figure 4 (a) Original profile (b) final profile after valley removal (c) and the difference

5. Conclusions

This paper has demonstrated the use of morphological filters and wavelets for outlier analysis. While multi-resolution analysis partitions a signal into many bands with very high computational speeds, scale-space approach is computationally expensive. Faster algorithms [4][5] are available for line structuring elements that enhance speed considerably. Scale-space seems to provide better valley separation with limited edge effects along the valleys.

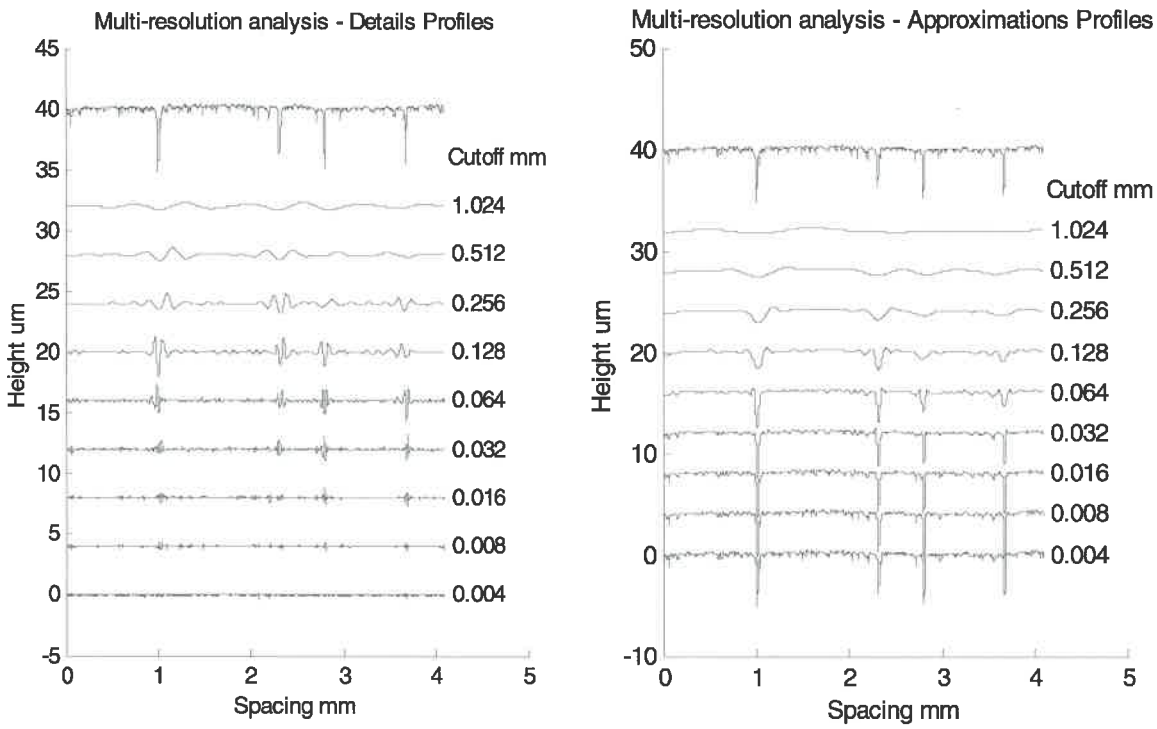

Fig 5 Scale space analysis to remove outliers – the details are plotted on the left, the approximations on the right

6. References

1. Srinivasan V., "Discrete Morphological filters for Metrology", Proceedings of the 6th IMEKO ISMQC Symposium on Metrology for Quality Control in Production, TU Wien, Austria, 1988
2. Chen X., Raja J., Simanapalli S., "Multi-scale of engineering surface', Int. J. Mach. Tools Manufacts. Vol. 35, No.2, 1995
3. Liu, X., "Advanced Techniques for Separation of Roughness, Waviness and Form ", Ph.D. dissertation, University of North Carolina at Charlotte, 1999.
4. Demin Wang, Dong-Chen He, "A fast implementation of 1-D grayscale morphological filters", IEEE transactions on circuits and systems-II: Analog and Digital signal processing, vol 41, no.9, September 1994
5. M.H.Sedaaghi, "A direct implementation of open-closing in morphological filtering", Electronic Letters, vol 33, no. 3, January 1997

Off-axis White Light Scatter Interferometry with 0.5m Transmissive Optical Elements

Anthony E Gee

School of Industrial and Manufacturing Science (B50)
Cranfield University, Cranfield MK43 0AL, England
a.e.gee@cranfield.ac.uk

Keywords: Scatter, interference, white light, optical components, testing.

1. Scattering from Thick Glass Reflectors

Newton (1730) observed interference with a back-silvered concave spherical mirror whose transmissive front surface scattered light due to fine particles or abrasive scratches ground on it. Light was incident on it from a pinhole at the centre of curvature. The direct image of the pin-hole was reflected back to a screen and around it he observed a set of interference rings. de Witte (1967) has reviewed white light scattering interferometry, detailing a number of techniques.

For normal incidence, Dyson (1958) simplifie d the explanation of Newton's arrangement using a second-surface plane-partial mirror with scattering first surface, as shown in Fig.1.

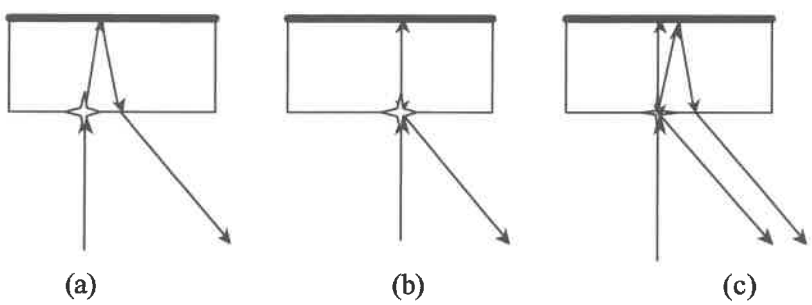

Figure 1. Normal Incidence Scattering Interference (Dyson 1958)

He explained the action in terms of components of a single (surface-normal) light ray either:

(a) forward-scattered obliquely on entry by a scatter element and, reflected off the back surface, avoiding the scatterer;

or

(b) some of the light incident at the scatterer is transmitted unscattered into the glass, reflected normally by the second surface along a reciprocal path and scattered by the element on emergence.

Combining these:

(c) corresponding scattered components from (a) and (b) interfere in the scatter far-field direction and the effects observed/displayed.

It might be added that matching energy/direction characteristics cause far-field scattered rays to interfere over a range of scatter-angles about the normal.

Because of the reciprocal incidence path in (b), the scatterer necessarily acts (at least partially) as beam energy-partitioner, dependent on dimension, shape and nature, accounting for the contrast observed in the central bright fringe viewed on axis.

Such interference can arise in any transmissive optical component with a partially-reflecting front surface and total- or partially-reflecting rear surface and constant or 'slow' changes of optical path delay between them across the interfering wave-fronts.

2. Oblique Incidence and High Fringe Contrast

Dyson's plane mirror arrangement was viewed both in collimated and divergent white light. With the divergent source, a ring-pattern was observed, manifesting increasing chromatic separation with increasing path difference with field pattern scale set by source/mirror geometry. Viewed on-axis (using a partially-reflecting mirror) the source-lamp reflection coincides with the central (bright) spot.
The pattern and source reflection was observed firstly in normal adjustment using a beamsplitter and then directly off axis as shown in Fig.2. From a mirror 5-8m away, the fringe-pattern can be viewed from alongside the light source either directly unaided from about 80mm off-axis, (typical pupil/temple separation) or by employing a miniature television camera closer to the axis.
Using white light interferometry, zero path-difference is indicated by the white/brightest fringe straddled by dark rings. In the off-axis condition, this is observed coinciding with the source reflection but, with a non-central fringe-ring and the ring-pattern central spot now manifests weaker fringe contrast and colour-separation indicating non-zero path-difference, according to how many fringes removed it is from the equal-path (but now off-axis) condition.

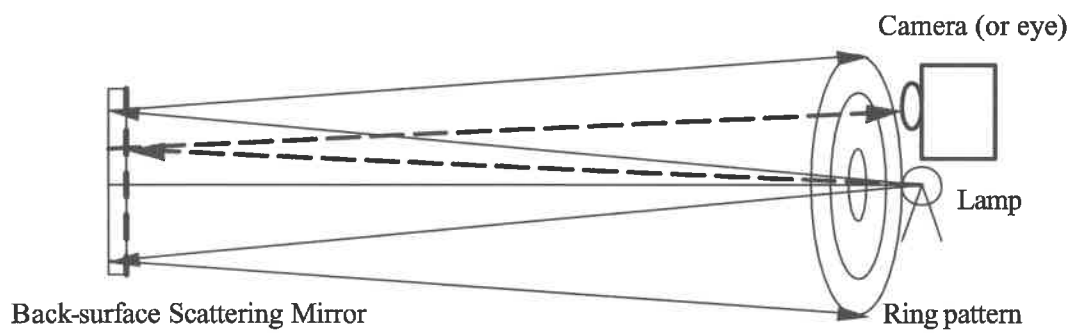

Figure 2. Simplified Off-Axis Viewing
(Observed source reflection ray-path indicated by heavy chain line).

Using different mirrors, scatterers and distributions, fringes adjacent to the bright equal-path off-axis condition invariably showed high contrast, indicating well-balanced contributing amplitudes/intensities due to action not apparent in the normal incidence cases shown in Fig 1. This seemed worthy of further investigation and a balance mechanism became apparent.

3. Scatter Balancing for High Fringe Contrast

At non-normal incidence (in divergent light viewed off-axis), two equal energy rays of light encounter any one scatterer as shown in Fig.3. (a) shows the ray directly incident from the source and forward-scattered obliquely to the angle of refraction into the glass on entry, reflected at the back (silvered) surface to finally emerge from the first surface alongside the scatterer.

A second ray, as in Fig.3(b), is incident parallel with the first ray onto the first surface, and laterally offset from the scatterer. As it does not encounter a scatterer on incidence, it is refracted unscattered into the glass, reflected from the back surface to be scattered on emergence.

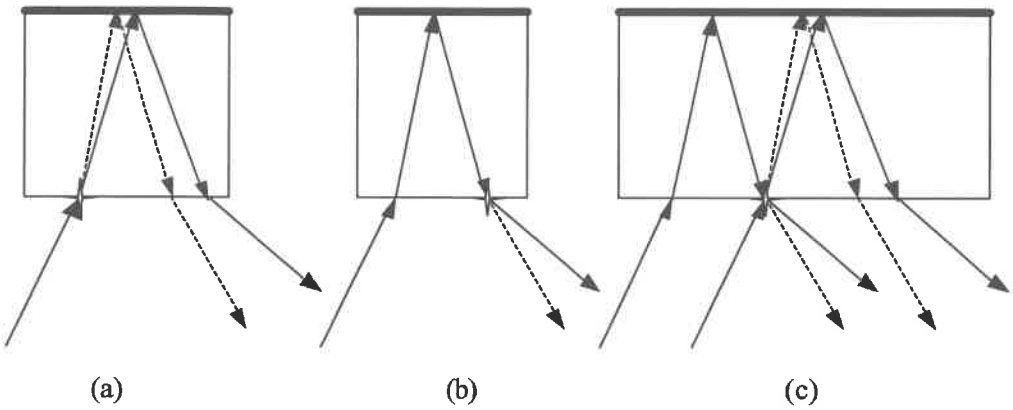

Figure 3. Balanced forward scattering from obliquely incident light, either:
(a) on entry to first surface or (b) on emergence from it
and (c) combining both from the same scatter-element. (Non-scattered paths shown dashed).

We see that from each scatterer, a laterally-sheared corresponding pair of rays emerge as shown in Fig.3(c), having travelled close parallel optical paths. Scattered in a given direction by the same scatterer, they have similar amplitudes and so generate high-contrast interference fringes in the far field.

4. Scatter Spatial Separation for High Fringe Intensity

Burch (1970, 1993) observed that there appeared to be an optimal spacing for maximum fringe intensity at greater spacing than that corresponding to 50% occupancy of the aperture by scatterers. For a given scatter angle, optimum scatterer spacing can be calculated as shown in Fig.4.

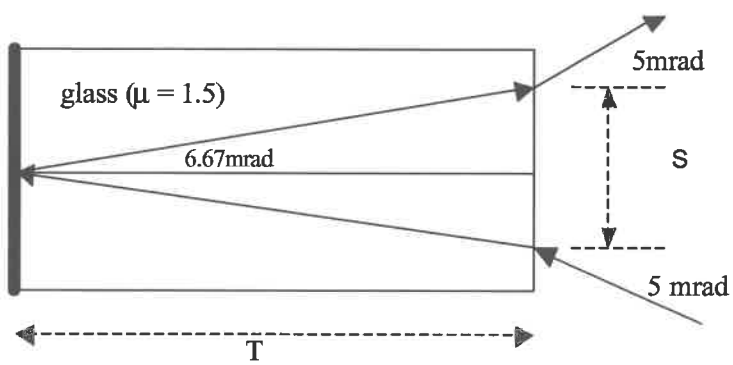

Figure 4. Offset angles and spacing for optimum scatterer density

With 8m source/mirror separation and 80 mm eye-source offset, the total included angle at the (now offset) zero order condition is 10mrad. This includes 5mrad incidence angle at the first glass surface, 3.33mrad refraction angle inside the glass (of refractive index 1.5) and 6.67mrad total reflection offset angle at the back surface. With glass 10mm thick (T), the emergent reflected ray is displaced 67μm laterally (S). To avoid vignetting rays from one scatterer by the next, lateral spacing between scatterers should exceed this value, thereby defining maximum scatterer density.

Due to the lateral shearing action, the technique can be employed for measuring effects of this order of scale. With large optical elements of perhaps 0.1m thickness, the shear increases to 0.67mm and, with an increase of offset angle by a factor or five to 50mrad, the lateral shear can be increased to more than 3mm so long as the aperture is large enough to support sufficient scatter elements to permit fringes to be seen at this low scatterer-density.

5. Utility of White Light Fringes

By definition, white light interferometry employs light of short coherence, with near equal paths and fringe visibility falling off either side of the zero order. The clarity of the zero order fringe however has much metrological merit in identification of this condition. Because of the intrinsic ability to discriminate to within one visible fringe, white light interference can be employed to determine when two optical components are in optical phase as in optical arrays (Gee 1995).

However, with a divergent source, the system produces a ring pattern permitting the arrangement to extend to any axisymmetric system or component, e.g. a lens. The ring pattern density is then dependent on the radial path change gradient which can be compensated by a complementary element of known performance.

6. Conclusions

Subject to limitations on shearing path length differences, where a large refractive component needs to be examined at spatial increments across the aperture of the order of between tens of micrometres and perhaps fractions of a millimetre, Newton's white light scatter interference may be of utility. It requires no beamsplitter or test component and has been employed with apertures of up to 0.5m. Dyson's (1958) normal incidence explanation has been expanded to account for autonomous remarkable brightness and contrast of near zero order fringes when viewed off-axis. The scatterer density limitation observed by Burch (1970) has been quantified.

7. Acknowledgments

I am grateful to Edward Palmer of Hampton, Middlesex, England, for bringing to my attention wide aperture white light scatter interferometry using second surface mirrors and for subsequent discussions. (Modestly, he declined co-authorship). My late colleague, James M Burch, formerly Visiting Professor at Cranfield, is acknowledged for introducing me to the powerful simplicity of white light scatter interferometry requiring neither laser nor polished surface.

8. References

Burch J M (1970) *Interferometry with Scattered Light* pp213-237 of J Home Dickson (ed.) 'Optical Instruments and Techniques 1969' Oriel, Newcastle (Proc ICO Conf Reading 1969)

Burch J M (1993) Private Communication

Dyson J (1958) *Interferometers* Appendix B (pp377-392) of Strong J (1958) *Concepts of Classical Optics* W H Freeman, San Francisco CA; (see particularly pp 382-383)

Gee A E (1995) *The Grating Array: Sub-micrometre Control of Five Degrees of Freedom,* ASPE Spring Meeting, Tucson, AZ, April, 1995: Proc ASPE vol 11 pp50-53 (Am Soc Prec Eng, Raleigh, NC)

Newton I (1730) *Opticks* London 4th edn, (2nd Book, Pt IV, *Observations Concerning the Reflexions and Colours of thick transparent polish'd Plates*) reprinted (1952 & 1979) Dover, New York NY, pp289-312

de Witte A J (1967) *Interference in Scattered Light* Am J Phys vol 35 pp301-313

Zone plate interferometer using a liquid crystal panel as a diffraction grating - Proposal on the compensation method of systematic error -

Kazuhide KAMIYA[*a], Takashi NOMURA[*a], Seiichi OKUDA[*a],
Hatsuzo TASHIRO[**b], Kazuo YOSHIKAWA[**b]
[a] Facility of Engineering, Toyama Prefectural University,
[b]Facility of Engineering, Toyama University
* Kurokawa, Kosugi-machi, Toyama 939-0398, Japan,
** Gofuku, Toyama, Toyama 930-8555, Japan

Keywords: zone plate interferometer, liquid crystal panel, compensation method, systematic error, shape measurement, common path interferometer, phase shift method

Introduction

Common path interferometers are key devices for shape measurements of optical elements and precision machine parts. A zone plate interferometer is a type of common path interferometer,[1)] in which wavefronts generated by a diffraction grating called the zone plate are used as a standard surface for measurement. In other words, the zone plate functions as a null lens. The production process of the zone plate is simpler than the manufacturing process of a null lens because the zone plate pattern is obtained from calculations using geometric conditions and because it is possible to manufacture the zone plate by optical lithography. However, custom-made zone plates are required in order to measure various shapes.

We proposed the use of the pattern displayed on the liquid crystal panel as a diffraction grating.[2)] As a result, an interference fringe showing the shape of the plane mirror was obtained. The interference fringes were analyzed by the phase shift method. However, use of the liquid crystal panel resulted in measurement error, since it was not designed specifically for use with the interferometer. In this paper, a method of reduceing the measurement error is proposed.

Zone plate interferometer

Figure 1 shows a schematic diagram of the zone plate interferometer with a liquid crystal panel. The zone plate is illuminated by a laser light source. The light beam passing through the liquid crystal zone plate functions as a measurement light beam. The light beam diffracted by the zone plate on the liquid crystal panel functions as a reference light beam. The measurement light beam reflects off the surface being tested and is distorted by the error in the shape of the surface being tested. The reference light beam reflects off the center of the surface being tested and is not influenced by the surface being tested because the reflecting area is very small. The measurement light beam and the reference light beam pass and diffract again at the liquid crystal zone plate. Both light beams converge on a small spot at the aperture stop. Unnecessary light beams are removed almost completely by the aperture stop. Interference fringes are obtained on

the image plane of the charge-coupled device (CCD) camera. The interference fringes include measurement error caused by the shape error and configuration error of the optical elements constituting the interferometer. The method of compensation of the error caused by the heterogeneity of the liquid crystal panel is described in the next section.

Method of the compensation

Compensation of the error is carried out by rewriting the pattern displayed on the liquid crystal panel. In other words, the light beam diffracted at the pattern can be controlled. An error map is not made for compensation of the measured value on the interferometer. The procedure for the compensation is as follows.

1) It is assumed that the interferometer does not have error and the original pattern of the zone plate is calculated. An example of an original zone plate is shown in Fig.2.
2) A known shape is measured by the zone plate interferometer using the original pattern of the zone plate.
3) The difference between the known shape and the measured shape is regarded as the systematic error of the interferometer. A modulated pattern is designed in order to compensate the error. Figure 3 shows an example of a modulated zone plate.

In the method of correcting the measured value using the error map, the light beam is distorted during the measurement. However, in the proposed method, the light beam distortion has been corrected. Figure 4 shows the process in which the corrected reference light beam is generated from the light beam distorted by the modulated zone plate.

Liquid crystal panel

Experiments were conducted using a liquid crystal panel, as shown in Fig.5. The specifications of the liquid crystal panel are as follows. The panel (KOPIN Cyber Display 320 Monochrome) with 320 x 240 pixels and thin film transistors was used. Each pixel was addressed by the active matrix method. The interval between adjacent pixels, both horizontal and vertical, was is 15 μm. The gray level of the display of the panel was over 256.

Experimental results

Experiments were carried out to confirm the validity of the proposed method. The error of the liquid crystal panel was estimated using a plane mirror with an accuracy of $\lambda/20$. The experimental results showed that the error caused by the nonuniformity of the liquid crystal panel can be corrected by the proposed method.

Conclusions

In this paper, a method of reducing the measurement error caused by the nonuniformity of the liquid crystal was proposed. The experimental results established the validity of the proposed method.

Acknowledgment

This study is financially supported in part by Grant-in-Aid for Encouragement of Young Scientists (A) (11750102) from the Ministry of Education, Science, Sports and Culture, Japan.

References

1. R. N. Smartt, "Zone plate interferometer," Appl. Opt., 13, 1093 (1974).

2. K. Kamiya, T. Nomura, H. Miyashiro, K. Yoshikawa, H. Tashiro, "Application of liquid crystal panel as diffraction grating to zone-plate interferometer," Proc. ASPE, 353 (1996).

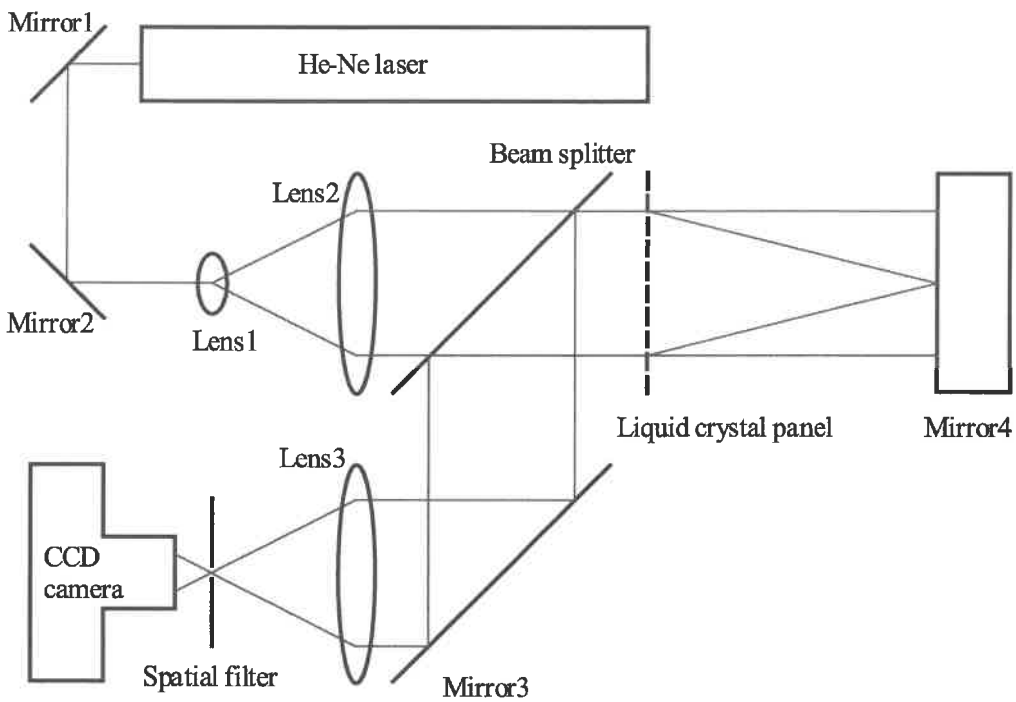

Fig.1 Schematic diagram of zone plate interferometer with a liquid crystal panel

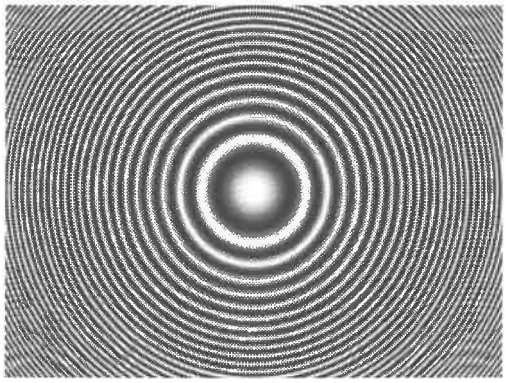

Fig.2 Original zone plate

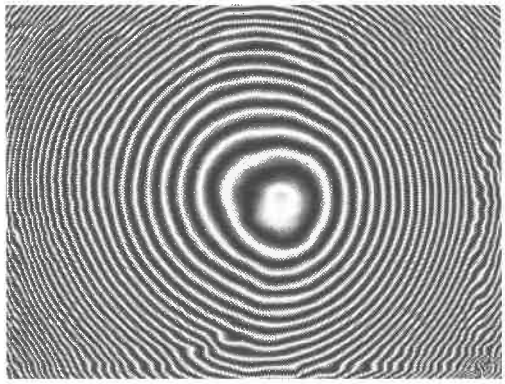

Fig.3 Modulated zone plate

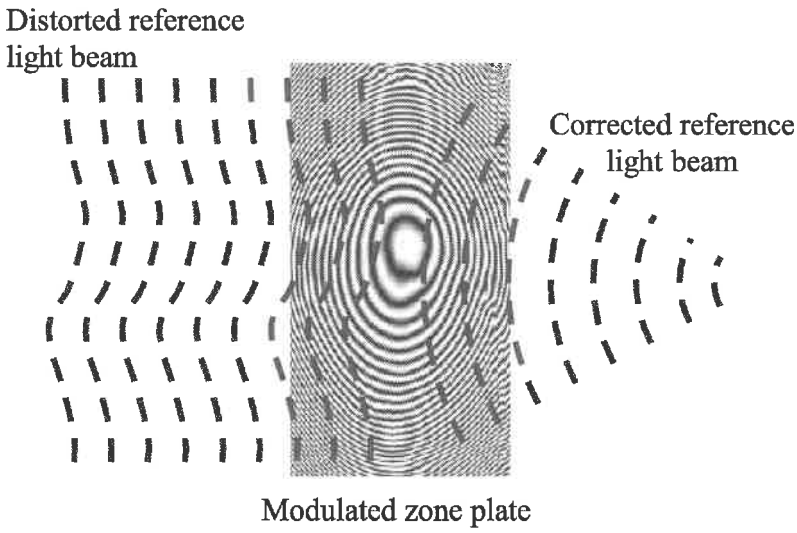

Fig.4 Compensation of the distorted reference light beam by the modulated zone plate

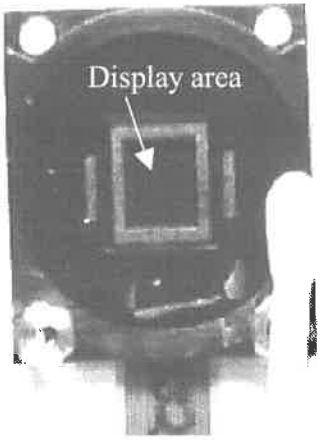

Fig.5 Liquid crystal panel

A Study of Grinding Marks in Semiconductor Wafer Grinding

Somasundaram Chidambaram and Z.J. Pei
Dept. of Industrial and Manufacturing Systems Engineering,
Kansas State University, Manhattan, Kansas 66506.

1. Introduction

Integrated circuits are a part of everyone's life today. They are used in building of all kinds of electronic devices from a radio to the most sophisticated satellites. These integrated circuits are constructed on semiconductor wafers and are later diced and assembled into their final assemblies. Manufacturing of semiconductor wafers to meet the ever increasing demand and quality needs is a constant challenge.

One of the important processes in manufacturing of semiconductor wafers and Integrated circuits is grinding process. Grinding is done to reduce the thickness and improve the surface quality of the wafer at a high throughput. Hence, its use in wafer manufacturing is increasing. Grinding is finding some newer applications in the manufacturing process such as partially replacing lapping and polishing operations. The grinding operation is generally used in two places. The first place is to remove the waviness from the initial sliced wafer and to restore parallelism between the front and the back surface. Secondly, the grinding is done on the backside by a process called "backgrinding" after construction of circuits on the front side.

One phenomenon in wafer grinding is the generation of grinding marks. The depth and the orientation of grinding marks play an important role in determining the quality of the wafer produced. Even though the grinding marks produced by wafer grinding are uniform with radial alignment, the orientation of the grinding marks varies significantly for the sliced die. This causes variation in the die strength of the wafer produced. It is important that the surface quality and the die strength of the wafer produced by grinding process be optimized. To achieve this we need to understand thoroughly the process of semiconductor wafer grinding and predict the generation of grinding marks.

This paper studies the most commonly used semiconductor wafer grinding process namely, the cup wheel grinding (in other words "wafer grinding", "backgrinding" or "surface grinding"). It first presents an analytical model to predict the locus of the grinding lines and the distance between two adjacent grinding lines. Then the locus and distance of grinding marks predicted by the model are compared with experimental results.

2. Development of Mathematical Model

The literature most relevant to grinding marks includes analyses on vertical-spindle surface grinding using conventional wheels [Shaw, 1996], diamond cup wheel grinding of parabolic and toroidal surface on ceramics for mirrors [Zhong and Venkatesh, 1994; Zhong and Nakagawa, 1996], and precision cylindrical face grinding using a narrow ring superabrasive wheel [Shih and Lee, 1999]. These analyses are instrumental to the model development for wafer grinding, but cannot be applied directly.

Fig. 1 shows the setup of wafer grinding. The grinding wheel is modeled as a single-point cutter and it removes the work material from the edge to the center along the curve MO as shown in Fig. 2. Two coordinate systems are used to define all the points on the wafer and the grinding wheel as shown in Fig. 2. The origin of the grinding wheel's coordinate system U-V is at the center of the grinding wheel and the origin of the chuck's coordinate X-Y is at the

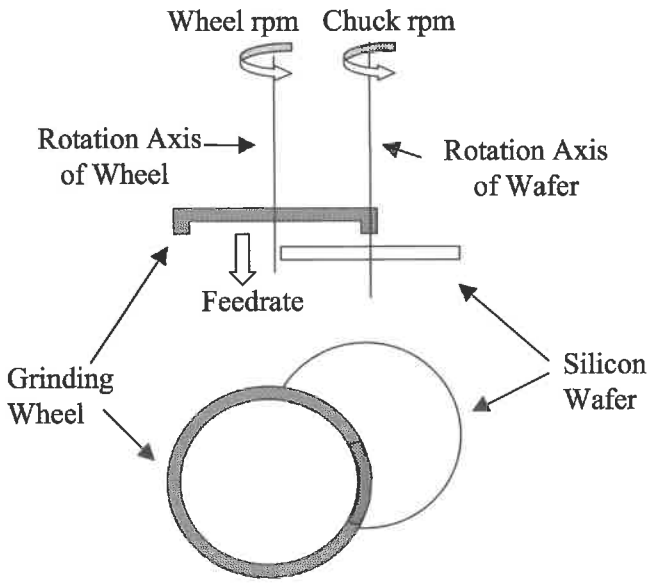

Fig. 1. Illustration of semiconductor wafer grinding.

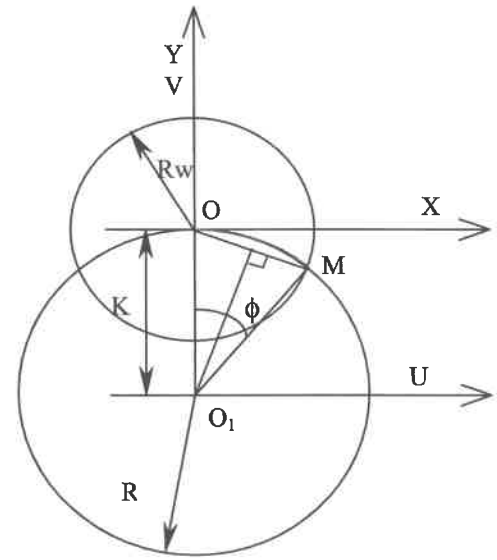

Fig. 2. Illustration of coordinate systems.

center of the chuck. The grinding wheel coordinate system is offset from the chuck's coordinate system along the Y-axis by a distance $-K$. In this case K is equal to R, the radius of the grinding wheel. The grinding wheel revolves about its center O_1 at N_s rev/sec. The wafer revolves about its center O at N_c rev/sec. and the wafer has radius R_w. Thus, there are four input parameters in this model: R, N_s, N_c, and R_w.

For the grinding wheel in Fig. 2, any point on the edge of the grinding wheel can be defined with respect to the *U-V* coordinate system by following equations

$$u = R.\cos(2\pi.N_s.t) \tag{1}$$

$$v = R.\sin(2\pi.N_s.t) \tag{2}$$

where, $t = 0$ is set initially at coordinates (*R*, 0).

The points in the *U-V* coordinate system can be transformed to the *X-Y* coordinate system by following equations

$$x = u = R.\cos(2\pi.N_s.t) \tag{3}$$

$$y = v - k = R.\sin(2\pi.N_s.t) - K \tag{4}$$

The time taken for point P with coordinates (*R*, 0) in the *U-V* coordinate system starting with time $t = 0$ to reach point M at the edge of the wafer can be calculated using basic geometry as shown in Fig. 2.

Thus, the range of t lies between

$$t_1 \le t \le \frac{1}{4N_s}$$

where t_1 is,

$$t_1 = \frac{1}{2\pi N_s}\left(\frac{\pi}{2} - 2.\arcsin\left(\frac{R_w}{2R}\right)\right) \tag{5}$$

and the time at which the nth grinding mark starts is given by

$$t_n = \frac{1}{2\pi N_s}\left(\frac{\pi}{2} - 2.\arcsin\left(\frac{R_w}{2R}\right)\right) + \frac{n-1}{N_s} \quad \text{where } n = 1,2,3\ldots \qquad (6)$$

However the above-described point P is not the point on the profile of the grinding mark. This point P is offset to P' on the wafer due to the simultaneous revolution of wafer as shown in Fig. 3. Angles θ_0 and $\Delta\theta$ and the distance r (r =OP=OP') with respect to the chuck's coordinate system are necessary to calculate the coordinates of point P'. These parameters are defined by pure geometry as shown in following equations

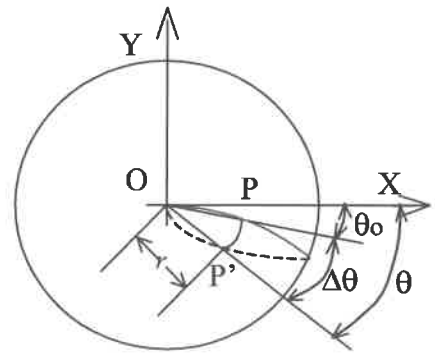

Fig.3. Offset of point P to P' due to wafer rotation.

$$\theta_0 = \arctan\left(\frac{y}{x}\right) \qquad (7)$$

$$\Delta\theta = 2\pi.N_c.(t - t_1) \qquad (8)$$

$$\theta = \theta_0 - \Delta\theta \qquad (9)$$

The distance of point P' from the origin O can be found out from the coordinates of P as P and P' should lie at the same distance from the origin O or on the same circle.

$$r = \sqrt{x^2 + y^2} \qquad (10)$$

Thus, the coordinates of P' can be written as (x_1, y_1)

$$x_1 = r.\cos(\theta) \qquad (11)$$

$$y_1 = r.\sin(\theta) \qquad (12)$$

3. Validation of the Model

The model was validated using the experimental results of Pei and Strausbaugh [2001] and Oh et al. [2001]. The grinding conditions used in these experiments are shown in Table 1. Fig. 4 shows some magic mirror pictures of ground wafers and the corresponding graphs of grinding marks generated by the presented model. From the figure it can be seen that the graphs have a very close resemblance with the grinding marks on the wafer surface. Both the curvature and the distances match to a close extent. The grinding marks were generated for one chuck revolution initially. In case of very high chuck speeds the grinding marks that fall in between the first and second grinding mark of the first revolution of the chuck were generated by using Eq. 6.

Table 1. Grinding parameters used in experiments [Pei and Strausbaugh, 2001; Oh et al., 2001]

Grinding wheel speed Ns rev/s (rpm)	Chuck speed Nc rev/s (rpm)	Grinding wheel radius R (mm)	Wafer radius Rw (mm)	Figure
36.25 (2175)	0.6667 (40)	140	100	Fig. 4 a
36.25 (2175)	9.8333 (590)	140	100	Fig. 4 b
72.5 (4350)	0.6667 (40)	140	100	Fig. 4 c
68.8833 (4133)	10.3833 (623)	140	100	Fig. 4 d

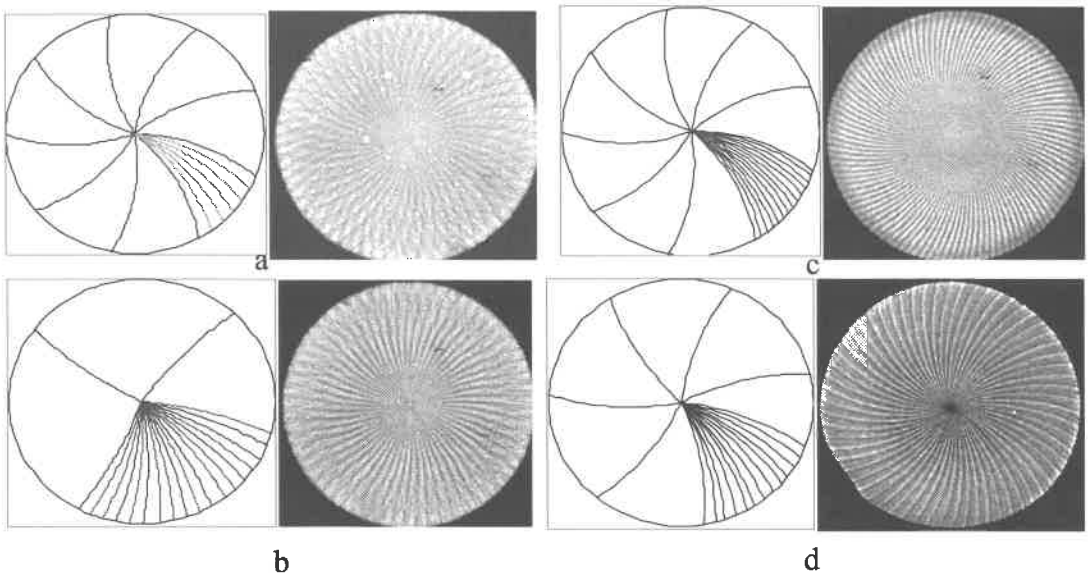

Fig. 4. Comparison of predicted grinding lines with magic mirror pictures.
(Note: Only about ¼ of grinding lines are drawn.)

4. Conclusion

A mathematical model has been developed to predict the grinding marks on the surface of semiconductor wafers induced by wafer grinding. The grinding marks generated by the model were compared with magic mirror pictures of experimental results. There seemed to be a very close resemblance in terms of curvature as well as the distance between two successive grinding marks.

Acknowledgement

Financial support was provided by the Department of Industrial and Manufacturing systems Engineering and the Advanced Manufacturing Institute of Kansas State University.

References

[1] Oh, H.S., Park, S.E., Jeong, S.M., Kim, S.S., and Lee, H.L., 2001, "Process induced mechanical damage and fine grinding process parameters," to appear at The Fourth International Symposium on Advances in Abrasive Technology (ISAAT'2001), November 6-9, Yonsei University, Seoul, Korea.

[2] Pei, Z.J., and Strasbaugh, A., 2001, "Fine grinding of silicon wafers: designed experiments," accepted to appear in International Journal of Machine Tools and Manufacture.

[3] Shih, A.J., and Lee, N.L., 1999, "Precision cylindrical face grinding," Precision Engineering, Vol. 23, pp. 177-184.

[4] Zhong, Z., and Venkatesh, V.C., 1994, "Generation of parabolic and toroidal surfaces on silicon and silicon-based compounds using diamond cup grinding wheels," Annual of CIRP, Vol. 43, No.1. pp. 323-326.

[5] Zhong, Z., and Nakagawa, T., 1996, "Grinding of aspherical SiC mirrors," Journal of Materials Processing Technology, Vol. 56, pp. 37-44.

Optimization of Cooling Effect in the Grinding with Mist Type Coolant

H. Z. Choi, S. W. Lee, D. J. Kim

Korea Institute of Industrial Technology
35-3, HongChonRi, IbJangMyun, ChonAnSi, 330-825, Korea

ABSTRACT

Coolant generally contains the extreme pressure additives such as chlorine, sulfur and phosphorus to improve the grinding efficiency, but the severity of environmental pollution due to these additives always has been proposed. Mist type coolant is one of the cooling materials developed for preventing heat generation on the grinding point instead of coolant. It is so effective that it can increase the surface integrity of workpiece, decrease considerable machining cost and in the end prevent the environmental pollution.

This study focused on the methods for increasing the cooling effect in grinding using mist type coolant. First, grinding characteristics in the grinding with mist type coolant were compared with that of coolant and compressed cold air. And then mist type coolant supply and grinding conditions for increasing the cooling with respect to workpiece quality were considered. As a result, it is possible to get the surface integrity and cooling effect as much as coolant.

Key words : Extreme pressure additives, Grinding Efficiency, Environmental problem, Mist type coolant Cooling material, Cooling effect, Surface integrity, Grinding temperature, Energy ratio

1. Introduction

Coolant has great performances such as lubrication, cooling and penetration. Especially, it contains the extreme pressure additives such as chlorine, sulfur and phosphorus to improve the grinding efficiency. But these chemical materials cause several environmental problems. The dry grinding with compressed cold air was one of the grinding methods that have developed for solving these environmental problems. It could prevent the environmental pollution through only using -10 ~ -40℃ of compressed air and also decrease the considerable machining cost due to coolant. Nevertheless, it is not enough to get the sufficient grinding performance and cooling effect because it has no lubricant material on the grinding point. The semi-dry grinding with mist type coolant uses small amount of coolant for the lubrication on the grinding point. These grinding methods not only can improve the surface integrity of workpiece but also reduce the environmental pollution by minimizing the use of coolant. But it could not achieve the cooling effect as much as coolant.

Therefore, in this study, the grinding experiments using coolant, mist type coolant were performed and methods to increase the cooling effect of the grinding using mist type coolant were analyzed. First, the surface integrity of workpiece such as surface roughness, roughness, residual stress and energy ratio into workpiece were measured to analyze the grinding characteristic of mist type coolant. And then, the grinding experiments according to the supply method of mist type coolant and grinding condition like wheel speed were performed. Through these experiments, the cooling effect in grinding using mist type coolant could be increased as much as that of coolant.

2. Experimentation

2.1 Fundamentals of Cooling Effect in Grinding

The main characteristic of grinding in comparison to other machining processes is the relatively large contact area between the wheel and workpiece and the high friction between the abrasive grains and workpiece surface. It causes high heat generation on the grinding point, resulting in a high risk of thermal

damage to the workpiece surface layer. The semi-dry grinding using mist type coolant generally uses 5~300ml/min of coolant for cooling lubrication. This cooling lubrication largely depends on the proper lubrication environment for preventing the film boiling on the grinding arc between wheel and workpiece. The film boiling on the grinding arc can be escaped as the amount of mist type coolant increases and its particle size become large. The mist type coolant also has to be supplied on the wheel surface prior to the grinding point. In this experiment, the mist type coolant supply was fixed on the wheel surface prior to the grinding point. Through observing the flow of mist type coolant with CCD CAMERA, 200*ml*/min of mist type coolant was decided. Its particle size was 24μm.

2.2 Experimental Conditions

In this experiment, surface grinder and CNC cylindrical grinding machine, WA(White Alumina) grinding wheel and SCM21 of crank shaft material were used. The experimental conditions are shown in Table 1. The cooling methods, depth of cut, wheel speed were used as the variables for the experiment.

Table 1 Experimental Conditions

Grinding machine		Surface grinder Cylindrical grinding machine		
Grinding wheel		WA80I/J7V, ~$Ø_o$305×25^t×$Ø_i$127		
Workpiece		SCM21	Carburizing and quenching, H_{RC} 58~60	
Grinding fluids	Coolant	Emulsion (4%)		
	Mist	Amount(ml/min)	100, 200	
		Temperature (℃)	-30	
Dressing conditions		Dresser	One-point diamond dresser	
		Depth of cut (a_d, μm)	10	
		Feed rate (f_d, mm/rev)	0.05	
Working conditions		Surface grinding	Depth of cut (a, μm)	20
			Wheel speed (v_c, m/sec)	20, 30
			Table feed speed (v_{ft}, mm/sec)	6
		Plunge grinding	Depth of cut (a, μm)	5, 10, 15, 20, 30
			Wheel speed (v_c, m/sec)	25, 30, 35, 40
			Workpiece speed (v_w, m/min)	18

2.3 Experimental Device

The experimental equipment was composed of two components. That is, mist type coolant nozzle and constant temperature water bathe. The nozzle makes coolant 10~24μm of particles and constant temperature water bathe controls the temperature of compressed cold air within ±0.5℃ over 5 hours.

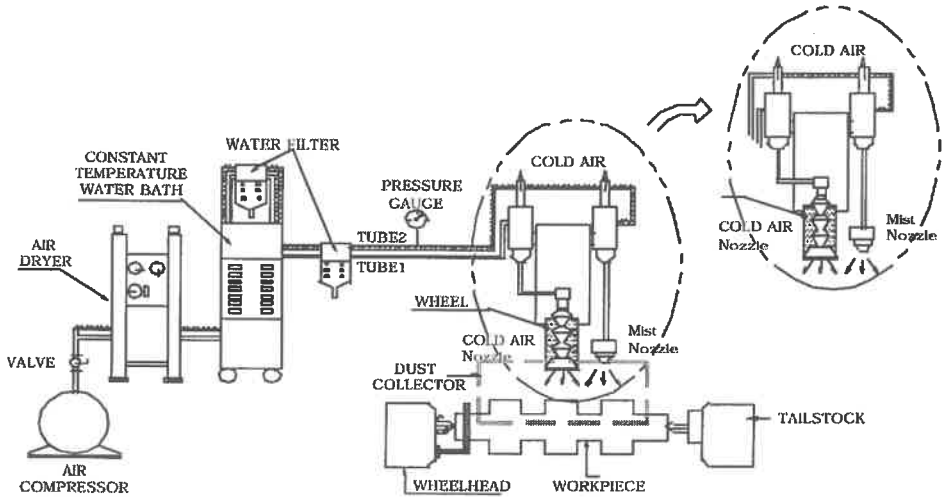

Fig. 1 Schematic Diagram of Experimental Equipment

3. Experimental Results and Inquiries

3.1 Surface Integrity in the Grinding using Mist Type Coolant

Fig. 2 shows the surface roughness and roundness of workpiece after grinding according to cooling methods. As shown in Fig. 2, the surface roughness was increased as much as coolant and roundness was even better than that of coolant due to low pressure force on the grinding point between wheel and workpiece. This results explain that small amount of mist type coolant only can increase the surface integrity of workpiece with keeping the lubrication well on the grinding arc and decrease the perpendicular pressure force (F_n) due to coolant.

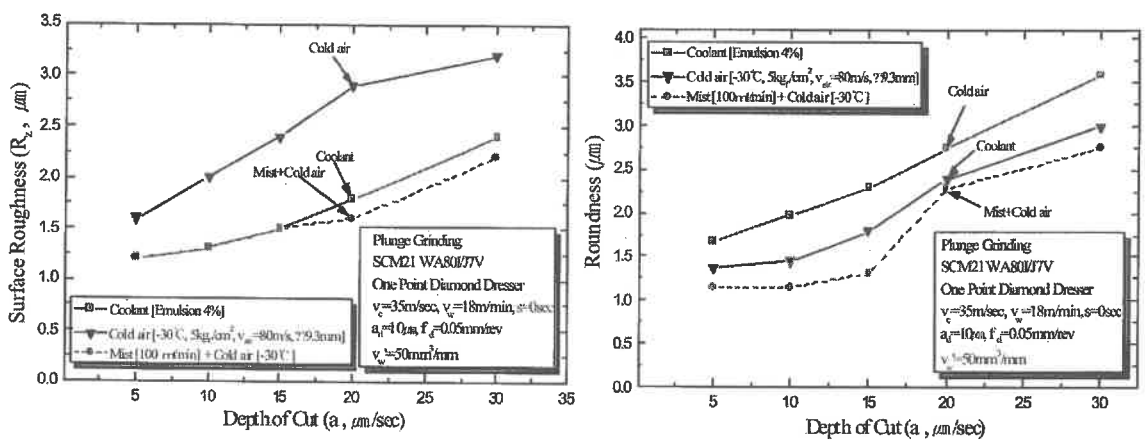

(a) Surface Roughness (b) Roundness

Fig. 2 Surface Integrity of grinding according to grinding methods

3.2 Cooling Effect in the Grinding using Mist Type Coolant

Fig. 3 shows the energy ratio conducted into workpiece among total grinding heat on the grinding point

during grinding and residual stress on the workpiece surface after grinding. As shown in Fig. 3, the energy ratio of coolant was 26.83%, mist 31.04% and compressed cold air 43.47%. These heat energy conducted into workpiece generates the tensile residual stress in contrast to that by mechanical process. At result, the residual stress in the grinding using coolant showed the compressed residual stress to depth of cut 30μm, but mist type coolant showed the tensile stress over depth of cut 15μm.

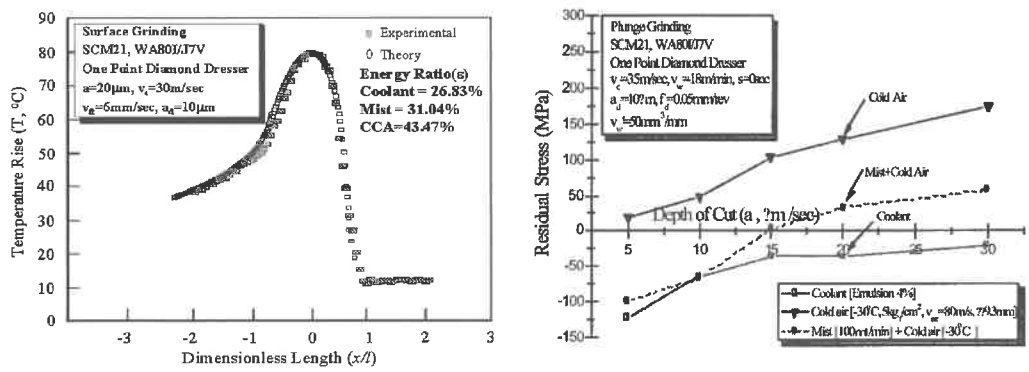

(a) Energy Ratio (b) Residual Stress

Fig. 3 Energy Ratio into Workpiece and Residual Stress

4. Conclusions

The experiments to optimize cooling effect in the grinding using mist type coolant were carried out. The conclusions are drawn as follows:

1) The surface roughness in the grinding using mist type coolant was increased as much as coolant and roundness was even better then coolant due to low pressure force generated on the grinding point.
2) The energy ratio into the workpiece in the grinding using coolant was 26.83%, but mist type coolant is 31.04%. And, in case of residual stress, coolant showed the compressed residual stress to 30μm of depth of cut, but mist type coolant showed the tensile residual stress over 15μm of depth of cut. Because it is not enough to get sufficient cooling effect on the grinding point
3) The supply method of mist type coolant on the peripheral surface of grinding wheel and approximate 200*ml*/min (particle size=24μm) of mist type coolant for optimizing the cooling effect were selected. The grinding condition like wheel speed was also considered as a grinding variable.

5. Reference

1. H. Z. Choi, S. W. Lee, H. D. Jeong, "A comparison of the cooling effects of the compressed cold air and coolant for cylindrical grinding with CBN wheel", Proceeding of AFDM, pp 319~322, 1999
2. H. Z. Choi, S. W. Lee, J. S. Ahn, "A study on the surface integrity for the cylindrical grinding with compressed cold air", ISAAT, pp. 187~192, 1998.
3. H. Z. Choi, S. W. Lee, J. S. Ahn, "A comparision of the cooling effects of the compressed cold air and coolant for the cylindrical grinding", International euspen conference, pp. 416~419, 1999.
4. H. Z. Choi, S. W. Lee, D. J. Kim and H. D. Jeong, "Grinding of Spindle Shaft Material with Mist Type Coolant", The 4th ISAAT, pp.279-284, 2000.
5. Toenshoff, H. K., Brinksmeier, E. Choi, H. Z., "Abrasive and their influence on force, temperatures and surface", International grinding conference, SME Technical paper MR86-626, June 1986.
6. C. Guo, "Energy Partition and Cooling During Grinding", Proceeding of 3rd International Machining & Grinding Conference, SME, Session 214, 1999

Grinding Temperature Measurements in MgO-PSZ Using Infrared Spectrometry

A. C. Curry[+], A J. Shih[+], J. Kong, S. B. McSpadden, R. B. Dinwiddie* and R. O. Scattergood[+]*
[+]North Carolina State University, Raleigh, NC 27695
**Oak Ridge National Laboratory, Oak Ridge, TN 37831*

Introduction

When the grinding wheel specifications are properly chosen, a SiC grinding wheel performs remarkably well for grinding partially stabilized MgO-ZrO_2 ceramics (MgO-PSZ). Rather surprisingly, the highest G-ratios are obtained at higher grinding rates for the SiC wheel. This, and the fact that SiC grinding wheels can be readily shaped for use in precision cylindrical form grinding, has been exploited for cost-effective production of PSZ components in automotive applications [1]. Several important effects were noted in studies on SiC-grinding of MgO-PSZ [2]. X-ray diffraction showed that the monoclinic phase was not present in the grinding chips. In contrast, the ground surfaces contained excess, relative to unground surfaces, of the monoclinic phase. This implies that the local hot-spot (flash) temperatures generated in PSZ grinding chips must be at least 1500 K, while the overall surface remains at a lower temperature. It has also been suggested that very high hot-spot temperatures would soften the ceramic and thereby contribute to the excellent grinding performance observed with SiC wheels. Motivated by these studies, the research reported here was undertaken to measure the grinding temperatures when using SiC wheels for grinding a 9 mol% MgO-PZS Coors ceramic.

A number of researchers have undertaken the task of determining the temperatures generated during grinding [3-7]. These can be divided into two classes. The first uses detectors such as infrared cameras to measure the intensity of the source output without discriminating between different wavelengths. Calibration techniques are needed to correlate the absolute intensity with source temperature and this can be difficult. In contrast, other methods use the ratio of two or more intensities at specific wavelengths to determine temperature in conjunction with blackbody radiation curves. As long as emissivity and other parameters are independent of wavelength over the measurement range, these do not have to be determined independently. A spectrometer-based method of this kind was used for the results reported here.

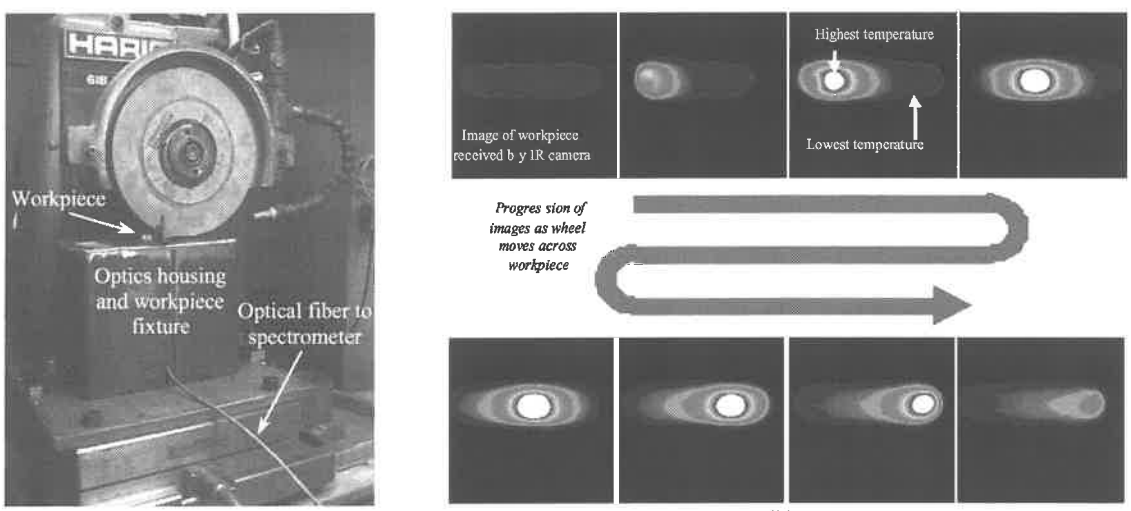

(a) (b)

Figure 1. a) Test setup. b) Infrared images of the grinding contact zone in a).

Experimental Procedure

Grinding tests were done on a Harig surface grinder. The table speed was fixed at 150 mm/s. The wheel speeds used were 3500, 4000 and 4500 rpm (37, 42 and 47 m/s surface cutting speed, respectively).

Downfeeds (depths-of-cut) were 0.0025, 0.005 and 0.0075 mm. The grinding wheel was a specially selected 220 mesh SiC grit vitreous bond wheel with a 200 mm diameter [1]. Water-based Cimtech 500 synthetic coolant at 5 % concentration was used during grinding. Sample fixtures, optics and other details of the grinding procedure are given in [8]. Temperature measurements were conducted using an Ocean Optics USB2000 near-infrared CCD array spectrometer. Since zirconia ceramics are transparent in the near infrared, a transmission technique was implemented. This permits measurements to be made with grinding coolant present. Light transmitted through the MgO-PSZ workpiece was collected and fed to a 600 μm diameter multi-mode optical fiber which is carried to the spectrometer aperture for intensity measurements. The test setup is shown in Figure 1a. Figure 1b shows images of the grinding contact region taken using an infrared camera. These were not used for temperature measurement, but they do show the distribution of intense infrared radiation transmitted through the specimen during grinding. The spatial resolution of the spectrometer was insufficient to resolve individual grinding grits and the spectrometer aperture will contain grinding grit-workpiece hot spots distributed over a backgound. The effective temperatures determined from the source spectra must therefore be interpreted with the aid of simulations. Further details of the testing procedure along with additional data will be published elesewhere [2].

Analysis Method and Results

The measured source spectrum, $R(\lambda)$, is assumed to be emitted by a graybody source, hence,

$$R(\lambda) = \frac{c_1}{\lambda^5\left(e^{\frac{c_2}{\lambda T}} - 1\right)} \tag{1}$$

where c_1 is a constant accounting for the (unknown) emissivity, transmissivity, aperture constant, etc., and $c_2 = hc/k = 14390$ μmK. Assuming that c_1 is independent of λ over the measurement range, eq.(1) can be written as

$$SR(\lambda) = E(\lambda, T) = \frac{1}{\lambda^5\left(e^{\frac{c_2}{\lambda T}} - 1\right)} \tag{2}$$

where S is an adjustable scaling factor independent of λ and $E(\lambda,T)$ is the blackbody function. For the temperatures and wavelengths of interest, $\exp(-c_2/\lambda T) << 1$ and eq.(2) can be reduced to

$$\ln\left(\frac{1}{\lambda^5 R(\lambda)}\right) = \frac{c_2}{T}\frac{1}{\lambda} + \ln S \tag{3}$$

This is the basis of the data-analysis technique. A "best fit" of $R(\lambda)$ to $E(\lambda,T)$ is obtained by treating S and T as adjustable parameters. A plot of $\ln(1/\lambda^5 R)$ vs. $1/\lambda$ should be a straight line. Using a linear least-squares fit over the wavelength measurement range adopted for the tests, $0.75\ \mu m \le \lambda \le 0.95\ \mu m$, the temperature T and scale factor S can be determined from the slope and intercept, respectively.

Figure 2 shows the results obtained for increasing grinding downfeeds at 3500 rpm wheel speed. The top frame in each plot is the spectrometer output function, $R(\lambda)$, for the grinding conditions indicated while the bottom frame shows the least-squares fit (solid line) according to eq. (3). The solid curve through the $R(\lambda)$ data is the fitted blackbody curve, $E(\lambda,T)$, for the temperature and scale factor determined. Similar plots were obtained for other grinding conditions used in this study. The results for the temperatures are summarized in Table 1. For each set of grinding conditions, the average values and standard deviations reported in Table 1 correspond to 4-5 tests using workpieces with different thickness.

The temperatures in Table 1 are the order of 3000K for all conditions. No strong trends for the effect of grinding conditions on the temperature can be identified. There does appear to be a slight decrease in temperature when downfeed is increased at constant wheel speed or when wheel speed is increased at constant downfeed. However, these changes are close to the measurement standard deviations.

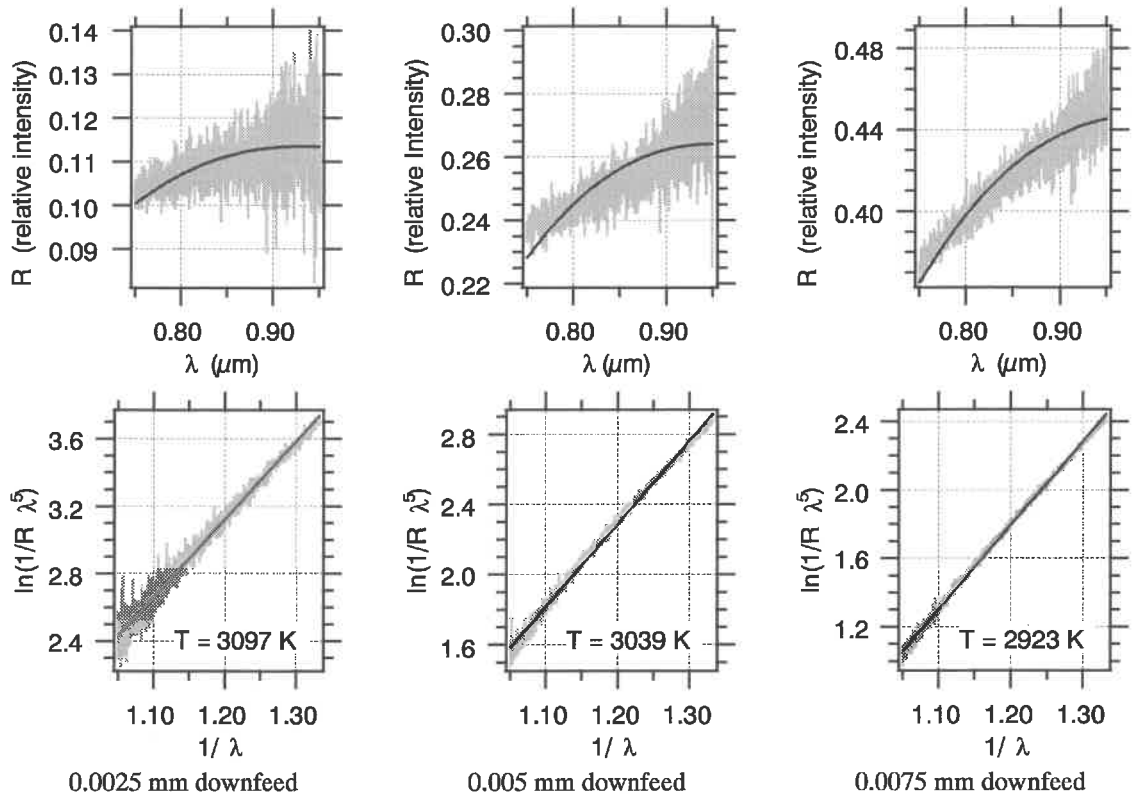

Figure 2. Spectrometer data and analysis results for the downfeeds indicated.

Speed (rpm)	3500	3500	3500	4000	4500
Downfeed (mm)	.0025	.005	.0075	.005	.005
Average T (K)	3089	3045	2955	3019	2999
Deviation (K)	13.2	23.2	22.6	11.9	27.1

Table 1. Summary of Temperature Measurements

The estimation of temperature based on eq. (3) produces an *effective* graybody source temperature. If a distribution of temperature exists within the source, then the effective temperature represents an average over this distribution. In view of the non-linear temperature dependence of the blackbody radiation function, $E(\lambda,T)$, the averaging process will be strongly biased with respect to temperature. The nature of this averaging process for grinding can be understood by using simulation calculations. Because of the localized contacts between grinding grits and workpiece material, there will be a distribution of grinding hot-spots within the aperture field-of-view of the spectrometer. During the duration of a measurement, the hot-spot distribution varies in both spatial and time coordinates. It will be sufficient to consider a time-average, bimodal spatial variation of temperature such that, within the aperture, there is an area fraction f_h of hot-spot temperature, T_h, combined with an area fraction $f_b = 1 - f_h$ of lower background surface temperature, T_b. The spectral power density received within the spectrometer aperture will then be proportional to the area-average function, $E_{avg}(\lambda) = f_h E(\lambda,T_h)+(1-f_h)E(\lambda,T_b)$, where $E(\lambda,T)$ is given by eq. (2). In order to determine an effective temperature for this simulated distribution, set $R(\lambda) = E_{avg}(\lambda)$ for specified values of T_h, f_h and T_b, then solve for T using linear least-squares regression via eq. (3). Fig. 3a shows the results for T_h = 3000K, 500K $\leq T_b \leq$ 3000K and different values of the area fraction f_h of hot spots (Hot Area). The effective temperature is the same as the hot-spot temperature if $T_b = T_h$ or if T_b is less than about one-third of T_h. In the intermediate range, the effective temperature depends on the percentage

of hot-spot area . Assuming T_b < 1000K and an area fraction of grinding hot-spots of 5 % to be reasonable estimates for grinding [2], the temperatures in Table 1 can be taken as representative of the grinding hot-spot temperatures.

The hot-spot temperatures shown in Table 1 are very high (9 mol % MgO-PSZ melts at about 2700K). Such high temperatures are favored by the very low thermal conductivity for PSZ. Usual experience dictates that hard structural ceramics cannot be ground with common abrasives such as SiC because the high forces lead to excessive wear and/or damage of the grinding grit. Diamond grinding must be used. It therefore appears that grinding mechanisms for PSZ are facilitated by high hot-spot temperature to the extent that SiC grinding wheels become a practical choice. The SEM micrograph of a typical grinding chip is shown in Fig. 3b. Ductile-like chip morpholgy, similar to metal machining, is evident. Furthermore, the chip surfaces show a granular/globular appearance that is at least suggestive of partial melting on the chip surface. The formation of hot, ductile chips is consistent with high hot-spot temperatures and this must facilitate the grinding process.

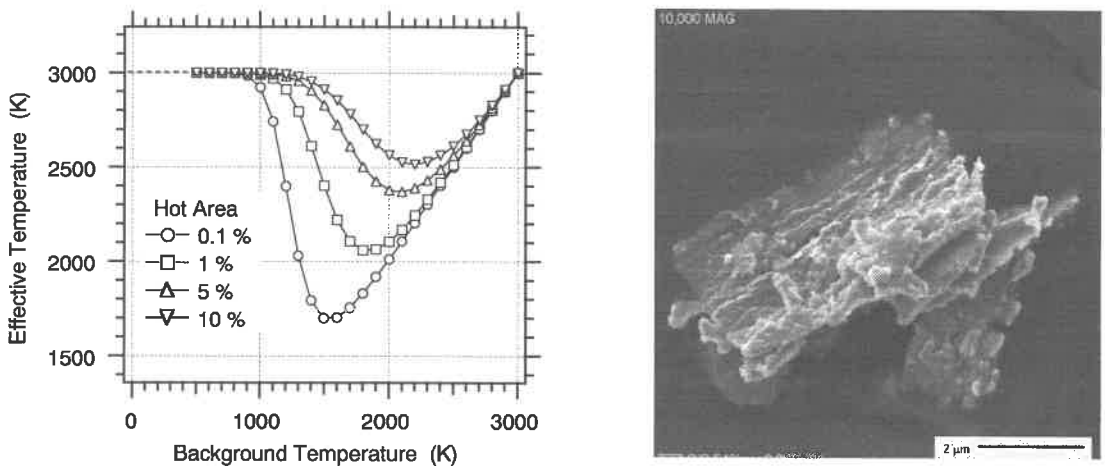

(a) (b)

Figure 3. a) Simulations for the effective temperature. b) SEM micrograph of a MgO-PSZ grinding chip.

Summary and Conclusions

A spectrometer method was developed to measure the grit-workpiece interface temperatures for grinding MgO-PSZ. Advantage was taken of the fact that PSZ is transparent in the near infrared and measurements were made using transmitted light. Hot-spot temperatures the order of 3000K were obtained. In addition, the high temperatures produce ductile-like chips. Thermal softening at grinding grit-workpiece interfaces was therefore be identified as an important contributing factor for the success of SiC grinding wheels for high-rate, high G-ratio grinding of PSZ parts in high-volume production applications.

Acknowledgements

Support for this research was provided by the User Program, High-Temperature Materials Laboratory, Oak Ridge National Laboratory and the National Science Foundation (Dr. K. P. Rajurkar, program director).

References

1. A. J. Shih, A. J. Shih and T.M. Yonushonis, US Patent Number 6,030,277 (2000).
2. A. C. Curry, et. al., submitted to *J. Am. Ceram. Soc.* (2001).
3. T. Ueda, K. Yamada, and T. Sugita, *Jour. Eng Ind* [114], 317-321 (1992).
4. R. Hebbar, R., S. Chandrasekar and T. N. Farris, *J. Am. Ceram. Soc.,* [75], no. 10, 2742-2748 (1992).
5. M. V. Swain and R. H. J. Hannink ,*J. Am. Ceram. Soc.,* [72] no. 8, 1358-1364 (1989).
6. J. O. Outwater and M. C. Shaw, *Trans ASME*, 73-86 (1952).
7. S. Kohli, C. Guo, S. Malkin, *Jour. Eng Ind* [117], 160-168 (1995).
8. A. C. Curry, MS Thesis, North Carolina State University (2001).

Force Modeling in Vibration Assisted Cutting

Xiaorui Fan and Michele H. Miller
Michigan Technological University, Houghton, MI

Introduction

Experiments have repeatedly demonstrated that vibration assistance can make cutting forces decrease. For instance, in grinding tests performed under dry conditions, the average force decreased by 15% when 3 kHz vibration was introduced [1]. Some research has been done to explain this phenomenon. Astashev, for example, developed a force model that includes the effect of vibration parallel to the cutting direction [2]. His model explains how forces reduce for a workpiece material whose strength is independent of cutting speed. The model predicts force reduction as a function of the ratio of maximum vibration speed to cutting speed. A large ratio leads to more force reduction. When the ratio is less than one (when cutting velocity exceeds maximum vibration velocity), vibration no longer affects the cutting force. Nazarenko proposed a theoretical model for friction behavior in the presence of mechanical vibration at various angles to motion direction [3]. If the vibration is parallel to the sliding direction, the equations for predicting force reduction are similar to Astashev's. For vibrations normal and transverse to the sliding direction, friction force would also decrease.

Our research focuses on vertical vibration (normal to the cutting direction). Astashev's mechanism does not apply in this case. However, we will make use of Nazarenko's model when considering friction between the chip and tool rake face.

Figure 1 shows a 2-dimensional view of the orthogonal single point cutting process. Key parameters include depth of cut (t_o), chip thickness (t_c), cutting speed (V), chip velocity (V_c), shear angle (ϕ) and rake angle (α). Some of these parameters are prescribed: depth of cut, cutting speed, and rake angle. Shear angle, chip thickness, and chip velocity cannot be prescribed directly. They depend on material properties and rake face friction as well as t_o, V, and α.

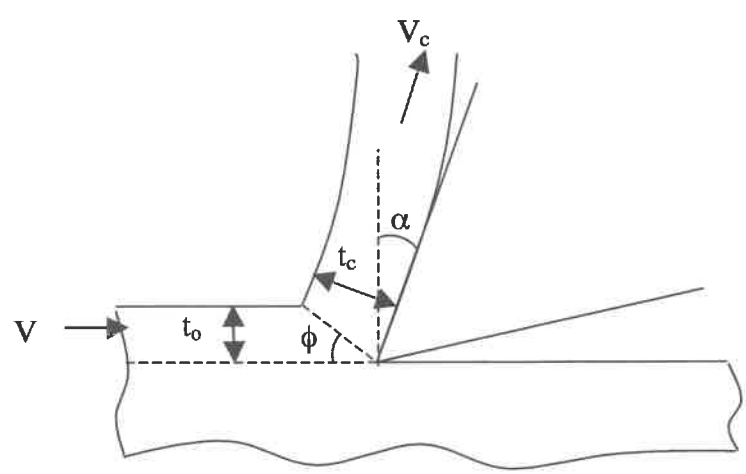

Fig. 1: Geometry of single point cutting

Introducing high frequency vibration in the vertical direction (applied to tool or workpiece) causes all these parameters to change during the machining process. Depth of cut varies in a straightforward way. The relative cutting speed between tool and workpiece changes in amplitude and direction. If the rake angle is defined using a reference perpendicular to the cutting direction, then it too changes continuously with vibration. So, t_o, V, and α modulate

continuously about their nominal values. Changes in these parameters, in turn, influence the shear angle ϕ, the chip thickness t_o, and the chip velocity V_c. Finally, rake face friction is influenced by the ratio of chip velocity to tool velocity. Since shear angle depends on rake face friction, the relationship amongst all the variables appears quite complex. Figure 2 depicts a map of the various factors and their interrelationships.

The shear angle plays a key role in determining forces in single point cutting; however, it is difficult to predict even in the simple case of no vibration assistance. Of the various models devised for predicting shear angle [4,5], none works well for all cases.

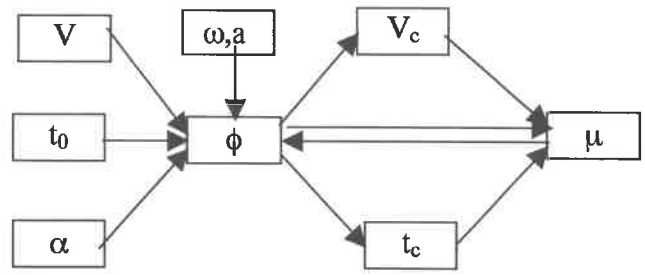

Fig.2: Interrelationships of cutting parameters

Simplified Force Model

Our first step in modeling how vibration influences force is to make a simple assumption about how vibration affects the shear angle. We assume that the shear plane angle with respect to a fixed coordinate system remains constant and assume the shear angle with respect to the cutting direction varies. Figure 3(a) shows a snapshot of the cutting geometry when the tool is at the top or bottom of its vibration cycle. In this case, the cutting direction is horizontal, and the shear angle is ϕ_1. Figure 3(b) shows a snapshot when the tool is at its maximum vibration velocity. The instantaneous cutting direction rotates up, and the shear angle ϕ_2 is less than ϕ_1.

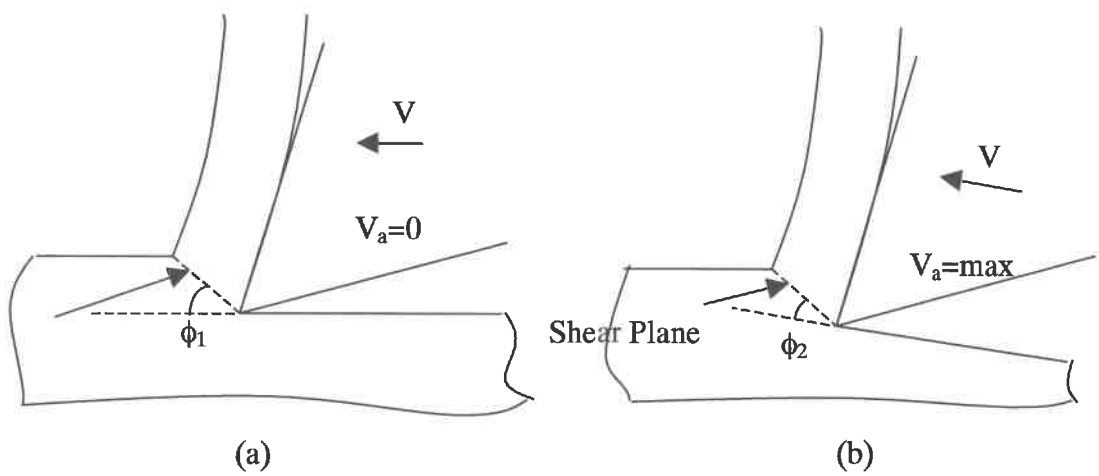

Fig. 3: Schematic of cutting with vertical vibration

The instantaneous shear angle using this assumption is:

$$\phi_2 = \phi_1 - \arctan\left(\frac{V_a}{V}\right) \qquad \text{where } V_a = a\omega \sin \omega t \tag{1}$$

Suppose V=1 m/s, ϕ_1=20°, and α=0°. Fig. 4 shows how ϕ_2 changes with time for a couple of different vibration conditions.

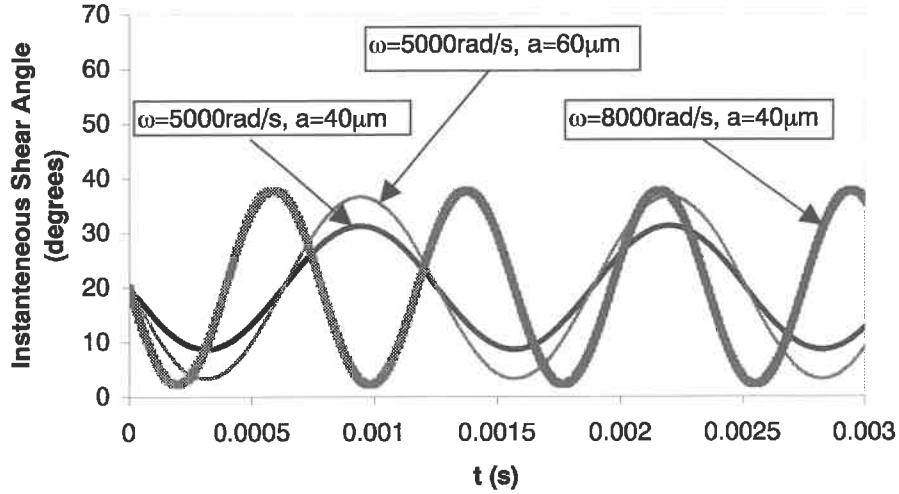

Fig. 4: Shear angle variation (V=1 m/s, ϕ_1=20°, and α=0°)

Chip Velocity and Average Friction Coefficient

Based on our prediction for shear angle, we can now calculate how the chip velocity modulates. Then we can compare the chip velocity to the vibration velocity of the tool rake face. The chip velocity can be calculated from:

$$V_c = V \cdot \frac{t_o}{t_c} = V \cdot \frac{\sin\phi}{\cos(\phi - \alpha)} \tag{2}$$

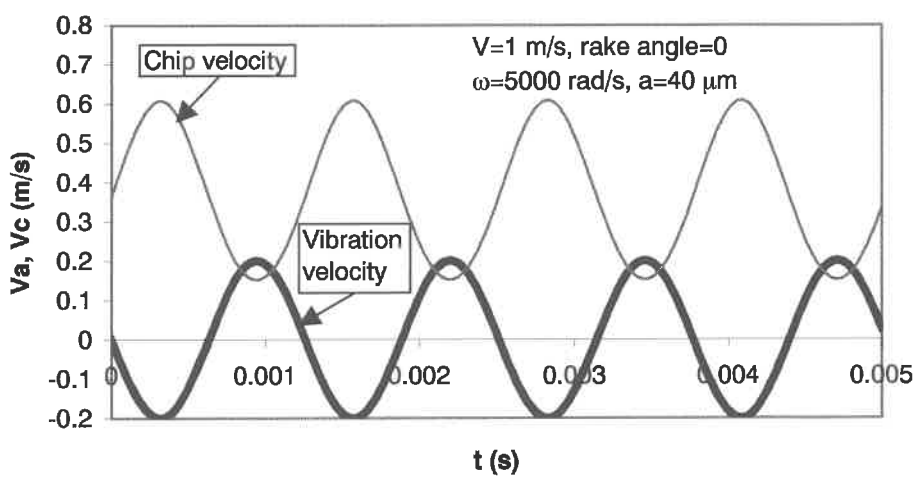

Fig. 5: Comparison of V_a (bold line) and V_c

For the case of V=1 m/s, ϕ_1=20°, α=0°, ω=5000 rad/s, and a=40 μm, Fig. 5 shows the variation in chip velocity (based on Eqs 2 and 1) and vibration velocity. According to Fig. 5, the vibration

velocity exceeds the chip velocity for a short time during each vibration cycle. At these times, the friction force between the chip and tool changes direction. Consequently, when averaged over many cycles, the friction force is less than its nominal value.

Increasing the vibration frequency or amplitude increases the amount of time that the vibration speed exceeds the chip velocity and thus further reduces the average friction force. Fig. 6 shows the reduction in rake face friction force as maximum vibration velocity increases. If the vibration velocity can be made high enough, significant reductions in friction force (and thus overall machining forces) are possible.

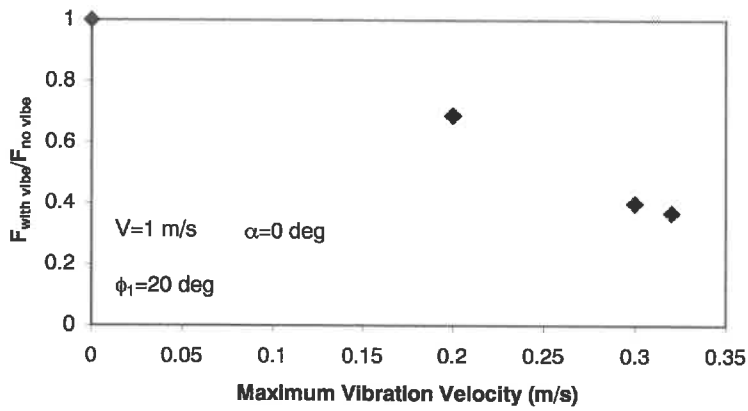

Fig.6: Reduction in rake face friction (note that an ω of 5000 rad/sec and an *a* of 40 μm produces a maximum vibration velocity of 0.2 m/s)

Conclusions

This model, based on a simple geometric assumption about the shear angle, predicts that moderately high vibration frequencies (thousands of rad/sec) can produce significant force reductions. However, further refinement of the shear angle assumption is necessary. Future work will investigate the effects of depth of cut and friction force variation on the shear angle. In addition, single point cutting experiments will be done to determine how the vibration frequency and amplitude actually affect the force on the rake face.

References

[1] Chen, P., W. Qu, M. H. Miller and A. Chandra, "Thermal Effects in Vibration Assisted Grinding," *Proc. of the ASPE Annual Meeting*, 2000, pp. 86-89.

[2] Astashev, V. K. "Effect of Ultrasonic Vibration of a Single-point Tool on the Process of Cutting," *Journal of Machinery Manufacture and Reliability*, No. 3, 1992, pp. 65-70.

[3] A. F. Nazarenko, A. F. "Study of Vibrations Effect on Friction," *Journal of Friction and Wear,* Vol. 15, No. 4, 1994, pp. 36-39.

[4] Merchant, M. E., "Mechanics of the Metal Cutting Process," *J. Appl. Phys.,* Vol. 16, No. 5, 1945, p. 267.

[5] Lee, E. H., and B. W. Shaffer, "The Theory of Plasticity Applied to a Problem of Machining," *J. Appl. Mech.,* Vol. 18, No. 4, 1951, p. 405.

Water Jet Assisted In-Process Cleaning and Dressing of Grinding Wheels

Lit Ming Gho and Michele H. Miller
Michigan Technological University, Houghton, MI

Introduction

Grinding of ceramics is costly due to low material removal rates, need for frequent wheel dressing, and the generation of subsurface damage, which may necessitate a secondary process. One way to improve productivity is to perform in-process dressing using electrolysis, mechanical, water jet, or other means [1,2]. In-process dressing maintains consistent wheel sharpness and reduces the heat generated during machining. In-process methods are particularly important for fine grit wheels such as those used in ceramics grinding because they prevent chip loading, thus lowering the frictional forces in the contact zone.

This project further investigates water-jet assisted dressing and how to optimize wheel condition while minimizing wheel removal. Water jet parameters under consideration are feed rate, depth of engagement, standoff distance, nozzle diameter, and water pressure. We make measurements of wheel roughness, wheel erosion rate, and ground workpiece roughness as we evaluate the effectiveness of this method.

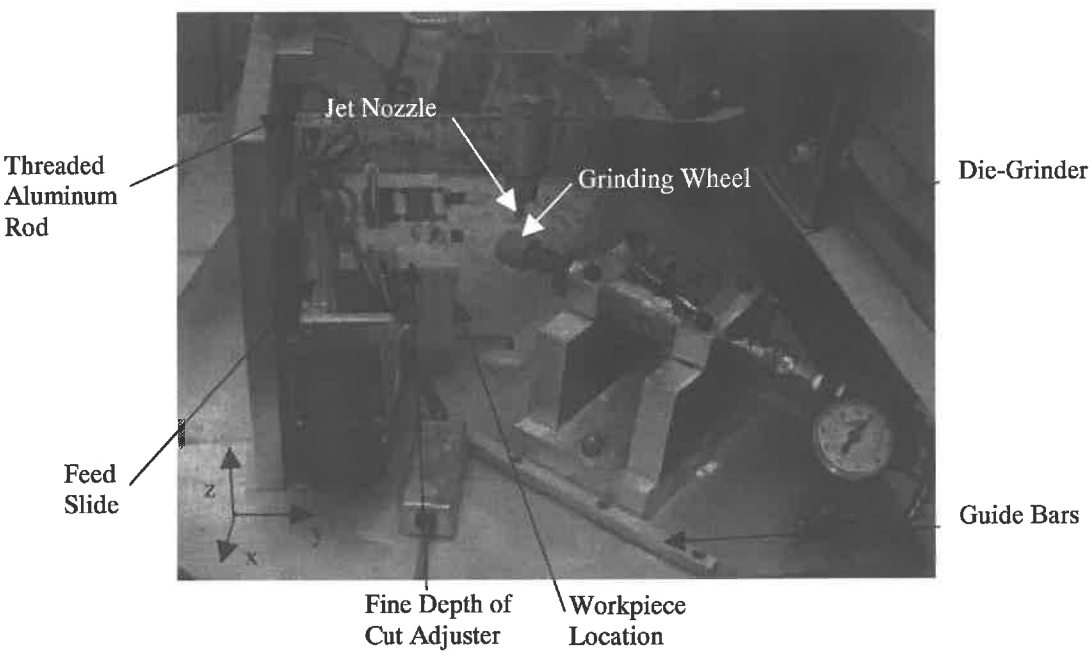

Figure 1: Side View of Experimental Setup

Experimental Setup

The in-process dressing system used in this research consists of a specially designed grinding module and a commercial abrasive water jet machine. Figure 1 provides a better understanding of this setup. The grinding module consists of a die-grinder, fine depth-of-cut adjuster, linear motion feed slide, coolant delivery system, support frame, and the grinder's holder. When the wheel rotates and the feed slide moves in the X direction, a groove is created on the workpiece surface. The feed slide is low speed in order to minimize heat generation and subsurface damage during ceramic machining. The fine depth-of-

cut adjuster uses a micrometer (parallel to the X direction) and demagnifying wedge to control the depth of cut in the Y direction.

A threaded aluminum rod screwed into the base plate of the feed slide provides up and down adjustment of the feed slide position in the Z direction. This allows several grooves to be ground parallel to each other on the same workpiece. The die-grinder holder is placed at a 45 degree angle to the work surface. The grinding wheel must be trued at a 45 degree angle so that the trued surface will be parallel to the workpiece. Air pressure controls wheel rotational speed. Finally, a coolant system is available to deliver water during grinding of ceramics.

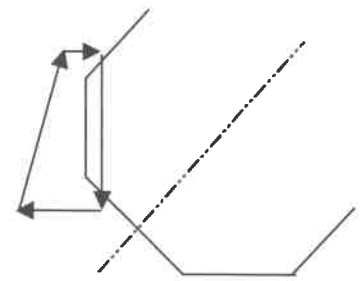

Figure 2: Top view of wheel showing jet nozzle scanning path

To accomplish in-process dressing, the jet scans along the edge of the pre-trued wheel surface as shown in Figure 2. The starting position for each experiment is determined by "touching off" the trued wheel surface with a low water pressure jet.

Table 1: Factors in fractional factorial design of experiment

Factor	High Level	Low Level
Feed Rate	10 in/min	5 in/min
Depth of Engagement	0.001 in	0.00001 in
Standoff Distance	3.156 in	0.781 in
Nozzle Diameter	0.045 in	0.03 in
Pressure	55 ksi	15 ksi

Wheel Surface Texture Measurements

A two level fractional factorial design was used to identify the effect of the important jet factors on wheel surface texture. Sixteen tests were done on 60 grit aluminum oxide wheels with combinations of the conditions shown in Table 1. Surface roughness of the dressed wheels was measured using a Cobra laser profile scanner. Analysis showed that none of the factors has an especially significant effect on surface roughness.

We then carried out an additional set of experiments in which pressure was the only factor varied. Figure 3 shows the variation in wheel surface roughness with jet pressure (each point is the average of 10 measurements). Wheel roughness is not especially sensitive to pressure, but pressures of 35 to 45 ksi give the highest roughness.

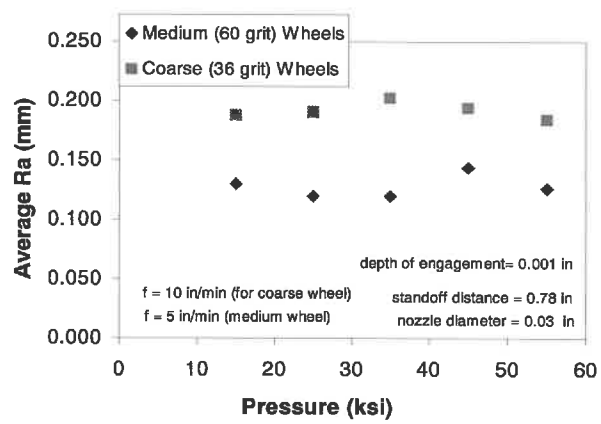

Figure 3: Effect of jet pressure on wheel surface roughness

Wheel Erosion Measurements

A low wheel erosion rate due to dressing is desirable. Wheel erosion rates were measured under a variety of water jet operating conditions with the jet shooting perpendicular to the wheel (on top rather than on the edge). Erosion was measured after shooting at a spinning wheel and after shooting at a stationary wheel. The results show that erosion rate is particularly sensitive to water pressure but also feedrate and nozzle size. For a spinning wheel, erosion rate is approximately proportional to $(\text{pressure})^{5.3}$ and to $(\text{feedrate})^{-0.8}$. For a stationary wheel, erosion rate is approximately proportional to $(\text{pressure})^{3}$ and to $(\text{feedrate})^{-0.75}$.

In-Process Dressing Tests

We performed in-process dressing tests: with aluminum oxide wheels grinding steel and with diamond wheels grinding silicon carbide. The objective is to measure wheel cleanliness, workpiece surface finish, and wheel wear rate.

Table 2 describes the experimental conditions for the aluminum oxide wheel tests. Figure 4 shows the grinding ratio (work material removed/wheel loss) for the tests with the 0.03 in nozzle size. "Pure grinding" indicates the grinding ratio for grinding without dressing. For most of the tests, the grinding ratio is higher with jet assisted dressing than without. Perhaps this indicates that dressing maintains a cleaner, sharper wheel which lessens temperatures in the grinding zone. However, mist from the water jet may also reduce temperatures. Figure 4 indicates that higher feedrates tend to produce higher grinding ratios. Note that when the nozzle feed rate increases, the number of times the nozzle scans the wheel increases; and with each scan, the nozzle is programmed to step another 0.0001 in into the wheel. Figure 4 also suggests there is a tradeoff with pressure. On the one hand, higher pressures erode the wheel faster; on the other hand, higher pressures maintain a sharper wheel.

Figure 5 shows the workpiece surface finish of the steel workpiece for the tests with the 0.03 in nozzle size. The roughness of most workpieces is higher than the pure grinding condition. This may be because water jet dressing tends to make the wheel surface rougher which might in turn make the work surface rougher.

Table 3 describes the conditions for the diamond wheel tests. Figure 6 shows the grinding ratio for the tests with the 10/20 μm grit wheel and 0.3 in/min slide feedrate. In all cases, the grinding ratio is higher for the pure grinding without dressing. This is opposite of the result with the aluminum oxide wheels. The difference may be that the diamond wheels have a resin binder which erodes more easily when hit with the water jet. Figure 7 shows the surface roughness of the silicon carbide workpieces ground with the 10/20 μm wheel and dressed with 0.03 in nozzle diameter. In all

Table 2: In-process dressing and grinding conditions (alum. ox. wheels)

Workpiece	3"x1½"x1/2" 4140 steel
Wheel	alum. ox., 60 grit size, 1 in dia.
Wheel speed	9940 rpm
Slide feedrate	0.3 in/min
Depth of cut	0.0025 in
Coolant	Off
Nozzle feedrate	3, 5, 10 in/min
Nozzle diameter	0.03, 0.045 in
Water pressure	16, 20, 24 ksi
Depth of engagement	0.0001 in

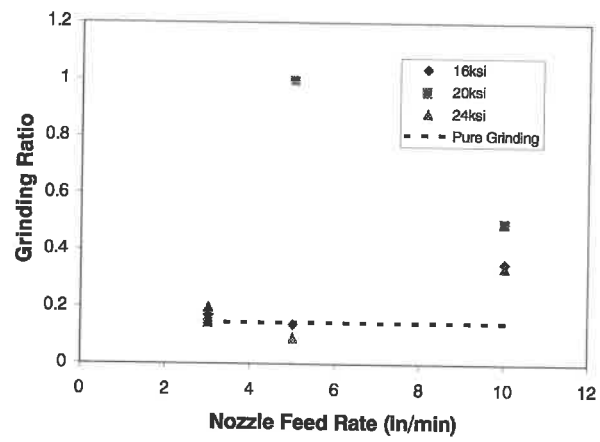

Figure 4: Grinding ratio of 60 grit wheel (0.03 in nozzle tests)

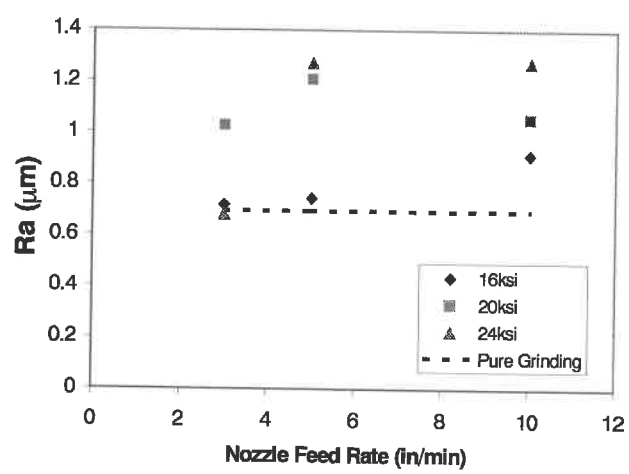

Figure 5: Surface roughness of steel workpiece (0.03 in nozzle tests)

cases, dressing produces rougher surface finish than grinding without dressing.

Conclusions

In evaluating the benefits of water jet assisted dressing, the results are mixed. In tests with aluminum oxide wheels grinding steel, jet assistance improved the grinding ratio. For both aluminum oxide wheels and diamond wheels, water jet dressing made the workpiece surface finish worse. Because the grinding in these tests was not aggressive, the wheel likely remained clean and sharp even without dressing. Perhaps benefits of water jet dressing would have been more evident with higher feeds and depths of cut and longer grinding times. Future work will investigate this possibility.

Table 3: In-process dressing and grinding conditions (diamond wheels)

Workpiece	Silicon carbide
Wheel	Diamond, resin bond, 75 concentration, 10/20 μm and 320 grit
Wheel speed	9940 rpm
Slide feedrate	0.05, 0.175, 0.3 in/min
Depth of cut	0.00125 in
Coolant	Water
Nozzle feedrate	3, 10 in/min
Nozzle diameter	0.03 in
Water pressure	15, 55 ksi
Depth of engagement	0.0001 in

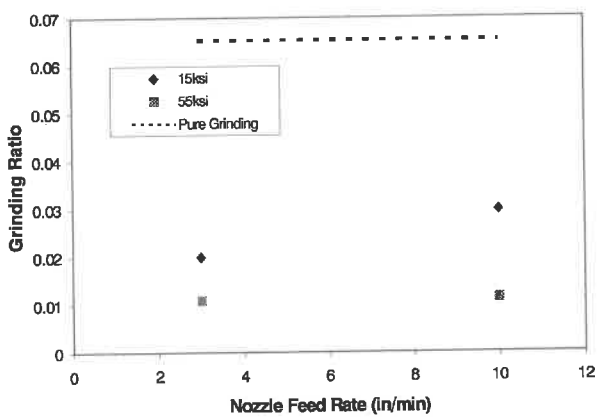

Figure 6: Grinding ratio for tests with 10/20 μm wheels and 0.3 in/min slide feedrate

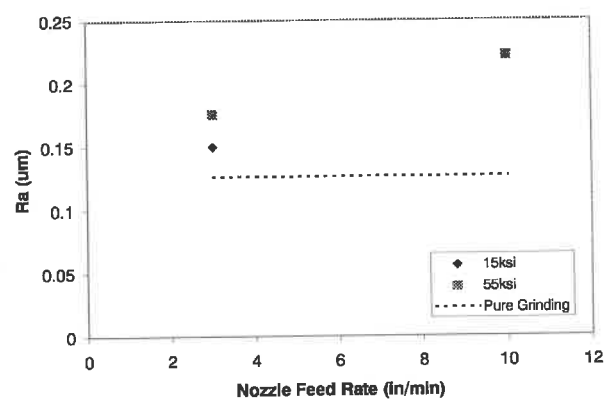

Figure 7: Surface roughness of silicon carbide workpiece for tests with 10/20 μm wheels and 0.3 in/min slide feedrate

References

[1] Ohmori, H. and T. Nakagawa, "Mirror Surface Grinding of Silicon Wafers with Electronic In-Process Dressing," *Annals of the CIRP*, Vol. 39, No. 1, 1990, pp. 329-332.

[2] Masatoshi Hirao, Masaki Izawa, Nobuaki Iguchi, Keiichi Shirase, Kunio Ootani, and Takeshi Yasui, "WaterJet In-Process Dressing (1st Report)," *Proceedings of 1999 ASPE Annual Meeting*, pp. 95-98.

[3] Hashish, M. and M. P. duPlessis, "Theoretical and Experimental Investigation of Continuous Jet Penetration of Solids," *ASME Journal of Engineering for Industry*, Vol.100, Feb 1978, pp. 88-94.

Abrasive Wear and Forces in Grinding of Silicon Carbide

Prasann B. Handigund, Michele H. Miller
Michigan Technological University, Houghton, MI

Introduction

Silicon carbide is one of the most widely used advanced ceramics. Its popularity is due to its suitability for high power electronics, high temperature electronics and radiation-hardened environments. It is also widely used as a cutting tool material. However, ceramics are difficult to manufacture because of their high hardness. To be able to use ceramics to their highest potential, cost efficient machining without any induced damage on the workpiece surface is required.

The two primary problems involved in grinding of ceramics are workpiece subsurface damage and wheel wear. Wheel wear, the topic of this research, impacts cost because it relates to the need for wheel redressing or replacement.

Self-dressing is a replenishment process for abrasive grits. The cutting process causes sharp abrasive grit edges to wear. As a cutting edge wears, the cutting force acting on the grit increases. When it becomes sufficiently high, the grit fractures or pulls out of the binder matrix exposing the next layer of grits. The self-dressing process is a beneficial effect of wheel wear.

The self-dressing process can be monitored by measuring the grinding force components (sum total of all grit forces). A new or newly dressed wheel cuts with low force. The force increases as grits wear and levels off as the wheel reaches an equilibrium condition. At this point the increase in grit forces is balanced by the reduction in force caused by a grit fracture or pull out. The grinding force at this equilibrium is important because it relates to the sharpness of the wheel and thus to the quality of the ground surface. The wheel wear rate associated with this equilibrium is important because it impacts tool costs. Proper selection of the grinding wheel would balance the needs for a sharp wheel and for low wear rates.

A model of the self-dressing process would help in the design of the optimum wheel. Modeling is complicated due to the interaction of various factors like abrasive grit size, workpiece hardness, binder hardness and infeed [1].

This paper focuses on a portion of the whole process: wear of individual grits and subsequent force increase. The paper describes an experimental technique for monitoring volumetric grit wear, percentage of active cutting grits, percentage of grit pullouts, and forces.

Technique for Measuring Wheel Wear

Measuring wheel wear is challenging because a wheel has thousands of potential cutting abrasives, and the ones doing the cutting are constantly changing. Methods for measuring wheel wear include: profilometry, imprint methods, scratch methods, dynamometry methods, thermocouple measurements, and microscopy (optical, SEM, and confocal). Each measuring technique has its advantages and limitations, according to factors such as resolution, measuring depth, ease of application, and data analysis and interpretation.

Most of the methods mentioned above require the wheel to be removed from the grinding machine. To overcome this limitation, a new method to measure wheel wear is adopted. Imprints of the wheel are made in a dental molding material and later studied using stereo scanning electron microscopy (SEM) [2]. To limit the number of abrasives under study, we use electroplated grinding wheels (100 mm diameter x 12.5 mm wide), specially made with a small abrasive section (25 x 12.5 mm). This type of wheel has a single layer of diamonds.

The abrasive section was micro indented so as to simplify location of grits under study.

A wheel mold can be made while the wheel remains on the grinding machine. Before making a mold, the wheel is cleaned of any debris using an ultrasonic cleaner. To make a mold, the abrasive section of the wheel is lowered into a small tray of molding material. After several minutes, the mold material is separated from the wheel.

Next, the small wheel mold (25x12.5x12.5 mm) is imaged using an SEM. The stereo SEM technique produces a digital elevated model (DEM) that can be analyzed for volume changes using imaging software. With this technique wear of individual abrasives can be monitored.

Validation of Measurement Technique

Testing was done to evaluate the accuracy of the mold and SEM measurement technique. Two brass rods were turned machined with different feeds (0.3 mm and 0.6 mm) to produce different surface finishes. These were measured with profilometry and stereo SEM. Negatives of these were developed using the mold material. These negatives were then measured using the stereo SEM. Figures 1-3 show the profiles from the three sources (profilometer measurement of brass rod, SEM measurement of brass rod, SEM measurement of the mold/negative of the brass rod) for the rod turned with a nominal feed of 0.3 mm.

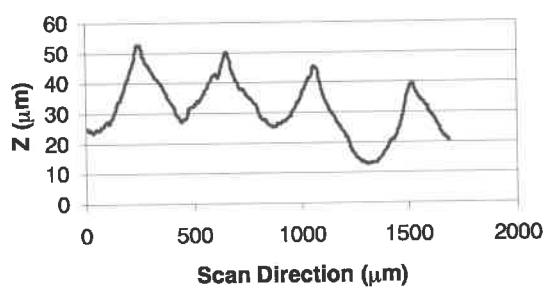

Figure 1: Profile of rod (profilometer)

Table 1 compares the peak-to-valley roughness R_{max} and feed spacing f for these three profiles. Table 2 compares the R_{max} and f for the rod turned at a nominal feed of 0.6 mm. The three types of measures are reasonably close. The profilometer scan included more length of the rod than the SEM. The SEM-mold profile appears inverted because it is the negative or imprint of the brass rods.

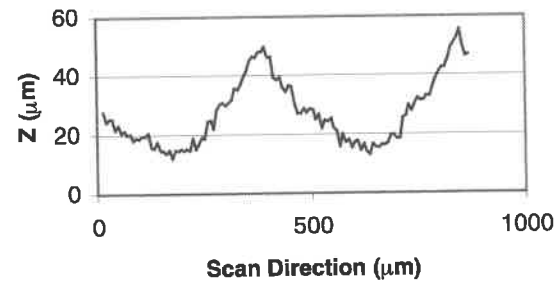

Figure 2: Profile of rod (SEM)

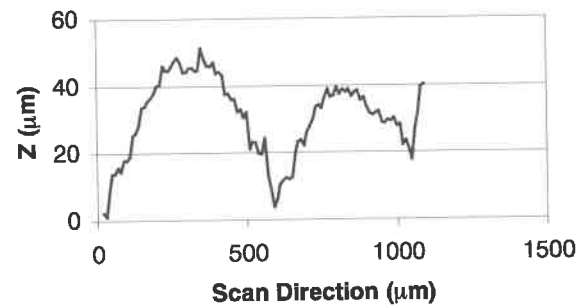

Figure 3: Profile of mold (SEM)

Table 1: Profile Measurements (Nominal Feed 0.3 mm)

	R_{max} (µm)	f (mm)
Profilometry	40	0.436
SEM Specimen	44	0.455
SEM Mold	48	0.460

Table 2: Profile Measurements (Nominal Feed 0.6 mm)

	R_{max} (µm)	f (mm)
Profilometry	122	0.630
SEM Specimen	120	0.617
SEM Mold	125	0.587

Profilometery is an established standard for measuring surface roughness; hence the SEM results were compared with profilometry. The fact that these tools give comparable surface measurements leads us to believe that the stereo SEM with imaging software can be used for quantitative measurements.

Additional tests were carried out to validate the mold and SEM technique for quantifying volume:

1) An object with a known volume (the anode of a AA battery cell) was molded and measured with the stereo SEM. The object volume is compared to the mold cavity volume.
2) Two molds of the grinding wheel (180 grit size) were developed. With the help of indent marks, the same grit was measured on both molds. This was done to understand the amount of variation due to the molding process.
3) On one mold the volume of one grit is measured five times. Some variation in this measurement is possible because the user has to manually mark the boundary of the grit when using the measurement software. Two extreme readings are presented in the following table.

Table 3 summarizes the results of these three tests.

Table 3: Variation in volume measurements

Test #			% Variation
1	12.56 mm^3 (object vol.)	14.07 mm^3 (mold vol.)	12
2	129,400 μm^3 (mold 1)	138,800μm^3 (mold 2)	7.3
3	665.3 μm^3 (min)	682.9 μm^3 (max)	2.6

Based on all these results, the mold and SEM technique is considered adequate for quantifying attritious wear of the grinding wheel.

Optical Microscopy in Wheel Wear Analysis

The volume measurements are made on a sampling of grits. This gives an indication of the attritious wear rate for individual cutting grits. Of the remaining two wear mechanisms (grit fracture and bond fracture/grit pullout), optical microscopy can provide information about the rate of grit pullout. In addition, by manually counting the number of wear flats, we can use optical micrographs to estimate the percentage of grits that are cutting grits. Figure 4 shows a cutting grit with a wear flat, a non-cutting grit, and a grit pull-out site. Since it is tedious to monitor wear flats and grit pull-outs over the entire abrasive area, wear flats and grit pull-outs are counted for sampled areas.

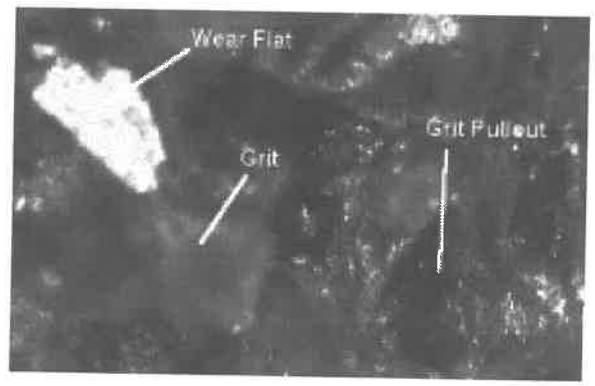

Figure 4: Optical micrograph (50X) showing wear flat, grit pull-out site, and non-cutting grit

Forces in Surface Grinding

Grinding generates forces between the wheel and the workpiece. In surface grinding, the total force vector exerted by the workpiece against the wheel can be separated into a tangential component F_t and a normal component F_n as shown in Figure 5.

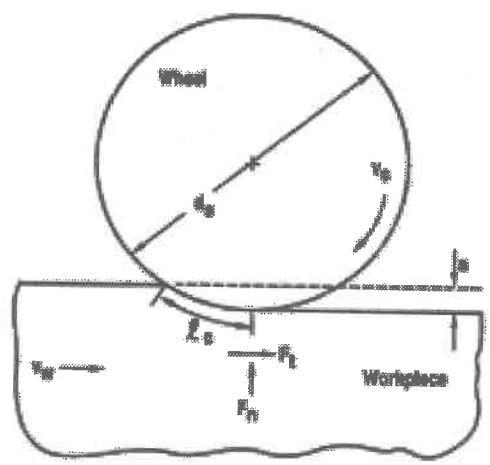

Figure 5: Force components in surface grinding

The grinding forces can be broken down into a cutting component and sliding component as follows:

$$F_t = F_{t,c} + F_{t,sl}$$
$$F_n = F_{n,c} + F_{n,sl}$$

where, $F_{t,c}$ and $F_{n,c}$ are the tangential and normal forces for cutting, and $F_{t,sl}$ and $F_{n,sl}$ are those for sliding.

Both the tangential and normal force components increase linearly with wear flat area [3]. The cutting force components are assumed to be unaffected by the size of the wear flats. The sliding force components are functions of: (a) the contact area between the workpiece and the wheel; (b) the coefficient of friction (for horizontal sliding force component only); (c) the contact pressure between wear flats and workpiece (for vertical sliding force component only). Assuming the last two factors constant, the sliding force components are linearly related to the area of contact between the workpiece and the wheel. This explains the linear relationship between the force components and the wear flats area.

Experimental Plan

We will conduct surface grinding experiments using electroplated diamond wheels and silicon carbide workpieces. We will monitor wheel wear (grit volume loss, percentage of grit pull-out) and forces with respect to volume of work material removed. Percentage of grit flats with respect to work material removed will also be measured. Factors such as depth of cut and grit size will be varied to determine their influence on the wear process. Table 4 outlines the grinding conditions.

Table 4: Grinding conditions

Workpiece mat'l: Silicon carbide
Grinding wheel: Electroplated diamond (1A1), 100 mm dia. X 12.5 mm with 25 mm x 12.5 mm abrasive patch, 180 and 100 grit sizes
Wheel speed: 15.42 m/s
Table speed: 0.0762 m/s
Wheel depth of cut: 2.5 μm and 5 μm
Coolant: Mobilmet 160 water-based
Mold material: 3M Express, light body fast set
Mold preparation frequency: Every 20 passes
Force measurement frequency: Every 20 passes
Wear flat and grit pullout measurement frequency: Every 40 passes.

References

[1] Miller, M. H. and T. S. Kakumanu, "Wear and Self-Dressing of Resin Bound Grinding Wheels," *Proc. of the ASPE Annual Meeting*, 1999, pp. 493-496.

[2] Personal communication with Dr. Ronald D Ott, Oak Ridge National Laboratory, Oak Ridge, Tennessee, October, 2000.

[3] Malkin, S. and N. H. Cook "The Wear of Grinding Wheels Part-I Attritious Wear," *Transactions of ASME*, Vol. 93, 1971, pp. 1120-1129.

STUDY ON A MEASURING METHOD FOR GRAIN CUTTING EDGES IN GRINDING WHEEL SURFACE

Masumi IZUMI*, Hwa-Soo LEE**, Shigeru INOUE***

*Hiroshima Institute of Technology, 2-1-1 Miyake, Saeki-ku, Hiroshima, 731-5193, JAPAN
**College of Science and Technology, Nihon University, 1-8-14 Kanda-Surugadai, Chiyoda-ku, Tokyo, 101-8308, JAPAN
***MAKINO SEIKI CO., LTD. 4029, Nakatsu, Aikawa-machi, Aiko-gun, Kanagawa, 243-0303, JAPAN

ABSTRACT

Present study aims to propose a measuring method for the grinding wheel profile and the distribution of cutting edges in the same time. As the results of experiments, cutting edges in the periphery of grinding wheels can be measured directly by the proposed contact method. And it is confirmed that the distribution, the density and the length of cutting edges can be easily measured by the present method simultaneously.

1.INTRODUCTION

A grinding wheel surface removes workpiece material. A wheel surface is closely related to a workpiece surface form and roughness. And then it is important to measure grinding cutting edges in a grinding wheel in order to carry out the precision grinding. Some measuring methods for grinding wheel surfaces have been developed [1-3]. However, any method to measure the profile of grinding wheel surface and grain cutting edges simultaneously cannot be found. In order to evaluate the grinding wheel surface quantitatively, the wheel surface, that is, the distribution of cutting edges and the surface profile of wheel surface have to be measured in the same time. From such a viewpoint, present study aims to develop a method to measure the surface profiles of grinding wheel surfaces and grain cutting edges simultaneously. And the experimental result with an newly designed instrument, it is confirmed that the proposed method can be used reliably.

2. A MEASURING INSTRUMENT AND METHOD

Figure 1(a) shows a measuring instrument for grain cutting edges developed in this study, which is loaded on a chuck of a surface-grinding machine. The detective part of measuring instrument is settled on an X-Y axis stage, which is able to move along the directions of a wheel axis and wheel radius. The detective part consists of spools, a direction roller, a guide, wire, an acoustic emission sensor (AE), a stepping motor and etc. An AE sensor, which cannot be seen in figure 1, is fitted to the guide. A wire is driven by a stepping motor. The wire goes through the guide, and is reeled by a spool. As shown in this figure, a wire is used as a stylus in this measuring system. The contact of a grinding wheel surface and a wire is detected by an AE sensor. By reeling the wire after every contact, the wire in the contact part can be kept fresh in every measurement. Hence, this instrument can be used to measure the grinding wheel surface in contact methods. In this study, X-axis and Y-axis are defined as the direction of grinding wheel axis, and as the vertical direction of a magnet-chuck respectively.

On the other hand, a photo interrupter is installed to the end of the spindle of a grinding machine as shown in Figure 1(b), and it generates pulse signals when a reference slit passes through the photo sensor. The origin of the rotational angle of grinding wheel can be calculated from these pulse signals.

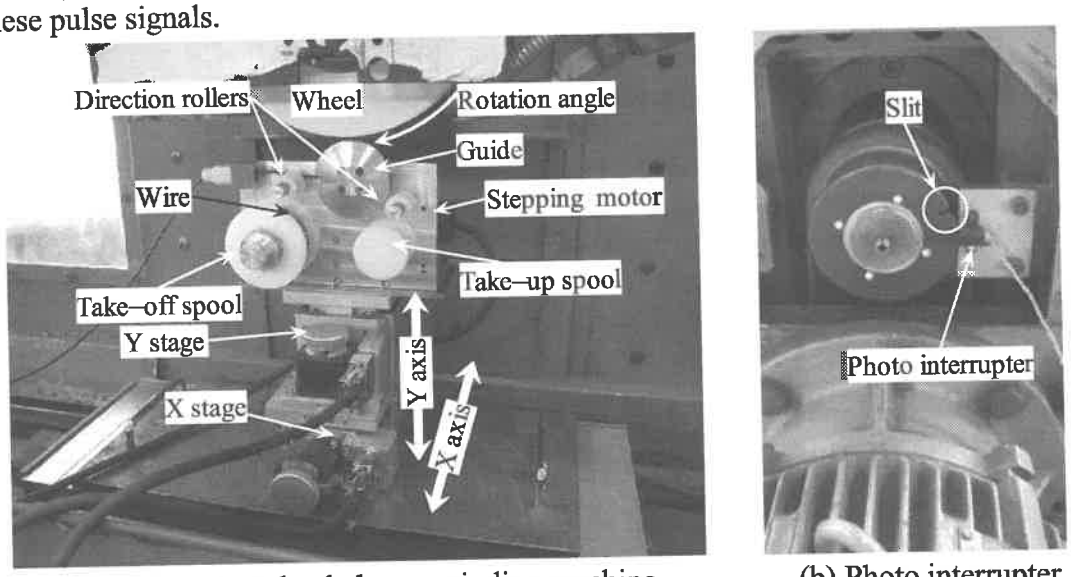

(a) An instrument loaded on a grinding machine (b) Photo interrupter

Figure 1 Measuring instrument

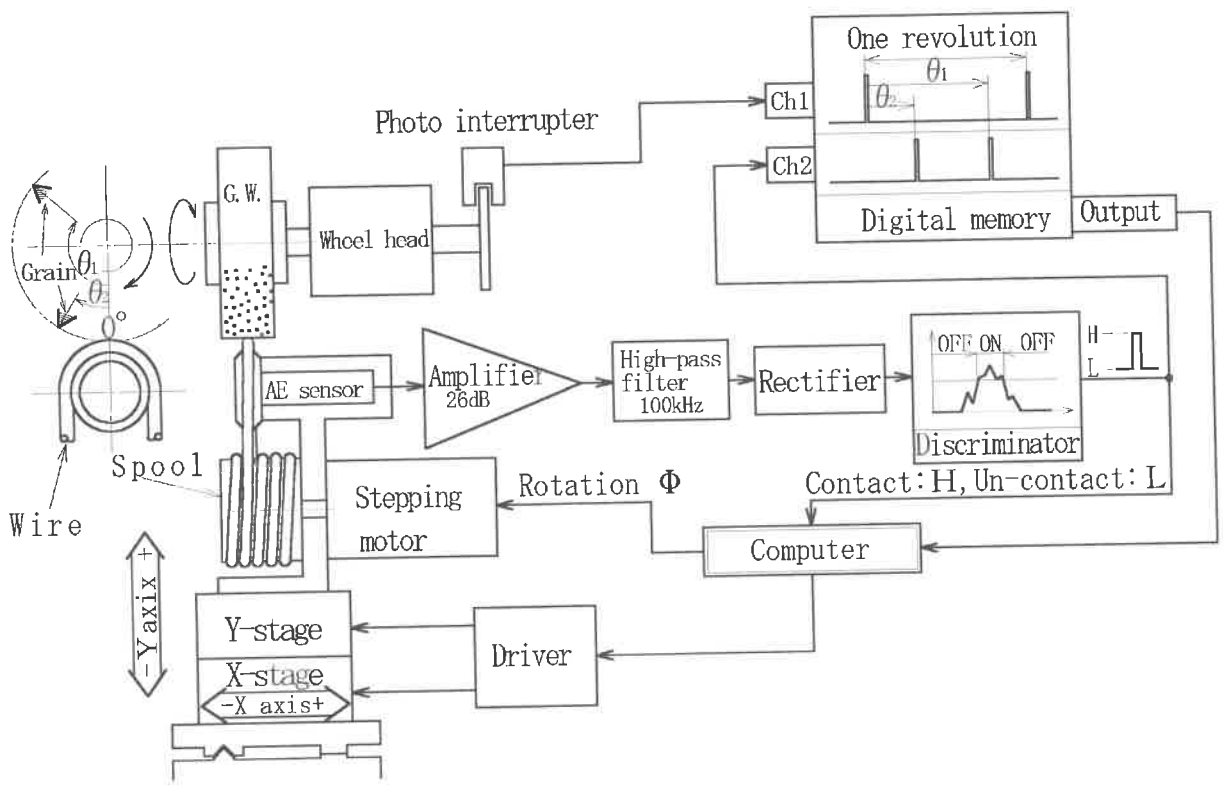

Figure 2 Measuring system

Figure 2 shows a schematic diagram of the present measuring system. A computer connected to a stepping motor, can send a command to role a spool, by which a fresh part of wire

is supplied to the top of the guide. The computer also controls the X-Y stage. Namely, the detecting part of the instrument is controlled in X-axis and Y-axis. The AE signal generated from the AE sensor due to the contact of grinding wheel and wire is transferred to an amplifier, a high-pass filter, a rectifier and a discriminator. The discriminator evaluates the contact of the wire to wheel and transmits the pulse signal to a digital memory. In the same time, lift up motion of the detective part is stopped.

Table1 Measuring condition

Grinding wheel	WA36G8V
Peripheral speed	1800m/min
AE sensor	500kHz
Wire	Tungsten, φ0.1mm
X-stage least incremental input	1μm
Y-stage least incremental input	0.5μm
Dressing condition	10μm×10pass(lead=0.1mm/rev) 5μm×10pass(lead=0.05mm/rev)

On the other hand, a digital memory records two pulse signals generated from the photo interrupter and the discriminator. A rotational angle of a grain cutting edge in a grinding wheel surface from a reference point is calculated. Measuring condition of this experiment is shown in table 1.

3. DISTRIBUTION OF GRAIN CUTTING EDGES AND GRINDING WHEEL PROFILE

Figure 3 shows a measured example of distribution of grain cutting edges and geometrical shape of grinding wheel. Figure (a) shows a grinding wheel profile, and figure (b) shows grain cutting edge distribution of figure (a). From figure (b), the distribution of cutting edges can be evaluated. Some of the grain cutting edges are converging in the same rotational angle These aligned cutting edges indicate one cutting edge is continuing. From these results, it can be known that the length of grain cutting edge is about 0.08mm in this case.

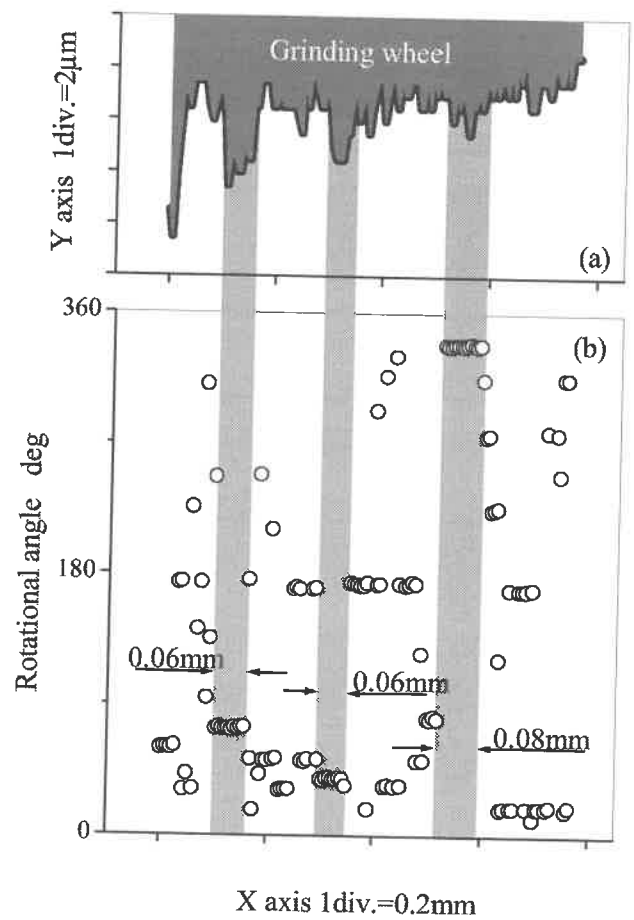

Figure3 Grinding wheel surface and grain cutting edges distribution

4. THE DISTRIBUTION OF GRAIN CUTTING EDGE AND ITS DENSITY

Figure 4 shows the distribution of cutting edges measured after dressing and after grinding. In this experiment S45C (HRC33) was used as a workpiece. The distribution of after dressing shown in figure 4 (a) is the coarsest in three results. Namely the number of grains in after dressing is the least. And it has a tendency that the number of grains increases and their distribution becomes dense in the grinding process. This tendency may be

caused as follows. That is, in the grinding process, grain cutting edges are gradually worn and released, and then, the distribution of grains height also decreases. The numeric values of density are shown in figure 4. The density of cutting edge at the after dressing is $0.04mm^{-2}$. And it increases to $0.098mm^{-2}$ with the progress of grinding process and saturated. As shown in figure 4, it is clarified that the number and the density of cutting grains in wheel surface can be evaluate quantitatively by using the measuring method proposed in the present study.

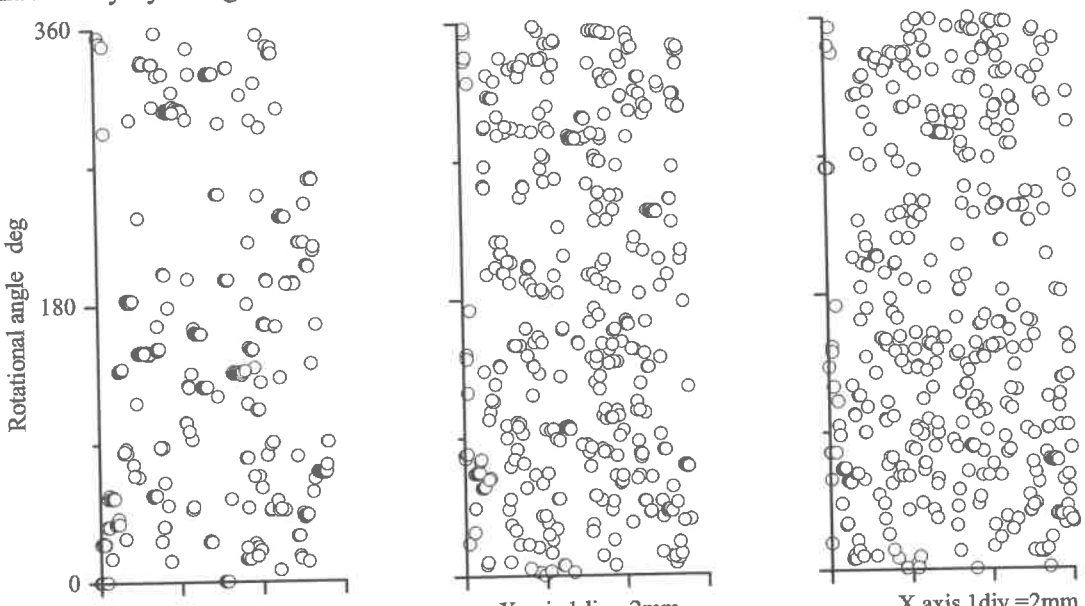

X axis 1div.=2mm
Number of grains=201
Density of cuttin edge=$0.045mm^{-2}$
(a)After dressing

X axis 1div.=2mm
Number of grains = 428
Density of cuttin edge=$0.095mm^{-2}$
(b)Removal value=$23mm^3/mm$

X axis 1div.=2mm
Number of grains = 439
Density of cuttin edge=$0.098mm^{-2}$
(c)Removal value = $47mm^3/mm$

Figure 4 Grain cutting edge distribution

5. CONCLUSIONS

In this study, a measuring method of grinding wheel surface profile and the distribution of cutting edge is proposed. The results obtained in this study are summarized as follows.

(1) The geometrical shape of grinding wheels and the distribution of cutting edges can be measured precisely in the same time.

(2) The distribution of cutting edge can be evaluated quantitatively.

(3) As the results shown above, the condition of grinding wheel surface can be evaluated precisely.

REFERENCES

[1]Seiki MATSUI, Jun'ichi TAMAKI, Studies on measuring method of wheel surface topography (4th Report)--Stylus Method --, JSPE, 50,4 (1984), (in Japanese).

[2]Akira HOSOKAWA, Heiji YASUI, Yukihisa KANAO, Kaoru SATO, Characterization of the grinding wheel surface by means of image processing (1st Report)--Post-process measurement of abrasive grain and cutting-edge distribution on the wheel surface --, JSPE, 62,9 (1996) 1297, (in Japanese).

[3]Masumi IZUMI, Hwa-Soo LEE, Tadashi WAKABAYASHI, Shigeru INOUE, Development of a measuring instrument for grinding wheel peripheral shapes, Proc. ASPE 2000 Annual meeting, 377.

In-situ three-dimensional observation of active abrasive grains on a grinding wheel during grinding of brittle materials

Akira Kanai*, Fumio Inaba* and Masakazu Miyashita**

*Ashikaga Institute of Technology, Ashikaga, Tochigi, Japan
**Nano-Tec Associates, Kokubunji, Tokyo, Japan

Abstract: This paper is a report of three-dimensional observation of active abrasive grains on a grinding wheel. The topographies of the wheel surface of a metal bonded diamond wheel were observed during grinding brittle. The change in active abrasive grains of cutting edges for accumulated chip volume was investigated.

Keywords: ultra-precision grinding, grinding of brittle material, grinding wheel, abrasive grain, topography of wheel surface,

1. Introduction

Grinding is the material removal process that is characteristic in generating minute chips by a grinding wheel with a large number of cutting edges of abrasive grains. For the precision machining process the size of chip is very important because it dominantly influences the machining quality of surface roughness, dimensional accuracy and sub-surface damage. In machining of brittle materials the size is especially important because it decides the mode of material removal. In cutting process the size of chip can be deterministically designed by specifying a cutting tool and cutting conditions. However in grinding the size cannot be deterministically estimated from the specification of a grinding wheel and grinding conditions, because they give little information about cutting edges.

Grinding to be high precision material removal process is derived from the minute size of chip. However at present a process engineer cannot design the size. It results from cutting edges to be in a black box. We have to know how many abrasive grains are active during material removal, how far active abrasive grains are apart from each other, how high active abrasive grains protrude and how much active grains wear. Those information about cutting edges is absolutely essential for grinding process to be revolutionarily improved from the technology based on the wheel depth of cut to the one on the grain depth of cut and from the material removal process based on cut-and-try to on the deterministic theory.

The authors had proposed the method of the in-situ three-dimensional observation of active grain distribution on a grinding wheel fixed to a grinding spindle at the annual meeting of ASPE in 1999. In the present paper the method was applied to grinding tests of brittle materials with a metal bonded diamond wheel and the change in active abrasive grains on a grinding wheel during material removal process were studied.

2. Three-dimensional observation of active abrasive grains during grinding

The topography of both the wheel surface and the ground surface were in-situ observed on a grinding machine by the definite chip volume during grinding a piece of work-piece. Figure 1 shows the set-up of the observation. Table 1 is the specification of the three-dimensional surface profiler to observe both the wheel surface and the machined surface on a grinding machine. The

conditions of traverse grinding test are listed in Table 2.

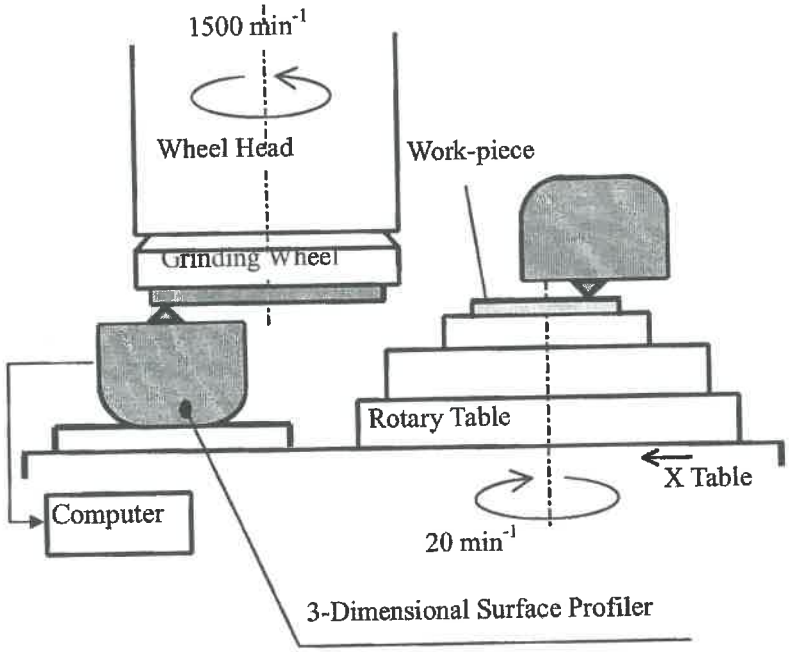

Fig. 1 Set-up of in-situ observation

Table 1. 3D surface profiler

Traverse area	1mm x 1mm max in X and Y
Gauge resolution	3 nm minimum
Max data size	500 x 500 points
Stylus tip radius	5 μm

Table 2. Grinding conditions

Grinding wheel	SD800N75M, Cup wheel (ϕ150×W3)
Work piece	Soda lime glass (□75×t1.7)
Work piece revolution	20 rpm
Grinding wheel revolution	1500 rpm
Wheel depth of cut	1.0 μm
Traverse rate	0.4 mm/sec

3. Results

Figure 2 and 3 the topographies of the grinding wheel surface. The vertical scale in Fig. 2 is adjusted to the height of the topography and the one in Fig. 3 is fixed for all of topography. Each topography in both Fig. 2 and 3 is the one to be observed by accumulated chip volume of 3000 mm^3 after dressing and clearly shows the change in active abrasive grains of cutting edges. Fig. 2 gives us the information about wear of abrasive grains and Fig. 3 does the one about the change of the grain top of cutting edge. The quantitative parameters to estimate the cutting edges on a grinding wheel can be derived from those topographies.

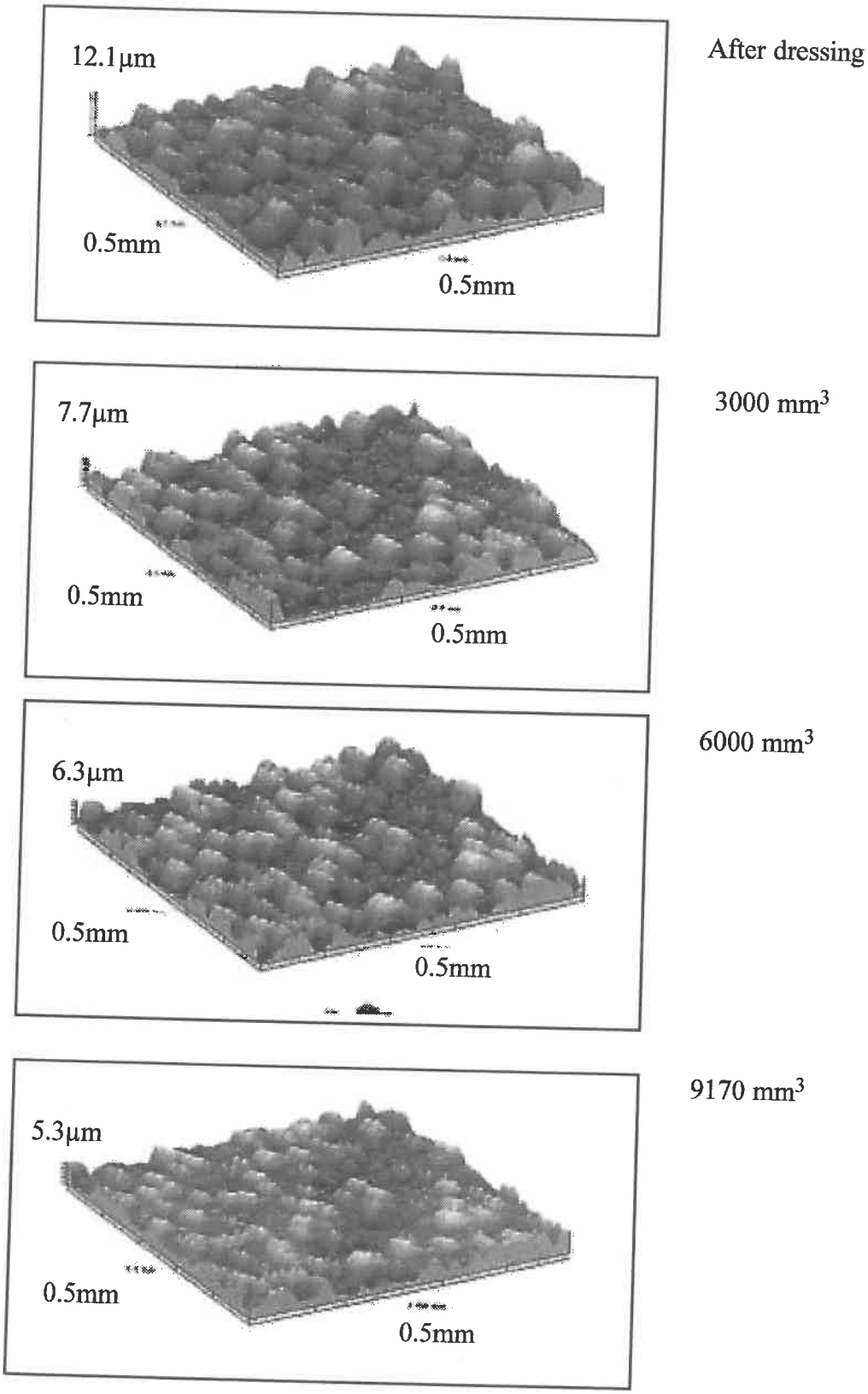

Fig. 2 Topography of wheel surface

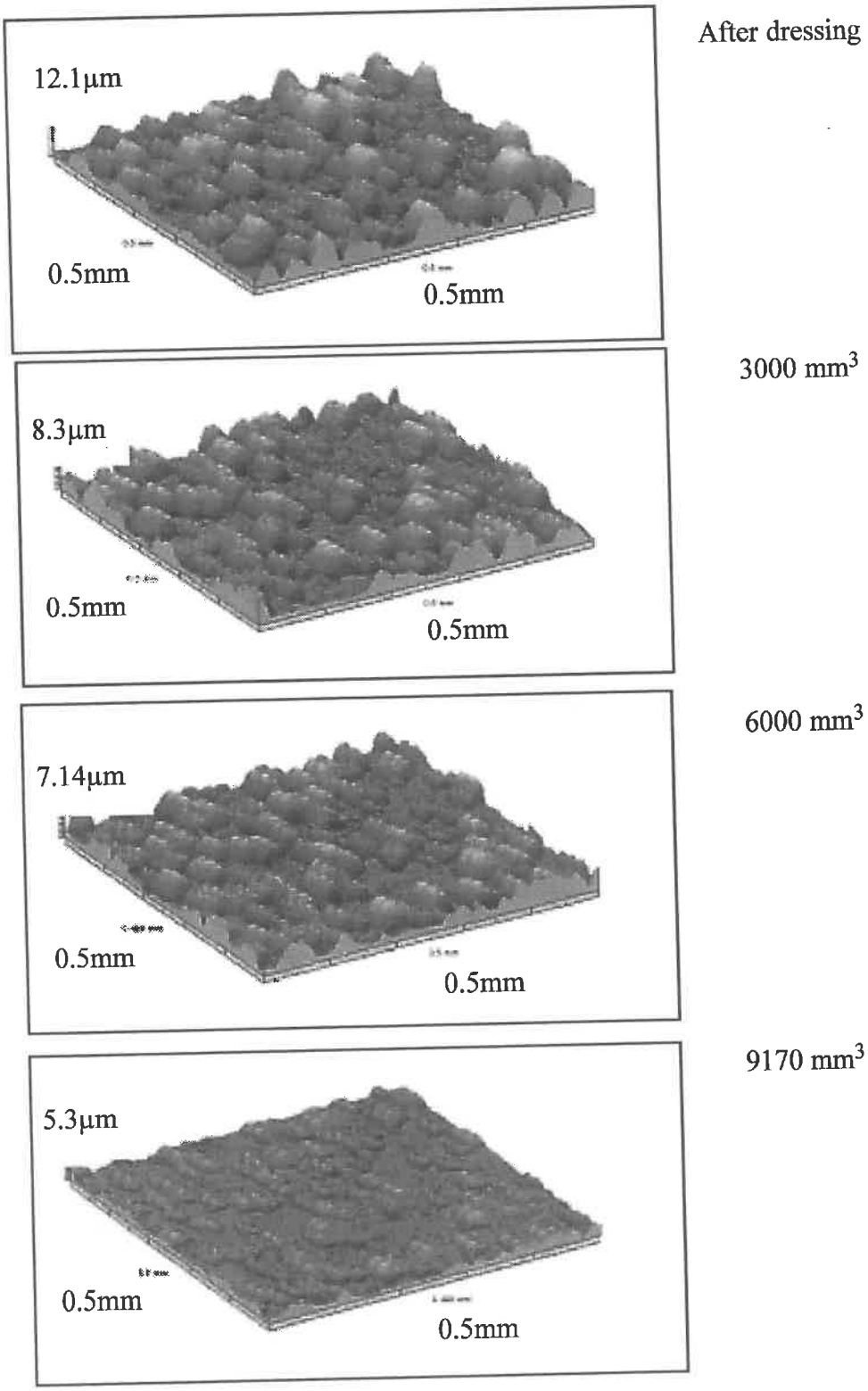

Fig. 3 Topography of wheel surface -2

FIGHTING SURFACE DAMAGES OF SILICON WAFERS – FINE-TUNED WAFER PROCESSING WITH ROTATIONAL GRINDING

Fritz Klocke, Dietmar Pähler
Fraunhofer Institute of Production Technology IPT, Aachen, Germany

SUBSURFACE DAMAGES IMPOTRANT FOR WAFER QUALITY

Within today's computerised world the demand for high-quality silicon wafers as the base for nearly any microchip is enormous but not easily satisfied. This is mainly due to the problems one encounters when machining brittle silicon with efficient process lay-outs under the command of constantly rising quality requirements. The driving parameters in wafer manufacture can be reduced to four outstanding factors:

- Quality of the wafer surface,
- Geometry of the wafer,
- Duration of the process and
- Total costs of the processing.

At the Fraunhofer Institute of Production Technology IPT rotational low-damage grinding processes are investigated among others for the manufacture of high-quality silicon wafers. Within the process lay-out particular attention is paid to the virtual avoidance of subsurface damages (SSD) with values below 2 µm employing a ductile material removal mechanism.

ADJUSTING PROCESS LAY-OUT TO DUCTILE MATERIAL REMOVAL

The ductile removal of material is found to be superior in terms of SSD compared to the traditional brittle removal. The future wafer manufacturing chain will consist of an integrated and adjusted process flow, starting from multi-wire slicing via two rotation grinding stages for micro- and nano-finishing (e.g. rough and finish grinding) to rotational polishing.
The adjusted process flow will pay particular respect to the quality of the wafer surface by introducing ductile machining as the last rotational grinding stage. The shift of modus towards the ductile material removal is technically archived by reducing the depth of penetration of the grinding wheel's grains into the silicon wafer. Even though ductile grinding reduces the material removal rate it results in practically damage-free wafers. This results in wafers with nearly polished-like surface qualities and minimised sub surface damages. There is a correlation between SSD and surface quality that is used here. Surface qualities of silicon wafers are $R_a > 0.3$ µm, $R_t > 4$ µm and SSD > 5 µm for rough grinding and R_a approx. 3 nm and SSD < 2 µm for fine grinding.

The choice of the grinding wheel is determining the removal mode employed. To achieve the values mentioned different grinding wheels with resin and vitrified bonding systems were used along with variations of grain size and concentration. It was found that grain sizes below D9 achieve sustainable improvements over coarser grains as **picture 1** shows the distinct characteristics of different D-values regarding their impact on the machined wafer surface; the transition from brittle to ductile machining occurs at

the value of D9. Furthermore, the best SSD values were consequently achieved with the very fine D3 grain.

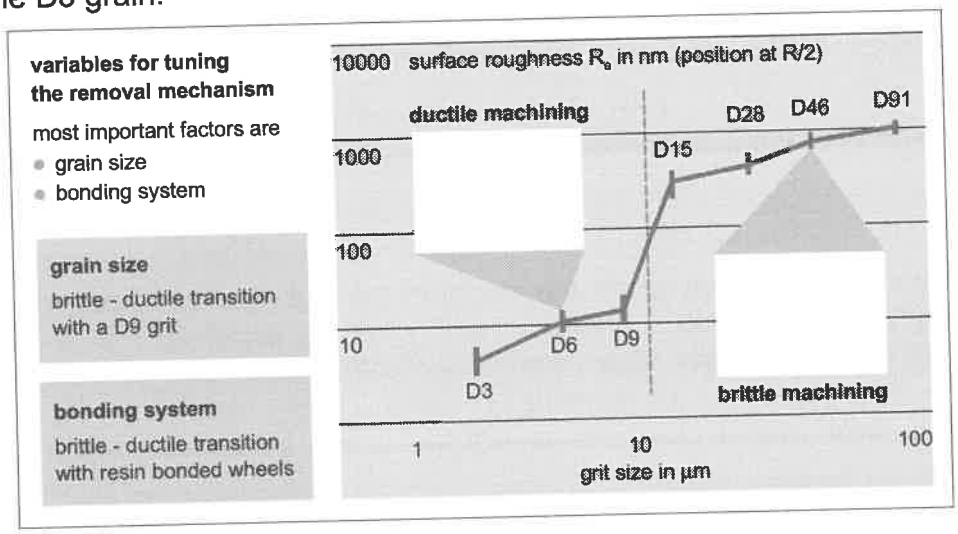

Picture 1: The transition from brittle to ductile machining depends vastly on the grain size used. The turning point was found between D9 and D15.

Regarding grain concentration it was found that higher values give a clear advantage; a C200 value was found to be appropriate for the testings done. A typical sample of a well-machined surface in the wafer's center produced with our D6 C200 grinding wheel can be seen in **picture 2**. Surface quality values of the silicon wafer are fulfilling the requirements well with $R_a < 6$ nm and R_t –values fare below 100 nm.

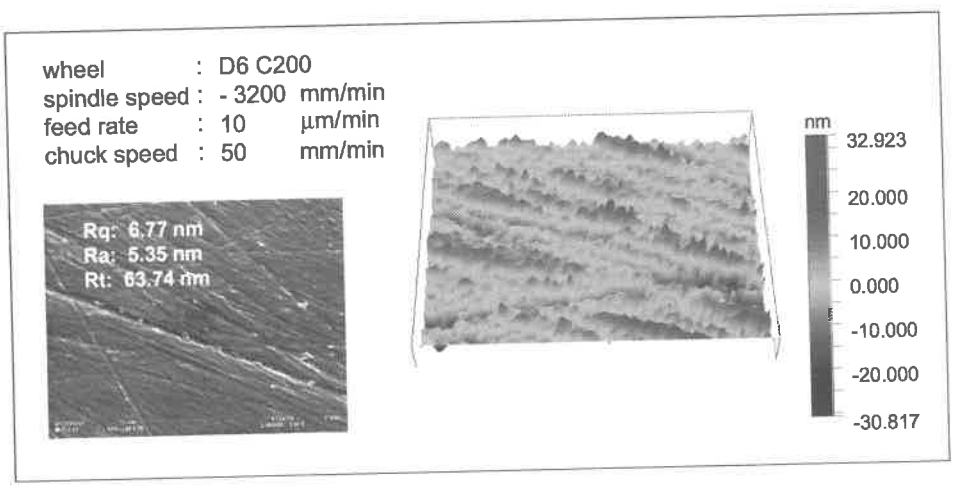

Picture 2: Sample of a well-machined wafer surface with superior R_a and R_t –values by use of the proposed process lay-out.

Using the same grinding wheel can also result in inferior qualities (**picture 3**). Even though similar parameters were used, the results are devastating. Therefore, the fine-tuned combination of all components is imperative for the successful ductile material removal. As for the bonding system a resin-bond grinding wheel proofed to be superior.

The bonding defines parameters such as the thermal and chemical stability, the wheel's toughness and elasticity.

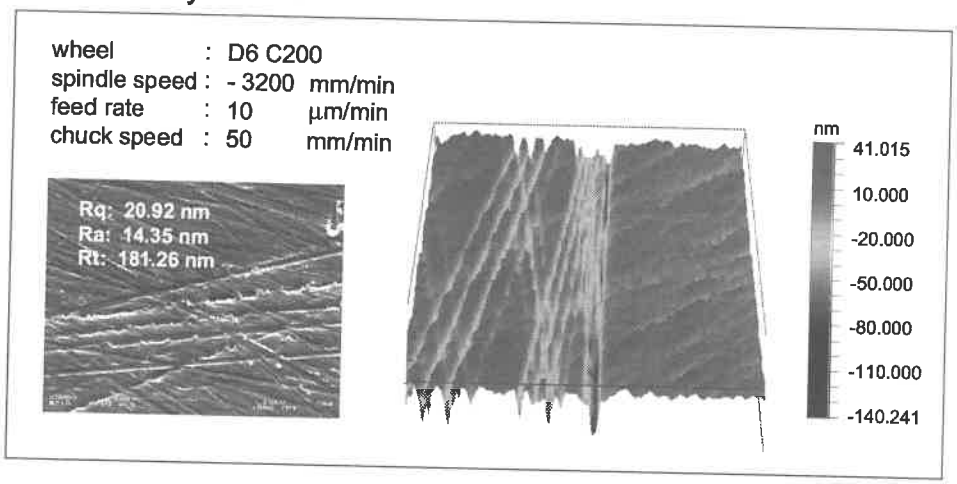

Picture 3: Using the same process lay-out with inappropriate machining parameter might as well result in inferior wafer qualities.

CONSIDERATION OF PROCESS PARAMETERS IMPORTANT

Therefore, the process parameters are an important aspect to be thoroughly considered when designing the process lay-out. As a rule of thumb, high spindle speeds combined with low material removal rates result in the best R_a-values. Process parameters also allow for the change in the removal mechanism employed as shown in **picture 4**.

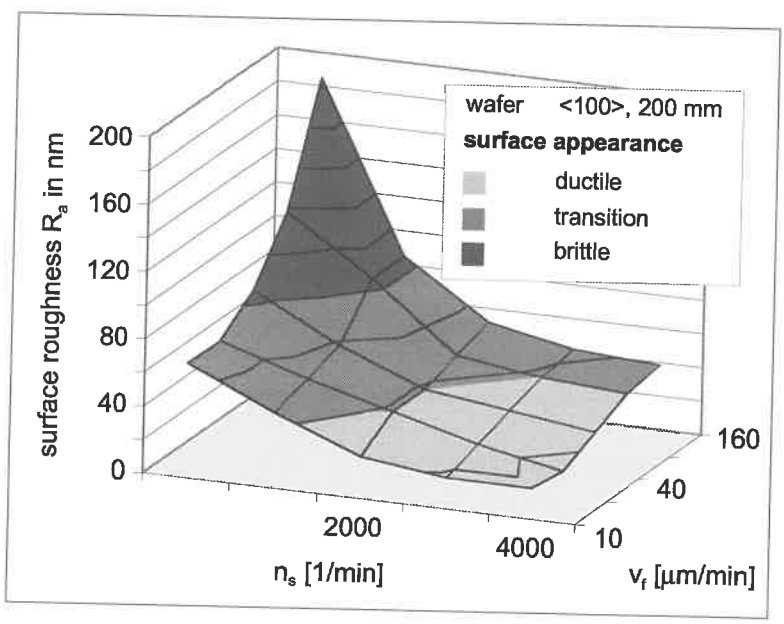

Picture 4: There is a wide range of machining parameters resulting in very different surface qualities. But only very few combinations suite today's demands well.

Ductile machining can be achieved with different combinations of the spindle speed n_s and the feed rate v_f. For instance, ductile material removal takes already place at speeds of $n_s = 1750\ min^{-1}$ and feed rates of $v_f = 20\ \mu m/min$ using our investigated customised grinding-wheel. The most desirable results are found only at the very small tip of the combination-landscape, with spindle speeds of $n_s \approx 3500\ min^{-1}$ and feed rates of $v_f \approx 20\ \mu m/min$ for this particular grinding-wheel. With these parameters the surface qualities were found to be in the range of $R_a \approx 0.03\ \mu m$ and below.

CO-ORDINATED PROCESSING FIGHTS SSD EFFICIENTLY

It is the fine-tuned combination of each parameter investigated that gives the proposed process lay-out with two rotational grinding stages its unique advantages regarding subsurface damages. Furthermore, there is no definite optimum but a range of good combinations (**picture 5**). Among the preferred grinding wheels with fine grains the spindle speed proofed to be a considerable variable: Spindle speeds for best R_a –values are not necessarily the same for perfect R_t –values. Using D3 wheels in the range of $n_s \approx 3500\ min^{-1}$ gives the most perfect results for machining silicon wafers in the ductile grinding mode with virtually damage free surfaces.

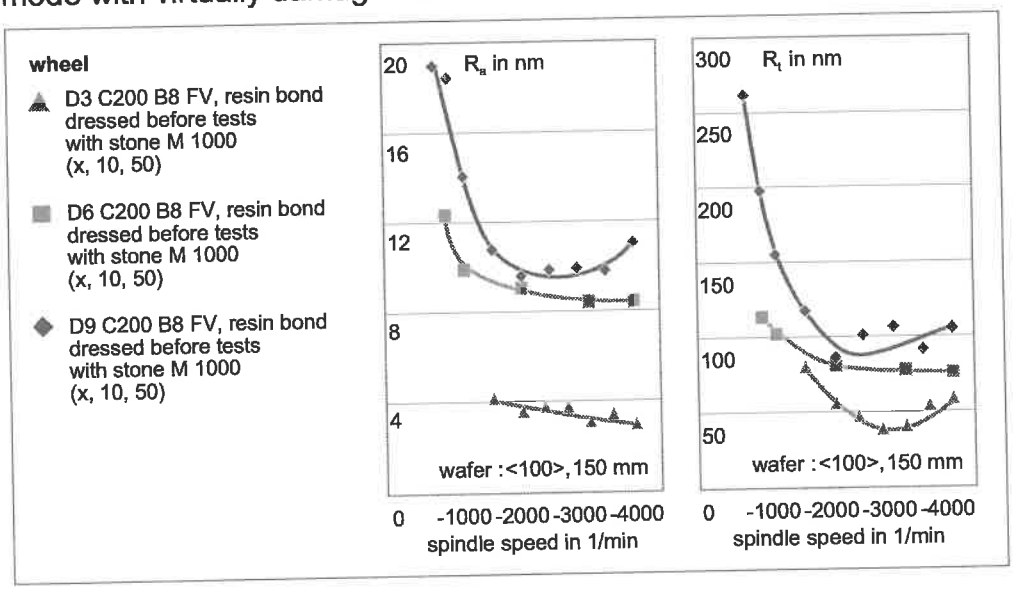

Picture 5: Spindle speeds determine surface finish in ductile regime mode grinding; superior values are obtained with rotational grinding at high speeds.

References

Klocke2001: Klocke, F., Pähler, D., Jakob, A. *Precision Machining of Future Silicon Wafers – Grinding and Slicing Techniques for Flawless Qualities*. Proc. of 2nd euspen Int. Conf., Turin; May 27th-31st 2001, pp.656-659.

Klocke2000: Klocke, F., Gerent, O., Pähler, D., Jakob, A. *Flat rates on future silicon wafers: precision grinding*. Industrial Diamond Review 2000; 2:pp. 149-56.

Nishi2000: Nishi, Y., Doering, R., *Handbook of Semiconductor Manufacturing Technology*. New York: Marcel Dekker, 2000.

Pei2001: Pei,Z.J.; Strasbaugh, A. *Fine grinding of silicon wafers*. Int. Jornal of Machine Tool & Manufacture 41, pp. 659-672.

Wire Electrical Discharge Truing of Metal Bond Diamond Grinding Wheels

B. K. Rhoney, A. J. Shih, and R. O. Scattergood, North Carolina State University, Raleigh, NC 27695
S. B. McSpadden and R. Ott, Oak Ridge National Laboratory, Oak Ridge, TN 37831
J. A. Akemon, D. J. Gust, T. M. Yonushonis, and M. B. Grant, Cummins Inc., Columbus, IN 47201

Abstract

Cylindrical wire EDM profile truing of the metal bond diamond wheel for precision form grinding of ceramics is presented in this report. First, a corrosion-resistant, precise spindle with the high-electrical current capability for wire EDM truing of grinding wheel was fabricated. An arc profile was adopted in order to determine form tolerances capabilities of this process. Results show the wire EDM process can generate μm-scale precision form on the diamond wheel efficiently. The wheel, after truing, was used to grind the silicon nitride and grinding forces, surface finish of ground components, and wheel wear were measured. The EDM trued wheel showed a reduction in grinding force from that of the stick dressed wheel. Surface finishes between the two truing methods were similar. In the beginning of the grinding, significant wheel wear rate was identified. The subsequent wheel wear rate stabilized and became considerable lower.

1. Introduction

As the applications of engineering ceramics broadened, the shape of these parts has become more complicated and the form tolerance specifications are more stringent [1]. An efficient and cost-effective method to grind a ceramic component with a complicated shape is to generate the desired form on a diamond grinding wheel and then plunge the shaped wheel into the ceramic workpiece. Based on this approach, the technical challenge has shifted from grinding the workpiece to shaping or truing the diamond grinding wheel. This study investigates the wire Electrical Discharge Machining (EDM) as a process for truing of a metal bond diamond wheel.

Traditionally, a stationary or rotary diamond tool is used to true a grinding wheel to generate the desired form. Shih [2] has studied the wear of the rotary diamond tool for truing of a vitreous bond diamond grinding wheel and demonstrated that the wear of diamond tool is significant under a wide range of process parameters. Instead of using the mechanical force to break the diamond, the wire EDM process uses the thermal energy or electrical sparks between a thin, traveling wire and the rotating grinding wheel to remove the bond around the diamond. Three popular grinding wheel bonding systems are: metal, resin, and vitreous. The EDM process requires the workpiece, in this case the grinding wheel, to be electrically conductive, thus a metal bond wheel is selected.

The configuration of Wire Electrical Discharge Truing (WEDT) process is illustrated in Fig. 1(a). The relative motion between the grinding wheel and traveling wire is controlled by the X and Y slides in a two-axis wire EDM machine to generate the intricate form on a rotating metal bond diamond wheel. Top view of the trajectory of the wire and the form generated on the wheel is shown in Fig. 1(b). Besides the wire EDM, the die-sinking EDM can also be used for truing the metal bond diamond wheel [3]. The literature survey found a lack of research studying the use of the wire EDM method to create μm-level truing of metal bond wheel. Nor was there any data on the EDM trued wheels grinding performance. These become the objectives of this research.

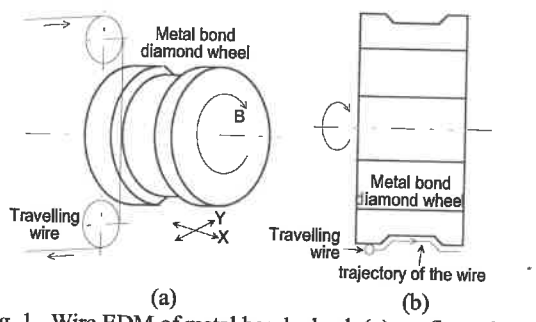

Fig. 1. Wire EDM of metal bond wheel, (a) configuration of the operation, (b) top view of the trajectory of the wire.

2. Spindle Design

Due to corrosive environment of the EDM process, a corrosion resistant and precise spindle suitable for truing the metal bond grinding wheel was constructed. Spindle runout was reduced to sub-μm level by precision grinding and assembly. Ceramic bearings were used to support the shaft to assure no EDM erosion of the bearings. To transfer the heavy current flow from the spindle shaft to the shaft housing, a shunt carbon brush was used. A DC motor was selected due to good voltage speed control. In order to smoothly transfer rotation from the motor to the spindle shaft a 6.2 mm diameter round grooved polyethylene pulley and belt were employed. A standard grinding adapter was used to mount the wheel to the spindle shaft.

3. Achievable Form Tolerance

The ability to create a precise form into the grinding wheel was the goal of WEDT. In order to

quantify the level of precision achievable, an arc profile was adopted. This form has two arcs of radii 0.665 and 1.05 mm as shown in Fig 2. First, the 1200 ANSI grit bronze bond diamond grinding wheel was profiled to shape using the WEDT process. Then, a piece of machineable plastic was ground. In order to see how the form errors change after an initial grind, a piece of zirconia was ground followed by another piece of machineable plastic.

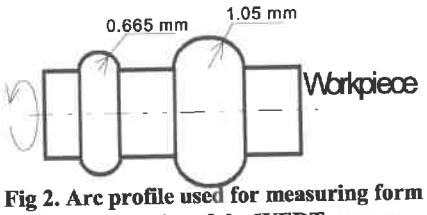

Fig 2. Arc profile used for measuring form error capabilities of the WEDT process.

Table 1. Results of form error measurement.

Table of Form Error		Before Grind		After Grind	
Large Arc	*Cutoff (mm)*	*0.08*	*0.25*	*0.08*	*0.25*
(1.05 mm rad)	W_t (μm)	11.69	9.16	10.45	6.25
Small Arc	*Cutoff (mm)*	*0.08*	*0.25*	*0.08*	*0.25*
(0.665 mm rad)	W_t (μm)	5.45	3.47	1.69	1.07

The two plastic profiled cylinders were then measured for form error using a Rank-Taylor Talysurf profilometer, with a 0.5mm ball stylus. The data from the arcs were then passed through one of two filters with cutoff values of 0.08 and 0.25mm. The results are shown in Table 1. These form error values, W_t, are recorded as the peak-to-valley values after the appropriate filtering. From these values two trends are noted: first, the form error of the large arc is nearly double that of the smaller arc, and, secondly, the form error decreases after the grinding of the zirconia for both arcs. The reason for the reduction in form error after initial grinding was studied using the stereo-SEM. Results showed that some of the diamonds in the "as trued" wheel surface were protruding nearly half of their size. However, after only a slight presence of force in grinding these diamonds are fractured to a height which can support the load during grinding.

4. Grinding Study

A grinding study was developed to compare the performance of the WEDT wheel against a single point diamond trued and stick dressed wheel. After the wheel was trued it was then dressed using a 220 ANSI mesh silicon carbide stick. This will remove some of the metal matrix from around the diamond for chip clearance. With WEDT the truing and dressing were performed simultaneously, thus no stick dressing was required

Once the wheels were prepared, silicon nitride tiles from Toshiba (TSN-10) were ground. The samples are 42.5 mm long (along direction of table feed) and have a width of 6.35 mm. The width of the wheel is 12.7 mm, enabling wheel wear data to be collected. The sample was aligned to the middle of the wheel leaving ungrounded areas near both edges of the wheel. As the parts are ground a groove will be created into the middle of the wheel due to wear. This groove from the wheel can be transferred to create a step into a plastic wear block. This step on the wear block can be measured to determine the progressive wear of the wheel.

The grinding machine was the ELB BD10 with 22.4 kV ball bearing spindle and ball screw slide. The coolant was TRIM 413A with 5% concentration. The 8 inch diameter Norton Scepter diamond wheel (ME 178393 D-2-MX876D-1/4) at 36.6 m/s surface speed was used. The table speed was 127 mm/min, depth of grind was 3.81 mm, specific material removal rate was 8 mm^2/s with 1.03 cm^3 of silicon nitride removed per pass. After each grinding pass through the silicon nitride, a pass was also taken trough the plastic wear block. In addition, the silicon nitride samples were replaced after each pass, in order to measure any changes in surface finish of the samples.

4.1. Forces

Grinding forces were captured in the vertical and horizontal directions using a Kistler 9257B 3-axis force dynamometer. Spindle power was measured using a Hall-effect power sensor which was installed on the ELB grinder. A DC voltage output signal from the sensor is given relative to the spindle load, which is then converted to power by a calibration constant. The output signal was passed through a low-pass RC filter, with cutoff frequency of 442 Hz.

As mentioned previously the horizontal and vertical forces were measured during grinding. However, as shown in Fig 3, these forces are not the same as the tangential and normal forces, respectively, due to the large arc of machining caused by a deep depth of cut. As the depth of cut, t in Fig. 3, increases the tangential and normal forces begin to slide up the machining arc.

Tangential force, as the name implies, is the force that is tangential to the wheel's surface. Torque on the wheel is the product of tangential force and wheel

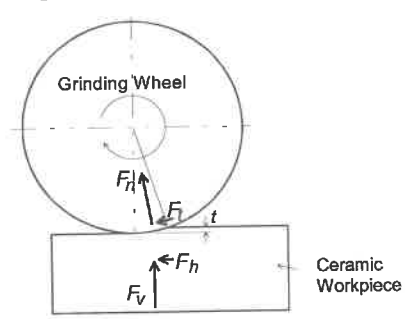

Fig 3. Diagram of grinding forces for deep DOC.

radius. Likewise, spindle power load on the wheel is the product of torque and angular velocity. By having the power (P_s), and the horizontal force (F_h), and vertical force (F_v) known, the tangential (F_t) and normal forces (F_n) can be calculated. Since the resultant force of the vertical and horizontal forces is the same as that of the tangential and normal forces, the relationship can be made that:

$$F_n^2 + F_t^2 = F_h^2 + F_v^2 \qquad (1)$$

Then, the tangential force is just the spindle load divided by the wheel surface speed (V_s).

$$F_t = \frac{P_s}{V_s} \qquad (2)$$

By rearranging Eqs. (1) and (2), the normal force can be calculated.

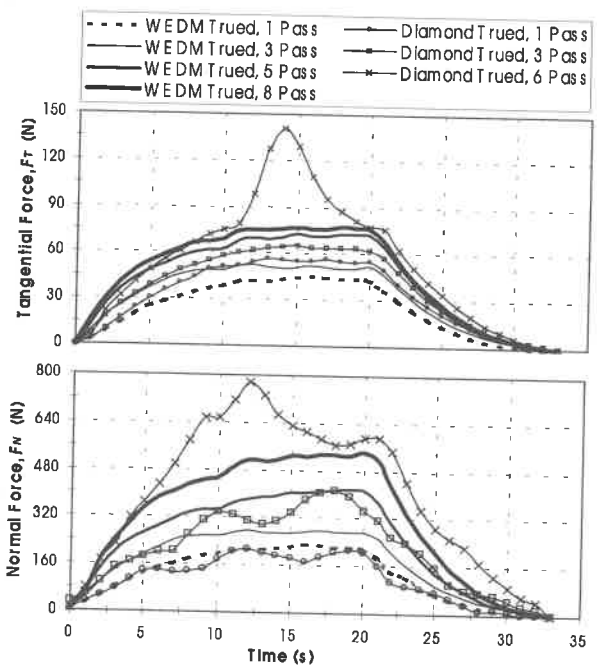

Fig 4. Forces generated during silicon nitride grinding.

Fig 4 shows the tangential and normal force results after the conversion. Notice that the EDM wheel has tangential forces that are 20% lower than that of the stick dressed wheel. This remains the case until the sixth pass, where the stick dressed wheel begins to break down. The forces produced by the stick dressed wheel began to increase drastically, which causes the diamonds on the surface to fracture or pull out. This also occurred with the EDM trued wheel, but after 15 passes.

Normal forces generated when grinding with the traditionally dressed wheel are also 20 – 40% higher than forces produced when grinding with the EDM trued wheel. On the sixth pass, the normal force reached nearly 800 N for the traditionally dressed wheel. While on the eighth pass, the EDM wheel was only seeing forces around 500 N.

4.2. Surface Finish and Wheel Wear

Since the samples were removed after each pass, they were measured to establish surface finish trends. The measurements were made using a Talysurf with a standard diamond 2 μm radius tip, and a 0.25 mm cutoff. Results in Fig 5 show that both truing methods produce components of similar roughness. As the wheel is continually used the surface finish of the components improves. This can be contributed to an increase in the diamonds' wear flat.

The depth of the groove created in the wheel, due to the wheel wear, is also shown in Fig 5. An initial high wear rate, shown by the slope of the line, is noted for both truing methods. However, after the first pass,

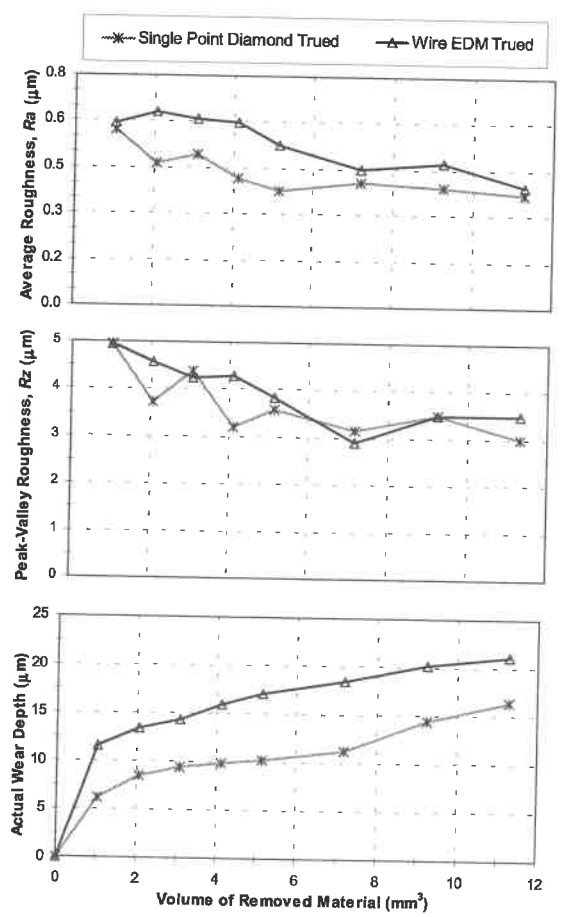

Fig 5. Surface finish of ground silicon nitride samples and wheel wear during grinding.

both wheels seem to stabilize at the same wear rate, or have the same slope. The higher initial wear rate of the EDM trued wheel was determined to be caused by fracturing of over-protruding diamonds on the wheel surface. It was also noted that form error was not increased due to diamond fracture, since the form is placed in the metal matrix and not in the diamonds themselves.

5. SEM Investigation of Wheel Wear

Stereo SEM was used to study the high initial wheel wear rate of the EDM trued wheel. Figure 6 shows a diamond that is protruding from the EDM trued wheel surface about 29 μm. All of the diamonds measured in WEDT surface were in the range 3-35 μm. The size of the average diamond in this wheel is about 60 μm.

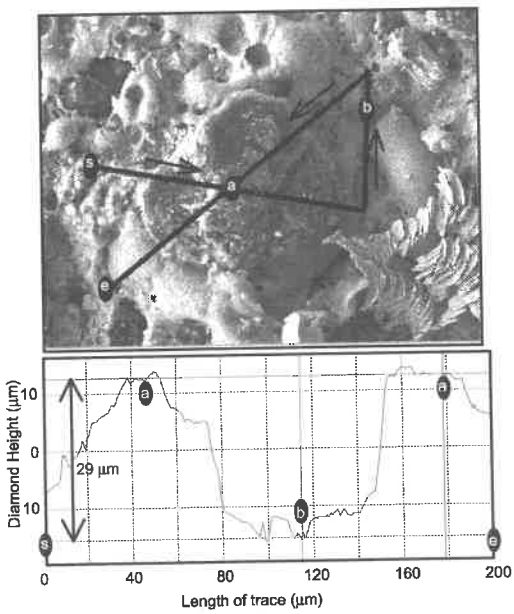

Fig6. Stereo-SEM profile of WEDT virgin wheel surface.

A section of the same wheel was used to grind silicon nitride. A single light pass was used to determine the diamond height after only a slight presence of grinding force. The results show that those forces reduced the diamond height range to 3 – 13 μm.

Figure 7 shows two diamonds that are active, as seen by the rub marks on top of the diamonds. The stereo SEM reveled that the diamond (b) is at the same height as the working plane, while the diamond (c) is 6 μm above the working plane.

Conclusions

Wire Electrical Discharge Truing (WEDT) is capable of producing μm-level precision forms in metal bonded super-abrasive wheels. WEDT wheels have reduced grinding force as compared to a stick

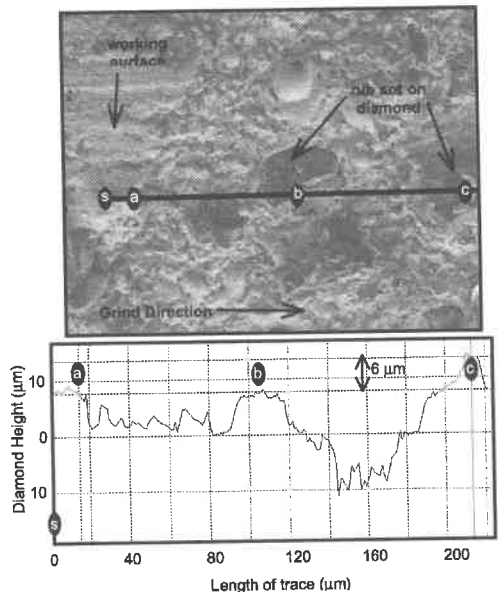

Fig 7. Stereo-SEM profile of lightly ground wheel surface.

dressed wheel. WEDT wheels are also capable of delaying wheel breakdown, which increases the interval for which redressing is required. The surface finish of components ground with a WEDT diamond wheel are similar to those ground with a stick dressed wheel. Wheel wear rates of the EDM trued wheel stabilizes after the initial introduction of grinding forces. It was noted that this diamond fracture did not increase the form error, since the form was placed in the metal matrix by spark erosion and not the diamonds themselves.

Acknowledgement

The authors gratefully acknowledge the support by Cummins Inc., National Science Foundation (K. P. Rajurkar, Program Director), and the High Temperature Materials Laboratory User Program, Oak Ridge National Laboratory, managed by UT-Battelle, LLC, for the U.S. Department of Energy under contract number DE-AC05-00OR22725.

References

[1] W. F. Mandler, T. M. Yonushonis, K. Shinosawa, "Ceramic success in diesel engines," 6th International symposium on ceramic materials and components for engines, K. Niihara et al. (Ed.) Arita, Japan: 1997 137-141.

[2] A.J. Shih, "Rotary truing of the vitreous bond diamond grinding wheels using metal bond diamond disks," Machining science and technology, 2 (1998) 13-28.

[3] Suzuki, K. and Uematsu, T. and Nakagawa, T. "On-machine trueing/dressing of metal bond diamond grinding wheels by electro-discharge machining," *CIRP Annals*: 1987.

Machining of Aspherical Opto-Device Utilizing Parallel Grinding Method

Masaru Saeki[1,2], Tsunemoto Kuriyagawa[1], Joo-Sang Lee[3] and Katsuo Syoji[1]

[1]Department of Mechatronics and Precision Engineering, Tohoku University
Aramaki Aoba 01, Aoba-ku, Sendai 980-8579, Japan
[2]Olympus Optical Co., Ltd., Tokyo 192-8507, Japan
[3]Nambu University, Kwangju 506-302, Korea

Introduction

Recently, a demand of aspherical optics increases as key parts for achieving miniaturization and better image quality of an optical instrument. Especially the needs of the improvement in image quality for the latest digital image equipments are increasing steadily, and a high accuracy of aspherical lens has strongly been required. Most of aspherical lenses that are widely used are produced by a plastic injection molding. As the plastic lenses do not have enough accuracy and environmental resistance, glass lenses are required. Therefore, the development of the more precise grinding technology for the aspherical glass lenses and glass molding dies is required.

As a processing method that responds to the needs, authors devised a new grinding technique called as a "parallel grinding method" which performs an arc-envelope grinding method [1] [2], using an ultra-fine grit diamond wheel with an arc-trued cross-sectional profile [3]. In this paper, form accuracy and roughness of the ground surface utilized the parallel and conventional grinding methods are compared and investigated, and the more precise grinding system for the parallel grinding method is developed.

Parallel Grinding Method

Grinding method for the most mainly applying to the machining of the axisymmetric aspherical lens is shown in Figure 1. The system has the vertical wheel axis, and the grinding is performed by simultaneous 2-axis control of X and Z directions [4]. As the rotational direction of the workpiece and the cutting direction of the wheel are perpendicular at the grinding point, the grinding marks are formed in radial direction of the workpiece. The conventional system is called as a "cross grinding method". As a V-shaped wheel is normally used, furthermore, the grinding point is fixed and the wheel wear is concentrated at the point. Therefore, it is difficult to obtain a high form accuracy using the cross grinding method.

To solve this problem, the parallel grinding method is developed. As the wheel axis in the new method is installed as shown in Figure 2, the rotational direction of the workpiece and the cutting direction of wheel at the grinding point become parallel. Therefore, the grinding marks become circular

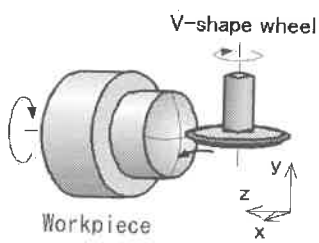

Fig. 1 Cross grinding method

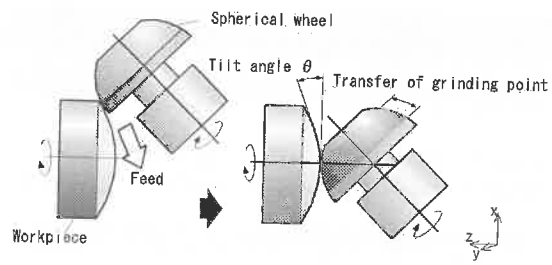

Fig. 2 Parallel grinding method

and the ground surface roughness is significantly improved compared to that achieved by conventional method. In the new method, furthermore, the grinding point is changed along the wheel profile, and the wheel wear decreases remarkably to obtain the better form accuracy of the ground aspherical profile.

Comparison of Ground Surface

To clarify the difference of ground surface characteristics between parallel and cross grinding methods, grinding tests were carried out using the ultra-precision aspheric grinding system as shown in Figure 3. The system installs 3-axis sliding tables and two air spindles for a workpiece and a wheel. The sliding tables use non-circulation type V-V roller guide ways, and are driven by the simultaneous three-axial numerical controlled servomotors with minimum infeed resolution of 10 nm. Moreover, the spindles are supported using an ultra-precision aerostatic bearing with a run-out of 100 nm below. The X and Z axes sliding tables were used in the tests of the cross grinding method, and the X and Y axes sliding tables were used in the parallel grinding method.

To compare only the difference of surface characteristics of a parallel and cross grinding methods, a flat surface was ground, not an aspherical surface. Material of the workpiece is tungsten carbide (WC) for glass lens molding dies. The spherical grinding wheel was used, which was trued and dressed

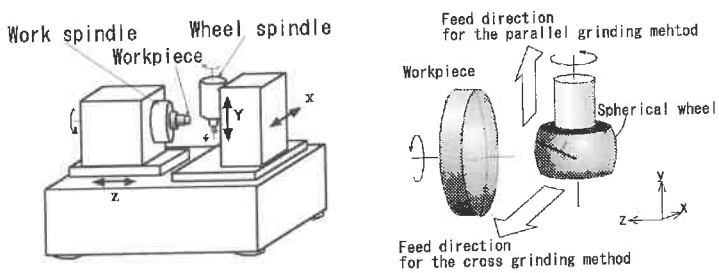

Fig. 3 Schematic diagram of the experiment apparatus

Table 1 Grinding conditions

Wheel: SD3000B, Spherical, d=10 mm	
Rotational speed	30000 rpm
Depth of cut	1 μm
Feed rate	1 mm/min
Workpiece: WC 10 mm in diameter	
Rotational speed	500 rpm
Coolant	Solution type

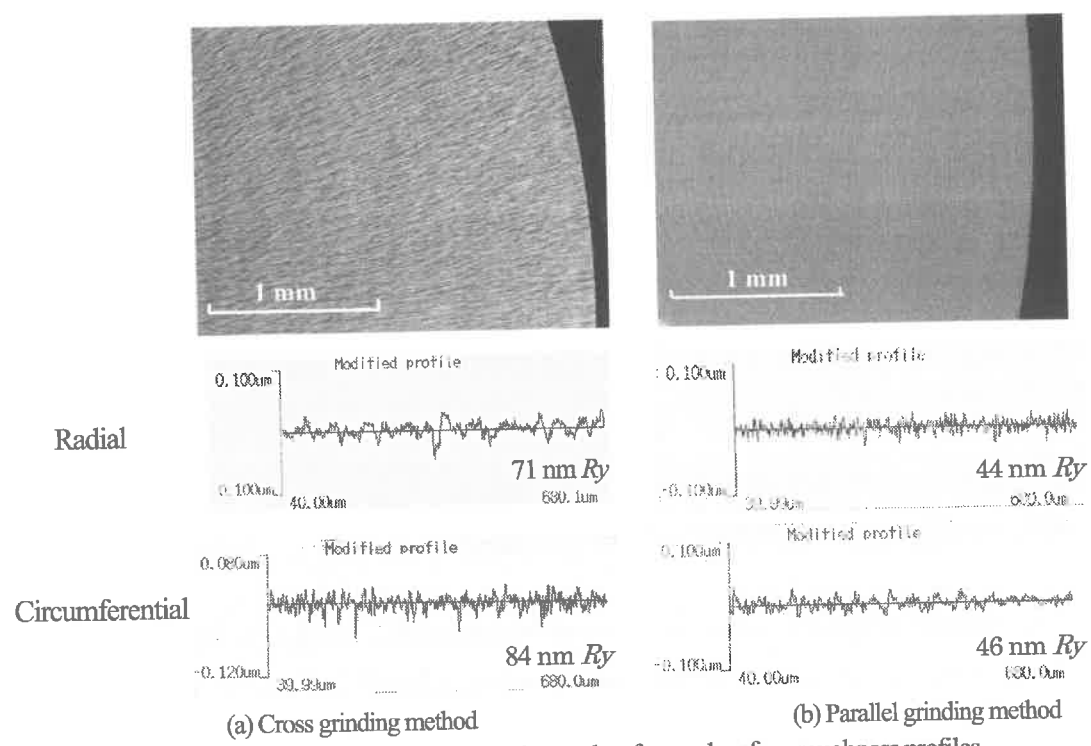

(a) Cross grinding method (b) Parallel grinding method

Fig. 4 Nomarski micrograph of ground surface and surface roughness profiles

into spherical shape using a curve generating method [5]. Grinding conditions is shown in Table 1.

Figure 4 shows Nomarski microphotographs and roughness profiles of the ground surface. Regardless of measurement direction, roughness of ground surface by the parallel grinding method is finer. It is because the number of effective cutting edge in a parallel grinding method becomes larger than that in a cross grinding method.

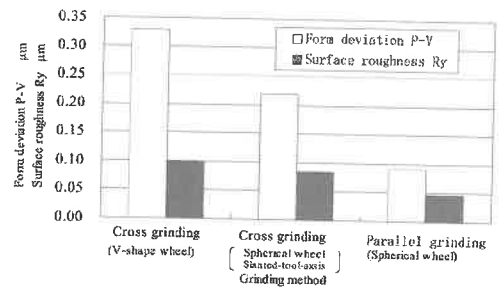

Fig. 5 Surface roughness and form deviation

Next, aspherical grinding tests were carried out to compare the difference of the form deviation by each method. Figure 5 shows the result of the form deviation of the aspherical die and the surface roughness. It is clear that the ground surface quality by the parallel grinding method is remarkably better than the conventional method.

Development of Axisymmetric aspheric parallel grinding system

Based on the findings in the previous section, an ultra-precision axisymmetric aspheric grinding machine was manufactured for a parallel grinding method. Figure 6 shows a whole system and a close-up view of the working area. The specification of the machine is listed in Table 2. The machine has X and Z axes of oil hydrostatic slide tables with 1 nm resolution. The workpiece spindle is mounted on the X slide table and the wheel spindle mounted on the Z slide table, and both spindles are supported by the oil hydrostatic bearing. The wheel spindle is inclined to the workpiece spindle at 0 to 90 degrees in a horizontal plane.

An equation of aspherical shape is as follows:

$$Z(X)=\frac{C_v X^2}{1+\sqrt{1-(K+1)C_v^{\,2}X^2}}+\sum_{i=1}^{m}C_i X^i \ , \qquad (1)$$

where X is radial position, $Z(X)$ is axial position and Cv, k, Ci (i =1-m) are aspherical constants. After rough grinding using SD600B wheel, it was finished by SD3000B wheel. Other grinding conditions were same as in Table 3. Grinding flowchart is shown in Figure 7. In finish grinding process, based on the form error curve measured after each grinding process, compensation-grinding processes were repeated to 2 times.

The aspheric glass lens of 30 mm in diameter and 52 mm of curvature was ground. Figure 8 shows the results of the surface roughness and the form deviation from the theoretical shape. The form

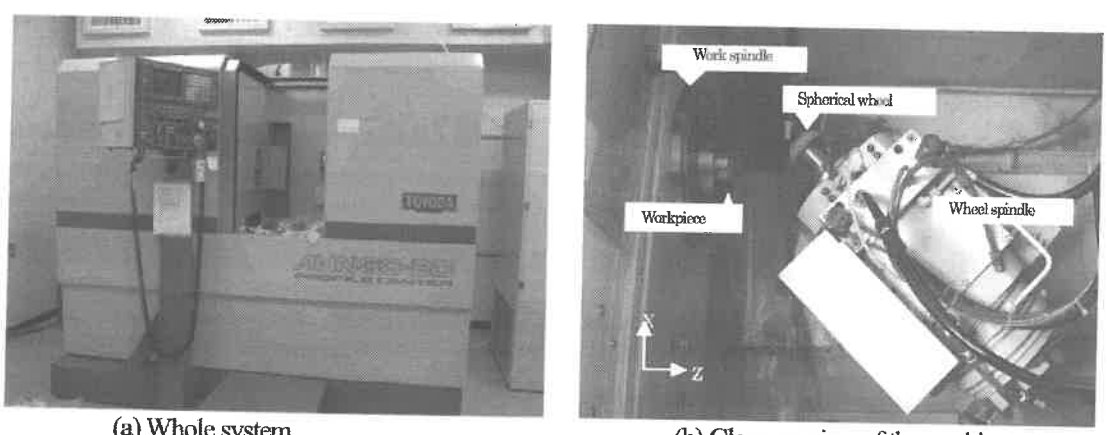

(a) Whole system (b) Close-up view of the working area

Fig. 6 Photograph of ultra-precision aspheric grinding system

Table 2 Specification of the newly developed grinding machine

Wheel spindle	Oil hydrostatic bearing spindle
	5000 rpm in maximum
Work spindle	Oil hydrostatic bearing spindle
	1000 rpm in maximum
X and Z axes	Oil hydrostatic slide
Feed resolution	1 nm
Maximum workpiece	600 mm in diameter

Table 3 Grinding conditions

Wheel : SD3000B, spherical, d=75 mm	
Rotational speed	5000 rpm
Depth of cut	1 μm
Feed rate	3 mm/min
Workpiece	FSL 30mm
Rotational speed	200 rpm
Coolant	Solution type

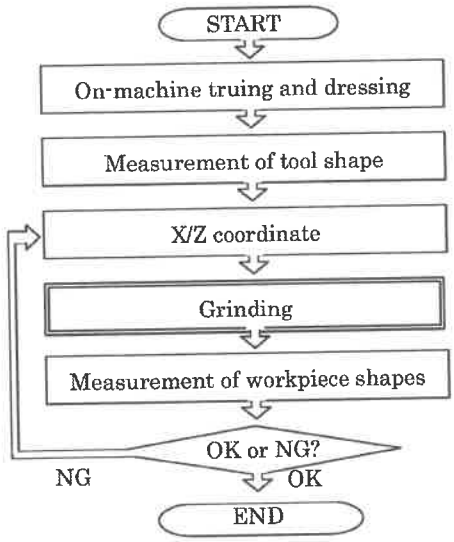

Fig. 7 Aspherical grinding process

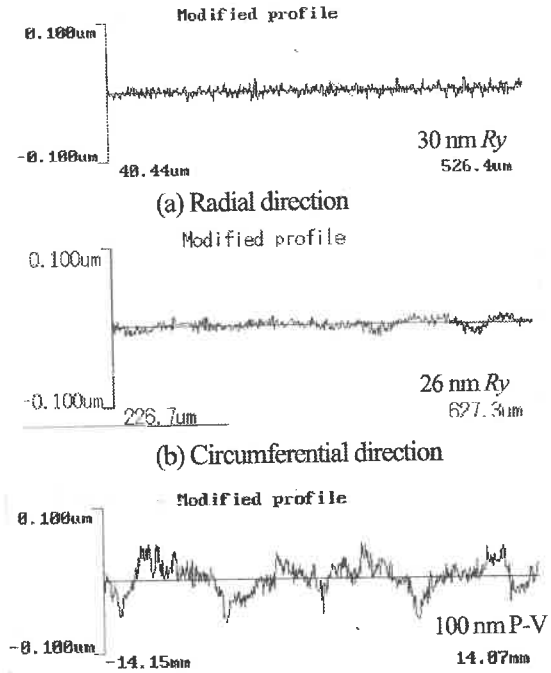

Fig. 8 Surface roughness and the form deviation

accuracy and roughness were approximately 100 nm P-V and 30 nm *Ry* respectively.

Conclusions

1) Surface roughness and form deviation by a conventional cross grinding method and a newly developed parallel grinding method were compared. It is clear that a better surface quality is obtained by the parallel grinding method.

2) Ultra-precision axisymmetric aspheric grinding system for the parallel grinding method was developed, and the aspherical glass lens with a 100 nm form accuracy and 30 nm *Ry* was successfully ground.

References

[1] T. Kuriyagawa, K. Syoji and L. Zhou, Precision Form Truing and Dressing for Aspheric Ceramic Mirror Grinding Machining of Advanced Materials, NIST Special Publication 847, 6 (1993) 325-331.

[2] T. Kuriyagawa, M. S. Sepasy and K. Syoji, A new grinding method for aspheric ceramic mirrors Journal of Materials Processing Technology, 62 (1996) 387-392.

[3] M. S. Sepasy, T. Kuriyagawa, K. Syoji and T. Tachibana, Ultra-Precision Arc Truing and Dressing of Diamond Wheels for Aspheric Mirror Grinding International Journal of Japan Society Precision Engineering, 31,4 (1997) 263-268.

[4] H. Suzuki, S. Kodera, S. maekawa, N. Morita, E. Sakurai, K. Tanaka, H. Takada, T. Kuriyagawa, and K. Syouji, Study on precision grinding of micro aspherical surface, J.Japan Soc.Prec.Engg.,1998,64(4):619-623.

[5] T. Kuriyagawa, J. Lee, M. Saeki and K. Syoji, Micro Truing/Dressing for Small-Sized Aspherical Mirror Grinding Advances in Abrasive Technology IV, (2001) . (Proceedings of the 4th International Conference on Abrasive Technology)

PRECISION GRINDING OF MICRO FRESNEL SHAPE AND PRECISION GLASS MOLDING OF MICRO FRESNEL LENS

Hirofumi Suzuki[1)], Toshiro Higuchi[2)], Masahiko Nishioka[3)], Takayuki Kitajima[4)], Akinori Yui[4)], Shigeki Okuyama[4)], Hideo Shibutani[1)] and Osamu Horiuchi[1)]

1) Toyohashi University of Technology, Aichi, Japan, 2) University of Tokyo, Tokyo, Japan, 3) Toshiba Machine, Numadu, Japan, 4) National Defense Academy, Yokosuka, Japan

Abstract

This paper deals with the precision grinding of micro fresnel molding die and glass molding for micro fresnel lens with some micro grooves. Fresnel lenses are useful for the next generation type of optical devices because of its thin structure and excellent optical characteristics. A grinding system of 4-axes (X, Y, Z, C) and a new grinding method with vertically controlled grinding spindle were developed. In a feasibility study of the fresnel shape grinding with the developed system, the molding dies of tungsten carbide for glass lenses were ground in trial. And micro glass fresnel lenses were glass-pressed with the ground WC die in trial. The grinding results show that a form accuracy of about 0.1 μmP-V and surface roughness of about 10 nmRy were obtained and this new grinding system and glass molding system are useful.

Keywords: micro fresnel glass lens, axi-symmetric aspherical surface, precision grinding, diamond wheel, tungsten carbide dies, glass molding

1. Vertically controlled grinding method and grinding system

A schematic diagram of newly developed micro fresnel grinding system is shown in **Fig.1**. As a wheel, a disk type of diamond wheel which edge was trued as a sharp knife edge was used and the wheel scanned along the workpiece radial position vertically. The wheel air spindle rotated vertical and the workpiece air spindle rotated horizontally. The feature of this grinding system was that the wheel rotated in the parallel with the workpiece rotational direction at the grinding point. With the NC-controlled sharp edged wheel, the axi-symmetric aspherical fresnel shaped workpiece will be generated.

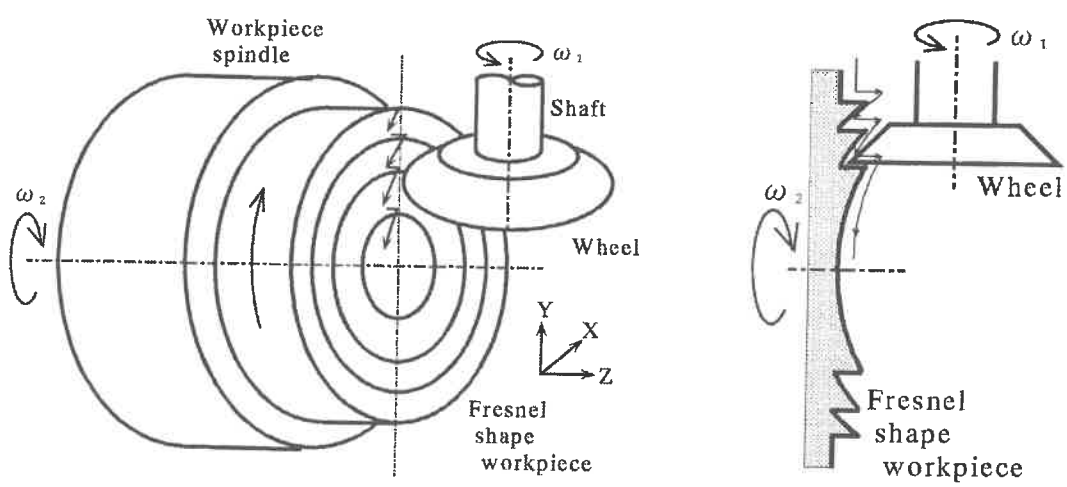

(a) Schematic illustration (b) Cross-section BB

Fig.1 Schematic diagram of newly developed micro fresnel grinding system

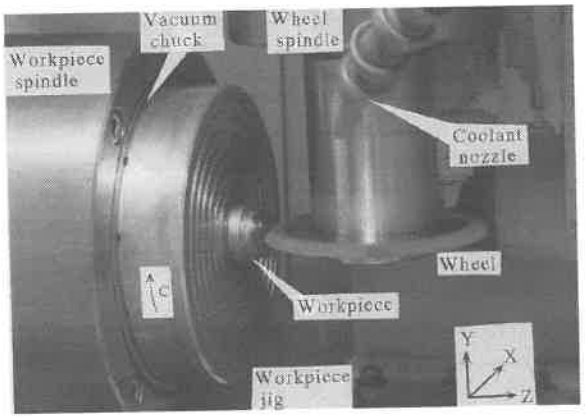

Fig.2 A view of aspherical grinding machine

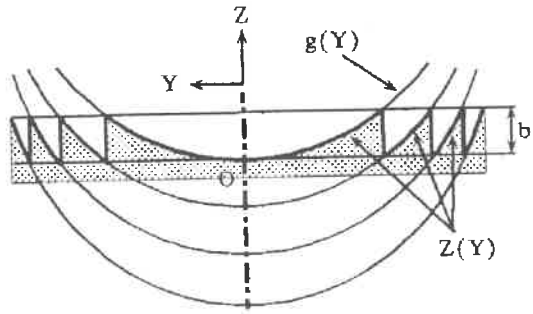

Fig.3 Shape of a target fresnel surface

Table 1 Grinding conditions

Wheel	Resinoid-bonded diamond
Grain size	#1200
Diameter	Φ70 mm
Rotational rate	2×10^4 rpm
Depth of cut	2 μm
Feed rate	0.025 – 0.4 μm/rev
Coolant	Solution type

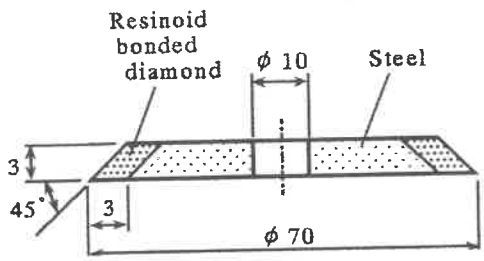

Fig.4 Shape of a diamond wheel

2. Grinding system and grinding method

(a) Grinding machine

A view of the simultaneous 4-axes (X, Y, Z, C) controlled grinding machine is shown in **Fig. 2**. The grinding spindle was actuated in X, Y and Z-axes by the linear scale feedback system of 1 nm positioning resolutions. The grinding spindle and workpiece spindle were equipped with air bearings and the maximum rotational rate of grinding wheel was 4×10^4 rpm and that of workpiece spindle was 3×10^3 rpm. In this grinding experiments, the grinding spindle was simultaneous 2-axes (Y, Z) controlled. The wheel horizontal position was adjusted with X-axis table and was fixed in the aspherical grinding.

(b) Grinding conditions

The workpiece shape shown in **Fig. 3** was tested, which outer diameter was about 4 mm. The material was tungsten carbide of ultra-fine particles for glass press molding. The grinding conditions are shown in **Table 1**. As a wheel, a resinoid bonded diamond wheel of #1200 in a grain size was used. This was because to decrease the wheel wear which will cause the workpiece form error. The wheel feed fate was varied between 0.025 - 0.4 mm/min in order to decrease the grinding force change. The 45 degrees sharpen wheel in **Fig. 4** was trued on the machine by using a disk type of #200 diamond wheel vacuum-chucked in the workpiece spindle.

3. GLASS MOLDING SYSTEM AND METHOD

(a) Glass molding press machine

Fig.5(a) shows a view of glass molding press machine and **Fig.5(b)** shows a view of molding die installed in the press machine. Dies with outer diameters of up to 110 mm can be mounted to make possible the molding of a number of small diameter lenses in a single operation. **Fig.5(c)** shows a view of molding unit. Infrared heating system can heat the dies and glass

materials quick and distributed equalize for greater productivity. Cooling of the dies and glass lenses are carried out by a cooling system with water and nitrogen gas. **Table 1** shows specifications of the press machine. Maximum heating temperature is 800 °C and maximum pressing force is 2 $\times 10^4$ N. The die temperatures are measured with thermocouples and controlled accurately by the NC controller system.

(b) Glass molding process

Fig.6 shows a schematic diagram of a glass molding process. At first, a ball of glass material is set between the upper die and lower die. And at the second process, the molding unit is purged with nitrogen gas, and glass material is heated by the infrared heating system and pressed with load. Finally, after cooling the molding dies and the molded lenses by the cooling system with cold water and nitrogen gas, the glass lenses are ejected. In this molding experiment, the dies material of tungsten carbide was used and the surface was coated with platinum (Pt) by sputter deposition. The molding conditions are shown in **Table 2**.

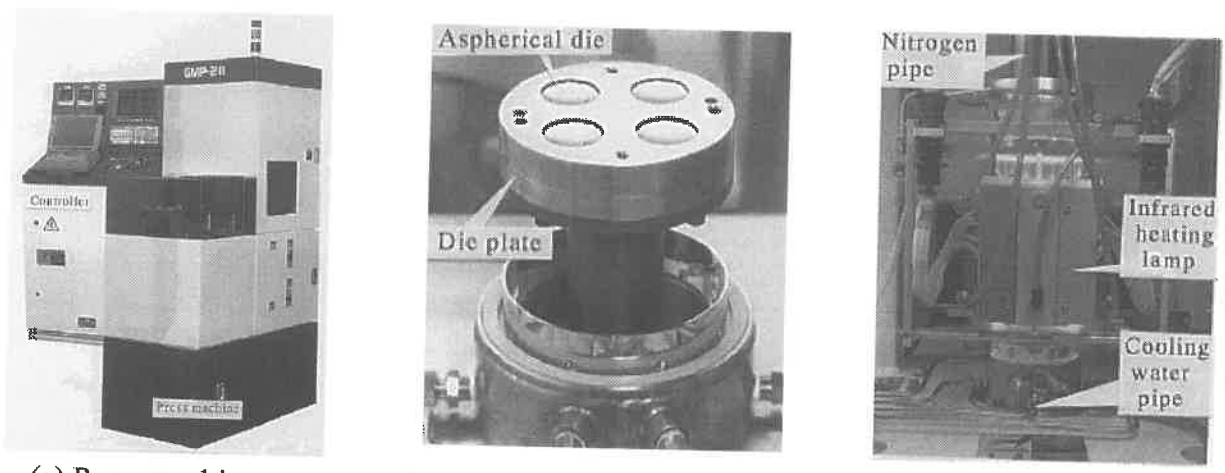

(a) Press machine (b) Molding die and die plate (c) Infrared heating system

Fig.5 Views of glass molding press machine

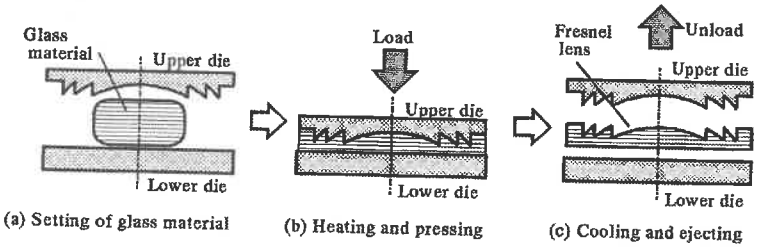

(a) Setting of glass material (b) Heating and pressing (c) Cooling and ejecting

Fig.6 Glass molding process

Table 2 Glass molding conditions

Glass material	L-BAL42
Transformation temperature	506 °C
Sag temperature	538 °C
Softening temperature	607 °C
Molding die	Binderless WC
Coating material	Pt
Molding temperature	550 - 580 °C
Pressing force	250 - 4000 N

4. Grinding and glass molding results

3 dimensional topographies of a ground workpiece (WC) and a molded lens are shown in **Fig.7**. The form profiles were measured by non-contact type of laser scanning instrument (Mitaka-kohki, NH-3). The form profiles of the cross section in the radial direction are shown in **Fig.8**. The profiles were measured with contact type of surface measurement instrument (Matsushita, UA-3P) with a 2 μm diamond stylus. From the measured profiles, it was found that the sharp edge was created comparatively precisely. The form deviation profile of ground

workpiece compared with the reference form and calculated from Fig.8 is shown in **Fig.9**. In case of a die, the form accuracy of about 0.3 μmP-V was obtained and high accuracy was kept.

Conclusions

A grinding system of 4-axes, vertically controlled new grinding method and a disk type of wheel with a sharp knife edge were developed. In a feasibility study of the fresnel shape grinding, the molding die of tungsten carbide for glass lens were ground in trial. From the experiments it was clarified that ultra-precision grinding of micro fresnel shape could be performed with a resinoid bonded diamond wheel. Then the glass lenses were molded. From the grinding experiments, the form accuracy of about 0.1 μmP-V and the surface roughness of about 0.03 μmRy were obtained, and it was clarified that precision grinding and molding of micro fresnel shape could be performed by the newly developed micro grinding system and glass molding method.

References

[1] H. Suzuki, et al.: Precision Grinding of Micro Fresnel Lens Molding Die, Proceedings of 1st euspen, (1999)318.

[2] H. Suzuki, et al.: Precision Grinding of Molding Die and Glass Molding in Micro Optical Components, Proceedings of 9th ICPE, (2001)126.

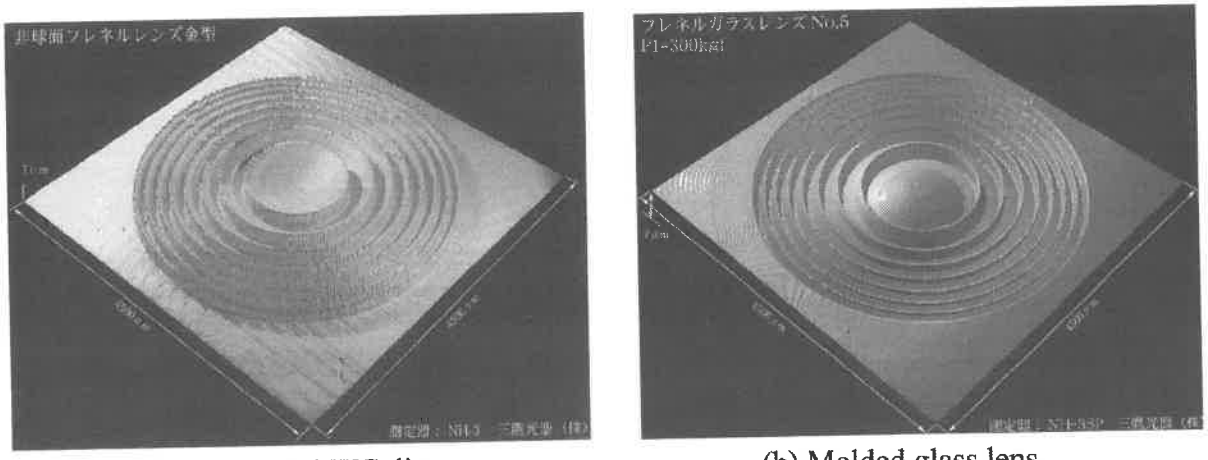

(a) Ground WC die (b) Molded glass lens

Fig.7 3-dimensional topography of fresnel surface

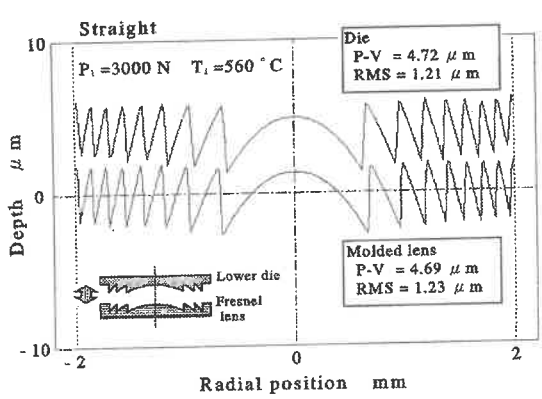

Fig.8 Profiles of cross sections

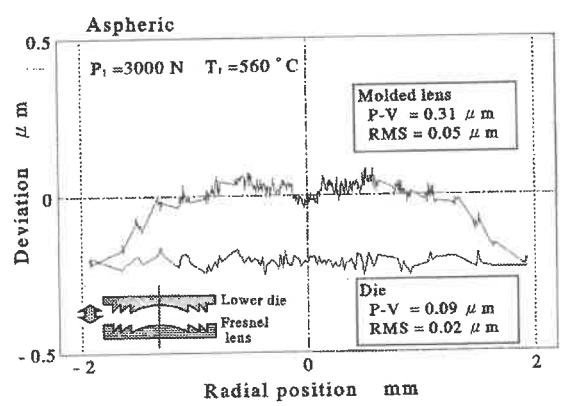

Fig.9 Deviation profiles

EVALUATION OF GRINDING CONDITIONS USING DYNAMIC COMPONENTS OF GRINDING FORCE IN CENTERLESS GRINDING

Yongbo WU and Masana KATO,
Department of Machine & Intelligence Systems Engineering, Akita Prefectural University
Tsuchiya-Ebinokuchi 84-4, Honjo, Akita 015-0055, JAPAN
Katsuo SYOJI and Tsunemoto KURIYAGAWA
Department of Mechatronics and Precision Engineering, Tohoku University
Aramaki-Aoba 01, Sendai 780-8579, JAPAN
Toru TACHIBANA
Micron Machinery Co.,Ltd, Uwano Zao 578-2, Yamagata 990-2301, JAPAN

1. Introduction

In a centerless grinding operation the workpiece rounding mechanism is very complicated, and it is difficult to optimize the grinding conditions for minimizing the workpiece roundness error. Authors had proposed the optimum grinding conditions [1]. However, the selected process parameters based on the proposed optimum grinding conditions might become unsuitable as the grinding wheel and regulating wheel are wore down during grinding. Consequently, in order to re-setup the optimum grinding conditions efficiently and certainly, automatically selecting the process parameters are necessary. For this purpose, an evaluation function of grinding conditions called the waviness decrease rate had also been provided [2].

To build the closed-loop control system for the process parameters, however, it is necessary to find a practical way to measure the waviness decrease rate. In this paper, a relationship between the waviness decrease rate and the dynamic components of grinding force was investigated analytically. It was found that the frequency characteristics of the waviness decrease rate shows a similar tendency to that of the dynamic components of grinding force. Then, a grinding force measurement system was built and measurement and evaluation of the grinding force were carried out. As a result, it was confirmed that the grinding conditions could be evaluated using the dynamic components of grinding force.

2. Principle of obtaining the waviness decrease rate from the dynamic components of grinding force

Fig.1 shows the geometrical arrangement of centerless grinding. R_{wo} is the radius of the workpiece average circle. Let a waviness component on the workpiece ground for i revolutions at frequency n be a vector $r_i(jn)$ on the complex number plane, the component on the initial workpiece (i=0) and that on one ground for N revolutions (i=N) can be expressed as $r_0(jn)$ and $r_N(jn)$, respectively. Then a relationship between $r_0(jn)$ and $r_N(jn)$ will be as follows [2].

$$r_N(jn) = \kappa_r^N(jn) r_0(jn) \tag{1}$$

Where

$$\kappa_r(jn) = 1 \Big/ \left[1 + \frac{\kappa}{1-\kappa} \left\{ 1 - \frac{\sin\gamma}{\sin(\phi+\beta)} e^{-j(\phi-\alpha)n} + \frac{\sin(\phi-\alpha)}{\sin(\phi+\beta)} e^{-j(\pi-\gamma)n} \right\} \right] \tag{2}$$

is called the waviness decrease rate [2], and κ=$K_m/(K_m+K_s)$(K_m, the machine stiffness and K_s, the grinding stiffness)[3].

Generally the amplitudes of waviness on initial workpiece in low frequency region are bigger than that in high frequency region. Therefore, in order to decrease roundness error the grinding conditions must be set-up so that the waviness decrease rate $\kappa_r(jn)$ in low frequency region becomes as smaller as possible according to Eq.(1). Thus, if frequency characteristics of $\kappa_r(jn)$ has been obtained in practice, the grinding conditions could be evaluated with this standard.

To find a practical way for obtaining the frequency characteristics of $\kappa_r(jn)$, a relation of it to the frequency characteristics of the dynamic component of grinding force was discussed as bellow.

First, assuming the grinding force is proportional to the depth of cut gives a relationship between the dynamic component of grinding force and the waviness component as Eq.(3) [2].

$$F_{Gni}(jn) = K_s \Delta_i(jn) = K_s\{r_i(jn) - r_{i-1}(jn)\} \quad (3)$$

where $F_{Gni}(jn)$ is the dynamic component of grinding force at frequency n in the i th revolution of grinding, and $r_i(jn)$, $r_{i-1}(jn)$ are the waviness components at frequency n in i th and (i-1) th revolution of grinding respectively. Then, next formula can be obtained from Eq. (3).

$$r_N(jn) = r_0(jn) + F_{GnS}(jn)/K_s \quad (4)$$

where $F_{GnS}(jn) = \sum_{i=1}^{N} F_{Gni}(jn)$ (5)

Substituting Eq.(1) in Eq.(4) and arranging it, an equation is obtained as Eq.(6).

$$\kappa_r^N(jn) = 1 + \frac{1}{K_s}\frac{F_{GnS}(jn)}{r_0(jn)} \quad (6)$$

Eq. (6) shows that on the complex number plane the vector $\kappa_r^N(jn)$ is obtained by moving only 1 parallel along the real axis, after the vector $F_{GnS}(jn)/r_0(jn)$ is expanded (or reduce) in magnification of $1/K_s$, as K_s is a real number. Therefore, according to the mapping principle of the complex number [4], the frequency characteristics of $F_{GnS}(jn)/r_0(jn)$ will be same as that of $\kappa_r^N(jn)$. Consequently, when the initial workpiece waviness $r_0(jn)$ has been known, the frequency characteristics of $\kappa_r^N(jn)$ can be obtained by measuring $F_{GnS}(jn)$.

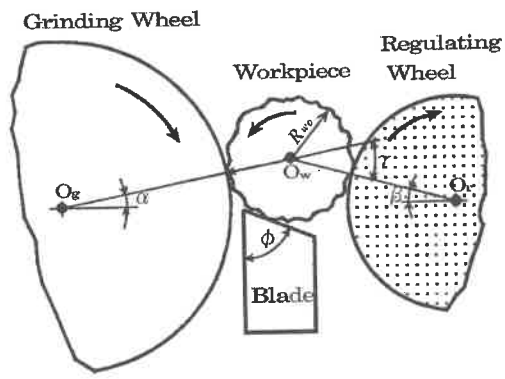

Fig.1 Geometrical arrangement of centerless grinding

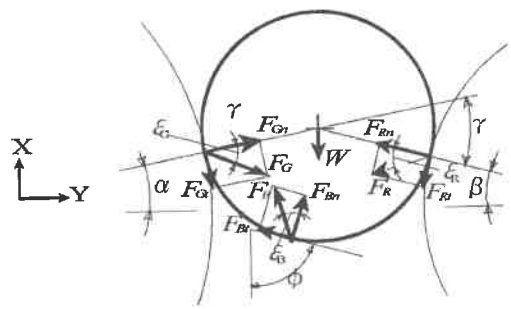

Fig.2 Forces on workpiece

3. Measuring method of dynamic components of grinding force

As above mentioned, the waviness decrease rate $\kappa_r(jn)$ can be obtained from the dynamic component of normal grinding force F_{Gn}. However in centerless grinding, it is very difficult to measure F_{Gn}. In this work, instead of F_{Gn} the force on the blade is used to obtain $\kappa_r(jn)$ in a way as bellow.

Figure 2 shows the forces on the workpiece. Let the vertical (X direction) component of the force F_B on the blade be $F_{Bx}(\theta)$, a relationship between $F_{Gn}(\theta)$ and $F_{Bx}(\theta)$ is obtained from the equilibrium of forces on workpiece as bellow [5].

$$F_{Gn}(\theta) = K_B F_{Bx}(\theta) - K_W W \quad (7)$$

where $K_B = \dfrac{\sin(\varepsilon_B - \varepsilon_C + \phi + \beta)\cos\varepsilon_G}{\sin(\varepsilon_G + \varepsilon_C - \gamma)\sin(\varepsilon_B + \phi)}$, $K_W = \dfrac{\cos(\varepsilon_C - \beta)\cos\varepsilon_G}{\sin(\varepsilon_G + \varepsilon_C - \gamma)}$,

and θ is the workpiece rotation angle measured from the grinding start point. The angles ε_B and ε_C depend on the friction coefficients between the workpiece and the blade, the regulating wheel, respectively. The angle ε_G is determined by the ratio of normal component of grinding force to its tangential component. Because the geometrical arrangement (β, γ, ϕ) and the angles ε_B, ε_C, ε_G are independent of the grinding time in a grinding cycle, the coefficients K_B, K_W can be regarded as constant.

As the workpiece rotation angle θ is proportional to the grinding time, doing Laplace transform of Eq.(7) on i th revolution of grinding ($2\pi(i-1) \le \theta \le 2\pi i$) gives a relationship between $F_{Gni}(jn)$ and $F_{Bxi}(jn)$ at frequency n as bellow.

$$F_{Gni}(jn) = K_B F_{Bxi}(jn) \quad (8)$$

Then substituting Eq.(8) in Eq.(5) and arranging it, an equation is obtained as following.

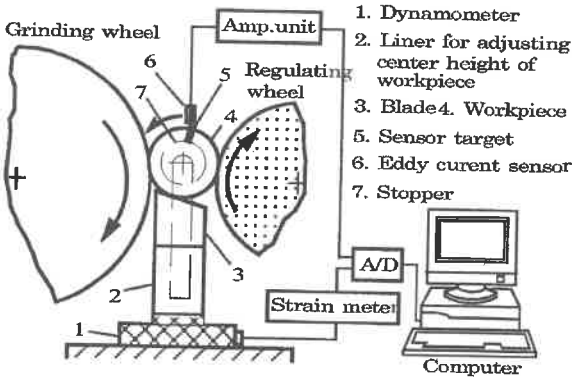

Fig. 3 Sketch of experimental system

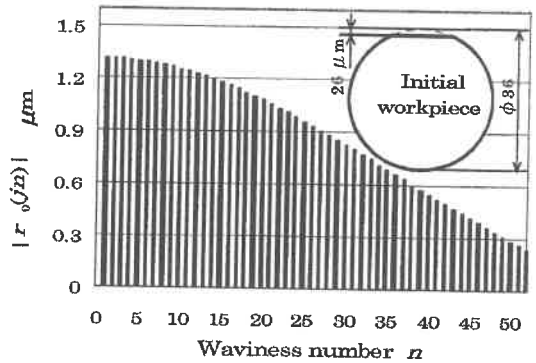

Fig. 4 initial workpiece

$$F_{GnS}(jn) = K_B F_{BxS}(jn) \tag{9}$$

where

$$F_{BxS}(jn) = \sum_{i=1}^{N} F_{Bxi}(jn) \tag{10}$$

As K_B is a real number, the frequency characteristics of $F_{BxS}(jn)$ should be equal to that of $F_{GnS}(jn)$ according to the mapping principle of complex number. Consequently, we know from Eq.(9) and Eq.(6) that the frequency characteristics of $\kappa_r^N(jn)$ can be obtained by measuring $F_{BxS}(jn)$.

A measuring system for $F_{BxS}(jn)$ was produced as shown in **Fig. 3**. The output signal of the dynamometer is used to obtain $F_{Bxi}(jn)$ (i=1,2,…,N). To extract the signal every revolution of workpiece, a trigger signal is necessary to divide the signal for each revolution. In this system, the trigger signal is obtained by detecting the position of a small iron piece (the sensor target) stuck on the workpiece with an eddy type proximity sensor The analog signal of dynamometer is sampled through an A/D board by a personal computer. The sampling rate was set at 400Hz.

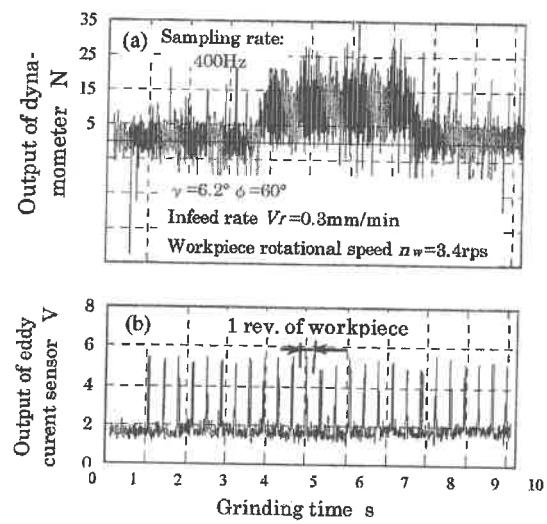

Fig. 5 Outputs of experimental system

4. Measurement of frequency characteristics of force on blade

Ferrite rings (36mm in outer diameter, 16mm in inside diameter 12mm in width) were ground on the produced experimental system, and the frequency characteristics of the output signal of dynamometer are calculated. Experimental procedures are as follows.

To begin with, the initial workpieces with a flat (see **Fig. 4**) are prepared. Next, centerless infeed grinding operations are carried out under the given grinding conditions, and the output signal of dynamometer and proximity sensor are incorporated into the computer. Then, the output signal is treated by FFT method to obtain the dynamic components for every revolution of workpiece, $F_{Bxi}(jn)$(i=1,2,3,…) responding to the trigger signal from proximity sensor. Thus, the parameter $F_{BxS}(jn)/r_0(jn)$ can be calculated using Eq.(10) and data in Fig. 4. Changing the center height by using different liners, the experiment on the above procedure was repeated. **Fig.5** (a) and (b) show an example for the outputs of dynamometer and proximity sensor, respectively.

Figure 6 shows the frequency characteristics of parameter $F_{BxS}(jn)/r_0(jn)$ obtained experimentally. Obviously, the frequency components of $F_{BxS}(jn)/r_0(jn)$ in low-frequency region of

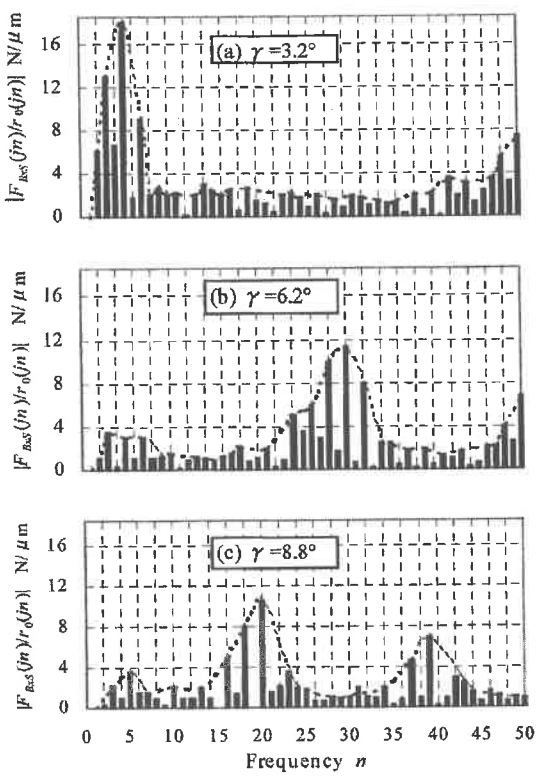

Fig.6 Frequency characteristics of parameter $F_{BxS}(jn)/r_0(jn)$

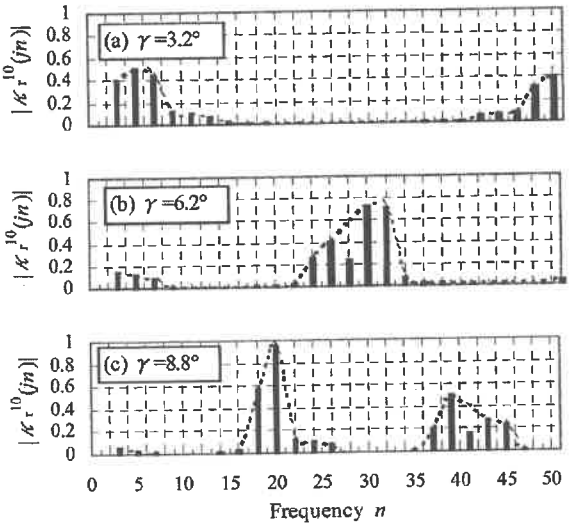

Fig. 7 Frequency characteristics of waviness decrease rate

N=3-7 are comparatively bigger than others at γ=3.2° (see Fig.6(a)). In the meantime, in the case of γ=6.2° (see Fig.6(b)), the high frequency components such as in 28-32Hz, especially at 30Hz are bigger than others. Furthermore, as the center height increase to γ=8.8°(see Fig.6(c)), the component at 20Hz is biggest.

To confirm the supposition mentioned in section 3 that the $\kappa_r(jn)$ can be obtained from the vertical component $F_{Bxr}(jn)$ of force on the blade, the calculated results of $\kappa_r^N(jn)$ (here N=10) with Eq.(2) are shown in Fig. 7. In comparison with Fig.6 and Fig.7, it is obvious that frequency characteristics of $F_{GrnS}(jn)/r_0(jn)$ and $\kappa_r^N(jn)$ agree with each other for all of the center height angle. Like this, it is confirmed experimentally that the grinding conditions can be evaluated by obtaining the frequency characteristics of the waviness decrease rate, which can be obtained by measuring dynamic component of vertical component of force on blade.

5. Summary

The evaluation of grinding conditions in centerless grinding was attempted by measuring the dynamic components of grinding force. The obtained results can be summarized as: (1) the frequency characteristics of the waviness decrease rate can be obtained by measuring that of the dynamic components of grinding force, (2) the frequency characteristics of the dynamic components of grinding force can be specified by measuring that of the dynamic component of vertical force on the blade, (3) the measuring system, which is mainly composed of a thin-type dynamometer was produced, and measurement experiments were carried out, as the result, it was confirmed that the grinding conditions can be evaluated using the dynamic components of vertical force on the blade.

Reference

(1) Y. Wu, K. Syoji, T. Kuriyagawa and T. Tachibana: Studies on centerless grinding (1st Report), J. of JSPE, 62(3), 433(1996).

(2) Y. Wu, K. Syoji, T. Kuriyagawa and T. Tachibana, Studies on centerless grinding (2nd Report), J. of JSPE, 65(6), 862(1999).

(3) W.B.Rowe and M.M.Barash: Computer Method for Investigating the Inherent Accuracy of Centerless Grinding, Int. J. MTDR, 4(1964) 91.

(4) K. Hiroike, T. Morida and M. Tanaka: Applied mathematics, Kyouritu-shuppan, 6.

(5) S. Yonetsu: Centerless grinding process and grinder, Nikkan-kougyo shinbun-sha, (1966).

DEVELOPMENT OF DEAD-END GRINDING MACHINE WITH LINEAR MOTOR DRIVEN TABLE

Akinori Yui, Shigeki Okuyama and Takayuki Kitajima
National Defense Academy
1-10-20, Hashirimizu, Yokosuka, Japan
Keiichi Kosugi
Okamoto Machine Tool Works, LTD.
3009 Gobara, Annaka, Gunma, Japan

Abstract

High efficient grinding machine for a small and precision tie-bar-cut punch is required from information technology allied industries. High Speed Stroke Grinding (HSSG) machine equipped with linear motor driven table is developed to response this demand. Since the table acceleration is controlled at a constant value, table speed always changes during the grinding operation. Table speed and cross sectional area of the generated chip under the HSSG is theoretically estimated, and they are also investigated exponentially to clarify the optimum grinding conditions for HSSG.

Key words: Dead-end grinding, Linear motor, Table acceleration, Tie-bar-cut punch, Mean chip cross sectional area, HSSG machine

1. Introduction

Since information technology has attained a rapid progress, demands for the applications of integrated circuits are rapidly expanding. The large numbers of the sophisticated IC lead frames, which are usually produced by the high-speed press machines, are necessary for the integrated circuits. The press machines are equipped with the precision tie-bar-cut punches, which should be very accurate and reliable, and the punches must be supplied quickly.

In order to manufacture the tie-bar-cut punches effectively, development of a highly efficient dead-end grinding machine has been required. Because conventional surface grinding machines has low table speed and large over-travel.

This paper describes a newly developed high-speed stroke surface-grinding (HSSG) machine equipped with a linear motor driven table for dead-end grinding.

2. HSSG system developed

High efficient surface grinding machines are roughly divided into two kinds. One is a creep feed grinding machine, which is characterized by an extremely slow table speed and large depth of cut. The other is a speed-stroke grinding machine, which realizes very high table speed under the shallow depth

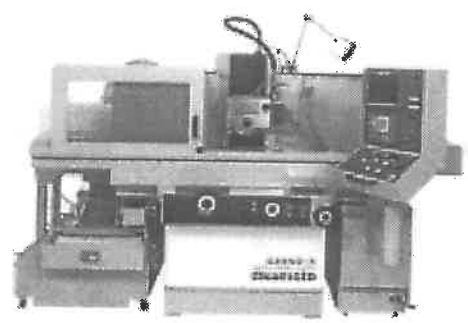

Fig.1 Surface grinding machine with linear motor driven table (HSSG) system

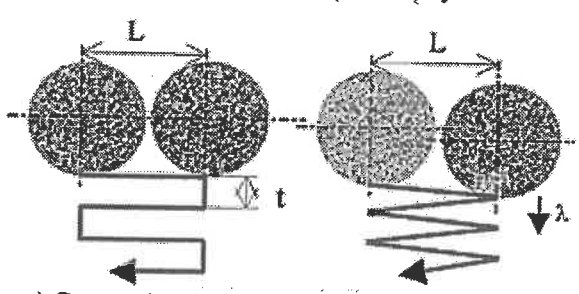

a) Conventional plunge grinding b) HSSG method

Fig.2 Schematic view of HSSG and conventional grinding methods

of cut. The HSSG machine is evolved from the speed stroke grinding machines. An appearance of the newly developed machine is shown in Fig.1. This machine has a function of continues wheel down feed under the high-speed stroke grinding operations as shown in Fig.2.

Table 1 shows the performance of the machine table developed. The linear motor driven table is suitable for realizing the very high table speed. The maximum speed of this table is 1.667m/s (100m/min), which is 4 to 5 times as much as the conventional machine tables.

To construct the table of lightweight and high rigidity, alumina ceramics are adopted for the main component of the table because of its high young's modulus.

As shown in Fig.3, a pair of permanent magnets is attached under the table and a pair of motor coils is installed in the saddle of the machine. This configuration is applied to eliminate the table mass and to balance the magnetic forces [1]. Since the linear motor table system does not have any mechanical transmission elements, it is easy to achieve high-speed motion with small energy loss [2].

Figure 4 shows the relationship between table position and table speed under the constant table acceleration. Because of the limitation of a laser measuring instrument, maximam tabel speed was set at 1.2m/s. The table speed shows an exponential inclease and declease under the constant acceleration and deceleration. Mesured data through the laser interfelometor (HP-5519B) almost agree to the estimated value.

Increase in table speed demands enhancement in wheel speed for a grinding efficiency. Then, the test machine was designed to realize the wheel speed of 200m/s, which is 7 times as much as the conventional machines.

3. Frequency of table reciprocation

In order to fully exploit the advantages of the HSSG machine developed it is necessary

Table 1 Performance of the machine table

Maximum table acceleration	19.6m/s^2
Maximum table speed	1.667m/s
Table stroke	300mm
Total mass of table unit	28kg
Power of linear motors	4.2kW
Resolution of table positioning	0.0001mm

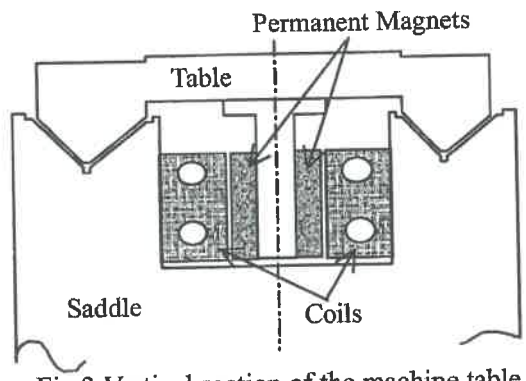

Fig.3 Vertical section of the machine table

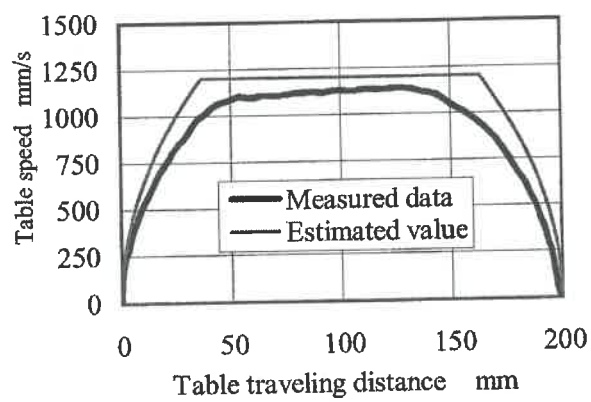

Fig.4 Comparison of measured table speed and estimated one under the constant table acceleration (α=19.6m/s^2, L=200mm)

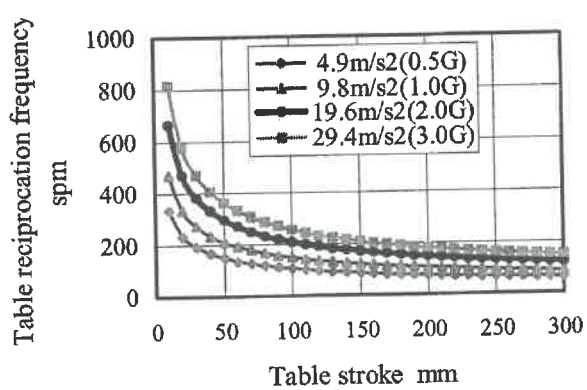

Fig.5 Relationship between table stroke and reciprocation frequency under the constant table acceleration

to achieve high frequent table reciprocation.

Frequency of the table reciprocation, S, can be estimated using table acceleration, α, and table stroke length, L.

$$s = 15 \cdot \sqrt{\frac{\alpha}{L}} \tag{1}$$

α is given by the following equation:

$$\alpha = \frac{F - W \times G \times \mu}{W} \tag{2}$$

where, F is power of linear motor, W is table mass, G is gravitation, and μ is coefficient of slide way friction.

Figure 5 shows the relationship between table stroke length and frequency of the table reciprocation. Owing to the application of a linear motor to the table drive system, the table has attained the performance of 469 reciprocations per minute at 20mm stroke.

4. Table speed under constant acceleration

Figure 6 shows change in table speed with time under the constant table acceleration in short stroke. In this condition, table speed v, is given by equation (3)

$$v = \alpha \cdot \tau \tag{3}$$

where, τ is time elapsed.

In case of the conventional grinding machines, which make use of the hydraulic table drive systems, the tables maintain their speed during grinding. On the other hand, table speed under the constant table acceleration changes exponentially. v will be given by equations (4) and (5).

$$v = \sqrt{2 \cdot \alpha \cdot l} \quad \left(\text{where}, 0 < l \le \frac{L}{2}\right) \tag{4}$$

$$v = \sqrt{2 \cdot \alpha \cdot (L - l)} \quad \left(\text{where}, \frac{L}{2} < l \le L\right) \tag{5}$$

where, ℓ is table position from the starting point of grinding. The table will be accelerated until it reaches the center of the table stroke according to the equation (4) and it is decelerated after passing the center of the stroke according to the equation (5) as shown in Fig.7.

5. Mean chip cross sectional area

Workpiece removal process in grinding can be qualitatively described by introducing the parameter a_m, mean chip cross sectional area, which is given by equation (6) [3].

$$a_m = \omega^2 \cdot \frac{v}{V} \cdot \sqrt{\frac{t}{D}} \tag{6}$$

where, ω is average cutting edge distance, V is wheel speed, t is wheel depth of cut and D is diameter of a grinding wheel.

Under the HSSG operation, t always changes. Because, grinding wheel is continuously down fed and table speed changes exponentially. Therefore, effective wheel depth of cut, t, can be given by the

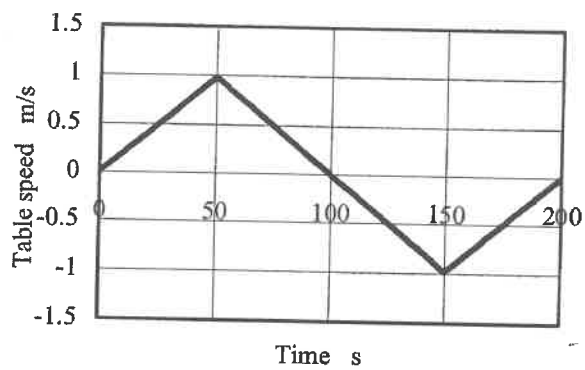

Fig.6 Change in table speed with time elapsed under the constant table acceleration (L=100mm, α=19.6m/s^2)

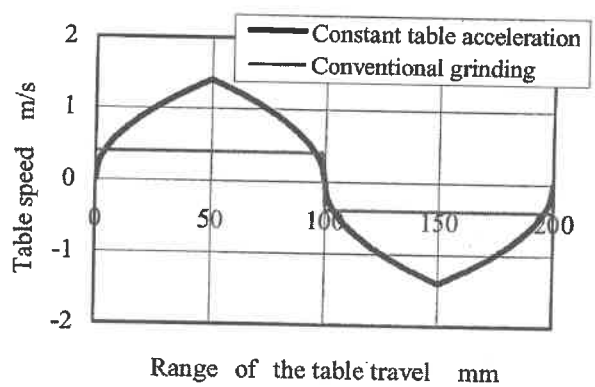

Fig.7 Change in table speed with table traversing distance (α=19.6m/s^2, v=0.4m/s, L=100mm)

following equation.

$$t = \lambda \cdot \sqrt{\frac{2 \cdot l}{\alpha}} \qquad (7)$$

where, λ is wheel down feed rate.

Therefore, the mean chip cross sectional area under HSSG, a_m, will be given by the equations (8) and (9).

$$a_m = \omega^2 \cdot \frac{\sqrt{2 \cdot \alpha \cdot l + \lambda^2}}{V} \cdot \sqrt{\frac{2 \cdot \lambda \cdot \sqrt{\frac{2 \cdot l}{\alpha}}}{D}} \qquad (8)$$

(where, $0 < l \leq \frac{L}{2}$)

$$a_m = \omega^2 \cdot \frac{\sqrt{2 \cdot \alpha \cdot (L-l) + \lambda^2}}{V} \cdot \sqrt{\frac{2 \cdot \lambda \cdot \left(\sqrt{\frac{4 \cdot L}{\alpha}} - \sqrt{\frac{2 \cdot (L-l)}{\alpha}}\right)}{D}} \qquad (9)$$

(where, $\frac{L}{2} < l \leq L$)

The mean cross chip sectional area has a peak value at the center of the table stroke as shown in Fig.8. The shape of the curve changes with the parameters, α and λ. In order to achieve the higher process efficiency, a_m should not be too small. Inversely, a_m should not be too big in order to avoid the extreme wheel wear.

Figure 9 shows a SEM photograph of chips generated by HSSG. Various sizes of chips can be observed, and the chip cross sectional areas are within 1.5×10^{-6} to 2.7×10^{-5} mm^2. These values almost agree with the estimated a_m through the equations (8) and (9).

6. Conclusions

1) A linear motor is applied to the table drive system of a surface-grinding machine, and the motor significantly increases the table speed and frequency of table reciprocation.
2) Under the HSSG operation, table speed and effective wheel depth of cut always change, and the generated chip size also changes during grinding.
3) High efficient dead-end grinding of the tie-bar-cut punch can be realized by HSSG machine developed.

References

[1] T.Kobayashi, I.Inasaki, H.Aoyama, A.Yui, A.Horikoshi, *Proc.IMTP*, 77 (1998), pp.77-83.

[2] I.Inasaki, Annals of the CIRP, Vol.48, No.1,(1999),pp.243-246.

[3] Toenshoff H.K., et al ; Annals of the CIRP, Vol.41, No.2, (1992), pp.677-688.

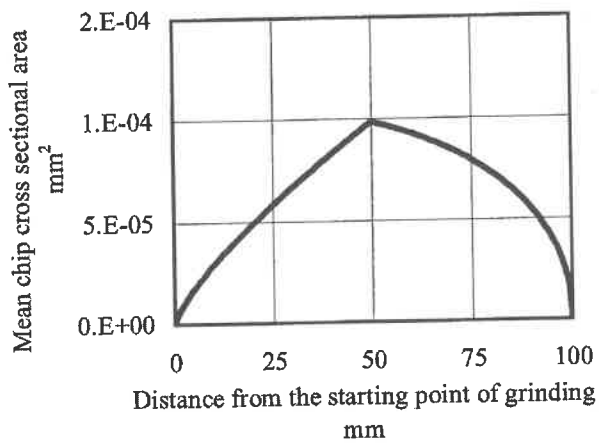

Fig.8 Change in mean chip cross sectional area under HSSG (ω=0.5mm, V=30m/s, λ=0.1mm/s, D=200mm, L=100mm, α=19.6m/s^2)

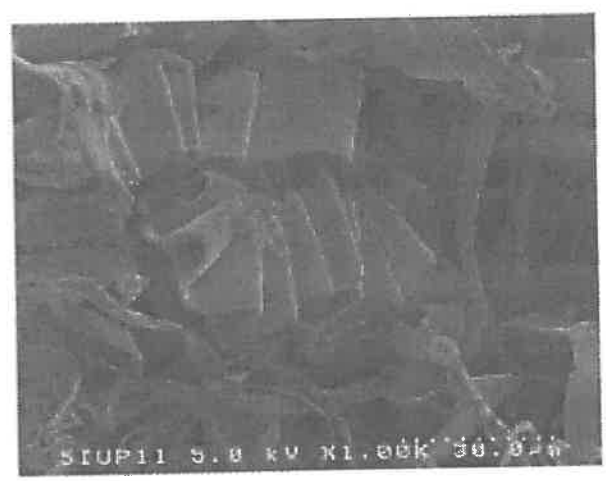

Fig.9 SEM photograph of chips by HSSG process (SK-3 H_RC58, λ=0.1mm/s, L=25mm)

Material Development of Si_3N_4-SiC Composites for Machining Application

Won Tae Kwon[1], June Seuk Park[1], Kyung Jae Kim[1] and Young-Wook Kim[2]
[1] Department of Mechanical and Information Engineering
[2] Department of Materials Science and Engineering
University of Seoul, Seoul 130-743, Korea

Composites of Si_3N_4-SiC that contained up to 30 wt% of dispersed SiC particles were fabricated via hot-pressing with an oxynitride glass. The mechanical properties and the cutting performance of resulting ceramic composites were investigated. By fixing the composition as Si_3N_4-20wt% SiC, the effect of sintering time on the microstructure, the mechanical properties, and the cutting performance were also investigated. The longer the sintering time is, the larger the grain size of SiC is. The fracture toughness(K_{IC}) of the Si_3N_4-SiC ceramic composites increased with the increase of grain size, while the flexural strength(σ) decreased. For machining SCM440, the insert with 20wt% SiC sintered for 8 hours showed the longest tool life while the insert with 20wt% SiC sintered for 12 hours showed the longest tool life for machining gray cast iron.

1. Introduction

One approach for tailoring properties is to combine the properties of different materials. Examples are SiC-TiC composites for improved fracture toughness [1,2] and Si_3N_4-SiC composites for improved strength [3,4]. A new approach that has received much less attention for developing advanced ceramic cutting tools is the incorporation of SiC in Si_3N_4 with oxynitride additives. SiC has higher hardness and oxidation resistance, whereas Si_3N_4 has better strength and thermal-shock behavior. In the present study, Si_3N_4-SiC ceramic composites that contained up to 30 wt% of dispersed SiC particles were fabricated via hot-pressing with an oxynitride glass. The microstructure, mechanical properties, and cutting performance of the resulting ceramics were investigated.

2. Experiments and Results

Commercially available β-SiC(Ultrafine, Ibiden Co., Ltd., Nagoya, Japan), α–Si_3N_4(Grade E10, Ube Industries, Tokyo, Japan), β–Si_3N_4(Grade SN-P21, Denkikagaku, Tokyo, Japan), were used as the starting powders. The combination of SiO_2(reagent grade, Kanto Chemical Co., Tokyo, Japan), MgO(high purity grade, Wako Pure Chemical Industries Ltd., Osaka, Japan), Y_2O_3(99.9% pure, Shin-Etsu Chemical Co., Tokyo, Japan), Al_2O_3(99.9% pure, Sumitomo, Chemical Co., Tokyo, Japan), and AlN(Grade F, Tokuyama Soda, Co., Tokyo, Japan) was used as the sintering additive [3]. Each sample was mixed and ball milled in ethanol for 24 h using polyethylene jar and SiC ball. The mixed

slurry was dried, subsequently sieved through a 60 mesh screen and hot-pressed at 1760°C under a pressure of 25 MPa in N_2 atmosphere. The composition and sintering conditions are given in Table 1. The hot pressed composites were cut and ground to make SNGN120416. The cutting performance of home made ceramic inserts were compared with commercial Si_3N_4 inserts (AS10, Taegu Tec, Tague, Korea). The mechanical properties of the home-made and commercial inserts were measured and compared in Table 2.

Home-made inserts have similar or a little bit lower fracture toughness, while they have higher hardness and Young's modulus than commercial insert. The cutting condition was 160m/min., 0.2mm/rev., 0.25mm depth of cut for machining of heat-treated AISI4140 (H_{RC}:58) and 330m/min., 0.2mm/rev. and 0.5mm depth of cut for machining of gray cast iron. All experiments were executed under dry cutting condition. Tool life was considered to be finished when the flank wear reached 0.3mm. To determine the effect of the sintering time on the characteristics of the cutting tool, the inserts with 20wt% SiC composition and various sintering time were manufactured and tested. The results are given in Fig. 2. Wear of SCN1 grew so fast that its life was finished in 30sec. SCN4 and SCN8 showed the similar performance with commercial tool before cutting time reached 30 sec after which wear grew faster than commercial tool. SCN8-20 has the longest tool life among them. No apparent relationship between mechanical characteristics and cutting performance was revealed by comparison Table 2 and Fig. 1. It may attribute to the fact that tool life is also affected by the other properties such as surface finish, density, grain size, and the size and the number of the inherent defects in the

Table 1. List of composition and sintering condition

Sample	Batch(wt%)			Sintering Time
	SiC	α-Si_3N_4	β-Si_3N_4	
SCN1-20	20	71	1	1hr
SCN2-20	20	71	1	2hr
SCN4-20	20	71	1	4hr
SCN8-5	5	86	1	8hr
SCN8-10	10	81	1	8hr
SCN8-20	20	71	1	8hr
SCN8-25	25	66.1	0.9	8hr
SCN8-30	30	66.1	0.9	8hr
SCN12-20	20	71	1	12hr
SCN16-20	20	71	1	16hr
SCN24-20	20	71	1	24hr

Table. 2 Mechanical properties of ceramic cutting tool materials

Sample	Fracture Toughness ($MPa \cdot m^{1/2}$)	Hardness (GPa)	Bulk Density (g/cm^3)
Si_3N_4	6.0	15.5	3.2
SCN1-20	4.5 ± 0.2	16.4	3.154
SCN2-20	5.2 ± 0.3	16.2	3.14
SCN4-20	4.7 ± 0.1	16.6	3.175
SCN8-5	6.5 ± 0.2	14.9	3.182
SCN8-10	5.7 ± 1.2	15.5	3.183
SCN8-20	4.7 ± 0.2	16.3	3.177
SCN12-20	5.5 ± 0.1	16.2	3.187

insert. Since SCN8-20 shows the best result, the sintering time for the development was set to 8 h and the composition of β-SiC was changed from 5 to 30 wt%. As shown in Fig. 2, the insert with 5wt% SiC had the shortest tool life. Generally, the more the amount of SiC, the longer the tool life, until the composition of SiC reaches 20wt%, after that tool life is getting shorter.

Next experiments were carried out to find the cutting performance of the developed ceramic inserts for machining gray cast iron. The cutting condition was set to one of the recommended condition whose cutting speed 330m/min., feed rate 0.2mm/rev. and 0.5mm depth of cut. The effect of the

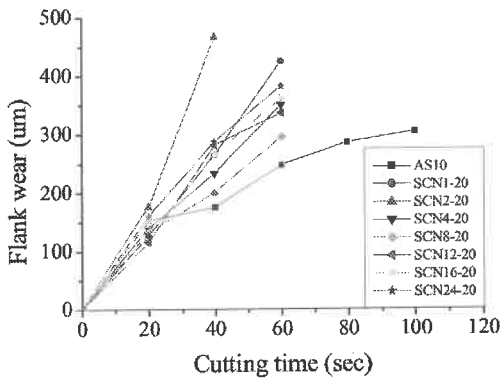

Fig. 1 Flank wear curve of different sintering time SCN-series during machining heat treated SCM440 with 160m/min cutting speed, 0.2mm/rev. feed rate and 0.25mm depth of cut

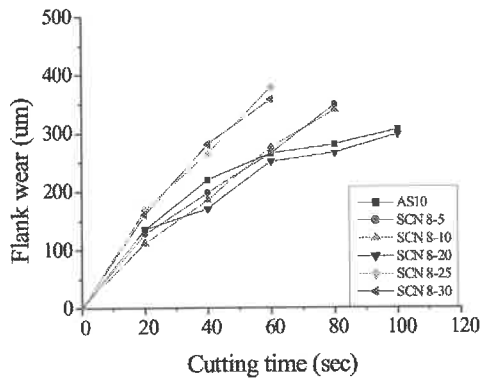

Fig. 3 Flank wear curve of different SiC content SCN-series during machining gray cast iron with 330m/min cutting speed, 0.2mm/rev. feed rate and 0.5mm depth of cut

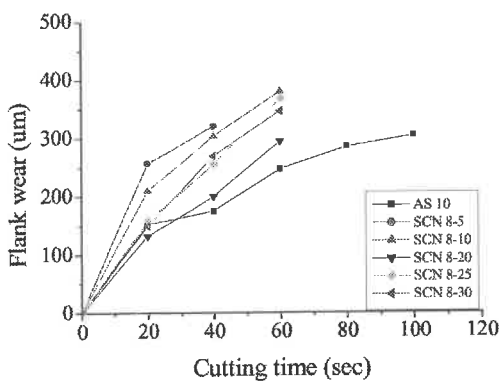

Fig. 2 Flank wear curve of different SiC content SCN-series during machining heat treated SCM440 with 160m/min cutting speed, 0.2mm/rev. feed rate and 0.25mm depth of cut

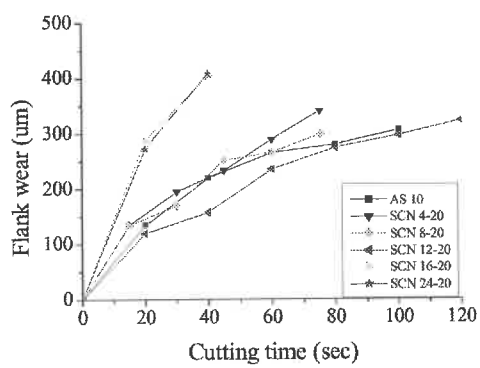

Fig.7 Flank wear curve of different sintering time SCN-series during machining gray cast iron with 330m/min cutting speed, 0.2mm/rev., feed rate and 0.5mm depth of cut

amount of SiC on the cutting performance was investigated and shown in Fig. 3. SCN8-20, which had the longest tool life during machining the heat-treated SCM440 had the longest tool life, again. In this case, the tool life of the SCN8-20 was longer than that of the commercial insert. The inserts with the SiC composition over 25wt% showed the poor cutting performance for machining gray cast iron.

The effect of the sintering time on the cutting performance was investigated and shown in Fig. 4. The composition of SiC was fixed as 20 wt%. For the inserts with relatively short sintering time (4 h), the tool life was short. As the sintering time is longer, so is the tool life until the sintering time reaches 12 h. The cutting performance of the inserts with 16 and 24 h deteriorated severely.

3. Conclusions

$SiC-Si_3N_4$ ceramics were manufactured and the effect of the sintering time and the composition was investigated for machining heat-treated SCM440 and gray cast iron. The insert with 8 h sintering time and 20 wt% SiC showed the best cutting performance for machining SCM440 and the inserts with 12 h and 20 wt% SiC for gray cast iron. No apparent relationship between mechanical characteristics and cutting performance was revealed.

Acknowledgement

This work was supported by Korea Research Foundation under Grant No. KRF-99-042-E00133

References

1. K.S. Cho, Y.-W. Kim, H. J. Choi, and J. G. Lee, "In Situ-Toughened Silicon Carbide-Titanium Carbide Composites," J. Am. Ceram. Soc., 79 [6] 1711-1713 (1996).
2. Y.-W. Kim, S. G. Lee, Y. I. Lee, "Pressureless Sintering of SiC-TiC Composites with Improved Fracture Toughness," J. Mater. Sci., 35, 5569-5574 (2000).
3. Y.-W. Kim, Y. I. Lee, M. Mitomo, H. J. Choi, and J. G. Lee, "Fabrication and Mechanical Properties of Silicon Carbide-Silicon Nitride Composites with Oxynitride Glass," J. Am. Ceram. Soc., 82 [4] 1058-1060 (1999).
4. Y.-W. Kim and M. Mitomo, "Fabrication and Mechanical properties of Silicon Carbide-Silicon Nitride Nanocomposites," J. Mater. Sci., 35, 5885-5890 (2000).

BURR FORMATION IN MICRO-MILLING

Kiha Lee[1], Ingo Essel[2], David A. Dornfeld[1]
1. University of California at Berkeley, Berkeley, CA
2. University of Technology at Aachen (RWTH), Aachen, Germany

Key words: burr formation, micro-machining, micro-burr, micro-milling

Abstract

Experimental studies on micro-milling in aluminum 6061-T6, stainless steel 304 and copper 110 have been carried out. A range of different cutting chip loads and depths of cut using 127μm, 254μm and 635μm diameters were considered. The influence of the cutting parameters on burr size and burr type was observed. A comparison to burr formation in different materials is presented.

Introduction

A phenomenon similar to the formation of chips is the formation of burrs at the end of a cut. Burrs are undesirable because they present a hazard in handling machined parts and can interfere with subsequent assembly operations. Thus, they must be removed in subsequent deburring processes to allow the part to meet specified tolerances.

A number of burr removal processes exist for conventional machining and except for the cost, can be conveniently applied. In the micro-machining process, however, the burr is very difficult to remove and, more importantly, the burr removal can seriously damage the workpiece. Conventional deburring operations cannot easily apply to micro-burrs.

Micro-milling here refers to machining with miniaturized end mills as small as 20μm. The miniaturized end mills have similar cutter geometries as conventional machine tools.

Research on burr formation in micro-milling of stainless steel, brass, aluminum and cast iron [1] [2] [3] has been reported. Micro burr formation, however, with respect to cutting conditions has been studied only in aluminum so far [3]. The fundamental mechanisms are not well understood. In this paper, the size and type of burr created in aluminum 6061-T6, stainless steel 304 and copper 110, are studied.

Chu [3] conducted a set of conventional slot and step milling tests to analyze burr formation in milling aluminum, 6061-T6 and reported milling burr types. Chu reported that the cutting speed has an insignificant influence on burr formation and larger feed per tooth induces large burrs in the feed direction. A series of experiments has been performed to investigate burr formation of three different materials in micro-milling.

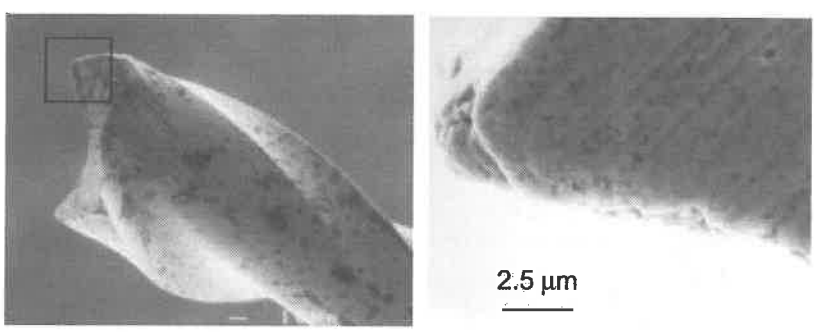

Figure 1. SEM of 127μm micro-mill (left) and its magnified cutting edge (right)

Experimental setup

For machining three materials two flute end mills (Figure 1), provided by RobbJack Corp., were used. It is a stub length version with a small cutting length for only low aspect ratios. Figure 1 illustrates 10,000 times magnified view of the major cutting edge, which is located at the left side of the top view. The cutting edge radius is around 1.3 μm. A micro end mill was attached to a Mori Seiki CNC Drilling Center TV-30. Micro-drop coolant was used.

To ensure the correspondence of burr formation in slot-milling with different tool diameters, the ratio of depth of cut to tool diameter was constant for each diameter, so that the ratio varies in the same range. The feed per tooth to tool radius ratio was also constant for every tool and it increased in five steps. The middle values of depth of cut and feedrate have been selected as recommended from a tool manufacturer, Table 1.

Table 1. Experimental cutting conditions

Diameter [mm]	v_c [m/min]	Depth of [μm]	Feedrate [mm/min]
0.635	15	40, 79, 119, 159, 318*	38, 75, 113, 150, 188
0.254	6	16, 32, 48, 64, 127*	15, 30, 45, 60, 75
0.127	3	8, 16, 24, 32, 64*, 127**	8, 15, 23, 30, 38, 64**

*only used for milling the copper alloy and aluminum, **only for aluminum

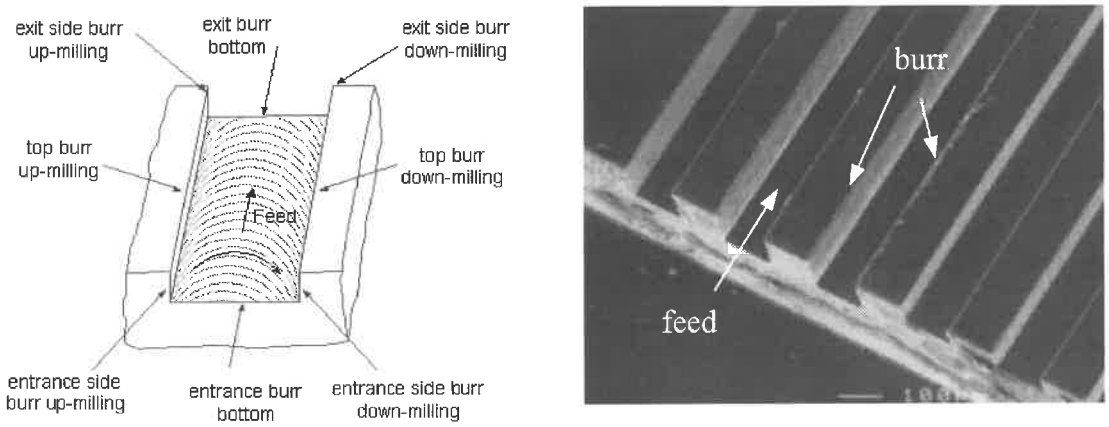

Figure 2. Burr definition and its location in slot milling (left) and machined slots (right)

Results

Burr definition and its location in slot milling can be seen in Figure 2. The entrance side burrs at up-milling as well as the exit side burr at down-milling were minimal because they are both characterized by tool entrance. For this reason they were not evaluated. Also, the bottom burr at the entrance side was too small for a reasonable evaluation.

Figure 3. Entrance of slot, aluminum (left), stainless steel (medium), copper (right)

Thus, five different burr types were important for the analysis of the influence of cutting parameters on burr formation: the entrance side burrs at the down-milling side, the top burrs from up- and down-milling, the exit burrs at the bottom of the slot and finally the exit side burrs at the up-milling side.

Entrance burrs

Curl-type entrance side burr was formed, Figure3. With higher feedrate, the burr size slightly increases for all the materials. The increase of the depth of cut resulted in a clear increase of the burr length for aluminum and copper. No similar result was not observed in stainless steel. Longer burr was formed in stainless steel, compared to other two materials. The lower strength of the copper and aluminum enabled a better fracturing and so less material was formed to the burr. From bottom to top at the entrance side in aluminum and copper, the burr size increases, because the cutting edge underneath end-mill first exits the workpiece and pushes the material to the top.

Top burrs

In slot milling operations top burrs occur at two different locations. As shown in Figure 4, one type of top burr is formed at the up-milling side and the other at the down-milling side of the cut. These burrs are difficult to remove in micro slot milling. Conventional deburring operations cannot easily remove these burrs. In milling aluminum, wavy-type burr is created when the tool enters the top surface of the workpiece with high feedrate. A ruptured-type burr results when the tool exits. With higher feedrate, the burr size increases. Depth of cut has an insignificant influence on burr formation in aluminum.

For stainless steel, at the upper side of the photo (Figure 4) the top burr from up-milling shows an orientation to the right, which is similar to the direction of the material flow as a result of tool rotation and feed motion. The bottom side of the photo displays the top burr from down-milling. As it can be seen in the photo it is a kind of rollover burr. Regarding the influence of an enhancement of depth of cut it can be reported that the top burrs from up- and down-milling decreased significantly. Up to the ratio of depth of cut to diameter, 3/16, burr size decreases. After that, burr increases as depth of cut increases because of tool wear. The results from milling stainless steel showed somewhat decreasing top burr on both when the feedrate was raised up to the degree in which tool wear increases. The main reason was the transient to a more regular burr on both sides.

As can be seen in Figure 4, milling the copper brought very good results with respect to the top burr formation at small depths of cut. Considerable top burrs first occurred when cutting with a high depth of cut, a half diameter depth. With higher feedrate, the burr size increases.

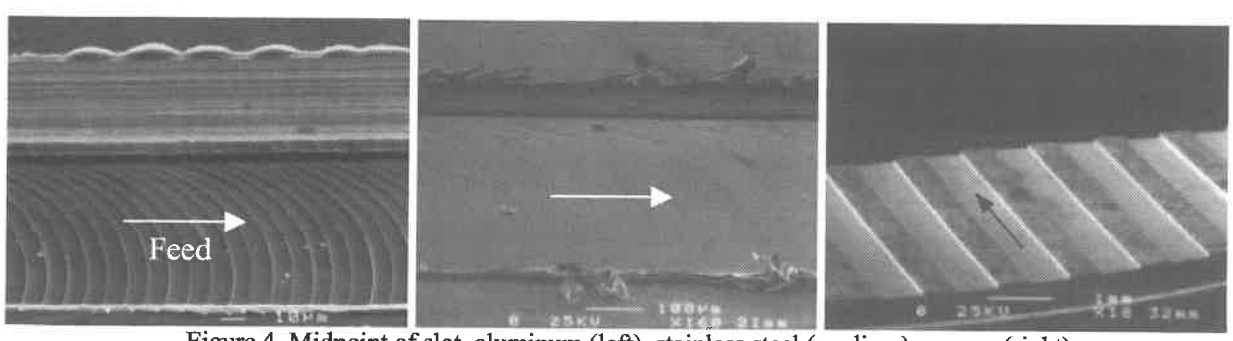

Figure 4. Midpoint of slot, aluminum (left), stainless steel (medium), copper (right)

Figure 5. End of slot, aluminum (left), stainless steel (medium), copper (right)

Exit burrs

Exit side burrs were always created in milling aluminum regardless of depth of cut and feed. As seen in Figure 5, it is a flag-type burr. The length of burr is roughly same as the width of slot. This burr is easier to be removed than top burr since it is attached to the workpiece slightly. Exit burr at the foot of slot in aluminum can hardly be observed.

In stainless steel, large bottom burr was formed. At the small depth of cut to 1/16 diameter-ratio the bottom burr and the exit side burr merged. The bottom burr height was bigger than the depth of cut of the slot, which leads to the conclusion, that the material was not only bent but also plastically deformed in the feed direction as can be seen in Figure 5. The burr height of the bottom burr slightly decreased with a raise of the feedrate at this small depth of cut. At higher feedrates, finally a large exit side burr was formed with smaller bottom burr.

The experimental results from micro-milling in copper did not take after stainless steel but aluminum. There was no transition from a bottom burr to a side burr formation. Concerning the exit side at up-milling in copper, it can be noted that three different types of workpiece edges occurred. It consists of a fin type burr which can be seen in Figure 5, the flag burr which occurred mainly at higher depths of cut and a sharp and small burr as a consequence of the detachment of fin type burr or flag burr.

Acknowledgments

This work was supported by the Consortium on Deburring and Edge Finishing (CODEF) at University of California at Berkeley. Information is available at http://lma.berkeley.edu. The authors thank Robbjack Corp. for supporting the work.

References

1. Damazo, B. N., Davies, M. A., Dutterer, B. S., Kennedy, M. D., 1999, "A summary of micro-milling studies," *1st International Conference of the European Society for Precision Engineering and Nanotechnology*, Bremen, Germany, 31 May - 4 June, 1999. 322-324
2. Schaller, T., Bohn, L., Mayer, J., Schubert, K., "Microstructure grooves with a width of less than 50μm cut with ground hard metal micro end mills," *Precision Engineering* 1999, Vol. 23, 229-235.
3. Lee, K., Stirn, B., Dornfeld, A., "Burr Formation in Micro-Machining, Aluminum, 6061-T6," *10th, International Conference on Precision Engineering*, Japan 2001
4. Chu, C. H., Integrated Edge Precision Machining, Ph.D. dissertation, Department of Mechanical Engineering, University of California at Berkeley, 2000

Reduction of Tensile Residual Stress and Cutting Force under High Speed Cutting

M. Nakao*, Y. Chen*, J. Konno*, Y. Hatamura** and N. Morita***

*The University of Tokyo, 7-3-1 Hongo, Bunkyo-ku, Tokyo 113-8656, JAPAN
** Kogakuin University
*** Chiba University

1. Introduction

High speed machining, not only enhances machining efficiency, but is effective in cutting hard steel and shapes with high aspect ratio like fins. In recent years, metal cutting of parts for information machines have applied the technique in milling micro structures using small size end mills at high speed. Hardly any research, however, has been made on how the cutting speed affects the cutting force or residual stress on the finished surface, or on the optimum machining conditions.

Our study aims at clarifying how the machining speed changes the residual stress on the finished surface and the machining force. For this study, we cut aluminum alloy at high speed using a single crystal diamond tool and a carbide end mill.

2. Residual Stress in High Speed Cutting

2.1 Stress Measurement Method

X-ray allows measuring stress distribution without contact or destruction. This method, which measures the change in Bragg angle from residual stress when the X-ray is reflected, however, has thin incidence depth, which is 1/10 of the layer of a few 10s μm depth affected by machining. Ultrasonic, on the other hand, measures the velocity when ultrasonic wave transmits on the surface, and this depth of travel approximately equals the depth of the affected layer, allowing more accurate measurement [1]. Fig. 1 shows the principle of ultrasonic measurement. Casting an ultrasonic wave on the specimen surface leaks part of it from the specimen surface. This leaky surface elastic wave (A-B-O-C-D) interferes with the perpendicular reflection wave (E-O-E) to intensify or weaken each other depending on the distance z between the lens and the specimen.

Fig. 2 sketches the interference wave intensity when z varies. The horizontal axis is the x-direction scan distance and the vertical, the lens-specimen distance. Naming the intesified area from interference z1, z2, and z3 from the top, the pitch (z1-z2 or z2-z3) quantitatively gives the surface elastic wave velocity (call sonic speed). The measurement range (B-C) is ϕ 10 μm when z is smallest. This sonic speed depends on the material surface stress, thus, residual stress on the machined surface is found by finding the relation between stress and sonic speed for the specimen material beforehand.

We used an ultrasonic microscope (Hitachi Construction Machinery HSAM200) for measuring the sonic speed. We measured the stress and sonic speed relation ahead of time by loading stress to the specimen within the microscope with a 4 point bending stress loading device.

2.2 Sonic Speed Dependent on Stress and Roughness

Our preparatory test applied surface stress to the aluminum-magnesium tempered alloy (A5052-O) with the 4 point bending stress loading device and for each stress value, plotted sonic speed at an arbitrary point. Fig. 3 shows the relation between the aluminum alloy surface stress and sonic speed derived from Fig. 2. The alloy had its mirror surface smoothed by a lapping process for this measurement. The change in sonic speed from the data in Fig. 3 is its difference when the material is stress free and when loaded. Tensile stress is noted positive, and compression negative. The ultrasonic microscope had resolution of 15 m/s and shows +/-30 m/s variation when free of load depending on the crystal orientation. To remove this dependency on orientation, we slightly marked a 200 μm square area with ultraviolet laser then the measured location repeated within +/- 5 μm.

Fig. 3 shows that sonic speed reduces with tensile stress and it increases with compression. The change is proportional to the stress within +/-60 MPa. The change of sonic speed is not proportional to the stress off the 60 MPa limit due to plastic deformation.

We next prepared a specimen with a surface rough but heat treated and annealed to remove the residual stress. Fig. 4 shows the relation of surface roughness and sonic speed. The symbols indicate sonic speed at each measurement point. The figure shows that sonic sound

largely varies (+/-500 m/s) when the surface is no longer a 0.1 μm (p-p) mirror surface. This is due to the change in ultrasonic wave path (BOC in Fig. 1) with a rough surface. Fig. 5 shows interference data like Fig. 2 when the surface is rough; 6 μm (p-p). The figure shows, when the surface roughness increases, the large change happens in z1, z2, and z3 as the measurement point moves in the x-direction. This wave form is not synchronized with the x-direction and the BOC path widens with greater z to be affected by the surrounding roughness, and as a result, the sonic speed gave more variation as Fig. 4 shows. Fig. 6 is the stress and sonic speed correlation similar to Fig. 3. Measurements taken at the same location have wider variation and larger change in sonic speed, however, similarly to Fig. 3, the sonic speed changes negatively in tensile area, and positively in compression.

2.3 Residual Stress on High Speed Cutting Surface

We measured the sonic speed on aluminum alloy after planer cutting with a single crystal diamond tool and a carbide tool (front rake: 0 degrees, relief angle: 5 degrees), and rotational cutting with a carbide end mill. We prepared the cutting area in the same manner using ultraviolet laser marking and narrowed the measurement point to a single point.

2.3.1 Residual Stress in Planar Cutting

Fig. 7 shows the change in sonic speed on the cut surface with white symbols, and on the uncut with black symbols. The depth of cut was 10 μm and width 900 μm. From the figure, the uncut reference surface was confirmed to have no stress, but the cut surface had some residual stress. Cutting speed of 0.1 m/s caused tensile stress in the range 10-50 MPa, whereas 8 m/s gave compression of about 35 MPa. Tensile stress turned to compressive at 5 m/s. We believe the reason is the heat contained in the chips with higher speed machining to reduce the tensile heat stress on the cut surface, however, we have not gathered enough data to prove this theory. Fig. 8 shows similar results with the carbide tool. But the larger radius of the cutting edge made the larger compression stress.

2.3.2 Residual Stress in Rotational Cutting

We measured the residual stress under 4 different conditions of cutting depth 0.5 μm and 2.5 μm and cutting direction upward and downward. Fig. 9 shows the 2.5 μm depth downward cutting made compression stress, but the 0.5/2.5 μm depth upward cutting reduced tensile stress as linear cutting speed increased from 5 m/s to 10 m/s.

3. Cutting Force in High Speed Cutting

3.1 Force Measurement Method

We fixed the aluminum alloy work on a table, driven by a linear motor of a milling machine, and measured the cutting force to identify the relation between cutting speed and cutting force. For this test, we installed a 3-axis sensor (KISTLER 9256A) with an accelerometer to cancel the effect of inertia. Fig. 10 shows the measured output, measured acceleration, and the resulting waveforms of subtracting the later from the former. The later figures show the inertia with the work table acceleration.

3.2 Cutting Force in High Speed Cutting

Fig. 11 shows the horizontal component Fy and vertical component Fz to relate them to the cutting speed of aluminum alloy. Fy and Fz increase with the cutting speed when it is 3 m/s or less, and decreases again when the cutting speed exceeds 3 m/s. Fig. 12 is the resulting cutting force with a carbide tool, showing the same trend with Fig. 11. The reason is, we believe, the tool speed exceeding the speed of heat diffusion, causing temperature rise on the rake contact surface of the chips that lubricates the interface to reduce friction.

4. Conclusion

We clarified the relation between the cutting speed and surface residual stress, and the cutting speed and cutting force so that we can find the effect of high speed machining on the cutting surface of aluminum alloy. Ultrasonic measurement of the surface residual stress revealed that when the cutting speed exceeds 4-5 m/s, the residual stress turns from tensile to compressive. Also, measuring the cutting force with a force sensor that compensates for inertia showed that the force is maximized when the cutting speed is 2-3 m/s

References

[1] K. Yoshida, et al.: *J. Jpn Soc. Precis. Eng.*, **64**: pp. 1679, 1998.

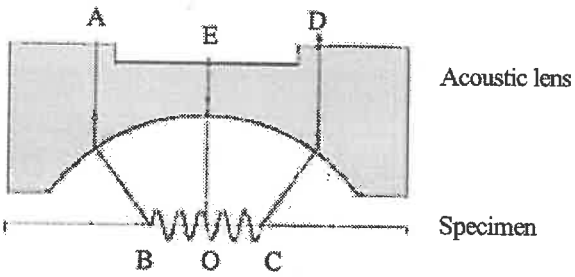

Fig. 1: Principle of ultrasonic wave measurement

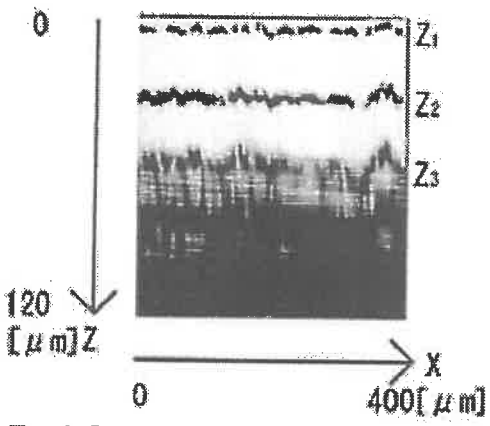

Fig. 2: Image generated by ultrasonic wave microscope on the smooth surface

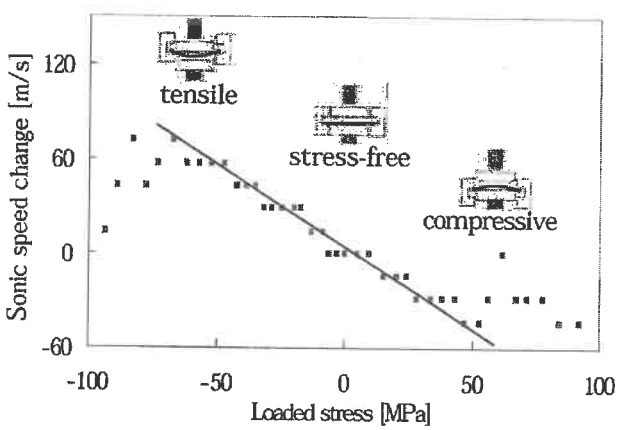

Fig. 3: Change of sonic speed when stress is applied to aluminum alloy with 4 point bending stress loading device on the smooth surface

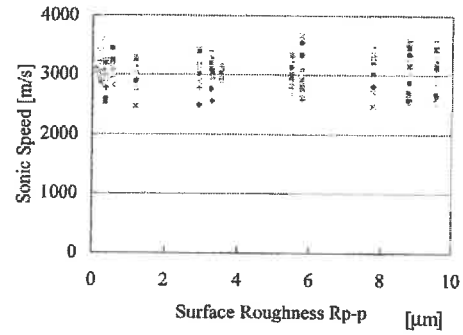

Fig. 4 Relation of surface finish and sonic speed

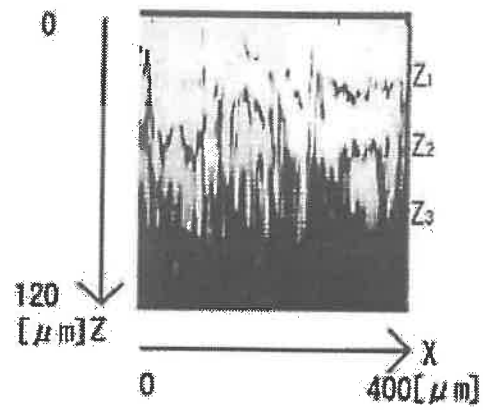

Fig. 5: Image generated by ultrasonic wave microscope on the rough surface

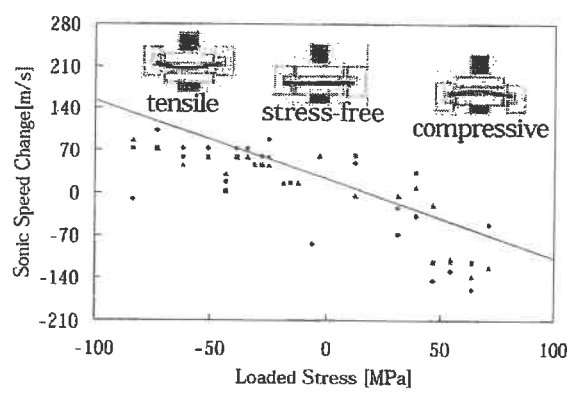

Fig.6: Change of sonic speed when stress is applied to aluminium alloy 4 point bending stress loading device on the rough surface

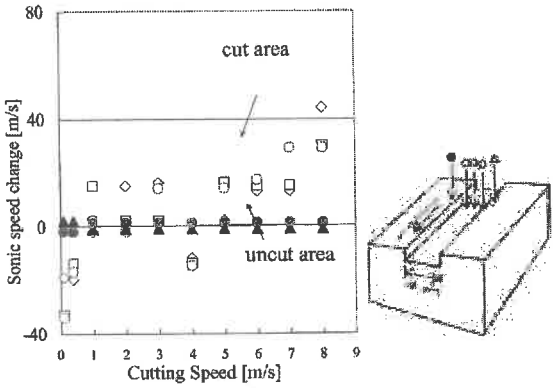

Fig. 7: Relation of aluminum alloy cutting speed and sonic speed change using diamond tool

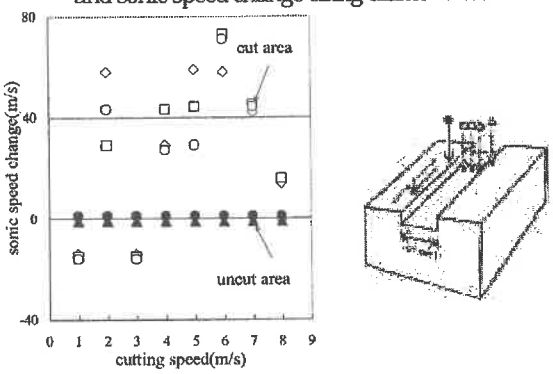

Fig. 8: Relation of the aluminum cutting speed and sonic speed change using carbide tool

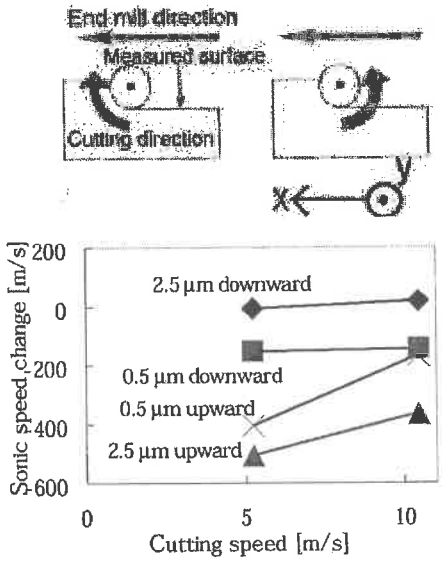

Fig. 9: Relation of cutting speed and sonic speed change in y-direction

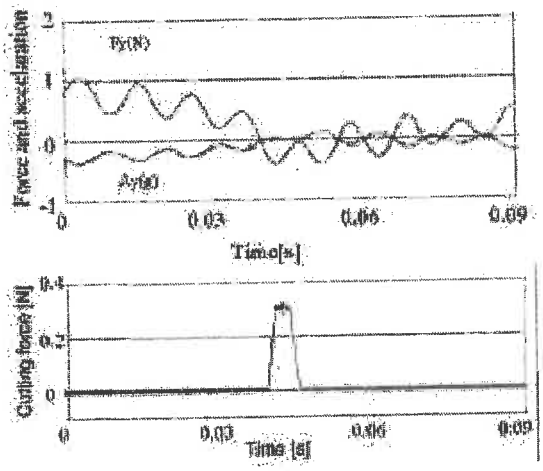

Fig.10 Sensor output and compensated cutting force

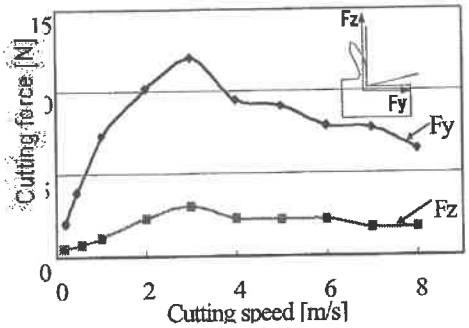

Fig. 11: Relation of aluminum alloy cutting speed and cutting force using diamond tool

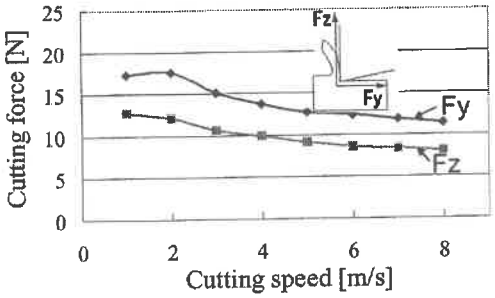

Fig. 12: Relation of aluminum cutting speed and cutting force using carbide tool

SINGLE-POINT DIAMOND MACHINING OF SILICON

Brian P. O'Connor, Robert D. Grejda, Byron R. Knapp, Eric R. Marsh
The Machine Dynamics Research Laboratory
The Pennsylvania State University
University Park, PA 16802

Introduction

Silicon is an attractive material for electronic components and infrared optics, but an expensive material to manufacture due to its material properties. The use of silicon in these applications requires optical quality surfaces as well as tight geometric form tolerances. In machining of brittle materials such as silicon, light depths-of-cut, small feed rates, and stiff machine tools are required to produce mirror-like surfaces with minimal sub-surface damage.

The current trend in manufacturing silicon is to use numerous grinding, lapping, and polishing steps to produce optical quality, damage-free surfaces. However, silicon has the advantage of being a diamond-turnable material based upon its chemical composition [1]. In diamond turning of silicon, tool wear is significant, which results in an increase in machining forces and an increase in surface roughness and sub-surface damage. Previous work done on chemically similar diamond indicates that machining silicon along preferred crystallographic directions lowers machining forces and suggests optimal machining conditions for directional processes such as flycutting, grinding, and lapping [2]. Previous researchers have investigated the ductile-to-brittle transition effects and the ability to produce optical quality surfaces using single-point diamond turning techniques [3-5].

In ductile-regime machining of brittle materials, plastic deformation dominates as the main material removal mechanism instead of brittle fracture. Fracture mechanics may yield a possible explanation into the laws governing ductile/brittle material removal [3][5][7]. Based upon the Griffith fracture criteria for brittle materials, a critical depth, t_c, for crack initiation under a sharp indenter yields the equation,

$$t_c = \psi \cdot \left(\frac{E}{H}\right) \cdot \left(\frac{K_c}{H}\right)^2 \tag{1}$$

where ψ is a dimensionless parameter that depends on the indenter (or tool) geometry, E is the elastic modulus, H is the hardness, and K_c is the fracture toughness [6-7]. As Blake and Scattergood have shown, there are important similarities between quasi-static indentation and diamond turning [3]. They have shown that the critical depth, t_c, will separate brittle fracture from ductility in precision machining of brittle materials. Since silicon is an anisotropic crystal, the critical chip thickness (critical depth) required to machine in a purely ductile fashion varies as a function of crystallographic orientation. It is therefore proposed that ψ will vary as a function of crystallographic orientation as well as tool geometry. The machining forces are also found to vary as the machining direction changes on the crystal face. The objective of this research is to characterize the ductile-to-brittle transition depth and machining forces as a function of crystallographic orientation on the (001) silicon face.

Experimental Setup

All experimental results are obtained from diamond flycutting tests conducted on a flycutting test-bed at the Machine Dynamics Research Lab at Penn State. A novel approach using two spindles (one workpiece and one flycutter) is implemented to characterize the machining forces and critical chip thickness over the entire (001) face of monocrystalline silicon. The machine design allows very light, non-overlapping cuts to be made while minimizing tool track length and sensitivity to workpiece flatness. Figure 1 shows the experimental test-bed on a Moore No. 3 UMM base with two Professional Instruments 4R air bearing spindles.

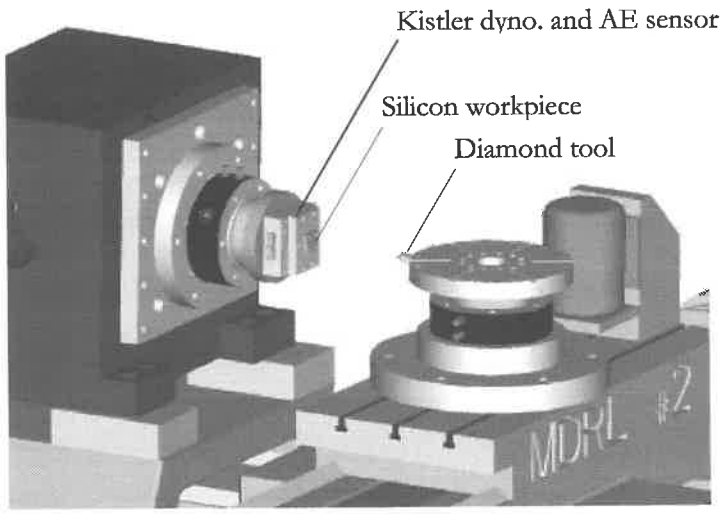

Figure 1: Experimental test-bed used in silicon flycutting experiments.

The two-spindle approach allows for a varying depth-of-cut to be taken over a variety of crystallographic machining directions in a single test setup. The flycutter spindle is setup to operate at 180 rpm while the workpiece spindle rotates at 1 rpm, although a variety of speeds from 0-500 rpm are possible. This allows for cuts to be taken every 2° over the entire crystal face in a single test setup. Figure 2 shows an SEM micrograph of multiple cuts taken on a silicon workpiece using the two-spindle approach.

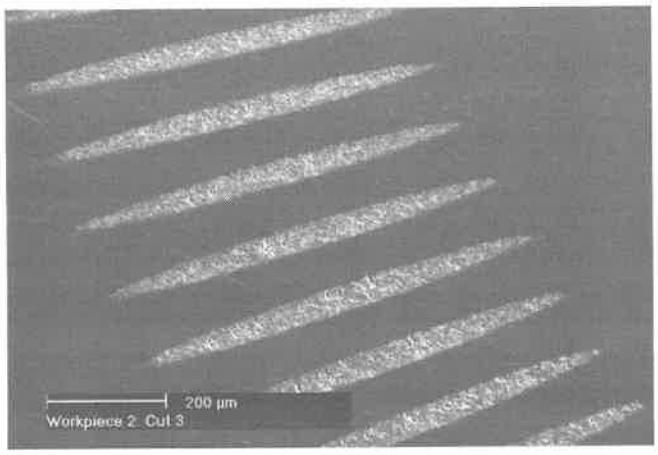

Figure 2: SEM micrograph of multiple cuts taken on a silicon workpiece.

Machining forces are measured using a high-resolution Kistler MiniDyn 3-Component Dynamometer (Type 9256) mounted to the workpiece spindle. Since extremely light depths-of-cut (on the order of 100 nanometers) are required to machine in the ductile regime, a Kistler acoustic emission sensor is mounted to the workpiece chuck in order to detect tool-workpiece contact. Scanning electron microscopy is used to analyze and measure the machined workpieces.

Results

The cutting forces, as well as the ductile-to-brittle transition depth, are found to exhibit the same four-lobed pattern seen in diamond. A typical force vs. crystallographic orientation measurement is shown in Figure 3.

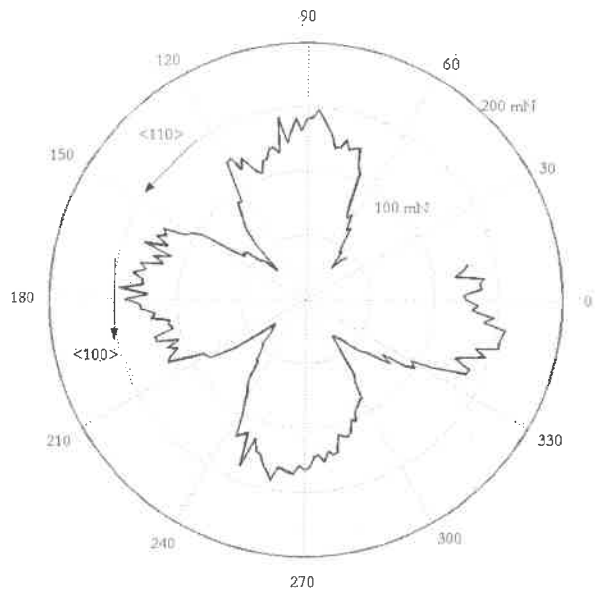

Figure 3: Thrust force as a function of crystallographic orientation on the (001) face,

The critical chip thickness is shown to vary as a function of machining direction. Figure 4 shows SEM micrographs of individual cuts taken in two different directions on the (001) face.

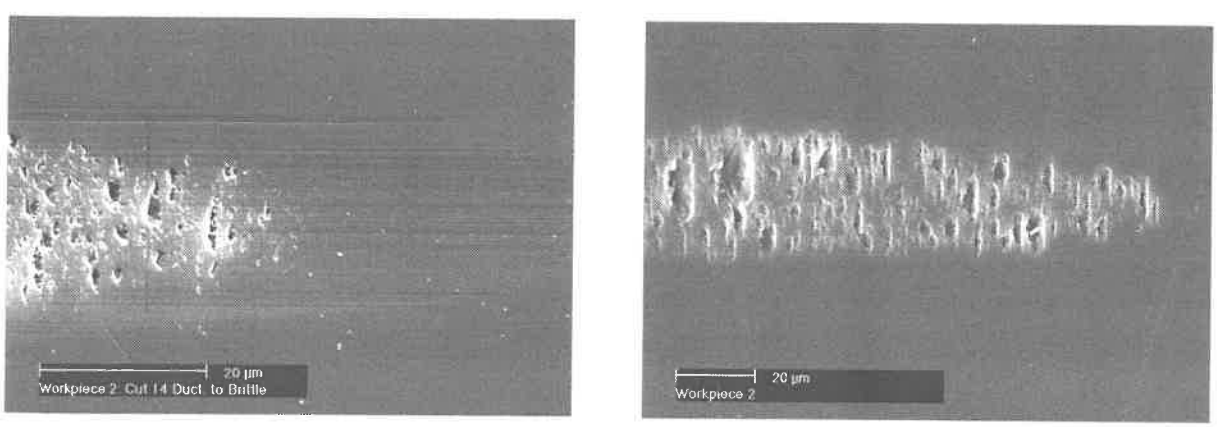

(a) (b)

Figure 4: (a) SEM micrograph of a cut taken along the <100> machining direction.
(b) SEM micrograph of a cut taken along the <110> machining direction.

Notice that along the <100> direction, the transition from ductile machining to brittle fracture is clear. Along the <110> machining direction, the transition occurs much sooner in the cut indicating a smaller critical depth in that direction. It is interesting to note that the <110> direction is the preferred cleavage plane for (001) silicon. As a result, this direction is shown to have a smaller critical chip thickness than the <100> direction.

With the knowledge of tool geometry (0.72 mm radius, 0° rake diamond tool supplied by Edge Technologies), the critical chip thickness can easily be calculated by measuring the width of the cut where the ductile-to-brittle transition occurs. With the valid assumption that the tool nose radius, R, << t_c, the critical chip thickness is calculated from simple geometry by,

$$t_c = \frac{w^2}{8 \cdot R} \tag{2}$$

where w is the width of the cut at the ductile-to-brittle transition (measured by SEM) and R is the tool nose radius. For example, from Figure 4a, a 0.72 mm tool produces a width of 25 μm at the ductile-to-brittle transition, which results in a critical chip thickness of 110 nm. This same procedure is used to quantify the critical chip thickness around the entire (001) crystal face.

Conclusions/Future Work

By using the proposed two-spindle approach, the ductile-to-brittle transition and machining forces can accurately be measured over the entire crystal face without "history" effects present in conventional facing-cut methods. The knowledge of machining forces and ductile-to-brittle transition for any crystallographic orientation allows for the optimal machining direction to be chosen. This knowledge is beneficial for directional-dependent processes such as grinding, flycutting, and lapping.

Future work is planned that investigates the effect of tool geometry (rake angle, nose radius, etc.) on the machining forces and ductile-to-brittle transition. Also, studies are planned that would quantify tool wear as a function of crystallographic orientation.

Acknowledgements

The authors would sincerely like to thank Dave Arneson and Mel Liebers of Professional Instruments, Newman Marsilius III from Moore Tool Company, and Don Martin from Lion Precision. In addition, funding from Aerotech, Kistler Instrument Corporation and Edge Technologies is greatly appreciated.

References

[1] Paul, E., et. al., "Chemical aspects of tool wear in single point diamond turning." *Precision Engineering*, 1996.

[2] Kim, George. "Technical details of silicon machining behavior from a diamond toolmaker's perspective." *Proceedings of ASPE Spring Topical Meeting on Silicon Machining*, 1998.

[3] Blake, P., and Scattergood, R. "Ductile-regime machining of germanium and silicon." *Journal of the American Ceramic Society*, 1990.

[4] Taylor, J., et. al. "Diamond turning of silicon for optics applications." *LLNL Technical Report*, 1987.

[5] Blackley, W., and Scattergood, R. "Ductile-regime machining model for diamond turning of brittle materials." *Precision Engineering*, 1991.

[6] Lawn, B., and Evans, A., "A model for crack initiation in elastic/plastic indentation fields." *Journal of Material Science*, 1977.

[7] Bifano, T, Dow, T., and Scattergood, R., "Ductile-regime grinding: A new technology for machining brittle materials." *Journal of Engineering for Industry*, 1991.

PROFILE GENERATION FOR BRITTLE MATERIALS BY USING ULTRA-PRECISION LATHE WITH ON-MACHINE MEASUREMENT SYSTEM

Ichiro Ogura, Yuichi Okazaki
Fine Manufacturing System Group
Institute of Mechanical Systems Engineering
National Institute of Advanced Industrial Science and Technology (AIST),
Tsukuba 305-8564, Japan

1. Introduction

Ductile mode machining[1)] of brittle materials, such as optical glasses, enables high-precision optical devices to be produced without the use of a mold. Compared to grinding, single point diamond (SPD) turning is more suitable for high-spatial-frequency profile generation. Therefore, if a ductile mode machining technique employing SPD is established, it will become possible to fabricate new types of optical devices having minute patterns on aspheric profiles.

We have previously presented our experimental results on the machining of brittle materials using a practical SPD ultra-precision lathe with a fast tool servo (FTS)[2)]. In that study, the plunge-cut experiment[3)] was performed on brittle materials in several different atmospheres, and it appeared that an ethanol atmosphere was best for BK7 cutting. However, the depth of cut in the experiment was denoted only by the tool infeed, so the effect of the surface profile or skew angle when the work was attached to the chuck was not taken into account. For exact control of the depth of cut, information on the surface profile is important. In the present study, we constructed an on-machine measurement system to measure the surface profile before cutting. This system can create the cutting data from the measurement results. By applying profile measurement results to plunge-cut experiments on brittle materials, it was confirmed that our system enables works to be cut without being affected by the surface profile.

A profile generation experiment on brittle materials was performed taking the profile surface into consideration. This was a preparatory experiment for generating minute patterns on an aspheric profile. A concave micro lens array was cut on the surface profiles. After machining, generation of the lens array was confirmed by interferometric observation.

2. Ultra-precision lathe with on-machine measurement system

Fig. 1 shows a schematic diagram of the ultra-precision lathe with the on-machine measurement system. Using a piezoelectric actuator, the FTS can control depth of cut at a 2 nm resolution, with a frequency response of 2 kHz. A diamond-cutting tool is set on the FTS. The radius of the cutting tool is 0.2 mm, and the rake angle is 0 degree. Contact between the FTS diamond bite and work surface is detected from changes in the servo signal.

A capacitance type sensor is set by the side of the FTS and scans the surface of the work by main axis rotation and x-axis slide feeding. By using a double-buffered DAQ (data acquisition) board synchronizing main axis encoder pulse, this system can measure 2048 points per 1 rotation. The rotation speed of the spindle axis is 90 rpm. The feeding speed of the x-axis slide in measurement was set at 1.0 mm/min in all of the experiments.

The data sampling sequence of the double buffer is as follows: The first buffer in the double buffer acquires data until the buffer is filled up. When the first buffer is filled, the second buffer starts to acquire data. The computer saves the data of the first buffer to a file while the second buffer is acquiring data. When the second buffer is filled, the same procedure is performed. The double buffer repeats these operations and records data.

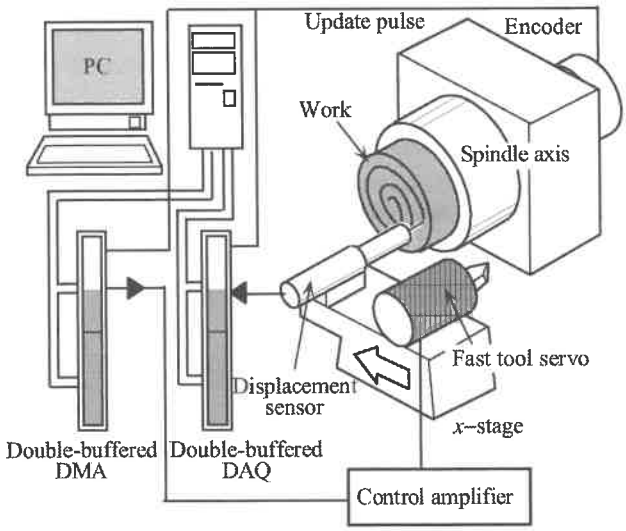

Fig. 1 Ultra-precision lathe with on-machine measurement system

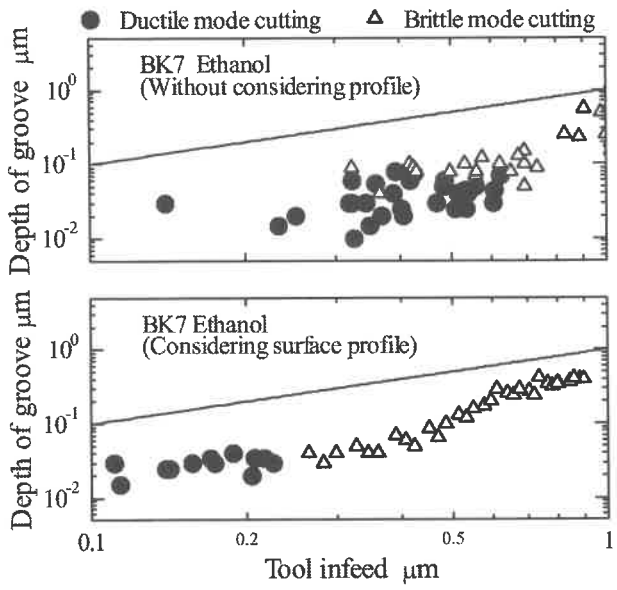

Fig. 2 Results of plunge-cut experiments

The amount of tool feeding is determined with reference to the profile data of each point. Therefore, the FTS can ensure the exact depth of cut for the work without being affected by the surface profile or setting errors.

The cutting data are sent to the double-buffered DMA (direct memory access) board. The DMA operates similarly to the DAQ board. It outputs a data stream to the control amplifier using two buffers.

3. Results of plunge-cut experiments

Plunge-cut experiments were performed to demonstrate the validity of our system. In these experiments the FTS applied the plunge-cut to the work increasing the depth of cut with the main axis rotation. BK7 was selected as the work for cutting. Before cutting, the test work was measured by the on-machine measurement system. The tool infeed data were generated so as to make the amount of infeed for the test work linearly increase with the main axis rotation. Cutting was performed three times at different radii.

After the cutting experiments, the surfaces of the test works were observed by Nomarski differential interference microscope, and the transition from ductile mode cutting to brittle mode cutting was identified. The amount of tool infeed was calculated from the starting point of the cutting mark, and a surface topographic measurement apparatus was used to measure the depth of groove. In this way, the relationships between tool infeed, depth of groove, and groove state under several atmospheres were finally obtained.

Fig. 2 shows the results of the plunge-cut experiments. In this figure, two results – without considering the surface profile, as in the past method, and considering the surface profile – are shown. Comparing these results, it is clearly seen that the ductile mode widely overlaps the brittle mode when the surface profile is not considered.

Of course, some area of overlap between the ductile and brittle modes is to be expected, because these results were obtained from three cutting marks, and the respective ductile-brittle transitions affected by the crack distribution are not perfectly identical. However, the results show overlaps occurring at a depth of cut of 300 nm or more. The reason is, as shown in Fig. 3, that plunge-cut tool infeeding was affected by the profile of the work surface, and the real depth of cut was different from the expected value.

On the other hand, when the profile of the work surface is taken into consideration, there is no overlapping between the ductile and brittle modes. This shows that the effect of the surface profile was

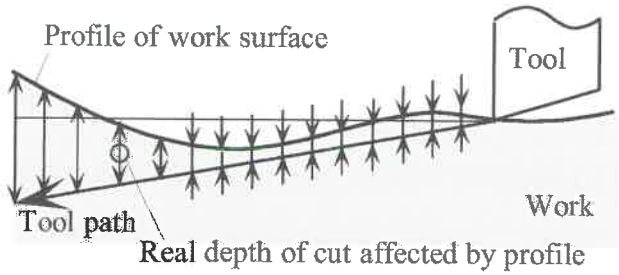

Fig. 3 Schematic diagram of plunge cut

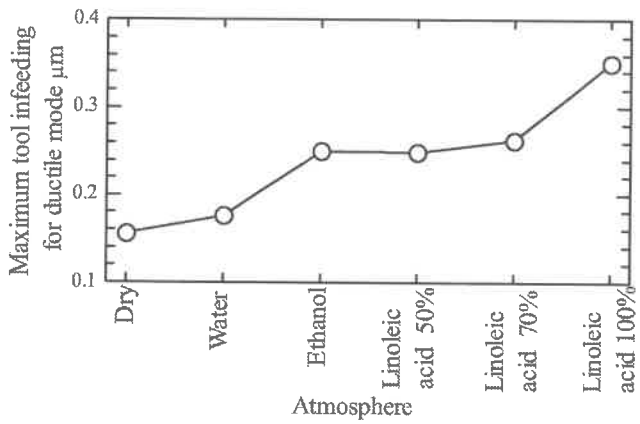

Fig. 4 Plunge-cut experiment under several atmospheres

cancelled by the generation of cutting data from the on-machine measurement results. These results demonstrate the validity of the on-machine measurement system and assure the reliability of the experimental results.

4. Effect of cutting atmosphere

In our previous study, we obtained the result that ethanol provided the best condition for ductile cutting of BK7, even if these results were affected by the profile of the work surface.

This time, we performed plunge-cut experiments under several atmospheres, taking the surface profile of the work into consideration. The test work was soda lime, and the atmospheres selected were dry, water, ethanol, and linoleic acid. The linoleic acid was diluted by ethanol, to give concentrations of 50%, 70%, and 100%.

Fig. 4 shows the results of the experiments. This figure shows the maximum tool infeed for ductile mode under several atmospheres. The dry and water atmospheres are not suitable for ductile cutting mode, whereas ethanol is a good atmosphere in these experiments also. Linoleic acid is a much better atmosphere, however, with concentrations 50% and 70% providing similar or slightly better results than ethanol.

We believe that these results are mainly attributable to a reduction of friction between the material surface and the cutting bite. Reduced friction causes less crack propagation and increases the maximum depth of cut in ductile mode. In addition, a chemical effect on the glass surface can be expected.

5. Profile generation experiment

Using an ultra-precision lathe, a basic profile generation experiment was performed on brittle material. In this study, a concave micro lens array was selected for profile generation. The material used was soda lime. The diameter of the material was 30 mm, and that of the machined area was 23 mm. The feeding speed of the x-axis in the ultra-precision lathe was set at 0.4 mm/min. The cutting atmosphere was linoleic acid diluted to 50% by ethanol.

Fig. 5 shows the cutting data chart for the FTS. This chart includes the profile surface to maintain ductile mode cutting. The maximum depth of cut was 250 nm. The diameter of each lens was 300 micron, and the interval of each lens was 200 microns.

The result of the profile generation experiment is shown in Fig. 6. This figure shows the measurement result obtained by WYKO interferometer (NT-2000). Throughout the cutting area there is almost no brittle cutting zone, but ductile mode cutting marks.

Fig. 7 shows section profiles of the micro lens. These profiles should correspond because the cutting data for the micro lens was symmetric with the center axis of each lens. But Fig. 7 does not show good correspondence.

The reason is that the tip of the cutting bite changes due to wear, so that the motion copying of the cutting bite was not performed perfectly. Indeed, observation under a microscope after cutting showed

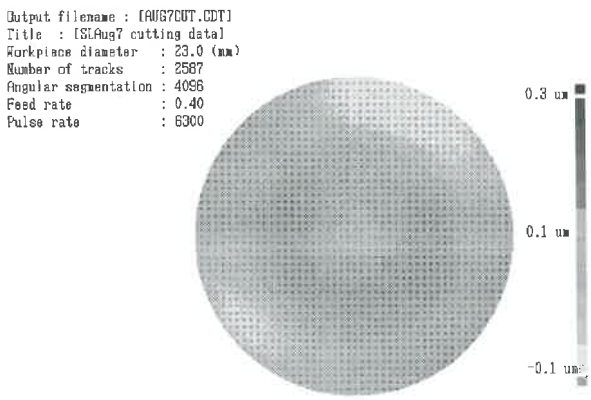

Fig. 5 Cutting data chart for the profile generation

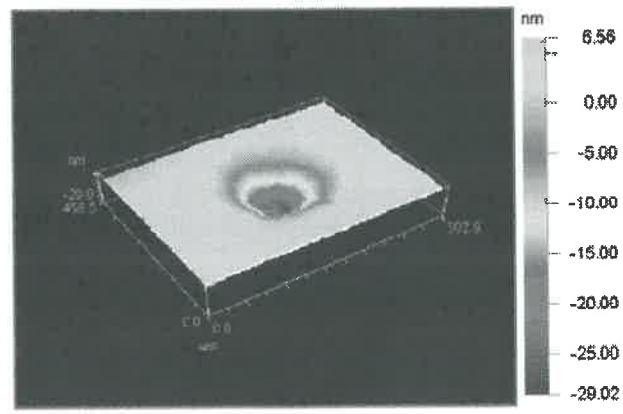

Fig. 6 Results of profile generation experiment

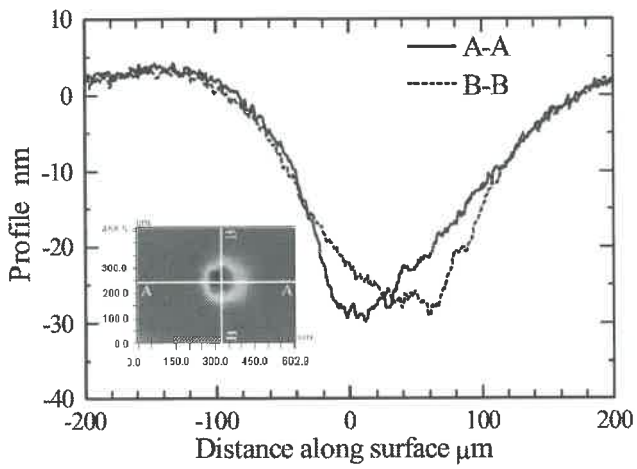

Fig. 7 Section profiles of micro lens

wear of the cutting bite.

The maximum depth of the lens is almost 30 nm. This result has validity because, as seen in the relationship between tool infeed and depth of groove in Fig. 2, the depth of groove will be 30 nm when the tool infeed is 250 nm, allowing maximum tool infeed in ductile mode. Of course, Fig. 2 shows the results for BK7 under an ethanol atmosphere, not soda lime under linoleic acid and ethanol. But almost the same relationship was obtained for this material and atmosphere.

In this experiment, only nanometer-order depth of profile was obtained. To fabricate a practical optical device, at least micrometer-order profiles are required. A deeper form without brittle cracks will be obtained by carrying out repetitive cutting.

6. Summary

This study can be summarized as follows.

(1) We have constructed an on-machine measurement system for an ultra-precision lath. Plunge-cut experiments showed that our system is able to cut works without being affected by the surface profile.

(2) The effect of the cutting atmosphere was investigated. For dry, water, and ethanol atmospheres, the same tendencies were obtained as in our previous study. Linoleic acid provides the best atmosphere for soda lime.

(3) A profile generation experiment was performed. In this study, a micro lens array on the profile surface was tested. For almost all cut surfaces, a ductile mode lens array was obtained. The profile of the lens was not symmetrical with the center axis of each lens. The main reason for this is wear of the cutting bite.

References

1) T. Bifano, T. Dow, and R. Scattergood: Ductile Regime Grinding: A New Technology for Machining Brittle Materials. ASME, J. Eng. Ind., 113, 5 (1991), 184.

2) I. Ogura and Y. Okazaki: Ductile-Regime Turning of Brittle Materials by Single Point Diamond, Proc. 15th ASPE (2000), 58.

3) E. Brinksmeier, W. Preub, and O. Riemer: From Friction to Chip Removal. An Experimental Investigation of the Microcutting Process. Proc. 8th Intern. Prec. Eng. Seminar (1995), 335.

MICROMACHINING BY CNC SLOTTING USING A STEERED TOOL

Thomas Schaller, Klaus Schubert
Forschungszentrum Karlsruhe GmbH, Karlsruhe, Germany

Abstract

CNC slotting is proposed as a new microcutting technique using profiled tools. The tools are mounted onto a CNC cutting machine instead of the standard spindle. The direction of the cutting edge is adjusted ("steered") to the actual cutting direction in the XY-plane by rotation around the Z axis. Cutting is performed similarly to usual milling, the minimum tool path radius being limited by the tool geometry only. CNC slotting allows to machine narrow curvilinear trenches and sharp inner edges and the cutting of steel using diamond tools. Applications are seen in machining of structural details for finishing microstructure workpieces, namely, the fabrication of steel molds for microreplication.

Keywords: Micromachining, slotting, profiled microtool

Microtools

Microcutting always starts with the choice of a microtool. Depending on the cutting method, a rotating tool (drill, end-mill) or a profiled tool ("chisel") is used.

All types of rotating tools are commonly used for the removal of large volumes, for high cutting speeds, and for a variety of materials and geometries. In the cutting of microstructure details, their main drawback is the limited minimum size due to tool stability, especially of multi- and spiral-fluted end-mills. Microstructure details depend on the size of the tool, e.g. the radius of inner edges cannot be less than the tool radius. Commercially available are tungsten carbide straight and ball end-mills down to 100 µm diameter. There are experimental examples of cutters with 50 µm diameter and less [1, 2] as well as diamond end-mills with 200 µm minimum diameter. Their applicability is limited to special purposes or materials and prototype structures, their lifetime often being rather short.

Profiled tools with a huge variety of shapes are well-known from turning, broaching, planing, and slotting. In most cases, they are more stable compared to the fragile end-mills. For microcutting, mainly diamond tools are used, which provide an excellent cutting edge quality and shape. Unfortunately, their use is – if not used in tricky setups, e.g., ultrasonic excitation – restricted to nonferrous materials, which means a severe restriction for the fabrication of replication tools, where steel is the first-choice material.

Micromachining

Milling can be considered to be the most applied and most versatile cutting technique. It is a standard manufacturing process and also used for the machining of microstructures. But there are

problems arising from the miniaturization of the tools: Microcutting using rotating microtools implies an increase of the rotational spindle speed to achieve the theoretically required cutting speed. With tool diameters of 100 µm and below, however, the performance of conventional spindles is far beyond a technological limit. Nonetheless "slow" cutting of brass and steel produces satisfying results [1, 3].

Techniques characterized by the use of profiled tools do not necessarily require high speed. This also applies to turning which is the most common technique using a non-rotating tool. But these techniques are usually limited to linear or circular tool or workpiece motions, which is sufficient for many industrial applications and structures. A machining technique to overcome the speed restriction is flycutting using profiled tools as a "single-tooth-cutter" mounted on a spindle, but structures to be cut are strictly linear.

Slotting as a linear technique has proved its potential for cutting microstructures since the early 70s: Into long metal rods complex shaped grooves were cut by using profiled diamond tools, the rods being used to build up a nozzle for uranium isotope separation, which marks the starting point of micromachining at the Forschungszentrum Karlsruhe [4]. This gives rise to the assumption that micromachining can be done with profiled tools at relatively low cutting speeds. The cutting method proposed here is to overcome the restrictions of linear or rotational symmetry using profiled tools instead of the fragile rotating ones.

3D Slotting

The machine setup for three-dimensional slotting is achieved by replacing the spindle of a 3- or 5-axes CNC milling machine by a profiled microtool. The movement of the tool relative to the workpiece is performed by travel and rotation of the CNC axes, and for the cutting of curvilinear trenches the cutting edge of the tool has to be steered to the actual cutting direction.

The most general solution for steering will be a rotation of the tool with respect to the former spindle axis. A setup for adjustment and rotational action of profiled microtools is in preparation. Prior to the realization of real 5 axes and three-dimensional machining, there will be a 2.5-dimensional approach: A planar workpiece will be moved by travel of the X and Y axes, the vertical feed is provided by Z axis travel, and the actual rotation angle of the tool will be calculated from the changes of the X and Y coordinates and transformed into computer-controlled rotary motion of the tool. This will enable the manufacture of curved trenches without rotational motion of the workpiece. For evaluation purposes an optional manual control of the tool rotation will be implemented.

Another approach without any change of the machine hardware is the simultaneous travel of a rotational stage and the linear axes, but with the tool fixed. While the cutting edge is steered by rotation of the workpiece depending on the actual cutting direction in the XY-plane, the X and Y axes control the position of the workpiece. The Z axis is used for vertical feed. A special case is the cutting of structures with rotational symmetry, the symmetry axis coinciding with the axis of the rotational stage – that basically corresponds to the setup of a lathe. All other structures require travel of the X and Y axes depending on the actual cutting position *and* direction. For

circular structures, the terms for directional XY correction can be calculated from simple trigonometry.

Programming of machine motion for the cutting of curvilinear structures was performed for trenches composed of linear and circular elements. The tool path was reduced to polygons, and for each polygon point the corresponding rotation angle and XY coordinates were determined using spreadsheet calculations. The calculated data were transformed into NC command lines for machine programming and directly transferred to the machine.

Results

Cutting tests were performed on a KERN HSPC 2216 machine. Profiled diamond and tungsten carbide tools of various dimensions and cutting edges (triangular or rectangular shape, sharp tip or 50 μm minimum width) were used for cutting brass and steel. The tools were fixed at the machine spindle position. Cutting was done by simultaneous travel of XY axes and rotation of the A axis (parallel to Z). Vertical feed was controlled by movement of the Z axis.

Cutting tests have shown that linear, circular, and dead-ended trenches and pyramid structures could be machined. Sample pictures are shown below. A low cutting speed and the use of a lubricant ensured a low thermal load of the cutting edge, resulting in no obvious wear problems when cutting steel with diamond tools. Cutting lengths may depend on tool and structure dimensions as well as on material combinations and still have to be determined. A first application example is a mold insert for the replication of lab chips with intersecting walls of less than 5 μm inner radius of curvature.

Concluding Remarks

The proposed machining method is not aimed at replacing existing ones, but considered to represent a useful supplement. Because of the limited material removal rate and cutting speed, it may be applied as a finishing step in machining both complex shapes and difficult-to-cut materials.

References

1. Schaller Th, Bohn L, Mayer J, Schubert K, Prec. Eng. 23 (4), 229-235 (1999).
2. Vasile MJ, Friedrich CR, Kikkeri B, McElhannon R, Prec. Eng. 19 (2-3), 180-186 (1996).
3. Adams DP, Vasile MJ, Krishnan ASM, Prec. Eng. 24 (4), 347-356 (2000).
4. Patent DE-PS 24 19 192 (1977).

Figures

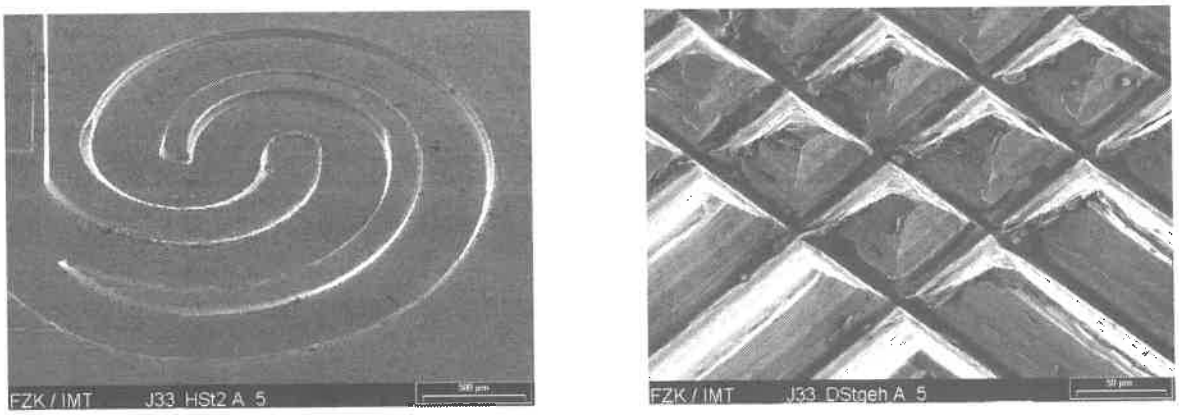

SEM of a meander structure (left) and pyramids (right). The meander was cut into tool steel (X2 NiCoMo 18 9 5) by using a rectangular tungsten carbide tool. The pyramids were cut into the same tool steel, but hardened to >55 HRC using a triangular diamond tool.

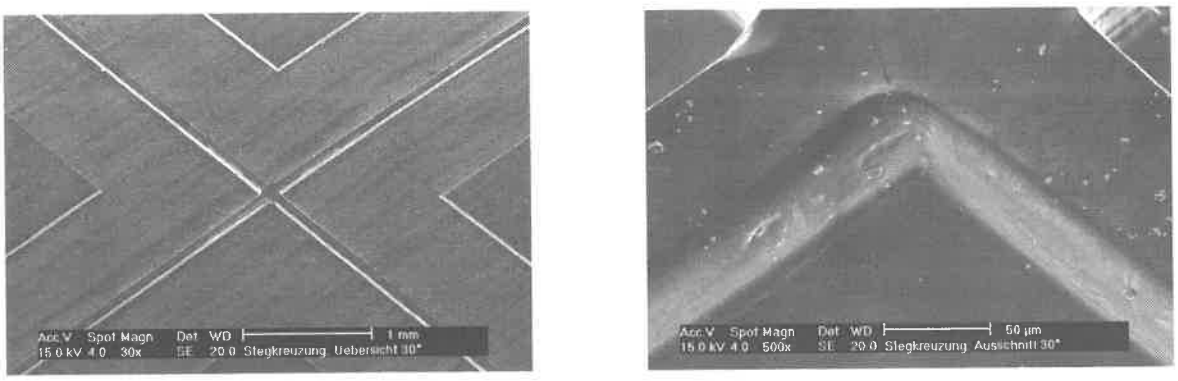

SEM overview and detail view of crossed channels with the radius of the inner edges minimized, for the replication of a lab-on-a-chip channel structure. Workpiece material is tool steel (X2 NiCoMo 18 9 5) cut by using a rectangular tungsten carbide tool and deburred by electrochemical polishing after cutting.

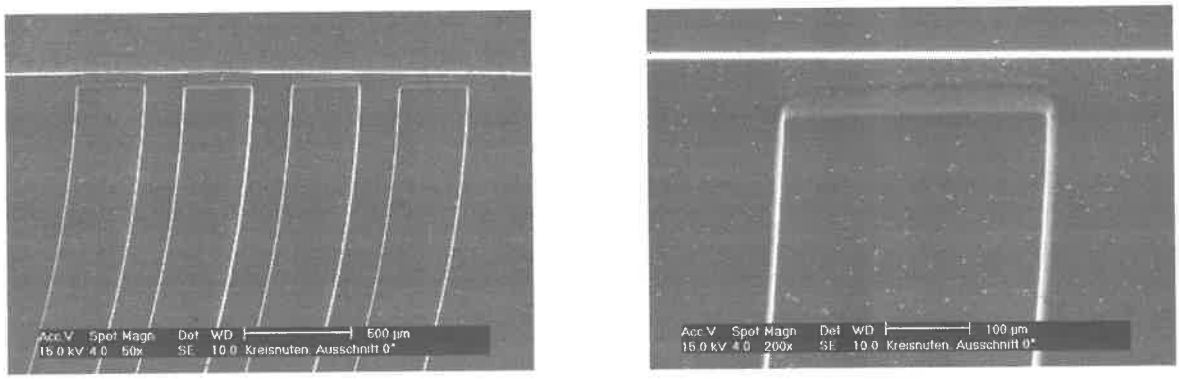

SEM overview and detailed view of circular trenches with a "dead end" cut into tool steel (X2 NiCoMo 18 9 5) by using a rectangular tungsten carbide tool and deburred by electrochemical polishing after cutting.

BURR FORMATION IN MICRO-DRILLING

Boris Stirn[1], Kiha Lee[2], David A. Dornfeld[2]
1. University of Technology at Aachen (RWTH), Aachen, Germany
2. University of California at Berkeley, Berkeley, CA

Key words: burr formation, micro-machining, micro-burr, micro-drilling

Abstract

Experimental studies on micro-drilling in aluminum alloy and steel have been carried out. Drilling experiments with different feed to diameter ratios, cutting speeds and 130μm, 250μm, 500μm drills were conducted. The influence of the cutting parameters on burr size and burr type was observed. A comparison to burr formation in conventional drilling is presented.

Introduction

Most machining processes produce burrs. These burrs cause several problems for product quality and functionality as they can interfere with assembly of parts or may reduce the fatigue life. Deburring of micro-structures is especially difficult due to bad accessibility and tight tolerances. In some cases, due to part fragility or edge tolerances, deburring of micro-parts is not possible. Therefore, reducing burr is very important in micro-machining. Understanding the burr formation and its dominant parameters is essential for predicting and reducing burr. Very few studies [1] [2] have been performed on the burrs resulting from micro-drilling. Micro-burr formation in aluminum alloy has been investigated with respect to cutting conditions [2]. The fundamental mechanisms are not well understood.

Previous research [3] had established basic burr types in the conventional drilling of low ally steel. Burr shape is the most important because the burr size, and as a result, deburring cost is greatly dependent on it. Three different shapes of burrs were observed as seen in Figure 1. The uniform burr has relatively small and uniform burr height and thickness around the hole periphery. The crown burr has a larger and irregular height distribution around the hole. The transient burr is a type of burr formed in the transient stage between the uniform burr and the crown burr.

The work presented in this paper investigates the factors which significantly influence the burr formation process in micro-drilling. The burrs which result from micro-drilling in the different materials have been characterized and are compared to conventional drilling. Analysis of the data for the effect of diameter, cutting speed and feedrate and the mechanics of burr formation in micro-drilling are addressed. Burr shape of micro-burr is investigated.

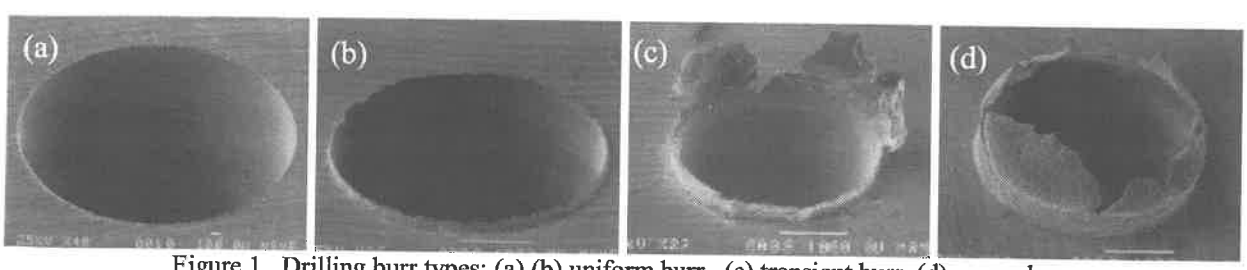

Figure 1. Drilling burr types; (a) (b) uniform burr , (c) transient burr, (d) crown burr

Experimental setup

Drilling experiments in 6061-T6 aluminum and 25MoCrS4 steel (similar to AISI 4130) were conducted in 21 speed and feed variations, Table 1. The cutting parameters are based on recommendations by the tool manufacturer. Three different diameters, 130μm, 250μm, 500μm, are tested. Figure 2 shows 250μm drill and its cutting edge, of which radius is 3μm. A micro drill was attached to a Mori Seiki CNC Drilling Center TV-30 or Cameron Micro Drill Press MD-90. Micro-drop coolant was used. The height and thickness were measured using SEM pictures. Other current methods to measure burr size such as contact method, optical microscope method, etc, cannot easily apply to micro-burr due to small size. Measuring burr thickness is more difficult than height due to the irregularity of the shape using SEM. The measurements of the five holes were averaged for each cutting parameter.

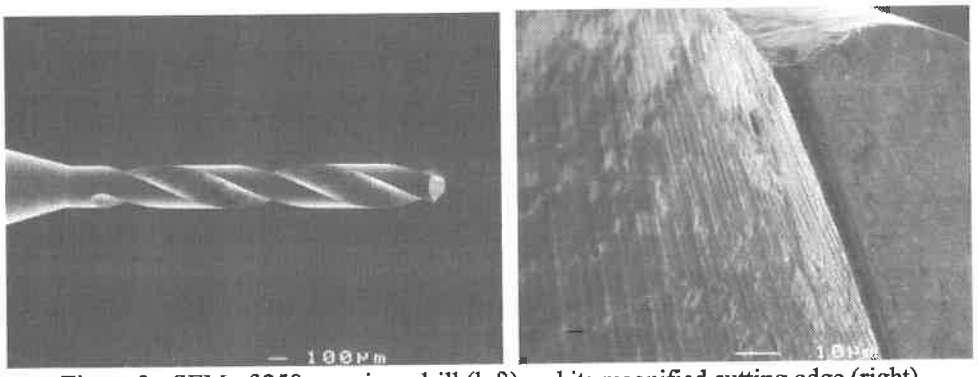

Figure 2. SEM of 250μm micro-drill (left) and its magnified cutting edge (right)

Table 1. . Experimental cutting conditions

Parameter	Aluminum	Steel
Diameter	130μm, 250μm, 500μm	
feed/diameter	0.00625 – 0.1	0.005 – 0.08
feed/rev [μm]	0.81 – 50	0.65 – 40
RPM	6000 – 19500	4000 – 7600
Cutting speed [m/min]	2.5 – 30.6	1.6 – 11.9

Results

Aluminum micro-burr

A tendency of increasing height with increasing feed was observed, Figure 3. The effect of cutting speed is not clear. The burrs created by the 250 μm and 500 μm drill shows similar tendencies with respect to the feed rate. No large difference of burr height in 130 μm drill from one feed/diameter ratio to the next was observed compared to other two bigger drills. The comparison of the average burr heights at different drill sizes shows a minimum at 250 μm. The effect of speed is not consistent concerning burr thickness as both higher and lower speed creates a thicker burr. The values of burr thickness correspond to the values of height. Higher feed rate produces thicker burr.

Figure 4 shows micro-burr chart with the 250μm drill according to feedrate and speed. Micro-burr type is similar to conventional drilling. Uniform burr is observed only in the lower feed. No uniform burr cannot be seen in the 130μm drill. Again the effect of increasing feed is

confirmed as the formation mechanism changes to crown burr formation. No consistent effect of speed was observed.

Steel micro-burr

The burr height is a function of the feed as observed in the drilling of aluminum, Figure 5. Increasing feed has the effect of increasing height. With the 500μm drill, increases in speed also increases burr height, which increases from 37 μm at low speed to 52μm at medium speed. The value goes down slightly to 50 μm at high speed. In the case of the 250μm, the burr height at low speed (27 μm) is higher than at medium (17 μm) and high speed (18 μm). Using 130μm, the height at different speeds does not vary much. The feed shows the same effect on burr thickness that was observed on burr height. The cutting speed has no significant effect on the thickness.

The burrs at the lowest three feed rates show mostly uniform burr formation, Figure 6. With the highest feedrate the SEM shows very clearly a crown burr formation. In the second highest feedrate, the burr parts with crown characteristics and the big cap fragments indicate the transition between the uniform and the crown burr formation. No uniform burr was observed when the 130 μm drill was used.

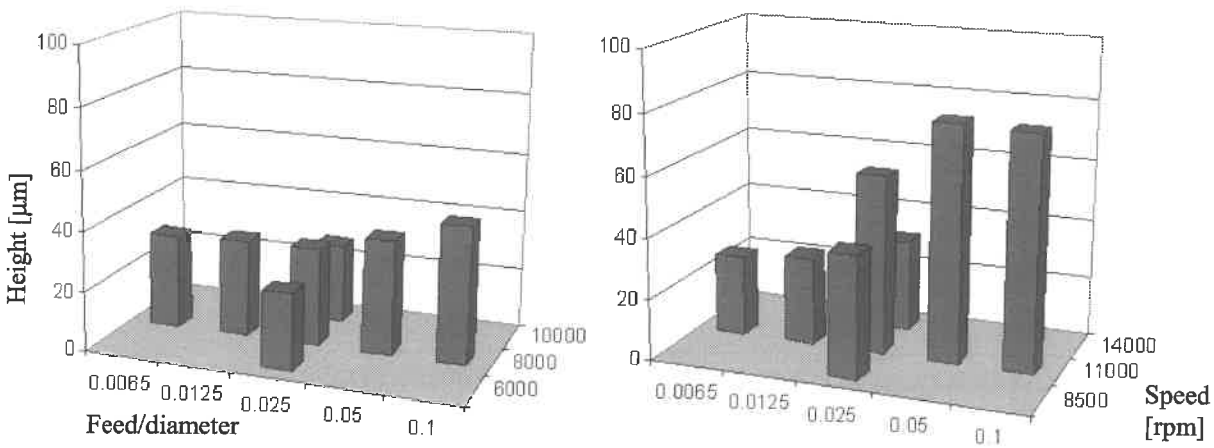

Figure 3. Burr height of aluminum in 130μm diameter (left) and 250μm diameter (right)

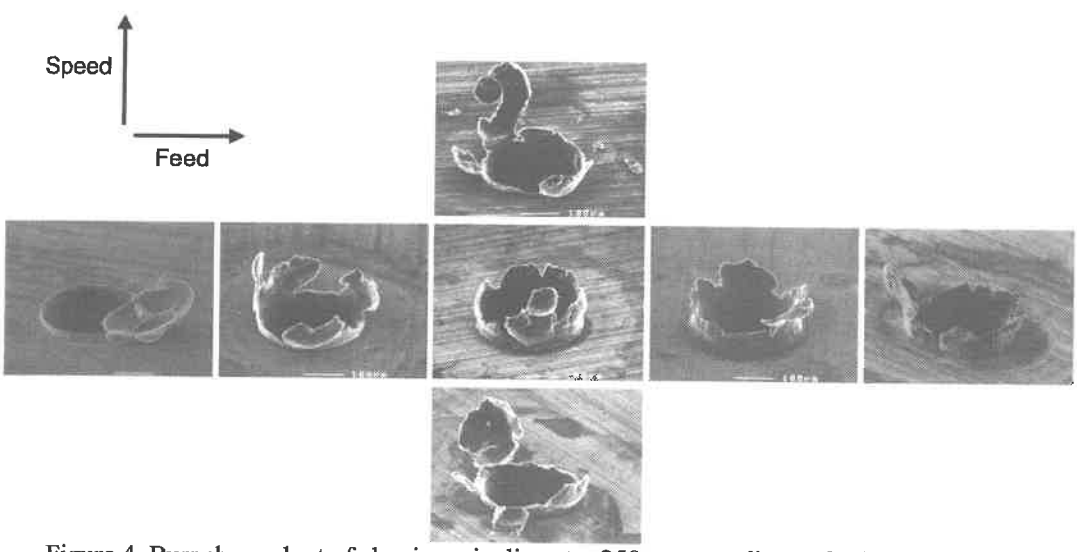

Figure 4. Burr shape chart of aluminum in diameter 250μm according to feedrate and speed.

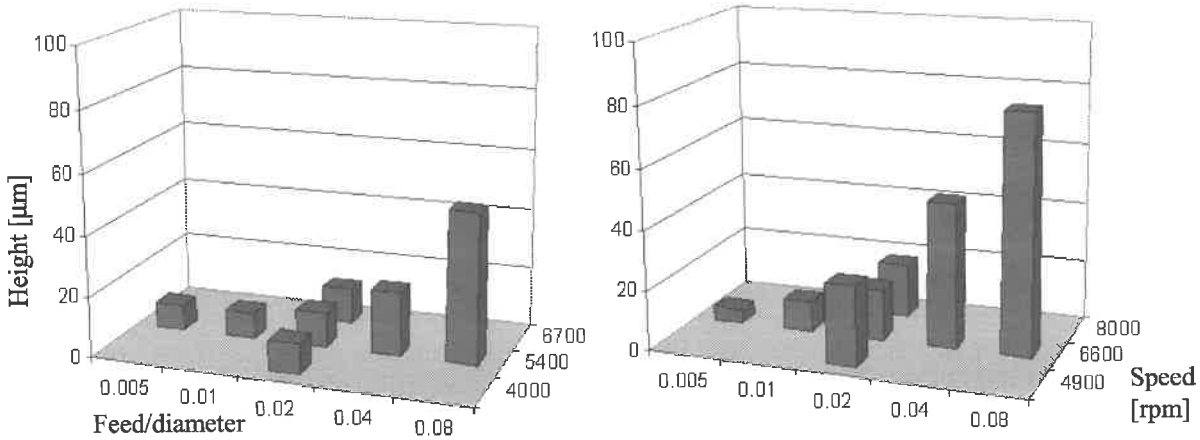

Figure 5. Burr height of steel in 130µm diameter (left) and 250µm diameter (right)

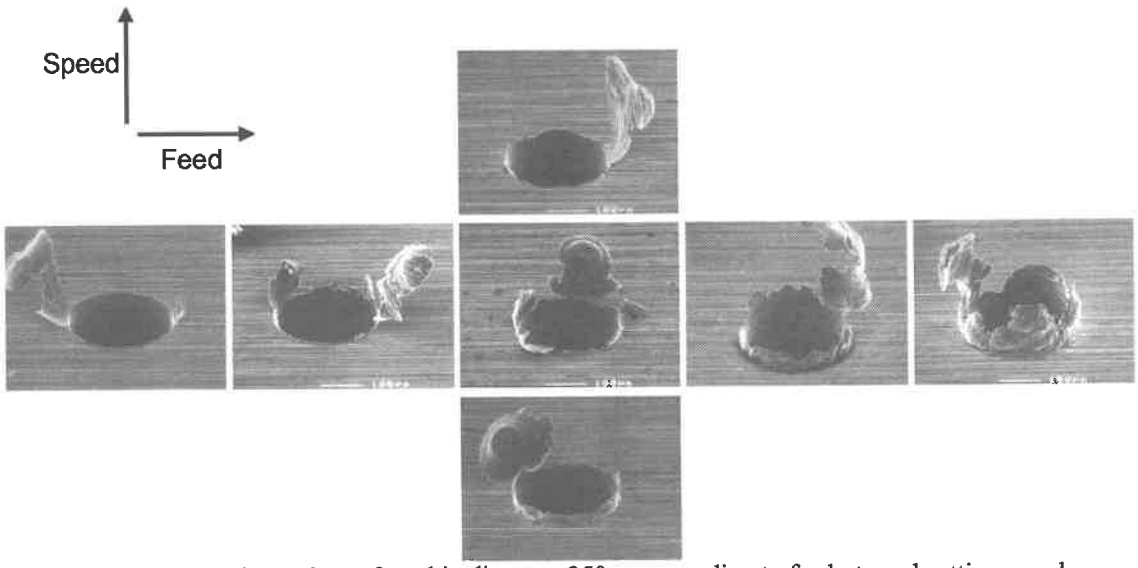

Figure 6. Burr shape chart of steel in diameter 250µm according to feedrate and cutting speed.

Acknowledgments

This work was supported by the Consortium on Deburring and Edge Finishing (CODEF) at University of California at Berkeley. Information is available at http://lma.berkeley.edu.

References

1. Sugawara, A., and Inagaki, K., "Effect of workpiece structure on burr formation in micro-drilling," *Precision Engineering* 1982, Vol. 4, No. 1, 9-14
2. Lee, K., Stirn, B., Dornfeld, A., "Burr Formation in Micro-Machining, Aluminum, 6061-T6," *10th, International Conference on Precision Engineering*, Japan 2001
3. Min, S., Kim, J., Kim, Dornfeld, D., "Development of a Drilling Burr Control Chart for Low Alloy Steel, AISI 4118," *Proc. the 5th Asia Pacific Conference on Materials Processing*, Seoul, Korea, June, 2001

A Basic Study on Slurry Actions and Slicing Characteristics of Multi-wire Saw

Hitoshi SUWABE, Ken-ichi ISHIKAWA, and Akihisa KITAJIMA
Kanazawa Institute of Technology : 7-1 Ohgigaoka, Nonoichi, Ishikawa 921-8501 Japan
e-mail : suwabe@neptune.kanazawa-it.ac.jp
Michio UNEDA
Japan Defense Agency : 1-2-10 Sakae, Tachikawa, 190-8533, Japan

1. Introduction

The silicon wafers as the base plate of IC or LSI are mass-produced by large sized ingot. The mass-production of silicon wafers bears one part of development of electronics industry. The multi-wire saw is one of the slicing methods for semiconductor materials. This slicing method uses tensioned thin wire and slurry (mixed working fluid of abrasive grains). And, this slicing method has some problems on the slurry characteristics and actions and slicing accuracy in case of the slicing of large sized silicon ingot. There are some papers for slurry characteristics on multi–wire saw [1]. Although the slurry actions during the processing affect the large effect for slicing efficiency and accuracy, authors have known few papers for the slurry actions.

Therefore, authors direct our attention to the slurry action to enter into processing area in case of the work descent type of multi-wire saw. And, this study aims to clear the slurry actions on the thin wire tool, the relation between the slurry action and slicing efficiency, and the mechanism of processing. In this paper, the high speed camera observed the slurry actions on the wire, and the slurry amounts on the wire were measured. And, another report [2] described about multi-wire saw used low frequency vibration. This wire saw system vibrates the wire to improve enter of carried slurry in slicing area. The report was clear that the slicing efficiency showed increase of 50-100%. Therefore, in this paper, the slurry actions in case of vibrated wire are observed, and the vibration effects are considered from viewpoint of slurry actions.

2. Experimental apparatus and methods

2.1 slurry amount and actions

Figure 1 shows the measurement method of slurry amount on the wire. Here, the slurry amount is defined by total slurry amount on the wire at the separate point of 50 mm from

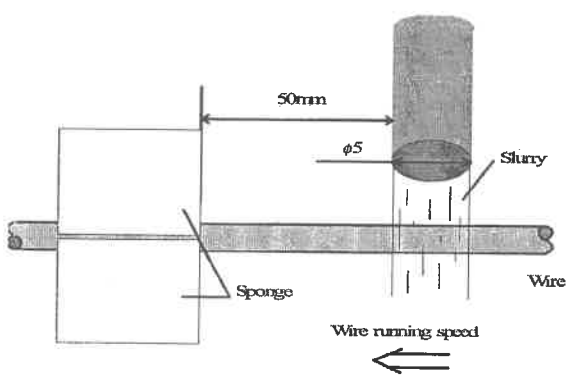

Fig.1 Measurement method of slurry amount

supplied point of slurry. At the measurement of the slurry amount, the slurry is supplied on the wire, and the wire runs. The sponges caught the slurry on the wire at the measurement point, and the slurry amount is measured.

Figure 2 shows the method to observe slurry actions on wire. The observation method applies the slurry on wire and observes the slurry action on wire at the arbitrarily point from supplied point.

Table 1 shows the experimental conditions of slurry actions.

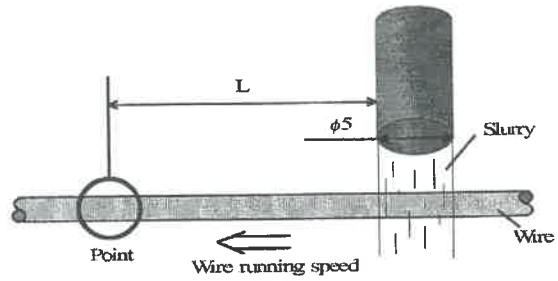

Fig.2 Observation method of slurry actions

Table 1 Experimental conditions of slurry action

Slurry	Base oil	PS-LW-1
	Grains (Size)	GC#800 (14μm)
Slurry concentration		35 wt%
Wire diameter		Piano wire ϕ0.2 mm
Wire running speed		20~200 m/min
Frequency		56 Hz
Amplitude		1.0 mm

2.2 Slicing method

Figure 3 shows the mechanism of multi-wire saw. This wire saw is the descent type of the workpiece. The slurry is supplied continuously and uniformly on the wire. In case of the vibration slicing, the wire vibrates by the four eccentric grooved rollers at the processing area. And, this wire saw has a characteristic that the frequency of wire changes with the wire running speed.

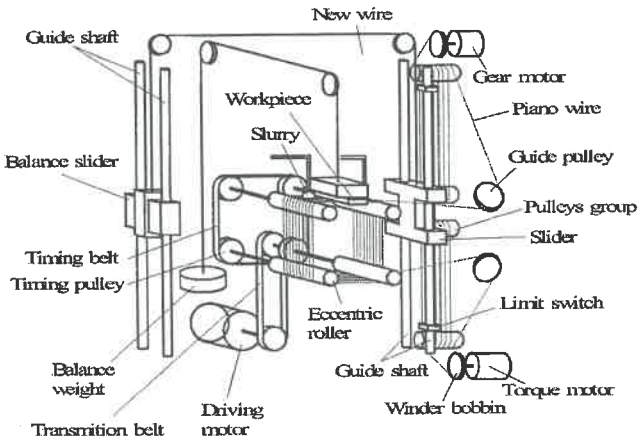

Fig.3 Mechanism of multi-wire saw

Table 2 Experimental conditions of slicing

Workpiece (size)	Soda glass (100*25*10t)
Slurry	PS-LW-1 + GC#800
Slurry concentration	35 wt%
Wire	Piano wire, ϕ0.2 mm
Wire tension	19.6 N
Working load	0.65, 0.77 N/wire
Wire running speed	200, 300, 400, 480 m/min
Frequency	13, 20, 27, 32 Hz
Amplitude	1.5 mm

Table 2 shows the experimental conditions of slicing.

3. Slurry actions and slicing characteristics in non-vibration slicing

Figure 4 shows relationship between slurry amount and wire running speed. When the wire running speed is less than 60 m/min, the slurry amount increases linearly with accelerating of wire running speed. And, at the area of 60 m/min over, the increase of slurry amount shows very small value. Figure 5 shows the observation results of slurry actions by

high-speed camera. As shown in Figure 5-(a), the slurry in case of 20m/min of wire running speed becomes like small balls at observation point of L=80 mm. And, in case of 100m/min, the slurry film under the wire is observed at the same point. In case of high wire speed, the carried slurry in the processing area observes uniformly film to compare with the case of low wire speed. On the other hand, the slurry film under wire is observed at L=0 mm (this slurry film defines as bottom film.). This bottom film brings by supplied slurry and carried slurry for wire running direction. Therefore, authors expect that the carried slurry amount in processing area is increase to get widely bottom film.

The two slurry nozzles is prepared to increase the carried slurry in the processing area. And, these nozzles are set over the wire for wire running direction. The slurry amounts on the wire measure by changing the length between two slurry nozzles. Figure 6 shows relationship between length of two nozzles and slurry amount. As shown in Figure 6, the slurry amount on the wire increases by using two nozzles. But, it is clear that the over-length of two nozzles decreases the carried slurry amounts.

Figure 7 shows the behavior of slicing efficiency by two type of supply method. It is clear that the cutting efficiency in case of improved supplying slurry nozzles shows the value efficiency of 1.2 times to compare with the with the case of previous supplying

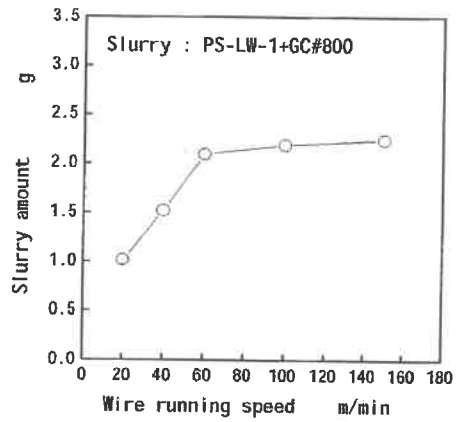

Fig.4 Behavior of slurry amount on the wire

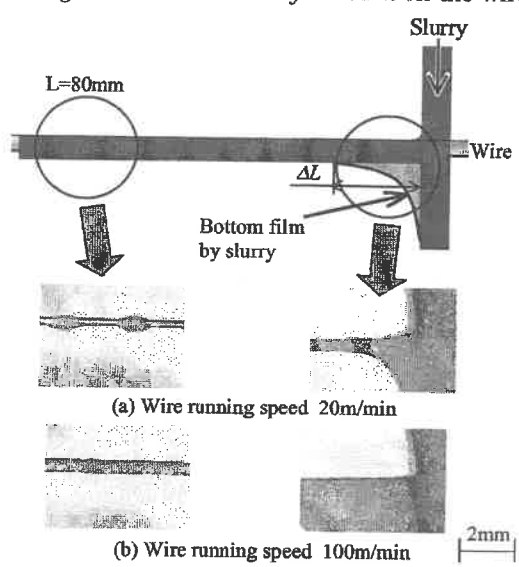

Fig.5 Slurry action in case of non-vibration

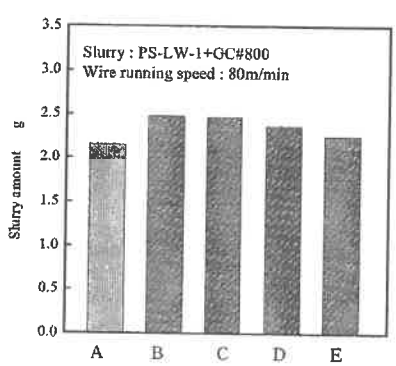

A: one slurry pipe, B: 2mm, C: 4mm, D: 7mm, E: 10mm

Fig. 6 slurry amount of two nozzles

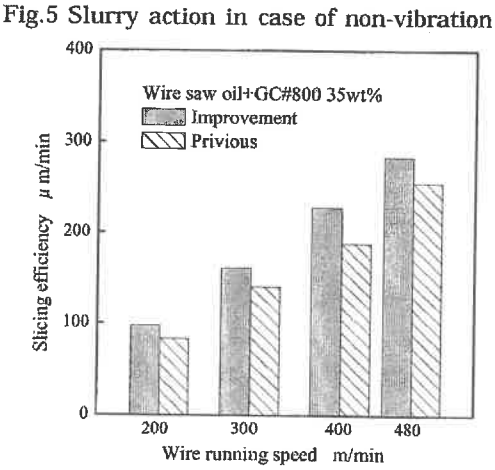

Fig.7 Behavior of slicing efficiency by two type of supply method

slurry.

4. Slurry actions and slicing characteristics in vibration slicing

Figure 8 shows the slicing efficiency in case of non-vibration and vibration slicing. The slicing efficiency in vibration slicing is lager than one of non-vibration. When the wire running speed is 200 m/min, the difference of slicing efficiency between non-vibration and vibration slicing shows 32 μm/min, and the difference of slicing efficiency at wire running speed of 400 m/min is 123 μm/min. These difference values are in proportion to increasing rate of wire running speed. This vibration effect is occurred by the change of frequency.

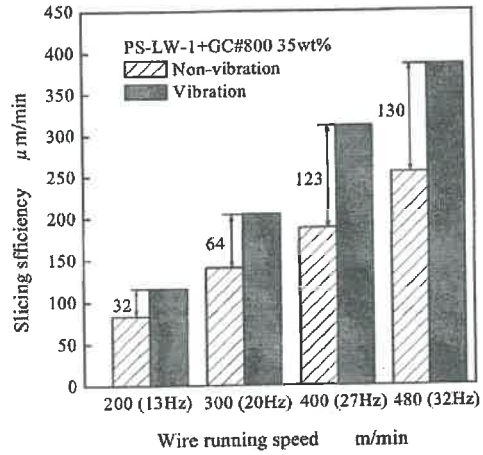

Figure 8 slicing efficiency in vibration slicing

The slurry actions on vibrated wire observe by high speed camera to be clear vibration effect. Figure 9 shows the observations of slurry action. The experimental conditions are wire running speed: 60 m/min, amplitude: 1.0 mm, frequency: 60 Hz. In case of non-vibration, the carried slurry in processing area is hung under the wire. But, in case of vibration, the carried slurry rounds on the wire for up and down direction. As the slurry on the wire moves, the carried slurry amount in processing area increases to compare with non-vibration.

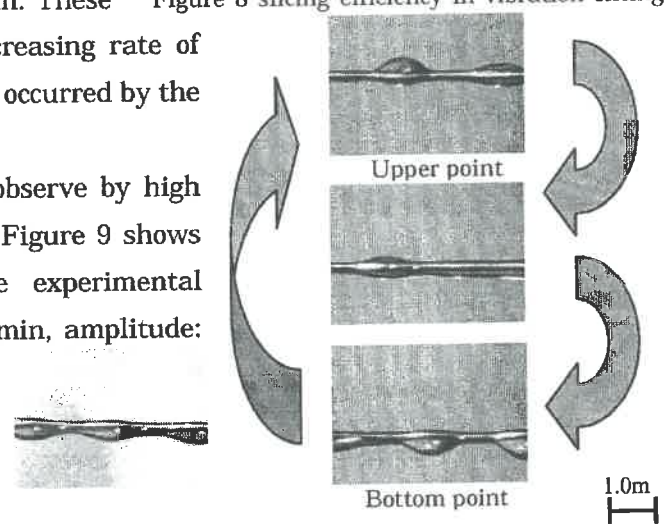

(a)Non-vibration (b) Vibration

Figure 9 Behavior of carried slurry in vibration

5. Conclusions

The slurry actions and slicing efficiency are studied, and the followings are clear.

1. When the two slurry nozzle for wire running direction is used, the amount of carried slurry in the processing area increases. And, the slicing efficiency shows the increase of approximately 10%.
2. The amount of carried slurry in the processing area is affected by bottom film under wire.
3. As the results of vibration wire saw, the hanged slurry rounds on the wire by vibration acceleration, and the amount of supplied slurry increases.

Reference

1. K. ISHIKAWA, H. SUWABE et al., J. Japan Soc. Prec. Engg., 66(6),912(2000). (in Japanese)
2. K. ISHIKAWA, H. SUWABE, Proc. Prec. Engg.(ICPE'97), 1, 253(1997).

Chatter Modeling and its Diagnostics in Endmilling

Moon Chul Yoon[a], Young Kook Kim[a], Hyun Deog Cho[b], Seong Kun Kim[c]

[a] School of Mechanical Engineering, PuKyong University, Pusan, Korea
[b] School of Mechanical Engineering, Kyungil University, Hayang, Korea
[c] School of Mechanical Engineering, Hoseo University, Asan, Korea

Abstract

In this study, the static and dynamic characteristics of the endmilling process were modeled and the analytic realization of a chatter mechanism was discussed. In this regard, we have discussed the comparative assessment of recursive time series modeling algorithms that can represent the machining process and detect abnormal machining behaviors in a precision endmilling operation. In this study, simulation and experimental work was performed to show malfunction behaviors. For this purpose, new recursive least square method (RLSM) was adopted for the on-line system identification and monitoring of a machining process; we can apply these new algorithms in a real process for detection of abnormal chatter. Also, the stability lobe of chatter was analyzed by the varying parameter of cutting dynamics in regenerative chatter mechanics.

Introduction

For the removal of malfunction behavior, it is very important to predict machining error, happening behaviors of chatter and cutting forces. The cutting force includes many machining behaviors and this factor has been the main object of this type of study such as detection and analysis of tool wear and fracture. Also, in this study, we have used the ARMA spectrum method especially recursive least square method algorithm for the analysis and detection of chatter frequency and have traced the change of stability borderline according to the design factor of machine tools such as natural frequency, the damping factor and the specific cutting force. Also, we proposed the stable and unstable regions of chatter according to the parameter of spindle revolution. In this study we have proposed the tendency of cutting dynamics in the endmilling operation

RLSM Modeling and Spectrum Analysis

For the analysis of the endmilling operation we used a mathematical modeling method of time series such as the ARMA (auto regressive moving average) modeling method. By acquiring the real time data of machining system for the endmilling, we definitely define the machining system and analyze the characteristics of the endmilling operation with the modeling parameter, especially for the case of malfunction behavior such as chatter. By configuring the diagnostic system for on-line monitoring we can certify the behaviors of malfunction behavior of the endmilling. The experimental signal for the time series modeling is the cutting force of tool dynamometers. Also, the ARMA spectrum by the RLSM algorithm was analyzed in each condition of malfunction. This algorithm may be applicable to turning, boring, drilling turning, grinding and nontraditional machining of each removal process. The other signal besides the cutting force may also be used for the on-line analysis of the machining system. We can represent the general ARMA discrete model of order (n,m) and the model may be represented in the endmilling operation as the following.[3)]

$$(1 + a_1 z^{-1} + a_2 z^{-2} + \dots + a_n z^{-n})x(t) = (1 + b_1 z^{-1} + b_2 z^{-2} + \dots + a_m z^{-m})a(t) \quad (1)$$

where, a_i, $i = 1, 2, \dots, n$: autoregressive parameter, b_i, $i = 1, 2, \dots, m$: moving average parameter

$z^{-1}x(t)=x(t-1)$, z^{-1} : backshift operator, $a(t)$: white noise, $E[a(t)]=0$

$E[a(t)a(t-u)] = \sigma_a^2 \delta_u$, δ_u : Kronecker Δ function

For the analysis of ARMA modeling and its spectrum, there are approximately two classified methods; These are on-line and off-line. In this study we used the RLSM which is the former type of on-line.[3)] Briefly speaking, times series data $x(t)$ may be modeled by this ARMA model of order(n, m) and its recursive algorithm may be summarized as follows:[3)]

$$\varphi(t) = [\, -x(t-1), \dots, -x(t-n), e'(t-1), \dots, e'(t-m) \,]'$$

$$e = x(t) - \varphi^t(t)\theta(t-1) \quad (2)$$

$$R(t) = \left(I - \frac{R(t-1)\varphi(t)\varphi^t(t)}{\lambda(t) + \varphi^t(t)R(t-1)\varphi(t-1)}\right)\frac{R(t-1)}{\lambda(t)} \quad (3)$$

$$K(t) = \frac{R(t-1)\varphi(t)}{\lambda(t) + \varphi^t(t)R(t-1)\varphi(t-1)} \quad (4)$$

$$\theta(t) = \theta(t-1) + K(t)e(t) \quad (5)$$

$$e'(t) = x(t) - \varphi^t(t)\theta(t) \quad (6)$$

but, $\lambda(t+1) = \lambda\,\lambda(t) + (1 - \lambda)$ $\quad (\lambda = 0.99, \quad \lambda(0) = 0.95)$

where, parameter $\lambda(t)$ is the forgetting factor which is in general approximately 1. The initial condition of α is a very large constant and may be selected in the following.

$$R(0) = \alpha I, \quad \theta(0) = 0, \quad \varphi(0) = 0$$

After ARMA modeling parameter $\theta(t)$ with the RLSM, we can get the power spectrum of the system by the

direct form transfer function and it can be represented as follows:[3)]

$$H(z)=\frac{N(z)}{D(z)}=\frac{b_o+b_1z^{-1}+b_2z^{-2}+\ldots+b_mz^{-m}}{1+a_1z^{-1}+a_2z^{-2}+\ldots+a_nz^{-n}} \tag{7}$$

Where, by substituting z with e^{jwT}, we can get the power spectrum and phase spectrum.

Chatter Modeling

Fig. 1 shows the components of the dynamic chip thickness according to vibration between the tool and workpiece after one edge passes another that already passed before. In this figure, the movement to x direction doesn't influence the geometry of the workpiece because the workpiece of remained part is directly removed.

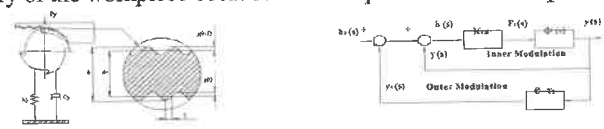

(a) (b)

Fig. 1 Wave generation and block diagram of chatter dynamics

So, we can simplify the model of the endmilling between tool and workpiece as the system of a two order ordinary differential equation with one degree in y-direction mathematically. When the endmill starts to rotate and we can let the depth of cut be as $y(t)$ in the present cutting edge case, having passed, and the depth of cut as $y(t-T)$, The dynamic chip thickness of this model may be represented in following eq. (8)

$$h(t)=h_0-[y(t)-y(t-T)] \tag{8}$$

Also, the cutting dynamics between the endmill and workpiece may be represented by the following equation:

$$m_y\frac{d^2y}{dt^2}(t)+c_y\frac{dy}{dt}(t)+k_y\,y(t)=F_f(t)=K_f\,ah(t)=K_f\,a[h_0+y(t-T)-y(t)] \tag{9}$$

Where, if $y(t)$-$y(t-T)$ is larger than h_0, then the chip thickness is not less than 0 and then we leave it as directly 0. By Laplace transform of eq. (8) and (9) we can summarized as follows.

$$\Phi(s)=\frac{y(s)}{F_f(s)}=\frac{\omega_n^2}{k_y(s^2+2\zeta\omega_n s+\omega_n^2)} \tag{10}$$

By substituting $y(s)$ with $h(s)$, we can get the following eq.

$$\frac{h(s)}{h_0(s)}=\frac{1}{1+(1-e^{-sT})K_f\,a\Phi(s)} \tag{11}$$

If we let the root of characteristic equation be $s=\sigma+j\omega_c$. The characteristic function becomes

$$1+(1-e^{-j\omega_cT})K_f\,a_{lim}\Phi(j\omega_c)=0 \tag{12}$$

Both real and imaginary parts of the characteristic equation must be zero. If the imaginary part is considered, it is the following.

$$G\sin\omega_cT+H(1-\cos\omega_cT)=0 \quad\text{and}\quad \tan\Psi=\frac{H(\omega_c)}{G(\omega_c)}=\frac{\sin\omega_cT}{\cos\omega_cT-1} \tag{13}$$

Where Ψ is the phase shift of the structure's transfer function. The spindle speed (n[rev/s]) and chatter frequency (ω_c or f_c) have a relationship and the vibration waves left on the surface of the workpiece is[4)]:

$$f_c[Hz]\cdot T[s]=\frac{f_c}{n}=k+\frac{\varepsilon}{2\pi} \tag{14}$$

where, k is the integer number of waves and $\varepsilon/2p$ is the fractional wave generated. angle ε represents the phase difference between the inner and outer modulations, where the phase shift between inner and outer waves is $\omega_c=3\pi+2\psi$. The corresponding spindle period (T[s]) and spindle revolution (n[rev/min]) is found to be

$$T=\frac{2k\pi+\varepsilon}{2\pi f_c}\rightarrow n=\frac{60}{ZT} \tag{15}$$

The critical depth of cut a_{lim} may be given by equating the real part of the characteristic equation to zero[4)].

$$a_{lim}=\frac{-1}{K_f\,G[(1-\cos\omega_cT-(H/G)\sin\omega_cT]} \tag{16}$$

Cutting Force and Spectrum Analysis

We used four-fluted HSS endmill of 12 mm in diameter manufactured by Taewha Co. and SM45C workpiece in this experiment. The tool dynamometer for measuring the cutting force is a piezo type Kistler(Model Type 9272) tool dynamometer. We also used a charge amp. For amplifying cutting force we used cassette data recorder

(TEAC MR-10) for saving the measured force. By using the A/D converter (DT3001) the digitized cutting force is stored in the PC and finally analyzed. Also, using the oscilloscope (HUNG CHANG 5504, 40MHz) we can see the signal of stored data directly. The raw data and power spectrum may be plotted and then calculated, respectively. By using the algorithm of the RLSM we can get the behaviors of parameter and the relationships between parameter and machining characteristics. Also, the total menu of the program is constructed by DTVEE software that is very convenient for the configuration of on-line connection between developed software and other displaying tools having the internal function language. In this study, the sampling frequency for acquiring the cutting force data in this experiment was selected as 1 kHz.

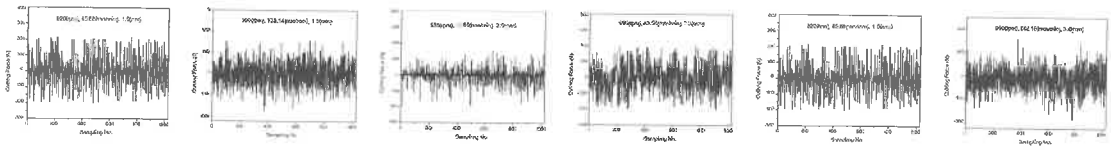

(a) (b) (c) (d) (e) (f)

Fig. 2 Cutting force signal for experiment

Fig. 2 (a) shows the signal having no chatter, (b) and (f) shows chattering for No.6 and No.17, respectively. Also, (c) and (d) shows a very mild chatter for No.7 and No.10, respectively. Fig. 2(e) shows that chatter happened more in severe for the condition of No.14, with greater axial depth. In the figure, the sudden change of signal appear more vividly in larger depth of cut; these phenomena are the irregularities of signal which have more dynamic properties during the cutting condition of larger depth of cut excessively. In general, for the condition of sudden fracture, the cutting force also changes suddenly and shows these trends. So, these properties may frequently occur in fracturing and also affects the residual parameter of ARMA modeling. However, in this study the chatter characteristics don't affect the residual parameters of the ARMA parameter. Therefore, the residual parameter is not a good parameter for the prediction of chattering.[3] by treating the data of Fig.2, and transforming the time series data into frequency domain, we were able to get the ARMA power spectrum. In this analysis we selected the order of ARMA modeling as (10,5). In Fig.2, the natural mode was calculated by the RLSM. The calculated normalized modes for the condition of 520 rpm are 0.064(64Hz), 0.129 (129Hz), 0.25 (250Hz) and 0.33 (330Hz). For the condition of 990 rpm, its characteristics appear at the point of 0.129, 0.258, 0.33, 0.37 and 0.42. In this study, as the spindle speed becomes high; the chatter characteristics of higher frequency begin to decrease. As a result, the higher chatter frequency disappears.

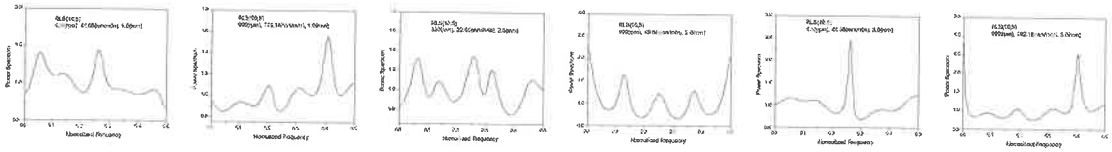

(a) (b) (c) (d) (e) (f)

Fig. 3 Power spectrum by RLSM analysis

Fig. 3(a) shows the spectrum by using the cutting force signal for 520 rpm with a RLSM algorithm. In the spectrum we can see the clear natural mode at 0.064 and 0.258. Also, this mode is the frequency of tools passing by converting and analysis. As we get the power spectrum of higher order, other modes of weak one may be sensed, in a slightly shifted mode. Fig.3 (b) and (f) is the case of No. 6 and 17, respectively on the condition of 990 rpm. If we machined the workpiece with higher feed, and chatter occurred, its mode was calculated at 0.42(420Hz) by the RLSM algorithm. It is a type of higher chatter frequency than the former. Fig.3(c) is the power spectrum for the cutting condition in 520 rpm and 2.0 mm depth. The natural modes appear at 0.064, 0.129, 0.258 and 0.33. Fig.3 (d) is the power spectrum of cutting condition for No. 10, and its natural modes appear at 0.129, 0.258 and 0.37. This natural frequency was verified as a tool passing frequency. Also, Fig. 3(e) is the case of spindle speed and depth of cut for 520 rpm and 3.0 mm, respectively. The analyzed natural mode appears clearly at 0.258 and this phenomenon is the result of dynamic property during cutting by the cutting edge. In all these investigations, we can see that as the higher the cutting speed and depth of cut is selected, the lower chatter frequency may disappear. This is true especially at the case of 990 rpm, where, the higher chatter frequency disappears. Also, as the spindle speed of 520 rpm moves to that of 990 rpm, the chatter frequency in middle range may disappear and a little appears at the higher frequency range. This phenomenon is very similar to that of Chiou's results[5]. The spectrum by RLSM is a very clear and convenient method for analyzing, especially with less data than conventional FFT and off-line ARMA spectrums.[4] Moreover, it has the advantage of calculating the algorithm's ARMA parameter in each step of the processing.

Stability Lobe of Chatter

Fig. 4(a) represents the stability lobe of chatter for the case of cutting dynamics having the property ω_n = 160Hz, ζ = 0.2, K_f = 2100 N/mm^2 by using eq. (20) and absolute stability region for the positive integer range of k(=0.6). It is stable below the stability lobe boundary region and unstable at the upper region of its boundary. The chatter frequency appears at the revolution of the unstable region and it may be converted to chatter frequency. Therefore, there are two types of chatter, with low and high frequency. According to the natural frequency, damping factor and specific cutting force, the chatter region moves to other region. If we increase the specific cutting force K_f, the transient axial depth of cut region becomes lower and in more possibility of chatter may occur for the case of a larger axial depth of cut. For the case of aluminum alloy and steel, the specific cutting force is K_f = 800 N/mm^2 and 2100 N/mm^2, respectively, where, the specific cutting force of steel is larger than aluminum, so the transient axial depth of cut shifts upward and the total stability region becomes larger. The point A is in the condition of Fig. 3(e) and there is no chatter. Moreover, its analyzed and converted revolution is matched to 520 rpm. Also, the mode of 0.258 (258Hz) is not a chatter mode but proves to be a tool passing frequency. The natural mode of 0.42 (420Hz) in Fig.3 (f) is chatter frequency and it corresponds to point B of chatter stability lobe region. The point C is an stable region and there is no tendency of chatter in Fig. 3(a). The two modes are detected and it proves to be the tool passing frequency because the cutting edge is four.

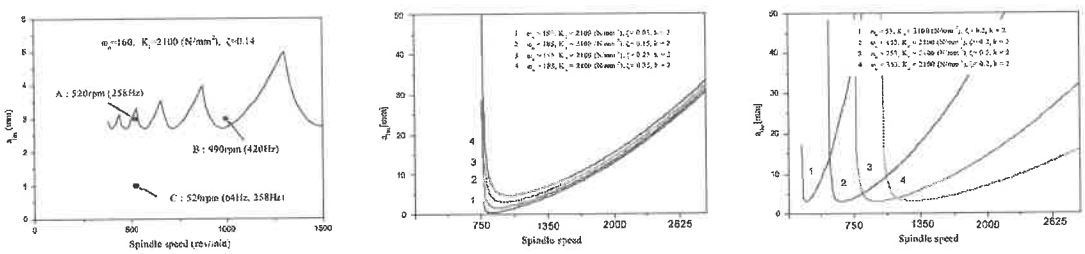

(a) (b) (c)

Fig.4 Stability lobe of chatter boundary for endmilling

Fig.4(a) shows the variation of the stability lobe borderline according to the change of the damping factor for ω_n = 185Hz and K_f = 2100 N/mm^2. As we increase the damping factor, the stable lobe borderline moves upward and the stable region becomes wider and moves to shift right. As we increase the damping factor the stable region also becomes wider (b). Fig.4(c) shows the variation of the stability borderline according to the change of natural frequency for ζ= 0.2 and K_f = 2100 N/mm^2. As we increase the natural frequency, the stability lobe borderline for the case of k = 2 moves to shift right and the region becomes narrow. Therefore, by considering the results of this study, we can predict the desirable cutting condition to avoid chatter by the appropriate selection of spindle speed and axial depth of cut. Moreover, these results may be used for the design of a machine tool having appropriate parameters of cutting dynamics for endmilling.

Conclusion

1) As we increase axial depth of cut and cutting speed, higher chatter frequency may occur rather than lower chatter frequency, after which, another high chatter frequency exist in the condition of a 990 rpm spindle speed. Also, as we increase axial depth of cut, the power of chatter frequency becomes higher.

2) We can get the exact power spectrum with a little sampled data by the RLSM and the analysis of the dynamic property of cutting force. By the analysis of stability borderline, we can predict the stable and unstable regions. As we increase the damping factor and specific cutting force of chattering dynamics, the area of stability becomes wider. Also, the natural frequency increases the lobe shifts to the right. Therefore, this result may be used as data for designing and manufacturing machine tools with no chattering.

References

[1] B. K. Fussell, K. Srinivasan, "An Investigation of the End Milling Process Under Varying Machining Conditions," *Trans of ASME, J. of Eng. Ind.*, Vol. 111, pp. 149-157, 1989.

[2] S. C. Lin, R. J. Yang, "Force-based Model for Tool Wear Monitoring in Face Milling," *Int. J. Mach. Tools and Manufacture*, Vol. 35, No. 9, pp. 1201-1211, 1995.

[3] M. C. Yoon, H. D. Cho, S. K. Kim, "A Study on Diagnostics of Machining System with ARMA Modeling and Spectrum Analysis," *KSMTE*, Vol. 8, No. 3, pp. 42-51, 1999.

[4] Yusuf Altintas, "Manufacturing Automation", Cambridge Univ., pp. 33-46, 2000.

[5] M. C. Yoon, H. D. Cho, S. K. Kim, Y. K. Kim, H. G. Cho, "A Study on the Modeling and Analysis of Chatter in Turning Operation," *KSMTE*, Vol. 10, No. 4, pp. 1-8, 2001.

[6] Y. K. Kim, M. C. Yoon, M. K. Ha, S. B. Sim, "A Study on the Modeling and Diagnostics on Chatter in Endmilling Operation," *KSPE*, to be published in October 2001.

COMPENSATION OF SPINDLE UNBALANCE-INDUCED VIBRATION USING AN ELECTROMAGNETIC EXCITER

Jae Sam Ahn, Sun Min Kim, N. P. Mahalik, and Sun Kyu Lee
Kwang-Ju Institute of Science and Technology, Gwangju, Korea

ABSTRACT

Recently, high speed cutting technology is widely adapted in the manufacturing process due to the increased demand of quality and productivity. Well-known high-speed cutting systems are motorized spindles. It is convinced that the profile of spindle rotation changes over the period of time due to the tool wear or tool change, which deteriorates not only machining quality but also tool life significantly. Therefore, automatic spindle balancing with respect to the spindle rotating condition becomes an essential requirement for high speed and high precision machining systems.

This paper presents an automatic compensating scheme for spindle unbalance using an electromagnetic exciter (EME). The proposed scheme provides several advantages such as compensation of spindle unbalance-induced exciting force, spindle monitoring, and accurate control since it uses non-contact excitation based on electromagnetism. In the proposed system, the spindle unbalance-induced force is measured by vibration sensors and used as the feedback. Accordingly the electromagnetic force is applied to the spindle rotor in the counter side that corresponds with the measured unbalance force.

In this paper, to implement the compensating system, the controller is designed and also the spindle-bearing system is built up. The experimental results indicate that the proposed method is very effective to compensate the spindle unbalance-induced exciting force in real time.

Key words: compensation of spindle unbalance-induced vibration, electromagnetic exciter (EME), spindle bearing system

1. INTRODUCTION

During the metal cutting process, the vibration on the spindle is generated by the spindle unbalance force or chattering by interaction between workpiece and tool in machining [1]. High speed and intensive cutting performance is significantly deteriorated by vibration caused by the spindle unbalance force and the chatter [2]. This also degrades the quality and productivity of the process. In this paper, the vibration due to the spindle unbalance force is addressed.

In general, the spindle unbalances are compensated by addition of mass to the opposite side corresponding to the spindle unbalance force, which is measured by using vibration sensors [2]. However, this method is mainly used at the initial state. Thus, the spindle unbalance force, which is generated over long time operation, is not compensated. Or even though possible, it is a troublesome work because this method needs to be done manually.

On the other hand, automatic balancing methods are adapted in real machine, however, it is frequently constrained by spindle configuration [3].

In this paper, a spindle system using an electromagnetic exciter (EME) has been proposed to compensate the spindle unbalance-induced vibration automatically as an alternative, but effective method. The proposed spindle system is composed of spindle bearing system using an EME, a control system, and a controller for compensation of the spindle unbalance force.

The proposed EME based scheme used in the spindle system offers several advantages such as excitation of the spindle by non-contact way and flexible way of changing the excitation frequency and magnitude [4].

The main works in this paper are summarized as design and development of sophisticated spindle system using an EME, configuration of control system by using sensory devices, and a DSP-based controller board, and development of controller to compensate the spindle unbalance. Experiments are conducted and the results are presented.

2. SYSTEM CONFIGURATION

The spindle system using an EME is applied to reduce the vibration caused by the spindle unbalance force.

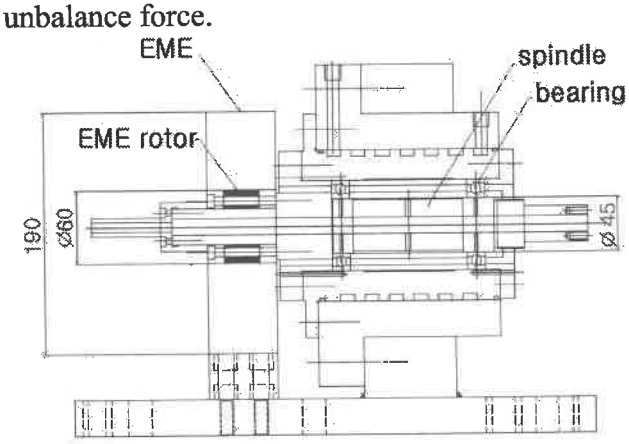

(a)

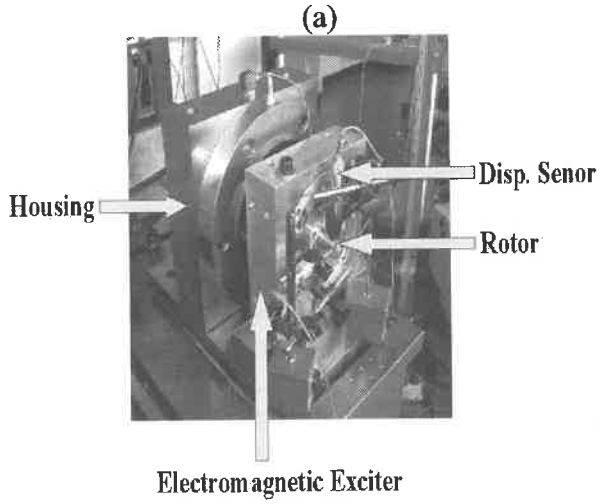

(b)

Fig.1 Spindle system using an EME (a) Schematic diagram (b) photo

The spindle unbalance-induced vibration is compensated with non-contact way by attractive force that is generated by the EME. The spindle system is composed of a spindle bearing system using an EME, a control system, and a controller as shown in Fig.1, 2.

In the custom-built spindle system using the EME, the EME is located in front of the front bearing of conventional spindle-bearing system as shown in Fig. 1. The EME is composed of four horseshoes electromagnets arranged in round shape and located by 90° between one magnet and each neighborhood magnet. Each electromagnet consists of two magnet poles. In addition, eight magnet poles of four electromagnets are arrayed by NNSSNNSS polar arrangements.

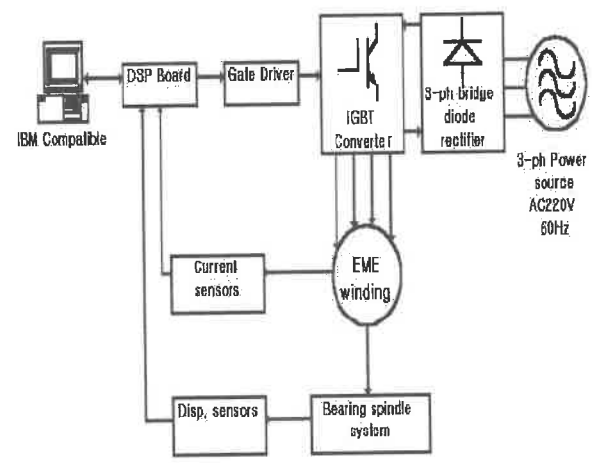

(a)

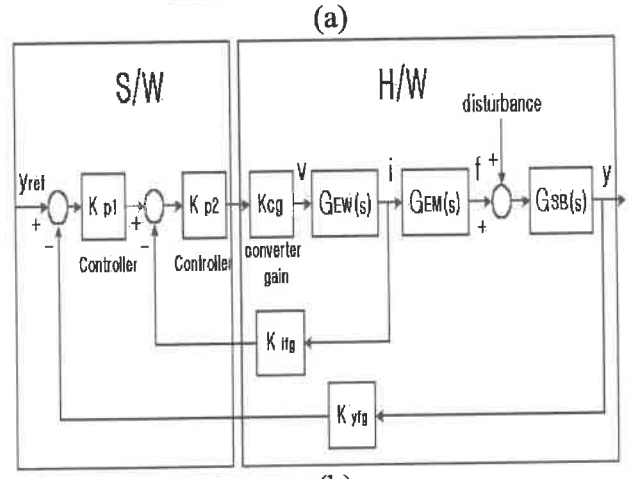

(b)

Fig. 2 Block diagram of (a) control system (b) controller

Secondly, the control system consists of four CTs, two capacitance displacement sensors, four IGBT converters, and a DSP based controller board as shown in Fig. 2 (a). The CTs are to measure winding coil currents of four electromagnets and the displacement sensors are to detect the radial displacement of the spindle shaft. Besides, four IGBT converters, asymmetric bridge type converters, are to supply electromagnets of the EME with electric power according to compensation signal. The DSP controller board is used for real-time control [5].

The controller consists of a current feedback controller and displacement feedback controller where $G_{EW}(s)$, $G_{EM}(s)$, and $G_{SB}(s)$ are transfer functions of electrical circuit of winding coil, electromagnetic structure of the EME, and mechanical system of spindle bearing system respectively. Furthermore, K_{p1}, K_{p2}, K_{ifg}, K_{yfg}, and K_{cg} are proportional gains of current and displacement controller, and current and displacement feedback gains, converter gain respectively. Moreover, v, i, f, y, and y_{ref} are winding input voltage, winding coil current, electromagnetic force generated by the EME, displacement of y-axis, and displacement command, respectively as shown in Fig. 2 (b).

3. EXPERIMENTAL RESULTS

The FRF experimental results represent performance of the proposed spindle system before compensation and after compensation as shown in Fig. 3.

The V-Y open loop bode plot in the proposed spindle system represents that the BW is 4[Hz] and the phase delay, which deteriorates the stability of system, becomes bigger as the frequency increases as shown in Fig. 3(a). Therefore, the controller is designed by considering this low BW and phase delay. Controller gains were tuned using trial and error method in the experimental setup.

The y_{ref}-y bode plot with the controller to compensate the spindle unbalance force shows that the BW is 385[Hz] and phase delay is improved as shown in Fig. 3 (b). Consequently, this controller is proved to be very effective because the controller makes the system response more rapid and improves the system stability by reducing the phase delay.

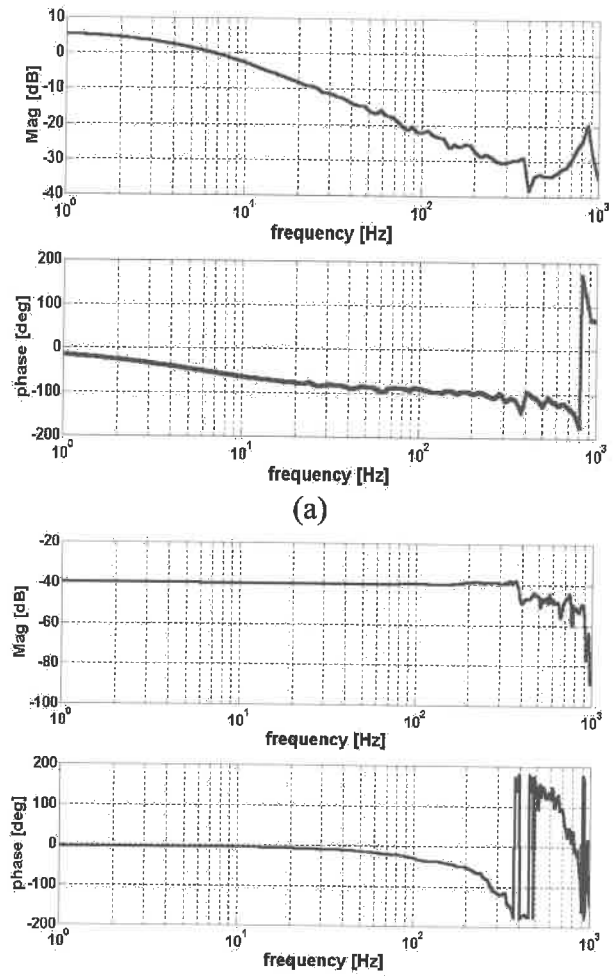

Fig. 3 Frequency response of the proposed spindle system (a) V-Y (input voltage vs. displacement at y axis) bode plot at open loop (b) Y_{ref}-Y (reference input voltage vs. displacement at y axis) bode plot with controller

The compensation result of the spindle unbalance-induced vibration is shown in Fig. 4. When the spindle with unbalance is rotated by 3000[rpm], the vibration with 50[Hz], which has the shape of oval type whose long radius and short radius are 5.5[μm] and 3.5[μm] respectively, is generated as shown in Fig.4. The vibration is reduced by implementing the

controller for compensation of the spindle unbalance about 40%; the long radius is lessened from 5.5[μm] to 2.5[μm] and the short radius from 3.5[μm] to 2[μm]. This experimental result indicates this proposed EME-based spindle system is very effective to compensate the spindle unbalance.

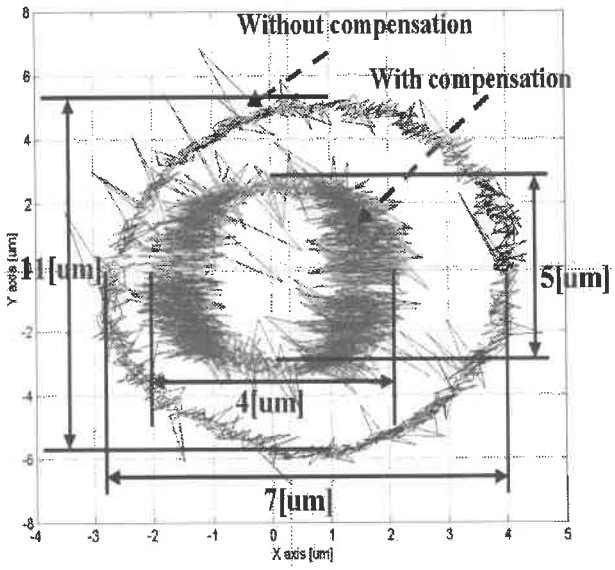

Fig. 4 Vibration compensation result due to spindle unbalance (vibration 50[Hz] in 3,000 [rpm])

4. DISCUSSION

To compensate the effect of spindle unbalance, firstly the spindle system using an EME and the control system were built up. And then the controller for compensation of the spindle unbalance was developed. Finally, this controller was implemented in the experimental setup. As a result, we obtained the bandwidth of 385[Hz]. In addition, when the spindle with unbalance was rotated with 3,000[rpm], the vibration was reduced to about 40% by implementing the controller. These experimental results showed this proposed spindle system was very effective to compensate the spindle unbalance.

However, there was limit because of increase of the phase delay in the frequency band above 100[Hz].

Therefore, it is needed to try to improve the performance of the controller. Furthermore, though the characteristic of non-linearity caused by the interaction between electromagnetic force and input voltage in the proposed spindle system was not considered in this paper, a controller using nonlinear control method should be developed.

5. CONCLUSION

In this paper, the spindle system using an EME was proposed to compensate the spindle unbalance-induced vibration. In the proposed spindle system, the vibration due to the spindle unbalance was monitored using vibration sensors and was compensated by electromagnetic attractive forces generated by the EME, which were excited by anti-direction forces corresponding to the measured unbalance.

6. ACKNOWLEDGEMENT

This research was supported by the Brain Korea 21 fund of the Ministry of Education in Korea. The authors express sincere gratitude to the Ministry of Education.

7. REFERENCES

1. S. A. Tobias, *"Machine Tool Vibration"*, Black & Son, London, 1965
2. Fredric F., Enrich, *"Handbook of Rotor Dynamics"*, Mcgrawhill, 1992
3. Yasusuke JINNOUCH, "Automatic Balancer-Static Balancing and Transient Response of a Multiball Ballancer", Trans. JSME(in Japanese), Vol. 59, pp. 79~84,1993
4. D. J. Song, S. M. Kim, and S. K. Lee, *"Monitoring of Stiffness of Spindle Bearing using Electro Magnetic Exciter"*, the Fall Session Conference of KSPE, 1999
5. G. H. Im, P. S. Shin, W. H. Kim, W. Y. Son, and W. M. Kim, *"The Study of Switched Reluctance Motor and Driver"*, KERI

ERRORS IN ALUMINUM MICRO-SCALE GROOVES PRODUCED WITH WIRE EDM FOR SUBSEQUENT GRINDING

Mathieu Barraja, Prem Rachakonda, and R. Ryan Vallance
Precision Systems Laboratory, University of Kentucky, Lexington, KY *

Abstract

This paper presents initial results from investigating the manufacture of high precision micro-scale vee-grooves fabricated in Aluminum 6061-T6. The manufacturing process being tested includes three primary steps. The first step produces the rough shape of the vee-grooves using conventional wire electro discharge machining (wire EDM). The second step coats the grooves with a hard layer using the Sandford process. The final step will produce precise vee-grooves with smooth surfaces by grinding away a portion of the hard coating. In this paper, we describe the fabrication process, assess the surfaces of the vee-grooves, and evaluate manufacturing variation in the form of the vee-grooves prior to the grinding step. The recast layer and coating thickness were investigated using metallography. The variation in the 2D form of the grooves was investigated with an algorithm for extracting 2D geometric parameters from a 3D point cloud measured with stylus profilometry.

Keywords: wire EDM, hard coating, vee-grooves, microfabrication

Introduction

In micro-scale devices, there is interest in the production of grooves and channels for locating microstructures and for micro-fluidics in heat exchangers and reactors. Micro grooves and channels can be manufactured with material removal processes such as etching [1], mechanical cutting with miniature cutters [2,3], and non-traditional micro machining [4]. Alternatively, they can be formed with processes such as coining [5] and molding.

The objective in this work is to investigate the suitability of a process for producing micro vee-grooves in aluminum 6061-T6 with processes and equipment that are readily available. Etching processes are not readily available to most manufacturers and are not appropriate for aluminum. Mechanical cutting, which is readily available, produces burrs that are significant at this length scale [6] and are difficult to remove. For these reasons, we are investigating a process based on wire electro discharge machining (wire EDM) and precision grinding. For testing purposes, we are manufacturing vee-grooves with nominal width, depth, and aperture angles of approximately 180 μm, 156 μm, and 60 degrees, respectively, after grinding.

Description of the Process

The first step in the manufacturing process is to cut the general shape of the vee-grooves using conventional wire EDM. Wire EDM is applicable for any conductive material, and many EDM machines are capable of using wires with diameters as small as 50.8 μm. Wire EDM can therefore produce a wide variety of groove geometries with lengths up to many millimeters. Unfortunately, wire EDM generates a recast layer produced by the re-solidification of molten metal. This undesirable surface is clearly visible with scanning electron microscopy (SEM) as shown in Fig 1. The

* *Precision Systems Laboratory, Mechanical Engineering, University of Kentucky, 210-A CRMS Building, Lexington, KY 40506. http://www.engr.uky.edu/psl.*

imprecision of the vee-grooves and the rough surface justify grinding after EDM.

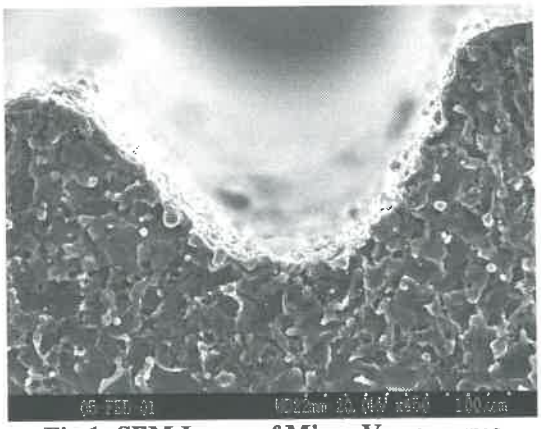

Fig 1: SEM Image of Micro Vee-grooves Following Wired EDM Operation

Prior to grinding, a hard coating was applied to the aluminum grooves using the Sandford process [7]. The Sandford process is an electrochemical process that produces a sapphire-like structure on the surface of aluminum parts by generating an oxide-coating layer. The coating penetrates the base metal and builds up on the surface. The hardness of the coating results in excellent abrasion resistance and is readily ground.

The third and final step in the manufacturing process will be to grind the precise shape of the vee-grooves into the coating to satisfy requirements for surface finish and tolerances.

At this time, we have fabricated a set of sample parts that are now ready for the grinding operation. The results of the grinding step will be described in future work following a careful study of achievable tolerances and surface finishes. In the remainder of the paper, we describe the nature of the coated surfaces and the manufacturing variation of the grooves prior to the grinding operation.

Metallography Study

A metallographic study was conducted to characterize the vee-grooves after wire EDM and after applying the hard coat layer. Hence, we can identify the effects of both steps on the final precision of the vee-grooves. The metallography study consisted of slicing the manufactured parts, mounting the parts, grinding and polishing the parts' endfaces, and finally observing the faces with an optical microscope.

A part cut with wire EDM but before coating was studied to characterize the recast layer observed in Fig 1. The recast layer produced a generally rough profile around the perimeter of the part that varied in thickness from between 4 μm and 8 μm as shown in Fig 2.

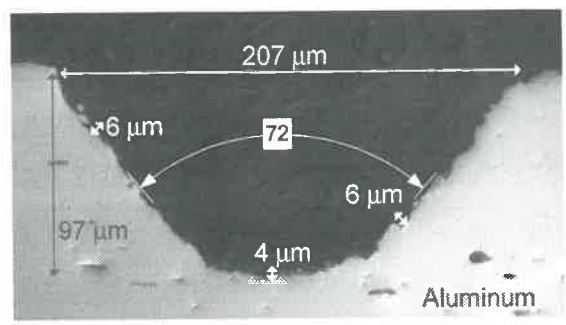

Fig 2: Metallography Study of a Vee-Groove Produced with Wire EDM

Fig 3 shows an image of a vee-groove after coating with the Sandford process. The thickness of the coating layer was not uniform, and it varied with the geometry of the vee-groove. On the sloped surfaces, the thickness was typically about 32 μm thick, but the thickness was only 16 μm at the bottom of the grooves. A thicker coating layer is achievable with a longer coating time, and may be necessary if gross errors exist during grinding.

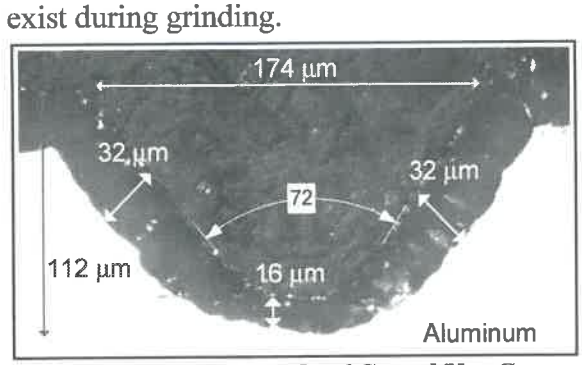

Fig 3: Metallographic Study of Coated Vee-Groove

Stylus Profilometry of Grooves

The accuracy and variation of the grooves' 2D shape was assessed prior to coating. Since the width, depth, and length of the grooves were approximately 170 μm, 150 μm, and 4 mm (before grinding), a 3D approach over the area of the grooves was necessary. Stylus profilometry was selected as the measurement technique since it provided suitable resolution in the z direction (~1 nm) over the necessary scan area (4 mm x 4.6 mm).

The stylus (~0.2 μm diameter) traveled along a path in the horizontal plane and recorded the height of the surface. The surface was scanned in a raster fashion by measuring a set of parallel traces. Traces were sequentially measured across the set of parallel grooves (x direction) with an increment in the y direction of 50 μm. The scan velocity in the x direction was 200 μm/s, and it sampled the height of the surface at 1 μm intervals. Thus a 3D point cloud of data points was collected, and it is shown in Fig 4 along with the ideal geometry.

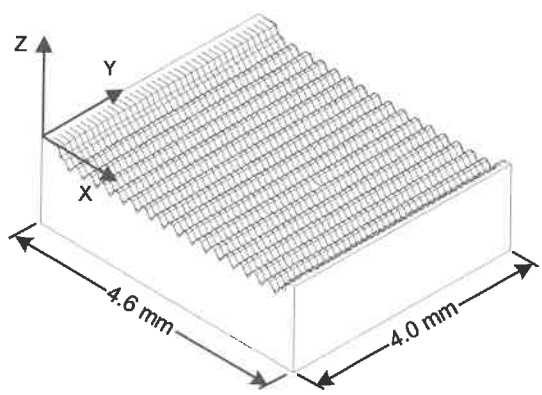

Fig 4: Point Cloud from Profilometry Traces

The manufacturing variation in the vee-grooves is observed after projecting the 3D point cloud onto a 2D plane intersecting the parallel vee-grooves. In Fig 5, it is evident that the EDM process did not remove the material at the very bottom of the grooves.

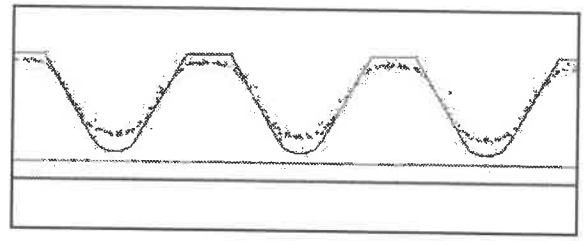

Fig 5: 3D Profilometry Data Projected onto a 2D Plane for Comparison to Ideal Model

Variation in Groove Shape

As shown in Fig 6, a vee-groove can be parametrically represented in two dimensions with four parameters and their manufacturing errors:

1. angle of aperture, α,
2. inclination angle, γ, which is the angle between the groove's bisector and a vertical line (ideally γ equals zero),
3. depth to the virtual vertex, h, and the
4. radius of curvature, r, at the bottom of the groove.

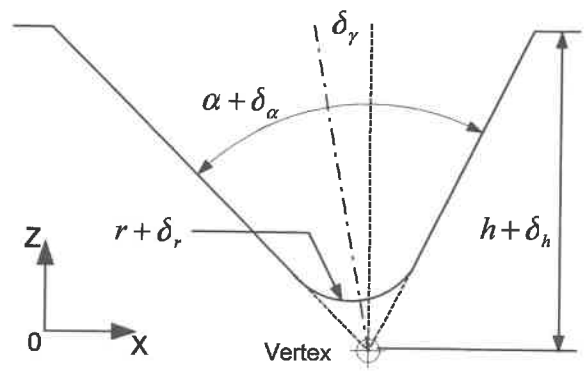

Fig 6: Manufacturing Errors in a Vee-Groove

We developed a simple algorithm that calculates the geometric parameters shown in Fig 6 from the measured profilometer data. For each vee-groove in a 2D trace, the algorithm fitted a straight line to the inclined edges and determined their slope and intersection. Thus two half-angles for every groove were calculated: the left one, β_L, and the right one, β_R. The angle of aperture was determined as the sum of the half angles. The intersection of the two fitted lines gave the coordinates of the groove's virtual

vertex, and so the dimension, h, was determined. The inclination angle was calculated as half the difference between β_L and β_R.

Using this algorithm on 40 traces and 16 grooves per trace yielded the geometric parameters of 640 2D grooves. Statistics characterizing the mean and variation of the parameters are shown in Table 1.

Conclusions

This paper introduced a manufacturing process to make micro-scale vee-grooves in Aluminum 6061T6 and a metrology procedure to measure their dimensional variation. Surface roughness and variation were found to be significant after EDM and coating, and so grinding remains necessary. A metallography study showed that variation in the thickness of the coating layer depended upon groove geometry. The thickness of the coating in the depth of the groove was approximately half the thickness on the flat surfaces.

Despite the dimensional variation after wire EDM and coating, the grooves are acceptable for subsequent grinding operations. The results of the grinding operation will be presented in future work.

Table 1: Statistics of 2D Geometric Parameters Describing Vee-Groove Variation

		Estimate of the Mean (95% Confidence Interval)			Estimate of the Variance (95% Confidence Interval)		
Feature	*Target value*	*Lower Limit*	*Estimated Mean*	*Upper Limit*	*Lower Limit*	*Estimated Variance*	*Upper Limit*
Left half angle (degrees)	30.0	34.41	34.63	34.84	7.1	7.9	8.9
Right half angle (degrees)	30.0	35.07	35.30	35.54	8.2	9.2	10.3
Aperture (degrees)	60.0	69.59	69.93	70.27	16.9	18.8	21.1
Inclination (degrees)	0.0	-0.49	-0.34	-0.19	3.5	3.8	4.3
Height (microns)	150	130.9	131.4	131.8	25.7	28.6	32.0

References

[1] Madou, M. *Fundamentals of Microfabrication.* CRC Press. New York, New York. 1997.

[2] Vasile, M.J., C.R. Friedrich, B. Kikkeri, and R. McElhannon. "Micrometer-Scale Machining: Tool Fabrication and Initial Results". *Precision Engineering.* Vol. 19. 1996. p. 180-186.

[3] Schaller, Th., L. Bohn, J. Mayer, and K. Schubert. "Microstructure Grooves with a Width of Less than 50 μm cut with Ground Hard Metal Micro End Mills". *Precision Engineering.* Vol. 23, No. 4. October 1999. p. 229-235.

[4] Masuzawa, T. and H.K. Tönshoff. "Three-Dimensional Micromachining by Machine Tools". Keynote Paper. *Annals of the CIRP.* Vol. 46, No. 2. 1997. p. 621-628.

[5] Hirt, G. and B. Rattay. "Coining of Thin Plates to Produce Micro Channel Structures". *Initiatives of Precision Engineering at the Beginning of a Millennium.* Proceedings of the 10th Int. Conf. on Precision Engineering. JSPE. Yokohama, Japan. July 18-20, 2001. Kluwer Academic Publishers, Boston, MA. p. 32-36.

[6] Lee, K., B. Stirn, and D.A. Dornfeld. "Burr Formation in Micro-Machining Aluminum, 6061-T6". *Initiatives of Precision Engineering at the Beginning of a Millennium.* Proceedings of the 10th Int. Conf. on Precision Engineering. JSPE. Yokohama, Japan. July 18-20, 2001. Kluwer Academic Publishers, Boston, MA. p. 47-51.

[7] Sanford Process. http://www.sanfordprocess.com

THE FABRICATION OF NANO-ROUGHNESS STANDARDS FOR THE CALIBRATION OF ATOMIC FORCE MICROSCOPES

Hans H. Gatzen and Christos Kourouklis
Institute for Microtechnology, Hanover University, Germany

Key Words: Atomic force microscope (AFM), roughness standard, nanogrinding, calibration

Abstract---For calibrating an atomic force microscope (AFM), nano-roughness standards are required. Only a calibrated AFM allows the user to perform reproducible measurements in accordance with national and international standards. So far, such AFM standards are not available. This paper is presenting an approach for fabricating nano-roughness standards with a selfrepeating quasirandom pattern. By using nanogrinding as the fabrication technology, randomly shaped, shallow furrows are ground in brittle materials. The profile of the furrows remains constant over the width of a standard and can be reproduced repeatedly.

1 Introduction

Roughness standards are used for the calibration of surface measurement systems. For calibrating classic profilometers with a stylus tip radius down to 2 μm, various roughness standards are available. However, the use of scanning probe microscopes such as the atomic force microscope (AFM) or the scanning tunneling microscope (STM) necessitates the development of new calibration standards. The resolution of these instruments is three orders of magnitude greater than for classic profilometers. Surface assessment methods for roughness values smaller than 20 nm are specified in ISO 4288 [1], while specifications for calibration standards to measure the surface texture are described in ISO 5436 [2]. According to standard type D1, contact stylus instruments as stated in ISO 3274 [3] require roughness standards with a recurring quasistatistical profile (repeating in the measurement direction). Although ISO 3274 does not call out atomic force microscopes, the same type of standards lends itself for calibrating these types of devices. According to ISO 4288, irregularly ground profiles with a CLA roughness R_a ranging from 6 nm to 20 nm have to be measured with a cutoff wavelength λ_c of 80 μm. With a turning process utilizing an ultraprecision lathe, programmed to create an appropriate quasirandom roughness profile, it is possible to fabricate roughness standards with an R_a of 25 nm [4]. This is the lower limit for the finest range specified in ISO 4288. At present, for R_a smaller 25 nm, no adequate roughness standard is available. Therefore, no appropriate calibration of an AFM for nanosurface analysis is available today.

To create such a standard, the following requirements have to be fulfilled. In correspondence to ISO 5436, the profile has to be irregular, but repeating itself exactly every 5 x λ_c. Hence, the profile length is 400 μm for a cut off wavelength of 80 μm. This applies for standards with roughness values down to an R_a of 6 nm. Furthermore, a future version presently under consideration will define nano-roughness standards for R_a smaller than 6 nm. The cutoff wavelength λ_c will be 40 μm and the profile length 200 μm. For this roughness range, a new method for calibrating AFMs is proposed. Assuming that the visual field of an AFM is 50 μm, the following calibration method based on ISO 3274 shall be applied (see Figure 1). In each of six successive scanning fields with an overlap of 20 μm, ten linescans are performed. Each scan has a length of 40 μm, two consecutive linescans are shifted 1 μm against each other. Thus, the whole scanning field encompasses an area of 200 μm x 100 μm. Within this field, the profile characteristics have to be constant normal to the measurement direction for the starting point not to affect calibration.

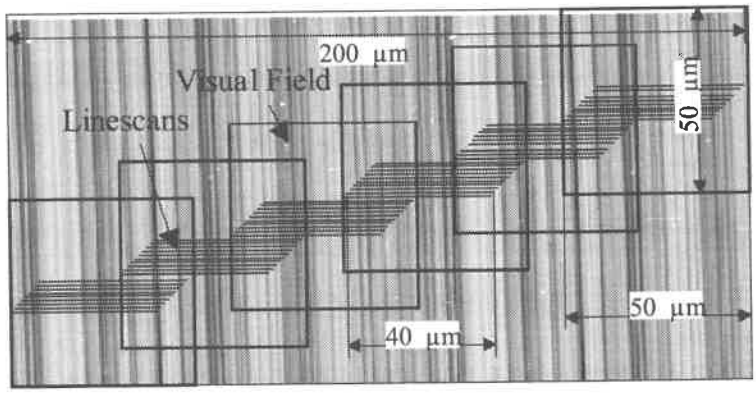

Fig. 1 Standardized measurement linescan pattern

2 Fabrication of Nano-roughness Standards Using Nanogrinding

2.1 Nanogrinding

Nanogrinding is an ultraprecision machining process used for the ductile mode machining of brittle materials [5]. The cutting grit is diamond which is embedded in the surface of a soft metallic plate. Nanogrinding is an ideal method for fabricating nano-roughness standards: in hard and brittle materials it achieves a constant cutting performance over the processing time, as well as CLA roughness values R_a down into the subnanometer range [5,6].

The kinematics of the workpieces and the tool for nanogrinding are similar to those for lapping. The workpieces mounted on a workpiece holder revolve on a rotating nanogrinding plate [5]. However, for fabricating a nano-roughness standard, the workpiece has to be held at a constant angle to the grinding plate's rotational direction. By doing so, linear furrows are machined on the surface of the workpiece.

To identify suitable materials for nano-roughness standards, nanogrinding experiments were conducted with different probe materials. Materials investigated were silicon, metal coatings on silicon, glass, and sapphire. Only silicon and sapphire showed a suitable surface topography. Figure 2 depicts the nanoground surface of a silicon workpiece. The topography of the silicon sample features a nearly constant profile shape along the furrows over the depicted surface area of 100 µm x 100 µm. Topography measurements in other areas of the same sample showed the same results. The furrows have a constant width and are free of chipping. The sample shown was nanoground with polycrystalline diamond with a grit of 1.5 µm - 3 µm. With the same diamond grit sapphire was machined, the result is depicted in Figure 3. The topography is similar in appearance as the silicon sample in Figure 2. Furrows are collateral and coplanar, another benefit of the nanogrinding process. The CLA roughness R_a of the silicon sample is 8.5 nm and that of the sapphire sample 4.2 nm. The roughness was averaged over three separate linescans normal to the direction of the furrows (similar to those shown in Fig. 2). The chosen workpiece pressure for the silicon and the sapphire

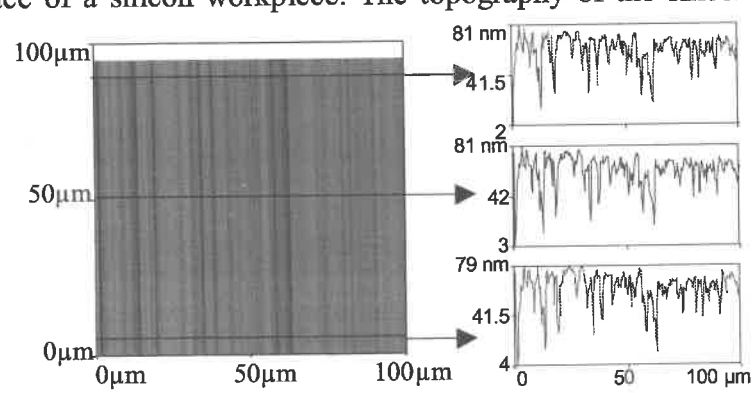

Fig. 2 Surface profile of a nanoground silicon probe

samples was set to approx. 120 kPa. Based on these results silicon and sapphire were chosen as the materials for the fabrication of the nano-roughness standards. If for STM an electrical conductivity beyond that of doped silicon is required, the standards may be plated with a thin conductive layer.

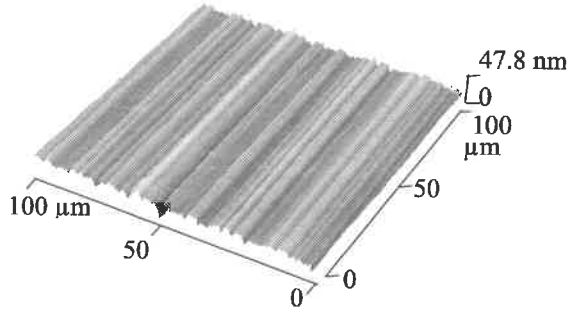

Fig. 3 AFM micrograph of a nanoground sapphire

2.2 Tooling

The tool for nano-roughness standard fabrication has to meet the following requirements. First of all the sample to be machined has to be held in place at a fixed position, not allowing any movement exceeding 1 µm during machining. This is necessary since the overlap between two consecutive profile ranges may not exceed 1% of their profile length (e.g. 4 µm for 400 µm of profile length). For doing so, the tool is firmly attached to the lapping machine's frame. In order to facilitate coplanar machining, a gimbaled workpiece holder was developed. Figure 4 depicts the tool engaging the nanogrinding plate. The tool has a linear positioning system for the translational displacement of the sample. It can be moved for a whole profile length with a precision of ±1 µm. A roller system allows to follow the nanogrinding plate at a given radius, thus eliminating errors due to the plate's eccentricity. The plate area creating the desired roughness profile range, both inside and outside, is separated by grooves from the rest of the plate. Figure 5 depicts the resulting ridge area determining the length of a profile range. The upper surface of the ridge shows the typical roughness of the soft metal on nanogrinding plates which is in the micrometer range. This roughness is a result of using pumice when conditioning the plate [7].

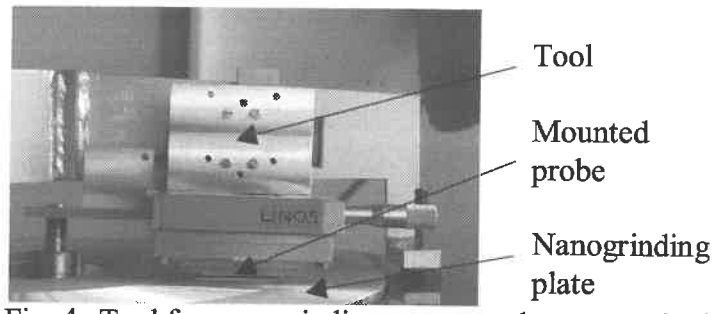

Fig. 4 Tool for nanogrinding nano-roughness standards

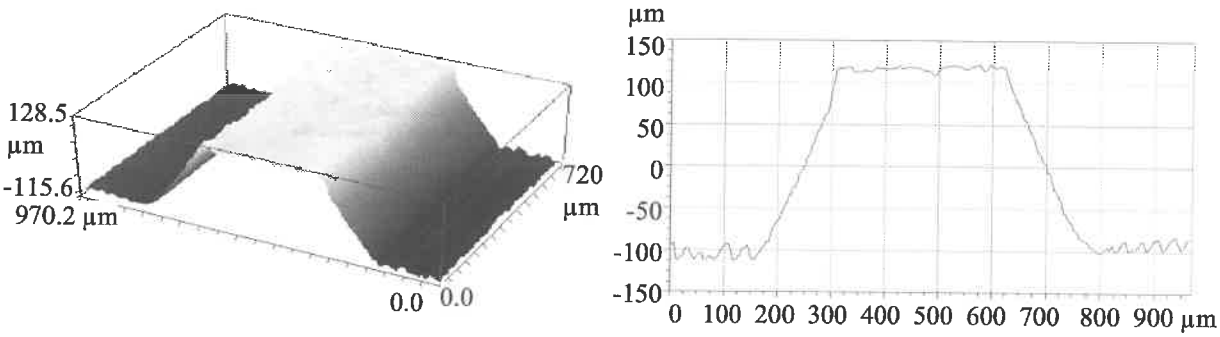

Fig. 5 Profile of a nano-roughness profile ridge on the nanogrinding plate after conditioning and diamond impregnation (White Light Interferometer (WLI) measurement)

2.3 Results

First investigations were performed with a ridge width between 300 µm and 350 µm. Using a diamond grit of 1.5 - 3 µm, silicon samples were machined. Figure 6 depicts the results. The machining was carried out in the following way. First the sample was placed on the ridge area of the grooved plate and machined for five minutes. After stopping the machine, the tool with the sample was lifted up then, using a micrometer screw, the sample was shifted by a distance of 340 µm equivalent to the length of a profile range. This process was then repeated two times. By doing so, three adjacent profiles were ground. The line scan in Fig. 6, right, shows the machining result: an irregular nano-roughness pattern, repeating every 340 µm.

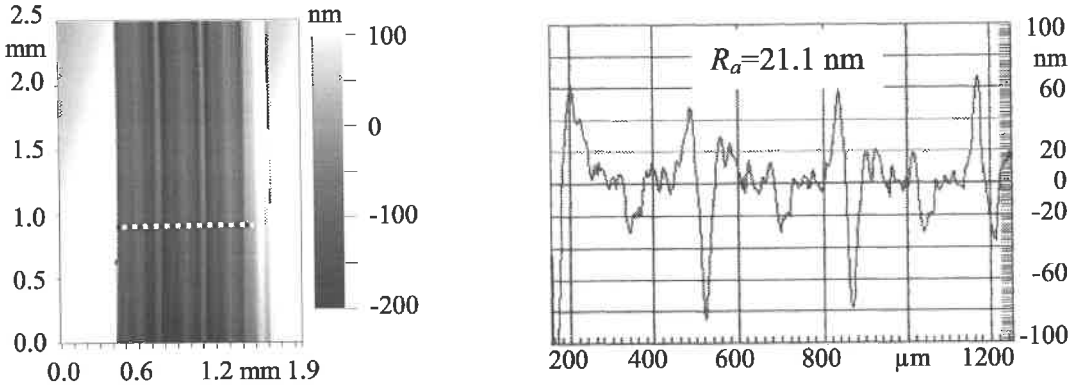

Fig. 6 Nanoground quasirandom profile on a silicon probe (left, WLI) and profile shape (right, profiler measurement)

3 Conclusions

The results clearly show that nanogrinding is very well suited for fabricating nano-roughness standards. By choosing an appropriate tooling, a quasistatistical surface nano-roughness profile may be created. Both silicon and sapphire may be used as a probe material for the nano-roughness standards. First tests with a new tool for the creation of profile repetitions prove the capability of the process to fabricate nano-roughness standards on common lapping machines.

4 Acknowledgments

This research is sponsored in part by the German Ministry of Education and Research (bmb+f). The authors are indebted to R. Krueger-Sehm, Physikalisch-Technische Bundesanstalt (PTB), Braunschweig, Germany, for providing insight into surface calibration standard requirements. Furthermore, the authors would like to acknowledge the cooperation of Nanosensors, Wetzlar, Germany, as well as a sponsoring by the Cray Foundation, Hanover, Germany, providing support for attending the conference.

References

[1] DIN EN ISO 4288, Rules and procedures for the assessment of surface texture, 1998

[2] DIN EN ISO 5436-1, Measurement standards - Part 1: Material measures, 2000

[3] DIN EN ISO 3274, Nominal characteristics of contact (stylus) instruments, 1998

[4] Hillmann, W., et. al.: Superfeine Raunormale (Superfine Roughness Standards). Qualität und Zuverlässigkeit, vol. 42, Carl Hanser Verlag, München 1997.

[5] Gatzen, H.H., Maetzig, J.C: Nanogrinding. Precision Engineering, vol. 21, Sep-Dec, Elsevier Science Ltd, Oxford, Engl, pp. 134-139, 1997

[6] Siekmann, H.: Arbeitsscheibenoptimierung beim Nanoschleifen (Plate Optimization for Nanogrinding). Fortschr.-Ber. VDI Verlag, Düsseldorf 2001

[7] Gatzen, H.H., Siekmann, H.: Plate Topography Influence on the Nanogrinding Process. Proceedings, 14th ASPE Annual Meeting, Monterey, California, pp. 83-86, 1999

Analysis of Cutting Forces in Ball End Milling

Hideaki Onozuka* , Yohei Asakawa* , Masashi Sawa* , Toshio Yamanaka* ,
Yukio Maeda* , Kazushi Watanabe ** , Takuji Tajima **
*Production Engineering Research Laboratory , Hitachi , Ltd.
292 Yoshida-cho , Totsuka-ku , Yokohama 244-0817 , Japan
**Hitachi Via Mechanics , Ltd.
2100 Imaizumi , Ebina 243-0488 , Japan

1.Introduction

By the improvement of machine tools and cutting tool materials , cutting efficiency has been increased in late years. Ball end mills are commonly used for machining of dies. But during the machining of dies , cutting forces act on an end mill affects the cutting accuracy due to the bending of the tool as shown in Fig.1. In order to predict the accuracy of machined surface , it is necessary to predict cutting forces.

There have been many researches on cutting forces while slotting by ball end mills[1) 2)]. But it is necessary to select small depth of cut in the machining of hardened materials. While slotting by using ball end mill in the condition of small depth of cut , geometrical shape of uncut chip becomes complex , and analyzing method is not found in such case. This paper reports the new method to predict the cutting forces in the case that depth of cut is small and shape of chips becomes complex.

In the new method , at first , uncut chip thickness is calculated under the assumption that end mill is fully immerged. Then the uncut chip thickness of the part which is already cut and stock material does not exit is set to be 0.

2.Experimental Procedure and Conditions

A vertical machining center (YASDA YBM-640V) was used for the cutting experiments. Maximum spindle revolution is 20000rpm , and a HSK shank which has high repetition accuracy in tool exchanging was adopted. And maximum table speed is 10000mm/min for each x , y , z axis. The run out of end mill was arranged to be within 5μm.

Cutting conditions are shown in Table 1. Experimental setup is shown in Fig.2. Piezo-electric dynamometer (Kistler 9257B) was used for measuring cutting forces , and specimen was fixed on the dynamo meter.

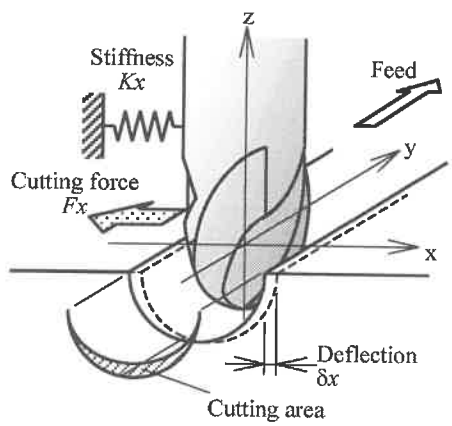

Fig.1 Deflection of end mill and cutting force

Table 1 Cutting conditions

Tool	Ball End Mill ϕ10 R5 WC(TiAlN coated)
Work	HPM1(HRC40)
Cutting Conditions	Spindle rotation 3000min^{-1} Axial depth of cut (*Ad*) 0.1mm Feed rate (*fz*) 0.1mm/tooth
Coolant	Oil

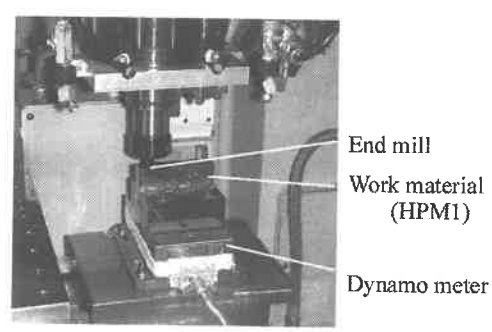

Fig.2 Experimental setup

3. Analysis of cutting forces

3.1 Geometry of cutting edge

Forces act on cutting edge are analyzed by rigid cutting force model. At first cutting edge is divided into small elements. Fig.3 shows the shape of an ball end mill observed from the bottom face. In this research , coordinates of several points on the cutting edge were sampled , and they are interpolated using spline curve. And then the curve was divided into 90 elements along the angle from x-y plane as shown in Fig.4. Position of each small elements $\vec{P}_i$, tangent of cutting edge $\vec{H}_i$, and phase shift from the center edge ϕ_i was calculated from the results.

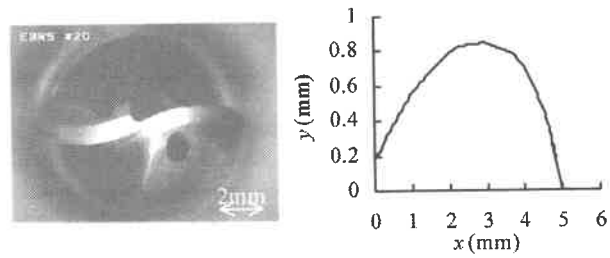

Fig.3 Observation results of cutting edge

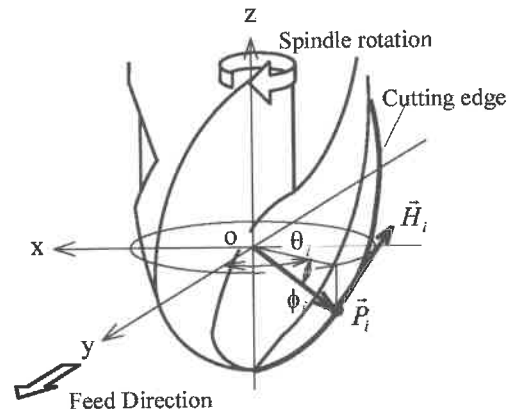

Fig.4 Data of divided elements on cutting edge

3.2 Cutting area

Cutting area $\Delta a_i(\theta)$ loaded on cutting edge while slotting under the condition that axial depth of cut equals cutter radius is expressed as following equation by using feed rate(fz) , position of the element(ϕ_i) , rotation angle of the cutter(θ) , cutter radius (R) ;

$$\Delta a_i(\theta) = fz \cdot \cos\phi_i \cdot \sin\theta_i \cdot R \cdot \Delta\phi \qquad (1)$$

But when the axial depth of cut is small , shape of cutting area projected to feed direction becomes like a new moon as shown in Fig.5 because there exists an air cut area. In the case that shape of cutting area becomes complex , limit rotation angle for each element should be calculated as a boundary condition. But this procedure requires complex calculation. Therefore , in this research , new method was proposed as follows.

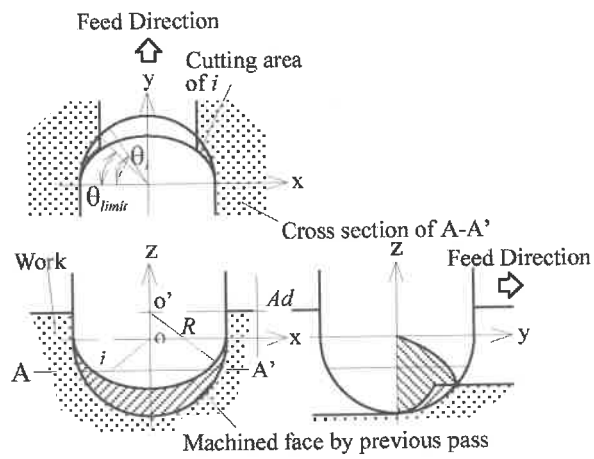

Fig.5 Schematic drawing of cutting area

At first , calculate cutting area $\Delta a_i(\theta)$ for all the elements without considering air cut area. Then if the small element is located inside the circle which center is o' and radius is R , set the cutting area 0 (o' is the center of ball nose of previous path of round trip cutting.) . This operation is expressed as following ;

$$(Ad - z_i(\theta))^2 + x_i(\theta)^2 \le R^2 \Rightarrow \Delta a_i = 0 \qquad (2)$$

Fig.6 shows the cutting area of various position on cutting edge calculated by proposed method.

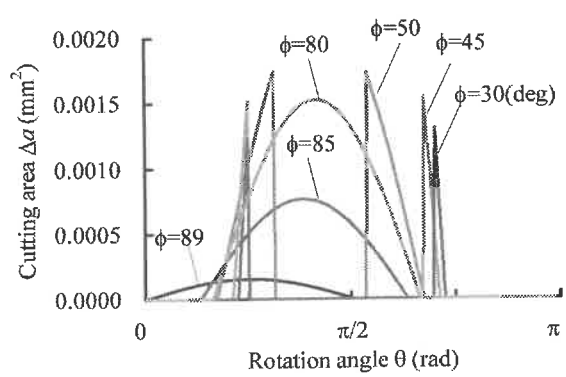

Fig.6 Cutting area of various position on cutting edge

Cutting condition was shown in Table.1. In this result , cutting area changes continuously at the bottom , but it becomes interruptive at the outer side. And phase shift is also simulated correspoinding to the helix angle of the cutter.

3.3 Direction and magnitude of cutting force

In this research , principal cutting force $\vec{Ft}_i$ is assumed to act toward the normal direction to the rake face of each element as shown in Fig.7. Rake face consists of position vector from the ball nose center $\vec{P}_i$ and tangent vector $\vec{H}_i$ of the element. And normal cutting force $\vec{Fn}_i$ is assumed to act toward the center. By these assumption , cutting force act on specific element is expressed as following equation.

$$\vec{Ft}_i = \frac{\vec{P}_i(\theta)\times\vec{H}_i(\theta)}{\left|\vec{P}_i(\theta)\times\vec{H}_i(\theta)\right|}\cdot(Kt\cdot\Delta a_i(\theta)+Pt\cdot R\cdot\Delta\phi) \qquad (3)$$

$$\vec{Fn}_i = \frac{\vec{P}_i(\theta)}{\left|\vec{P}_i(\theta)\right|}\cdot(Kn\cdot\Delta a_i(\theta)+Pn\cdot R\cdot\Delta\phi) \qquad (4)$$

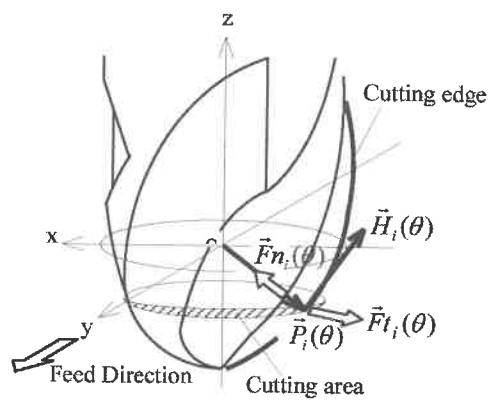

Fig.7 Assumption of direction of cutting forces

Kt, Pt, Kn, and Pn are cutting coefficient that depends on work materials. In this research cutting coefficients of HPM1(Hardness : HRC40) are decided by cutting experiments as follows;

Kt=2500 (N/mm^2) , Pt=5 (N/mm) , Kn=2500 (N/mm^2) , Pn=5 (N/mm) (5)

Cutting force acts on specific cutting edge is expressed as following equation ;

$$\vec{F}_1(\theta)=\sum_{i=1}^{N}\left(\vec{Ft}_i(\theta)+\vec{Fn}_i(\theta)\right) \qquad (6)$$

where N is the number of elements.

Force acts on another cutting edge $\vec{F}_2$ is expressed as follows because phase difference between 2 edge is π/2.

$$\vec{F}_2(\theta)=\vec{F}_1(\theta-\pi) \qquad (7)$$

4. Results and Discussion

Fig.8 shows the relationship between rotation angle and position of cutting edges. Rotation angle of cutter is considered to be π/2 when outer side of edge cuts the material. Fig.9 shows the example of calculated results. Measured cutting forces are also indicated in the figures. In this result , although the value of analyzed forces are different from measured forces , the characteristics of wave form of analyzed cutting forces correspond to the other.

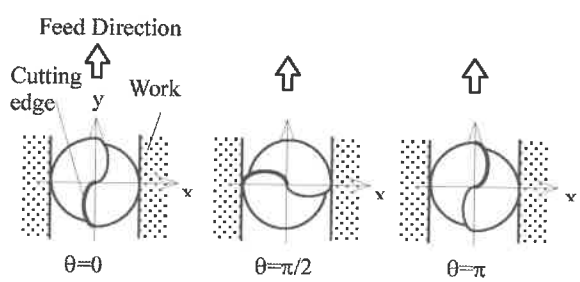

Fig.8 Relationship between rotation angle and position of cutting edge

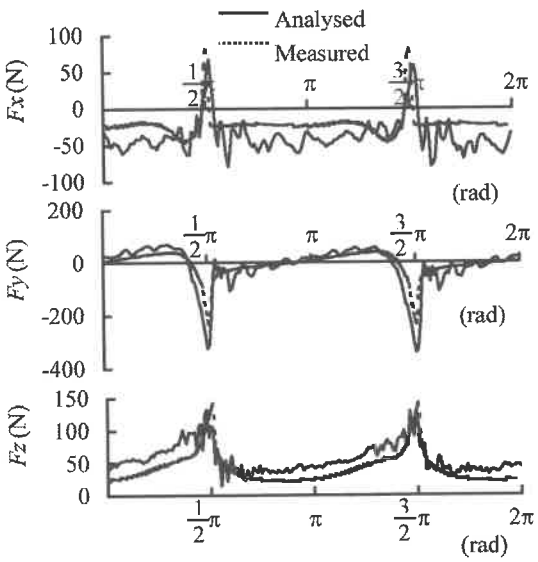

Fig.9 Results of analyzed and measured cutting forces

In the same figure , it is also found that cutting force acts toward the left to the feed direction when cutting edge finishes the side of work material.

5. Conclusions

In this paper , a new method to analyze the cutting forces of ball end milling is proposed and the predicted cutting forces are evaluated. Results are clarified that:

(1) By the new method , it became possible to analyze the complex geometrical shape of uncut chip , and the wave form of predicted cutting force correspond to measured one.

(2) While slotting with small depth of cut , direction of cutting force acts normal to feed direction changes with in 1 rotation.

(3) When the cutting edge finishes the side , cutting force acts toward the left to the feed direction.

6. References

1) Fujii , Terai : Ball-nose End Mills Simulator –Simulation of a Cutting Force- , JSPE , (1988) 2031 (in Japanese).

2) Altintas : Prediction of Ball End Milling Forces , Journal of Engineering for Industry , (1996) 188

Cylindrical Wire Electrical Discharge Machining Process Development

Jun Qu[+], Albert J. Shih[+], Ron O. Scattergood[#], and Samuel B. McSpadden[*]
[+]Department of Mechanical and Aerospace Engineering, North Carolina State University
[#]Department of Materials Science and Engineering, North Carolina State University
[*]High Temperature Materials Lab, Oak Ridge National Laboratory

Abstract

Results of applying the wire Electrical Discharge Machining (EDM) process to generate precise cylindrical forms on hard, difficult-to-machine materials are presented. A precise, flexible, and corrosion-resistant underwater rotary spindle was designed and added to a conventional two-axis wire EDM machine to enable the generation of free-form cylindrical geometries. A detailed spindle error analysis identifies the major source of error at different frequency. The mathematical model for the material removal of cylindrical wire EDM process is derived. Experiments were conducted to explore the maximum material removal rate for cylindrical and 2D wire EDM of carbide and brass work-materials. Compared to the 2D wire EDM, higher maximum material removal rates may be achieved in the cylindrical wire EDM. For carbide parts, an arithmetic average surface roughness and roundness as low as 0.68 and 1.7 μm, respectively, can be achieved. Surfaces of the cylindrical EDM parts were examined using Scanning Electron Microscopy to identify the craters, sub-surface recast layers and heat-affected zones under various process parameters.

1. Introduction

Electrical Discharge Machining (EDM) is a thermoelectric process that erodes workpiece material by a series of discrete electrical sparks between the workpiece and an electrode flushed by or immersed in a dielectric fluid. The EDM process is particularly suitable for machining hard, difficult-to-machine materials. The cutting force in the EDM process is small, which makes it ideal for fabricating parts with miniature features.

The concept of cylindrical wire EDM is illustrated in Fig. 1. A rotary axis is added to a conventional two-axis wire EDM machine to enable the generation of a cylindrical form. An example of the diesel fuel system injector plunger machined using the cylindrical wire EDM method is shown in Fig. 2.

The idea of using wire EDM to machine cylindrical parts has been reported by Dr. Masuzawa's research group at University of Tokyo [1-4]. Cylindrical pins as small as 5 μm in diameter can be machined [4].

In this study, instead of machining small-diameter pins, the focus is on exploring high material removal rate (MRR) in the cylindrical wire EDM process. The material removal rate data was not reported in Masuzawa's research [1-4].

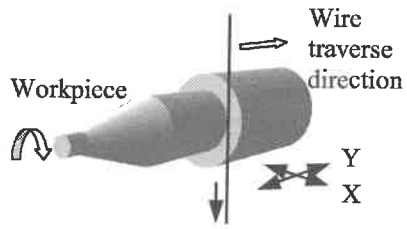

Fig. 1 The concept of cylindrical wire EDM process

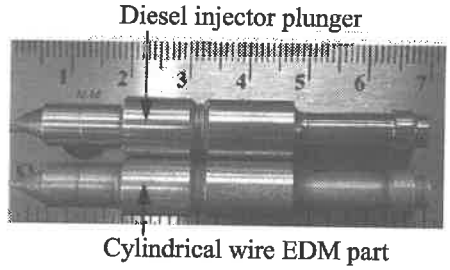

Fig. 2 A cylindrical wire EDM part with the same shape as the diesel engine injector plunger

Investigations have been carried out to analyze and improve the surface integrity of parts created by die-sinking EDM [5, 6] and wire EDM [7, 8]. This study investigates the surface finish and roundness of cylindrical wire EDM parts and explores possible ways to adjust process parameters to achieve the best possible surface integrity. Scanning Electron Microscopy (SEM) has been a common tool to examine EDM surfaces [6, 7]. This study uses SEM to quantify and compare sub-surface damage for various EDM process parameters and material removal rates.

2. Spindle Design and Error Analysis

The rotating workpiece is driven by a spindle, which is submerged in a tank of deionized water. This spindle must meet the following design criteria: accuracy, flexibility, high current electrical connection, and corrosion Resistance. The underwater spindle used in this study is shown in Fig. 3.

Spindle error is an important parameter that can affect the maximum material removal rate, roundness, and surface finish of cylindrical wire EDM parts. The Donaldson reversal principle [9] was applied to measure the spindle error. Results of the maximum spindle errors at 10 different speeds are shown in Fig. 4.

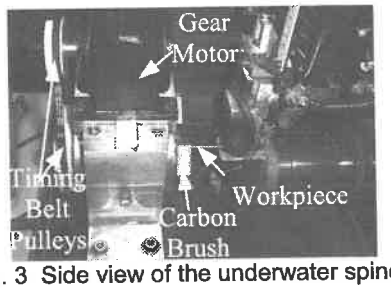

Fig. 3 Side view of the underwater spindle

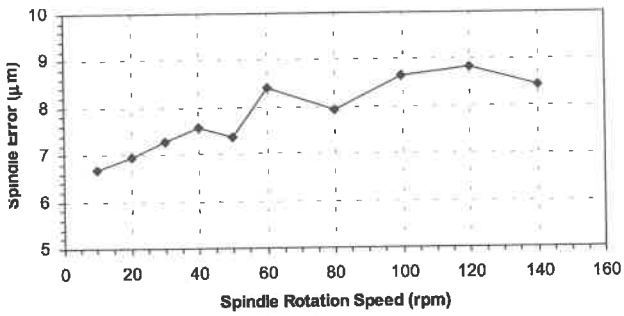

Fig. 4 Spindle error vs. rotational speed

Fourier transformation was applied to analyze the spindle runout data to identify the source of error, as shown in Fig. 5. Four major peaks are identified.

(i) f_0: This is the major peak, which is caused by the off-center error. The position of this peak always corresponds to the spindle rotational speed.
(ii) f_1: This is always equal to five times of f_0, possibly caused by the form error on bearing races.
(iii) f_3 and f_4: These two frequencies, 60 and 120 Hz, remain unchanged for different motor rotational speeds. They are possibly caused by the DC motor.

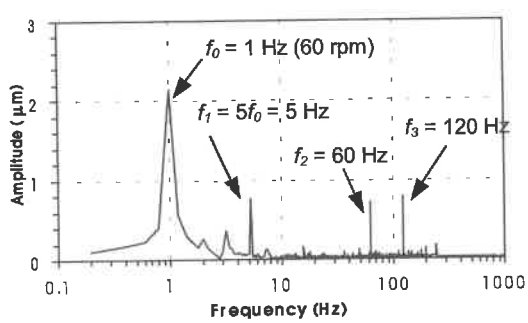

Fig. 5 Spindle error at rotation speed of 60 rpm

3. Material Removal Rate Modeling

The process parameters for modeling the material removal rate in cylindrical wire EDM of a free-form shape are illustrated in Fig. 6. R is the original radius of the workpiece. r_e is the radius of the effective circle, C_e, which equals the wire radius, r_w, plus the width of the gap between the wire and the workpiece. r is the distance from the lowest point of the effective circle to the rotational axis of the workpiece. v_f, is the wire feed rate. α is the angle from the positive X-axis to v_f. The range of α is from $-\pi/2$ to $\pi/2$.

The Material Removal Rate (MRR) in cylindrical wire EDM of a free-form surface is derived in [10].

$$MRR = v_f \cdot \pi[(R^2 - r^2)\cos\alpha + 2rr_e(1-\sin\alpha-\cos\alpha) + r_e^2(2-2\cos\alpha+(\frac{\pi}{2}-2-\alpha)\sin\alpha)] \quad (1)$$

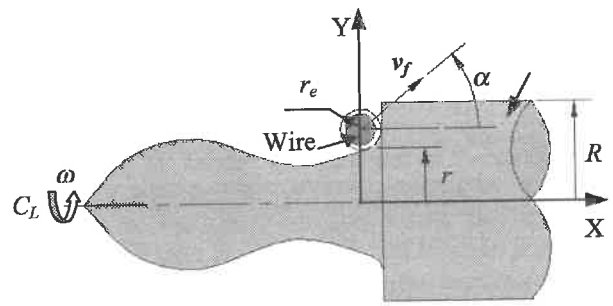

Fig. 6 Parameters in the cylindrical wire EDM

4. Experiment on Maximum MRR

The machine setup and process parameters for the cylindrical wire EDM experiment are listed in Table 1. Two parameters, the part rotational speed, ω, and wire feed rate, v_f, are varied in this study to investigate their effect on the cylindrical wire EDM of two different work-materials.

Table 1. Cylindrical wire EDM process setup.

Wire EDM machine	Brother HS-5100	
Wire manufacturer	Charmilles Tech., BercoCut	
Wire material	Brass	
Wire diameter (mm)	0.25	
Workpiece material	Brass	Carbide
Spark cycle (μs)	20	28
On-time (μs)	14	14
Wire speed (mm/s)	15	18
Wire tension (g)	1500	1500
Gap voltage (V)	45	35

The maximum material removal rate (MRR_{max}) is an important indicator of the efficiency and cost-effective of the process. Tests are designed to find the MRR_{max} in both the cylindrical and 2D wire EDM. Two test configurations to measure the MRR_{max} in cylindrical wire EDM are illustrated in Fig. 7(a) and 7(b). Two 2D wire EDM tests, as shown in Figs. 7(c) and 7(d), are also conducted on the same work-material to evaluate the difference in MRR_{max}.

In Fig. 7(a), α is set to 0 degree and v_f is gradually increased to the limiting speed, when the short circuit

error occurs. This v_f is recorded as $v_{f,max}$ and the MRR_{max} can be calculated using Eq. (1). Another test configuration, as shown in Fig. 7(b), has constant α and v_f. As the wire cuts into the workpiece, the material removal rate is gradually increased. At the position when the short circuit error occurs, the MRR is recorded as MRR_{max}. Two test configurations to find MRR_{max} for 2D wire EDM at different thickness are shown in Figs. 7(c) and 7(d). The v_f was gradually increased to find the MRR_{max}. Results of MRR_{max} are summarized in Tables 2 to 4.

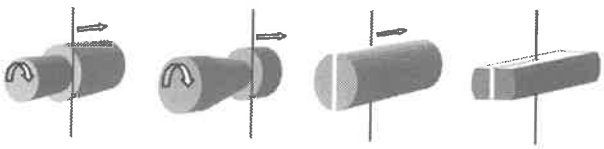

(a) (b) (c) (d)

Fig. 7 Test configurations to find the MRR_{max} in cylindrical and 2D wire EDM

Table 2 MRR_{max} for test configuration in Fig. 7(a).

Material	R (mm)	3.18			2.54	
	r (mm)	2.54	1.59	0.75	1.59	0.75
Brass	$v_{f,max}$ (mm/min)	5.72	2.69	2.13	5.33	3.46
	MRR_{max} (mm^3/min)	**65.2**	**64.1**	**63.7**	**65.7**	**64.0**
Carbide	$v_{f,max}$ (mm/min)	1.42	0.81	0.66	1.55	1.02
	MRR_{max} (mm^3/min)	**16.2**	**19.3**	**19.7**	**19.1**	**18.9**

Table 3. MRR_{max} for test configuration in Fig. 7(b).

Material	v_f (mm/min)	α (degree)	-15	-30	-45
Brass	3.81	r_{min} (mm)	2.16	2.01	1.65
		MRR_{max} (mm^3/min)	**65.5**	**68.3**	**69.6**
Carbide	1.02	r_{min} (mm)	2.02	1.95	1.17
		MRR_{max} (mm^3/min)	**19.1**	**18.7**	**20.9**

Table 4. MRR_{max} for test configurations in Figs. 7(c) and 7(d).

Material	t (mm)	r_e (mm)	$v_{f,max}$ (mm/min)	MRR_{max} (mm^3/min)
Brass	6.35	0.183	23.9	**55.5**
	3.23	0.183	37.8	**44.7**
Carbide	6.35	0.163	4.32	**8.94**
	3.23	0.163	8.00	**8.42**

Several observations can be extracted from the results in Table 2-4.

1. The brass has higher MRR_{max} than the carbide.
2. The results from the two test configurations for cylindrical wire EDM at different sizes and angles are close to each other. This verifies the concept as well as the mathematical model for the cylindrical wire EDM material removal rate.
3. The MRR_{max} for cylindrical wire EDM in Tables 2 and 3 is greater than the 2D wire EDM results in Table 4. The possible cause may be better flushing conditions in the cylindrical wire EDM.

5. Surface Finish and Roundness

Cylindrical wire EDM experiments were conducted to investigate the surface finish and roundness generated under different process parameters and to verify the surface finish model [11]. The goal of the experiment was to achieve the best possible surface finish and roundness by adjusting two critical process parameters, the wire feed rate and pulse on-time. The cutting configuration shown in Fig. 7(a) with $\alpha = 0$, $R = 2.59$ mm, and $r = 2.54$ mm was used.

Figure 8 shows the surface finish and roundness results. The shorter pulse on-time and lower feed rate, in general, created better surface finish and roundness. Shorter pulse on-time generates smaller sparks, which, in turn, creates smaller craters and better surface finish. This can be verified in the SEM micrographs of EDM surfaces. The best R_a and roundness generated on carbide are 0.68 and 1.7 μm, respectively. These values are comparable to that of rough grinding, which makes the cylindrical wire EDM process suitable for precision machining of the difficult-to-machine materials.

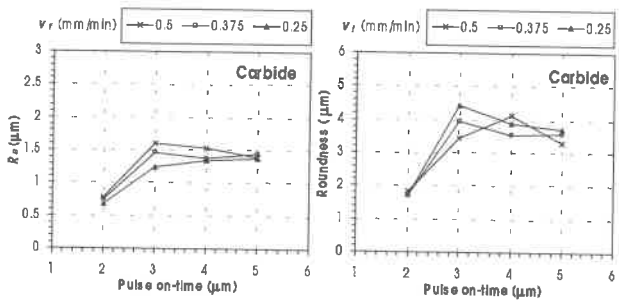

Fig. 8 The surface finish and roundness of cylindrical wire EDM parts.

6. SEM Micrographs of EDM Surface and Sub-Surface

SEM is used to examine the surface and sub-surface of cylindrical wire EDM carbide parts.

6.1 Craters. The cylindrical wire EDM surfaces are observed using the SEM machine to compare the surface texture and crater size. Under shorter pulse on-time, electrical sparks generate smaller craters on the surface. For carbide parts, as shown in Fig. 9, the rough estimate of the crater size is about 50, 30, and 20 μm under 14, 5, and 2 μs pulse on-time, respectively.

6.2 Sub-Surface Recast Layers and Heat-Affected Zones. The recast layer is defined as the material melted by electrical sparks and resolidified on the surface without being ejected nor removed by flushing. Below the recast layer is the heat-affected

zone. For the carbide material, the cobalt matrix melts and resolidifies in the heat-affected zone.

SEM micrographs of the cross-section of carbide parts are shown in Fig. 9. The recast layer, bubbles in the recast layer, and heat affected zone of three carbide samples are identified. Under high MRR at 14 μs pulse on-time, the recast layer, about 3 μm thick, can be clearly recognized on the surface. Thinner recast layers, less than 2 μm, exist on samples machined using shorter pulse on-time. Bubbles can be identified in the recast layers of all three carbide samples. Anon [5] has proposed that these micro-bubbles were generated by thermal stresses and tension cracking in the recast layer. As shown in Fig. 9, the depth of the heat-affected zone is estimated to be about 4, 3, and 2 μm on the carbide with 14, 5, and 2 μs pulse on-time, respectively.

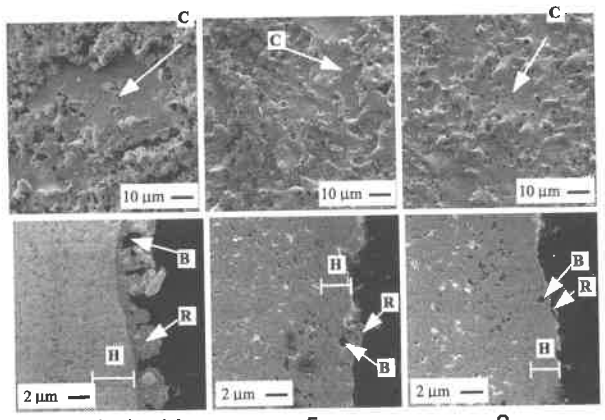

On-time (μs): 14 5 2

Legend: **C**: Crater, **R**: Recast layer, **B**: Bubble, **H**: Heat affected zone.

Fig. 9 SEM micrographs of surfaces and cross-sections of cylindrical wire EDM parts.

4. Conclusion

The feasibility of applying the cylindrical wire EDM process for high MRR machining of free-form cylindrical geometries was demonstrated in this study. The mathematical model for the MRR of cylindrical wire EDM of free-form surfaces was derived. Two experimental configurations designed to find the maximum MRR in cylindrical wire EDM were proposed. Results of each test configurations match each other, which validates the concept. The maximum MRR for the cylindrical wire EDM was higher than that in 2D wire EDM of the same work-material. This indicates that the cylindrical wire EDM is an efficient material removal process. The surface integrity and roundness of cylindrical wire EDM carbide and brass parts were investigated. Experiments demonstrated that good surface finish and roundness could be achieved in the cylindrical wire EDM process. The craters, recast layers, and heat-affected zones were observed, and their sizes were estimated using the SEM.

Acknowledgement

The authors gratefully acknowledge the support by National Science Foundation Grant #9983582 (Dr. K. P. Rajurkar, Program Director). Portion of this research was sponsored by the User program in the High Temperature Material Lab, Oak Ridge National Lab and the Heavy Vehicle Propulsion Systems Materials Program, US Department of Energy.

References

[1] Masuzawa, T., Fujino, M., Kobayashi, K., and Suzuki, T., 1985, "Study on Micro-Hole Drilling by EDM," *Bull. Japan Soc. of Prec. Eng.*, Vol. 20, No. 2, pp. 117-120.

[2] Kuo, C.-L., Masuzawa, T., and Fujino, M., 1992, "High-Precision Micronozzle Fabrication," *IEEE Micro Electro Mechanical Systems '92, Travemunde Germany*, Feb. 4-7, pp. 116-121.

[3] Masuzawa, T., Kuo, C.-L., and Fujino, M., 1994, "A Combined Electrical Machining Process for Micronozzle Fabrication," *Annals of CIRP*, Vol. 43, pp. 189-192.

[4] Masuzawa, T. and Tonshoff, H. K., 1997, "Three-Dimensional Micromachining by Machine Tools," *Annals of CIRP*, Vol. 46, pp. 621-628.

[5] Anon, 1987, "Controlling EDM Surface Integrity," American Machinist & Automated Manufacturing, Vol. 131, No. 11, pp. 80-83.

[6] Rajurkar, K. P. and Royo, G. F., 1989, "Effect of R.F. Control and Orbital Motion on Surface Integrity of EDM Components," *Journal of Mechanical Working Technology*, Vol. 20, pp. 341-352.

[7] Williams, R. E. and Rajurkar, K. P., 1991, "Study of Wire Electrical Discharge Machined Surface Characteristics," *Journal of Mechanical Processing Technology*, Vol. 28, pp. 127-138.

[8] Gokler, M. I. and Ozanozgu, A. M., 2000, "Experimental Investigation of Effects of Cutting Parameters on Surface Roughness in the WEDM Process," *International Journal of machine Tools & Manufacture*, Vol. 40, pp. 1831-1848.

[9] Slocum, A. H., 1992, *Precision Machine Design*, Prentice Hall.

[10] Qu, J., Shih, A. J., and Scattergood, R., "Development of the Cylindrical Wire Electrical Discharge Machining Process, Part I: Concept, Design, and Material Removal Rate," Submitted to *Journal of Manufacturing Science and Engineering.*

[11] Qu, J., Shih, A. J., and Scattergood, R., "Development of the Cylindrical Wire Electrical Discharge Machining Process, Part II: Surface Integrity and Roundness," Submitted to *Journal of Manufacturing Science and Engineering.*

Dimensional Control for Composite Manufacturing

Chensong Dong, Chuck Zhang, Ben Wang

Department of Industrial Engineering, FAMU-FSU College of Engineering
Tallahassee, FL 32310-6046

1 Introduction

As the development of industry, composite materials are more and more taking the place of traditional metallic materials. Fiber-reinforced composite materials consist of fibers of high strength and modulus embedded in or bonded to a matrix with distinct interfaces (boundary) between them. They have some better characteristics over metallic materials such as higher combined strength and modulus, lighter in weight, high damage tolerance, better thermal stability, high internal damping and resistance to corrosion.

Dimensional control of composite parts has gained more and more attention in recent years. Good dimensional accuracy can effectively reduce the cost of assembly of large composite structures, ensure part functions, and helps to achieve excellent surface integrity. Thus, it is essential for the precision applications of composite materials.

The problem of dimensional control of composite parts comes from the anisotropic nature of fiber-reinforced materials. Geometric deformation of composite parts can be classified as process-induced and structure-induced. Primary causes include crosslinking, non-uniform thermal expansion, shrinkage, residual stresses induced in curing process, and residual stress induced in the cooling down process.

The preliminary results of dimensional control for composite manufacturing are presented. Using a simple case, it is shown that deformation due to the temperature change in processing can be well predicted and compensated.

2 Finite Element Analysis

The deformation of a flat E-glass/epoxy panel is analyzed. The dimensions of the panel are shown in Fig. 1. The stacking sequence is $(0/90)_2(\pm45)_2(0/90)_2$.

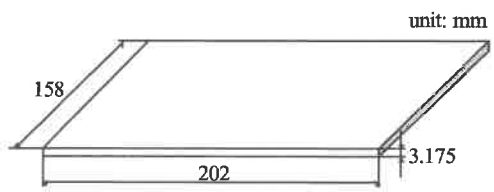

Fig. 1 Flat panel

The fiber volume fraction is about 49%. The mechanical properties and the CTEs of lamina are calculated as:

E_{11}	37.91 GPa
E_{22}	9.22 GPa
G_{12}	4.94 GPa
ν_{12}	0.23
α_{11}	8×10^{-6} m/m per °C
α_{22}	33×10^{-6} m/m per °C

The panel is cured at the temperature of 190°C and gradually cooled down to room temperature (21.67°C).

The deformation of the panel is analyzed using MSC.MARC. The mesh of the flat panel is shown in Fig. 2. Quadratic elements are used. The mechanical properties are CTEs of 0° lamina are inputted. The material is defined as composite. For each layer, fiber orientation and thickness are specified. In order to calculate the deformation of the panel, a base point should be defined. In this case, the centroid of the panel is used as the reference point. In calculation, the six degrees of freedom of the point are constrained to eliminate any rigid body movement. The temperature change is defined using boundary conditions and initial conditions.

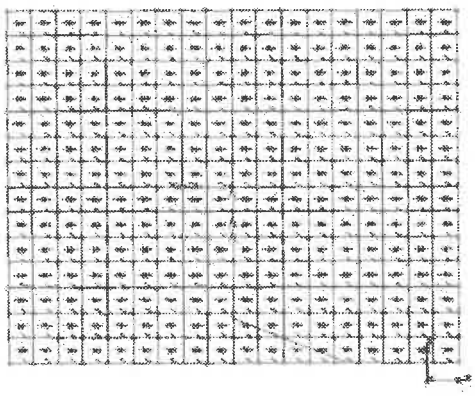

Fig. 2 Mesh of the flat panel

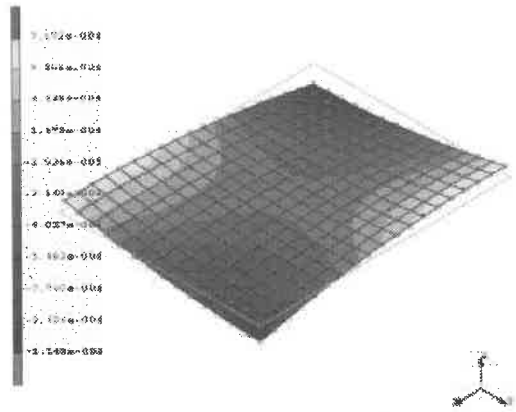

Fig. 3 Deformation of the flat panel

After calculation, the deformation of the panel is shown in Fig. 3. The peak value is 0.70mm and the valley value is –1.15mm.

3 Experiments

For the purpose of verification, several parts are fabricated using the same processing parameters, material parameters.

Two flat panels were fabricated in order to test the repeatability of deformation. These two panels are summarized as follows.

mass of fibers (g)	mass of panels (g)	fiber volume fraction (%)
122.08	183.14	49.60
122.25	189.81	47.68

After the panels were fabricated, they were measured on the coordinate measuring machine to obtain the error profiles. The panels are measured in gridded form, as shown in Fig. 4. The grid size is 10mm.

Fig. 10 Measurement to the panel

2D ERROR MODELS AND MONTE CARLO SIMULATIONS FOR BUDGETING VARIATION IN OPTICAL-FIBER ARRAY CONNECTORS

Prem Rachakonda, Mathieu Barraja, and R. Ryan Vallance,
Precision Systems Laboratory, University of Kentucky, Lexington, KY *

Sepehr Kiani and John Lehman
Teradyne Connection Systems, Nashua, NH †

Abstract

Connecting two fiber-optic cables requires precise alignment between the fibers in each cable so that most of the light is transmitted across the connection. Achieving minimal power loss is challenging for connector designers and manufacturers since a variety of situations attenuate the amount of signal transmitted. Preventing these situations requires stringent control throughout the manufacturing process, including fiber production, ferrule production, and fiber termination. This paper describes 2D error models and a method to simulate variation in the manufacture of connectors for arrays of single-mode optical fibers using Monte Carlo technique. This simulation enables designers to relate the effects of manufacturing variation to the statistics of transmission losses in the connectors. The ability to conduct sensitivity studies and combine errors is a powerful tool, which can help designers allocate and budget errors in the manufacture of fiber-optic connectors.

Keywords: Ferrule, Fiber-Optic Connectors, Transmission Losses, Monte Carlo Simulation

Introduction

Fiber-optic connectors provide separable interfaces between two fiber-optic cables. Despite being separable, the connection must have precise alignment to ensure that light is transmitted across the interface. In array connectors, the ends of two fiber ribbon cables are terminated in two ferrules. The primary function of the ferrules is to precisely align the fibers so that signal transmission across the connection is maximized. In MT-type ferrules, this is achieved with a pair of alignment pins extending from the face of the male ferrule that slide into alignment holes in the face of a female ferrule. Fig 1 illustrates a typical MT ferrule connector system joining two ribbon cables.

Achieving minimal power loss at a separable connection is challenging for designers and manufacturers of ferrules. Preventing the situations that cause transmission losses requires careful control throughout the entire manufacturing processes. Extreme precision and accuracy is necessary to prevent even the slightest relative error in the position or orientation of two connected fibers.

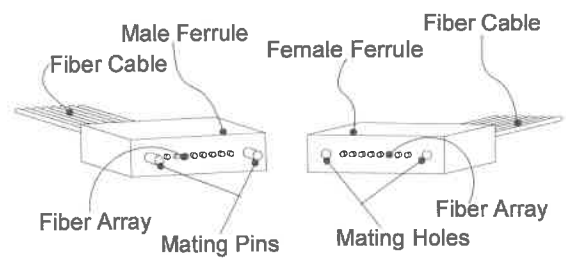

Fig 1: Male and Female Ferrule

This paper describes a 2D error model and simulation for budgeting variation in the manufacture of new MT-type ferrules used in array connectors for single-mode optical fibers. The approach simulates variation in the fibers, ferrules, termination process, and mating process to determine the statistics of transverse offsets and signal losses at the interface.

* *Precision Systems Laboratory, Mechanical Engineering, University of Kentucky, 210-A CRMS Building, Lexington, KY 40506. http://www.engr.uky.edu/psl.*
† *Teradyne Connection Systems, Nashua, NH. http://www.teradyne.com.*

Factors Affecting Transmission Losses

A variety of circumstances attenuate the amount of transmitted light between two ferrules, including: angular misalignment, longitudinal offsets, transverse offsets, mismatch of fiber parameters, mismatch of numerical aperture, core mismatch, poor concentricity, and surface finish.

In this paper, we model and simulate only two-dimensional manufacturing variation. The variation arises in the production of fibers, the production of ferrules, the termination of fibers within ferrules, and finally when two ferrules are connected together. As shown in Fig 2, 2D manufacturing variation will produce transverse offsets between two fibers, core concentricity errors within individual fibers, and mismatch between core diameters. Each of these contributes to signal loss.

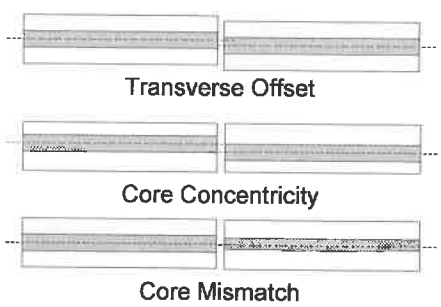

Fig 2: Contributors to 2D Connector Losses

Error Models for Production Steps

Errors in Fiber Production

Optical fibers consist of two concentric regions. The fiber core is located at the center of the fiber and has a nominal diameter of about 8.2 μm (single-mode fiber). A cladding that has a nominal diameter of 125 μm (single-mode fiber) surrounds the core. Light is transmitted through the fiber by internal reflections that occur at the interface between the core and cladding.

Our error model for fiber production considers three types of variation illustrated in Fig 3. The cladding diameter and core diameters vary between their upper and lower tolerance limits. Additionally, the core can be offset from the center of the cladding and can be described by an error vector.

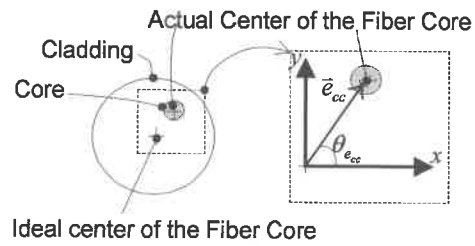

Fig 3: Error Model for Fiber Production

Errors in Ferrule Production

MT-type ferrules are typically molded from fiber-filled phenolic resins. A male ferrule consists of two pins (φ~0.7 mm) that protrude from the ferrule face and a linear array of holes that span the line between the centers of the pins. A female ferrule consists of two alignment holes (for pins) and a linear array of fiber holes that span the line between the centers of the alignment holes.

Our error model for the production of ferrules allows variation in the location of the alignment pins, alignment holes, and fiber holes. The variation is modeled with 2D position vectors that locate the center of a circle from its ideal position. In addition, the diameters of the pins, alignment holes, and fiber holes are allowed to deviate from their nominal values. Fig 4 illustrates these errors in a male/female ferrule.

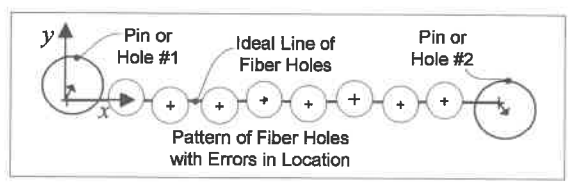

Fig 4: Error Model for Ferrule Production

Errors in Ferrule Termination

The assembly of the fibers into the ferrules occurs during termination. The protective shell of the ribbon cable is stripped away to expose the fiber cladding. The fibers are then slid into the fiber holes of the ferrule and bonded in place. Therefore, a slight amount of clearance between the hole ID and fiber OD is necessary. Finally, the faces of the ferrules and protruding fibers are polished.

Our error model for ferrule termination randomly locates the fibers within the fiber holes. The random location is specified with a

BASIS FOR MICRO-FACTORY: CNC MICROMACHINE TOOLS

L. Ruiz-Huerta
Laboratory of Mechatronics, Instrumentation Center, National Autonomous University of Mexico.
Circuito Exterior S/N, Cd. Universitaria, Coyoacán, 04510, A.P. 70-186 México, D.F.
e-Mail: leoruiz@servidor.unam.mx

***Abstract*--The problem of development micro-factories is discussed. Micro-factories can help to reduce the consumption of resources (energy and materials), and space; can help to increase productivity. We propose to use micro machine tools (CNC), to create micro-cells of production. The base feature of micro-factories is the flexibility of production. Main requirements to micro CNC machines tools and control systems are described as well as prototypes of the developed micro machine tools and testing results are presented.**

I. INTRODUCTION

The size of a micro-factory depends not only on the size of the factory equipment; depends on the size of the products too. The principles for flexible manufacturing (cells) of micro factories, could be use in micro-mechanics and micro-factories.

At present, small size mechanical devices are produced by equipment, which demands large rooms, large amount of energy and high labor cost. Modern microelectronics and control devices permit to create fully automated micro mechanical equipment corresponding to de size of produced devices and finally -fully automated micro-factories (desktop factories). They will produce low cost micro mechanical devices [1].

We know two possible ways for micro-factories creation. First way, is to use modern micro electronic technology for manufacturing low cost micro details of sub-millimeter sizes, and the second, to use conventional technology of mechanical treatment of materials by low cost micro mechanical CNC equipment (micro machine tools, micro assembly devices, micro testing devices etc.)[1].

The first approach is used very widely for manufacturing micro sensors and micro actuators [2,3], but it has some limitations connected with the problems of 3-D details manufacturing. Very difficult problems present also automatic assembly of micro devices, because 2-D details have no special surfaces, which facilitate assembly process. The second way has no such problems, but demands low cost micro equipment, which is absent at present. In the [5] main principles of such equipment creation are proposed. Micro mechanical equipment is to be made as a sequential generations of micro machine tools and micro assembly devices. Each next generation must have smaller sizes than previous one and must be produced by the equipment of previous generation.

II. THE MAIN REQUIREMENTS TO THE MICRO MACHINE TOOLS

At first, the micro machine tools must be sufficiently (but not superfluous) precise. We consider the first generation of micro machine tools as the equipment for producing details having overall sizes from some hundred microns to some millimeters. In this case they must provide tolerances of some microns [1]

Developed micro machine tools, at least the machine tools of first generation, must be multifunctional. The simplest multifunctional micro machine tool must have 4 or 5 degrees of freedom (DOF) 3-translation axis and 1 or 2

rotary axis. Micro machine tool must use the simplest types of stepping motors and the simplest sensors. It's preferable not use industrial motors and sensors, because the future next generation micro equipment will demand the possibility of producing all the components of micro equipment using the same micro equipment.

It's important to ensure the simplicity of manufacturing and assembly of micro machine tools. For this purpose all the complementary components of the machine tool must be as simple as possible.

For mass parallel manufacturing process which will decrease amount of human labor it's necessary to develop such a system of sensors and such a control system which facilitate combining of huge number of micro machine tools in the frame of desktop micro factory, controlled by one operator.

III. STATE OF THE ARTS IN THE MICRO MACHINE TOOLS DEVELOPMENT

Mechatronics Lab. had developed and tested some prototypes of first generation machine tools. The main idea was to make prototypes as simple as possible, and to use minimum of industrial components, for scaling down developed micro machine tool in future generations.

A. CNC Prototype

The prototype is shown in the figure 1. On the base (1) the guides (2), (4), (6), for 3 carriages (3), (5), (7) are installed by the sequential scheme, i.e. each subsequent guide is installed on the previous carriage for to provide translation movements along the axis X, Y, Z. The spindle case (10) with spindle (11) also is installed on the base. The drives for carriages and for spindle use stepping motors (8) with gearboxes (9). The spindle has clamp for to grip workpiece by turning, drill by drilling or mill by milling. Support (12) with cutter and two parallels metal pins for measurement of turned work piece diameter. By milling and drilling special gripper for workpiece should be installed on the carriage (7). The mayor components of the MMT are made in brass and aluminum.

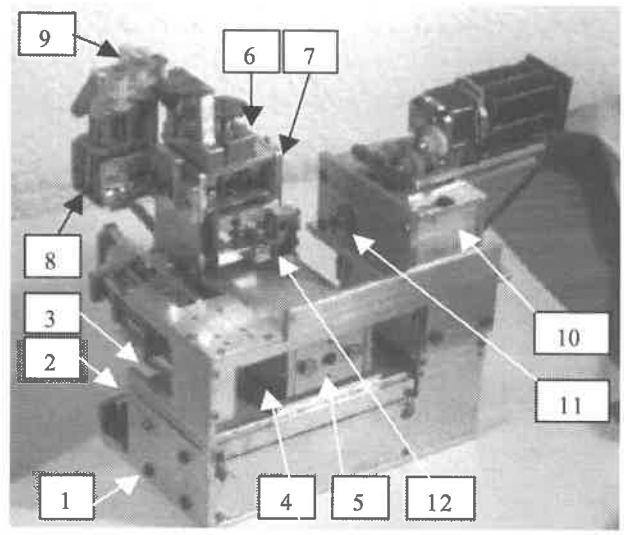

Figure 1. CNC Micro Machine Tool.

1) Components

The main components of the prototype are:

1. Stepping Motors. We make our stepping motors with 4 steps per revolution and they can be forced to make 8 half steps. They are used in the mode of high-speed rotation.
2. Carriage. The guides for carriage were made as the round bars. It simplifies the manufacturing, assembly and scaling down processes. For reasons of robustness we decide to include some ball of bearings compensate errors of guide's adjustment.
3. Transmission. It includes leading screws and gearboxes to reduce the speed of motors and increase the torque. All translation axes include the same configuration (reductor, screw, stepping motor).

2) Control

The feedback from the machine tool to the personal computer was realized on the base of four contact sensors, three of them are used to

determine home position of the carriages, and one is used to determine the moment of the contact of any tool with workpiece. This contact we used for determining relative positions of different instruments needed for the whole manufacturing process, and for measurements in the manufacturing process. We use electrical contact sensor and could have the feedback only from metal workpiece. If we need to make details from plastic, we made at first the same detail from metal, and then repeated the manufacturing process with plastic workpiesces. In principle it is possible to use other types of contact sensors (for example, acoustical contact sensor) to treatment of workpieces from any materials.

The control system, acquire the signal check of sensors, using the PC's parallel port. In order to get the control of the MMT, we assigned a specific task for the A port (sends data form PC to MMT); the B port (receives data form sensors and motors); and, finally the C port (gives the control signals to the system). The second prototype of control system is showed in the fig. 2.

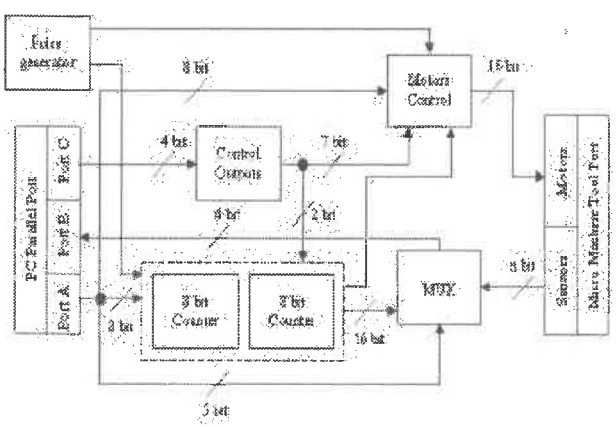

Fig. 2. Control System

3) Description

The MMT has 130?160?85mm, and is controlled by PC. The MMT, has three translation axes (X, Y, and Z), and one rotational. The axis X and Z, have 20 mm of displacement, and Y-axis has 35 mm. All of them have the same configuration. The resolution is 1.9?m per step of motor.

B. Test Pieces

Examples of the pieces that could be manufactured with this MMT are showed in figure 3. Those photos are compared with a match head. The sizes of the devices are showed in the table 1.

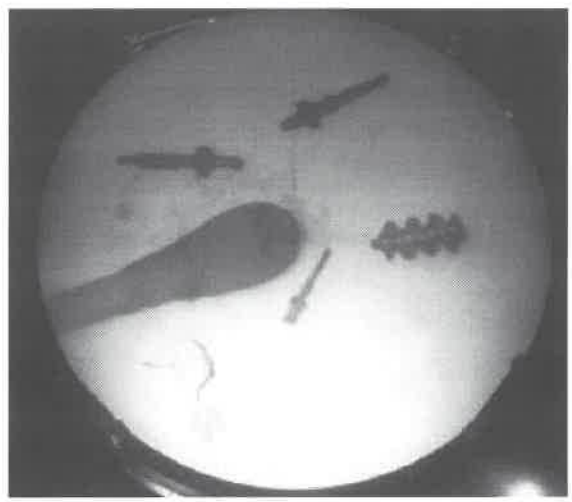

Figure 3. Test Pieces

The minimal sizes of pieces are investigated now. The main goal of this MMT development were the low cost of hardware and the relative easy to reduce its sizes in future for new generations of machine tools with low dimensions. Actually we are working in applications (micro filters, micromanipulators, etc.), and in new prototypes of MMT.

Description	Theory Value	Real Value
Gear		
External diameter	1700?m	1695?m
Internal diameter	800?m	802?m
Number of teeth	12	12
Screw		
Head Diameter	1580?m	1585?m
Screw Diameter	800?m	796?m

Deep of spiral	30?m	32?m
Total longitude	----	3290?m
Spiral Longitude	----	1185?m
Spirals per mm.	7.2	7.24
Worm Screw		
Screw Diameter	2600?m	2610?m
Deep of spiral	650?m	645?m
Total longitude	----	3300?m
Spiral Longitude	2500?m	2610?m
Spirals per mm.	1	1.15

Table 1. Test pieces values.

IV. Discussion

We proposed to use downsizing of conventional mechanics, with simple details, to reduce the cost. At first, we developed one MMT, with possibilities to milling, turning, etc. This MMT is the basis for develops larger structures of manufacture (cells, modules, factories, etc.). We consider that the basis for cheaper devices is parallel productions with low cost equipment. The low cost equipment is possible if we design simple hardware with possibilities to downsizing. To increase the potential of this MMT, is necessary to developed new systems of control and configure the first prototype of micro cell of production. This cell could contain at least two MMT and one or two manipulators. This configuration will help us to manipulate materials (and products), to perform an assembly processes.

V. Conclusions

We propose to make the micro factories on the base of miniaturized mechanical equipment. Such equipment permits to preserve all the types of existing mechanical technologies, manufacture the details of any shape and use any materials. Small sizes of equipment make it possible not only save the room, energy consumption and materials, but permit also to use relatively low precision equipment, because absolute tolerances decrease with decreasing of equipment sizes. Low cost of micro equipment will permit to organize mass parallel production of micro devices at the micro factories. To obtain low cost micro equipment it's necessary to make it in the form of sequential generations. Each generation has the sizes smaller than previous one, and is to be made with previous generations of equipment.

VI. Acknowledgements.

Special thanks to Professor Dr. Ernst Kussul and Alberto Caballero-Ruiz by your support in this work. This work was supported by CONACyT project 339944-U and DGAPA UNAM project IN-118799

VII. Reference

[1] Kussul E., Ruiz L., Caballero A., Kasatkina l., Baydyk T; CNC machine tools for low cost micro devices manufacturing; First International Conference on Mechatronics and Robotics; St.-Petesburg, Russia; 2000, Volume1; pp 98-103

[2] Various authors 1987-1996 Proc. IEEE Mechanical Systems Workshops (IEEE)

[3] Gabriel K J 1994 ARPA MEMS Program. Vision Statement (ARPA/ETEO)

[4] Micromachine Center Japan 1994-1995 Introductory. Course Micromachine No. 7-13

[5] E Kussul, D Rashkovskij, T Baidyk and S Talayev, 1996, Micromechanical engineering: a basis for the low- cost manufacturing of mechanical microdevices using microequipment, *J. Micromech. Microeng.* 6 410-425.

[6] Microfactory; 2nd International Workshop on Microfactories, Fribourg, Switzerland, Octubre 9-10, 2000, Swiss Foundation for Research in Microtechnology.

An Internet based Collaborative Filtering Scheme for Surface and Form Metrology Information

S. H Bui and Jay Raja
Surface and Form Metrology Group
Center for Precision Metrology
University of North Carolina at Charlotte
Charlotte, NC 28223

4.1 Introduction

This paper outlines the development of an information system using collaborative filters. There are a number of resources related to metrology on the World Wide Web such as books, journals, articles or information published by experts in industry and academia. It is a challenge for the user is to find best resources in a given context that fits his or her interests. Currently, the users have to spend a lot of effort to look for resources and spend time reading them to see if they meet their needs. One way to approach this problem is to use collaborative filtering technique. Collaborative filtering systems make use of reaction and opinion of people that have already seen a piece of information to make predictions about the value of that piece of information for people who have not yet seen it. By applying appropriate algorithms used to filter information, this system can guide the users to relevant resources or resources that have best quality in context.

4.2 Algorithm

At present, there is more information delivered than before. Engineers and scientists will be overwhelmed with the amount of information that they have to process everyday. The problem of information overload leaves the user unable to track information they want. In recent work, it has been shown that information can be filtered using several methods, such Kill files /Score files, Programmable Agents, or Intelligent Agent [1] using keyword search. The drawback of the keyword search is coarseness of information. For instance, some information contains keywords that are of interest to you, but their contents are not relevant. To resolve this problem, collaborative filtering technique must be used to filter or predict what information should be provided to the user. This technique tries to match the preferences of an audience to other audience in making recommendation. The filtering can be done by data mining [2], singular value decomposition (SVD) [3], or neighborhood-based methods [4]. A problem in prediction is spacing. If we form a matrix of users versus item to use prediction, we can have some empty cells in rows or column because someone will not enter feed back information after they check it out. To approach to this problem, SVD is used to reduce the dimension of the rating matrix to make more density of rating on data. This reduces the error in prediction due to sparsity of data. The following describes the SVD algorithm used to filter information [3].

SVD is a matrix factorization technique that factors matrix M into three matrices

$$M = U \cdot S \cdot V' \qquad (1)$$

where U and V are orthogonal matrices of size $m \times r$ and $n \times r$.

S is diagonal matrix $r \times r$, which contains all singular value of matrix M.

S_r with rank r is reduced to S_k, which contains k largest diagonal values. Reconstruction of $M_k = U_k S_k V'_k$ can minimizes the Frobenius norm $\|M-M_k\|$ over all rank-k matrices. M is a rating

matrix where its rows present the user elements and its columns present items that are rated. Following shows how to use SVD to predict rating scores.

1. Fill the null entries in the matrix by replacing each null entry with the column average of the corresponding column.
2. Normalize the matrix by replacing each entry $m_{i,j}$ by $(m_{i,j} - \overline{m}_i)$ where $\overline{m}_i$ is the row average of the ith row.
3. Decompose the matrix M into U, S, an V matrices
4. Reduce the $r \times r$ matrix S to dimension k by keeping k largest diagonal values of the matrix S
5. Compute two resultant matrices $U_k S_k^{1/2}$ and $S_k^{1/2} V_k^{'}$. This gives a prediction scores.
6. De-normalize the prediction scores by adding the user average back into each prediction score

SVD can be used to form neighbors and to generate top-N recommendations for the user. Following steps shows how to form neighbors in the reduced space and generate top-N recommendation.

1. Decompose the original user-product matrix M into S, U, V using SVD
2. Reduce the $r \times r$ matrix S to dimension k by keeping k largest diagonal values of the matrix S
3. Reduce the matrix U, V to dimension k
4. Compute the matrix product $U_k S_k^{1/2}$
5. Use Cosine similarity and the matrix product $U_k S_k^{1/2}$ to form the neighbors

After the neighbors are formed, the Top-N recommendation list can be found by two techniques, Center-based and Aggregate neighborhood [2].

Center-based: Top-N recommendation can be found by scanning through the rated documents of each of the u neighbors and performing a frequency count on them. The rated document list is then sorted and the N most frequently rated documents are returned as recommendations to the user [3].

Aggregate neighborhood: scheme forms a neighborhood of size u, for a customer c, by first picking the closest neighbor to c. Then the remaining u-1 neighbors are selected as follows. At a certain point, let there be j neighbors in the neighborhood N, where j<u. The algorithm then computes the centroid of the neighborhood. The centroid of N is defined as $\vec{C}$ and is computed as $\vec{C} = \frac{1}{j}\sum_{\vec{V} \in N} \vec{V}$. The user w, such that $w \notin N$ is selected as the j+1-st neighbor only if, w is closest to the centroid $\vec{C}$. Then the centroid is recomputed for j+1 neighbors and the process continues until |N|=u [3].

4.3 Features

The collaborative system is designed using object oriented programming technique. The main components of the system are the user interface classes and the background processing classes. All the classes of the system have been developed using Servlet. Component architecture of the system is shown in the figure below. Servlets connect to a database using Java Database Connectivity (JDBC) driver. They retrieve information from the database and input them to the

SVD algorithm to make a recommendation. Database is designed using relational databases and Oracle. Database stores information of documents being viewed and rated from the user, rating scores, and the user information.

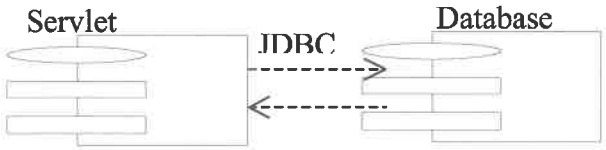

Figure 4.1 Component Architecture

The system consists of the following features:

- Provide a content management mechanism where a content provider can submit information to a central server. Content is reviewed by content editor before it can be published.
- Provide a surface finish catalog where all information is indexed in categories. The user can add links of their web site to the catalog or submit technical paper or surface finish data to a catalog.
- Provide a search engine where the user can search information from a database base on a categorized or general search.
- Run on Internet or Intranet.
- Provide a recommendation engine where it can guide the user top N list of relevant information used to analyze surface finish.
- View comments from other users. The user can rate and give comments on a particular document stored in a database.
- Provide the feature where the system can predict rating scores based on small and large size of rating data.
- Provide the user a unique interface that they can view, or rate information.

4.4 Interfaces

Figure 4.2 Documents with their rating score is displayed on a web browser

Figure above (4.2) shows how documents and rating scores are displayed on Surface Finish Catalog Interface. This screen shows the documents under "basic filtering" category. On this screen, the user can see rating score, title, author, abstract of documents, and content provider information. To access a document in detail, the user clicks on a title and the screen shown in figure 4.3 is displayed. This screen contains three frames. On the left frame, the user can rate the document, view comments from other users and top 10 recommend documents, and give feed back. When the user clicks on links at the left frame, the output is displayed on the bottom right frame as shown below. At the top right frame, the user can view a document in detail. The document can be from a data file located from the web server or from other websites.

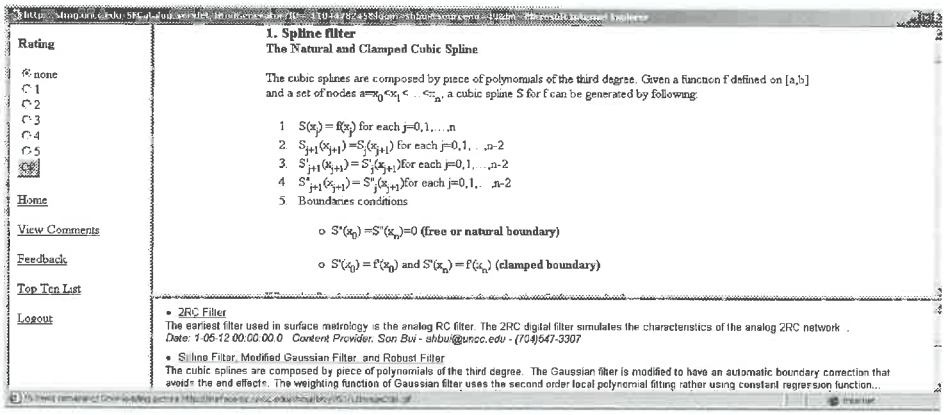

Figure 4.3 Rating document, top –N recommended document, and detail view of a documents screens

4.4 Conclusion

Collaborative filtering is one of the techniques used to filter information based on user references. Collaborative filtering is particularly useful in rating items that are hard to quantify such as ideas, feelings and thought. Also it can enhance information filtering systems by measuring, in dimensions beyond that of simple content, how well an item meets a user's need or interest. Collaborative filtering system guides the users to relevant resources or resources that have best quality in context and in timely manner.

4.5 References

1. Miller, N., Riedl, J., and Konstan, J. Experiences with GroupLens: MakingUsenet useful again. Proceedings of the 1997 Usenix Winter Technical Conference. Jan 1997.
2. 2. Sarwar, B. M., Karypis, G., Konstan, J. A., and Riedl, J. "Analysis of Recommender Algorithms for E-Commerce". To be presented at the *ACM E-Commerce 2000 Conference.* Oct. 17-20, 2000.
3. Sarwar, B. M., Karypis, G., Konstan, J. A., and Riedl, J. "Application of Dimensionality Reduction in Recommender System -- A Case Study". Full length paper at *ACM WebKDD 2000 Web Mining for E-Commerce Workshop* .
4. Herlocker, J., Konstan, J., Borchers, A., Riedl, J. An Algorithmic Framework for performing Collaborative Filtering. To appear in Proceedings of the 1999 Conference on Research and Development in Information Retrieval. Aug. 1999.

Abrasive Process for Reclaiming Semiconductor Wafers

G. Kremen*~, L. Igelshteyn*, S. Feigyn*, S. McSpadden^, R. Parten^, J. Bai. ^

Semiconductor circuit manufacturers require two qualities of crystalline silicon wafers: "prime" and "reclaim". Reclaim wafer may consist of a silicon substrate with semiconductor components implanted and/or diffused into one wafer surface. Reclaiming then involves removing the layers and portions of the underlying wafer.

Chemical stripping one of the most common techniques used in reclaiming semiconductor wafers. The process has serious disadvantages such as environmental hazards and chemical exposure to the population. It is unsuitable for removing surface layers from large diameter wafers (6 inches and more). A mixture of nitric acid (NHO3) and hydrofluoric acid (HF) is one of the etching compositions used for the reclamation of silicon wafers.

As device manufacturers begin the characterization of their 300-mm processes, almost every department in the fab will use reclaim. In the thin film department, high quality reclaim wafers will be used for LTO, PSG oxide, nitride, poly, and metals monitoring. Additionally, wafers to check spin 071 layers may be reclaim material. During furnace operations, reclaim will be used to check oxide thickness and diffusion depths, as well as sodium levels in CMOS applications.

The aim for reclaim wafering is to omit chemical striping and remove as little silicon as possible while producing as little subsurface damage (SSD) as possible. The amount of SSD directly corresponds to the time and amount of stock removal of silicon on a CMP operation. CMP is the most expensive process of all the operations in wafer manufacturing. The less silicon removed the more times a customer can reclaim the same wafer and re-use it.

The Magnetic Abrasive Process (MAP) is a relatively new technique to remove material from the surfaces of a workpeice by subjecting it to a magnetic abrasive powder in a magnetic field. In this paper we measure and compare the surface roughness, crystal damage and the depth of this damage within prime and reclaim silicon wafers machined using MAP and traditional technologies.

The set up for machining of silicon wafers is taken from US patent number 6,146,245 of Scientific Manufacturing Technologies Inc. (SMT Inc.).

Table 1 shows sample types as well as the parameters that were measured.

* Scientific Manufacturing Technology Inc. (SMT Inc.)
^ Oak Ridge National Laboratory (ORNL)
~ To whom correspondence should be addressed tel: 718-272-4070,
Fax: 718-272-4072, email: SciMT@aol.com

In order to more precisely describe roughness, the following parameters were calculated: R_p – maximum height of the profile above the mean line within the assessment length, R_v – maximum depth of the profile below the mean line with the assessment length, and R_t – maximum peak-to-valley height of the profile in the assessment lengths.). In order to assess the quality of the crystal, the x-ray rocking curve measurements were performed using synchrotron radiation with a wavelength of 0.155nm. The SSD was characterized via cross-sectional Transmission Electron Microscopy.

Observing parameter R_t, it can be seen that maximum peak-to-valley height (6.01μm) occurs after etching, and minimum height (0.09μm) occurs on a prime polished wafer; and the second-lowest height (0.19μm) occurs on a polished wafer with film before reclaiming. A reclaim wafer after MAP has a peak-to-valley height of 0.45μm, which is five times smaller that that of a prime wafer after lapping alone (2.25μm). The C-CMAP machining route compares favorably to the C-CL-CLE in terms of surface roughness. It is important to mention that final surface roughness after MAP is 0.45 μm as compared to 0.09 μm and 0.19 μm for CMP and FFO, respectively.

The appearance of the surface of wafers after the C-FMAP route is mirror-like with multiple scratches (like grinding marks). These scratches are believed by some to indicate the presence of a large amount of SSD, a low crystal quality or micro cracks. The x-ray data refute this belief.

Table 2 lists the Full Width at Half Maximum (FWHM) values obtained from the rocking curves at Si (111) reflection from the Si wafers processed at different conditions. The data taken from a near perfect Si crystal are used as standard in order to obtain the instrumental resolution. The FWHM provides a measure of the mosaicness of the sample, which would correspond to SSD. The CMAP3 machining route is only slightly more damaged than the CLEP machining route.

As shown from Table 2 above, the three wafers processed with MAP (CMAP1, CMAP2 and CMAP3) has narrower FWHM than those processed using traditional processes CL and CLE. In fact, the best result from the MAP processed wafers, 15.34 arcsec in FWHM, is even close to that of the wafer processed with the three traditional processes (lapping, etching, and CMP), which is 12.60 arcsec in FWHM. If we use MAP then we can eliminate lapping and etching. CMP after MAP is only used to decrease surface roughness.

The bright field TEM images allow convincing depth measurement of SSD. Figure 1 shows defects such as dislocation at the surface of the wafer penetrating to 0.5 micron. A typical lapped wafer has SSD depth of about 10-15 microns. The Kobe-process-induced SSD is less then 8 microns.

SMT Inc. process allows the removal of films from silicon wafers without environmental or chemical hazards. In order to remove 2-5 μm of films from reclaim wafers, today's traditional technologies remove 25-50 μm of silicon, which removes a 10-30 μm deep

layer of SSD. In contrast, the MAP removes 2-5 μm of films and 1-1.5 μm of silicon wafer, which removes a 0.5 μm deep layer of SSD.

TABLE 1. TYPES OF WAFERS

Samples Characterizations	As Cut (C)	As Cut & Lapped (CL)	As Cut, Lapped & Etched (CLE)	As Cut, Lapped & Etched, Polished (CLEP)	As Cut & MAP (CMAP)	Photoresistor Film & MAP (FMAP)	Oxide film Not Removed (FFO)
Surface Roughness	yes	yes	yes	yes	yes	yes	yes
Crystal Damage	yes	yes	yes	yes	yes	yes	no
Subsurface Damage	no	no	no	no	no	yes	no

Table 2. FWHM of the rocking curves

Sample	FWHM (arc sec)
C	127.15
CL	69.80
CLE	165.31
CLEP	12.60
CMAP1	24.01
CMAP2	41.80
CMAP3	15.34
FMAP	N/A
Silicon Standard	10.98

Figure 1

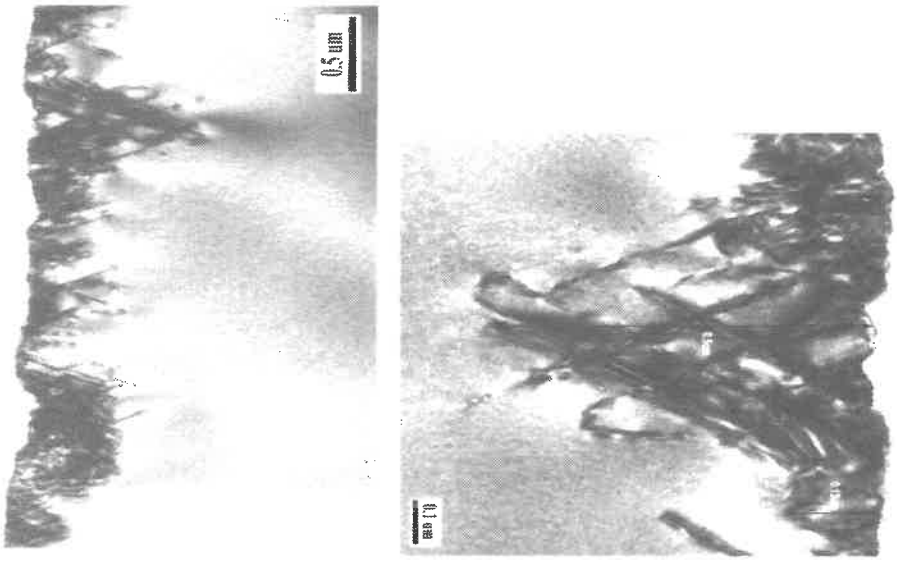

Acknowledgements

This research was performed in part at the High Temperature Materials Laboratory, Oak Ridge National Laboratory and Oak Ridge National Laboratory's beamline X-14A at the National Synchrotron Light Source, Brookhaven National Laboratory. Research sponsored by the Assistant Secretary for Energy Efficiency and Renewable Energy, Office of Transportation Technologies, as part of the High Temperature Materials Laboratory User Program, Oak Ridge National Laboratory, managed by UT-Battelle, LLC, for the U.S. Dept. of Energy under contract No. DE-AC05-00OR22725.

References

1. U.S. Patent number: 5,855,735 Date of Patent: January 5, 1999 "Process for Recovering Substrate". Takada et al.
2. "Method and Device for Machining Flat Parts" U.S. Patent, Patent Number: 6,146,245 Date of Patent: November 14, 2000. Kremen, G., Igelshteyn, L., Feigyn, S.
3. Kremen, G.Z., Feigyn, S., Igelshteyn, L., Elsayed, E.A., "Material removal Rate and of the Surface Roughness of the Magnetic-Abrasive process", *3rd International Machining and Grinding Conference on October 4-7, 1999 in Cincinnati, Ohio.*
4. "Magneto-Abrasive powder and method of producing the same," U.S. Patent, Patent Number: 5,846,270 Date of Patent: December 8, 1998. Feigyn, S., Kremen, G.Z., Igelshteyn, L.
5. H.K. Tonshoff, W.v.Schmeiden, I.Inasaki, W.Konnig, G.Spur "Abrasive Machining of Silicon". Annals o f the CIRP Vol. 39/2/1990
6. TEM Analysis for Scientific Manufacturing Technologies Inc. JOB #01090103026 (ref #: 01150).
7. Cutler, R. "The President's Corner",www.exsil.com. January 2001

MICRO ULTRASONIC ABRASIVE MACHINING FOR THREE-DIMENSIONAL MILLI-STRUCTURES OF HARD-BRITTLE MATERIALS

Tsunemoto Kuriyagawa[1], Tatsuya Shirosawa[2], Oshamu Saito[3] and Katsuo Syoji[1]

[1] Department of Mechatronics and Precision Engineering, Tohoku University
Aramaki Aoba 01, Aoba-ku, Sendai 980-8579, Japan
[2] Optoelectronic System Laboratory, Hitachi Cable, Ltd.
[3] Department of Mechanical Engineering, Tohoku Gakuin University

Introduction

The size of every component for opto-electrical devices or micro electro-mechanical systems (MEMS) has been reduced in recent years due to progress in opto-digital communications technology. The demands for micro-sized holes, slits and 3D structures of hard brittle materials such as ceramics and glass are considerable, and this has stimulated research into new methods and systems for a micro-mechanical fabrication [1]-[4].

In this study, we developed an ultrasonic vibration spindle capable of supporting an ultrasonic vibrator unit with an aerostatic bearing and rotating a small-diameter tool with high precision while providing axial ultrasonic vibration. A prototypal machining system was then manufactured that allows the small-diameter tool to be moved in three dimensions under numerical control. As shown in Figure 1, the machining of holes (drilling) is performed under 1-axis control, slits are machined under 2-axis control, and 3D structures are machined under 3-axis control. In this paper, we machined a micro-hole in glass, and basic machining characteristics including the influence of tool diameter and tool rotation were examined.

Micro Ultrasonic Abrasive Machining System

Micro ultrasonic abrasive machining is characterized by the use of smaller tools (micro tools) than those used in conventional ultrasonic abrasive machining. This results in a series of new problems and issues such as the manufacture of smaller tools, tool breakage, the mechanism of

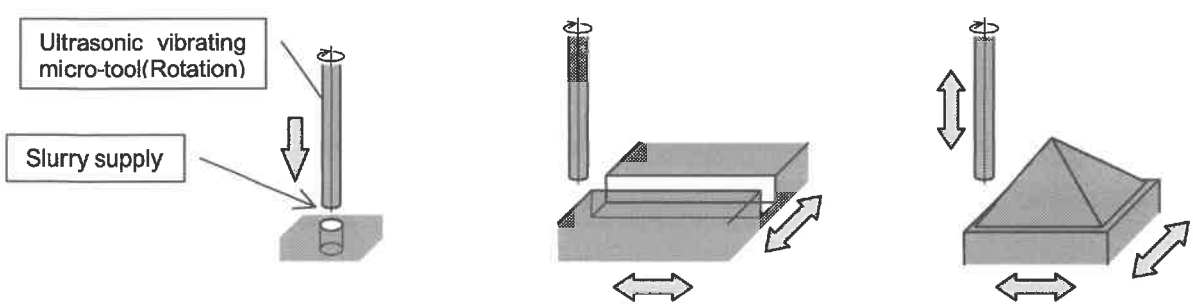

(a) Holes (b) Slots (c) 3D structures

Figure 1. Micro-mechanical fabrication using ultrasonic machining

applying machining pressure, and maintaining adequate supply of abrasive particles between the tool and the workpiece.

Based on the elaborate calculation and design, a micro ultrasonic abrasive machining system was manufactured. A schematic of the equipment are shown in Figure 2. The equipment consists of an aerostatic ultrasonic vibration spindle (hereinafter referred to as an ultrasonic head), a three-axis NC sliding table for three-dimensional movement of the small-diameter tool mounted on the head, a dynamometer for monitoring the machining force, and an ultrasonic torsion-vibration grinding unit for on-machine shaping of the tool. The equipment is constructed such that the ultrasonic head is fed vertically by the sliding table (Z-axis), which is driven by ball screws and an AC servomotor.

Aerostatic Ultrasonic Vibration Spindle: The structure of the ultrasonic head is shown in Figure 3. Here, the aerostatic bearing supports the entire vibrator unit, which consists of a Langevin-type vibrator, cone and hone. Rotation is produced by the DC servomotor via a rubber coupling. The vibrator is supplied with power (rated output is 25 W) from the slip ring attached to the coupling. The tool is securely fastened and fixed using the collet chuck at the tip of the hone. The vibration characteristics at the tip of the hone were measured using an optical non-contact displacement meter (response frequency; 80 kHz). According to the measurement, the vibrator frequency is 25 kHz and the maximum amplitude at the tip of the hone is 20 μm p-p. The holding rigidity of the aerostatic bearing is 21 N/μm in the radial direction and 39 N/μm in the axial direction. The maximum rotation speed is 1000 rpm, with a run-out of 0.7 μm at the axis end. The three axes were simultaneously numerically controlled using a PC-based motion controller (DMC-1000, GALIL), with a minimum infeed resolution of 0.25 μm and an infeed speed of 0.5 μm/s to 2.0 mm/s.

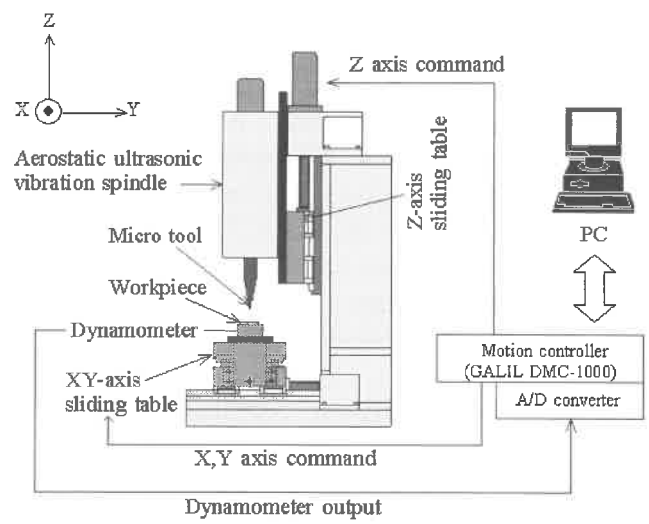

Figure 2. Micro ultrasonic machining system

Machining pressure Control: The system was designed such that the machining force can be constantly monitored by the dynamometer attached to the XY-stage in order to control tool infeed numerically using the computer and hence maintain a constant machining force. When the minimum set machining force was 100 mN or larger, a small piezoelectric dynamometer was used (9256A2,

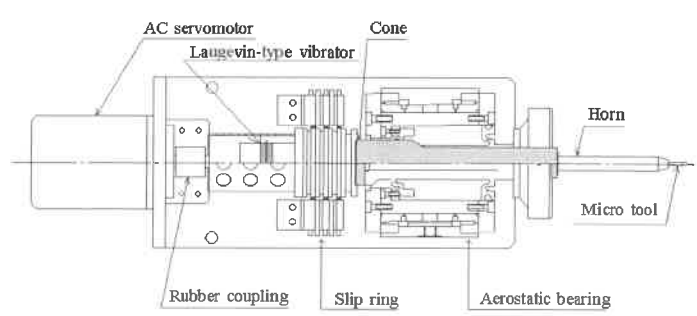

Figure 3. Aerostatic ultrasonic vibration spindle

Kistler). Accurate measurement by the piezoelectric dynamometer was impossible at minimum set machining force of less than100 mN due to drift and noise. Therefore, under low machining force conditions, a double-beam strain gauge dynamometer (LC4001, A&D) with a resolution of 0.1 mN, a maximum allowable load of 1.2 N, a natural frequency of 51 Hz (measured value), and a rigidity of 4.52 mN/μm (measured value), was used instead. The machining force was measured every 10 ms at total of 50 times, and the average of these measurements was used for machining pressure control.

On-Machine Shaping of Micro Tool: In this experiment, ultra-fine-particle tungsten-carbide alloy was used for the tool. The tool was shaped as shown in Figure 4(a). The cylindrical surface of a tungsten carbide rod fixed to the tip of the ultrasonic head was ground using the side of the diamond wheel. Torsional ultrasonic vibration was applied to the diamond wheel in order to grind the tool to a narrower diameter, as the application of such vibration has been shown to reduce the grinding force [5]. A typical shaped tool is shown in Figure 4(b).

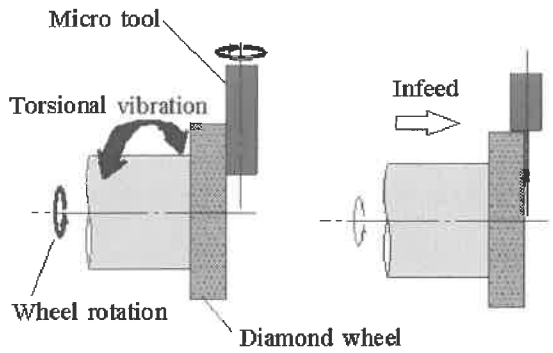

(a) Ultrasonic grinding of micro tool

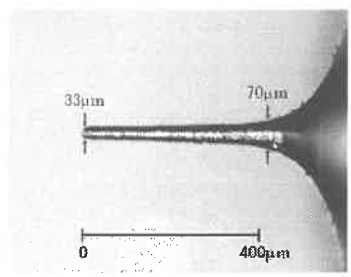

(b) Shaped micro tool

Figure 4. On-machine shaping

Machining Tests

Although the target application of this system is the fabrication of three-dimensional shapes containing grooves and holes, in this study we conducted a simple drilling experiment in order to clarify the basic machining characteristics of the system.

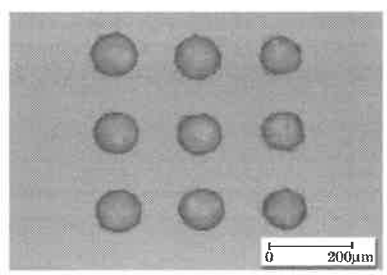

(a) Machined holes

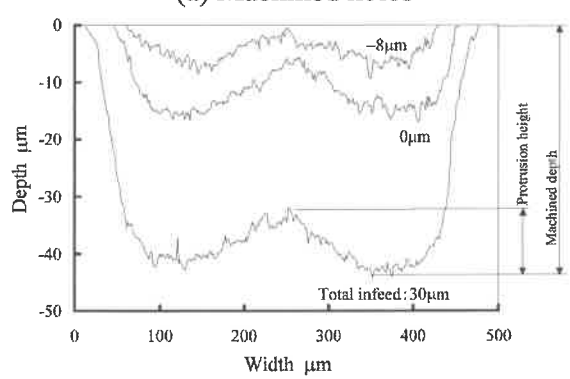

(b) Change of cross-sectional profile

Figure 5. Holes and protrusion height

Initially, the tool was applied without rotation in order to assess the effect of tool rotation. Figure 5(a) shows a photograph of a hole created using a 79 μm-diameter tool. Although there is topographical variation in the base of the hole profile, as shown in Figure 5(b), the machined depth was taken as the distance between the workpiece surface and the deepest point in the hole. As is clear from the figure, a rise is left in the center of the hole. Such protrusions were not observed for small-diameter tools (80 or 160

μm). However, this means that even small-diameter tools produce cavitation [6], which has a significant effect on the machining process.

The change in protrusion height with the progress of machining was examined for various rotation speeds using the 370 μm-diameter tool. The result is shown in Figure 6(a). The protrusion height tended to increase with machining time. However, the protrusion height and the rate of increase reduced when the tool was rotated. In particular, at the rotation speed of 1000 rpm, the protrusion height remained virtually constant throughout the machining process without increase. Specifically, it was found that the protrusion height could be reduced to less than half the normal protrusion height by rotating the tool.

When the tool was rotated, both the machining speed and tool wear increased. As shown in Figure 6(b), rotating the tool approximately doubled the machining speed, and the machining speed did not decrease over time, whereas the machining speed decreases with the progress of machining when the tool is not rotated. This effect was found to be largely independent of the tool rotation speed; simply rotating the tool produced this effect.

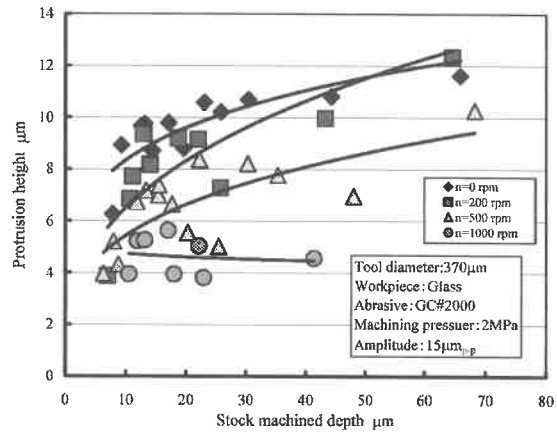

(a) Protrusion height

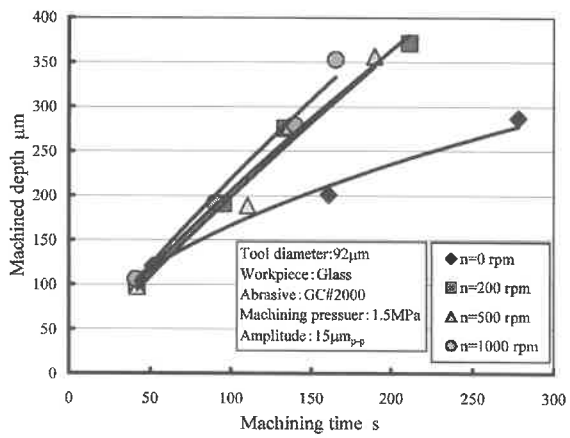

(b) Machining efficiency

Figure 6. Machining characteristics

Conclusion

A micro ultrasonic abrasive machining system was developed as one method of micro mechanical fabrications of micro-sized holes, slits and 3D structures. It has been found that rotating the tool not only decreases the severity of protrusions along the machining path, but also improves machining speed.

References

[1] Takeuchi, Y., Nishie, M., Sawada, K. and Sada, T., Machining of Micro-parts by Ultra-precision Milling Machine, J. of Japan Socciety for Precision Engineering, (in Japanese), Vol. 62, No. 8 (1996), p.1132-1135.

[2] Onikura, H. and Ohnishi, O., Ultrasonic Vibration Micro-Drilling, (in Japanese), Proceedings of Society of Grinding Engineers, (1999), p.175-176.

[3] Egashira, K. and Masuzawa, T., Application of Ultrasonic Machining to Micromachining, Seisankennkyu, (in Japanese), Vol. 49, No. 9 (1997) p.389-394.

[4] Egashira, K. and Masuzawa, T., Microultrasonic Machining by the Application of Workpiece Vibration, Annals of the CIRP, Vol. 48, No. 1 (1999) p.131-134.

[5] Ultrasonic Engineering, (in Japanese), Corona Publishing, (1993) p.199, 222.

[6] Saito, O., Kuriyagawa, T. and Syoji, K., Protrusion Appearance and Abrasive Behavior between Tool-Workpiece Interface in Ultrasonic Die Sinking, J. of Society of Grinding Engineers, (in Japanese), 44, 4 (2000) p.169-175.

PRODUCTIVE ANISOTROPIC ETCHING WITH EXCIMER LASER ASSIST

Nobuyuki Moronuki, Kenji Uchiyama and Akinori Takayama
Tokyo Metropolitan University, 1-1 Minami-Ohsawa, Hachioji, Tokyo 192-0397, JAPAN

1.Introduction

Anisotropic etching of silicon produces regular shapes that consist of {111} crystal planes because the etching rate against this plane becomes the minimum to the specific etchant [1, 2], however, the removal rate is limited. The combined process of the laser and the etching is already introduced to breakthrough the limitation [1], but in many cases the chemical reaction is promoted by heat, and the accuracy is limited. The UV lasers suit for the micromachining because the thermal effect becomes small [3]. This paper proposes a combined process of the excimer-laser processing and the anisotropic etching to obtain both high productivity and high accuracy. Figure 1 shows the concept. The laser processing or the laser-assisted etching (LAE) produces the rough profile, and then the anisotropic etching finishes the regular profile.

2. Basic properties of the process

Figure 2 shows the setup for the rough profiling process. An attenuator regulates the energy density of the excimer laser (KrF: 248nm) and a rectangular aperture shapes the beam profile. Then, the beams are focused on the workpiece. The workpiece is put in air or pure water for the laser processing, or in KOH solution for the LAE. In the LAE process, the SiO_2 layer for the etching mask is also removed with rectangular pattern, thus no mask-patterning process is necessary. The environment temperature was kept at 293K. In the subsequent anisotropic etching, the workpiece was dipped in KOH solution (35wt%) of which temperature was kept at 333K.

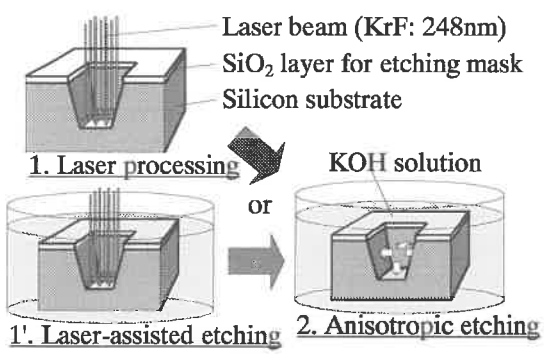

Fig.1 Concept of the combined process

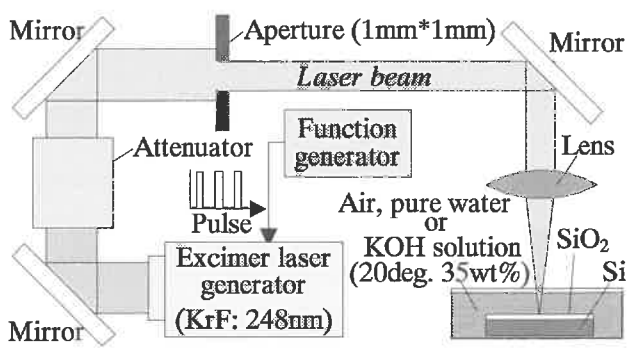

Fig.2 Experimental setup

Table 1 summarizes the experimental conditions including the anisotropic etching. The substrate orientation is only (100) in this case. The energy density was changed to investigate the optimum energy level. The repetition rate of the laser was set at low frequency, because the bubbles generated after the irradiation of laser intercept the next coming pulses. After the processing, the removed thickness and the roughness of the bottom surface were measured. The processing time is one hour in each case. The etching rate is also shown in the table.

Figure 3 shows the relationship between the energy density of the laser and the removal rate. The removal rate increases with the energy density. It is found that the removal rate of the laser processing in water becomes larger than that in air. It is considered that the plume generated

by laser pulses raises the local pressure and flow away the fragments effectively. When the energy density is low, the removal rate of the LAE became larger than the others.

Table 1 Experimental conditions

Laser processing	Substrate	Silicon (100)
	Energy density [kJ/m^2]	3, 3.5, 4, 8, 12
	Repetition rate	50Hz
Laser-assisted etching	Substrate	Silicon (100) with oxide layer of 1μm thick
	Energy density [kJ/m^2]	2.6, 3, 3.4, 6.8, 10.2
	Repetition rate	50Hz
	Etchant (etching rate)	KOH 35wt%, 293K (1.2μm/hr against (100))
Anisotropic etching	Etchant (etching rate)	KOH 35wt%, 333K (25μm/hr against (100))

Figure 4 shows the relationship between the energy density and the roughness of the bottom surface. It is found that the surface obtained by the laser processing in water becomes rough in spite of the high removal rate. The properties of the LAE are almost the intermediate of those of the laser processing and laser processing in water. The strong correlation is observed between the removal rate and obtained roughness.

The properties in lower energy density are obviously different from that in the higher one. The energy supplied by the laser irradiation truly activated the reaction of etching. When the energy density is 3.5 kJ/m^2, the removal rate of the LAE becomes three times larger than the others. Of course, the removal rate with etching only is negligible at this temperature. However, the surface roughness becomes worse, and regular shapes that are proper to anisotropic etching were not observed. Thus, some finishing process becomes necessary.

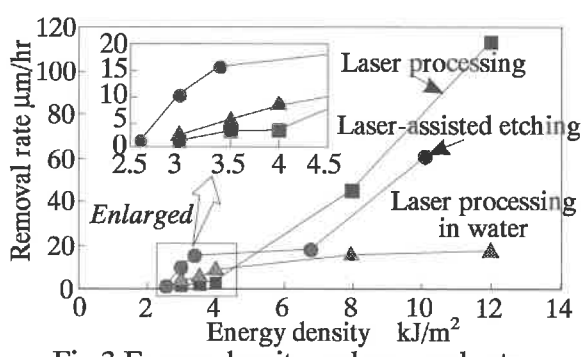

Fig.3 Energy density and removal rate

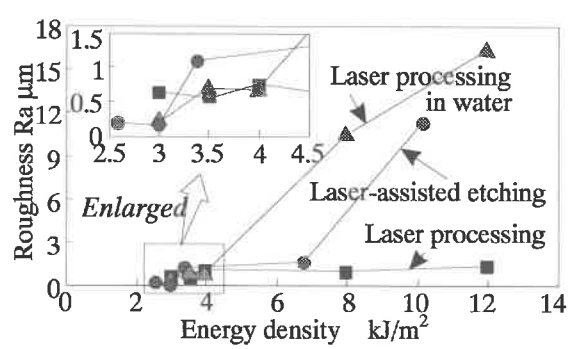

Fig.4 Energy density and obtained roughness

3. Combined process

To cope with the higher removal rate and the smooth roughness, two types of combined process were attempted; one is the laser processing and subsequent anisotropic etching; the other is the LAE and subsequent anisotropic etching. In these experiments, the substrate orientation was (100) or (110) with oxide layer of 1μm thickness.

3.1 Laser processing and subsequent anisotropic etching

Figure 5 shows the change of profiles from the laser processing to the anisotropic etching. A SEM was used for the observation, where the cross section was observed after cutting the sample with dicer. The experimental conditions are shown in the figure. In this case, the repitition rate of the laser was set at 10Hz to obtain smoother surface. It is found that the profile

after the laser processing is not accurate and the surface is rough though a steep and deep pit could be made. The effect of the substrate orientation can not be observed in the laser processing. After the anisotropic etching, regular shapes that consist of crystal plane {111} or {100} were obtained as shown in the lower part of the figure. In case of the (110) substrate, through hole with 300μm-depth was obtained. In case of (100) substrate, deep and overhanged shape was obtained but it has become asymmetric because of the inaccuracy of the preceding process.

3.2 Laser-assisted etching and subsequent anisotropic etching

To improve the geometrical accuracy, the LAE was adopted in the rough profiling process. Figure 6 shows the results. After the LAE process, a V-shape with flat bottom was obtained. The sidewalls are not {111} planes considering the inclination angle 50.4 degrees. After the anisotropic etching, the regular and accurate shapes were obtained. The shape obtained on (100) substrate is pyramidal of which sidewall inclined 54.7 degrees just same as the theory, and that on (110) substrate is a hexagonal pit with parallel sidewalls. The obtained depth was limited up to 100μm and the removal rate was not necessarily higher than that of anisotropic etching.

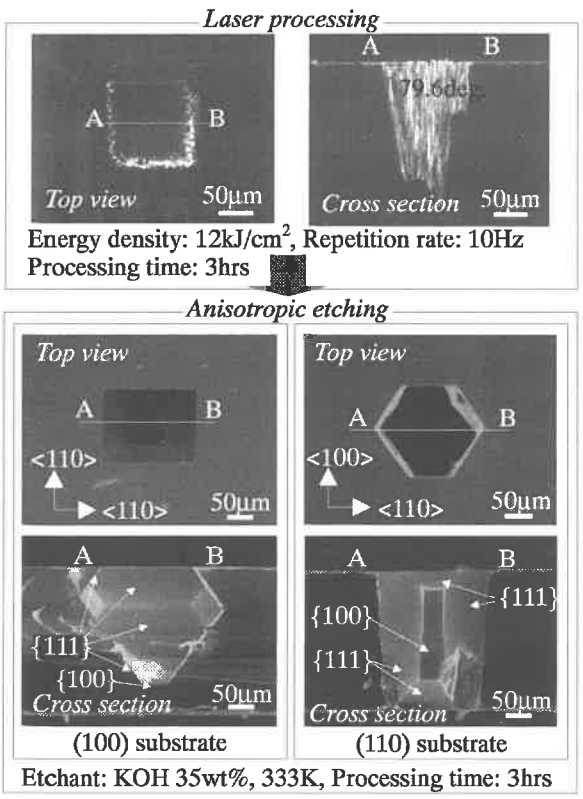

Fig.5 Results of laser and etching process

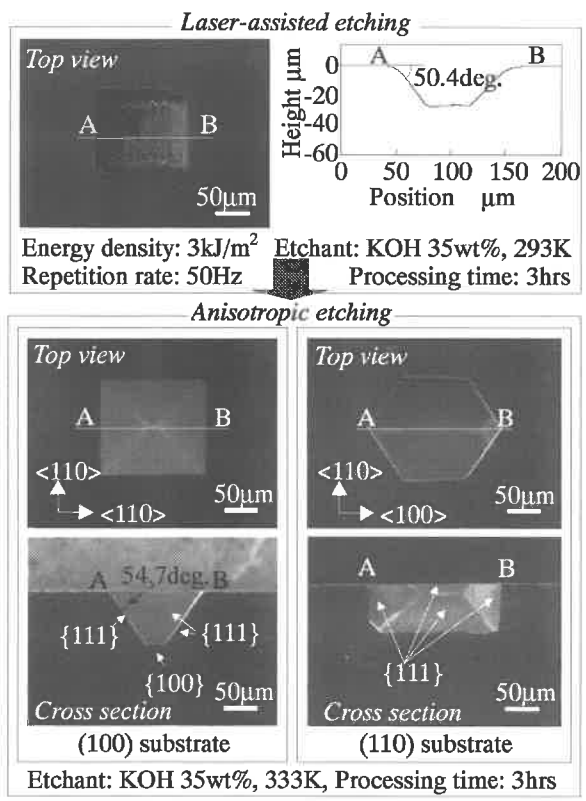

Fig.6 Results of LAE and etching process

Figure 7 summarizes the expected regular shapes that can be obtained by these processes. The final shapes are assumed to consist of {111} and {100} planes, where the etching rate against {100} is the maximum. The shapes that have {100} plane are the temporary one and gradually converge to the shapes that consist of {111} planes. The roughness of {100} plane is also good and such shape is sometimes adopted [4].

The proposed process can also produce irregular shapes that cannot be obtained in the normal anisotropic etching as shown in Fig.8. In this case, the incident angle of the laser

irradiation was not normal to the substrate but set at 35.3 degrees and a tilted pit was produced. This process was performed in water to obtain deep shape. The profile after the laser processing is not accurate (left), however, the deep and directional machining was performed. Then the regular shape was obtained by the anisotropic etching (right). The obtained inclination angle 145.7 degrees have some error because the theoretical one is 125.3 degrees.

The dry etching such as Deep RIE can produce deep structure with various cross-sectional shapes. However, sometimes the sidewalls become tapered or steps are observed on the sidewall. On the other hand, the proposed process can produce smooth and accurate sidewalls though the shape is limited by the crystal regularity. The typical shapes are the parallel walls or V-grooves. Such structures are considered to be applicable to optic or fluidic devices.

In the proposed process, the geometrical accuracy of the rough profiling strongly affects the final accuracy. The reason of insufficient accuracy in the above results is considered as the fluctuation of laser energy both in spatial distribution and/or along time. More stable laser source is necessary to apply this process for the practical use.

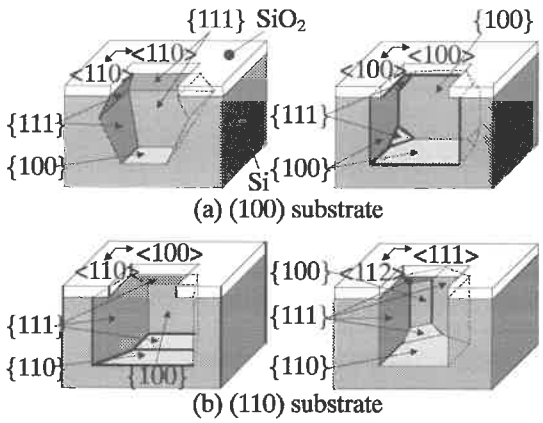

Fig.7 Expected regular-shape

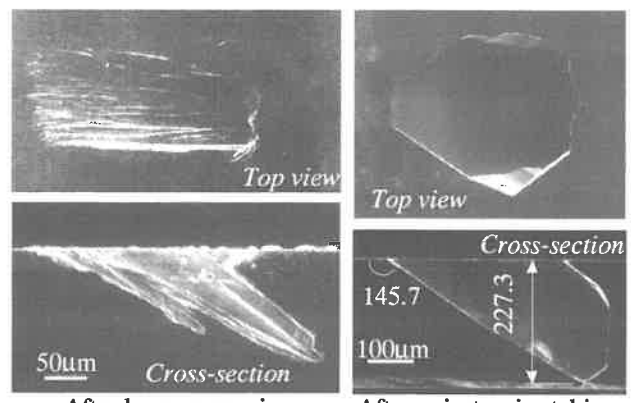

After laser processing After anisotropic etching

Fig.8 Example of irregular shape on (100) substrate

4. Conclusions

The improvement of the removal rate in anisotropic etching of silicon was attempted using the excimer laser assist. The results are summarized as follows.

- The basic properties of the laser processing both in water and air and the laser-assisted etching were made clear.
- Combined processes were proposed, in which the laser processing and the anisotropic etching are utilized to obtain deep and accurate shapes simultaneously.
- Irregular shape, that is difficult to produce with the normal anisotropic etching, was obtained with the help of the laser-assisted process.

References

[1] Madou M. Fundamentals of Microfabrication, CRC Press, 1997.
[2] Moronuki N, Uchiyama K. Linear Motion Microsystem Fabricated on a Silicon Wafer, Proc. of ASPE, 1999, pp.291-4.
[3] Toenshoff HK, Alvensleben FV, Temme T, and Willmann G. Review on Laser Micro Structuring, Proc. of 1st Euspen, Vol.2, 1999, pp.16-9.
[4] Schropfer G et al. Multi-axial bulk-micromachined silicon accelerometers with capacitive or optical read-out, Proc. of 4th Japan-France Congress on Mechatronics, 1998, pp491-6.

USING DROP-ON-DEMAND TECHNOLOGY FOR MANUFACTURING GRIN LENSES

H.-J. Trost, S. Ayers, T. Chen, W.R. Cox, M.E. Grove, and R. Hoenigman
MicroFab Technologies, Inc., Plano, Texas, USA

Overview

Lenses with gradient index of refraction (GRIN) are used to reduce focal spot sizes and correct chromatic aberrations found in lenses made of homogeneous materials. Current production methods for GRIN lenses suffer from two main limitations: For radial and spherical gradients, ion exchange in glass preforms is used, limiting their sizes to several millimeters dictated by diffusion lengths and rates of the selected ion species. For axial gradients, plates of different indices of refraction are stacked, fused at high temperatures ($1000°C$), cored and machined [1], requiring extensive tooling adjusted for the specific parameters of the lens. Lens diameters and focal lengths of 100 mm are possible. Drop-on-demand technology allows to construct either of these GRIN variants, or even mixtures, with a simple data-driven process, providing lots of flexibility for covering a wide range of lens parameters.

Existing small GRIN lens designs address applications in optics (communications, scanning), medicine (endoscopes [2]), and some other fields compatible with the few-mm size limit. Larger size axial GRIN lenses find use in, e.g., laser beam welders [3] and slide projectors. Our work is driven by interest in fast lenses with much larger focal lengths beyond 1 m for operation in the visible and infrared ranges of the optical spectrum, and focal spot sizes in the order of 5 μm. We have worked out a detailed design for a printing machine tailored to the task of printing lenses and performed various experiments to develop suitable optical materials and to study options in the manufacturing process. This is a project in progress. The machine has yet to be built and printing of full size lenses to be begun.

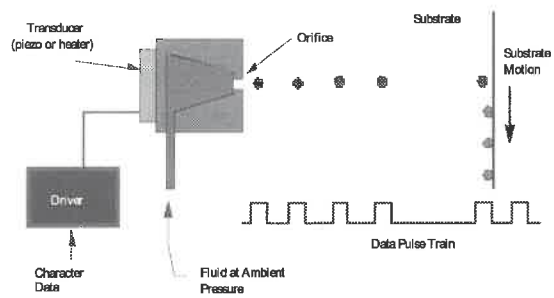

Figure 1: *Principle of drop-on-demand dispensing.*

Drop-on-Demand Printing

The most common use of drop-on-demand technology is found in ink-jet printers. The fundamental element consists of a piezoceramic cylinder fitted around a small glass tube with a narrow orifice (as is the case for the application discussed here) or a piezoceramic block with a number of fluid channels directly machined into it. The underlying principle of operation is the creation of acoustic waves in the fluid column by the piezo actuator which then, under proper shaping of the stimulating pulse to the piezo element, leads to controlled ejection of single droplets (Figure 1)[4].

A number of companies worldwide are applying this technology to many other fields that can benefit from precise dispensing of fluids in very small unit quantities. Among others, these include biotechnology and medicine, flat panel displays, adhesives, optical microlenses and solder bump bonding. This list is ordered roughly in terms of the fluid temperature needed

to sustain drop-on-demand dispensing. Optical materials usually require temperatures in the order of 150°C for direct dispensing. We have years of experience with high-temperature dispensing [5, 6] and are applying that technique here as well (Figure 2).

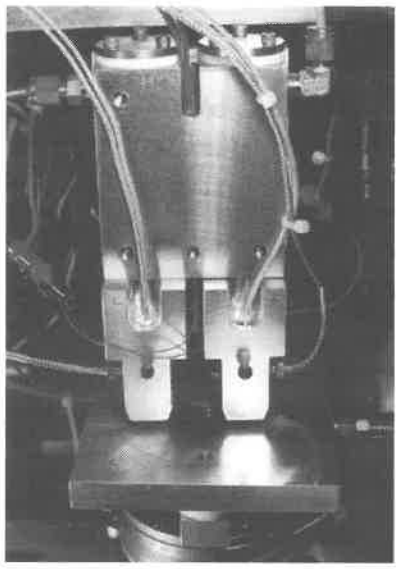

Figure 2: *Heated dual print head.*

Technical Implementation

We build our print stations with the dispensing head held in a fixed position and the substrate being moved to produce the desired pattern. By convention, the substrate (glass for experiments, glass, silicon and other substrates for custom applications), moves horizontally in the x-y plane. A third stage, usually moving vertically (z axis), positions the print head or heads closely above the substrate. It also supports a downward looking camera that can be used to survey printed patterns without relocating the substrate off of the motion table.

Large lenses cannot be created simply by piling up droplets in a single position, expecting spreading on the surface to take care of the sizing of the lens and surface tension of the fluid to assure the proper shape. Therefore, we have added a precision rotational stage on top of the x-y table to allow building up lenses ring by ring for a layer, and then, through raising the print head, layer by layer for its full shape (Figure 3). The x and y stages then serve mainly to provide the centering of the rings and the selection of the print head.

The optics field in general demands a variety of fluids to be dispensed with precisions down to 1-3 μm (3 std. dev.). To date, we have accomplished a relative placement accuracy of better than 2 μm (1 std. dev.) in arrays of microlenses [7]. It appears that this result is dominated by the properties of the motion system and the currently used software corrections.

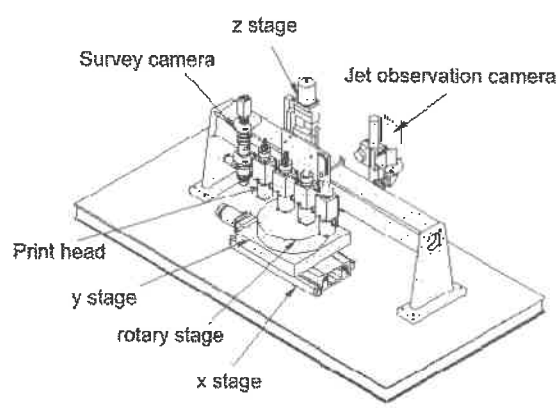

Figure 3: *GRIN lens printer concept.*

For small lenses of diameters in the order of 300-330 μm, we have achieved errors on diameter of less than 0.6%, and on focal length (also around 300-330 μm) of less than 1.1% (both 1 std.dev.). These are indicators of the good control over drop sizes and surface effects.

Requiring a focal spot size of 5 μm at a focal length of 1 m for a thin 100 mm diameter plano-convex lens implies that the droplet placement be clearly better than 5 μm so that the local radius and center of curvature are maintained within that limit across the whole lens area. We are aiming at positioning in the x-y plane to better than 1 μm and along the perimeter of every circle of better than 5 μm. Our current design calls for air-bearing x and

y stages and a direct drive rotary stage.

The desired variation of the index of refraction is accomplished by using different fluids. Our machine is laid out to support four fluids in separate heads on the machine (Figure 3). Because of the ring-by-ring and layer-by-layer construction, we can implement both radial and axial gradients at the same time.

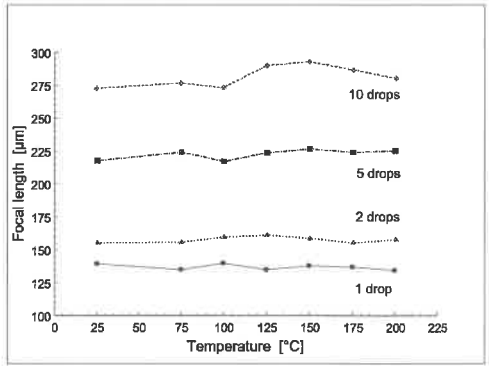

Figure 4: *Focal length vs baking temperature for different lens sizes (numbers of droplets)*

Printing GRIN Lenses

Various of our projects in the optics sector are centered around creating small lenses on flat substrates like glass plates or on the ends of fibers. The former are useful for building massively parallel optical switches while the latter include, e.g., efficient and stable couplings for single fibers. The basic lens is spherical, coming about quite naturally when one or a few droplets are dispensed at a fixed location. The drop-on-demand technology does allow us to also make quite odd-shaped lenses, e.g., hemielliptical or even nearly-square based ones.

Once printed, the optical material is cured by exposure to ample heat or UV light. For small lenses, the curing process is quite uncritical in terms of maintaining a specified focal length; e.g., a wide variation of the baking temperature will affect the focal length only to within a very few percent (Figure 4). This also implies that the lenses remain unaffected by large temperature variations in their operating environment.

The basic printing strategies are quite simple, as shown in Figures 5 and 6. The time needed to produce a single lens is not small, however. Assuming a dispense droplet rate of up to about 1 kHz, spacings of 120 μm between rings, between droplets around a ring and between layers, 100 mm lens diameter and 2 mm lens thickness, we will need about 6 hours for a single lens. The thickness and diameter match a plano-convex lens with 1 m focal length and a refractive index of n~1.4. The 120 μm spacings correspond to droplets of 2 nL volume or 135 μm diameter which are large for our dispensing devices but we have reliably produced droplets of tin-lead solder of this size before.

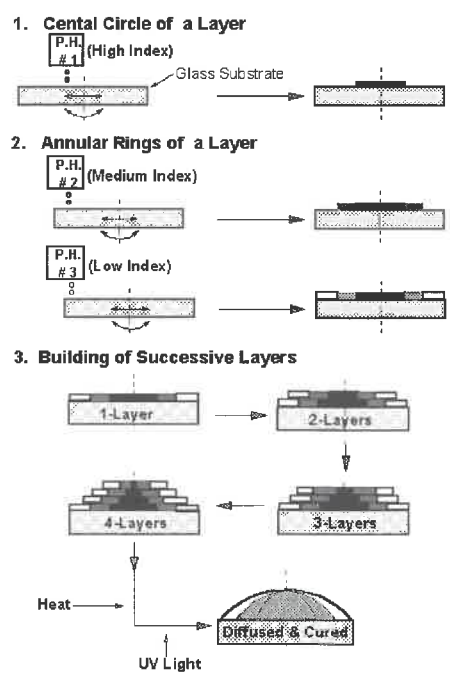

Figure 5: *Process steps for radial GRIN lenses.*

Beyond the machine construction and tuning, the optical materials require attention as well. Although we are able to operate our dispensers at temperatures up to over 300°C, many materials are not available to us due to their much higher melting temperatures. We are developing optical adhesives in-house which can be dispensed at 100-150°C and provide different indices of refraction. Curing is accomplished by UV exposure, which is applied only a the every end of the manufacturing processes (Figure 5). This provides for the opportunity to allow diffusion to occur at the interface between the different optical materials and also avoids the formation of reflective or absorptive skins in that area.

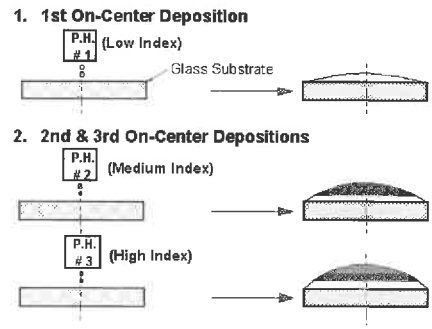

Figure 6: *Printing steps for axial GRIN lenses.*

We can test the material properties by printing small lenses on an existing print station. The example in Figure 7 shows effectively a measurement of the difference in index of refraction for two materials. The slopes (2.5, 3.0) can be converted into indices of refraction (1.4, 1.333) using the thin-lens approximation. As the approximation is not quite appropriate, the absolute sizes of the indices are inaccurate but their difference (0.067) is expected to be close to reality.

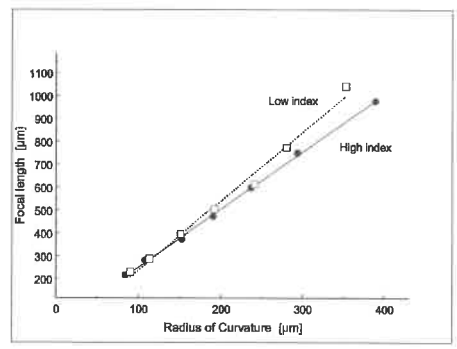

Figure 7: *Focal length vs. radius of curvature for small lenses with different indices of refraction.*

Summary

Drop-on-demand technology offers new avenues in the development and production of macroscopic optically corrected lenses. The primary benefit is the avoidance of mechanical tool making and setting dependent on lens parameters and added flexibility in the design, allowing to combine radial and axial gradient approaches.

References

[1] P.K. Manhart and R. Blankenbecler, Optical Engineering 36 (1997) 1607-1621.

[2] M. Humayun and P.S. Jensen, 2nd Int'l Congress High Care 2000, Bochum 25-27 Feb. 2000.

[3] B.V. Hunter et al., Proceedings ICALEO 81E (1996) 173-182.

[4] D.B. Wallace, ASME Pub. 89-WA/FE-4 (1989).

[5] W.R. Cox et al., IMAPS International Journal of Microcircuits & Electronics Packaging 20 (1997) 89-95.

[6] D.J. Hayes et al., U.S. Patents 5,498,444 (1994), 5,707,684 (1998).

[7] H.-J. Trost et al., Proc. 15th Annual Meeting of ASPE, 22-27 Oct. 2000, Scottsdale, AZ (ASPE, Raleigh, NC, USA 2000), pp.580-583.

LASER ASSISTED CHEMICAL MECHANICAL POLISHING FOR PLANARIZATION

Keiichi KIMURA : Sony Corporation
GCO West Tour, Osaki East Tec, 1-11-1 Osaki, Shinagawa-ku, Tokyo, 141-0032 JAPAN

Takashi MIYOSHI, Yasuhiro TAKAYA, Satoru TAKAHASHI : Osaka University
Yamadaoka 2-1, Suita-shi, Osaka 565-0871 JAPAN

1. Introduction

As the Moore's Law predicted, VLSI's scaling down of design rules has been developing steadily. The increase in the number of interconnection layers requires high planarity on individual surface of layers because the irregularities of the layers must be less than the DOF (Depth of Focus) of the projection lens of the Wafer Stepper. Moreover, the applications of the Cu interconnects, Low-k materials and the Dual Damascene processes have been started to the VLSI structure for achieving higher calculation speed and for preventing the increase in resistance and capacity of interconnect layers. At the Dual Damascene process, CMP is a key process that is required for removing accumulated copper to the designed level and for forming wire lines. Thus, CMP technology has developed along with the progress of VLSI's materials and processes.

However, the principle of material removal was not changed from the conventional method, where wafers were polished with rotated polishing pad with pressure load and slurry feed.

The essential factors for the evaluation of CMP processes are a)ununiformity within wafers, b) global planarity within die, c) throughput. Although the higher level of ununiformity can be achieved with material removal simulation technique [1], it is difficult to improve the planarity within a die with the conventional polishing method.

Thus, the material removal technology that removes off the intended small portions of the material in the arbitrary small area on the surface of wafer, is required. The goal of this research is the development of microscopic material removal method by means of chemical mechanical polishing technology.

2. Concept of the Laser Assisted CMP process

2-1 Planarization process on the Interlayer dielectric film

Cook [2] suggested the polishing mechanism of glass, and it seems that CMP process for ILD (Interlayer Dielectric) follows the material removal mechanism. The material removal processes consist of the following two processes, working alternatively:

(1) Formation of chemical reactive layer;

(2) Mechanical removal of chemical reactive layer.

Therefore, the planarity can be realized after removing the top of bumps as controlling these processes. In general, to fulfill these requirements, hard and small elastic deformable polishing pads has been widely used. However, the surface of polishing pad is rough and fluffy, therefore it cannot be controlled for contact positions and pressure appropriately.

As a conclusion of these considerations, the conventional polishing method stated above, is not capable of controlling the material removals at the specific position on wafer surface.

2-2 Basic concept of Laser Assisted CMP

The basic concept of the material removal and planarization in this research is the followings;

(1) Increasing the polishing speed locally with formation of chemical reactive layer

(2) Restricting polishing area with aggregated marks formed by Laser irradiation

Fig. 1 illustrates the schematic diagram of these two mechanisms. By Laser irradiation, chemical reacted layer is generated rapidly, and thus, the increase of material removal speed of polishing is

References

1. T.Doi, Details of Semiconductor CMP Technology, Kogyo Chosakai Publishing Co., Ltd. 2001
2. International Technology Roadmap for Semiconductors, 2000 Edition
3. F.W.Preston, The theory and design of plate glass polishing machines, J. Society of Glass Tech., 1972, 214-256

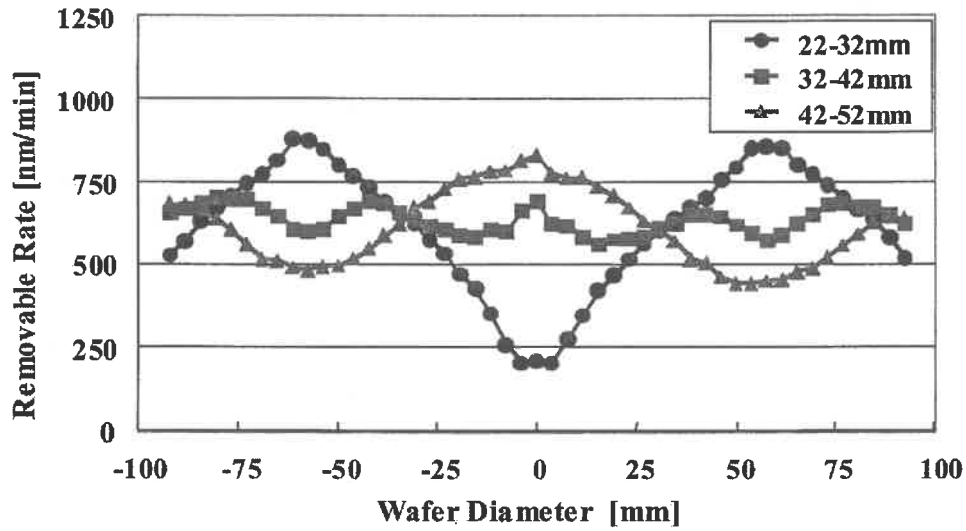

Figure 3 Polishing profiles

Position [mm]	22-32	32-42	42-52
Time [%]	19.5	36.6	43.9
Speed [mm/min]	686	600	800

Table 2 Dwelling time and Oscillation speed on every 10mm range

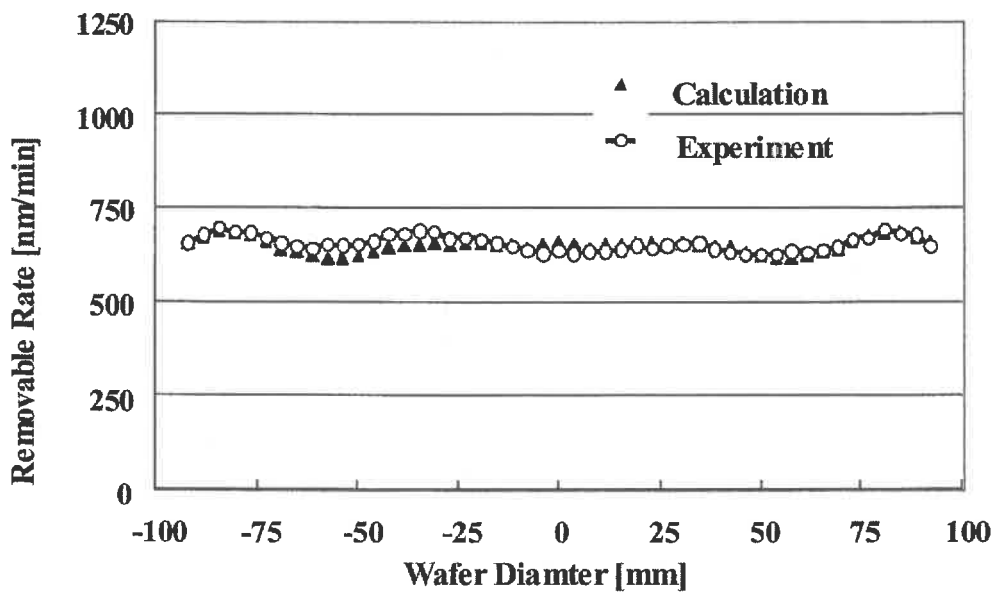

Figure 4 The comparison of experiment and calculation

High Removal Rate Ultra-Smoothness Polishing of NiP Plated Aluminum Magnetic Disk Substrate with Colloidal Silica

Heiji YASUI*, Tomohiko FUKAMACHI*, Shigehiko SAKAMOTO*
*:Dept. of Mechanical Engineering & Materials Science,
Kumamoto University, Kumamoto 860, Japan

1. Introduction

To produce the low cost compact magnetic disk of high storage capacity, the high productive ultra-smoothness polishing technic of the magnetic disk substrate has been strongly requested. In our previous researches[1]-[4], the optimum ultra-smoothness polishing conditions of the electroless nickel phosphorus plated aluminum substrate with the alumina abrasive of 0.5μm in nominal diameter are examined and discussed under the range of polishing conditions in the substrate manufacturing factories limited to the conventional polishing machine. A few of polishing experiments[5] using colloidal silica abrasive are also executed. From the results, when using colloidal silica abrasive, it is found that the surface smoothness is much better than alumina abrasive while the removal rate is much smaller than alumina abrasive. Toward the future from the present, in company with the trend to the storage capacity of 100Gb per a disc substrate, ultra-smoothness formed the colloidal silica abrasive, together with high removal rate obtained by alumina abrasive will be strictly required.

The research aims to make it possible to polish NiP plated aluminum magnetic disk substrate surface to the smoothness of below 0.4nm(Ra) with the high removal rate, using colloidal silica abrasives. In order to accomplish high removal rate polishing, the influence of the high polishing speed on the polishing results is investigated.

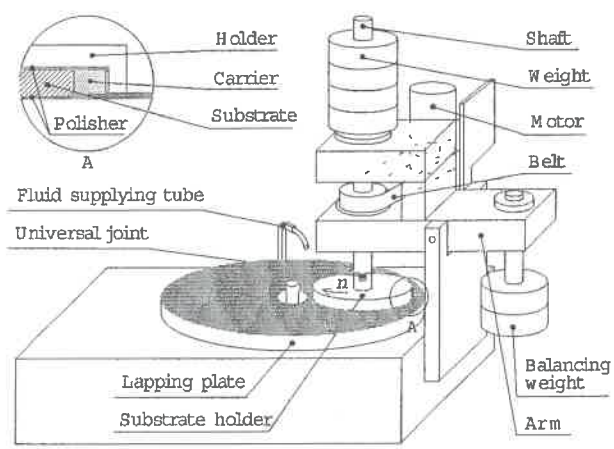

Fig.1 Shematic view of polishing machine

Table 1 Experimental conditions

Workpiece	NiP Plated Aluminum Magnetic Disk
Polisher	Non-woven Urethanform :ANM (Hardness20°)
Polishing fluid	Abrasive:SiO_2 (ϕ80nm) Abrasive Content C_g:10.0wt% Supply flux S_g:6.0g/min
Polishing Condition	Pressure P:3.7-11.1kPa Speed V_a:1.5-9.0m/s

2. Experiments

To carry out the high speed polishing experiments, the polishing machine which can gets the polishing speed over 9m/s, is newly manufactured by reconstructing the polishing one used in the previous

pressures. The minimum terminal removal depths required to attain the terminal slight undulation and the terminal surface roughness are about 2.5μm and 2μm, respectively. The minimum terminal removal depth depends on the surface smoothness before polishing. Accordingly the surface smoothness formed before polishing is one of the important points related to the productive efficiency in the polishing of disc substrate.

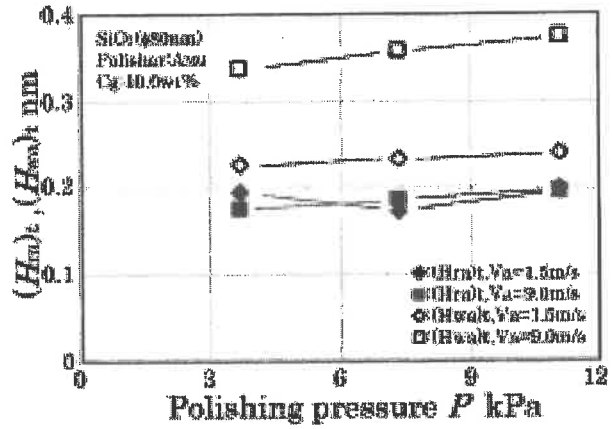

Fig.8 Influence of the terminal slight undulation and surface roughness on polishing speed

Figure 8 shows the Influence of the polishing pressure and the polishing speed. on the terminal smoothness. From the figure, the (*H*ra)t is found to keep about 0.2nm(Ra) in the whole region of the polishing pressure of 3.7kPa to 11.1kPa for both polishing speeds of *V*a=1.5m/s and *V*a=9m/s. The (*H*wa)t, on the other hand, tends to have extremely slight increase with the increase of polishing pressure. The (*H*wa)t of about 0.3nm(Ra) at *V*a=9m/s is larger than that of about 0.2nm(Ra) at *V*a=1.5m/s.

4. Summary

The main results obtained are as follows:

(1) The slight undulation and the surface roughness by polishing the substrate converge finally to the terminal values corresponding to a given polishing condition..

(2) The surface roughness is influenced little by the polishing speed and pressure. The terminal slight undulation of 0.3nm(Ra) at *V*a=9m/s is larger than that of 0.2nm(Ra) at *V*a=1.5m/s.

(3) The substrate removal depth for all the polishing conditions examined increases linearly with polishing time.

(4) The substrate removal rate becomes larger for higher polishing speed and pressures.

Reference

[1] H. Yasui *et al.*: A study on Nano-surface Polishing of Magnetic Disk Substrate, Proc. 7th Int. Precision Engg. Seminar, Kobe, Japan (1993) pp. 688-699.

[2] H. Yasui *et al.*: Studies on High Flatness of Magnetic Disk Substrate with Al_2O_3 Abrasives (1st Report), J. Japan Soc. Prec. Engg., Vol.60, No.1(1994) pp.128-132.

[3] H. Yasui *et al.*: A Few Nanometers' Flatness Polishing of NiP Plated Magnetic Disk Substrate with Al_2O_3 Abrasives, Proc. 3rd Int. Conf. Ultraprecision in Manufacturing Engg., Aachen Germany(1994) pp.438-441.

[4] H. Yasui *et al.*: Studies on High Flatness of Magnetic Disk Substrate with Al_2O_3 Abrasives (2nd Report), J. Japan Soc. Prec. Engg., Vol.60, No.11(1994) pp.1631-1636.

[5] H. Yasui *et al.*: Effect of Ultra Smoothness Polishing of Magnetic Disk Substrate on Magnetic Head Slider Flying Height, Proc. 8th Int. Precision Engg. Seminar, Compiegne, France (1995) pp.386-389.

Authors Index

Abackerli, Alvaro Jose . . . 237
Abbe, Makoto . . . 231
Ahn, Jae Sam . . . 485
Akemon, Jeffery L. . . . 429
Aketagawa, Masato . . . 107
Allen, James J. . . . 32
Amatucci, Edward G. . . . 135, 200
Ames, Lawrence . . . 103, 349
Aoyama, Hisayuki . . . 204
Arii, Shiro . . . 119
Asakawa, Yohei . . . 497
Ayers, Scott . . . 533
Bai, Jian Ming . . . 521
Barraja, Mathieu . . . 489
Barrett, Robert . . . 349
Barrett, Stephanie . . . 349
Bauer, Markus G. . . . 123
Bell, Ray . . . 103, 349
Benavides, Gilbert L. . . . 32
Benson, Robert . . . 349
Bieg, Lothar . . . 32
Borchardt, Bruce R. . . . 82
Bordatchev, Evgueni V. . . . 281
Bosco de Aquino Silva, Joao . . . 241
Brand, Christopher J. . . . 98
Büchner, Hans-Joachim . . . 23
Bui, Son Hoang . . . 517
Bullock, Jonathan Bowling . . . 273
Bunch, Robert . . . 135
Butler, Nat . . . 40
Caballero-Ruiz, Alberto . . . 325
Camargo, Carlos Augusto . . . 237
Cerniway, Matthew A. . . . 92
Chan, Hau-Lam Harley . . . 369
Chang, In-Bae . . . 172
Chang, Jee-Uk . . . 172
Chang, Kuo-Ming . . . 365
Chen, Carl G. . . . 15, 40, 216
Chen, Ting . . . 533
Chen, Yu-yen . . . 457
Cheraghi, S. Hossein . . . 245, 297
Cherukuri, Harish P. . . . 98
Chidambaram, Somasundaram . . . 393
Cho, Hyundeong . . . 481
Choi, Hon-Zong . . . 397
Choi, Hyun-Seung . . . 156
Cohen, Lester . . . 40
Cole, Addison D. . . . 269
Colonna de Lega, Xavier . . . 44
Corbett, John . . . 220
Cox, W. Royall . . . 533
Cross, Gene . . . 349
Curry, Adam C. . . . 401
Dagalakis, Nicholas G. . . . 135, 200
de Groot, Peter J. . . . 44
de Sousa, André Roberto . . . 353
Deck, Leslie L. . . . 115
Delalandre, Jerome . . . 220
Desta, Mesay T. . . . 298
Diaz, Rosemary T. . . . 103, 349
Dinwiddie, R. B. . . . 401
Dong, Chensong . . . 505
Dornfeld, David A. . . . 453, 475
Dow, Thomas A. . . . 28, 66, 92, 123, 224
Dubovitsky, Serge . . . 103
Dumont, Philip . . . 349
Dutta, Kalyan . . . 103, 349
Dyer, Stephen W. . . . 102*
Eom, TaeBong . . . 156
Essel, Ingo . . . 453
Fan, Xiaorui . . . 405
Fang, Cheng-Yen . . . 365
Feigyn, Savva . . . 521
Feng, Hsi-Yung (Steve) . . . 289
Fitsos, Pete . . . 160
Fu, Sheng Yu . . . 249, 381
Fuchiwaki, Ohmi . . . 204
Fukamachi, Tomohiko . . . 545
Furutani, Katsushi . . . 164
Gaillard, Jay . . . 212
Gao, Wei . . . 285, 333
Gao, Yongsheng . . . 257, 265, 329, 341, 377
Gardner, Tom E. . . . 245
Garrard, Kenneth P. . . . 28
Gatzen, Hans H. . . . 493
Gee, Anthony E. . . . 220, 385
Gho, Lit Ming . . . 409
Gill, David D. . . . 66
Grant, Marion B. . . . 429
Grejda, Robert D. . . . 58, 461
Grigg, David A. . . . 44
Grove, Michael E. . . . 533
Grünwald, Rainer . . . 23
Gust, Darryl J. . . . 429
Halverson, Peter . . . 103, 349
Han, Dong-Chul . . . 172
Handigund, Prasann B. . . . 413
Hara, Kazutoshi . . . 152
Hara, Seiichiro . . . 373
Hatamura, Yotaro . . . 36, 457
Hausotte, Tino . . . 23
Hayashi, Akira . . . 305

*Extended abstract not available at press time.

Heilmann, Ralf K. 15, 40, 216
Heinrich, Matias D. 224
Hetland, Gregory A.. 301
Higuchi, Toshiro. 437
Hii, King-Fu 168
Hiraki, Yutaka. 62
Hocken, Robert J. 261
Hoenigman, Rick. 533
Holmes, Buck 349
Honda, Satoshi 208
Horikawa, Oswaldo 293
Horiuchi, Osamu 437
Hoshino, Susumu 541
Huang, Peisen S.. 285
Igelshteyn, Leonic 521
Inaba, Fumio 421
Inoue, Shigeru. 417
Ishikawa, Akira 541
Ishikawa, Ken-ichi 477
Isobe, Sho 152
Izumi, Masumi 417
Jäger, Gerd 23
Jeong, Sung Ho. 127, 180
Jiang, Guohua. 297
Johnston, Gabriel 144
Jokiel Jr., Bernhard 32
Jun, Jay 19
Kagawa, Yoshihito 111, 144, 361
Kami, Yoshihiro 119
Kamiya, Kazuhide 389
Kanai, Akira. 152, 421
Karino, Takashi 196
Kato, Masana 441
Katsurada, Ken 305
Kethara Pasupathy, Trichy M. 301
Kiani, Sepehr. 509
Kim, D. J. 397
Kim, J. Y. 156
Kim, Kyung Jae 449
Kim, Oui-Serg 172
Kim, Seong Kun. 481
Kim, Sun-Min. 485
Kim, Young Guk. 481
Kim, Young-Wook 449
Kimura, Keiichi. 537
Kitajima, Akihisa 477
Kitajima, Takayuki 437, 445
Kiyono, Satoshi 285, 333
Klocke, Fritz. 425
Knapp, Byron R. 58, 461
Knapp, Wolfgang 88
Kong, John 401
Koning, Robert J.. 176
Konkola, Paul T.. . . . . 15, 40, 216
Konno, Jojiro 457
Kosugi, Keiichi. 445
Kourouklis, Christos. 493
Kramar, John A.. . . . . 19, 135
Kremen, Gennady Z. 521
Kudoh, Ryusei. 164
Kumarappa, Shiva. 148
Kumbera, Thimmaiah G. 98
Kuriyagawa, Tsunemoto 433, 441, 525
Kvamme, Todd. 349
Kwon, Ho Nam 127
Kwon, Won Tae 449
Lay, Oliver P. 103
Leary, David. 349
Lee, Byung-Ha. 180
Lee, Hwa-Soo 417
Lee, Il Hwan. 50
Lee, Jong Hyun 127
Lee, Joo-Sang. 433
Lee, Kiha 453, 475
Lee, Sang-Ho 172
Lee, Sang-Wook 172
Lee, Seok Woo 397
Lee, Sun-Kyu. 127, 156, 180, 485
Lee, Young-Kyoon 180
Lehman, John 509
Leifhelm, Burkhard 54
Liebman, Michael K. 131
Lin, Yizhen. 253
Liu, Jiancheng. 144
Liu, Xiangyang. 249
Liu, Xiaojun 377
Lui, Kam-Wa 365
Maeda, Yukio. 497
Mahalik, N. P.. 485
Marsh, Eric R. 58, 461
Martin, Osborne A. 103, 273
Marusich, Troy D.. 98
Matsumiya, Sadayuki 111
Matsumoto, Kiyoshi 36
McGuirk, Michael. 40
McSpadden, Samuel B.. . . . . 401, 429, 501, 521
Medicus, Kate M.. 357
Menske, Eberhard. 23
Miller, Michele H.. . . . . 405, 409, 413
Mishima, Nozomu 184
Mitsui, Kimiyuki 305
Mitsui, Takahiko. 541
Mitsuishi, Mamoru. 196
Miyashita, Masakazu. 152, 421
Miyoshi, Takashi 537
Mizumoto, Hiroshi 119
Mohri, Naotake 164
Mongrard, Oliver 40
Monnelly, Glen. 40
Moon, Jun Hee 188

Mori, Masahiko 144
Mori, Toshimichi 160, 192
Morita, Noboru 192, 457
Moronuki, Nobuyuki 529
Morse, Edward P. 277, 301, 337
Mueller, Ulrich 361
Muralikrishnan, Bala 249, 381
Nagel, D. J. 317
Nakao, Masayuki 36, 457
Nakao, Yohichi 317
Nayfeh, Samir Ali 139
Negishi, Nobuhiko 92
Nikumb, Suwas K. 281
Nishioka, Masahiko 437
Nomura, Takashi 389
O'Connor, Brian P. 461
Ogura, Ichiro 465
Okazaki, Yuichi 192, 465
Okuda, Seiichi 389
Okusa, Takenori 36
Okuyama, Shigeki 437, 445
Onozuka, Hideaki 497
Oosone, Tomoaki 373
Orji, Ndubuisi George 381
Orrego, Roxana M. Martinez 237
Ott, R. 429
Ozono, Shigeo 321
Pahk, Heui Jae 50, 188
Pähler, Dietmar 425
Park, Jun Seok 449
Parker, David H. 86*
Parten, R. 521
Pati, G. S. 15, 40, 216
Patten, John A. 98
Payne, Beverly F. 143*
Pei, Zhi-Jian 393
Penzes, William B. 19
Perkins, Patrick 349
Phillips, Steven D. 82
Polvani, Robert Stephen 48*
Prabhukumar, G. P. 148
Qin, P. 265
Qu, Jun 501
Rachakonda, Prem Kumar 489, 509
Rahim, Abdur 36
Raja, Jayaraman 249, 381, 517
Rao, A. M. 212
Rea, David 82
Rensing, N. M. 317
Rerkkumsup, Pongpun 107
Rhoney, Brian K. 429
Rhorer, Richard L. 143*
Ricker, George R. 40
Robertson, Alec P. 229
Ruiz-Huerta, Leopoldo 513
Sadanand, Bindu 212
Saeki, Masaru 433
Saito, Oshamu 525
Sakamoto, Shigehiko 545
Sakata, Masato 62
Sasajima, Kazuyuki 313
Sato, Tsuyoshi 233
Sawa, Masashi 497
Scattergood, Ronald O. 401, 429, 501
Schalcosky, David 58
Schaller, Thomas 469
Schattenburg, Mark Lee 15, 40, 216
Scheuerman, Vincent P. 19
Schmitz, Tony L. 357
Schneider, Carlos Alberto 353
Schott, Walter 23
Schubert, Klaus 469
Scire, Fredric E. 19
Scott, Mark 349
Senga, Tatsuya 541
Shaklan, Stuart Bruce 103, 349
Shen, Yin-Lin 253, 317
Shibutani, Hideo 437
Shih, Albert J. 401, 429, 501
Shimizu, Yuki 333
Shirosawa, Tatsuya 525
Sklad, Mateusz P. 369
Slocum, Alexander H. 229
Smith, Philip T. 212
Sohn, Alex 28, 66, 92
Song, In-Cheon 180
Spence, Allan D. 369
Spero, Robert 103, 349
Stephenson, David J. 220
Stirn, Boris 475
Stoup, John 82
Stubbs, David 349
Sugimoto, Yoshiaki 160
Suwabe, Hitoshi 477
Suzuki, Hirofumi 437
Syoji, Katsuo 433, 441, 525
Tachibana, Toru 441
Tajima, Takuji 497
Takada, Koji 107
Takagi, Toshio 107
Takahashi, Masaaki 313
Takahashi, Satoru 537
Takamasu, Kiyoshi 321
Takaya, Yasuhiro 537
Takayama, Akinori 529
Takenaka, Ryo 196
Tao, Zhengsu 257
Tashiro, Hatsuzo 389
Teague, E. Clayton 19
Tomita, Yoshiyuki 152

*Extended abstract not available at press time.

Trinkle, Christine A. 212
Trost, Hans-Jochen 533
Trumper, David L. 131
Tse, S. 233
Tsukada, Tadao 265
Tsukahara, Shinichiro 152
Uchiyama, Kenji 529
Uda, Yutaka 541
Uneda, Michio 477
Vallance, Robert Ryan 168, 212, 489, 509
Varanasi, Kripa Kiran 139
Vona, Marsette A. 131
Walter, Mark M. 176
Wang, Ben 505
Wang, Chunhai 261
Wang, Ke 337
Wang, Zhongyu 265
Warisawa, Shin'ichi 196
Watanabe, Kazushi 497
Watanabe, Tomonori 107
Weck, E.h. Manfred 54
Weikert, Sascha 88
Wilhelm, Robert G. 273, 301
Willoughby, Patrick J. 229
Winzenz, Wayne 102*
Wolsing, Eric 168
Wu, Yongbo 441
Xie, T. 341
Yabuya, Makoto 119
Yamada, Tomihiko 285
Yamamoto, Eiichi 541
Yamanaka, Toshio 497
Yamazaki, Kazuo 111, 144, 160, 361
Yanagi, Kazuhisa 373
Yang, L. 341
Yang, Yue 111
Yasui, Heiji 62, 545
Yonushonis, T. M. 429
Yoon, Moon-Chul 481
Yoshikawa, Kazuo 389
Youden, David H. 70
Yui, Akinori 437, 445
Zhang, Chuck 505
Zhang, X. 317
Zhang, Xianping 269
Zhao, Feng 103, 345, 349
Zhao, Xiaoping 213
Ziegert, John C. 82
Zou, Zhihua 277

**Extended abstract not available at press time.*